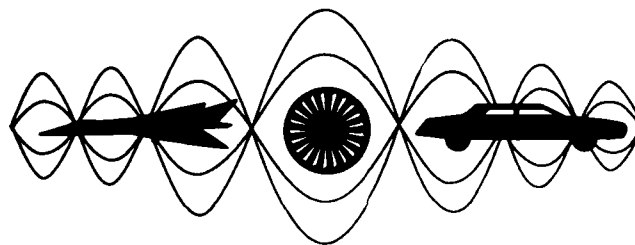AD-A286 730

PROCEEDINGS

SECOND INTERNATIONAL CONGRESS ON RECENT DEVELOPMENTS IN AIR- AND STRUCTURE-BORNE SOUND AND VIBRATION

MARCH 4-6, 1992   AUBURN UNIVERSITY, USA

95-01103

DTIC
ELECTE
S FEB 2 8 1995 D
G

Edited by

Malcolm J. Crocker

P. K. Raju

95 3 31 002

volume 1

PROCEEDINGS

DTIC
ELECTE
FEB 2 8 1995
S
G
D
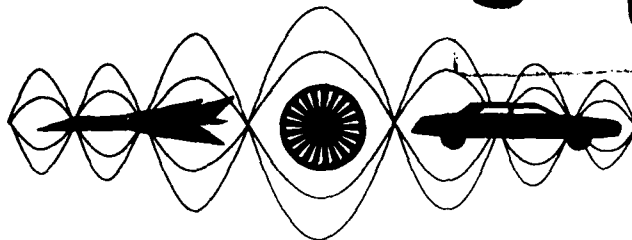
SECOND INTERNATIONAL CONGRESS ON RECENT DEVELOPMENTS IN AIR- AND STRUCTURE-BORNE SOUND AND VIBRATION

MARCH 4-6, 1992   AUBURN UNIVERSITY, USA

ONR

N00014-92-J-1525

Edited by

Malcolm J. Crocker

P. K. Raju

Volume 1

SECOND INTERNATIONAL CONGRESS
ON RECENT DEVELOPMENTS IN
AIR- & STRUCTURE-BORNE
SOUND AND VIBRATION

MARCH 4-6, 1992

Auburn University
USA

Sponsored by **AUBURN UNIVERSITY** in cooperation with
THE INTERNATIONAL COMMISSION ON ACOUSTICS OF IUPAP
and with the following professional societies:

ACOUSTICAL SOCIETY OF AMERICA
ACOUSTICAL SOCIETY OF THE NETHERLANDS
ACOUSTICAL SOCIETY OF THE RUSSIAN FEDERATION
AMERICAN HELICOPTER SOCIETY
AMERICAN SOCIETY OF MECHANICAL ENGINEERS
ASSOCIATION BELGE DES ACOUSTICIENS
ASSOCIAZIONE ITALIANA di ACUSTICA
AUSTRALIAN ACOUSTICAL SOCIETY
THE CANADIAN SOCIETY FOR MECHANICAL ENGINEERING
DEUTSCHE ARBEITSGEMEINSCHAFT FÜR AKUSTIK (DAGA)
INSTITUTE OF ACOUSTICS, UNITED KINGDOM
INSTITUTE OF NOISE CONTROL ENGINEERING/JAPAN
INSTITUTE OF NOISE CONTROL ENGINEERING/USA
INSTITUTION FOR MECHANICAL ENGINEERS, UNITED KINGDOM
THE AMERICAN SOCIETY FOR NONDESTRUCTIVE TESTING, INC.
VEREIN DEUTSCHER INGENIEURE (VDI-EDV), GERMANY
THE SOUTH AFRICAN ACOUSTICS INSTITUTE
SOCIÉTÉ FRANÇAISE D'ACOUSTIQUE
SOVIET ACOUSTICAL ASSOCIATION
ACOUSTICAL COMMISSION OF THE HUNGARIAN
ACADEMY OF SCIENCES

General Chairman—Malcolm J. Crocker, Mechanical Engineering Department
Program Chairman—P. K. Raju, Mechanical Engineering Department

Scientific Committee

Adnan Akay, Wayne State University, Michigan
Michael Bockhoff, Centre Techniques Des Industries Mecaniques, France
Brian L. Clarkson, University College of Swansea, United Kingdom
J. E. Ffowcs-Williams, University of Cambridge, United Kingdom
Robert Hickling, National Center for Physical Acoustics, Mississippi
G. Krishnappa, National Research Council of Canada
Leonid M. Lyamshev, Andreev Acoustics Institute, Moscow
Richard H. Lyon, Massachusetts Institute of Technology, Massachusetts
Gideon Maidanik, David Taylor Research Center, Maryland
M. L. Munjal, Indian Institute of Science, India
Alan Powell, University of Houston, Texas
Clemans A. Powell, NASA Langley Research Center, Virginia
J. N. Reddy, Virginia Polytechnic Institute & State University, Virginia
Herbert Überall, Catholic University of America, D.C.
Eric Ungar, Bolt Beranek and Newman, Massachusetts
V. V. Varadan, Pennsylvania State University, Pennsylvania
R. G. White, Institute of Sound and Vibration Research, United Kingdom

Organizing Committee

John E. Cochran, Auburn University (Aerospace Engineering)
Robert D. Collier, Tufts University (Mechanical Engineering)
Malcolm J. Crocker, Auburn University (Mechanical Engineering)
Malcolm A. Cutchins, Auburn University (Aerospace Engineering)
Ken Hsueh, Ford Motor Co., Allen Park, Michigan
Gopal Mathur, McDonnell Douglas, Long Beach, California
M. G. Prasad, Stevens Institute of Technology (Mechanical Engineering)
P. K. Raju, Auburn University (Mechanical Engineering)
Mohan Rao, Michigan Technological University (Mechanical Engineering)
Uday Shirahatti, Old Dominion University (Mechanical Engineering)

FOREWORD·

This three-volume book of proceedings includes the written versions of the papers presented at the Second International Congress on Recent Developments in Air- and Structure-Borne Sound and Vibration held at Auburn University March 4-6, 1992. The Congress was sponsored by Auburn University in cooperation with the International Commission on Acoustics of IUPAP and the 20 professional societies in 14 countries listed at the beginning of each volume. The support of this Commission and the professional societies has been invaluable in ensuring a truly international congress with participation from 30 countries. This support is gratefully acknowledged. In addition, the organizing committee would like to thank the National Science Foundation, the Office of Naval Research, the Office of Naval Research—Europe, the Alabama Space Grant Consortium, NASA, the College of Engineering and the Department of Mechanical Engineering of Auburn University for financial assistance.

Topics covered in the Proceedings include Sound Intensity, Structural Intensity, Modal Analysis and Synthesis, Statistical Energy Analysis and Energy Methods, Passive and Active Damping, Boundary Element Methods, Diagnostics and Condition Monitoring, Material Characterization and Non-Destructive Evaluation, Active Noise and Vibration Control, Sound Radiation and Scattering, and Finite Element Analysis.

The order in which the 217 papers appear in these volumes is roughly the same as they were presented at the Congress although the order is modified somewhat so they can be grouped in the topics above. There are also six keynote papers, including Professor Sir James Lighthill on Aeroacoustics and Atmospheric Sound, Professor Frank J. Fahy on Engineering Applications of Vibro-Acoustic Reciprocity; Dr. Louis Dragonette on Underwater Acoustic Scattering, Professor Robert E. Green on Overview of Acoustical Technology for Non-Destructive Evaluation, Professor David Brown on Future Trends in Modal Testing Technology and Professor Lothar Gaul on Calculation and Measurement of Structure-borne Sound. The papers in this book cover all major topics of interest to those concerned with engineering acoustics and vibration problems in machines, aircraft, spacecraft, other vehicles and buildings.

In the last 30 years, improvements in computers have allowed rapid developments in both theoretical and experimental analysis of acoustics and vibration problems. In the early 1960s statistical energy analysis (SEA) was first applied to coupled sound and vibration problems. In the early 1970s the finite element method (FEM) was first used in acoustics problems. In recent years considerable progress has been made with the boundary element method (BEM) in which discretization is confined to two-dimensional surfaces instead of three-dimensional fields. Some of these approaches have been combined for instance in SEA-FEM. The 1980s, which have also seen rapid advances in improved measurement techniques, could be called the decade of sound intensity, as it can now be used for rapid measurements of the in-situ sound power of a machine, to rank noise sources and determine transmission loss of structural partitions. Power flow in structures also now can be determined with the use of structural intensity measurements. Sound

and vibration signals are being used increasingly to diagnose the condition of machinery and to detect faults or to determine the properties of materials through non-destructive evaluation. There is also increased knowledge in sound radiation and scattering; in particular advances have occurred in scattering theory and in numerical solution techniques.

The organization and hosting of a conference is a considerable undertaking, and this Congress is no different. We would firstly like to thank all the authors who submitted their contributions promptly making publication of this book before the Congress possible. We would also like to acknowledge the assistance of the scientific committee and organizing committee who helped to completely organize some sessions. The staff of the Mechanical Engineering Department of Auburn University also provided valuable assistance. Our special thanks are extended to Rose-Marie Zuk who worked untiringly and efficiently on all aspects of the Congress program and this book, to Julia Shvetz who provided invaluable expert assistance in all areas of Congress planning in particular with travel arrangements for foreign guests, and to Olga Riabova for her hard work on Congress communications.

Malcolm J. Crocker, General Chairman
P.K. Raju, Program Chairman

TABLE OF CONTENTS

AUTHOR INDEX

KEYNOTE ADDRESSES

PAGE

KEYNOTE ADDRESS

A GENERAL INTRODUCTION TO AEROACOUSTICS
AND ATMOSPHERIC SOUND

Sir James Lighthill

A GENERAL INTRODUCTION TO AEROACOUSTICS AND ATMOSPHERIC SOUND

James Lighthill, Department of Mathematics, University College, London, WC1E 6BT, UK

1. BROAD OVERVIEW

This general introductory paper is devoted to INTERACTIONS OF SOUND WITH AIR, including **transmission through the atmosphere** and

both **generation of sound by** $\Big\}$**airflows**
and **propagation of sound in**

 (e.g. manmade flows — around aircraft or air machinery — or natural winds) as affected by the air's boundaries and atmospheric composition;

with (conversely) **generation of airflows by sound** (acoustic streaming).

From linear acoustics I utilise the properties of the **wave equation,** including

 (i) the the short-wavelength ray-acoustics approximation and

 (ii) the theory of multipole sources — with the long-wavelength compact-source approximation;

while from nonlinear accustics I use

 the physics of waveform shearing and shock formation[1].

Techniques special to Aeroacoustics and Atmospheric Sound are centred on the momentum equation for air. ITS DIFFERENCES FROM A WAVE-EQUATION APPROXIMATION INCLUDE

 A. Linear effects, of gravity acting on air stratified as meteorologists observe; effects which allow independent propagation of "internal" gravity waves and of sound, except at wavelengths of many kilometers when the atmosphere becomes a waveguide for global **propagation of interactive acoustic-gravity waves**[1];

AND (STILL MORE IMPORTANTLY) INCLUDE

 B. Nonlinear effects, of the momentum flux $\rho u_i u_j$; i.e. the flux — rate of transport across unit area — of any ρu_i momentum component by any u_j velocity component. This term, neglected in linear acoustics, acts like a **stress** (i.e. force per unit area — since rate of change of momentum is force). In particular,

 (i) an airflow's momentum flux $\rho u_i u_j$ **generates sound like** a distribution of (time-varying) imposed **stresses; thus not only do**

5

forces between the airflow and its **boundary** radiate sound as distributed **dipoles**, but also such **stresses** (acting on fluid elements with equal and opposite dipole-like forces) radiate as distributed **quadrupoles**[2,3];

(ii) the **mean** momentum flux $\langle \rho u_i u_j \rangle$ in any sound waves propagating through a sheared flow (with shear $\partial V_i / \partial x_j$) is a stress on that flow[1,4], and the consequent **energy exchange** (from sound to flow when positive, vice versa when negative) is

$$\langle \rho u_i u_j \rangle \partial V_i / \partial x_j \; ; \tag{1}$$

(iii) even without any pre-existing flow, energy-flux **attenuation** in a sound wave allows **streaming to be generated by unbalanced stresses** due to a corresponding attenuation in acoustic momentum flux — essentially, then, as acoustic energy flux is dissipated into heat, any associated acoustic momentum flux is transformed into a mean motion.[1,5]

AND ANOTHER (LESS CRUCIAL) MOMENTUM-EQUATION/WAVE-EQUATION DIFFERENCE IS

C. Nonlinear deviation of pressure excess $p-p_o$ from a constant multiple, $c_o^2(\rho-\rho_o)$, of density excess.

(a) For sound generation by airflows, this adds an isotropic term to the **quadrupole strength per unit volume**

$$T_{ij} = \rho u_i u_j + \left[(p-p_o) - c_o^2(p-p_o) \right] \delta_{ij} \; , \tag{2}$$

the last term being considered important mainly for **flows at above-ambient temperatures**;[2,6]

(b) for propagation of sound with energy density E through flows of air with adiabatic index γ, the mean deviation is about $(\frac{1}{2})(\gamma-1)E$, and the total **radiation stress**[7]

$$\langle \rho u_i u_j \rangle + \frac{1}{2}(\gamma-1)E\delta_{ij} \tag{3}$$

adds an isotropic pressure excess to the mean momentum flux (although the energy exchange (1) is unchanged in typical cases with $\partial V_i / \partial x_i$ essentially zero).

[And we may note that the very special case of **sound waves interacting on themselves** (in other words, **nonlinear acoustics**) may be interpreted as a

combined operation of the "self-convection effect" B and the (smaller) "sound-speed deviation" C.]

2. COMPACT SOURCE REGIONS

2.1. Sound generation by low-Mach-number airflows

The main nondimensional parameters governing airflows of characteristic speed U and length-scale L are **Mach number** $M = U/c$ (where, in aeroacoustics, c is taken as the sound speed in the **atmosphere** into which sound radiates) and **Reynolds number** $R = UL/v$ where v = kinematic viscosity. Low-Mach-number airflows are **compact** sources of sound, with frequencies

$$\left.\begin{array}{l}\text{narrow-banded at moderate R}\\\text{broad-banded at high R}\end{array}\right\}\text{INSTABILITIES}\begin{array}{c}\text{WHEN FLOW}\\ \\ \text{LEAD TO}\end{array}\left\{\begin{array}{l}\text{regular flow oscillations;}\\\text{extremely irregular turbulence.}\end{array}\right.$$

Since, in either case, a **typical frequency** ω scales as U/L (Strouhal scaling), the compactness condition $\omega L/c$ small is satisfied if $M = U/c$ is small.[3]

A **solid body** which, because of flow instability, is subjected to a fluctuating aerodynamic force F scaling as $\rho U^2 L^2$ (at frequencies scaling as U/L), radiates as **an acoustic dipole** of strength F, with mean radiated power $<\dot{F}^2>/12\pi\rho c^3$.
This **acoustic power** scales as $\rho U^6 L^2/c^3$ (a **sixth-power** dependence on flow speed). Therefore ACOUSTIC EFFICIENCY, defined as the ratio of acoustic power to a rate of delivery (scaling as $\rho U^3 L^2$) of energy to the flow, SCALES AS $(U/c)^3 = M^3$.

[Exceptions to compactness include bodies of high aspect-ratio; thus, a long wire in a wind (where the scale L determining frequency is its diameter) radiates as a lengthwise **distribution** of dipoles.]

Away from any solid body a compact flow (oscillating or turbulent, with frequencies scaling as U/L) leads to **quadrupole radiation** (see B(i) above) with total quadrupole strength scaling as $\rho U^2 L^3$. Acoustic power then scales as $\rho U^8 L^2/c^5$: an **eighth-power** dependence[2,3] on flow speed. In this case ACOUSTIC EFFICIENCY (see above) SCALES AS $(U/c)^5 = M^5$.

Such quadrupole radiation, though often important, may become **negligible**
NEAR A SOLID BODY when dipole radiation due to fluctuating body force
(with its **sixth-power dependence**) is also present.[8,9]

NEAR NOT NECESSARILY COMPACT BODIES a more refined calculation – using
Green's functions not for free space but for internally bounded space –
leads **in general** to the same conclusion : that quadrupole radiation with
its eighth-power dependence is negligible alongside the sixth-power
dependence of dipole radiation due to fluctuating body forces; **BUT
IMPORTANT EXCEPTIONS** to this rule include SHARP-EDGED BODIES, where
features of the relevant Green's function imply a **fifth-power** dependence
on flow speed of acoustic radiation from turbulence.[10,11,12,13]

2.2. Sound generation by turbulence at not so low Mach number

The **chaotic** character of turbulent flow fields implies that velocity
fluctuations at points P and Q, although they are **well correlated** when P
and Q are very close, become almost **uncorrelated** when P and Q are not
close to one another.

Reminder : statisticians define **correlation coefficient** C for the
velocities u_P and u_Q as $C = \langle v_P \cdot v_Q \rangle / \langle v_P^2 \rangle^{1/2} \langle v_Q^2 \rangle^{1/2}$ in terms of the
deviations, $v_P = u_P - \langle u_P \rangle$ and $v_Q = u_Q - \langle u_Q \rangle$, from their means.
When two uncorrelated quantities are combined, **their mean square
deviations are added up** : $\langle v_P + v_Q \rangle^2 = \langle v_P^2 \rangle + 2 \langle v_P \cdot v_Q \rangle + \langle v_Q^2 \rangle$
$$= \langle v_P^2 \rangle + \langle v_Q^2 \rangle \text{ if } C = 0.$$

Theories of turbulence define a *correlation length* ℓ, with

$$u_P \text{ and } u_Q \begin{Bmatrix} \text{WELL CORRELATED} \\ \text{UNCORRELATED} \end{Bmatrix} C \text{ close to } \begin{Bmatrix} 1 \\ 0 \end{Bmatrix} \text{when PQ is substantially } \begin{Bmatrix} < \ell \\ > \ell \end{Bmatrix}$$

Roughly speaking, **different regions of size** ℓ ("eddies") generate sound
independently, and the mean square radiated noise is the sum of the mean
square outputs from all the regions.[14]

Typical frequencies in the turbulence are of order $\omega = v/\ell$, where v is a
typical root mean square velocity deviation $\langle v^2 \rangle^{1/2}$, so that for each
region THE COMPACTNESS CONDITION $\omega\ell/c$ SMALL IS SATISFIED IF v/c IS
SMALL. Compactness, then, *requires only that a r.m.s. velocity*

deviation v (rather than a characteristic mean velocity U) be small compared with c — which is less of a restriction on M = U/c and can be satisfied at "not so low" Mach number.[6]

3. DOPPLER EFFECT

How is the radiation from such "eddies" modified by the fact that they are being convected at "not so low" Mach number? The expression DOPPLER EFFECT, covering all aspects of how the movement of sources of sound alters their radiation patterns, comprises (i) frequency changes,[1] (ii) volume changes,[2,3] (iii) compactness changes.[6,15]

3.1. Frequency changes

When a source of sound at frequency ω approaches an observer at velocity w, then in a single period $T = 2\pi/\omega$ sound emitted at the beginning travels a distance cT while at the end of the period sound is being emitted from a source that is closer by a distance wT. The wavelength λ (distance between crests) is reduced to

$$\lambda = cT - wT = 2\pi(c - w)/\omega \tag{4}$$

and the frequency heard by the observer (2π divided by the time λ/c between arrival of crests) is increased to the Doppler-shifted value[1]

$$\omega_r = \frac{\omega}{1 - (w/c)} : \text{ the relative frequency} \tag{5}$$

that results from relative motion between source and observer.

For an observer located on a line making an angle θ with a source's direction of motion at speed V, the source's velocity of approach towards the observer is $w = V\cos\theta$ and the relative frequency becomes

$$\omega_r = \frac{\omega}{1 - (V/c)\cos\theta} : \begin{Bmatrix} \text{augmented} \\ \text{diminished} \end{Bmatrix} \text{ when } \theta \text{ is an } \begin{Bmatrix} \text{acute} \\ \text{obtuse} \end{Bmatrix} \text{ angle.} \tag{6}$$

Such Doppler shifts in frequency are familiar everyday experiences.

3.2. Volume changes

When an observer is approached at velocity w by a source whose dimension (in the direction of the observer) is ℓ, sounds arriving simultaneously

9

from the source's $\begin{Bmatrix} \text{far} \\ \text{near} \end{Bmatrix}$ sides have been emitted $\begin{Bmatrix} \text{earlier} \\ \text{later} \end{Bmatrix}$ by a time τ (say). In the time t for sound from the far side to reach the observer, after travelling a distance ct, the relative distance of the near side in the direction of the observer was increased from ℓ to $\ell + w\tau$ before it emitted sound which then travelled a distance $c(t - \tau)$. Both sounds arrive simultaneously if

$$ct = \ell + w\tau + c(t - \tau), \text{ giving } \tau = \frac{\ell}{c-w} \text{ and } \ell + w\tau = \frac{\ell}{1-(w/c)} = \ell\omega_r/\omega. \quad (7)$$

The source's effective volume during emission is increased, then, by the Doppler factor ω_r/ω (since dimension in the direction of the observer is so increased whilst other dimensions are unaltered).[2,3]

If turbulent "eddies" are effectively being convected, relative to the air into which they are radiating, at velocity V, then equation (6) gives, for radiation at angle θ, the Doppler factor ω_r/ω which modifies both the frequencies at which they radiate and the effective volume occupied by a radiating eddy.

But equation (2) specifies the quadrupole strength T_{ij} per unit volume for such an eddy. Without convection the pattern of acoustic intensity around a compact eddy of volume ℓ^3 and quadrupole strength $\ell^3 T_{ij}$ would be

$$<(\ell^3 \ddot{T}_{ij} x_i x_j r^{-2})^2>/16\pi^2 r^2 \rho_o c^5 ; \quad (8)$$

and, since different eddies of volume ℓ^3 radiate independently, we can simply add up mean squares in the corresponding expressions for their far-field intensities. This gives

$$\ell^3 <(\ddot{T}_{ij} x_i x_j r^{-2})^2>/16\pi^2 r^2 \rho_o c^5 \quad (9)$$

as the intensity pattern radiated by unit volume of turbulence. THE DOPPLER EFFECT MODIFIES THIS, when the compactness condition is satisfied, BY FIVE FACTORS ω_r/ω (one for the change in source volume ℓ^3 and four for the frequency change as it affects the mean square of a multiple of the second time-derivative of T_{ij}) AND THIS INTENSITY MODIFICATION BY A FACTOR

$$[1 - (V/c)\cos\theta]^{-5} \quad (10)$$

brings about an important preference for forward emission.[15]

3.3. Compactness changes

As (V/c) increases, however, the Doppler effect tends to degrade the **compactness** of aeroacoustic sources in relation to forward emission. Not only does $\omega \ell/c$ increase in proportion to Mach number, but **an even greater value is taken by** $\omega_r \ell/c$, the ratio which must be small if convected sources are to be compact. A restriction on the extent (10) of intensity enhancement for forward emission as V/c increases is placed by these tendencies.[6,15,16]

They **can** develop, indeed, to a point where the compact-source approximation may appropriately be replaced by its opposite extreme: THE RAY-ACOUSTICS APPROXIMATION[1]. Thus, for **supersonic source convection** (V/c>1), the relative frequency (6) becomes infinite in

$$\text{the Mach direction } \theta = \cos^{-1}(c/V), \tag{11}$$

and radiation from the source proceeds **along rays emitted at this angle.**[17]

Explanatory note: the source's velocity of approach w towards an observer positioned at an angle (11) to its direction of motion is the sound speed c; thus, not only is the generated wavelength (4) reduced indefinitely (the ray-acoustics limit) but, essentially, different parts of a signal are observed **simultaneously:** the condition of **stationary phase** satisfied on rays[1].

Further note: the influences placing a limit on the signal propagated along rays may include **the duration δ of well-correlated emission** from turbulent "eddies"; and, also, may include nonlinear effects (see §4.2. **Supersonic Booms**).

3.4. Uniformly valid Doppler-effect approximations

Just as a **correlation length** ℓ for turbulence was specified in §2.2, so a **correlation duration** δ can be characterized by the requirement that moving eddies have
$$\left\{ \begin{matrix} \text{WELL CORRELATED} \\ \text{UNCORRELATED} \end{matrix} \right\} \text{ velocities at times differing by substantially } \left\{ \begin{matrix} <\delta \\ >\delta \end{matrix} \right\}.$$
Combined use of correlation length ℓ and duration δ affords an approximation to the radiation pattern from convected "eddies" that has

some value at all Mach numbers, spanning the areas of applicability of the compact-source and ray-acoustics approximations.

Figure 1 uses space-time diagrams where the space-coordinate (abscissa) is DISTANCE IN THE DIRECTION OF THE OBSERVER. Diagram (a) for unconvected "eddies" approximates the region of good correlation as AN ELLIPSE WITH AXES ℓ (in the space direction) AND δ (in the time direction). Diagram (b) shows such a region for convected "eddies" whose velocity of approach towards the observer is w; thus, it is Diagram (a) sheared by distance w per unit time.

Signals from far points F and near points N, in either case, reach the observer simultaneously -- as do signals from other points on the line FN -- if this line slopes by distance c (the sound speed) per unit time.

COMPACT-SOURCE CASE (i) WITH w/c SMALL : the space component of FN in Diagram (b) is $\ell[1-(w/c)]^{-1}$, just as in equation (7) for normal Doppler effect (neglecting finite δ).

RAY-ACOUSTICS CASE (ii) WITH w/c = 1 : the space component of FN is $c\delta$.

INTERMEDIATE CASE (iii) WITH w/c "MODERATELY" <1 : the space component of FN is ℓ multiplied by an enhancement factor

$$[(1-w/c)^2 + (\ell/c\delta)^2]^{-1/2} \tag{12}$$

which represents the effective augmentation of source volume due to convection.[15]

This enhancement factor (12) is applied not only to the volume term ℓ^3 in the quadrupole field (9) but also twice to each of the pair of twice-differentiated terms inside the mean square; essentially, because time-differentiations in quadrupole fields arise[1] from differences in the time of emission by different parts of the quadrupole source region (and the time component of FN in Diagram (b) is simply the space component divided by c). As before, then, five separate factors (12) enhance the intensity field; and, with w replaced by $V\cos\theta$, expression (10) for the overall intensity modification factor is replaced by

$$\{[1-(V/c)\cos\theta]^2 + (\ell/c\delta)^2\}^{-5/2} \tag{13}$$

This modification factor (13) affords us an improved description of the influence of Doppler effect not only on the preference for forward emission but also on the overall acoustic power output from convected

12

turbulence.[6,15] For example, Diagram (c) gives (plain line) a log-log plot of the average (spherical mean) of (13) as a function of V/c on the reasonable assumption that ℓ = 0.6Vδ. As V/c increases this average modification factor rises a little at first, but falls drastically like $5(V/c)^{-5}$ for V/c significantly >1.

Now low-Mach-number turbulence away from solid boundaries (§2.1) should radiate sound with an ACOUSTIC EFFICIENCY SCALING AS $(U/c)^5$ where U is a characteristic velocity in the flow. With V taken as that characteristic velocity (although IN A JET a typical velocity V of eddy convection would be between 0.5 and 0.6 times the jet exit speed), the modification of (say) an acoustic efficiency of $10^{-3}(V/c)^5$ for low Mach number by the average modification factor would cause acoustic efficiency to follow the broken-line curve in Diagram (c), tending asymptotically to A CONSTANT VALUE, 0.005, (aeroacoustic saturation) AT HIGH MACH NUMBER. Such a tendency is often observed for sound radiation from "properly expanded" supersonic jets (see below).

4. INTRODUCTION TO AIRCRAFT NOISE

4.1. Aero-engine and airframe noise

How are aeroacoustic principles applied to practical problems — such as those of studying aircraft noise with a view to its reduction?[18,19,20]

In any analysis of the generation of sound by airflows, we may need first of all to ask whether the geometry of the problem has features that tend to promote resonance. For example, a long wire in a wind (§2.1) generates most sound when vortex-shedding frequencies $\left\{ \begin{array}{l} \text{are fairly close to} \\ \text{and so can "lock on" to} \end{array} \right\}$ the wire's lowest natural frequency of vibration; giving good correlation of sideforces, and so also of dipole strengths, all along the wire.

Again, a jet emerging from a thin slit may interact with a downstream edge (parallel to the slit) in a resonant way;[21,22] with very small directional disturbances at the jet orifice being amplified by flow instability as they move downstream to the edge, where they produce angle-of-attack variations. Dipole fields associated with the resulting sideforces can at particular frequencies renew the directional disturbances at the orifice with the right phase to produce a resonant oscillation. Some musical wind

13

instruments utilize such **jet-edge resonances**, reinforced by coincidence with standing-wave resonances in an adjacent pipe.

But in the absence of such resonances (leading to enhanced acoustic generation at fairly well defined frequencies) AIRFLOWS TEND TO GENERATE ACOUSTIC "NOISE" whose reaction on the flow instability phenomena themselves is negligible.

Resonances analogous to the above which need to be avoided in aircraft design include, for example,

> (a) PANEL FLUTTER, generated at a characteristic frequency as an unstable vibration of a structural panel in the presence of an adjacent airflow;[23]

> (b) SCREECHING OF SUPERSONIC JETS from nozzles which, instead of being "properly expanded" so that an essentially parallel jet emerges, produce a jet in an initially non-parallel form followed by **shock waves** in the well known recurrent "diamond" **shock-cell pattern**; the first of these, replacing the edge in the above description, can through a similar **feedback of disturbances to the jet orifice** generate a powerful resonant oscillation.[22,24,25]

And undesirable resonances may also be associated with aeroengine combustion processes.[26] But we turn now to the **aircraft noise of a broad-banded character** that remains even when resonances have been avoided.

Then AERO-ENGINE JET NOISE PROPER[6] (that is, the part unrelated to any interaction of jet turbulence with solid boundaries) tends to **follow a broad trend** similar to that in Figure 1; where, however, because the eddy convection velocity V is between 0.5 and 0.6 times the jet exit speed U, the acoustic efficiency makes **a transition between a value of around** $10^{-4}M^5$ in order-of-magnitude terms for subsonic values of $M = U/c$ and an **asymptotically constant value of** 10^{-2} or a little less for M exceeding about 2.

The above tendency for M<1 implies that **noise emission from jet engines may be greatly diminished** if a given engine power can be achieved with a substantially LOWER JET EXIT SPEED, requiring of course a correspondingly larger jet diameter, L. Furthermore, with acoustic power output scaling as $\rho U^8 L^2/c^5$ (§2.1) **and jet thrust as** $\rho U^2 L^2$, NOISE EMISSION FOR GIVEN THRUST can be greatly reduced if U can be decreased and L increased by comparable factors.

Trends (along these lines) in aero-engine design towards large turbofan engines with higher and higher bypass ratios, generating very wide jets at relatively modest mean Mach numbers, have massively contributed to jet noise suppression (whilst also winning advantages of reduced fuel consumption). On the other hand, such successes in suppressing jet noise proper (originally, the main component of noise from jet aircraft) led to needs for a dedicated focusing of attention upon parallel reductions of other aircraft-noise sources:[27]

(a) those associated with the interaction of jet turbulence with solid boundaries – where sharp-edged boundaries (§2.1) pose a particular threat;

(b) fan noise emerging from the front of the engine and turbine noise from the rear;

(c) airframe noise including acoustic radiation from boundary-layer turbulence and from interaction of that turbulence with aerodynamic surfaces for control purposes or lift enhancement.

Some key areas of modern research on aero-engine and airframe noise are:

FOR JET NOISE, techniques for relating acoustic output to vorticity distributions,[28,29] and to any coherent structures[30,31], in jet turbulence; and for taking into account (cf §5.4) propagation through the sheared flow in a wide jet;[32,33]

FOR NOISE FROM FANS AND PROPELLERS, mathematically sophisticated ways of reliably estimating the extent of cancellation of dipole radiation from different parts of a rotating-blade system (alongside a good independent estimate of quadrupole radiation);[34]

FOR AIRFRAME NOISE, a recognition[35,36] that massive cancellations act to minimise noise radiation from boundary-layer turbulence on a flat surface of uniform compliance – and, therefore, that avoidance of sharp nonuniformities in airframe skin compliance may promote noise reduction.

4.2. Supersonic booms

In addition to aero-engine and airframe noise, any aircraft flying at a supersonic speed V emits a concentrated "boom"-like noise along rays in the Mach direction (11). I sketch the theory of supersonic booms with the atmosphere approximated as isothermal (so that the undisturbed sound speed takes a constant value c even though the undisturbed density ρ varies with altitude): a case permitting quite a simple extension of the nonlinear analysis of waveform shearing and shock formation.[1,37] Then the rays

continue as straight lines at the Mach angle for reasons summarized in the explanatory note below expression (11). (Actually, the slight refraction of rays by temperature stratification in the atmosphere, when taken into account in a generalized version of the theory, produces only somewhat minor modifications of the results.)

As such straight rays stretch out from a straight flight path along CONES with semi-angle (11), any narrow tube of rays has its cross-sectional area A increasing in proportion to distance r along the tube.[1,38] On linear theory[1], acoustic energy flux $u^2\rho cA$ is propagated unchanged along such a ray tube (so that $u(\rho r)^{1/2}$ is unchanged) where u is air velocity along it. On nonlinear theory, $u(\rho r)^{1/2}$ is propagated unchanged but at a signal speed altered to

$$c + \frac{\gamma + 1}{2} u \qquad (14)$$

by self-convection and excess-wavespeed effects.

This property can be described[1] by an equation

$$\left[\left\{\frac{1}{c} - \frac{\gamma + 1}{2} \frac{u}{c^2}\right\} \frac{\partial}{\partial t} + \frac{\partial}{\partial r}\right] u(\rho r)^{1/2} = 0 \qquad (15)$$

where the quantity in braces is the altered value of the reciprocal of the signal speed (14). Now a simple transformation of variables

$$x_1 = r - ct, \qquad t_1 = \int_0^r (\rho r)^{-1/2} dr, \qquad u_1 = \frac{\gamma + 1}{2} \frac{u}{c} (\rho r)^{1/2} \qquad (16)$$

is found to convert equation (15) into the familiar form

$$\frac{\partial u_1}{\partial t_1} + u_1 \frac{\partial u_1}{\partial x_1} = 0 \qquad (17)$$

which describes the waveform shearing at a uniform rate that is associated with shock formation and propagation in nonlinear plane-wave acoustics.

From amongst this equation's PHYSICALLY RELEVANT solutions – namely, those with area-conserving discontinuities (representing shocks) – the famous N-WAVE solution is the one produced by an initial signal (such as an aircraft's passage through the air) that is first compressive and then expansive. The rules[1] governing N-wave solutions of equation (17) are that

16

the discontinuity Δu_1 at each shock falls off like $t_1^{-1/2}$ while the space (change Δx_1 in x_1) between shocks increases like $t_1^{1/2}$. These rules for the transformed variables (16) have the following consequences for the true physical variables: at a large distance r from the flight path THE VELOCITY CHANGE Δu AT EACH SHOCK AND THE TIME INTERVAL Δt BETWEEN THE TWO SHOCKS VARY AS

$$\Delta u \approx \left[(\rho r) \int_0^r (\rho r)^{-1/2} dr \right]^{-1/2} \text{ AND } \Delta t \approx \left[\int_0^r (\rho r)^{-1/2} dr \right]^{1/2}. \tag{18}$$

On **horizontal rays** (at the level where the aircraft is flying), ρ is independent of r and the equations (18) take the greatly SIMPLIFIED FORM

$$\Delta u \approx r^{-3/4} \quad \text{AND} \quad \Delta t \approx r^{1/4} \tag{19}$$

APPROPRIATE TO CONICAL N-WAVES IN A HOMOGENEOUS ATMOSPHERE. Actually, the rules (19) apply also to the **propagation of cylindrical blast waves generated by an exploding wire**; since, here also, ray tube areas increase in proportion to r.

On **downward pointing** rays in an isothermal atmosphere ρ **increases exponentially** in such a way that the time interval Δt between shocks approaches the constant value obtained in (18) by making the integral's upper limit infinite.[1,38] On the other hand **the shock strength** (proportional to the velocity change Δu) includes the factor $(\rho r)^{-1/2}$ where the large increase in ρ from the flight path to the ground (as well as in r) enormously **attenuates the supersonic boom.** BELOW CONCORDE cruising at Mach 2, for example, an observer on the ground hears two clear shocks with an interval of around 0.5s between them, and yet with strengths $\Delta p/p$ only **about 0.001.**

5. PROPAGATION OF SOUND THROUGH STEADY MEAN FLOWS

5.1. Adaptations of ray acoustics

Useful information on sound propagation through steady mean flows[39,4] can be obtained by adaptations of the ray-acoustics approximation. I sketch these here before, first, applying them (in §5.3 below) to propagation through sheared stratified winds and, secondly, giving indications of how

effects of such **parallel mean flows** are modified at wavelengths too large for the applicability of ray acoustics.

Sound propagation through a steady airflow represents **an autonomous mechanical system**: one governed by laws that do not change with time. Then small disturbances can be Fourier-analysed in the knowledge that propagation of signals with different frequencies ω must proceed **without exchange of energy between them**.

Such disturbances of frequency ω involve pressure changes in the form $P\cos\alpha$ where P varies with position and **the phase α is a function of position and time** satisfying

$$\frac{\partial\alpha}{\partial t} = \omega : \text{THE FREQUENCY; AND} - \frac{\partial\alpha}{\partial x_i} = k_i : \text{THE WAVENUMBER,} \qquad (20)$$

A VECTOR with its direction normal to crests and its magnitude 2π divided by a local wavelength.

In ray theory for any wave system,[1,4] we assume that the wavelength is small enough (compared with distances over which the medium — and its motion, if any — change significantly) for a well defined relationship

$$\omega = \Omega(k_i, x_i) \qquad (21)$$

to link frequency with wavenumber at each position. Equations (20) and (21) require that

$$-\frac{\partial k_j}{\partial t} = \frac{\partial^2\alpha}{\partial x_j\partial t} = \frac{\partial\omega}{\partial x_j} = \frac{\partial\Omega}{\partial k_i}\left(-\frac{\partial^2\alpha}{\partial x_i\partial x_j}\right) + \frac{\partial\Omega}{\partial x_j} = \frac{\partial\Omega}{\partial k_i}\frac{\partial k_j}{\partial x_i} + \frac{\partial\Omega}{\partial x_j}, \qquad (22)$$

yielding the basic law (in Hamiltonian form) **for any wave system**:

$$\text{ON RAYS SATISFYING } \frac{dx_i}{dt} = \frac{\partial\Omega}{\partial k_i} \text{ WAVENUMBERS VARY AS } \frac{dk_j}{dt} = -\frac{\partial\Omega}{\partial x_j} ; \qquad (23)$$

equations easy to solve numerically for given initial position and wavenumber. However, the variations (23) of wavenumber ("refraction") produce no change of frequency along rays:

$$\frac{d\omega}{dt} = \frac{\partial\Omega}{\partial k_i}\frac{dk_i}{dt} + \frac{\partial\Omega}{\partial x_i}\frac{dx_i}{dt} = \frac{\partial\Omega}{\partial k_i}\left(-\frac{\partial\Omega}{\partial x_i}\right) + \frac{\partial\Omega}{\partial x_i}\frac{\partial\Omega}{\partial k_i} = 0, \tag{24}$$

so that rays are paths of propagation of the excess energy, at each frequency, associated with the waves' presence.

For sound waves we write k as the magnitude of the wavenumber vector, expecting that at any point the value of the relative frequency in a frame of reference moving at the local steady flow velocity u_{fi} will be $c_f k$ (the local sound speed times k); this implies[1,4] that

$$\omega_r = \frac{\partial\alpha}{\partial t} + u_{fi}\frac{\partial\alpha}{\partial x_i} = \omega - u_{fi}k_i, \text{ GIVING } \omega = \omega_r + u_{fi}k_i = c_f k + u_{fi}k_i \tag{25}$$

AS THE ACOUSTIC FORM OF THE RELATIONSHIP (21).

[Note: this rule (25) for relative frequency agrees with the Doppler rule (6), since the velocity of a source of frequency ω relative to stationary fluid into which it radiates is minus the velocity of the fluid relative to a frame in which the acoustic frequency is ω.]

Use of this form (25) of the relationship (21) in the basic law (23) tells us that

$$\frac{dk_j}{dt} = -k\frac{\partial c_f}{\partial x_j} - k_i\frac{\partial u_{fi}}{\partial x_j} \text{ ON RAYS WITH } \frac{dx_i}{dt} = c_f\frac{k_i}{k} + u_{fi}; \tag{26}$$

where the last terms in these equations represent adaptations of ray acoustics associated with the mean flow. For example, the velocity of propagation along rays is the vector sum of the mean flow velocity u_{fi} with a wave velocity of magnitude c_f and direction normal to crests.

5.2. Energy exchange between sound waves and mean flow

The excess energy (say, E per unit volume) associated with the presence of sound waves is propagated along such rays; in particular, if attenuation of sound energy is negligible, then

FLUX OF EXCESS ENERGY ALONG A RAY TUBE = CONSTANT. (27)

Note: this excess energy density E is by no means identical with the sound waves' energy density

$$E_r = \langle \tfrac{1}{2}\rho_f u_{sl} u_{sl} \rangle + \langle \tfrac{1}{2}c_f^2 \rho_f^{-1} \rho_s^2 \rangle = c_f^2 \rho_f^{-1} \langle \rho_s^2 \rangle \qquad (28)$$

(where the subscript s identifies changes due to the sound waves and the equality of the kinetic and potential energies makes E_r simply twice the latter) in a frame of reference moving at the local flow velocity (compare the definition (25) of ω_r). The kinetic-energy part of the excess energy density E is

$$\langle \tfrac{1}{2}(\rho_f + \rho_s)(u_{fl} + u_{sl})^2 \rangle - \tfrac{1}{2}\rho_f u_{fl} u_{fl}, \qquad (29)$$

which includes an extra term

$$\langle \rho_s u_{fl} u_{sl} \rangle = \langle \rho_s u_{fl} \frac{c_f}{\rho_f} \rho_s \frac{k_1}{k} \rangle = E_r \frac{u_{fl} k_1}{c_f k} = E_r\left(\frac{\omega}{\omega_r} - 1\right); \qquad (30)$$

and E is the sum of expressions (28) and (30), giving

$$E = E_r \frac{\omega}{\omega_r}; \quad \text{or, equivalently, either } E_r = E\frac{\omega_r}{\omega} \text{ or } \frac{E_r}{\omega_r} = \frac{E}{\omega}. \qquad (31)$$

THE QUANTITY E/ω, CALLED ACTION DENSITY IN HAMILTONIAN MECHANICS, is identical in both frames of reference, and equations (24) and (27) tell us that its flux along a ray tube is constant.[1,4]

But equation (31) shows too that **energy is exchanged between** (i) the acoustic motions relative to the mean flow and (ii) the mean flow itself. For example, where sound waves of frequency ω enter a region of opposing flow (or leave a region where the mean flow is along their direction of propagation) the ratio ω_r/ω increases AND SO THEREFORE DOES E_r/E: the sound waves gain energy at the expense of the mean flow.

The rate of exchange of energy takes the value (1) written down in §1. This is readily seen from the laws governing motion in an accelerating frame of reference, which feels

an inertial force = - (mass) × (acceleration of frame). (32)

If we use at each point of space a local frame of reference moving with velocity u_{fl} then fluid in that frame has velocity u_{sl} BUT IS SUBJECT TO AN ADDITIONAL FORCE (32); where, per unit volume, mass is ρ_f and the frame's acceleration is

$$u_{sj} \frac{\partial u_{f1}}{\partial x_j} \text{ GIVING FORCE} - \rho_f u_{sj} \frac{\partial u_{f1}}{\partial x_j} \text{ DOING WORK} - \rho_f \langle u_{s1} u_{sj} \rangle \frac{\partial u_{f1}}{\partial x_j} \quad (33)$$

per unit time on the local relative motions. This rate of energy exchange (33) proves to be consistent with the fact that it is the flux, not of E_r but of action E_r/ω_r, that is conserved along ray tubes.

Energy can be extracted from a mean flow, then, not only by turbulence but also by sound waves; and, in both cases, the rate of extraction takes the same form (33) in terms of perturbation velocities u_{s1}. It represents the effect (§1) of the

$$\text{MEAN MOMENTUM FLUX } \rho_f \langle u_{s1} u_{sj} \rangle \quad (34)$$

or Reynolds stress[40] with which either the sound waves or the turbulent motions act upon the mean flow. For sound waves, by equation (28) for E_r and by the substitution

$$u_{s1} = \frac{c_f}{\rho_f} \rho_s \frac{k_1}{k} \, , \text{ MEAN MOMENTUM FLUX} = E_r \frac{k_1 k_j}{k^2} \, ; \quad (35)$$

so that the Reynolds stress is a uniaxial stress in the direction of the wavenumber vector having magnitude E_r.

[Note : strictly speaking, the complete

$$\text{RADIATION STRESS } E_r \left(\frac{k_1 k_j}{k^2} + \frac{\gamma - 1}{2} \delta_{1j} \right) \text{ FOR SOUND WAVES} \quad (36)$$

includes not only the momentum flux (35) but also the waves' mean pressure excess

$$\frac{1}{2} \left(\frac{\partial^2 p}{\partial \rho^2} \right)_{\rho = \rho_f} \langle \rho_s^2 \rangle = \frac{\gamma - 1}{2} \frac{c_f^2}{\rho_f} \langle \rho_s^2 \rangle = \frac{\gamma - 1}{2} E_r \quad (37)$$

acting equally in all directions;[7] however (§1) this isotropic component produces no energy exchange with solenoidal mean flows.]

5.3. Propagation through sheared stratified winds

The extremely general ray-acoustics treatment outlined above for sound propagation through fluids in motion has far-reaching applications (in environmental and, also, in engineering acoustics) which, however, are illustrated below only by cases of propagation through **parallel flows, with stratification** of velocity as well as of temperature.[1,4] The x_1-direction is taken as that of the mean flow velocity $V(x_3)$ which, together with the sound speed $c(x_3)$, **depends only on the coordinate** x_3. Thus, V replaces u_{f1} in the general theory while c replaces c_f (and, for atmospheric propagation, x_3 is altitude). [Note : the analysis sketched here is readily extended to cases of **winds veering with altitude,** where u_{f2} as well as u_{f1} is nonzero.]

Either the basic law (23) or its ray-acoustics form (26) provides, in general, "refraction" information in the form of **THREE equations** for change of wavenumber; while the single, far simpler, equation (24) is a consequence of, but is by no means equivalent to, those three. By contrast, in the particular case when u_{f1} and c_f are independent of x_1 and x_2, equations (24) and, additionally, (26) in the **cases j = 1 and 2 give THREE simple results,**

$$\omega = \text{constant}, \ k_1 = \text{constant and } k_2 = \text{constant along rays}, \tag{38}$$

that may be shown fully equivalent to the basic law.

If now we write the wavenumber (a vector normal to crests) as

$$(k_1, \ k_2, \ k_3) = (\kappa \cos \psi, \ \kappa \sin \psi, \ \kappa \cot \theta), \tag{39}$$

so that κ is its **constant** horizontal resultant, ψ its **constant** azimuthal angle to the wind direction, and θ its **variable** angle to the vertical, and use equation (25) in the form

$$\omega = c(x_3)k + V(x_3)k_1 = c(x_3)\kappa \ \text{cosec}\theta + V(x_3)\kappa \cos \psi, \tag{40}$$

we obtain the important

$$\text{EXTENSION } \sin \theta = \frac{c(x_3)}{\omega \kappa^{-1} - V(x_3)\cos \psi} \text{ TO SNELL'S LAW} \tag{41}$$

from the classical case (V = 0) when the denominator is a constant. This extended law (41) tells us how θ varies with x_3 along any ray — whose path we can then trace, using equations (26) in the form

$$\frac{dx_1}{dt} = c(x_3)\cos \psi \sin \theta + V(x_3), \quad \frac{dx_2}{dt} = c(x_3)\sin \psi \sin \theta, \quad \frac{dx_3}{dt} = c(x_3)\cos \theta, \tag{42}$$

by simply integrating dx_1/dx_3 and dx_2/dx_3 with respect to x_3.

It follows that a ray tube covers the same horizontal area at each altitude, so that conservation of the flux of wave action E_r/ω_r along it implies that the vertical component

$$(E_r/\omega_r)(dx_3/dt) = E_r \, \kappa^{-1} \sin \theta \cos \theta \tag{43}$$

of wave action flux is constant along rays; from which, with equation (28), sound amplitudes are readily derived.

Wind shear is able to reproduce all the main types of ray bending[1] associated with temperature stratification, and often to an enhanced extent. Roughly, the downward curvature of near-horizontal rays in $(km)^{-1}$ comes to

$$3 \left\{ V'(x_3) \cos \psi + c'(x_3) \right\} \tag{44}$$

where the velocity gradients are in s^{-1} and the factor $3(km)^{-1}s$ outside the braces is an approximate reciprocal of the sound speed.[1,4]

Cases when (44) is negative: curvature is UPWARD; its magnitude with zero wind is at most 0.018 $(km)^{-1}$ (because temperature lapse rate in stable atmospheres cannot exceed $10°C$ per km, giving $c' = 0.006s^{-1}$) but with strong wind shear can take much bigger values for upwind propagation ($\psi = \pi$). In either case Figure 2(a) shows how the lowest ray emitted by a source "lifts off" from the ground, leaving below it a ZONE OF SILENCE (on ray theory — actually, a zone where amplitudes decrease exponentially with distance below that ray).

Cases when (44) is positive: curvature is DOWNWARD, as found with zero wind

in temperature-inversion conditions (e.g. over a calm cold lake) and even more with strong wind shear for downwind propagation ($\psi = 0$). Figure 2(b) shows how this leads to signal enhancement through multiple-path communication.

In summary, then, the very familiar augmentation of sound levels downwind, and diminution upwind, of a source are effects of the wind's shear (increase with altitude).

5.4. Wider aspects of parallel-flow acoustics

The propagation of sound through parallel flows at wavelengths too great for the applicability of ray acoustics can be analysed by a second-order ordinary differential equation. Thus, a typical Fourier component of the sound pressure field takes the form

$$p_s(x_3)e^{i(\omega t - k_1 x_1 - k_2 x_2)} \text{ with } \rho\frac{d}{dx_3}\left[\frac{1}{\rho(\omega-Vk_1)^2}\frac{dp_s}{dx_3}\right] + \left[\frac{1}{c^2} - \frac{k_1^2 + k_2^2}{(\omega-Vk_1)^2}\right]p_s = 0. \quad (45)$$

Equation (45) can be used to improve on ray acoustics

(a) near caustics (envelopes of rays) where it allows a uniformly valid representation of amplitude in terms of the famous Airy function, giving "beats" between superimposed waves on one side of the caustic and exponential decay on the other;[1]

(b) at larger wavelengths by abandoning ray theory altogether in favour of extensive numerical solutions of equation (45); and

(c) to obtain waveguide modes for sound propagation in a two-dimensional duct (between parallel planes).[41,42,43]

On the other hand, in the case of a three-dimensional duct carrying parallel flow $V(x_2,x_3)$ in the x_1-direction, equation (45) is converted into a partial differential equation (the first term being supplemented by another with d/dx_2 replacing d/dx_3, while k_2 is deleted) which is used

(d) to obtain waveguide modes in such ducts;

(e) in calculations of propagation of sound through the wide jets — modelled as parallel flows — typical (§4.1) of modern aero-engines; and,

(f) with aeroacoustic source terms included, in certain enterprising attempts at modelling jet noise generation and emission.[32,33]

6. ACOUSTIC STREAMING

6.1. Streaming as a result of acoustic attenuation

Sound waves act on the air with a Reynolds stress (34) **even when mean flow is absent** (so that subscript f becomes subscript zero). The j-component of force acting on unit volume of air is then

$$F_j = -\frac{\partial}{\partial x_i} \langle \rho_o u_{si} u_{sj} \rangle :$$

$$(46)$$

the force generating acoustic streaming.[5]

However the force (46) COULD NOT PRODUCE STREAMING FOR UNATTENUATED SOUND WAVES; indeed, their linearised equations can be used to show that

$$\text{IF } p^M = \langle \tfrac{1}{2} c_o^2 \rho_o^{-1} \rho_s^2 - \tfrac{1}{2} \rho_o u_{si} u_{si} \rangle \quad \text{THEN } F_j - \frac{\partial p^M}{\partial x_j} = \langle \frac{\partial}{\partial t}(\rho_s u_{sj}) \rangle$$

$$(47)$$

WHICH IS NECESSARILY ZERO (as the **mean value of the rate of change** of a bounded quantity). Accordingly, the fluid must remain at rest, responding merely by setting up the distribution p^M of mean pressure whose gradient can balance the force. [Note : actually, on the ray-acoustic approximation (28), p^M is itself zero, but the above argument **does not need to use this approximation.**]

ATTENUATION OF SOUND WAVES takes place

(a) **in the bulk of the fluid** through the action of viscosity, thermal conductivity and lags in attaining thermodynamic equilibrium (Ch. 6); and

(b) **near solid walls** by viscous attenuation in Stokes boundary layers

All these effects produce forces (46) which act to generate acoustic streaming. It is important to note, furthermore, that **even the forces due solely to viscous attenuation** – being opposed just by the fluid's own viscous resistance – generate mean motions which **do not disappear as the** viscosity μ tends to zero.[44,45,46,47]

6.2. Jets generated by attenuated acoustic beams

Attenuation of type (a) produces a streaming motion u_{fi} satisfying

$$\rho u_{fi} \partial u_{fj} / \partial x_i = F_j - \partial p / \partial x_j + \mu \nabla^2 u_{fj} \, . \tag{48}$$

Substantial streaming motions can be calculated from this equation **only with the left-hand side included;**[48] although in pre-1966 literature it was misleadingly regarded as "a fourth-order term" and so ignored — thus limiting all the theories to uninteresting cases when the **streaming Reynolds number** would be of order 1 or less.

We can use streaming generated by **acoustic beams** to illustrate the above principles. If acoustic energy is attenuated at a rate β **per unit length,** then a source at the origin which beams acoustic power P along the x_1-axis transmits a distribution of

$$\text{power } Pe^{-\beta x_1}, \text{ and therefore energy per unit length } c^{-1}Pe^{-\beta x_1}; \tag{49}$$

which is necessarily the integral of energy density, **and so also of the uniaxial Reynolds stress** (35), over the beam's cross-section. It follows that the force per unit volume (46), integrated over a cross-section, produces[5]

$$\text{A FORCE } c^{-1}P\beta e^{-\beta x_1} \text{ PER UNIT LENGTH in the } x_1\text{-direction.} \tag{50}$$

At high ultrasonic frequencies the force distribution (50) is rather concentrated, the distance of its **center of application** from the origin being just β^{-1} (which at 1 MHz, for example, is 24mm in air). Effectively, the beam applies at this center a **total force** $c^{-1}P$ (integral of the distribution (50)).

The type[1,5] of streaming motion generated by this concentrated force $c^{-1}P$ depends critically on the value of $\rho c^{-1} P \mu^{-2}$: a sort of Reynolds number squared, which is about $10^7 P$ in atmospheric air (with P in watts). Streaming of the low-Reynolds-number "stokeslet" type predicted (for a concentrated force) by equation (48) with the left-hand side suppressed is **a good approximation only for** $P < 10^{-6} W$.

For a source of power $10^{-4}W$, by contrast, the force $c^{-1}P$ generates quite a narrow laminar jet with momentum transport $c^{-1}P$, and **at powers exceeding** $3 \times 10^{-4}W$ **this jet has become turbulent,** spreading conically with semi-

angle about $15°$ and continuing to transport momentum at the rate $c^{-1}P$. Such turbulent jets generated by sound are strikingly reciprocal to a classical aeroacoustic theme!

At lower frequencies an acoustic beam of substantial power delivers a turbulent jet with a somewhat more variable angle of spread — but one which

at each point x_1 carries momentum transport $c^{-1}P(1 - e^{-\beta x_1})$,   (51)

generated by the total force (50) acting up to that point. This momentum transport in the jet represents the source's original rate of momentum delivery minus the acoustic beam's own remaining momentum transport (49). In summary, as acoustic power is dissipated into heat, the associated acoustic momentum transport is converted into a mean motion (which, at higher Reynolds numbers, is turbulent).[5]

6.3. Streaming around bodies generated by boundary-layer attenuation

Sound waves of frequency ω well below high ultrasonic frequencies have their attenuation concentrated, if solid bodies are present , in thin Stokes boundary layers attached to each body[1]. Then the streaming generated near a particular point on a body surface is rather simply expressed by using local coordinates with that point as origin, with the z-axis normal to the body and the x-axis in the direction of the inviscid flow just outside the boundary layer : the EXTERIOR flow. The Stokes boundary layer for an EXTERIOR flow

$(U(x,y),V(x,y))e^{i\omega t}$ has INTERIOR flow $(U(x,y),V(x,y))e^{i\omega t}\left[1-e^{-z\sqrt{(i\omega\rho/\mu)}}\right]$.(52)

[Note that my choice of coordinates makes $V(0,0) = 0$, and that the expressions (52) become identical outside the layer.] The streaming motion[1,5] is calculated from the equation

$$F_j^{INT} - F_j^{EXT} + \mu \partial^2 u_{fj}/\partial z^2 = 0,   (53)$$

with certain differences from equation (48) explained as follows:
  (a) the first term is the force (46) generating streaming within the boundary layer;
  (b) we are free, however, to subtract the second, since (see §24.6.1) it can produce no streaming, and, conveniently, the difference is zero outside the layer;

27

(c) gradients in the z-direction are so steep that the third term **dominates the viscous force** – and, indeed, in such a boundary layer, dominates also the left-hand side of equation (48).

The solution of equation (53) which vanishes at $z = 0$ and has zero gradient at the edge of the layer is obtained by two integrations, and its EXTERIOR value is

$$u_{fj}^{EXT} = \mu^{-1} \int_0^\infty \left(F_j^{INT} - F_j^{EXT} \right) z dz; \qquad (54)$$

where integration extends in practice, not to "infinity", but to **the edge of the layer within which the integrand is nonzero**. Expression (54) for the EXTERIOR streaming is yet again (see §6.1) **independent of the viscosity** μ since equation (52) makes $z dz$ of order $\mu/\rho\omega$; and it is easily evaluated.

At $x = y = 0$ (in the coordinates specified earlier) the EXTERIOR streaming (54) has

$$\text{x-component} \quad -U\frac{3\partial U/\partial x + 2\partial V/\partial y}{4\omega} \quad \text{and y-component} \quad -U\frac{\partial V/\partial x}{4\omega} , \qquad (55)$$

with zero z-component. This is a generalized form of the century-old RAYLEIGH LAW OF STREAMING (which covers cases when V is identically zero).

For the complete streaming pattern, expressions (55) are, effectively, **boundary values for its tangential component at the body surface** (because the Stokes boundary layer is so thin). Therefore, any simple solver for the steady-flow Navier-Stokes equations with specified tangential velocities on the boundary allows the pattern to be determined. **Important note: here, the inertia terms in the Navier-Stokes equations must NOT be neglected**, unless the Reynolds number R_s based on the streaming velocity (55) be of order 1 or less; when, however, the corresponding streaming motions would (as in §6.2) be uninterestingly small.

In the other extreme case when R_s is rather large (at least 10^3) the *streaming motion remains quite close to the body*[48] within **a steady boundary layer whose dimension** (relative to that of the body) **is of order** $R_s^{-1/2}$. This layer is by no means as thin as the Stokes boundary layer, but it does confine very considerably the acoustic streaming motion. Equations (55)

direct this motion **towards one of the EXTERIOR flow's stagnation points,** whence the steady-boundary-layer flow emerges as a jet — yet another jet generated by sound.[49,50]
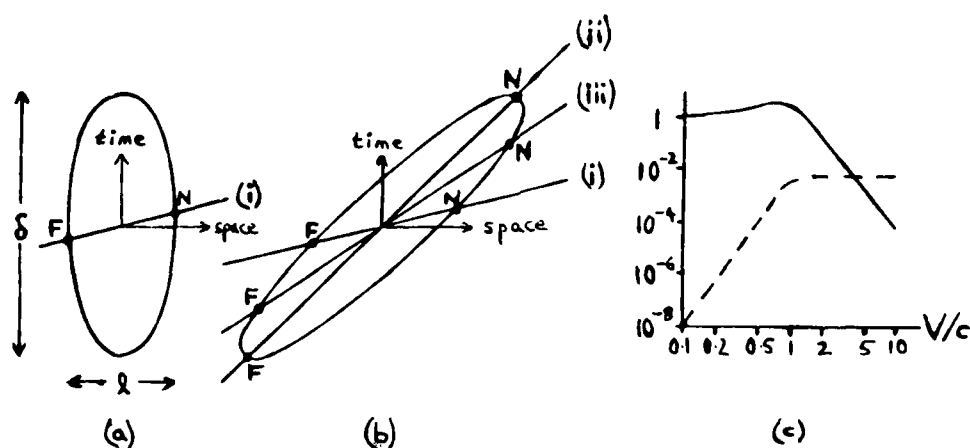
Figure 1. A uniformly valid Doppler-effect approximation.

Diagram (a) Space-time diagram for unconvected "eddies" of correlation length ℓ and duration δ.

Diagram (b) Case of "eddies" convected towards observer at velocity w; being Diagram (a) sheared by a distance w per unit time. Here, lines sloping by a distance c per unit time represent emissions received simultaneously by observer.
Case (i): w/c small.   Case (ii): w/c = 1.   Case (iii): intermediate value of w/c.

Diagram (c) ——————— Average modification factor (13).
------------- Acoustic efficiency, obtained by applying this factor to a low-Mach-number "quadrupole" efficiency of (say) $10^{-3}(V/c)^5$.

29

(a)   (b)
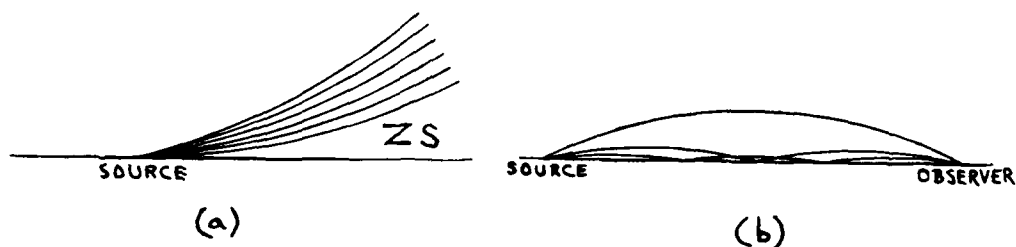
Figure 2. Effects of RAY CURVATURE (44) on propagation from a source
on horizontal ground.

Diagram (a). Rays of given UPWARD curvature (due to temperature lapse or
upwind propagation) can leave a Zone of Silence (ZS) below the ray
emitted horizontally.
Diagram (b). Rays of given DOWNWARD curvature (due to temperature
inversion or downwind propagation) can enhance received signals through
multiple-path communication.

REFERENCES

1.   LIGHTHILL, J. *Waves in Fluids*, Cambridge University Press 1978.

2.   LIGHTHILL, M.J. "On sound generated aerodynamically. I. General
theory", *Proceedings of the Royal Society A*, Vol. 211, 1952, pp. 564-
587.

3.   LIGHTHILL, M.J. "Sound generated aerodynamically. The Bakerian
Lecture", *Proceedings of the Royal Society A*, Vol. 267, 1962, pp. 147-
182.

4.   LIGHTHILL, J. "The propagation of sound through moving fluids",
Journal of Sound and Vibration, Vol. 24, 1972, pp. 471-492.

5.   LIGHTHILL, J. "Acoustic Streaming", *Journal of Sound and Vibration*,
Vol. 61, 1978, pp. 391-418.

6.   LIGHTHILL, M.J. "Jet Noise. The Wright Brothers Lecture", *American
Institute of Aeronautics and Astronautics Journal*,   Vol. 1, 1963,
pp. 1507-1517.

7. BRETHERTON, F.P. and GARRETT, C.J.R. "Wavetrains in inhomogeneous moving media" *Proceedings of the Royal Society A*, Vol. 302, 1968, pp. 529-554.

8. CURLE, N. "The influence of solid boundaries on aerodynamic sound", *Proceedings of the Royal Society A*, Vol. 231, 1955, pp. 505-514.

9. FFOWCS WILLIAMS, J.E. and HAWKINGS, D.L. "Sound generation by turbulence and surfaces in arbitrary motion", *Philosophical Transactions of the Royal Society A*, Vol. 264, pp. 321-342.

10. FFOWCS WILLIAMS, J.E. and HALL, L.H. "Aerodynamic sound generation by turbulent flow in the vicinity of a scattering half plane", *Journal of Fluid Mechanics*, Vol. 40, 1970, pp. 657-670.

11. CRIGHTON, D.G. and LEPPINGTON, F.G. "Scattering of aerodynamic noise by a semi-infinite compliant plate", *Journal of Fluid Mechanics*, Vol. 43, 1970, pp. 721-736.

12. CRIGHTON, D.G. and LEPPINGTON, F.G. "On the scattering of aerodynamic noise", *Journal of Fluid Mechanics*, Vol. 46, 1971, pp. 577-597.

13. CRIGHTON, D.G. "Acoustics as a branch of fluid mechanics", *Journal of Fluid Mechanics*, Vol. 106, 1981, pp. 261-298.

14. LIGHTHILL, M.J. "On sound generated aerodynamically. II. Turbulence as a source of sound", *Proceedings of the Royal Society A*, Vol. 222, 1954, pp. 1-32.

15. FFOWCS WILLIAMS, J.E. "The noise from turbulence convected at high speed". *Philosophical Transactions of the Royal Society A*, Vol. 255, 1963, pp. 469-503.

16. DOWLING, A.P., FFOWCS WILLIAMS, J.E. and GOLDSTEIN, M.E. "Sound production in a moving stream", *Philosophical Transactions of the Royal Society A*, Vol. 288, 1978, pp. 321-349.

17. FFOWCS WILLIAMS, J.E. and MAIDANIK, G. "The Mach wave field radiated by supersonic turbulent shear flows", *Journal of Fluid Mechanics*, Vol. 21, 1965, pp. 641-657.

18. CRIGHTON, D.G. "Basic principles of aerodynamic noise generation", *Progress in Aerospace Science*, Vol. 16, 1975, pp. 31-96.

19. GOLDSTEIN, M.E. *Aeroacoustics*, McGraw-Hill 1976.

20. GOLDSTEIN, M.E. "Aeroacoustics of turbulent shear flows", *Annual Reviews of Fluid Mechanics*, Vol. 16, 1984, pp. 263-285.

21. CURLE, N. "The mechanics of edge-tones." *Proceedings of the Royal Society A*, Vol. 216, 1953, pp. 412-424.

22. POWELL, A. "On edge-tones and associated phenomena", *Acustica*, Vol.3, 1953, pp. 233-243.

23. DOWELL, E.H. *Aeroelasticity of plates and shells.* Noordhoff 1975.

24. POWELL, A. "The Noise of Choked Jets", *Journal of the Acoustical Society of America*, Vol. 25, 1953, pp. 385-389.

25. HOWE, M.S. and FFOWCS WILLIAMS, J.E. "On the noise generated by an imperfectly expanded supersonic jet", *Philosophical Transactions of the Royal Society A*, Vol. 289, 1978, pp. 271-314.

26. CANDEL, S.M. and POINSOT, T.J. "Interactions between acoustics and combustions", *Proceedings of the Institute of Acoustics*, Vol. 10. 1988, pp. 103-153.

27. CRIGHTON, D.G. "The excess noise field of subsonic jets", *Journal of Fluid Mechanics*, Vol. 56, 1972, pp. 683-694.

28. POWELL, A. "Theory of vortex sound", *Journal of the Acoustical Society of America*, Vol. 36, 1964, pp. 177-195.

29. MÖHRING, W. "On vortex sound at low Mach number", *Journal of Fluid Mechanics*, Vol. 85, 1978, pp. 685-691.

30. RIBNER, H.S. "The Generation of Sound by Turbulent Jets", *Advances in Applied Mechanics*, Vol. 8, 1964, pp. 103-182.

31. FFOWCS WILLIAMS, J.E. and KEMPTON, A.J. "The noise from the large-scale structure of a jet", *Journal of Fluid Mechanics*, Vol. 84, 1978, pp. 673-694.

32. PHILLIPS, O.M. "On the generation of sound by supersonic turbulent shear layers", *Journal of Fluid Mechanics*, Vol. 9, 1960, pp. 1-28.

33. MANI, R. "The influence of jet flow on jet noise, Parts 1 and 2", *Journal of Fluid Mechanics*, Vol. 73, 1976, pp. 753-793.

34. PARRY, A.B. and CRIGHTON, D.G. "Asymptotic Theory of Propeller Noise", *American Institute of Aeronautics and Astronautics Journal*: Part I in Vol. 27, 1989, pp. 1184-1190 and Part II in Vol. 29, 1991, to appear.

35. POWELL, A. "Aerodynamic noise and the plane boundary", *Journal of the Acoustical Society of America*, Vol. 32, 1960, pp. 982-990.

36. CRIGHTON, D.G. "Long range acoustic scattering by surface inhomogeneities beneath a turbulent boundary layer", *Journal of Vibration, Stress and Reliability*, Vol. 106, 1984, pp. 376-382.

37. WHITHAM, G.B. "On the propagation of shock waves through regions of non-uniform area or flow", *Journal of Fluid Mechanics*, Vol. 4, 1958, pp. 337-360.

38. LIGHTHILL, M.J. "Viscosity Effects in Sound Waves of Finite Amplitude", pp. 250-351 of *Surveys in Mechanics* (ed. Batchelor, G.K. and Davies, R.M.), Cambridge University Press 1956.

39. BLOKHINTSEV, D.I. *Acoustics of a Nonhomogeneous Moving Medium*, Moscow: Gostekhizdat. Also available in English translation as *National Advisory Committee for Aeronautics Technical Memorandum* No.1399, Washington 1956.

40. REYNOLDS, O. "On the Dynamical Theory of Incompressible Viscous Fluids and the Determination of the Criterion", *Philosophical Transactions of the Royal Society A*, Vol. 186, 1895, pp. 123-164.

41. PRIDMORE-BROWN, D.C. "Sound propagation in a fluid flowing through an attenuating duct", *Journal of Fluid Mechanics*, Vol. 4, 1958, pp. 393-406.

42. MUNGUR, P. and GLADWELL, G.M.L. "Acoustic wave propagation in a sheared fluid contained in a duct", *Journal of Sound and Vibration*, Vol. 9, 1969, pp. 28-48.

43. SHANKAR, P.N. "On acoustic refraction by duct shear layers", *Journal of Fluid Mechanics*, Vol. 47, 1971, pp. 81-91.

44. RAYLEIGH, LORD *The Theory of Sound*, Vol. II, Second edition. Macmillan, London 1896.

45. NYBORG, W.L. "Acoustic streaming due to attenuted plane waves", *Journal of the Acoustical Society of America*, Vol. 25, 1953, pp. 68-75.

46. WESTERVELT, P.J. "The theory of steady rotational flow generated by a sound field", *Journal of the Acoustical Society of America*, Vol. †5, 1953, pp. 60-67.

47. NYBORG, W.L. "Acoustic Streaming", Chap. 11 in *Physical Acoustics, Principles and Methods* (ed. Mason, W.P.), Academic Press 1965.

48. STUART, J.T. "Double boundary layers in oscillatory viscous flow", *Journal of Fluid Mechanics*, Vol. 24, 1966, pp. 673-687.

49. RILEY, N. "Streaming from a cylinder due to an acoustic source", *Journal of Fluid Mechanics*, Vol. 180, 1987, pp. 319-326.

50. AMIN, N. and RILEY, N. "Streaming from a sphere due to a pulsating acoustic source", *Journal of Fluid Mechanics*, Vol. 210, 1990, pp. 459-473.

AEROACOUSTICS

**SECOND INTERNATIONAL CONGRESS ON
RECENT DEVELOPMENTS IN AIR- AND
STRUCTURE-BORNE SOUND AND VIBRATION**
MARCH 4-6, 1992   AUBURN UNIVERSITY, USA

VORTEX SOUND INTERACTION

A.P. Dowling
The University Engineering Department
Trumpington Street
Cambridge CB2 1PZ
UK

ABSTRACT

The interaction between vorticity and sound is twofold: unsteady vorticity generates sound but near a surface with a sharp edge incoming sound leads to the production of vorticity. The influence of scattering surfaces on the generation of sound by vorticity is reviewed within a unified framework. In particular, it is shown that the additional vorticity generated at the edges of an aperture in a rigid screen can act to reduce the scattered monopole field. Unsteady vortex shedding also occurs when a sound wave is incident upon a perforated plate, and leads to a reduction in the sound energy. Criteria are given for exploiting this mechanism to design panels, which absorb all the incident sound energy at a particular frequency.

INTRODUCTION

Lighthill's [1] theory of aerodynamic sound identifies the turbulent Reynolds stresses as a quadrupole source of sound in an unbounded fluid. It is sometimes convenient to use Powell's [2] reformulation of this theory, which emphasises the dependence of the noise-producing elements on local vorticity. One advantage of doing this is that vortical regions of the flow are often much more concentrated than the hydrodynamic region over which the Reynolds stresses are nonzero. Moreover, the development of the vorticity field can be described by simple kinematics.

We begin by considering the sound generated by a compact region of vorticity in unbounded space, and then go on to review the effects of nearby surfaces. An infinite plane rigid surface acts like a simple reflector [3] and produces, at most, a doubling in the quadrupole sound pressure generated by the vorticity in unbounded space.

A nearby rigid compact body leads to a scattered dipole field and can greatly enhance the radiated sound [4-6]. We illustrate this effect by discussing vorticity near an infinitely, long rigid cylinder of compact radius.

Vorticity near an aperture in plane boundary produces a fluctuating mass flux through the aperture and hence a scattered monopole sound field. The presence of an aperture can therefore lead to strong augmentation in the sound pressure generated at low Mach numbers by vorticity near a plane. We illustrate these effects by a detailed consideration of a compact circular aperture in an infinite plane surface. If the scattered field is assumed to be potential, infinite velocities are predicted around the rim of the aperture. In practice, viscous effects would be important in this region and lead to the generation of additional vorticity. This vortex shedding is in general a nonlinear phenomenon, but the presence of a mean bias flow through the aperture leads to vorticity that depends linearly on the local pressure fluctuations. We use the same model of this vortex shedding process

37

as Howe [7], but apply a different technique to solve the resulting integral equations. The unsteady vortex shedding is found to lead to a reduction in the amplitude of the scattered monopole sound, and to a change in its phase.

A sound wave incident upon an aperture in a plane surface generates unsteady vorticity in a similar way [7]. In the presence of a mean bias the flow, acoustic energy is converted into unsteady vortical motion and the unsteady vortex shedding provides a linear mechanism of sound absorption. Howe [7] calculated the absorptive properties of a screen with many circular apertures closely spaced on the wavelength scale. We summarise more recent results [8] for the sound absorbed by a screen perforated with a regular array of parallel slits. While absorption by circular apertures can be described by only two non-dimensional parameters, the slits interact with one another introducing an additional parameter. The maximum absorption coefficient for an isolated screen, perforated with either slits or circular holes is found to be 1/2.

The effectiveness of a perforated screen as a sound absorber can be greatly increased when a rigid surface is placed behind the screen [8,9]. We show that it is theoretically possible to absorb all the sound energy incident at a particular frequency, and indicate how the geometry and bias flow should be chosen to produce such highly absorptive liners. High absorption is predicted for suitably designed backed screens, whether they are perforated with slits or circular holes. Experimental results are presented, which show encouraging agreement with the theory.

SOUND GENERATED BY VORTICITY IN UNBOUNDED SPACE

Howe [10] showed the stagnation enthalpy, B, to be a convenient dependent variable to describe sound generation by vorticity. When the flow is isentropic, B is equal to $\int dp/\rho + \frac{1}{2} u^2$, where p is the pressure, ρ the density and u the particle velocity. In a linear acoustic field, $B'(x,t)$ reduces to $p'(x,t)/\rho_0$. The prime denotes a perturbation and the suffix o a mean value.

In a low Mach number isentropic flow, B satisfies the inhomogeneous wave equation [10]:

$$\left[\frac{1}{c^2} \frac{\partial^2}{\partial t^2} - \nabla^2\right] B = \text{div } L, \quad \text{where } L = \omega \times u. \tag{1}$$

The source velocity field, $u(x,t)$, can be regarded as incompressible (and therefore solenoidal) at low enough Mach numbers. ω is the vorticity vector and c the speed of sound.

The solution to Eq. (1) in unbounded space can be written down immediately. When the observer at x is in the far field and the vorticity is close to the origin, it is

$$B'(x,t) = -\frac{x_i}{4\pi|x|^2c} \frac{\partial}{\partial t} \int L_i (y, t-|x|/c + x.y/|x|c) \, d^3y. \tag{2}$$

This integral would vanish were it not for the retarded time variation over the region of vorticity, since for a solenoidal velocity field L can be expressed as a divergence:

$$L_i = \frac{\partial}{\partial y_j} (u_i u_j) - \frac{\partial}{\partial y_i} (\frac{1}{2} u^2). \tag{3}$$

For a compact source region, the retarded time variation can be expanded as a Taylor series. The result in Eq. (3) shows that the first term in the expansion integrates to zero, and we obtain

$$B'(x,t) = \frac{p'(x,t)}{\rho_0} = -\frac{1}{4\pi|x|^3c^2} \frac{\partial^2}{\partial t^2} \int (x.y) \, x.L (y, t-|x|/c) \, d^3y. \tag{4}$$

Equation (4) shows that the distant sound field is quadrupole [2] and Lighthill's

38

eighth-power scaling law [1] can be readily recovered.

SOUND GENERATED BY VORTICITY NEAR AN INFINITE RIGID PLANE

The momentum equation shows that $\nabla B = -\partial u/\partial t - \omega \times u$. The boundary condition of no normal acceleration on a fixed impenetrable surface S therefore reduces to

$\quad$ n.∇B = 0 on S, provided that the vorticity vanishes on the surface. $\hspace{2cm}$ (5)

To determine the sound generated by vorticity in front of the infinite rigid plane $y_1 = 0$, we need to solve the wave equation (1) with the boundary condition $\partial B/\partial y_1 = 0$ on $y_1 = 0$. This is readily achieved by using the half-space Green function, G_R.

$$G_R(y,\tau|x,t) = \frac{\delta(t-\tau-|x-y|/c)}{4\pi|x-y|} + \frac{\delta(t-\tau-|x^*-y|/c)}{4\pi|x^*-y|} \, . \hspace{1cm} (6)$$

with $x^* = (-x_1,x_2,x_3)$. The required solution is

$$B'(x,t) = - \int L_i \frac{\partial G_R}{\partial y_1} d^3y \, d\tau. \hspace{2cm} (7)$$

A repetition of the steps between Eqs. (2) and (4) shows that for x in the far field this reduces to

$$B'(x,t) = \frac{p'(x,t)}{\rho_o} = - \frac{1}{4\pi|x|^3c^2} \frac{\partial^2}{\partial t^2} \int \left[(x.y)x + (x^*.y)x^*).L(y,t-|x|/c)\right]d^3y \hspace{1cm} (8)$$

By comparison with Eq. (4), it is evident that the infinite plane acts like a simple reflector leading to at most a doubling in the radiated quadrupole sound field [3].

SOUND GENERATED BY VORTICITY NEAR A CYLINDER

A nearby rigid compact body leads to a scattered dipole field and can greatly enhance the sound radiated from vorticity [4-6]. We will illustrate this effect by considering vorticity near a fixed rigid cylinder, which is infinitely long with radius a. It is convenient to introduce a cylindrical coordinate system and write $y = (y_1,\sigma,\psi)$. The solution to Eq. (1) which satisfies n.∇B = 0 on the cylinder is given by

$$B'(x,t) = - \int L_i \frac{\partial G_c}{\partial y_1} d^3y \, d\tau. \hspace{2cm} (9)$$

where the Green function $G_c (y,\tau|x,t)$ satisfies

$$\left[\frac{1}{c^2} \frac{\partial^2}{\partial \tau^2} - \nabla^2\right] G_c = \delta(x-y,t-\tau), \quad \text{with} \quad \frac{\partial G_c}{\partial \sigma} = 0 \text{ on } \sigma = a. \hspace{1cm} (10)$$

Howe [11] has derived an approximation to $G_c(y,\tau|x,t)$ for use with compact sources. If the source at y is located well within a wavelength of the origin, and the observer at x is in the far field.

$$G_c \simeq \frac{1}{4\pi|x|} \delta(t-\tau-|x|/c) + \frac{y_1\cos\theta + (\sigma+a^2/\sigma)\sin\theta \cos(\psi-\phi)}{4\pi|x|c} \delta'(t-\tau-|x|/c) + \ldots \ldots \hspace{0.5cm} (11)$$

39

$(|x|, \theta, \phi)$ is the expansion of x in spherical polar coordinates, where θ is the angle between x and the 1-axis and ϕ is the azimuthal angle.

Substitution for $\partial G_c/\partial y_1$ from Eq. (11) into Eq. (9) would lead to an expression for the distant stagnation enthalpy in terms of the nonlinear source term L. This is the procedure followed by Hardin and Pope [12] when investigating the sound of a vortex ring moving past a cylinder. But here we will apply Mohring's method [13] of introducing a vector Green function. This enables us to obtain a source which depends only linearly on the vorticity and provides insight into the noise producing elements.

The approximation to G_c in Eq. (11) satisfies $\nabla^2 G_c \approx 0$, and so it is possible to define a vector Green function by curl $G = $ grad G_c. Simple algebra shows that the solution of this equation in cylindrical polar coordinates is

$$G = \frac{1}{4\pi|x|c} \left[\left(\sigma - \frac{a^2}{\sigma} \right) \sin\theta \, \sin(\psi-\phi), \; 0, \; \tfrac{1}{2}\sigma \, \cos\theta \right] \delta'(t-\tau-|x|/c). \tag{12}$$

Substitution of curl G for $\partial G_c/\partial y_1$ in Eq. (9) leads to

$$B'(x,t) \approx \frac{p'(x,t)}{\rho_0} = - \int L \cdot (\text{curl } G) d^3y \, d\tau. \tag{13}$$

After integration by parts and use of the vorticity equation, curl $L = -\partial\omega/\partial t$, this simplifies to

$$p'(x,t) = \rho_0 \frac{\partial}{\partial t} \int \omega . G \, d^3y \, d\tau$$

$$= \frac{\sin\theta}{4\pi|x|c} \frac{\partial^2}{\partial t^2} \int \left[\left(\sigma - \frac{a^2}{\sigma} \right) \sin(\psi - \phi)\omega_1 \right] d^3y + \frac{\cos\theta}{8\pi|x|c} \frac{\partial^2}{\partial t^2} \int \left[\sigma\omega_\psi \right] d^3y. \tag{14}$$

where the square brackets denote that the function they enclose is to be evaluated at retarded time $t-|x|/c$. The second term of the right-hand side of Eq. (14) appears to describe an axial dipole. However, the strength of the dipole depends on the rate of change of $\int \sigma\omega_\psi d^3y$, which is the axial impulse of the vorticity [14]. Since an infinitely long cylinder cannot exert an axial force on an inviscid fluid, this component of the impulse of the vortex system is constant and, as we might expect, the axial dipole is identically zero. It therefore follows from Eq. (14) that the axial component of the vorticity, ω_1, must be nonzero if the vortex sound field is to be of dipole type [4].

This has implications for the noise radiated by towed arrays. These are instrumentation packages in the form of long flexible cylinders, and are towed by ships and submarines to detect weak sound signals. We see from Eq. (14) that the main boundary-layer vorticity, which is azimuthal, does not radiate dipole sound unless the cylinder axis is curved.

SOUND GENERATION BY VORTICITY NEAR A CIRCULAR APERTURE

Let us now consider the sound generated by vorticity near a circular hole of radius a, in an otherwise rigid screen on $y_1 = 0$. The geometry is illustrated in Figure 1.

Without additional vortex shedding

We will suppose that both a and the distance of the vorticity from the aperture are small in comparison with the wavelength. The stagnation enthalpy satisfies Eq. (1) with $\partial B/\partial y_1 = 0$ on the rigid parts of the screen and B continuous through the aperture. The half-space Green function G_R in Eq. (6) may be used to convert Eq. (1) into an integral equation for

B'(x,t) and leads to

$$E'(x,t) = H(x_1) B_+(x,t) + H(-x_1) B_-(x,t) - \text{sgn}(x_1) \int_S G_R \frac{\partial B}{\partial y_1} dS \, d\tau, \tag{15}$$

where S is the surface of the aperture. $y_1 = 0$, $\sigma \leq a$, $0 \leq \psi \leq 2\pi$.

$$H(x_1) B_+(x,t) = -H(x_1) \int_0^\infty \int_{-\infty}^\infty \int_{-\infty}^\infty L_1 \frac{\partial G_R}{\partial y_1} d^3y \, d\tau \tag{16}$$

is the B-field produced in $x_1 > 0$ by vorticity in front of a rigid plane. Similarly

$$H(-x_1) B_-(x,t) = -H(-x_1) \int_{-\infty}^0 \int_{-\infty}^\infty \int_{-\infty}^\infty L_1 \frac{\partial G_R}{\partial y_1} d^3y \, d\tau \tag{17}$$

is the B-field produced in $x_1 < 0$ by vorticity behind a rigid plane. The last term in Eq. (15) describes the scattering effect of the aperture and represents a monopole sound field. For a low Mach number flow, this term makes the largest contribution to the distant sound field, and equation (15) reduces to

$$B'(x,t) = \frac{p'(x,t)}{\rho_0} = \frac{-\text{sgn}(x_1)}{2\pi|x|} \int_S \frac{\partial B}{\partial y_1} (y,t - |x|/c) dS \quad \text{for large } |x|. \tag{18}$$

The gradient $\partial B/\partial y_1$ within the aperture is to be determined by applying the requirement that B'(x,t) be continuous across the aperture to Eq. (15). This shows that $\partial B/\partial y_1$ must be the solution of the integral equation

$$2 \int_S G_R \frac{\partial B}{\partial y_1} dS \, d\tau = B_+(x,t) - B_-(x,t) \text{ for } x_1 = 0 \text{ and } |x| < a, \tag{19}$$

that satisfies $\partial B/\partial x_1 = 0$ on $x_1 = 0$ for $|x| > a$. After substituting for G_R from Eq. (6) and expressing x and y in terms of polar coordinates centred on the origin, $x = (0,\rho,\phi)$, $y = (0,\sigma,\psi)$, this integral equation becomes

$$\frac{1}{\pi} \int_S \frac{\partial B}{\partial y_1} \frac{\sigma \, d\sigma \, d\psi}{(\rho^2+\sigma^2-2\rho\sigma \cos(\psi-\phi))^{\frac{1}{2}}} = B_+(x,t) - B_-(x,t) \text{ for } \rho < a \tag{20}$$

An identical integral equation arises in the problem of determining the electrical charge distribution required on a disc to maintain a specified potential, and Copson [15] has determined the general solution.

In particular, if the vorticity is at a distance from the origin large in comparison with the aperture radius (although still small in comparison with the wavelength), $B_+(x,t)$ and $B_-(x,t)$ are approximately constant over the region $\rho \leq a$. The solution to Eq. (20) is then given in reference [15], Section 4.1:

41

$$\frac{\partial B}{\partial y_1} = \frac{B_+(0,t) - B_-(0,t)}{\pi(a^2 - \sigma^2)^{\frac{1}{2}}} \text{ for } \sigma < a. \tag{21}$$

When this expression for $\partial B/\partial y_1$ is substituted into Eq. (18), it leads to the far-field pressure perturbation

$$p'(x,t) = \frac{-sgn(x_1)\rho_o a}{\pi|x|} \left[B_+(0, t-|x|/c) - B_-(0, t-|x|/c) \right] . \tag{22}$$

This sound field is of monopole type, the strength of the equivalent monopole source depending on the product of $\pm 2\rho_o a$ with the difference in the incident B-fields, B_+-B_- [cf 16,17]. When the rigid plane surface had no aperture, we found the radiated sound field to be quadrupole (see Eq. (8)). Therefore, for a plate near a low Mach number flow, an aperture may lead to a significant enhancement in the radiated sound.

With vortex shedding

It is evident from Eq. (21) that the gradient $\partial B/\partial y_1$, and hence the particle velocity, is singular as σ tends to a. Hence, in practice, viscous effects will be important near the rim of the aperture and vorticity will be generated there. In general this vortex shedding would depend nonlinearly on the flow perturbations, but if there is a mean flow through the aperture the problem becomes linear.

We will use Howe's [7] simple model of this shedding process. Azimuthal vorticity is assumed to be generated around the rim of the aperture, and subsequently to be convected in the positive x_1-direction with the mean velocity $(U,0,0)$. Hence, for linear perturbations of frequency ω, the shed vorticity can be expressed in the form

$$\omega(y,\tau) = e_\psi \gamma \ H(y_1) \ \delta(\sigma-a) \ e^{-i\omega(\tau-y_1/U)}. \tag{23}$$

γ, the amplitude of the shed circulation per unit length, is to be determined by applying the Kutta condition [18] that the velocity at the rim of the aperture remain finite. This shed vorticity leads to an additional source term,

$$\omega \times u = e_\sigma \gamma U \ H(y_1) \ \delta(\sigma-a) \ e^{-i\omega(\tau-y_1/U)} , \tag{24}$$

in Eq. (15), which becomes

$$B'(x,t) = H(x_1) \ B_+(x,t) + H(-x_1) \ B_-(x,t) - H(x_1) \ \gamma Ua \int \frac{\partial G_R}{\partial \sigma} e^{-i\omega(\tau-y_1/U)} \ dy_1 d\psi d\tau$$

$$- sgn(x_1) \int_S G_R \frac{\partial B}{\partial y_1} \ dS \ d\tau. \tag{25}$$

For a low Mach number flow, the last term in Eq. (25), which describes a monopole source, makes the largest contribution to the distant sound field and

$$B'(x,t) = \frac{p'(x,t)}{\rho_o} = - \frac{sgn(x_1)}{2\pi|x|} \int_S \frac{\partial B}{\partial y_1} \ (y,t-|x|/c)dS \tag{26}$$

Again the gradient $\partial B/\partial y_1$ is to be determined from the condition that $B'(x,t)$ is continuous across the aperture, and $\partial B/\partial y_1$ vanishes on the rigid parts of the screen.

42

The problem for $B'(x,t)$ is equivalent to that solved by Howe [7] to determine the sound transmitted through a perforated screen. He used Tranter's method [19] to obtain the solution. The details of the analysis are complicated and conceal the simplicity of the solution. Here we will adopt a different approach.

Since $B'(x,t)$ is to be continuous across the aperture, equation (26) shows that $\partial B/\partial y_1$ is the solution of the integral equation:

$$2 \int_S G_R \frac{\partial B}{\partial y_1} \, dS \, d\tau = B_+(x,t) - B_-(x,t) - \gamma Ua \int \frac{\partial G_R}{\partial \sigma} e^{i\omega(\tau-y_1/U)} \, dy_1 \, d\psi \, d\tau \qquad (27)$$

for $x_1 = 0$ and $\rho < a$, that satisfies $\partial B/\partial x_1 = 0$ on $x_1 = 0$ for $\rho > a$. After substituting for G_R this integral equation becomes

$$\frac{1}{\pi} \int_S \frac{\partial B}{\partial y_1} \frac{\sigma \, d\sigma \, d\psi}{(\rho^2 + \sigma^2 - 2\rho\sigma \, \cos(\psi-\phi))^{\frac{1}{2}}} = B_+(0,t) - B_-(0,t)$$

$$- \frac{\gamma Ua}{2\pi} \int \frac{\partial}{\partial \sigma} \left[\frac{1}{\rho^2 + \sigma^2 - 2\rho\sigma \, \cos(\psi-\phi)} \right]_{\sigma=a}^{\frac{1}{2}} e^{-i\omega(t-y_1/U)} \, dy_1 \, d\psi,$$

$$(28)$$

provided B_+ and B_- are again approximately constant over the region $\rho \leq a$. The y_1 and ψ integrals in the last term in Eq. (28) are evaluated in the Appendix to show that the integral equation reduces to

$$\frac{1}{\pi} \int_S \frac{\partial B}{\partial y_1} \frac{\sigma \, d\sigma \, d\psi}{(\rho^2 + \sigma^2 - 2\rho\sigma \, \cos(\psi-\phi))^{\frac{1}{2}}} = B_+(0,t) - B_-(0,t) + i\gamma U \, a\kappa e^{-i\omega t} \int_0^\infty \frac{\lambda H_1^{(1)}(\lambda a) \, J_0(\lambda\rho) \, d\lambda}{\kappa^2 + \lambda^2},$$

$$(29)$$

where $\kappa = \omega/U$. This integral equation is in a particularly convenient form because Copson [15] has considered discs with a uniform potential and with a radial distribution proportional to $J_0(\lambda\rho)$ as special cases. We can use Copson's results to write down the solution to Eq. (29):

$$\frac{\partial B}{\partial y_1} = \frac{B_+(0,t)-B_-(0,t)}{\pi(a^2-\sigma^2)^{\frac{1}{2}}} + i\gamma U \, a\kappa e^{-i\omega t} \int_0^\infty \frac{\lambda H_1^{(1)}(\lambda a)}{\kappa^2+\lambda^2} \left[\frac{\lambda}{2} J_0(\lambda\sigma) + \frac{1}{\pi} \int_a^\infty \frac{t\cos(\lambda t)dt}{(t^2-\sigma^2)^{3/2}} \right] d\lambda, \text{ for } \sigma < a.$$

$$(30)$$

We have already noted that near the rim of the aperture where σ tends to a, the first term on the right-hand side of Eq. (30) has a square-root singularity. The last term on the right-hand side is also singular. We can bring out the form of this singularity explicitly by integrating the t-integral by parts. This leads to

$$\frac{\partial B}{\partial y_1} = \frac{B_+(0,t) - B_-(0,t)}{\pi(a^2 - \sigma^2)^{\frac{1}{2}}} + \frac{i \, \gamma \, U \, a \, \kappa \, F(St) \, e^{-i\omega t}}{\pi(a^2 - \sigma^2)^{\frac{1}{2}}} + \text{terms finite as } \sigma \to a \qquad (31)$$

where $St = \kappa a$ is the Strouhal number of the shed vorticity, $St = \omega a/U$

43

and $F(St) = \displaystyle\int_0^\infty \frac{z \cos z \, H_1^{(1)}(z) dz}{z^2 + (St)^2}$. $\qquad$ (32)

In order to satisfy the Kutta condition that $\partial B/\partial y_1$ remain finite as $\sigma \to a$, we must choose

$$\gamma = \frac{B_+(0,t) - B_-(0,t)}{U a \kappa F(St)} \, i \, e^{i\omega t} \qquad (33)$$

The calculation of the far-field pressure from Eq. (26), involves the evaluation of $\int \partial B/\partial y_1 dS = 2\pi \int \partial B/\partial y_1 \sigma \, d\sigma$. After substituting for $\partial B/\partial y_1$ from Eq. (31) and exchanging the order of the t and σ integrals, the remaining integrals are standard and lead to

$$\int \frac{\partial B}{\partial y_1} \, dS = 2a(B_+(0,t) - B_-(0,t)) + i2\gamma U \kappa a^2 E(St) \, e^{-i\omega t}. \qquad (34)$$

where $E(St) = \displaystyle\int_0^\infty -\frac{\sin z \, H_1^{(1)}(z) dz}{z^2 + (St)^2}$. $\qquad$ (35)

Once γ has been replaced by the form in Eq. (33),

$$\int \frac{\partial B}{\partial y_1} \, dS = 2a\left[B_+(0,t) - B_-(0,t)\right] \alpha(St), \qquad (36)$$

where $\alpha(St) = 1 - E(St)/F(St)$. $\qquad$ (37)

The far-field sound pressure is therefore given by Eq. (26) to be

$$p'(x,t) = - \frac{\text{sgn}(x_1)}{\pi |x|} \rho_0 \, a \, \alpha(St)\left[B_+(0, t - |x|/c) - B_-(0, t - |x|/c)\right] \qquad (38)$$

A comparison with Eq. (22) shows that the unsteady vortex shedding alters the radiated sound pressure at frequency ω, by the complex factor $\alpha(St) = 1 - E(St)/F(St)$, $St = \omega a/U$. The integrals defining $E(St)$ and $F(St)$ in Eqs. (35) and (32) can be converted into standard form [7]. This makes it straightforward to evaluate the function $\alpha(St)$, which is plotted in Figure 2. For Strouhal numbers less than 2, the unsteady vortex shedding leads to a considerable reduction in the amplitude of scattered monopole. Its phase is also changed.

TRANSMISSION OF SOUND THROUGH A PERFORATED SCREEN

Having considered scattering by a single aperture, we will now go on to investigate a rigid screen perforated by a uniform distribution of small circular apertures, each of radius a. A steady pressure difference produces a low Mach number mean flow through the perforations. Let us suppose that this is perturbed by a linear plane sound wave incident at an angle θ and that the incident pressure perturbations are $e^{i(k \cdot x \quad)}$, where $k = (k_1, k_2, k_3)$, $k_1 = \omega \cos\theta/c$.

If the separation between apertures is small in comparison with the wavelength, averaging over many apertures leads to a smoothed volume flow rate in the 1-direction, which we write as $Q \exp i(k_2 x_2 + k_3 x_3 - \omega t)$ per unit area of screen. Hence, far from the screen, the pressure perturbations are described by

44

$$p'(x,t) = e^{i(k.x-\omega t)} + e^{i(-k_1x_1 + k_2x_2 + k_3x_3-\omega t)} (1 - Q \rho_0 c/\cos\theta) \text{ in } x_1 \ll 0$$

$$= e^{i(k.x-\omega t)} Q\rho_0 c/\cos\theta \text{ in } x_1 \gg 0 \tag{39}$$

[7, equations (3.15) and (3.16)]

It is convenient to characterise the permeability of the screen·by an effective compliance, η, defined by

$$Qe^{i(k_2x_2 + k_3x_3 - \omega t)} = \frac{\eta}{i\omega\rho_0} [p']_{x_1=0^-}^{x_1=0^+} . \tag{40}$$

When the form for the pressure field in Eq. (39) is substituted into Eq. (40), it leads to

$$\frac{Q\rho_0 c}{\cos\theta} = \frac{1}{1-ik_1/2\eta} . \tag{41}$$

The transmission properties of the screen are described by Eq. (39) and depend only on the ratio k_1/η.

The volume flow rate through a single aperture is $(i\omega)^{-1} \int \partial B/\partial y_1 dS$. Through Eq. (36), we have obtained an expression for the relationship between this flux and the local difference in the B-field on either side of the aperture. When this is converted into the form in Eq. (40) it leads to

$$\eta = 2Na \; \alpha(St) = \frac{2\upsilon}{\pi a} \alpha(St) \tag{42}$$

where N is the number of apertures/unit area and υ $(= N\pi a^2)$ is the open-area ratio of the screen. $\alpha(St)$ is the known complex function of Strouhal number defined in Eq. (37). By substitution of this expression for η into Eqs. (39) and (41), we can recover Howe's result [7] for scattering from a screen with circular apertures.

A plate perforated by a regular array of parallel slits can be investigated in a similar way. Let us consider slits of width 2s, spaced a distance d apart. We are interested in the limit $\omega s \ll \omega d \ll c$. There is one major difference between the analysis for slits and circular apertures. For circular apertures, it has been sufficient to consider an isolated hole in detail, transmission across a perforated screen then being determined by superposition. For slits, the potential field of each slit decays slowly with distance and the geometry of the array of slits needs to be considered when setting up the integral equation for $\partial B/\partial y_1$. The details are given in reference [8] and lead to

$$\eta = \frac{\pi/2d}{\ell n2/\Phi - \ell n(\pi\upsilon)} \text{ (reference [8], Eq. (2.51))}. \tag{43}$$

υ is again the open-area ratio. $\Phi(St)$ is a complex function of the Strouhal number of the flow through the slits, $St = \omega s/U$, and is given in reference [8] Eq. (2.44).

The absorption coefficient Δ can be readily calculated from Eq. (39).

$$\Delta = 1 - |1-Q\rho_0 c/\cos\theta|^2 - |Q\rho_0 c/\cos\theta|^2 . \tag{44}$$

where Q is given by Eq. (41) and η is to be evaluated from Eq. (42) for circular apertures and from Eq. (43) for slits. Δ is plotted against Strouhal number in Figure 3 for various values of the parameters. For circular holes Δ is a function of only two non-dimensional parameters, St and $\upsilon/M\cos\theta$, where $M = U/c$ is the Mach number of the mean bias flow. For

slits there is an extra parameter, since the open-area ratio v appears explicitly.

It is straightforward to show that for any complex Q the maximum value of the function Δ, as described by Eq. (44), is ½. Thus Figure 3b shows an optimal case for both screens.

THE ABSORPTION OF SOUND BY A PERFORATED SCREEN WITH AN INFINITE RIGID BACKING PLANE

The effectiveness of a perforated screen as a sound absorber can be greatly increased when a rigid surface is placed behind the screen. Consider the geometry in Figure 4. Sound waves are incident from $x_1 > 0$ onto an infinite perforated plate positioned at $x_1 = 0$. A rigid wall occupies the plane $x_1 = -\ell$. For small $\omega a/c$ and $\ell \gg a$, the acoustic properties of the screen can be described by the smoothed boundary condition in Eq. (40). This, together with the condition of vanishing normal velocity on $x_1 = -\ell$ and continuity of the smoothed volume flow rate Q at $x_1 = 0$, specifies the sound field. We find that the reflection coefficient R is given by

$$R = \frac{ik_1/\eta + 1 - 1/\tan k_1\ell}{ik_1/\eta - 1 - 1/\tan k_1\ell}. \tag{45}$$

We will examine the case of circular apertures first. Then in the the absence of a bias flow $\eta = 2v/\pi a$ and, with the additional constraint that $\omega\ell\cos\theta \ll 1$, the reflection coefficient in Eq. (45) reduces to that determined by Leppington and Levine [20]. There is then a resonance for incident sound at frequency ω_c, where

$$\omega_c^2 = 2c^2 v/\pi a\ell\cos^2\theta, \tag{46}$$

the Helmholtz resonator frequency for the apertures and cavity. The screen appears to be perfectly soft at this frequency. When there is a mean bias flow through the screen, sound energy is converted into unsteady vortical flow. We can write the reflection coefficient R for a general frequency in terms of the non-dimensional frequency ω/ω_c, $\omega\ell\cos\theta/c$ and the Strouhal number $\omega a/U$. We are particularly interested in the absorption coefficient $\Delta = 1 - |R|^2$, which can be readily calculated once R has been determined. Intuitively, one might expect the maximum absorption to occur near the resonance frequency in Eq. (46).

Figure 5 shows a comparison between the theoretical absorption coefficient and measurements obtained in an impedance tube. The agreement between the theory and experiment is very encouraging. We see from Figure 5a that the theoretical prediction of total sound absorption, at a particular frequency, can be obtained in practice and that this high absorption is indeed obtained near the resonance frequency, ω_c. When the parameters are altered to produce a less efficient sound absorber, the correlation between the theory and experiment is still good, as shown in Figure 5b.

Figure 6 indicates how an effective sound absorber can be designed with circular apertures. For a given frequency, angle of incidence and cavity depth, the parameter $\omega\ell\cos\theta/c$ is fixed. The plate geometry should then be chosen so that ω_c, as defined in Eq. (46), is equal to the frequency of the incident sound. The appropriate Strouhal number can then be read from Figure 6, thus determining the bias flow velocity. This procedure was adopted to design the highly absorptive panel in Figure 5a.

We now turn our attention to parallel slits. Where there is no bias flow, $\phi = 1$ and η reduces to $\pi/2d\ell n(2/\pi v)$. There is then a resonance for incident sound for which

$$2k_1 d \, \ell n(2/\pi v) \tan k_1\ell = \pi. \tag{47}$$

Since $k_1 d$ is small, $\tan k_1\ell$ must be large at the resonance condition, i.e.

$$k_1\ell \simeq (n + \tfrac{1}{2})\pi \text{ for some integer n.} \tag{48}$$

46

When there is a mean bias flow through the screen,we might expect the maximum absorption to occur near the resonance condition in Eq. (48). This is confirmed by both the experimental and theoretical results in Figure 7. There is good agreement between theory and experiment and again high levels of absorption can be achieved if the plate parameters and the bias flow are chosen appropriately.

To design a backed screen, which will absorb all the sound of frequency ω incident at an angle θ, the cavity depth should be chosen so that $k_1\ell=\pi/2$. Next a convenient value of d/ℓ may be specified. Finally υ and M must be chosen to ensure that the absorption coefficient at $k_1\ell=\pi/2$ is unity. Plots of the form shown in Figure 8 aid this choice. They show that in fact there is a family of optimal pairs (υ,M). The designer can choose among them. A comparison of Figures 8a and 8b shows that the absorption coefficient is only weakly dependent on the ratio d/ℓ.

CONCLUSIONS

The generation of sound by vorticity has been reviewed within a unified framework and the scattering effects of surfaces have been discussed. In particular, it is shown that the additional vorticity shed at the rim of an aperture in a rigid screen can significantly reduce the scattered monopole field. The same mechanism can convert the energy in an incident sound wave into unsteady vortical flow. Criteria are given for designing perforated panels which absorb all the incident sound energy at a particular frequency.

REFERENCES

[1] Lighthill, M.J., 'On sound generated aerodynamically, Part I, General Theory', Proc. Roy. Soc. Lond. A 211, 564-587 (1952).

[2] Powell, A., 'Theory of vortex sound', J. Acoust. Soc. Amer., 36, 177-195 (1964).

[3] Powell, A., 'Aerodynamic noise and the plane boundary', J. Acoust. Soc. Amer., 32, 982-990 (1960).

[4] Obermeier, F., 'The influence of solid bodies on low Mach number vortex sound', J. Sound Vib., 72, 39-49 (1980).

[5] Kambe, T., Minota, T. & Ikushima, Y., 'Acoustic waves emitted by vortex-body interaction', Proc. IUTAM Symposium on Aero- and Hydro-Acoustics. Springer-Verlag, 21-28 (1986).

[6] Kambe, T., 'Acoustic emissions by vortex motions', J. Fluid Mech., 173, 643-666 (1986).

[7] Howe, M.S., 'On the theory of unsteady high Reynolds number flow through a circular aperture', Proc. Roy. Soc. Lond. A 366, 205-223 (1979).

[8] Dowling, A.P. & Hughes I.J., 'Sound absorption by a screen with a regular array of slits', J. Sound Vib. (to appear).

[9] Hughes, I.J. & Dowling A.P., 'The absorption of sound by perforated linings', J. Fluid Mech., 218, 299-335.

[10] Howe, M.S., 'Contributions to the theory of aerodynamic sound, with application to excess jet noise and the theory of the flute', J. Fluid Mech., 71, 625-673 (1975).

[11] Howe, M.S., 'The generation of sound by aerodynamic sources in an inhomogeneous steady flow', J. Fluid Mech., 67, 597-610 (1975).

[12] Hardin, J.C. & Pope, D.S., 'Ring vortex/cylinder sound production revisited', AIAA J., 26, 1163-1167 (1988)

[13] Mohring, W., 'On vortex sound at low Mach number', J. Fluid Mech., 85, 685-691 (1978).

[14] Lamb, H., Hydrodynamics, Cambridge University Press (1975).

[15] Copson, E.T., 'On the problem of the electrified disc', Proc. Edinb. Math. Soc., 3, 14-19 (1947).

[16] Rayleigh, J.W.S., The Theory of Sound, Vol. 2, Dover (1945).

[17] Ffowcs Williams, J.E., 'The acoustics of turbulence near sound-absorbent liners', J. Fluid Mech., 51, 737-749 (1972).

[18] Crighton, D.G., 'The Kutta condition in unsteady flow', Annual Review of Fluid Mechanics, 17, 411-445 (1985).

[19] Tranter, C.J., Integral Transforms in Mathematical Physics, Chapman & Hall (1966).

[20] Leppington, F.G. & Levine, H., 'Reflexion and transmission at a plane screen with periodically arranged circular or elliptical apertures'. J. Fluid Mech., 61, 109-127 (1973).

APPENDIX

Expanding the solution of $\nabla^2 \psi = \delta(x-y)$ in cylindrical polar coordinates shows that

$$\frac{1}{(y_1^2 + \rho^2 - \sigma^2 - 2\rho\sigma \cos(\psi-\theta))^{1/2}} = \frac{2}{\pi} \int_0^\infty \sum_{n=0}^\infty a_n I_n(k\rho) \, K_n(k\sigma) \, \cos n(\psi-\theta) \, \cos(ky_1) dk$$

for $\rho < \sigma$, where $a_0 = 1$, $a_n = 2$, $n \geq 1$. $\qquad$ (A1)

For the form on the right-hand side of Eq. (A1) it is easy to evaluate the ψ and y_1 integrals in Eq. (28).

$$\int_0^\infty \int_0^{2\pi} \frac{e^{i\kappa y_1} \, d\psi \, dy_1}{(y_1^2 + \rho^2 + \sigma^2 - 2\rho\sigma \cos(\psi-\theta))^{1/2}} = 4i\kappa \int_0^\infty \frac{I_0(k\rho) \, K_0(k\sigma) \, dk}{\kappa^2 - k^2} \, . \qquad (A2)$$

After differentiation with respect to σ, this leads to

$$\int \frac{\partial}{\partial\sigma} \left[\frac{1}{y_1^2 + \rho^2 + \sigma^2 - 2\rho\sigma \cos(\psi-\theta)} \right]^{1/2}_{\sigma=a} e^{i\kappa y_1} \, d\psi dy_1 = -4i\kappa \int_0^\infty \frac{I_0(k\rho) \, K_1(ka) \, kdk}{\kappa^2 - k^2} \, . \qquad (A3)$$

Howe [7] shows how the contour of integration in the last term in Eq. (A3) may be rotated in the clockwise direction onto the negative imaginery axis. In this way, we obtain

$$\int \frac{\partial}{\partial\sigma} \left[\frac{1}{y_1^2 + \rho^2 + \sigma^2 - 2\rho\sigma \cos(\psi-\theta)} \right]^{1/2}_{\sigma=a} e^{i\kappa y_1} \, d\psi dy_1 = -2\pi i\kappa \int_0^\infty \frac{\lambda H_1^{(1)}(\lambda a) J_0(\lambda\rho) d\lambda}{\kappa^2 + \lambda^2} : \quad (A4)$$

a result that is used in Eq. (29).
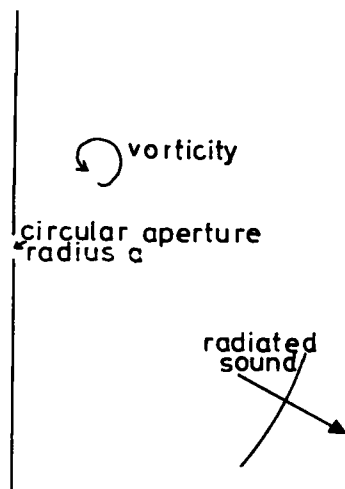
Figure 1 Scattering of sound by a circular aperture.
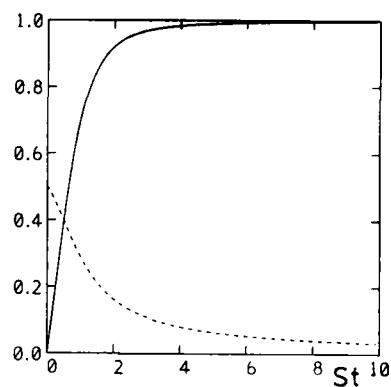
Figure 2 The variation of α with Strouhal number; ___ $|\alpha(St)|$, _____ - phase $\alpha(St)/\pi$.
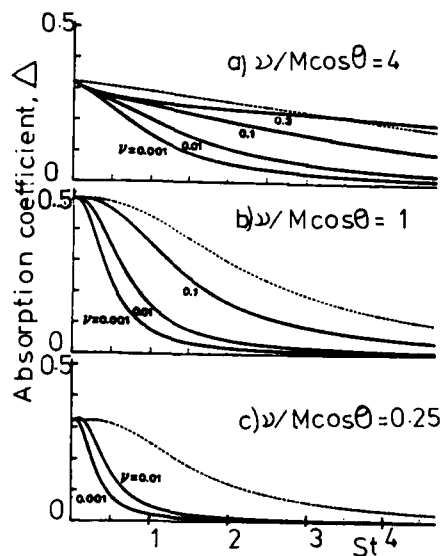
Figure 3 The absorption coefficient of a perforated screen as a function of St; ___ slits $(St=\omega s/U)$, --- circular apertures $(St=\omega a/U)$.
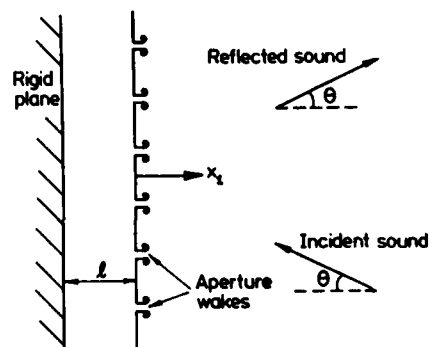
Figure 4 The geometry of the backed screen.

49
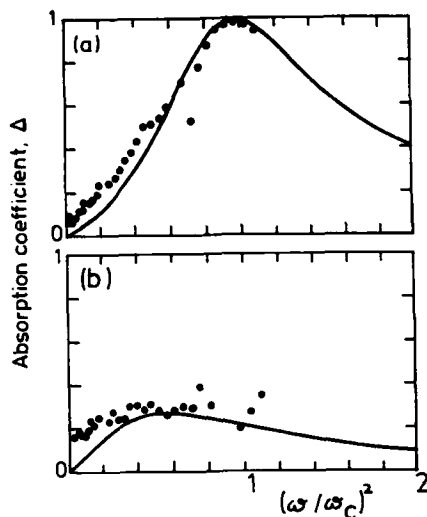
Figure 5 The absorption coefficient for a backed screen with circular apertures when a) $M = 0.014$, $a/\ell = 0.15$, $v = 0.025$, b) $M = 0.052$, $a/\ell = 0.032$, $v = 0.11$. ___ theory, • experiment [from 9].

Figure 6 The absorption coefficient for a backed screen with circular apertures at frequency ω_c [from 9].

Figure 7 The absorption coefficient for a backed screen with slits for $v = 0.1$, $d/\ell = 0.2$, $\theta = 0$;
$M = 0.06$, ___ theory,
• experiment, microphone spacing 91mm,
x experiment, microphone spacing 69mm
$M = 0.015$, --- theory,
o experiment, microphone spacing 91mm.
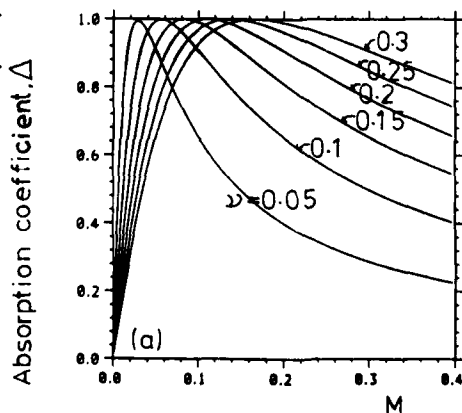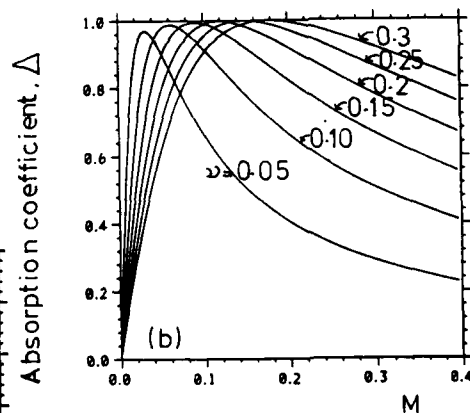
Figure 8 The absorption coefficient for a backed screen with slits as a function M for a) $d/\ell = 0.1$, b) $d/\ell = 0.2$, $\theta = 0$ and various v.

50

NUMERICAL PREDICTIONS IN ACOUSTICS

Jay C. Hardin
NASA Langley Research Center
Hampton, Virginia 23665-5225
U.S.A.

ABSTRACT

Computational Aeroacoustics (CAA) involves the calculation of the sound produced by a flow as well as the underlying flowfield itself from first principles. While one might think this endeavor would be a straightforward application of standard computational fluid dynamics (CFD) techniques, one soon finds that the physics of sound fields require careful tailoring of numerical approaches for successful aeroacoustic computations.

This paper describes the numerical challenges of CAA and recent research efforts to overcome these challenges. In addition, it includes the benefits of CAA in removing restrictions of linearity, single frequency, constant parameters, low Mach numbers, etc. found in standard acoustic analyses as well as means for evaluating the validity of these numerical approaches. Finally, numerous applications of CAA to both classical as well as modern problems of concern to the aerospace industry are presented.

INTRODUCTION

Classical acoustics considered small perturbations produced by a given source of sound in an ambient or, at most, a uniformly moving medium. The governing equations were linearized, restricting their validity to low Mach number, usually assumed a constant speed of sound, and often specified the source to be harmonic.

The first significant departure from this classical approach was made by Lighthill[1] who considered sound generation by turbulent jets. His theory retained the appearance of linearity, but did not specify the source, which appeared in the analysis through the nonlinear terms. Although Lighthill's work was a monumental advance, practical applications of his theory were still limited to low Mach numbers.

With the development of larger and faster computers, the field of Computational Aeroacoustics, where the sound produced by a flow as well as the underlying flowfield itself is computed from first principles, has become a practical reality. However, such calculations are not trivial extensions of compressive computational fluid dynamics codes, which are usually developed for steady flows and are thus designed to damp out oscillations, but must be carefully tailored to extract the acoustic quantities of interest. Successful CAA calculations must overcome the challenges produced by the small size and high frequencies of the quantities of interest, which

make damping and dispersion of waves undesirable, and the need for long time solutions, nonreflecting boundary conditions in greater than one dimension, as well as the nonlinear behavior at higher Mach numbers.

GOVERNING EQUATIONS

The complete set of equations[2] governing fluid flow are:

Mass

$$\frac{D\rho}{Dt} + \rho \nabla \cdot \vec{u} = 0 \tag{1}$$

Momentum

$$\rho \frac{Du_i}{Dt} = \rho F_i - \frac{\partial p}{\partial x_i} + \frac{\partial}{\partial x_i}\left[2\mu\left(e_{ij} - \frac{1}{3}\Delta\delta_{ij}\right)\right] \tag{2}$$

Energy

$$T\frac{DS}{Dt} = c_p \frac{DT}{Dt} - \frac{\beta T}{\rho}\frac{Dp}{Dt} = \phi + \frac{1}{\rho}\frac{\partial}{\partial x_i}\left(k\frac{\partial T}{\partial x_i}\right) \tag{3}$$

State

$$f(p, \rho, T) = 0 \tag{4}$$

which consist of six equations for the six unknowns, the density, ρ, pressure, p, temperature T, and three velocity components, u_i, if the energy equation is viewed as defining the entropy per unit mass, S. Here, F_i is the applied body force per unit mass, c_p, k, μ, and β are the specific heat at constant pressure, and coefficients of thermal conductivity, viscosity and thermal expansion respectively. Also, e_{ij} is the rate of strain, $\Delta = e_{ii}$, and ϕ is the viscous dissipation.

Air at normal temperatures and pressures is well approximated as a perfect gas[2] with constant specific heats. Thus, the equation of state may be taken to be

$$p = \rho RT \tag{5}$$

where R is the gas constant. If this relation is employed in Eq. (3), the energy equation may be integrated to show that

$$S - S_o = c_v \log(p/\rho^\gamma) \tag{6}$$

where c_v is the specific heat at constant volume and $\gamma = c_p/c_v = 1.4$. Finally, Eq. (6) may also be utilized to define the speed of sound, c, in the medium as

$$c^2(T) = \left(\frac{\partial p}{\partial \rho}\right)_s = \gamma RT$$

NUMERICAL SOLUTIONS

The governing equations developed above may, in theory, be solved numerically for the sound produced by any fluctuating fluid flow. Such "direct simulations" have been attempted by

several authors, including Brentner[3], Watson[4], and Lele[5], with varying degrees of success. These mixed reviews are not surprising when one considers the difficulties inherent in the calculation, especially for viscous flows.

The first of these difficulties might be called the "dynamic range" problem. Hydrodynamic pressure fluctuations in turbulent flows are typically of the order of 10^{-2} of the ambient pressure, while an intense sound wave (100 dB) is produced by pressure fluctuations of the order of 10^{-5} of the ambient pressure. Thus, the waves one is seeking are tiny compared to other fluctuations in the flow. Further, the frequencies of interest of these waves are typically of the order of kilohertz, since that is where the ear is most sensitive. However, numerical algorithms usually act as low pass filters. For example, consider the simple forward difference

$$\frac{d\hat{f}}{dt} = \frac{f(t + \Delta t) - f(t)}{\Delta t}$$

applied to estimate the derivative of a harmonic function of frequency ω, $f(t) = e^{i\omega t}$. One finds

$$\frac{d\hat{f}}{dt} = \left[\frac{\sin\frac{\omega\Delta t}{2}}{\frac{\omega\Delta t}{2}} \right] e^{i\omega\frac{\Delta t}{2}} \frac{df}{dt} \tag{7}$$

resulting in an amplitude dissipation given by the bracketed term in Eq. (7) and a dispersive phase error $\omega\Delta t/2$. Figure 1 displays the dissipative error as a function of frequency. Clearly, $\omega\Delta t$ must be very small for the acoustic frequencies of interest, or this error, which occurs every time step, will soon damp out the acoustic waves. It should be noted that this error can be reduced, but not eliminated, by more sophisticated higher order numerical schemes.

A second difficulty might be called the "multiple scales" problem. In a viscous flow, the smallest energy dissipating eddies have sizes which scale on the inverse of the Reynolds number, while acoustic waves have wave lengths that are proportional to the speed of sound. Thus, the acoustic scales of interest are ordinarily much larger than the smallest scales in the flow. Since numerical spatial derivatives have the same low pass characteristic as seen earlier for temporal derivatives, the requirements to both resolve the viscous scales and have a reasonable number of wavelengths of the acoustic field in the computational domain usually result in a prohibitive number of grid points. This has led to various low wavenumber approaches[6], such as Large Eddy Simulation (LES) and Renormalization Group Theory (RNG), which attempt to model the energy drain to small scales and compute only the larger ones. These techniques are based on the concept that the larger flow structures should be most efficient in radiation of sound. Other approaches compute only the near hydrodynamic field and use the Kirchhoff theory to determine the acoustic field[6] or attempt to split the viscous and acoustic parts of the problem[7].

A third difficulty might be called the "anisotropy" problem. If one considers the two dimensional wave equation

$$P_{tt} = c^2\left(P_{xx} + P_{yy}\right)$$

which is much simpler than the equations of interest, but to which they reduce for small perturbations in an ambient, 2D medium, one finds that the continuous equation admits the solution

$$P(x,y,t) = e^{i(\omega t - k_1 x - k_2 y)}$$

53

where $k_1^2 + k_2^2 = k^2$ and $k = \dfrac{\omega}{c}$ is the acoustic wavenumber. This solution corresponds to a plane wave propagating in the direction $\theta = \arctan(k_2/k_1)$ with respect to the positive x-axis. If one then discretizes the wave equation using second order central differences, one finds that the solution to the continuous equation will also be a solution to the discrete equation if and only if

$$\beta^2\left[1 - \cos\frac{k_1 c\Delta t}{\beta}\right] + \gamma^2\left[1 - \cos\frac{k_2 c\Delta t}{\gamma}\right] \qquad (8)$$

$$= 1 - \cos k c\Delta t$$

where $\beta = c\Delta t/\Delta x$ and $\gamma = c\Delta t/\Delta y$ are the CFL numbers in the two coordinate directions. The solution of equation (8)

$$\beta = \frac{k_1}{k} \qquad\qquad \gamma = \frac{k_2}{k} = \frac{\sqrt{k^2 - k_1^2}}{k}$$

which is plotted on Figure 2, shows that the optimum numerical parameters depend not only on the frequency of the wave, but also on its direction of propagation! Thus, numerical acoustic solutions are very sensitive to the grid employed in their computation. Physically, the optimum requires the next grid point to be at precisely the distance the wave will travel in one time step. Clearly this cannot be achieved in the general case and thus frequency and direction dependent dissipative and dispersive errors will creep into the solution. Again these errors can be reduced, but not eliminated, by more sophisticated numerical schemes such as the Finite Volume Method[3].

A final difficulty which might be mentioned is the need for "nonreflecting" boundary conditions. Typically, one is interested in radiation into an unbounded medium, but the computational domain is of necessity bounded. Thus, one must prescribe suitable conditions at the computational boundaries such that outgoing waves are not reflected. In one dimension, this is a straightforward task, but in higher dimensions, where waves can strike the boundary non-normally, development of nonreflecting conditions is more problematic. Some success has been achieved using characteristic conditions[4] and asymptotic conditions[8] based on an assumed form for the farfield solution.

VALIDATION

In spite of the difficulties mentioned above, significant progress toward the development of numerical solutions to acoustic problems, i.e. CAA, has been made. Most of this work has been of the nature of building a firm foundation of understanding upon which later work could stand.

In one dimension, the classical problems of a piston in a pipe and a pulsating sphere have been solved and compared with the standard linearized solutions at low Mach number. Figure 3 shows such a comparison. Here the numerical scheme[7] solved the complete set of inviscid governing equations using a MacCormack predictor-corrector scheme with $\beta = c\Delta t/\Delta r = 1/1+M$. As can be seen, the solutions at M=0.05 are identical. At higher Mach number, the numerical solutions have been compared with a perturbation series solution[9] to the full set of equations. For the piston in pipe problem, the numerical results agreed exactly with only one term of the perturbation series, even for Mach numbers where significant nonlinear effects were apparent. However, for the spherical pulsating sphere problem, differences are seen even with two terms of the perturbation series. Such a comparison is shown in Figure 4 at M=0.3. Here, the density perturbation has been multiplied by the distance r to remove the spherical spreading. Note that the numerical solution appears to steepen more quickly than the perturbation series result. Which of these results is correct and the reason for the discrepancy is still being explored.

In two dimensions, the problems of a pulsating sphere, piston in wall, accelerating cylinder, and sound propagation in a variable area duct with flow have been explored. The first, second, and some cases of the fourth of these problems are classical and thus linearized solutions exist for validation. A nonlinear perturbation series solution[9] has also been obtained for the first of these problems. Figure 5 displays a comparison between a MacCormack numerical scheme[4] and the linear theory for a straight duct carrying $M=0.5$ flow into which a low amplitude non-planar acoustic wave is inserted. Characteristic boundary conditions are employed at inflow and outflow. This work goes on to look at variable area ducts where no analytic solutions are available. Figure 6 displays the density perturbation radiated by a cylinder impulsively accelerated to $M=0.4$. Here, density is normalized by $r^{1/2}$ to remove the cylindrical spreading. This calculation[3] was achieved using the five stage time stepping method of Jameson. Although no analytic solution is available for this problem, the solution error was measured by computing the entropy of the solution, which should be zero in this invisid flow in the absence of shocks. The entropy was found to vary significantly with the fineness of the grid, again emphasizing the anisotropy problem in two dimensions.

Viscous flow computations in two dimensions include the compressible free shear layer work of Lele[5] mentioned earlier who compared a direct simulation with an acoustic analogy approach[1] yielding reasonable agreement. In addition, the present author and Lamkin are attempting such a comparison for the Aeolian tone radiation produced by uniform flow into a stationary cylinder.

In three dimensions, little work has been attempted due to the prohibitive cost of the computations. Berman and Orszag[10] are in the process of computing noise from a circular, but not assumed axisymmetric, jet using a spectral technique in conjunction with RNG modelling of the small scales. A preliminary result for the farfield noise spectrum at 90° to the jet axis of a $Re=10,000$ and $M=1$ jet is shown in Figure 7 as a function of Strouhal number. Note that the expected peak near the Strouhal number of 0.3 is not observed which may be attributed to aliasing from high wave numbers.

CONCLUSION

This paper has considered the development of Computational Aeroacoustics (CAA) where the sound radiation by a flow, as well as often the flow itself, are numerically computed from the full governing equations. The advantages and difficulties of this approach in addition to methods of verification and examples of its use are discussed. It may be concluded that the computational power to handle such problems, at least in two dimensions, now exists. Further, the physics of sound fields require tailoring of standard compressible fluid dynamic codes in order to successfully extract acoustic information.

REFERENCES

1. Lighthill, M. J.: On Sound Generated Aerodynamically. I. General Theory, Proc. Roy. Soc., Ser. A, Vol. 211, No. 1107, pp. 564-587. 1952.

2. Batchelor, G. K.: An Introduction to Fluid Dynamics, Cambridge University Press, 1967.

3. Brentner, K. S.: The Sound of Moving Bodies, Cambridge University Thesis, Dec. 1990.

4. Watson, W. R.: A Time Domain Numerical Theory for Studying Steady-State Acoustic Disturbance in Flow, George Washington University Thesis, 1991.

5. Lele, S. K.: Acoustic Radiation from Compressible Free Shear Layers, Private Communication, 1990.

6. Berman, C. and Ramos, J.: Simultaneous Computation of Jet Turbulence and Noise, AIAA Paper No. 89-1091, 1989.

7. Hardin, J. C. and Pope, D. S.: A New Technique for Aerodynamic Noise Calculation. To be presented at DGLR/AIAA 14th Aeroacoustics Conference, Aachen, Germany, May 11-14, 1992.

8. Bayliss, A. and Turkel, E.: Radiation Boundary Conditions for Wave-like Equations, Comm. Pure Appl. Math., Vol. 33, pp. 707-726, 1980.

9. Geer, J. F. and Pope, D. S.: Sound Generation by Vibrating Bodies—A Multiple Scales Approach, Private Communication, 1991.

10. Berman, C. and Orszag, S.: Direct Computation of Jet Noise, Private Communication, 1991.
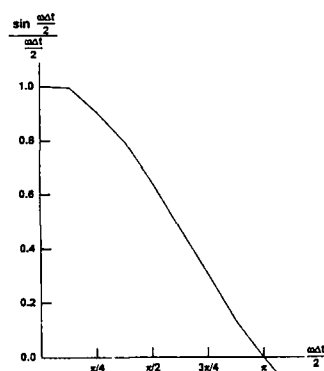
Figure 1: Frequency/Time Step Restriction
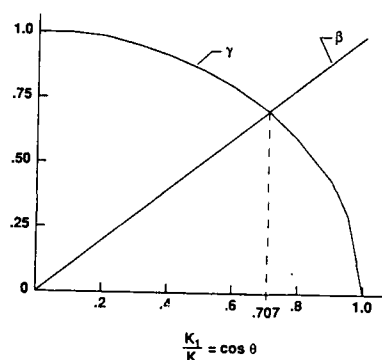
Figure 2: Optimum Numerical Parameters
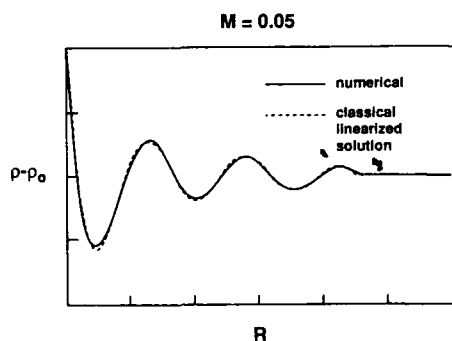
Figure 3: Pulsating Sphere Comparison
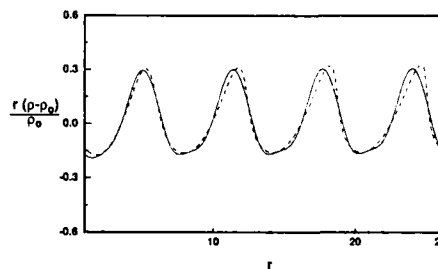
Figure 4: Pulsating Sphere Comparison, M=0.3,—Numerical, ---Perturbation Series
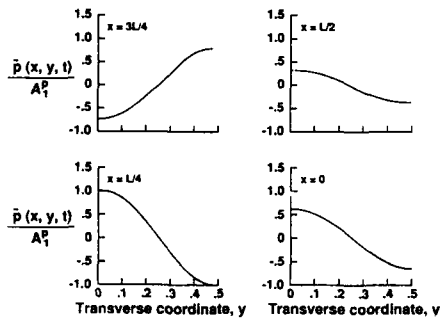
Figure 5: Duct Flow Comparison, M=0.5,
Theory and Numerical
Indistinguishable
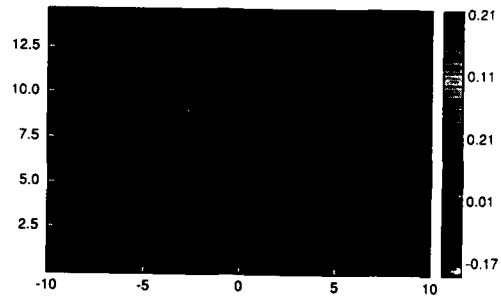
Figure 6: Accelerating Cylinder Radiation,
$r^{1/2}\rho'$ plotted

Figure 7: Predicted Jet Noise Spectrum

The Broadband Noise Generated by Very High Temperature, High Velocity Exhausts

S. A. McInerny
Dept. of Mechanical Engineering, California State University
1250 Bellflower Blvd., Long Beach, CA 90840-5005

ABSTRACT

The far-field noise of rockets is primarily generated by turbulence in the transonic region of the plume. Turbulence convection velocities in this region scale on the speed of sound in the exhaust, C_e. These convection velocities are supersonic with respect to the speed of sound in the atmosphere, resulting in a high acoustic radiation efficiency and large angle of maximum directivity. Since C_e is the characteristic flow velocity in this region, a dimensionless frequency based on the exhaust velocity, fD/U_e, results in a very low peak Strouhal number in the sound power spectrum. In this paper, properties of the rocket exhaust plume and their relationship to the radiated noise are examined and contrasted to those of lower temperature supersonic jets. It is concluded that extrapolations based on supersonic jet data are unreliable unless the data includes jets for which $U_e/C_e \gg 1$ and $C_e/C_o \geq 1.4$.

NOMENCLATURE

f frequency in Hz
p static pressure
C_e speed of sound in the exhaust at the nozzle exit plane
D nozzle exit diameter
ER nozzle expansion ratio (ratio of exit area to throat area)
L_c length of the laminar core
L_s length of the supersonic core
LOX/LH_2 liquid engines fueled by liquid oxygen and liquid hydrogen
$LOX/RP-1$ liquid engines fueled by liquid oxygen and rocket propellant (high grade carbon fuel)
$M_e = V_e/C_e$ Mach number based on flow velocity and speed of sound in the flow
$M_o = V_e/C_o$ Mach number based on flow velocity and speed of sound in the atmosphere
M_{c1}, M_{c2} convective Mach number of large scale turbulence structures on the high and low speed sides, respectively, of a two-dimensional shear layer, $M_{c1} = \frac{U_1 - U_c}{C_1}$ and $M_{c2} = \frac{U_c - U_2}{C_2}$
$SRBs$ solid rocket booster engines
$SSMEs$ second stage main engines on the Space Shuttle
T mean exhaust temperature (absolute) at nozzle exit plane
U_e exhaust velocity at nozzle exit plane
U_1, U_2 freestream velocities on high and low speed sides, respectively, of two-dimensional shear layer
γ_e ideal gas constant of the exhaust at the nozzle exit plane
ρ_e exhaust density at nozzle exit plane

INTRODUCTION

The experimental studies of Cole, von Gierke, et al [3, 1957] and Mayes et al [18, 1959], among others, established the key characteristics of rocket noise. These studies were followed by work by Ffowcs-Williams [7, 1963] and Lighthill [15, 1963] that clarified the dependence of the overall sound power on the flow velocity and provided a qualitative explanation of the high radiation efficiency and large directivity angle as consequences of

Mach wave radiation from turbulence in the plume. However, many aspects of the generation and radiation of rocket noise remained unclear. More recent work on supersonic shear layers and supersonic jets has provided an explanation for the extended length of the laminar core. Much of the theoretical work has been concerned with the spatial instability of the shear layer. This studies have identified the nature of the dominant flow disturbances in the shear layer as well as their phase velocities and wavenumbers, primarily for cold supersonic jets. However, these studies do not permit the prediction of laminar or supersonic core lengths and until recently (see Tam [30, 1989]) have not been extended to the high temperatures typical of rocket exhausts. See Table I.

The transition from instability waves to fully developed turbulence at the end of the laminar core with a subsequent transition from supersonic to subsonic flow is a very complex process, even for perfectly expanded flows. This process depends not only on the exhaust Mach number, $M_e = U_e/C_e$, but also on the ratio of the speed of sound in the flow to that of the ambient fluid, C_e/C_o. It is likely that this process will continue to elude prediction by theoretical and numerical methods for (at least) another decade.

Table 1: Typical Rocket Exhaust Parameters at Nozzle Exit Plane

	Titan solids	Saturn V	Saturn IB	Shuttle SSMEs
Engine Type	solids	LOX/RP-1	LOX/RP-1	LOX/LH$_2$
Nozzle ER	10	16	8	(55-75)
C_e - m/s	780	890	950	860
γ_e	1.19	1.2	1.2	1.23
ρ_e/ρ_o	0.12	0.06	0.09	0.04
T_e/T_o	6.2	6.9	7.3	4.5
p_e/p_o	0.71	0.48	0.78	0.20
V_e - m/s	2500	2900	2850	4000
V_e/C_e	3.2	3.5	3.0	4.7
V_e/C_o	7.4	9.0	8.4	11.8

OVERALL SOUND POWER

For high thrust rockets ($\geq 7 \times 10^5$N) the mean overall sound power is well predicted as 0.5% of the engine mechanical power.[25,6,15,9] The engine mechanical power, W_m, is equal to one half the product of the thrust, T, times the exhaust velocity. Thus, the overall acoustic power radiated by a rocket can be expressed as

$$W_a = \eta \frac{1}{2} T U_e \qquad (1)$$

where η is generally taken to be 0.005. This is to be compared to an efficiency of $10^{-4} M_e^5$ for subsonic jets.[15, Fig. 4] The high acoustic radiation efficiency of rockets was explained by Ffowcs-Williams [7] and Lighthill [15] to be the result of Mach wave radiation.

The thrust, neglecting a small pressure contribution when the flow is imperfectly expanded, is proportional to U_e^2. This results in a U_e^3 dependence for the noise generated by rockets, as predicted by Ffowcs-Williams [7], Lighthill [15] and later by Tam.[29] This prediction of Ffowcs-Williams was based on an order of magnitude estimate using the nozzle exhaust velocity as the characteristic velocity (for a stationary nozzle) and the nozzle exit diameter as the characteristic length scale. Although these scales do not appear appropriate without modification for prediction of peak frequencies or the peak radiation angle, the U_e^3 dependence is well established.

Figure 1 from von Gierke[33, 1961] illustrates the transition from the U^8 (or M^5U^3) dependence for subsonic jets to the asymptotic U^3 dependence. On this curve von Gierke has noted that the rocket data shown could equally well be fitted by a C_e^8 dependence if the "jet velocity effective for acoustic radiation" is taken to be "the sound velocity in the flow."[33] Other versions of Fig. 1 can be found in refs. [7,19]. The subsonic U^8 and high high Mach number U^3 dependence of the overall sound power are best illustrated in Ref. [7], where the data are plotted against the exhaust velocity as opposed to the Lighthill parameter.

Ffowcs-Williams also predicted that at sufficiently high Mach numbers ($M_o = U_e/C_o \gg 1$) the acoustic efficiency of a stationary rocket would depend only on the ratio of the mean exhaust density to that of the ambient fluid. Records of rocket noise experiments do not, in general, contain information on densities. Exhaust densities for different types rocket engines designed for lift-off (not highly too overexpanded at sea level) do not vary enough given the additional uncertainties introduced by multiple engine, trajectory and atmospheric effects to draw firm conclusions from launch data. However, the experiments of Hoch et al support Ffowcs-Williams' prediction.[11]

Hoch et al studied the effects of density on jet noise for exhaust velocities that were both subsonic and supersonic with respect to the atmospheric speed of sound. Their data indicate that the overall sound power decreases with decreasing density when $M_o > 1$ and that this decrease is proportional to $(\rho_e/\rho_o)^2$. Since the jet mechanical power is proportional to ρ_e, this finding supports an acoustic efficiency of ρ_e/ρ_o. In their experiments, Hoch et al used air as the working fluid and controlled the density of the exhaust by increasing the temperature. The effect of the variation in C_e/C_o along with ρ_e/ρ_o was not considered. The range of $M_o = U_e/C_o$ investigated was 0.4 to 2.5, whereas $M_e = U_e/C_e$ varied from only 0.4 to 1.2.
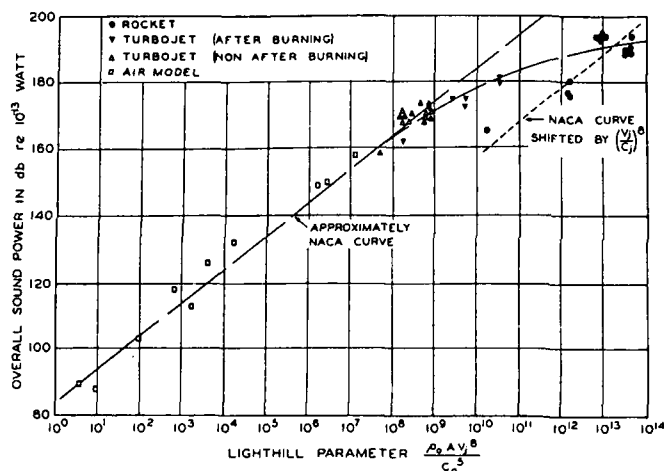
Figure 1. Overall Sound Power of model jets, turbo-jets, and rocket engines as funciotn of the Lighthill parameter. From Ref. [35].

LOCATION OF THE DOMINANT SOURCE REGION

The major sound source region for a rocket is some 25 to 35 exit diameters downstream of nozzle exhaust plane, compared to a distance of four to six diameters for subsonic jets.[25,18,19,6] See Figure 2 from Ref. [33]. This region is concluded to be the transonic region, centered on the supersonic core tip.[3,18,6] See Figure 9. There do not appear to have been, however, any direct measurements of the supersonic core length in rockets (for obvious reasons, see Table I). In fact, in some experimental rocket noise studies the transonic region seems to have been located by the region of maximum sound generation. The conclusion that this was this supersonic core tip was probably based on supersonic jet experiments such as those of Anderson et al [1, 1954] cited in Reference [5, 1963].

It is also unlikey that the length of the laminar core was ever measured in a rocket plume. References provide a variety of formulas for the lengths of the supersonic core, L_s [4,6,20], and the laminar core, L_c [20,14], as functions of M_e. These formulas do not predict asymptotic values for L_c/D and they differ widely in their predictions for values of M_e typical of rockets. Tracing the origin of these formulas, one finds that they are based primarily on supersonic jet data in the range of $M_e = 0.5$ to 2.4, a range of rapid change in behavior and trends.[11,14,13,31,32,27] The influence of temperature (or C_e/C_o) on the laminar core length was investigated over a limited range of M_e by Lau [13] in a follow on study to Ref. [14].

Based on the work of Papamoschou and Roshko [22,23] and Papamoschou [24], the ratio of the laminar core to the nozzle diameter can be expected to have an asymptotic value at high Mach numbers. Papamoschou and Rosko have shown that the dynamics and development of turbulent supersonic shear layers (two dimensional) depend on the convective Mach numbers of the turbulence $M_{c1} = \frac{U_1-U_c}{C_1}$ and $M_{c2} = \frac{U_c-U_2}{C_2}$, where U_c is the convection velocity of the large scale turbulence structures. Papamoschou and Roshko's experiments indicate that the spread rate of highly supersonic shear layers decreases to an asymptotic value of 0.2-0.25 times the incompressible rate as M_{c1} increases from 0.2 to somewhat less than 1.0.[22,23] Presuming these results can be extended to axi-symmetric compressible shear layers (see, for instance, Ref. [10]) L_c/D can be expected to have an asymptotic value four to five times its subsonic value. This places the laminar core tip in a rocket plume some 16 to 22 diameters

downstream of the nozzle exit plane.

It may be that the value of L_s/D also reaches an asymptotic value, but the data of Lau [13] suggests otherwise. Lau found that the mean flow velocity on the jet centerline plotted as a function of x/L_c, where x is the distance downstream of the nozzle exit plane, formed a universal curve. His data included jets in the range of $M_o = 0.3$ to 1.7 and $C_e/C_o = 1.0$ to 1.5. The decay of the mean velocity went through two stages, one upstream of the sonic core tip and one downstream. The rate of decay was more gradual in the supersonic region. Extrapolating (dangerous?) from Lau's Figure 10, one would expect the distance between the laminar and sonic core tips to continue to increase as M_e increases. This was also the conclusion of Nagamatsu et al.[20] The influence of temperature on the core lengths must also be accounted for. Space does not permit an adequate discussion of this dependence, but the laminar core length has been found to decrease, at least initially, with increasing temperature.[13,5]
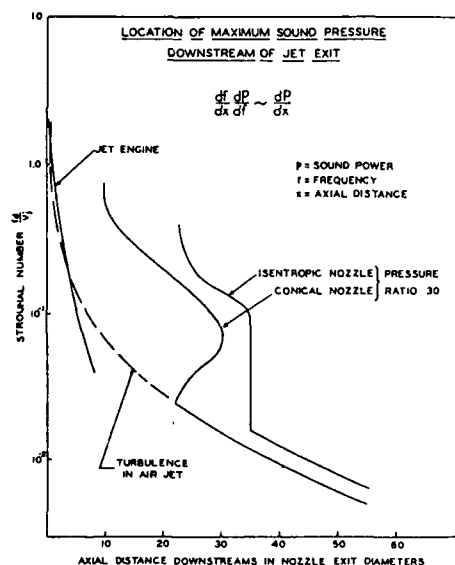
Figure 2. Dimensionless frequency as a function of apparent source position for turbo-jet engine and supersonic nozzles. From Ref. [35].

WHY THE SUPERSONIC CORE?

For any jet with an exit velocity greater than the ambient speed of sound ($M_o > 1$) Mach wave radiation can be expected downstream of the nozzle exit plane. The existence of this Mach wave radiation has been well established using shadowgraphs, schlieren photographs, holographic interferograms and double exposure interferograms. See, for example, Refs. [16,12,26,21]. The intensity of shadowgraphs and schlieren records are proportional to the second and first derivatives, respectively, of the density, so that both techniques are more sensitive to high frequencies and steep wavefronts. Lowson and Ollerhead noted that shadowgraphs of their supersonic jets ($M_e = 2.03$ to 3.17, $M_o = 1.5$ to 2.75, C_e/C_o from 0.58 to 1.3) indicated that the greater part of the sound is generated in the first few diameters, but that this contradicted the results of sound pressure measurements.[16]

Salant et al used holographic interferometry for which the image intensity was said to be proportional to the density.[26] In their photographs the "apparent edge of the jet coincided with the edge of the supersonic core..." It was suggested that "the subsonic mixing region is not visible, since the density difference (from ambient) in this region is too small to be detected." Measurements of density profiles (by Godderum [8]) which indicated a rapid increase in density in the immediate vicinity of the edge of the supersonic core were cited. In the experiments, Salant et al used jets of $M_e = 2.1$ to 2.7, but they were cold jets. Thus it is not suprising that the images did not show Mach wave radiation from, or substantial density fluctuations beyond, the supersonic core.

Oertel has used double exposure interferograms to study the Mach wave radiation of hot supersonic jets.[21] These jets included the range $M_e = 1$ to 4.4 and $C_e/C_o = 0.5$ to 3.2. In the paper reviewed by this author, the transonic region was not studied, but was mentioned as the focus of the next phase in a continuing program. Only one photograph with the transonic region in the field of view was included, but it clearly showed Mach wave radiation from the transonic region. It is not evident, however, what the values of M_e and C_e/C_o were for the jet in this photograph.

In the case of rockets, strong Mach wave radiation can be expected over a distance downstream of the nozzle

as great as thirty to fourty diameters. However, the dominant sound source remains fully developed turbulence. In contrast to subsonic jets it is the turbulence in the transonic region not at the end of the laminar core. As noted by von Gierke, "the supersonic portion of the gas stream radiates only negligible acoustic power."

Consider the case of fully developed, attached turbulent boundary layers. The rms pressure fluctuation at the surface can be expressed as a percentage of the freestream head,

$$p_{rms} = \beta \frac{1}{2}\rho U_\infty^2 \tag{2}$$

where the coefficient β is a function of the freestream Mach number, M_∞.[17,2,30] Data presented by Coe et al [2] indicate a mean value for β of 0.005 to 0.006 for $M_\infty \ll 1$, a large spread in values near $M_\infty = 1$ with a maximum of 0.006, and then a steady decrease to a mean of 0.004 for $M_\infty > 2$. The data in Fig. 66 of Speaker and Ailman [30] show a much more dramatic decrease in β with increasing M_∞ with a mean value of 0.0015 for $M_\infty \gg 1$. One curve in this figure (based on a referenced set of data) indicates a pronounced peak in β at $M_\infty = 1$. The boundary layer spectra presented in Coe et al and Speaker and Ailman also show a consistent decrease in peak levels with increasing Mach number.[30, Fig. 70][2, Fig. 10]. Wind tunnel data measured on a scale model of a launch vehicle fairing (unpublished data), when normalized by the freestream head, showed peak pressure fluctuation levels for M_∞ in the range of 0.8 to 0.9 for transducers located in regions unaffected by shocks. A pressure transducer located just downstream of a model seam that protruded into the boundary layer measured peak levels 5.0 dB greater than at other unperturbed locations on the fairing. Peak normalized pressure power spectral density levels for this transducer decreased 7.0 dB as the freestream Mach number increased from 0.86 to 0.9 (the local Mach number was higher), indicating a high sensitivity to small changes in Mach number.

Based on the "circumstantial" evidence presented in the previous paragraph, the pressure fluctuation coefficient in a rocket plume plume can be expected to increase downstream of the laminar core with a possible peak in the transonic region. Assuming the maximum sound source region is associated with maximum density and pressure fluctuations in the plume, this would help explain the association of maximum sound generation with the transonic region. The additional effects, in Eq. (2), of the increase in mean density and decrease in mean flow velocity have not been considered in this argument. Nonetheless, the transonic region can be expected to generate high level pressure fluctuations due to the extreme sensitivity to disturbances in the transonic flow regime.

OVERALL SOUND POWER DIRECTIVITY

For large rockets, $T > 7 \times 10^5 N$, the predominant radiation angle for overall sound power measured relative to the downstream exhaust axis is between $50°$ and $60°$.[26,6] This is a much larger angle than that for subsonic jets ($20°$ to $30°$) or turbojets. Overall sound power plots for rocket noise indicate a secondary lobe in the forward quadrant that is assumed to be shock associated noise.[11,34,21] Taking the peak directivity to be associated with radiation by turbulence in the transonic region, the angle of maximum sound radiation can be estimated as

$$\theta_{max} \approx cos^{-1} \frac{C_o}{\alpha C_e} \tag{3}$$

where αC_e is the turbulence convection velocity. Using $\alpha = 0.7$ produces values of $\theta_{max} =$ of $51°$ to $60°$ for $C_e = 780$ to 950 m/s typical of rockets (see Table I). This is in good agreement with measured peak directivities. This estimate neglects the effects of heat transfer and entrainment on C_e, which would tend to reduce θ_{max}, and refraction effects due to the high temperature gradients, which would tend to increase θ_{max}.

The ratio of the convection t$\bullet$ freestream velocity, α, for large turbulence structures is not well defined for supersonic shear layers. Papamoschou and Roshko proposed equality of convection Mach numbers, $M_{c1} = M_{c2}$, and obtained a formula which reduces to

$$\alpha(= \frac{U_c}{U}) = \frac{1}{1 + \frac{C_1}{C_2}} \tag{4}$$

for one fluid at rest, i.e. $U_2 = 0$.[23] However, Papamoschou found that the measured convection velocities of large scale structures in a turbulent shear layer, over a wide range of combinations of M_{c1} and M_{c2}, deviated substantially from the predictions of Eq. (4). He concluded that for a supersonic-subsonic shear layer, that is $M_1 > 1$ and $M_2 < 1$, the convection velocity of the large scale turbulence structures approaches the speed of the high speed fluid (i.e $U_c \rightarrow U_1$).[25] In Papamoschou's experiments, C_1 and C_2 were varied by using different gases on the two sides of the shear layer. Salant et al, using cold jets, measured convection velocities (of the structures generating Mach waves downstream of the nozzle) of $0.81 - 0.9 U_e$ for $M_e = 2.1$ and $0.74 - 1.13 U_e$ with an average value of 0.9 for $M_e = 2.6$ and 2.7.[27] These results are similar to those of Papamoschou, but the range of measured convection velocities for two the higher two Mach numbers in Salant's experiments suggests that there may have been two families of waves supported by the jet at these Mach numbers, like those identified by Oertel.

63

Oertel identified three families of wave structures travelling at three different speeds in his interferograms of hot, supersonic jets ($M_e = 1$ to 4.4 and $C_e/C_o = 0.5$ to 3.2).[22] The preferred speeds of these structures, $w'' < w < w'$, could be fitted to the equations

$$w = \frac{U_j}{1 + \frac{C_j}{C_o}} \tag{5}$$

$$w' = \frac{U_j + C_j}{1 + \frac{C_j}{C_o}} \tag{6}$$

$$w'' = \frac{U_j - C_j}{1 + \frac{C_j}{C_o}} \tag{7}$$

where U_j is the jet exit velocity and C_j the speed of sound in the jet. The first equation is identical to Papamoschou and Roshko's Eq. (4). Tam has identified these w waves as Kelvin-Helmholtz instability waves and the other families as supersonic and subsonic instability waves.[32] The subsonic waves are confined mainly to inside the jet and do not radiate sound. Tam predicted that the supersonic instability waves would exist only when

$$U_j > C_j + C_o \tag{8}$$

The cause for differences in the findings of Papamoschou [25], Salant et al [27] and Oertel [22] is not clear. Neither Pamoschou nor Salant measured the velocities predicted by Eq. (4) or (5). Papamoschou measured convection velocities of large scale structures in a turbulent two-dimensional shear layer using schlieren photographs; whereas Salant and Oertel measured velocities of the structures generating Mach waves in a developing annular shear layer using interferograms. Salant's jets were cold, while Oertel's were both hot and cold. What is clear is that the work of Papamoschou and Roshko, Oertel and Tam has introduced yet another significant combination of the variables U_e, C_e and C_o, given by Eq. (8); and that it has not been proven that temperature effects are fully accounted for in C_e. Returning to the convection velocity in the transonic region of a rocket plume, in this region the flow Mach number is near 1 so that use of the subsonic result $U_c \approx 0.7U$ is not unreasonable.

SOUND POWER SPECTRAL DISTRIBUTION

The peak in the sound power spectrum of rocket noise when plotted as a function of fD/U_e is close to 0.018.[6]. Cole, von Gierke, Kyrazis, Eldred, and Humphrey found that a Strouhal number based on the speed of sound in the exhaust, fD/C_e, provided an excellent collapse of rocket data, but did not fully collapse the spectra of rockets and cold, subsonic jets.[3] See Figure 3(a). That fD/C_e did not fully collapse rocket and subsonic jet data might be expected. The characteristic velocity for subsonic jets is less than C_e ($\approx C_o$) and the characteristic length for rockets may be somewhat larger than that for cold jets due to the continued spread of the shear layer from the laminar core to the transonic region. That C_e is the characteristic velocity for rocket noise was clearly seen by von Gierke.[35]

Eldred used a dimensionless frequency of fD_cC_t/V_cC_o.[4] The characteristic diameter, D_c, was taken equal to $D_t(p_t/p_o)$, where D_t was the nozzle throat diameter, p_t the static pressure at the throat, and p_o the atmospheric pressure beyond the nozzle exit plane. The characteristic velocity, V_c, was taken to be the velocity at the nozzle throat. Since the velocity at the throat of a supersonic, converging-diverging nozzle is C_t, this form of the Strouhal number reduces to $(fD_t/C_o)(p_t/p_o)$ for supersonic exhausts. This dimensionless frequency provided an excellent collapse of rocket, turbojet, and subsonic model jet data, as shown in Fig. 3(b) and confirmed by Potter and Crocker.[26] Since this Strouhal number does not depend on the flow conditions at the nozzle exit plane, the peak frequency in the noise spectra of overexpanded, underexpanded, and perfectly expanded supersonic exhausts with the same throat conditions and throat diameter are predicted to be equal. Despite the favorable collapse of data, and presumably due to a lack of theoretical justification, the Strouhal number in Fig. 3(b) was not carried forward by Eldred in later work.[6]

The experiments of Cole et al provided a wealth of information and a few additional findings are worth noting here. Near-field sound pressure levels were found to be strongly related to flame front stability for nozzles and propellants that had re-ignition of the exhaust gases in plume. The noise generated by two solid rockets of equal thrust, one with re-ignition in the plume and the other without, were compared. The near-field SPLs of the engine without reignition were found to be consistently lower. The far-field levels, however, were comparable. The effect of nozzle configurations on the generated noise was also examined "by replacing the standard conical nozzle of unit C (a solid rocket) with an ideally (shock free) expanded nozzle and a 'corrugated' nozzle. Neither the ideal nozzle, nor the corrugated nozzle, caused any significant change in the far field SPL distribution, or, therefore, in PWL from that of the standard nozzle. Examination of the near-field SPL distribution...shows that the near field is definitely affected by the type of nozzle in use. The near field levels produced by the corrugated nozzle were uniformly higher than those of either the standard or ideal nozzles. The greatest increases were at positions

closest to the nozzle and in the higher frequency bands." The "corrugated" nozzle was constructed by adding six, equally spaced, tapered top-hat type sections inside the standard nozzle. These sections did not extend into the throat. Norum and Seiner found a similar result when they introduced a tab at the nozzle lip in their shock noise experiments. They noted that the "use of a tab in convergent-divergent nozzles ... creates shocks of its own that result in an excess high frequency broadband noise."[21] These tabs were used to eliminate screech (not generated by rockets). The measurements of Cole et al did not include the forward quadrant where differences in shock noise levels might have been measured.

Cole et al's nozzle evaluation included studying the effects of a "jetavator." This consisted of a ring that extended 180° around the outside of the nozzle and pivoted "in such a fashion as to inpinge into the jet stream." The practical use of the "jetavator" was as a control surface used to effect guidance of the rocket in flight. It was found that "when the jetavator moved into the flow boundary there was an immediate and significant reduction in near field sound pressure levels. ...this reduction was greatest in the low frequencies, being 10-15 dB below the levels generated with no jetavator in the stream." This reduction in levels was correlated with a stabilization in the flame front in the plume; the jetavator moved the flame front up to the nozzle and stopped the flame front oscillations. However, "the far field levels and consequently the acoustic power were not significantly affected by changes in the flame front caused by the jetavator action."
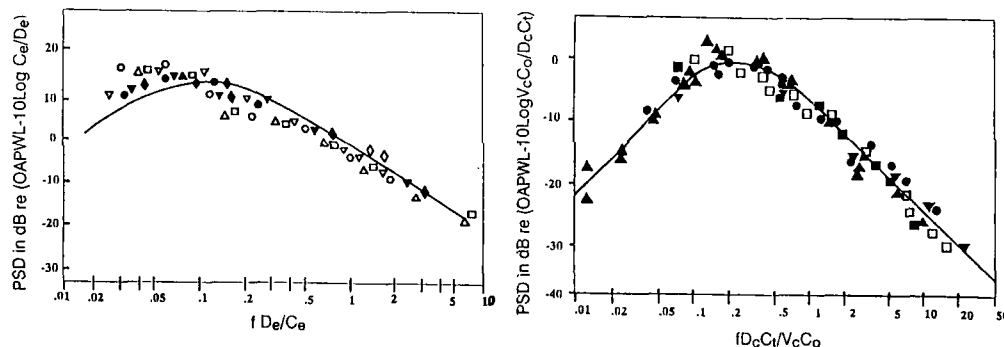
Figure 3. Dimensionless Rocket Noise Spectra. In a) from Ref. [3] the smooth solid curve is "the average of rocket, turbo-jet, and model jet data," symbols are rocket data for thrusts from 4450 N to 578,000 N, including solids and liquids. Data in b) from Ref. [4] includes afterburners, turbo-jets at military power, and supersonic and subsonic air jets.

CONCLUSION

The far-field sound power of rockets is controlled by turbulence in the transonic region of the plume. The characteristic velocity is the speed of sound in the exhaust, as seen by von Gierke.[35] Supersonic jet noise studies cannot be expected to accurately predict far-field rocket noise trends unless $M_e \gg 1$ and $C_e/C_o > 1.4$. The first condition guarantees an extended laminar core length of 16 to 22 diameters. The second insures that convection velocities in the transonic region remain supersonic with respect to the atmosphere. Differences in the normalized distance from the laminar core to the transonic region and, correspondingly, the extent of the dominant source region may require even greater values of C_e/C_o for similarity with rockets. Results obtained using supersonic jets in the range of $M_e = 0.7$ to 2.0 should not be extrapolated to higher Mach numbers as this is a region of rapid change in trends. Although turbulence in the transonic region controls the peak sound power levels in the far-field, shock noise appears responsible for the secondary lobe in the forward quadrant of the far-field directivity plots. Unlike peak far-field levels, shock noise in rockets may be sensitive to changes in nozzle configurations and protusions into the shear layer at nozzle exit plane. Cole et al found that near-field sound pressure levels are affected by such changes and that when re-ignition occurs in the plume the near-field levels are strongly correlated with the flame fronts.[3] These findings and the implications of the work of Tam (see Eq. 8) suggest that near-field sound pressure levels generated by rockets can never be modelled using cold jets.

ACKNOWLEDGEMENT

References

[1] Anderson, Arthur, and Johns, Frank, "Non- Dimensional Characteristics of Free and Deflected Supersonic Jets Exhausting in Quiescent Air," WADC-ED-5401, March 1954.

[2] Coe, C. F., Chyu, W. J., and Dods, J. B., Jr., "Pressure Fluctuations Underlying Attached and Separated Supersonic Turbulent Boundary Layers and Shock Waves," AIAA Paper 73-996, AIAA Aero-Acoustics Conference, 15-17 October 1973.

[3] Cole, J.N., von Gierke, H.E., Kyrazis, D.T., Eldred, K.M., Humphrey, A.J., "Noise Radiation from Fourteen Types of Rockets in the 1,000 to 130,000 Pounds Thrust Range," WADC Technical Report 57-354, December 1957.

[4] Eldred, K.,"Prediction of Sonic Exposure Histories," *Proceedings FATIGUE of Aircraft Structures*, WADC TR59-507, Wright Air Development Center, pp. 396-415, 11-13 August 1959.

[5] Eldred, K.E., White, R., Mann, M. and Cottis, M., "Suppression of Jet Noise with Emphasis on the Near Field," ASD-TDR-62-578, February 1963.

[6] Eldred, K. M., "Acoustic Loads Generated by the Propulsion System," NASA SP-8072, June 1971.

[7] Ffowcs Williams, J. E., "The Noise From Turbulence Convected at High Speed," *Phil. Trans. Roy. Soc. London*, vol. 255, pp. 469-503, 1963.

[8] Godderum, P. B., et. al., NACA Report 963, 1950. S

[9] Guest, S. H., "Acoustic Efficiency Trends for High Thrust Boosters," NASA Technical Note TN D-1999, July 1964.

[10] Gutmark, E., Schadow, K.C., and Wilson, K.J., "Effect of convective Mach number on mixing of coaxial circular and rectangular jets," *Phys. of Fluid A*, Vol. 3, No. 1, pp. 29-36, Jan. 1991.

[11] Hoch, R.G., Duponchel, J.P., Cocking, B.J., and Bryce, W.D., "Studies of the Influence of Density on Jet Noise," *Journal of Sound and Vibration*, Vol. 28, no. 4, pp. 649-668, 1973.

[12] Jones, I. S. F., "Finite Amplitude Waves from a Supersonic Jet," AIAA Paper 71-151, AIAA 9th Aerospace Sciences Meeting, N.Y., 25-27 January 1971.

[13] Lau, J. C., "Effects of exit Mach number and temprature on mean-flow and turbulence in round jets," *J. Fluid Mech.*, vol. 105, pp. 193-218, 1981.

[14] Lau, J. C., Morris, P. J., and Fisher, M. J., "Measurements in subsonic and supersonic free jets using a laser velocimeter," *J. Fluid Mech.*, vol 93, part 1, pp. 1-27, 1979.

[15] Lighthill, M.J., "Jet Noise," *AIAA Journal*, Vol 1, no. 7, pp. 1507-1517, July 1963.

[16] Lowson, M. V., and Ollerhead, J. B., "Visualization of Noise from Cold Supersonic Jets," *J. Acoust. Soc. of Amer.*, vol. 44, no. 2, pp. 624-630, 1968.

[17] Mabey, D. B., "Analysis and Correlation of Data on Pressure Fluctuations in Separated Flow," *J. Aircraft*, vol. 9, no. 5, pp. 642-645, September 1972.

[18] Mayes, William H., Lanford, Wade E., and Hubbard, Harvey H., "Near-Field and Far-Field Noise Surveys of Solid-Fuel Rocket Engines for a Range of Nozzle Exit Pressures," NASA TN D-21, August 1959.

[19] *Noise and Acoustic Fatigue in Aeronautics*, E. J. Richards and D. J. Mead, Eds., J. Wiley and Sons, London, 1968, Chapt. 7.

[20] Nagamatsu, H.T., Sheer, R.E., and Horvay, G., "Supersonic Jet Noise Theory and Experiments," *Basic Aerodynamic Noise Research*, NASA SP- 207, 1969.

[21] Norum, T. D., and Seiner, J. M., "Location and Propogation of Shock Associated Noise from Supersonic Jets," AIAA 80-0983, AIAA 6th Aeroacoustics Conf., 4-6 June 1980. See, also, Seiner and Norum (1980) cited below.

[22] Oertel, H., "Mach Wave Radiation of Hot Supersonic Jets by Means of the Shock Tube and New Optical Techniques," *Proc. of the 12th Intl. Symp. on Shock Tubes and Waves*, A. Lifshitz and J. Rom, Eds., pp. 266-275, Jerusalem, 1980.

[23] Papamoschou, D., and Roshko, A., "Observations of Supersonic Free Shear Layers," AIAA Paper 86- 0162, 1986.

[24] Papamoschou, D., and Roshko, A., "The Compressible Turbulent Shear Layer: An Experimental Study," *J. of Fluid Mech.*, Vol. 197, pp. 453-477, Dec. 1988.

[25] Papamoschou, D., "Structure of the Compressible Turbulent Shear Layer," AIAA Paper-89-0126, 27th Aerospace Sciences Meeting, Jan. 9-12, 1989.

[26] Potter, R.C., and Crocker, M.J., "Acoustic Prediction Methods for Rocket Engines, Including the Effects of Clustered Engines and Deflected Exhaust Flow," NASA CR-566, October 1966.

[27] Salant, R. F., Zaic, G. F., and Kolesar, R. R., "Holographic Study of the Mach Wave Field Generated by a Supersonic Turbulent Jet," *Proceedings of the Purdue Noise Control Conference*, Malcolm J. Crocker, Ed., 1971.

[28] Seiner, J. M., and Norum, T. D., "Aerodynamic Aspects of Shock Containing Jet Plumes," AIAA Paper 80-0965, AIAA 6th Aeroacoustics Conf., 4-6 June 1980. See also, Norum and Seiner (1980), cited above.

[29] Smith, D. J., and Johannesen, "The Effects of Density on Subsonic Jet Noise," *Aero- and Hydro-Acoustics*, IUTAM Symposium, Lyon 1985, G. Comte-Bellot and J. E. Ffowcs-Williams, Eds., Springer, Berlin, 1986.

[30] Speaker, W. V., and Ailman, C. M., "Spectra and Space-Time Correlations of the Fluctuating Pressures at a Wall Beneath a Supersonic Turbulent Boundary Layer Perturbed by Steps and Shock Waves," NASA CR-486, May 1966.

[31] Tam, C. K. W., "On the noise of a nearly ideally expanded supersonic jet," *J. Fluid Mech.*, vol. 51, pt. 1, pp. 69-95, 1972.

[32] Tam, C. K. W., "On the three families of instability waves of high speed jets," *J. Fluid Mech.*, vol. 201, pp. 447-483, 1989.

[33] Tanna, H.K., "An Experimental Study of Jet Noise Part I: Turbulent Mixing Noise," *Journal of Sound and Vibration*, Vol. 50, no. 3, pp. 405-428, 1977.

[34] Tanna, H.K., "An Experimental Study of Jet Noise Part II: Shock Associated Noise," *Journal of Sound and Vibration*, Vol. 50, no. 3, pp. 429-444, 1977.

[35] von Gierke, H. E., "Types of Pressure Fields of Interest in Acoustical Fatigue Problems," WADC Technical Report 59-676, *WADC - University of Minnesota Conference on Acoustical Fatigue*, March 1961.
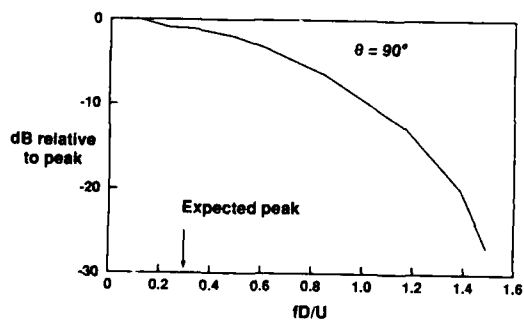
SECOND INTERNATIONAL CONGRESS ON
RECENT DEVELOPMENTS IN AIR- AND
STRUCTURE-BORNE SOUND AND VIBRATION
MARCH 4-6, 1992   AUBURN UNIVERSITY, USA

FLOW-INDUCED NOISE AND VIBRATION OF CONFINED JETS

Kam W. Ng
Applied Research and Technology
Office of Naval Research
Arlington, VA 22217-5000
U.S.A.

ABSTRACT

A theoretical model was developed to study the wall pressure and vibratory motion of
a cylindrical duct which is excited by a confined turbulent jet flow resulting from fluid
flow through orifices in the duct. Based on flow field measurements, the blocked surface
pressure was calculated using Lighthill's method, and then used to drive the fluid-filled
shell.   The wall pressure and pipe wall acceleration were determined by solving the
coupled fluid solid interaction problem. The wall pressure was obtained by summing the
blocked surface pressure and the pressure due to the wall vibration.   An amplitude
modulated convecting wave field was used to simulate the moving acoustic sources of the
jet.   Analytical and experimental results for wall pressure and acceleration then were
compared for a wide range of parameters of interest. Results from comparisons showed
reasonably good agreement.

INTRODUCTION

Turbulence-generated noise due to high velocity flow through valves and restrictors
has been identified as one of the major noise contributors in piping systems. To predict
and reduce piping system noise, a better understanding of the noise generating mechanisms
and their interaction with the flow field and neighboring structures is needed. The noise
characteristics of flow through valves and restrictors with air,   steam, and gases have
been studied quite extensively.[1-7] However, studies of the noise characteristics of water
flow through valves and regulators have been limited, and the understanding of
flow-induced noise is far from satisfactory.
    The physical problem under investigation is illustrated in Fig. 1. In general, a
low-to-moderate flow approaches the flow restriction in a pipe. A high-velocity jet is
formed at the vena contracta immediately downstream of the orifice plate.   Near the
orifice plate, the jet is surrounded by a low velocity recirculation zone or reversed flow
region.   Further downstream, the jet shear layer grows until it reattaches to the pipe
wall. As shown in the figure, the flow field can be divided into two regions; namely, the
recirculating or developing region and the fully developed region. The developing region
of the jet is the noise production area in which the flow and noise characteristics are
very similar to those of a free jet. In this region, the jet mixing noise is the dominant
noise mechanism. However, the flow field can be modified by the presence of the pipe
wall, which can alter the noise generation. As compared to a free jet, the confined jet
differs significantly in acoustic radiation, propagation, and fluid/structural interaction
processes.
    In the following sections, the development of the solution for the wall pressure and
acceleration of a cylinder with an internal flow as shown in Fig. 1 is presented. First,
the development of the expressions for the blocked surface pressure is introduced and then
the vibratory response of the internally fluid loaded shell due to the blocked pressure is
addressed.
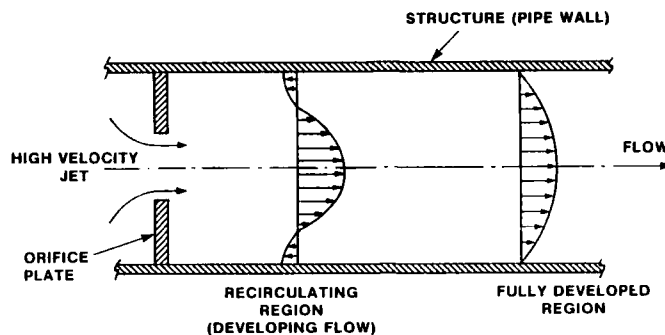
Figure 1- Development of confined jet

As a result of the complexity of the problem, numerous approximations are needed to simplify the analysis. Although significant extensions to the Lighthill theory of aeroacoustic noise have been developed by Bergeron[8] and most recently by Chase and Noiseux,[9] the present analysis neglects the compressibility of the fluid and is based on the Lighthill formulation which leads to an inhomogeneous Poisson's equation.

THEORETICAL DEVELOPMENT

The acoustic pressure on the wall of a cylinder with internal flow can be expressed as a superposition of two components: a blocked surface pressure and a pressure due to the induced vibration of the shell. The blocked surface pressure is defined as the near-field pressure generated by the fluid on the pipe wall surface, but with the surface rigid. This pressure is primarily due to the near-field hydrodynamic component of the turbulent jet flow which is influenced by its small scale and large-scale or coherent structures. A computational approach to this jet flow-induced noise model is shown in Fig. 2.
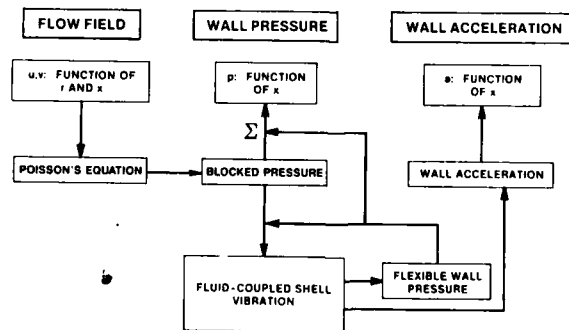
Figure 2--Noise model for fluid-filled shell vibration excited by a confined jet

Near-Field Jet Noise and Blocked Surface Pressure

Consider the flow field of a turbulent jet as shown in Fig. 1. The flow and pressure are governed by the conservation of mass and momentum equations for fluids. For the case of an incompressible fluid, the combination of the divergence of the momentum equation and the equation of conservation of mass, leads to the following inhomogeneous Poisson's equation[10] for the pressure

$$\frac{1}{\rho} \nabla^2 p = - \frac{\partial^2}{\partial x_i \partial x_j} u_i u_j \ , \tag{1}$$

where $u = u(x,t)$ and $p = p(x,t)$ are the instantaneous velocity and pressure, respectively.

68

In turbulent flow, the instantaneous velocity and pressure can be written as the sum of the mean and fluctuating quantities, i.e., $p(x,t) = P(x) + p'(x,t)$, and $u_i(x,t) = U_i(x) + u_i'(x,t)$. By substituting the mean and fluctuating quantities into Eq. (1) and then averaging with respect to time, the fluctuating pressure and momentum have been shown by Abdallah[10] to satisfy the following Poisson's equation, i.e.,

$$\nabla^2 p' = -M ,$$ (2)

where the source terms are

$$M = \rho \frac{\partial^2}{\partial x_i \partial x_j} (u_i'u_j' - \overline{u_i'u_j'} + 2U_i u_j') .$$

Here, the overbar denotes the time-averaged value. The fluctuating pressure in Eq. (2) is the near-field pressure generated by the turbulent jet. Since the compressibility of the fluid has been ignored, the pressure p' does not propagate as sound and thus is referred to as "pseudo sound." The blocked surface pressure noted earlier is equivalent to p' at the surface of the rigid wall.

To solve the Poisson's equation, a Green's function approach is now utilized. The Green's function in cylindrical coordinates $G(r,\theta,x/r_0,\theta_0,x_0)$ represents the response at point (r,θ,x) due to a unit point source at (r_0,θ_0,x_0). It is again noted that time delays effects are neglected here via the use of Poisson's equation vis-a-vis Helmholtz equation. The source term in Eq. (2) consists of the time dependent pressure fluctuations or sources at (r_0,θ_0,x_0) and the solution of Poisson's equation in terms of the Green's function can be interpreted as the result of summing responses due to the distribution of source fluctuations. This solution of Poisson's equation can be expressed as

$$p'(r,\theta,x,t) = \int_V M\, G(r,\theta,x/r_0,\theta_0,x_0)\, dV$$

$$- \int_S \frac{\partial p'}{\partial r} G(r,\theta,x/r_0,\theta_0,x_0)\, dS ,$$ (3)

where $G(r_0,\theta_0,x_0)$ is the solution of the nonhomogeneous equation

$$\nabla^2 G = -\frac{1}{r} \delta(r - r_0)\, \delta(\theta - \theta_0)\, \delta(x - x_0) ,$$

which satisfies the boundary condition $\partial G/\partial r = 0$ at the wall (i.e., $r = D/2$).

The Green's function $G(r,\theta,x/r_0,\theta_0,x_0)$ is readily obtained by standard methods[10] which lead to

$$G(r,\theta,x/r_0,\theta_0,x_0) = \sum_{n=0}^{\infty} \sum_{m=1}^{\infty} \frac{\varepsilon_n}{\pi D} \frac{\xi_{mn}}{\xi_{mn}^2 - n^2} \frac{1}{J_n^2(\xi_{mn})} \phi_{mn}(r_0,\theta_0)$$

$$\cdot \phi_{mn}(r,\theta) \exp(-2\xi_{mn}|x-x_0|/D) ,$$ (4)

where

$$\phi_{mn}(r,\theta) = J_n(2\xi_{mn} r/D) \cos[n(\theta - \theta_0)] ,$$

$$\varepsilon_n = 1 \quad n = 0 ,$$

$$\varepsilon_n = 2 \quad n \neq 0 .$$

J_n, is the Bessel function of the first kind of order n, and ξ_{mn} satisfies the equation $J_n'(\xi_{mn}) = 0$.

As shown by Abdallah[10], the dipole surface term in Eq. (3) is small compared with the Reynolds shear stress component of the quadrupole source. More specifically, on order of magnitude analysis by Abdallah[10] showed that the ratio of the volume integral to the surface integral in Eq. (3) is $(uL/\upsilon)^{1/2}$, where L is the length scale (i.e. radius of the pipe), u is the turbulent velocity scale, and υ is the kinematic viscosity. This conclusion agrees with the previous experimental work by Olsen, Miles, and Dorsch[11] that the surface dipole term is indeed small.

By neglecting the surface dipole term, Eq. (3) can be written as

$$p'(r,\theta,x,t) = \int_v G(r,\theta,x/y) \frac{\partial^2}{\partial y_i \partial y_j} H_{ij} \, dV_y \, , \tag{5}$$

where $y = (r_0, \theta_0, x_0)$ and

$$H_{ij} = -\rho(u_i'u_j' - \overline{u_i'u_j'} + 2U_i u_j') \, .$$

After using the identity

$$\frac{\partial}{\partial y_i} G \frac{\partial H_{ij}}{\partial y_j} - \frac{\partial}{\partial y_j} H_{ij} \frac{\partial G}{\partial y_i} = G \frac{\partial^2 H_{ij}}{\partial y_i \partial y_j} - H_{ij} \frac{\partial^2 G}{\partial y_i \partial y_j}$$

to eliminate $G(\partial^2/\partial y_i \partial y_j)H_{ij}$ and then applying the divergence theorem

Eq. (5) becomes

$$p'(r,\theta,x,t) = \int_v H_{ij} \frac{\partial^2 G}{\partial y_i \partial y_j} dV_y + \int_s G \, n_i \frac{\partial}{\partial y_j} H_{ij} \, dS_y - \int_s n_j H_{ij} \frac{\partial G}{\partial y_i} dS_y \, . \tag{6}$$

Since the wall is, at this atage, considered to be rigid, the velocity vanishes at the surface and the wall pressure fluctuation then becomes

$$p'(D/2,\theta,x,t) = \int_v H_{ij} \frac{\partial^2 G}{\partial y_i \partial y_j} dV_y \, . \tag{7}$$

The wall pressure fluctuation can thus be evaluated by multiplying the source magnitude H_{ij} at each point of the flow field by the corresponding local weighting function $\partial^2 G/\partial x_i \partial x_j$ and integrating over the whole source volume.

Consider the specific case of interest, i.e., an axisymmetric jet whose principal mean velocity is the axial component, and $\partial/\partial x \ll \partial/\partial r$. Representing the velocity field as $U_i = (U_x, U_r, 0)$, the continuity equation can be written as

$$\frac{1}{r} \frac{\partial}{\partial r} r \, U_r + \frac{\partial U_x}{\partial x} = 0 \, ,$$

which gives U_r/U_x of the order l/L where l and L are the length scales in the r and x direction, respectively. Assuming an axially symmetric source distribution (i.e., $\partial/\partial \theta = 0$), Eq. (7) becomes

$$p'(D/2,x,t) = \rho \int_v S_{ij} \frac{\partial^2 G}{\partial y_i \partial y_j} dV_y \, , \tag{8}$$

where the source term S_{ij} is defeined to be:

$$S_{ij} = u_i'u_j' - \overline{u_i'u_j'} + 2u_i'U_j \delta_{j1}$$

and the Green's function is now

70

$$G(D/2,x/r_o,x_o) = \sum_{m=1}^{\infty} \frac{1}{\pi D} \frac{1}{\xi_m} \frac{J_o(2\xi_m r_o/D)}{J_o(\xi_m)} \exp(-2\xi_m |x-x_o|/D) \ .$$

Differentiating the Green's function with respect to x_o and r_o, the local weighting function $\partial^2 G/\partial x_i \partial x_j$ becomes

$$\frac{\partial^2 G}{\partial x_o \partial r_o} = - \frac{4}{\pi D^3} \sum_{m=1}^{\infty} \frac{\xi_m J_1(\xi_m r_o/R)}{J_o(\xi_m)} \exp(-\xi_m |x-x_o|/R) \ . \tag{9a}$$

and $p'(D/2,x,t)$ can then be expressed as

$$p'(D/2,x,t) = - \frac{4\rho}{\pi D^3} \int_V (u_i'u_j' - \overline{u_i'u_j'} + 2u_i'U_j \delta_{j1})$$

$$\cdot \sum_{m=1}^{\infty} \frac{\xi_m J_1(\xi_m r_o/R)}{J_o(\xi_m)} \exp(-\xi_m |x-x_o|/R) \ dV \ . \tag{9b}$$

Vibratory Response and Pressure Field

An approach is presented in this section to evaluate the vibratory response and pressure field of a fluid-filled shell excited by a harmonic, axisymmetric axially varying blocked pressure. The vibratory response is first analyzed, then followed by an analysis of the wall pressure due to the wall vibration.

1. Forced Vibration of Shell

Consider a thin circular shell of infinite length, which is filled with a dense fluid (i.e., water). The vibratory motion of the shell can be described by the Donnell-Mushtari shell equations as presented by Leissa[12] as

$$\begin{bmatrix} \begin{bmatrix} & & \\ & L_{ij} & \\ & & \end{bmatrix} \end{bmatrix} \begin{bmatrix} u_s \\ v_s \\ w_s \end{bmatrix} - m_s \frac{\partial^2}{\partial t^2} \begin{bmatrix} u_s \\ v_s \\ w_s \end{bmatrix} = - \begin{bmatrix} p_x \\ p_\theta \\ p_r \end{bmatrix} + \begin{bmatrix} 0 \\ 0 \\ p_a \end{bmatrix} \ , \tag{10}$$

where u_s, v_s, and w_s are the axial, circumferential, and radial components of the displacement vector in the x, θ, and r directions. The L_{ij}'s are differential operators, m_s is the mass density per unit area of the shell, and p_x, p_θ, and p_r are the mechanical excitations per unit area which act on the shell in the x, θ, and r directions. The additional pressure p_a is the acoustic pressure which acts on the shell as a result of the excitation of the fluid via the vibration of the shell.

To analyze the response of a cylindrical shell to a generalized harmonic excitation pressure, it is convenient to express the shell displacements and excitation pressure as spatial Fourier transforms, i.e.,

$$U = \frac{1}{\sqrt{2\pi}} \int_{-\infty}^{\infty} \sum_s \sum_n \hat{U}_{ns} \cos(n\theta) \exp[jk_{ns}x - j\omega t + j\pi/2] \ dk_{ns} \ , \tag{11a}$$

$$V = \frac{1}{\sqrt{2\pi}} \int_{-\infty}^{\infty} \sum_s \sum_n \hat{V}_{ns} \sin(n\theta) \exp[jk_{ns}x - j\omega t] \ dk_{ns} \ , \tag{11b}$$

$$W = \frac{1}{\sqrt{2\pi}} \int_{-\infty}^{\infty} \sum_s \sum_n \hat{W}_{ns} \cos(n\theta) \exp[jk_{ns}x - j\omega t] \ dk_{ns} \ , \tag{11c}$$

$$P_r = \frac{1}{\sqrt{2\pi}} \int_{-\infty}^{\infty} \sum_s \sum_n \hat{P}_r \cos(n\theta) \exp[jk_{ns}x - j\omega t] \, dk_{ns} \quad . \tag{11d}$$

Substituting Eqns. (11-a) through (11-d) into the original equations of motion (Eq. 10) of the fluid-filled shell gives the spectral equations of motion for $p_x = p_\theta = 0$:

$$
\begin{bmatrix} L_{11} & L_{12} & L_{13} \\ L_{21} & L_{22} & L_{23} \\ L_{31} & L_{32} & L_{33} \end{bmatrix}
\begin{bmatrix} \hat{U}_{ns} \\ \hat{V}_{ns} \\ \hat{W}_{ns} \end{bmatrix}
=
\begin{bmatrix} 0 \\ 0 \\ \hat{P}_r \Omega^2 / \rho_s h \omega^2 \end{bmatrix} \quad . \tag{12}
$$

The elements of the differential operator L_{ij} are given by

$$L_{11} = -\Omega^2 + (k_{ns}a)^2 + \frac{1}{2}(1-\nu)n^2 \quad ,$$

$$L_{12} = \frac{1}{2}(1+\nu)n(k_{ns}a) \quad ,$$

$$L_{13} = \nu(k_{ns}a) \quad ,$$

$$L_{21} = L_{12} \quad ,$$

$$L_{22} = -\Omega^2 + \frac{1}{2}(1-\nu)(k_{ns}a)^2 + n^2 \quad ,$$

$$L_{23} = n \quad ,$$

$$L_{31} = L_{13} \quad ,$$

$$L_{32} = L_{23} \quad ,$$

$$L_{33} = -\Omega^2 + 1 + \beta^2[(k_{ns}a)^2 + n^2]^2 - FL \quad , \text{ and}$$

$$FL = \Omega^2(\rho_f/\rho_s)(a/h)(k_s{}^r a)^{-1}[J_n(k_s{}^r a)/J_n{}'(k_s{}^r a)] \quad .$$

In these expressions, Ω is the non-dimensional frequency $\Omega = \omega a/c_1$; c_1 is the extensional phase speed of the shell material; k_{ns} is the structural wavenumber; a is the mean radius of the shell; ν is the Poisson's ratio; β is the thickness parameter given by $\beta^2 = h^2/12a^2$; n is the circumferential order of the shell; and the fluid loading term FL is associated with the acoustic pressure which is due to the presence of fluid acting on the shell wall. In the FL term given by Fuller[13], ρ_f is the fluid density, ρ_s is the density of the shell material, and h is the shell thickness.

The solution of the forced vibration problem can be obtained via the Fourier transform technique. From the spectral equations of motion (Eq. 12), the spectral radial displacement, as a function of $k_{ns}a$, is

$$\hat{W}_{ns} = \hat{P}_r \frac{\Omega^2}{\rho_s h \omega^2} \frac{L_{11}L_{22} - L_{12}L_{21}}{\det |L|} \quad . \tag{13}$$

The radial displacement is obtained by performing the inverse transform on Eq. (13). It should be noted that for the axisymmetric case, (i.e., $n = 0$) the differential operators L_{12}, L_{21}, L_{23}, and L_{32} vanishes. Thus, in the axisymmetric case, the radial displacement becomes

$$W(x) = \frac{1}{\sqrt{2\pi}} \frac{\Omega^2}{\rho_s h \omega^2} \int_{-\infty}^{\infty} \hat{P}_r \frac{L_{11}L_{22}}{\det |L|} \exp(jk_s x) dk_s \quad . \tag{14}$$

The integral in Eq. (14) can be solved using the residue theorem. Consequently, the radial velocity and acceleration can be obtained by multiplying Eq. (14) by $-j\omega$ and $(-j\omega)^2$ respectively.

72

2. Pipe Wall Pressure Fluctuations

As discussed previously, the pipe wall pressure is the sum of the blocked surface pressure and the pressure contribution from the pipe wall vibration. The evaluation of the blocked surface pressure was presented in the previous section and the pressure due to the wall vibration is developed here.

Consider an infinite-length shell with radius a, filled with dense fluid (i.e., water). The shell is set in motion by axisymmetrically distributed sources on the inside of the pipe. The harmonic pressure due to the vibratory motion of the pipe wall is governed by the Helmholtz equation:

$$[\nabla^2 + k^2] \; P(r,x,\omega) = 0 \; . \tag{15}$$

Introducing the Fourier transform pair

$$\hat{P}(r,k_x,\omega) = \int_{-\infty}^{\infty} P(r,x,\omega) \; \exp \; (-jk_x \; x) \; dx \; ,$$

and

$$P(r,x,\omega) = \frac{1}{2\pi} \int_{-\infty}^{\infty} \hat{P}(r,k_x,\omega) \; \exp \; (jk_x \; x) \; dk_x \; ,$$

the Fourier transform of Eq. (15) is

$$[\; \nabla_r^2 + (k^2 - k_x^2)] \; \hat{P}(r,k_x,\omega) = 0 \; , \tag{16}$$

where ∇_r^2 is the operator in cylindrical coordinates. The solution of Eq. (16) can be written as

$$\hat{P} = A_0 J_0(k_r r) \; , \tag{17}$$

where J_0 is the Bessel function of order zero and A_0 is to be determined. Applying the boundary condition at the wall, r = a,

$$\frac{d}{dr} \hat{P} \; \bigg|_{r=a} = -jk\rho_f c_f \; \hat{\dot{W}} \; ,$$

the constant A_0 can be expressed as

$$A_0 = - \frac{jk\rho_f c_f}{k_r J_0{}'(k_r a)} \; \hat{W} \; , \tag{18}$$

where $\quad \hat{\dot{W}} = \frac{a \; F_0}{c_1{}^2 2\pi\rho_s h} \; [\frac{L_{11}L_{22}}{\det |L|}] \; (-j\omega) \; .$

Eq. (17) now becomes

$$\hat{P}(a,k_x) = [\frac{-jk\rho_f c_f}{k_r J_0{}'(k_r a)} \; J_0(k_r a)] \; \hat{W}(a,k_x) \; . \tag{19}$$

By taking the inverse transform, the pressure is

$$
P(a,x,\omega) = - \frac{\rho_f c_f F_o \omega}{4\pi^2 c_1^2 \rho_s h} \int_{-\infty}^{\infty} \frac{ka}{k_r a} \frac{J_o(k_r a)}{J_o'(k_r a)} [\frac{L_{11}L_{22}}{\det|L|}] \exp(jk_x x) dk_x a \ .
$$

(20)

The form of the complex integral, Eq. (20), is very similar to Eq. (14). Again, using the residue theorem, the pressure due to shell wall vibration at $x = 0$ can be written as

$$
\bar{P}(a,x,\omega) = -j \frac{F_o \omega^2}{2\pi c_1^2} (\frac{\rho_f}{\rho_s})(\frac{a}{h}) \sum_{s=1}^{\infty} \frac{J_o(k_r a)[L_{11}L_{22}]}{(k_r a)J_o'(k_r a) \det|L|'} \exp(jk_x x) \ ,
$$

(21)

where the terms in the sum are evaluated at the poles of the integrand and ' represents differentiation with respect to the argument.

Wall Pressure Fluctuations and Forced Vibration in Shell Excited by Random Sources

It is well known that turbulent jet flow is a random process in space and time. Therefore wall pressure and flow-excited vibration fields associated with the confined jets are also random functions of space and time. To quantify the wall pressure and pipe wall vibratory response, a statistical averaging method must be used.

First, consider the blocked surface pressure that is due to the near-field hydrodynamic component of the axisymmetric turbulent jet flow. The equation relating the blocked harmonic surface pressure to the fluctuations in momentum is obtained by Fourier transforming Eq. (9b), i.e.,

$$
P_b(x,a,\omega) = \int_V S(x_o,r_o,\omega) \frac{\partial^2 G}{\partial x_o \partial r_o}(x,a|x_o,r_o) \ dV \ ,
$$

where $S(x_o,r_o,\omega)$ is the source spectrum at point (x_o,r_o) and is given by

$$
S(x_o,r_o,\omega) = \rho \int_{-\infty}^{\infty} (u_i'u_j' - \overline{u_i'u_j'} + 2u_i'U_j\delta_{j1}) \exp(-j\omega t) \ dt \ .
$$

The complex conjugate of blocked pressure $P_b(x,a)$ at point x' is

$$
P_b^*(x',a,\omega) = \int_{V'} S^*(x_o',r_o',\omega) \frac{\partial^2 G^*}{\partial x_o \partial r_o}(x',a|x_o',r_o') \ dV' \ .
$$

(22)

By multiplying Eq. (8) with Eq. (22) and ensemble averaging the product, the following expression for the cross spectral density of the pressure is obtained:

$$
\langle P_b(x,a,\omega)P_b^*(x',a,\omega)\rangle = \iint_{V'V} \langle S(x_o,r_o,\omega)S^*(x_o',r_o',\omega)\rangle \frac{\partial^2 G}{\partial x_o \partial r_o}(x,a|x_o,r_o)
$$
$$
\cdot \frac{\partial^2 G^*}{\partial x_o' \partial r_o'}(x',a|x_o',r_o') \ dV \ dV' \ .
$$

(23)

The mean squared blocked pressure at a point x is simply obtained by letting $x' = x$ in Eq. (23).

74

In order to determine the velocity of the wall as a function of axial position in the turbulent jet flow, the transfer mobility $Y(x-x_o)$, which is defined as the ratio of pipe wall radial velocity at x' to a ring harmonic excitation force applied at point x_o is now introduced. It then follows from the preceeding definition and Eq. (14) that $Y(x-x_o)$ can be expressed as:

$$Y(x-x_o) = \frac{-j\omega^2}{2\pi\omega\rho_s h} \int_{-\infty}^{\infty} \frac{L_{11}L_{22}}{\det|L|} \exp[-jk_s(x-x_o)] \, dk_s \quad , \tag{24}$$

which can be simply evaluated using the residue theorem. Finally, after a straight forward application of superposition, it follows that the wall velocity can be expressed as

$$\dot{W}(x,\omega) = \int_{x_o} Y(x-x_o) \, P_b(x_o,a,\omega) \, dx_o \quad . \tag{25}$$

An expression for the mean squared velocity of the wall as a function of position can now be obtained. Following a similar procedure of the blocked pressure, the cross spectral density of the velocity can be expressed as

$$\langle \dot{W}(x,\omega)\dot{W}^*(x',\omega)\rangle = \int_{x_o'} \int_{x_o} Y(x-x_o)Y^*(x'-x_o')\langle P_b(a,x_o,\omega)P_b^*(a,x_o',\omega)\rangle dx_o dx_o' \quad . \tag{26}$$

The mean squared velocity of the wall as a function of x is simply obtained from Eq. (26) by letting $x' = x$. It is noted that the cross spectral density of the blocked pressure, as specified in Eq. (23) is contained in Eq. (26).

Special Case

The solution of the fluid-coupled shell vibration problem for the specific blocked pressure distribution is presented in this section. Results are presented for a random blocked surface pressure. The random blocked surface pressure is intended to represent the physics of the confined jet flow. More specifically, the cross spectral density of the pressure is assumed to result from hydrodynamic pressure fluctuations which are uncorrelated in the radial direction, but are correlated in the x direction near the jet exit. The uncorrelated pressure fluctuations in the radial direction reflect the random motion of the turbulent jet, whereas the correlated pressure fluctuations in the x direction reflect the motion of the large-scale coherent structures near the jet exit.[14]

A general expression for evaluating the cross spectral density of the blocked pressure is presented in Eq. (23). In this special case, it was assumed that the pressure fluctuations are uncorrelated in the radial direction, and the local weighting function $\partial^2 G/\partial x_o \partial x_i$ can be approximated by a Dirac delta function in the x direction. With these assumptions, Eq. (23) can be simplified and the mean squared blocked pressure can be expressed as

$$\langle P_b(x,a,\omega)^2\rangle = \int_V \langle S(r_o,\omega)^2\rangle \, |\frac{\partial^2 G}{\partial x_o \partial r_o}(x,a|x_o,r_o)|^2 \, dV \quad . \tag{27}$$

In the pipe wall response calculations, it was assumed that the blocked pressure has a triangular distribution, and the pressure fluctuations are correlated in the x direction. With these assumptions, Eq. (26) could be reduced to

$$\langle \dot{W}(x'\omega)\dot{W}^*(x',\omega)\rangle = P_o^2 \int_{x_o'} \int_{x_o} Y(x-x_o)Y^*(x'-x_o')A(x_o,\omega)A^*(x_o',\omega)$$

$$\cdot \exp[-j\omega/V_c(x_o-x_o')]dx_o dx_o' \quad , \tag{28}$$

where $A(x,\omega)$ is the triangular pressure distribution.

75

NUMERICAL AND EXPERIMENTAL RESULTS

The theoretical development of the blocked surface pressure, pipe wall acceleration, and pressure contribution due to shell vibration was presented. In this section, results from the numerical calculations are presented and discussed. Calculations of the blocked surface pressure are presented first, followed by the pipe wall acceleration and pressure contribution from the wall vibration. Lastly, the numerical results of the wall pressure and acceleration are compared with the experimental data.

Fluid-Filled Shell Vibration

Consider the vibration of a fluid-filled shell. For a free vibration solution to exist, the determinant of the matrix operator in Eq. (12) must be equal to zero. Expansion of the determinant yields the characteristic equation. The characteristic equation of the coupled system is complex due to the presence of the desired eigen roots in the argument of the Bessel functions in the fluid loading term. The roots of the characteristic equation were found by using a complex root searching technique as introduced by Fuller.[15] For the cases of purely real or imaginary values, a simple stepping procedure was used to locate a change of sign in the characteristic equation. The roots of the characteristic equation correspond to the structural wavenumber and are denoted as k_{ns}.

In the present study, efforts were focused on the calculations of the wall pressure and pipe wall response due to an axisymmetic turbulent jet inside the pipe. Before the analysis of the forced response of the fluid-filled shell, it is necessary to consider the free vibration problem. Furthermore, the roots of the characteristic equation correspond to the poles of the complex integral that appears in the inverse Fourier transform. In evaluating the complex integral, the method of residues was used. This method involves the summation of residues at the poles. The roots of the characteristic equation for the various branches s were plotted against the normalized frequency.

Dispersion curves for the axisymmetric mode (n = 0) of a 5.1-cm (2-in.) diameter, 6.4-mm (0.25-in.) thick Plexiglas shell have been obtained. The frequency range of interest is from 100 to 2500 Hz. It should be noted that this frequency range is much below the ring, cut-off and critical frequencies. The results show most of the dispersion curves are independent of frequency, except the first two branches (s = 1 and s = 2). The material properties used in the calculations are representative of the Plexiglas test section used in the experimental investigation. Material properties are summarized in Table 1.

Table 1-- Material properties for numerical calculations

Material	Young's Modulus (N/m^2)	Poisson's Ratio	Density (kg/m^3)	Wave Speed (m/sec)
Plexiglas	4.137×10^9	0.355	1388	1846
Water	–	–	1000	1500

Near-Field Jet Noise and Blocked Surface Pressure

The equation relating the near-field jet pressure fluctuations to the velocity fluctuations was presented in Eq. (9b). In the rigid wall case, the near-field pressure fluctuations are equivalent to the blocked surface pressure. As shown in Eq. (8), the blocked surface pressure is obtained by integrating the product of the source term and local weighting function $\partial^2 G/\partial x_i \partial x_j$ in the source region. The source term consists of the velocity fluctuations $u_i'u_j'$, time-averaged of $u_i'u_j'$, and the interaction of mean velocity and fluctuating velocity $2u_i'U_j$. The magnitude of the source term was determined experimentally, i.e., from the laser Doppler velocimeter (LDV) data; and the weighting function as shown in Eq. (9a) was derived analytically.

In general, the $2u_i'U_i$ is the dominant component in the source term. As discussed previously, near the jet exit the axial mean velocity U is much larger than the radial mean velocity V, and its velocity fluctuations u' and v'; thus, the major contribution in the source term is from the $2u'U$ term. It should be noted that further downstream, the axial mean velocity U decays, and hence the $2u'U$ term may not be dominant.

76

Theoretically, the source term can be determined from the flow field data; however, it requires that the measurements of all points be taken simultaneously. During the test, the LDV measurements were taken at different points at different times. Experimental results showed the time history of the velocity cor. onents are relatively independent of the time interval. Accordingly, the flow field da:a were assumed to be stat'onary, and the source term was calculated using LDV measured data.

It was pointed out earlier that, in spite of the forward scattering mode and particle filtering efforts, the data rates of the LDV measurement were only up to 5000 samples per second. As compared with other similar LDV systems, these data rates were relatively high. In overcoming the low data rate problem, various interpolation schemes were considered to enhance the velocity data. Since the source calculations were performed in the frequency domain, the interpolations were applied on a velocity versus time basis. Several interpolation schemes and various curve fittings were attempted. Results showed the Lagrangian interpolation polynomial to be the most appropriate and the third order is sufficient. The third-order polynomial was based on a four-point interpolation scheme given by Abramowitz and Stegun.[16]

The local weighting function $\partial^2 G/\partial x_i \partial x_j$, as given by Eq. (9a) is an oscillatory function. It has been found that as the number of terms m increases, the number of maxima and minima increases; and also the weighting is substantially large near the wall. It should be pointed out that the exponential term in Eq. (9a) has a strong influence on the weighting function in the axial direction. In that the amplitude of the weighting function drops off rapidly with increasing x/R.

During the test program, for each axial location x, the velocity measurements were taken at 11 radial points, i.e., values of r/R range from 0.0 to 0.925. Because of the oscillatory nature of the weighting function, spatial averaged values of the weighting function at each LDV measurement point were used in the blocked pressure calculations. The averaged values were obtained by integrating the weighting function in each annular area representing the particular measurement point. Fig. 3 illustrates the division of the annular areas or bands. Calculations showed that the averaged weighting function approach was independent of the number of terms used in Eq. (9a), and the amplitude of the weighting function was bounded near the wall. The value of m (number of terms) used in the numerical calculations was 32.

Based on the statistical approach as presented previously, the cross spectral density of the surface pressure fluctuations were evaluated according to Eq. (23). In the calculations, it was assumed that the velocity fluctuations are uncorrelated in the radial direction. This assumption was verified by the experimental results. In the experimental study of confined jets conducted by Abdallah[10], she also observed that the velocity fluctuations are uncorrelated in the radial direction.

As discussed previously, the blocked pressure was evaluated by multiplying the source magnitude S_{ij} at each point of the flow field by the corresponding local weighting function $\partial^2 G/\partial x_i \partial x_j$ and integrating over the whole source volume. Because the local weighting function decays rapidly with x, $\partial^2 G/\partial x_i \partial x_j$ was approximated by a Dirac delta function in the x direction. With this approximation, Eq. (23) could be simplified and the mean squared blocked pressure can be expressed as Eq. (27).
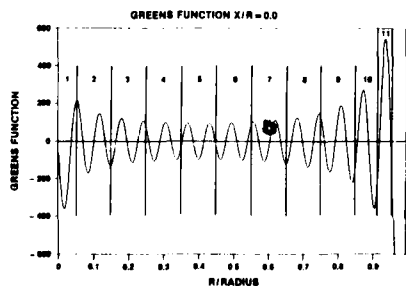
Figure 3--Green's function and division of annular bands
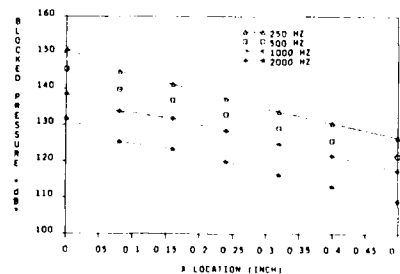
Figure 4--Blocked surface pressure vs location

Based on calculations, the spectral characteristics of the blocked surface pressure are very similar to the measured wall pressure. As discussed previously, the total wall pressure is the sum of blocked surface pressure and pressure contribution from the wall vibration. Therefore, wall pressure comparison cannot be made until the pressure contribution from the pipe wall vibration is quantified.

Results of the pressure calculations showed that the blocked pressure from sources at a specific x_0 indeed decays quite rapidly with distance $|x-x_0|$. For example, in Fig. 4, the blocked surface pressure decays more than 20 dB for relative x of 1.27 cm (0.5 in.). Plots of blocked pressure versus relative axial location for several frequencies are shown in Fig. 4. In general, the decay of blocked pressure is independent of frequency. These results support the use of the Dirac delta function as noted previously.

Fluid-Coupled Shell Vibration with Confined Jet Excitation

As discussed previously, the pipe wall response was obtained by solving the characteristic or spectral equations of the fluid-filled shell vibration problem. The spectral radial displacement has been given in Eq. (14). Consequently, the radial velocity and acceleration were obtained by differentiating Eq. (14).

To calculate the pipe wall acceleration, it is required to specify the blocked excitation pressure distribution as a function of x. As discussed previously, the blocked surface pressure decays rapidly and linearly with x. A special case was presented earlier, in which a relatively simple form of an amplitude modulated convecting wave field was used as the blocked surface pressure. Hence, the blocked excitation pressure distribution was assumed to be triangular. The width of the triangular distribution 2L, is associated with the pressure correlation length.

The response of the pipe wall due to excitation by a harmonic ring load was calculated. A plot of the ratio of wall acceleration to peak pressure P_0 versus location is shown in Fig. 5 for several frequencies. As shown, the wall acceleration decays quite rapidly for x less than 2.54 cm (1 in.). It should be noted that the decay at high frequencies is less than the decay at low frequencies.

Based on the statistical approach as presented previously, the cross spectral density of the pipe wall velocity was evaluated according to Eq. (26). In the calculations, it was assumed that the pressure fluctuations are correlated in the x direction. The correlated pressure fluctuations reflect the occurrence of large-scale coherent structures in the jet developing region. As shown and discussed by Ng[14], the high coherence functions in wall pressure data are attributed to the large-scale coherent structures.

The expression for the pipe wall velocity due to an amplitude modulated convecting wave field was presented in Eq. (28). As discussed previously, the blocked pressure was assumed to have a triangular distribution. In the calculations the half width L, which here corresponds to the correlation length scale, was allowed to vary with frequency in a manner which is similar to the experimental results presented by Clinch[16] for the pipe flow. The correlation length was assumed to be a function of the jet diameter. Specifically, the values of L range from about 3 jet diameters at 2 kHz to about 12 jet diameters at 100 Hz. Results showed the calculated wall acceleration spectra agree well with the experimental data.

Pipe Wall Pressure Due to Flexible Wall Vibration

The shell wall pressure calculations were obtained by solving the fluid-filled shell vibration problem with the blocked surface pressure as the excitation source. An expression relating the flexible wall pressure to the blocked pressure was given in Eq. (21). In the evaluation of the sum of residues, the summation was truncated at s = 10.

A typical flexible wall pressure spectrum is shown in Fig. 6. As shown, the flexible wall pressure spectrum is lower than the blocked surface pressure, particularly at the low frequencies. For the range of frequencies of interest, the blocked surface pressure is dominant.
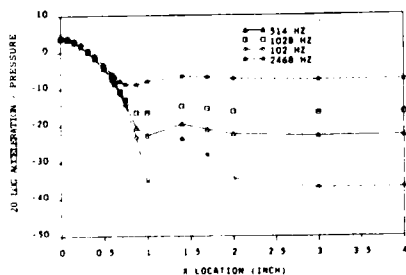
Figure 5--Wall Acceleration vs location
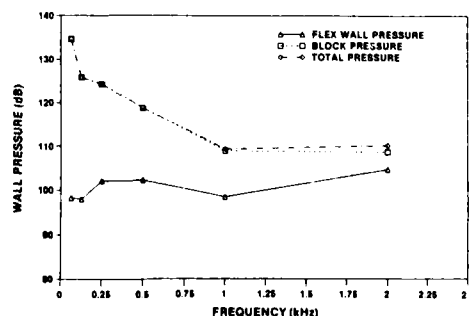
Figure 6--Flexible wall pressure spectrum

78

Comparison with Experimental Data

1. Wall Pressure

The wall pressure was calculated by summing the blocked surface pressure and flexible wall pressure. Because the blocked surface pressure is dominant for the range of frequencies of interest, the flexible wall pressure has no significant contribution on the wall pressure calculations. The expressions for the blocked pressure and flexible wall pressure were presented in Eqs. (9b) and (21). It was assumed that the pressure fluctuations are uncorrelated in the radial direction, and the local weighting function $\partial^2 G / \partial x_i \partial x_i$ can be approximated by a Dirac delta function in the x direction.

A typical comparison of the calculated wall pressure with experimental data is shown in Fig. 7 for the 1.00-in diameter jet. The agreement is reasonably good, except for the pipe flow case in which the calculated spectrum is higher than the measured spectrum by about 6 db. In general, the calculated wall pressure spectra are higher than the measured spectra in the high frequencies. Because of the low data rates associated with the LDV data, the accuracy of the calculated wall pressure spectra decreases for frequencies above 2 kHz.

2. Pipe Wall Acceleration

Typical calculated wall acceleration spectrum is shown in Fig. 8 for the 1.50-in diameter jet. For comparison purpose, the measured wall acceleration spectrum is also plotted. As shown, the calculated wall acceleration spectrum agrees reasonably well with the acceleration measurements. In most cases, the model overpredicts slightly in the low frequencies, i.e, for frequencies less than 500 Hz.
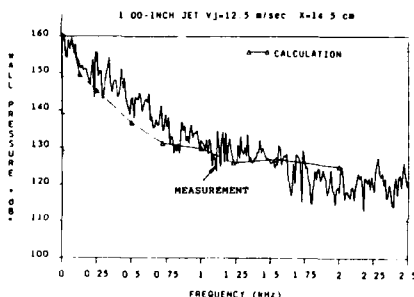
Figure 7--Wall pressure spectra comparison - 1.00-inch jet
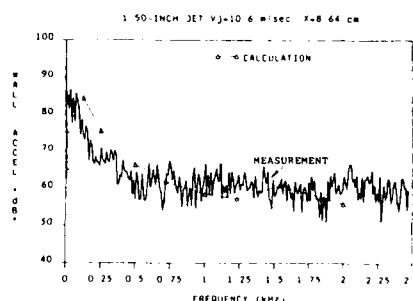
Figure 8--Wall acceleration spectra comparison - 1.5inch jet

CONCLUSIONS

A noise model was developed to calculate the wall pressure and the response of the pipe wall due to the turbulent jet flow in the pipe. An approach has been presented to evaluate the wall pressure fluctuations and pipe wall acceleration due to the excitation of turbulent jet flows. Based on flow field measurements, the blocked surface presssure was calculated using the Lighthill method, and then used to drive the fluid-filled shell. The wall pressure and pipe wall acceleration were determined by solving the coupled fluid solid interaction problem. The wall pressure was obtained by summing the blocked surface pressure and the pressure due to the wall vibration.

Principal results and conclusions to be drawn from the study are as follows:

1. The source strength based on the Lighthill's method was calculated from the experimentally determined turbulence structure of the jet flow. The source term is controlled by the interaction of the mean axial velocity and axial velocity fluctuations.

2. The blocked surface pressure was obtained by integrating the product of the source term and the local weighting Green's function in the source region. Because the weighting function is an oscillatory function, spatial averaged values of the weighting function at each LDV measurement point were used in the blocked pressure calculations. The amplitude of the local weighting function increases toward the wall and decays rapidly in the axial direction. The blocked pressure is controlled by the sources near the wall since the values of the local weighting function are dominant near the wall region.

3. The random nature of the turbulent jet was incorporated into a statistical analysis of the jet sources. Specifically, the acoustic pressure was assumed to result from hydrodynamic pressure fluctuations which are uncorrelated in the radial direction, but are correlated in the axial direction near the jet exit. The uncorrelated pressure fluctuations in the radial direction reflect the random motion of the turbulent jet,

whereas the correlated pressure fluctuations in the axial direction reflect the motion of the large-scale coherent structures near the jet exit.

4. The width of the triangular pressure distribution for the statistical calculations was chosen to represent the correlation length scale of the pressure fluctuations. The correlation length scale is a function of frequency. Specifically, the values of L range from about 3 jet diameters at 2 kHz to about 12 jet diameters at 100 Hz.

5. Numerical results showed that the blocked pressure is dominant as compared to the pressure due to the wall motion. The blocked pressure decays faster than the pipe wall acceleration with respect to the axial location. In the pipe wall response, the low frequencies decay faster than the high frequencies.

6. Numerical results have demonstrated that the noise model is capable of relating the flow field and acoustic field of confined jet flows. Results from the analytical model showed good agreement with the measured wall pressure and pipe wall acceleration.

7. Although the analytical development and noise model focused on the prediction of flow-induced noise and vibration of confined jets, the analytical noise model can also be applied to the pipe flow noise prediction problem.

ACKNOWLEDGMENTS

REFERENCES

1. G. Reethof, "Turbulence-Generated Noise I - Pipe Flow," Ann. Rev. Fluid Mech., 333-367 (1978).

2. J. L. Walter, "Coincidence of Higher Order Modes - A Mechanism of the Excitation of Cylindrical Shell Vibrations Via Internal Sound," Ph.D. Thesis, Penn State University 1979.

3. A. C. Fagerlund, "A Theoretical and Experimental Investigation of the Effects of the Interaction between an Acoustic Field and Cylindrical Structure on Sound Transmission Loss," Ph.D. Thesis, University of Iowa, 1979.

4. K. W. Ng, "Aerodynamic Noise Generation in Control Valves," ASME Paper 80-WA/NC-8, 1980.

5. H. T. Loh, "Circular Pipe Wall Vibratory Response Excited by Internal Acoustic Fields," M.S. Thesis, Penn State University, 1981.

6. M. P. Norton and M. K. Bull, "Mechanisms of the Generation of External Acoustic Radiation from Pipes due to Internal Flow Disturbances," J. Sound Vib., 94(1) 105-146 (1984).

7. B. Stahl, "An Experimental Investigation of Noise Generated by Turbulence in a Pipe Flow Behind a Discontinuous Area Enlargement," DFVLR, Dissertation (D. of Eng.), November 1985.

8. R. F. Bergeron, "Aerodynamic Sound and the Low-Wavenumber Wall-Pressure Spectrum of Nearly Incompressible Boundary-Layer Turbulence," J. Acoust. Soc. Am., 54, 123-133 (1973).

9. D. M. Chase, and C. F. Noiseux, "Turbulent Wall Pressure at Low Wavenumbers: Relation to Nonlinear Sources in Planar and Cylindrical Flow," J. Acoust. Soc. Am., 72, 975-982 (1982).

10. S. A. Abdallah, "On the Wall Pressure Fluctuations and the Flow Field Structure Distal to a Modeled Stenosis," Ph.D Thesis, University of Houston, 1984.

11. W. A. Olsen, J. H. Miles, and R. G. Dorsch, "Noise Generated by Impingement of a Jet upon a Large Flat Plate," NASA TN D-7075, 1972.

12. A. W. Leissa, "Vibration of Shells," NASA SP-288,1973.

13. C. R. Fuller, "The Mobility of an Infinite Circular Cylindrical Elastic Shell Filled with Fluid," J. Sound Vib., 87, 409-427 (1983).

14. K. W. Ng, "Fluctuating Wall Pressure and Vibratory Response of a Cylindrical Elastic Shell due to Confined Jet Excitations," Ph.D. Thesis, University of Rhode Island, 1988.

15. C. R. Fuller and F. J. Fahy, "Characteristics of Wave Propagation and Energy Distributions in Cylindrical Elastic Shells Filled with Fluid," J. Sound Vib., 81, 501-518 (1982).

16. M. Abramowitz and I. A. Stegun, "Handbook of Mathematical Functions with Formulas, Graphs, and Mathematical Tables," National Bureau of Standards, 1964.

17. J. M. Clinch, "Measurements of the Wall Pressure Field at the Surface of a Smooth-Walled Pipe Containing Turbulent Water Flow," J. Sound Vib., 9, 398-419 (1969).

SECOND INTERNATIONAL CONGRESS ON
RECENT DEVELOPMENTS IN AIR- AND
STRUCTURE-BORNE SOUND AND VIBRATION
MARCH 4-6 1992   AUBURN UNIVERSITY USA

STRUCTURAL-ACOUSTIC COUPLING IN AIRCRAFT FUSELAGE STRUCTURES

Gopal P. Mathur and Myles A. Simpson

Douglas Aircraft Company
McDonnell Douglas Corporation
3855 Lakewood Blvd, MC 36-60
Long Beach, CA 90846, U.S.A.

ABSTRACT

Results of analytical and experimental investigations of structural-acoustic coupling phenomenon in an aircraft fuselage are described. The structural and acoustic cavity modes of DC-9 fuselage were determined using a finite element approach to vibration analysis. Predicted structural and acoustic dispersion curves were used to determine possible occurrences of structural-acoustic coupling for the fuselage. An aft section of DC-9 aircraft fuselage, housed in an anechoic chamber, was used for experimental investigations. The test fuselage was excited by a shaker and vibration response and interior sound field were measured using accelerometer and microphone arrays. The wavenumber-frequency structural and cavity response maps were generated from the measured data. Analysis and interpretation of the spatial plots and wavenumber maps provided the required information on modal characteristics, fuselage response and structural-acoustic coupling.

INTRODUCTION

The sound transmission and radiation characteristics of aircraft fuselage structures are strongly dependent on the structural-acoustic coupling inside the fuselage shell. A knowledge of fuselage shell modes and their coupling with the cavity modes can be valuable in the design of both passive and active noise control treatments. In recent years, analytical and experimental studies have been conducted on the coupling mechanism of a vibrating finite circular cylindrical shell and its interior cavity, closed with rigid end caps using mode matching technique [1]. The mode matching technique requires expanding the shell wall displacement in terms of acoustic modes. In the case of practical structures, such as an aircraft fuselage, it is often difficult to map and distinguish between different spatial modes as many shell modes contribute to the response. The wavenumber matching method, on the other hand, overcomes this difficulty of spatial mode matching technique.

In the wavenumber matching technique, acoustic and structural wavenumber maps or dispersion diagrams are superposed to study structural-acoustic coupling. Some of the lower order shell modes are acoustically fast below the ring frequency. Such modes can be efficient radiators if they can couple with similar cavity modes. The structural-acoustic coupling occurs for those acoustic and structural modes that are of same axial and circumferential orders [2]. This equality of circumferential and axial wavenumbers (or modes) is also known as coincidence condition. Although the coupled acoustic and structural modes differ

81

from the respective uncoupled modes, they may be assumed to resemble closely their uncoupled components for the purposes of approximate analysis. This paper presents results of analytical and experimental investigations on the structural-acoustic coupling phenomenon in an aircraft fuselage using wavenumber matching approach.

THEORETICAL BACKGROUND

Aircraft fuselage structure, in general, is a complex stiffened shell and does not conform to the idealized form of a circular cylindrical shell. The cylindrical shell analysis, however, is useful in understanding the flexural wave motion in such structures. A brief introduction to wavenumber (or k-space) analysis of structural-acoustic coupling is first presented for a uniform cylindrical shell.

The flexural wave motion in a uniform cylindrical shell can be characterized by axial (or longitudinal) and circumferential wavenumbers, k_a and k_c. The non-dimensional wavenumber functions, $\hat{k}_a$ and $\hat{k}_c$, for the structural vibration of an idealized cylindrical shell are [3]:

$$\hat{k}_a = k_a \left(\frac{h^2 R^2}{12(1-\mu^2)} \right)^{\frac{1}{4}}$$

$$\hat{k}_c = k_c \left(\frac{h^2 R^2}{12(1-\mu^2)} \right)^{\frac{1}{4}}$$

where $k_a = \left(\frac{m\pi}{L} \right)$ and $k_c = \left(\frac{N}{R} \right)$, and m is the axial mode number, N is the structural circumferential mode number, R and L are the radius and length of the cylinder respectively, and μ is the Poisson ratio. The formula for natural frequencies of a cylindrical shell can be expressed in the following form [3]:

$$\omega_{mN} = \left((\hat{k}_a^2 + \hat{k}_c^2)^2 + \frac{\hat{k}_a^4}{(\hat{k}_a^2 + \hat{k}_c^2)^2} \right)^{\frac{1}{2}} \omega_r$$

where ω_r is the ring frequency of the cylinder.

The acoustic modes of a rigid-walled cylindrical waveguide take the following form [4]:

$$p_{mn}(r, \phi, z) = P_{mn} \frac{sin}{cos} (n\phi) J_n(k_r r) cos(k_z z)$$

where J_n is the Bessel function, m is axial mode order, n is the acoustic circumferential mode order, P_{mn} is pressure amplitude, and (r, ϕ, z) denote a cylindrical coordinate system. The radial wavenumber k_r is determined by the zero normal-particle wall boundary condition as characteristic solutions k_r^{np} of the equation:

$$\left[\frac{\partial J_n(k_r r)}{\partial r} \right]_{r=R} = 0$$

where n indicates the number of diametral pressure nodes and p the number of concentric circular pressure nodes (radial mode order).

The axial and radial wavenumbers satisfy the acoustic wave equation resulting in the following dispersion relationship for the cylindrical cavity:

$$k_z^2 + (k_r^{np})^2 = k^2$$

where k is acoustic wavenumber ($= \omega/c_0$) and c_0 is speed of sound. The axial (k_a) and circumferential (k_c) wavenumbers and the modal frequencies for the cylindrical cavity are given by:

$$k_a = (k_z)|_{z=L} = \frac{m\pi}{L}$$

$$k_c = (k_r^{np})|_{r=R} = \frac{\gamma_{np}}{R}$$

$$\omega_{mnp}^2 = (\frac{c}{2\pi})^2 \left(k_a^2 + k_c^2\right)$$

where γ_{np} are characteristic solutions of the equation $[J_n'(k_r)]_{r=R} = 0$ for the cylindrical cavity.

In order to understand the acoustic waveguide behavior of aircraft fuselage cavity, uncoupled acoustic modal characteristics of an equivalent hardwalled, stiffened cylindrical shell were first studied using the matrix difference equation (MDE) method [5]. This method is a computer code developed at Douglas Aircraft Company using a finite element approach to vibration analysis; the basic simplifying assumption is that the structure is spatially periodic or repetitive, meaning that it is a longitudinal array of identical substructures. The computer code is applicable to coupled structural-acoustic modes representing the fuselage structure and the air inside.

DESCRIPTION OF TEST PROGRAM

All tests were conducted in the Douglas Aircraft Company (DAC) Fuselage Acoustics Research Facility (FARF). The facility consists of the aft section of a DC-9 aircraft fuselage, noise and vibration sources, a multi-channel digital data acquisition and processing system, and an anechoic chamber to house the fuselage section. Figure 1 shows the fuselage test section, with the frame station and longeron numbering system.

The fuselage shell and cavity were excited by a single mechanical shaker. The input signal to the shaker was broadband random between 100 and 1000 Hz. The shaker was mounted on a support structure, and attached to the right side of the fuselage at station 718, longeron 9. An array of accelerometers was mounted on the left side of the fuselage. This 13x15 array had a longitudinal spacing of 9.5 inches and a circumferential spacing of 15.4 inches. The accelerometer on the left side at station 718 just under longeron 9 was used as a reference accelerometer for vibration measurements.

Within the cabin, an array of 75 microphones shown in Figure 2 was used to measure interior noise levels at 13 stations (approximately 19 inches apart) from station 547 to station 779. For these measurements the reference microphone was located on the cabin centerline, approximately 20 inches above the floor and 40 inches in front of the interior loudspeaker at the front of the cabin. Further details of instrumentation and measurements are given in Reference [6].

DISCUSSION OF RESULTS

The uncoupled acoustic modes of an equivalent hardwalled, stiffened cylindrical shell were determined using a MDE model. The radius (R=65.8 inch) and length (L=380 inch) of the cylindrical shell cavity are the same as that of the FARF (DC-9) fuselage. The MDE model of the hardwalled cylindrical shell consisted of 20 substructures, each substructure being 19 inches long. Figure 3 shows sample predicted acoustic pressure contours for the (m=3, n=2, p=0) mode. The circumferential (n) and radial (p) mode ordering of these acoustic modes can be done by either comparing the predicted contours with those obtained from the classical theory for circular cylindrical shells or by identifying the modal distribution of acoustic pressures.

The acoustic and structural dispersion diagrams for uncoupled modes of the cylindrical shell are shown superimposed in Figure 4. For a given circumferential mode order, equality of axial wavenumber (or mode

order) gives the coincidence condition. At coincidence, optimum conditions exist for transfer of energy between these modes. The mode coupling would occur where structural and acoustic dispersion curves coincide or cross each other for the same axial and circumferential mode order. Figure 4 indicates that the coincidence between the lower-order circumferential shell modes (e.g. N=0 and 1) and the lower-order circumferential acoustic modes (e.g. n=0 and 1) and low radial order (p=0), can occur at frequencies close to the acoustic mode cutoff frequencies. Between the lowest acoustic mode cutoff frequency and the ring frequency, there can be several such coincidences; any one shell mode can be coincident with all the acoustic modes of equal circumferential order (n) and increasing radial order (p). Multiple coincidences between the lower order structural and acoustic curves may also occur since portions of these curves run parallel to each other (e.g. the N=0 structural curve and the (n=0, p=4) acoustic curve). The chance of coincidence for the higher order shell modes (N = 4 and above), however, becomes less as the structural curves tend to rise rapidly and run parallel to the lower order acoustic curves.

The MDE model of the hardwalled cylindrical cavity was modified to represent the flexible wall test fuselage. The coupled modal frequencies and mode shapes for the fuselage were determined using the MDE model. Figure 5 shows the cavity spatial pressures predicted at 118 Hz. This predicted (n=2, p=0) acoustic mode compares very well with the measured cavity mode at 105 Hz (see Figure 6). The difference in frequencies is likely due to the simplified model used for predictions.

The structural and acoustic dispersion curves for the fuselage were constructed using the MDE method and are shown in Figure 7. These dispersion curves, particularly for the lower-order modes, appear to be very similar to those obtained for the equivalent cylindrical shell. It may be observed from Figure 7 that structural-acoustic coupling can occur for the (1,1) structural mode and the (1,1,0) acoustic mode, in the frequency range from 60 to 70 Hz (below the frequency range measured during the test program). The figure also shows that structural acoustic coupling may occur for the (3,2) structural mode and the (3,2,0) acoustic mode, in the frequency range from 120 to 150 Hz.

Measured fuselage acceleration levels and cabin noise levels under broadband shaker excitation were used to define the structural and cavity modal characteristics of the fuselage. The wavenumber spectrum analysis approach was used to examine the structural-acoustic coupling for the FARF fuselage, between the (3,2) structural mode and the (3,2,0) acoustic mode. The spatial domain data for the vibration response was obtained using the 13x15 array of accelerometers mounted on the left side of the fuselage. The interior sound field was mapped using a three-dimensional array of microphones, comprised of the microphones in a ring around the periphery of the cabin adjacent to the sidewall (i.e., ring 5 on Figure 2), at each of 13 stations within the cabin. The k-space vibration response was obtained by implementing two-dimensional spatial Fourier transforms (at each temporal frequency) on the spatial domain data.

The circumferential wavenumbers and mode orders of the structural and acoustic cavity modes are related by the following relationships: $k_c = N/R$ for the structural mode and $k_r^{np} = \frac{\gamma_{np}}{r}|_{r=R}$ for the acoustic cavity mode, where n and p are circumferential and radial mode numbers for acoustic modes respectively. The axial mode numbers may also be calculated from the axial wavenumbers using $k_a = \frac{m\pi}{L}$. Since acceleration and pressure wavenumber-frequency spectra are complex functions, only magnitude of these functions will be shown in the form of contour plots.

The k-space vibration reponse of the fuselage at 105 Hz due to the shaker broadband excitation is shown in Figure 8. The k-space acoustic response of the FARF cavity at the same frequency obtained from the ring 5 array of microphones is shown in Figure 9. It may be observed in Figure 8 that a number of structural modes (N=2 to 7) contribute to the response of the FARF structure at 105 Hz. The acoustic modes contributing to the FARF cavity response are found (Figure 9) to be in the range of n=1 to 3 with the n=2 mode being the most dominant. Although the N=2 structural mode is not resonant at 105 Hz, it has spatial contribution at this frequency and shows up with somewhat diminished amplitude in the vibration wavenumber plot. It therefore appears from Figures 8 and 9 that the N=2 structural mode is coupling with the n=2 acoustic mode, in agreement with the earlier predictions.

CONCLUSIONS

Analytical and experimental investigations were conducted on the DC-9 aft fuselage test section to study the shell and cavity modal characteristics and the structural-acoustic coupling characteristics of the fuselage. The matrix difference equation (MDE) method based on finite element approach was used to study the structural-acoustic coupling and to make mode coupling predictions for a cylindrical shell and the FARF fuselage. Coupling of the structure and acoustic cavity is expected to occur at only those frequencies for which there is a structural mode and a cavity mode of identical axial and circumferential mode order.

The test fuselage was excited by a shaker with broadband random input and vibration response was measured with an array of accelerometers on the left side of the structure. Interior noise levels were measured at 13 locations along the length of the cabin with an array of microphones throughout the cabin cross-section. The structural and cavity mode shapes were derived from the measured accelerometer and microphone data.

To define the primary modes contributing to the fuselage vibration and cavity acoustic pressure at selected frequencies, a wavenumber analysis of the measured data was undertaken. The resulting wavenumber maps confirmed the MDE predictions that the $N=2$ structural mode would couple with the $(n=2, p=0)$ circumferential cavity mode; from the measurements this was found to occur at 105 Hz.

The wavenumber analyses were found to be very useful in defining the structural-acoustic behavior of the fuselage. The wavenumber-frequency maps provide information about the structural-acoustic response of the fuselage/cavity that is usually not obtainable from conventional analyses based in the spatial domain.

ACKNOWLEDGEMENTS

REFERENCES

[1] Silcox, R. ar J H. Lester, "Propeller Modelling Effects on Interior Noise in Cylindrical Cavities with Application to Active Control," AIAA Paper 89-1123, presented at the 12th Aeroacoustics Conference held at San Antonio, TX, April 10-12, 1989.

[2] Fahy, F., *Sound and Structural Vibration: Radiation, Transmission and Response*, Academic Press Inc. (1985).

[3] Szechenyi, E., "Modal Densities and Radiation Efficiencies of Unstiffened Cylinders Using Statistical Methods," J. Sound Vib. 19, 1971, pp.65-81.

[4] Morse, P. M., *Vibration and Sound*, McGraw-Hill Company, New York (1948) (Reprinted by The Acoustical Society of America, 1981).

[5] Denke. P. H., "The MDE Method for Aircraft Cabin Interior Noise Prediction," ASME Paper 892372, presented at the SAE Aerospace Technology Conference and Exposition held at Anaheim, CA, September 25-28, 1989.

[6] Simpson, M. A., G. P. Mathur, M. R. Cannon, B. N. Tran and P. L. Burge, "Fuselage Shell and Cavity Response Measurements on a DC-9 Test Section," NASA Contractor Report NASA CR-187557, August 1990.
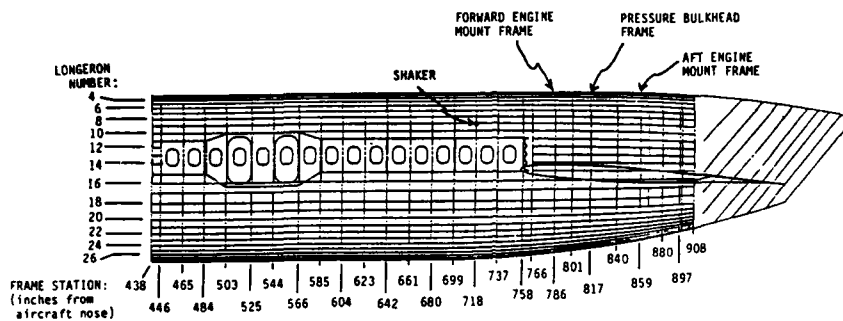
Figure 1: The DC-9 fuselage test section, showing frame and longeron numbering.
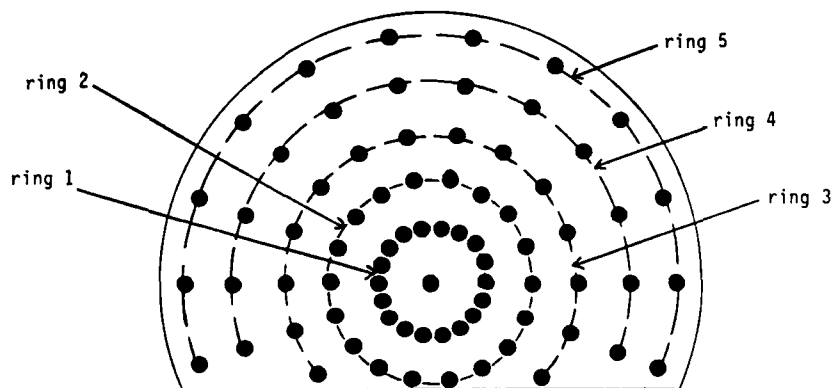
Figure 2: The interior microphone array.
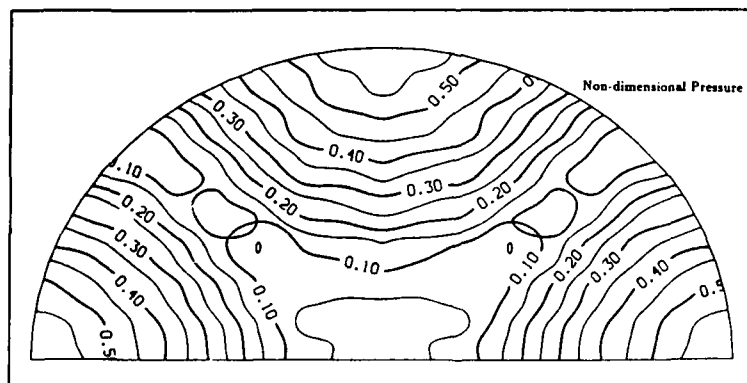
Figure 3: Predicted uncoupled ($m=3$, $n=2$, $p=0$) mode for a cylindrical cavity.
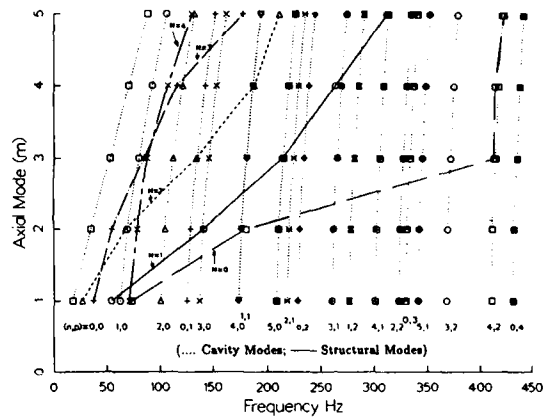
Figure 4: Structural and acoustic dispersion curves for identifying coupled modes for a cylindrical shell.
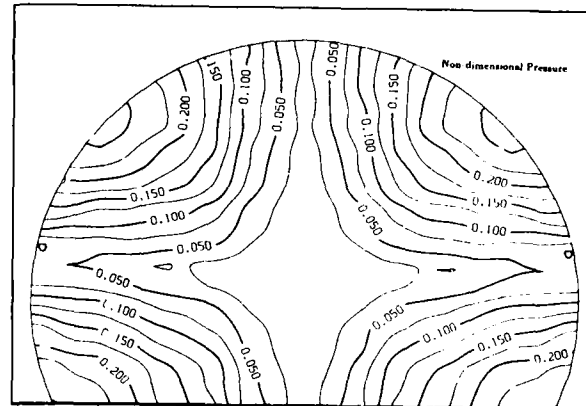
Figure 5: Predicted coupled (n=2, p=0) mode for the test fuselage cavity at 118 Hz.
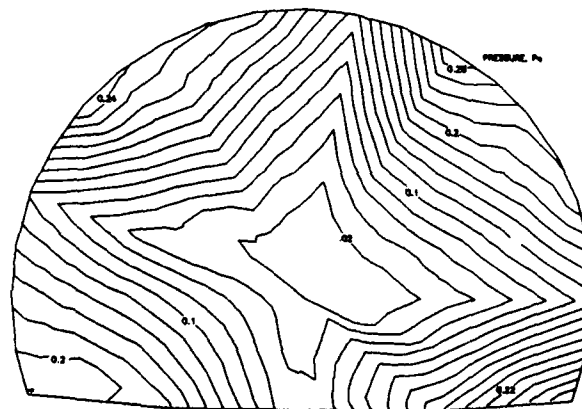
Figure 6: Sample measured coupled cavity mode of the test fuselage at station 718 (105 Hz).
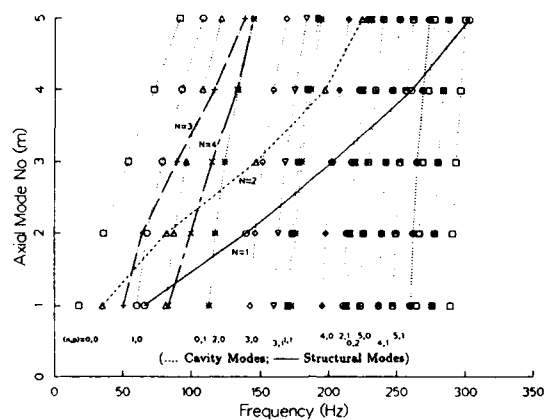
Figure 7: Structural and acoustic dispersion curves for identifying coupled modes for the test fuselage.
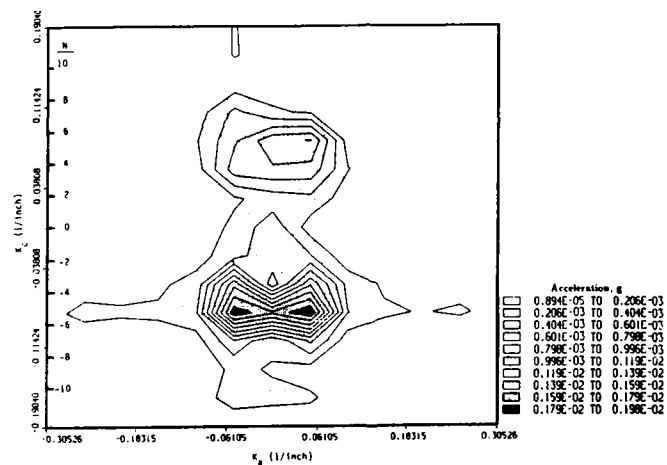
Figure 8: Acceleration wavenumber plot for shaker excitation, 105 Hz.
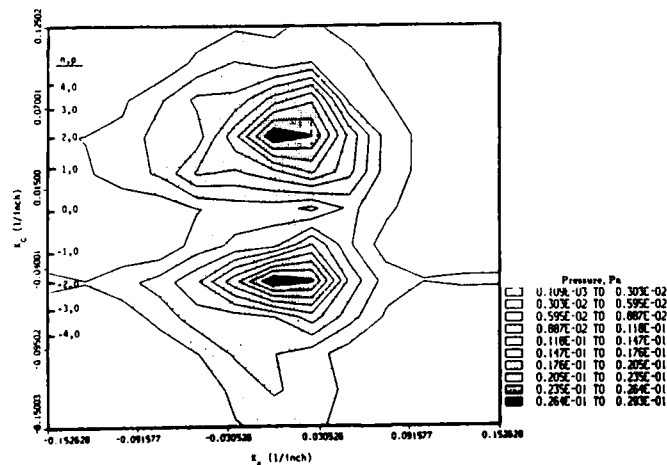
Figure 9: Pressure wavenumber plot for shaker excitation, 105 Hz.
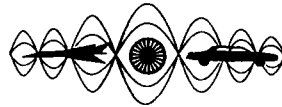
88

**SECOND INTERNATIONAL CONGRESS ON
RECENT DEVELOPMENTS IN AIR- AND
STRUCTURE-BORNE SOUND AND VIBRATION**

MARCH 4-6, 1992   AUBURN UNIVERSITY, USA

RESPONSE VARIABILITY OBSERVED IN A REVERBERANT
ACOUSTIC TEST OF A MODEL AEROSPACE STRUCTURE

Robert E. Powell

Cambridge Collaborative Inc.
689 Concord Avenue
Cambridge, Massachusetts   02138
U.S.A.

ABSTRACT

   One of the most difficult concepts to grasp in Statistical Energy Analysis is that structural response can be considered a random variable. It is instructive to perform statistical analyses on actual test data in order to investigate assumptions about the distribution of response. These types of analyses are rarely carried out because of the relatively low number of measurements typically obtained during a test. This paper presents a statistical analysis of the structural response during a reverberant acoustic test of a prototype aerospace component. The test article was the mass/thermal/acoustic model of the photovoltaic power management and distribution system for the NASA Space Station Freedom. The analysis takes advantage of the large number of acceleration sensors located on component attachment screws to conclude that the spatial variation of power spectral density (PSD) averaged in third octave bands can be described by a lognormal probability distribution.

INTRODUCTION

   One of the most useful concepts of Statistical Energy Analysis (SEA) is that the dynamic response of acoustical and structural systems can be modeled as a random variable. The subject of this paper is the description of the spatial probability distribution of a set of structural responses measured during a reverberant acoustic test of the Mass/Thermal/Acoustic Model (MTAM) of the photovoltaic power management and distribution system for the NASA Space Station Freedom. Prediction of the distribution of responses is of considerable importance in setting random vibration test levels for all of the components to ensure their reliable functioning after being exposed to the launch vibroacoustic environment.

Background
   Third octave band sound pressure *levels* measured in the aerospace launch environment are commonly accepted to be random variables following a normal (gaussian) probability distribution. This means that the mean-square pressure responses in each band follow a *lognormal* distribution. It is simple to envision the flight-to-flight variability of the acoustic environment carrying over to the ensuing structural response of a payload   More difficult to grasp is that the same factors contributing to the spatial variability in the interior acoustic field—distributed excitation, multi-modal response, and spatial variation of mode shapes—can create structural responses that appear spatially random, even if the structure is considered perfectly linear and deterministic.

   Once the concept of spatially random structural response is accepted, the next problem is to define its statistics. The U.S. aerospace industry standard for describing the maximum expected *acoustic* environment is a third octave band spectrum where the level in each band is defined as equal to or greater than the value at the ninety-fifth

percentile value at least 50 percent of the time. Prediction of this value from test data requires an assumption of the underlying probability distribution function in order to estimate the ninety-fifth percentile at a 50% confidence level. The set of band levels predicted by this method is commonly denoted as the P95/50 acoustic spectrum.

It would be useful if similar statistical procedures could be followed in characterizing structural response. In particular, SEA predictions of average response and variability require an assumption of a probability distribution in order to assign a P95 level. There is no "/50" involved in the theoretical prediction, because it is determined for the population rather than being estimated from sampled data. The unknown variable in an SEA prediction is the average—or mean—of the mean-square vibrational response in a frequency band. The actual mean-square response of a structural element varies in space. With an infinite number of sensors during a test, one could determine the mean and higher moments of spatial variation. Assuming there are no other sources of variability, the P95 response is the mean-square response exceeded by only 5% of the structure. Because the mean-square is non-negative, its amplitude distribution cannot be symmetric about the mean, as is the gaussian, or normal distribution. A gamma distribution was suggested as a convenient form in the initial paper on SEA confidence intervals by Lyon and Eichler [1], but they did not present any experimental data or theory to support that particular choice. This material also appeared in the 1975 textbook by Lyon [2] describing SEA methods. A study of structural responses during several reverberant acoustic tests at Lockheed and at the NASA Jet Propulsion Laboratory is presented in [3]. The conclusion of that study was that third octave band PSD responses are lognormally distributed, but that a better fit to data is obtained if a skew factor of 1.2 is applied. A true lognormal distribution would have a skew factor of one.

Structural similarity between measurement locations—in acoustic coupling, structural damping, and impedance—is critically important for the assessment of probability distribution. Because of the relatively few structural response sensors available from flight tests, there is a tendency to lump all of the sensors from a payload into a single ensemble. Since bare panels tend to respond more strongly than those highly loaded by components, there are often two or more distributions with different means being combined into a single, bimodal distribution. The assumptions underlying the P95 calculations are then violated.

In this paper, a set of data from a reverberant acoustic test of a large prototype aerospace payload is analyzed to determine whether the spatial variation of structural response can be described by a lognormal distribution. Acceleration PSD spectra from 73 sensors on attachment locations of similar components were processed into third octave band average PSD, with 23 bands per spectrum from 20 Hz to 3.15 kHz center frequencies. The raw data was transformed to decibels, and the levels in each band were normalized to zero mean and unit variance. The resulting 1679 samples were tested for goodness-of-fit to a normal distribution. The Kolmogorov-Smirnov test statistic indicated that the log-scaled data could have been drawn from a normal distribution with a significance level of 0.2. This means that one in five datasets of this size drawn from a true normal distribution would have poorer fit to the theoretical gaussian distribution. The conclusion is that the third octave average PSD responses on these components were spatially lognormal when excited by a reverberant acoustic field.

MTAM ACOUSTIC TEST

The test article was the Mass/Thermal/Acoustic model (MTAM) of the photovoltaic power management and distribution system for the NASA Space Station Freedom. The Work Package Four team includes the NASA Lewis Research Center, Rocketdyne Division of Rockwell International, Ford Aerospace, and Lockheed. Cambridge Collaborative, Inc. provides support to NASA Lewis on acoustic and vibration analysis. The MTAM prototype was constructed and tested by Rocketdyne to help verify the structural design concepts, as well as design analysis procedures.

The major elements included a structural strongback to support 26 large component boxes, known as orbital replacement units (ORUs); bulkheads supporting a thermal radiator and gimbal cylinders for positioning the solar array; and four large boxes containing the stowed photovoltaic array blankets. The most sensitive electronic equipment, including batteries for the entire power system, is to be packaged into ORUs to facilitate on-orbit replacement. Figure 1 is a sketch of the structural strongback with 13 ORUs on each side. The longer dimension spans the cargo bay of the shuttle orbiter during launch. Each ORU is held onto the structure by two acme screws—designed for quick removal and replacement of the ORUs after the space station is assembled and operational. The six large ORUs on each side contain the battery cells for storing the solar energy converted by the photovoltaic array. The smaller ORUs include cooling pumps and control electronics for the power management system.

The MTAM acoustic test was designed and run by Rocketdyne and took place in October and November 1990 at the Martin Marietta Waterton Test Facility near Denver, Colorado. The vibration data gathered during the acoustic test was extensive—260 channels of narrow band (1 Hz Δf) acceleration spectra for each of seven acoustic test levels. Twenty-six triaxial accelerometers were allocated to the acme screw attachment locations, resulting in 78 channels of vibration data for structurally-similar locations.

DATA REDUCTION

For this study, data from only the highest of the seven acoustic test levels was considered. The following steps were followed in reducing the test data from the acme screw triaxial accelerometers:

1) Calculate one-third octave band averages of PSD for each channel using 1 Hz narrow band PSD. Reasonably good data was available from 20 Hz to 3.15 kHz center frequencies (23 bands).

2) Plot the reduced data on a log-log scale to screen out any channels with noise contamination or dropouts. Five of 78 channels were rejected due to noise contamination, leaving 73 spectra for further analysis.

3) In each band, calculate mean and sample standard deviation of the third octave PSD.

4) Convert the PSD data to decibels by a 10 Log(PSD) transformation. In each band, calculate decibel mean and sample standard deviation.

5) Normalize the dB data to a single zero-mean, unit-variance ensemble by subtracting the band mean from each sample and then dividing the result by the standard deviation in that band.

Third Octave Averaging and Data Screening

Figure 2 illustrates a typical third octave average spectrum compared to a narrow band curve. The third octave average is seen to follow the trend of the narrow band data, but the peak levels are reduced about 3 to 6 dB by the band averaging. Figure 3 is a surface plot of the log PSD for all 78 channels and 23 frequency bands. In Figure 4, the same data is shown sorted by descending response in the 20 Hz band, to show the contamination by low-frequency noise. One channel has obvious broadband noise contamination, and several others appear to have a suspiciously linear frequency spectrum. The five channels with 20 Hz PSD greater than 0.1 g^2/Hz were rejected from further processing because of the apparent noise contamination.

STATISTICS OF RESPONSE

Means and sample variances in each frequency band were calculated on both PSD responses and PSD levels in decibels.
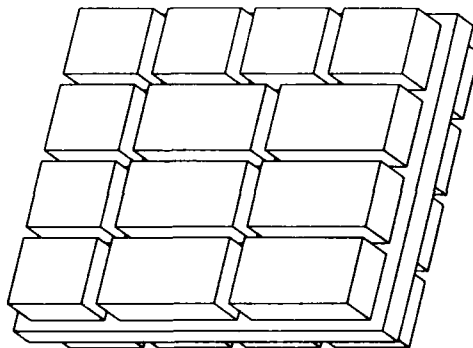
Figure 1. Sketch of the MTAM strongback with 26 orbital replacement units.
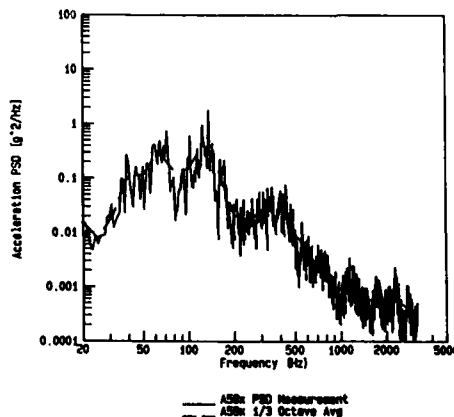
Figure 2. Example of third octave average data reduction.

91
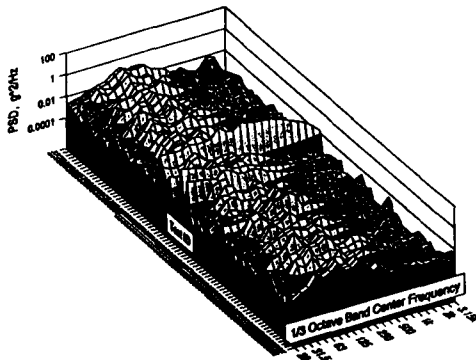
Figure 3. Surface plot of measured PSD for Figure 4. Data from Figure 3 sorted by 20 Hz
MTAM acme screws.   third octave.
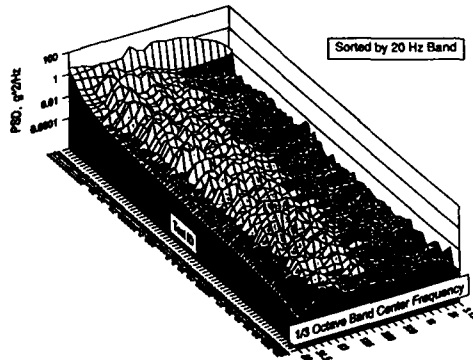
$$m_{PSD} = \frac{1}{N} \sum_i PSD_i \tag{1}$$

$$s^2_{PSD} = \frac{1}{N-1} \sum_{i=1}^{N} (PSD_i - m_{PSD})^2 \tag{2}$$

$$m_{dB} = \frac{1}{N} \sum_{i=1}^{N} dB_i \tag{3}$$

$$s^2_{dB} = \frac{1}{N-1} \sum_{i=1}^{N} (dB_i - m_{dB})^2 \tag{4}$$

where N is the number of samples (channels), m is the mean, s is the sample standard
deviation, dB_i is defined as

$$dB_i = 10 \, Log_{10} \, PSD_i \tag{5}$$

and PSD_i is the value of the power spectral density for the i'th accelerometer. Assuming
that the PSD responses are drawn from a lognormal distribution, the PSD levels in dB are
normally distributed. The P95/50 level is obtained from the sample mean and the sample
standard deviation by

$$P95/50_{dB} = m_{dB} + K \, s_{dB} \tag{6}$$

where

$$K = 1.645 \left[\frac{N-1}{\chi^2(N-1,.5)} \right]^{\frac{1}{2}} \tag{7}$$

The 1.645 factor in K is simply the number of true standard deviations above the mean for
the 95th percentile in a normal distribution—the critical value of a standardized normal
distribution for a probability of 0.95. The second factor scales the sample standard
deviation to the true standard deviation with 50% confidence [4]. $\chi^2(N-1,.5)$ is the
critical value of the chi-square distribution with N-1 degrees of freedom for a
probability of one-half. For large N the second factor tends to unity. For small
numbers of samples the chi-square distribution is highly skewed, so that even though the
sample variance is an unbiased estimate of true variance, the 50% confidence limit is
somewhat higher than the expected (mean) value. For example, $\chi^2(5-1,.5)=3.36$, so that
the second factor in Eq. (7) is 1.09 and K=1.79 if there are only 5 samples.
    The value p of the P95/50 PSD in g^2/Hz is obtained from the $P95/50_{dB}$ by

$$p = 10^{\left[\frac{P95/50_{dB}}{10} \right]} \quad g^2/Hz \tag{8}$$

Similarly, the value of the lognormal mean in g^2/Hz is obtained from the decibel mean by

92

$$m_{lognorm} = 10^{\left[\frac{m_{dB}}{10}\right]} \quad g^2/Hz \tag{9}$$

An alternate calculation of the P95/50 was performed to check the lognormal assumption. If the PSD distribution is truly lognormal, the lognormal mean and natural log standard deviation can be calculated from the corresponding PSD statistics by [5]

$$\hat{m}_{lognorm} = \frac{m_{PSD}}{\sqrt{1 + C^2}} \quad g^2/Hz \tag{10}$$

$$\hat{s}_{ln} = \sqrt{\ln[1 + C^2]} \tag{11}$$

where C^2 is the normalized variance of the PSD data

$$C = s_{PSD}/m_{PSD} \tag{12}$$

Note from Eq. (10) that the PSD mean is always greater than the lognormal mean. The P95/50 PSD can then be estimated by

$$\hat{p} = \hat{m}_{lognorm} \exp[K \hat{s}_{ln}] \tag{13}$$

This is simply a restatement of Eq. (6) and (8), using natural rather than common logarithms, except that the estimates of mean and standard deviation will be biased if the responses do not follow a lognormal distribution. A non-dimensional peak factor can be formed by taking the ratio of p to m

$$\hat{r} = \hat{p}/m_{PSD} \tag{14}$$

Figure 5 is a plot c. $\hat{r}$ and C^2 versus frequency bands for the MTAM acme screw acceleration measurements. For this data, the normalized variance was between 1 and 7. The r ratio showed much less variation, staying between 2.4 and 3.8, with an average value of 3.1 (5.0 dB). This nondimensional value can be compared to similar calculations from other data. Reference [3] describes a data study of several reverberant acoustic tests on spacecraft that suggests an r factor of 5.5 (7.4 dB) for third octave bands. This ratio is affected by damping, modal density, bandwidth, and mode shape [1].

Spectra of $\hat{p}$, m_{PSD}, and $m_{lognorm}$ for the test data are shown in Figure 6. A comparison between the two calculations for the lognormal mean and P95/50 is displayed in Figure 7. The decibel mean curve given by Eq. (9) is the only one of the three spectra in Figure 7 not dependent on the lognormal assumption. The agreement between the two methods suggests that the distribution of the data is very close to lognormal.

Comparison to Theoretical Distributions
Test data can be readily compared to various theoretical distributions by constructing an *observed cumulative distribution function* S_i

$$S_i(x) = P(PSD \leq x) \tag{15}$$

that is the probability that a sample will be less than a given level x, with no other knowledge than the existing sampled data. For a set of samples, in this case a set of PSDs from a given third octave band, the function S_i is calculated by sorting the numbers in increasing order. The PSDs x_i are each assigned a probability value $S_i = i/N$, where i is their index (position) in the sorted list. The resulting cumulative distribution function (c.d.f.) increases by a fixed value 1/N at each sampled PSD value x_i in a stairstep curve.

The observed c.d.f. for the 73 measured MTAM acme screw PSDs from the 20 Hz third octave band are shown in Figure 8. The PSD values are plotted on the abscissa with a log scale. Two theoretical distribution functions are also shown for comparison in Figure 8: a lognormal and a gamma distribution. The lognormal distribution was obtained by normalizing the PSD decibel levels to have zero mean and unit variance

$$z_i = [dB_i - m_{dB}]/s_{dB} \tag{16}$$

and assigning the standardized normal distribution c.d.f. $F(z_i)$ as the ordinate.

93
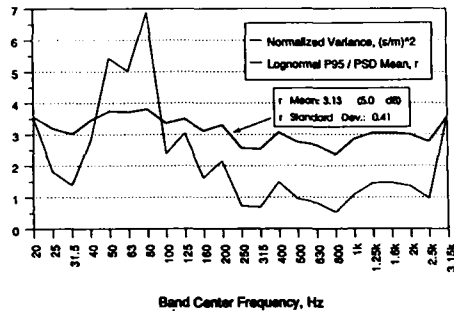
Figure 5. Statistics of variation for third octave response.
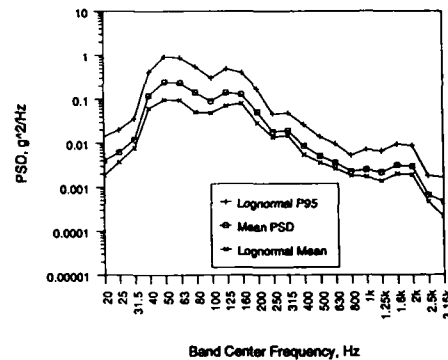
Figure 6. Spectra of third octave PSD statistics.
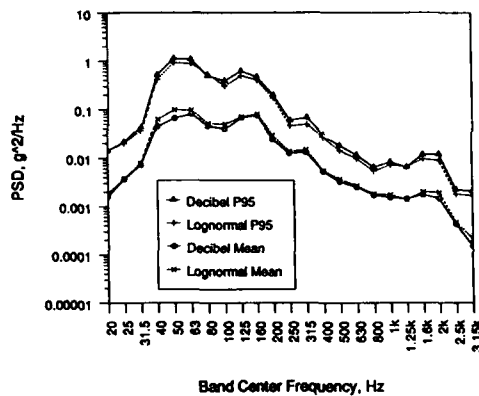
Figure 7. Spectra of statistics with and without log transformation.
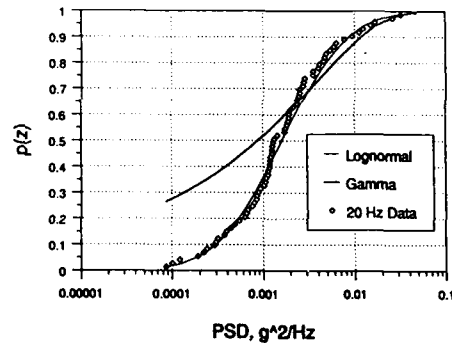
Figure 8. Cumulative distribution function of 20 Hz band PSD.

$$F(z_i) = \frac{1}{\sqrt{2\pi}} \int_{-\infty}^{z_i} \exp[-(1/2)z^2] \, dz \qquad (17)$$

For the gamma distribution, as suggested by Lyon and Eichler [1], the c.d.f. is given by

$$P(a,b) = \frac{\gamma(a,b)}{\Gamma(a)} \qquad (18)$$

where γ is the incomplete gamma function, Γ is the gamma function, and the arguments are [1]

$$a = m_{PSD}^2 / s_{PSD}^2 \qquad (19)$$

$$b = PSD_i m_{PSD} / s_{PSD}^2 \qquad (20)$$

The 20 Hz data appears symmetrical (on the log scale) about the lognormal mean, while the gamma distribution is skewed. The fit to the lognormal curve is quite good.

Once the decibel levels are standardized to zero mean and unit variance by Eq. (16), data from all of the 23 frequency bands can be combined into a single set of 1679 samples—73 channels of 23 bands. A histogram was constructed with bin edges from -5.5 to +5.5, and with all of the bins having unit width—1 standard deviation. Figure 9 shows the relative frequency of the measured acme screw levels compared with that of the normal distribution. The comparison is very close. Additional summary statistics on the complete normalized dataset are shown in Table I.

94

Kolmogorov-Smirnov Test for Goodness-of-Fit

The c.d.f. curve S_i for the complete (log-transformed) dataset is shown in Figure 10, compared with the theoretical normal curve. The data is nearly indistinguishable from the theoretical curve over much of the range. A powerful quantitative test for goodness-of-fit with continuous data is the *Kolmogorov-Smirnov* test [6]. The statistic for this test is the maximum absolute difference between the observed c.d.f. and the theoretical c.d.f.

$$D = \underset{i}{Max} \ |F_i - S_i| \qquad (21)$$

TABLE I. SUMMARY STATISTICS ON ACME SCREW LOG PSD

Statistic	Test Value	Standard Normal Distribution
N	1679	1679
Median	0.038	0
Skew	-0.299	0
Kurtosis	3.35	3

The larger D is, the more confidence we have that the test data does not come from the assumed distribution. Because the sampling distribution for D is known, a probability can be calculated of the likelihood that D would exceed some value D_o for samples taken from a known distribution. This probability can be called the *level of significance* for setting a limit on the maximum D that might be accepted as being from the assumed distribution. The level of significance is usually set at a relatively small value, such as 0.05, so that there is only a one in twenty chance of rejecting a sample actually drawn from the assumed distribution. A fairly rigorous test would set the level of significance to 0.2, possibly rejecting one in five "good" tests. The corresponding critical value of D for a sample size over 35 is given by [6]

$$D_o(0.2) = \frac{1.07}{\sqrt{N}} \qquad (22)$$

which gives $D_o(0.2)=0.026$ for N=1679. For the data in Figure 10, D=0.022, which is less than $D_o(0.2)$. The hypothesis that the band PSDs follow a lognormal distribution is accepted at a 0.2 level of significance.
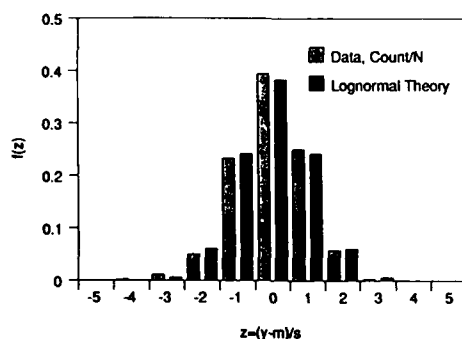
Figure 9. Relative frequency distribution of 1679 PSD samples.
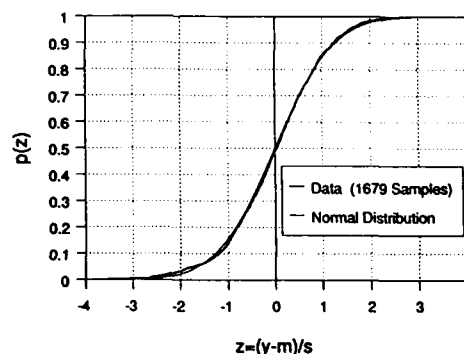
Figure 10. Cumulative distribution function of log PSD.

EXAMPLE WITH A NON-HOMOGENEOUS DATASET

Several of the MTAM structures had acceleration responses that were clearly bimodal at lower frequencies, that is, the responses split into two groups with different means. Five triaxial and eight uniaxial accelerometers were mounted directly to the strongback structure. The triaxial sensors were located on the interior, away from the two end bulkheads, while the uniaxial sensors were generally within 0.4 m of the bulkheads. All of the uniaxial sensors were oriented in the z (normal) direction. The entire test article was supported in the z direction by trunnion pins on the bulkheads, close to the corners of the strongback.

Because of the proximity of the high-impedance trunnion supports, the eight uniaxial sensor responses were much lower below 200 Hz than the fifteen triaxial channels. Grouping the two sets of sensors into a single dataset created a bimodal distribution

that obviously violated the lognormal assumption behind the P95/50 calculation. In Figure 11, the lognormal mean in third octave bands is displayed for the two calculation methods: Eqs. (9) and (10); and for two sample sizes: the 15 triaxial channels only, and all 23 channels. Only the decibel mean calculation is significantly biased by the inclusion of the eight low data samples. Figure 12 compares the same datasets with the two P95/50 calculation methods: Eqs. (8) and (13). Here the inclusion of the eight low data samples causes the P95/50 prediction with the log transformation (decibel, all) to *increase* by up to 4 dB. This occurs in spite of the low mean prediction in Figure 11 because the low samples greatly increased the decibel standard deviation.

CONCLUSIONS

This paper has described the spatial probability distribution of a set of structural responses measured during a reverberant acoustic test of the Mass/Thermal/Acoustic Model (MTAM) of the photovoltaic power management and distribution system for the NASA Space Station Freedom. Structural similarity between measurement locations—in acoustic coupling, structural damping, and impedance—is important for the assessment of probability distribution. While it may be difficult to discard data from the limited quantity available from a test, a reasonable procedure would be to separate data channels that appear to have a different response, and to calculate separate P95/50 values for the different groups.

A statistical data study was performed for a subset of the MTAM test data. The Kolmogorov-Smirnov test statistic indicated that the third octave average PSD responses on these components were spatially lognormal when excited by a reverberant acoustic field. Two procedures for estimating the P95/50 level were demonstrated to agree well for the component attachment sensors. One calculates the mean and standard deviation of log-transformed PSD, while the other uses PSD mean and standard deviation directly. The two methods gave different results when applied to another set of responses that contained several channels of much lower response than the majority. The dataset should be at least approximately lognormal in order to obtain consistent results.
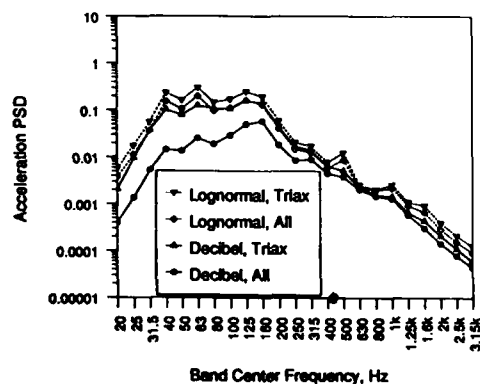
Figure 11. Comparison of mean predictions for the MTAM strongback
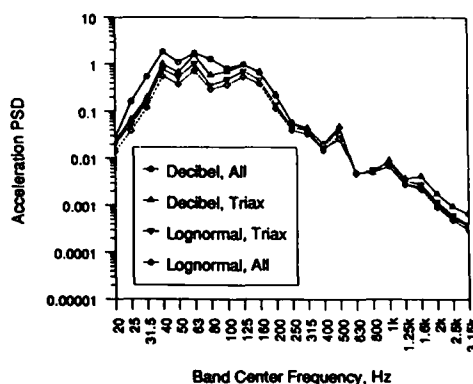
Figure 12. Comparison of P95/50 predictions for the MTAM strongback

REFERENCES

[1]   Lyon, R.H. and Eichler, E., "Random Vibration of Connected Structures," J. Acoust. Soc. Am., 36(7), July 1964, pp.1344-1354.
[2]   Lyon, R.H., *Statistical Energy Analysis: Theory and Applications*, M.I.T. Press, Cambridge, Massachusetts, 1975.
[3]   Badilla, G., et al, "Vibroacoustic Payload Environment Prediction System (VAPEPS)," Workshop Notes, Jet Propulsion Laboratory, Pasadena, 16-18 August 1988, p.12-30.
[4]   Harnett, D.L., Statistical Methods, Third Edition, Addison-Wesley, Reading, Massachusetts, 1982, p.292.
[5]   Shigley, J.E., and Mischke, C.R., Mechanical Engineering Design, Fifth Edition, McGraw-Hill, New York, pp.163-164.
[6]   Harnett, D.L., **Statistical Methods**, Third Edition, Addison-Wesley, Reading, Massachusetts, 1982, p.712, A58.

**SECOND INTERNATIONAL CONGRESS ON
RECENT DEVELOPMENTS IN AIR- AND
STRUCTURE-BORNE SOUND AND VIBRATION**
MARCH 4-6, 1992   AUBURN UNIVERSITY, USA

RESPONSE OF LAUNCH PAD STRUCTURES TO RANDOM ACOUSTIC EXCITATION

Ravi Margasahayam and Valentin Sepcenko
Boeing Aerospace Operations, Inc.

Raoul Caimi
NASA Engineering Development (DM-MED-11)

John F. Kennedy Space Center, FL 32899
U.S.A.

ABSTRACT

Two solutions (probabilistic and deterministic) for the random vibration problem are presented in this paper from the standpoint of their applicability to predict the response of ground structures subjected to acoustic loading during the launch of a Space Shuttle. Deficiencies of the probabilistic method, especially to predict response in the low-frequency regime, prompted the development of the deterministic analysis, which offers a valid alternative. Challenges associated with the implementation of these response solutions in a commercially available Finite Element Method (FEM) code are briefly addressed.

INTRODUCTION

The design of launch pad structures, particularly those having a large area-to-mass ratio, is governed by launch-induced acoustics, a relatively short random transient with input pressure amplitudes having a non-Gaussian distribution (figure 1). The factors influencing the acoustic excitation and resulting structural responses are numerous and cannot be predicted precisely. The purpose of this on-going research program at NASA's Kennedy Space Center (KSC) is threefold:

   a.   To characterize the launch-induced acoustic environment

   b.   To develop methods to predict the response of pad structures

   c.   To implement the proposed method in a FEM code

BACKGROUND

One purpose of taking acoustic measurements during Space Shuttle launches is their application to structural response analysis and environmental testing. The choice of a response analysis method is subject to observations drawn from these measurements. Since the acoustic pressure field is extremely complex, it does not lend itself to a simple analytical description or field idealization nor does there exist a unique response analysis method. Based on experience and observations, however, two different approaches (probabilistic and deterministic) to the response analysis emerged [1].

The first approach, called probabilistic, is based on the classical solution of the random vibration theory [2,3]. The analysis assumes a stationary input/response relation and requires a definition of the acoustic field in terms of power spectral density (PSD) and cross-power spectral density (CPSD). The second approach, called deterministic, is a more recent development prompted primarily by a deficiency of the former method to predict response in the low-frequency range of the launch transient, where most major pad structure resonances are observed. Response spectra (RS), together with pressure correlation lengths (PCL's), provide a platform for deterministic analysis of structural responses [4,5].

RESPONSE ANALYSIS METHODS

Probabilistic Method
    The exact solution for a steady-state response of a linear structure in a random stationary acoustic field, which may or may not be homogeneous, written in terms of PSD and CPSD of modal coordinates is:

$$\Phi_{qq} = H_m \cdot b^T \cdot dA \cdot \Theta_{pp} \cdot dA \cdot b \cdot H_m^* \tag{1}$$

$$kxk \quad kxk \quad kxn \quad nxn \quad nxn \quad nxn \quad nxk \quad kxk$$

where Φ is the solution matrix of k modal coordinates of k normal modes and H_m is the matrix of modal frequency response functions (FRF's). Θ_{pp}, b, and dA are the acoustic load matrix, the matrix of n modal displacements at n loaded points due to k normal modes, and the diagonal matrix of contributory areas at n nodal points.

    Major computational problems and the complexities associated with the definition of the acoustic load matrix, Θ_{pp}, in the exact solution necessitated the search for a simplified response solution. This search was also influenced by two concepts from the theory of random processes: the white noise excitation having a PSD of a constant intensity, K psi²/hertz, which extends from zero to an infinite frequency; and the white noise decay, which defines CPSD of a white noise excitation. The variation of a white noise CPSD along a single axis, x, between points x_1 and x_2 is defined by:

$$\Theta_{pp}(x_1,x_2,\omega) = K \cdot \exp(-\alpha \mid x_2 - x_1 \mid) \cdot \exp(-i\beta\omega(x_2 - x_1)) \tag{2}$$

where α and β are constants that, presumably, may be adjusted to fit experimental data. Terms containing α and β are magnitude and phase expressions of white noise decay in equation 2.

    The concept of white noise decay and the possibility of an analytical definition appeared to have facilitated the definition of Θ_{pp} in equations 1 and 2. Recent research has indicated that this is true even if the acoustic field is not a white noise [of constant intensity K, but characterized by a frequency-dependent PSD given by $S_p(f)$]. Then the matrix Θ_{pp} may be normalized by a scalar function $S_p(f)$, so that:

$$\Theta_{pp} = S_p(f) \cdot Nc \tag{3}$$

$$nxn \qquad nxn$$

where Nc is the matrix of normalized CPSD (NCPSD). The concept of such normalization may be applied to any type of acoustic field. In a homogeneous acoustic field, main diagonal elements of Nc are all constant, real, and equal to 1.0. Phase relations in Nc remain the same as in Θ_{pp}. If the field is assumed to have white noise decay, then off-diagonal elements are complex analytical functions and are given by the right-hand side of equation 2 except for the K term.

    It is important to note two limitations of a white noise decay field. First, the magnitude is not a function of frequency; and secondly, the phase is a linear function of frequency with a slope

being proportional to the relative distance $x_2 - x_1$, in equation 2. Contrary to the assumptions of a white noise decay model, Shuttle measurements indicate a strong dependence on Mag(Nc) on frequency. Consequently, response predictions made by FEM programs that do not allow input of frequency-dependent and general complex functions in the definition of Θ_{pp} or Nc matrices will not be accurate. Moreover, the measurements confirm a linear phase trend with frequency and the dependence of slope on relative distance, this dependence is not quite linear (figure 2).

Deterministic Solution

The basic premise behind the concept of response spectra is that a total structural response consists of uncoupled responses in individual structural vibration modes. Then, the response in a mode can be obtained by integrating the equation of motion for that mode in the time domain. If the time history of a generalized modal load is known, then the integration is possible and it does not matter whether or not the generalized modal load is a random transient. In this integration process, the input is treated as a deterministic pressure time history; however, the definition of a corresponding generalized modal load contains elements of a random response analysis, and it is uniquely related to the PSD of the generalized modal load contained in equation 1.

A given transient pressure time history, p(t), has a PSD, $S_p(f)$, which is derivable by a normalized averaging procedure and does not require an assumption of a stationary random process. An examination of two NCPSD's based on past Shuttle launches for "short" and "long" processing intervals indicates similarity, regardless of p(t) being a transient. Therefore, functions derivable from NCPSD's, such as PCL's and correlated pressure distribution (CPD), may be assumed to be time invariant for the duration of the launch pressure transient. Consequently, for a structural vibration mode, the product of a normal modal displacement and a corresponding CPD is also time invariant. This product, when integrated over the area of the structure, defines a generalized modal load for a constant and unit p(t). Thus, for a time variable p(t), the generalized modal load for a j-th mode is proportional to p(t), and may be written as follows:

$$GL_j(t) = AJ_j \cdot p(t) \qquad (4)$$

where AJ_j is the above-mentioned integrated product, independent of time. The PSD of a generalized modal load is given by:

$$Sgl_j(f) = (AJ_j)^2 \cdot S_p(f) \qquad (5)$$

The equation of motion for a j-th mode (omitting the subscript for brevity) in terms of generalized modal coordinate, q, is:

$$\ddot{q} + 2\xi\Omega\dot{q} + \Omega^2 q = (AJ/M) \cdot p(t) \qquad (6)$$

where M, Ω, and ξ are parameters of the j-th mode, generalized modal mass, circular resonance frequency, and modal damping. The equation of motion, equation 6, is solved (integrated) for a variable q/(AJ/M), assuming zero initial conditions and an array of frequencies, $f = \Omega/2\pi$, so as to include resonances of all modes of interest. Similar to well-known shock spectra, only the peak (maximax) values are retained in the solution. Since a solution corresponds to each of the assumed frequencies, q = q(f), for presentation purposes the plotted variable on response spectra plots is:

$$Y(f) = q(f) / (AJ/M/\omega^2) \qquad (7)$$

Then, in applications, the maximax value of q(f) is obtained from the plotted quantity Y(f), as follows:

$$q(f) = Y(f) \cdot (AJ/M/\omega^2) \qquad (8)$$

using values of AJ, M, and $\omega = \Omega$ for a particular mode of interest. When response coordinates are computed for k modes, it is convenient to arrange them as main diagonal elements of a kxk maximax response matrix Q. Then peak response values, R_s, of internal stresses, reactions, etc., are computed by a simple multiplication of a stress matrix, S_q, due to normalized modes by the peak values of corresponding modal response coordinates:

$$R_s = S_q \cdot Q$$

(9)

$$kxk \quad kxk \quad kxk$$

The total response from all k modes is usually computed as a square root of the sum of squared responses of individual modes. Responses in closely spaced modes are often summed up directly. The major difficulty in obtaining a response solution by means of response spectra is in the computation of the AJ-factor associated with each generalized modal load. Reference [5] addresses this problem and provides diagrams of J-coefficients for a few types of beam structures (corresponding A is a normalizing constant equal to a beam span). Whenever a complete (in all three directions in space: X, Y, and Z) set of NCPSD's are available, AJ-factors can be computed "exactly" for any type of structure by means of equation 11.

The deterministic solution also has its drawbacks. The main drawback is the peak generalized modal load that, in multispan structures and in modes higher than fundamental, may require a few trials in order to ensure an absolute peak.

Deterministic Versus Probabilistic
The relation between deterministic and probabilistic solutions is much closer than it appears to be, although the results of analysis by each method may differ. An important relation between the two is obtained by the comparison of PSD's of generalized modal loads defined by each type of solution. For the probabilistic solution, from equations 1 and 3, the PSD's are defined by the main diagonal elements of the matrix:

$$[\, b^T \cdot dA \cdot Nc \cdot dA \cdot b \,] \cdot S_p(f)$$

(10)

$$kxn \quad nxn \quad nxn \quad nxn \quad nxk$$

where $S_p(f)$ is a scalar multiplier with a physical meaning of an acoustic pressure PSD. The matrix in brackets is a complex Hermitian function of frequency, since its component matrix Nc is Hermitian and frequency dependent. A corresponding deterministic definition of generalized modal load PSD's is given in equation 5. Note that each AJ_j term in equation 5 is a function of a discrete resonance frequency of j-th normal mode.

By equating 5 and 10 and cancelling $S_p(f)$ appearing on each side of the equation:

$$[AJ_j \, (f{=}f_j)]^2 = DIAG_{jj} \, [b^T \cdot dA \cdot Nc \cdot dA \cdot b]_{\bullet \, f{=}f_j}$$

(11)

where $DIAG_{jj}$ designates a j-th element on the main diagonal of the matrix in brackets, computed at the frequency f_j of the j-th mode resonance. Thus, each method (probabilistic or deterministic) defines a generalized modal load and its PSD in a consistent manner through identical computations.

Factors AJ(f) in equation 11 define a vibroacoustic coupling between a structure through its modal matrix b, and an acoustic field correctly characterized by its matrix Nc of NCPSD's. This definition of AJ(f) is a smooth and continuous function of frequency. Beyond this common point at equation 11, the probabilistic and deterministic methods of response analysis diverge. The details differentiating a probabilistic from a deterministic approach to response analysis are

addressed in three areas: the account of modal coupling, computations of peak responses, and the effect of basic assumptions inherent in the probabilistic method.

Effect of Modal Coupling
        Whereas a probabilistic solution provides an exact account of coupling between different modes, the deterministic solution does not account for modal coupling. The question is how important is this modal coupling effect; when and where does it occur; and can it be neglected in the analysis?

        Modal coupling (energy transfer between closely spaced modes) becomes significant for two reasons: (1) the spacing between resonant frequencies is less than the larger half-power-point bandwidth of adjacent resonances and (2) when modal displacements of coupled modes overlap within a substantial area of a structure.

        An examination of measured strain PSD's on diverse launch pad structures did not disclose any merged or closely spaced peaks in the PSD's. Peaks corresponding to fundamental modes governing the design were all distinct in these strain data. Modal coupling commonly occurs between much higher modes than the fundamental, especially in the high-frequency range where modal density is also high; but these modes seldom if ever govern the design of launch pad structures having resonances below 20 hertz.

Mean Square Versus Peak Response
        The probabilistic method computes a mean square value of the response. The peak response, required in design applications, has to be estimated from a probabilistic distribution of amplitudes, which is most often assumed. More often than not, experimental data on amplitude probability distributions is lacking, while data on joint probabilities is totally nonexistent. Thus, a designer has little choice but to assume a normal distribution. Shuttle measurements are clearly non-Gaussian.

        The deterministic method, however, computes a peak response. Since input response spectra (RS) are obtained from Shuttle measurements, computed peak responses reflect a prior experience, eliminating the need to resort to a hypothetical distribution. Clearly, penalty for Gaussian distribution assumption leads to a 22-percent error in design values.

Stationary Versus Transient Response
        The probabilistic solution contains an inherent assumption that the input is a stationary (weakly stationary) random process. Consequently, the response is also a stationary random process, although solutions exist for a case when a structure is being excited from zero initial conditions (the input still must remain stationary for the theory to apply).

        In reality, actual input is a transient with a duration that for some frequencies does not contain a sufficient number of cycles to induce a full resonance. Vibration modes with resonances below 20 hertz are never fully excited. If one considers that practically all fundamental resonances of launch pad structures and their elements are below 20 hertz, and most are below even 10 hertz, then the use of the probabilistic method leads to overestimation of the predicted responses. A deterministic solution fully accounts for the transient characteristic of an input pressure time history. To appreciate the full effect of a lift-off transient (on these response solutions), the reader is directed to compare response spectra and power spectra for the Shuttle (figure 3).

FINITE ELEMENT IMPLEMENTATION

        In the past, only PSD's were used in applications, while CPSD's, required for the solution to be realistic and accurate, were substituted by assumed models of acoustic fields. One such model, called white noise decay, was incorporated into a widely used FEM code [6] for random response analysis application. For example, the widely used MSC/NASTRAN program accepts only a constant and frequency-independent definition of the Nc matrix (X+iY terms). It is clear from

101

Shuttle measurements that the white noise decay model does not reflect the reality of the launch-induced acoustic field as outlined in the section, Probabilistic Method.

The definition of the acoustic load matrix Θ_{pp}, in the probabilistic solution (equation 1) is a formidable task even if it were available. It requires the definition of a CPSD between any two loaded points of a structural model. For example, a structure with 50 loaded points requires as many as 2,500 complex (real and imaginary) functions. Thus, most FEM codes never incorporated exact solutions in their programs. A few codes (ASKA II, NISA II, etc.) allowed an unrestricted definition of real components only [7,8]. Recently, NISA II has incorporated a general form of Θ_{pp}, which includes both real and imaginary functions. However, the problem of inputting a large number of complex functions still exists.

Presently, the response spectra method has a drawback. There is not a single commercial FEM code that has the capability to use response spectra (the deterministic method). Their use has been limited to simple structures where, after modal analysis is completed, responses could be computed manually. Thus, both deterministic and probabilistic methods face a setback at the present time.

SUMMARY AND CONCLUSIONS

This paper attempts to focus on the missing characteristics of an acoustic field that involves cross-functions and defines the vibroacoustic coupling between the structure and the acoustic field. The focus is on the normalized form of CPSD (NCPSD) rather than CPSD. The former is more general than the latter for characterizing the observed acoustic field and may even be transportable to other pad locations. The probabilistic solution for a mean square response and a deterministic solution based on response spectra both require information contained in NCPSD's. Literally, thousands are needed in the probabilistic method; however, only a few are needed in the deterministic method. NCPSD's are also a sole source for computing PCL and CPD required by the deterministic method.

In this paper, the state-of-the-art probabilistic solution is reviewed and its critique presented to alert the user about differences between the exact solution and its simplified versions implemented in various commercially available FEM codes. Besides describing a basic theory behind the concept of response spectra (used in the deterministic method), a critical comparison of both the probabilistic and the deterministic methods of response analysis is outlined. Perhaps the usefulness of each method should be judged on how well the launch environment fits assumptions of each model. It should not be surprising to find that within a certain range of parameters, frequencies, etc., either method may be preferred over the other. Within the low-frequency range (0 to 20 hertz) of launch pad structure resonances, however, the deterministic method is simpler, more feasible, and more accurate than the probabilistic solution, thereby, offering a valid alternative technique [1,9].

In spite of limitations, both methods have a rightful place in the analysis, and should be evaluated further. Future effort should be directed toward implementation of these methods in a commercially available FEM code for general purpose application.

ACKNOWLEDGMENT

REFERENCES

1. GP-1059, Volume III, "Environment and Test Specification Levels Ground Support Equipment for Space Shuttle System Launch Complex 39," Kennedy Space Center, November 1991.

2. Lin, Y.K., "Probabilistic Theory of Structural Dynamics," McGraw-Hill, 1967. Reprinted by Kreiger Publishing Co., 1976.

3. Elishakoff, I., "Probabilistic Methods in the Theory of Structures," Wiley-Interscience, New York, 1983.

4. KSC-DM-3147, "Procedure and Criteria for Conducting a Dynamic Analysis of Orbiter Weather Protection System on LC-39B Fixed Service Structure," Kennedy Space Center, September 1987.

5. KSC-DM-3265, "Computation of Generalized Modal Loads in an Acoustic Field Defined by a Distribution of Correlated Pressures," Kennedy Space Center, August 1989.

6. MSC/NASTRAN USER'S MANUAL, MacNeal Schwendler Corporation, Los Angeles, California, 1990.

7. NISA II USER'S MANUAL, Engineering Mechanics Research Corporation, Troy, Michigan, 1990.

8. ASKA II - Linear Dynamic Analysis Random Response, Report ASKA UM 218, Institut für Statik und Dynamik der Luft-und Raumfahrtkonstruktionen, University of Stuttgart, Germany, 1978.

9. Robson, J.D., "Probabilistic and Deterministic Solutions of Random Vibration Response Problems," Journal of Acoustic Society of America, May 1973, pp 392-395.
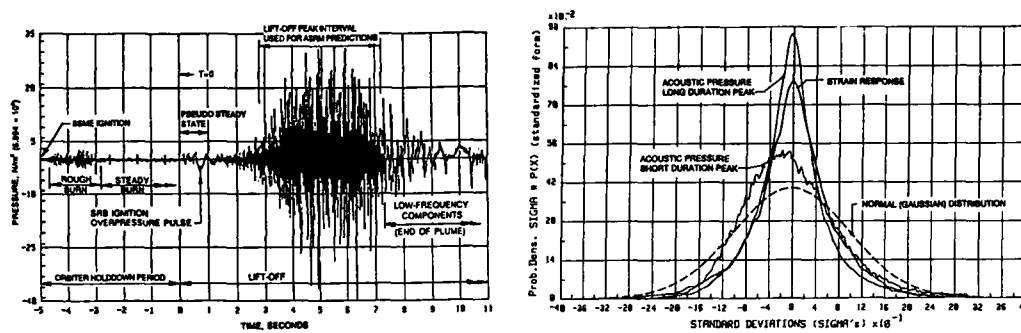
Figure 1. Time Periods, Intervals of the Launch Environment,
and Typical Acoustic Input/Strain Response Distribution
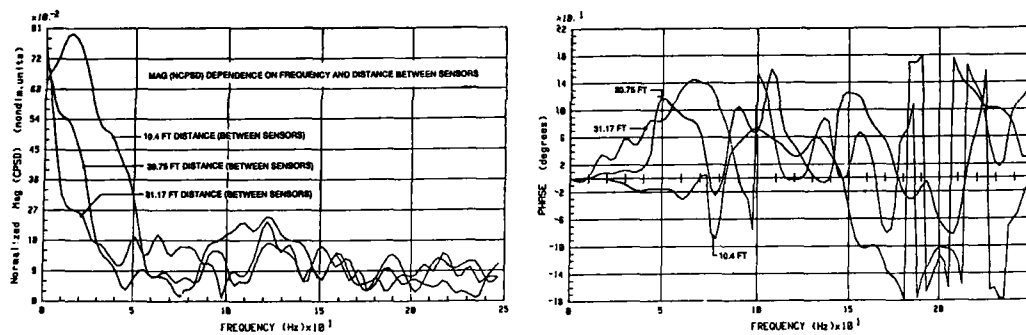
Figure 2. Normalized Mean Pressure Cross Power Spectra
Magnitude and Phase
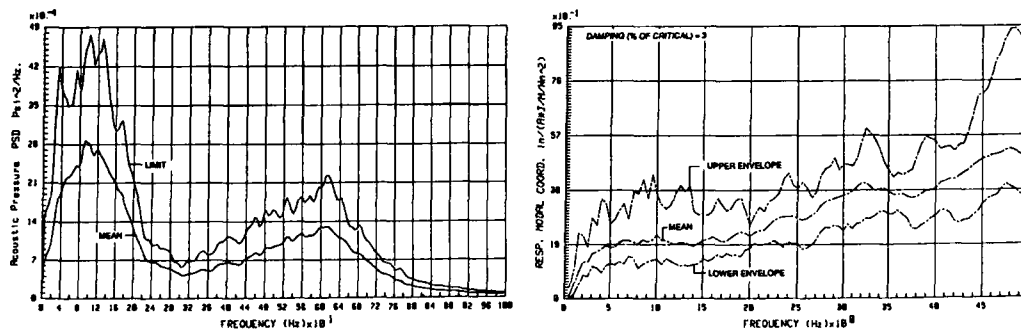
Figure 3. Lift-Off Peak Pressure Power Spectra and
Response Spectra on the FSS at 125 Feet

104

**SECOND INTERNATIONAL CONGRESS ON
RECENT DEVELOPMENTS IN AIR- AND
STRUCTURE-BORNE SOUND AND VIBRATION**

MARCH 4-6, 1992   AUBURN UNIVERSITY, USA

SONIC BOOM MINIMIZATION: MYTH OR REALITY?

Kenneth J. Plotkin
Wyle Laboratories
Arlington, VA 22202
U.S.A.

ABSTRACT

Sonic boom, the audible shock pattern of a supersonic vehicle, is an important issue for contemplated advanced supersonic transports and for operation of supersonic military aircraft. Physical realities make sonic boom unavoidable. However, there are promising opportunities to shape sonic booms from supersonic transports so that their perceived loudness may be acceptable. Current efforts toward developing acceptable minimum-boom aircraft are discussed. These include both aircraft configuration studies and psychoacoustic studies to establish acceptability criteria. Atmospheric turbulence is known to distort sonic booms. The potential for turbulent distortion to affect the loudness of sonic booms is discussed.

GENERATION OF SONIC BOOM

The pressure field around a slender axisymmetric body travelling at supersonic speed is given by:[1,2]

$$\delta p\ (x - \beta r, r)\ =\ p_o\ \frac{\gamma M^2\ F\ (x - \beta r)}{(2\ \beta r)^{1/2}} \tag{1}$$

where p = pressure
   p_o = undisturbed ambient pressure
   x = axial coordinate (body fixed)
   r = radius
   γ = ratio of specific heats
   M = Mach number
   β = $\sqrt{M^2 - 1}$ = Prandtl–Glauert factor

and

$$F(x)\ =\ \frac{1}{2\pi} \int_o^x \frac{A''\ (x)}{(x - \xi)^{1/2}}\ d\xi \tag{2}$$

where A is the cross-sectional area of the body as measured by the normal projection of cuts along planes aligned with the Mach angle $\mu = \sin^{-1}(1/M)$. The quantity F(x) is known as the Whitham F-function,[1,2] and represents the normalized amplitude pattern of a cylindrical acoustic wave. Noting that the second derivative of A with respect to the axial coordinate appears in Eq. (2), it is straightforward to interpret Eq. (2) as an axial distribution of simple sources.

Eqs. (1) and (2) were derived for an axisymmetric body. Walkden[3] showed that the same form applies to complete aircraft by considering particular azimuthal directions (i.e., downward, to the side, etc.) and replacing area A with an equivalent area representing combinations of the fuselage area, wing thickness, a component of lift, and contributions due to wing/fuselage interference. Each component of equivalent area depends on Mach cuts and load components aligned with the particular azimuth. It is common to view the equivalent area and resultant F-function to be a combination of volume and lift components. For simple configurations, the volume component is axisymmetric and the lift component depends on the cosine of the azimuth. It is important to note that the net boom depends on the combination of components. Desired low-boom F-functions are obtained by balancing the components, analogous to minimization of supersonic wave drag by area rule techniques.

The F-function is derived from linearized supersonic flow theory which was originally developed to calculate aerodynamic loads,[4,5] and is intimately related to those loads. Attempts to avoid sonic boom by devising vehicles with zero F-functions have inevitably met with failure. Certain unique bodies (the Busemann biplane and Ferri ring wing) have finite volume but zero F-function. They also have zero lift and zero drag, and substantial practical difficulties. With regard to the component of boom due to lift, conservation of momentum dictates that this must reach the ground. Reference 6 contains a good evaluation of certain classes of apparently boomless aircraft. While unique boomless configurations can be entertaining (as can sleight of hand), they are beyond the scope of this paper. That sonic booms will reach the ground is inevitable. It is not, however, inevitable that they will be a problem, as will be discussed shortly.

PROPAGATION AND AGING

Eqs. (1) and (2) describe linear acoustic waves propagating cylindrically in a uniform medium. As sonic booms propagate toward the ground, two significant phenomena occur:

- Temperature and wind gradients cause the waves to curve, affecting amplitudes and location somewhat. Amplitude is also affected by acoustic impedance gradients. Except for particular situations (focusing and locations where rays curve upward), the impedance gradient affects amplitude much more than refraction does.

- Although wave amplitudes are sufficiently weak for Eqs. (1) and (2) to be valid near the aircraft, they are sufficiently strong that over long propagation distances they cause significant distortion to the shape of the boom. The increasing distortion accompanying increasing distance (or increasing propagation time) is often referred to as aging.

These two phenomena are illustrated in Figure 1. Refraction causes the general concavity of the wave pattern. Nonlinear distortion is illustrated by sketches of the wave at three distances. Nonlinearity manifests itself in positive portions of the wave propagating faster, and negative portions slower, so that the wave "steepens", and shock waves will eventually form. Landau[7] showed that the ultimate shape of a weak positive pulse is triangular: a shock followed by a linear expansion. For an aircraft signature which is generally positive in the front and negative in the rear, the asymptotic far field shape is an N-wave, shown at the bottom of Figure 1. N-waves were experimentally demonstrated by DuMond et al.[8] in the 1940s.

In the early 1950s, Whitham developed his elegant rule for calculating aged signature shapes. His rule is a second-order theory, presented in the context of being a uniformly valid first-order theory. He began with the premise that the linear acoustic solution gave the amplitude correct to first order. This solution, however, gave a wave location based on acoustic propagation, which was exact only for infinitesimal waves: a zero order result. His rule was thus to accept the pressure given by Eq. (1), but to correct the location (the argument of F, x − βr) to first order. The ambient sound speed is replaced by the first-order perturbed sound speed. Since this is a linear adjustment, the distortion of each element of the signature is proportional to its amplitude. A simple construction yields the shape of an aged signature, as sketched in Figure 2. At some point, however, a positive slope will steepen into a shock wave. Continuation of the second-order steepening construction yields an impossible triple-valued region. By incorporating the linearized Rankine–Hugoniot shock relations, Whitham explicitly accounted for shock formation. He also showed that the location of the shock was determined by a simple area balance (sketched as the shaded regions in Figure 2) of the second-order (i.e., first-order corrected location) construction. It is fascinating to see that Whitham's rule, which is presented as a "uniform first order" theory and is usually viewed as second order, actually incorporates (via the shock) third-order elements.

106

Whitham showed that the asymptotic far-field signature was an N-wave, and that the amplitude depended only on an integral of the F-function. This far-field result applies when so much aging has occurred that most of the original signature has been absorbed into the shock. The loss of information of the original signature corresponds to the entropy increase. The presence of the shock also provides an implicit accounting for dissipation. The amplitude of a cylindrically spreading N-wave in a uniform atmosphere decays with distance as $r^{-3/4}$, versus $r^{1/2}$ for a linear acoustic wave.

Whitham's result that the far-field N-wave result includes the aircraft only as an integral of the F-function enables the development of simple scaling laws. If equivalent area is written as a normalized form, one can derive this integral as a product of aircraft length, weight, and a "shape factor". This was exploited by Carlson in a simplified boom calculation scheme.[9] For the present discussion, a significant result of Carlson's analysis is that shape factors do not vary substantially between aircraft types: for a given length and weight, there is perhaps a 20 percent difference across most aircraft types. Length and weight enter the scaling laws as fractional powers, so that doubling or halving size or weight affects boom by less than a factor of two.

FAR-FIELD VERSUS MID-FIELD SIGNATURES

The relative insensitivity of N-wave booms to aircraft configuration and size presents an apparently bleak situation for reducing boom. The two shock waves in an N-wave are obviously intrusive, containing substantial acoustic energy within the audible frequency range. Virtually all flight test results showed N-waves, in good agreement with the Whitham/Walkden theory. Except, however, for the occasional extra detail seen in booms from large aircraft such as the B-70.

A significant turning point in boom minimization was the observation by McLean[10] that N-waves were not inevitable. For most supersonic aircraft – fighters less than 100 feet long – far-field N-wave conditions were usually satisfied. For large aircraft, of length several hundred feet, he noted that distortion due to aging was not necessarily large compared to the original signature length. Signatures at the ground would be mid-field, retaining some details associated with the aircraft's detailed configuration, rather than far-field N-waves. This observation raised the possibility of designing booms which, while obeying the laws of physics, would have a different (and possibly less intrusive) shape than N-waves.

LOW-BOOM SIGNATURES AND THEIR LOUDNESS

If the frequency spectrum of an N-wave boom is considered, most of the audible frequency content is associated with the shock waves. Duration of a boom affects only the lowest frequencies. Low-boom concepts concentrate on this aural dominance of the shock waves in the perception of booms. Concepts for shaped low booms thus center on shock amplitude being the single most important parameter, to be minimized with little regard for the effect on other parts of the signature.

Figure 3 shows potential low-boom signatures based on "reduce the shock" concepts. Relative to a "normal" N-wave (a), one might use added aircraft length to obtain reduced shocks at the cost of greater duration (b). A flat-top boom (c) considers that shocks may be reduced without paying a duration penalty if plateaus are allowed after the bow shock and before the rear shock. The plateaus are considered to be inaudible. A minimum-shock boom (d) is an extension of this concept, in that there could be maxima not associated with the shocks. The signature shape near each maximum is sufficiently smooth that only low frequencies, below the range of hearing, are involved.

N-wave sonic booms have tended to be described only by their peak overpressure, which isolated sonic boom response studies from the mainstream of psychoacoustic descriptors. Several researchers have applied noisiness[11] or loudness[12] metrics to N-wave booms, with satisfactory results. A key issue is whether such metrics can accurately predict the perceived loudness of shaped minimum booms. This was answered in dramatic fashion by a recent study at NASA–Langley.[13] where human subjects were exposed to a variety of N-wave and shaped booms in a sonic boom simulator. Annoyance ratings by the subjects were interpreted as subjective loudness, and correlated with various calculated metrics. Figure 4 shows the results for peak overpressures and the loudness method of Reference 12, which is based on Stevens Mark VII loudness. Peak pressure itself is a poor predictor, but loudness (perceived level) shows excellent correlation with subjective loudness.

107

The significance of Figure 4 cannot be overemphasized. The potential benefit of shaped signatures is no longer based on qualitative speculation of the importance of the shocks, but is quantified by a mainstream psychoacoustic metric. While these results were for booms as heard outdoors, analysis of the transmission of booms into structures indicate that the audible benefit of shaped booms applies indoors as well.[14] The effect of shaped booms on structures (including secondary effects such as rattle) is not yet clear, but studies are in progress.

DESIGNING FOR LOW BOOM

Designing a low-boom aircraft is an inverse process, conducted in two stages. First, it is necessary to know what kind of F-function will age into the desired shape. Second, it is necessary to establish what configuration will yield that F-function. Neither step has a unique solution. The first step is particularly difficult when considering the entropy increase as a signature ages.

The first stage has been solved for N-waves, flat-top and minimum shock signatures. Using calculus of variations, Jones[15] demonstrated that a minimum far-field N-wave would result from an impulsive (delta function) F-function. George[16] noted that at a mid-field position this would yield an N-wave of some amplitude. If the F-function has an impulse followed by a plateau of that amplitude, the result is a flat-top boom. If a compression follows the impulse, with slope gentle enough that a shock does not form, a minimum shock signature results. Figure 5 illustrates George's general low-boom F-function, considering both front and rear shocks.[17]

George's result is valuable for two reasons. First, it provides an optimum solution to a formally intractable problem. Second, it is a form which is mostly straight lines and can be easily described by about half a dozen parameters. This eases the second part of the problem, establishing a configuration to achieve the F-function. Eq. (2) can be inverted to yield the required equivalent area distribution, and for the parameterized George F-function this step is essentially algebraic.

The above process does not uniquely determine a configuration. First, the number of parameters in the F-function will not necessarily correspond to the number of independent design variables available. Second, the equivalent area distribution can be any combination of lift and volume. The result of the process is additional constraints to consider in aircraft configuration design. A number of parametric studies have been performed evaluating tradeoffs between low boom and performance. Reference 18 is a very good example of such analyses.

Two particular aspects of George's minimum F-function are the initial impulse and the slow growth of effective area following the impulse. The impulse requires high load at the nose, which is often implemented by blunting the nose. This incurs a drag penalty, offset somewhat by the fact that there is less drag away from the nose and that interior room may be increased. Generally, up to some point, useful boom reduction can be achieved with modest drag penalties. Sohn[19] proposed obtaining the initial spike via a canard, obtaining useful lift as a by-product, although other performance penalties were found to exist. The slow growth of effective area following the impulse generally translates into the lifting surfaces being farther back than would normally be desirable, causing adverse effects on balance and trim. Structural difficulties can be introduced by, for example, requirements for particularly slender components.

A number of papers, such as References 17 through 19, provide detailed analyses of boom reduction. The bottom line is that if reduced sonic boom is desirable, it is a design goal which must be traded with other design parameters. Potential for low boom increases if other compromises are possible. For first-generation SSTs designed in the 1960s, performance requirements precluded any such compromises. Aircraft technology has advanced to the point where tradeoffs are feasible. Recent studies, such as Reference 20, show that sonic boom loudness reductions of 10 to 15 dB (relative to first-generation SSTs) are not impossible. As technology improves, the practicality of such improvements will increase.

CONCLUSIONS

A review has been presented of sonic boom theory and minimization concepts. We have seen the issue of boom reduction change from "Is it possible?" to "Is it feasible?" to "Is it practical?" Sohn[20] has pointed out that boom reduction is a matter of advancing technology, and that his low-boom results follow from trading on such advances. It is encouraging to see that some recent studies of low-boom design present consequences in terms of design and operating costs. This is quite different from questions of whether boom can be reduced at all. It will be very interesting to see whether the current generation of supersonic transport studies yields practical low-boom designs, or whether we must wait for the next generation.

108

REFERENCES

1. Whitham, G.B., "The Flow Pattern of a Supersonic Projectile", *Communications on Pure and Applied Mathematics, 5,* 301-348, 1952.

2. Whitham, G.B., "On the Propagation of Weak Shock Waves", *J. Fluid Mech., 1,* 290-318, 1956.

3. Walkden, F., "The Shock Pattern of a Wing-Body Combination, Far From the Flight Path", *Aeronautical Quarterly, IX* (2), 164-194, 1958.

4. Hayes, W.D., "Linearized Supersonic Flow", Ph.D. Thesis, California Institute of Technology, 1947.

5. Jones, R.T., "Theory of Wing-Body Drag at Supersonic Speeds", NACA RM A53H18a, 1953.

6. Resler, E.L., "Reduction of Sonic Boom Attributed to Lift", *Second Conference on Sonic Boom Research,* Schwartz, I.R. (Ed.), NASA SP-180, May 1968.

7. Landau, L.D., "On Shock Waves at Large Distances From the Place of Their Origin", *J. Phys. USSR, 9,* 496, 1945.

8. DuMond, J.W.M., Cohen, E.R., Panofsky, W.K.H., and Deeds, E., "A Determination of the Wave Forms and Laws of Propagation and Dissipation of Ballistic Shock Waves", *JASA, 18* (1), 97-118, 1946.

9. Carlson, H.W., "Simplified Sonic Boom Prediction", NASA Technical Paper 1122, 1978.

10. McLean, F.E., "Some Nonasymptotic Effects on the Sonic Boom of Large Airplanes", NASA TN D-2877, June 1965.

11. Zepler, E.E., and Harel, J.R.P., "The Loudness of Sonic Booms and Other Impulsive Sounds", *J. Sound and Vibration 2,* 249-256, 1965.

12. Johnson, D.R., and Robinson, D.W., "The Subjective Evaluation of Sonic Bangs", *Acustica, 18* (5), 1967.

13. Shepherd, K.P., Sullivan, B.M., Leatherwood, J.D., and McCurdy, D.A., "Sonic Boom Acceptability Studies", First Annual High-Speed Research Workshop, May 14-16, 1991.

14. Brown, D., and Sutherland, L.C., "Outdoor-to-Indoor Response to Minimized Sonic Booms", First Annual High-Speed Research Workshop, May 14-16, 1991.

15. Jones, L.B., "Lower Bounds for Sonic Bangs", *J. Roy. Aeron. Soc., 65,* 1-4, 1961.

16. George, A.R., "Lower Bounds for Sonic Booms in the Mid-Field", *AIAA Journal, 7,* 1542, 1969.

17. Seebass, A.R., and George, A.R., "Design and Operation of Aircraft to Minimize Their Sonic Boom", *J. Aircraft, 11,* (9), 509-517, 1974.

18. Darden, C.M., "Study of the Limitations of Linear Theory Methods as Applied to Sonic Boom Calculations", AIAA Paper 90-0368, January 1990.

19. Sohn, R.A., "Overview of Sonic Boom and HSCT Design Considerations", paper presented at AIAA Aeroacoustics conference, April 1989.

20. Sohn, R.A., "Sonic Boom Configuration Minimization", First Annual High-Speed Research Workshop, May 14-16, 1991.
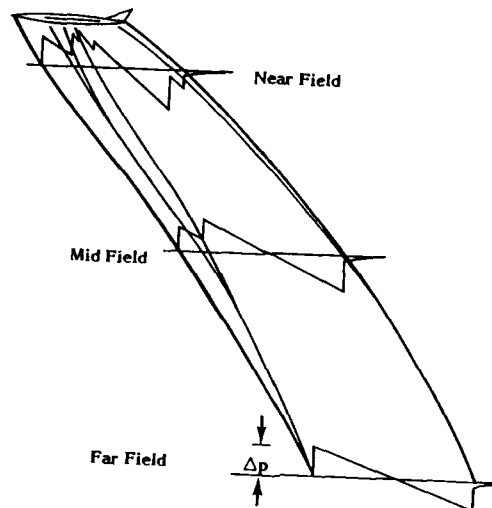
Figure 1. Sonic Boom Generation, Propagation, and Signature Evolution.
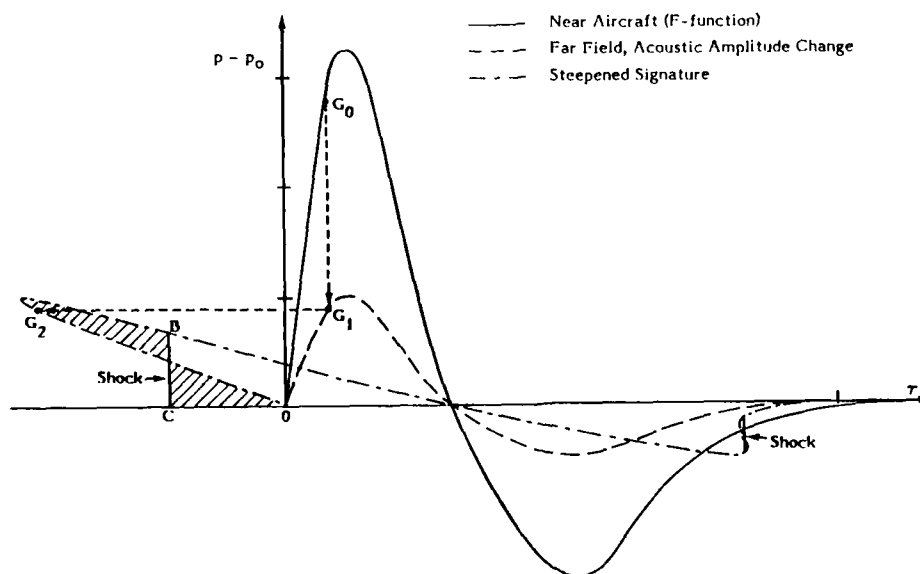
Figure 2. Evolution and Steepening of Sonic Boom Signature.
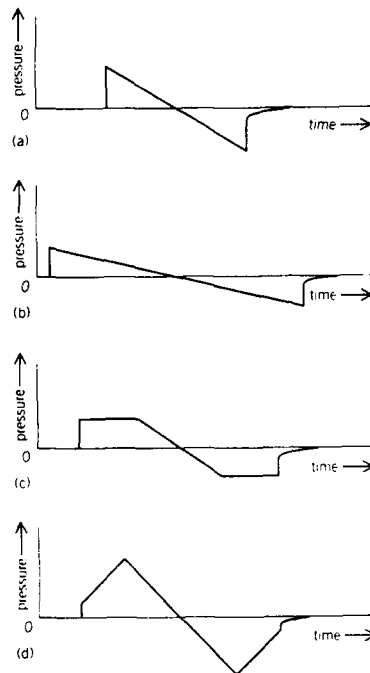
Figure 3. Various Reduced-Noise Sonic Booms Compared
With a Normal N-Wave.
(a) Normal N-Wave.
(b) Extended-Duration Sonic Boom.
(c) Flat-Top Sonic Boom.
(d) Minimum-Shock Sonic Boom.
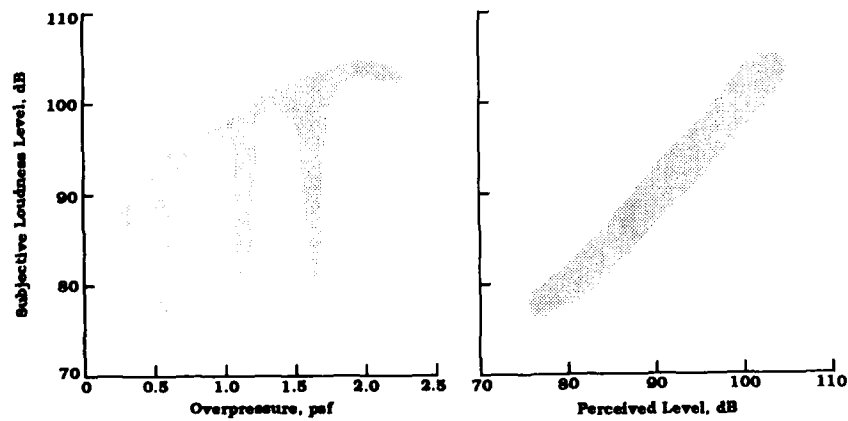
Figure 4. Prediction of Subjective Response to Sonic Booms.[13]

111
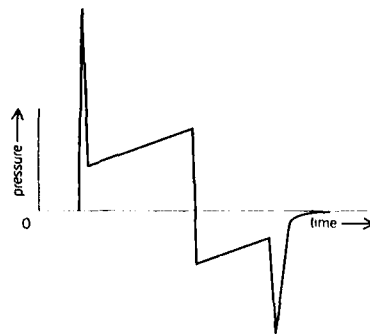
Figure 5.   F-Function That Will Age Into a Minimum-Shock Sonic Boom.[17]

SECOND INTERNATIONAL CONGRESS ON
RECENT DEVELOPMENTS IN AIR- AND
STRUCTURE-BORNE SOUND AND VIBRATION
MARCH 4-6, 1992   AUBURN UNIVERSITY, USA

CONTROL OF SUPERSONIC THROUGHFLOW TURBOMACHINES DISCRETE FREQUENCY NOISE GENERATION BY AERODYNAMIC DETUNING

Sanford Fleeter
School of Mechanical Engineering
Purdue University
West Lafayette, Indiana 47907

ABSTRACT

Substantial improvements in supersonic and hypersonic flight vehicles can be obtained by utilizing supersonic throughflow fans and compressors. However, the environmental impact of such future propulsion systems must be considered, for example their noise generation. In this regard, progress in engine noise control is dependent on developing an increased fundamental understanding of turbomachinery noise generation and on novel methods for controlling this noise which do not impose performance penalties on the engine. In this paper, a mathematical is developed to analyze the effects of aerodynamic detuning on the discrete frequency noise generation of supersonic axial flow rotors, with the detuning achieved by alternating the circumferential spacing of adjacent rotor blades. This model is then applied to baseline uniformly spaced twelve bladed rotors and detuned configurations of these baseline rotors, with the effect of this aerodynamic detuning on the discrete frequency noise generation determined by considering the relative magnitudes of the gust generated unsteady aerodynamic lift. This study demonstrated that, dependent on the specific blade row and flow field geometry, alternate blade circumferential spacing aerodynamic detuning is a viable passive discrete frequency noise generation control technique for supersonic throughflow rotors.

NOMENCLATURE

C	airfoil chord
$[CG]^n$	gust influence coefficient airfoil n
M_∞	inlet Mach number
R_1, R_0	reference airfoils of detuned cascade
S	baseline tuned cascade spacing
S_d	detuned cascade spacing
c	perturbation speed of sound
w_g	transverse gust amplitude
k	reduced frequency, $\omega C/U_\infty$
u	dimensionless perturbation chordwise velocity
v	dimensionless perturbation normal velocity
w	complex amplitude of gust
x	dimensionless chordwise coordinate
y	dimensionless normal coordinate
β	interblade phase angle
β_d	detuned interblade phase angle
$\overrightarrow{\Delta W}$	mean and instantaneous velocity difference vector
ε	level of aerodynamic detuning
ω	gust frequency

113

INTRODUCTION

In the design of high performance gas turbine engines, acoustic analyses are a necessary evil. This is because overall engine performance is not improved by noise control considerations. In fact, state-of-the-art noise control techniques often decrease performance while adding weight and increasing the complexity of the engine. As a result, progress in engine noise control is dependent on developing an increased fundamental understanding of turbomachinery noise generation, i.e., fan, compressor and turbine generated noise, and on novel methods for controlling this noise generation which do not impose engine performance penalties [1].

Unsteady flow phenomena are responsible for turbomachinery noise generation, with the discrete frequency noise generated by periodic blade row interactions a primary noise source. Namely, turbomachine blade rows are subject to spatially nonuniform inlet flow fields, with upstream airfoil wakes convecting downstream widely believed to be the most important noise generation mechanism. The interaction of the rotor with these nonuniform spatial inlet flows results in periodic unsteady aerodynamic lift forces on the rotor blading which are the source of discrete frequency acoustic radiation.

This paper is concerned with supersonic blade row discrete frequency noise generation and control. This is a result of the renewed interest in supersonic and hypersonic flight vehicles having focused attention on engines which can either sustain efficient supersonic cruise or serve as boosters for acceleration to moderate supersonic velocities. For such applications, turbofan engine cycle studies have shown that substantial improvements can be obtained with supersonic throughflow fans and compressors. With the increasing concern regarding environmental issues, such advanced propulsion systems are being scrutinized closely for their environmental impact. One such concern is the noise generation of the engine, with the discrete frequency noise generation of supersonic throughflow blade rows of particular interest herein.

Blade row unsteady aerodynamic analyses are based on two-dimensional models applied in a strip theory technique, with a two-dimensional, typical element of the blade row represented by an equally spaced airfoil cascade. Thus, in the supersonic axial flow regime of interest, a flat plate airfoil cascade embedded in a supersonic flow field with a supersonic leading edge locus is considered, Figure 1. To predict the discrete frequency noise generation of the blade row, the inlet wake is decomposed into unsteady aerodynamic gust components parallel and normal to the blade row, u and v, Figure 2. These gusts are then harmonically decomposed, u^+ and v^+, with each harmonic frequency individually considered. The harmonic gust generated unsteady aerodynamic lift forces acting on the blading are then calculated with blade row unsteady aerodynamic gust response models. As the noise generation is proportional to the square of the magnitude of this unsteady lift, it is essential to both accurately analyze these unsteady lift forces and to develop passive control design capabilities to minimize the discrete frequency noise generation.

Aerodynamic detuning is defined as designed passage-to-passage variations in the unsteady aerodynamic flow field of a blade row. As small changes in blade row solidity typically do not have a large effect on aerodynamic performance, alternate nonuniform circumferential blade spacing has been shown theoretically to have a beneficial effect on blade row aeroelasticity [2, 3, 4]. Thus, it is also of interest to investigate the effect of alternate nonuniform circumferential airfoil spacing on the fundamental driving mechanisms associated with discrete frequency noise generation, namely the unsteady aerodynamic lift forces generated on the rotor blading as well as the resulting discrete frequency noise generation.

In this paper, the effect of aerodynamic detuning on the discrete frequency acoustic radiation of a rotor operating with a supersonic relative inlet velocity with a supersonic axial component is investigated. As small changes in blade row solidity typically do not have a large effect on aerodynamic performance, alternate nonuniform circumferential blade spacing is the aerodynamic detuning technique considered. A two dimensional typical airfoil section approach is utilized. A mathematical model is developed to predict the unsteady aerodynamic forces acting on the airfoil cascade. The inlet distortion is modeled as a transverse gust convected with the mean flow past the cascade. The unsteady aerodynamics due to the convection of this transverse gust past a stationary airfoil cascade are determined by developing an influence coefficient technique which is appropriate for both uniformly spaced, i.e., tuned, rotors and aerodynamically detuned rotor configurations. The effects of this aerodynamic detuning on discrete frequency noise generation of supersonic axial flow rotors are then demonstrated by applying this math model to baseline twelve bladed rotors, with the discrete frequency noise generation determined by considering the relative magnitude of the gust generated unsteady aerodynamic lift of the tuned and detuned cascades [5].

UNSTEADY AERODYNAMIC MODEL

To predict the discrete frequency noise generation of a turbomachine rotor blade, a mathematical model is developed to analyze the unsteady aerodynamic lift generated on a supersonic blade row by a convected transverse gust.

Aerodynamically Detuned Cascade

Alternate blade circumferential spacing aerodynamic detuning is considered. Introducing this detuning into the baseline uniformly spaced or tuned cascade results in two reference passages: an increased spacing or decreased solidity passage and a decreased spacing or increased solidity passage. Also, as schematically depicted in Figure 3, there are two reference airfoils for each passage, denoted by R_0 and R_1. The aerodynamically detuned airfoil cascade can be considered as being comprised of two uniformly spaced cascades, each having a spacing of S_d which is twice that of the baseline cascade. The circumferential spacing between adjacent airfoils S_1 and S_2 is specified by the level of aerodynamic detuning ε.

$$S_{2,1} = (1 \pm \varepsilon) S \qquad (1)$$

where S is the spacing of the baseline cascade and S_1 and S_2 are the airfoil spacings of the detuned cascades.

Unsteady Flow Field

The fluid is assumed to be a perfect gas with the flow inviscid, irrotational, adiabatic and isentropic. The unsteady continuity and Euler equations are linearized by considering the unsteady flow to be small as compared to the steady flow field. Assuming harmonic time dependence, the dependent variables are the nondimensional chordwise, normal, and sonic perturbation velocities, u, v and a, respectively. The nondimensional chordwise, normal, and sonic perturbation velocities are then given by Equation 2.

$$\frac{\partial u}{\partial x} + \sqrt{M_\infty^2 - 1}\, \frac{\partial v}{\partial y} + M_\infty^2 \frac{\partial a}{\partial x} + ik M_\infty^2 a = 0$$

$$\frac{\partial u}{\partial x} + \frac{\partial a}{\partial x} + iku = 0 \qquad (2)$$

$$\frac{\partial u}{\partial y} - \sqrt{M_\infty^2 - 1}\, \frac{\partial v}{\partial x} = 0$$

where $k = \omega C / U_\infty$ is the reduced frequency.

Boundary Conditions

The airfoil surface flow tangency boundary condition requires that the normal component of the perturbation velocity v is equal to the normal velocity of the airfoil. The gust boundary condition on the nth airfoil is developed by considering a small transverse gust of amplitude w_g superimposed on and convected with the uniform throughflow with a mean velocity U_∞.

$$v_n(x, y_s, t) = w_g\, e^{i(k(t-x)+n\beta)} \qquad (3)$$

where x is the nondimensional airfoil chordwise coordinate as measured from midchord, t is nondimensional time and y_s denotes the airfoil surface.

This boundary condition is specified in terms of the interblade phase angle β. For blade row interaction discrete frequency noise generation, the interblade phase angle is specified a priori, being fixed by the aerodynamic forcing function and the circumferential spacing of the blade row of interest. For a uniform circumferentially spaced airfoil cascade subject to an inlet gust, the interblade phase angle between two adjacent airfoils β is a function of the airfoil spacing for a given forcing function harmonic. Analogously, for the aerodynamically detuned cascade, the interblade phase angle between two adjacent airfoils of each set β_d is a function of the airfoil spacing for a given harmonic of the inlet gust w_g.

Flow Field Solution

The solution to the system of partial differential equations and boundary conditions which describe the unsteady flow field, Equations 1, 2 and 3, are obtained by the method of characteristics [6]. The compatibility equations, which are the ordinary differential equations that act along the characteristics, are given in Equation 4.

$$\left(\frac{\partial u}{\partial x}\right)_{\xi} - \left(\frac{\partial v}{\partial x}\right)_{\xi} + ik \frac{M_{\infty}^2}{M_{\infty}^2 - 1} (u - a) = 0$$

$$\left(\frac{\partial u}{\partial x}\right)_{\eta} + \left(\frac{\partial v}{\partial x}\right)_{\eta} + ik \frac{M_{\infty}^2}{M_{\infty}^2 - 1} (u - a) = 0 \qquad (4)$$

$$\left(\frac{\partial u}{\partial x}\right)_{str} + \left(\frac{\partial a}{\partial x}\right)_{str} + ik = 0$$

where the subscripts ξ, η and str indicate that the relation is valid along the right or left running Mach lines of the streamline direction, respectively.

Uniformly Spaced (Tuned) Cascade Solution

The formulation of the basic unsteady aerodynamic mathematical model is now complete. For the uniformly spaced or tuned cascade, finite differences are used to solve the system of three differential equations in three unknowns, Equation 4, at the intersection of the characteristics for the chordwise, normal and sonic dimensionless perturbation velocities, u, v and a, subject to the specified transverse gust boundary condition. The unsteady perturbation pressure on the surfaces of the reference airfoil are then determined from the perturbation sonic velocity. Finally the airfoil nondimensional unsteady aerodynamic lift L is calculated.

$$L = \int_0^1 \Delta p (x, y_s, t) \, dx \qquad (5)$$

where Δp denotes the nondimensional unsteady pressure difference across the chordline of a reference airfoil of the uniformly spaced cascade.

Detuned Cascade Solution

This method of characteristics solution procedure for the perturbation velocity components can also be applied to the two passages of the supersonic axial flow aerodynamically detuned cascade under consideration. However, this requires complete reanalysis of the cascade for every detuned interblade phase angle of interest. This limitation is overcome in the model developed herein by utilizing an unsteady aerodynamic influence coefficient technique [3] to predict the unsteady aerodynamic lift on the two reference airfoils of the alternate circumferentially spaced detuned cascade due to the convected gust.

$$L_{R_0, R_1} = \left([CG]^0{}_{R_0, R_1} w_{R_0} + [CG]^1{}_{R_0, R_1} w_{R_1}\right) e^{i\omega t} \qquad (6)$$

where w_{R_0, R_1} are the complex gust amplitudes and the double subscript notation is a means of expressing two equations, one for each of the two reference airfoils.

To determine the influence coefficients [CG], the unsteady aerodynamic gust response model for the two-reference passage detuned cascade is utilized directly with the modification of the airfoil surface boundary conditions on the two reference airfoils. The gust influence coefficients are determined by specifying a unit amplitude gust on the reference airfoil R_0 and the detuned interblade phase angle β_d with a zero normal velocity on reference airfoil R_1. The influence coefficients $[CG]^1{}_{R_0, R_1}$ are determined in an analogous manner but with reference airfoil R_0 and R_1 reversed, namely, by specifying a unit amplitude gust normal velocity on reference airfoil R_1 and a zero normal velocity on reference airfoil R_0.

The complex gust amplitudes w_{R_0} and w_{R_1} are related to the Fourier coefficients or a general inlet distortion and to the airfoil spacing. Thus, for a given harmonic of the inlet distortion, these amplitudes are related by the detuned interblade phase angle between the two adjacent reference airfoils β_d and the level of aerodynamic detuning ϵ.

116

$$w_{R_0} = w_{R_1} e^{-i(1-\varepsilon)\beta_d/2} \tag{7}$$

The resulting unsteady aerodynamic lift on the two reference airfoils of the detuned cascade is given in Equation 8.

$$L_{R_0, R_1} = w_{R_0} \left([CG]^0{}_{R_0, R_1} + e^{i(1-\varepsilon)\beta_d/2} [CG]^1{}_{R_0, R_1} \right) e^{i\omega t} \tag{8}$$

Thus, with the influence coefficients $[CG]^0$ and $[CG]^1$ determined for a given detuned cascade configuration, the unsteady aerodynamic lift on the two reference airfoils if determined for any detuned interblade phase angle by the simple complex algebraic addition of these influence coefficients.

DISCRETE FREQUENCY NOISE GENERATION

This unsteady aerodynamic model is utilized to predict the discrete frequency noise generated by considering the magnitude of the gust generated unsteady aerodynamic lift on the reference airfoils of the tuned and detuned cascades [5]. In particular, the relative noise generation is determined by considering the magnitude of the gust generated unsteady aerodynamic lift LWG of the baseline tuned and detuned cascades.

$$LWG = \frac{1}{2} |L_{R_0} + L_{R_1}| \tag{9}$$

Thus a decrease in the aerodynamically detuned cascade value of LWG as compared to the baseline turned cascade value quantifies the reduction in the noise generation due to the aerodynamic detuning. As the sound pressure level is proportional to $(LWG)^2$, the effect of the aerodynamic detuning on noise generation can also be expressed in terms of decibels.

$$\Delta dB = 20 \, Log_{10} \left| \frac{LWG_\varepsilon}{LWG_{\varepsilon=0}} \right| \tag{10}$$

where the subscript ε indicates LWG for the detuned cascade and $\varepsilon = 0$ denotes the LWG for the baseline tuned cascade.

RESULTS

The effect of alternate blade aerodynamic detuning on the discrete frequency noise generation characteristics of a supersonic throughflow rotor is demonstrated by considering two baseline uniformly spaced twelve bladed rotors and alternate circumferentially spaced aerodynamically detuned variations of each. In particular, the mathematical model developed herein is utilized to predict the relative noise generation of the detuned rotors as compared to the tuned rotor over the complete range of gust interblade phase angle values.

Baseline & Detuned Rotor Geometries

With a supersonic inlet flow field, waves of finite strength originate from the leading and trailing edges of the airfoils in the cascade representing the flow geometry of the rotor. With a supersonic axial velocity component, the airfoil trailing edge waves are always downstream of the other airfoils. However, the airfoil leading edge waves may be reflected from the surfaces of adjacent airfoils. Two such cascade flow geometries are of interest, herein termed Cascade F and Cascade K. As schematically depicted in Figure 4, Cascade F has one airfoil leading edge wave reflection, whereas Cascades K has one reflection of both the airfoil leading edge waves.

Three alternate circumferential spacing, aerodynamically detuned configurations of each cascade geometry are considered: 10%, 20% and 30% detuning. For Cascade F, as the level of aerodynamic detuning is increased, the wave reflection on the pressure surface of reference airfoil R_1 moves toward the leading edge whereas the pressure surface reflection on the reference airfoil R_0 moves toward the trailing edge. The left running Mach wave from the leading edge of reference airfoil R_1 does not intersect airfoil R_0 for the baseline, 10% or 20% detuning. However, with 30% detuning, it intersects the suction surface of airfoil R_0. For Cascade K, as the level of aerodynamic detuning is increased, the wave reflection on the pressure surface of reference airfoil R_1 also moves toward the leading edge while the wave reflection on the pressure surface of airfoil R_0 moves toward the trailing edge. The left running Mach line from the leading edge of airfoil R_0 intersects the suction surface of airfoil R_1 with 10% and 20% aerodynamic detuning and moves toward the trailing edge as the level of aerodynamic detuning increases. With 30% aerodynamic detuning, the Mach line does not intersect the suction surface of blade R_1. The left running Mach line form the leading edge of airfoil R_1 intersects the suction surface of blade R_0 for all levels of detuning and moves toward the leading edge as the level of aerodynamic detuning is increased.

<u>Discrete Frequency Noise Generation</u>

For cascades utilizing aerodynamic detuning without the incorporation of splitters, the results of the noise generation study for Cascades F and K are shown in Figures 5 and 6. Cascade F with 10% and 20% the alternate blade circumferential spacing aerodynamic detuning results in discrete frequency noise reduction for all interblade phase angle values, with a maximum decrease for detuned interblade phase angle of 180°. However, with 30% aerodynamic detuning, there is an increase in the discrete frequency noise generation for interblade phases of 120° and 240°. For Cascade K, alternate blade spacing aerodynamic detuning increases the discrete frequency noise generation for all interblade phase angles, with the exception of a detuned interblade phase angle of 300° with 10% and 20% detuning.

SUMMARY AND CONCLUSIONS

A mathematical model has been developed to analyze the effects of aerodynamic detuning on the discrete frequency noise generation of supersonic axial flow rotors. The aerodynamic detuning was achieved by alternating the circumferential spacing of adjacent blades. The unsteady aerodynamics due to a transverse gust convected past a stationary cascade was determined by developing an influence coefficient technique appropriate for both aerodynamically tuned (uniformly spaced) and detuned rotor configurations. The discrete frequency noise generation was then determined by considering the magnitude of the gust generated unsteady aerodynamic lift on the reference airfoils of the tuned and detuned cascades. The effects of this unsteady aerodynamic detuning on the discrete frequency noise generation of supersonic axial flow rotors were then demonstrated by applying this model to two baseline twelve bladed rotors and aerodynamically detuned variations of these rotors. This study demonstrated that, dependent on the specific blade row and flow field geometry, aerodynamic detuning is a viable passive discrete frequency noise generation control technique for supersonic throughflow rotors.

REFERENCES

1. Gliebe, P.R., "Aeroacoustics in Turbomachines and Propellers - Future Research Needs," *6th International Symposium on Unsteady Aerodynamics, Aeroacoustics and Aeroelasticity in Turbomachines and Propellers*, September 1991.

2. Hoyniak, D. and Fleeter, S., "Aerodynamic Detuning Analysis of an Unstalled Supersonic Turbofan Cascade," *ASME Journal of Engineering for Gas Turbines and Power*, Vol. 108, No. 1, January 1986, pp 60-67.

3. Hoyniak, D. and Fleeter, S., "Forced Response Analysis of an Aerodynamically Detuned Supersonic Turbomachine Rotor," *Journal of Vibration, Acoustics, Stress, and Reliability in Design*, Vol. 108, April 1986, pp. 117-124.

4. Spara, K.M. and Fleeter, S., "Supersonic Turbomachine Rotor Flutter Control by Aerodynamic Detuning," *AIAA Paper 89-2685*, July 1989.

5. Goldstein, M.E., *Aeroacoustics*, McGraw Hill, New York, 1976.

6. Platzer, M.F. and Chalkley, H.G., "A Study of Supersonic Cascade Flutter," *Master's Thesis, Naval Postgraduate School*, Monterey, California, June 1972.
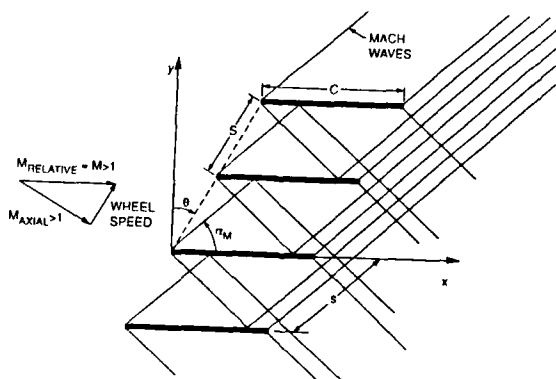
Figure 1. Supersonic axial flow flat plate cascade
flow field
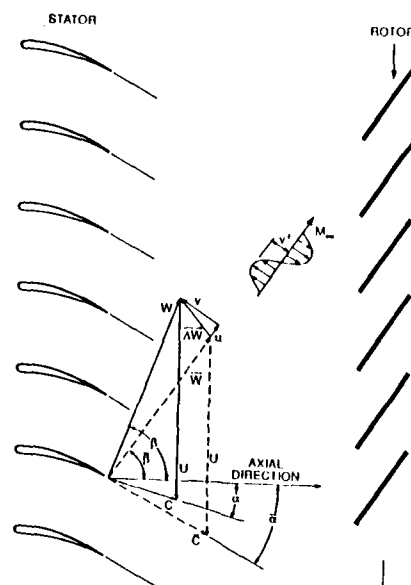
Figure 2. Transverse gust convected past flat plate
cascade
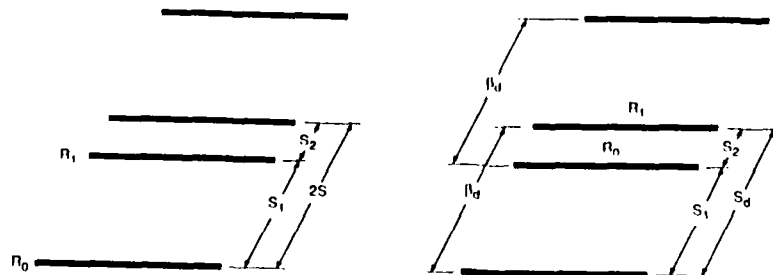
Figure 3. Alternate spacing cascade aerodynamic
detuning
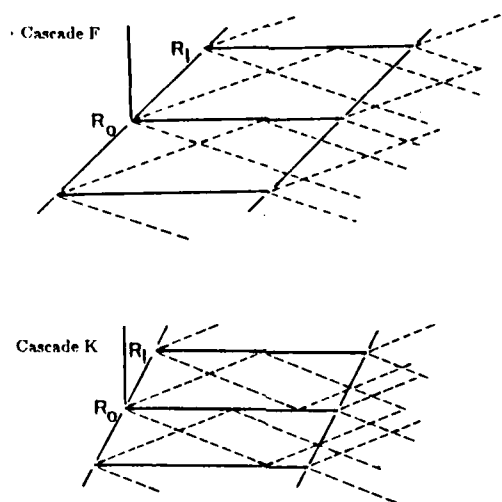
Figure 4. Baseline cascade flow geometries
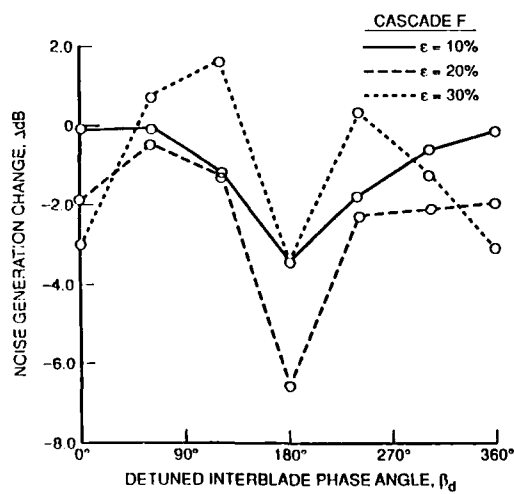
Figure 5. Aerodynamic detuning effect on Cascade F noise generation
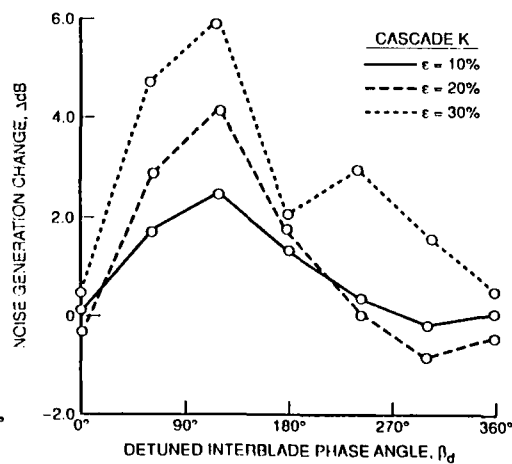
Figure 6. Aerodynamic detuning effect on Cascade K noise generation
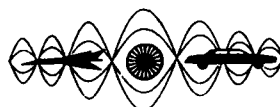
**SECOND INTERNATIONAL CONGRESS ON
RECENT DEVELOPMENTS IN AIR- AND
STRUCTURE-BORNE SOUND AND VIBRATION**

MARCH 4-6, 1992   AUBURN UNIVERSITY, USA

COMPARISON OF RADIATED NOISE
FROM SHROUDED AND UNSHROUDED PROPELLERS

Walter Eversman
Mechanical and Aerospace Engineering
and Engineering Mechanics
University of Missouri-Rolla
Rolla, Missouri 65401

ABSTRACT

A finite element model is created for the generation, propagation, and radiation of steady, rotor alone noise and rotor and exit guide vane interaction noise of a ducted fan. In the case of rotor alone noise the acoustic source is represented by a rotating lifting line of thrust and torque dipoles distributed radially on the blade. In the case of interaction noise the acoustic source is a stationary lifting line of torque and thrust dipoles which represents the fluctuating lift on the exit guide vane created by the velocity deficit associated with wakes in the steady velocity field behind the rotor. In the configurations considered in the present study, emphasis is on ducted fans or ducted propellers for which the by-pass ratio is very large. In this case the usual assumption is made that the fan, or propeller, is operating in a mean flow environment which is uniform and the same as the forward flight velocity. The flow acceleration in the inlet, acceleration in the fan duct, and jet free shear layer are not accounted for in the present model. The model accounts for the noise generation process, the propagation through the inlet and fan duct, and the radiation to the near and far field.

The major issue addressed in the computational examples is the relationship between the far field radiated Sound Pressure Level (SPL) and directivity and the fan tip speed. In the case of rotor alone noise it is shown that due to the effect of finite duct length and mean flow velocity in the duct there can be significant SPL in the far field at large angles to the duct axis, even for subsonic tip speeds. In the case of interaction noise it is found that the radiated field can be significant near the duct axis.

INTRODUCTION

Ultra high by-pass ratio turbo-fan engines and ducted or shrouded propellers are attractive from the standpoint of propulsive efficiency. In addition there are possible advantages to be gained in radiated noise levels due to the imbedding of the propeller or fan acoustic source within the nacelle or shroud. An unducted propeller generates an acoustic field which tends to produce high levels on the sideline, and therefore may create unaccceptable noise levels in the interior of the aircraft. A ducted propeller is restricted in the way in which it can radiate to the near and far field. It is known that steady, rotor alone noise, created by blade loading, is a principle source mechanism for unducted propellers. It is generally assumed that in the case of a ducted propeller the rotor alone noise is not propagated to the far field if the tip speed does not exceed the speed of sound. This result, due to pioneering work of Tyler and Sofrin [1], is true for rotor generated noise in a thin annulus with the absence of duct mean flow.

In the case of ducted fans and propellers an additional source mechanism exists associated with the presence of exit guide vanes (EGV). The EGV operate in a helical velocity field behind the rotor, which is for the most part steady and defined in direction by the thrust of the rotor. The mainly steady character of the rotor generated velocity is periodically interrupted by the viscous wakes downstream of the individual rotating blades. The EGV produce lift in response to the rotor velocity field, and because of the fluctuating velocity field behind the rotor, produce fluctuating lift and provide an

121

acoustic source mechanism. This interaction source mechanism was also addressed by Tyler and Sofrin [1] and was shown to have the potential for the creation of acoustic modes of very low angular order. Modes of this type will propagate and radiate with a directivity pattern which may produce high levels near the axis of symmetry.

The purpose of the work presented here is to investigate the differences in the radiated acoustic fields of ducted and unducted propellers of the same thrust operating under similar conditions. Hanson [2] has created a comprehensive acoustic model for unducted propellers which accounts for spanwise and chordwise details of the blade loading. It is not the intent in the present study to focus on such a refined model. Instead, the approach is to generate a very simple source model, similar to the lifting line theory suggested by Gutin [3], to concentrate on the propagation and radiation effects introduced by the duct, and to compare the acoustic performance of similar ducted and unducted propellers based on the same source model.

The finite element method (FEM) has been used in previous studies to model the wind tunnel acoustic testing of propellers and the free field acoustic radiation of propellers [4-7]. In the present study the FEM is used to model the ducted propeller in the free field. This combines the propeller modeling previously reported and some aspects of earlier work on the prediction of the radiated acoustic field from turbofan engine inlets [8-9].

The generation, propagation, and radiation of sound from a ducted fan is described in this study by the convected wave equation with volumetric body forces. Body forces are used to introduce the blade loading for rotating blades and stationary exit guide vanes. For an axisymmetric nacelle or shroud, the problem is formulated in cylindrical coordinates. For a specified angular harmonic the angular coordinate is eliminated and a two dimensional representation results. A finite element discretization based on nine node quadratic isoparametric elements is used.

Geometry and Coordinate System

In this investigation the acoustic field is represented in a cylindrical geometry with the axis of the propeller or rotor/nacelle designated as the x axis. It is assumed that the nacelle/centerbody combination is axially symmetric and that the inlet flow field is axially symmetric. The acoustic field is periodic in the angular coordinate of the cylindrical system. It is represented as the components of a Fourier Series in the angular coordinate θ. The acoustic field for each angular component, or "angular mode," is represented by a field equation in only the axial and radial components x, r of the cylindrical system.

Figure 1 shows an idealized geometry for a rotor/nacelle arrangement. Noise sources related to the rotating blades and the interaction of the blades with stationary exit guide varies can be modeled.

The steady velocity field in and around the nacelle is assumed to be uniform. For many applications, notably the case of the ultra high bypass fan or the ducted propeller this is probably satisfactory. For other cases it may be necessary to model the flow in and around the nacelle. It may also be required to consider the effects of the shear layer in the interface between the fan exhaust and the surrounding steady flow.

Mathematical Model

The acoustic field is described by the convected wave equation with body forces

$$\nabla^2 p^* - \frac{1}{c^2}\frac{D^2 p^*}{Dt^{*2}} = \rho_o \nabla \cdot \bar{f}^* \tag{1}$$

where p^* is the acoustic pressure, ρ_o is the ambient density, c is the ambient speed of sound, and $\bar{f}^*$ represents the body force per unit mass acting on the fluid. $\rho_o \bar{f}^*$ is the body force per unit volume.

Equation (1) is in dimensional form. In the development which follows a nondimensional form of equation (1) is used with the following scaling

$$x = \frac{x^*}{L} \ , \quad p = \frac{p^*}{\rho_o c_o^2}, \quad u = \frac{u^*}{c_o} \ , \quad t = \frac{c t^*}{L}, \quad \bar{f} = \frac{L}{c_o^2} \bar{f}^*$$

t^* is the dimensional time, x^* is any of the linear spatial coordinates, and u^* is any of the fluid velocity components. The reference length L is the propeller radius R. The nondimensional form of the acoustic field equation is

$$\nabla \cdot \ (\nabla p - M^2 \ \frac{\partial p}{\partial x} \ \bar{i} - \bar{f}) - 2M \ \frac{\partial^2 p}{\partial x \partial t} - \frac{\partial^2 p}{\partial t^2} = 0 \qquad (2)$$

where M is the mean flow Mach number.

The body force per unit mass $\bar{f}$ is related to the force exerted on the fluid by the rotating blade or stationary vane.

The major idealization in this model is the assumption that the interior and external flow are uniform and at the flight Mach number. This is required because a pressure formulation has been chosen to introduce the acoustic source model for the rotor or EGV via equivalent body forces acting on the fluid. This is consistent with previous models of propellers [4-7]. In the pressure formulation it is required that the flow field be uniform in order that the acoustic field equations can be reduced to the convected wave equation. Nonuniform flow near the inlet lip and the jet shear layer are not considered.

The models used for the propeller or rotor and exit guide vane acoustic sources are discussed briefly in the following sections.

<u>Blade Loading</u>

The blade loading of the propeller or rotor is considered as the only source of rotor alone noise. No effects of blade thickness are modeled in this investigation. Blade loading is based on isolated lifting surface theory using a strip analysis. The discussion of Dommasch, Sherby and Connolly [10] is directly relevant to the model used here.

Figure 2 shows an airfoil section at the radius r from the hub. The local angle of attack of the section at radius r depends on the inflow velocity, U, the relative velocity due to rotation $r\Omega/U$, where Ω is the angular velocity of the rotor or propeller, and the blade twist ϕ . If the total thrust T is specified and if the loading is assumed to be linearly varying from hub to tip, the thrust and torque components per unit propeller span can be written

$$l_t = l_{tip} \cos\beta \ (\frac{r}{R}) \qquad l_m = l_{tip} \sin\beta \ (\frac{r}{R}) \qquad (3)$$

where l_{tip} is the lifting per unit span at the rotor blade tip, R is the rotor blade radius, and β is the inflow angle shown in Figure 1.

<u>Rotor Alone Noise</u>

Rotor alone noise generation is viewed from the perspective of a source fixed in space which is active during the passage of a blade with its associated lift distribution. It is assumed that the duration of passage of the blade past a fixed point is $\tau = a/\Omega r$ where a(r) is the projection of the blade chord on the rotor plane, r is the radial location, and Ω is the angular speed of the rotor. The strength

123

of the source representing the blade passage is taken as the negative of the lifting pressure differential across the blade, approximated by $l(r)/c(r)$ where $c(r)$ is the local chord.

If the passage of N_B blades is considered at arbitrary angular position θ, the nondimensional volumetric force representing rotor alone noise can be written

$$f_t = -\frac{1}{\rho c_o^2} (\frac{l_t(r)}{a}) \delta(x) \sum_{m=-\infty}^{\infty} C_m e^{imN_B \eta t} e^{-imN_B \theta} \tag{4}$$

$$f_m = \frac{1}{\rho c_o^2} (\frac{l_m(r)}{a}) \delta(x) \sum_{m=-\infty}^{\infty} C_m e^{imN_B \eta t} e^{-imN_B \theta} \tag{5}$$

where

$$C_m = \frac{\sin m N_B \Omega \tau + i(\cos m N_B \tau - 1)}{2\pi m}$$

and $\eta = \Omega R/c$ is the nondimensional rotor speed which is also the rotor tip Mach number.

EGV Interaction Noise

In order to estimate the noise generating mechanism of the exit guide vanes (EGV) in their interaction with the rotating blades, a simplified model has been constructed. This model assumes that the EGV are on the average under the influence of a steady lift dictated by the magnitude and direction of the absolute velocity field leaving the rotor. This can be approximated from a knowledge of the steady blade loading in the rotor stage. The flow field downstream of the rotor is not steady, but is interrupted by the wakes downstream of the blade trailing edges. The velocity deficit in the wake, which is dependent on the distance downstream of the blade trailing edge, creates a fluctuating lift on the EGV. It is this fluctuation which becomes the noise source. The model used is based on quasi-steady strip theory aerodynamics and is intended only as an estimate of the actual source mechanism.

With this type of model and with an analysis based on N_v guide vanes being affected by N_B blades, it is determined that an approximation for the nondimensional volumetric loading for EGV noise source can be written

$$f_t = \frac{(1-\epsilon)}{\rho_o c_o^2} \left(\frac{l_s}{r}\right) \sin\alpha_2 \, \delta(x) N_v N_B \sum_{n=-\infty}^{\infty} \sum_{m=-\infty}^{\infty} F_n G_n e^{inN_B \eta t} e^{-i(nN_B - mN_v)\theta} \tag{6}$$

$$f_m = \frac{(1-\epsilon)}{\rho_o c_o^2} \left(\frac{l_s}{r}\right) \cos\alpha_2 \, \delta(x) \, N_v N_B \sum_{n=-\infty}^{\infty} \sum_{m=-\infty}^{\infty} F_n G_n e^{inN_B \eta t} e^{-i(nN_B - mN_v)\theta} \tag{7}$$

where

$$F_n = \frac{\sin n N_B \Omega \tau + i(\cos n N_B \Omega \tau - 1)}{2\pi n N_B}, \qquad G_m = \frac{1}{2\pi} \tag{8}$$

and τ is an estimate of the time taken for a rotor wake to sweep across an EGV.

The steady lift per unit span on an EGV, l_s, can be estimated from an elementary theory of turbomachines [11]. The velocity deficit parameter ϵ in the wake is quantified by

$$\epsilon = \left(1 - \frac{1}{x_d}\right)^2 \qquad (9)$$

and x_d is the distance downstream of the leading edge of the EGV behind the rotating blade leading edge, measured in blade chords.

Note that equations (6) and (7), the temporal harmonics, are integer multiples of the blade passage frequency, as in the rotor alone case. The angular harmonics are differences in integer multiples of the numbers of blades and vanes. For example, for 8 blades and 7 vanes, with $n = 1$ and $M = 1$, the angular harmonic is $M_\theta = 1$. For the rotor alone case the lowest angular harmonic would be $M_\theta = 8$. For subsonic tip speed the rotor alone fundamental angular mode may be cut off while the EGV fundamental angular mode may radiate at relatively low angles to the axis of symmetry.

FINITE ELEMENT FORMULATION

Equation (2) is the field equation which governs the radiated sound field generated by the distribution of body forces $\vec{f}$ which are defined in the case of rotor alone noise by equations (4) and (5) and in the case of EGV interaction noise by equations (6) and (7). References [4-9] give details of the finite element discretization of equation (2).

COMPUTATIONAL RESULTS

In this study both rotor alone noise and EGV interaction noise for a shrouded propeller noise will be compared to unshrouded propeller noise for a fixed thrust. In the case of rotor alone noise both subsonic and supersonic tip speeds are considered, while for EGV interaction noise only the subsonic tip speed case is considered. In the rotor alone case there is a distinct difference in the subsonic and supersonic tip speed cases, while in the EGV interaction no fundamental difference is attributed to the difference in rotor speed.

A. Nacelle and Propeller Configuration

A model scale propeller and nacelle is considered here. The propeller has four or eight blades and is of dimensional radius 0.311 m (1.02 ft). The blade chord is taken to be uniform at 0.052 m (0.17 ft). The nondimensional propeller angular velocity is taken as $\eta = 0.8$ in the subsonic case and $\eta = 1.2$ in the supersonic case. For a speed of sound of 1125 ft/sec, this corresponds to an angular speed $\Omega = 8426$ RPM for the subsonic case and $\Omega = 12639$ RPM for the supersonic case. The nacelle geometry is shown in Figure 3. In the unshrouded propeller case no centerbody is present. This has only a slight effect on the propeller loading. The source location, whether rotor alone or EGV interaction, is just ahead of the center of the nacelle. The flow velocity inside and outside of the nacelle is $M = 0.4$.

B. Rotor Alone Noise

Figures 4 and 5 are summaries of the polar radiation directivity for four and eight blade shrouded propellers with comparisons to similar unshrouded propellers. Both supersonic and subsonic tip speeds are shown. Figure 4 is the four blade case. For supersonic tip speed, $\eta = 1.2$, the (4,1) mode (fourth angular, first radial) is cut off with cutoff ratio $\xi_{41}(1.2) = 0.988$ while at subsonic tip speed it is cut off with cut off ratio $\xi_{41}(0.8) = 0.66$. The corresponding attenuations based on the cut off ratio in the duct length of 1.3R are 8.6 dB and 41 dB. It is seen that the peak radiated noise at a distance of ten duct radii is 120 dB created by the unshrouded propeller (this sets the scale level for the plot). The shrouded supersonic propeller has a peak level of about 109. The unshrouded subsonic propeller

peaks at 113 dB while the shrouded subsonic propeller peaks at about 75 dB. The relationship of the SPL levels of the shrouded propellers below those of the unshrouded propellers is consistent with the projected attenuations due to the cutoff phenomenon, though not numerically equivalent. The comparison of the SPL levels of the two shrouded propellers shows an additional attenuation for the subsonic case which is also consistent, and close to the 33 dB predicted theoretically.

For the eight blade propeller a somewhat different picture emerges, as shown in Figure 5. For supersonic tip speed the (8,1) mode is propagating with ξ_{81} (1.2)= 1.085, but for the subsonic tip speed it is cut off with ξ_{81} (0.8)= 0.72 with a calculated attenuation of 69 dB. Reference to Figure 5 shows that the shrouded propeller at supersonic tip speed creates the highest SPL and sets the scale level at 130 dB. The corresponding unshrouded propeller has a peak level about 10 dB lower. The unshrouded subsonic propeller peaks at about 108 db and the corresponding shrouded case is heavily attenuated at only about 39 dB (just barely seen near the origin of the figure), consistent with, but larger than, the attenuation attributable to the cut off phenomenon. The interesting feature here is the high peak SPL of the shrouded propeller. The (8,1) mode for the supersonic case is cut on, as opposed to the (4,1) mode being slightly cut off for the four blade propeller. It appears that the mechanics of wave propagation in the duct enhances the radiation of the ducted propeller noise when the mode is cut on.

C. EGV Interaction Noise

To demonstrate the radiation of EGV noise a case with eight rotating blades and seven stationary vanes located one blade chord downstream is considered. The lowest angular mode excited at blade passage frequency is $M_\theta = 1$. Figure 6 shows the radiated directivity in this case for a subsonic rotor with $\eta = 0.8$. The radiated field is noted to oeak relatively near the axis of symmetry, characteristic of the well cut on $M_\theta = 1$ mode. The lev. 's in this case are much lower than the unshrouded propeller, but very much higher than the subsonic rotor alone case.

SUMMARY

Several important observations can be made. 1) Contrary to the usual understanding of the Tyler and Sofrin result [1], supersonic tip speed rotor noise can be cut off if the tip Mach number is only slightly in excess of unity and if the number of blades is relatively small. If there are many blades, the fundamental angular mode number is large, and the Tyler and Sofrin result for thin annuli becomes more relevant. 2) Shrouding of subsonic tip speed propellers is a very effective means of controlling rotor alone noise. 3) There appears to be no benefit in terms of the peak radiated SPL for shrouded supersonic propellers when the fundamental mode is propagating. 4) For shrouded subsonic rotors, EGV noise becomes the dominant source.

REFERENCES

1. Tyler, J. M. and Sofrin, T. G., "Axial Flow Compressor Noise Studies," Society of Automotive Engineers Transactions 70, pp. 309-332, 1962

2. Hanson, D.B., "Near Field Frequency Domain Theory of Propeller Noise," AIAA Paper 83-0688, 1983.

3. Gutin, L., "On the Sound Field of a Rotating Propeller," NACA TM 1195, 1948 (originally in Russian 1936).

4. Eversman, W. and Steck, J. E., "Finite Element Modeling of Acoustic Singularities with Application to Propeller Noise," Journal of Aircraft, Vol. 23, No. 4, April 1986, pp. 275-282.

5. Eversman, W. and Baumeister, K. J., "Modeling of Wind Tunnel Wall Effects on the Radiation Characteristics of Acoustic Sources," Journal of Aircraft, Vol. 23, No. 6, June 1986, pp. 455-463.

6. Baumeister, K. J. and Eversman, W., "Effects of Wind Tunnel Wall Absorption on Acoustic Radiation of Propellers," Journal of Propulsion and Power, Vol. 5, No. 1, January-February 1989, pp.56-63.

7. Eversman, W., "Analytical Study of Wind Tunnel Acoustic Testing of Propellers," Journal of Aircraft, Vol. 27, No. 10, October,1990, pp.851-858.

8. Eversman, W., Parrett, A. V., Preisser, J.S., and Silcox, R. J., "Contributions to the Finite Element Solution of the Fan Noise Radiation Problem," ASME Journal of Vibration, Acoustics, Stress, and Reliability in Design, Vol. 107, No. 2, February 1985, pp. 216-223.

9. Preisser, J. S., Silcox, R. H., Eversman, W. and Parrett, A. V., "A Flight Study of Tone Radiation Patterns Generated by Inlet Rods in a Small Turbofan Engine," Journal of Aircraft, Vol. 22, No. 1, January 1985, pp. 57-62.

10. Dommasch, D. O., Sherby, S. S. and Connally, T. F., Airplane Aerodynamics, Pitman, New York, 1967, pp. 219-233.

11. Vincent, E. T., The Theory and Design of Gas Turbines and Jet Engines, McGraw-Hill, New York, 1950, pp.324-335.
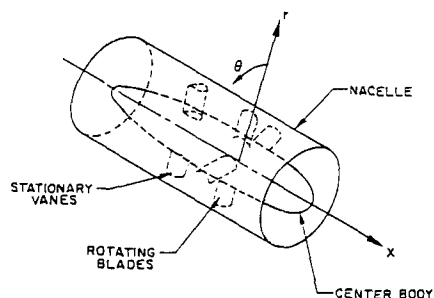
Figure 1. Geometry of Shrouded Propeller or Rotor.
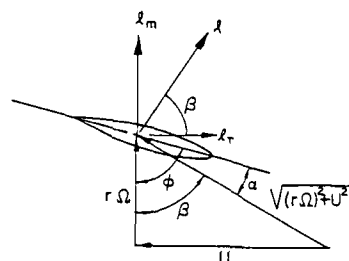
Figure 2. Velocities and Inflow Angles Experienced by a Blade Element.
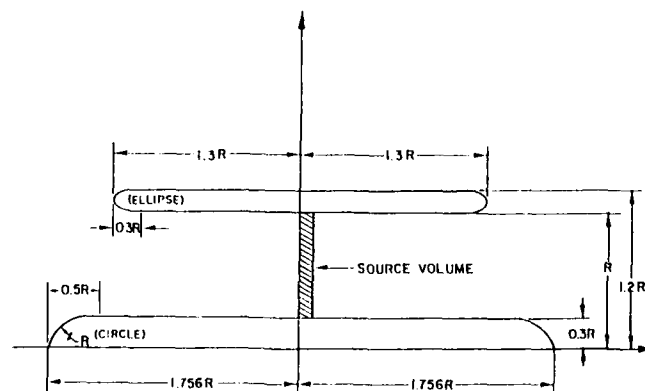
Figure 3. Idealized Shrouded Rotor for Example Cases.

SCALE LEVEL   120.14
FLOW MACH NO.   -0.40
INLET MACH NO.   -0.40
ANGULAR MODE NO.   4

POLAR SPL DIRECTIVITY
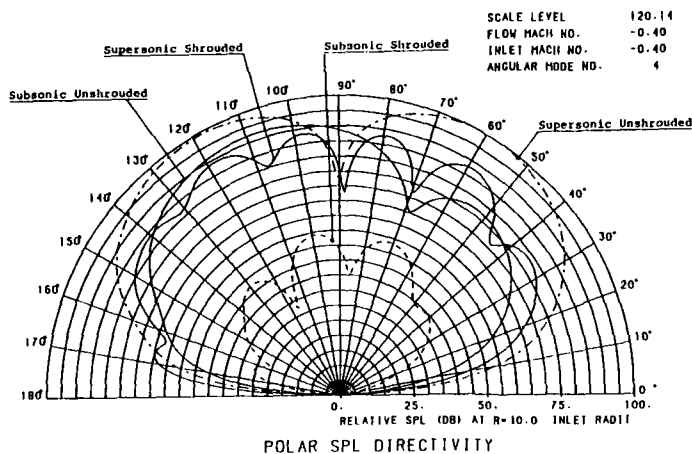
Figure 4. Radiated Acoustic Field for Four Blade Propeller, Rotor Alone.
Actual SPL is Relative SPL + 20.14 dB.

SCALE LEVEL   130.50
FLOW MACH NO.   -0.40
INLET MACH NO.   -0.40
ANGULAR MODE NO.   8

POLAR SPL DIRECTIVITY
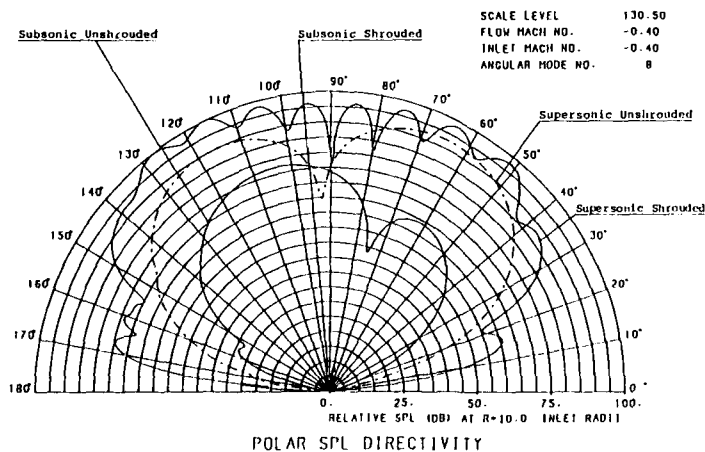
Figure 5. Radiated Acoustic for Eight Blade Propeller, Rotor Alone.
Actual SPL is Relative SPL + 30.5.

WAVE NO.   6.40
ANGULAR MODE NO.   1
SCALE LEVEL   101.15

POLAR SPL DIRECTIVITY
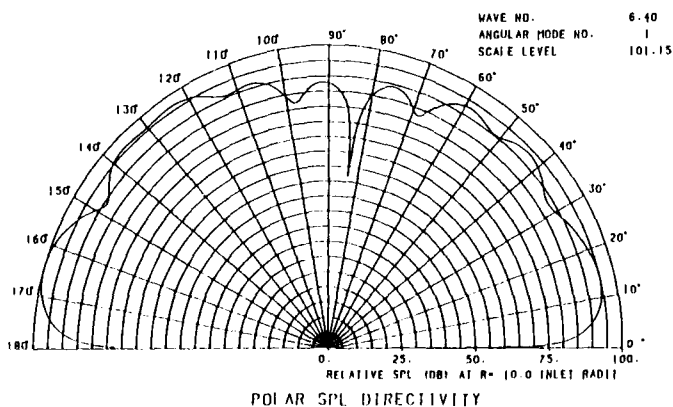
Figure 6. EGV Interaction Noise. Eight Blades, Seven Vanes, M_θ = 1.
Actual SPL is Relative SPL + 1.15.

128

SECOND INTERNATIONAL CONGRESS ON
RECENT DEVELOPMENTS IN AIR- AND
STRUCTURE-BORNE SOUND AND VIBRATION
MARCH 4-6, 1992 AUBURN UNIVERSITY, USA

NOISE AND VIBRATION ANALYSIS IN PROPELLER AIRCRAFT BY ADVANCED EXPERIMENTAL MODELING TECHNIQUES

Herman Van der Auweraer
Dirk Otte

LMS International
Interleuvenlaan 65
3001 Leuven - Belgium

ABSTRACT

Noise and vibration control measures in large structures such as aircraft need the development of a representative model of the complex vibro-acoustic system, built up by the fuselage, the trim panels and the cabin cavity. The complexity of such systems often results in a failure of the classical multiple degree-of-freedom parameter estimation techniques to obtain a consistent modal model.

This paper discusses some alternative experimental modelling techniques for such complex vibro-acoustic systems, based on singular value decomposition of a measured FRF-matrix. The physical significance of this orthogonal decomposition on the FRF-matrix is explored. Two related modeling concepts, Principal Field Shape Analysis and the U-vector Expansion Method (Impedance Modelling) are introduced. A case study on a twin propeller aircraft, featuring Principal Field Shape Analysis is presented and commented. Finally, issues to be investigated more thoroughly are mentioned and current research topics are outlined.

INTRODUCTION

Noise and vibration reduction measures in complex vibro-acoustic systems, such as aircraft, not only require a thorough understanding of the operating (in-flight) behaviour, but also demand the development of a representative model for the system.

In the case of an aircraft, the investigated structural-acoustical system, consisting of fuselage, trim panels and cabin cavity is very complex and is characterised by high damping values and high modal density, and consequently high modal coupling. In addition, the measured response fields resulting from forced excitation ground tests show a dominantly propagating nature, even around resonance. This is due to dissipation by damping and outside radiation and results in response location dependent phase shifts.

These factors make that the classical multiple degree-of-freedom modal parameter estimation techniques fail to obtain a consistent modal model, consisting of resonance frequencies, modeshapes and damping factors. The longitudinal shape and the strong coupling between the structure and the cabin cavity are other factors that jeopardise the success of a full scale modal analysis.

The application of Statistical Energy Analysis (SEA) might also not be appropriate, because the problem frequencies and modal overlapping are not high enough (e.g. propeller blade pass frequencies in a propeller aircraft), and because one is still interested in obtaining detailed characteristic acoustic field and structural deflection shapes.

This "twilight zone" between the Modal Analysis application area and the SEA application field is often referred to as the "mid-frequencies". Some recently introduced experimental modeling techniques are based on Singular Value Decomposition, which is an established robust and stable data reduction tool.

This conceptual paper discusses the Singular Value Decomposition on measured FRF-matrices as a basic technique for some experimental impedance modeling methods. The physical meaning of this

orthogonal decomposition is explored and its relation to the Complex Mode Indication Function (CMIF) is outlined. A more appropriate modeling method for complex vibro-acoustic systems, Principal Field Shape Analysis, is introduced. An example, concerning a twin-propeller aircraft is discussed. The U-vector Expansion Method, leading to a more global impedance modeling is presented as a logical extension of Principal Field Shape Analysis. Finally, some current research topics are outlined.

PRINCIPAL FIELD SHAPE ANALYSIS

Singular Value Decomposition of an FRF-matrix

Suppose a system, which is excited in N_{REF} degrees of freedom (DOFs), and of which the response is measured in N_{RSP} DOFs. All measured Frequency Response Functions (FRFs) then form a $(N_{RSP} \times N_{REF})$-matrix $[H(f)]$.

At each spectral line, one can perform a singular value decomposition of $[H(f)]$:

$$[H(f)] = [U(f)] \lceil S(f) \rfloor [V(f)]^H \tag{1}$$

($[..]^H$: complex conjugate transpose, Hermitian transpose)

$[U(f)]$ is a $(N_{RSP} \times N_{RSP})$ unitary matrix ($[U(f)]^H [U(f)] = \lceil I \rfloor$) of which the columns are the left singular vectors. $\lceil S(f) \rfloor$ is a $(N_{RSP} \times N_{REF})$ pseudo-diagonal matrix, with diagonal entries containing the singular values s_i in descending order. $[V(f)]$ is a $(N_{REF} \times N_{REF})$ unitary matrix, ($[V(f)]^H [V(f)] = \lceil I \rfloor$) containing in its columns the right singular vectors.

$[U(f)]$ is also often referred to as a $(N_{RSP} \times N_{REF})$ matrix, keeping the first N_{REF} columns. $\lceil S(f) \rfloor$ is then denoted as a square diagonal $(N_{REF} \times N_{REF})$ matrix.

The singular values are real and non-negative and per definition ...ɇ square roots of the eigenvalues of a normal matrix of $[H(f)]$. $[U(f)]$ and $[V(f)]$ are complex, both matrices are also obtained as eigenvector matrices by an eigenvalue decomposition of the resp. normal matrices $[H(f)] [H(f)]^H$ and $[H(f)]^H [H(f)]$.

$$[H(f)] [H(f)]^H = [U(f)] \lceil L(f) \rfloor [U(f)]^H \tag{2}$$

$$[H(f)]^H [H(f)] = [V(f)] \lceil L(f) \rfloor [V(f)]^H \tag{3}$$

$\lceil L(f) \rfloor$ contains the eigenvalues l_i in descending order.

$$l_i(f) = s_i^2(f) \tag{4}$$

Some remarks about the complex elements of the singular vectors need to be made. The Hermitian matrix $[H(f)] [H(f)]^H$ can be written as:

$$[H(f)] [H(f)]^H = [A] + j[B] \tag{5}$$

The eigenvalue decomposition of the symmetric matrix $\begin{bmatrix} [A] & -[B] \\ [B] & [A] \end{bmatrix}$ ($[A]$ symmetric, $[B]$ antisymmetric) results in a set of double eigenvalues, corresponding with couples of orthogonal eigenvectors $\begin{Bmatrix} -\{U_{bi}\} \\ \{U_{ai}\} \end{Bmatrix}$ and $\begin{Bmatrix} \{U_{ai}\} \\ \{U_{bi}\} \end{Bmatrix}$. These two eigenvector correspond to one complex eigenvector, indeed,

130

$$({U_{Ai}} + j{U_{Bi}}) \cdot j = -{U_{Bi}} + j{U_{Ai}} \tag{6}$$

This means that the eigenvectors are determined only up to a factor $e^{j\theta} = \cos\theta + j\sin\theta$. The same reasoning can be followed for $[V(f)]$. However, when the phase of a singular vector ${U_i}$ is chosen, ${V_i}$ is completely defined.

The U-vectors, multiplied by the corresponding singular values, form a $(N_{RSP} \times N_{REF})$ matrix $[H'(f)] = [U(f)] \lceil S(f) \rfloor$, they can be considered as the FRF-matrix referring to a set of virtual or principal inputs, related to the physical references by the unitary transformation matrix $[V(f)]$.

$$[H(f)] = [H'(f)] [V(f)]^H \tag{7}$$

Alternatively, one can consider $[U(f)]$ as a unitary transformation matrix to a set of N_{REF} virtual or principal responses:

$$[H(f)] = [U(f)] [H'(f)] \tag{8}$$

with $[H'(f)] = \lceil S(f) \rfloor [V(f)]^H$.

The singular value decomposition of $[H(f)]$ also offers some data reduction possibilities. At a specific frequency, one can assume that the response of the structure is dominated by a finite number of modes. A number N_{RNK} modes will be dominant and will describe the column space of $[H(f)]$. As the number of singular values different from zero, (or, in practice, larger than a certain threshold) denotes the rank of the matrix, it also denotes the dimension of the column space (and of the row space) of $[H(f)]$. Consequently, the number of effective modes at frequency f, controllable at the reference DOFs, is revealed by the number of significant singular values.

The FRF-matrix can then be approximated, taking into account a limited set of significant singular values and corresponding singular vectors.

$$[H(f)] \approx [U(f)]_{RNK} \lceil S(f) \rfloor_{RNK} [V(f)]^H_{RNK} \tag{9}$$

The first N_{RNK} U-vectors are linear combinations of the (unknown) mode vectors.

In the following, it will be implicitly assumed that this data reduction is performed and that the smallest dimension of the concerned matrices is N_{RNK}.

Complex Mode Indication Function (CMIF)
The SVD of the FRF-matrix at each spectral line may form the basis of modal parameter estimation and is then referred to as the Complex Mode Indication Function (CMIF) [1]. The CMIFs are defined as the squares of the singular values of the FRF-matrix.

$$CMIF_k(f) = s_k^2(f) = l_k(f) \tag{10}$$

$$(k = 1, 2, ..., N_{RNK})$$

where $CMIF_k(f)$ is the k-th CMIF at frequency f. In practical calculations, as the number of responses might largely exceed the number of inputs, the $(N_{REF} \times N_{REF})$ normal matrix $[H(f)]^H [H(f)]$ is calculated at and its eigenvalue decomposition performed, with much less memory requirements. The CMIF plot is the plot of these eigenvalues on a log magnitude scale as a function of frequency.

131

For lowly damped structures and frequency bands that allow clear distinction of resonance frequencies, the peaks of $CMIF(f)$ indicate the existence of modes and the corresponding damped natural frequencies. More peaks at one frequency reveal repeated modes. The left singular vectors $\{U_i(f_p)\}$ at these frequencies f_p denote the unscaled modeshapes and the right singular vectors $\{V_i(f_p)\}$ the modal participation vectors. In order to estimate accurate damped natural frequencies and damping factors, single DOF parameter estimation methods can be applied to enhanced FRFs for each mode. The enhanced FRF $\hat{h}(f)$ for the k-th repeated mode at f_p is defined as

$$\hat{h}(f) = \{U_k(f_p)\}^H [H(f)] \{V(f_p)\} \tag{11}$$

The above considerations implicitly assume a mass matrix to be identity. In practical cases however, as the modeshapes and modal participation vectors are only orthogonal w.r.t. the mass matrix, the FRF-matrix need to be weighted by some estimation of the mass matrix, resp. the reduced mass matrix, in order to cope with the fact that mode shapes are orthogonal to the mass matrix. Only in that case, the singular vectors will coincide with the modes, resp. modal participation vectors.

$$[H(f)]_{WGT} = [M_\phi]^{1/2} [H(f)] [M_L]^{1/2} \tag{12}$$

$[H(f)]_{WGT}$ is the weighted ($N_{RSP} \times N_{REF}$) FRF matrix; $[M_\phi]$ is the mass matrix of size ($N_{RSP} \times N_{RSP}$); M_L is the ($N_{REF} \times N_{REF}$) reduced mass matrix. The a priori estimation of these mass matrices is certainly a weak point of the CMIF parameter estimation method.

Principal Field Shapes

When dealing with the kind of complex systems mentioned in the introduction, the singular values of the unweighted FRF-matrix will not clearly reflect the existence of damped natural frequencies. The high damping and modal overlapping and the fact of not taking into account an unknown mass matrix make that the U-vectors related to the CMIF-peaks (if peaks are distinguishable at all) generally are complex linear combinations of several hidden normal modes. The corresponding enhanced FRFs also would show different peaks, not allowing for proper resonance frequency and damping factor estimations.

Principal field shape analysis only makes use of the left singular vectors as such, weighted by the corresponding singular values: the principal field shapes are defined as the first N_{RNK} vectors $\{U_i(f) \cdot s_i(f)\}$. The principal field shapes correspond in fact to the columns of the ($N_{RSP} \times N_{RNK}$) FRF-matrix $[H'(f)]$. The first principal inputs relate to the dominant singular values and correspond to the responses with maximum amplitude.

$$[H'(f)] = [U(f)] \lceil S(f) \rfloor \tag{13}$$

Hence, $[H'(f)]$ is related to the original FRF-matrix by a unitary coordinate transformation $[V(f)]$ (Equation 7).

If the U-vectors must describe the whole system response vector space at a given frequency, all system modes should be controllable by the chosen set of input locations. This means that no mode vector should be orthogonal to the vector space formed by the reference DOFs. Practically, this condition means that, for structural excitation, at least one shaker should not be positioned in a node of a mode. Also, the number of references must exceed the number of active modes at each frequency. This condition is also posed for classic multiple reference modal analysis testing.

If not all system modes can be controlled via the chosen reference DOFs, one only obtains a partial model, valid for the chosen excitation locations. In that case one should try to represent the operating conditions as close as possible, so that at least these system modes, contributing in operating conditions, can be excited. As for a twin-propeller aircraft, the primary in-flight condition is direct airborne sound radiation from the propellers, leading to a distributed force field at the fuselage exterior, excitation of the fuselage near the propeller plane is to be preferred.

Anyhow, even if all system modes can be addressed, the calculated U-vectors will be dependent on the choice of reference DOFs. Different reference DOF configurations may lead to a U-vector set describing the same response space, but the principal direction vectors generally will be different. This means the principal field shapes for a certain set of references are not a property of the system, but only a way, between others, to describe the system.

The excited system, say A (e.g. the aircraft fuselage, described by acceleration signals) may be coupled to another system B (e.g. the cabin cavity, described by acoustic pressure signals), the latter being described by an FRF-matrix $[H_B(f)]$. The columns of that FRF-matrix also refer to the same references of the excited system A. Consequently, the coordinate transformation $[V(f)]^H$ can be applied to $[H_B(f)]$. The coupled system responses can then be described in a similar way by the column vector set of $[H'_B(f)]$, referring to the principal references of system A. These field shapes are directly related to the principal field shapes of the excited structure and allow an understanding of the coupling between both systems.

$$[H_B(f)] \quad = \quad [H'_B(f)] \, [V(f)]^H \qquad\qquad (14)$$

Again, only a partial model is obtained: only the subspace of B containing the modes that are controllable by the used references in A is spanned by $[H'_B(f)]$.

A singular value decomposition of the complete FRF-matrix, containing the responses of both coupled systems is also possible. In that case, the issue of correctly scaling different types of DOFs, such as accelerations or velocities and sound pressures, may rise, as this directly affects the resulting U-vectors and singular values. This issue is currently being investigated.

Case Study

A fully trimmed Saab 340 aircraft was instrumented with accelerometers on a number of fuselage frames and with microphones in several cabin cavity sections. In total, 276 structural DOFs on the fuselage and 208 acoustical DOFs were measured. Different excitation configurations, structural as well as acoustical (by loudspeakers inside the aircraft) were tried out. In this paper, structural excitation by 6 shakers on one fuselage frame section is discussed.

Fig. 1 shows the singular values of the FRF-matrix as a function of frequency, between 70 and 120 Hz. Estimating the number of dominant singular values, and hence the number of effective modes, is not obvious; neither is the determination of resonance frequencies. Fig. 2 represents the first principal field and clearly shows which frame was excited. It is revealed that, due to the high damping, the fuselage response shows a forced nature. Except for their amplitude, the individual frame responses are similar, but shifted in phase, which jeopardises the success of any modal parameter fitting method.

Further analysis was focused on the first two principal deflection shapes of the excited frame and the corresponding acoustic field shapes in two neighbouring cabin sections. Two frequencies were selected: 102.5 Hz, where the first singular value slightly peaks, and 85 Hz, which is the first bladepass frequency in normal flight conditions. To visualise the acoustic fields, the microphone grids were presented as wireframes, and the pressures were visualised as vectors, orthogonal to the sections. This allows for an animated display of the response field, making it possible to interpret the amplitude/phase information as sound field shapes or (combinations of) acoustic modes. Fig. 3 shows the 102.5 Hz results (A-structural, B-cavity), whereas Fig. 4 shows the 85 Hz results. In both figures, the left part represents the first principal shape, the right part the second principal shape.

At 102.5 Hz, some real modes of the fuselage frame are recognised, each one clearly coupled to specific acoustic field shapes (Fig.3). The second deflection shape shows at earheight out of phase vibrations at each side, favouring an acoustic side-side mode. At the first field shape, these sides vibrate in phase and rather favourise longitudinal modes; the top of the frame however moves out of phase and corresponds with a coupled acoustic top-down mode.

At 85 Hz, the more forced (one side dominant) and complex (not monophase; less clear modes) deflection shapes of the excited frame again correspond well with the coupled acoustic behaviour. (Fig.4)

133

U-VECTOR EXPANSION METHOD

The singular value decomposition of the FRF-matrix also forms the first step in the procedure of obtaining an impedance model of the total system, based on U-vector expansion [2].

Based on reciprocity considerations and reduced rank assumptions of the FRF-matrix, the orthogonal U-vector set, which in fact describes the dynamic behaviour of a subset of the total dynamic system, is used to estimate the characteristics of the whole system. Basically, the method consists of a reconstruction of a full square FRF-matrix, based on the measured submatrix.

A full ($N_{RSP} \times N_{RSP}$) FRF-matrix can be decomposed as follows:

$$[H(f)]_{FULL} = [\Psi] \lceil \Lambda(f) \rfloor [\Psi]^T \qquad (15)$$

where $[\Psi]$ is an ($N_{RSP} \times N_{RNK}$) matrix containing in its columns the mode shapes, independent (only orthogonal w.r.t. the mass matrix) contributing in the frequency range of interest. These modeshapes are independent of frequency and span the vector space of the system responses. $\lceil \Lambda(f) \rfloor$ is a frequency-dependent ($N_{RNK} \times N_{RNK}$) diagonal matrix based on the system eigenvalues (resonance frequencies and damping values).

As $[H(f)]_{FULL}$ is assumed symmetrical, it can also be decomposed using the previously calculated U-vectors, obtained by SVD of the ($N_{RSP} \times N_{REF}$) submatrix $[H(f)]$.

$$[H(f)]_{FULL} = [U(f)] [H''(f)] [U(f)]^T \qquad (16)$$

$[H''(f)]$ is a ($N_{RNK} \times N_{RNK}$) (N_{RNK} depending on the number of significant singular values in $[H(f)]$) square matrix, generally not diagonal. In order for Equation (16) to be (approximately) correct, the U-vectors should also span the total system response space, or, N_{RNK} needs to be the rank of $[H(f)]$ as well as of $[H(f)]_{FULL}$. This means that the vectors of $[U(f)]$ not only span the column space of $[H(f)]$ but also the column space of $[H(f)]_{FULL}$. If all system modes, active at frequency f, are present in the measured FRF-matrix, which means that they can all be excited, are controllable, all column vectors of the full FRF-matrix should still belong to that space. $[H''(f)]$ can be estimated starting from:

$$[H(f)] = [U(f)] [H''(f)] [\overline{U}(f)]^T \qquad (17)$$

$[\overline{U}(f)]$ is the matrix formed by the ($N_{REF} \times N_{RNK}$) elements of $[U(f)]$, related to the excitation DOFs. It should be noted that this matrix is not unitary, its columns are not orthogonal and might even be dependent. The column vectors of $[\overline{U}(f)]$ are the projections of the U-vectors in the N_{RNK}-dimensional space, defined by the right singular vector basis $[V(f)]$.

$[H''(f)]$ can then be computed as follows:

$$[H''(f)] = [U(f)]^H [H(f)] ([\overline{U}(f)]^T)^{-1} \qquad (18)$$

or also,

$$[H''(f)] = \lceil S(f) \rfloor [V(f)]^H ([\overline{U}(f)]^T)^{-1} \qquad (19)$$

An important issue is the inversion of the truncated matrix $[\overline{U}(f)]$. Indeed, this matrix isn't unitary anymore and may be rectangular. Possibly, a pseudo-inverse solution could be envisaged here. This can be done by a singular value decomposition of $[\overline{U}(f)]$:

$$[\overline{U}(f)] = [U(f)]_U \lceil S(f) \rfloor_U [V(f)]_U^H \qquad (20)$$

Because of the singular vector matrices are unitary and the singular values matrix is diagonal, the pseudo-inverse of $[\overline{U}(f)]$ can be written as:

$$[\overline{U}(f)]^+ = [V(f)]_U \lceil S(f) \rfloor_U^{-1} [U(f)]_U^H \qquad (21)$$

As the vectors of $[\overline{U}(f)]$ describe the same vector space as $[V(f)]$, it can be expected that all N_{RNK} singular values of $[\overline{U}(f)]$ are significant.

A new singular value decomposition on this matrix would give the global U-vector or principal field shape set, which in case of a mass matrix proportional to the identity matrix, would be proportional to the mode vectors. The number of non-zero singular values would evidently be N_{RNK}.

CONCLUSIONS AND CURRENT RESEARCH TOPICS

Principal Field Analysis and U-Vector Expansion are currently subject to a feasibility study. Several issues still need to be studied more thoroughly.

In order to obtain a global vibro-acoustic impedance model based on U-vector expansion, including all coupled systems, not only the scaling of the different responses, but also fulfilling the reciprocity requirement for vibro-acoustic and acoustic-vibration FRFs (quantities for the acoustic inputs) need to be investigated more thoroughly. Vibro-acoustic reciprocity was recently discussed by Fahy [3].

In order to cancel out measurement errors due to frequency shifts and data inconsistencies over a certain frequency band, methods are currently developed that globally describe the "average" dynamic behaviour in that frequency band (which may contain several resonance frequencies)[4] [5]. The information of a number of frequency lines may be reduced to one "averaged" FRF-matrix. One then obtains a principal field shape set, representing the dynamic behaviour in that frequency range. A feasibility study on linking this method to the U-vector expansion method is currently on-going.

REFERENCES

1. SHIH, C.Y., TSUEI, Y.G., ALLEMANG, R.J., BROWN, D.L., *Complex Mode Indication Function and Its Application to Spatial Domain Parameter Estimation*, Mechanical Systems and Signal Processing, Vol. 2, Nr. 4, pp. 367-377, 1988.

2. W.G. HALVORSEN, P.S. BARNEY, D.L. BROWN, *Developing Impedance-Type Models of Structural/Acoustic Systems* Sound and Vibration, Aug. 1991, pp.18-26.

3. FAHY, F.J., *The Reciprocity Principle and Applications in Vibro-Acoustics* Presented at the 9th FASE Symposium on New Acoustical Measurement Methods, Balatonfured, Hungary, 7-9 May, 1991.

4. LEURIDAN, J., DE VIS, D., GRANGIER, H., AQUILINA, R. *Coupling of Structures Using Measured FRFs: Some Improved Techniques* Proc. 13th Int. Seminar on Modal Analys Leuven, Belgium, 1988, 19 pp.

5. OTTE, D., LEURIDAN, J., GRANGIER, H., AQUILINA, R. *Prediction of the Dynamics of Structural Assemblies Using Measured FRF-data: Some Improved Data Enhancement Techniques* Proc. 9-th Int. Modal Analysis Conference, Florence, Italy, 1991, pp.909-918.
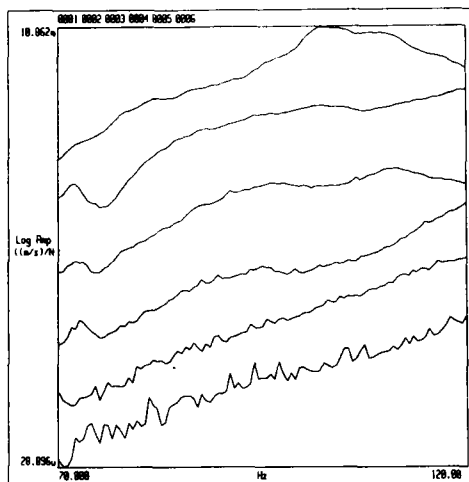
Figure 1 : Singular Values (70 - 120 Hz)

Figure 2 : First Principal Field (Structure), 102.5 Hz

Figure 3A : First (L) and Second (R) Field Shape (Structure), 102.5 Hz

Figure 3B : First (L) and Second (R) Field Shape (Cavity), 102.5 Hz

Figure 4A : First (L) and Second (R) Field Shape (Structure), 85 Hz
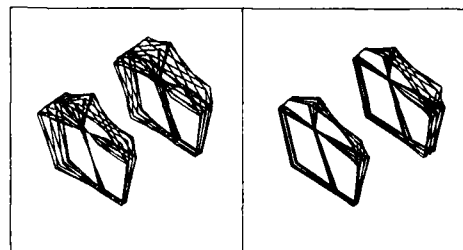
Figure 4B : First (L) and Second (R) Field Shape (Cavity), 85 Hz

AERODYNAMIC NOISE GENERATED BY CASCADED AIRFOILS

Gerald C. Lauchle and Lori Ann Perry
Penn State University
Applied Research Laboratory and
Graduate Program in Acoustics
P.O. Box 30
State College, PA 16804 U.S.A.

ABSTRACT

Louvers are routinely used in heating, ventilation and air conditioning (HVAC) systems to direct exit airflow in preferred directions. Fundamentally, a louver system is a cascade of small airfoils all operating at a common angle of attack. The noise radiated from such a cascade is more complicated than simply the sum of the emissions from N independent airfoils, where N is the number of foils in the cascade. The complication arises because of blade-to-blade interactions and increasing blockage (solidity) as N gets large. Indeed the turbulence structure over the individual blades may be altered as the solidity increases which can have an effect on the aerodynamic noise produced. In this study, these fundamental issues are addressed experimentally. A typical, small, plastic louver vent (register) used in automotive HVAC applications is considered. Sound pressure level data are acquired 45° off the exit centerline in an anechoic environment when air is supplied to the louver from a remote quiet airflow source. Flow velocity, angle of attack, and N are the primary independent variables in these experiments from which velocity and solidity scaling laws are being developed.

INTRODUCTION

A louver is oftentimes placed at the exit of a heating, ventilation and air conditioning (HVAC) system to cover the opening, to act as a finger or hand guard, and to provide directional control of the exit airflow. The louver is basically a cascade of small airfoils each operated at a common angle of attack. Airfoils operated under steady and nonsteady (as well as uniform and nonuniform) inflow conditions create noise because of several different mechanisms. These mechanisms relate to the character of the flow - laminar, turbulent, or separated; to the geometry of the leading and trailing edges - sharp or blunt; and to the angle of attack which, essentially, influences the type of flow over the surface. Under subsonic conditions, turbulence in the inflow, wake, or turbulent boundary layer creates relatively inefficient quadrupole radiation. However, as the turbulence interacts with the leading or trailing edges of an airfoil, non-acoustic wavenumber components of the turbulent pressure fluctuations get scattered into more efficient dipole radiators [1-3]. In many applications it is the trailing edge that is responsible for most of the noise radiation from small airfoils at low flow velocities.

The Reynolds number based on airfoil chord length, C and free-stream velocity, U is defined by UC/ν, where ν is the kinematic viscosity of air. If the Reynolds number is smaller than about 2×10^5, then the flow entering the trailing edge (TE) region will be laminar. The noise from the TE will be tonal

in nature due to a Helmholtz instability in the periodic wake vorticity. The frequency of the radiation will scale as a Strouhal number, $f\ell/U$ = constant, where ℓ is typically the boundary layer thickness, δ for sharp trailing edges; or h, the TE thickness for blunt terminations. As the angle of attack increases, local flow separation will occur on the airfoil and the tonal nature of the radiation disappears and the sound becomes broadband in character. For high Reynolds numbers, the boundary layer transitions from laminar-to-turbulent on the surface of the foil. Then TE noise is governed by the scattering of the turbulent boundary layer (TBL) pressure fluctuations by the edge discontinuity. For sharp or blunt edge shapes, the spectrum of radiation is continuous. For some combinations of TBL thickness and TE bluntness, a broadband "hump" of energy sometimes appears in the noise spectrum and can be related to random vortices being shed from the edge which form a quasi-random wake structure. These bands of energy scale, usually, on the thickness of the near wake.

In the study reported here, a small louver vent used in automotive HVAC applications is considered. The study is experimental with a primary goal of determining the spectrum of radiated sound under various independent operating conditions (velocity, angle of attack, and number of blades, N) and relating these data to the physical aeroacoustic mechanisms expected. For those aerodynamic mechanisms identified, efforts are devoted to modification of the device to alter the fluid mechanics and hopefully reduce the noise radiation. Because the louver is a set of several small airfoils, the experimental methodology includes measuring the noise from individual foils and components in order to establish the hierarchy of noise sources. The results presented here are preliminary in that the project continues at this writing. The interpretations and conclusions are based on only one angle of attack, zero degrees; acoustic data for other angles will be presented at a later time.

EXPERIMENTAL APPARATUS AND PROCEDURES

Figure 1 shows photographs of the louver vent under consideration. In the Fig. 1a view, the flow is from left to right. This louver is designed to fit into a 9.5 cm orifice. A tie rod connects the four airfoils together so that they can pivot together through common angles. When closed (90° angle of attack), each blade nests within steps molded into each blade. Thus, the flow surfaces have pronounced discontinuities as sketched in Fig. 3. As seen, the boundary layer formed over the blade is prone to separation induced by a forward (FWD) facing step on the bottom, and a backward (BWD) facing step on the top side. The highest flow velocity considered is 16.2 m/s, and the chord is only 27 mm, so the maximum chord Reynolds number is 2900; the boundary layer is laminar before it reaches the steps.

Airflow is supplied by a 20 HP centrifugal blower situated outside a large anechoic chamber and contained within a sound isolation box. The inlet to the blower is acoustically treated by use of a commercial muffler. As sketched in Fig. 4, a flexible air hose connects the air source to another plenum box inside the anechoic chamber. This plenum eliminates all turbulence in the approach stream (due to its large volume) and provides acoustically-treated baffles to attenuate the air source noise. The anechoic chamber [4] is reflection free down to 70 Hz and is equipped with a portable wire mesh floor to support the test apparatus. At the exit of the plenum box, investigators have the option of placing the louver vent directly within the opening (circular orifice), or adding pipe and turbulence screens for the study of turbulence ingestion noise. For this presentation, the louver was placed directly within the plenum exit orifice without the optional piping and turbulence generators. The air source is controlled by a three-phase invertor, so the flow velocity can be set to any desired value between 4.8 and 34 m/s.

Velocity is measured with a Pitot-static pressure probe. Particular volume flow rates were required in the tests and these were established from probe scans across the open jet orifice without the louver. When the louver is placed in the orifice, flow velocities necessarily increase at constant airflow due to the blockage created by the louver blades. Thus, presented data for the open jet alone will show a lower test velocity than those data acquired when the louver is in the flow path. Velocities for the louver in place, were measured between the two center louver blades.

Sound pressure level data were acquired with a 1/2-inch B&K microphone (Type 4133) situated 45° off the centerline of the exit jet and at 1 meter from the plane of the orifice. Amplification was achieved from an Ortec Differential AC Amplifier (Type 9454). Acoustic data acquisition was performed using a Zonic System 7000 8-channel parallel signal processor. A VAX Station 3100 computer controls the processor and performs the spectral computations. Data were taken at a 12.8 kHz sampling rate which provides spectral estimates up to 5 kHz. A Hanning window was used for spectral smoothing, 256 ensembles were used in spectral averaging, and the effective analysis bandwidth is 6.25 Hz.

RESULTS AND DISCUSSION

The measured overall sound pressure level as a function of airflow velocity for three different configurations is shown in Fig. 4. The open jet data suggest classical jet noise which is composed of acoustically compact quadrupoles; the mean-square acoustic pressure increases with the eighth power of flow velocity [5]. When the louver housing containing only one of the center blades is placed in the exit orifice of the plenum box, the acoustic pressure depends on the sixth power of flow velocity which is expected for the dipole source mechanisms of TE flow. The same acoustic mechanism exists when all blades are in the louver as indicated by the "plus-circle" data points of Fig. 4. The louver in this particular data set was modified by removal of the tie rod and the individual blades were filled with body putty and sanded smooth as to eliminate the FWD and BWD facing steps. Other data obtained before the blade modification also show a sixth power law dependence on velocity.

Power spectra of the radiated acoustic pressure are shown in Fig. 5 for the housing of the louver vent without blades. Within one or two dB, these spectra are identical to those measured for the circular orifice without the housing. The large energy band at very low frequencies is velocity dependent (eighth power law) and is basically jet induced. As will be shown in the following results, this band of energy persists in the measured spectra regardless of the number or geometry of blades installed in the housing.

When all four blades are in the louver vent housing (stock configuration), noise increases occur at all frequencies above 500 Hz, Fig. 6. The effect of removing blades, one at a time, is demonstrated in Fig. 7 for the maximum velocity considered. Systematic decreases in sound pressure levels are observed for most of the spectral range as blades are eliminated, but a pronounced narrow-band component appears in the 3500 Hz range which is related to the bottom blade of the vent. A closer examination of the noise radiated by this bottom blade is given in Fig. 8. Inspection of the blade (see Fig. 1) reveals a "thumb tread" molded onto the blade surface which appears as periodically-spaced set of six ridges. The height, h of these ridges is 0.5 mm and Strouhal scaling using this height causes the velocity-dependent peaks of Fig. 8 to collapse to a common Strouhal number of $S = fh/U = 0.12$. The ridges are spaced at $L = 3$ mm, and using this length scale, $S = 0.72$. The ridges were removed from the blade and the acoustic measurements repeated. Figure 9 shows the spectral results and it is clear that the thumb tread was responsible for the narrow-band energy observed in the previous figure. This narrow-band energy does not appear in the as-designed stock louver runs of Fig. 7. A definite reason has yet to be proven, but blade-to-blade interaction mechanisms are believed to be the underlying physics. When there is a blade operating adjacent to the one with the thumb tread, the thumb tread-induced tone is suppressed. The interaction probably destroys the vortices shed from the ridges which cause tonal radiation.

The rearward and forward facing steps on the individual louver blades are responsible for a considerable portion of the high-frequency radiated sound. This can be demonstrated by comparing Fig. 10 with Fig. 6, where the data of Fig. 10 were obtained for a louver vent in which the steps were filled in with body putty and sanded smooth. Noise reductions above 500 Hz are in the 3 to 6 dB range.

CONCLUSIONS

A systematic investigation is underway to identify the mechanisms of aerodynamic sound generation from small subsonic airfoils operated in cascade, and to use this diagnostic information to modify the designs for noise reduction. Examples of our findings have been presented here and initial conclusions are as follows·

- When individual blades are added one-at-a-time to make up a louver vent, the noise increases in proportion to the number of blades to a point where blade-to-blade interaction may alter the aerodynamics of a given blade and the noise character may change.

- Rearward and forward facing steps molded into individual blades are predominant sources of radiated sound. By removing them, 3 to 6 dB noise reduction may occur.

- A circular louver housing without blades radiates predominantly quadrupole sound which obeys an eighth power dependence on flow velocity.

- The small airfoils mounted in the louver housing radiate more intensely than the jet alone owing to the dipole mechanisms of flow over surfaces with free edges. A sixth power dependence of this dipole noise on flow velocity was found. The steps that are present on these blades also behave as dipole sources of sound because the power law dependence does not change with blade surface modification.

ACKNOWLEDGEMENTS

REFERENCES

1. Ffowcs Williams, J. E. and Hall, L. H. Aerodynamic Sound Generation by Turbulent Flow in the Vicinity of a Scattering Half-Plane. J. Fluid Mech. 40, 1970, pp. 657-670.

2. Howe, M. S. A Review of Trailing Edge Noise. J. Sound Vib. 61, 1978, pp. 437-465.

3. Blake, W. K. and Gershfeld, J. L. The Aeroacoustics of Trailing Edges. Lecture Notes in Engineering. Frontiers in Experimental Fluid Mechanics (Gad-el-Hak, M., ed.), Springer-Verlag, Berlin, 46, 1989, pp. 457-532.

4. Marhoe, R. C., Lauchle, G. C. and Kargus, W. A. Quiet Wall Jet Facility for Basic Aero/Hydroacoustics Research. ASME Book NCA Vol. 10 (Farabee, T. M. and Arndt, R. E. A., eds.), 1991, pp. 69-73.

5. Lighthill, M. J. Sound Generated Aerodynamically. II Turbulence as a Source of Sound. Proc. Roy. Soc. A 222, 1952, pp. 1-32.
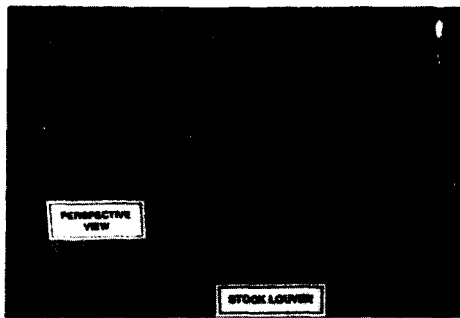
Figure 1--Photograph of louver vent investigated, a) front view;
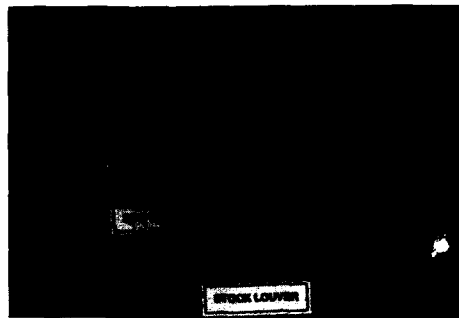
b) side view
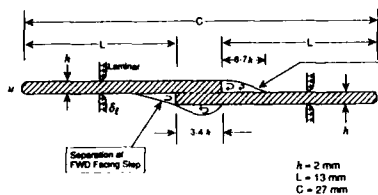
Figure 2--Cross-sectional view of a typical louver blade in unit evaluated
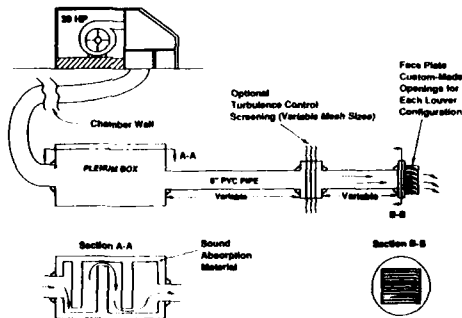
Figure 3--Louver noise experimental setup
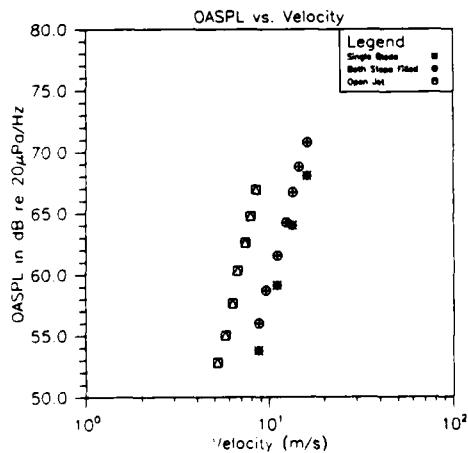
Figure 4--Dependence of overall sound pressure level on flow velocity
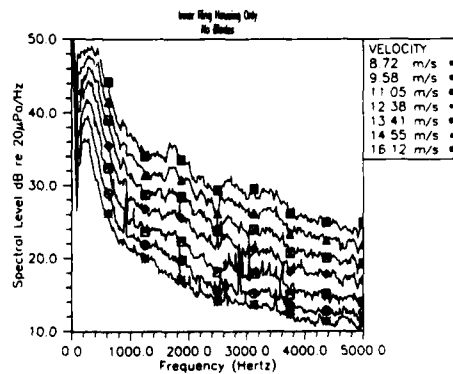
Figure 5--Power spectra of the sound pressure for the orifice jet with louver ring housing

141
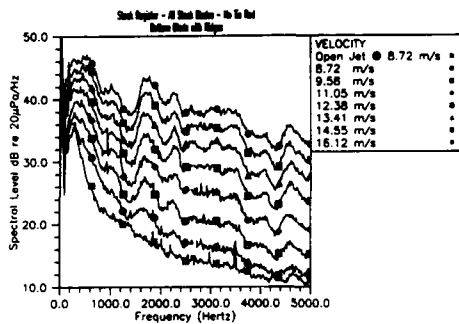
Figure 6--Power spectra of the sound
pressure for the as-designed stock louver
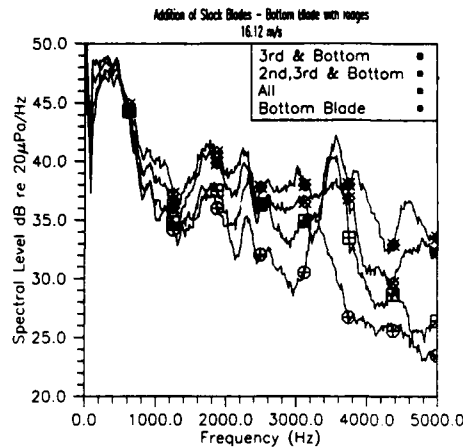
Figure 7--Power spectra of the sound
pressure for individual and multiple
blades in the louver
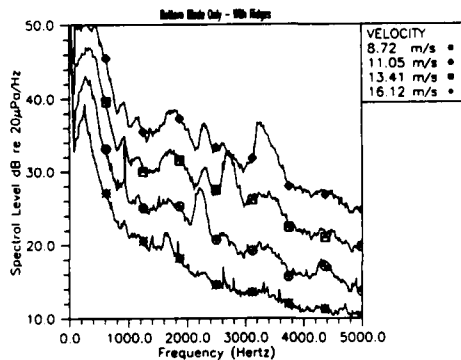
Figure 8--Power spectra of the sound
pressure for the bottom blade only with
thumb tread ridges in place
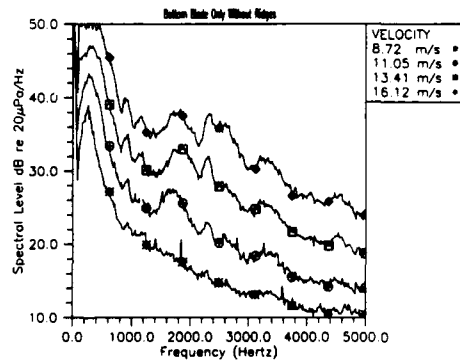
Figure 9--Power spectra of the sound
pressure for the bottom blade only with
thumb tread ridges removed
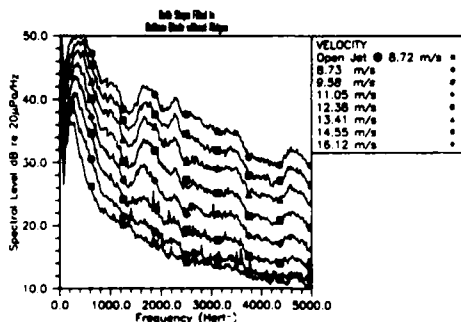
Figure 10--Power spectra of the sound
pressure for the register vent when the
steps on all blades are filled and smoothed

142

VIBRATION ISOLATION OF AVIATION POWER PLANTS
TAKING INTO ACCOUNT
REAL DYNAMIK CHARACTERISTICS OF ENGINE AND AIRCRAFT

V.S.Baklanov,V.M.Vul
A.N.Tupolev Aviation Science and Technical Complex
Moskow
RSFSR

ABSTRACT

Multiple connection structural system "engine-mount-airframe" is considered
and choice strategy for vibration isolation devices is presented,taking into ac-
count real dynamic characteristics of engines and airframe in attachment points.
In the present paper results of extensive experimental studies of various
engines and aircraft bodies dynamic compliances are generalized, as well as these
of airframe acoustic response functions calculated by the impedance testing tech-
nique in 10...1000 Hz frequency range.
As an exemple we consider the improved D30-KU engine vibration isolating attach-
ment on the TU-154M aircraft.

INTRODUCTION

Acoustic comfort in flight and passenger compartments is achieved through
the matching of frequency-dependent characteristics of engine and aircraft bodies;
this is of special importance when multi-shaft turbine engines are used on aircrafts.
To satisfy the requirements of vibration and acoustic comfort in the flight
and passenger compartments of modern aircrafts expected levels of noise and vibra-
tion from main sources are to be known by the design stage.
One of the main aircraft noise and vibration sources is its power plant.
The present paper deals with the structure-borne noise due to the reemission
by the structure components-sush as fuselage casing excited by the engine vibra-
tion action in attachment points.

TRANSMISSION MODEL

Using the multiple connection mathematical model "engine-moint-airframe" with
generalizad dynamic characteristics (mechanical impedance etc.) in attachment po-
ints,the equation is obtained to estimate the level of engine power dynamic act
ion on the airframe [1]:

$$\left\{ R_E \right\} = \left(\left[C_{EM} \right] + \left[C_{AM} \right] \right)^{-1} \cdot \left[C_{ES} \right] \left\{ F_S \right\} , \qquad (1)$$

where $\left[C_{EM} \right], \left[C_{AM} \right]$ are square matrices of dynamic compliances of respectively engine and airframe mount structures in attachment points;
$\left[C_{ES} \right]$ is the matrix of engine structure transferred compliances from excitation forces application points to attachment ones; $\left\{ F_S \right\}$ is the matrix-column of excitation forces in engine components.

Using real engine and airframe compliance data obtained experimentally [2] the coupled motion limits in the "engine-mount-airframe" structural system were studied anda possibility to produce a one-dimensional mathematical model for each attacment point was examined.

The analysis of obtained characteristics had shown considerable variation of dynamic compliances (input and transferred) ratios in the excitation frequency range (see Fig.1).

Taking into account these dependencies the possibility to neglect transferred compliances may be examined through comparison of matrix rates of the following type [3]:

$$N = \sqrt{\sum_{i,j=1}^{m} |C^{ij}|^2} , \qquad N^* = \sqrt{\sum_{i=1}^{m} |C^{ii}|^2} , \qquad (2)$$

where N and N^* are euclidian rates of full and diagonal matrices of the structure, respectively.

Then the variable $\alpha = \frac{N - N^*}{N}$ may be referend to as the system connectivity ratio.

The calculations executed have show that, α being sufficiently small (less then 0,5%),the whole system "engine-mount-airframe" decomposes into m non-connected systems which are considerably easier to analize.

If engine mounting attachment are dynamically independent and motion is uni-directional,the expression for the force acting from the engine side in the i-th attachment point may be transformed to:

$$R_E^i (\omega) = \left(C_{EM}^{ii}(\omega) + C_M^{ii}(\omega) + C_{AM}^{ii}(\omega) \right)^{-1} \sum_{k=1}^{q} C_{ES}^{ki}(\omega) \cdot F_S^k(\omega), \qquad (3)$$

where $\sum_{k=1}^{q} C_{ES}(\omega) \cdot F_S^k(\omega)$ is engine vibratory motion in the hypothetical case of the engine being not cunstrained in the vibration sense.

Considering each of m engine structure attachments to airframe as a separate action sourse,we determine the total acoustic pressure ρ^n in some point n of the pressurized cabin as a sum of acoustic pressures due to each of these sorces:

$$P_c^n (\omega) = \sum_{i=1}^{m} H_A^{in}(\omega) \cdot R_E^i (\omega) , \qquad (4)$$

where $H_A^{in}(\omega)$ is the structure frequency response defined as the acoustic pressure $\rho^n(\omega)$ in the point n divided by the dynamic force $F^i(\omega)$ applied to the point i and producing this pressure:

$$H_A^{in}(\omega) = \frac{\rho^{ni}(\omega)}{F^i(\omega)} \qquad (5)$$

The noise being expressed in dB,let us rewrite this formula in the following form which is more convenient for the measurment of the characteristic:

$$L_{H_A}^{in}(\omega) = L^{ni}(\omega) - 20 \lg \bar{F}_{\mathcal{H}}^i(\omega) , \qquad (6)$$

where $L_{H_A}^{in}(\omega)$ is soud pressure level (SPL) transfer function, $L^{ni}(\omega)$ is the noise level in dB within the aircraft cabin which is generated by a constant , for the experiment,excication force , $\bar{F}_{\mathcal{H}}^i(\omega)$ is the exitation force amplitude to the unit force ratio.

So,for the i-th attachment point the expected noise level in pressurized cabin due to the vibratory action of the aircraft power plant accounting for the engine vibratory motion,engine and airframe dynamic compliance matrices and interior SPL responses,may be calculated according to the formula:

$$L^{ni}(\omega) = L_{H_A}^{in}(\omega) + 20\lg\left(C_{ES}^{ii}(\omega) + C_M^i(\omega) + C_{AS}^{ii}(\omega)\right)^{-1} \cdot \frac{V_E^i(\omega)}{\omega \cdot F_{\mathcal{H}}^i(\omega)} \quad , \tag{7}$$

where $F_{\mathcal{H}}^i(\omega)$ is the vibrator excitation force in the i-th attachment point,
$V_E^i(\omega)$ is the amplitude of engine body vibration in the i-th attachment point,
ω -circular frequency.

Adding together separate sources powers we get the total noise level due to the vibratory action of the power plant.

The analitical expression thus obtained allows to formulate the requirements to the power plant to limit vibroacoustic action and to choose the most effective ways to decrease it.

EXPERIMENTAL DATA

A well-known test technique was used:structures were excited by an electro-dynamic shaker while the harmonic input force amplitude being constant and its frequency varying authomatically within the studied range.

Measurment were done in a hangar in silence mode,aircraft pressurized cabin doors being baattened down.During the tests the interferences level was monitored.

The noise was measured at passenger's and pilot's heads level according to current rules of sertification testing in aircraft passenger and flighting compart-ments. The sound pressure level data presented herein are refereced to $P_0 = 2 \cdot 10^{-5} \, N/m^2$.

Vibration pickups were placed on the seat rails along the pressurized cabin, on the pres⊾ ⁀ dome,on engine nacelles.On the engines , vibration pickups were placed at mount attachment points and also on some engine components.

The information was processed with the use of a magnetic recorder unit , a 2-channel analizer and an XY-recorder. From the digital output of the analizer the information was transmitted to a digital cassette recorder in order to create a databank;then it was loaded in a computer to make necessery calculations, e.g. to estimate the expected noice level due to the engine vibratory action.

The dynamic characteristics analysis of several turbofan engine demonstrates similaraty and allows the frequency range of interest to be divided into several sub-ranges,which are characterized by the engine cetrain dynamic behaviour;that is, for every such subrange a sufficienty simple and reliable mathematical model can be provided.

Thus the upper limit of rigid body behaviour of a turbine engine was determi-nad-it is about 25-30 Hz.It is shown that above 30 Hz the engine behaves as an elastic-inertial system with multiple resonances.The identification of these re-sonances allowed to relate them to natural frequencies of some engine components (rotors,gear boxes,accessories attached to engine cassing etc.)

Above 100 Hz the engine corresponds to the elastic-dissipative model,its damping and elasticity levels depending on the action appliication point and direction.

The engine body dynamic compliance (module) characteristics are represented in Fig.2 for different directions of mount excitation;that allows to identify the transverse motion natural frequency of one of the rotors.

In the experiments the linearity principle validity was checked and the limits of reciprocity were determined.

The spectrograms of acoustic response indicate multiple resonances of the com-partment air volume (noice level variations are up to 20-30 dB).The comparison of the acoustic response of some point of the TU-154M aircraft with the same cha-racteristic of the DC-9 aircraft [7] demonstrates a strong similarity of aircraft structures properties (Fig.3).

145

An example of the dynamic compliance variation of the structure in some engine attachment point is show in Fig.4;the same characteristic of the DC-9 aircraft engine attachment bracket is also show [8].

The use of real dynamic characteristics for separate mount was earlier considered in a one-dimensional way because of insufficient information,but even then the authors in the conclusion of their paper laid down a program of a detailed study and pointed out the necessity of the relationship between the sound pressure in the compartment and the forces applied to the fuselage from the engine side to be taken into account [8].

A study is known where the light airplane transmission model included engine mount dynamic characteristics in the attachment points and the acoustic response of selected cabin interior points,defermintd by what is generally referred to as point and transfere impedance testing,but the engine was still modeled as a rigid body [9]

Our analysis of body dynamic compliance of several Soviet engines differing both by the thrust levels (10000...20000 Kg) and the bypass ratios (from 0.5 to 5.0), allowed to improve considerably the turbine engine dynamic model in the rotor frequency range.

The investigation of the airframe SPL transfer function from engine vibratory action application of the points (attachment points) to the cabin resulted in determination of each engine (or attachment point) constribution to the pressurized cabin vibroacoustic field and allowed to dispose the vibration isolation means accordingly.

This method application is exemplified by the design of the improved engine mount vibration isolation in middle-sized airliner, where the matching of frequency dependent characteristics of engine bodies and aircraft is achieved through the right choice of moint parameters.

To evaluate the contribution of each engine vibration isolating mount in case of multiengine power plant a method was elaborated in flight tests to dismatch the operating conditions of engines taking into account the test equipment resolution and rotor slip in order to separate individual engine contributions.

Acoustic characteristics of the pressurized cabin were determined for different cruising conditions - firstly for rigid engine mounts and then for various vibration isolating mounts (elastic, elastic-inertial with narrow-band vibration absorbers).

The use of the new vibration isolating engine mount resulted in reduction of engine discrete tones in the rotor frequency range by 8...12 dB and of the noise in octave bands containing rotor harmonics - by 6...10 dB (see Fig.5).

This allowed to reduce the total SPL within the compartments by 3...5 dB(A). The results obtained agree with calculations.
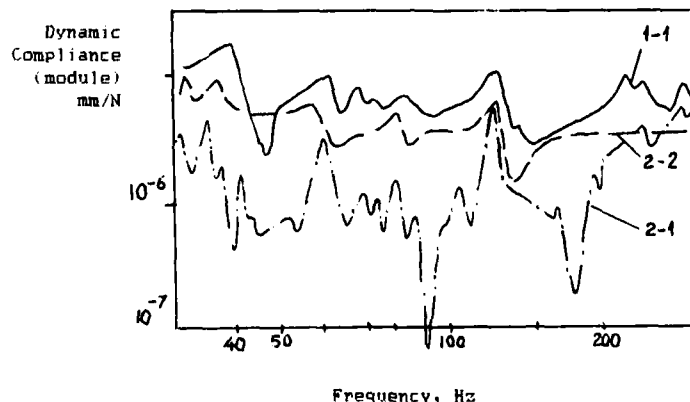
Frequency, Hz
Figure1. Comparison of dynamic compliances (input and transferred)
1-1,2-2-input;2-1-transferred
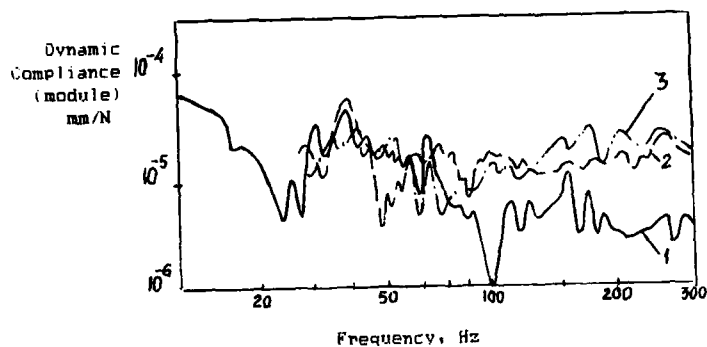
Figure2. Engine dynamic compliances (module) for different directions of exitation
1-in the diametrical;2-in the longitudinal;3-50°from diametrical
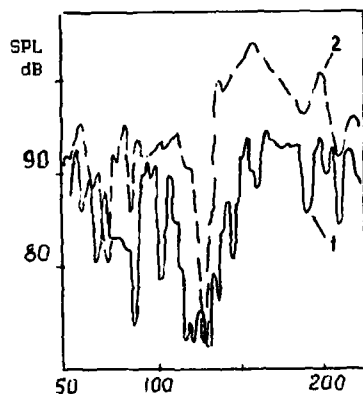
Figure 3. Comparison of SPL
transfer function spectra
1-TU-154M,2-DC-9
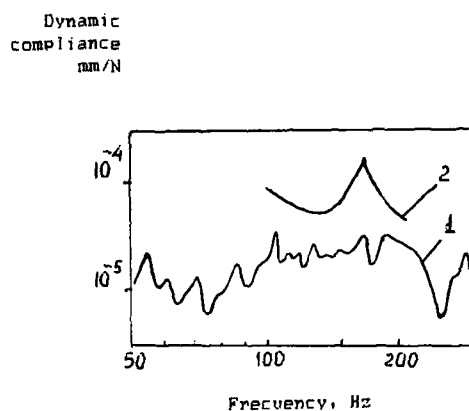
Figure 4. Comparison of airframe
dynamic complances in
engine attachment point
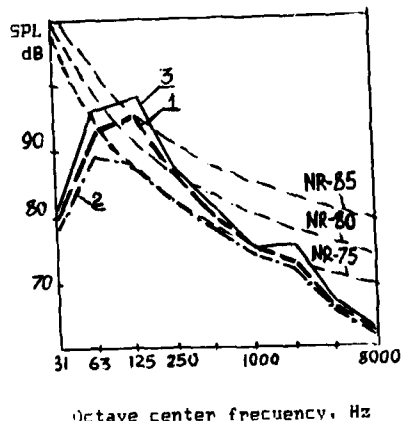
Figure 5. Effectivness of improved vibration isolation mount
1-regular isolator,2-improved , 3 ·rigid

REFERENCES

1.Бакланов В.С., Вуль В.М. "Оценка структурного шума, возбуждаемого вибрациями
  двигателей". Доклады VII Всесоюзной конференции по аэроакустике. ЦАГИ 1981,
  стр.207-208
2.Вуль В.М., Попков В.И., Агафонов В.К., Бакланов В.С. "Исследование динамических
  характеристик двигателя, стенда и объекта в местах опорных связей". Виброционная
  прочность и надежность двигателей и систем летательных аппаратов. Научный сборник.
  Куйбышевский авиационный институт, 1980, с. 62-68
3.Lankaster P.Theory of matrices. Academia Press. New-York-London,1969
4.Вуль В.М.,Бакланов В.С. "Влияние связанных колебаний сложных динамических систем
  на оценку эффективности виброизоляции." Доклады X Всесоюзной акустической конферен-
  ции. Москва, Акустический институт АН СССР, 1983, с.65-68
5.Бакланов В.С. Вуль В.М. "Требования к авиационной силовой установке с позиции огра-
  ничения виброакустического воздействия". Проблемы энергетики воздушного транспорта.
  Труды ЦИАМ N 1272, Москва, 1990, с. 169-175
6.Агафонов В.К., Бакланов В.С., Вуль В.М., Попков В.И., Попов А.В. "Исследование виб-
  роакустических и динамических характеристик самолета и двигателя в местах опорных
  связей". Доклады Всесоюзной конференции "Борьба с шумами и вибрацией". Судостроение.
  Ленинград, 1991, с. 121-131
7.Van Dyke J.D.,Schendel Jr, I.W.,Gunderson C.O.,Ballard M.R. "Cabin Noise Reduction
  in the DC-9". Paper 667-401,presented at the AIAA Commercial Aircraft Design
  Meeting,June 1967
8.Rubin S., Biehl F.A. "Mechanical Impedante Approach to Engine Vibration Transmission
  Info an Aircraft Fuselage".Paper 670873. Aeronautic and Spase Engineering and Manufac
  turing Meeting. Los Angeles, Cflif. October 2-6, 1967
9.Unruh J.F. "Procedure for Evalution of Engine Isolators for Reduced Structure-Borne
  Noise Transmissiom". Journal of Aircraft, Vol.20,January 1983,p.76-82

PASSIVE DAMPING
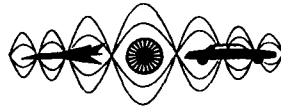
ANALYSIS OF CONSTRAINED-LAYER DAMPING OF FLEXURAL AND EXTENSIONAL WAVES IN INFINITE, FLUID-LOADED PLATES

Pieter S. Dubbelday
Naval Research Laboratory, USRD
P.O. Box 568339
Orlando, FL, 32856-8339
U.S.A.

ABSTRACT

This study contains a mathematical analysis of constrained-layer damping (CLD) in plates of infinite extent, with an emphasis on the physical understanding of some special features, including fluid loading. Previous work is expanded to cover extensional waves. Some essential aspects of fluid loading may be understood by applying thin-plate theory. Therefore thin-plate theory of extensional waves in a fluid-loaded plate was developed as a counterpart to that for flexural waves. The description and examples of CLD follow three models: the first is an extension of Kerwin's 1959 model, the second a hybrid model for which the base plate is treated by exact elasticity theory, and finally a fully exact model for all three layers. Examples and comparisons are given.

NOMENCLATURE

c_p extensional wave speed for thin base plate

c_d dilatational wave speed for thin base plate

c_3 extensional wave speed for thin constraining layer

c_o wavespeed in medium

d_i $= h_i/2$; h_i-layer thickness

E_i Young's modulus for three layers

E_i^e extensional modulus for three layers; $E^e = E/(1-\nu^2)$

F fluid-loading parameter

i index of layers: 1-base plate, 2-elastomer, 3-constrained layer

k wavenumber in plate, $k = k'-i\alpha$

k_o wavenumber in medium

q^s $= \sigma_+ + \sigma_-$

w displacement perpendicular to plate

α attenuation coefficient

ν_i Poisson's ratio for three layers

ρ_i density of three layers

G_2 complex shear modulus of elastomer, $G_2 = G_2'(1+i\beta)$

g complex shear parameter, $=G_2/(k'^2 E_3{}^e h_2 h_3)$, $g=g'(1+i\beta)$

r $=3/4$ for flexural, $=1/2$ for extensional waves

ρ_o density of medium

$\sigma_{+,-}$ stresses at opposite sides of plate

τ $= [(k/k_o)^2 -1]^{1/2}$

w_c characteristic frequency for extensional waves in fluid-loaded plate

Ω dimensionless frequency, $\Omega = w/w_c$

INTRODUCTION

The principle of constrained-layer damping of acoustic waves consists of attaching a thin elastomer layer with high viscoelastic loss plus a stiff covering layer to a bar, plate, or structure. This stiff layer forces the elastomer into shear, with concomitant large loss, as compared with purely extensional loss in the elastomer without cover layer. Although the loss tangent of the shear modulus G is almost the same as the loss tangent in the Young's modulus E, the energy loss in the constrained layer is of the order $1/kh_2$ of that in an unconstrained layer.

This physical explanation of the effect is represented in a classical paper by E.M. Kerwin [1]. His model gives good results within the given restrictions: flexural waves at low frequency in a main plate with thin additional layers. Extensional waves are not considered, and fluid loading is not readily introduced.

In order to retain the advantage of Kerwin's model of providing an explicit algebraic expression for the attenuation coefficient in terms of geometric and elastic parameters, the model was extended and compared with more exact formulations, a "hybrid" model and an exact model [2,3].

In this study the analysis is extended to cover extensional waves. Since flexural waves were discussed in previous publications [2,3], only some of their features will be mentioned here. For most combinations of plate and medium, the flexural wave speed in the plate, which increases from zero at zero frequency, reaches a value equal to the speed in the medium, at a certain frequency. Thus one distinguishes radiating and non-radiating ("subsonic") waves in the plate. This phenomenon does not occur for extensional waves in most cases.

HIERARCHY OF MODELS

In the case of flexural waves in a fluid-loaded plate, physical insight was obtained by using thin-plate theory. A parallel thin-plate theory for extensional waves in a fluid-loaded plate is presented. The formalism for extensional waves in terms of the hybrid model and fully exact model is the same as for flexural waves.

The extended Kerwin model includes extensional waves. It is represented by the following expression,

$$\alpha/k' = (r\beta) \frac{E_3{}^e h_3}{E_1{}^e h_1} \frac{g'[1 - (c/c_3)^2]}{[1 - (c/c_3)^2 + g']^2 + \beta^2 g'^2} \qquad (1)$$

The following outline lists the three models for constrained layer damping used in the examples, with their characteristic properties.

152

1. Extended Kerwin model
   a. Flexural or extensional waves   b. Inertia of constraining layer
   c. Complex shear parameter   d. Wave speed from thick-plate theory

2. Hybrid model
   a. Exact elasticity theory for   b. Other two layers as in Kerwin
      base plate
   c. Flexural and extensional waves   d. With or without fluid loading

3. Exact model
   a. Exact theory for all layers   b. Flexural and extensional waves
   c. With or without fluid loading

In all the following examples of the analysis the base plate and additional layers have physical and geometric parameters as listed in table I. The (complex) shear modulus of the elastomer is assumed independent of frequency, in order to emphasize the mechanical aspects of the technique without viscoelastic effects.

THIN-PLATE THEORY FOR EXTENSIONAL WAVES IN FLUID-LOADED PLATE

Thin plate theory for flexural waves in a fluid-loaded plate may be found in Ref.[4]. It appeared difficult to derive an analogous expression for extensional waves directly. Therefore the problem was approached as follows.

One starts from the structural equations for waves in plates obtained from exact elasticity theory by integrating and averaging along the direction perpendicular to the plate. From this, one may derive a thick-plate theory for extensional waves [5]. Fluid loading is represented by the sum of the stresses at both sides of the plate, given as $q^s = \sigma_+ + \sigma_-$. Thin-plate theory follows by dropping terms containing the factor (kd). (In this section all quantities refer to the base plate.) The result is equivalent to adding a fluid-loading term F to the familiar equation for extensional waves in a plate,

$$[E/(1-\nu^2)] \, \partial^2 w/\partial x^2 + F = \rho \, \partial^2 w/\partial t^2 \qquad (2)$$

where F is given by

$$F = [1 - (c/c_d)^2] \, (kd)^2 \, q/(2d) \qquad (3)$$

Assuming a harmonic wave, with space and time dependence expressed by exp i(wt-kx), where the x-coordinate is in the direction of the wave parallel to the plate's surface, and introducing a new variable τ by $k^2 = k_o^2(1+\tau^2)$, Eq.(2) is replaced by an algebraic equation in terms of τ. For fluid loading on both sides one has $q = 2 w^2 \rho_o w /(k_o \tau)$ and Eq.(2) becomes

$$\tau^3 - \Omega \tau^2 + \tau [1-(c_o/c_p)^2] - \Omega [1-(c_o/c_d)^2] = 0 \qquad (4)$$

where a characteristic frequency w_c and a corresponding dimensionless frequency Ω are introduced by $w_c = (\rho/\rho_o) \, c_p^2/(c_o d)$ and $\Omega = w/w_c$,

The characteristic frequency ω_c for brass in water is 0.26×10^6 rad/s, and thus for the frequency region where thin-plate theory may be applied, the non-dimensional frequency Ω is very small. As a consequence there exists a small real root, for small Ω namely

$$\tau - \Omega \frac{1 - (c_o/c_d)^2}{1 - (c_o/c_p)^2} \tag{5}$$

This root corresponds to a non-radiating wave in the plate, with a constant speed slightly less than the speed in the medium, (for low frequency).

By synthetic division one determines the quadratic equation for the two remaining complex conjugate roots,

$$\tau^2 + a\,\tau + b = 0, \tag{6}$$

where $a = -\Omega \dfrac{(c_o/c_p)^2 - (c_o/c_d)^2}{1 - (c_o/c_p)^2}$ and $b = 1 - (c_o/c_p)^2$

One of these gives a wave number with positive attenuation constant α.

In Fig. 1 a comparison is shown of the relative attenuation α/k', according to thin-plate theory and to exact elasticity theory, first for two-sided fluid loading. Although the boundary conditions for extensional waves cannot be satisfied for one-sided fluid loading without additional flexural waves, one might take half the value of q^s as given before, and carry this through the analysis. The results in Fig. 1 show that the attenuation for one-sided fluid-loading thus computed does not compare well with the exact-elasticity result.

CONSTRAINED PLATE IN VACUUM

In Fig. 2, a threefold comparison is shown for the relative attenuation constant for extensional waves propagating in a constrained plate, without fluid loading, for three models. The sharp dip in attenuation near 15 kHz is due to an "equivoluminal mode", whereby the tangential velocity component at the faces of the plate is zero, thus no shear exists in the elastomer layer. Of course this feature does not show up in the extended Kerwin model.

FLUID-LOADED, CONSTRAINED PLATE

Flexural waves
Various typical features for damping of flexural waves by radiation and viscoelastic effects may be seen in Fig. 3. One sees that in the high-frequency range the total attenuation is mostly due to radiation. In the middle range the attenuation is due to viscoelastic damping in the elastomer. At the low frequency end a feature appears of high damping due to radiation. It may be pointed out that this is a consequence of the infinite extent of the plate; for finite plates this "radiation" would not be expected to be found in the farfield. See Ref. [3] for further details.

Extensional waves

In Fig.4, a comparison is shown for the relative attenuation constant as a function of frequency for a constrained plate loaded by fluid on both sides, on the side of the added layers, and on the opposite side, computed by exact elasticity theory. One sees that for a large frequency region there is not much difference between the curves, except for a factor of two between the double-sided and one-sided fluid loading. At the low frequency end the curves for the two cases part, while at the high frequency side two of the curves converge and the third one follows a different path. If one compares this figure with Fig.1, one sees that the damping due to the elastomer layer does not make much difference in the total attenuation, except for a different structure at the high-frequency end.

In all the various configurations for extensional waves studied here, there is little variation of the phase speed from that for a single, unloaded plate. This is quite different from the behavior of the phase speed for flexural waves at high frequencies [3].

REFERENCES

1. E.M. Kerwin, "Damping of flexural waves by a constrained viscoelastic layer", J.Acoust.Soc.Am. 31, 1959, 952-962.
2. P.S. Dubbelday, "Constrained-layer model investigation based on exact elasticity theory", J.Acoust.Soc.Am. 80, 1986, 1097-1102.
3. P.S. Dubbelday, "Constrained-layer damping analysis for flexural waves in infinite fluid-loaded plates", J.Acoust.Soc.Am. 90, 1991, 1475-1487.
4. M.C. Junger and D. Feit, Sound, Structures, and Their Interaction, MIT, Cambridge, 2nd ed., 1986, Secs. 8.1 and 8.2
5. P.S. Dubbelday, "Contribution of antisymmetric and symmetric waves to the reflection of sound in a fluid by a thick, homogeneous plate", NRL Memo. Rep. 4312, Naval Research Laboratory, Orlando, FL, 1980.

TABLE I. Material and geometric parameters and derived quantities.		
Base plate, brass	**Elastomer layer (hypothetical)**	
h_1 = 10 cm E_1 = 104 Pa	h_2 = 1.24 mm	ρ_2 = 1100 kg/m^3
ν_1 = 0.37 ρ_1 = 8500 kg/m$_3$	$G_2{}'$ $\approx$ 10 MPa	β = 1.0
G_1 = 38 GPa c_p = 3765 m/s	Bulk modulus = 1.0 GPa	
ω_c = 0.26 Mrad/s	**Constraining layer, aluminum**	
Fluid, water	h_3 = 2.48 mm	E_3 = 71 GPa
ρ_o = 998 kg/m^3 c_o = 1481 m/s	ν_3 = 0.33	ρ_3 = 2700 kg/m^3
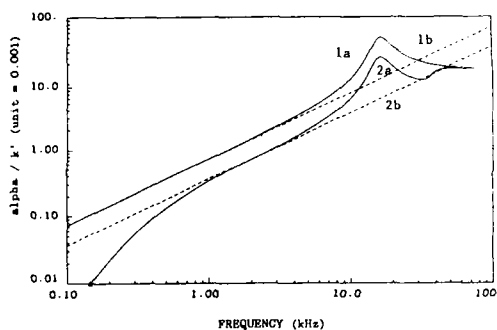
Figure 1. Extensional wave; single,
fluid-loaded plate. Fluid on:
1-both sides; a-exact b-thin plate
2-one side;   a-exact b-thin plate
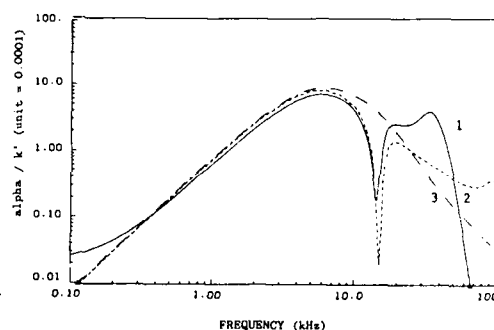
Figure 2. Extensional wave;
constrained plate in vacuum. Model:
1-exact; 2-hybrid; 3-extended Kerwin
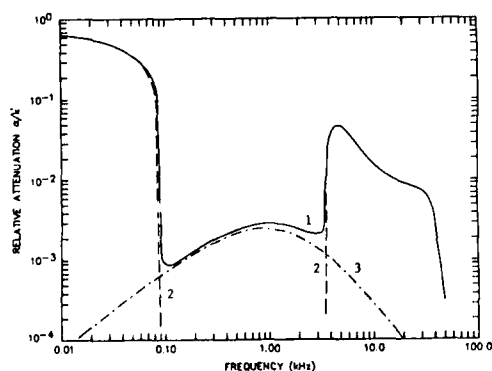
Figure 3. Flexural wave; exact model.
1-constrained plate, water on elas-
tomer side; 2-single plate, water on
one side; 3-constrained plate in
vacuum
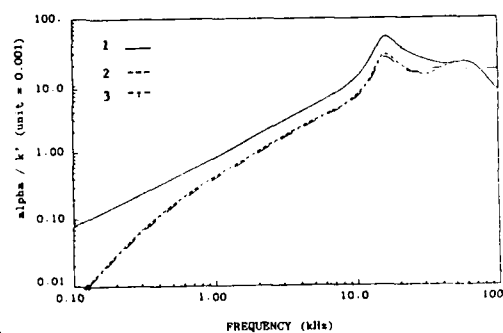
Figure 4. Extensional wave, constrained
plate. 1-water on both sides; 2-water on
elastomer side; 3-water on opposite
side. Exact model.

156

Effect of Partial Coverage on the Effectiveness of a
Constrained Layer Damper on a Plate

M. R. Garrison, R. N. Miles,
J. Q. Sun and W. Bao
Department of Mechanical and Industrial Engineering
State University of New York
P.O. 6000
Binghamton, New York 13902-6000
U.S.A.

ABSTRACT

An analysis is presented of the random vibration of a plate which is partially covered by a constrained layer damper that incorporates a spacer layer to enhance damping effectiveness. The spacer layer is assumed to be rigid in shear and to have no bending stiffness. The spacer enhances the damping effectiveness by inducing additional shear deformation in the adhesive layer. The analytical model accounts for both shear and thickness deformation of the adhesive layer. A parametric study is conducted to optimize the position, coverage area, and the thickness of the damper. It is found that the incorporation of the spacer layer permits the use of a damper having reduced coverage area, and hence, less added weight without compromising damping effectiveness.

I. INTRODUCTION

In the past, laminated beams and plates with viscoelastic cores have received a considerable amount of attention in an attempt to reduce the resonant bending vibration of various structures. By bonding a relatively thin stiff member to the structure with a viscoelastic adhesive, energy from the structure is dissipated when strain is induced in the adhesive during vibration. The thin stiff member, a constraining layer, was designed to induce shear strain in the adhesive layer. Previous studies have shown that the constraining layer should be stiff in bending as well as in tension to increase the effectiveness of the damper [1]. In constrained layer damping applications, it has been accepted that by increasing the thickness of the constraining layer the strain in the adhesive layer could also be increased. However, the constraining layer was an elastic solid, such as aluminum, which added a considerable mass when the thickness was increased. In 1959, Whittier [2] was the first to observe that the addition of a spacer layer to a laminated structure with a viscoelastic core could enhance the damping performance by increasing the shear strain in the adhesive layer. This configuration is commonly referred to as a stand off damper. Ungar [3] presented an analysis of stand off dampers for simply-supported beams with uniform coverage. It has also been shown experimentally that a spacer layer can be constructed which has the desired properties and provides the predicted performance [4,5]. In the present study, an analytical model is presented to facilitate the design of stand off dampers for plates.

The incorporation of a spacer in a constrained layer damper will increase both the effectiveness and the total mass of the treatment. Since the added mass is a primary concern, especially in aerospace applications, some form of compensation is necessary. One way to off-set the increase in mass is to use only partial coverage of the primary layer. This will, of course, reduce the damping performance. It is very difficult to anticipate the amount of reduction in performance that will result from reducing the coverage area. A primary objective of the present study is to examine the performance of a spaced damper on a partially covered plate. Partial coverage of the structure can be an efficient means of reducing the total mass by eliminating the damping treatment in areas where the effectiveness is low. To obtain an optimal design, it is helpful to employ an analytical model of the system response.

Models of the effects of partial coverage on a beam have been presented by several investigators [6-8]. The model of a partially covered plate is, however, considerably more complex in comparison to the beam.

For example, in an attempt to simplify the problem, Ozguven [9] reduced the primary layer with the applied damping treatment down to a single layer by representing the system as a single hysteretic damping element for each mode. Lall, Asnani and Nakra [10] also studied the partially covered plate, using only single term solutions for the longitudinal displacements of the constraining layer and the transverse displacement of the primary layer. The model generated here includes a large number of complex resonant modes to describe the responses of the base plate and the constraining layer as a complete system. This is the first study of a partially covered plate that includes enough detail to provide reliable design guidelines.

In comparing the performance of the dampers that do not cover the entire primary layer, it must be noted that the damping effectiveness will depend on where the response is determined. In an attempt to obtain an unbiased measure of damper performance, the figure of merit used here consists of the spatial average of the response power spectral density due to spatially uncorrelated homogeneous white noise.

The primary result of the present study is that the incorporation of a spacer can provide better performance with less added weight through the use of partial coverage. As the coverage area is reduced, however, it is important to know how to position the damping treatment to obtain optimum performance. The results presented in the following indicate that a thin strip of stand off damping treatment placed slightly off-center on the primary layer provides a highly weight efficient design.

II. ANALYTICAL MODEL

The system studied here consists of a traditional constrained layer damper with a spacer added to induce additional strain, as shown in figure 1 (a). The analytical model is created beginning with the formulation of the mass and stiffness matrices. The solution to the eigen problem is then used in modeling the response of the primary layer to a random excitation. The basis for the analytical model comes from Hamilton's principle:

$$\delta \int_{t_1}^{t_2} [T - V] \, dt + \delta \int_{t_1}^{t_2} W \, dt = 0. \tag{1}$$

II.1 Mass and Stiffness Matrices

The first step in formulating the mass and stiffness matrices is to obtain the kinetic and potential energies. The potential energy expression for each layer is written in terms of the elastic stresses and strains. It is necessary to begin by defining the displacement fields of each layer. Figure 1 shows the orientation of the layer displacements. The displacement field for the adhesive layer is written in terms of the assumed displacements of the primary layer, $U_1(x,y,t)$, $V_1(x,y,t)$, $W_1(x,y,t)$, and of the constraining layer, $U_3(x,y,t)$, $V_3(x,y,t)$, $W_3(x,y,t)$. The assumption is made that the adhesive layer displacements can be obtained by linear interpolation between the two outer layer displacements. As shown in figure 1 (b), the line connecting points a and b through the adhesive layer is assumed to be straight. Using this assumption, the relationships for the displacement field in the adhesive layer are

$$U_2(x,y,z,t) = \frac{U_3 + \frac{h_3}{2}\frac{\partial W_3}{\partial x} - U_1 + \left(\frac{h_1}{2} + h_s\right)\frac{\partial W_1}{\partial x}}{h_2} z + \frac{U_3 + \frac{h_3}{2}\frac{\partial W_3}{\partial x} + U_1 - \left(\frac{h_1}{2} + h_s\right)\frac{\partial W_1}{\partial x}}{2},$$

$$V_2(x,y,z,t) = \frac{V_3 + \frac{h_3}{2}\frac{\partial W_3}{\partial y} - V_1 + \left(\frac{h_1}{2} + h_s\right)\frac{\partial W_1}{\partial y}}{h_2} z + \frac{V_3 + \frac{h_3}{2}\frac{\partial W_3}{\partial y} + V_1 - \left(\frac{h_1}{2} + h_s\right)\frac{\partial W_1}{\partial y}}{2}, \tag{2}$$

$$W_2(x,y,z,t) = \frac{W_3 - W_1}{h_2} z + \frac{W_3 + W_1}{2}.$$

The displacement relationships for the spacer layer may be expressed in terms of the displacements of the primary layer.

$$U_s(x,y,z,t) = U_1(x,y,t) - \frac{\partial W_1}{\partial x}\left(\frac{h_1}{2} + \frac{h_s}{2} + z\right)$$

$$V_s(x,y,z,t) = V_1(x,y,t) - \frac{\partial W_1}{\partial y}\left(\frac{h_1}{2} + \frac{h_s}{2} + z\right) \tag{3}$$

$$W_s(x,y,z,t) = W_1(x,y,t)$$

In order to obtain the elements of the mass and stiffness matrices we will first construct expressions for the strain and kinetic energies of the system [11]. The assumption that the material in each layer is linearly elastic

158

and isotropic leads to well known relationships for stress and strain in terms of the displacements. The two outer layers are assumed to behave according to elementary plate theory. Once the displacements, stresses and strains have been defined, the strain and kinetic energies can be written as

$$\mathcal{V}_1 = \frac{1}{2} \int_{-\frac{h_1}{2}}^{\frac{h_1}{2}} \int_0^{ly_1} \int_0^{lx_1} (\sigma_{x_1}\epsilon_{x_1} + \sigma_{y_1}\epsilon_{y_1} + 2\tau_{xy_1}\gamma_{xy_1})dxdydz \quad \text{and} \quad \mathcal{T}_1 = \frac{1}{2}\rho_1 h_1 \int_0^{ly_1} \int_0^{lx_1} (\dot{U}_1^2 + \dot{V}_1^2 + \dot{W}_1^2)dxdy. \quad (4)$$

The same procedure is followed to obtain the energy expressions for the constraining layer. Similarly, the strain energy of the adhesive layer is

$$\mathcal{V}_2 = \frac{1}{2} \int_{-\frac{h_2}{2}}^{\frac{h_2}{2}} \int_0^{ly_3} \int_0^{lx_3} \left[\sigma_{x_2}\epsilon_{x_2} + \sigma_{y_2}\epsilon_{y_2} + \sigma_{z_2}\epsilon_{z_2} + 2\left(\tau_{xy_2}\gamma_{xy_2} + \tau_{xz_2}\gamma_{xz_2} + \tau_{yz_2}\gamma_{yz_2}\right)\right] dxdydz. \quad (5)$$

The kinetic energies of the adhesive layer and the spacer have the same form as for the outer two layers.

The unknown displacements are expanded in the following form

$$U_1(x,y,t) = \sum_{i=1}^{N_{U_1}} A_i(t)cos(n_i\pi x/lx_1)cos(m_i\pi y/ly_1)$$

$$V_1(x,y,t) = \sum_{i=1+N_{U_1}}^{N_{U_1}+N_{V_1}} A_i(t)cos(n_i\pi x/lx_1)cos(m_i\pi y/ly_1) \quad (6)$$

$$W_1(x,y,t) = \sum_{i=1+N_{U_1}+N_{V_1}}^{N_{U_1}+N_{V_1}+N_{W_1}} A_i(t)sin(n_i\pi x/lx_1)sin(m_i\pi y/ly_1)$$

$$U_3(x,y,t) = \sum_{i=1+N_{U_1}+N_{V_1}+N_{W_1}}^{N_{U_1}+N_{V_1}+N_{W_1}+N_{U_3}} A_i(t)cos(n_i\pi x/lx_1)cos(m_i\pi y/ly_1)$$

$$V_3(x,y,t) = \sum_{i=1+N_{U_1}+N_{V_1}+N_{W_1}+N_{U_3}}^{N_{U_1}+N_{V_1}+N_{W_1}+N_{U_3}+N_{V_3}} A_i(t)cos(n_i\pi x/lx_1)cos(m_i\pi y/ly_1) \quad (7)$$

$$W_3(x,y,t) = \sum_{i=1+N_{U_1}+N_{V_1}+N_{W_1}+N_{U_3}+N_{V_3}}^{N_{U_1}+N_{V_1}+N_{W_1}+N_{U_3}+N_{V_3}+N_{W_3}} A_i(t)sin(n_i\pi x/lx_1)sin(m_i\pi y/ly_1).$$

The unknown functions $A_i(t)$ are in the form of a partitioned vector, which provides a mapping between the displacement fields, equations (6) and (7), and the partitioned mass and stiffness matrices. In each expansion n_i and m_i are selected so that any desired number of half-waves is included in each direction. If $\mathcal{V}$ and $\mathcal{T}$ are the total strain and kinetic energies of the system, the elements of the mass and stiffness matrices, $[M]$ and $[K]$, are written as

$$M_{ij} = \frac{\partial^2 \mathcal{T}}{\partial \dot{A}_i(t)\partial \dot{A}_j(t)}, \qquad\qquad K_{ij} = \frac{\partial^2 \mathcal{V}}{\partial A_i(t)\partial A_j(t)}. \quad (8)$$

II.2 Random Excitation

In the previous section, the mass and stiffness matrices were obtained for the system. Using these results, we will now describe the effects of the damping treatment on the plate if it is subjected to a stationary random loading. It will be assumed that the excitation is applied to the primary layer in the transverse direction. In this study, the excitation field is taken to be totally uncorrelated in both space and time, or a "rain on the roof" excitation. In order to develop the response due to a spatially uncorrelated random excitation, we begin by using the form of the primary layer response as shown in equation (6). The results of section II.1 are substituted into equation (1) to give

$$[K]\{A\} + [M]\{\ddot{A}\} = \{f\}. \quad (9)$$

159

The elements of $\{f\}$ are

$$f_i(t) = \int_0^{lx_1} \int_0^{ly_1} f(x,y,t)\phi_i(x,y)dydx, \tag{10}$$

for $N_{U_1} + N_{V_1} < i \leq N_{U_1} + N_{V_1} + N_{W_1}$ and $f_i(t) = 0$ for all other values of i. The finite Fourier transform of $f_i(t)$ is

$$F_i(\omega,T) = \frac{1}{2\pi} \int_{-T}^{T} f_i(t)e^{-i\omega t}dt. \tag{11}$$

The finite Fourier transform of equation (9) is then

$$[K]\{A(\omega,T)\} - \omega^2[M]\{A(\omega,T)\} = \{F(\omega,T)\}. \tag{12}$$

The damping properties of the viscoelastic material are included by letting the elastic moduli be complex. When complex moduli are used in the results of section II.1, the elements of the stiffness matrix given in equation (8) become complex. Modal analysis is used to obtain the frequencies and mode shapes corresponding to equation (12). The solution to the complex eigen problem allows $A_i(\omega,T)$ to be written as

$$A_i(\omega,T) = \sum_{l=1}^{N} \mathcal{H}_{il}(\omega)F_l(\omega,T), \quad \text{where} \quad \mathcal{H}_{il}(\omega) = \sum_{j=1}^{N} U_{lj}H_j(\omega)U_{ij}, \qquad H_j(\omega) = \frac{1}{\omega_j^2 - \omega^2} \tag{13}$$

and U_{ij} are the elements of a modal column matrix, $[U]$.

The single sided power spectral density [12] of $W_1(x,y,t)$ is

$$G_{W_1W_1}(\omega,x,y) = \lim_{T \to \infty} \frac{2\pi}{T} E[|W_1(x,y,\omega,T)|^2], \tag{14}$$

where $E[\cdot]$ denotes the expected value. Because the performance of the damping material is likely to depend strongly on position, a figure of merit is used in this study that consists of a spatial average of the response power spectral density. Determining this 'averaged' response turns out to be computationally simple once the complex modal column matrix, $[U]$, has been obtained. The spatial average of the response spectrum over the plate is

$$R(\omega) = \frac{1}{lx_1ly_1} \int_0^{lx_1} \int_0^{ly_1} G_{W_1W_1}(\omega,x,y)dydx. \tag{15}$$

For a spatially uncorrelated excitation field this may be shown to be [13]

$$R(\omega) = \frac{lx_1ly_1}{16} G_{ff}(\omega) \sum_{i=1+N_{U_1}+N_{V_1}}^{N_{U_1}+N_{V_1}+N_{W_1}} \sum_{l=1+N_{U_1}+N_{V_1}}^{N_{U_1}+N_{V_1}+N_{W_1}} |\mathcal{H}_{il}(\omega)|^2. \tag{16}$$

III. RESULTS AND CONCLUSIONS

The analytical model has been created to produce the spatial average of the response spectrum for the simply-supported plate with a stand off damper. The goal of the study is to show that the stand off damper provides an improvement in damping effectiveness over the conventional constrained layer damper. In addition, some general guidelines can be presented for the optimization of position, partial coverage, and the thickness of the adhesive and spacer layers. The method of design for the thickness of the adhesive and spacer layers has been outlined using the results obtained from the analytical model.

All of the results are obtained using an aluminum primary layer which is 53.3cm long, 20.3cm wide and 0.190cm thick. The material properties of the primary layer are held constant throughout the study. To include structural damping in the primary layer, Young's modulus is allowed to be complex in the form $E_1(1 + i\beta_1)$, where E_1 is 68.9GPa and the loss factor, β_1, is 0.005. The specific weight, $\rho_1 g$, is $27.1 \frac{kN}{m^3}$ so that the density of the aluminum is $2762 \frac{kg}{m^3}$. Poisson's ratio, η_1, is 0.3. The damping treatment, consisting of the adhesive, spacer

160

and constraining layers, will have variable geometry, but the material properties will be constant. It will be assumed that the spacer and constraining layers always have the same x and y dimensions as the adhesive layer. As in the primary layer, the Young's modulus of the adhesive layer is taken to be is complex, where, in the form $E_2(1 + i\beta_2)$, E_2 is 3.45MPa and β_2 is 1.0. For the adhesive layer, $\rho_2 g$ is $10.0\frac{kN}{m^3}$, giving a density of $1024\frac{kg}{m^3}$, and Poisson's ratio, η_2, is 0.3. For the spacer layer, $\rho_s g$ is $4.45\frac{kN}{m^3}$, giving a density of $454\frac{kg}{m^3}$. The spacer is assumed to have the ideal properties of an infinite shear stiffness and a negligible bending stiffness. The constraining layer is always assumed to be aluminum with the same material properties as the primary layer and a thickness of 0.025cm, unless otherwise specified.

In this study the primary layer is simply supported and the damper is not attached with any mechanical fasteners (see figure 1), but only through the adhesive layer. The displacement fields for the primary and constraining layers are defined in equations (6) and (7), where the number of terms in the expansion has been left as a variable. For the results in this study 9 terms were used in both the x and y directions for $W_1(x, y, t)$ and $W_3(x, y, t)$. The displacements $U_1(x, y, t)$, $V_1(x, y, t)$, $U_3(x, y, t)$ and $V_3(x, y, t)$ are expanded with 5 terms in the x and y directions. This gives a total of 262 degrees of freedom.

In the process of optimization of partial coverage and position (see figure 2), the goal is to reduce the coverage area of the damping treatment without causing a substantial loss in effectiveness. Since the motion is already restricted at the edges due to the boundary conditions, it seems reasonable that damping the motion some distance away from the boundaries will be the most effective solution. This observation is evident if a given coverage area is positioned differently with respect to the edges of the primary layer.

Figures 2.1, 2, 7, and 8 show a strip of damping material at four different positions on the primary layer. Figure 3 shows the narrow band data for the spatial average of the primary layer response spectrum as a function of frequency. From this plot it is not clear which configuration provides the best performance. The process of selection is dependent on the frequency range of interest. Since the configurations perform differently in different frequency ranges, it is not reasonable to perform the optimization based only on a single number or performance index, such as an integration over frequency. In order to reduce the amount of data for comparison, the narrowband data can be plotted in octave band format. The narrowband data is added up over each octave band and plotted as a single value for the corresponding frequency band. Figure 4 shows the octave band data for the configurations in figure 2. From figure 4, the configuration shown in figure 2.7 generally has the best performance.

A similar comparison can be made for variation of coverage shown in figures 2.3, 4, 9, and 10, placed across the plate instead of along the length of the plate. Figure 5 shows the performance of this set of configurations. From the data presented in figures 4 and 5, it is evident that the long thin strip, shown in figure 2.7, is able to damp more of the modes on the primary plate. This suggests that the strips extending the length of the plate can damp a majority of the modes with waves in both directions on the plate. The strip extending across the primary plate is not able to damp waves traveling across the plate which do not pass through the coverage area. Knowing that the damping treatment has low performance when it is located near the edges of the primary layer leads to the conclusion that is not necessary to cover that area. The results suggest that it is best to cover nearly all of the length of the plate and as much of the width as possible, but position the damping treatment at an offset from the center of the primary plate if the coverage is narrow.

In an attempt to minimize the weight which the damping treatment adds to the primary layer, an effort is made to reduce the coverage area. The effect of partial coverage is not only an optimization of the size of the coverage area, but also the position. Figures 2.5, 6, 11, and 12 show what might be an obvious way to reduce the coverage area. In figure 6, the reduction in coverage produces an approximately uniform reduction in performance over the frequency range of interest. From the information obtained in figures 4 and 5, however, it seems reasonable to pursue a coverage which is as long as possible, while not reducing the width unreasonably. This method produces an improved performance.

The optimization of the partial coverage of a structure with a constrained layer damper with a spacer layer added is not straight forward. The coverage area and position must be optimized simultaneously, while also considering the thickness of the adhesive and spacer layers.

REFERENCES

[1] R.N. Miles and P.G. Reinhall 1986 *ASME Journal of Vibration, Acoustics, Stress, and Reliability in Design* **108**, 56–64. An analytical model for the vibration of laminated beams including the effects of both shear and thickness deformation in the adhesive layer.

[2] J.S. Whittier 1959 *WADC Technical Report 58-568: Wright Air Development Center*. The effect of configurational additions using viscoelastic interfaces on the damping of a cantilever beam.

[3] Eric E. Ungar, "Damping of Panels," in *Noise and Vibration Control*. Leo L. Beranek (Eds.), Institute of Noise Control Engineering: Washington, DC, 1988, pp. 434–475.

[4] M. Parin, Dr. L.C. Rogers, M. Falugi and Dr. Y. Moon 1989 *Proceedings of Damping '89, Volume II, Paper No. IBA*. Practical stand off damping treatment for sheet metal.

[5] M. Parin, V. Levraea, A. Pacia, and L. Rogers 1991 *Proceedings of Damping '91, Volume I, Paper No. BAB*. An investigation of add-on damping treatment for life extension of the F-15 upper outer wing skin.

[6] A.K. Lall, N.T. Asnani, and B.C. Nakra 1988 *Journal of Sound and Vibration* **123**, 247–259. Damping analysis of partially covered sandwich beams.

[7] Stefan Markus 1974 *Acta Technica CSAV* **19**, 179–194. Damping mechanism of beams partially covered by constrained viscoelastic layer.

[8] L.J. Pulgrano 1962 *64th Meeting of the Acoustical Society of America, Washington*. Effectiveness of partial coverage for constrained layer damping treatments.

[9] H. Nevzat Ozguven 1982 *Mecanique-Materiaux-Electricite* **389-391**, 282–286. Mathematical modeling for dynamic response analysis of partially coated or laminated plates - an energy approach.

[10] A.K. Lall, N.T. Asnani, and B.C. Nakra July 1987 *Transactions of American Society of Mechanical Engineers Journal of Vibration, Acoustics, Stress, and Reliability in Design* **109**, 241–247. Vibration and damping analysis of rectangular plate with partially covered constrained viscoelastic layer.

[11] Irving H. Shames and Clive L. Dym 1985 *Energy and Finite Element Methods in Structural Mechanics*. Hemisphere Publishing Corporation: New York, NY.

[12] Y.K. Lin 1967 *Probabilistic Theory of Structural Dynamics*. Robert E. Kreiger Publishing Co.: Malabar, Florida.

[13] M.R. Garrison, 1991, M.S. Thesis, Mechanical and Industrial Engineering Dept., Watson School, State University of New York at Binghamton, Vibration damping treatments for a plate subjected to random excitation.
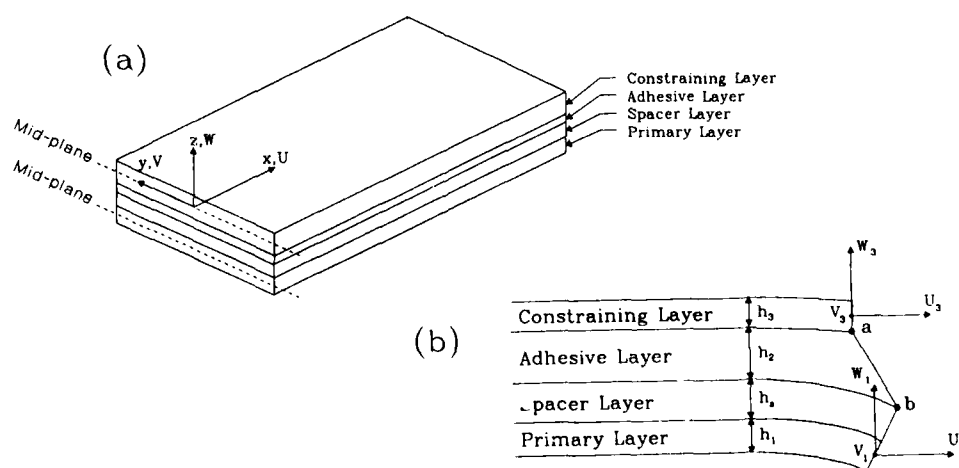
Figure 1. This figure shows (a) the sandwich plate cross-section, its coordinate system and (b) the deformed cross-sectional view.
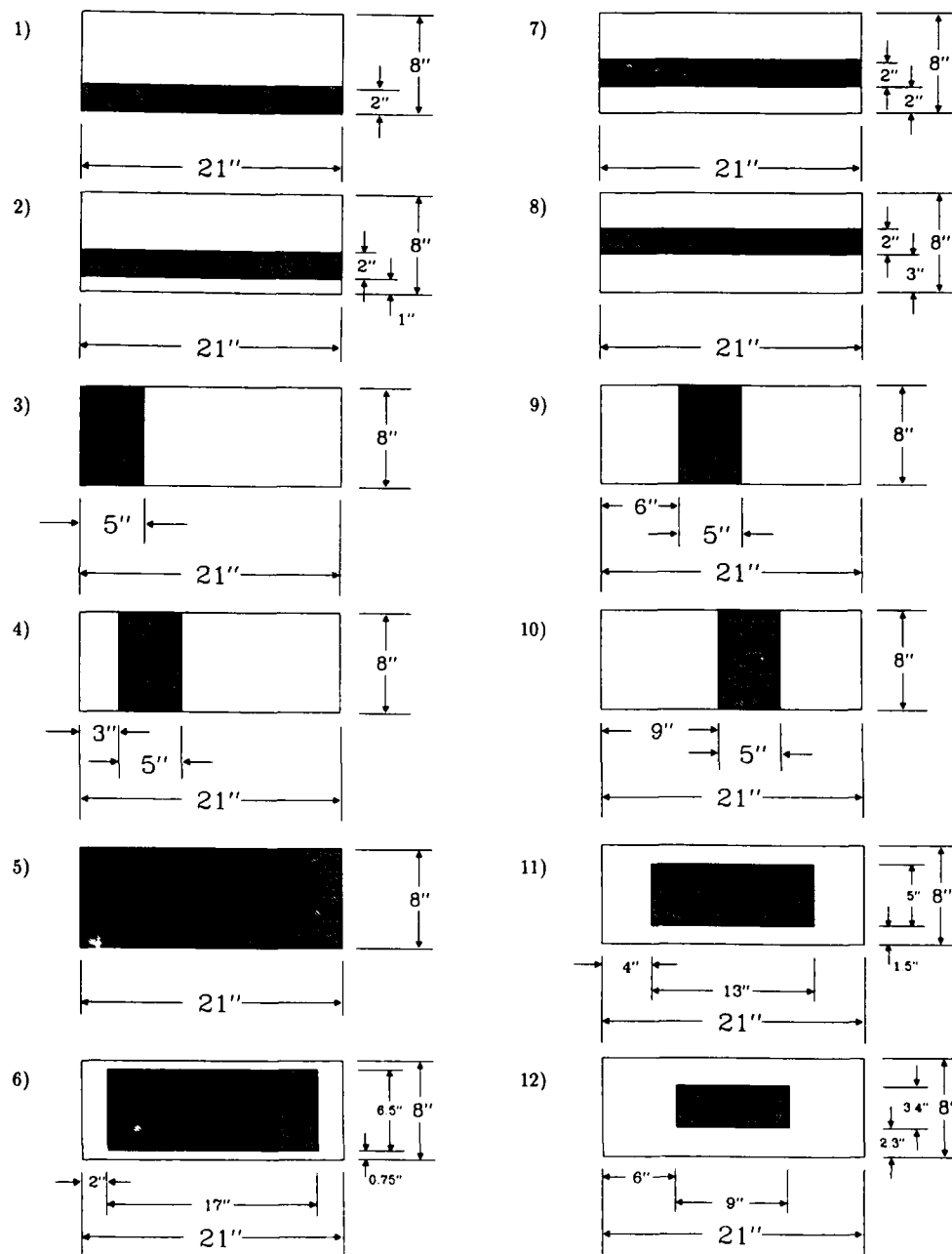
Figure 2. Geometrical description of partial coverage of the primary plate, using a 0.005 inch adhesive layer, a 0.1 inch thick spacer layer and a 0.01 inch thick constraining layer. The shaded region represents the damping treatment.

Predicted Random Response Spectra

Predicted Random Response Band Levels
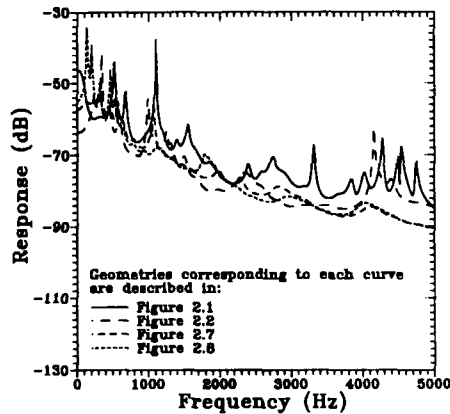
Figure 3. The predicted random response spectra due to a spatially uncorrelated, stationary Gaussian white noise, for the geometries shown in figure 2. An expression for the spatial average of the response spectrum is given in equation (16).
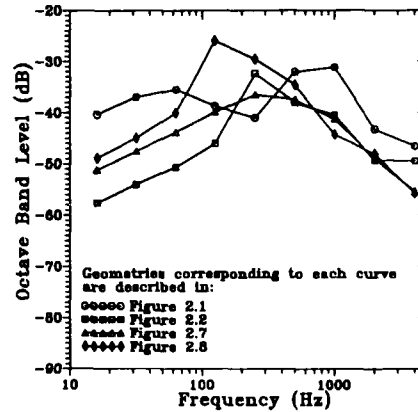
Figure 4. The predicted random response, plotted in normalized octave band levels for the geometries shown in figure 2. Each band level is obtained by a summation of the narrow band data over each octave band. The octave band levels will be normalized since the auto spectrum of the excitation is assumed to be unity.

Predicted Random Response Band Levels

Predicted Random Response Band Levels
Effect of Reduction in Coverage Area
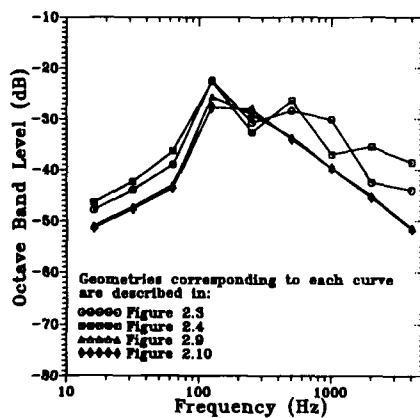
Figure 5. The predicted random response, plotted in normalized octave band levels, as in figure 4, for the geometries in figures 2.
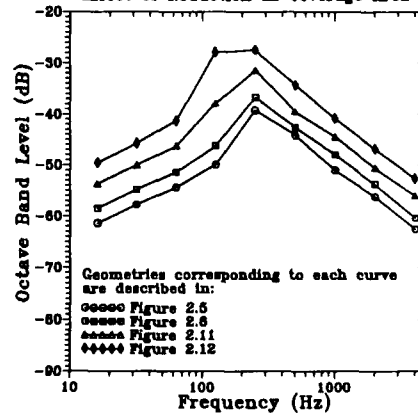
Figure 6. Predicted random response spectra, plotted in normalized octave band levels, as described in figure 4, for the geometries shown in figures 2.
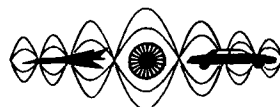
REDUCTION OF NOISE AT STEEL SHELLS WORKING BY
USING VIBRODAMPING COVERS OF MULTIPLE USE

Victor F. Asminin,
Sergey I. Chotelev, Yury P. Chepulsky
Voronezhsky Lesotechnichesky Institute
Voronezh 394000
USSR

In machine building, ship building and ship repairs, railway transport works and other industries there are widely used production operations connected with thin steel shells working. Important, that a steel shell itself is a dominating noise source where high frequency sound vibration (over 1000 Hz) appears as a consequence of its mechanic excitation.

In production such operations are considered as the most unfavourable to their noise factor (110-115 dBA).

Vibrodamping cover has been developed and a batch of it has been produced. It is fixed to a shell owing to its magnetic properties. The cover is made of rubber base with finely divided magnetic filler.

Vibrodamping cover of multiple use (VCMU) is rather elastic to provide its tight attaching to a shell, it has stable magnetic properties that may be lost in the result of structural failure during its longterm use.

The authors after theoretical and experimental investigations have developed the optimal content of magnetic filler in a rubber base to ensure highly effective damping properties of VCMU and reliability of magnetic attachment on the vibrating shell.

DEVELOPMENT OF VCMU

Rubber with finely divided magnetic filler is a well known conditioned material assuming magnetic properties at pulsed magnetization. Barita ferrite ($BaO.6Fe_2O_3$) posessing rather high magnetic properties at low cost is widely used as a magnetic filler. Such rubber possesses stable magnetic properties even in the conditions of intensive vibration, temperature interval of VCMU usage is from -10° to $+40^\circ C$.

But you hardly can find any information about using rubber with magnetic filler as damping covers. Thus, the following problems were put and solved:

- investigations in formulation and technology of rubber with magnetic filler to find out the effect on its magnetic and damping properties, optimization of compounding;
- has been received matematical expression of conditions of reliable magnetic fixing of VCMU to an excited shell;
- has been experimentally researched the effect of magnetic fixing to a cover in comparison with adhesive fixing on the efficiency of damping (loss factor η).

As a result the optimal content of the magnetic filler has been determined 85-87%(weight) when acceptable damping properties and reliable fixing are ensured. It has been proved that at the considerable amount of magnetic filler the rubber compounding of covering material practically does not influence the loss factor η. So, the rubber compounding for VCMU should be selected to meet the conditions of its presumptive application and chemical properties of acceptable rubbers.

To research damping properties of cover of rubber with magnetic filler the Oberst method has been used, according to which research samples were attached to a carrier steel rod in which torsional vibration was excited. This method allows to fix the cover being researched on a carrier steel rod both in adhesive and magnetic way.

Thus, one could observe the loss factor alteration in the system rod-cover in dependence of excitation frequency (f) and way of cover fixing.

Influence of excitation vibration f on η value of cover samples was analized using magnetized and not magnetized cover samples with magnetic filler of 87% (weight) at magnetic and adhesive way of fixing. Thickness of used cover samples was h_2=4mm, of rod h_1=2mm. There was determined advancing growth of η at magnetic fixing (in comparison with adhesive) with frequency of growth.

It was assumed that the effect , characterizing magnetic fixing of the cover is connected with friction of cover and rod on the contact surface - an additional factor of vibrating energy dissipation.

ESTIMATION OF VCMU ACOUSTIC EFFICIENCY

To estimate acoustic efficiency of VCMU and to prove positive effect of surface friction at fixing of cover a special method and plant for experimental research have been developed. The plant consists of a steel plate 500x500x2mm with angles fastened to a frame and excitation device placed under the plate. The excitation device is a motor with rotation speed n=1300rpm with a flexible shaft, on a free end of which a shell striker is fixed. Thus, in these excitation conditions noise emitted by the plate is assumed to be constant by aural perception, because time interval between pulses is T<0,05 s. The plant construction ensures stability of excitation conditions, that is very important for comparative testing. The testing was carried out in a reverberation chamber.

The results of measurements proved good efficiency of VCMU and magnetic fixing. Spectral analysys of acoustic emission of the plate with covers of different area showed efficiency of magnetic way of fixing to reduce sound vibration of frequency over 500-1000Hz.

Fig. 1 shows dependences of reduction of noise level ΔL against areas of cover S_2 and plate S_1 and magnetic (1) and adhesive(2) fixing. It is proved that damping efficiency is higher at magnetic fixing rather than at adhesive, that is caused by surface friction. In fig.2 there is a plot of Δ L as a function of magnetic attraction F_m. It is evident that growth of Δ L depends on growth of F_m value. At small values of F_m that can't provide cover fixing, Δ L does not grow, with growth of F_m value Δ L grows to a certain limit. At the constant value of F_m value of friction coefficient μ was varied by changing of the plate roughness and addition of rough lubricant (to imitate contamination).

In fig. 3 there is a plot of Δ L growth against μ , which is approximated by a linear function.

On the base of above-stated a conclusion was made that vibration energy W losses in a sandwich plate-cover (at magnetic fixing) are summed up of:

$$W = W_{int} + W_{out}$$

where W_{int} - internal friction losses inside cover, W_{out} - dry friction losses to cover and plate contact surface.

Thus damping cover can't be considered "hard" or "soft" type of covers, attached by adhesive where damping occurs only at the expense of internal losses in the cover material itself. VCMU forms the new - third - type of covers, named by the authors "movable".

RESULTS OF PRACTICAL APPLICATION OF VCMU

The main positive features of this facility for noise reduction
are: high acoustic efficiency, low price and easy use (at any culture
of production).

The experience of VCMU application at overhaul of refrigirator
shells showed reduction of noise in a shop for 10-12 dBA, inside a
shell - for 15 dBA. In both cases a shell is covered with vibrodamping
cover of multiple use for only 25-30% of the whole area of the shell.

BIBLIOGRAPHIC REFERENCES

1. Modern magnetic materials open up new markets.Eng. Materials and
Design, 1985, 29, Nr 7, p.p. 35-38
2. Oberst H. Über die DÄmpfung der Biegeschurngungen dÜnner Bleche
durch Festhaftende Beläge. Acoustiche Beihefte, 1952,2,4,p.181-195
3. Асминин В.Ф., Чепульский Ю.П., Юдин Е.Я. О возможности применения
магнитотвердых резин в вибропоглощающих покрытиях// Проблемы Охраны
Труда: Тез. докл. 5 Всесоюзной межвузовской конф. Рубежное, 16-18 сент.
1986г. - Рубежное, 1986.-С.138-139.
4. Асминин В.Ф. Магнитный способ фиксации вибродемпфирующего покрытия
и его влияние на акустическую эффективность/ Воронеж. Лесотехн. ин-т.-
Воронеж 1989.-13с.-Библиогр.:5 назв.-Рус.-Деп.в ВНИИТЭМР, №202мш89.

Figure 1

167

$\Delta L, dB(A)$

Figure 2

$\Delta L = -2.569 + 47.262 * M$
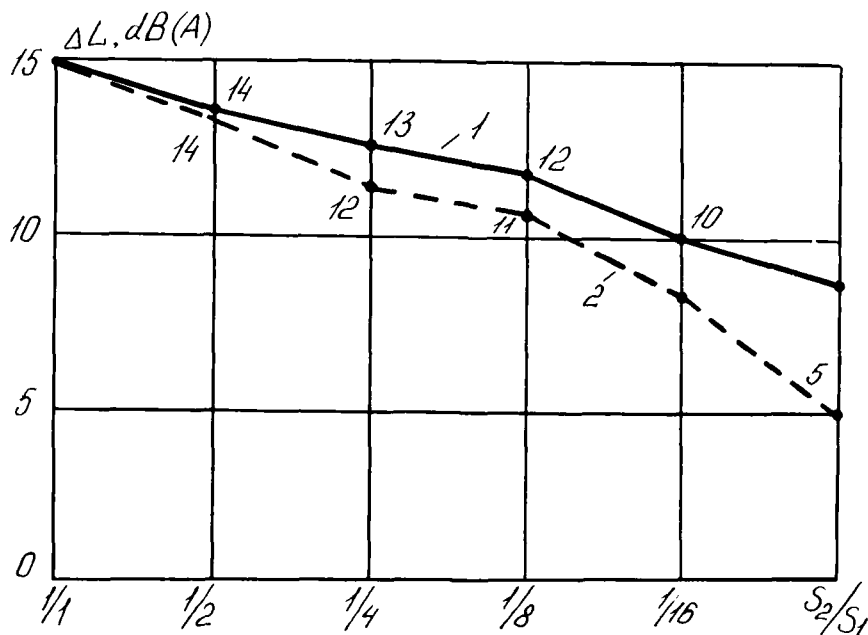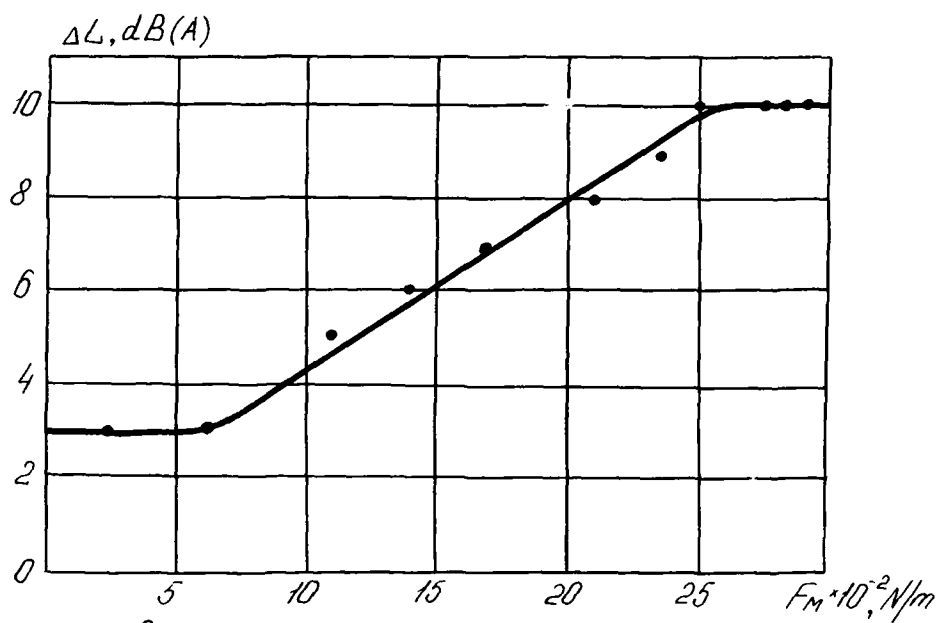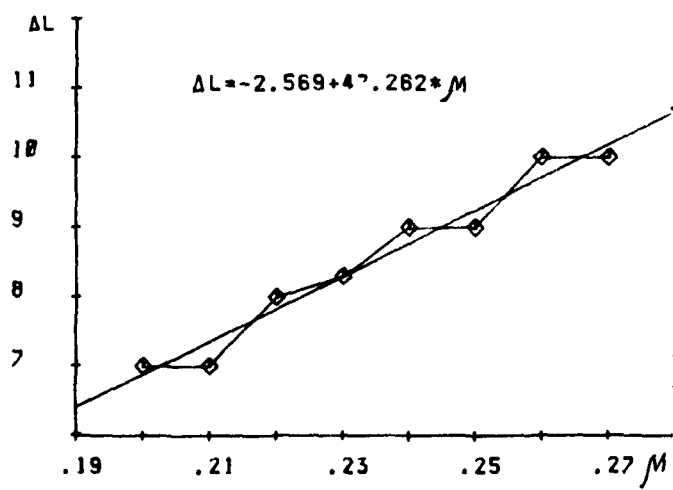
Figure 3

SIMULTANEOUS DESIGN OF ACTIVE VIBRATION CONTROL AND PASSIVE VISCOELASTIC DAMPING

Michele L. D. Gaudreault
Ronald L. Bagley
Brad S. Liebst
Department of Aeronautics and Astronautics
Air Force Institute of Technology
Wright-Patterson AFB, Ohio

ABSTRACT

Structural engineers have found that passive damping can reduce the amount of active damping required. Conversely, improperly designed passive damping can inadvertantly increase system reaction times, reducing control effectiveness. This paper presents several techniques for blending active vibration control and passive viscoelastic damping. Viscoelasticity is modelled using classical techniques. To avoid the dependence on initial conditions, solution techniques for sub-optimal, state independent solutions are developed, including a closed form solution for classical modelling techniques.

The advantages and disadvantages of the different solution techniques are discussed with respect to computation requirements and performance. A numerical example illustrates the similarities and differences of the various techniques.

INTRODUCTION

No existing method of vibration suppression offers an optimal blend of viscoelastic damping and active control. Traditional methods make the structure as rigid as possible, approximate the residual damping as viscous, and then design an optimal controller with respect to a predetermined cost function [1]. Although the controller effectively stabilizes resonances at specific frequencies, problems arise when the structure has modes at closely spaced frequencies. This is typically the case with large space structures, which often have closely spaced, low resonant frequencies. To stabilize the associated modes, passive dampers are added [2]. What is the "best" size for the passive dampers? If one does not design passive and active control elements simultaneously, higher weight costs are likely, which is important for space structures.

To overcome these problems, Mar encouraged viewing damping as a creative force in design [3]. Along these lines, several recent research efforts have been aimed at designing a damped structure, then designing a controller for it [4, 5, 6]. Simonian, Major, and Gluck point out that incorporating passive damping in an active control design must be done so that the deficiencies of one technology are compensated by the strengths of the other [7]. They propose an iterative scheme that uses modal strain energy analysis to determine the modal damping. A hybrid cost function is used to determine the tradeoffs. Fowler, et al., implemented a variation of this method in a computer program [8].

Gaudreault, et al. [9], present a method for simultaneous design of active vibration control and passive viscous damping. The concept is expanded to the case of viscoelastic damping in this paper.

OPTIMIZING VISCOELASTIC DAMPING AND ACTIVE CONTROL SIMULTANEOUSLY

We will consider problems in which the viscoelastic dampers have been constructed so that one component of strain dissipates the energy. Hence the mechanical properties of the damper can be derived

from a scalar relationship between stress and strain in the material. The standard linear viscoelastic model relating stress and strain is [10]

$$\sigma(t) + \sum_{i=1}^{k} b_i \frac{d^i \sigma(t)}{dt^i} = E_0 \epsilon(t) + \sum_{i=1}^{j} E_i \frac{d^i \epsilon(t)}{dt^i} \tag{1}$$

Assuming the viscoelastic material is initially undisturbed, the equations of motion of a structure in the Laplace domain using this classical model for viscoelastic damping are

$$s^2 \mathbf{M} \mathbf{x} + \frac{G_0 + \sum_{i=1}^{j} G_i s^i}{1 + \sum_{i=1}^{k} b_i s^i} \mathbf{K}_v \mathbf{x} + \mathbf{K} \mathbf{x} + \mathbf{B} \mathbf{u} = 0 \tag{2}$$

The matrix $\mathbf{K}_v$ is symmetric and can be written as $\mathbf{b}_v \mathbf{C} \boldsymbol{\Phi}_v$ where $\boldsymbol{\Phi}_v = \mathbf{b}_v{}^T$ and $\mathbf{C}$ is a diagonal matrix of the unknown damper coefficients.

Defining $b_0 = 1$ and multiplying through by $\sum_{i=0}^{k} b_i s^i$ one obtains

$$\mathbf{M} \sum_{i=0}^{k} b_i s^{i+2} \mathbf{x} + \mathbf{b}_v \left[\mathbf{C} \sum_{i=0}^{j} G_i s^i \boldsymbol{\Phi}_v \mathbf{x} \right] + \mathbf{K} \sum_{i=0}^{k} b_i s^i \mathbf{x} + \mathbf{B} \sum_{i=0}^{k} b_i s^i \mathbf{u} = 0 \tag{3}$$

Writing the equation in the time domain with the highest derivative on $\mathbf{x}$ separated out, and defining the passive damping forces as

$$\mathbf{v} = \mathbf{C} \boldsymbol{\Phi}_v \sum_{i=0}^{j} G_i \frac{d^i}{dt^i} \mathbf{x} \tag{4}$$

gives

$$b_k \mathbf{M} \frac{d^{k+2}}{dt^{k+2}} \mathbf{x} + \mathbf{M} \sum_{i=2}^{k+1} b_{i-2} \frac{d^i}{dt^i} \mathbf{x} + \mathbf{b}_v \mathbf{v} + \mathbf{K} \sum_{i=0}^{k} b_i \frac{d^i}{dt^i} \mathbf{x} + \mathbf{B} \sum_{i=0}^{k} b_i \frac{d^i}{dt^i} \mathbf{u} = 0 \tag{5}$$

Hence the highest derivative on $\mathbf{x}$ can be written as

$$\frac{d^{k+2}}{dt^{k+2}} \mathbf{x} = -\frac{1}{b_k} \mathbf{M}^{-1} \left[\mathbf{M} \sum_{i=2}^{k+1} b_{i-2} \frac{d^i}{dt^i} \mathbf{x} + \mathbf{K} \sum_{i=0}^{k} b_i \frac{d^i}{dt^i} \mathbf{x} \right] - \frac{1}{b_k} \mathbf{M}^{-1} \mathbf{B} \sum_{i=0}^{k} b_i \frac{d^i}{dt^i} \mathbf{u} - \frac{1}{b_k} \mathbf{M}^{-1} \mathbf{b}_v \mathbf{v} \tag{6}$$

This can also be written as

$$\frac{d^{k+2}}{dt^{k+2}} \mathbf{x} = -\frac{1}{b_k} \left[\mathbf{M}^{-1} \mathbf{K} \mathbf{x} + \mathbf{M}^{-1} \mathbf{K} b_1 \dot{\mathbf{x}} + \sum_{i=2}^{k} \left(b_{i-2} + \mathbf{M}^{-1} \mathbf{K} b_i \right) \frac{d^i}{dt^i} \mathbf{x} + b_{k-1} \frac{d^{k+1}}{dt^{k+1}} \mathbf{x} \right]$$
$$- \frac{1}{b_k} \mathbf{M}^{-1} \mathbf{B} \sum_{i=0}^{k} b_i \frac{d^i}{dt^i} \mathbf{u} - \frac{1}{b_k} \mathbf{M}^{-1} \mathbf{b}_v \mathbf{v} \tag{7}$$

By letting

$$\mathbf{y} = [\ \mathbf{x}^T \quad \dot{\mathbf{x}}^T \quad \ddot{\mathbf{x}}^T \quad \cdots \quad d^{k+1} \mathbf{x}^T / dt^{k+1} \ ]^T$$
$$\mathbf{a}_i = -\frac{b_i}{b_k} \mathbf{M}^{-1} \mathbf{K} \qquad\qquad i = 0, 1$$
$$\mathbf{a}_i = -\frac{1}{b_k} [b_{i-2} \mathbf{I} + \mathbf{M}^{-1} \mathbf{K} b_i] \qquad i = 2, \ldots, k$$
$$\mathbf{a}_{k+1} = -\frac{b_{k-1}}{b_k} \mathbf{I}$$

Eq. (7) can be written as the following first order system.

$$\dot{\mathbf{y}} = \begin{bmatrix} 0 & \mathbf{I} & 0 & \cdots & 0 \\ 0 & 0 & \mathbf{I} & \ddots & \vdots \\ \vdots & & \ddots & \ddots & 0 \\ 0 & 0 & \cdots & 0 & \mathbf{I} \\ \mathbf{a}_0 & \mathbf{a}_1 & \mathbf{a}_2 & \cdots & \mathbf{a}_{k+1} \end{bmatrix} \mathbf{y} + \begin{bmatrix} 0 \\ \vdots \\ 0 \\ -\frac{1}{b_k} \mathbf{M}^{-1} \mathbf{B} \end{bmatrix} \sum_{i=0}^{k} b_i \frac{d^i}{dt^i} \mathbf{u} + \begin{bmatrix} 0 \\ \vdots \\ 0 \\ -\frac{1}{b_k} \mathbf{M}^{-1} \mathbf{b}_v \end{bmatrix} \mathbf{v}$$

$$= \mathbf{A} \mathbf{y} + \mathbf{B}_1 \sum_{i=0}^{k} b_i \frac{d^i}{dt^i} \mathbf{u} + \mathbf{B}_v \mathbf{v} \tag{8}$$

170

For active control, we are interested primarily in constant gain feedback of $\mathbf{x}$ and $\dot{\mathbf{x}}$. Therefore we constrain

$$\mathbf{u} = \mathbf{G_r}[\ \mathbf{x}^T \quad \dot{\mathbf{x}}^T\ ]^T = \mathbf{G_r}\mathbf{I_r}^T\mathbf{y}$$

$$\text{where} \quad \mathbf{I_r}^T = \begin{bmatrix} \mathbf{I} & 0 & 0 & \cdots & 0 \\ 0 & \mathbf{I} & 0 & \cdots & 0 \end{bmatrix}$$

Note that $\mathbf{v}$ is of the form

$$\mathbf{v} = \mathbf{C}\begin{bmatrix} G_0\mathbf{\Phi_v} & G_1\mathbf{\Phi_v} & \cdots & G_0\mathbf{\Phi_v} & 0 & \cdots & 0 \end{bmatrix}\mathbf{y} \tag{9}$$
$$= \mathbf{C\Phi y} \tag{10}$$

In order to simultaneously design active feedback control and the damper coefficients, consider a variation of the standard linear quadratic regulator (LQR) performance index used in control theory in which the passive damping forces are weighted as well:

$$J = \int_{t_0}^{\infty} \frac{1}{2}\left([\mathbf{x}^T\ \dot{\mathbf{x}}^T]\mathbf{Q}_r\begin{Bmatrix} \mathbf{x} \\ \dot{\mathbf{x}} \end{Bmatrix} + \mathbf{u}^T\mathbf{R}\mathbf{u} + \mathbf{v}^T\mathbf{S}\mathbf{v}\right)dt \tag{11}$$

We have specific reasons for weighting the passive damping forces like the active control forces. When implementing a damping design using viscoelastic solids, one must take into account the temperature sensitivity of the damping medium. Modest changes in temperature due to absorbed mechanical energy can dramatically alter the damping properties of both fluids and solids. Hence we are motivated to limit in some fashion the mechanical energy absorbed by any given damper as well as limit the peak value of its damping force. The quadratic damping term weighted with $\mathbf{S}$ appearing in the performance index, Eq. (11), serves this end rather nicely.

Define $\mathbf{Q}$ such that

$$\mathbf{y}^T\mathbf{Q}\mathbf{y} = \begin{bmatrix} \mathbf{x}^T & \dot{\mathbf{x}}^T \end{bmatrix}\mathbf{Q}_r\begin{Bmatrix} \mathbf{x} \\ \dot{\mathbf{x}} \end{Bmatrix} \tag{12}$$

Thus the problem is to determine the $\mathbf{C}$ and $\mathbf{G_r}$ that:

$$\begin{aligned} \text{Minimize:} \quad J &= \int_{t_0}^{\infty} \tfrac{1}{2}(\mathbf{y}^T\mathbf{Q}\mathbf{y} + \mathbf{u}^T\mathbf{R}\mathbf{u} + \mathbf{v}^T\mathbf{S}\mathbf{v})dt \\ \text{subject to:} \quad \dot{\mathbf{y}} &= \mathbf{A}\mathbf{y} + \mathbf{B}_1\sum_{i=0}^{k}b_i\frac{d^i}{dt^i}\mathbf{u} + \mathbf{B_v}\mathbf{v} \\ \mathbf{u} &= \mathbf{G_r}\mathbf{I_r}^T\mathbf{y} \\ \mathbf{v} &= \mathbf{C\Phi y} \end{aligned} \tag{13}$$

Using the method of Lagrange multipliers to append the constraints to the performance index gives

$$\begin{aligned} J = \int_{t_0}^{\infty} &\left[\frac{1}{2}(\mathbf{y}^T\mathbf{Q}\mathbf{y} + \mathbf{u}^T\mathbf{R}\mathbf{u} + \mathbf{v}^T\mathbf{S}\mathbf{v}) - \boldsymbol{\lambda}_1^T(\dot{\mathbf{y}} - \mathbf{A}\mathbf{y} - \mathbf{B}_1\sum_{i=0}^{k}b_i\frac{d^i}{dt^i}\mathbf{u} - \mathbf{B_v}\mathbf{v})\right.\\ &\left. -\boldsymbol{\lambda}_2^T(\mathbf{u} - \mathbf{G_r}\mathbf{I_r}^T\mathbf{y}) - \boldsymbol{\lambda}_3^T(\mathbf{v} - \mathbf{C\Phi y})\right]dt \end{aligned}$$

Now $\mathbf{y}, \mathbf{u}$, and $\mathbf{v}$ are taken to be independent, which implies that $\mathbf{G_r}$ and $\mathbf{C}$ are independent of these quantities also. By definition, $\boldsymbol{\lambda}_1, \boldsymbol{\lambda}_2,$ and $\boldsymbol{\lambda}_3$ are independent of each other and of $\mathbf{y}, \mathbf{u}, \mathbf{v}, \mathbf{G_r}$ and $\mathbf{C}$. Hence, to minimize J, take its variation and set it equal to zero.

Since all variations are independent, we obtain the following equations to be satisfied in addition to the three constraint equations.

$$0 = \dot{\boldsymbol{\lambda}}_1 + \mathbf{A}^T\boldsymbol{\lambda}_1 + \mathbf{Q}\mathbf{y} \tag{14}$$

$$\mathbf{u} = -\mathbf{R}^{-1}\sum_{i=0}^{k}(-1)^i b_i\mathbf{B}_1^T\frac{d^i}{dt^i}\boldsymbol{\lambda}_1 \tag{15}$$

$$\mathbf{v} = -\mathbf{S}^{-1}\mathbf{B_v}^T\boldsymbol{\lambda}_1 \tag{16}$$

$$\boldsymbol{\lambda}_2^T = \boldsymbol{\lambda}_3^T = 0 \tag{17}$$

171

The multiple derivatives on $\boldsymbol{\lambda}_1$ in Eq. (15) are apparently disconcerting, but the special form of the problem resolves this difficulty for us rather nicely. Note that Eq. (14) yields $\dot{\boldsymbol{\lambda}}_1 = -\mathbf{Q}\mathbf{y} - \mathbf{A}^T\boldsymbol{\lambda}_1$, so

$$\mathbf{B}_1^T\dot{\boldsymbol{\lambda}}_1 = \mathbf{B}_1^T(-\mathbf{Q}\mathbf{y} - \mathbf{A}^T\boldsymbol{\lambda}_1) = -\mathbf{B}_1^T\mathbf{A}^T\boldsymbol{\lambda}_1 \tag{18}$$

since $\mathbf{B}_1^T\mathbf{Q} = 0$ for $k \geq 1$. Therefore,

$$\mathbf{B}_1^T\ddot{\boldsymbol{\lambda}}_1 = -\mathbf{B}_1^T\mathbf{A}^T\dot{\boldsymbol{\lambda}}_1 = \mathbf{B}_1^T\mathbf{A}^T(\mathbf{Q}\mathbf{y} + \mathbf{A}^T\boldsymbol{\lambda}_1) = (-1)^2\mathbf{B}_1^T(\mathbf{A}^T)^2\boldsymbol{\lambda}_1 \tag{19}$$

since $\mathbf{B}_1^T\mathbf{A}^T\mathbf{Q} = 0$ for $k \geq 2$. It follows easily that

$$\mathbf{B}_1^T\tfrac{d^i}{dt^i}\boldsymbol{\lambda}_1 = (-1)^i\mathbf{B}_1^T(\mathbf{A}^T)^i\boldsymbol{\lambda}_1 \qquad \text{for } i \leq k \tag{20}$$

Thus we have that

$$\mathbf{u} = -\mathbf{R}^{-1}\mathbf{B}_1^T\left(\sum_{i=0}^{k} b_i(\mathbf{A}^T)^i\right)\boldsymbol{\lambda}_1 \tag{21}$$

This can be written more compactly by letting $\mathbf{I}_A = \sum_{i=0}^{k} b_i(\mathbf{A}^T)^i$. Thus

$$\mathbf{u} = -\mathbf{R}^{-1}\mathbf{B}_1^T\mathbf{I}_A\boldsymbol{\lambda}_1 \tag{22}$$

Eqs. (13), (16), and (22) imply that

$$\mathbf{G}_r\mathbf{I}_r^T\mathbf{y} = -\mathbf{R}^{-1}\mathbf{B}_1^T\mathbf{I}_A\boldsymbol{\lambda}_1 \tag{23}$$
$$\mathbf{C}\boldsymbol{\Phi}\mathbf{y} = -\mathbf{S}^{-1}\mathbf{B}_v^T\boldsymbol{\lambda}_1 \tag{24}$$

Since we desire $\mathbf{G}_r$ and $\mathbf{C}$ to be constant, these two equations require that $\boldsymbol{\lambda}_1 = \mathbf{P}\mathbf{y}$ where $\dot{\mathbf{P}} = \mathbf{0}$. With this constraint and $\mathbf{y}$ not specified, Eqs. (23) and (24) lead to

$$\mathbf{G}_r\mathbf{I}_r^T = -\mathbf{R}^{-1}\mathbf{B}_1^T\mathbf{I}_A\mathbf{P} \tag{25}$$
$$\mathbf{C}\boldsymbol{\Phi} = -\mathbf{S}^{-1}\mathbf{B}_v^T\mathbf{P} \tag{26}$$

Now $\mathbf{I}_r^T\mathbf{I}_r = \mathbf{I}$, so

$$\mathbf{G}_r = -\mathbf{R}^{-1}\mathbf{B}_1^T\mathbf{I}_A\mathbf{P}\mathbf{I}_r \tag{27}$$

In our attempt to solve for $\mathbf{P}$, the multiple derivatives on $\mathbf{u}$ become a concern. But note that $\dot{\mathbf{u}} = \mathbf{G}_r[\ \dot{\mathbf{x}}^T\ \ddot{\mathbf{x}}^T\ ]^T = \mathbf{G}_r\mathbf{I}_r^T\hat{\mathbf{I}}_1\mathbf{y}$ where

$$\hat{\mathbf{I}}_1 = \begin{bmatrix} 0 & \mathbf{I} & 0 & \cdots & 0 \\ 0 & 0 & \mathbf{I} & \ddots & \vdots \\ \vdots & \vdots & \ddots & \ddots & 0 \\ \vdots & \vdots & & \ddots & \mathbf{I} \\ 0 & 0 & \cdots & \cdots & 0 \end{bmatrix} \tag{28}$$

It follows that

$$\frac{d^i}{dt^i}\mathbf{u} = \mathbf{G}_r\mathbf{I}_r^T\left(\hat{\mathbf{I}}_1\right)^i\mathbf{y}$$

Hence, we obtain

$$\sum_{i=0}^{k} b_i\frac{d^i}{dt^i}\mathbf{u} = \sum_{i=0}^{k} b_i\mathbf{G}_r\mathbf{I}_r^T\left(\hat{\mathbf{I}}_1\right)^i\mathbf{y} = \mathbf{G}_r\mathbf{I}_r^T\left[\sum_{i=0}^{k} b_i\left(\hat{\mathbf{I}}_1\right)^i\right]\mathbf{y}$$

Defining

$$\mathbf{I}_{12} = \left[\sum_{i=0}^{k} b_i\left(\hat{\mathbf{I}}_1\right)^i\right]$$

we can write $\dot{\mathbf{y}}$ as

$$\dot{\mathbf{y}} = \mathbf{A}\mathbf{y} - \mathbf{B}_1\mathbf{R}^{-1}\mathbf{B}_1^T\mathbf{I}_A\mathbf{P}\hat{\mathbf{I}}_r\mathbf{I}_{12}\mathbf{y} - \mathbf{B}_v\mathbf{S}^{-1}\mathbf{B}_v^T\mathbf{P}\mathbf{y} \tag{29}$$

172

Note that Eq. (14) can be written as

$$0 = P\dot{y} + A^T{}_1 y + Qy \tag{30}$$

Substituting for $\dot{y}$ in Eq. (30) gives

$$P(Ay - B_1 R^{-1} B_1^T I_A P \hat{I}_r I_{12} y - B_v S^{-1} B_v{}^T P y) + A^T P y + Qy = 0 \tag{31}$$

which leads to the non-symmetric quadratic matrix equation

$$PA + A^T P - PB_1 R^{-1} B_1^T I_A P \hat{I}_r I_{12} - PB_v S^{-1} B_v{}^T P + Q = 0 \tag{32}$$

This equation can be solved for P using the technique outlined in the Appendix.

Since Eq. (26) in general will not be satisfied by a diagonal C, we seek the diagonal C that gives the best least squares fit. Equivalently, minimize the Frobenius norm

$$\|C\Phi + S^{-1} B_v^T P\|_F \tag{33}$$

where P is the solution of Eq. (32). (The Frobenius norm of a matrix w is defined as the square root of the sum of the squares of the elements of the matrix - $\|w\| = [\sum \sum w_{ij}^2]^{1/2}$.) This is a linear minimization problem and has a closed form solution [9]. The elements of C are

$$c_{ii} = \frac{\sum_{j=1}^{n} \phi_{ij} w_{ij}}{\sum_{j=1}^{n} \phi_{ij}^2}; \qquad c_{ij} = 0 \quad \text{for} \quad i \neq j \tag{34}$$

If m is the number of damper coefficients, and n is the length of y, Φ and w are $m \times n$ matrices. For our problem,

$$w = -S^{-1} B_v{}^T P \tag{35}$$

This solution also has the added attraction of guaranteed positive values of c_i [9]. The active control gains are given by Eq. (27).

If the viscoelastic material is modelled using only one derivative on stress and only one on strain, we can consider methods of refining our choice of damper coefficients and active control gains. One method considers minimizing the average value of the cost functional over the unit ball $\|y_0\| = 1$. The second method minimizes the maximum value of the cost functional over the unit ball $\|y_0\| = 1$.

The value of the cost functional can be expressed in terms of the initial state:

$$J = \frac{1}{2} y_0^T P_1 y_0 \tag{36}$$

where P_1 satisfies

$$P_1(A + B_1 G_r I_r{}^T I_{12} + B_v C\Phi) + (A + B_1 G_r I_r{}^T I_{12} + B_v C\Phi)^T P_1 + (Q + I_r G_r{}^T R G_r I_r{}^T + \Phi^T C S C\Phi) = 0 \tag{37}$$

The average value of the cost functional over the unit ball is given by

$$\overline{J} = \frac{1}{2n} \text{trace } P_1 \tag{38}$$

Hence, minimizing the trace of P_1 minimizes the average value of J over the unit ball $\|y_0\| = 1$, regardless of system order. In this method, given C, one solves first for G_r using

$$G_r = -R^{-1} B_1^T I_A P I_r \tag{39}$$

where P satisfies

$$P(A + B_v C\Phi) + (A + B_v C\Phi)^T P - PB_1 R^{-1} B_1^T I_A P \hat{I}_r I_{12}(Q + \Phi^T C S C\Phi) = 0 \tag{40}$$

(This equation is derived using the method above, but assuming C is known. The matrices I_A and I_{12} have slightly differen definitions in Eq. (40) than in Eq. (32).) Then P_1 is calculated using Eq. (37). Iteration with respect to C is carried out until the trace of P_1 is minimized.
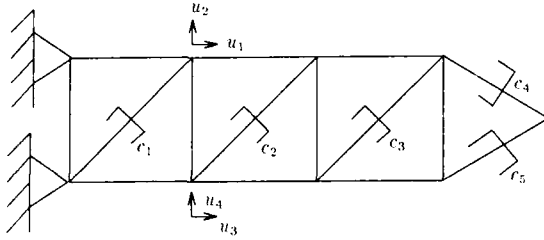
Figure 1: Example Problem – Truss Structure

A similar approach is used for minimizing the maximum value of J for all $\|\mathbf{y}_0\| = 1$. This approach requires determining the two norm of $\mathbf{P}_1$, since

$$J = \frac{1}{2}|\mathbf{y}_0^T\mathbf{P}_1\mathbf{y}_0| \leq \frac{1}{2}\|\mathbf{y}_0\|^2\|\mathbf{P}_1\|_2 = \frac{1}{2}\|\mathbf{P}_1\|_2 \tag{41}$$

In this method, iteration with respect to $\mathbf{C}$ is carried out until $\|\mathbf{P}_1\|_2$ is minimized, using Eqs. (37), (39), and (40). This approach might be very conservative in general, since the $\mathbf{y}_0$ that maximizes $\mathbf{P}_1$ may not be encountered very often.

EXAMPLE PROBLEM

Consider the two-dimensional viscoelastically damped aluminum truss in Fig. 1. In the figure, the u_i's represent active control forces, and the c_i's represent the unknown damper coefficients that we wish to determine. The viscoelastic material was modelled using one derivative on stress and one on strain. The parameters for the model were

$$
\begin{aligned}
G_0 &= 6.8948 \times 10^3 \text{ N/m}^2 \quad (1.0 \text{ lb/in}^2) \\
G_1 &= 4.8264 \times 10^4 \text{ N-s/m}^2 \quad (7.0 \text{ lb-sec/in}^2) \\
b_1 &= 0.001 \text{ sec}
\end{aligned}
$$

Using the method presented above the equations of motion can be written in the state space form:

$$\dot{\mathbf{y}} = \mathbf{A}\mathbf{y} + \mathbf{B}_1 \sum_{i=0}^{k} b_i \frac{d^i}{dt^i}\mathbf{u} + \mathbf{B}_v\mathbf{v} \tag{42}$$

The state space vector $\mathbf{y}$ is 42×1. There are four control inputs and five damping coefficients, so $\mathbf{u}$ is 4×1 and $\mathbf{C}$ is 5×5 diagonal. Therefore, $\mathbf{A}$ is 42×42, $\mathbf{B}$ is 42×4, $\mathbf{B}_v$ is 42×5, and $\mathbf{\Phi}$ is 5×42. The parameters of the system are:

$$
\begin{aligned}
EA &= 1.5179 \times 10^6 \text{ N} \quad (3.4125 \times 10^5 \text{ lb}) \\
\rho A &= 8.3564 \text{ N-s}^2/\text{m}^2 \quad (1.212 \times 10^{-3} \text{ lb-s}^2/\text{in}^4)
\end{aligned}
$$

The length of the horizontal elements is 4.572m (15 ft) while the vertical elements are 3.048 m (10 ft). The length of the two elements with dampers c_4 and c_5 is 4.819 m (15.81 ft). Thus, the diagonal elements with dampers c_1, c_2, and c_3 are 5.495 m (18.03 ft) in length. There are 0.454 kg (1 lbm) point masses at every node, with an 0.907 kg (2 lbm) point mass at the tip. The undamped natural frequencies ranged from 1.2 hz to 50.8 hz.

The state weighting matrix $\mathbf{Q}_x$ was chosen such that $\mathbf{y}^T\mathbf{Q}\mathbf{y}$ equalled the total mechanical energy in the system. Thus $\mathbf{Q}_x$ was formed using the mass and stiffness matrices, $\mathbf{M}$ and $\mathbf{K}$. The weighting matrices are

$$\mathbf{Q}_x = \begin{bmatrix} \mathbf{K} & 0 \\ 0 & \mathbf{M} \end{bmatrix}, \quad \mathbf{R} = 0.1\mathbf{I}, \quad \mathbf{S} = 0.01\mathbf{I} \tag{43}$$

Table 1: Example Problem Results

	min $\|\mathbf{H}\|_F$	min trace $\mathbf{P}$	min $\|\mathbf{P}\|_2$
c_1	19.43	19.90	24.69
c_2	13.22	13.05	17.64
c_3	13.48	13.59	22.32
c_4	18.51	18.20	23.02
c_5	17.85	17.52	18.91
time	2 min	20 hr 4 min	20 hr 43 min
ζ – Passive only	.0005 to .0400	.0005 to .0397	.0007 to .0533
ζ – Complete Solution	.0110 to .0409	.0110 to .0405	.0116 to .0537

The values of the damper coefficients for the three solution techniques, along with their approximate computation times, are given in Table 1. The solution techniques were run on a VAX 6420 using MATLAB routines. The minimization algorithm utilized is the Nelder-Mead simplex method [11]. The active control gains are computed using Eq. (27). The range of damping ratios with just the viscoelastic portion of the solution implemented is shown in Table 1, as well as the range of damping ratios for the complete solution. Although the active control did not noticeably increase the higher damping ratios, there was a significant improvement in the lightly damped modes, which tended to occur at the lower frequencies.

SUMMARY

The need for simultaneous optimization of damping and active vibration control is driven primarily by the potential use of large flexible structures in space. This paper presents several new design techniques to determine optimal blending of passive viscoelastic damping and active vibration control. The techniques are based on modified versions of the standard linear quadratic regulator cost functional of optimal control theory. Two iterative techniques are developed in addition to a closed form solution.

The proposed cost functional treats passive damping as a separate control force, which results in an additional energy term in the cost functional. The closed form solution is a least squares solution. One iterative technique minimizes the maximum value of the proposed cost functional. The other iterative technique minimizes the average value of the proposed cost functional. All three techniques yielded similar performance relative to each other, although the closed form solution took considerably less computation time.

ACKNOWLEDGEMENT

REFERENCES

[1] Soovere, J., and Drake, M. L., *Aerospace Structures Technology Damping Design Guide, Vol. I: Technology Review*, AFWAL TR-84-3089-VOL-1, Dec. 1985. (AD-A178313)

[2] Lasiecka, I., and Triggiani, R., "Increasing the Margin of Stability of Arbitrarily Finite Modes of Flexible Large Space Structures with Damping," AFOSR-TR-890328, Dec. 1988. (AD-A206487)

[3] Mar, J. W., "Some Musings on How to Make Damping a Creative Force in Design," *AFWAL Vibration Damping 1984 Workshop Proceedings*, Nov. 1984. (AD-A152547)

[4] Burns, J. A., and Fabiano, R. H., "Feedback Conrol of a Hyperbolic Partial-Differential Equation with Viscoelastic Damping," AFOSR TR-880575, Apr. 1988. (AD-A192896)

[5] Hannsgen, K. B., and Wheeler, R. L., "Energy Decay and Boundary Control for Distributed Parameter Systems with Viscoelastic Damping," AFOSR TR-89-1895, Jul. 1989. (AD-A216468)

[6] Oden, J. T., Tworzydlo, W. W., and Martins, J. A., "Computational Methods for Nonlinear Dynamic Problems in Solid and Structural Mechanics: Progress in the Theory and Modeling of Friction and in the Control of Dynamical Systems with Frictional Forces," AFOSR TR 89-0627, Mar 89. (AD-A208763)

[7] Simonian, S. S., Major, C. S., and Gluck, R., "An Experimental Study of Passive Damping and Active Control of Large Space Structures," *AFWAL Vibration Damping 1984 Workshop Proceedings*, Nov. 1984. (AD-A152547)

[8] Fowler, B. L., Gibson, W. C., Smith, K. E., and Johnson, C. D., "Passive Damping Techniques for Beam Control Structures," AFWL TR-88-97, Apr. 1989. (AD-B133313)

[9] Gaudreault, M. L. D., Liebst, B. S., and Bagley, R. L., "Simultaneous Design of Active Vibration Control and Passive Viscous Damping," AIAA Guidance, Navigation, and Control Conference. Aug 12-14, 1991, p.90. (AIAA 91-2611)

[10] Christensen, R. M., *Theory of Viscoelasticity: An Introduction*, Academic Press, New York, 1971.

[11] Woods, D. J., Report 85-5, Dept. of Math Sciences, Rice University, May 1985.

APPENDIX

This appendix describes the method for solving Eqs. (32) and (40). The method will be demonstrated using Eq. (32):

$$\mathbf{Q} + \mathbf{PA} + \mathbf{A}^T\mathbf{P} - \mathbf{PB}_1\mathbf{R}^{-1}\mathbf{B}_1^T\mathbf{I}_A\mathbf{P}\hat{\mathbf{I}}_r\mathbf{I}_{12} - \mathbf{PB}_v\mathbf{S}^{-1}\mathbf{B}_v{}^T\mathbf{P} = 0$$

This equation is quadratic in $\mathbf{P}$, but is not solvable by any handy algorithms. Newton-Raphson is a standard technique and we employed it as follows: First define

$$\mathbf{Q(P)} = \mathbf{Q} + \mathbf{PA} + \mathbf{A}^T\mathbf{P} - \mathbf{PB}_1\mathbf{R}^{-1}\mathbf{B}_1^T\mathbf{I}_A\mathbf{P}\hat{\mathbf{I}}_r\mathbf{I}_{12} - \mathbf{PB}_v\mathbf{S}^{-1}\mathbf{B}_v{}^T\mathbf{P} \qquad (44)$$

We wish to find $\mathbf{P}$ such that $\mathbf{Q(P)}=0$. Approximate $\mathbf{Q(P)}$ by

$$\mathbf{Q(P)} = \mathbf{Q(P_0)} + D\mathbf{Q[P_0]}(\mathbf{P} - \mathbf{P_0}) + o(\|\mathbf{P} - \mathbf{P_0}\|) \qquad (45)$$

where the operator $D\mathbf{Q[P_0]}$ represents the Fréchet derivative of $\mathbf{Q}$ at $\mathbf{P_0}$ and $o(\mathbf{P})$ represents terms of higher order. Let $\mathbf{H} = \mathbf{P} - \mathbf{P_0}$.

Since $\mathbf{Q}$ is a function of $\mathbf{P}$,

$$D\mathbf{Q[P_0]}(\mathbf{H}) = \frac{d}{d\alpha}\mathbf{Q(P_0} + \alpha\mathbf{H)}|_{\alpha=0} \qquad (46)$$

Carrying out the calculation,

$$D\mathbf{Q[P_0]}(\mathbf{H}) = \mathbf{HA} + \mathbf{A}^T\mathbf{H} - \mathbf{HB}_1\mathbf{R}^{-1}\mathbf{B}_1^T\mathbf{I}_A\mathbf{P}_0\hat{\mathbf{I}}_r\mathbf{I}_{12} - \mathbf{P}_0\mathbf{B}_1\mathbf{R}^{-1}\mathbf{B}_1^T\mathbf{I}_A\mathbf{H}\hat{\mathbf{I}}_r\mathbf{I}_{12}$$
$$-\mathbf{HB}_v\mathbf{S}^{-1}\mathbf{B}_v{}^T\mathbf{P}_0 - \mathbf{P}_0\mathbf{B}_v\mathbf{S}^{-1}\mathbf{B}_v{}^T\mathbf{H} \qquad (47)$$

This may not look much better than $\mathbf{Q(P)}$, but at least it is linear in $\mathbf{H}$. The equation we wish to solve for $\mathbf{H}$ is

$$D\mathbf{Q[P_0]}(\mathbf{H}) + \mathbf{Q(P_0)} = 0 \qquad (48)$$

Note that this equation is similar to a Lyapunov equation, although some of the terms do not have $\mathbf{H}$ on the left or right, but in the middle. To get around this difficulty, note that $\hat{\mathbf{I}}_r$ is an identity matrix with the bottom third diagonal all zeros. Therefore approximate $\mathbf{H}\hat{\mathbf{I}}_r$ and $\mathbf{H}\widehat{\mathbf{I}_{12}}$ by $\mathbf{H}$ where appropriate in $D\mathbf{Q[P_0]}(\mathbf{H})$. This results in the simplification,

$$D\mathbf{Q[P_0]}(\mathbf{H}) = \mathbf{HA} + \mathbf{A}^T\mathbf{H} - \mathbf{HB}_1\mathbf{R}^{-1}\mathbf{B}_1^T\mathbf{I}_A\mathbf{P}_0\hat{\mathbf{I}}_r\mathbf{I}_{12} - \mathbf{P}_0\mathbf{B}_1^T\mathbf{I}_A\mathbf{H}$$
$$-\mathbf{HB}_v\mathbf{S}^{-1}\mathbf{B}_v{}^T\mathbf{P}_0 - \mathbf{P}_0\mathbf{B}_v\mathbf{S}^{-1}\mathbf{B}_v{}^T\mathbf{H} \qquad (49)$$

With this approximation,

$$D\mathbf{Q[P_0]}(\mathbf{H}) + \mathbf{Q(P_0)} = 0 \qquad (50)$$

becomes a Lyapunov equation, easily solved by a simple routine in MATLAB. The updated estimate of $\mathbf{P}$ is $\mathbf{P_0} + \mathbf{H}$.
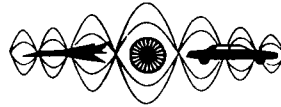
SECOND INTERNATIONAL CONGRESS ON
RECENT DEVELOPMENTS IN AIR- AND
STRUCTURE-BORNE SOUND AND VIBRATION
MARCH 4-6, 1992 AUBURN UNIVERSITY, USA

A SUBRESONANT METHOD FOR MEASURING MATERIAL DAMPING
IN LOW FREQUENCY UNIAXIAL VIBRATION

George A. Lesieutre
Kiran M. Govindswamy
Aerospace Engineering Department
The Pennsylvania State University
University Park, PA 16802
U.S.A.

ABSTRACT

A method for accurately determining the inherent, possibly low, damping of engineering materials at low frequencies is presented. A specimen made of the material to be characterized is connected in series with a reference specimen of low or calibrated damping and forced in low frequency (<10 hz) uniaxial vibration. Because the specimens are instrumented identically with strain gages and forced at frequencies orders of magnitude lower than any resonant frequencies, the phase difference between the resulting strain signals is proportional to the difference in damping between the specimens. The phase difference at a given forcing frequency is measured in the time domain as a time delay between the signals. Relative material loss factors (tangents of phase angles) are measured with accuracy better than 10^{-4}. Potential applications are discussed.

INTRODUCTION AND BACKGROUND

Passive damping is important because it governs resonant response levels and transient settling times of uncontrolled dynamic systems. However, when structural motion due to operational disturbances must be minimized to meet demanding performance requirements, control augmentation may be appropriate. An accurate description of the dynamic behavior, including damping, of such precision structures is necessary to facilitate the design of robust, fast-responding, linear-time-invariant structural control systems [1].

The damping of large precision space truss structures is of particular interest. Several features of such structures indicate the need for a test method capable of measuring low damping in low frequency axial vibration:

• Advanced composite materials are ideal for such applications because of excellent tailorable mechanical and thermal properties, as well as the possibility of modest levels of damping [2]. For reasons of precision, integrity and predictability of performance, composite structures often have relatively few mechanical joints at which relative motion of adjacent surfaces is allowed. One result of such construction is that structural damping can be dominated by material contributions and can often be quite low (modal damping ratios of <0.001) [3].

• In addition, large truss structures being considered for future space missions will often have vibration modes with frequencies below 1 hz [4]. For typical member sizes, especially with pinned end connections, individual struts experience such global vibration as oscillatory, low frequency axial loads [2].

Available resonant and subresonant test methods are inadequate for direct characterization of low damping in low frequency axial vibration. Resonant techniques, generally reliable for low damping measurements, require the use of impractically large specimens or added mass to lower the natural frequency into a range of interest. Due to the difficulty of measuring very small phase angles, subresonant techniques in common use are typically limited to the characterization of relatively high damping materials such as viscoelastic polymers [5].

The goal of this work was to develop and demonstrate a test method capable of accurately measuring the frequency-dependent low damping of materials in low frequency axial vibration.

177

OVERVIEW OF THE TECHNIQUE AND RELATED WORK

In the subject technique, a specimen made of the material to be characterized is connected in series with a reference specimen of low or calibrated damping and forced in low frequency uniaxial vibration. The specimens are instrumented identically with strain gages and forced at frequencies orders of magnitude lower than any resonant frequencies, ensuring that the phase difference between the resulting strain signals, $\Delta\phi$, is proportional to the difference in axial damping between the specimens. In this approach, the phase difference at a given forcing frequency is measured directly in the time domain as a delay or time shift between the signals.

Consider a time harmonic uniaxial stress, σ, common to both specimens:

$$\sigma = \sigma_0 e^{i\omega t} \tag{1}$$

where σ_0 is the amplitude, and ω is the circular frequency. Material damping causes the strain to lag the stress:

$$\varepsilon = \varepsilon_0 e^{i(\omega t - \phi)} \tag{2}$$

where ε_0 is the cyclic strain amplitude and ϕ, the loss angle, is non-negative. Note that the loss angle will generally be different for the reference and primary specimens. Since the strain field in the specimens is homogeneous, the material loss factor, η, is related to the loss angle:

$$\eta = \tan(\phi) \tag{3}$$

And, for "light" damping, the effective modal damping ratio, ζ, for a larger structure made from the material is:

$$\zeta = 0.5\ \eta \tag{4}$$

The small relative loss factor of the specimen with respect to the reference specimen, η_{rel}, is given by:

$$\eta_{rel} = \eta_{spec} - \eta_{ref} = \tan(\phi_{spec}) - \tan(\phi_{ref}) \sim \Delta\phi \tag{5}$$

Several other approaches have been used to experimentally determine axial material damping properties at low frequencies. A classical approach involves measuring the area of the stress-strain hysteresis loop obtained under cyclic loading [3, 4, 6, 7]. The area enclosed by the hysteresis loop, A, is given approximately by:

$$A = \pi\sigma_0\varepsilon_0\ \eta \tag{6}$$

The accuracy of the hysteresis loop area technique can be sensitive to truncation and numerical integration errors [6]. Moreover, the use of hydraulic testing machines and associated load cells can introduce undesirable mechanical noise and phase errors [2, 8].

Gibson [4] estimated the area of the hysteresis loop using an electromechanical plotter. However, the useful frequency range was limited to below 0.1 hz due to phase lags introduced by the plotter. More recently, Ray et al. [7] and Wren and Kinra [8] employed a FFT technique to transform the generally noisy stress and strain signals to the frequency domain and retained the 6 terms nearest to the excitation frequency to reconstruct the time signals and hysteresis loops. Lin et al. [6] used a strain–strain hysteresis loop technique with truncation error compensation to determine the relative loss factors of two materials.

This paper describes an experimental technique developed to make accurate phase and damping measurements in the time domain. Initial error analysis indicated the feasibility of making low frequency damping measurements of suitable accuracy ($<10^{-4}$ radians) using available, moderately-priced precision instrumentation.

EXPERIMENTAL APPARATUS AND PROCEDURE

Fig.1 shows a schematic of the experiment setup. Cylindrical specimens of various materials were instrumented "identically" with a pair of semiconductor strain gages (Micron Instr. SS-080-050-500P, gage factor of 140) aligned with the specimen axis, on diametrically opposite sides. A half bridge circuit was used for increased sensitivity to axial strains, with two passive gages for temperature compensation. Both strain bridges were excited by a single precision voltage source (Lambda Electronics LQ411). Polycrystalline aluminum was chosen as a reference material because its loss factor at low frequencies and strain levels in uniaxial vibration is very small ($<10^{-4}$).

An electrostrictive actuator (AVX Corp. CO60020A) was used to force axial vibration of the specimens. The specimens were sized on the basis of the actuator characteristics, with nominal dimensions of 20 mm length, 4 mm outer diameter and 3 mm inner diameter. A linear region of actuator operation (50 ± 14 Volts) was identified in an initial calibration run. The actuator was connected in series with the reference and primary specimens, and the assembly placed under a compressive preload of about 40 N in a micrometer clamp. The compressive preload ensured that the specimens remained loaded throughout testing.

A function generator (HP 3314A) was used in conjunction with a power amplifier (Burleigh Instr. PZ-150M) to drive the actuator. Electrically-shielded wires and boxes were used to reduce noise, and differential connections used to avoid ground loops. The strain signals were digitized by a 16 bit A/D board (National Instr. NB-MIO16X) installed in a Macintosh IIfx. Digitized data was acquired and partially analyzed under the control of a Virtual Instrument (V.I.) built using LabVIEW software (National Instr.). Fig. 2 shows the front panel of the V.I. including two axial strain waveforms acquired during a test of different aluminum specimens.
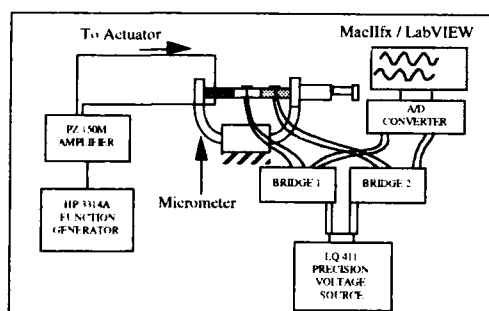
Figure 1--A schematic of the experimental setup.   Figure 2--Front panel of the Data Acquisition V.I.
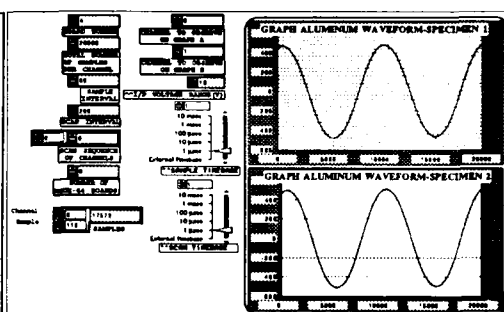
DATA ANALYSIS

A design stage uncertainty analysis was performed to identify the parameters that govern the accuracy of the phase measurement [9]. The results were used to define the following data analysis approach.

The sampling rate and/or the number of points per channel are varied with frequency to ensure that a fixed, integer number of cycles are sampled in each channel at the specified forcing frequencies. The D.C. bias in each channel is removed by numerical averaging and approximate signal zero crossing times are identified on each channel. In the vicinity of each of these crossings, least square lines are fit over a small fraction of a cycle to better estimate the "true" zero crossing times. These zero crossing times are then corrected to account for the time delay in sampling between channels, and the net time delay (phase difference) between the channels is found.

The phase difference between channels is calculated at all the available zero crossings and a mean loss factor and the standard deviation are calculated. This statistical approach employs "noisy" time domain data directly, avoiding possible phase corruption associated with various filter concepts.

INITIAL RESULTS

At the time of writing of this paper, some testing was still in progress. In an initial run, two channels of sine signals were acquired directly from the function generator. The amplitude of the signals was adjusted to simulate those that would ensue from two instrumented aluminum specimens under test conditions. The oscillation frequency was varied from 0.5 hz to 10 hz and the apparent loss factor and the standard deviation were computed at each frequency. Six thousand points were sampled per channel and six cycles were used for the calculations. The sampling rate ranged from 500 hz to 10,000 s⁻¹ for forcing frequencies ranging from 0.5 to 10 hz, respectively.

The apparent loss factor varied randomly about zero, with no frequency-dependent trend observed. The average of these apparent loss factors was 6.1×10^{-5} radians (3.5×10^{-3} degrees), with typical standard deviations of 2.4×10^{-4}. At a forcing frequency of 1 hz, this phase angle corresponds to a time lag of 9.76 μsec.

A test run was made with two aluminum specimens over the frequency range from 0.5 to 10 hz. The relative loss factors were very repeatable, with standard deviations on the order of those obtained using the function generator signals directly. However, the loss factors did vary with frequency, with values on the order of 10^{-3}. These are believed to be real differences arising from the use of excessive adhesive on the specimens.

179

POTENTIAL APPLICATIONS

As previously noted, this technique is suitable for characterization of the possibly low damping of structural materials envisioned for use in large precision space structures. In addition, it is also well-suited for accurate characterization of materials with higher damping, such as viscoelastic polymers.

The damping of a structural component is also sensitive to the kind, location and density of any microstructural flaws present. Because specimens are subject to a macroscopically homogeneous strain field in this technique, it might be especially useful for non–destructive evaluation of materials with uniformly-distributed flaws. Such materials include ceramic composites subjected to repeated high-temperature thermal cycling.

Finally, this technique could be used in any application requiring an accurate determination of the phase difference between two sinusoidal signals.

SUMMARY

A low-cost method for accurately determining the possibly low inherent damping of various engineering materials at low frequencies in uniaxial vibration has been developed. Accuracies of better than 10^{-4} in loss factor have been demonstrated. This approach is distinguished from others by:

• the use of identically-instrumented reference and primary specimens to determine relative damping;

• the determination of small phase differences between noisy signals directly in the time domain as time delays between zero crossings; and

• the use of statistical methods and straightforward data reduction to provide high, quantifiable accuracy.

REFERENCES

1. von Flotow, A.H. and Vos, D.W., "The Need for Passive Damping in Feedback Controlled Flexible Structures," *Proc.Conf. on Recent Advances in Active Control of Sound and Vibration* , pp 593-603, 1991.

2. Lesieutre, G.A., "Graphite/Metal and Carbon-Carbon Composites for Precision Maneuvering Spacecraft," NSWC TR 89-332, 11 August, 1989.

3. Smith, S. and Yee, R.C., "A New Technique for the Characterization of Structural Materials under Dynamic Loading," AIAA Paper 78-510.

4. Gibson, R.F., "Vibration Damping Characteristics of Graphite/Epoxy Composites for Large Space Structures," NASA Conference Publication 2215, *Large Space Systems Technology - 1981*, 1982, pp. 123-132.

5. Read, B.E., and Dean, G.D., "The Determination of Dynamic Properties of Polymers and Composites," John Wiley & Sons, New York, 1978.

6. Lin, C.H. and Plunkett, R., "A Low-Frequency Axial Oscillation Technique for Composite Material Damping Measurement," Journal of Composite Materials, Vol. 23, January 1989, pp. 92-105.

7. Ray, A.K., Kinra, V.K., Rawal, S.P.and Misra, M.S., "Specific Damping Capacity of Metal-Matrix Composites in Tension-Tension Fatigue," Damping 1986 Proceedings, FC-1-CF-16 (1986).

8. Wren, G.G. and Kinra, V.K., "Damping in Metal Matrix Composites: Theory and Experiment," Department of Aerospace Engineering Report, Texas A&M University, February 1990.

9. Govindswamy, K.M., "A Subresonant Method for Measuring Material Damping in Low-Frequency Uniaxial Vibration," M.S. Thesis, Aerospace Engineering, The Pennsylvania State University, 1992.
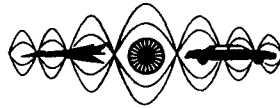
SECOND INTERNATIONAL CONGRESS ON
RECENT DEVELOPMENTS IN AIR- AND
STRUCTURE-BORNE SOUND AND VIBRATION
MARCH 4-6, 1992   AUBURN UNIVERSITY, USA

Passive Damping Technology

Eric M. Austin
Conor D. Johnson, Ph.D.
CSA Engineering, Inc.
2850 West Bayshore Road
Palo Alto, CA 94303
U.S.A.

ABSTRACT

This paper presents a brief review of techniques for designed-in passive damping for noise and vibration control. Designed-in passive damping for structures is usually based on one of four damping technologies: viscoelastic materials, viscous fluids, magnetics, or passive piezoelectrics. These methods are discussed and compared. The technology of using viscoelastic materials for passive damping is discussed in more detail than the other methods since it is presently the most applicable for surface treatments for noise control. Testing and characterization of viscoelastic materials and design methods for passive damping are discussed. An example showing the benefits of a passive damping treatment for an acoustic problem is presented.

INTRODUCTION

Passive damping plays a major role in suppressing structure-borne sound and vibrations. The primary effects of increased damping in a structure are reduction of vibration amplitudes at resonances, with corresponding decreases in stresses, displacements, fatigue, and sound radiation; increase sound isolation (transmission loss) of the structure above the frequency at which the propagation speed of the bending wave in the structure equals the speed of sound in air; attenuation of structure-borne waves propagating in the structure; and more rapid decay of free vibrations and therefore reduction of noise generation. Passive damping may be broken into two classes: inherent and designed-in. Inherent damping is damping that exists in a structure due to friction in joints, material damping, rubbing of cables, etc. The level of inherent damping in a structure is usually less than 2 percent structural. Designed-in damping refers to passive damping that is added to a structure by design. This damping supplements inhe; nt damping, and it can increase the passive damping of a structure by substantial, predictable amounts.

Designed-in passive damping for structures is usually based on one of four damping technologies: viscoelastic materials, viscous fluids, magnetics, or passive piezoelectrics. Each of these damping mechanisms must be understood in order to select the most appropriate type of damping treatment. The paragraphs below describe each mechanism, and Table 1 presents a comparison.

Viscoelastic Materials

Passive damping using viscoelastic materials (VEMs) is found widely in both commercial and aerospace applications. Viscoelastic materials are elastomeric materials whose long-chain molecules cause them to convert mechanical energy into heat when they are deformed. Perhaps the most important advantage of VEMs is their high loss factor and low storage modulus. The loss factor is a measure of the energy dissipation capacity of the material, and the storage modulus is a measure of the stiffness of the material. The storage modulus (shear modulus) is important in determining how much energy gets into the viscoelastic material, and the loss factor determines how much energy is dissipated. Both the shear modulus and loss

Table 1: Primary passive damping mechanisms and related information

	TYPE OF DAMPING MECHANISM			
	Viscoelastic Materials	Viscous Devices	Magnetic Devices	Passive Piezoelectrics
Types of Treatments	All	Strut Dampers and TMDs	Strut Dampers and TMDs	Strut Dampers
Temperature Sensitivity	High	Moderate	Low	Low
Temperature Control	Embedded Heaters	Heaters	None Needed	Embedded Heaters
Loss Factor	High	High	Low	Low
Frequency Range	Wide	Moderate	Moderate	Moderate
Weight	Low	Moderate	High	Moderate

factor of VEMs are temperature and frequency dependent, though of the two temperature has a greater effect on damping performance.

Viscous Devices

These devices dissipate energy via a true velocity-dependent mechanism, typically by forcing a fluid through a precision orifice. Although the actual viscous damping coefficient is usually not frequency dependent, the viscous damping force ($c\omega$) is obviously frequency dependent. Viscous dampers are most effective for axial deformations. The levels of loss obtainable by a viscous device are higher than those obtainable with VEM-based struts, but a price is paid in the "bandwidth" of effectiveness. That is, a viscous damper is usually effective at damping only modes in a relatively narrow frequency range. As with VEM damping treatments, the effectiveness of viscous dampers is affected by changes in temperature, but to a lesser degree. This change is due to the viscosity of the fluid changing.

Viscous damping mechanisms have been adapted to address bending deformations, but it is not the most direct and efficient use of the technology. This approach is thus not attractive for situations dominated by panel bending, such as many acoustics-driven problems.

Magnetic Devices

With advancements in the production of powerful magnetics, magnetic (eddy current) damping is proving to be a viable solution to problems where temperature extremes are a factor. As with fluid-based systems, this technology produces a true, velocity-dependent viscous damping force. However, the damping coefficients of magnetic devices are much less than viscous devices. The power and effectiveness of the magnetics are relatively unaffected by changes in temperatures.

This is another technology that is not well suited for most bending problems. However, magnetic TMDs have been shown to be effective in harsh environments where neither viscoelastic or viscous damping mechanisms are possible.

Passive Piezoelectrics

Piezoelectric ceramic materials have the unique ability to produce a strain when subjected to an electrical charge, and, conversely, they produce a charge when strained mechanically. A piezoelectric material can be used as a passive damping element in a structure by shunting it with a passive electrical circuit, thereby turning vibrational strain energy into electrical energy that can be dissipated as heat energy by a resistor. Two types of shunted circuits exist: a resistor alone and a resistor in series with an inductor. In resistor-shunting, the voltage created is run through a circuit in series with a resistor that dissipates the electric energy. The theoretical maximum loss factor for this configuration is 0.425, this making it less efficient than a good viscoelastic material. Shunting with a resistor and inductor, along with the inherent capacitance of the piezoceramic, creates a resonant LRC circuit that is analogous to a mechanical tuned-mass damper (TMD), except that it counters vibrational strain energy instead of kinetic energy. This can result in loss factors higher than 0.425, but how much higher depends on the amount of inductance. For

Table 2: Primary implementations of passive damping and associated design methods for space structures

	TYPE OF TREATMENT				
	Strut Dampers	Constrained Layers	Tuned-Mass Dampers	Joint/Interface Dampers	Embedded Dampers
Target Modes	Global	Member Bending and Extension	Narrow Frequency Range, Any Mode Shape	Local or Global	Member Bending and Extension
Primary Design Method	Modal Strain Energy	Modal Strain Energy	Complex Eigenvalues	Joint Test or Modal Strain Energy	Modal Strain Energy
Special Features	Removable, Lightweight	Flexible, Wide Bandwidth	Low Cost, Low Weight	Low Weight Low Volume	Embedded, Low Outgassing

large inductance, one needs a large, heavy inductor. Active inductors using power amplifiers have been built, but this defeats the purpose of a passive system. Some advantages of piezoceramics are that they have some structural stiffness, are relatively temperature independent, and can be used for both sensors and actuators.

PASSIVE DAMPING CONCEPTS

Although passive damping if often attributed to friction or other such "accidental" mechanisms, designed-in damping using high-loss materials and techniques can yield energy dissipation that is orders of magnitude higher and much more predictable. *All passive damping treatments share a common goal:* absorb significant amounts of strain energy in the modes of interest and dissipate this energy through some energy-dissipation mechanism. The effectiveness of all passive damping methods varies with frequency and temperature, through some more than others.

For each of the basic passive damping *mechanisms*, there are several choices for implementation. Damped struts are commonly used in truss-type structures, though they can also be used to damp structures where two or more parts of the structure are deforming relative to each other. Constrained layer treatments are surface treatments where the damping material is sandwiched between the base structure and a constraining layer. This type of damping treatment is most commonly used to damp bending modes of surfaces (shell-type modes). A tuned-mass damper (TMD) is a vibration damping device attached to the structure at or near an antinode of a troublesome mode of vibration. These devices transfer energy at a particular resonance to two new system resonances, each highly damped. A small increase in damping may be achieved by placing damping material in joints. The advantage of this type of damping is that it requires very little added weight. Embedded dampers can be constructed of viscoelastic materials or passive piezoelectrics. Table 2 summarizes the primary passive damping concepts along with their typical uses.

VEM TESTING AND CHARACTERIZATION

As stated previously, viscoelastic materials are temperature and frequency dependent. VEMs must therefore be tested over both temperature and frequency ranges to characterize the material accurately. VEM test methods fall into two broad classes: resonant and nonresonant.

Resonant tests infer VEM properties from measured normal mode properties of some simple structure that includes the viscoelastic material, such as a sandwich beam. Resonant tests have the advantage of being relatively insensitive to both gain and phase errors in the transducing systems. However, a major disadvantage is that the measurement is indirect; material proｐrties are inferred from modal properties by working backwards through some theoretical solution. Also, material properties are obtained only at discrete frequencies.

Nonresonant tests, often called complex stiffness tests, utilize a VEM sample connected to a rigid fixture and loaded dynamically, usually in shear. The force transmitted through the specimen and the resulting deformation across it are transduced directly. Damping is determined from the phase angle by which the displacement lags the force. Stiffness, or storage modulus, is determined from the ratio of in-phase force to displacement. Stiffness and loss factor are obtained as almost continuous functions of frequency and at discrete temperatures.
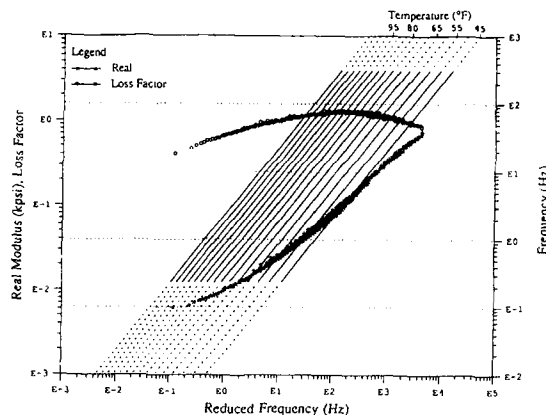
Figure 1: Reduced-temperature nomogram

Using the test data measured at selected temperatures and frequencies, a process known as characterization is used to determine the material properties at all combinations of temperature and frequency [1] [2]. The actual process of characterization is complex and rather involved. A layman's view is to determine a functional relationship (the temperature shift function (α_T)) between temperature and frequency such that both the storage modulus and loss factor at any temperature and frequency can be determined. Incorrect characterization can lead to major errors in property data. The end result of characterization is a viscoelastic material nomogram (also called the international plot). Figure 1 gives an example and its use for 3M's Y-966.

Once a material has been characterized accurately, its parameters may be placed into a database. The computer may then perform searches for materials that meet specific engineering criteria in a method exactly analogous to reading the international plot. Since these searches are based solely on the characterization parameters, the importance of quality data and characterization methods should not be underestimated.

PASSIVE DAMPING DESIGN METHODS

Passive damping treatments for complex structures are usually designed using finite element techniques. The frequency and temperature dependencies of passive damping mechanisms must be taken into account during the design. Damping design is not just the selection of a high loss mechanism (material, device) for the temperature range of interest; it is an integrated structural and materials design process. To achieve damping, two conditions must be met: significant strain energy must be directed into the high loss mechanism for all modes of interest, and the energy in the mechanism must be dissipated. The first condition requires most of the design effort and is dependent on structural properties, location, mode shapes, stiffness, wave lengths, thickness of material, etc. The second condition is met by selecting the mechanism with the proper loss factor that matches the designed stiffness.

Before the design of the passive damping treatment can begin, it is imperative that the true nature of the problem be understood thoroughly. The designer must have in mind some figure of merit, which could be as simple as the response of a fundamental mode of a panel or as complicated as the RMS beam jitter of multiple optics in an optical system due to acoustic excitation. In any case, the engineer must determine whether the problem is a single mode or many modes over a broad frequency band. In the later case, the precise modes that are driving the figure of merit must be identified. Knowing all of this, the proper damping mechanism, analysis technique, and hardware can be chosen.

Methods for finite element analysis of damped structures can generally be categorized as either a damping treatment design method or a response prediction method. The damping treatment design methods are used to determine the proper selection of design variables that will lead to high damping in modes of interest. These methods predict the amount of damping in each mode. The response prediction methods are used to predict the performance of damped structures but may be used for design purposes.
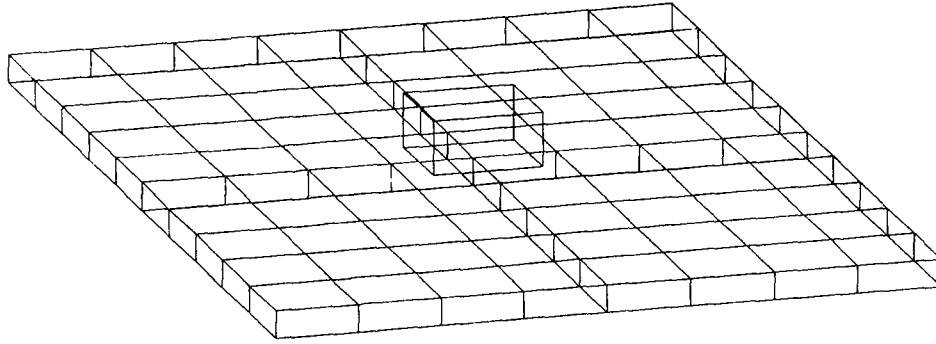
Figure 2: Finite element model of the stiffened panel

The two major damping treatment design methods are the Modal Strain Energy (MSE) [3] method and the complex eigenvalue (CEV) method, with the MSE method being the most widely used. Using the MSE method, the modal damping of a structure may be approximated by the sum of the products of the loss factor of each material and the fraction of strain energy in that material for each mode. In the case of a multi-material system, the system loss is given by

$$\eta^{(r)} = \sum_{i=1}^{M} \eta_i \frac{SE_i^{(r)}}{SE^{(r)}}, \tag{1}$$

where η_i = material loss factor for material i, $SE_i^{(r)}$ = strain energy in material i when the structure deforms in natural vibration mode r, and $SE^{(r)}$ = total strain energy in natural vibration mode r.

The MSE method is an approximation of the complex eigenvalue method, which treats the viscoelastic material as complex. The advantages of the MSE method are that it uses normal mode analysis, which is much more efficient computationally than complex eigenanalysis, and that it calculates the distribution of strain energy in the structure, which aids in determining the best location for the damping treatment.

The response prediction methods include the modal and direct frequency response methods and the modal and direct transient response methods. The modal frequency response analysis method is efficient, but uses modes based on constant stiffness, even though the damping may be a function of frequency. This method is reasonably accurate as long as the calculated response frequency range is not over a decade. The direct frequency response method uses frequency-dependent complex material properties, which makes this method accurate but very expensive computationally. The modal transient response method again uses modes calculated using constant stiffness, while the direct transient response analysis method can handle complex material properties.

PASSIVE DAMPING EXAMPLE

One example of the application of passive damping is a stiffened panel supporting a simulated component that is sensitive to its vibration environment. To simulate excitation by an acoustic field, a random pressure loading is applied over the surface of the panel. The chosen figure of merit is the RMS (0–1,000 Hz) of the displacement PSDs normal to the panel and about the axes in the plane of the panel. The analysis is performed with a finite element model using MSC/NASTRAN in which the panel and ribs are modeled with plate elements, and the component is a lumped mass. For visualization, a massless box had been attached to the lumped mass, as shown in Figure 2.

The first step is to determine which modes contribute the most to the figure of merit. For the displacement normal to the panel, it is easy to rationalize that the fundamental bending mode dominates this resonance. However, for the rotational displacements, the fundamental mode along with the either the second (for θ_x) or third (for θ_y) modes are of equal importance. The displacement PSD for the x rotation, along with its forward sum, is shown in Figure 3.

If only the normal displacement were important, this problem would be a good candidate for a tuned-mass damper, since this displacement PSD is strongly dominated by just the fundamental mode. However,
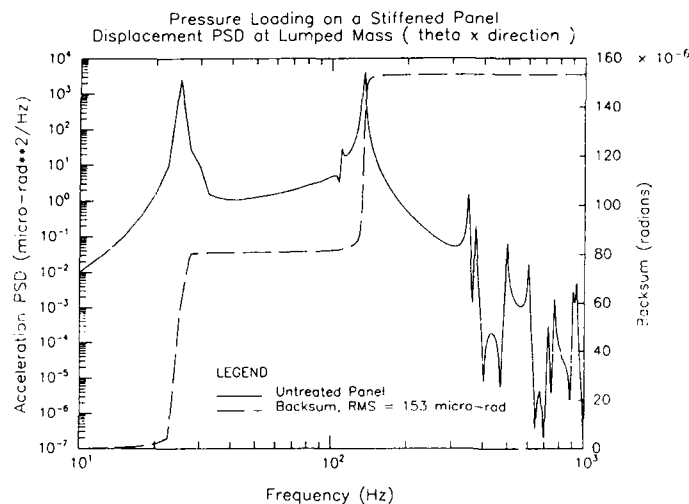
Figure 3: Displacement PSD for θ_x with forward sum

there are several modes that need to be addressed, so a constrained-layer treatment is more appropriate for this case.

There are five basic design parameters for a constrained-layer treatment: thickness of the constraining layer, modulus of the constraining layer, thickness of the VEM, modulus of the VEM, and placement of the treatment. In most practical situations, some of this parameters are determined by outside factors such as constraints on weight, CTE, space, etc. Where weight is a factor, it usually advantageous to make the constraining layer from advanced materials, such as metal matrix or graphite-epoxy [5]. For this example, the constraining layer is made from the same material as the base panel: aluminum. Also, assume that the entire top surface of the panel, including under the component, is covered by the constrained-layer damping treatment. A brief trade study with the remaining parameters showed that the VEM should be 0.006" thick and have a shear modulus near 250 psi. This trade study is documented in Table 3.

Table 3: Summary of trade study for add-on constrained-layer damping treatment

VEMT	VEMG	CL	% MSE in VEM		
(inches)	(psi)	(inches)	Mode 1	Mode 2	Mode 3
0.010	250	0.05	5.41	6.57	5.43
0.010	250	0.10	10.0	11.43	8.93
0.010	250	0.15	13.65	15.02	11.49
use CLT = 0.10 as baseline, now vary VEMG					
0.010	50	0.10	5.61	4.93	3.15
0.010	2000	0.10	7.18	9.44	10.05
0.010	1000	0.10	9.09	11.82	11.42
use VEMG = 250 for baseline, now vary VEMT					
0.002	250	0.10	8.05	10.53	10.44
0.005	250	0.10	9.77	12.14	10.53
0.004	250	0.10	9.49	12.01	10.77
0.006	250	0.10	9.93	12.11	10.22
Runs for final predictions of MSE in modes 1–3					
0.006	95*	0.10	8.88	n/a	n/a
0.006	280†	0.10	n/a	12.21	10.48

*3M Y-966 shear modulus at ∼ 25 Hz

†3M Y-966 shear modulus at ∼ ¹30 Hz

Table 4: Reductions in RMS values resulting from passive damping

	RMS		
	z (μinches)	θ_x (μrad)	θ_y (μrad)
Untreated	483	153	191
With Damping	83	40	43

There are three variations on this concept that bear mentioning:

1. The damping treatment could be shrunk so that it covered a smaller portion of the base panel.

2. The panels themselves could be constructed from a sandwich of metal and VEM.

3. Instead of a constraining layer, the VEM could be sandwiched between the base structure and built-up sections (I-Beams, C-channels, hat sections, etc.).[5] [6]

Each of these alternatives is likely to result in additional weight savings, though they are not discussed in this paper.

A trade study showed that the shear modulus of the VEM should be approximately 250 psi. One material that fits this closely for the three modes of interest is 3M's Y-966 (see Figure 1). The shear modulus and loss factor for this VEM at 25 and 130 Hz are approximately (95 psi,1.17) and (280 psi,1.3), respectively [7]. Two additional runs were then made with these values to get a better approximation for the MSE in the modes of interest. They are also reported in Table 3. These values of modal strain energy were subsequently multiplied by the loss factors for their respective frequencies and used to predict the responses of the structure with the added damping treatment. The RMS values are given in Table 4, and the effects are shown clearly by the PSD in Figure 4.
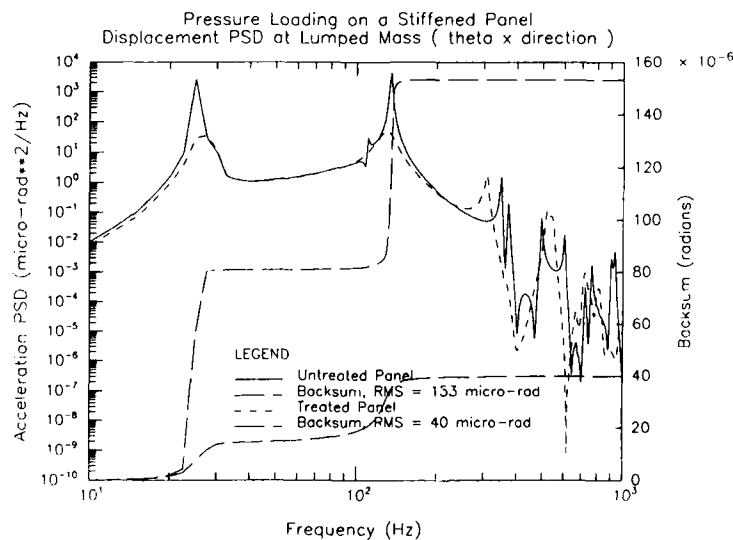
Figure 4: Effect of Passive Damping

References

[1] Fowler, B.L., "Interactive Processing of Complex Modulus Data," *Dynamic Elastic Modulus Measurements in Materials*, ASTM STP 1045, 1989.

[2] Rogers, L.C., "An Accurate Temperature Shift Function and A New Approach to Modelling Complex Modulus," *Proceeding of 60th Shock and Vibration Symposium*, November 1989.

[3] Johnson, C.D. and Kienholz, D.A., "Finite Element Prediction of Damping in Structures with Constrained Viscoelastic Layers," *AIAA Journal*, Vol. 20, No. 9, September 1982.

[4] Campbell, W.A. and Mariott, R.S., "Outgassing Data for Selecting Spacecraft Materials," NASA Reference Publication 1124, Revised.

[5] Yiu, Y.C., Austin, E.M., and Zeigler, M.L., "Designing a Dynamically and Thermally Stable Sensor Platform using Passive Damping and Metal Matrix Composites," *Proceeding of 61st Shock and Vibration Symposium*, October 1990.

[6] Stahle, C.V., and Staley, J.A., "Integral Damping of Component Mounting Panels," *Proceedings of AIAA Dynamics Specialists Conference*, AIAA Paper 84-1040-CP, 1984.

[7] Austin, E.M., Allen, B.R., and Fowler, B.L., "Report on Testing of Viscoelastic Materials Under DAMMPS Phase I," CSA Report 90-10-02, October 1990.
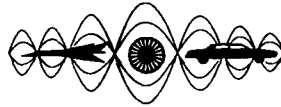
SECOND INTERNATIONAL CONGRESS ON RECENT DEVELOPMENTS IN AIR- AND STRUCTURE-BORNE SOUND AND VIBRATION

MARCH 4-6, 1992   AUBURN UNIVERSITY, USA

RECENT APPLICATION OF THE PASSIVE DAMPING TECHNOLOGY

Ahid D. Nashif
Anatrol Corporation
4120 Birch Street, #108
Newport Beach, CA   92660

ABSTRACT

The use of damping technology to control the vibrational amplitude of structures has been increasing recently due to the availability of an extensive data base on the properties of materials with different environments, and efficient experimental and analytical techniques to evaluate the effectiveness of damping treatments when used in different applications. This paper describes some of the recent passive damping applications that have been used in different industries. Specifically, the application of this technology to control the vibrational amplitude in various components found in the automotive. sporting goods, aerospace, and computer industries is described.

INTRODUCTION

Passive damping as a technology has been around for many years.   Specifically, the unconstrained and constrained layer damping treatments have been analyzed and developed, at least for simple structures, since the early 50's [1,2]. The tuned vibration absorber has been investigated even earlier for the case of low [3] and high [4] damping capabilities in the spring elements. Since those early days, this technology continued to be refined by many researchers and organizations, but its impact to solve noise and vibration problems has been limited until the last few years.   This can be mainly attributed to the availability of better damping materials, and analytical and experimental tools to determine the effectiveness of damping treatments when applied to various structural components [5].

Advances in the material technology include new materials that have high damping capabilities, while being resistant to the operating environment such as temperature, solvents. aging, loading, etc.   These materials have been measured for their dynamic behavior and characterized as analytical functions in terms of temperature, frequency, static loading. dynamic loading, creep, and stress relaxation. Several data bases now exist to assist the users in selecting the appropriate materials for given requirements.

Using this material technology, along with newer and more efficient analytical and experimental tools for modeling the dynamic behavior of structures, designers have been able to concentrate on the practical aspects of implementing damping into various products including those of mass production. Actually, the majority of applications today for the damping technology are found in both the automotive and appliance industries which are high volumes and usually cost conscience [5].

This paper describes some of the latest and most interesting applications for various industries. Two types of damping treatments will be discussed. The first type is the constrained layer damping with its application to control disc brake squeal in the automotive industry and the suspension of disc drives in the computer industries. The second type is the tuned vibration absorber for two different applications. One, is where this device is used to introduce damping into the system as for controlling tennis racket vibration, and the other when used to increase the dynamic stiffness for reducing the aircraft fuselage vibrations.

Damping of Automotive Disc Brakes

Analyzing and controlling brake noise have been going on for many years for a variety of vehicles. However, as asbestos lining materials are being phased out, especially when replaced with semi-metallic ones, controlling brake noise became an important issue in the automotive industry to reduce warranty costs. Such new lining materials have higher friction forces and lower damping capabilities than the old asbestos ones, and therefore create the conditions for a number of noise problems to occur in the vehicle. Of these, the most important one occurs whenever the dynamics of the rotor match those of the brake pads at a given frequency or a number of frequencies which lead to brake squeal [6].

To illustrate the dynamics affecting brake squeal consider Figure 1 in which a dynamic force (in the brake static condition at room temperature) is applied to a rotor and the response is measured as a function of brake line pressure. The frequency range that is selected in this figure is similar to that where the brake squeal occurs. Other conditions such as temperature and humidity also affect brake squeal and, therefore, should also be investigated, but will not be discussed here.

At zero pressure when the rotor is not in contact with the brake pads, the frequency response is high with low damping. However, as the pressure is increased and the pads start to contact the rotor, the response becomes considerably lower and with much higher damping. This is due to the high joint damping between the rotor, and the pads which are still vibrating as rigid bodies, while the rotor is deforming in a given modal pattern at this frequency. As the pressure continues to increase, it can be seen that the response becomes higher again and with low damping. This condition occurs whenever the dynamics of the rotor match those of the pads and the new system starts to vibrate in-phase which generates little joint damping. The deformation pattern for the system at this condition is shown in Figure 2, which matches the actual operating deflection shape that occurs during squeal condition.

Two approaches are usually used to control the above mentioned condition. One is to mismatch the two dynamics between the rotor and the pads, however, this approach is not always satisfactory because of the large number of resonances in the system, especially as they continue to change with increasing wear. The other is to introduce enough damping into the system. Several ways and locations have been investigated to introduce damping into disc brakes and the most successful has been the constrained layer damping treatment when applied to the back of the brake pads, as illustrated in Figure 3. Such a treatment works whenever the pad starts vibrating in-phase with the rotor in a given mode so that the steel constraining layer causes the damping layer to undergo shear deformation and thereby dissipates the unwanted vibrational energies. Typical performance for such a treatment is shown in Figure 4. As can be seen in this figure, and as always expected, the constrained layer damping treatment works effectively over a given temperature range that is governed by the material properties, geometry and the dynamics of the system. If such a temperature range is not sufficient, then it is necessary to use different materials, geometries, and/or multiple constrained layers. Most new vehicles now are equipped with constrained layer damping treatments on the brake pads.

Damping of Disc Drive Suspension

Damping of the flexures in disc drives is needed to control the resonant vibration in the suspension and thereby eliminates the read/write errors associated with such resonances [7]. A typical constrained layer damping treatment on a flexure is shown in Figure 5. The design of the damping treatment includes the determination of the dynamic behavior of the flexure, the measurements of the properties of the damping material to be used, the design of the damping configuration and its location on the flexure and finally the verification of the performance of the treatment.

The dynamic response of the flexure is shown in Figure 6 which is measured while the disc is spinning to properly simulate the boundary conditions. A number of resonances are seen in the frequency response, and their importance is dependent on the specific application. For example, earlier disc drives were affected by the first bending mode of the suspension, while present designs are more affected by the sway mode. The mode shapes of vibration of those two resonances are shown in Figure 7. Knowing which one of the two modes to control is an important factor in the design of the damping treatment. To illustrate this point, the modal strain energy is shown in Figure 8 for each mode. Since the damping treatment needs to be applied at the locations of maximum strain energy for optimum performance, then it can be seen that the damping treatment of Figure 6 is good for the 1st bending mode and not for the sway mode.

Figure 9 represents the measured and analytically predicted performance for a constrained layer damping treatment as a function of temperature for the first bending mode of vibration. The design of this treatment included the optimization of the selection of the damping material, its thickness, and the thickness of the constraining layer to achieve a given damping level over the operating temperature range. This type of damping treatment plays an important role in the design of the high performance disc drives.

Damping of Tennis Racket Vibration
The response of several sporting goods, especially those that are hand held, such as tennis rackets, baseball bats, and golf clubs are being investigated today as for the case of hand-held tools. This is because whenever such devices are hand held and operated, their dynamics couple with those of the arm, or whole body, and in many cases lead to objectionable feel from the vibration. In the case of tennis rackets, both noise and vibration conditions occur during ball impacts. However, the vibration felt in the hand is becoming more important to control especially as new high stiffness composite rackets are being developed.

Figure 10 represents the driving point frequency response measured on a composite racket to illustrate its resonances up to 1000 Hz in the case of free-free boundary conditions (not hand-held). The first bending mode of the racket and first bending mode of the strings are illustrated in Figures 11 and 12. The string mode illustrated in Figure 12 is the dominant one for noise, while the bending mode of the racket is the one that is felt in the arm. This is illustrated in Figure 13 for the hand-held condition and measurements were made on both the arm and the racket. It can be seen in this figure that the arm now is coupled with the racket and the new system mode of vibration is causing bending in the arm.

In the case of high stiffness rackets, which have low inherent damping, the arm becomes the dominant damping mechanism for the racket vibration. In other words, as the system resonates in the mode of Figure 13, the arm is dissipating the majority of the vibrational energy which leads to tiring in the arm, and in part to aggravating "tennis-elbow". This is perhaps better seen in Figure 14 which illustrates two responses of the racket when it is hand-held and free-free. It can be seen form this figure that the damping in the system is increased by about a factor of ten when the racket is hand-held.

To improve on the response of the system it is necessary to introduce higher damping into the racket, either by a material change or additional devices, than that introduced by the arm. Whenever this occurs, then the racket or the device will do the work to dissipate the energy instead of the arm, and thereby lead to better and more comfortable feel during playing conditions. Even though many devices have been tried, and claim to reduce the vibration of the racket, very few have been as good as the damping introduced by the hand, and therefore become ineffective when the racket is hand-held. However, tuned vibration absorbers, when properly designed and selected to have high damping in the rubber element, could introduce high damping into the system for a low weight penalty.

Figure 15 represents the response of the hand-held racket with a tuned vibration absorber that has a weight of only 3% of the racket. It can be seen in the figure that significant damping has been introduced into the system, which leads to more comfortable playing conditions. Because of such improvements, similar tuned devices are now being considered for other hand held sporting goods, such as baseball bats.

Damping of Aircraft Fuselage Vibration

Controlling the amplitude of vibration of the fuselages on aircrafts is a key factor in reducing the interior noise, especially for the propeller driven ones. For such aircrafts the important frequencies to address are the fundamental and second blade passage frequencies. However, because such frequencies are usually below 200 Hz, the damping approach is not very effective because the response of the frames of the fuselage is more of the forced type rather than of resonant one. Thus, increasing the stiffness of the frames becomes the recommended approach to reduce the vibrational response for a given input force.

Typical ways of introducing higher stiffness into the fuselage, such as increased skin thickness or stiffer frames are not very effective for significant noise reductions, because of the weight penalty involved. An alternate approach is to increase the dynamic stiffness around the frequency of excitation to introduce a notch in the frequency response. This can be accomplished by using tuned vibration absorbers that are attached to the frames at the point of maximum amplitude so that when the frame is vibrating, the mass of the absorber is vibrating out-of-phase with the frame, which leads to the desired reduction.

Figure 16 illustrates the response of an aircraft frame before and after the addition of tuned vibration absorbers that are tuned for different frequencies. This figure illustrates that the response of the frame is of the forced vibration type and that the tuned vibration absorbers could introduce significant stiffness into the system. Lower damping in the rubber element will lead to further increases in stiffness, but the width of the notch becomes narrower, which could cause the absorber to be ineffective if the operating engine speed is going to vary greatly. Proper designs of the damping in the rubber element and mass is based on the operating engine speed and weight budget.

Figure 17 represents the actual vibration of a number of frames during typical flight conditions with and without the tuned vibration absorbers. This level of vibration reduction is also seen in the response of the trim panel (see Figure 18) which is the primary radiator affecting the interior noise. Typical interior noise reductions of four to six dBA's have been achieved by using this approach, which is significant for the low weight and cost penalties. Because such reductions, tuned vibration absorbers are now being considered not only to retrofit existing aircrafts, but also in the design of new ones [8].

CONCLUSIONS

The application of the passive damping technology to control the noise and vibration levels of components found in various industries has been discussed. The increased use of this technology illustrates that it is now one of the important tools available to designers when dealing with controlling the unwanted dynamics of structures in an efficient and cost effective ways.

REFERENCES

1.   H. Oberst and K. Frakenfeld, "Uber die Dampfung der Biegeschwingungen dunner Bleche durch festhaftende Belage," Acustica, 2, 1952.

2.   D. Ross, E.E. Ungar, and E.M. Kerwin Jr., "Damping of Plate Flexural Vibrations by Means of Viscoelastic Laminate," Structural Damping, ASME, New York, 1959.

3.   J.P. Den Hartog, Mechanical Vibrations, 4th Edition, McGraw-Hill, New York. 1956.

4.   J.C. Snowdon, "Vibration and Shock in Damped Mechanical Systems," Wiley, New York, 1968.

5.   Proceedings of Damping 91, Airforce System Command, Wright-Patterson Air Force Base, Ohio, WL-TR-91-3078, August 1991.

6.   T.M. Lewis and P. Shah, "Analysis and Control of Brake Noise," SAE 872240, 1987.

7.   Head/Media Technology Review Conference, Las Vegas, Nevada, November 11, 1990.

8.   Aviation Week and Space Technology, January 6, 1992.
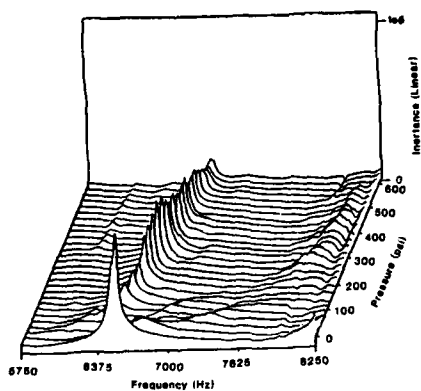
Figure 1: Frequency Response Measurement on the Assembled System
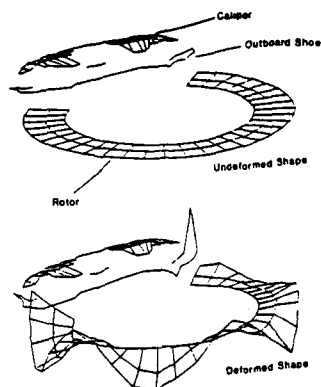
Figure 2: Mode Shape of Vibration
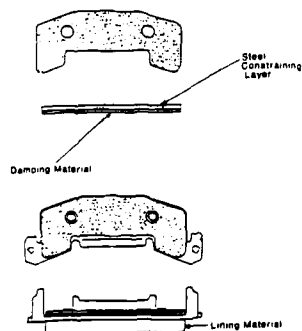
Figure 3: Constraining Layer Damping Treatment Applied to a Brake Shoe
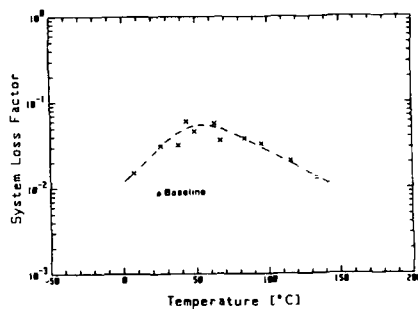
Figure 4: Performance of a Constrained Layer Damping Treatment on a Brake System

Figure 5: Typical Damping Treatment on a Disc Drive Suspension
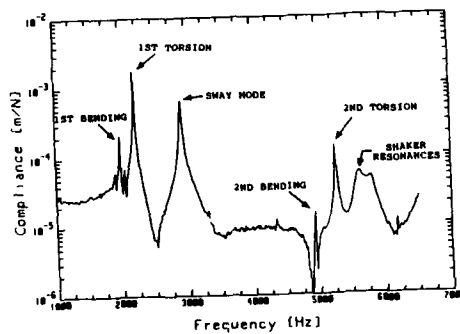
Figure 6: Frequency Response Function Measurement on a Typical Suspension

193
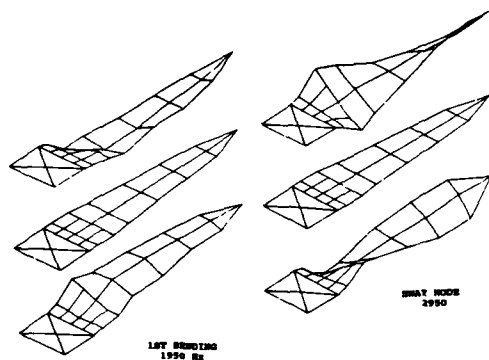
Figure 7: Mode Shapes of Vibration
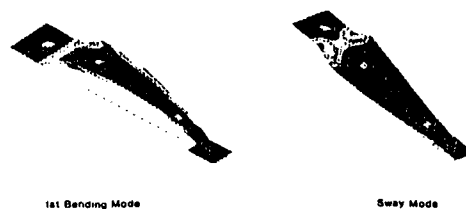
Figure 8: Modal Strain Energy Distribution
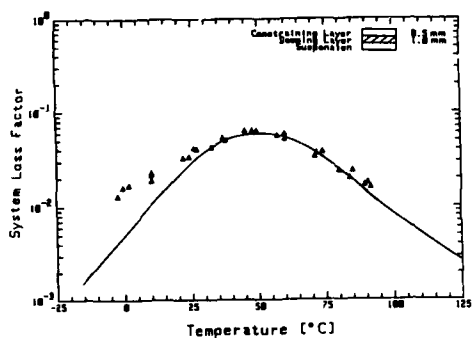
Figure 9: Comparison Between Predicted and Actual Loss Factor Values for a Typical Constrained Layer Treatment
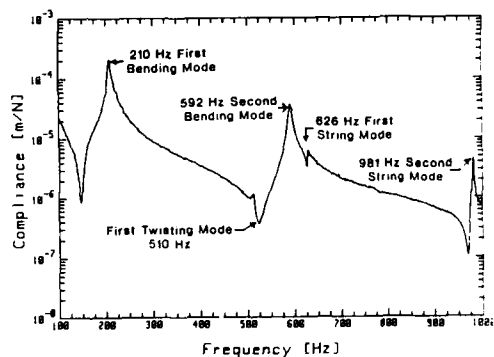
Figure 10: Compliance Plot for a Composite Racket
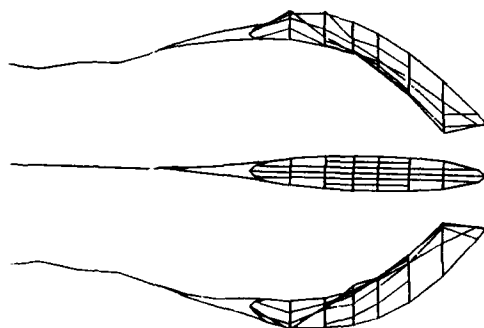
Figure 11: First Bending Mode
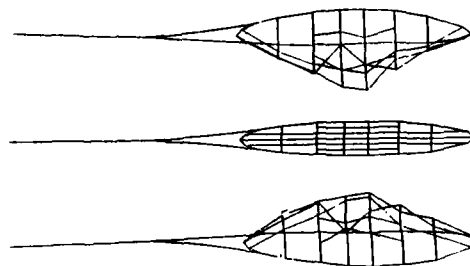
Figure 12: First String Mode
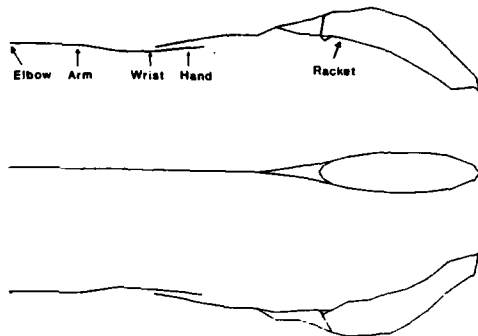
Figure 13. First Bending Mode of Racket and Arm
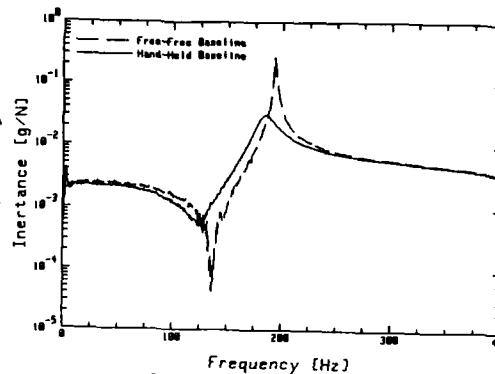
Figure 14 Comparison Between Free-Free and Hand-Held Response
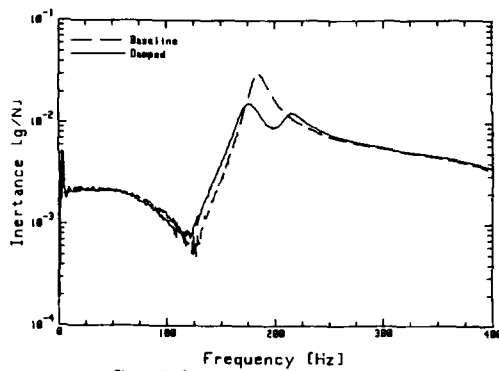
Figure 15 Comparison Between Baseline and Damped Response on the Hand-Held Case
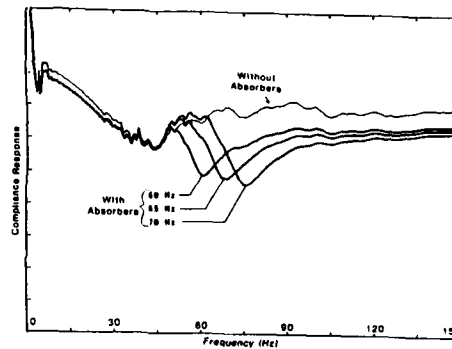
Figure 16: Response of Fuselage Frame with Absorbers Tuned to Different Frequencies
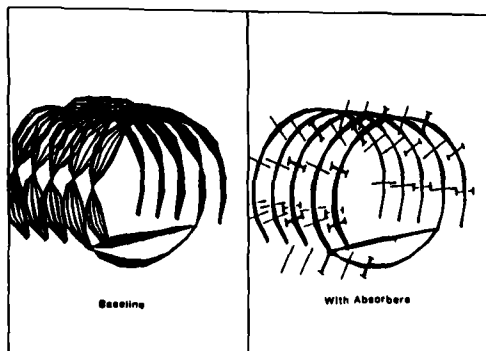
Figure 17: Effect of Tuned Vibration Absorbers on Reducing the Fuselage Vibration During Flight Cruise Condition
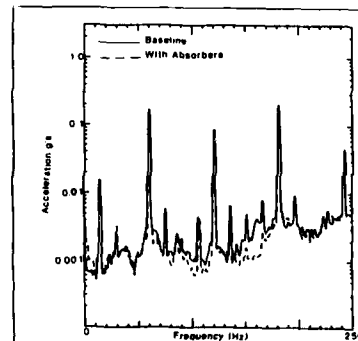
Figure 18 Effect of Tuned Vibration Absorbers on Reducing the Trim Panel Vibration During Flight Cruise Conditions
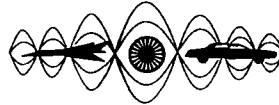
SECOND INTERNATIONAL CONGRESS ON
RECENT DEVELOPMENTS IN AIR- AND
STRUCTURE-BORNE SOUND AND VIBRATION
MARCH 4-6, 1992   AUBURN UNIVERSITY, USA

MATERIAL AND STRUCTURAL DYNAMIC PROPERTIES OF
WOOD AND WOOD COMPOSITE PROFESSIONAL BASEBALL BATS

Robert D. Collier
Department of Mechanical Engineering
Tufts University
Medford, MA 02155
U.S.A.

ABSTRACT

The objectives of the current research are to: (1) evaluate the static and dynamic material and structural properties of different types of baseball bats and (2) develop relationships between design parameters and hitting performance. A new 6.35 cm (2.5 in.) OD wood composite bat and a professional hardwood bat have comparable stiffnesses, material elasticity, modal response and acoustic signatures. The wood composite bat, however, has experienced no breakage in extended field hitting due to its enhanced fracture toughness and higher breaking strength. Controlled hitting tests yield statistically comparable performance levels for both bats. The performance of the wood composite bat remains unchanged after 2000 hits. The dynamic properties of 6.98 cm (2.75 in). OD high performance tubular construction aluminum alloy bats and their acoustic signatures differ significantly from those of wood and wood composite bats.

INTRODUCTION

To our knowledge, there are no standard laboratory test procedures for measuring the structural characteristics and properties of baseball bats and only relatively simple analytical models for relating these measurements to field performance. As Professor Adair of Yale University states in his recent book, The Physics of Baseball.(1)

"It may seem curious that the physics of baseball is not at all under control. We cannot calculate from first principles the character of the collision of an ash bat with a sphere made up of layers of tightly wound yarns...", and

"Baseball, albeit rich in anecdote, has not been subject to extensive quantitative studies of its mechanics, hence, models of baseball are not as well founded as they might be..."

The overall objective of the research discussed in this paper is to develop a practical understanding of the relationships between the engineering properties of baseball bats and their field performance as a component of the batter-bat-ball dynamic system. The specific objectives are to:

(1)   Analyze the material properties and structural characteristics of three types of bats: wood, wood composite, and aluminum.

(2)   Develop and validate analytical models for exchange of energy in bat-ball collisions including the role of surface elasticity and the extent of the "sweet-spot" area.

(3)   Develop and implement laboratory static and dynamic testing methods and demonstrate their relevance to design parameters and performance characteristics of baseball bats.

197

(4) Develop and implement field testing measurement and analysis procedures to complement laboratory testing methods and to quantify batter-bat-ball performance metrics.

(5) Develop and implement integrated laboratory and field testing procedures to determine durability of all types of bats.

The experimental results presented in this paper were devised to obtain relative structural static and dynamic data for three purposes: (1) provide bat design guidance for selection of materials and structural parameters of wood composite bats; (2) develop a more comprehensive understanding of how and why the various bat designs work and perform as they do; and (3) establish hitting performance and durability measures.

The initial technical approach is to conduct full scale laboratory experiments on the three types of bats and correlate the results with full scale field hitting performance measurements. This paper deals only with the experimental phase of the research; concurrent analytical models and research in the dynamics of the bat-ball collision and energy exchange and will be discussed in subsequent papers.

Table 1 lists the major bat design factors and physical measurement issues which relate to bat performance.

TABLE 1. Baseball Bat Properties

WEIGHT total Distribution Centers of Mass	VIBRATION Modal analysis Impact Response	DURABILITY Structural integrity Surface elasticity Dents and plasticity
DIMENSIONS Diameter and length Shape and form	MATERIAL ELASTICITY Ball deformation Bat deformation Surface strain	ACOUSTICS Time wave forms Sound signatures Hit location
STIFFNESS Modulus Beam deflection	STRENGTH Fracture Deformation	SWEETSPOT Size and location Energy Transfer Adjustability

Table 2 lists representative weights, lengths and diameters of the bats discussed in this paper.

TABLE 2   Bat Description

TYPE	DIA. CM.	LENGTH CM.	WT. GMS.
WOOD	6.35 (2.5in)	86.36 (34in)	904.1 (31.9oz)
WOOD COMPOSITE	6.35 (2.5in)	86.36 (34in)	906.5 (32.0oz)
ALUMINUM	6.98 (2.75in)	86.36 (34in)	878.5 (31.0oz)

A general description of the bat materials and structural configuration is as follows:

1. Professional hardwood: solid northern white ash, 2. Baum wood composite: solid unibody, composite core with integrated northern white ash outer structure; and 3. Aluminum alloy: Thin-wall tube, (0.127-0.343cm/0.050-0.135in) thickness.

Note: Aluminum bats are designed for higher performance with a larger diameter and longer barrels. A high performance wood composite bat has also been designed and tested with comparable performance to that of the aluminum bat.

LABORATORY MEASURFMENTS-STATIC PROPERTIES

There are three principal material-structural properties of baseball bats which relate to performance and durability: (1) stiffness; (2) fracture mechanics and breaking strength; and (3) material elasticity.

(1) The overall stiffness in bending is measured with the Instron universal testing machine as illustrated in Figure 1. A specially designed fixture was developed for positioning and clamping the bats. Representative results are shown in Figure 2 for the three types of bats. The wood and wood composite bats have comparable stiffnesses although it should be noted that wood bats have a larger range of stiffnesses due to the variableness in natural wood materials. The aluminum bats, on the other hand are generally about twice as stiff as the wood and wood composite structures. The stiffness of wood composites can be adjusted through selection of materials and structural configurations.

(2) The static breaking strength of bats has been measured in both the fixed cantilever and three point bending test configurations. Comparative results for the latter configuration are shown in Figure 3 where the load is applied through a baseball on the barrel of a simply supported bat. The load-deflection curve is based on the maximum deflection measured in the handle where the breakage occurs (wood and wood composite) or permanent deformation (aluminum) occurs. The results indicate that the breaking strength of wood composites approaches the limit of aluminum bats and is significantly greater than natural wood bats. The breaking strength of bats under large static deflections in either laboratory test configuration does not, of course, simulate the breaking strength of bats under dynamic impact loads in actual batting situations. However, these tests have provided information on fracture mechanisms which are useful for design and manufacturing objectives.

The results of full scale durability hitting tests corroborate laboratory results in that no wood composite bats have been broken during major league testing by 14 teams nor in the 2000 hit live hitting tests with 121 km/hr (75 mph) Jug machine pitching. Wood bats, as is well known, can fracture readily if the ball-bat collision takes place off the sweet spot. Aluminum bats do not fracture under normal conditions.

(3) The material elasticity of bats plays an important role in the energy exchange during bat-ball contact. The material deforms under impact and this deformation must remain in the elastic range in order to maintain its structural integrity and bat performance. Figure 4 shows that the relative local displacement of a typical hardwood is 50% or more greater than that of an aluminum cylinder. The relative local displacement of the wood composites depends on the combination of materials and thus can be designed to meet a given elasticity requirement. In the case under discussion, the elasticity of the wood and wood composite bats under cycling loads are found to be directly comparable and remain in the elastic range for cycling loads up to several thousand pounds. The relationship of material elasticity to durability and performance is the subject of current research.

LABORATORY MEASUREMENTS-DYNAMIC PROPERTIES

Modal analysis of the baseball bats provides information on the dynamic properties including (i) resonant frequencies; (ii) mode shapes; and (iii) vibration damping. The resonant frequencies and their associated vibration damping values are shown in Table 3 below.

TABLE 3. Bat Natural Frequencies and Damping Values

FREQUENCY AND DAMPING

BAT/MODE	1		2		3		4		5	
	Hz	%C_c	Hz	%C_c	Hz	%C_c	Hz	%C_c	Hz	%C_c
Wood H&B C271	150	2.54	518	1.27	1041	0.82	1655	0.79	2339	0.77
Aluminum Easton	204	1.48	636	0.49	1324	0.31	-	-	-	-
Wood Composite Baum P9	160	2.59	524	1.24	1040	0.98	1650	0.92	2387	0.93

The fundamental frequency of the Baum wood composite is slightly higher (160 vs. 150Hz) than the H&B C271. The higher ordered resonant frequencies are essentially the same. The damping values are also comparable for all resonant frequencies. The aluminum bat has higher natural frequencies and lower damping. The frequency response functions (for a given impact point) are shown in Figure 5 for the wood and aluminum bats. The two higher frequencies of the aluminum bat at 2.1 and 2.8 KHz are not beam modes but rather shell vibrations of the aluminum barrel which, of course, are not present in the solid bats. These are the frequencies which radiate efficiently and are shown to correspond with the acoustic signature, i.e., ringing sound of the aluminum bat.

The vibration modes of the wood and wood composite bats associated with the natural frequencies tabulated in Table 2 are shown in Figure 6. The location of the nodes are the same for both bats for all frequencies. For example, for the fundamental frequency, the node of the barrel for both bats is precisely 18.1cm (7-1/8in) from the end of the bat.

FIELD MEASUREMENTS

Full scale evaluation of bats has been performed with the participation of the Tufts Varsity baseball team. The evaluation includes measurement and analysis of: (1) acoustic signatures, (2) hitting performance comparisons; and (3) durability testing. Pitching is accomplished with a Jugs machine standardized to a 121 km/hr (75 mph) ball velocity. Batters hit in a statistical procedure with alternative bats and distances were measured by radial markers within the first third base lines. Results are summarized as follows:

(1) Acoustics: Three typical signatures are shown in Figure 7 for the wood, wood composite and aluminum bats respectively. The time records of the bat-ball collision indicate contact times during ball and bat deformation in the order of 1-4 ms. The broadband impulse and frequency response functions of the wood and wood composite bats yield an acoustic signature dominated by a broadband of frequencies characterizing the familiar "crack-of-the-bat". The trained ears of the majority of batters, coaches and audio experts are unable to distinguish between these two solid bats. On the other hand, the acoustic signature of the aluminum bat is dominated by resonant frequencies associated with the two shell modes identified in modal analysis at frequencies of 2.1-2.3 and 2.8 KHz. This is the instantly recognizable "ping" and, due to the highly correlated modal responses of the barrel and their radiation efficiencies, results in significantly higher radiated sound pressure levels.

200

(2) Hitting Performance: The hitting performance of the 6.35 cm (2.5in) diameter wood and wood composites bats are shown to be statistically comparable in Figure 8. Each of the first three test acts involved a total of 300 hits on each of the new bats. The overall differences in average hitting distances was 2.5%. The second three sets of tests (4, 5 and 6) demonstrated comparable performance between a used wood composite bat (2000 plus hits) and a new wood bat with an overall difference in average hitting distances of less than 0.6%.

The results of the field tests confirmed laboratory measurements in as much as the similar static and dynamic properties of the wood and wood composite bats resulted in comparable performance levels.

(3) Durability: The strength and durability of the wood composite exceeded the design objective of 2,000 hits without a fracture. The sustained performance of the wood composite indicates that the material elasticity and structural integrity did not change as a result of durability testing.

ACKNOWLEDGEMENTS

REFERENCES

1. Adair, Robert K The Physics of Baseball, Harper and Rowe, Publishers, 1990.

INSTRON TEST CONFIGURATION FOR STIFFNESS

FIGURE 1

STATIC STIFFNESS - BAT COMPARISONS

FIGURE 2

FIGURE 3

MAXIMUM BEAM DEFLECTION IN HANDLE - CM

FIGURE 4

DISPLACEMENT AT POINT OF LOAD   CM x 10⁻³

BAT ELASTICITY - BARREL COMPRESSION LOAD

LOUISVILLE (H & B) HARDWOOD BAT MODEL C271 PRO
ACCELERATION FREQUENCY RESPONSE, POSITION 1

FIGURE 5   LOUISVILLE (H & B) ALUMINUM BAT MODEL TPX BBL
ACCELERATION FREQUENCY RESPONSE, POSITION 1

202

Measurement Locations

NOTE: NODES ARE AT SAME LOCATIONS FOR BOTH BATS FOR ALL
MODES OF VIBRATION.

VIBRATIONAL MODES OF BOTH H&B C271 WOOD AND
BAUM AAA PRO MODEL WOOD COMPOSITE BATS

FIGURE 6

ACOUSTIC SIGNATURES

FIGURE 7

203

AVERAGE HITTING DISTANCES

FT

■ COOPER C271
□ BAUM AAA PRO

SET   1   2   3   4   5   6

New Cooper C271
New AAA Pro Model

New Cooper C271
Used AAA Pro Model
(2030 Hits)

PERFORMANCE TEST RESULTS
COOPER C271 WOOD AND BAUM AAA PRO MODEL WOOD COMPOSITE.

PERFORMANCE TESTS: PRE-DURABILITY, SETS 1-3
NEW BAUM P17 AND NEW COOPER C271/C27

TEST	BAUM P17	COOPER C271/C27
Set 1: 9/16/91		
Total swings	157	179
Total hits counted	102	101
(incl. < 200		
Total hits measured	71	68
(200' and above)		
Average distance	261	268
	Percentage Difference: 2.68%	
Set 2: 9/17/91		
Total swings	113	118
Total hits counted	82	82
(incl <200)		
Total hits measured	68	61
(200 ft and above)		
Average distance	269	271
	Percentage Difference: 0.74%	
Set 3: 9/18/91		
Total swings	182	181
Total hits counted	117	117
(incl < 200)		
Total hits measured	89	80
(200 and above)		
Average distance	279	267
	Percentage Difference: 3.96%	

PERFORMANCE TESTS: POST DURABILITY SETS 4-6 USED
BAUM AAA PRO MODEL (P12, 2030 HITS)
AND NEW COOPER C271(C9)

TEST	BAUM P12	COOPER C271/C9
Set 4: 9/27/91		
Total swings	176	161
Total hits counted	115	116
(incl. < 200)		
Total hits measured	77	89
(200' and above)		
Average distance	249.6	250.2
	Percentage Difference: 0.24%	
Set 5: 10/1/91		
Total swings	161	154
Total hits counted	119	110
(incl. < 200)		
Total hits measured	96	91
(200' and above)		
Average distance	235.4	233.3
	Percentage Difference: 0.89%	
Set 6: 10/3/91		
Total swings	93	64
Total hits counted	69	47
(incl. < 200)		
Total hits measured	61	38
(200 and above)		
Average distance	233.3	234.9
	Percentage Difference: 0.6%	

FIGURE 8

204

SECOND INTERNATIONAL CONGRESS ON RECENT DEVELOPMENTS IN AIR- AND STRUCTURE-BORNE SOUND AND VIBRATION

MARCH 4-6, 1992   AUBURN UNIVERSITY, USA

THE DAMPING EFFICIENCY OF METAL AND COMPOSITE PANELS

Mr. Richard M. Weyer
Applied Research Laboratory
The Pennsylvania State University
Post Office Box 30
State College, PA 16804
USA

and

Mr. Richard P. Szwerc
Code 1944
David Taylor Research Center
Department of the Navy
Bethesda, MD 20084
USA

ABSTRACT

The dissipation of energy in metal and composite free panels has been experimentally measured using two independent techniques in both air and water. The measured loss factors resulting from the two measurement techniques compare favorably in both media.

The damping efficiency, as defined by Dubbleday and Fausett [3], is experimentally determined for each of the panels. Frequency regimes of effectiveness for mechanical damping treatments are indicated, and the dominance of radiation losses is shown for panels in water near the coincidence frequency.

NOMENCLATURE

A_p	surface area of panels
B_i	flexural rigidity of layer i
C_o	wave speed of fluid medium
C_L	wave speed of panel material
f_i	frequency, Hz
G_i	storage shear modulus of layer i (imaginary part)
$H_{m,n}$	distance between neutral axes of layers "m" and "n"
h	panel thickness
K_i	extensional stiffness of layer i
m''	mass per unit area of panel
$R(f)$	room constant
σ_{RAD}	radiation efficiency
λ	wavelength
ρ_o	density of fluid
ρ_P	density of panel material
ϕ_{PP}	spectral density of radiated acoustic pressure
ϕ_{aa}	spectral density of panel acceleration
η_s	loss factor of viscoelastic material
μ_p	Poisson's ratio
ω	circular frequency, $2\pi f$, rads/sec
ν	kinematic viscosity

1.0 INTRODUCTION

The ability to minimize the vibrational response of structures to various forms of excitation is highly desirable for many reasons. Many methods are employed to control unwanted vibration such as constrained layer damping treatments [1], the use of highly damped composite materials [2], and active control schemes. However, some of the methods are very expensive and difficult to incorporate into the design and the manufacture of a structure. If a structure happens to be loaded by a fluid, the structural engineer can often utilize an alternate damping mechanism inherent to the structure, the energy loss due to acoustic radiation. Kinetic energy in a panel is partially dissipated by conversion into acoustic radiation and at some frequencies, especially in a dense fluid, this means of energy dissipation can be the dominant damping mechanism. In fact, at frequencies greater than the acoustic coincidence frequency, most of the structural energy is converted into acoustic radiation.

Energy decay is viewed herein as the result of the dissipation of energy from a structure without regard for the dissipation mechanism. A more rigorous term for this decay is the loss factor. The loss factor is the fraction of the kinetic energy in a structure which is dissipated in a cycle of vibration. Damping is the process by which the energy decay occurs. When not associated with a specific mechanism, the terms energy decay, loss factor, and damping are roughly comparable. If the specific mechanism is known, or thought to be known, we refer to it by the specific mechanism, i.e. the mechanical loss factor, or mechanical damping.

Damping efficiency is defined by Dubbleday and Fausett [3] as the ratio of the energy dissipated through mechanical damping to the total energy dissipation by all possible means. As alluded to above, the damping efficiency decreases as frequencies approach the acoustic coincidence frequency and the radiation damping becomes the dominant energy dissipation mechanism. Recently, Dubbleday and Fausett have presented an analytical expression for the determination of damping efficiency. In this article, we will present experimental evidence which supports the theoretical developments presented by Dubbleday and Fausett.

Loss factor measurements are made in air and in water on undamped and highly damped metal and composite material panels. When the loss factor measurements from air and water are compared, the data from the denser fluid are shown to yield elevated loss factors at all frequencies. However, the increase in loss factor is especially dramatic as the coincidence frequency is approached and these data are seen to be independent of the mechanical loss factor of the panels and depend only on the radiation damping of the panels.

As a result, we conclude that for panels in a dense fluid medium, the mechanical damping efficiency decreases at frequencies approaching the coincidence frequency. Therefore the effectiveness of mechanical damping treatments to control structural vibration as frequencies approach the coincidence frequency is limited. Instead, the radiation loss factor becomes the dominant loss mechanism above coincidence where the damping efficiency is low.

2.0 DESCRIPTION OF PANELS

The panels used in these experiments varied in materials and construction. Four panels were used; two were made of a metal alloy, and two were made of a composite material. All of the panels had dimensions of 10 inches width and 16 inches length. The metal panels were 1.1 inches thick and the composite panels were 1.5 inches thick.

Two variations of the metal panels were tested. The first panel was simply a solid block of metal machined to the appropriate dimensions. The second panel contained a layer of constrained layer damping material. The damping layer was a 1/32-inch thick viscoelastic material bonded to the base of the panel with binary epoxy. The constraining layer was a 1/16-inch thick metal sheet bolted into place. Figure 1 shows the metal panels used in these experiments.

The composite material panels were fabricated from layers of woven graphite fibers embedded in an epoxy resin. The first panel was made up of two solid panels of 3/4-inch thickness glued face to face to give a total thickness of 1.5 inches. The second panel was more complicated since it contained two constrained layers of damping and a filled void. Figure 2 shows the construction details of this panel. The constrained damping layers were 1/32-inch thick and were deeply embedded on only one side of the panel. The void was created by casting a pocket in each of two 3/4-inch panels which were then glued together to give the total panel thickness of 1.5 inches. The void was filled with an enhanced molding compound.

For ease of identification, we have assigned the following designations to each of the panels and these will be used throughout the remainder of this article. Panel 1

206

refers to the solid metal alloy panel, Panel 2 is the damped metal alloy panel, Panel 3 is the solid composite panel, and Panel 4 is the damped composite panel. Table 1 summarizes the panels used during these experiments.

3.0 LOSS FACTOR MEASUREMENT PROCEDURE

Loss factor measurements were conducted in air and water for each of the panels. Two independent methods were used to make the measurements. The first, referred to as the reverberation time method is based on measuring the 60 dB decay time of the panel vibrational energy in 1/3 octave bands. The second, referred to as the 3 dB down method, is based upon measuring the half power points associated with the resonance frequencies of the panel. Both of these methods are well known techniques for the determination of the loss factor of a structure [7].

The reverberation time method relates the exponential decay of vibrational energy in a panel to the loss factor of the panel. The measurement is relatively simple to conduct. The panel is suspended by a thin elastic chord from a single attachment point to approximate the free-free boundary condition. An elastic chord is recommended so that any losses caused by the attachment are kept to a minimum. The panel is then excited by an impact, typically by a small hammer. An accelerometer mounted at a corner of the panel senses the acceleration and the decaying signal is passed to a 1/3 octave filter, amplified, and finally stored in a digital oscilloscope. The oscilloscope trace is read by a computer which displays the logarithm of the signal resulting in a straight line. The straight line is analytically fit and the loss factor can be directly determined from the slope of the line. Equation (1) shows the relationship:

$$\eta(f) = 1/(\beta \tau f_o) \tag{1}$$

where η is the frequency dependent loss factor, B is a constant, τ is the slope of the line, and f_o is the center frequency of the 1/3 octave band of interest.

The 3 dB down method is a classic measurement technique that involves locating the resonance frequencies of the panel and observing the frequency bandwidth for which the magnitude of the resonance response has decayed by one-half, or 3 dB. Equation (2) shows how the loss factor is calculated using this method:

$$\eta(f) = \Delta\omega/\omega_o \tag{2}$$

where η is the frequency dependent loss factor, $\Delta\omega$ is the bandwidth about the frequency of resonance defined by the 3 dB down points from the peak, and ω_o is the frequency at resonance.

Care must be taken to locate resonance frequencies that represent only one mode of vibration of the panel. Multiple modes may be smeared together and distort the results if their frequencies are in close proximity to one another. Therefore, this method is usually handicapped as the frequency and the modal density of the panel increase. Contrasting the limitation imposed on the 3 dB down method is the fact that as the modal density of the panel increases, the more effective the reverberation time method becomes, since averaging the decay rates of all of the modes gives a better estimate of the loss factor. At low frequencies where there are few modes, or in bands where no modes exist, the reverberation time method must be used with caution.

The 3 dB down measurements were conducted by hanging the panels in the same manner as described for the reverberation time method to simulate free-free boundary conditions. One of two sources was used to excite the panels into vibration. All of the panels were excited with a mechanical shaker that was glued directly to the panel through a force gauge and driven by a swept sine wave. Some of the panels were excited acoustically by placing a speaker near the panel and driving the speaker with a swept sine wave. The advantage of the acoustic method is its nonintrusive nature; however, its results, particularly in water, tended to be limited in frequency since the source output rolled off significantly as the frequency increased making it difficult to excite the panel. The panel vibrational responses were measured using an accelerometer, or in some cases a laser vibrometer. Agreement in loss factor between the two means of excitation was very good and no effort has been made here to distinguish between the methods in the results.

It should be pointed out that all of the panel loss factor measurements that used the reverberation time method were conducted at the David Taylor Research Center (DTRC), and the 3 dB down measurements were made at both the Applied Research Lab at Penn State (ARL) and DTRC. Part of the interest in conducting these measurements was to see if the results of the two independent measurement techniques agreed. In air it was expected that they would be the same, but in water there were fundamental differences in the

207

facilities where the measurements were conducted that raised concerns. At DTRC the water measurements were conducted in a large 10' x 13' x 13' tank, which is described in detail by Blake, et. al. [5]; while at ARL the water measurements were conducted in a small 5.83' x 2.42' x 1.83' tank. However, as the results will show, the resulting loss factor values agreed quite well.

Comparisons of the measured loss factors via the reverberation time method and the 3 dB down method were made for all of the panels in air and water. In general, the agreement between the methods is good. Figures 3 and 4 show typical results of such a comparison. Figure 3 shows the comparison of the two methods for a composite panel in air, and Figure 4 shows the comparison for a composite panel in water. The frequency limitation of the 3 dB down method is clearly evident in the figures. The method's reliance on low modal density hinders its use as frequency increases. The reverberation time method is inherently subjective when it comes to fitting a line to the energy decay slope. As a result, these data can appear quite scattered and it is best to present them as a group of individual points or as a band describing the limits of the range of those points.

4.0 DETERMINATION OF DAMPING EFFICIENCY

Recall that the damping efficiency is defined by Dubbleday and Fausett [3] as the ratio of the energy decay which can be attributed solely to the mechanical damping of the structure to the total energy decay in that structure. In an analytical investigation, it is relatively simple to separate the effects of different loss mechanisms. Experimentally, it is more difficult because the techniques that measure energy loss cannot usually discriminate between the causes of the loss.

The principal mechanisms for energy dissipation in panels which are suspended in a free-free boundary condition are viscous losses, mechanical losses, and radiation losses. Viscous losses can be attributed to the energy expended by the panel during the creation of local disturbances in the surrounding fluid. Mechanical losses can be attributed to energy transfer into the support fixtures and to energy dissipation by strains induced within the vibrating panel. According to Nashif, et. al. [1], this is the primary means by which constrained layer damping treatments increase the energy decay rate in a structure. Finally, energy can be dissipated by the conversion of kinetic energy into acoustically radiated energy.

The first part of this investigation is to experimentally determine the energy loss, or damping level which is due solely to the mechanical losses associated with the panels. Ideally, the measurement of the mechanical energy decay in a freely suspended panel would be made in a vacuum in order to eliminate the likelihood of viscous and acoustic radiation losses. Then the measured decay would be due solely to the mechanical losses within the panel. However, from a practical point of view, in-vacuo measurements were not possible. Instead, the experimental method is based on two approximations. First, it can be shown that a panel freely suspended in air will experience such light fluid loading that viscous loading will be negligible. Secondly, if the panels are suspended using a relatively thin elastic chord, then the panel is essentially in a free-free boundary condition and experiences no losses due to the support fixtures.

Guidance was supplied to the experimental determination of the mechanical losses by making two supporting calculations. The radiation loss factor of the panels in air is calculated so that an estimate may be made of the frequency at which acoustic radiation represents the dominant loss mechanism. The mechanical loss factor is also calculated. Note that it is this mechanical damping level which the experiment seeks to obtain.

The loss factor due to viscous losses is calculated according to Blake [5]. He defines the viscous loss factor as:

$$\eta_v = 4.4 \; \rho_o/\rho_p \; 1/h \; (v/\omega)^{1/2} \tag{3}$$

Figure 5 is the result of this calculation for the metal and composite panels freely suspended in air.

When the wave speed in the panel equals the wave speed in the surrounding fluid, most of the vibrational energy will be converted and radiate as acoustic energy. The frequency at which this occurs is referred to as the coincidence frequency. Blake [6] shows that the coincidence frequency for a panel is:

$$f_c = c_o^2/\pi \; 1/c_L h \; (3(1 - \mu_p))^{1/2} \tag{4}$$

Below the coincidence frequency, a fraction of the panel vibrational energy is converted to acoustic radiation. This amount can be described by the radiation loss

208

factor which can be estimated using the theory of Cremer, Heckl, and Ungar [7]:

$$\eta_r = \rho_o c_o \sigma_{RAD}/\omega m''$$ (5)

The estimated radiation loss factors of the metal and composite panels in air according to Equations (4) and (5) are shown in Figure 6. This estimate of the radiation loss factor is made by using Equation (5). The radiation efficiency is assumed to have a positive slope of approximately 25 dB/decade as the frequencies approach coincidence. This assumption is based on prior experience and is consistent with other published work [10]. The acoustic coincidence frequency for these panels in air is determined from Equation 4.

The amount of mechanical damping which a constrained layer damping treatment will cause in a panel has been described by Ungar [9]. If η_m is the mechanical damping of the panel, it can be calculated by:

$$\eta_m = \eta_s YX \left(1 + (2 + Y) X + (1 + Y) \left(1 + \eta_s^2\right) X^2 \right)^{-1}$$ (6)

where $X = G'_2 \omega_2 (\lambda/2\pi)^2$ $(1/K_1 + 1/K_3)$ and $Y = H_{31}^2/(1/K_1 + 1/K_3)(B_1 + B_3)$. Figure 7 shows the results of the calculation based on Equation (6) of the mechanical damping in the damped composite and the damped metallic panels. Figures 8 and 9 contain all of the calculated loss mechanisms for the freely suspended damped metal and composite panels in air, respectively.

The measurements of the loss factor of the panels in air should result in the levels depicted in Figures 8 and 9. Observe that the mechanical loss factor is the dominant loss mechanism over the majority of the frequencies. The experimental methods limit the upper frequency of the experimental data to 40 kHz. Therefore, over the entire frequency range of this experiment, the energy loss measurements in air are controlled by the mechanical damping. It should be noted that the upper frequency limit of accelerometer data is typically considered to be approximately 20 kHz in the most ideal situation. However, because these measurements require only relative acceleration levels, and not absolute levels, data up to 40 kHz has been included.

5.0 EXPERIMENTAL RESULTS

The dissipation of energy in both metal and in both composite material panels has been measured in air and in water using the experimental methods described in section 3.0. In the following sections, we will discuss the results of these measurements, and make comparisons to the calculations described above.

5.1 Results in Air

In Figure 10, the loss factor measurements of composite material Panels 3 and 4 are presented. A comparison of the loss factor measurement of Panel 4 with the mechanical, radiation, and viscous loss factor calculations shown in Figure 9 indicates that all of the measured energy decay is due to the mechanical damping.

Similarly, Figure 11 shows the loss factor measurements of metal Panels 1 and 2. A comparison of the measured losses of panel 2 to the calculated mechanical, radiation, and viscous loss factors for Panel 2 shown in Figure 8 also shows that all of the measured energy dissipation is due to the mechanical damping. Therefore, the energy decay of both the metal and composite material panels in air is dominated by mechanical losses.

The undamped metal and composite material panels (1 and 3) are not included in the above comparisons since the Ungar equations for calculating the mechanical damping of a panel require the application of a constrained layer damping treatment.

These results demonstrate that the first requirement for determining the damping efficiency, the mechanical damping quantity, has been satisfied.

5.2 Results in Water

Figure 12 is a comparison of the in-air and in-water loss factor measurements from Panel 3. Observe that for the in-water measurements the loss factor in the mid-frequency range has been elevated slightly while significant increases have occurred in the higher frequencies. Figures 13-15 are the in-water energy decay measurements for Panels 4, 1, and 2 respectively, compared with the in-air measured data for each of the panels. Note that these comparisons are qualitatively similar to the results shown in Figure 12. The in-water data for all of the panels show total losses which are elevated above the mechanical loss factors of the panels, particularly at higher frequencies.

The cause of the increased high frequency loss factors can be determined by calculating the radiation loss factor in water. For improved accuracy, this calculation

is not based upon an estimate of the panel radiation efficiency, as was sufficient in air. Rather, this calculation is based upon a direct measurement of the radiation efficiency of these panels. The in-water data analysis is felt to require a more rigorous determination of the radiation loss factor because preliminary data indicated that radiation damping had become the dominant mechanism of energy loss for the panels in water.

The experimental approach for the determination of the radiation efficiency is summarized both by Blake [6] and Cremer, Heckl, and Ungar [7]. In short, the panels are suspended in a reverberant tank, excited with random noise via an electrodynamic shaker, and the ratio of the resulting average sound pressure levels in the tank to the spatially averaged vibration levels of the panels is obtained. As developed by Blake [6], the relationship between the acoustic pressure, the vibration amplitude of the panels, and the radiation efficiency of the panels is:

$$\sigma_{RAD} = (\pi/\rho_o c_o)^2 \ f^2 R(f) \ 1/A_p \ \phi_{pp}(f)/\phi_{aa}(f) \tag{7}$$

The radiation loss factor is calculated from the measured radiation efficiency by the relationship in Equation (5).

Figure 16 shows the measured radiation efficiency of the four panels in water. The radiation loss factor is calculated using the data in Figure 16 and Equation (5) and compared to the energy decay measurements of each of the four panels in water.

In Figure 17, the loss factor measurements of metal Panels 1 and 2 are plotted along with the calculation of the radiation loss factor for these panels. Observe the good agreement between the measured high frequency data and the calculated radiation loss factor. Similarly, Figure 18 is a comparison of the measured loss factor from composite material panels 3 and 4 and the calculation of the radiation loss factor for each of them. Good agreement is also seen in the high frequency region here.

The comparison in Figures 17 and 18 suggests that the elevation in the loss factors at high frequencies after submerging the panels in water is due to acoustic radiation damping of the panels. The earlier comparisons in Figures 13-15 suggested that the low to mid-frequency loss factors are controlled by the mechanical damping. Clearly these data show that mechanical damping is not the most efficient mechanism of energy decay for the fluid loaded panels in the frequency range near and above the coincidence frequency.

5.3 Damping Efficiency

The damping efficiency of Panels 1-4 in water is now determined based upon the definition given by Dubbleday and Fausett [3]. Figure 19 shows the damping efficiency for Panels 1 and 2, and Figure 20 shows it for Panels 3 and 4. The damping efficiency is easily determined by taking the ratio of the curves displayed in Figures 12-15, since it has been shown that the in-air loss factors are dominated by the mechanical damping of the panels. In all cases, the damping efficiency decreases as the frequency increases. This behavior qualitatively agrees with the findings of Dubbleday and Fausett as illustrated in Figure 21. Note that Figure 21 is taken directly from the paper by Dubbleday and Fausett.

For Panels 1 and 2, where the mechanical damping of Panel 2 has been increased greatly by the application of the constrained layer damping treatment, the damping efficiency has been greatly increased. The effectiveness of the mechanical damping on controlling the vibration of the panel has resulted in an extension of the frequency range where the damping treatment is beneficial.

For Panels 3 and 4, although the mechanical damping of the Panel 4 has been increased by approximately two, the frequency range where the damping treatment has an impact on the vibration is barely affected. The damping efficiency has been largely unaffected by the application of the constraining layer to Panel 4.

6.0 CONCLUSIONS

We have addressed several of the mechanisms that cause the dissipation of vibrational energy in structural panels. It has been shown for a panel immersed in a dense fluid, such as water, that energy dissipation due to acoustic radiation dominates the loss mechanisms as frequencies approach the coincidence frequency. As a result, the use of mechanical damping treatments to control energy decay in this frequency regime is inefficient.

Observe in Figure 19 that the application of a damping treatment to an undamped metal panel extended the frequency range of high values of damping efficiency. This result occurred because of the significant increase in energy decay caused by the damping treatment. However, in Figure 20, the damping efficiency of the composite

panels was barely affected by the application of the damping treatment. This result is due to the relatively high damping level of the initial composite panel, Panel 3.

It is important to make the distinction that although the amount of energy decay attributable to the mechanical damping treatment did increase on Panel 4 when compared to Panel 3 (Figure 10), the damping efficiency was largely unaffected. So, there are benefits to applying constrained layer damping treatments in the frequency region where the mechanical damping is the dominant loss mechanism; however, the treatment will not always expand the frequency range for which the damping treatment is intended to control the vibration.

This is significant to the structural engineer who is trying to decrease the vibration of a fluid loaded panel over a broader frequency range. What has been demonstrated here is that if a panel already has a high level of mechanical damping, increasing the energy decay through the use of mechanical damping treatments will not necessarily extend the frequency range of its effectiveness. The relatively simple calculations employed in this document can provide a designer with enough information to decide if it would be advantageous to increase the mechanical damping if the goal is to control the vibration at frequencies in the vicinity of coincidence.

Another important point demonstrated by these results comes from the comparison of several methods of determining the loss factor of a panel. Energy decay was measured by observing the half-power bandwidth of panel resonances and the reverberation time of energy in the panel. Both contact and non-contact measurement techniques were employed, and both mechanical impact and acoustic energy were used to excite the panel into vibration. Despite these variables, the loss factor data from all of the measurements was in good agreement. Energy loss due to acoustic radiation was also determined by measuring the radiation efficiency of the panels and calculating the radiation loss factor. The radiation loss factor obtained in this manner was found to be in good agreement with the measured loss factors near the coincidence frequency.

REFERENCES

1. A. D. Nashif, D. I. G. Jones, and J. P. Henderson, Vibration Damping, J. Wiley and Sons, 1985.

2. D. Barrett, "Damped Composite Structures", Composite Structures 18, 1991, pp. 283-294.

3. P. S. Dubbleday, and L. V. Fausett, "Constrained-layer Damping Analysis for Flexural Waves in Infinite Fluid-Loaded Plates", J. Acoust. Soc. Am. 90(3), Sep. 1991, pp. 1475-1487.

4. W. K. Blake, and L. J. Maga, "Chamber for Reverberant Acoustic Power Measurements in Air and in Water", J. Acoust. Soc. Am. 57(2), Feb. 1975, pp. 380-384.

5. W. K. Blake, "On the Damping of Transverse Motion of Free-Free Beams in Dense, Stagnant Fluids", Shock Vib. Bull., 42(4), Jan. 1972, pp. 41-55.

6. W. K. Blake, "The Radiation from Free-Free Beams in Air and in Water", J. Sound Vib., 33(4), 1974, pp. 427-250.

7. L. Cremer, M. Heckl, and E. E. Ungar, Structure-Borne Sound, Springer-Verlag, 1973.

8. E. Ungar, "Guide to Designing Highly Damped Structures", Machine Design, Feb. 14, 1963, pp. 162-168.

9. F. Fahy, Sound and Structural Vibration, Academic Press, 1985.
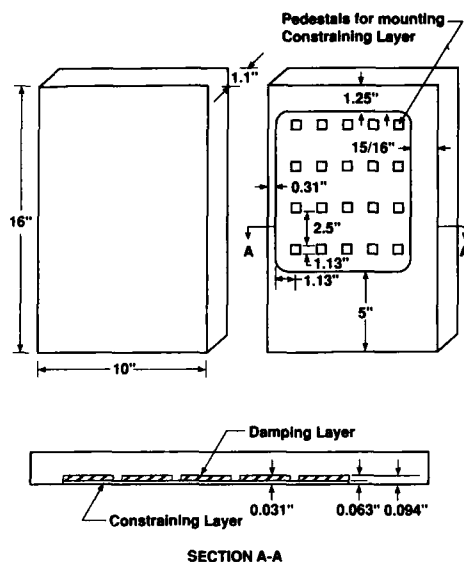
Figure 1. Metal Panel With and Without Constrained Layer Damping Treatment
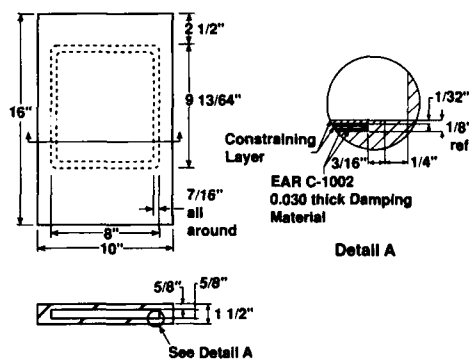
Figure 2. Composite Panel with Constrained Layer Damping Treatment Embedded in Panel

Table 1

Panel Number	Panel Description
1	Solid metal alloy
2	Metal alloy with constrained layer damping treatment
3	Solid composite material panel
4	Composite material panel with constrained layer damping treatment and a filled void
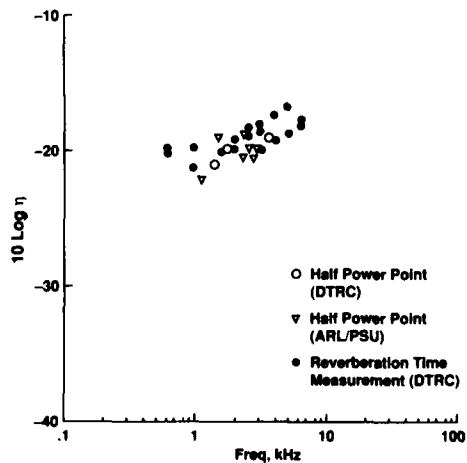
Figure 3. Comparison of Loss Factor Data Measured with Various Methods on a Composite Panel in Air.
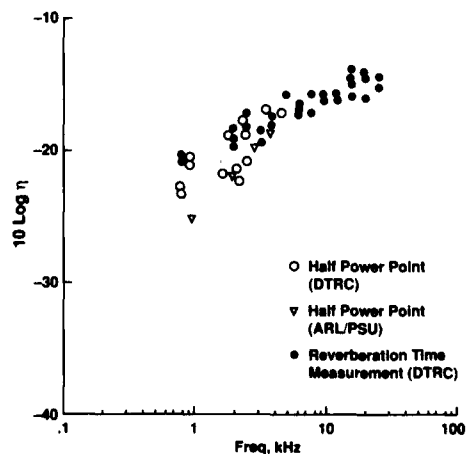
Figure 4. Comparison of Data Measured with Various Methods on a Composite Panel in Water.

212
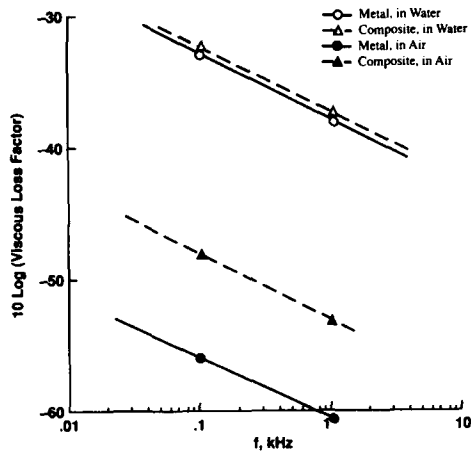
Figure 5. Viscous Loss Factor Calculations, Based on
Blake (4).

Figure 6. Estimated Radiation Loss Factor for Metal
and Composite Panels in Air.

Figure 7. Estimated Mechanical Loss Factor of Panels 2 and 4.
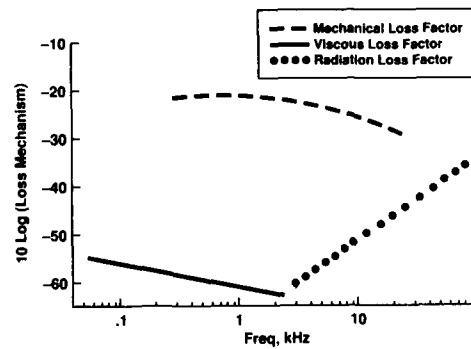
Figure 8. Summary of Estimated Loss Mechanisms for
Panel 2 in Air.

Figure 9. Summary of Estimated Loss Mechanisms for
Panel 4 in Air.
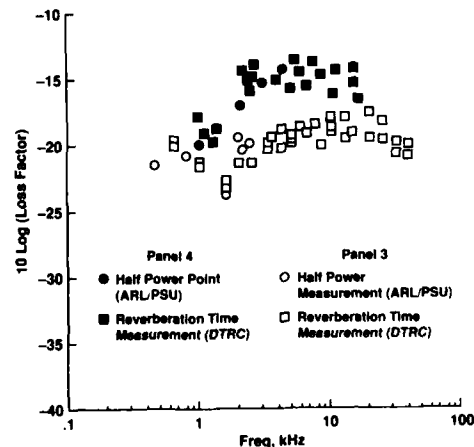
Figure 10. Comparison of Energy Decay Measurements on
Panels 3 and 4 in Air.

213
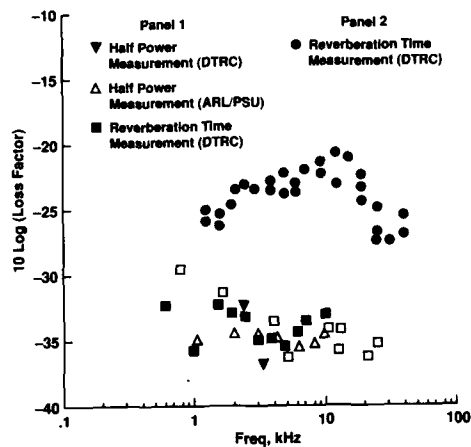
Figure 11. Comparison of Energy Decay Measurements on Panels 1 and 2 in Air.
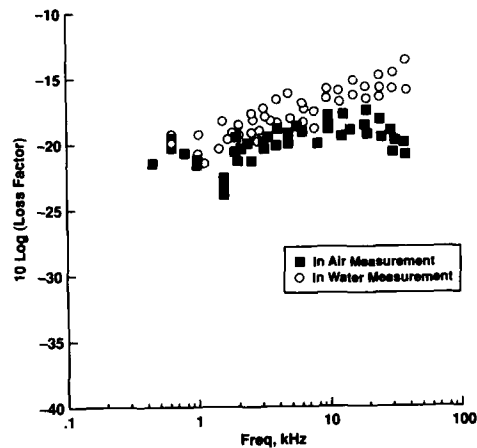
Figure 12. Comparison of Energy Decay Measurements on Panel 3 in Air and in Water.
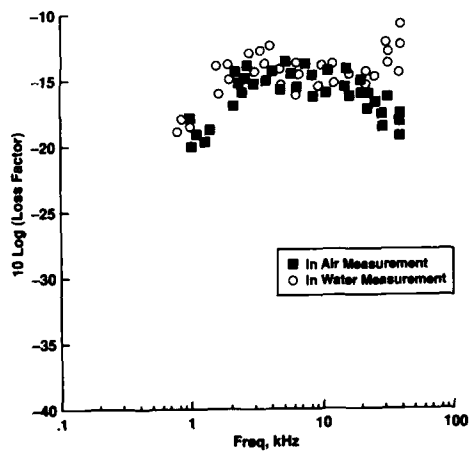
Figure 13. Comparison of Energy Decay Measurements on Panel 4 in Air and in Water.
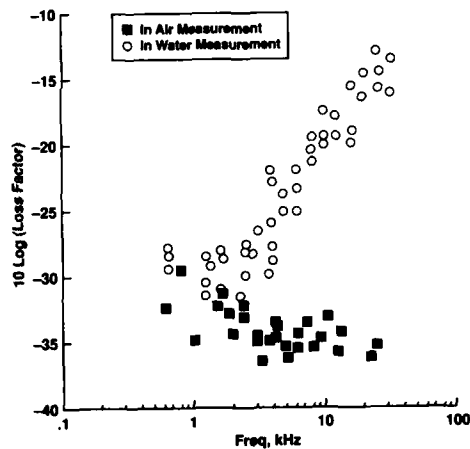
Figure 14. Comparison of Energy Decay Measurements on Panel 1 in Air and in Water.
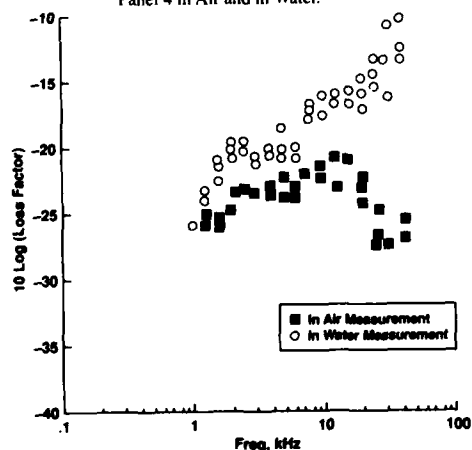
Figure 15. Comparison of Energy Decay Measurements on Panel 2 in Air and in Water.
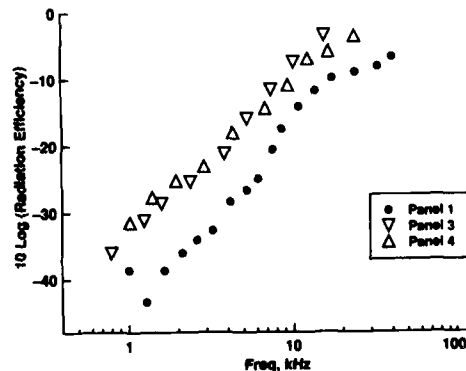
Figure 16. Radiation Efficiency Measurements on Panels 1,3,4.

214
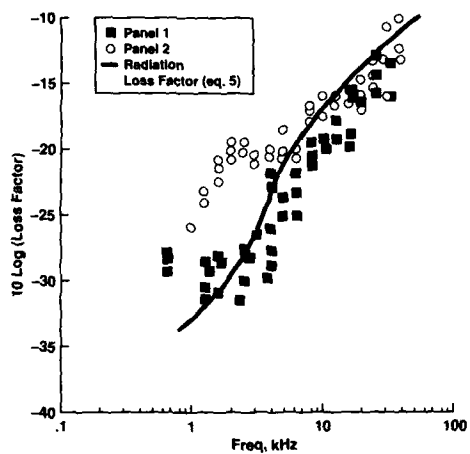
Figure 17. Comparison of Energy Decay Measurements of Panels 1 and 2 in Water and Radiation Loss Factor (based on Figure 16).
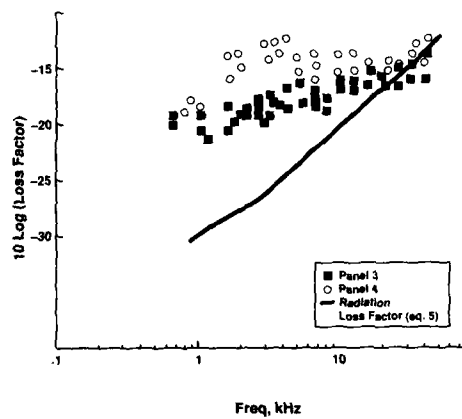
Figure 18. Comparison of Energy Decay Measurements of Panels 3 and 4 in Water, and Radiation Loss Factor (Based on Figure 14).
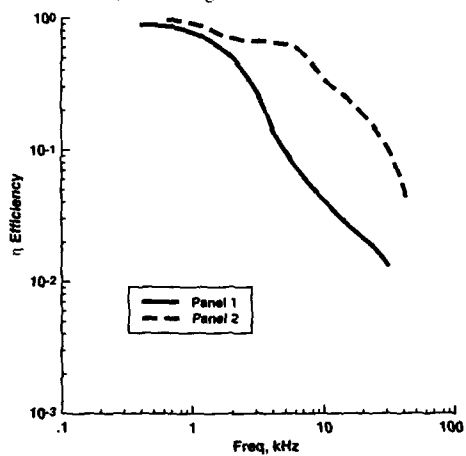
Figure 19. Experimentally Determined Damping Efficiency of Panels 1 and 2 in Water.
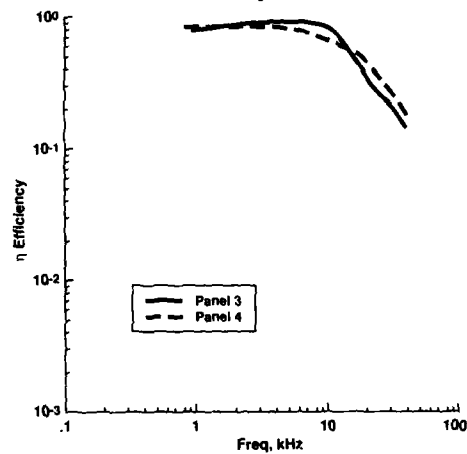
Figure 20. Experimentally Determined Damping Efficiency of Panels 3 and 4 in Water.
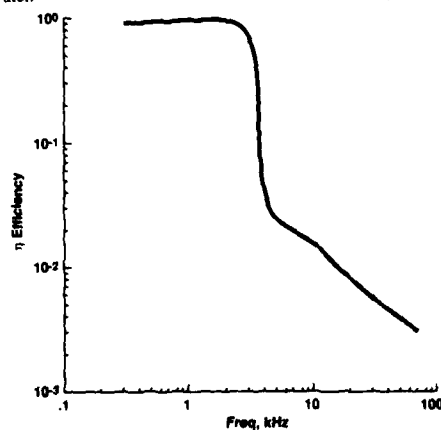
Figure 21. Analytically Determined Damping Efficiency of Damped Metal Panel in Water (from ref. 3).

215

DAMAGED INDUCED DAMPING CHARACTERISTICS

OF GLASS REINFORCED EPOXY COMPOSITES

Max A. Gibbs and Mohan D. Rao
Mechanical Engineering Department
Michigan Technological University
Houghton, MI 49931 USA

Anne B. Doucet
Mechanical Engineering Department
Louisiana State University
Baton Rouge, LA 70803 USA

ABSTRACT

The objective of this research effort is to characterize the effect of impact damage on the damping capacity and dynamic modulus of glass fiber/epoxy composites. Unidirectional and cross-ply laminates were impacted over a range of impact energies. The absorbed energy was measured during the test. Damaged modes were characterized using a scanning electron microscope for the various combinations of layup and impact energy. Damping measurements were made before and after impact and the results are correlated to the observed damage modes and measured values of absorbed impact energy. Assessment of damage using damping as a parameter shows good promise as a non-destructive test tool in composites, as the method does not involve time-consuming scanning of the whole structure.

INTRODUCTION

A thorough understanding of the vibration damping capacity of fiber reinforced polymer composites is essential for the successful design and use of these materials in structural and non-structural applications. Most structural systems subjected to dynamic loading accumulate damage in their service environment. In order to assure safety, it is necessary that this damage be monitored to assess its occurrence, location and extent for subsequent repair and compensation. Damage may be interpreted and monitored from changes in the dynamic properties, viz. stiffness and damping of the structure. It has been recognized that damage due to impact in any mode will greatly influence on the damping capacity of the material which will have to be characterized by experiment and analysis. Previous attempts in this area of damage assessment from vibration tests can be found in references 1 through 4.

In this pilot study, the effect of impact damage on the damping and natural frequency (related to the dynamic stiffness) of unidirectional and cross-ply glass reinforced epoxy composites have been studied through experiments. Damping capacity and natural frequencies of samples before and after impact have been measured using the frequency response function obtained by modal analysis type experiments. Damage modes have been characterized through a scanning electron microscope and attempts are made to correlate the measured changes in stiffness and damping of samples to observed damage modes.

EXPERIMENTAL PROCEDURE

Scotchply Type 1002 Glass fiber-reinforced composite laminates from 3M Corporation were used in the experiments. Both 'unidirectional' and [0/90] cross-ply laminates were used. The 'unidirectional' material actually has a spring orientation (denoted SO), the commercially available form of the unidirectional composite. A cross-ply is placed near the top and bottom of the laminate to provide strength in the 90° direction without significantly affecting the properties in the 0° fiber direction. The laminate layup is thus $[0/90/0_4]_s$. 15.2 x 8.9 cm impact specimens were machined with the 0° fiber direction in the long specimen axis. The laminate thicknesses were 3.5 mm and 3.2 mm for the SO and cross-ply material, respectively.

The impact tests were performed using an instrumented drop weight tower. The impact fixture, which holds the impactor tup, slides along steel guiding columns which are equipped with linear bearings. These linear bearings reduce the friction between the impact fixture and steel guiding columns, allowing the impactor to fall perpendicular to the specimen. The specimen is clamped along the short sides to supports providing a 11 cm x 8.9 cm rectangular opening.

The impact tup is conical steel impactor instrumented with two strain gages cemented 180° apart. The strain gages are connected to a strain gage conditioner and amplifier through a quarter-bridge circuit and this arrangement serves as a load cell. Using the quarter-bridge circuit, the two active gages act to eliminate bending contributions. The amplified output of strain-gage voltage is sent to a Nicolet 4094C digital oscilloscope which records the voltage vs. time impact history. The impactor was calibrated by loading it in compression and recording the linear relationship of strain voltage to the applied load. Using this calibration curve, the output voltage of the strain gage can be converted to impact load.

The energy absorbed by the impact specimen is given by the following formula:

$$U = v_0 \int_0^t F \, dt + g \int_0^t F t \, dt - 1/2M \left(\int_0^t F \, dt \right)^2$$

where U is impact energy absorbed by the specimen, v_0 is the velocity just before impact, M is the mass of the impactor, F is the impact force, g is acceleration due to gravity, and t is time. The last two terms of this equation represent higher order terms with respect to time and are neglected in the actual calculation of impact energy.

The velocity just before impact is measured using two photo diodes located near the bottom of one of the steel guiding columns. A timer is used to record the time interval when the impactor travels the 15.2 cm distance between the two photo-diode detectors. The average velocity over the 15.2 cm is then calculated. To allow investigations of impact energy on the material response, two additional impact weights were used with the conical impactor to provide three levels of impact weight; 1.02 kg, 1.25 kg, and 1.66 kg.

The frequency response function of each of damaged as well as the undamaged plates was measured using the setup as shown in Figure 1. The structure's frequency response function (ratio of acceleration to force) was utilized to determine the damping ratio ζ and the natural frequency ω_n. The structure was excited with an instrumented hammer at a point on one side of the damaged area and then the response was measured with a mini accelerometer. The frequency response function was measured on only the top layer of the laminate where the damaged was introduced. The structure was fixed at both ends so as to simulate the same boundary conditions that were used during impact tests. The fixed supports were made of two steel clamps with two steel spacers in between the plate. The specimen with the steel clamp was then fastened to a steel bed plate to prevent any motion between the support and the plate. The frequency range of interest was limited to 3kHz. Three modes of vibrations were analyzed to determine the damping ratio (ζ) and the natural frequency (ω_n). The impact energy absorbed by the glass fiber composites ranged from 0 to 126 Joule for the unidirectional fibers and 0 to 115 Joule for the cross-ply laminates.
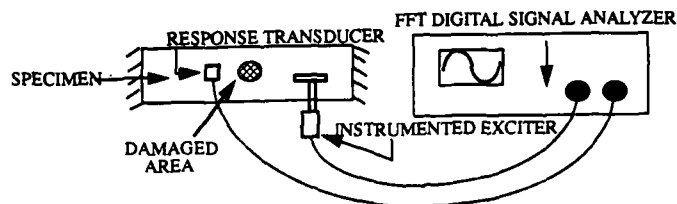
Figure 1. Experimental Set-up

RESULTS

A typical frequency response plot as obtained using the HP35660 FFT analyzer is shown in Figure 2. It shows three modes in the frequency range of interest. Damping ratios for each mode was estimated using a single-degree of freedom curve-fitting technique available in the SMS Modal Analysis Software. Figures 3 through 6 show the variation of ω_n and ζ with respect to impact energy for both the unidirectional and cross-ply samples. These results are summarized in Tables 1 and 2. Table 1 shows the damping ratio and natural frequencies for the unidirectional fiber orientation composites for three modes of vibration. A general increase in ζ for the first mode can be seen as the amount of impact energy is increased in the plates.

Table 1. Damping and Frequency Results
Unidirectional Fibers

Energy (J)	Mode 1		Mode 2		Mode 3	
	Hz	ζ	KHz	ζ	KHz	ζ
0	710	1.76	1.52	0.66	2.75	0.84
69	625	1.67	1.45	0.72	2.56	0.98
73	722	1.76	1.55	0.71	2.83	0.82
94	723	2.07	1.60	0.66	2.89	0.79
98	691	3.17	1.53	0.71	2.72	1.24
121	626	2.37	1.49	0.67	2.71	0.84
126	677	3.31	1.54	0.68	2.84	0.84

Table 2. Damping and Frequency Results
Cross-Ply Fibers

Energy (J)	Mode 1		Mode 2		Mode 3	
	Hz	ζ	KHz	ζ	KHz	ζ
0	652	3.37	1.42	0.68	2.56	0.84
56	608	1.42	1.47	0.68	2.57	1.04
60	584	1.53	1.47	0.58	2.52	0.79
89	605	1.83	1.42	0.61	2.49	0.83
92	602	1.73	1.45	0.59	2.56	0.81
110	595	1.63	1.39	0.60	2.45	0.78
115	594	2.92	1.47	0.58	2.56	0.76

Analysis of the microstructure of the unidirectional plates reveals a significant crack that formed through the thickness. As the number of events and amount of energy increases, the number of cracks through the interior 0° plies increases. These cracks interact as shown in Figure 7. A 100% to 200% increase in damping is noticed for the first mode of the unidirectional laminate. There is always delamination where the crack meets the first 0/90 interface. The cracks interface with one another cause an increase in the energy absorption of the plate which in turn results in a higher damping capacity. The second and third modes for the unidirectional fibers has a some-what similar increase in damping ratios as compared to the undamaged plate, but this increase appears to be less significant for higher frequencies.

Table 2 shows the damping and natural frequencies for the cross-ply laminated plates. The damping ratio ζ appears to decrease for the first mode as the impact energy absorbed by the plates is increased. Analysis of the microstructure for the cross-ply laminates reveals some interesting results. At low amounts of impact energy and events, matrix cracks are predominately seen through the bottom ply and some delamination at the 0/90 interface. As the number of events and amount of energy is increased, the number of delaminated interfaces increase and finally cracks form between them. This microstructure can be seen in Figure 8. For the second and third modes, the damping ratio shows no noticeable increase or decrease that would be significant to be attributed to impact damage. The damping ratio decrease in the first mode for the cross-ply plates was significant enough to show that if damage occurred at a low frequency, the structure's frequency response function can be utilized to detect damage. The damage is more evenly distributed and is horizontal to the impact with the cross-ply lami-nates while the cracks are large and through the thickness in the unidirectional laminates. The plane of measure-ment for the unidirectional and cross-ply plates was the top plane where the damage was induced. For the unidirectional plates, the effect of the damage could be measured since the crack was through the thickness while for the cross-ply, the damage was initially at the bottom surface and finally propagate toward the surface where the measurement was made.
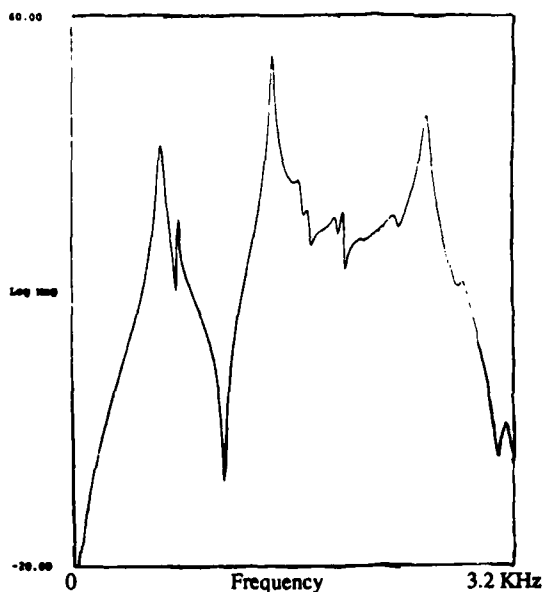
Figure 2. Frequency Response Plot of Unidirectional Plate
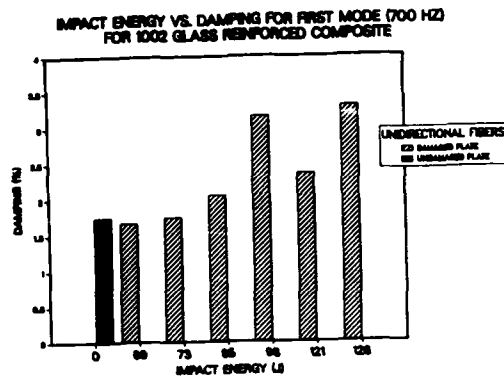
Figure 3.
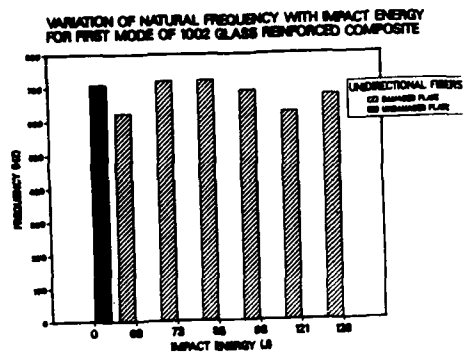
Figure 4.
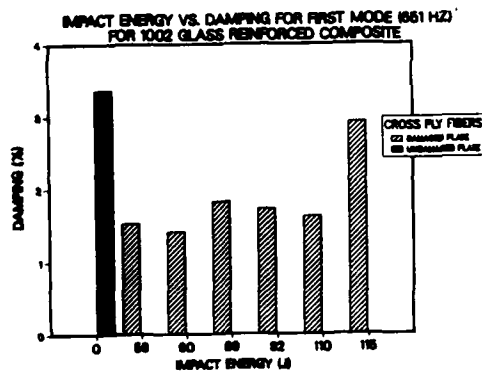
Figure 5.
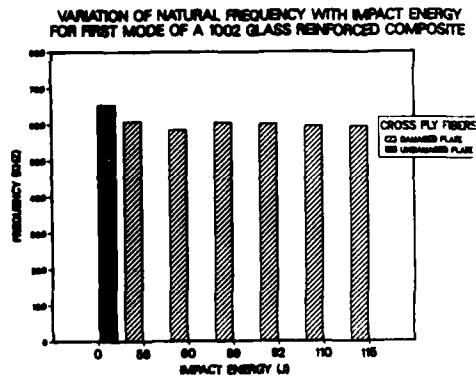
Figure 6.

Figure 7. Microstructure of Unidirectional Laminates
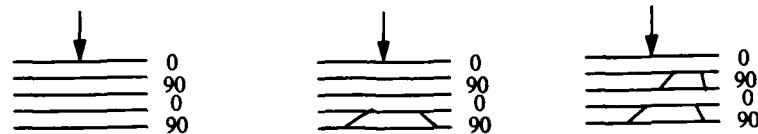
Figure 8. Microstructure of Cross Ply Laminates

CONCLUSION

The use of glass fiber/epoxy composites for many structural applications has greatly increased in the recent years along with a need to monitor the structure to insure its safety in a dynamic environment. Impact damage to these structures can be monitored by utilizing the structure's frequency response function to measure its damping capacity. For damage induced at low frequencies (below 1 KHz), an increase in damping capacity is very evident for unidirectional orientated fibers while a significant decrease in damping capacity for cross-ply orientated fibers was noticed. Damping changes at the higher frequencies (greater than 1 KHz) were not significant enough to detect damage induced into the structure. The increase in the damping capacity for the unidirectional fibers can be attributed to the formation of microcracks as noticed in the microstructure. The matrix crack develops through the entire thickness as the damaged is increased causing crack interfacing which perhaps improves the laminate's energy absorption. For the cross-ply fibers, the damage affected the bottom surface initially and as the damaged increased the cracks propagate horizontally toward the surface. The damage lowered the damping capacity of the cross-ply fibers at low frequencies (below 1 KHz), the reason for this is not clear and needs further research. To determine the effects of damage to the damping characteristics of cross-ply fibers, the structure's frequency response function must be measured on the damaged surface. Further work needs to be done on how to monitor damage at higher frequencies (above 1KHz) and detect the damage through non-contact methods.

REFRENCES

[1] Springer, W.T., Lawrence, K.L. and Lawley ,T.J., "*Damage Assessments Based on the Structural Frequency-Response Function*," Experimental Mechanics, March 1988, 34-36.

[2] Cawley, P. and Ray, R., "*A Comparison of the Natural Frequency Changes Produced by Cracks and Slots*," ASME Vol. 110, July 1988, 366-369.

[3] Wolff, T. and Richardson, M., "*Fault Detection in Structures from Changes in Their Modal Parameters*," 7th IMAC proceedings, 1989, 87-92.

[4] Cawley, P. and Adams, R.D., "*The Location Of Defects In Structures From Measurements Of Natural Frequency*," Journal Of Strain Analysis Vol 14 No.2, 1979, 49-56.

SECOND INTERNATIONAL CONGRESS ON RECENT DEVELOPMENTS IN AIR- AND STRUCTURE-BORNE SOUND AND VIBRATION

MARCH 4-6, 1992   AUBURN UNIVERSITY, USA

ON THE FLEXURAL DAMPING OF TWO MAGNESIUM ALLOYS AND A MAGNESIUM METAL-MATRIX COMPOSITE

Squadron Leader Graeme G. Wren
Royal Australian Air Force
Department of Defence - Air Force Office
Russell Offices
Canberra, ACT 2600
AUSTRALIA

Vikram K. Kinra
Aerospace Engineering Department
Texas A&M University
College Station, TX 77843
U.S.A.

ABSTRACT

The dimensional extent of large space structures make them prone to vibrations which can attain large amplitudes even under modest impulsive or cyclic loading. In addition, stability during dynamic manoeuvres requires short settling times. Therefore, the incorporation of damping into space structures is necessary. The need to develop low-complexity, lightweight, high-strength, dynamically stable structures for the space environment has necessitated the search high damping materials. Studies of magnesium and its alloys demonstrate that these materials possess very high damping compared to other metals. Recent studies have shown that when magnesium is alloyed with particular solute species having very low solid solubilities ($<1\%$) such as Al, Cu, Sn, Zr, Mn or Si, the characteristically high damping of magnesium is preserved while the mechanical properties are enhanced. In addition, both damping and the amplitude dependence of damping increases with decreasing solute atom concentration. This paper presents damping data on a recent magnesium MMC, Pitch 55 graphite fibres in a matrix of Mg-0.6%Zr (P55Gr/Mg-0.6%Zr) and two magnesium alloys, Mg-0.6%Zr and Mg-1.0%Mn. These data support the conclusions of other researchers who estimated and measured the damping of Mg-0.6%Zr and a similar alloy, Mg-Mg$_2$Ni, having a very low solid solubility of Ni (0.1%). Finally, a comparison between the measured damping of the Mg-0.6%Zr alloy and the $[0_8]$ P55Gr/Mg-0.6%Zr composite is presented to quantify whether the addition of strength-enhancing fibres contributes to, detracts from, or otherwise influences the high damping properties of the matrix. It is noted that the data presented herein pertains to flexural damping and thus provides a globally-averaged measure of damping. This compendious study is an extract from a more comprehensive doctoral investigation of damping in advanced composites.

NOMENCLATURE

A_o	amplitude at t_o
$A(t)$	amplitude at time t
E	Young's modulus
E'	Storage modulus (real part of the complex modulus)
E″	Loss Modulus (imaginary part of the complex modulus)
f_r	resonant frequency (cycles/second)
m	slope of straight line
Q^{-1}	inverse quality factor
t	time
t_o	initialization time, $t=0$
W	maximum elastic energy stored during a cycle

δ logarithmic decrement
$\mu\varepsilon$ micro-strain
ε_i accuracy of experimental measurement, i
ζ, ξ damping ratio
η loss factor
ϕ phase angle by which the applied stress leads the resulting strain (loss angle).
ψ specific damping = $\Delta W/W$
ω frequency in radians/second = $2\pi\phi$

INTRODUCTION

Composite materials, in general, have been utilized for many aerospace structural applications because of their ability to be taylored to meet specific strength and weight requirements. In particular, recent attention has focused on the use of metal-matrix composites (MMC's) for space structural applications because of the growing need for high-strength, low-weight materials which are impervious to the inherently hostile environment. The candidate materials to be used in the fabrication of MMC's are varied. Of the available fibres, Pitch 55 or Pitch 100 graphite fibres seem to be favoured [1,2,3]. Of the many metals available, matrices possessing a high level of material damping have been viewed as the most promising candidates for use in advanced composites to enhance dynamic stability [4-7].

Studies of magnesium and its alloys have shown that these materials possess very high damping compared to other metals [8,9]; one alloy, Mg-0.6%Zr, *has been known to possess* high damping for some time [10]. Recent studies [11] have shown that when magnesium is alloyed with particular solute species having very low solid solubilities (<1%) such as Al, Cu, Sn, Zr, Mn or Si, the characteristically high damping of magnesium is preserved while the mechanical properties are enhanced. In addition, both damping and the amplitude dependence of damping increases with decreasing solute atom concentration [12].

Although the literature presents some studies of damping in magnesium alloys [10,11,12,13], there is very limited data on the damping capacity of magnesium MMC's [14,15]. Because of the continuing need to investigate the degree of damping offered by new MMC candidates for use in space structural applications, this paper has been compiled to present damping data on a recent magnesium MMC, namely Pitch 55 graphite fibres in a matrix of Mg-0.6%Zr (P55Gr/Mg-0.6%Zr). In addition, the damping measurements of two magnesium alloys, namely Mg-0.6%Zr and Mg-1.0%Mn, are presented to support the conclusions of other researchers [10,11,12] who estimated and measured the damping of Mg-0.6%Zr and a similar alloy, Mg-Mg$_2$Ni, having a very low solid solubility of Ni (0.1%). Finally, a comparison between the measured damping of the Mg-0.6%Zr alloy and the [0$_8$] P55Gr/Mg-0.6%Zr composite is presented to quantify whether the addition of strength-enhancing fibres contributes to, detracts from, or otherwise influences the high damping properties of the matrix.

It is noted that the data presented herein pertains to flexural damping and thus provides a globally-averaged measure of damping. A detailed discussion of the various measures of damping is presented in a comprehensive doctoral investigation of damping in advanced composites [16] from which this paper was extracted.

PREVIOUS RESEARCH

When magnesium is alloyed with particular solute species which have very low solid solubilities (<1%), such as Zr, Mn, Al, Cu, Sn, Ni, or Si, the characteristically high damping of magnesium is preserved while the mechanical properties are enhanced [10,11]. The high damping of pure magnesium and these particular alloys is due to the ease of dislocation motion along the basal slip planes. Small additions of alloying elements (<1%) result in the formation of localized precipitates. It is believed that the presence of this second phase increases the dislocation density in the high-purity magnesium phase without inhibiting dislocation movement to a significant degree. This results in these alloys displaying a higher damping capacity than that observed in unalloyed magnesium [12]. The typical microstructure of these hypoeutectic alloys consists of large grains of primary Mg surrounded by a eutectic mixture in a matrix of Mg; the eutectic mixture is typically of the form Mg$_2$R, where R represents the alloying species [14]. The grains produced by the small additions of an alloying element, particularly zirconium, are evenly distributed, equiaxed and have random orientations. Because the grains are equiaxed, the break-away phenomena can occur at very low applied stresses in grains where the orientation is 45°, and therefore subject to the maximum resolved shear stress [12].

Sugimoto, Niiya, Okamoto and Kishitake [11] investigated the damping capacity of Ni, Cu, Al, and Sn magnesium alloys using a resonant beam apparatus. They showed that the damping and Young's modulus were strong functions of the grain size of the primary magnesium. It was observed that when the grain size was smaller than 10μm, the mobility of the dislocations was decreased which in turn decreased the damping. They concluded that enhanced damping and amplitude-dependence of damping in magnesium alloys was produced when (1) the solubility of alloying elements was very low (<1%) and (2) when the primary magnesium grains were dendritic or globular in shape and larger than about 10 microns in size. Weissmann and Babington [10] developed a cast polycrystalline Mg-0.6%Zr alloy for the making of guided missile components, such as the housing, instrument plate and gyro mounting brackets for the main guidance section, because of its high damping characteristics. They determined that the damping properties of this alloy are not affected by machining, aging or finishing and, although heat treatments do not affect the unmachined alloy, a reduction in damping has been observed following heat treatments of machined samples.

Factors which decrease damping are increased alloy concentration, rapid solidification and deformation. It has been shown that both damping and the amplitude dependence of damping increase with decreasing solute atom concentration [10,11] and that slow solidification rates of these alloys maximizes damping by allowing greater dislocation mobility due to larger grain sizes [14]. The decrease in damping following deformation occurs by the formation of preferred orientations due to the deformation [12,13].

THE DEFINITION OF DAMPING USED

The definition of damping used herein is the *specific damping capacity*, ψ, which is defined as the energy dissipated during one cycle of motion divided by the maximum elastic energy stored during the cycle:

$$\psi = \frac{\Delta W}{W} \qquad (1)$$

Although there are many other definitions and interpretations for this quantity in the literature, they will not be discussed here; the reader is referred to a detailed discussion of these definitions elsewhere [16]. *The reader is strongly cautioned that the origins of each definition of damping are varied and that the mathematical meaning of each definition, although supposedly being for the same quantity, can in fact be quite different.* However, these definitions approach equality for small damping, say, $\tan\phi < 0.1$, and the relationships between them are given by:

$$\psi = 2\pi\eta = 2\pi\tan\phi = 2\pi E^*/E' = 2\delta = 2\pi Q^{-1} = 4\pi\zeta = 4\pi\xi \qquad (2)$$

SPECIMENS

The specimens examined in this study are neat Mg-0.6%Zr and Mg-1.0%Mn magnesium alloys and a P55Gr/Mg-0.6%Zr metal-matrix composite. The dimensions and thermoelastic properties of all specimen constituents are given in Tables 1 and 2, respectively. All specimens were provided by Martin Marietta Aerospace Corporation, Denver, Colorado.

The P55Gr/Mg Laminate Specimens

The [0₈] P55Gr/K1A-Mg (Mg-0.6%Zr) composite specimens were fabricated by FMI Incorporated [17] using a vacuum investment casting process as shown in Figure 1 [18]. The panels were carefully hand-sanded to a thickness of approximately 2 mm (0.08 in) and specimens were cut from the panels using a diamond wheel. This laminate was examined using a scanning electron microscope (SEM). Representative SEM samples were cut from the laminate using a diamond saw and then polished to a mirror finish of 0.5 micron using successively finer grades of diamond paste. The samples were ultrasonically cleaned following each polishing step to remove residue which may cause scoring of the surface and obscure detail. Examination of the four electron-micrographs, Figure 2, show that in general there is good matrix infiltration. However, the lowest magnification micrographs show a small degree of voiding in these composites. This qualitative evidence of voiding is presented to aid interpretation of the experimental results presented herein and demonstrate that a continuum mechanics approach to modelling of damping in these composites could be justified.

The Experimental Method

Apparatus

The experimental apparatus, shown in Figure 3, comprises a cantilevered beam, a Bruel and Kjaer M0002 electromagnetic transducer for vibrational excitation, a Wavetek Model 164 frequency generator and a NAD 2200 power amplifier to drive the excitation transducer, a strain gage connected to a Micro-Measurements BAM-1 strain gage bridge to detect vibrational motion, and a Data Precision Model 6000/611 waveform analyzer interfaced with a Hewlett Packard 217/9000 computer via an IEEE bus to acquire and reduce data. To exclude air-damping all tests were conducted in a vacuum chamber at a vacuum of 0.013 Pa (0.1 micron of Hg); a Cenco Hypervac 25 vacuum pump was used for this purpose. All specimens tested were non-magnetic. Therefore, to couple the specimen with the magnetic field of the transducer, high permeability discs 9mm in diameter and 0.3mm thick were bonded to the extreme ends of each specimen using super glue. The combined mass of these end tabs were typically less than 0.2% of the specimen mass. The transducers are specified to exert an attractive magnetic force of 0.02 Newtons at a specimen/transducer separation of two millimetres (mm) from the permeability discs [19]. The NAD 2200 amplifier was used so that strain amplitudes of up to $600\mu\varepsilon$ could be attained. Calibration procedures are discussed in Reference [16]. The estimate of error in the measured values of specific damping and modulus are $\varepsilon_\psi = \pm 1 \times 10^{-3}$ and $\varepsilon_E = \pm 4\%$, respectively.

Experimental Procedure

With reference to Figure 3, the output voltage from the waveform generator was connected via the amplifier to the electromagnetic transducer. The waveform generator was tuned to the flexural resonant frequency of the specimen. Vibrational motion was detected by the strain gage attached near the beam root and resonance was determined by monitoring the amplitude of oscillation c c digital oscilloscope. After steady-state vibration was achieved, the current to the excitation transducer was in ..upted allowing the specimen's oscillation to freely decay. At the same time a computer program was initiated. The free vibrational decay of the specimen was amplified and stored in digital form by the Data 6000 which then determined the voltage of each positive peak of the waveform. These values were passed to the computer via an IEEE 488 interface. The internal clock of the computer was used to obtain the time corresponding to each amplitude data point. Damping was determined using the logarithmic decrement technique.

It is not uncommon for spurious modes to become excited. Whenever this happens, mechanical energy is consumed by both modes but is attributed only to the mode under examination. Therefore, the measured damping is greater than its true value. This phenomenon is virtually impossible to detect in the time domain. However, it is very easy to guard against it in the frequency domain: the two modes will show up very clearly as two separate peaks in the Fourier transform of the signal. A typical time domain signal is shown in Figure 4; the corresponding FFT is given in Figure 5. It is clear that no spurious modes are excited.

Data Reduction - The Logarithmic Decrement Technique

The logarithmic decrement is a well known measure of damping obtained from the cyclic decay of free vibrations and provides a globally-averaged measure of damping [16]. This technique involves inducing steady-state vibration at the resonant frequency of the specimen and then allowing the vibrations to decay freely. In the past the damping capacity has been calculated using only two experimental data values obtained from the amplitude decay curve. Therefore, the experimental error of the resultant damping value is dependent on the experimental error (scatter) of only two data points out of typically 100 data values collected. A more accurate method is to average out the scatter inherent in each data point by using as many data points as possible to determine the value of damping. By rearranging the well-known expression for the logarithmic decrement, the result can be viewed as a linear equation:

$$\ln\left[\frac{A_o}{A(t)}\right] = \frac{\psi f_r}{2}[t-to] \qquad (3)$$

Plotting $\ln[A_o/A(t)]$ as a function of $[t-t_o]$ the gradient of the resulting curve is $0.5\psi f_r$. The material damping value is then:

$$\psi = \left[\frac{4\pi}{\omega}\right] m \qquad (4)$$

Typical free-decay and reduced curves are given in Figure 6. The points between 90% and 10% of the maximum amplitude were used to calculate damping. A least squares fit algorithm was then used to determine an interpolated line of best fit passing through the experimental data and the damping calculated from the gradient of this line. Typical standard errors for the linear interpolation routine were of the order of 1×10^{-4}.

RESULTS AND DISCUSSION

Flexural Damping of Mg-1%Mn and Mg-0.6%Zr Alloys

Results for Mg-1%Mn and Mg-0.6%Zr are shown in Figures 7 and 8, respectively, and Table 3. The size of the symbols used represent the mean plus one standard deviation. The mean damping of the Mg-1%Mn alloy between 15-50 Hz and 55 $\mu\varepsilon$ was $\psi \approx 3.5 \times 10^{-2}$ and that for the Mg-0.6%Zr alloy was $\psi \approx 7 \times 10^{-2}$. The experimental data is compared with the thermoelastic damping calculated using the thermoelastic properties listed in Table 2. Figures 7 and 8 show that the damping of the Mg-0.6%Zr alloy is higher and more strain-amplitude dependent over the range 15$\mu\varepsilon$ to 55$\mu\varepsilon$ than for the Mg-1%Mn alloy. In both cases the measured damping is significantly higher than the thermoelastic damping. These observations support the following findings, the latter of which was observed by Sugimoto, Niiya, Okamoto and Kishitake [11]:

a. due to the prominence of the dislocation damping mechanism in pure magnesium and low concentration magnesium alloys, one would expect the measured damping of these materials to be significantly higher than the thermoelastic damping; and

b. higher damping and strain amplitude dependence is observed for lower alloy concentrations.

Flexural Damping of the [0₈] P55Gr/Mg-0.6%Zr Composite

Since the experimental evidence supports the conjecture that the high damping in pure magnesium and low concentration magnesium alloys is primarily due to dislocation motion, then one would suspect that the addition of 46% volume fraction of fibres would have a noticeable effect on damping. The mobility of dislocations will not only be dependent upon the inter-fiber spacing, which as shown in Figure 2 varies greatly throughout the composite, but also upon the spacing between the Mg_2Zr and Mg_2Mn precipitates within the matrix. Although there is no quantitative information pertaining to the "inter-precipitate" spacing for the P55Gr/0.6%Zr composite, Steckel and Nelson [14] measured the distance (or "plate spacing" in their terminology) between Mg_2Si precipitates in a P55Gr/Mg-1%Si composite to be approximately 3μm; this comparison is based on the assumption that the microstructure of the P55Gr/Mg-1%Si composite is representative of the microstructure of the P55Gr/0.6%Zr composite based on a comparison of damping measurements found in the literature [16, Figures 29 and 64]. If this assumption holds, then one explanation for the decreased level of damping in the P55Gr/0.6%Zr composite could be that the 10 micron minimum size of the primary magnesium regions necessary for the high damping properties observed by Sugimoto, Niiya, Okamoto and Kishitake [11], is clearly not satisfied. In addition to inter-fiber and inter-precipitate spacing, the mobility of dislocations will be hindered by the fiber-matrix interface. Even though the interfaces themselves may be regions of dislocation formation due to the difference in the thermal expansion coefficients of the fibre and matrix (Table 2), they will impede dislocation motion by being both a physical barrier, and potential sites for dislocation pinning. It is therefore reasonable to expect that the measured damping of a Gr/Mg-Zr composite will be significantly less than that of the neat magnesium alloy matrix.

The damping of three P55Gr/0.6%Zr specimens (designated A-25, B-11 and B-12) was measured. The data from three specimens is shown in Figure 9 and Table 3. As expected the damping of the composite is much less than that of the neat magnesium alloy. This is shown more clearly in Figure 10 in which a separate experimental comparison of the damping in a Mg-0.6%Zr alloy and the P55Gr/0.6%Zr composite was conducted. The mean damping of $\psi \approx 6 \times 10^{-2}$ for the Mg-0.6%Zr alloy between 15-50 Hz compares to a mean damping for the P55Gr/Mg-0.6%Zr composite of approximately $\psi \approx 1.5 \times 10^{-2}$. It is evident from this comparison that the high damping properties of the magnesium alloys investigated are not preserved in the composite; that is, the high damping properties of the magnesium alloys investigated do not provide enhanced damping of the composite.

227

A closing comment. Although we have shown that the damping of a Gr/Mg composite is significantly less than that possessed by the neat matrix, the presence of an alloying element having very low solid solubility in the matrix still enhances the damping of the composite to some degree. This is evidenced by the work of Steckel in which the Mg_2Si precipitates in a Gr/Mg-1%Si composite produced higher damping than in a Gr/Mg-0%Si composite [15].

CONCLUSIONS

The damping of neat Mg-0.6%Zr and Mg-1%Mn alloys and a P55Gr/Mg-0.6%Zr composite was measured. The results for the neat alloys show that the measured damping of these materials was significantly higher than the thermoelastic damping and that higher damping and strain amplitude dependence is observed for lower alloy concentrations. The comparison between the neat alloys and the P55Gr/Mg-0.6%Zr composite showed that the high damping properties of the magnesium alloys investigated are not preserved in the composite.

REFERENCES

1. DiCarlo, J.A., Unpublished work received personally from D.A. DiCarlo, NASA-Lewis Research Center, Cleveland, Ohio, 44135.
2. Timmerman, N.S., and Doherty, J., "Loss Factors in Metal Matrix Composites," Army Materials and Mechanics Research Center, Final Report, AMMRC TR 84-22, June, 1984.
3. Bhagat, R.B., Amateau, M.F., and Smith, E.C., "Damping Behavior of Squeeze Cast Planar Random Carbon Fiber Reinforced 6061 Aluminum Matrix Composite," to appear in Journal of Composite Technology and Research.
4. Lesieutre, G.A., "Damping in Unidirectional Graphite/Metal Composites and Material Design Potential," Sparta Incorporated, Laguna Hills, California, 1987.
5. Persh, J., "Materials and Structures, Science and Technology Requirements for the DOD Strategic Defence Initiative, Ceramic Bulletin, Vol. 64, No. 4, 1985, p. 555.
6. Ashley, H., "On Passive Damping in Large Space Structures," AIAA Paper No. 82-0639, 23rd Structures, Structural Dynamics and Materials Conference, April 1982, p. 56.
7. Trudell, R.W., Curley, R.C., and Rogers, L.C., "Passive Damping in Large Space Structures," AIAA Paper 80-0677-CP, presented at the 21st AIAA/ASME/ASCE/AHS Structures, Structural Dynamics and Materials Conference, Seattle, Washington, May, 1980.
8. Stanton, L.R., and Thompson, F.C., "A Note on the 'Damping' Characteristics of Some Magnesium and Aluminum Alloys," Journal of the Institute of Metals London, Vol. 69, Part 1, 1943.
9. James, D.W., "High Damping Metals for Engineering Applications," Materials Science and Engineering, Vol. 4, 1969, p. 1.
10. Weissmann, G.F., and Babington, W., "A High Damping Magnesium Alloy for Missile Applications," ASTM Proceedings, Vol. 58, 1958, p. 869-892.
11. Sugimoto, K., Niiya, K., Okamoto, T., and Kishitake, K., "A Study of Damping Capacity in Magnesium Alloys," Transactions of the Japan Institute of Metals, Vol. 18, 1977, pp. 277-288.
12. Sugimoto, K., Matsui, T., Okamoto, T., and Kishitake, K., "Effect of Crystal Orientation on Amplitude Dependent Damping in Magnesium," Transactions of the Japan Institute of Metals, Vol. 16, 1975, pp. 647-655.
13. Schwaneko, A.E., and Nash, R.W., "Effect of Preferred Orientation on the Damping Capacity of Magnesium Alloys," Metallurgical Transactions, Vol. 2, 1971, p. 3453.
14. Steckel, G.L., and Nelson, B.A., "Mechanical Damping Behavior of Graphite-Magnesium," Aerospace Corporation Report No. TOR-0086(6726-01)-1, The Aerospace Corporation, El Segundo, California 90245, 10 October, 1985.
15. Steckel, G., "Material Damping Behavior of Gr/Al Composites," Aerospace Corporation, El Segundo, California, ONR Report No. TOR-0084-A-5726-01(-1), October 1985.
16. Wren, G.G., and Kinra, V.,K., Damping in Metal-Matrix Composites - Theory and Experiment, Department of Aerospace Engineering Report, Texas A&M University, College Station, Texas 77843 - Based on the Doctoral

Dissertation of Graeme G. Wren entitled "A New Technique for Measuring Axial Damping and It's Application to Metal-Matrix Composites", Texas A&M University, College Station, Texas 77843, May 1990.

17. FMI Incorporated, 666 North Hague, Columbus, Ohio 43204, Tel. (614) 272-5785.

18. Rawal, S.P., Misra, M.S., Jackson, J., and Goddard, D., "Novel Processing Techniques to Fabricate Gr/Mg Composites for Space Applications," Final Report MCR-88-635, Naval Sea Systems Command Contract N00024-84-C-5306, 1988.

19. Bruel & Kjaer Product Data Sheet for the MMOO2 Magnetic Transducer, Bruel and Kjaer Instruments Inc., 5111 West 164th Street, Cleveland, Ohio, 44142.

20. Rawal, S.P., Armstrong, J.H., and Misra, M.S., "Interfaces and Damping in Metal-Matrix Composites," Martin Marietta Aerospace Corporation, Denver, Colorado, Report No. MCR-86-684, December 1986.

Table 1. Dimensions of the Flexural Specimens

Specimen ID	Length (cm)	Width (cm)	Thickness (cm)
Mg/0.6%Zr			
1	14.20	1.26	0.198
2	14.15	1.26	0.196
Mg/1%Mn			
1	14.88	1.26	0.198
2	15.01	1.26	0.193
[08] P55Gr/Mg-0.6%Zr			
A-25	20.70	1.25	0.152
B-11	19.28	1.28	0.150
B-12	17.22	1.28	0.152

Table 2. Thermoelastic Properties of the Materials Studied

Material	E GPa	K GPa	G_{LT} GPa	r_{LT}	ρ g/cm^3	α μm/m°C	k W/m°K	C_p J/kg°K	V_f
Mg/Zr (K1A)	44.9	55.3	16.6	0.35	1.74	27.0	122.8	1046.6	
Mg/Mn (M1A)	44.2	55.3	16.6	0.35	1.74	26.0	137.7	1046.6	
P55Gr Fiber (10μmm) L	380.0	6.9	2.1	0.20	2.00	-1.25	120.9		
T	9.7		3.7	0.30		20.3			
P55Gr/Mg-0.6%Zr [0g]	164.8		16.5	0.35	1.91	26.6	110.5	1046.5	0.47
P55Gr/Mg-1%Mn [0g]	166.2		16.5	0.35	1.89	26.6	110.5	1046.5	0.46

Table 3. Experimental Values of the Mechanical Properties in Flexure

Material	ρ g/cm^3	E GPa	ψx10^{-2} @ 55 μs
Mg/0.6%Zr			
Specimen 1	1.83	46.88	7.0
Specimen 2	1.74	44.13	6.8
Mg/1%Mn			
Specimen 1	1.85	45.51	3.6
Specimen 2	1.80	44.68	3.4
[0g] P55Gr/Mg-0.6%Zr			
Specimen A-25	1.94	163.20	1.3
Specimen B-11	1.91	165.68	1.5
Specimen B-12	1.91	159.90	1.6
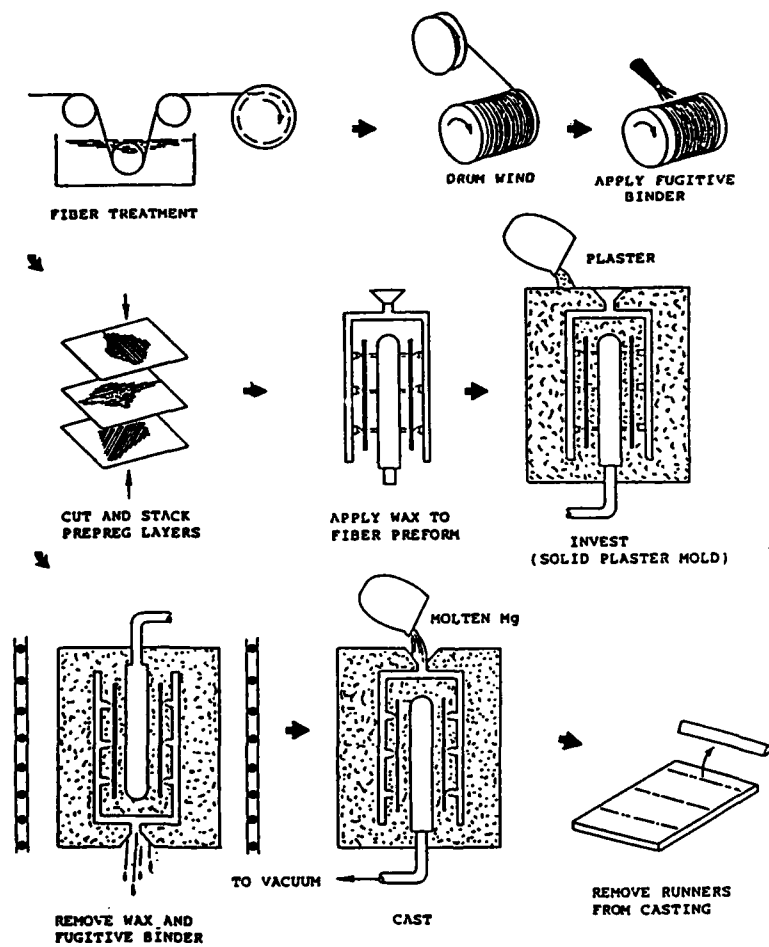
Figure 1 Schematic of Investment Casting Procedure Used to Fabricate the Gr/Mg Composite [20]

1000μm

1000μm

100μm

100μm
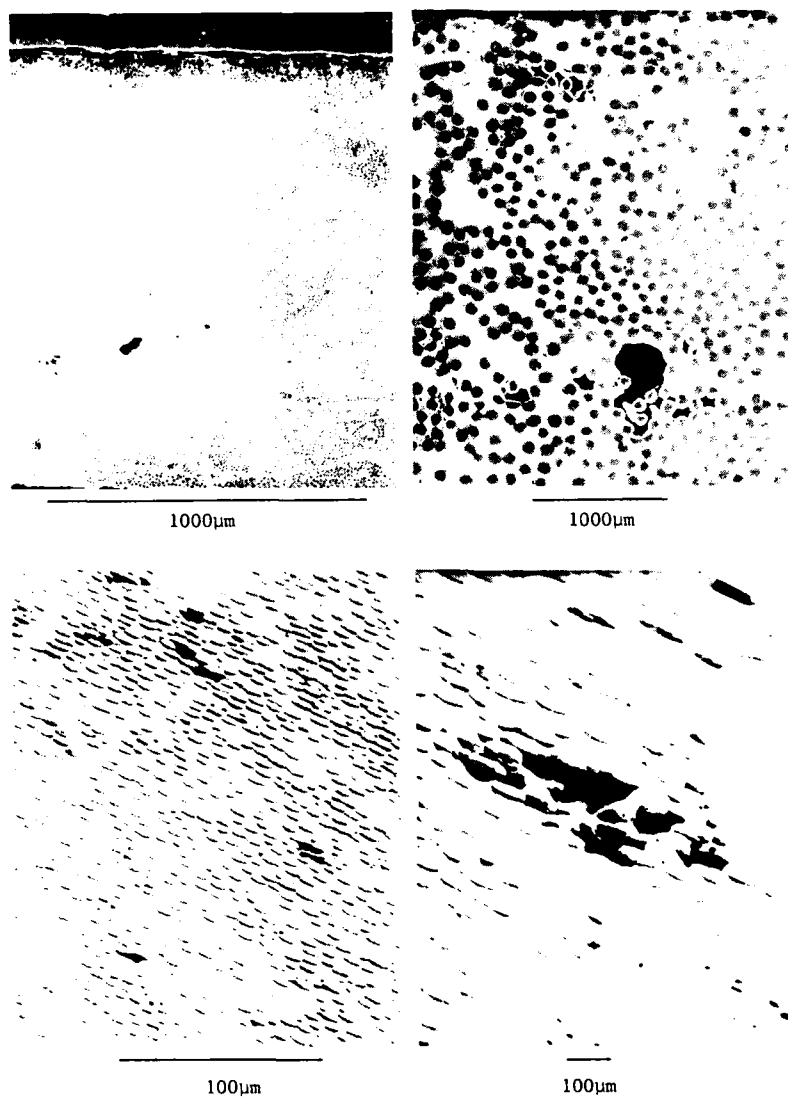
Figure 2 Electron-Micrographs of [0g] P55Gr/Mg Composite (450X)
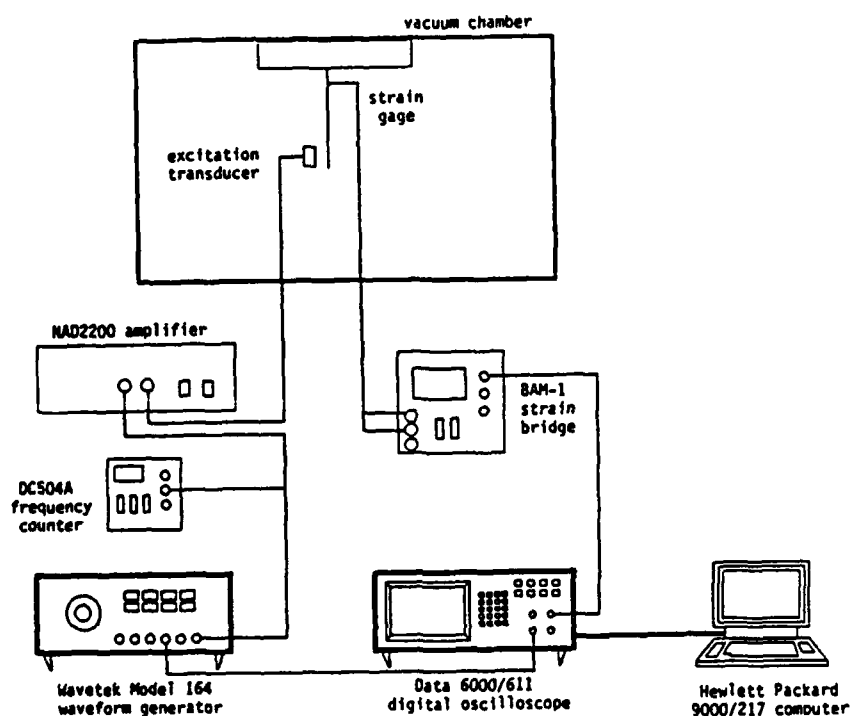
Figure 3 Experimental Apparatus
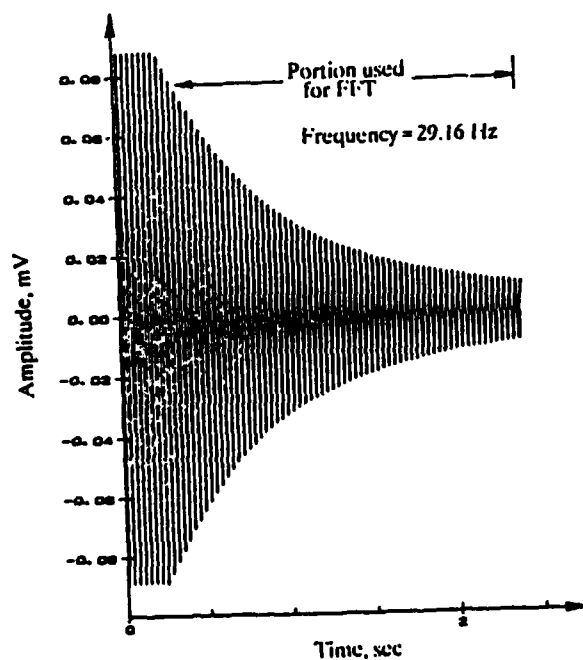
Figure 4 Time Domain Signal of Decay Waveform

232

Frequency = 29.16 Hz

Amplitude (volts)
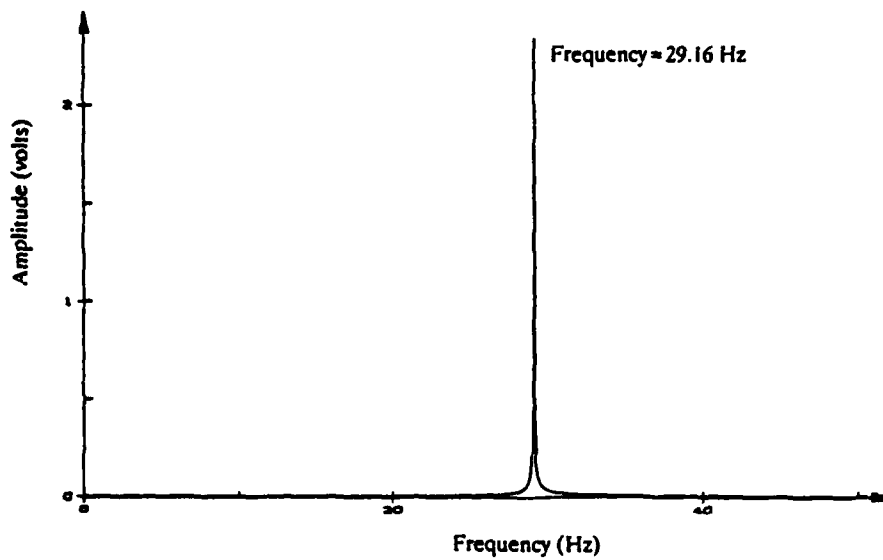
Frequency (Hz)

Figure 5 FFT of the Decay Waveform

Amplitude

time

$\ln[A_0/A(t_i)]$

$\psi/4\pi$

$\omega(t_1-t_0)$
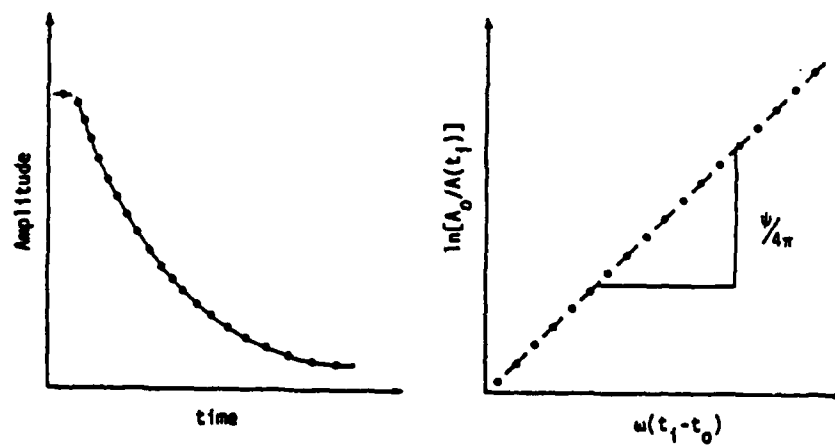
Figure 6 Typical Free-Decay and Reduced Experimental Data
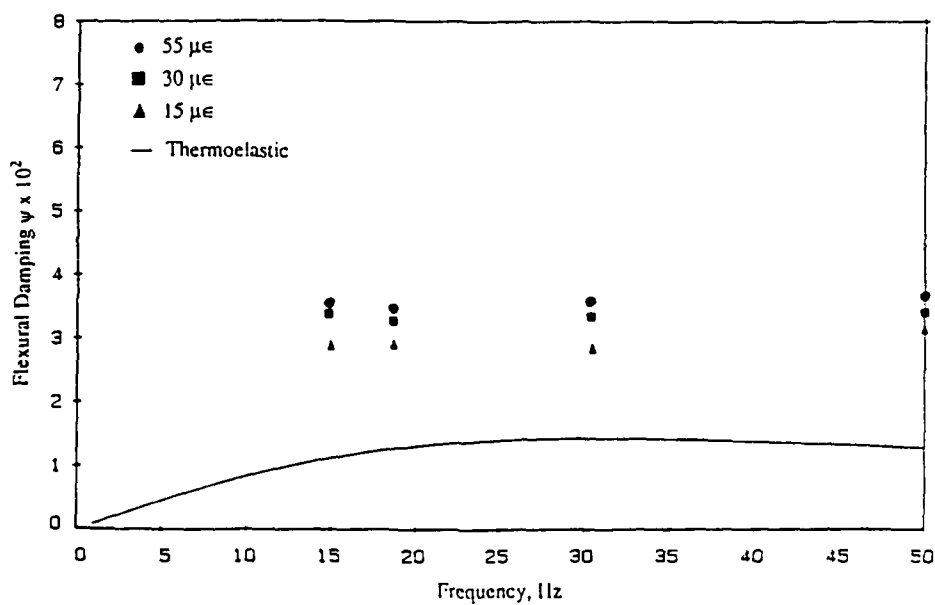
Figure 7 Flexural Damping vs Frequency for the Mg-1%Mn Alloy
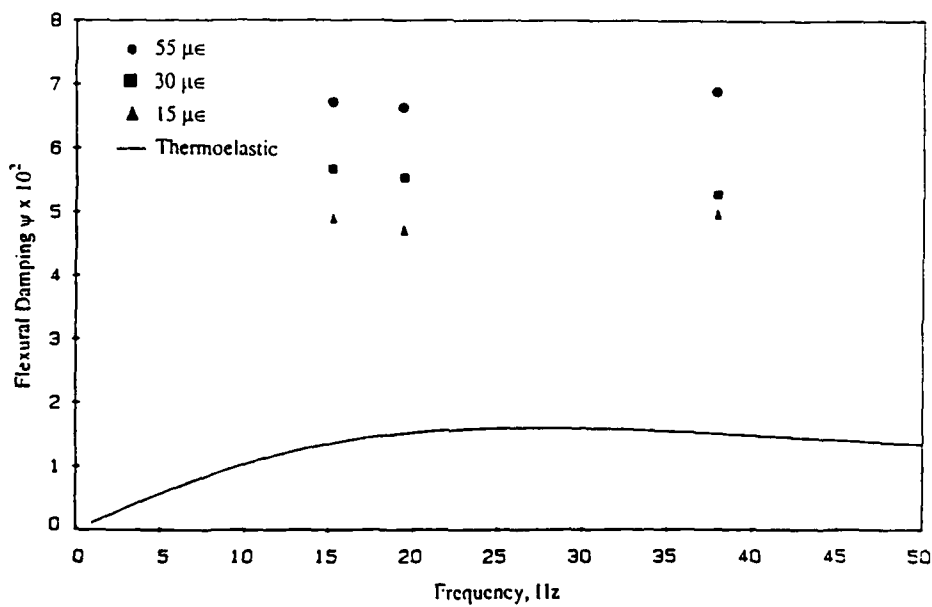
Figure 8 Flexural Damping vs Frequency for the Mg-0.6%Zr Alloy

234
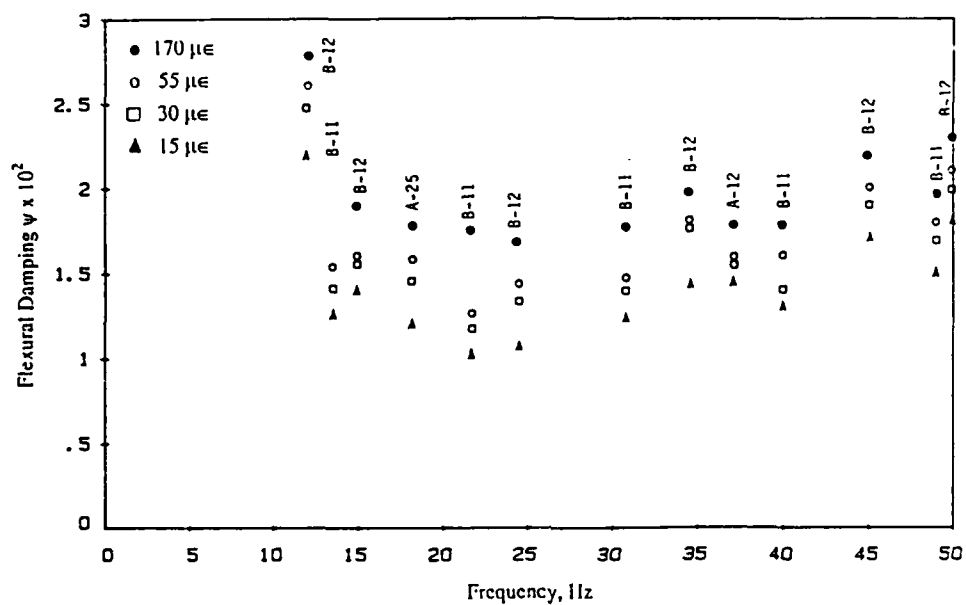
Figure 9 Flexural Damping vs Frequency and Strain Amplitude for [0₈] P55Gr/Mg-0.6%Zr Composite
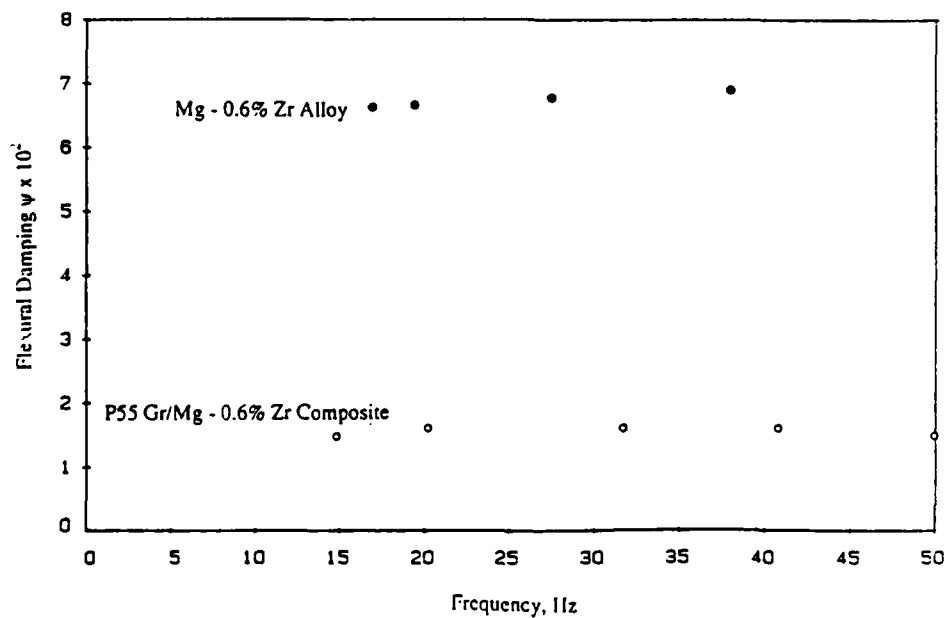
Figure 10 Comparison Between the Damping of the Mg-0.6%Zr Alloy and the [0₈] P55Gr/Mg-0.6%Zr Composite
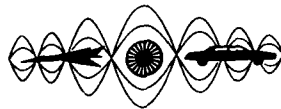
DAMPING IN AEROSPACE COMPOSITE MATERIALS

A.Agneni, L.Balis Crema, A.Castellani
Università di Roma "La Sapienza"
Dipartimento Aerospaziale
Via Eudossiana,16 - Roma (Italy)

ABSTRACT

In this work some experimental results gained by the authors are presented:in particular the ones on specimens of carbon and Kevlar fibers in epoxy resin, materials which are used in many aerospace structures (control surfaces and wings in aircraft, large antennas in spacecraft, etc.). In the first part of the paper some experimental methods of estimating damping ratios are reviewed: either in the time domain and in the frequency domain. In a second section, some damping factor estimates from experimental tests are shown; in order to evaluate the effects of the aerospace environment, damping factors have been obtained in a typical range of temperature, namely between $+120°C$ and $-120°C$, and in a pressure range from room pressure to 10^{-6} torr. Finally a theoretical approach for predicting the bounds of the damping coefficients is shown and predictional data is compared with experimental results.

NOMENCLATURE

a's, b's	polynomial coefficients
f_n	natural frequency (Hz)
h(t)	impulse response
$h_H(t)$	Hilbert transform of the impulse response
n	number of modes considered in the FRF
$|r|$	residue amplitude
s	complex variable of the Laplace transform
u(t)	Heaviside step function
w(t)	free decay response amplitude
z(t)	complex signal
A's, R's	fitting constants
E_c	storage modulus (Pa)
E_c''	loss modulus (Pa)
E_f	fiber Young's modulus (Pa)
E_m	matrix Young's modulus (Pa)
T_{60}	time at which the amplitude decays at -60dB
V_m	matrix volume fraction
ζ	damping ratio

ζ_{cL}	lower bound value of composite damping ratio
ζ_{cU}	upper bound value of composite damping ratio
ζ_f	fiber damping ratio
ζ_m	matrix damping ratio
ζ_0	damping ratio at room temperature
$\zeta_{HILBERT}$	damping ratio estimated by Hilbert method
ζ_{MDOF}	damping ratio estimated by a MDOF FRF fitting
ζ_{SMS}	damping ratio estimated by SMS code
η	loss factor
σ	decay rate
τ	time constant
ϕ	residue phase
ω_d	damped angular frequency
ω_n	natural angular frequency
Δf	frequency increment
Δt	time interval (s)

INTRODUCTION

Damping characteristics are of the utmost importance in evaluating the behaviour of the aerospace structures under mechanical and acoustic excitations; in fact these excitations are of the broadband type and it is impossible to avoid mechanical resonances. Therefore it is the damping of the structure that limits the effects of the vibration environment. Of course an high damping in a structure can be obtained by using additive high-loss non-structural materials or concentrate dampers, taking account of some restrictions due to weight penalties, material outgassing and temperature effects.

This paper focuses its attention on damping characteristics of composite structural materials and outlines the work carried out by the authors on damping ratio predictions and estimates in aerospace composite materials.

Damping in composite materials is the sum of the damping in the constitutive phases weighted by the contribute of each of them to total strain energy: fiber modulus is much greater than the one of the matrix, so most of the strain energy is in the fiber and it is possible to increase the material damping by increasing the fiber damping.

A particular attention has been paid to the different behaviour of carbon and Kevlar fiber composites: in CFRP an inverse relationship between damping and Young's modulus has been found out, whereas in Kevlar composites the damping ratio is nearly independent of stiffness and composite technology (fabric or laminate).

Tests have been carried out in order to evaluate the effects of pressure and temperature, in a range of interest of aerospace structures, on damping ratios of carbon and Kevlar fiber composites.

Experimental methods to estimate damping factors have been investigated, particularly with the aim of evaluating light damping values, as it is necessary when losses in carbon, glass and Kevlar fibers must be measured.

DAMPING ESTIMATION TECHNIQUES

A particular attention has been paid by the authors to the evaluation of the damping ratio especially from signals truncated at the end of the observation window [1], [2], [3], [4], that is from impulse responses characterized by low natural frequencies and light damping ratios, typical for large space structures.

A short description of some methods, used to estimate the damping factor, is presented.

Time Domain Techniques

A classic approach of damping measurement from a free decay response is the logarithmic decrement; since its estimation is based on the determination of successive cycle amplitudes, when the

decay rate is low enough, only few cycles are contained within the observation window, and therefore it is not possible, especially in presence of noise, to get statistically reliable results. An improvement of the method can be obtained rectifying the free response, so that also the negative half periods are available for the measurements.

A further improvement is achieved by the Bruel & Kjaer Complex Modulus Apparatus, which is particularly suitable for damping factor evaluation from low-loss small specimens. The sample, generally clamped at one end, is excited at its natural frequency (f_n) tuning the oscillator of the electronic equipment to resonance and, once the maximum amplitude of oscillations is gained, the input signal is cut out and the free decay is rectified, demodulated, filtered (in order to remove the ripple) and finally sent to a paper level recorder. Because the amplitude is plotted in semi-log scale, measured the amplitudes $w(t)$ at two time instants (t_1 and t_2), the loss factor is given by [5]:

$$\eta = \frac{\ln\left[\dfrac{w(t_1)}{w(t_2)}\right]}{\pi f_n \Delta t} \tag{1}$$

where $\Delta t = t_2 - t_1$. If the final value of the amplitude is chosen such as $w(t_2) = 10^{-3}\, w(t_1)$, that is -60dB below the initial value, the previous equation is reduced to the classic T_{60} relationship: $\eta \cong 2.2/(f_n T_{60})$.

A similar technique, used by Herlufsen [6], takes advantage of the Hilbert transform as amplitude demodulator of the impulse response, $h(t)$. In fact, for a SDOF system, the time function:

$$h_H(t) = -|r|\, e^{-\sigma t} \cos(\omega_d t + \phi) \tag{2}$$

(where σ is the decay rate, ω_d is the damped angular frequency, $|r|$ and ϕ are the residue magnitude and phase respectively) under proper conditions, can be considered the Hilbert transform of the impulse response:

$$h(t) = [\,|r|\, e^{-\sigma t} \sin(\omega_d t + \phi)\,]\, u(t) \tag{3}$$

where u(t) is the Heaviside function, that takes account of the causality of the impulse response. Thus from the complex signal $z(t) = h(t) + jh_H(t)$ it is possible to achieve the decaying exponential envelope:

$$|z(t)| = \sqrt{\left[h(t)\right]^2 + \left[h_H(t)\right]^2} = |r|\, e^{-\sigma t} \tag{4}$$

Plotting it on the dB scale, the time constant $\tau = \sigma^{-1}$ corresponds to the interval within which the envelope decays of about -8.7dB. For light damping, the natural angular frequency can be estimated from the peak of the frequency response function magnitude and then the damping factor is given by: $\zeta = (\tau \omega_n)^{-1}$. In presence of additive noise, because τ is estimated using only two points of the envelope, it is necessary to lower it by averaging a certain number of FRFs. This trouble is overcome, at least for not very high noise levels, estimating the decay rate from the slope of the straight line obtained by a linear least square fitting of the instantaneous envelope, plotted in a semi-log plane [1]. On the other hand, the damped angular frequency is given by the slope of the straight line, which fits (in the least square sense) the total phase, that is the argument of the complex function z(t) [2]:

$$\theta(t) = \arctan\left[\frac{h_H(t)}{h(t)}\right] = \omega_d t + \phi - \frac{\pi}{2} \tag{5}$$

From σ and ω_d it is straightforward to get the damping ratio:

$$\zeta = \sigma \left(\sigma^2 + \omega_d^2 \right)^{-1/2} \qquad (6)$$

This approach thoroughly exploits the advantages resulting from the complex signal [3], [4]. Obviously, as the previous techniques, the ones based on the Hilbert transform can analyze a single mode and therefore it must be filtered out from the FRF before the processing mentioned above.

Frequency Domain Techniques

The half power approach is a rapid and simple method, but provides damping ratio estimations with unacceptable errors when the signal is truncated at the end of the observation window. Errors due to this phenomenon, firstly pointed out by Clarkson and Mercer for correlation functions [7], were studied and quantified by White [8], [9]. This drawback could be overcome multiplying the decaying time function by an exponential window, in order to limitate truncation, and later on correcting the estimated damping ratio; unfortunatelly, the use of this type of window produces an artificial coupling between near modes and then the method could produce another type of error and estimates could be again unacceptable.

A much better approach consists in a least square fitting of the FRF, or of a part of it, by a rational fraction (MDOF technique):

$$H(s) \left. \right]_{s=j\omega} = \frac{\displaystyle\sum_{k=0}^{m} b_k s^k}{\displaystyle\sum_{l=0}^{2n} a_l s^l} \Bigg]_{s=j\omega} \qquad (7)$$

The method consists in finding the roots - poles, which contain all the information (damping ratios and damped angular frequencies) necessary to obtain damping ratios - of the characteristic polinomial, denominator of the above fraction, and after to expand Eq.(7) into partial fractions, that in turns permits to get complex residues:

$$H(\omega) \left. \right]_{s=j\omega} = \left[\sum_{i=1}^{n} \left(\frac{r_i}{s-p_i} + \frac{r_i^*}{s-p_i^*} \right) + R(s) \right]_{s=j\omega} \qquad (8)$$

If the software can only fit a mode at a time, as it happens for the release of the SMS Modal Analysis System 3.0 [10], Eq.(7) can be reduced to:

$$H(s) \left. \right]_{s=j\omega} = \frac{R_2(s+\sigma) + R_1 \omega_d}{s^2 + (2\sigma) s + \omega_n^2} + A_0 + A_1 s + A_2 s^2 \Bigg]_{s=j\omega} \qquad (9)$$

where ω_n is the natural angular frequency and the terms A_0, A_1 and A_2 take account of the effects due to the modes out of the considered frequency band. Generally no problems arise if the modes are not tightly coupled, but also in this case, if impulse responses are truncated and the residues must be correctly estimated, an exponential window could be applied and so coupling increases and damping ratios might result to be misestimated. In this case, the method based on the Poisson's sum formula could be applied, in fact it does not procure coupling and permits to correct the estimated residue values in magnitude and phase [11].

A comparison of damping ratios estimated by different methods is reported in Tab.1 and Tab.2; all the evaluations have been obtained from FRFs and from reconstructed impulse responses achieved by a dual channel analyzer (SD 375). Broadband excitations have been gained by a PCB impact hammer. The different specimens, clamped at one end, were made of Kevlar fiber composites.

Table 1 - First mode damping ratios obtained by SMS, MDOF and Hilbert approaches.

frequency (Hz)	ζ_{SMS} (x 10^3)	ζ_{MDOF} (x 10^3)	$\zeta_{HILBERT}$ (x 10^3)
25.5	6.95	7.01	6.78
35.0	9.34	8.95	8.85
47.5	8.36	8.16	8.05

Table 2 - Higher mode damping ratios obtained by MDOF and Hilbert approaches.

frequency (Hz)	226.1	290.8	308.6	655.1	915.5	1011.0	1683.8	1888.9
ζ_{MDOF} (x 10^3)	12.09	13.84	12.04	11.60	10.81	10.55	8.45	14.28
ζ_{HIL} (x 10^3)	11.66	13.75	12.02	11.54	10.85	10.32	8.71	16.85

In the following figures (Fig.1, Fig.2 and Fig.3) are presented the instantaneous envelope, the total phase and the FRF, real and imaginary parts, relative to a test case.
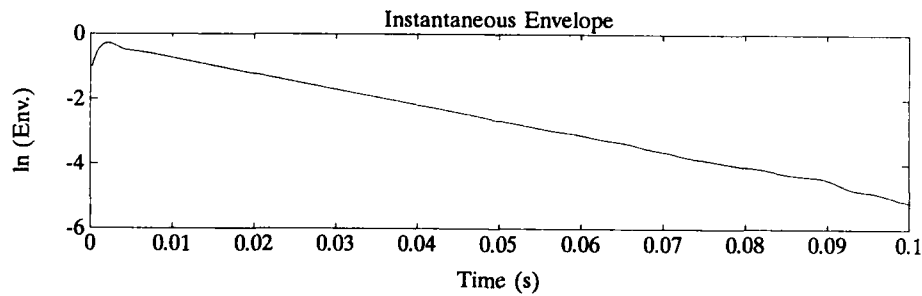
Fig.1 - Instantaneous envelope obtained by the Hilbert approach
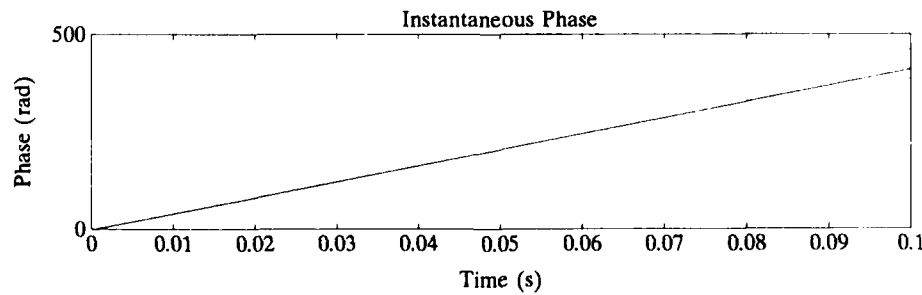
Fig.2 - Total phase obtained by the Hilbert approach

241
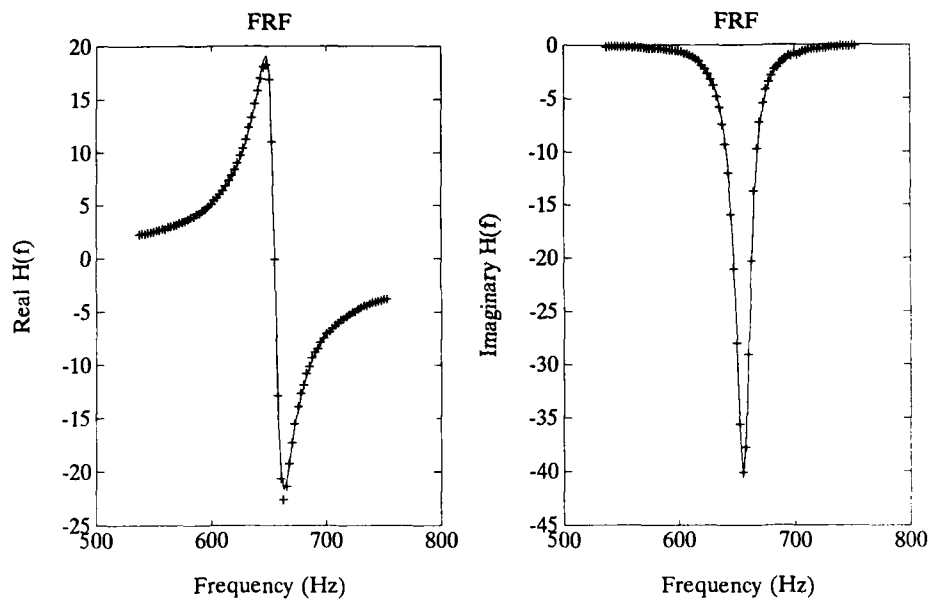
Fig.3 - Fitting of real and imaginary parts of experimental data (+) by MDOF

EXPERIMENTAL TESTS

A series of experimental results gained by the authors in the last years is presented. The effects connected with space environment, namely pressure and temperature, on damping factors have been considered. Some tests have been carried out in room conditions and other ones in the environmental chamber of the Aerospace Department, where a vacuum level in the order of 10^6 torr can be achieved; other tests have been done in function of the temperature, from room conditions to $+120°C$ and $-120°C$.

Damping factors have been measured by the free decay method in a frequency range from 10 (Hz) to 800 (Hz). Frequencies have been gained from different geometry specimens, excited at their first three modes.

Tests have been carried out on laminated and fabric aerospace composite materials (carbon and Kevlar fibers in epoxy resin) supplied by Italian firms Agusta and Alenia.

Carbon Fiber Composites

A set of specimens in carbon fiber have been tested: the specifications of all the specimens are shown in Tab.3, the prepreg has been made by Ciba-Geigy (fiber type Courtaulds E/HMS, resin type 920).

Pressure effects. In Fig.4 damping coefficients versus pressure are shown. A decrease of damping ratio as the pressure lowers from the atmospheric value to 10^6 torr has been pointed out: this effect is more significant for the thinnest samples, that present a decrease in the order of 25% of the value estimated at atmospheric pressure. The pressure variation causes also a frequency shift, due to the air mass around the specimen: frequencies increase with the decreasing of pressure as shown in Fig.5, where the $\Delta f/f$ ratio (Δf is the frequency increment and f is the value at 10^6 torr) versus frequency is reported [12].

Table 3 - Carbon fiber specimen characteristics

Specimen	Number of laminae	Laminate lay-up	Length (mm)
A1	8	[90/90/90/90]$_s$	250
A2	8	[0/0/0/0]$_s$	250
B1-B2-B3	8	[0/90/90/0]$_s$	200-250-400
C1-C2-C3	16	[0/90/90/0]$_s$	250-300-400
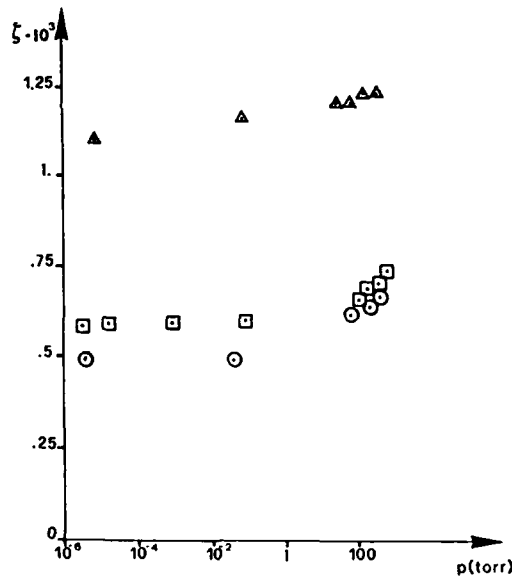
Fig.4 - CFRP damping ratios vs. pressure [12]
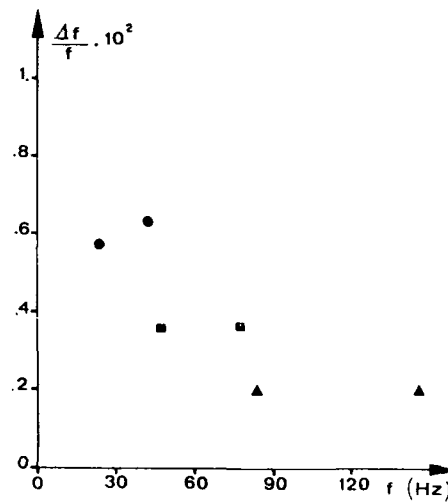
Fig.5 - Δf/f versus frequency [12]

Temperature effects. Some tests, in the temperature range between room conditions and 120°C, are shown in Fig.6: ζ_0 is the damping ratio at room temperature and ζ is its value at the current temperature. It is possible to see a remarkable increase of damping starting from a temperature of about 90°C, this effect is consistent with the cure cycle of the laminating procedure at 125°C and around the curing temperature there is also a significant decreasing for the storage modulus value: this is a typical effect of the α-transition for the epoxy resin [12]. The effects on damping coefficient of low temperatures, until -120°C, have been investigated: in Fig.7 damping values versus temperature are shown. Damping factors, in a first range of decreasing temperature, increase and reache a maximum for a typical temperature value and after they decrease. This behaviour is peculiar for the β-transition in epoxy resin, besides the temperature range, from -30°C to -90°C, and the value where the maximum damping ratio occurs are also typical of the β-transition in the material mentioned above [13].
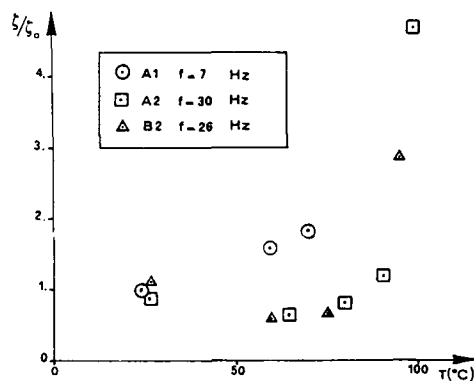
Fig.6 - CFRP ζ's vs. high temperatures [12]
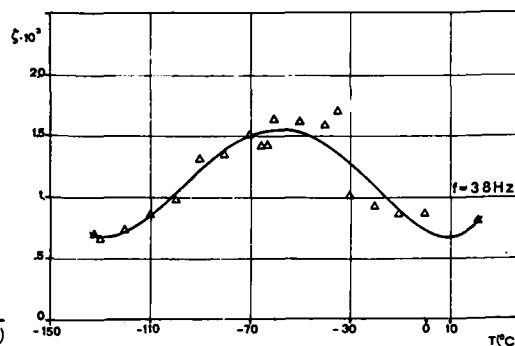
Fig.7 - CFRP ζ's vs. low temperatures [13]

Kevlar Fiber Composites

Some Kevlar fiber laminate and fabric specimens in epoxy resin, reported in Tab.4, have been tested. The damping ratio in Kevlar composites is generally higher than in similar carbon or glass fiber composites and it is significantly higher in high stiffness composites.

Table 4 - Kevlar fiber specimen characteristics

Specimen F = fabric L = laminate	Number of laminae	Laminate lay-up	Cut-off angle (degree)	Length (mm)
A (L)	16	unidirectional	0	200
B (L)	16	unidirectional	45	200
C (F style 285)	18	$[(0/90)_4/0]_s$	0	200
D (F style 285)	18	$[(0/90)_4/0]_s$	45	200
E (F style 285)	18	$[(0/90\pm45)_2/45]_s$	0	200
F (F style 120)	20	$[(0/90)_5]_s$	0	230
G (F style 120)	20	$[(0/90)_2(\pm45)_2/(0/90)_2]_s$	0	230

Frequency effects. Damping ratios in function of frequency are shown in the following figure (Fig.8): an insignificant variation in damping values has been obtained, as it appears from the previous figure [14].

Temperature effects. Damping ratios versus temperature, in the range from the room value to -120 °C, are presented in Fig.9: as the temperature decreases, the damping factor reaches values that are lower than the ones measured at room temperature and this effect can be connected with a significant decreasing of the damping ratio in fibers [13].
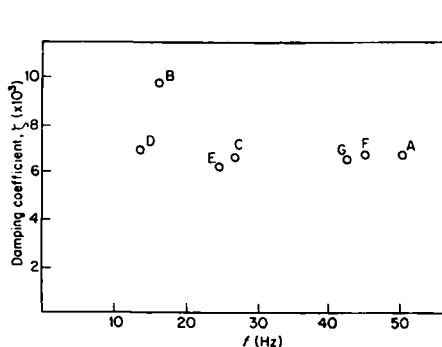
Fig.8 - Kevlar damping ratio vs. frequency [14]
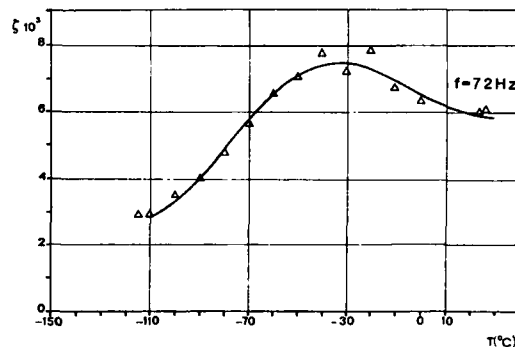
Fig.9 - Kevlar ζ's vs. low temperatures [13]

The analysis of the experimental tests, in carbon fiber composites, has confirmed the intuitive idea that it is possible to get a relationship between damping ratios and storage modulus: that is a significant decreasing of damping factor with the increasing of stiffness, as it also happens in glass fiber composites. On the contrary, damping factor in Kevlar composites is nearly constant in function of Young's modulus and it does not depend on the composite type, fabric or laminate.

Damping ratio versus Young's modulus for Kevlar fiber are compared with the similar data for carbon and glass fiber composites in Fig.10; the Kevlar different behaviour is due to the fact that in its case both the two constitutive phases, fiber and matrix, behave as viscoelastic materials and the fiber damping has the same order of magnitude of the matrix damping, whereas in carbon and glass fiber composites, fibers may be considered as an elastic phase [14].
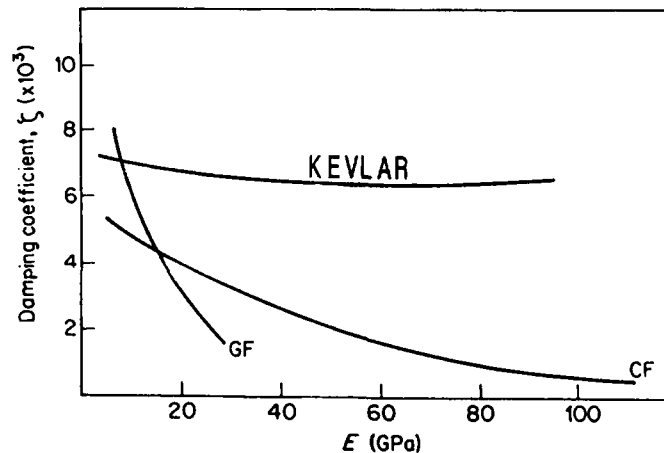
Fig.10 - CFRP, GFRP and Kevlar ζ's vs. Young's modulus [14]

DAMPING PREDICTION IN COMPOSITE MATERIALS

Basic properties of fiber and matrix (Young's moduli E_f and E_m, damping ratios ζ_f and ζ_m) must be used in evaluating damping characteristics of composites; if it is possible to consider that only one phase in the composite material behaves as a viscoelastic one, then the correspondence principle may be used to evaluate upper and lower bounds for damping factors [15]. The lower bound is given by the

245

following relationship:

$$\zeta_{cL} = \frac{V_m \, \zeta_m \, E_m + (1 - V_m)\zeta_f \, E_f}{E_c} \qquad (10)$$

while the upper bound is provided by:

$$\zeta_{cU} = \frac{V_m \zeta_m \, E_m E_f^2 + (1 - V_m)\zeta_f \, E_f E_m^2}{E_c(V_m E_f + (1 - V_m)E_m)^2} \qquad (11)$$

where V_m is the matrix volume fraction and the subscript c stands for composite.

These relationships can be used in the case of CFRP and GFRP, but not in the case of Kevlar fiber composites, where the fiber too behaves as a viscoelastic phase. It is possible to predict the damping factor by strain energy methods. If the specimen is considered as a bending composite beam, the damping factor can be evaluated by:

$$\zeta_c = \frac{\left[\dfrac{E_f E_m}{E_c}\right] (\zeta_m - \zeta_f) + \zeta_f E_f - \zeta_m E_m}{E_f - E_m} \qquad (12)$$

Some experimental results, carried out on carbon fiber specimens, are compared with the predicted lower and upper bounds in Fig.11 (where E''_c is the coefficient of the imaginary part of the complex modulus, that is $E''_c = 2\zeta_c E_c$). In Fig.12 the predicted Kevlar fiber damping is compared with experimental results.
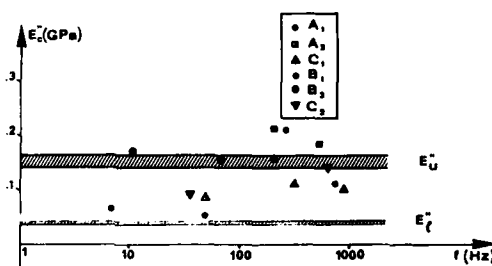
Fig.11 - CFRP loss modulus, upper and lower bounds vs. frequency [15]
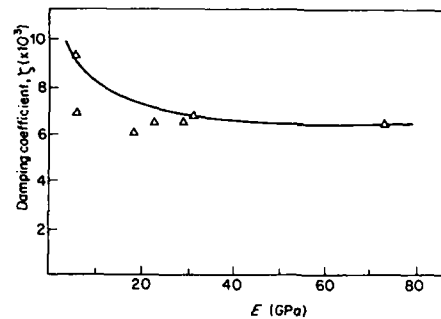
Fig.12 - Kevlar experimental ζ's with the predicted line [14]

Many authors have considered the behaviour of damping characteristics in composite materials both by theoretical analysis and by experimental tests [16], [17], [18]. Finite element codes have been studied in order to evaluate the damped response of composite structures [19]. In damping evaluation of structural elements, the effects of the mode shapes on ζ's have been also pointed out.

Studies on metal matrix composites [20], proposed improvements of damping in carbon fiber composites by using high damping fibers [21] and studies on damping in composite structural joints [22] are of particular interest for applications in aerospace structures.

ACKNWOLEDGEMENTS

REFERENCES

[1] A.Agneni, L.Balis Crema:"Misura del fattore di smorzamento con l'impiego della trasformata di Hilbert", Atti del Dipartimento Aerospaziale, DAURS 84.02, 1984.

[2] A.Agneni, L.Balis Crema:"A new proposal for time domain SDOF components estimation", l'Aerotecnica-Missili e Spazio, vol.65, n.4, 1986, pp.167-175.

[3] A.Agneni, L.Balis Crema:"Analytic signals in the damping coefficient estimation", Proc. Int. Conf. "Spacecraft Structure and Mechanical Testing", ESA SP-289, 1988, pp.133-139.

[4] A.Agneni, L.Balis Crema:"Damping measurements from truncated signals via Hilbert transform", Mechanical System and Signal Processing, 3(1), 1989, pp.1-13.

[5] B.E.Read, G.D.Dean:"The determination of dynamic properties of polymers and composites", Adam Hilger Ltd., 1978, pp.86-91.

[6] H.Herlufsen:"Dual channel FFT analysis (part II)", Bruel & Kjaer Technical Review no.2, 1984.

[7] B.L.Clarkson, C.A.Mercer:"Use of cross correlation in studying the response of lightly damped structures to random forces", AIAA Journal, vol.3, no.12, 1965, pp.2287-2291.

[8] R.G.White:"Use of transient excitation in the dynamic analysis of structures", Journal of Royal Aeronautical Society, 73, 1969, pp.1047-1050.

[9] R.G.White:"Evaluation of the dynamic characteristics of structures by transient testing", Journal of Sound and Vibration, 15, 1971, pp.147-161.

[10] Structural Measurements Systems (SMS), Modal Analysis System. Operating Manual:"Theory of Operation", 1985.

[11] A.Agneni, L.Balis Crema, A.Paolozzi:"On the use of Poisson's sum formula to avoid truncation effects", Proc. of Florence Modal Analysis Conference, Florence 10-12 Sept. 1991, pp.645-654.

[12] L.Balis Crema, R.Barboni, A.Castellani:"Structural Damping of Composite Materials for Space Applications", AGARD CP-327, 1983, pp.12-1,12-8.

[13] L.Balis Crema, A.Castellani, V.F.Polcaro:"Low Temperature Effect on Damping Coefficients of Aerospace Composite Materials", ASME Composite Material Technology PD-Vol.37, 1991, pp.33-36.

[14] L.Balis Crema, A.Castellani, U.Drago:"Damping Characteristics of Fabric and Laminated Kevlar Composites", Composites, 1989, pp.593-596.

[15] L.Balis-Crema, R.Barboni, A.Castellani, I.Peroni:"Tests and Prediction of Composite Material Viscoelastic Behavior for Large Space Structures", l'Aerotecnica Missili e Spazio, 1983, pp.205-210.

[16] R.G.Ni, R.D.Adams:"The Damping and Dynamic Moduli of Simmetric Laminated Composite Beams-Theoretical and Experimental Results", Journal of Composite Materials, 1984, pp.104-121.

[17] D.X.Lin, R.G.Ni, R.D.Adams:"Prediction and Measurement of the Vibrational Damping Parameters of Carbon and Glass Fibre-Reinforced Plastics Plates", Journal of Composite Materials, 1984, pp.132-152.

[18] R.D. Adams:"A Review of the Damping Mechanisms in Advanced Fibre-Reinforced Composites", Proc. of Damping 1986 AFWAL-TR-86-3059, pp. FG1-FG22.

[19] D.A.Saravanos, C.C.Chamis:"Computational Simulation of Damping in Composite Structures", Journal of Reinforced Plastics and Composites, 1991, pp.256-278.

[20] V.K.Kinra, G.G.Wren, K.B.Milligan:"Damping in Metal-Matrix Composites: Theory and Experiment", ASME Composite Material Technology PD-Vol.37, 1991, pp.25-31.

[21] G.A.Lesieutre, D.Christiansen, W.Whatley, S.Yariagadda:"Improved Composite Material Damping Using High Damping Graphite Fibers", ASME Composite Material Technology PD-Vol.37, 1991, pp.21-24.

[22] M.D.Rao, M.J.Crocker, P.K.Raju:"Study of the damping capacity of structural joints made of graphite epoxy composite material", Proc. of Damping 1989 WRDC-TR-89-3116, pp.HDB-1 to HDB-22.

SECOND INTERNATIONAL CONGRESS ON
RECENT DEVELOPMENTS IN AIR- AND
STRUCTURE-BORNE SOUND AND VIBRATION
MARCH 4-6, 1992   AUBURN UNIVERSITY, USA

TRANSVERSE VIBRATION AND DAMPING ANALYSIS OF DOUBLE-STRAP JOINTS*

Mohan D. Rao and Shulin He
Mechanical Engineering and Engineering Mechanics Department
Michigan Technological University
Houghton, MI 49931
U.S.A.

ABSTRACT

This paper presents an analytical model to predict the damping of adhesively bonded double-strap joints under transverse vibration. The differential equations of motion of the joint system are derived using the energy method and Hamilton's principle. It is assumed that the energy dissipated by the joint system is contributed by both the shear and longitudinal deformation of the adhesive layers. The combination of natural boundary conditions, forced boundary conditions, and continuity conditions yields the frequency equations to predict the system resonance frequencies and modal loss factors. The effects of structural parameters and material properties of the adhesive layer on the system modal loss factors and resonance frequencies are also studied.

INTRODUCTION

Double-strap joints are one type of structural joints that are gaining wide applications in many aerospace structures which are joint dominated. All structures must have sufficient damping to keep vibration and acoustic response within acceptable limits. It is well known that adding a layer of viscoelastic material between any two bonded parts of the joint (as in a sandwich structure) will improve both the stress distribution and damping capacity of the joint system. This would, however, results in certain penalties in other structural properties such as stiffness, strength and weight. There is a strong need to develop passively damped joints which would give favorable trade-offs between damping benefits and associated stiffness and strength penalties. The current trend in the designed-in incorporation of viscoelastic materials in the joints for passive vibration control has resulted in many innovative means to enhance the inherent damping in structures subjected to dynamic loading. Despite these impressive developments, unfortunately, research in the area of analytical modeling of damping of structural joints, especially double-strap joints is relatively unexplored. The objective of this research is a continuing effort to develop theoretical models to predict the damping capacity of adhesively bonded simple structural joints incorporating viscoelastic damping materials. Previous modeling efforts by the authors have included damping of single lap joints [2, 3], curved sandwich beams [4], longitudinal vibration of double-strap joints [5].

In this paper, the authors have developed a dynamic model to predict the damping and resonance frequency of a double-strap joint system under transverse vibration. A parametric study has been conducted to study the effects of various design parameters on the system modal damping capacity and resonance frequencies. This is an extension of the work on the longitudinal vibration of the same system formulated by the authors [5].

---

* This is an abridged version of a paper submitted for review by the Journal of the Acoustical Society of America [1].

I. FORMULATION OF THE ANALYTICAL MODEL
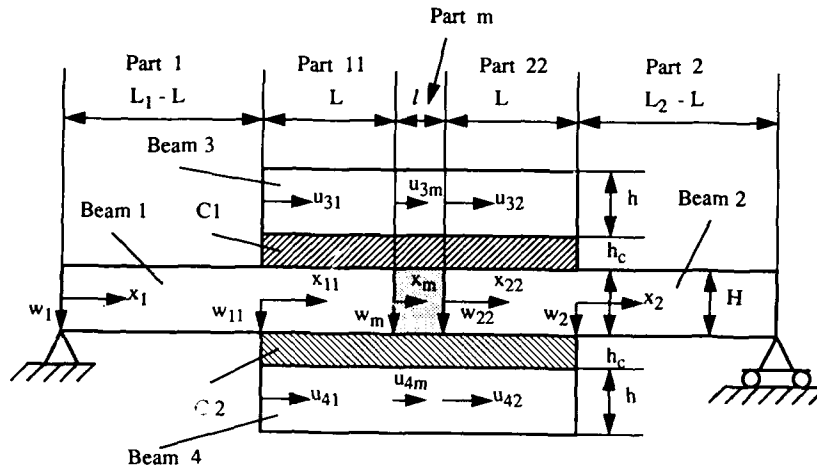
Figure 1 -- The double-strap joint system chosen for study

The double-strap joint system is shown in Figure 1. The two primary beams and the upper and lower constraining beams are assumed to be orthotropic, while the adhesive layers are modeled as linear viscoelastic materials. The middle connecting beam (spacer material) is a small piece of aluminum usually included to strengthen the joint. The shear and longitudinal deformations of the adhesive layers are included. But the longitudinal inertia of the joint system is neglected. Also, the joint is assumed to be symmetric with the primary beams. The total system is hypothetically divided into five parts, as shown in Figure 2.

(a) Part 11

(b) Part m

(c) Part 22
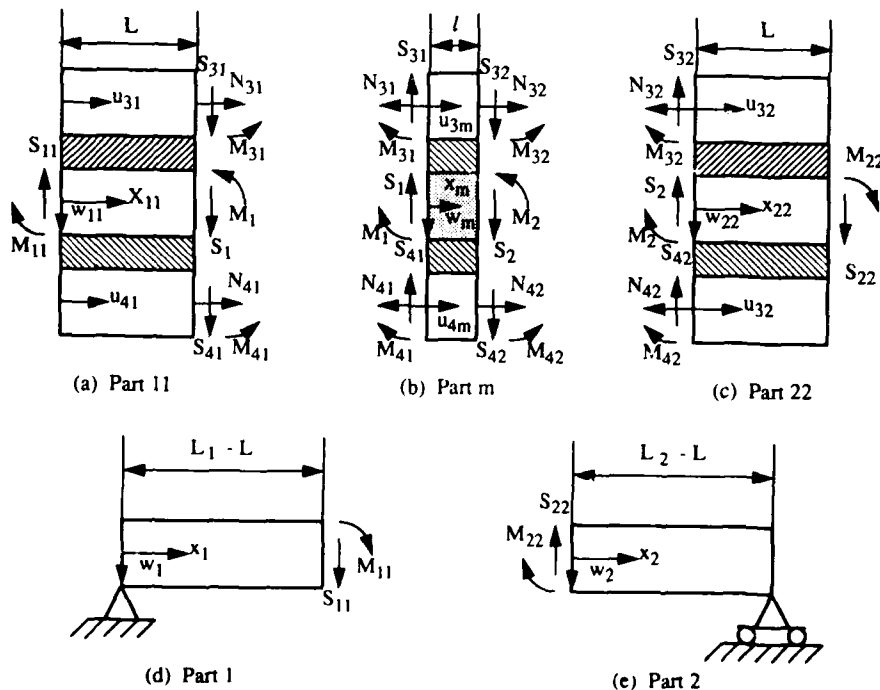
(d) Part 1

(e) Part 2

Figure 2 -- Hypothetical division of the joint system for study

A. Analysis of part 11 and part 22

Figure 2(a) shows the coordinate system and free body diagram of part 11 with all the forces acting on it. Due to the symmetry of the composite beam, the middle surface of beam 1 is the neutral surface of the composite system.

Suppose the composite system has unit width. Let w_{11} be the transverse displacement of the composite beam, and u_{31} and u_{41} be the longitudinal deformations of beams 3 and 4 respectively. Then from $\sum F_{x_{11}} = 0$, we can show that

$$u_{31} = -u_{41}. \tag{1}$$

The potential energy in C_1 and C_2 are given by

$$V_{C_1} + V_{C_2} = \frac{1}{2}\int_0^L \left(\left[\frac{E_c^* h_c}{3(1-\upsilon_c^2)} (u_{31}')^2 + G_c^* h_c \left(\frac{c}{h_c} w_{11}' - \frac{u_{31}}{h_c} \right)^2 \right] + \left[\frac{E_c^* h_c}{3(1-\upsilon_c^2)} (u_{41}')^2 + G_c^* h_c \left(\frac{c}{h_c} w_{11}' + \frac{u_{41}}{h_c} \right)^2 \right] \right) dx_{11} \tag{2}$$

where $c = h_c + (\frac{h+H}{2})$, $w_{11}' = \frac{\partial w_{11}}{\partial x_{11}}$, $u_{31}' = \frac{\partial u_{31}}{\partial x_{11}}$ and $u_{41}' = \frac{\partial u_{41}}{\partial x_{11}}$.

The contribution of potential energy of beams 1, 3 and 4 is

$$V_1 + V_3 + V_4 = \frac{1}{2}\int_0^L \left[\frac{E}{12} (H^3 + h^3)(w_{11}'')^2 + Eh((u_{31}')^2 + (u_{41}')^2) \right] dx_{11}. \tag{3}$$

The total potential energy is then $V = V_1 + V_3 + V_4 + V_{C_1} + V_{C_2}$.

The total kinetic energy of the composite beam in part 11 after neglecting longitudinal inertia is

$$T_1 + T_3 + T_4 + T_{c1} + T_{c2} = \frac{1}{2}\int_0^L [\rho(H + 2h) + 2\rho_c h_c] \dot{w}_{11}^2 dx_{11} \tag{4}$$

where in Eqs. (4) and (5), $\dot{w}_{11} = \frac{\partial w_{11}}{\partial t}$ and $w_{11}'' = \frac{\partial^2 w_{11}}{\partial x_{11}^2}$. E is the Young's modulus of the three beams. H, h and h_c are the thicknesses of the primary beams, constraining beams and adhesive layers respectively. ρ and ρ_c are the material density of the beams and the adhesive layers. E_c^* and G_c^* are the complex elastic and shear modulus of the viscoelastic layer. Under harmonic vibration, we can express E_c^* and G_c^* as $E_c^* = E_c'(1 + i\eta_{c1})$ and $G_c^* = G_c'(1 + i\eta_{c2})$, in which E_c' and G_c' are the storage moduli, and η_{c1} and η_{c2} are the loss factors corresponding to extensional and shear deformation of the viscoelastic material. In current analysis, we assume that $\eta_{c1} = \eta_{c2} = \eta_c$ which is a common assumption made with many damping materials. Values of E_c' and G_c' corresponding to a frequency and temperature can be obtained from material data sheets supplied by the manufacturers [6].

Work done by external forces is given by

$$W = (M_{11}w_{11}' - S_{11}w_{11})|_{x_{11}=0} + [N_{31}u_{31} + N_{41}u_{41} + (S_{31} + S_{41} + S_1)w_{11}]|_{x_{11}=L}$$

$$- (M_{31} + M_{41} + M_1)|_{x_{11}=L} + \int_0^L q_{11}\delta w_{11} dx_{11}, \tag{5}$$

where $q_{11}(x_{11}, t)$ is the distributed excitation force applied to part 11 which is not shown in Figure 2(a). Applying Hamilton's principle $\delta\int_{t_1}^{t_2} (T - V + W) dt = 0$ and using Eq. (1), we obtain the differential equations of motion for part 11 to be

$$\frac{E}{12}(H^3 + 2h^3)\frac{\partial^4 w_{11}}{\partial x_{11}^4} - \frac{2c^2 G_c^*}{h_c}\frac{\partial^2 w_{11}}{\partial x_{11}^2} + m\frac{\partial^2 w_{11}}{\partial t^2} - \frac{2cG_c^*}{h_c}\frac{\partial u_{41}}{\partial x_{11}} = q_{11}(x_{11}, t), \text{ and} \tag{6}$$

$$\left[Eh + \frac{E_c^* h_c}{3(1-\upsilon_c^2)} \right]\frac{\partial^2 u_{41}}{\partial x_{11}^2} - \frac{G_c^*}{h_c}u_{41} - \frac{cG_c^*}{h_c}\frac{\partial w_{11}}{\partial x_{11}} = 0, \tag{7}$$

where $m = \rho(H + 2h) + 2\rho_c h_c$. m represents the mass per unit length of the composite beam. The natural boundary conditions obtained as a by product of the variational principle are given by

$$\left\{ \left[\frac{E}{12}(H^3 + 2h^3)\frac{\partial^3 w_{11}}{\partial x_{11}^3} - \frac{2cG_c^*}{h_c}(c\frac{\partial w_{11}}{\partial x_{11}} + u_{41}) \right]\delta w_{11} - \frac{E}{12}(H^3 + 2h^3)\frac{\partial^2 w_{11}}{\partial x_{11}^2}\delta w_{11}' \right\} \Big|_0^L$$

$$- (S_{11}\delta w_{11} - M_{11}\delta w_{11}')|_{x_{11}=0} + [(S_1 + S_{31} + S_{41})\delta w_{11} - (M_1 + M_{31} + M_{41})\delta w_{11}']|_{x_{11}=0}$$

$$- 2\left[\frac{E_c^* h_c}{3(1-\upsilon_c^2)} + Eh \right]u_{41}'\delta u_{41} \Big|_0^L + (N_{41} - N_{31})|_{x_{11}=L} = 0 \tag{8}$$

251

Since the study of the modal loss factors and system resonance frequencies is our interest, we can assume the whole joint system have resonance frequencies ω_n, and let $w_{11}(x_{11},t) = W_{11}(x_{11})e^{i\omega_n t}$ and $u_{41}(x_{11},t) = U_{41}(x_{11})e^{i\omega_n t}$. Then under harmonic vibration at a resonance, excitation force $q_{11}(x_{11},t)$ will be $\frac{\pi}{2}$ degree *out of phase* with $w_{11}(x_{11},t)$ and balance the damping force of the composite beam. Therefore, s:milar to what is discussed by Mead and Markus [7], we can assume that $q_{11}(x_{11},t) = i\omega_n^2\eta m w_{11}(x_{11},t)$, where η corresponding to the system modal loss factors. Then Eq. (6) and Eq. (7) become

$$\frac{E}{12}(H^3+2h^3)\frac{\partial^4 W_{11}}{\partial x_{11}^4} - \frac{2c^2 G_c^*}{h_c}\frac{\partial^2 W_{11}}{\partial x_{11}^2} - m\omega_n^2(1+i\eta)W_{11} - \frac{2cG_c^*}{h_c}\frac{\partial U_{41}}{\partial x_{11}} = 0, \text{ and} \tag{6-a}$$

$$\left[Eh + \frac{E_c^* h_c}{3(1-v_c^2)}\right]\frac{\partial^2 U_{41}}{\partial x_{11}^2} - \frac{G_c^*}{h_c}U_{41} - \frac{cG_c^*}{h_c}\frac{\partial W_{41}}{\partial x_{11}} = 0. \tag{7-a}$$

Using non-dimensional quantities $\bar{x}_{11} = \frac{x_{11}}{L_1}$, $\bar{W}_{11} = \frac{W_{11}}{H}$, $\bar{U}_{41} = \frac{U_{41}}{H}$, $\bar{E}_c = \frac{E_c^*}{E}$, $\bar{G}_c = \frac{G_c^*}{E}$, $\bar{h}_c = \frac{h_c}{H}$, $\bar{h} = \frac{h}{H}$, $\bar{c} = \frac{c}{H}$, $\bar{\rho}_c = \frac{\rho_c}{\rho}$ and $\bar{\omega} = \frac{\omega_n\sqrt{(1+i\eta)}}{\omega_0}$, where $\omega_0 = \frac{H}{2L_1^2}\sqrt{\frac{E}{3\rho}}$, and let $D_{11} = \frac{\partial}{\partial\bar{x}_{11}}$, we can express Eq. (6-a) and Eq. (7-a) in a matrix form:

$$\begin{bmatrix} a_1 D_{11}^4 - b_1 D_{11}^2 - c_1 & -d_1 D_{11} \\ -c_2 D_{11} & a_2 D_{11}^2 - b_2 \end{bmatrix}\begin{bmatrix} \bar{W}_{11} \\ \bar{U}_{41} \end{bmatrix} = \begin{bmatrix} 0 \\ 0 \end{bmatrix} \tag{9}$$

where, $a_1 = 1 + 2\bar{h}^3$, $b_1 = \frac{24\bar{c}^2}{\bar{h}_c}(\frac{L_1}{H})^2\bar{G}_c$, $c_1 = (1+2\bar{h}+2\bar{\rho}_c\bar{h}_c)\bar{\omega}^2$, $d_1 = \frac{24\bar{c}}{h_c}(\frac{L_1}{H})^3\bar{G}_c$, $a_2 = \bar{h} + \frac{\bar{E}_c\bar{h}_c}{3(1-v_c^2)}$, $b_2 = \frac{\bar{G}_c}{\bar{h}_c}(\frac{L_1}{H})^2$ and $c_2 = \frac{\bar{c}}{\bar{h}_c}(\frac{L_1}{H})\bar{G}_c$.

Solving Eq. (9) by applying $\bar{W}_{11}(\bar{x}_{11}) = Ae^{\lambda\bar{x}_{11}}$ and $\bar{U}_{41}(\bar{x}_{11}) = Be^{\lambda\bar{x}_{11}}$, we obtain

$$\bar{W}_{11}(\bar{x}_{11}) = \sum_{n=1}^{6} A_n e^{(\lambda_n\bar{x}_{11})}, \text{ and } \bar{U}_{41}(\bar{x}_{11}) = \sum_{n=1}^{6} f_n A_n e^{(\lambda_n\bar{x}_{11})}, \tag{10}$$

where $0 \leq \bar{x}_{11} \leq \frac{L}{L_1}$, $f_n = \frac{c_2\lambda_n}{a_2\lambda_n^2 - b_2}$, $n = 1, ..., 6$, and $\lambda_1, ..., \lambda_6$ are the six eigenvalues of Eq. (9). $A_1, ..., A_6$ are six arbitrary constants.

Analysis of Part 22 of the joint system, shown in Figure 2(c), is exactly the same as part 11 except for the boundary conditions. Here let $w_{22}(x_{22},t) = W_{22}(x_{22})e^{i\omega_n t}$ and $u_{42}(x_{22},t) = U_{42}(x_{22})e^{i\omega_n t}$, we get

$$\bar{W}_{22}(\bar{x}_{22}) = \sum_{n=1}^{6} C_n e^{(\lambda_n\bar{x}_{22})}, \text{ and } \bar{U}_{42}(\bar{x}_{22}) = \sum_{n=1}^{6} f_n C_n e^{(\lambda_n\bar{x}_{22})}, \tag{11}$$

where $\bar{x}_{22} = \frac{x_{22}}{L_1}$, $\bar{W}_{22} = \frac{W_{22}}{H}$, $\bar{U}_{42} = \frac{U_{42}}{H}$, and $C_1, ..., C_6$ are another six arbitrary constants. In addition, there are six boundary conditions corresponding to part 22.

B. Analysis of part m

The analysis of part m, shown in Figure 2(b), is similar to part 11 or part 22 except for some minor difference. The central beam here has a different material from the two constraining beams. Suppose the density of the material of the central beam be ρ_m and Young's modulus be E_m. Let $w_m(x_m,t) = W_m(x_m)e^{i\omega_n t}$, $u_{4m}(x_m,t) = U_{4m}(x_m)e^{i\omega_n t}$ and external excitation load be $q_m(x_m,t) = i\omega_n^2\eta(\rho_m H + 2\rho h + 2\rho_c h_c)w_m(x_m,t)$. we get

$$\bar{W}_m(\bar{x}_m) = \sum_{n=1}^{6} B_n e^{(\alpha_n\bar{x}_m)}, \text{ and } \bar{U}_{4m}(\bar{x}_m) = \sum_{n=1}^{6} B_n g_n e^{(\alpha_n\bar{x}_m)}, \quad 0 \leq \bar{x}_m \leq \frac{l}{L_1}, \tag{12}$$

where $g_n = \frac{c_2\alpha_n}{a_2\alpha_n^2 - b_2}$, $n = 1, ..., 6$, and $\alpha_1, ..., \alpha_6$ are the six eigenvalues for this part. $B_1, ..., B_6$ are six arbitrary constants. Again, here we get six additional boundary conditions.

C. Analysis of part 1 and part 2

The coordinate systems for part 1 and part 2 are shown in Figure 2(d) and 2(e) respectively. The analysis of these two parts are straight forward Euler-Bernouli beam analysis. Let $w_1(x_1,t) = W_1(x_1)e^{i\omega_n t}$ and $w_2(x_2,t) = W_2(x_2)e^{i\omega_n t}$. We have

$$\overline{W}_1(\bar{x}_1) = D_{11}\sin\beta\bar{x}_1 + D_{12}\sinh\beta\bar{x}_1, \qquad 0 \leq \bar{x}_1 \leq (1 - \frac{L}{L_1}) \tag{13}$$

$$\overline{W}_2(\bar{x}_2) = D_{21}\left[\sin\beta\bar{x}_2 - \tan\beta\,(1 - \frac{L}{L_1})\cos\beta\bar{x}_2\right] + D_{22}\left[\sinh\beta\bar{x}_2 - \tanh\beta\,(1 - \frac{L}{L_1})\cosh\beta\bar{x}_2\right] \tag{14}$$

where $\overline{W}_1 = \dfrac{W_1}{H}$, $\overline{W}_2 = \dfrac{W_2}{H}$, $\bar{x}_1 = \dfrac{x_1}{L_1}$, $\bar{x}_2 = \dfrac{x_2}{L_1}$, $\beta = \sqrt{\bar{\omega}}$ and $0 \leq \bar{x}_{22} \leq (1 - \frac{L}{L_1})$. D_{11}, D_{12}, D_{21} and D_{22} are four arbitrary constants. There are four natural boundary condition equations corresponding to these two parts.

D. Derivation of the frequency equation

The foregoing analysis has produced 22 boundary equations with 22 arbitrary constants and 10 interfacial forces. Considering the continuity of displacements and slopes at interfaces $x_{11} = 0$, $x_m = 0$, $x_{22} = 0$ and $x_2 = 0$, we get 10 more continuity equations. We can eliminate the 10 interfacial forces and the four arbitrary constants D_{11}, D_{12}, D_{21} and D_{22} from the above 32 boundary equations and get 18 homogeneous equations with A_1, ..., A_6, B_1, ..., B_6, C_1, ..., C_6 being unknowns. Expressed in a matrix form, it is $[A]\{V\} = 0$, where $\{V\} = [A_1...A_6$, $B_1 ... B_6, C_1 ... C_6]^T$ and $[A]$ is an 18×18 matrix with complex elements.

For a non-trivial solution of $\{V\}$, we must have
$$\det[A] = 0, \tag{15}$$
which is the system frequency equation. The roots of Eq. (15) yield the eigenvalues ω_n and η of the joint system. Once the eigenvalues are evaluated, the corresponding eigenvectors $\{V\}$ can be found. A computer program has been developed on an IBM 4381 system to obtain the numerical solution of Eq. (15).

II. NUMERICAL RESULTS

Let D_R and D_I be the real and imaginary parts of the determinant of matrix $[A]$. Then both D_R and D_I will be functions of η and $\bar{\omega}_n$, where $\bar{\omega}_n = \dfrac{\omega_n}{\omega_0}$. As every non-zero element of $[A]$ is a complex transcendental function with $\bar{\omega}^2 = \bar{\omega}_n^2(1 + i\eta)$ appearing as an independent variable, special searching technique needs to be employed to find the roots of Eq. (15). One such searching strategy that has been preciously developed by the authors [5] is also employed here to obtain the numerical results. The details of this search strategy are described in [5].

The material properties of the adhesive layer and their frequency, temperature dependence are needed for input to the program. Considerable research is being done in the area of analytical modeling of frequency and temperature effects on the damping and modulus of viscoelastic materials [7]. Although data on the shear modulus and loss factor of damping materials corresponding to a frequency and temperature are available in the data sheets supplied by the manufacturers, these data are not useful, here, since we don't know the resonance frequencies of the system. However, based on the experimental data, and curve-fitting, some formulae are available to find the values of G_c' and η_c corresponding to a frequency F and a temperature T. The empirical formulae for $G_c'(T, F)$ and $\eta_c'(T, F)$ developed in reference [8] by Drake is utilized in this study.

The material of the beam chosen here is Graphite/Epoxy which has an elastic modulus E along the fiber direction and the connecting part in the middle is chosen to be aluminum.

The variations of system resonance frequency $\bar{\omega}_n$ and modal loss factor η with the adhesive thickness h_c for the first four modes are plotted in Figure 3 and Figure 4.
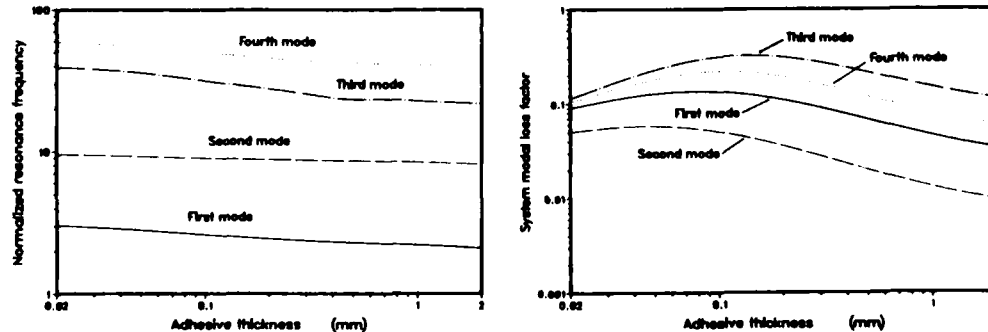
Figure 3 -- Variation of ω_n with adhesive thickness h_c Figure 4 -- Variation of η with adhesive thickness h_c

The lap ratio $\frac{L}{L_1}$ was set to be 0.5. 3M ISD-112 damping material was chosen and the operating temperature was assumed to be atmospheric (T = 21.1°C or 70°F). h_c was varied from 0.02 mm to 2 mm in Figures 3 and 4. Observation of these figures shows that $\bar{\omega}_n$ decrease with h_c for all the four modes, but η takes on maximum values near $h_c = 0.1$mm.

The overlap ratio $\frac{L}{L_1}$ is another parameter being studied. The $\bar{\omega}_n$ - $(\frac{L}{L_1})$ and η - $(\frac{L}{L_1})$ curves are shown in Figure 5 and Figure 6. The damping material and temperature are kept unchanged. The adhesive thickness h_c was kept to be 0.5 mm. From Figure 5 it is clear that the variation of $\bar{\omega}_n$ with $(\frac{L}{L_1})$ is not very significant for all the four modes. But increasing $\frac{L}{L_1}$ will greatly increase the system modal loss factors η especially when $\frac{L}{L_1} < 0.5$ as seen in Figure 6.
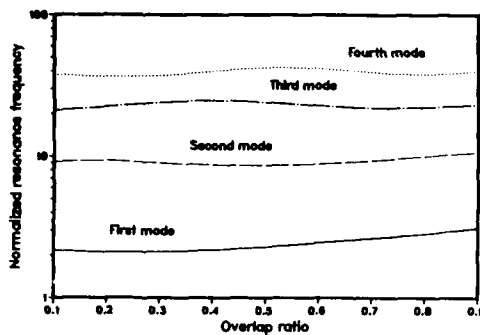
Figure 5 -- Variation of ω_n with overlap ratio
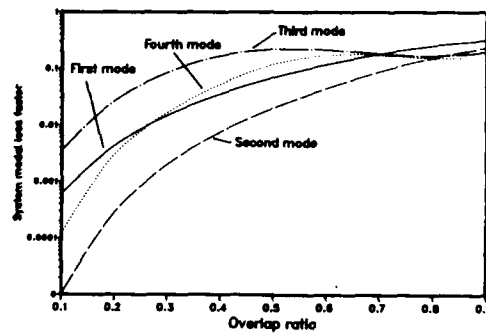
Figure 6 -- Variation of η with overlap ratio

The variation of $\bar{\omega}_n$ and η with temperature T is also studied. The shear modulus G_c' and loss factor η_c of almost all damping materials are highly temperature dependent [6]. The damping material in this case was still unchanged, and we set $h_c = 0.5$ mm and $\frac{L}{L_1}$ = 0.5. T was varied from -12.2°C (10°F) to 65.6°C (150°F). The results are plotted in Figure 7 and Figure 8. Observation shows that for ISD-112 damping material, $\bar{\omega}_n$ decreases with T for the first two modes. For the third and fourth modes, $\bar{\omega}_n$ takes on peak values somewhere between T = -12.2°C (+10°F) and T = 10°C (50°F), and then decrease with T. The variation of η with T is more dramatic and interesting. Figure 8 shows that for 3M ISD-112 material, η reaches its maximum values between T = -1.11°C (+20°F) and T = 21.11°C (+70°F) and decrease sharply with T after T > 21.11°C. This behavior is consistent with what is observed normally with these type of damping materials [6].
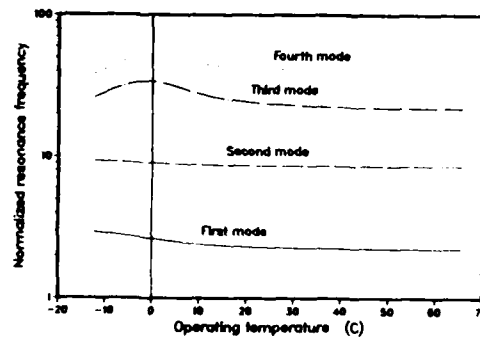
Figure 7 -- Variation of ω_n with temperature T
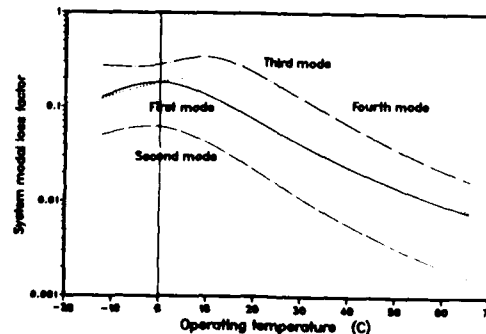
Figure 8 -- Variation of η with temperature T

Table 1 shows the $\bar{\omega}_n$ and η values for seven different damping materials chosen here for the case when h_c =

0.5 mm, $\frac{L}{L_1}$ = 0.5 and T = 21.11°C. Data like these are invaluable in the selection of damping material in the joint design.

Table 1: Resonance Frequency and Modal Loss Factor of the Joint System for Different Damping Materials at Room Temperature

Damping Material	Mode 1		Mode 2		Mode 3		Mode 4	
	$\bar{\omega}_n$	η	$\bar{\omega}_n$	η	$\bar{\omega}_n$	η	$\bar{\omega}_n$	η
Soundcoat LT	2.2245	0.00567	8.5779	0.00133	21.824	0.01445	40.368	0.00755
3M ISD-113	2.2005	0.02382	8.5881	0.00578	21.759	0.06619	40.447	0.03335
Soundcoat MN	2.2175	0.02839	8.6258	0.01135	22.478	0.16703	41.257	0.10144
3M ISD-112	2.2913	0.06779	8.6680	0.02022	23.199	0.21322	42.505	0.11969
Dyad 601	1.9210	0.04855	7.5777	0.02376	22.571	0.33232	40.896	0.22611
3M ISD-110	2.5916	0.14535	8.9468	0.03706	29.933	0.16385	47.508	0.08961
Soundcoat D	2.6671	0.02573	8.5565	0.01562	38.193	0.03580	56.846	0.03313

The accuracy of the numerical data obtained in the study can be checked by the mode shape plotting. As eigenvalues are complex quantities, we may plot the real and imaginary parts, or the magnitude and phase of the mode shape function. One example of mode shape plotting for the first four modes when h_c = 0.5 mm, $\frac{L}{L_1}$ = 0.5,

T = 21.11°C and ISD-112 damping material is shown in reference [1]. These plots clear show the validity of the numerical data obtained in the searching process.

III. CONCLUSION

A theoretical analysis for the study of transverse vibration of adhesively bonded composite double-strap joint system is presented in this paper. Energy method and Hamilton's principle are used to derive the system governing equations of motion and natural boundary conditions. The adhesive material is modeled as a viscoelastic and complex modulus approach is utilized to model its material properties. The solution of the governing equations for simply supported ends of the system has been achieved by solving a 18 × 18 matrix equation with complex elements. A special searching strategy has been employed to predict the system the resonance frequencies (ω_n) and modal loss factors (η). A parametric study has been conducted to study the variation of ω_n and η with various structural and geometric parameters of the system.

It has been found that an increase in the overlap ratio leads to an increase in the damping capacity of the joint without significant loss in the system stiffness. But an increase in adhesive thickness h_c results in increased damping only up to a certain limit. Values of h_c beyond 0.1 mm leads to significant decrease in the stiffness of the system with little damping benefits. Temperature plays a major role in the damping of the system. As expected, the resonance frequency of the joint system decreases with temperature, while the loss factor increases gradually and appears to take on a maximum value near the glass transition temperature of the damping material. Values of ω_n and η are generated for seven different damping materials which will be useful in the design of these joints.

REFERENCES

1. Rao, M. D., and He, S., "Transverse Vibration and Damping Analysis of Adhesively Bonded Double-Strap Joints," in review by the J. of the Acoustical Society of America.
2. He, S., and Rao, M. D., "Vibration Analysis of Adhesively Bonded Composite Lap Joint, Part I - Theory," J. Sound and Vibration, in press.
3. Rao, M. D., and He, S., "Vibration Analysis of Adhesively Bonded Composite Lap Joint, Part II - Numerical Solution," J. Sound and Vibration, in press.
4. He, S., and Rao, M. D. , "Prediction of Loss Factors of Curved Sandwich Beams," accepted by J. Sound and Vibration.
5. He, S., and Rao, M. D., "Longitudinal Vibration and Damping Analysis of Adhesively Bonded Double-Strap Joints," accepted by the ASME J. of Vibration and Acoustics.
6. Nashif, A. D. , Jones, D. I. G., and Henderson, J. P., "Vibration Damping," Wiley, New York, 1985.
7. Mead, D. J., and Markus, S., "The Forced Vibration of A Three-Layer, Damped Sandwich Beam with Arbitrary Boundary Conditions," J. Sound and Vibration, Vol. 10, No. 2, 1969, pp. 163- 175.
8. Drake, M. L., "Section 7.1 - Fourth-order Beam Theory," Vibration Damping Short Course Notes, University of Dayton Research Institute.
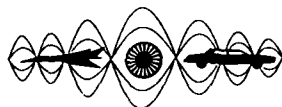
SECOND INTERNATIONAL CONGRESS ON
RECENT DEVELOPMENTS IN AIR- AND
STRUCTURE-BORNE SOUND AND VIBRATION
MARCH 4-6, 1992   AUBURN UNIVERSITY, USA

DAMPED ADVANCED COMPOSITE PARTS

David John Barrett
Naval Air Development Center
Advance Structures Technology Branch (Code 6043)
Warminster, Pennsylvania 18974-5000, USA

Christopher A. Rotz
Department of Manufacturing Engineering & Engineering Technology
Brigham Young University
Provo, Utah 84602

ABSTRACT

Recent demonstrations have shown that commercially available damping materials and advanced composite materials can be cocured into hybrid structural forms. Experiments indicate that the processing does not degrade the damping materials and that excellent structural damping properties can be obtained. In construction, the thin film damping materials are manipulated and placed essentially the same as the plies of graphite-epoxy. Damping materials can therefore be easily incorporated into complex structural parts. This paper discusses the design opportunities that are possible through the use of this type of construction.

INTRODUCTION

The oscillating aerodynamic loads that aircraft experience have grown in intensity as the speed and maneuverability of aircraft have improved. These loads excite resonant responses in the aircraft structure that often lead to fatigue, damage and component failure. Damped structural parts offer a way of safely resisting these dynamic loadings and, out of necessity, such parts will be a feature of future aerospace vehicles.

A novel method of constructing damped parts is the cocuring of damping materials and advanced composite materials into hybrid structural forms. Several researchers have experimented with this method of fabrication and they have reported good success [1-5]. From their work it can be concluded that commercially available damping materials, that have good thermal stability, can be routinely incorporated into advanced composite parts. The damping materials were found to retain their favorable properties under the pressures and temperatures of a standard autoclave cure cycle for graphite-epoxy without any special precautions being required during the construction and processing. The finished advanced composite parts were found to have excellent damping properties.

Besides offering an efficient method of construction, the cocuring of damping materials and advanced composite materials introduces new design opportunities. For instance, structural designs can be considered which take advantage of the orthotropic properties of advanced composites to increase the effectiveness of damping treatments [6-12]. Laminated construction can also offer design options that can lead to improved structural performance [11-14]. Finally, the flexibility of placing and arranging uncured materials prior to consolidation allows for the design and construction of new laminate architecture that can lead to improvements in stiffness, strength and structural damping.

COCURED PARTS

An example of cocured construction can be found in an effort [5] that examined both unstiffened and hat stiffened panels. The panels were made of IM6/3501-6 tape using a standard (1.5 mm (.006 in)) and an ultrathin (.094 mm (.0037 in)) thickness. The damping materials were 3M's AF-32 and ISD-112 film adhesives each with a thickness of .254 mm (.010 in).

The unstiffened panels were made with the standard ply thickness. A baseline undamped panel was constructed with a stacking sequence of $[0_{13}]$. The damped panels were laid up in a $[0_6/d/0_6]$ stacking sequence (the letter d is used to indicate the location of the damping layer). In all cases the plates were square with an edge dimension of 300 mm (12 in).

A baseline undamped hat-stiffened panel was made of ultrathin plies laid up in a combination of $0°, ±45°$ and $90°$ layers. Two damped hat stiffened panels were made identical to the baseline case except for the addition of damping layers of AF-32 in one and ISD-112 in the other. The damping layers were placed in the flange and legs of the hat and in the mid-surface of the skin (see Figure 1). In each case the hat was formed with a Teflon mandrel whose cross-section was 57 mm (2.25 in) wide at the base, 38 mm (1.5 in) wide at the top, and 23 mm (.90 in) in height. The hat stiffened panels had edge dimensions of 180 mm (7 in) by 460 mm (18 in).

During laminate fabrication the adhesive films were handled in essentially the same way as the stiffness plies. All panels were cured in an autoclave at $177°C$ ($350°F$) and 550 KPa (80 psi) using a conventional cycle. Microscopic examinations of the cured-part cross sections revealed that the damping layers had remained intact, had bonded well to the stiffness layers, and showed no evidence of excessive flow, absorption into the epoxy, or thermal degradation. C-scans confirmed that good bonding was achieved in all cases.

After curing, the unstiffened panels were cut into beam specimens 25 mm wide x 250 mm (1 in x 10 in) long, with the fibers aligned parallel to the longer dimension. The first two natural frequencies and modal damping values were measured at room temperature with the beams cantilevered from a rigid support. The beam specimens were also tested statically to determine their stiffness and strength. The results of these tests are summarized in Table 1.

As expected the beam study showed that there is a trade-off between static and dynamic properties in that increases in damping were accompanied with a loss in static properties. For example, the values of the modal damping at the first natural frequency were increased 230% for the AF-32 panel and 600% for the ISD-112 panel, while the flexural strengths were decreased to 55% and 39% of their original levels, respectively. In evaluating these results it should be realized that in many situations the value of damped structure can far outweigh any concern over stiffness and strength. For example, a structural element may be far overdesigned for static strength to prevent it from failing in fatigue.

The hat-stiffened panels were tested in a free-free configuration. Sufficient tests were run to determine the natural frequencies, modal damping values, and mode shapes of the first three modes of vibration. The measured dynamic properties are summarized in Table 2.

The lowest vibration mode consisted of the panel flanges bending in the vertical direction (flange flapping). For this mode, the damping of the AF-32 panel was slightly higher than that of the baseline. However, the damping in the ISD-112 panel was three times higher.

The next measured response was deduced to be a twisting of the panel flanges. The results show that in this mode the baseline panel exhibited a relatively high inherent damping, presumably due to the shearing of the graphite-epoxy. Although the damped panels were not specifically designed to resist this mode of response, either through the selection or placement of the damping materials, the ISD-112 panel still showed an increase in damping.

The third mode consisted of a longitudinal bending of the whole specimen. In the design of the test articles, the damping layer in the flange of the hat was carried down into the legs. This allowed the inner and outer faces of the hat to flex relative to one another. Because of this the damping layer could be sheared in longitudinal bending and thereby be able to dissipate bending energies of vibration. In this mode the damping increased by more than a 100% for the AF-32 panel and by nearly 1000% for the ISD-112 panel.

The high damping in the longitudinal bending mode indicated that the internal design features were working successfully. The fundamental skin mode was also significantly damped. The most efficient design of the hat stiffened panel would be to use ISD-112 in the base panel (to maximize the damping in the skin) and AF-32 in the hat stiffener (to retain good static properties while achieving desirable levels of damping).

STRESS COUPLING

Orthotropic materials can be used in structures to create a coupling between normal and shear strains (Stress Coupling). For instance, a ply of fiber reinforced graphite-epoxy will behave anisotropically if the fibers are oriented off-axis with respect to the direction of any in-plane loads. That is, an in-plane tensile force will produce an in-plane

shear deformation as well as an in-plane extension. In a part that is a hybrid of composite materials and damping materials, the shear deformations due to stress coupling can be used to load the damping layers. Therefore the possibility exists that stress coupling could be used to increase the energy dissipation.

An example of a hybrid stress coupled part is a tension-compression tubular member consisting of three concentric cylinders (see Figure 2). In this design the inner and outer cylinders consist of a fiber reinforced material while the middle cylinder is formed from a layer of damping material. When the fibers in the cylinders are oriented at an angle with respect to the central axis of the member, the inner and outer cylinders will rotate and deform under axial loads. These rotations will shear the damping layer and thereby provide a means to dissipate vibrational energy. An initial analysis of this design concluded that maximum effectiveness could be achieved if the fiber orientations were varied along the cylinder's length [6]. A recent work [10] has examined a tube in which the fiber orientations are varied by reversing the ply orientations at several specially designed joints along the tube. Analytical and experimental analysis found this design to yield good stiffness and damping properties.

Stress coupling can also be applied to flexural members, such as the damped panels previously discussed. Depending upon the ply layup, laminates can be constructed that contain extensional-shear, extensional-bending/twisting and bending-twisting couplings. Damping plies located in the layup can be made to shear under the deformations associated with these couplings.

Previous work on stress coupled hybrid laminates has yielded disappointing results [11 & 12]. Ply layups were found that could improve the structural damping, but this benefit was achieved at a greatly reduced static stiffness. The overall effect was, in spite of the improved damping level, an increase in the forced response of the stress coupled plates.

To examine this point, consider the dynamic response of a simply supported semi-infinite plate subjected to a steady state transverse harmonic excitation. The dynamic properties and response of this plate were determined through an analysis based on an anisotropic laminated damped plate theory [11] that employs Mead's Forced Mode Method [15]. The plate is a three layered construction consisting of top and bottom face sheets and a core of damping material. The face sheets consist of AS4/3501-6 graphite-epoxy with a fiber volume fraction of 60% and a ply thickness of .127 mm (.005 in). The damping layer consists of Soundcoat's D polymer with a thickness of .051 mm (.002 in). The computations accounted for the temperature and frequency dependence of the material properties and were performed for a temperature of $115\,^{\circ}$C ($240\,^{\circ}$F). The plate's width was taken to be 50 cm (20 in).

The ply orientations were referenced with respect to the plate's width with the layup specifications being $[\theta_5/-\theta_5/d/\theta_5/-\theta_5]$. Stress coupling occurs in this design when the angles of theta are greater than 0 degrees. Note that no stress coupling occurs for the laminate $[0_5/0_5/d/0_5/0_5]$, which will serve as the baseline structure from which to judge the performance of the stress coupled designs. The amplitude of the midspan transverse deflection was used to measure the response of the plate. For each individual forced mode this measure was normalized with respect to the corresponding response of the baseline plate.

Table 3 shows the results of the computations for the first six forced flexural modes. In each mode the structural damping in seen to increase with increasing off-axis fiber orientations. However, in spite of the improvement in damping, the forced response also increases. As in previous studies, this increased response is attributed to the loss in static stiffness.

If in the stress coupled plates, some of the plies are restricted to remain oriented across the width of the plate, then the loss of stiffness is minimized. In a previous work [12] laminates with ply specifications of $[0_N/\theta_{(10-N)}/-\theta_{(10-N)}/0_N/d/0_N/\theta_{(10-N)}/-\theta_{(10-N)}/0_N]$ where N ranges from 1 to 4 were analyzed. These laminates were found to have no design advantages. Another analytical study [13] examined a laminate in which the off-axis plies were confined to the inner sides of the face sheets. Favorable results were found as will be demonstrated here.

Consider a set of plates with ply layups of $[0_5/-\theta_5/d/\theta_5/0_5]$. The dynamic properties of these plates were computed (see Table 4) and it was found that the structural damping increases with increasing off-axis orientations. Now however, the dynamic response decreases since the loss in stiffness is not as great.

Table 4 also shows that the best performance is obtained with theta values of 90 degrees. This is at first puzzling, since cross-ply plates in this situation do not contain any stress coupling. The conclusion then is that an effect other than stress coupling is acting to improve the structural performance. These improvements have been attributed to compliant layering.

COMPLIANT LAYERING

In the previous example, the face sheets of the most effective design had inner plies that were oriented 90 degrees from the direction of the plate's width. Since a ply of graphite-epoxy is flexible in the directions transverse to the fibers, the inner plies of this configuration are more compliant along the width than the baseline design. This type of layup is called a compliant layered design and studies of such configurations have found interesting results.

Compliant layering in a sandwich construction is defined as the replacement of the inner sides of the face sheets with a material that is less stiff than the removed material. The effect of this replacement is to reduce the in-plane extensional stiffness of the face sheets. This allows the face sheets to undergo greater in-plane translations. These translations were found to increase the rate of core shearing which reduced the amplitude of the response [13].

To demonstrate the effect of compliant layering, a sandwich construction with metallic face sheets was examined (metallic face sheets were chosen to simplify the demonstration and to broaden the solution base). The semi-infinite plate again served as the analytical test structure. The plate has a width of 610 mm (24 in). The face sheets of the baseline structure are composed of .762 mm (.030 in) of carbon steel. The damping material is ISD-112 with a thickness of .051 mm (.002 in). The compliant layered plate has bimetallic face sheets. The outside layer is a carbon steel sheet with a thickness of .635 mm (.025 in) while the inner layer is a 2024 aluminum sheet with a thickness of .127 mm (.005 in). The aluminum and steel layers are assumed to be rigidly bonded together. The computations were run for room temperature properties using the previous analysis procedure.

Table 5 shows the results of the computations for the first ten forced flexural modes. In each mode the compliant layer design led to an increased loss factor and a reduced resonant response. Note that the compliant layer design is 11% lighter than the baseline design. The increase in resonant frequency in the lower modes is attributed to this reduction in mass.

NEW DESIGNS

One of the advantages of cocuring damped composite parts is that new designs are achievable. The ease of cutting, draping and interleafing uncured materials makes this possible. Also, simple fabrication procedures allow the build-up of complex but desirable laminate architecture.

As an example, consider the "Floating Layer" design shown in Figure 3. The name comes from the strips of fiber reinforced tape that are attached to the inner sides of the face sheets at only one end of a strip. The rest of the strip extends into and is surrounded by the damping material. As the face sheets deflect under transverse vibration, the floating layers will be pushed and pulled through the damping material. This should lead to additional shearing of the damping material and higher energy dissipation. Note that floating layers can be used to stress "dead" areas of the damping layer such as the midspan region of a simply supported damped sandwich beam vibrating in it's fundamental mode.

Another design example is a glass reinforced damping layer. Preliminary fabrication experiments have shown that if a layer of ISD 112 is placed on top of a dry glass mat, then during autoclave processing the damping material will penetrate the mat and coat the glass fibers. Additional experiments have shown that plies of graphite epoxy can be added as top and bottom face sheets to the damping layer and the dry mat prior to curing. The cured assembly was found to remain intact. Future specimens of this type will be tested for stiffness, strength and structural damping. If the glass mat can be prevented from binding the face sheets together, then the damping layer will be properly sheared. In addition, the glass mat will increase the stiffness, possibly the strength and, by making the stress fields in the damping layer more complex, the structural damping.

CONCLUSIONS

From this body of work several conclusions can be made:

1. Cocuring is a viable construction option for the building of damped primary (stiffeners and structural shapes) and secondary (skins) structure.

2. Stress coupling and compliant layering offer design advantages in special structural situations.

3. Internal architectural features can be designed to promote the efficiency of damping applications.

4. Damped advanced composite parts will be a fruitful area for further research and development.

REFERENCES

1. Schmidt, K., Curtis, F., Muziani, E. and Amore, L., "RELSAT Damped Equipment Panels - Fabrication," Proceedings of Damping '89, Paper JBD, AFWAL-TR-89-3116, February 1989.

2. Bronowicki, A. and Diaz, P., "Analysis, Optimization, Fabrication and Test of Composite Shells with Embedded Viscoelastic Layers," Proceedings of Damping '89, Paper GCA, AFWAL-TR-89-3116, February 1989.

3. Belknap, F., "Vibration Reduction of Composite Structures Using Constrained Layer Damping Techniques, "Proceedings of the 32nd AIAA/ASME/AHS/ASCE Structures, Structural Dynamics and Materials Conference, 1991, pp. 2391-2396.

4. Griffen, C. and Drake, M., "Composite/Vibration Damping Panels", University of Dayton Research Institute Technical Memorandum, July 1, 1991.

5. Rotz, C. A. and Barrett, D. J., "Cocured Damped Layers in Composite Structure," SAMPE Quarterly Journal, January 1992.

6. Barrett, D. J., "A Design for Improving the Structural Damping Properties of Axial Members," Paper HCB, Proceedings of Damping '89, West Palm Beach, FL, February 1989.

7. Chen, G. and Wada, B. K., "Passive Damping of Vibrations in Truss Structures," NASA Jet Propulsion Laboratory Report NPO-17609/7113, November 1990.

8. Belknap, F. and Kotsmatka, J. B., "Vibration Suppression of Thin Walled Composite Tubes Using Embedded Viscoelastic Layers," Paper HAC, Proceedings of Damping '91, San Diego, CA, February 1991.

9. Dolgin, B., "Composite Struts Damp Vibration," NASA Jet Propulsion Laboratory Report NPO-17914/7407, April 1991.

10. Olcott, D. D., Rotz, C. A., and Barrett, D. J., "Improved Damping in Composite Tubes through Stress Coupling and Co-Cured Damping Layers," 23rd International SAMPE Technical Conference, Kiamesha Lake, NY, October 1991, pp 373-387.

11. Barrett, D. J., "An Anisotropic Laminated Damped Plate Theory," Journal of Sound and Vibration, March 1992, Vol. 153(3).

12. Barrett, D. J., "On the Use of Stress Coupling in Damped Plates," Journal of Sound and Vibration (In peer review).

13. Barrett, D. J., "The Effect of Compliant Layering on Damped Beams," Paper BBB, Proceedings of Damping '91, San Diego, CA, February 1991.

14. Saravanos, D. A., "The Effect of Interply Damping Layers on the Dynamic Response of Composite Structures," Proceedings of the 32nd AIAA Conference, Paper AIAA-91-1124-CP, 1991.

15. Mead, D. J. and Markus, S., "The Forced Vibration of a Three Layer Damped Sandwich Beam with Arbitrary Boundary Conditions," Journal of Sound and Vibration 10(2), 1969, pp. 163-175.

TABLE 1 SUMMARY OF TEST RESULTS FOR BEAM SPECIMENS

Measured Natural Frequencies and Modal Damping Values for Cantilever Beams

Damping Material	Mode 1		Mode 2	
	ω (Hz)	η (%)	ω (Hz)	η (%)
Baseline (None)	62.5	1.2	417	0.3
AF-32	62.6	2.7	420	2.0
ISD-112	55.6	7.2	376	7.3

Note: ω is the natural frequency and η the modal damping for the indicated mode

Damping Material	Short Beam Shear Strength (Interlaminar)		Flexural Strength		Flexural Modulus	
	MPa	(Ksi)	MPa	(Ksi)	GPa	(Msi)
Baseline (None)	123	(17.8)	1340	(194)	132	(19.1)
AF-32	91	(13.2)	1190	(173)	72	(10.5)
ISD-112	83	(12.0)	527	(76)	47	(6.8)

Measured Static Properties

TABLE 2 SUMMARY OF TEST RESULTS FOR HAT-STIFFENED PANEL SPECIMENS

Measured Natural Frequencies and Modal Damping for Hat-Stiffened Panels						
Mode Description	Baseline Test Article		AF-32 Test Article		ISD-112 Test Article	
	ω (Hz)	η (%)	ω (Hz)	η (%)	ω (Hz)	η (%)
Flange Flapping	307	1.3	336	1.7	313	4.2
Flange Twisting	334	2.4	385	2.1	347	3.8
Longitudinal Bending	751	1.1	815	2.7	725	10.7

Note: ω is the natural frequency and η the modal damping for the indicated mode.

TABLE 3 RESULTS OF THE STRESS COUPLED PLATE STUDY

Modal Loss Factor (%) of $\theta_5/-\theta_5/d/\theta_5/-\theta_5$			
Mode	θ = 0°	θ = 5°	θ = 10°	θ = 15°
1	21.3	22.9	25.3	26.4
2	24.0	26.7	31.3	34.6
3	21.4	24.1	29.2	33.4
4	18.6	21.2	26.1	30.3
5	16.3	18.7	23.2	27.4
6	14.4	16.6	20.8	24.7

TABLE 4 RESULTS OF THE STRESS COUPLED PLATE STUDY

Modal Loss Factor (%) of $0_5/-\theta_5/d/\theta_5/0_5$			
Mode	θ = 0°	θ = 15°	θ = 45°	θ = 90°
1	21.3	23.3	25.5	26.0
2	24.0	32.4	42.9	45.5
3	21.4	32.1	48.6	53.3
4	18.6	29.7	49.3	55.4
5	16.3	27.0	48.0	55.0
6	14.4	24.6	45.8	53.5

Normalized Resonant Response (cm/cm) of $\theta_5/-\theta_5/d/\theta_5/-\theta_5$			
Mode	θ = 0°	θ = 5°	θ = 10°	θ = 15°
1	1.00	1.03	1.09	1.18
2	1.00	1.04	1.11	1.18
3	1.00	1.04	1.12	1.19
4	1.00	1.04	1.13	1.21
5	1.00	1.05	1.13	1.21
6	1.00	1.05	1.14	1.22

Normalized Resonant Response (cm/cm) of $\theta_5/-\theta_5/d/\theta_5/-\theta_5$			
Mode	θ = 0°	θ = 15°	θ = 45°	θ = 90°
1	1.00	.917	.870	.864
2	1.00	.809	.698	.686
3	1.00	.785	.663	.651
4	1.00	.774	.657	.649
5	1.00	.770	.658	.651
6	1.00	.768	.659	.659

TABLE 5 RESULTS OF THE COMPLIANT LAYERED PLATE STUDY

Computed Forced Frequencies (ω), Loss Factors (η) and Normalized Resonant Response (R)						
Mode	Steel Design			Bimetallic Design		
	ω (Hz)	η (%)	R	ω (Hz)	η (%)	R
1	9.7	4.09	1.0	10.3	4.15	99
2	34.2	15.8	1.0	36.2	16.8	94
3	69.9	24.2	1.0	73.8	26.7	91
4	116	29.1	1.0	121	33.2	89
5	172	31.7	1.0	178	37.3	88
6	238	32.9	1.0	244	39.7	88
7	313	33.2	1.0	320	40.9	87
8	399	33.1	1.0	404	41.4	87
9	495	32.6	1.0	498	41.4	87
10	601	32.0	1.0	601	41.1	87
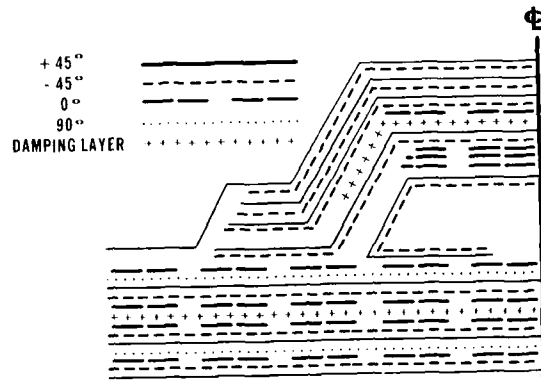
FIGURE 1. LAYUP DIAGRAM FOR THE HAT-STIFFENED DAMPED PANELS
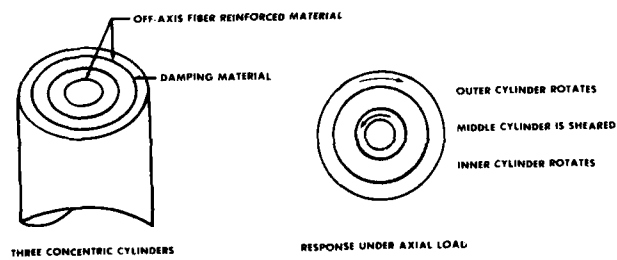
FIGURE 2. STRESS COUPLED TUBE DESIGN
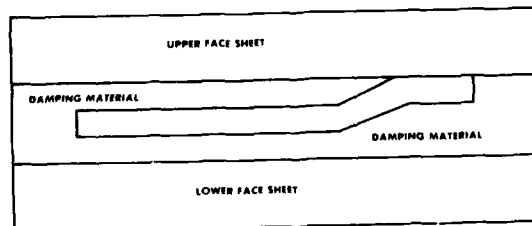
FIGURE 3. DETAIL OF "FLOATING LAYER" DESIGN
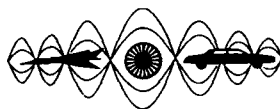
DAMPING OF LAMINATED COMPOSITE BEAMS WITH MULTIPLE VISCOELASTIC LAYERS

Shulin He and Mohan D. Rao

Department of Mechanical Engineering - Engineering Mechanics

Michigan Technological University

Houghton, MI 49931

ABSTRACT

This paper presents a theory for the damping and vibration analysis of composite beams with multiple viscoelastic damping layers. The damping layers are constrained (or sandwiched) by anisotropic laminated beams. The laminate theory for composite materials as well as the energy method are employed in the analysis. The in-plane shear strains of the damping layers and the constraining laminated beams are included. Closed form solutions are obtained for a general composite beam with N layers of damping material under simply supported boundary conditions. Numerical examples are presented for the cases of single, double and triple damping layers along with a study of the variation of loss factors with structural parameters such as the ply orientation of a laminae in a certain constraining laminated beam.

INTRODUCTION

In recent years, lot of research work has been focused on the analysis of anisotropic laminated damped beams and plates. Tujimota, et al [1] used both experimental work and theory for a sandwich beam with isotropic face plates to study the damping characteristics of multi-layer composite sandwich plates. In some cases, especially for anisotropic case, their experimental results diverged a lot from the numerical results. This discrepancy was attributed to the anisotropicity of each of the face plates. Mukhopadhyay and Kingsbury [2] pointed out that when the sandwich plate undergoes flexural deformation, the anisotropic facings will not only deform under normal strain, but also undergo shear deformation in its own plane. This is due to the coupling between the bending and extensional motion, and also between shear and extensional deformation. The additional in-plane shear deformation in the face plates will influence the in-plane shear deformation of the damping layer, which will not happen in conventional sandwich beams with isotropic facings. Also when the beams or plates are composite materials, the material damping of the face plates need to be included in the analysis. A comprehensive model to predict the damping of composite laminated beams with a single damping layer is developed by Barrett [3].

In this paper, the authors have derived a comprehensive, yet simple model to study the dynamic behavior of multi-damping layer composite beams with laminated composite constraining layers. The authors believe that the dominating factors which affect the damping efficiency of the composite beam include the shear deformation of the damping layers both in xz-plane and in xy-plane (in-plane). In current analysis, the in-plane shear deformations of the damping layers as well as that of the constraining layers are included. The model also shows why the theory for conventional sandwich beam and plate doesn't work for the case in which the constraining layers are anisotropic beams.

I. THEORY

The multi-damping layer composite beam with laminated constraining layers (beams) is shown in Figure 1. The following basic assumptions are made in current analysis.
(1) The composite beam has unit width and total length L and has (2N-1) damping layers and 2N constraining laminated beams and the ith laminated beam has N_i layers of plies.
(2) The composite beam is symmetric with respect to the xy-plane and is simply supported.
(3) The in-plane (xy plane) shear strain of the damping layers and the constraining laminated beams as well as the extensional strain of the constraining laminated beams and the shear strain of the damping layers in xz-

plane are included. But the in-plane shear strains in the laminated beams and the xz-plane shear strains of the damping layers are constant through their thickness.

(4) The extensional strains in the damping layers are included, but only the transversely inertia of the composite beam is included.

(5) The shear and elastic moduli of the damping material is linear viscoelastic and complex modulus approach is used for both the damping material and the lamina material.

(6) All the σ_y's and σ_z's of each layer are zero.
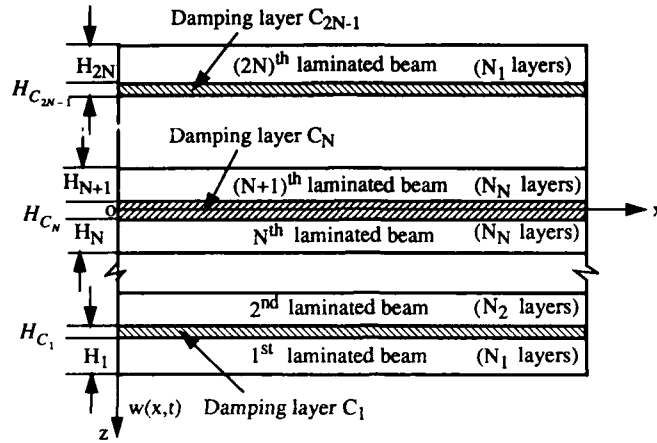
Figure 1 -- Configuration of the composite beam with multiple damping layers

In addition, the transverse displacement $w(x,t)$ is assumed to be the same for every layer of the composite beam as shown in Figure 1. Also we introduce another 2N independent variables to describe the strain and deformation field of the whole system. Let $\gamma_{xz}^{C_1}, ..., \gamma_{xz}^{C_N}$ be the xz-plane shear strains of damping layers C_1 to C_N respectively and $\gamma_{xy}^{(1)}, ..., \gamma_{xy}^{(N)}$ be the xy-plane (in-plane) shear strains of laminated beams 1 to layer N respectively. Due to the symmetry of the composite beam with respect to xy-plane, we have

$$H_1 = H_{2N}, ..., H_i = H_{(2N+1)-i}, i = 1, ..., N, \quad H_{C_1} = H_{C_{2N-1}}, ..., H_{C_i} = H_{C_{2N-i}}, i = 1, ..., N-1,$$

$$\gamma_{xz}^{C_{2N-1}} = \gamma_{xz}^{C_1}, ..., \gamma_{xz}^{C_{2N-i}} = \gamma_{xz}^{C_i}, i = 1, ..., N-1, \text{ and } \gamma_{xy}^{(2N)} = -\gamma_{xy}^{(1)}, ..., \gamma_{xy}^{(2N+1-i)} = -\gamma_{xy}^{(i)}, i = 1, ..., N$$

where $\gamma_{xz}^{C_i}, i = N+1, ..., 2N-1$, are the xz-plane shear strains of the damping layers N+1 to 2N-1 which locate on the negative z direction and $\gamma_{xy}^{(i)}, i = N+1, ..., 2N$, are the xy-plane shear strains of the constraining laminated beams N+1 to 2N which also locate on the negative z direction.

1.1. Strain energy analysis of the composite beam

Since the y and z directional normal stresses of each layer are assumed to be zero, only the displacement along the x direction (axial direction) of the beam needs to be defined. The longitudinal displacement field of the composite beam can be described as follows.

For the ith laminated beam:

$$u_i(z, x, t) = z\frac{\partial w}{\partial x} - \left(\frac{H_{C_N}}{2}\gamma_{xz}^{C_N} + \sum_{k=i}^{N-1} H_{C_k}\gamma_{xz}^{C_k}\right), i = 1, ..., N \tag{1}$$

where $z_c^i \le z \le z_c^i + H_i$, $z_c^i = \frac{H_{C_N}}{2} + \sum_{k=i}^{N-1} H_{C_k} + \sum_{k=i+1}^{N} H_k$, and

$$u_i(z, x, t) = -u_{2N+1-i}(-z, x, t), i = N+1, N+2, ..., 2N. \tag{2}$$

The longitudinal displacements of the damping layers are approximated as constant through their thickness. For damping layer C_i, we have $u_{C_i}(x, t) = \frac{1}{2}\left[u_i\big|_{z=(z_c^i-H_{C_i})} + u_{i+1}\big|_{z=z_c^i}\right]$, i.e.

$$u_{C_i}(x, t) = (z_c^i - \frac{1}{2}H_{C_i})\frac{\partial w}{\partial x} - \left[\frac{1}{2}(H_{C_i}\gamma_{xz}^{C_i} + H_{C_N}\gamma_{xz}^{C_N}) + \sum_{k=i+1}^{N-1} H_{C_k}\gamma_{xz}^{C_k}\right] \text{ for } i = 1, 2, ..., N-1, \tag{3}$$

and $u_{C_i}(x, t) = -u_{C_{2N-i}}(x, t)$ for $i = N+1, ..., 2N-1$. $\tag{4}$

Through the above displacement description, we can determine the strain field of the composite beam. The strain field of the ith laminated beam corresponding to $\sigma_x^{(i)}$ and $\tau_{xy}^{(i)}$ can be shown to be

$$\varepsilon_x^{(i)}(z,x,t) = z\frac{\partial^2 w}{\partial x^2} - \left(\frac{H_{C_N}}{2}\frac{\partial \gamma_{xz}^{C_N}}{\partial x} + \sum_{k=i}^{N-1} H_{C_k}\frac{\partial \gamma_{xz}^{C_k}}{\partial x}\right), \gamma_{xy}^{(i)}(x,t) = \gamma_{xy}^{(i)}(x,t) \text{ for } i = 1,...,N, \tag{5}$$

and $\quad \varepsilon_x^{(i)}(-z,x,t) = -\varepsilon_x^{(2N+1-i)}(z,x,t), \gamma_{xy}^{(i)}(x,t) = -\gamma_{xy}^{(2N+1-i)}(x,t) \text{ for } i = N,...,2N. \tag{6}$

The strain field of damping layer C_i corresponding to $\sigma_x^{C_i}$, $\tau_{xy}^{C_i}$ and $\tau_{xz}^{C_i}$ can be shown to be

$$\varepsilon_x^{C_i}(x,t) = (z_i - \frac{1}{2}H_{C_i})\frac{\partial^2 w}{\partial x^2} - \left[\frac{1}{2}\left(H_{C_i}\frac{\partial \gamma_{xz}^{C_i}}{\partial x} + H_{C_N}\frac{\partial \gamma_{xz}^{C_N}}{\partial x}\right) + \sum_{k=i+1}^{N-1} H_{C_k}\frac{\partial \gamma_{xz}^{C_k}}{\partial x}\right], \tag{7}$$

$$\gamma_{xy}^{C_i}(z,x,t) = \gamma_{xy}^{(i+1)} + \frac{1}{H_{C_i}}[z - (z_c^i - H_{C_i})][\gamma_{xy}^{(i)} - \gamma_{xy}^{(i+1)}], \quad z_c^i - H_{C_i} \le z \le z_c^i, \tag{8}$$

and $\quad \gamma_{xz}^{C_i}(x,t) = \gamma_{xz}^{C_i}(x,t) \text{ for } i = 1,2,...,N-1. \tag{9}$

Also, $\quad \varepsilon_x^{C_i}(x,t) = -\varepsilon_x^{C_{2N-i}}(x,t), \gamma_{xy}^{C_i}(-z,x,t) = -\gamma_{xy}^{C_{2N-i}}(z,x,t), \gamma_{xz}^{C_i}(-z,x,t) = \gamma_{xz}^{C_{2N-i}}(z,x,t) \tag{10}$

for $i = N+1,...,2N-1$. As for the damping layer C_N, since the middle surface of this layer is the neutral surface, $\varepsilon_x^{C_N}$ is approximated to be zero. The shear strains of this layer are given by

$$\gamma_{xz}^{C_N}(x,t) = \gamma_{xz}^{C_N}(x,t), \text{ and } \gamma_{xy}^{C_N}(z,x,t) = \frac{2z}{H_{C_N}}\gamma_{xy}^{(N)}(x,t), -\frac{H_{C_N}}{2} \le z \le \frac{H_{C_N}}{2} \tag{11}$$

Consider the ith laminated beam in the positive z direction ($i = 1,2,...,N$) which has N_i layers of laminae and assume that the angle between the fiber direction of the jth layer and the x-axial direction is $\theta^{(i,j)}$. For the jth layer of the ith beam, applying the stress-strain formula relations (see reference 5), we have

$$\begin{bmatrix} \sigma_x^{(i,j)} \\ \sigma_y^{(i,j)} \\ \tau_{xy}^{(i,j)} \end{bmatrix} = \begin{bmatrix} \overline{Q}_{11}^{(i,j)} & \overline{Q}_{12}^{(i,j)} & \overline{Q}_{16}^{(i,j)} \\ \overline{Q}_{12}^{(i,j)} & \overline{Q}_{22}^{(i,j)} & \overline{Q}_{26}^{(i,j)} \\ \overline{Q}_{16}^{(i,j)} & \overline{Q}_{26}^{(i,j)} & \overline{Q}_{66}^{(i,j)} \end{bmatrix} \begin{bmatrix} \varepsilon_x^{(i,j)} \\ \varepsilon_y^{(i,j)} \\ \varepsilon_{xy}^{(i,j)} \end{bmatrix} \tag{12}$$

where $\overline{Q}_{11}^{(i,j)}$ to $\overline{Q}_{66}^{(i,j)}$ are the element of the transformed reduced stiffness matrix of the jth layer of the ith constraining beam. Here $\sigma_y^{(i,j)} = 0$ is assumed. Then the strain energy density of the jth layer of the ith beam is given by

$$U_o^{(i,j)} = \frac{1}{2}(\overline{Q}_{11}(i,j))(\varepsilon_x^{(i,j)})^2 + \frac{1}{2}(\overline{Q}_{66}(i,j))(\gamma_{xy}^{(i,j)})^2 + \overline{Q}_{16}(i,j)\varepsilon_x^{(i,j)}\gamma_{xy}^{(i,j)}, \tag{13}$$

where $\overline{Q}_{11}(i,j) = \overline{Q}_{11}^{(i,j)} - \frac{(\overline{Q}_{12}^{(i,j)})^2}{\overline{Q}_{22}^{(i,j)}}, \overline{Q}_{16}(i,j) = \overline{Q}_{16}^{(i,j)} - \frac{\overline{Q}_{12}^{(i,j)}\overline{Q}_{26}^{(i,j)}}{\overline{Q}_{22}^{(i,j)}}, \overline{Q}_{66}(i,j) = \overline{Q}_{66}^{(i,j)} - \frac{(\overline{Q}_{26}^{(i,j)})^2}{\overline{Q}_{22}^{(i,j)}}.$

Then the strain energy of the ith constraining laminated beam can be integrated by

$$U^{(i)} = \int_0^L \left[\sum_{j=1}^{N_i}\left(\int_{z_j^{(i)}}^{z_{j+1}^{(i)}} U_o^{(i,j)} dz\right)\right]dx \tag{14}$$

for unit width and $i = 1,2,...,N$, in which $z_1^{(i)} = z_c^i$ and $z_{N_i}^{(i)} = z_c^i + H_i$.

Due to the symmetry of the composite beam, we can show that $U^{(i)} = U^{(2N+1-i)}$ for $i = N+1,...,2N$.

The total strain energy contributed by the laminated beams then is given by $U_B = 2\sum_{i=1}^{N} U^{(i)}$.

The strain energy in damping layer C_i, $i = 1,...,N-1$, can be calculated from

$$U^{(C_i)} = \frac{1}{2}\int_0^L\left\{\int_{z_c^{i+1}}^{z_c^i}\left[E_{C_i}(\varepsilon_x^{C_i})^2 + G_{C_i}(\gamma_{xy}^{C_i})^2 + G_{C_i}(\gamma_{xz}^{C_i})^2\right]dz\right\}dx \tag{15}$$

where E_{C_i} and G_{C_i} are the complex elastic and shear modulus of the damping layer.

The strain energy of damping layer C_N is given by

$$U^{(C_N)} = \frac{H_{C_N} G_{C_N}}{2} \int_0^L \left[(\gamma_{xz}^{C_N})^2 + \frac{1}{3} (\gamma_{xy}^{(N)})^2 \right] dx. \tag{16}$$

As for the other N-1 damping layers, we can show that $U^{(C_i)} = U^{(C_{2N-i})}$ for $i = N+1, ..., 2N-1$. Then the total straining energy contributed by the 2N-1 damping layers are given by $U_B = U^{(C_N)} + 2 \sum_{i=1}^{N-1} U^{(C_i)}$.

Considering only the transverse inertia, we can find that kinetic energy of the composite to be

$$T = \frac{1}{2} \int_0^L m \left(\frac{\partial w}{\partial t}\right)^2 dx \tag{17}$$

where $m = 2\rho_N H_N + \rho_{C_N} H_{C_N} + \sum_{i=1}^{N-1} 2 (\rho_i H_i + \rho_{C_i} H_{C_i})$ is the density of the composite beam in unit length and ρ_i and ρ_{C_i}, $i = 1, 2, ..., N$, are the lamina material and the damping material densities respectively.

Assume the energy dissipated in the composite beam is balanced by the work done by the external distribution load $q(x, t)$. Then work done by $q(x, t)$ is given by

$$W = \int_0^L q(x, t) w(x, t) dx \tag{18}$$

The system differential equations of motion can be retrieved by the application of the Hamilton's principle which is given by

$$\delta \int_0^{\Delta t} [T - (U_B + U_C) + W] dt = 0. \tag{19}$$

1.2. Derivation of the frequency equation

To find the system modal loss factors and resonance frequency, we can use the Ritz method. Suppose the simply supported composite beam is under time harmonic vibration. The comparison functions for $w(x, t)$, $\gamma_{xz}^{C_i}$ and $\gamma_{xy}^{(i)}$, $i = 1, 2, ..., N$ can be written as

$$w(x, t) = \sum_{n=1}^{\infty} A_n \sin\frac{n\pi x}{L} e^{i\omega t}, \quad \gamma_{xz}^{C_i}(x, t) = \sum_{n=1}^{\infty} B_{in} \cos\frac{n\pi x}{L} e^{i\omega t}, \quad \gamma_{xy}^{(i)}(x, t) = \sum_{n=1}^{\infty} C_{in} \sin\frac{n\pi x}{L} e^{i\omega t} \tag{20}$$

where A_n, B_{in}, C_{in}, $i = 1, 2, ..., N$ and $n = 1, 2, ...$ are arbitrary constants to be determined. ω is the vibration frequency.

Considering the first n modes of vibration, we can substitute Eqs. (20) into Eq. (19) by setting $q(x, t) = 0$ and ω to be a complex quantity, i.e. $\omega^2 = \omega_r^2 (1 + i\eta)$, where ω_r corresponds to the resonance frequency and η corresponds to the modal loss factor. The variation of w, $\gamma_{xz}^{C_i}$ and $\gamma_{xy}^{(i)}$ can be carried on the arbitrary constants A_n, B_{in}, C_{in}. After some mathematical manipulation, we obtain the following homogeneous equations

$$\begin{bmatrix} k_{1,1} - \omega_r^2 m (1 + i\eta) & k_{1,2} & \cdots & k_{1,2n+1} \\ k_{1,2} & k_{2,2} & \cdots & k_{2,2n+1} \\ \cdots & \cdots & \cdots & \cdots \\ \cdots & \cdots & \cdots & \cdots \\ \cdots & \cdots & \cdots & \cdots \\ k_{1,2n+1} & k_{2,2n+1} & \cdots & k_{2n+1,2n+1} \end{bmatrix} \begin{bmatrix} A_n \\ B_{1n} \\ \cdots \\ B_{Nn} \\ C_{1n} \\ \cdots \\ C_{Nn} \end{bmatrix} = \begin{bmatrix} 0 \\ 0 \\ \cdots \\ 0 \\ 0 \\ \cdots \\ 0 \end{bmatrix} \tag{21}$$

where $k_{i,j}$, $i = 1, 2, ..., 2n$ and $j = 1, 2, ..., 2n$ are constant coefficients resulted from the variational process.

Let the cofactor of $k_{i,j}$ in the coefficient matrix be $K_{i,j}$ and let the determinant of $K_{i,j}$ be $\Delta K_{i,j}$. Then setting the determinant of the coefficient matrix of Eq. (21) to zero, we have

$$[k_{1,1} - \omega_r^2 m (1 + i\eta)] \Delta K_{1,1} + \sum_{j=2}^{2n+1} k_{1,j} \Delta K_{1,j} = 0 \tag{22}$$

268

which is the system frequency equation, from which we get ω_r and η in closed form solutions

$$\omega_r = \sqrt{\frac{1}{m}Re\,(K_{III})} \quad \text{and} \quad \eta = \frac{Im\,(K_{III})}{Re\,(K_{III})} \tag{23}$$

where $K_{III} = k_{1,1} - \dfrac{1}{\Delta K_{1,1}}\left(\displaystyle\sum_{j=2}^{2n+1} k_{1,j}\Delta K_{1,j}\right)$. The above formulas work for the case of 2N laminated beams

and 2N-1 damping layers. If the composite beam consists of 2N damping layers and 2N+1 laminated beams, the procedure to find ω_r and η is the same except that we will have (N+1) $\gamma_{xy}^{(i)}$ variables.

II. NUMERICAL EXAMPLES

First, numerical results are generated to compare the present model with Barrett's model [3]. The composite sandwich beam has layups of $0_4/\theta_2/d/\theta_2/0_4$, in which d is the damping layer. Barrett's data are input to our program. The least-squares curve fitting method is used to define a six order polynomial to find the shear modulus of the SJ 2015X, Type 112 damping material corresponding to a frequency at $20°C$. Loss factors η of the composite beam corresponding to the first three modes are plotted in Figure 2. It can be observed that data resulted from our model is very close that of Barrett's model for the first mode. As for the second and third modes, some minor difference exists between these two models when the ply angle varies from 10 degrees to 60 degrees. Figure 3 plots the normalized resonance frequency of the first three modes versus the ply angle θ, from which we can see that the ply angle doesn't seem to affect the stiffness of the composite beam. It could be due to the fact that those plies with angle θ are close to the neutral surface and the total number of these plies are only half of all the plies with zero ply angle. So changing the ply angles of the inner layers can enhance the damping capacity of the sandwich composite beam without significantly reducing the stiffness of the composite beam.
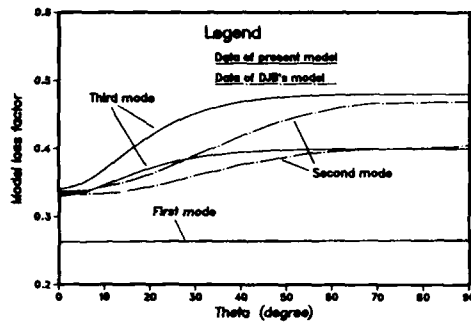
Figure 2. Comparison of η of present model with Barrett's model
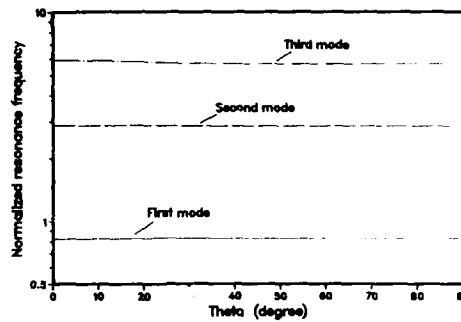
Figure 3. Variation of resonance frequency with ply angle in current model
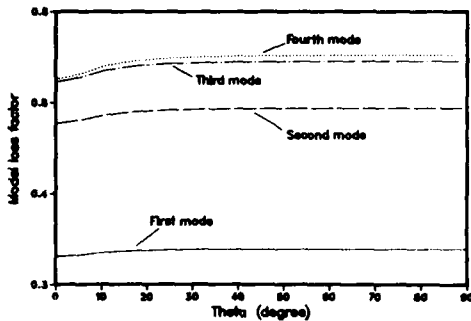
Figure 4. Variation of η with the ply angle θ of the central beam
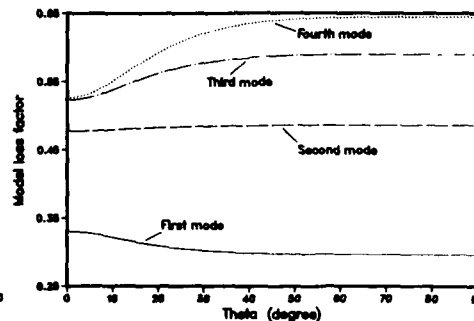
Figure 5. Variation of η with the ply angle of the inner two layers of two outer beams

Next, consider the case of double damping layer composite beams which have laminate code of $0_6/d/\theta_4/d/0_6$ and $0_4/\theta_2/d/0_4/d/\theta_2 0_4$. Each lamina has the same geometrical and mechanical properties as that in Barrett's model, and the 3M ISD-112 damping material is chosen. The formulae for calculating the shear storage modulus $G'_c\,(T,f)$ and material loss factor $\eta_c\,(T,f)$ of the damping material corresponding to a frequency f and environmental temperature T can be referred from reference [4]. Figure 4 (laminate code $0_6/d/\theta_4/d/0_6$) and Figure

5 (laminate code $0_4\theta_2/d/0_4/d/\theta_20_4$) show the variation of modal loss factor η of the composite beam with θ for the first four modes at $T = 20^o$. Numerical results shows that although increasing the ply angle of the central beam or the that of the two inner layers of the two outer beams can increase η the increase of η with the ply angle of the two inner layers of the top and bottom beams is more significant as can be observed from Figure 5. It is obvious that the ply angle of the central beam and that of the two outer beams have different effect in changing the modal loss factor of the double damping layer composite beam.

Numerical example of the triple damping layer composite beam is also studied. Again each lamina and the damping material is kept as the same above. Figure 6 and Figure 7 show the composite beam loss factor versus θ for two different layups $0_4/d/\theta_4/d/\theta_4/d/0_4$ and $0_4\theta_2/d/0_2/d/0_2/d/\theta_20_4$ at $T = 20^o$ respectively. It can be observed that both the ply angle of the two inner beams (corresponding to layups $0_4/d/\theta_4/d/\theta_4/d/0_4$) and those of the two outer beams (corresponding to layups $0_4\theta_2/d/0_2/d/0_2/d/\theta_20_4$) have significant effect on the modal loss factor. It is interesting to observe that η of the first mode decreases with θ in Figure 6.
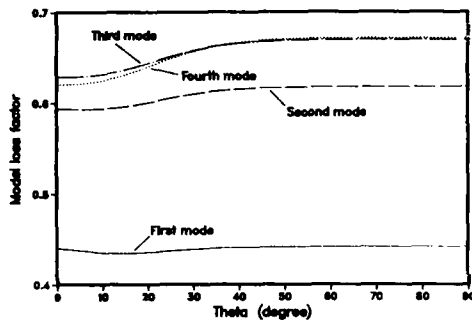
Figure 6. Variation of η with the ply angle
θ of the two inner beams
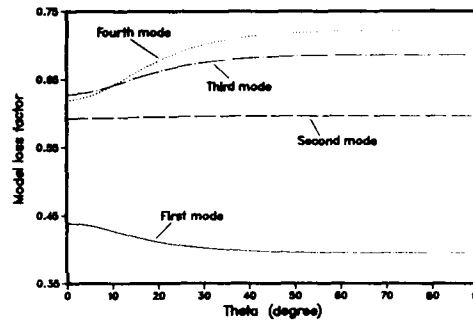
Figure 7. Variation of η with the ply angle of the
inner two layers of beam 1 and beam 4

Further parametric study will be conducted in the future to observe the effects of the different damping materials, operating temperature, thickness of damping layers on the modal loss factor of the composite beam. Also, effects of different layups of a composite beam with same number of damping layers on the modal loss factor of the composite beam will also be studied..

III. CONCLUSION

This paper describes a comprehensive vibration analysis of laminated composite beams that incorporate multiple viscoelastic damping layers. The location of damping layers are chosen to maximize the energy dissipation capacity and thus damping of the beam system. Laminated composite beam theory, Hamilton's principle and Ritz method are utilized to develop equations for predicting the system natural frequencies and modal loss factors of simply supported beams in closed form. Numerical results for the case of single, double and triple damping layers show that changing the ply angles of the laminae in the inner beams or near to the symmetric plane of the composite beam may benefit the damping capacity without losing the stiffness of the composite beam. Optimal ply angles of the laminas of a composite beam with multi-damping layers can be found to get maximum modal loss factor for certain damping material and environmental temperature using the above analytical model.

REFERENCES

1. Tujimoto, J., et al, "Mechanical Properties for CFRP/Damping-Material Laminates," Paper presented at the International Conference on Composite Materials, July, 1991, Honolulu, Hawaii.
2. Mukhopadhyay, A. K., and Kingsbury, H. B., "On the Dynamic Response of A Rectangular Sandwich Plate with Viscoelastic Core and Generally Orthotropic Facings," J. Sound and Vibration, Vol. 47, NO. 3, 1976, pp. 347 - 358.
3. Barrett, D. J., "An Anisotropic Laminated Damped Plate Theory," NADC-90066-60, 1990.
4. Drake, M. L., Vibration Damping Short Course Notes, University of Dayton Research Institute, Dayton, Ohio, 1989.
5. Jones, R. M., "Mechanics of Composite Materials," Hemisphere Publishing Company, 1980.
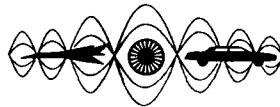
FUNDAMENTAL STUDY ON DEVELOPMENT OF
HIGH-DAMPING STRUCTURAL CABLE

Hiroki Yamaguchi and Rajesh Adhikari
Division of Structural Engineering and Construction
Asian Institute of Technology
GPO Box 2754, Bangkok 10501
Thailand

ABSTRACT

The modal damping of structural cables is conceived to be increased by using a damping treatment. An attempt is made to analytically estimate the modal damping of a composite Parallel-Wire-Strand Cable which is to be made by introducing some viscoelastic material between strands and the outer cover pipe. The effect of such damping treatment on the modal damping is discussed in terms of energy loss factors in axial and bending deformations. It is found that the magnitude of the bending loss factor is higher than that of the axial loss factor and hence the contribution of the bending loss factor to the modal damping can be significant. The possibility of developing structural cables with high damping performance is finally discussed.

INTRODUCTION

The use of viscoelastic layer as a mean to increase energy loss in plates under flexural vibrations is frequently encountered in the acoustic, mechanical and aerospace engineering fields [1, 2]. Viscoelastic materials in this damping treatment are found to dissipate energy when subjected to alternating stresses through the disruption of the molecular bonds of their long chain molecules. A similar treatment when applied to structural cables may also be expected to yield higher amount of energy loss in them and thereby increasing damping in the structural cables. If such a treatment is found to be effective then external devices like oil dampers or cable-tie systems, which are present-day-practice [3], would be unnecessary in order to reduce wind-induced cable vibrations in cable stayed bridges. Since the treated damping will inherently be associated with the cable, the effectiveness would be wider ranged than the external damping devices.

In the present paper, the possibility of developing a high-damping structural cable by utilizing high strength of steel and high energy dissipation characteristics of some viscoelastic materials is investigated. Since the prefabricated strand cables, such as New-PWS (Nippon Steel Corporation) or Hi-Am cable (BBR), have a thin outer cover pipe for the protection of strands against environmental effects, some viscoelastic material might be introduced between strands and the outer cover during their fabrication process. An attempt is made to analytically estimate the loss factor of a composite parallel-wire-strand (PWS) cable which is made by introducing some viscoelastic material in between the gaps left by the strands and also between strands and the outer cover pipe. Here the loss factor is defined as the ratio of the dynamically dissipated energy to the elastic energy stored per cycle and is conveniently represented by the coefficient of the imaginary part of the complex stiffness. It is assumed in the analysis that the introduction of viscoelastic material in the gaps does not alter the strand configuration and hence the damping characteristics of the original cable. Only the additional damping due to the introduction of viscoelastic material is discussed.

DAMPING TREATMENT IN STRUCTURAL CABLE

Composite Cable

The cross section of a typical prefabricated PWS Cable is shown in Fig. 1.(a). This type of cable is provided with an outer cover pipe, usually made of polyethylene, which protects the inner strands against the environmental effects. In this paper, viscoelastic material is to be introduced between the strands and the outer

cover pipe in order to increase the vibration damping of the cable. The outer cover pipe in such cables with the damping treatment can act as so called constraining layer to the viscoelastic layer inside and the properties of the outer cover is also to be changed. The schematic diagram of such a cable, hereafter termed as composite cable, is shown in Fig. 1.(b)

(a) Typical Prefabricated Cable   (b) Composite Cable
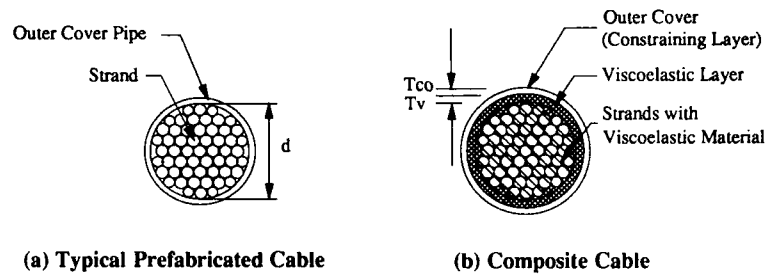
Fig. 1 Cross Section of Structural Cable.

Modal Damping in Composite Cable

The total potential energy U associated with a cable under flexural vibration may be attributed to the sum of potential energy of initial tension U_t, the strain energy due to the axial deformation U_a and the strain energy due to the bending deformation U_b. Of all these energies, the contribution of the initial tension is dominant in the case of cable and the contribution of strain energy of axial and bending deformation can be generally neglected, i.e.

$$U = U_t + U_a + U_b \doteq U_t \tag{1}$$

As for the energy dissipation D in the ordinary cable, it has been found that the major source of damping energy is the energy dissipated in axial deformation, D_a [4]. The energy dissipated in bending deformation, D_b, however, may not be negligible in the case of the above mentioned composite cable and hence the energy dissipation of composite cable is assumed to have two sources. Using energy loss factors η_a and η_b associated with both of the deformational modes, the total dissipated energy can be represented by

$$D \doteq D_a + D_b = 2\pi(\eta_a U_a + \eta_b U_b) \tag{2}$$

Therefore the modal damping ratio, which is defined as the ratio of the damping energy to the potential energy, is obtained for the flexural vibration in the composite cable as

$$\xi = \frac{D}{4\pi U} \doteq \frac{1}{2}\left(\frac{U_a}{U_t}\eta_a + \frac{U_b}{U_t}\eta_b\right) \tag{3}$$

Since all of the potential energies can be estimated analytically by using the calculated mode shape, it is essential to estimate two kinds of loss factor of the composite cable, i.e. the loss factor in axial deformation η_a and the loss factor in bending deformation η_b, for discussing the effectiveness of the damping treatment based on the modal damping ratio of Eq. (3).

LOSS FACTOR OF COMPOSITE CABLE IN AXIAL DEFORMATION

Analysis

In the present analysis of the composite cable with regular hexagonal arrangement of strands the following assumptions are introduced :

a) The lay angles of the strands are quite small and can be neglected. This assumption is justifiable because the lay angle of the outermost strand in a PWS Cable is only about 3.5° [5, 6].

b) The introduction of viscoelastic material and the modification of the cover pipe do not affect on the configuration of the strand cable.

c) The strands and the outer cover are treated to be nondissipative. Only the additional damping due to the damping treatment of viscoelastic material is considered.

d) The bond between strands and viscoelastic filaments, and the bond between the viscoelastic layer and the outer cover are perfect. There is no relative slip at the interfaces.

272

Suppose the composite cable is subjected to axial loading P, the total axial load is then to be taken by three parts of the composite cable in Fig. 1(b); the part of strands with viscoelastic material, the viscoelastic layer and the outer cover pipe or the constraining layer. Considering the compatibility condition of equal axial strains in three parts of the cable in Fig. 1(b), one can easily obtain the equivalent axial stiffness EA of the composite cable, which is nondimensionalised by the stiffness of the original untreated cable $(EA)_{cable}$, as

$$\frac{EA}{(EA)_{cable}} = 1 + \{4e_v t_v(t_v + 1) + 4e_{co} t_{co}(t_{co} + 2t_v + 1)\}\left(\frac{(1 + 2N)^2}{1 + 3N + 3N^2}\right) \tag{4}$$

where the following nondimensional parameters are introduced:

$$e_v = \frac{E_v}{E_{cable}}, \quad e_{co} = \frac{E_{co}}{E_{cable}}, \quad t_v = \frac{T_v}{d}, \quad t_{co} = \frac{T_{co}}{d} \tag{5.a,b,c,d}$$

E_v, E_{co} and E_{cable} are Young's moduli of viscoelastic layer, the outer cover and the cable (2.0×10^{11} N/m^2 assumed), respectively. d is the diameter of original cable as defined in Fig. 1(a) without damping treatment. T_v and T_{co} are thickness of the viscoelastic layer and the thickness of the outer cover both of which are shown in Fig. 1(b). N in Eq. (4) is the number of strand layers in the cable.

The possible range of the Young's modulus ratio of the viscoelastic material e_v is estimated to be from 5×10^{-8} to 2.5×10^{-2} by considering the Young's modulus of some commonly available viscoelastic materials, which can be estimated to be in the range of 1×10^4 N/m^2 to 5×10^9 N/m^2 (see Appendix), whereas the modulus ratio of the cover material e_{co} can be made to have any value between 0.005 (for some epoxy resins) and 1.0 (for steel pipe). As for the ranges of thickness ratios of both of the added layers, i.e. t_v and t_{co}, these nondimensional parameters can not be more than 0.1 to 0.2 because of practical constraints. Furthermore, it is mathematically evident that the term in brackets containing N in Eq. (4) is insensitive to the value of N and can be of the order of one. Therefore, the second term of Eq. (4) can be considerably small and the nondimensional equivalent axial stiffness given by Eq. (4) is close to 1.

With this characteristics of the equivalent axial stiffness, introducing the complex modulus $E_v^* = E_v(1 + i\eta_v)$ for the viscoelastic material and separating real and imaginary parts gives the approximate expression for the equivalent axial loss factor of the composite cable, nondimensionalised by the loss factor of the viscoelastic material, as

$$\frac{\eta_a}{\eta_v} = e_v\left[\{4e_v \cdot t_v(t_v + 1) + 1\}\left(\frac{(1 + 2N)^2}{1 + 3N + 3N^2}\right) - 1\right] \tag{6}$$

Possible Magnitude of Axial Loss Factor

In view of the insensitivity of the term containing N in Eq. (6), the equivalent axial loss factor of the composite cable is affected only by the parameters associated with the viscoelastic layer, i.e. the Young's modulus ratio of the material e_v and the thickness ratio t_v.
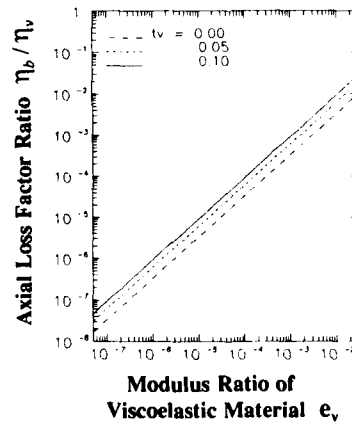
Fig. 2 Axial Loss Factor versus Young's Modulus Ratio for Different Thickness Ratio t_v of Viscoelastic Layer.

273

In order to investigate the axial loss factor quantitatively, the effect of the modulus ratio of the viscoelastic layer on the axial loss factor ratio of composite cable is shown in Fig. 2 for different values of thickness ratio of the viscoelastic layer. As can be seen in Fig. 2, the axial loss factor of composite cable is greatly influenced by the modulus of viscoelastic material while the thickness does not affect much on the loss factor. It can be estimated from Fig. 2 that a moderate value of $e_v = 5 \times 10^{-6}$ and $\eta_v = 1.0$ with $t_v = 0.05$ for the viscoelastic layer would give us a loss factor of about 3×10^{-6} which is very small. However, if e_v is increased to say 2.5×10^{-2} and t_v to 0.1 then the expected loss factor can be about 2×10^{-2} which would give a modal damping equal to 1 percent of the critical damping ($\xi = \eta/2 = 0.01$).

Therefore, it can be concluded here that viscoelastic material with higher Young's modulus and higher loss factor is preferable in order to get larger axial loss factor in composite cable.

LOSS FACTOR OF COMPOSITE CABLE IN BENDING DEFORMATION

Analysis

In case of bending deformation, the composite cable is modelled as a central rod (for the strand cable) placed inside laminated cylindrical shells (for the viscoelastic layer and the outer cover) with radii equal to R_2 and R_3 (Fig. 3(a)) and this model of composite cable subjected to pure bending as shown in Fig. 3(b). Timoshenko type shell theory is applied [7] only to the viscoelastic layer in order to take into account of the shear deformation in the viscoelastic layer whereas the shear deformations in the central rod and in the outer cover are neglected. Following assumptions are made here in addition to the previous assumptions on the axial deformation:

(a) Cross Section   (b) Applied Moment   (c) Strain Profile
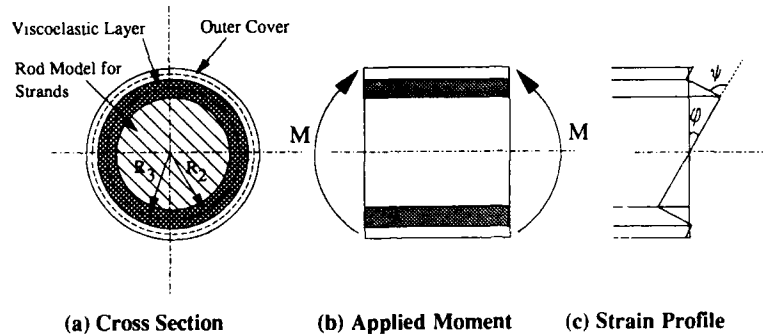
Fig. 3 Composite Cable in Bending.

a) The shear deformation is taken into account only in the viscoelastic layer. This assumption is justifiable for the case of a viscoelastic layer which has modulus of elasticity lower than those of the central rod and the outer cover material.

b) There is no radial deformation in the shell walls because of the high rigidity of the central solid rod and perfect bond at the interfaces.

c) The loss factor of the strands with viscoelastic filaments in the gaps is neglected.

The applied bending moment is again to be carried by three parts of the composite cable; the central rod, the viscoelastic layer and the outer cover. The bending moment carried by each part can be evaluated by considering the bending stress distribution in each part which is obtained from the strain profile as shown in Fig. 3(c). Thus obtained total bending moment is a function of the curvature and the shear deformation, and the equivalent bending stiffness of the composite cable can be defined as the ratio of the bending moment to the curvatures. After some manipulations, the equivalent stiffness of the composite cable, nondimensionalised by the bending stiffness of the cable without damping treatment, is easily derived as

$$\frac{EI}{(EI)_{cable}} = 1 + e_v((1+2t_v)^4 - 1) + e_{co}((1+2t_v+2t_{co})^4 - (1+2t_v)^4)$$

$$- 8e_v t_v^2 \left((1+t_v)^2 + \frac{t_v^2}{3} + \frac{2}{3}t_v(1+t_v)\right)\frac{\partial \psi}{\partial \phi}$$

$$- 16e_{co}t_{co}t_v \left((1+2t_v+t_{co})^2 + \frac{t_{co}^2}{3}\right)\frac{\partial \psi}{\partial \phi} \tag{7}$$

274

where ϕ and ψ are the deflection angle and the shear deformation as defined in Fig. 3(c) and the bending stiffness of cable $(EI)_{cable}$ is taken to be equal to the bending stiffness of a rod of diameter d. The first three terms in Eq. (7) account for the bending stiffnesses of the central rod, viscoelastic layer and the outer cover, respectively, and the last two negative terms are the reduction in bending stiffness due to the shear deformation in the viscoelastic layer.

In order to specify the relation between the shear angle ψ and the deflection angle ϕ, it is assumed, same as the case of laminated plate [1], that both the added layers and the central rod experience the same sinusoidal flexural vibration. Since the shear strain in the viscoelastic layer is to be caused by the net force increment in the outer cover layer, the following relation is derived after some manipulations [8, 9]:

$$\frac{\partial \psi}{\partial \phi} = \left[\frac{\partial \psi}{\partial x}\right]\Big/\left[\frac{\partial \phi}{\partial x}\right] = \frac{R_3/T_v}{1+g} \tag{8}$$

The nondimensional parameter g in Eq. (8) is termed as shear parameter and is defined as

$$g = \frac{G_v}{p^2 E_{co} T_{co} T_v} \tag{9}$$

where G_v is the shear modulus of the viscoelastic layer and p is the wave number which, in case of cables with mode number n and length L, is given by

$$p = n\pi/L \tag{10}$$

The characteristics of the equivalent stiffness in Eq. (7) with Eqs. (8 ~ 10) is investigated by estimating the possible ranges of each of parameters. The ranges of e_v, e_{co}, t_v and t_{co} remain same as in the case of axial deformation. The range of G_v can be approximated to be equal to that of E_v which was discussed earlier (Appendix). Therefore, for cables with the mode number n equal to 1 to 5 and the diameter equal to about 1 percent of the cable length, the range of the shear parameter g is estimated to be 1×10^{-3} to 1×10^{7}. For this range of g and the ranges of e_v, e_{co}, t_v and t_{co}, it can be shown that the stiffness ratio of composite cable as defined by Eq. (7) can be approximately equal to 1.

With this approximation, the bending loss factor of the composite cable can now be determined as follows by substituting complex elastic moduli, E_v and G_v, of the viscoelastic layer and assuming the same loss factors for the shear modulus and Young's modulus.

$$\eta_b = (\alpha_1 - \alpha_2 + \alpha_3)\eta_v \tag{11}$$

where

$$\alpha_1 = e_v((1+2t_v)^4 - 1) \tag{12.a}$$

$$\alpha_2 = 4e_v t_v\left((1+t_v)^2 + \frac{t_v^2}{3} + 2t_v(1+t_v)\right)(1+2t_v+t_{co})\frac{1}{(1+g)^2 + (g\eta_v)^2} \tag{12.b}$$

$$\alpha_3 = 8e_{co}t_{co}\left((1+2t_v+t_{co})^2 + \frac{t_{co}^2}{3}\right)(1+2t_v+t_{co})\frac{g}{(1+g)^2 + (g\eta_v)^2} \tag{12.c}$$

The first term in the bracket in Eq. (11) is the contribution to the total equivalent bending loss factor due to the bending of the viscoelastic layer, the second negative term is due to the interaction of bending and shear deformation in the viscoelastic layer and the third term is due to the shear in viscoelastic layer caused by the outer cover.

Possible Magnitude of Loss Factor in Bending Deformation

It is seen from Eq. (11) that the equivalent bending loss factor η_b of the composite cable is roughly proportional to the loss factor of the viscoelastic material η_v although there are small contributions of nonlinear terms of η_v in Eqs. (12.b,c).

The effect of the properties of the viscoelastic layer on the equivalent bending loss factor η_b can be depicted in Figs. 4 and 5. Fig. 4 shows the effect of Young's modulus of viscoelastic material e_v on bending loss factor and Fig. 5 shows the effect of thickness of viscoelastic layer t_v on bending loss factor. In both of the Figs. 4 and 5 the bending loss factor is plotted versus the shear parameter g which is ranged within a

previously discussed values. The presence of a peak value of loss factor is clearly observed in both of the figures and the bending loss factor is much dependent on the shear parameter. Moreover, it is found from these two figures that the maximum bending loss factor is not affected significantly by the modulus and thickness of the viscoelastic layer, instead the bending loss factor is found to go through a maximum value as a function of shear parameter g.

Since the deformation in the viscoelastic layer is primarily shear deformation, the effect of the properties associated with the outer cover, i.e. its modulus ratio e_{co} and thickness ratio t_{co}, would have greater effect on the equivalent bending loss factor. Therefore the effect of the properties of the outer cover on maximum bending loss factor $\eta_{b\,max}$ is next discussed. Fig. 6 gives the maximum value of the bending loss factor which can be obtained for the case of $e_v = 5 \times 10^{-6}$, $t_v = 0.05$ and $\eta_v = 1.0$. It is found from Fig. 6 that the maximum bending loss factor can be increased by increasing either t_{co} or e_{co} or both. For example, if $t_{co} = 0.01$ then for $e_{co} = 0.005$ a loss factor of the order of 1×10^{-4} is obtained whereas for the same value of t_{co} the expected loss factor increases to 0.02 when e_{co} is increased to 1. Suppose t_{co} is also increased to 0.05 then the expected loss factor can be about 0.1 which would give us a modal damping (for the case of bending only) equal to 5 percent of critical damping.
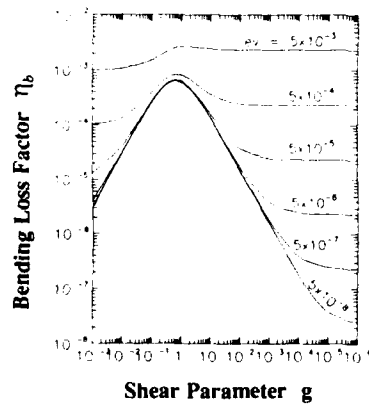
Shear Parameter g

Fig.4 Bending Loss Factor versus Shear Parameter for Different Modulus of Viscoelastic Layer.

($t_v = 0.05$, $\eta_v = 1.0$, $t_{co} = 0.05$, $e_{co} = 0.005$)
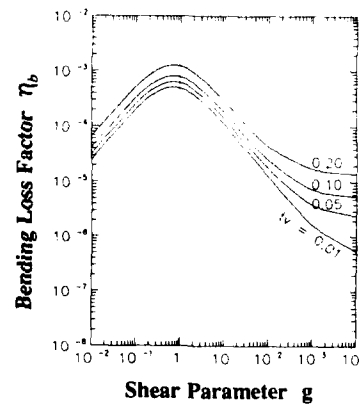
Shear Parameter g

Fig.5 Bending Loss Factor versus Shear Parameter for Different Thickness of Viscoelastic Layer.

($e_v = 5 \times 10^{-6}$, $\eta_v = 1.0$, $t_{co} = 0.05$, $e_{co} = 0.005$)

Outer Cover Thickness Ratio t_{co}
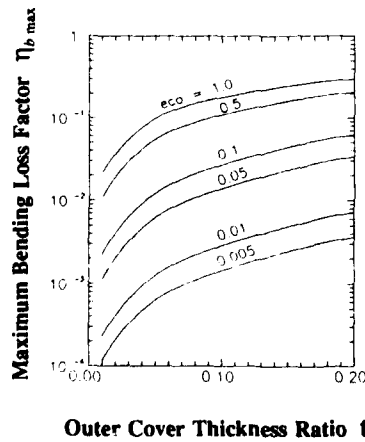
Fig.6 Maximum Loss Factor with modulus and thickness of outer cover.

Therefore, it can be concluded from above discussions that the equivalent bending loss factor η_b is affected significantly by three major factors; loss factor of the viscoelastic material, the shear parameter and the properties of the outer cover. The dependency of the bending loss factor on the loss factor of the viscoelastic material is roughly proportional, whereas the maximum bending loss factor (obtained under the condition of optimum shear parameter) can be increased by increasing either the Young's modulus of the outer cover or thickness of the outer cover or both.

Optimum Shear Parameter and Maximum Loss Factor

The presence of optimum shear parameter g, for which the loss factor in bending deformation is maximum, was discussed above and also it was found that the maximum loss factor in bending deformation is not affected by the modulus ratio e_v and thickness ratio t_v of the viscoelastic layer. Therefore an approximate expression for the maximum loss factor can be obtained by neglecting the effect of viscoelastic layer on the loss factor of the composite cable as

$$\eta_{b\,max} \doteq \alpha_3 \cdot \eta_v$$

$$\doteq 8 e_{co} t_{co} \left[(1+2t_v+t_{co})^2 + \frac{t_{co}^2}{3} \right] (1+2t_v+t_{co}) \frac{g}{(1+g)^2 + (g\eta_v)^2} \eta_v \tag{13}$$

with the following optimum value of the shear parameter which is determined by setting $\partial\eta/\partial g = 0$.

$$g_{opt} = \frac{1}{\sqrt{1 + \eta_v^2}} \tag{14}$$

The accuracy of above formula was checked numerically and was found to be satisfactory.

POSSIBILITY OF DEVELOPING HIGH-DAMPING-CABLE

It was found in the above two sections that for a composite cable with $e_v = 5\times10^{-6}$, $t_v = 0.05$, $\eta_v = 1.0$ and $e_{co} \approx 0.005$, the axial loss factor η_a is equal to 3×10^{-6} while the bending loss factor η_b can be 6×10^{-4}. That is, the magnitude of the bending loss factor for the composite cable is found to be greater than the axial loss factor whereas the bending loss factor of ordinary cable is generally negligible. Therefore the damping caused by bending loss factor may not be negligible in case of composite cables. Since the contribution of the bending loss factor to the modal damping of the composite cable depends on the ratio of the bending strain energy U_b to the potential energy of initial tension U, as shown in Eq. (3), a further study on the damping analysis [10] of the composite cable is hence needed in order to estimate the effectiveness of such type of damping treatment on modal damping of structural cable.

Based on above discussions, it can be said that there is a possibility of increasing the modal damping of the usual structural cables by giving them a damping treatment as outlined in present paper.

CONCLUDING REMARKS

The magnitude of energy loss factor of a composite structural cable, which is made by introducing viscoelastic material in between strands and the outer cover of a Parallel-Wire-Strand (PWS), was investigated analytically. Two modes of deformations, i.e. axial and bending deformations, were considered. The brief conclusions obtained through the present study are summarized as follows :

1) Effect of viscoelastic layer, i.e. its modulus and relative thickness, has a significant effect on the axial loss factor whereas its effect on bending loss factor is not significant and can be neglected.

2) The loss factor in bending deformation can be greater than the loss factor in axial deformation. This means that the energy loss caused by bending may play an important role in the damping of the composite cable.

3) There is an optimum value of shear parameter for which the bending loss factor is maximum.

4) The loss factor in bending deformation can be increased by increasing either the Young's modulus or thickness of the outer cover or both.

Increased bending loss factor may increase the modal damping of the composite cable and hence a new type of cables with superior damping performance, i.e. High-Damping Cables, may be developed, while further study on the damping analysis of the composite cable are next to be done.

REFERENCES

1. Ross, D., Ungar, E. E. and Kerwin, E. M. Jr., 'Damping of Plate Flexural Vibration by Means of Viscoelastic Laminae', *Structural Damping, ASME*, New York, 1959, pp. 49-87.
2. Hamme, Richard N., 'Vibration Control by Applied Damping Treatments', in Haris, C. M. and Crede, C. E. (ed.), *Shock and Vibration Handbook Vol. II'*, McGraw Hill Book Company. 1961, pp. 37-1-37-34.
3. Matsumoto, M., Yokoyama, K., Miyata, T. and Yamaguchi, H., 'Wind-Induced Cable Vibration of Cable-Stayed Bridges in Japan', *Canada-Japan Workshop on Bridge Engineering*, Canada, Japan, Sept. 25-27, 1989.
4. Yamaguchi, H., 'Damping Characteristics of Suspended Cables in Flexural Oscillation', Structural Dynamics : Recent Advances (*Proc. Of 4th Int. Conf.*), Elsevier Applied Science, 1991, pp. 606-615.
5. Gimsing, N.J., *Cable Supported Bridges - Concept and Design*, John Wiley & Sons Ltd., 1983.
6. NEW-PWS - *A Report by Nippon Steel Corporation, Japan.*
7. Tu, Yi-Yuan, 'Vibrations of Elastic Sandwich Cylindrical Shells', *ASME, Journal of Applied Mechanics*, Dec. 1960, pp. 653-662.
8. Karasudhi, P., *Foundations of Solid Mechanics*, Kluwer Academic Publishers, 1991.
9. Timoshenko, S. and Goodier, J.N., *Theory of Elasticity*, 2d ed., New York, McGraw-Hill, 1951.
10. Yamaguchi, H. and Jayawardena, S.J.K.L.L., 'Analytical Estimation of Vibration Damping in Cable Systems', *Proc. of 8th Int. Conf.on Wind Eng.*, London, Canada, July 1991 (to be published).
11. Jones, D.I.G., 'Damping Material for Vibration and Sound Control', in Faulkner L.L. *Handbook of Industrial Noise Control*, Industrial Press Inc., New York, 1976, pp. 218-232.
12. Nasif, A.D., Jones D.I.G. and Henderson, J.P., *Vibration Damping*, John Wiley & Sons Ltd., 1985.

APPENDIX

The elastic and the damping properties of commonly available viscoelastic materials for damping treatments are given in References [11] and [12]. The relations between Young's and shear moduli and the corresponding loss factors are summarized for various viscoelastic materials in Figs. A(a) and A(b). The figures were obtained by using the data in the references with the conditions of temperature of 20° C and the frequency of 10 Hz which are reasonable for the vibration problems of structural cables.

(a) Young's Modulus and its Loss Factor   (b) Shear Modulus and its Loss Factor
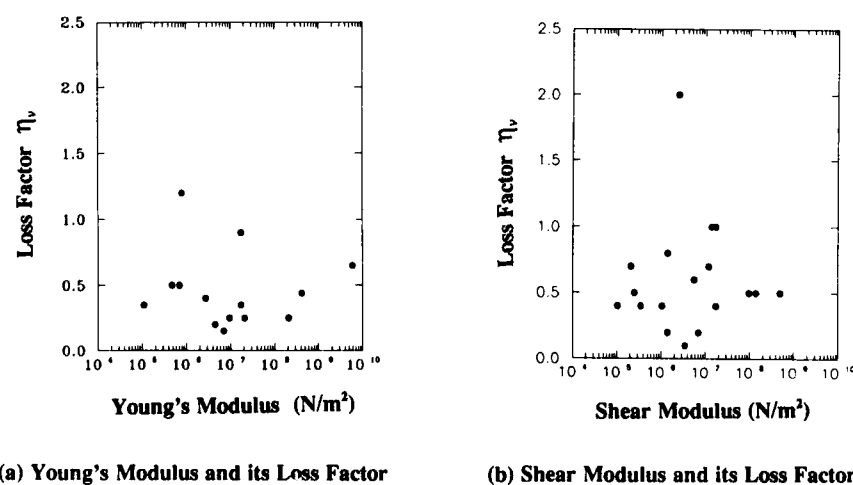
Fig. A Elastic and Damping Properties of Viscoelastic Materials
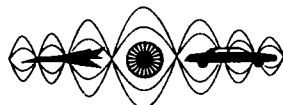
VISCOUS DAMPING OF LAYERED BEAMS WITH MIXED BOUNDARY CONDITIONS

Eugene T. Cottle, Capt, USAF
ASD/YZEE
WPAFB, OH 45431

December 21, 1991

ABSTRACT

For many years, viscoelastic materials have been used in damping treatments to control vibration. To optimize a design, the designer must predict frequencies and loss factors as a function of design parameters. Models of layered beams have been developed, but to date, analytical solutions have assumed boundary conditions to be the same for all layers.

Solutions to equations of motion of a layered beam are presented which permit each elastic layer to have its own boundary conditions. The equations are solved for the longitudinal displacement of both elastic layers, as well as the lateral displacement of the composite beam. Results of test cases verify the equations against known solutions, and illustrate the effect of mixed boundary conditions on the calculation of frequency and damping factor.

INTRODUCTION

Constrained layer damping treatments, usually in the form of damping tape, have been used for many years to reduce structural vibration. In order to understand the damping mechanism, analysts have studied the equations of motion of layered beams, such as the one shown in Figure 1. A layered beam consists of a viscoelastic layer between two elastic layers.

Analytical solutions to the equations of motion of a layered beam have historically assumed the boundary conditions for all layers to be the same. In this paper, the equations of motion are solved for the more general case in which the elastic layers can have different boundary conditions.

This paper presents solutions to the equations of motion of a layered beam, in which the elastic layers can have different boundary conditions. The equations of motion, the general solution, and numerical results for several interesting boundary conditions are shown. It is shown that considering different boundary conditions for each elastic layer can significantly effect the calculation of the beam equivalent damping. This has important implications for design of damping treatments. A more detailed treatment can be found in reference [2].
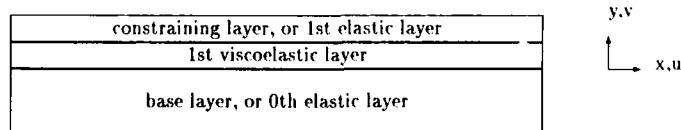
Figure 1: Constrained Layer Damping Treatment

CONVENTIONS

It is necessary to briefly explain the convention used in this paper to quantify viscous damping, and to explain the functional form of the frequency dependency of the complex shear modulus.

There are a number of ways to quantify the damping of a system. They include the loss factor, percent critical damping, viscous damping factor, log decrement, complex frequency, etc. These quantities are related [10, 2-7]. Only two quantities will be used in this paper. One will be the complex damped natural frequency of vibration, $\omega = \omega_R + \omega_I i$, where the subscripts R and I denote the real and imaginary parts of a quantity, and $i = \sqrt{-1}$. The other will be the loss factor η.

The relationship between the loss factor and the complex frequency is:

$$\eta = \frac{2\omega_R\omega_I}{\omega_R^2 - \omega_I^2} \qquad \text{or} \qquad \eta \approx \frac{2\omega_I}{\omega_R} \qquad \text{for} \qquad \omega_I \ll \omega_R \qquad (1)$$

A distinction must be made between the 'beam equivalent loss factor', η_b, and the loss factor of the material in the beam. For a homogeneous beam, the loss factor of the beam is equal to the loss factor of the material. However, for the layered beam, the loss factor defined by Eqn 1, will, in general, be different than the loss factor of the material in the adhesive layer. In this paper, the beam equivalent loss factor, η_b, will be defined in terms of the complex natural frequency of vibration, as shown in Eqn 1.

The development which follows permits all moduli to be complex, and to be functions of frequency and temperature. However, for the calculations in this paper, only the shear modulus of the viscoelastic layer was considered frequency dependent, and temperature dependence was not considered. The functional form of the frequency dependence of the shear modulus was taken from reference [12, 1-13,503-511]. It has the form

$$G = B(1) + \frac{B(2)}{1 + B(5)\,[B(3)/(fi)]^{B(6)} + [B(3)/(fi)]^{B(4)}} \qquad \text{where} \qquad \begin{array}{lll} G & = & \text{Complex shear modulus} \\ f & = & \text{frequency} \\ B(1)\ldots B(6) & = & \text{curve fit parameters} \end{array}$$

$$(2)$$

Material properties were taken from reference [12, 263-270], and are listed in Table 1.

EQUATIONS OF MOTION

The equations of motion are similar to those which have been derived in the literature [5] [8] [13]. The equations can be derived by applying Hamilton's principle [6, 44] to the layered beam. Figure 1 shows the directions of the lateral displacements, v, and the longitudinal displacements, u. Plane strain is assumed [9, 220]. It is also assumed that kinetic energy of rotation is small compared to translational kinetic energy. The beam is assumed to have unit width. Lateral (y-direction) displacements are assumed equal for all layers. Finally, it has been assumed [3] [5] that

$$G_{v1}t_{v1}\gamma_{v1}^2 \quad \gg \quad G_{e0}t_{e0}\gamma_{e0}^2 + G_{e1}t_{e1}\gamma_{e1}^2 \qquad (3)$$

$$E_{v1}t_{v1}\left[\frac{1}{2}\left(\frac{\partial u_{e1}}{\partial x} + \frac{\partial u_{e0}}{\partial x}\right)\right]^2 \quad \ll \quad E_{e0}t_{e0}\left(\frac{\partial u_{e0}}{\partial x}\right)^2 + E_{e1}t_{e1}\left(\frac{\partial u_{e1}}{\partial x}\right)^2 \qquad (4)$$

The equations of motion are

$$D_T\frac{\partial^4 v}{\partial x^4} + (\rho t)_T\frac{\partial^2 v}{\partial t^2} - G_{v1}t_{v1}d_1\left[\frac{1}{t_{v1}}\left(\frac{\partial u_{e1}}{\partial x} - \frac{\partial u_{e0}}{\partial x}\right) + d_1\frac{\partial^2 v}{\partial x^2}\right] = 0$$

$$E_{e0}t_{e0}\frac{\partial^2 u_{e0}}{\partial x^2} + G_{v1}\left(\frac{u_{e1} - u_{e0}}{t_{v1}} + d_1\frac{\partial v}{\partial x}\right) = 0 \qquad (5)$$

$$E_{e1}t_{e1}\frac{\partial^2 u_{e1}}{\partial x^2} - G_{v1}\left(\frac{u_{e1} - u_{e0}}{t_{v1}} + d_1\frac{\partial v}{\partial x}\right) = 0$$

where

x	$=$	spatial coordinate (see Figure 1)	$(\rho t)_T$	$=$	$\rho_{e0}t_{e0} + \rho_{e1}t_{e1} + \rho_{v1}t_{v1}$
y	$=$	spatial coordinate (see Figure 1)		$=$	mass per unit area
t	$=$	time (no subscript)	E	$=$	modulus of elasticity
ρ	$=$	density	G	$=$	shear modulus
t	$=$	thickness (subscripted)	d_1	$=$	$1 + (t_{e1} + t_{e0})/(2t_{v1})$
v	$=$	lateral (y-direction) displacement	D_T	$=$	$(E_{e0}t_{e0}^3)/[12(1 - \nu_{e1}^2)] + (E_{e1}t_{e1}^3)/[12(1 - \nu_{e1}^2)]$
u	$=$	longitudinal (x-direction) displacement	γ_{v1}	$=$	$(u_{e1} - u_{e0})/t_{v1} + d_1\partial v/\partial x$
				$=$	shear strain in the viscoelastic layer

The subscripts $e0$, $v1$, and $e1$ denote the 0th elastic layer, the 1st viscoelastic layer, and the 1st elastic layer, as shown in Figure 1. The notation is intended to facilitate generalization to multiple viscoelastic and elastic layers [13].

The boundary conditions result from the integration by parts in the application of Hamilton's principle. The conditions which must be satisfied, at $x = 0$ and $x = L$, are

$$
\begin{aligned}
\partial u_{e0}/\partial x &= 0 & \text{or} & & u_{e0} &= 0 \\
\partial u_{e1}/\partial x &= 0 & \text{or} & & u_{e1} &= 0 \\
G_{v1}d_1t_{v1}\left[(u_{e1} - u_{e0})/t_{v1} + d_1(\partial v/\partial x)\right] - D_T(\partial^3 v/\partial x^3) &= 0 & \text{or} & & v &= 0 \\
\partial^2 v/\partial x^2 &= 0 & \text{or} & & \partial v/\partial x &= 0
\end{aligned}
\tag{6}
$$

These equations of motion and boundary conditions compare with published results in the early literature [3] [5] [8], except Eqns 6 consider the longitudinal displacements of the elastic layers separately [13]. Note that in Eqns 5, u_{e0} and u_{e1} appear only as a difference. Considering boundary conditions on the composite beam, as has been done historically, is equivalent to considering boundary conditions on the difference between u_{e0} and u_{e1}. In that case, only six boundary condition equations result [8].

GENERAL SOLUTION OF THE EQUATIONS OF MOTION

Eqns 5 will be solved simultaneously, rather than combining them into a single sixth order equation, as is usually done [5] [8] [13]. Since the problem of interest is steady state oscillatory motion, displacements will be assumed to be periodic functions of time. It is customary [4] [3] [5] to assume a solution of the form

$$
v = e^{i\omega t}Ae^{px} \quad ; \quad u_{e0} = e^{i\omega t}Be^{px} \quad ; \quad u_{e1} = e^{i\omega t}Ce^{px}
\tag{7}
$$

Solving the equations requires finding values for p, A, B, C, and ω which satisfy Eqns 5 and 6. Note that Eqns 7 assume the solution is separable. Assuming a separable solution implies that mode shapes are expected which are not a function of time, as in the steady state. The orthogonality of the solutions [5] guarantees the uniqueness of the steady state solution, but a transient solution of this form may not be unique.

Substituting Eqns 7 into Eqns 5 and dividing through by $e^{i\omega t}$ and e^{px} results in a set of simultaneous algebraic equations. They can be written in matrix form as follows

$$
\begin{bmatrix}
[D_T p^4 - (\rho t)_T \omega^2 - G_{v1}t_{v1}d_1^2 p^2] & G_{v1}d_1p & -G_{v1}d_1p \\
G_{v1}d_1p & [E_{e0}t_{e0}p^2 - (G_{v1}/t_{v1})] & G_{v1}/t_{v1} \\
-G_{v1}d_1p & G_{v1}/t_{v1} & [E_{e1}t_{e1}p^2 - (G_{v1}/t_{v1})]
\end{bmatrix}
\times
\begin{Bmatrix} A \\ B \\ C \end{Bmatrix}
=
\begin{Bmatrix} 0 \\ 0 \\ 0 \end{Bmatrix}
\tag{8}
$$

Finding the solution to Eqns 8 is an eigenvalue problem. A nontrivial solution requires the determinant of the three by three matrix to = 0:

$$
p^8 - G_{v1}\left[\frac{t_{v1}d_1^2}{D_T} + \frac{1}{t_{v1}}\left(\frac{1}{E_{e1}t_{e1}} + \frac{1}{E_{e0}t_{e0}}\right)\right]p^6 - \frac{\omega^2(\rho t)_T}{D_T}p^4 + \frac{(\rho t)_T \omega^2 G_{v1}}{D_T t_{v1}}\left(\frac{1}{E_{e1}t_{e1}} + \frac{1}{E_{e0}t_{e0}}\right)p^2 = 0
\tag{9}
$$

Eqn 9 is the characteristic equation. It differs from the characteristic equation published in the literature [3] [8] in that it has a double zero root. The double zero root is the result of considering longitudinal displacements of the individual elastic layers separately.

The roots of Eqn 9 will be designated p_j. These are eigenvalues of the system. Mead and Markus [5] demonstrated that, for $p_j \neq 0$, the associated eigenfunctions are orthogonal. For $p = 0$, the eigenfunctions can be made orthogonal by choosing proper linear combinations of them [6, 142].

For $p_j \neq 0$, the eigenfunctions are determined by solving for B and C in terms of A in Eqns 8. It can be shown that [2]

$$
B_j = \left[\frac{(\rho t)_T \omega^2 - p_j^4 D_T}{t_{v1}d_1 E_{e0}t_{e0}p_j^3}\right]A_j = \beta_j A_j \quad \text{and} \quad C_j = \left[\beta_j + \frac{p_j^4 D_T - p_j^2 G_{v1}t_{v1}d_1^2 - (\rho t)_T \omega^2}{G_{v1}d_1 p_j}\right]A_j = \gamma_j A_j
\tag{10}
$$

These expressions relate the lateral displacement of the composite beam to the longitudinal displacements of the individual elastic layers.

For $p_j \neq 0$, there are now only six unspecified constants, $A_1 \ldots A_6$. Since there are eight boundary conditions, two more constants are expected. The two additional constants will result from the double zero root in the characteristic equation. For $p_j = 0$, it can be shown that [2]

$$
\begin{array}{ll}
\underline{\text{for } \omega \neq 0} & \underline{\text{for } \omega = 0} \\
B_8 = C_8 & B_8 = C_8 \\
B_7 = C_7 & B_7 - C_7 = d_1 t_{v1} A_8 \\
A_7 = A_8 = 0 & A_7 \text{ and } A_8 \quad \text{unspecified}
\end{array}
$$

The two unspecified constants, A_7 and A_8, correspond to rigid body lateral translation and rotation. If $\omega = 0$ satisfies the boundary conditions, that case must be considered separately. It will not be treated here.

The general solution to Eqns 5 is then

$$v = e^{i\omega t} \left[\sum_{j=1}^{6} (A_j e^{p_j x}) \right] \quad ; \quad u_{e0} = e^{i\omega t} \left[\sum_{j=1}^{6} (\beta_j A_j e^{p_j x}) + B_7 + B_8 x \right] \quad ; \quad u_{e1} = e^{i\omega t} \left[\sum_{j=1}^{6} (\gamma_j A_j e^{p_j x}) + B_7 + B_8 x \right]$$
$$(11)$$

The solution is now determined to within eight arbitrary constants, $A_1 \dots A_6$, B_7 and B_8, corresponding to the eight boundary conditions which need to be satisfied. It now remains to find the complex frequency of vibration, ω, which satisfies a particular set of boundary conditions. Specific boundary conditions are considered next.

BOUNDARY CONDITION MATRICES

Substituting Eqns 11 into Eqns 6 results in a set of eight simultaneous equations in the eight constants $A_1 \dots A_6$, B_7 and B_8, and frequency. Nontrivial solutions will exist only when the determinant of the boundary condition matrix is zero. Solving the equations requires finding the complex frequency which drives the determinant to zero. In contrast to the boundary conditions on the composite beam, where the boundary condition matrix is six by six [8], for mixed boundary conditions, in general the matrix will be eight by eight. When the boundary conditions are the same for each elastic layer, the matrix reduces to six by six. In this section, boundary conditions are presented for several important cases. Numerical results will be presented in the next section.

Both Base and Constraining Layers Fixed-Free

The case where both the base and constraining layers fixed at $x = 0$ and free at $x = L$ is of interest because it duplicates approximate solutions which are available in the literature [11, 5-24]. It will be used for comparison purposes. The boundary conditions are

	at $x = 0$			at $x = L$		
$\partial v/\partial x$	=	0		$\partial u_{e0}/\partial x$	=	0
v	=	0		$\partial u_{e1}/\partial x$	=	0
u_{e0}	=	0		$\partial^2 v/\partial x^2$	=	0
u_{e1}	=	0		$G_{v1} d_1 t_{v1} \left[\frac{u_{e1} - u_{e0}}{t_{v1}} + d_1 \frac{\partial v}{\partial x} \right] - D_T \frac{\partial^3 v}{\partial x^3}$	=	0

$$(12)$$

Substituting Eqns 11 into Eqns 12 produces a set of eight simultaneous equations in the eight constants, $A_1, \dots, A_6$, B_7 and B_8. In this case, because both elastic layers have the same boundary condition, the constants B_7 and B_8 can be eliminated from the system, reducing the number of simultaneous equations to be satisfied to six.

Base Layer Fixed-Free; Constraining Layer Free-Free

This is an example of mixed boundary conditions. Comparing this case to the previous one will illustrate the effect of considering mixed boundary conditions on the loss factor. The boundary conditions are

	at $x = 0$			at $x = L$		
$\partial v/\partial x$	=	0		$\partial u_{e0}/\partial x$	=	0
v	=	0		$\partial u_{e1}/\partial x$	=	0
u_{e0}	=	0		$\partial^2 v/\partial x^2$	=	0
$\partial u_{e1}/\partial x$	=	0		$G_{v1} d_1 t_{v1} \left[\frac{u_{e1} - u_{e0}}{t_{v1}} + d_1 \frac{\partial v}{\partial x} \right] - D_T \frac{\partial^3 v}{\partial x^3}$	=	0

$$(13)$$

Since the boundary conditions on the elastic layers are different at $x = 0$, the constants B_7 and B_8 cannot be eliminated. In this case, the boundary condition matrix will be eight by eight, and all eight constants, $A_1 \dots A_6$, B_7, and B_8 must be found.

Base Layer Simply Supported; Constraining Layer Free-Free

This boundary condition was selected for comparison with known solutions. It is similar to the simply supported composite boundary condition which was the first case solved in the literature [5]. The boundary conditions are; at both $x = 0$ and $x = L$,

v	=	0		$\partial^2 v/\partial x^2$	=	0
u_{e0}	=	0		$\partial u_{e1}/\partial x$	=	0

$$(14)$$

In this case, B_7 can be eliminated from the system, and the boundary condition matrix will be seven by seven.

Table 1: Test Case Data [11, 5-26] [12, 263-270]
Base Layer, aluminum; Adhesive Layer, SoundCoat
DIAD no. 606; Constraining Layer, aluminum

Variable	Value	Units	Variable	Value	Units	Variable	Value	Units
L	0.254	meter	E_{e0}	$6.8900e10$	Pascal	B(1)	$0.2e6$	Pascal
t_{e0}	5.0800e-3	meter	ρ_{e0}	$2.7700e\ 3$	(kg)/meter^3	B(2)	$1200.0e6$	Pascal
ν_{e0}	0.3300		t_{v1}	2.5400e-4	meter	B(3)	$0.3e7$	Hz
ρ_{v1}	$9.6900e\ 2$	(kg)/meter^3	E_{e1}	$6.8900e10$	Pascal	B(4)	0.55	
t_{e1}	2.5400e-4	meter	ρ_{e1}	1.0	(kg)/meter^3	B(5)	1.5	
ν_{e1}	0.3300					B(6)	0.1	

Base Layer Simply Supported; Constraining Layer Attached-Free

This is a variation on the simply supported boundary condition shown in Eqns 14, and will be used to illustrate the effect of permitting mixed boundary conditions. The constraining layer is 'rigidly connected' to the base layer at $x = 0$, such that all layers rotate together at that end; and is free at $x = L$. The constraining layer will have a non-zero enforced displacement at $x = 0$.

At first glance this appears to be a non-homogeneous boundary condition. All the boundary conditions considered so far have been homogeneous. An arbitrary enforced nonzero displacement is a non-homogeneous boundary condition. However, the enforced displacement in this case is not arbitrary, but is related to the slope of the beam. For small rotations, at $x = 0$

$$u_{e1} \approx -\left(\frac{t_{e0} + t_{e1}}{2} + t_{v1}\right) \frac{\partial v}{\partial x} = -t_{v1} d_1 \frac{\partial v}{\partial x} \tag{15}$$

Since $\partial v/\partial x$ contains only terms in $A_1 \ldots A_6$, this displacement can be included in the left-hand side of the boundary condition equation, and the boundary condition is seen to be homogeneous. The boundary conditions are

$$
\begin{array}{ccc}
\underline{\text{at}\quad x = 0} & & \underline{\text{at}\quad x = L} \\
v = 0 & & v = 0 \\
\partial^2 v/\partial x^2 = 0 & & \partial^2 v/\partial x^2 = 0 \\
u_{e0} = 0 & & u_{e0} = 0 \\
u_{e1} = -t_{v1} d_1 (\partial v/\partial x) & & \partial u_{e1}/\partial x = 0
\end{array}
\tag{16}
$$

Neither B_7 nor B_8 can be eliminated, and the boundary condition matrix will be eight by eight.

NUMERICAL RESULTS

Numerical results of sample calculations are presented for the boundary conditions in the previous section. Several test cases are presented. The first demonstrates that the formulation which has been presented correctly predicts the natural frequencies of a cantilever beam. The next case predicts the natural frequencies of a simply supported beam, to compare the predictions with those based on sixth order theory [5]. Finally, for both the cantilever and simply supported boundary conditions, a comparison is made between cases in which the boundary conditions are the same for each layer, and those in which the boundary conditions differ between layers. The loss factor is calculated for these cases, to illustrate that the different predicted results can effect damping design.

A note must be made about coding the equations for solution on a computer. The boundary condition matrices tend to be very ill conditioned [1, 175]. Care must be taken to maximize accuracy. The numerical results presented here were calculated using double precision complex arithmetic. Also, to improve the accuracy of the calculation of the determinant, total pivoting was used in the gaussian elimination algorithm, rather than the more common scaled partial pivoting [1, 159].

In order to have a test case against which the results could be compared, the physical parameters were taken from a sample calculation in the damping design guide listed as Ref [11, 5-26]. The material properties and curve fit parameters for use in Eqn 2 were taken from the third volume of the design guide [12, 263-270]. Except where noted, the shear modulus of the viscoelastic layer was permitted to vary with frequency according to Eqn 2, but temperature was held constant. Except where noted, the data listed in Table 1 was used for the test cases.

Comparing Cantilever Boundary Conditions With Simple Theory

If the mass and stiffness of the top two layers of the beam are made small, the natural frequencies predicted by Eqns 11 and 12 should approach the frequencies of a homogeneous cantilever beam. The frequencies of a

Table 2: Data Used for Cantilever Boundary Condition Calculations

Data Used In Eqns 11 and 12			Data Used In Eqn 17		
Variable	Value	Units	Variable	Value	Units
E_{e1}	1.00e 4 + 0.0i	Pascal	E	6.89e10	Pascal
G_{v1}	1.00 + 1.0i	Pascal	I	1.09e-8	meter^4
ρ_{v1}	1.00	(kg)/meter^3	L	0.254	meter
ρ_{e1}	1.0	(kg)/meter^3	m/L	14.0716	(kg)/meter

Table 3: Results of Cantilever Boundary Condition Calculations
Frequencies are in radians/second

Mode	Eqn 17 Predicted	Eqns 11 and 12 Real	Imag	error in Real freq	Mode	Eqn 17 Predicted	Eqns 11 and 12 Real	Imag	error in Real freq
1	398.59	422.23	0.0000	5.9 %	4	13705.93	14519.03	0.0000	5.9 %
2	2497.92	2646.10	0.0000	5.9 %	5	22656.89	24000.99	0.0001	5.9 %
3	6994.25	7409.17	0.0000	5.9 %	6	33854.47	35853.33	0.0001	5.9 %

homogeneous cantilever beam are the roots of the transcendental equation [7, 224-227]

$$\cos \lambda L \cosh \lambda L = -1 \qquad where \qquad \lambda^4 = \frac{\omega^2 m}{EI} \qquad (17)$$

Data listed in Table 2 was used to predict natural frequencies using both formulations. The mass and stiffnesses of the upper two layers were made as small as possible without causing numerical problems. Data not listed in Table 2 was unchanged from that shown in Table 1. Note that, in this case, the shear modulus, G_{v1}, was held constant for all frequencies, rather than letting it vary according to Eqn 2. Table 3 lists the resulting natural frequencies for the first six modes as predicted by Eqn 17, and the complex frequencies predicted by Eqns 11 and 12.

Note in Table 3 that the imaginary frequencies predicted by Eqns 11 and 12 are zero or very small, suggesting small damping, as required. All real frequencies are 5.9% high. This could be the result of letting the parameters of the top layers be small, but not zero.

Comparing Simply Supported Boundary Conditions With Simple Theory

Historically, the first boundary condition solved for the layered beam was the simply supported case [5]. The solution is of the form

$$v = D \sin \left(\frac{n \pi x}{L} \right) \qquad and \qquad u_{e1} = F \cos \left(\frac{n \pi x}{L} \right) \qquad (18)$$

where

D	=	a constant	F	=	a constant
n	=	the mode number	π	=	3.14159 ...
x	=	distance along the length of the beam	L	=	the length of the beam

The expression for v in Eqn 18 can be found in the literature [5]. The expression for u_{e1} can be justified intuitively with a simple argument. When the composite beam is deflected upward in the center, the longitudinal displacement of the top layer should be zero in the center. It should also be some negative value at $x = 0$ and the same positive value at $x = L$. It is not immediately apparent what form the longitudinal deflection of the base layer (u_{e0}) would take, since it is restrained at both ends. It now remains to be demonstrated that the formulation presented in this paper degenerates to solutions of the form in Eqn 18 for the case in which the base layer is simply supported and the constraining layer is free.

It can be shown that, in order for the solution to Eqns 11 and 14 to degenerate into the form of Eqns 18, the following conditions must be met [2]. First, exactly one pair of roots to Eqn 9 must satisfy

$$p_R = 0 \qquad and \qquad p_I = \pm \frac{n \pi}{L} \qquad (19)$$

The subscript R denotes the real part and the subscript I denotes the imaginary part of a quantity. The coefficients $A_1 \ldots A_6$ from Eqn 11 and $\gamma_1 \ldots \gamma_6$ from Eqn 10 must satisfy the following conditions:

$$
\begin{aligned}
A_{k,R} + A_{l,R} &= 0 & (\gamma_{k,R} A_{k,R} - \gamma_{k,I} A_{k,I}) + (\gamma_{l,R} A_{l,R} - \gamma_{l,I} A_{l,I}) &\neq 0 \\
A_{k,I} - A_{l,I} &\neq 0 & (\gamma_{k,R} A_{k,I} - \gamma_{k,I} A_{k,R}) - (\gamma_{l,R} A_{l,I} - \gamma_{l,I} A_{l,R}) &= 0
\end{aligned}
\qquad (20)
$$

Table 4: Conditions on Constants A and γ, Simply Supported Boundary Condition

Mode 1:
$$p_1 = 21.15 + 8.49i; \quad p_3 = 0.00 - 12.38i; \quad p_5 = 12.18 + .23i$$
$$p_2 = -21.15 - 8.49i; \quad p_4 = 0.00 + 12.38i; \quad p_6 = -12.18 - .23i$$

$$A_{1,R} + A_{2,R} = -8.18E - 04; \quad (\gamma_{1,R}A_{1,R} - \gamma_{1,I}A_{1,I}) + (\gamma_{2,R}A_{2,R} - \gamma_{2,I}A_{2,I}) = +4.93E - 04$$
$$A_{1,I} - A_{2,I} = -1.24E - 03; \quad (\gamma_{1,R}A_{1,I} - \gamma_{1,I}A_{1,R}) - (\gamma_{2,R}A_{2,I} - \gamma_{2,I}A_{2,R}) = +5.57E - 04$$
$$A_{3,R} + A_{4,R} = -2.07E - 03; \quad (\gamma_{3,R}A_{3,R} - \gamma_{3,I}A_{3,I}) + (\gamma_{4,R}A_{4,R} - \gamma_{4,I}A_{4,I}) = -3.78E - 02$$
$$A_{3,I} - A_{4,I} = +1.32 \quad ; \quad (\gamma_{3,R}A_{3,I} - \gamma_{3,I}A_{3,R}) - (\gamma_{4,R}A_{4,I} - \gamma_{4,I}A_{4,R}) = +5.52E - 05$$
$$A_{5,R} + A_{6,R} = +2.89E - 03; \quad (\gamma_{5,R}A_{5,R} - \gamma_{5,I}A_{5,I}) + (\gamma_{6,R}A_{6,R} - \gamma_{6,I}A_{6,I}) = +9.67E - 05$$
$$A_{5,I} - A_{6,I} = +1.14E - 03; \quad (\gamma_{5,R}A_{5,I} - \gamma_{5,I}A_{5,R}) - (\gamma_{6,R}A_{6,I} - \gamma_{6,I}A_{6,R}) = +1.89E - 05$$

Mode 2:
$$p_1 = 29.95 + 12.00i; \quad p_3 = 24.19 + 1.00i; \quad p_5 = 0.00 - 24.74i$$
$$p_2 = -29.95 - 12.00i; \quad p_4 = -24.19 - 1.00i; \quad p_6 = 0.00 + 24.74i$$

$$A_{1,R} + A_{2,R} = -8.62E - 12; \quad (\gamma_{1,R}A_{1,R} - \gamma_{1,I}A_{1,I}) + (\gamma_{2,R}A_{2,R} - \gamma_{2,I}A_{2,I}) = +1.16E - 11$$
$$A_{1,I} - A_{2,I} = -2.14E - 11; \quad (\gamma_{1,R}A_{1,I} - \gamma_{1,I}A_{1,R}) - (\gamma_{2,R}A_{2,I} - \gamma_{2,I}A_{2,R}) = +1.20E - 11$$
$$A_{3,R} + A_{4,R} = -1.18E - 10; \quad (\gamma_{3,R}A_{3,R} - \gamma_{3,I}A_{3,I}) + (\gamma_{4,R}A_{4,R} - \gamma_{4,I}A_{4,I}) = -2.07E - 11$$
$$A_{3,I} - A_{4,I} = +1.85E - 10; \quad (\gamma_{3,R}A_{3,I} - \gamma_{3,I}A_{3,R}) - (\gamma_{4,R}A_{4,I} - \gamma_{4,I}A_{4,R}) = +2.19E - 11$$
$$A_{5,R} + A_{6,R} = -1.34E - 10; \quad (\gamma_{5,R}A_{5,R} - \gamma_{5,I}A_{5,I}) + (\gamma_{6,R}A_{6,R} - \gamma_{6,I}A_{6,I}) = +1.88E - 02$$
$$A_{5,I} - A_{6,I} = -0.83 \quad ; \quad (\gamma_{5,R}A_{5,I} - \gamma_{5,I}A_{5,R}) - (\gamma_{6,R}A_{6,I} - \gamma_{6,I}A_{6,R}) = +8.08E - 12$$

for constants A and γ corresponding the root pair $p_{k,l}$ which satisfy Eqn 19, and

$$A_{k,R} + A_{l,R} = 0 \quad (\gamma_{k,R}A_{k,R} - \gamma_{k,I}A_{k,I}) + (\gamma_{l,R}A_{l,R} - \gamma_{l,I}A_{l,I}) = 0$$
$$A_{k,I} - A_{l,I} = 0 \quad (\gamma_{k,R}A_{k,I} - \gamma_{k,I}A_{k,R}) - (\gamma_{l,R}A_{l,I} - \gamma_{l,I}A_{l,R}) = 0 \tag{21}$$

for constants A and γ corresponding root pairs $p_{k,l}$ which do not satisfy Eqn 19.

The results of calculations for the data in Table 1 are shown in Table 4. The calculated results demonstrate that, when the base layer is simply supported, the solution to Eqns 11 and 14 degenerate into the form of Eqns 18, as required.

Demonstrating the Effect of Considering Mixed Boundary Conditions

Solving the equations of motion of a layered beam sheds light on the prediction of the damping of a structure. Tables 5 and 6 illustrate that considering mixed boundary conditions in the solution of the equations of motion does effect the calculation of the beam equivalent damping. Beam equivalent damping was calculated according to Eqn 1, after finding the complex frequency, ω, which satisfied the boundary conditions. The shear modulus of the viscoelastic layer, G_{v1}, was permitted to vary with frequency according to Eqn 2.

Table 5 compares the damping predicted by Eqns 12 and 13 for the two cantilever boundary conditions. Also shown for comparison, is the calculation of the damping according to approximate formulae in a damping design guide [11, 5-29], for a three layer cantilever beam. The damping differs for the different boundary conditions. The damping predicted by Eqns 12 and 13 also differ from the predictions of the design guide, sometimes markedly. It is also important to note that each case predicts a different frequency and mode shape at which maximum damping occurs. That has important implications for design optimization.

Table 6 makes similar comparisons for the simply supported boundary conditions in Eqns 14 and 16. Again, the damping differs between boundary conditions, as does the frequency and mode at which maximum damping occurs.

CONCLUSION

This paper has presented solutions to the equations of motion of a layered beam in which the elastic layers are permitted to have different boundary conditions. It was shown that, for boundary conditions which approximate cases for which simple theoretical solutions are available, the formulation presented in this paper compares well with those theoretical solutions. It was also shown that considering mixed boundary conditions affects the prediction of beam equivalent damping, and the frequency and mode at which maximum damping occurs.

Table 5: Comparison of Complex Frequencies for Cantilever Boundary Conditions

	Const. Layer Fixed-Free			Const. Layer Free-Free			Design Guide		
Mode	Real	Imag	η_b	Real	Imag	η_b	Real	Imag	η_b
1	437.14	2.78	0.0127	421.02	4.17	0.0198	410.48	4.17	0.0203
2	2697.53	36.32	0.0269	2678.24	25.19	0.0188	2511.78	40.46	0.0322
3	7495.15	114.71	0.0306	7474.49	96.74	0.0259	6946.62	105.29	0.0303
4	14588.14	234.25	0.0321	14570.69	212.39	0.0292	13525.28	180.31	0.0267
5	23990.36	381.06	0.0318	23976.29	358.02	0.0299	22271.59	260.66	0.0234
6	35692.67	547.31	0.0307	35681.46	524.36	0.0294	33184.20	344.23	0.0207

Table 6: Comparison of Complex Frequencies for Simply Supported Boundary Conditions

	Const. Layer Rigid-Free			Const. Layer Free-Free		
Mode	Real	Imag	η_b	Real	Imag	η_b
1	1199.22	14.07	0.0235	1221.86	14.46	0.0237
2	4780.24	66.14	0.0277	4820.67	75.75	0.0314
3	10704.32	161.38	0.0302	10753.82	182.75	0.0340
4	18942.83	288.94	0.0305	18996.25	319.32	0.0336
5	29488.11	440.83	0.0299	29542.05	478.50	0.0324
6	42331.97	608.42	0.0287	42385.70	651.11	0.0307

References

[1] Samuel D. Conte and Carl de Boor. *Elementary Numerical Analysis, An Algoritmic Approach*. McGraw Hill, 1980.

[2] Eugere T. Cottle. Damping of layered beams with mixed boundary conditions. Master's thesis, Air Force Institute of Technology, Wright Patterson AFB, OH, 1990. DTIC number AD-A230665.

[3] R. A. DiTaranto. Theory of vibratory bending for elastic and viscoelastic layered finite-length beams. *Journal of Applied Mechanics*, pages 881–886, December 1965.

[4] Edward. M. Kerwin, Jr. Damping of flexural waves by a constrained visco-elastic layer. *Journal of the Acoustical Society of America*, 31:952–962, July 1959.

[5] D. J. Mead and S. Marcus. The forced vibration of a three-layer, damped sandwich beam with arbitrary boundary conditions. *Journal of Sound and Vibration*, 10:163–175, 1969.

[6] Leonard Meirovitch. *Methods of Analytical Dynamics*. McGraw Hill, 1967.

[7] Leonard Meirovitch. *Elements of Vibration Analysis*. McGraw Hill, 1986.

[8] D. K. Rao. Frequency and loss factors of sandwich beams under various boundary conditions. *Journal of Mechanical Engineering Science*, 20(5):271–282, 1978.

[9] Adel S. Saada. *Elasticity Theory and Applications*. Robert E. Krieger Publishing Company, Inc., 1974.

[10] J. Soovere and M. L. Drake. Aerospace structures technology damping design guide, volume i - technology review. Technical Report AFWAL-TR-84-3089, AFSC/AFWAL, 1985.

[11] J. Soovere and M. L. Drake. Aerospace structures technology damping design guide, volume ii - design guide. Technical Report AFWAL-TR-84-3089, AFSC/AFWAL, 1985.

[12] J. Soovere and M. L. Drake. Aerospace structures technology damping design guide, volume iii - damping material data. Technical Report AFWAL-TR-84-3089, AFSC/AFWAL, 1985.

[13] Peter J. Torvik. Damping of layered materials. In *30th AIAA/ASME/ASME/ASCE/AHS/ASC Structures, Structural Dynamics and Materials Conference*. AIAA, April 1989. AIAA 89-1422.
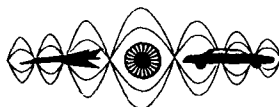
SECOND INTERNATIONAL CONGRESS ON
RECENT DEVELOPMENTS IN AIR- AND
STRUCTURE-BORNE SOUND AND VIBRATION
MARCH 4-6 1992 AUBURN UNIVERSITY USA

PASSIVE DAMPING APPLIED TO AIRCRAFT WING SKIN

Vincent J. Levraea, Jr., Captain USAF
Lynn C. Rogers, PhD, Consultant
Wright-Patterson AFB, OH 45433
U.S.A.

ABSTRACT

The purpose of this investigation was to develop candidate add-on damping treatments for the F-15 upper-outer wing skin. The upper-outer wing skin has experienced high cycle fatigue cracks caused by separated flow on the upper wing surface. The separated flow results during high load factor maneuvers and in turn, induces large vibratory loads on the upper wing skin and associated substructure. Damage accumulates due to the resonant vibration of local skin/stiffener modes. Two damping treatments resulted from the investigation. One was an external constrained-layer treatment and the other was an internal "stand-off" treatment. Estimates of the life extension factors for the external and internal damping treatments were 5 and 34 respectively.

INTRODUCTION

Modern fighter aircraft are expected to deliver high levels of performance resulting in large structural loads and often consequent premature failure of aircraft structural elements. Inherent with high performance are high vibration levels. One cause of large vibratory loads in fighter aircraft is separated flow. Within the separated flow environment it is often impossible to estimate the precise dynamic flow characteristics or loading conditions that aircraft components may experience during flight. Aircraft skins, in particular outboard wing skins, are relatively light weight structures which are extremely susceptible to vibration response induced by separated flow. These large vibratory loads can result in high cycle fatigue and a substantial reduction in the useful service life of the component.

The F-15 upper-outer wing skin (UOWS) panel has experienced cracks resulting from high cycle fatigue. The F-15 aircraft, shown in Figure 1, has sufficient thrust to perform sustained, high load maneuvers causing separated flow over the wing panel. This separated flow region contains high-level broad-band random pressure fluctuations and induces large vibratory response in the UOWS panel and associated wing substructure. The resulting elevated stresses over time cause high cycle fatigue cracks to form in the wing skin. Initially, the cracks were considered to occur only over a small portion of the skin closest to the wing tip. Later findings show that the entire UOWS is prone to cracking.

The UOWS was originally designed for a service life of 8000 hours. Unfortunately, the

initial service life realized was only 250 hours. Several modifications were incorporated by the contractor in the early 1980s to improve the fatigue life of the skin, including fortifying critical locations on the wing skin. These modifications only increased the life of the skin to approximately 1250 hours. The need still remained to increase the service life to the original design value of 8000 hours.

BACKGROUND

The F-15 UOWS is machined from a single block of 2024 aluminum and consist of the skin, integrally machined "T" stiffeners, and chemically milled pockets between the stiffeners. The thickness varies from location to location on the panel, but assuming a constant thickness of 2.032 mm (0.080 in) is sufficient for understanding the problem. Figure 2 shows the major substructure for the left wing. The UOWS extends from rib 155 to rib 224, and from the front spar to the rear spar. There are intermediate ribs at locations 172, 188, and 206. At rib 188, the front, main, and rear spars are at 10%, 45%, and 65% chord, respectively. Collectively, these members constitute the outer wing torque box. The wing skin measures approximately 1.524 m (5 ft) wide by 2.134 m (7 ft) long measuring along rib 188 and the main spar, respectively. Inboard of rib 155 the wing is "wet," that is, the volume is used for fuel storage. The outer torque box is "dry." Blind threaded, flush fasteners are used to attach the skin to the rib and spar substructure. A scrapped right-hand UOWS is shown in Figure 3. Visible in Figure 3 are the integral stiffeners and their runouts, spar and rib fastener holes, and various panel access holes. Stiffeners are numbered consecutively starting at the UOWS leading edge. The stiffeners are not clipped to the ribs but are allowed to move freely within the rib notch. Damage accumulates due to resonant vibration of local skin/stiffener modes. The cracks develop in the rib fastener holes adjacent to the stiffeners. Predominantly, the cracks initiate either perpendicular to the ribs or parallel to the stiffeners. Figure 4 shows a close-up of the cracks in the scrapped UOWS. Based on the crack patterns and the unclipped stiffener design, it was concluded that the skin cracks were most likely induced by stiffener rotation. Figure 5 gives a convenient shorthand designation for the spar-rib bays which will be used throughout the remainder of this report to aid the reader in locating specific portions of the UOWS.

FLIGHT TESTS

Flight test data were gathered to obtain UOWS response data during high load factor maneuvers and to assess the effectiveness of the damping systems. These test were conducted by McDonnell Aircraft Corporation, St. Louis MO. (MCAIR). The flight data collected for this investigation included the baseline response of the F-15 UOWS as well as the UOWS response with various candidate damping treatment configurations. Strain gages placed on internal and external surfaces of the panel were used to record the bulk of the response data. In some cases internal accelerometers were also used. Historically, many cracks have been discovered along stiffener #4. Based on past analyses, it was observed that the response data obtained at the intersection of stiffener #4 and rib 188 could be used to represent the response over the remaining panel. Thus, the analysis performed centered on the UOWS response measurements taken at this location.

The power spectral density (PSD), shown in Figure 6, was typical of the UOWS response at the intersection of stiffener #4 and rib 188 for an undamped panel. The flight conditions for this PSD were: 11° AOA, 5.9 g load factor, 0.80 Mach, 6096 m (20,000 ft) altitude, and 20.30 kPa (2.94 psi) dynamic pressure. Figure 6 shows high strain levels occurred in the 300 Hz to 400 Hz band. It was obvious that this peak results in the most significant contribution to cumulative high

cycle fatigue crack damage.

Several damping treatment configurations were flight tested. Unfortunately detailed data is not yet available and will not be available before printing of this report; thus no specific flight test results can be presented. The preliminary flight test results received from MCAIR are very promising and appear to significantly improve the UOWS fatigue life.

MODAL TESTS

To ascertain the cause of the problem, modal tests were conducted on a full-scale F-15A wing in the laboratory. Modal tests were performed on the baseline UOWS and the UOWS with various damping treatments applied. These tests were conducted using laser video holography and more traditional multi-accelerometer surveys. Tests were performed which concentrated separately on the individual responses of the skin and stiffeners. As a result of the modal testing, numerous closely spaced skin/stiffener modes were observed in the 300 Hz to 400 Hz frequency band which match the frequency band of the dominate peak observed in Figure 6. Mode shapes and other modal parameters were obtained from the transfer functions gathered during the modal surveys on the skin and stiffeners. A strong correlation was found between the resonant frequencies of the skin and the resonant frequencies of the stiffeners. This suggested that a damping treatment applied to both the skin and stiffeners may attenuate the vibration enough to yield a substantial increase in the service life of the UOWS.

DAMPING TREATMENTS

This study investigated the performance of 13 different candidate add-on damping treatment configurations under laboratory conditions. For brevity, only the two new damping treatments which were recommended for F-15 fleet retrofit are discussed in this paper. Past damping experience suggested that a constrained-layer damping treatment would offer the most viable, cost effective solution. A constrained-layer damping system consists of a layer of viscoelastic material (VEM) which is constrained by a metal layer. Often this type of damping system will be constructed of multiple constrained layers to achieve the desired level of damping. Whenever the structure undergoes bending, the metal layer will constrain the viscoelastic material, resulting in shear deformation of the VEM. Energy is dissipated due to this shear deformation.

An important part of designing a damping treatment is determining the environmental condition to which the treatment will be exposed and ensuring that the selected treatment will withstand and perform properly under these conditions. Critical environmental considerations include the operational temperature range for which damping is desired, the effects of the damping treatment on corrosion of the structure, and the effects of thermal aging on the performance of the damping treatment. Based on the flight conditions at which most of the damage is expected to occur, a temperature range of 10 °C (50 °F) to 23.9 °C (75 °F) was selected as the design temperature range of the damping treatments. Laboratory corrosion tests showed no degradation in corrosion resistance caused by the application of the recommended damping treatments. The corrosion test panels were exposed to a standard 30-day humidity corrosion environment in the laboratory consisting of 48.9 °C (120 °F), 98% relative humidity, and salt spray. The addition of the damping treatments had no effect on corrosion, primarily because the UOWS paint was not disturbed during installation. Extensive service experience with similar damping treatments has not revealed any corrosion problems. Satisfactory thermal aging characteristics were demonstrated in the laboratory for all materials used in the new damping treatments. The temperature exposure of 8 hours at 171.1 °C (340 °F) plus 48 hours at 132.2 °C (270 °F) was intended to be a conservative design condition for the 8000 hour life; however, these

exposure levels are believed to be much more severe than necessary. Thousands of hours of F-111 service data establish that the stagnation temperature exceeds 51.7 °C (125 °F) less than 1% of the time. Laboratory tests confirmed that thermal aging caused the damping material to stiffen slightly, which tended to increase damping treatment effectiveness. An additional issue of practicality is the ability to inspect the UOWS for structural integrity with the damping treatment installed. The damping treatment configurations used, in no instance covered up fasteners or locations where the cracks initiate. Therefore, the damping treatments will not hinder inspection of the UOWS either visually or radiographically and the treatments also will not impact removal or installation of the UOWS or other maintenance functions.

As previously mentioned, two new damping treatments were developed as a result of this investigation and recommended for F-15 fleet retrofit. The treatments consisted of an externally applied, field installable system and an internally applied, depot installable system. Figure 7 shows the recommended external multiple (4) constrained layer configuration. Two different constrained layers were used in the external treatment design. One consisted of a 0.051 mm (0.002 in) layer of ISD-112 VEM constrained by a 0.127 mm (0.005 in) layer of aluminum and the other was made of a 0.051 mm (0.002 in) layer of ISD-113 VEM also constrained by a 0.127 mm (0.005 in) layer of aluminum. Two each of these different constrained layers were used to build up the total of four constrained layers in the external treatment design. Two VEMs were used to broadened the effective temperature range of the damping treatment. The six outer most spar-rib bays were covered (R1, R2, R3, L1, L2, and L3) by the external treatment. Figure 8 is a photo of the external treatment installed on an F-15 wing.

The recommended internal treatment design is summarized in Figure 9. Starting at the wing skin, there was a 0.102 mm (0.004 in) layer of pressure sensitive adhesive (PSA) which performed as a VEM. Next there was a 2.032 mm (0.080 in) stand-off layer of syntactic foam configured to maintain high shear stiffness and low flexural stiffness. This was achieved by cutting a checker board pattern into the syntactic foam. Finally, three constrained layers of damping material were placed on top of the stand-off layer. The first constrained layer (from the bottom) consisted of 0.102 mm (0.004 in) of VEM constrained by 0.127 mm (0.005 in) of aluminum. The other two constrained layers each consisted of 0.051 mm (0.002 in) of VEM constrained by 0.127 mm (0.005 in) of aluminum. For all layers the Hueston Industries F-440 VEM was used. The internal damping treatment was applied in the chemically-milled pockets between the integral stiffeners for all 8 spar-rib bays shown in Figure 5. Additionally, there were viscoelastic links (VELs) placed between the caps of the integral stiffeners and the notches in the ribs. The VELs were located in all rib notch locations. The VEL material was slightly tacky at room temperature. A VEL thickness of 12.7 mm (0.50 in) was used to provide an interference fit. The purpose of the VEL was to provide a link (having both stiffness and damping) from the stiffener cap to ground (rib notch), thereby reducing stiffener rotation. Figure 10 shows the stand-off damping treatment applied to the internal surface of the wing skin. Figure 11 shows the VELs located in the rib notches.

RESULTS

A comparison between the frequency response of the baseline UOWS and the UOWS with the external damping treatment installed is presented in Figure 12. The acceleration Frequency Response Functions (FRFs) were integrated twice to obtain the compliance (displacement) FRFs; the compliance FRFs were assumed to be proportional to strain. Figure 13 makes a similar comparison for the internal damping configuration. Notice the dramatic, beneficial reduction in response due to the internal treatment. The comparisons in this report were made on the basis of RMS stress rather than by considering peak values. Figure 14 presents the equation used to

calculate the life extension factor. The ratio of the damped to the baseline response was raised to the proper exponent to give the life extension factor (ie, ratio of lifetimes). The RMS of the compliance FRF between 300 Hz and 400 Hz was the basis of the calculation.

Calculations made in this manner reveal that the UOWS with the external damping treatment will last 5 times as long as the baseline UOWS (bare UOWS); thus the life extension factor is 5. The life of the baseline UOWS is approximately 1250 hours; therefore, the projected life with the external damping treatment is 6250 hours. Obviously, this is only an estimate; however, it does provide a measure of performance for the damping treatments. A similar estimate for the internal damping treatment yielded a life extension factor of 34. The internal treatment is considered the primary configuration for resolving the UOWS high cycle fatigue cracking. This is because of the dramatic reduction in response achieved with it installed. Its large life extension factor should offset a variety of uncertainties not accounted for by this investigation, such as precise temperature at which damage accumulates, the fact that RMS strains were used instead of peak values, and potential changes in future operational usage.

CONCLUSIONS

Tests were conducted on 13 candidate add-on damping treatments for the F-15 UOWS. Of those tested, two damping treatments were recommended for F-15 fleet retrofit. One treatment was an externally applied constrained-layer treatment and the other was an internally applied stand-off treatment with viscoelastic links in the rib notches. The external and internal treatments resulted in life extension factors of 5 and 34, respectively. The damping treatments were thermally aged and corrosion tested; no adverse effects were noted. The recommended damping treatments are fully qualified for F-15 fleet retrofit and represent a viable, cost effective solution which will substantially improve the F-15 UOWS service life.

REFERENCES

1. Levraea, V., Rogers, L., Parin, M., and Pacia A., "Add-on Damping Treatment for Life Extension of the F-15 Upper-Outer Wing Skin", WL-TM-91-307-FIBG, WPAFB, OH, 1991.

2. Parin, M., Rogers L., Moon Y., and Falugi M. "Practical Stand Off Damping Treatment for Sheet Metal," Proceedings of Damping '89, Volume II, Paper No. IBA, February 1989.

3. Nashif, A., Jones, D., and Henderson, J., Vibration Damping, John Wiley & Sons, 1985.

4. Miles, R. "The Prediction of the Damping Effectiveness of Multiple Constrained Layer Damping Treatments" Presented at Acoustical Society of America, Massachusetts Institute of Technology June 11-15, 1979.
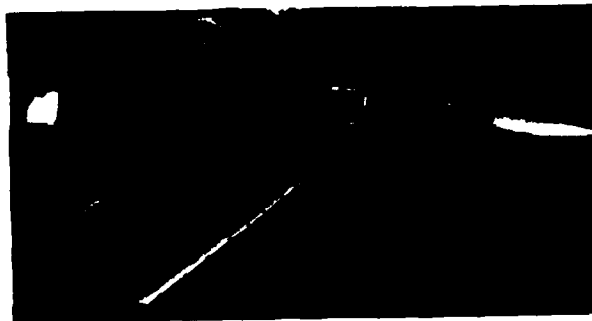
Figure 1. F-15 Aircraft
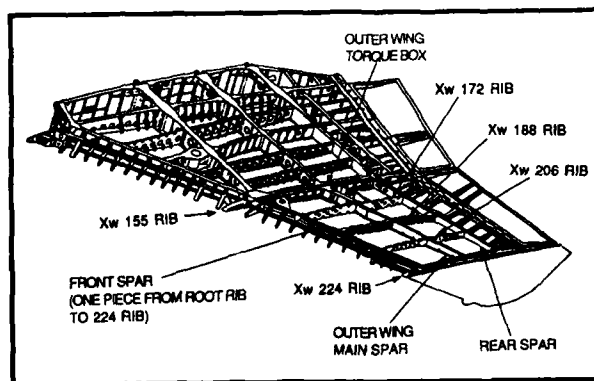
Figure 2. F-15 Wing Structure
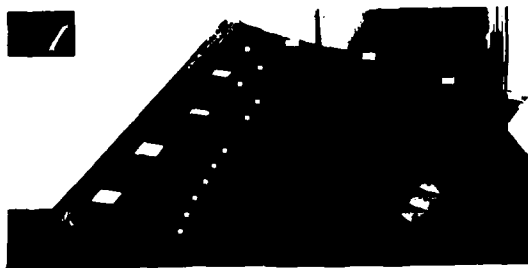
Figure 3. F-15 Upper-Outer Wing Skin Panel

Figure 4. Close-up of UOWS Fatigue Cracks
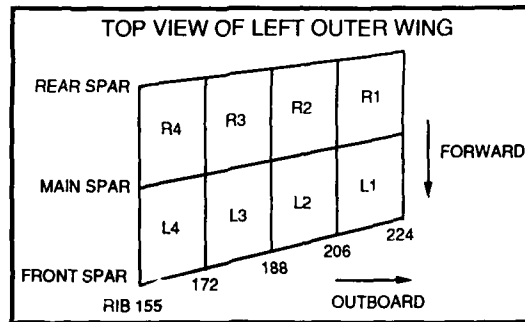
Figure 5. UOWS Spar-Rib Bay Designation
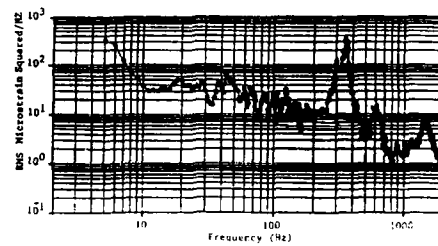
Figure 6. PSD of Strain Gage Flight Data
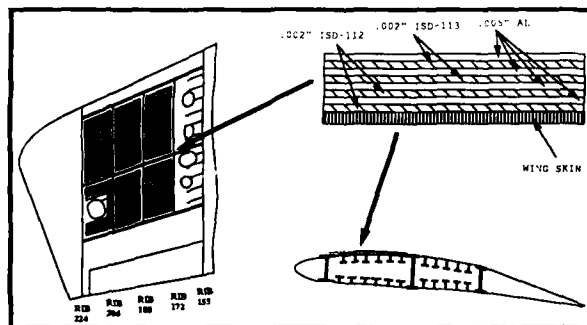
Figure 7. External Damping Treatment
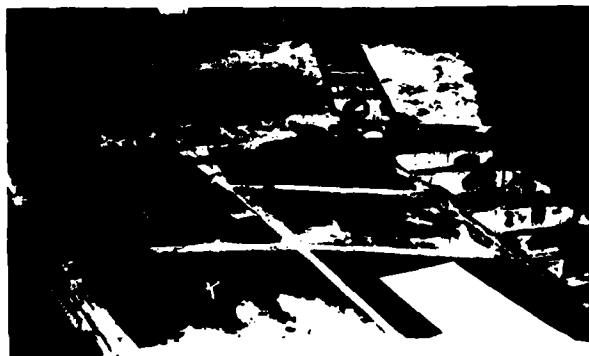
Figure 8. Installed External Damping Treatment
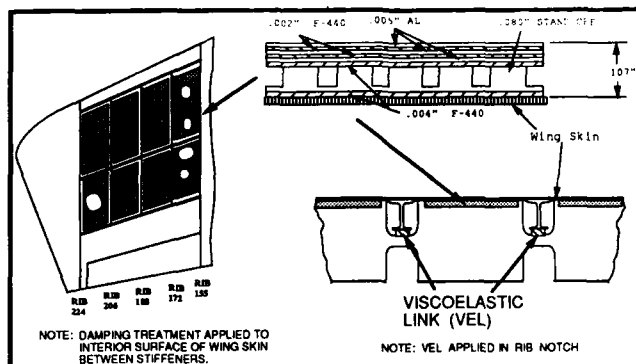
Figure 9. Internal Damping Treatment

Figure 10. Installed Internal Damping Treatment
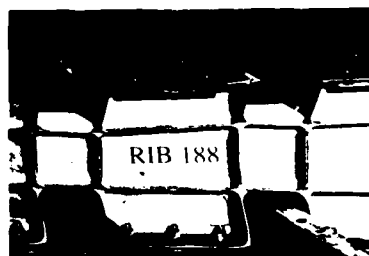
Figure 11. Typical Placement of VELs
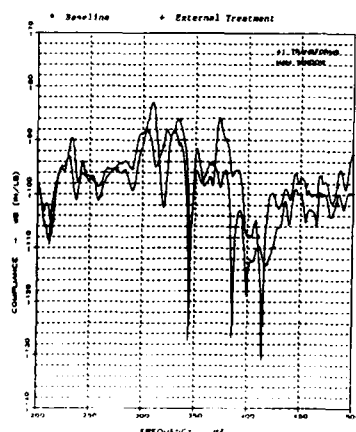
Figure 12. Comparison of Baseline UOWS and Externally Damped UOWS
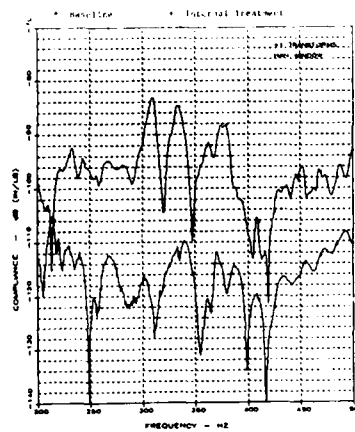
Figure 13. Comparison of Baseline UOWS and Internally Damped UOWS

$$Nd/Nu=(Sd/Su)^{-3.323}$$

WHERE

Nd = DAMPED LIFE
Nu = UNDAMPED LIFE
Sd = DAMPED STRESS
Su = UNDAMPED STRESS

Figure 14. Life Extension Calculation
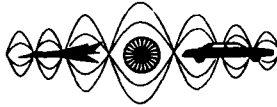
294

SECOND INTERNATIONAL CONGRESS ON
RECENT DEVELOPMENTS IN AIR- AND
STRUCTURE-BORNE SOUND AND VIBRATION
MARCH 4-6, 1992   AUBURN UNIVERSITY, USA

MEASUREMENT OF DAMPING OF CONCRETE BEAMS:

PASSIVE CONTROL OF PROPERTIES

Richard Kohoutek
Department of Civil and Mining Engineering
University of Wollongong
Wollongong 2500
AUSTRALIA

ABSTRACT
A forced vibration technique for the measurement of elastic modulus and loss factor of concrete beams, which includes resonant frequencies, is described. Several different beams made of plain concrete have been cast and deflections, exciting forces and phase shifts measured. The results indicate large differences of damping between resonant and non-resonant regions, but also considerable damping dependency on the concrete mix. The damping dependency on frequency and mix design could be used for a passive control of vibrations for structures. Furthermore, the method, which is exact in terms of the governing differential equation, can be also used for testing other materials.

1. INTRODUCTION

An important property in the analytical investigation of vibration of structures is damping of the material. In particular, for the analytical model of hysteretic damping, the determination of the properties of dynamic elastic modulus and loss factor is important. These properties are normally estimated from the response of a structure around its resonance frequency. This resonance condition leads typically to large amplitudes of vibrations and likely to some distortion of results if applied in the nonresonant part of a spectrum of the structure. An additional disadvantage is restriction of measured properties to the resonant frequency only.

A forced vibration of a simple beam for asphalt by Zaveri and Olsen [1] was adopted here and improved. The improvement was achieved by using dynamic deformation method for a simply supported beam. The advantage of the method is removal of the upper limit for a tested frequency, which is the first natural frequency of the tested specimen. The method presented here makes it possible to measure both properties, the elastic modulus and the loss factor for a frequency above as well as below the first and higher natural frequencies of the specimen. Furthermore, additional influences such as the mass of the core of the shaker and the accelerometer mass acting at midspan; shear deformations and rotary inertia of the beam; and overhang on both ends can be also included in the measured modulus and the loss factor.

To consider the need for a range of frequencies it must kept in mind that the first frequency of a building is within the first decades from zero, where the exciting frequency induced by machinery is 50 or 60 Hz, depending on the country, but also below as well as above this value, because of the need of gear boxes when rotating speeds of motors are unsuited to various needs in buildings. Hence, the range of frequency of interest is broad and not only related (preferably) to the resonant frequency of a structure.

2. PROBLEM FORMULATION

The theoretical model is shown in Figure 1 with the basic geometrical properties as indicated. It is assumed that the sinusoidal load applied will develop only small amplitudes of deformation, which will be within the linear range of the material of the specimen. Only the bending stress is considered to contribute to the deflection, which is furthermore small in respect to the dimensions of the beam. The bending of such a beam may be then described by an ordinary differential equation of fourth order and the dynamic load may be expressed in a matrix using frequency functions as presented in Kohoutek [2].
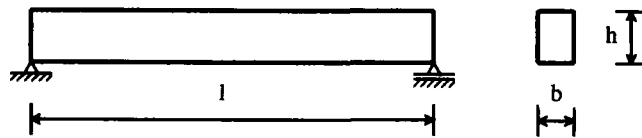
FIGURE 1: Geometry of a simply supported beam.

The most common types of damping are *viscous, dry friction* and *hysteretic*. The model of damping used here is that of *hysteretic* damping, where the stress-strain relationship is that the stress (harmonic force) leads the strain (deformation) by a constant angle, φ.

An harmonic strain, $\epsilon = \epsilon_o \sin \varphi\, t$, where the induced stress is $\sigma = \sigma_o \sin(\theta\, t + \varphi)$. Hence, an harmonic stress is $\sigma = \sigma_o \cos \varphi \sin \theta\, t + \sigma_o \sin \varphi \cos \theta\, t$ which is also $\sigma = \sigma_o \cos \varphi \sin \theta\, t + \sigma_o \sin \varphi \sin (\theta\, t + \pi/2)$. The last expression can be rewritten with use of a complex variable as:

$$\sigma = \sigma_o \cos \varphi \sin \theta t + i\, \sigma_o \sin \varphi \sin \theta t. \tag{1}$$

Hence a complex modulus E^* is,

$$E^* = \sigma/\epsilon = \sigma_o/\epsilon_o \cos \varphi + i\, \sigma_o/\epsilon_o \sin \varphi = E' + E'', \tag{2}$$

where the first component is storage modulus and the second is loss modulus. The loss factor η is a measure of hysteretic damping, $\eta = tan\,\varphi = E''/E'$. The relationships above lead to the angular difference between applied force $P(t) = P_o \sin \theta t$ and the displacement v_1 by a phase angle φ as derived thus.

Consider a beam loaded by a single periodic force $P(t) = P_o \sin \theta t$ in the midspan as shown in Figure 2. Three different models are considered here, a) simply supported beam on ideal hinges, b) semi-rigidly supported beam on marked with a cross inside of the circle, and c) semi-rigidly supported beam with overhang.

$P(t) = P_o \sin \theta t$ $P(t) = P_o \sin \theta t$ $P(t) = P_o \sin \theta t$
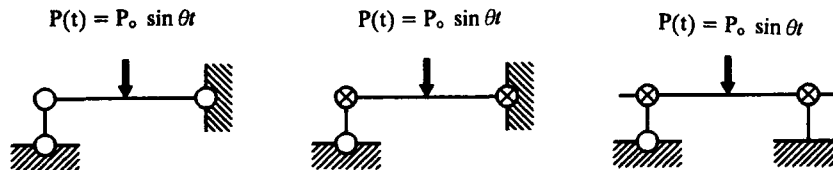
a) Ideal hinges   b) Semi-rigid supports   c) Semi-rigid supports with overhang
FIGURE 2: Three models of simply supported beam subjected to dynamic load.

296

The equilibrium of the dynamic moment and the dynamic shear force at the point under the load must be maintained for any value of t.

$$\Sigma M(t) = 0 \quad \text{and for the amplitudes} \quad M_{10} + M_{12} = 0 \tag{3}$$

where M_{10} and M_{12} are

$$M_{10} = \frac{EI}{l_1} F_7(\lambda_1) \xi_1 + \frac{EI}{l_1^2} F_9(\lambda_1) v_1 \qquad M_{12} = \frac{EI}{l_1} F_7(\lambda_1) \xi_1 - \frac{EI}{l_1^2} F_9(\lambda_1) v_1, \tag{4}$$

similarly for the periodic shear force $\quad \Sigma V(t) = P(t) \quad V_{10} + V_{12} = P \tag{5}$

$$V_{01} = \frac{EI}{l_2^3} F_{11}(\lambda) v_1 + \frac{EI}{l_2^2} F_9(\lambda) \xi_2 \qquad V_{12} = \frac{EI}{l_2^3} F_{11}(\lambda) v_1 - \frac{EI}{l_2^2} F_9(\lambda) \xi_2 \tag{6}$$

The matrix elements, after grouping the same components where ξ_1 is a rotation under the load P and v_1, is the deflection at the same point 1:

$$a_{11} = \frac{EI}{l_1} F_7(\lambda_1) + \frac{EI}{l_2} F_7(\lambda_2) \qquad a_{12} = 0$$

$$\tag{7}$$

$$a_{22} = \frac{EI}{l_1^3} F_{11}(\lambda_1) + \frac{EI}{l_2^3} F_{11}(\lambda_2) \qquad a_{21} = 0$$

The system for the amplitudes of ξ_1 and v_1, for any frequency of the load, is

$$a_{11}\xi_1 + a_{12}v_1 = 0$$

$$a_{21}\xi_1 + a_{22}v_1 = P(t) \tag{8}$$

and the solutions can be found exactly, in this case decoupled. The solution vector has the first component $\xi_1 = 0$ for any θ, and taking the amplitudes only, the second component v_1 (real part) is:

$$v_1 = \frac{4 P l^3 \left((-1 + \exp(-2\lambda)) \cos \lambda + (1 + \exp(-2\lambda)) \sin \lambda \right)}{\lambda^3 E' I (1 + \exp(-2\lambda)) \cos \lambda} \tag{9}$$

and subsequently taking a ratio of the amplitudes P/v_1 in combination of the relationship $E^* = E'(1 + i \eta)$,

$$P/v_1 = \frac{4 E' I \lambda^3 (1 + \exp(-2\lambda)) \cos \lambda + \eta \, 4 E I \lambda^3 (1 + \exp(-2\lambda)) \cos \lambda}{l^3 \left((-1 + \exp(-2\lambda)) \cos \lambda + (1 + \exp(-2\lambda)) \sin \lambda \right)}. \tag{10}$$

The loss factor $\eta = \tan \varphi$ and the modulus of elasticity can be calculated from the equation (10). Because the modulus is also included on the right hand side of the equation in λ, the iterative process used is numerical. However, the equation (10) is the exact solution of the differential equation [2] for flexural deformations of a beam. The solution for the basic support conditions is summarized in Appendix, and also in [2]. Where the rotary inertia and shear deformations can be included by using frequency functions of [2]. The result of application to equation (9), when including the influences of shear deformations and rotary inertia on the total deflection v_1

$$v_1 = \frac{4\,P\,\lambda^3(aa_o + dd_o)\{d_o(1 + \exp(-2d))\sin a - a_o(1 - \exp(-2d))\cos a\}}{E'\,I\,a_o d_o(aa_o + dd_o)^2(1 + \exp(-2d))\cos a} \tag{11}$$

and similar expressions can be derived for the ratio of P/v_1, followed by an iterative evaluation of E, thus including the influence of shear deformations and rotary inertia.

2.1 Influence of Support Conditions and Overhang

It is very difficult to create ideal support conditions, especially for a structure dynamically loaded. The dynamic performance is very sensitive to the support conditions, and when this influence is neglected it could lead to large errors in the estimate of a modulus.

Formulae have been developed to accommodate a variation of the support conditions and the above process for ideal hinge supports can be carried out numerically for semi-rigid supports. The same method can be used by creating a stiffness matrix for any other tested structure using Appendix and [2], also inclusive of an influence of rotary inertia and shear deformations of a specimen.

3. TESTING SET-UP

Beams were subjected to a sinusoidal force of varying frequency applied in the mid-span by an electromagnetic shaker. The tests were performed by selecting particular frequency and adjusting the displacement to be approximately constant. This led inevitably to a variation in the amplitude of the dynamic force, measured by a piezoelectric load cell. An accelerometer with a charge amplifier was the second channel into the Spectrum Analyzer to record a force, displacement, and a phase shift.

4. PROPERTIES OF CONCRETE BEAMS

The experimental programme is made up of seven plain concrete beams. The beam dimensions are shown in Figure 1, and mix proportions of the constituents follow in Table 1.

TABLE 1: Mix proportions of concrete beams

Beam #	Cement kg/m^3	Silica kg/m^3	Water kg/m^3	Fine A. kg/m^3	Coarse A. kg/m^3	High Dens. kg/m^3	Lightwt. kg/m^3	Superplast. l/m^3	Fibermesh kg/m^3	W/C	Slump mm
A	523	-	263	1363	-	-	-	-	-	0.5	170
B	557	-	267	937	996	-	-	-	-	0.48	165
C	557	-	197	937	689	747	-	-	-	0.35	10
D	557	-	223	937	689	-	153	-	-	0.40	80
E	557	-	223	937	-	-	574	-	-	0.40	85
F	518	39	156	937	996	-	-	8	-	0.28	105
G	557	-	228	937	996	-	-	-	4.5	0.41	75

with general characteristic of mixes as follows:
A - : Mix contains 100% mortar
B - : Mix containing 100 % natural aggregate
C - : Mix containing 75 % natural aggregate and 25 % high density aggregate
D - : Mix containing 100 % natural aggregate and 25 % lightweight aggregate
E - : Mix containing 100 % lightweight aggregate
F - : Mix containing 100 % natural aggregate with 7 % of cement replaced with silica fume
G - : Mix containing 100 % natural aggregate with Fibremesh

Cement used was normal Portland, type A, complying with the Australian Standard AS 1315-1982. *Silica fume* being a byproduct of the electric arc furnace production of silicon and ferro-silicon alloys. *Coarse aggregate* was 14 mm irregular shaped, crushed basalt. *Fine aggregate* used was river sand. *Lightweight aggregate* was common household ornamental garden stone, approximately 10 mm size. *High density aggregate* consisted of steel punchings of mild steel, approximately 15 mm diameter and 4 mm thickness. *Admixture* was a superplasticizer, to reduce the water/cement ratio and to maintain the workability. *Fibermesh* was micro-reinforcement polypropylene fibres, used normally to control shrinkage cracking.

TABLE 2: *Measured properties of concrete beams*

Beam #	Comp. S. MPa	Density kg/m³	Modulus* GPa	Damping** Log. Decr.	Nat.freq. 1 Hz	Modulus† GPa	Nat.freq. 2 Hz	Nat.freq. 3 Hz
A	44.5	2200	30	0.129	66.25	21.9	77	76.9
B	49.5	2360	35	0.294	65.0	22.6	79.5	80.4
C	56	2840	49	0.319	70.0	31.5	78.5	86.9
D	53	2300	35	0.317	72.5	27.4	68	81.35
E	45	2160	29	0.209	62.5	19.1	71.5	77.1
F	99	2440	52	0.199	70	27.1	80	96.6
G	45	2400	35	0.239	56.5	17.4	73	76.1

* calculated according to AS1012 Part 12 and 17 (1986)   Nat.freq.1 measured on hinges
** calculated by free decay test   Nat.freq.2 measured on rollers
† calculated from the first natural frequency 1   Nat.freq.3 calculated using E from AS1012

5. MODULUS OF ELASTICITY AND HYSTERETIC DAMPING OF CONCRETE BEAMS

A theory presented in section 2 above was applied to the concrete beams. The real part of modulus of elasticity is presented in Figure 3, considering only four beams; *A-beam (44.5 MPa)* made of mortar, *B-beam (49.5 MPa)* made of natural aggregate, *F-beam (99 MPa)* made of high strength concrete, and *G-beam (45 MPa)* made of natural aggregate with Fibremesh. The real part of modulus for the beams, *A,B,* and *F* differs substantially but it has similar trend, even for the high strength concrete *F*. However, the behaviour of beam *G* differs in the region below as well as above the natural frequency. There is substantial reduction of modulus on both sides of the natural frequency of the beam. Additional difference is a relative independence of the amplitude of modulus on the frequency of excitation when compared with other beams.
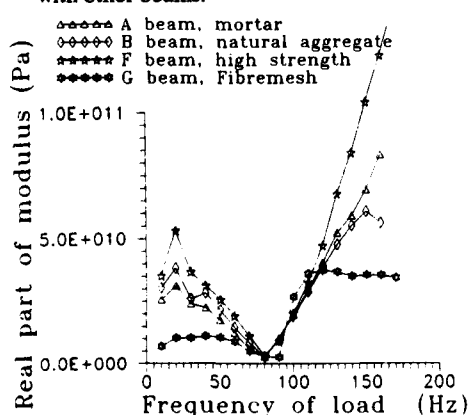
FIGURE 3. *Dependency of the real part of modulus on the frequency of loading.*
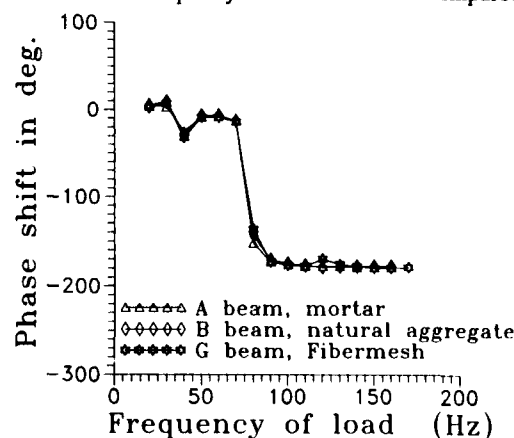
FIGURE 4. *Dependency of the phase shift on the frequency of loading.*

A phase shift for the same beams are shown in Figure 4, where the grouping of three beams A,B, and G is also apparent, however, the numerical values are different.

Specific Damping Capacity, used because of large value of φ, is defined as a ratio of an energy absorbed by the material against the energy supplied. This is an area of ellipse generated by the phase shift φ on two coordinates, a force and displacement; over the area of amplitudes of a force and displacement.

The area of an ellipse, for amplitudes of a force P_o and a displacement v_o, based on equation (1) is:

$$A_1 = P_o v_o \pi \sin \varphi, \tag{12}$$

and the energy supplied is $A_2 = P_o v_o$. Taking a ratio of A_1 / A_2 leads to the expression for a Specific Damping Capacity:

$$\psi = \pi \sin \varphi. \tag{13}$$

The results, shown here for the same beams, showing the measured phase shift φ and calculated Specific Damping Capacity ψ are in Figures 4, and 5.
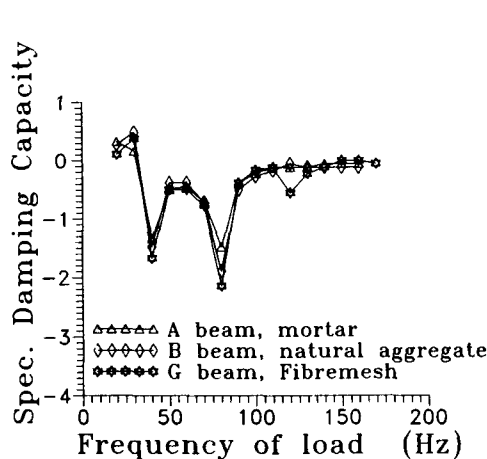
FIGURE 5. Dependency of damping
on the frequency of loading.
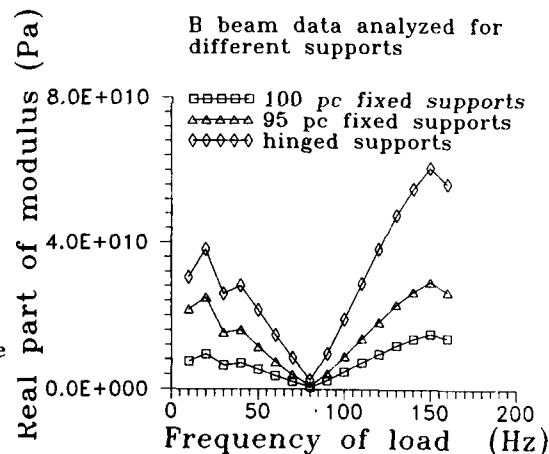
FIGURE 6. Relationship between a support conditions
and the real part of modulus.

The test arrangement, in particular the support conditions, have also marked influence on the results. This is shown in Figure 6, where the same measured data were analyzed for the three support conditions. Completely fixed supports, 95% fixity at the supports, and ideal hinges result in completely different modulus. It is noted, that the small change at the fixity has considerably larger effect on the result than the same change at a hinge (not shown here). Therefore in interpretation of data, some attention should be paid to creation known boundary conditions, which will be used correctly in the analysis. The beams tested here were supported on almost ideal hinges.

6. CONCLUSIONS

Several main points can be made from this first round of tests on beams made from plain concrete. The advantages of present test arrangement is in testing the global properties of concrete, on a large size of specimen. Furthermore, the stress distribution within the tested structure is similar to the real structural elements and includes real size aggregates and its properties. However, the disadvantage is the result, which clearly includes several mechanisms of damping without defining the individual contributions of each of three mechanism.

1) The modulus of elasticity for plain concrete is frequency dependent over the range of tested frequencies, in particular: below, above and at the first natural frequency of the specimen.
2) The Specific Damping Capacity measured by a phase shift is also frequency dependent.

3) It might be possible to vary damping properties of concrete at will by changing the composition of mix, therefore introducing additional design parameter for those structures where such property is required.
All main points of the present study need further investigation with a different concrete mixes and . possibly some variations in support conditions. However, the method of testing presented makes this forced vibration possible for any beam structures and materials. The solution presented is an exact in terms of the differential equation for a beam.

7. ACKNOWLEDGEMENT

8. REFERENCES

[1] ZAVERI, K. and OLESEN, H.P. (1972). "Measurement of Elastic Modulus and Loss Factor of Asphalt," Technical Review No.4, Bruel & Kjaer, pp. 3-15.
[2] KOHOUTEK, R, (1985). "Analysis of Beams and Frames," Chapter 4 in "Analysis and design of foundations for vibrations," pp. 99-156; P. Moore, ed., 512pp, 1985, published by A.A.Balkema.
[3] LAZAN, B.J. (1968). "Damping of materials and members in structural mechanics," Pergamon Press.
[4] MYKLESTAD, N.O. (1952) "The Concept of Complex Damping," J. of Applied Mechanics, pp. 284-286.

APPENDIX

FREQUENCY FUNCTIONS $F_i(\lambda)$

Transverse vibration without shear deformations and rotary inertia considered.

$$\lambda = l \left(\frac{m\theta^2}{EI}\right)^{1/4},$$

where E - Young's modulus, I - moment of inertia, m - mass per unit length, θ - loading frequency, l - length of the bar.

FUNCTION	LIMIT ($\lambda = 0$)
$F_1(\lambda) = -\lambda \dfrac{1 - \exp{-\lambda}(2\sin\lambda + \exp{-\lambda})}{\cos\lambda - \exp{-\lambda}(2 - \exp{-\lambda}\cos\lambda)}$	$F_1(0) = 2.00$
$F_2(\lambda) = -\lambda \dfrac{\sin\lambda - \cos\lambda + \exp{-2\lambda}(\sin\lambda + \cos\lambda)}{\cos\lambda - \exp{-\lambda}(2 - \exp{-\lambda}\cos\lambda)}$	$F_2(0) = 4.00$
$F_3(\lambda) = -\lambda^2 \dfrac{1 + \exp{-\lambda}(\exp{-\lambda} - 2\cos\lambda)}{\cos\lambda - \exp{-\lambda}(2 - \exp{-\lambda}\cos\lambda)}$	$F_3(0) = 6.00$

$$F_4(\lambda) = \lambda^2 \frac{\sin \lambda \, (1 - \exp{-2\lambda})}{\cos \lambda - \exp{-\lambda}(2 - \exp{-\lambda} \cos \lambda)} \qquad\qquad F_4(0) = -6.00$$

$$F_5(\lambda) = \lambda^3 \frac{1 + \exp{-\lambda} \, (2 \sin \lambda - \exp{-\lambda})}{\cos \lambda - \exp{-\lambda}(2 - \exp{-\lambda} \cos \lambda)} \qquad\qquad F_5(0) = -12.00$$

$$F_6(\lambda) = -\lambda^3 \frac{\sin \lambda + \cos \lambda + \exp{-2\lambda} \, (\sin \lambda - \cos \lambda)}{\cos \lambda - \exp{-\lambda}(2 - \exp{-\lambda} \cos \lambda)} \qquad\qquad F_6(0) = 12.00$$

$$F_7(\lambda) = \lambda \frac{2 \sin \lambda \, (1 - \exp{-2\lambda})}{\sin \lambda - \cos \lambda + \exp{-2\lambda} \, (\sin \lambda + \cos \lambda)} \qquad\qquad F_7(0) = 3.00$$

$$F_8(\lambda) = \lambda^2 \frac{1 + \exp{-\lambda} \, (2 \sin \lambda - \exp{-\lambda})}{\sin \lambda - \cos \lambda + \exp{-2\lambda} \, (\sin \lambda + \cos \lambda)} \qquad\qquad F_8(0) = 3.00$$

$$F_9(\lambda) = -\lambda^2 \frac{\sin \lambda + \cos \lambda + \exp{-2\lambda} \, (\sin \lambda - \cos \lambda)}{\sin \lambda - \cos \lambda + \exp{-2\lambda} \, (\sin \lambda + \cos \lambda)} \qquad\qquad F_9(0) = -3.00$$

$$F_{10}(\lambda) = -\lambda^3 \frac{1 + \exp{-\lambda} \, (2 \cos \lambda + \exp{-\lambda})}{\sin \lambda - \cos \lambda + \exp{-2\lambda} \, (\sin \lambda + \cos \lambda)} \qquad\qquad F_{10}(0) = -3.00$$

$$F_{11}(\lambda) = \lambda^3 \frac{2 \cos \lambda \, (1 + \exp{-2\lambda})}{\sin \lambda - \cos \lambda + \exp{-2\lambda} \, (\sin \lambda + \cos \lambda)} \qquad\qquad F_{11}(0) = 3.00$$

$$F_{12}(\lambda) = \lambda^3 \frac{\cos \lambda \, (1 + \exp{-2\lambda}) + 2 \exp{-\lambda}}{\sin \lambda - \cos \lambda + \exp{-2\lambda} \, (\sin \lambda + \cos \lambda)} \qquad\qquad F_{12}(0) = 3.00$$

$$F_{13}(\lambda) = -\lambda^3 \frac{1 - \exp{-\lambda} \, (2 \sin \lambda + \exp{-\lambda})}{2 \sin \lambda \, (1 - \exp{-2\lambda})} \qquad\qquad F_{13}(0) = 0.00$$

$$F_{14}(\lambda) = \lambda^3 \frac{\cos \lambda \, (1 - \exp{-2\lambda}) - \sin \lambda \, (1 + \exp{-2\lambda})}{2 \sin \lambda \, (1 - \exp{-2\lambda})} \qquad\qquad F_{14}(0) = 0.00$$

$$F_{15}(\lambda) = -\lambda \frac{\sin \lambda - \cos \lambda + \exp{-2\lambda} \, (\sin \lambda + \cos \lambda)}{\cos \lambda + \exp{-\lambda}(2 + \exp{-\lambda} \cos \lambda)} \qquad\qquad F_{15}(0) = 0.00$$

$$F_{16}(\lambda) = \lambda^2 \frac{\sin \lambda \, (1 - \exp{-2\lambda})}{\cos \lambda + \exp{-\lambda}(2 + \exp{-\lambda} \cos \lambda)} \qquad\qquad F_{16}(0) = 0.00$$

$$F_{17}(\lambda) = -\lambda^3 \frac{\sin \lambda + \cos \lambda + \exp{-2\lambda} \, (\sin \lambda - \cos \lambda)}{\cos \lambda + \exp{-\lambda}(2 + \exp{-\lambda} \cos \lambda)} \qquad\qquad F_{17}(0) = 0.00$$

$$f_1 = \cos \lambda - \exp{-\lambda}(2 - \exp{-\lambda} \cos \lambda)$$

$$f_2 = \sin \lambda - \cos \lambda + \exp{-2\lambda} \, (\sin \lambda + \cos \lambda)$$

$$f_3 = \cos \lambda + \exp{-\lambda}(2 + \exp{-\lambda} \cos \lambda)$$

ACTIVE CONTROL AND DAMPING
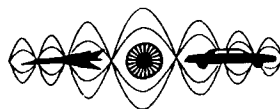
SECOND INTERNATIONAL CONGRESS ON
RECENT DEVELOPMENTS IN AIR- AND
STRUCTURE-BORNE SOUND AND VIBRATION
MARCH 4-6, 1992 AUBURN UNIVERSITY, USA

EXPERIMENTS ON THE ACTIVE CONTROL OF
TRANSITIONAL BOUNDARY LAYERS

P.A. Nelson, J.-L. Rioual and M.J. Fisher

Institute of Sound and Vibration Research
University of Southampton
England

ABSTRACT

Experimen' 'l results are presented which demonstrate that the streamwise position of the transition region of a flat plate boundary layer can be actively controlled. The means of co.'trol is through the application of suction through the surface of the plate, a progressive increase in suction rate being capable of producing transition at progressively larger distances downstream from the plate leading edge. A simple digital feedback regulator based on an integral control law is shown to be most effective in regulating the position of transition, an error signal being derived from measurements of pressure fluctuations on the surface of the plate.

1. INTRODUCTION

The maintenance of laminar flow in the boundary layer over the surface of a moving body will reduce both skin friction drag and the generation of flow noise. The pursuit of the former objective has motivated extensive research on laminar flow control, much of the early work being undertaken during the 1940's and 50's (see the recent review by Gad-el-Hak [1]). Renewed interest in the subject has been stimulated by the potential for vast savings in fuel costs that result from the maintenance of laminar flow over the wings of aircraft. One of the classical approaches to the stabilisation of a laminar boundary layer is to suck fluid through the surface over which the boundary layer develops. This technique was demonstrated by several workers in the 1940's [1] but has never reached widespread practical use, mainly because of the engineering difficulties in providing a suitable surface through which to withdraw the fluid. Many of these difficulties can now be overcome with the use of electron-beam drilled titanium sheet which provides a porous surface which is both rigid and smooth. There is also interest, however, in being able to monitor the effect of suction on the boundary layer whilst modifying the rate of suction through the porous surface. Clearly, the use of suction itself consumes power since a pump must be provided to withdraw the fluid. Ultimately, the aim would be to so optimise the distribution and rate of suction through a wing surface in order to minimise the total net power consumed in propelling the aircraft. In this work we take a first step towards this goal by showing that the state of the transitional boundary layer on a flat plate can be effectively monitored by measurement of the fluctuating surface pressures. Furthermore, we demonstrate that these measurements can be used to provide an "error signal" which can be used by a control system which regulates the suction flow rate in order to maintain the transition region in a desired streamwise position.

2. SURFACE PRESSURE FLUCTUATIONS DUE TO A FLAT PLATE BOUNDARY LAYER

All the experiments described below were performed in a small wind tunnel having a 305 mm × 230 mm working section. The tunnel could produce velocities in the working section up to 22 ms^{-1} with a turbulence level of 1%. A flat plate with an elliptical leading edge was installed in the tunnel as illustrated in Figure 1. The plate was 1.2 m in length and filled the 230 mm width of the working section. The plate was constructed of honeycomb core 12.7 mm in thickness to which was bonded 1.2 mm thick aluminium skins. The plate incorporated a suction panel in the position shown in Figure 1. The design of the panel was closely based on that reported by Reynolds and Saric [2]. This consisted of 9 suction strips each having a width of 16 mm with a separation of 4 mm between each strip. The surface used above the strips consisted of a finely drilled titanium sheet with 0.1 mm diameter holes randomly spaced by 1mm. This arrangement ensured a close to uniform distribution of surface suction over the area of the panel .

Pressure fluctuation measurements were made downstream of the suction panel by using an array of electret microphones mounted flush with the panel surface. The microphone signals were high pass filtered above a frequency of 800 Hz to remove the acoustic pressure fluctuations generated by the wind tunnel fan. Some typical time histories are illustrated in Figure 2. These results show clearly the development of the boundary layer from laminar to turbulent in the region downstream of the suction panel. The laminar region is characterised by the almost complete absence of pressure fluctuations, whereas the measurements made in the transition region show the development of turbulent spots, their 'intermittency' [3] increasing in the streamwise direction until the boundary layer becomes fully turbulent. The nature of the time histories detected by the microphones were found to be very similar to those detected by a hot wire anemometer traversed close to the positions of the microphones. Figure 3 illustrates the change in the distribution of rms pressure fluctuations produced by varying the flowrate through the suction panel. These results demonstrate the delay in transition that can be produced by increasing the suction flowrate. Furthermore, it is shown how the streamwise location of the transition region can be accurately determined from measurements of the surface pressure fluctuations.

3. ACTIVE CONTROL OF THE POSITION OF THE TRANSITION REGION

We will now show how the measurement of the distribution of surface pressure can be used in controlling the suction flowrate. Here we show that the transition region can be automatically held at a pre-specified streamwise location, irrespective of, for example, changes in the mean flow velocity. The desired location of the transition region can be specified in terms of the associated distribution of normalised rms pressures. We therefore specify that we wish the rms values of the outputs of a streamwise array of N microphones to be given by, for example, the vector

$$\mathbf{r}^T = \left[p_r(x_1) \, p_r(x_2) \dots p_r(x_N) \right] \tag{2}$$

Each element of the vector corresponds to a desired or "reference" value of the normalised rms pressure given by $p_r(x_n) = p_{rms}(x_n) / p_{turb}$, where p_{turb} is the rms pressure fluctuation associated with the fully turbulent flow in the boundary layer. Values of $p_r(x_n)$ therefore vary from 0 to 1 with streamwise location along the plate. A measure of the "error" in the location of transition can then be deduced by comparing the vector r with the vector y given by

$$\mathbf{y}^T(k) = \left[p(x_1, k) \, p(x_2, k) \dots p(x_N, k) \right] \tag{3}$$

where the elements $p(x_n,k) = p_{rms}$ $(x_n,k)/p_{turb}$ are the normalised rms pressures measured at a given time index k. We then define the error at a time index k by

$$e(k) = \sum_{n=1}^{N} \left[p_r(x_n) - p(x_n,k) \right] \tag{4}$$

This error signal is then operated on by a controller which modifies the suction rate to ensure that the error is driven to zero. The structure of the control system is therefore as illustrated in Figure 4(a), which has been drawn in the form of a classical feedback regulator. Note that the "output" of the "plant" y can also be influenced by "external disturbances" such as those due to a sudden change in the mean flow speed. An alternative way of representing the control system is that shown in Figure 4(b) where it is assumed that, since r takes a constant value, we need only consider the relationship between the value of the input u(k) to the "plant" and the error output e(k) at a given time index k. One can then simply regard the error output produced by a given control input (in the absence of external disturbances) as that resulting from the excitation of a single input/single output system.

4. DYNAMICS OF THE PLANT AND CONTROLLER

The nature of the error signal described above will be highly dependent on the time used to estimate the rms values of the pressure fluctuations produced at the microphones. Experiments showed that an averaging time of at least 10 seconds was required if the standard deviation of the resulting distribution of rms values was to be less than 10%. However, one would clearly wish the control system to operate over a much shorter timescale, with a response time of much less than ten seconds. For example, the reference vector of desired rms pressure values at four microphones placed at the streamwise locations $x_1 = 0.835$ m, $x_2 = 0.85$ m, $x_3 = 0.865$ m and $x_4 = 0.885$ m downstream of the leading edge can be defined as

$$r^T = \begin{bmatrix} 0.2 & 0.33 & 0.66 & 0.8 \end{bmatrix} \tag{5}$$

Figure 5 shows the corresponding sequence of values of e(k) computed following a step change in the control voltage supplied to the variable speed pump. Thus the controller (computer) outputs values u(k) to the speed controller at intervals of 0.36 s. The resulting error is computed at intervals of 0.36 s by sampling the time histories of the pressure fluctuations over a duration of 0.1 s. The step response illustrated in Figure 5 shows how the intrinsically intermittent nature of the pressure fluctuations produced in the transition region will result in a very "noisy" error signal when short duration data lengths are used to estimate its value. Also shown in Figure 5 is the response of the error to a step change in the input when averaged over an ensemble of 40 separately repeated experiments. The underlying response of the system is therefore, at least to a first approximation, characteristic of a first order system whose step response converges exponentially to its steady state value with a well defined time constant. Figure 6 shows the variation of the ensemble averaged relationship between the steady state values of e(k) as a function of the steady state value of the input u(k), the value of the voltage output to the suction pump speed controller. Figure 6 shows that at least over a certain range of the value u(k), the "plant" illustrated in the block diagram of Figure 4(b) can be considered as a linear system. A simple description of the dynamics of this system is given by the first order difference equation

$$e(k + 1) = ae(k) + bu(k) + w(k) \tag{6}$$

where the system dynamics are characterised by the parameters a and b. These take the approximate values of a = 0.01 and b = 2.4. The "noise" produced in the error signal when sampling over a short duration is represented by the signal w(k) which, to a first approximation, can be considered to be zero mean Gaussian white noise.

The noisy value of the error signal can be dealt with effectively by using what amounts to an integral controller. Thus, in terms of classical control theory [4], the input to the plant u(k) is simply made equal to the time integrated value of the error signal multiplied by a gain K. In discrete time this amounts to updating the controller output u(k) in accordance with

$$u(k + 1) = u(k) + Ke(k) \qquad (7)$$

where it has been assumed that in the equivalent continuous time case $u(t) = K\int e(t)dt$ or $du(t)/dt = Ke(t)$ and a finite difference approximation is made for $du(t)/dt$. This form of control, sometimes referred to as "incremental control" is particularly suited to the current problem since it is capable of automatically tracking a steady state reference set point (in this case zero error) even in the presence of unmodelled external disturbances (see, for example, Wellstead and Zarrop [5] for a full discussion). It is also interesting to note that the algorithm specified by equation (7) can be regarded as a special case of a stochastic approximation method for efficiently finding the zero value of what amounts to a "noisy" error function [6].

5. THE PERFORMANCE OF THE CONTROL SYSTEM

A typical result which illustrates the effectiveness of the control system is shown in Figure 7. This shows the development of the error signal e(k) and the controller input u(k) when a sudden change is made to the mean flow speed in the wind tunnel. This was accomplished by applying a step input to the speed control of the wind tunnel fan. The value of the controller gain K chosen in this case was given by 0.03, the system becoming unstable at a value of K of 0.045. The results demonstrate the excellent response of the system when an external disturbance is imposed. The error very rapidly recovers to a mean value of zero as the suction rate is automatically adjusted in order to compensate for the change in mean flow speed.

6. CONCLUSION

The preliminary experiments described demonstrate the feasibility of automatically controlling the streamwise location of the transition region in a flat plate boundary layer. Measurements of surface pressure fluctuations have been used successfully to both characterise the location of transition and to provide an error signal input to a suction rate control system.

REFERENCES

1.   M GAD-EL-HAK Flow control. Applied Mechanics Review **42**, 1989. 261-292.
2.   G A REYNOLDS and W S SARIC   Experiments on the stability of the flat plate boundary layer with suction AIAA Journal **24**, 1986 202-207.
3.   A D YOUNG Boundary layers, Blackwell Scientific, Oxford. 1989.
4,   R J RICHARDS   An Introduction to Dynamics and Control. Longman, New York. 1979.
5.   P E WELLSTEAD and M B ZARROP Self-Tuning Systems.   John Wiley, Chichester. 1991.
6.   H ROBBINS and S MONRO A stochastic approximation method. Ann. Math. Stat. **22** 1951 400-407.
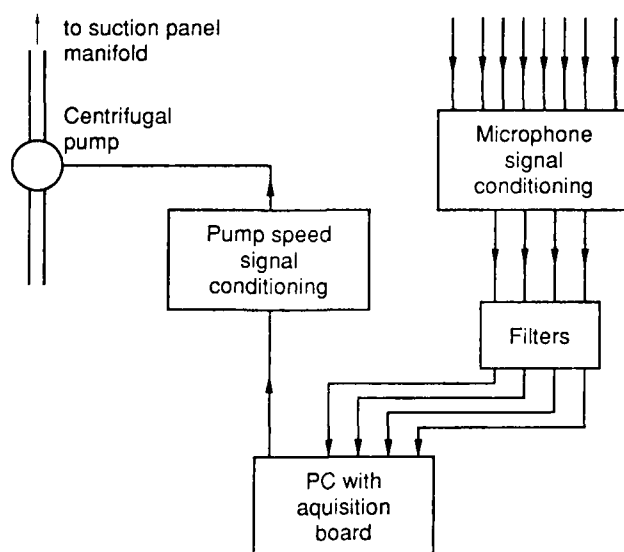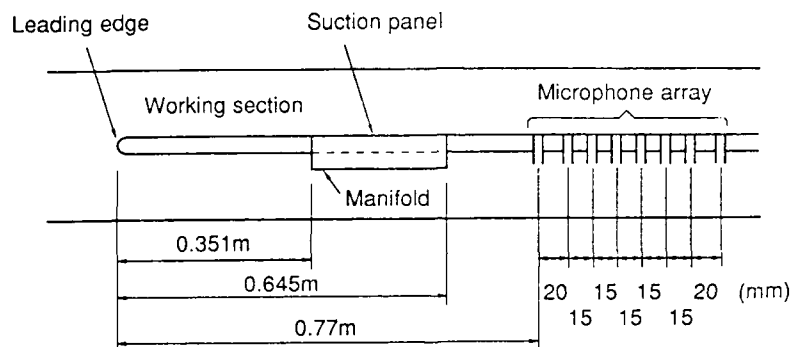
Figure 1   Schematic of test rig and suction rate control equipment.
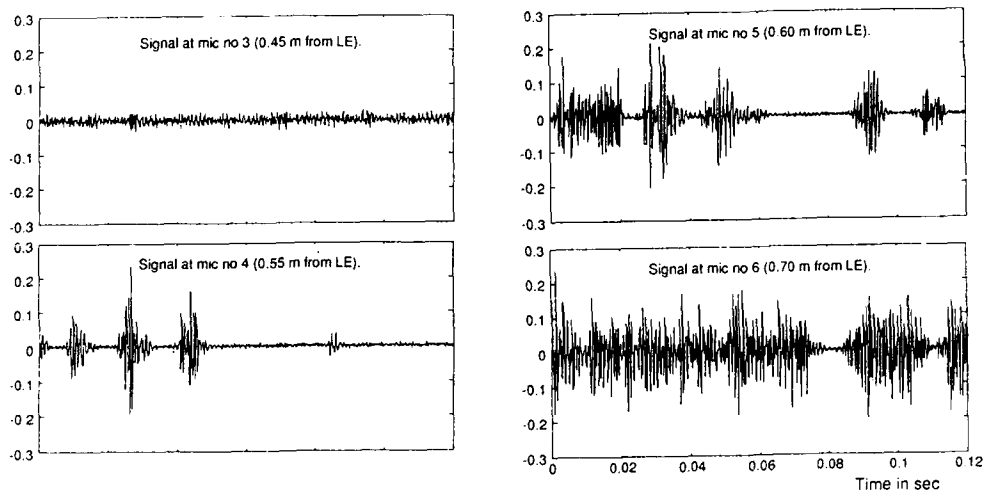
Figure 2: Pressure fluctuation time histories.
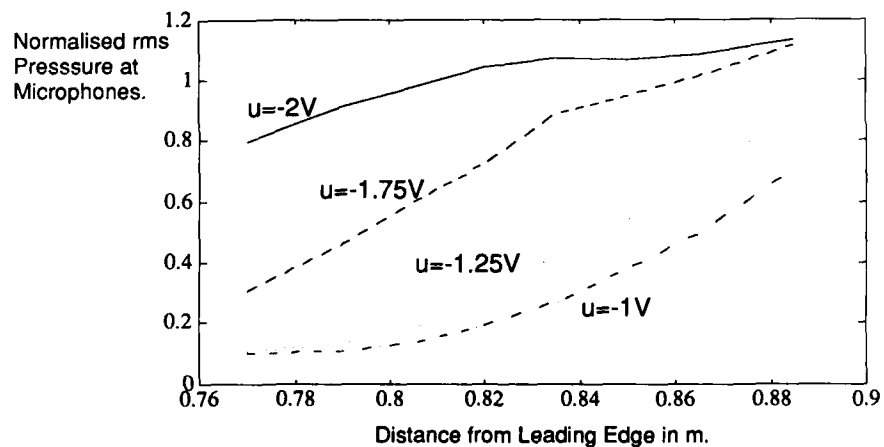
Figure 3   Pressure fluctuation rms distribution with changing suction,
where u defines the voltage output from the controller. The
results shown are for a mean flow speed Uo of 20 m/s.
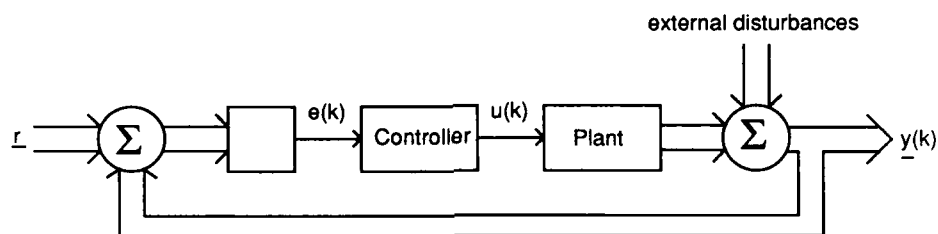
Figure 4 a): Control system structure.
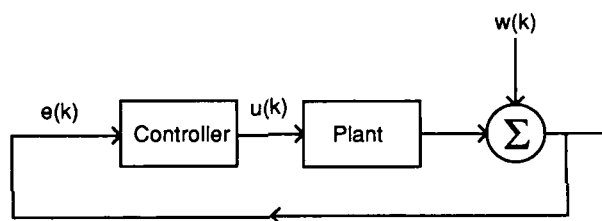
Figure 4 b): Alternative representation of the control system in terms
of the scalar variables u(k) and e(k).
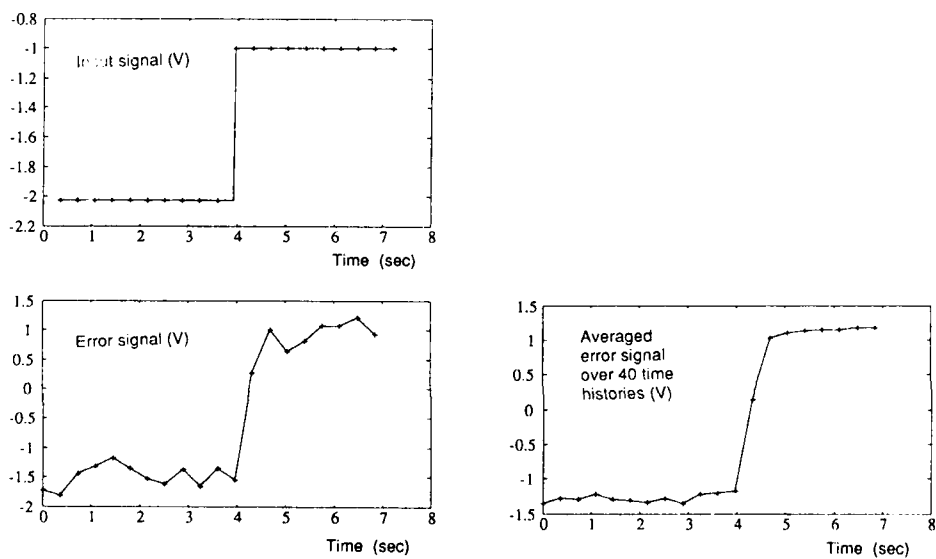
Figure 5: Time histories of the error response to step change
in controller input.
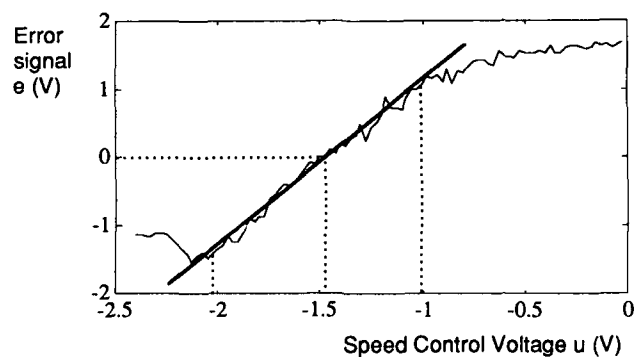
Figure 6: Steady state input/output of the plant.
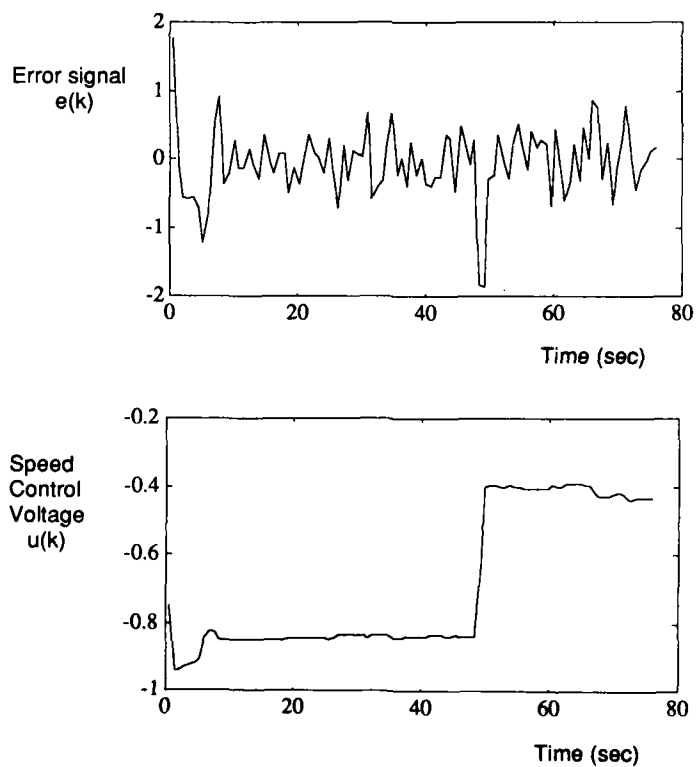
Figure 7: Controller Response to a sudden change in mean flow velocity, from Uo=15m/s to Uo=20m/s.

SECOND INTERNATIONAL CONGRESS ON
RECENT DEVELOPMENTS IN AIR- AND
STRUCTURE-BORNE SOUND AND VIBRATION
MARCH 4-6, 1992   AUBURN UNIVERSITY, USA

RECENT ADVANCES IN ACTIVE NOISE CONTROL

D. Guicking
Drittes Physikalisches Institut
University of Göttingen
D-3400 Göttingen
Germany

ABSTRACT

An overview is given of the worldwide progress which could be observed during the last few years in the field of active noise control. After presenting some statistical evaluation of the temporal and regional development (showing a still exponential increase of publications, and a shift from Europe to U.S.A. and Japan), commercially available products and their technical applications are briefly described, followed by an outline of recent theoretical and experimental laboratory research work.

INTRODUCTION

Active noise control—first proposed in 1933 [1], experimentally demonstrated in laboratory set-ups not before the early 50's [2], theoretically treated since the mid 60's [3], technical demonstration installations since 1980 [4, 5]—has led to commercially available products since about 1987 [6]. In the last few years, considerable progress has been made, although the application is still confined to acoustically "simple" problems. Somewhat older is active vibration control where similar techniques are applied and—mainly because of its importance for spacecraft and aircraft—greater activities can be observed. This paper does not intend to give a historical review of the development of active noise control since a number of such reports have been published in the past [e. g., 7–9], and particularly the recently published excellent first monograph on "Active Control of Sound" by NELSON and ELLIOTT [10] provides all necessary information. It is also assumed that the reader be familiar with the basic principles of active noise control, the cancellation of an existing sound by its negative replica or, more effective, the installation of an antiphase compensation source next to a primary sound source.

Active (usually electroacoustic) noise control is still widely considered somewhat exotic, the vast majority of noise reduction problems being solved with the technically much simpler (though not always cheaper) conventional passive methods of sound absorption or sound shielding. However, there are situations where these methods fail, particularly at low frequencies where passive means become either inefficient or too bulky for practical installations.

A fundamental problem to be solved in each active sound cancellation system is the requirement of highly precise control, temporal stability and reliability. This is the reason why the application of active systems became reasonable only after the development of powerful digital electronics. This is reflected in the temporal development of research activities on this subject as can be seen from the number of publications. Fig. 1 shows a histogram of publications on active controls where the number of references per year are plotted, 3460 of them being taken from a comprehensive dat. base [11], plus several hundred new entries, and about 1000 reliable citations where the papers have not yet been available. The frequency of publications is still increasing exponentially (the seeming drop in the last few years is due to incompleteness of data). Active *noise* control papers amount to about 1/3 of the total number.

REFERENCES ON ACTIVE CONTROLS

(January 1992)
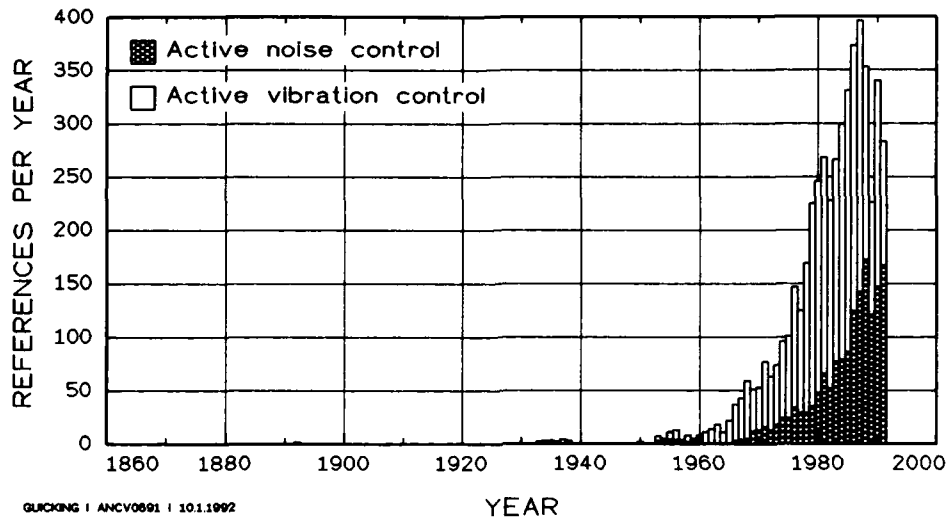
Fig. 1. Histogram of publications on active noise and vibration control.

The regional distribution can be seen from Fig. 2. Until very recently, Europe has been leading in this field, but meanwhile the U.S. and Japanese contributions are prevailing. This is even more pronounced for commercial products as will be outlined below.

REFERENCES ON ACTIVE NOISE CONTROL

(January 1992)
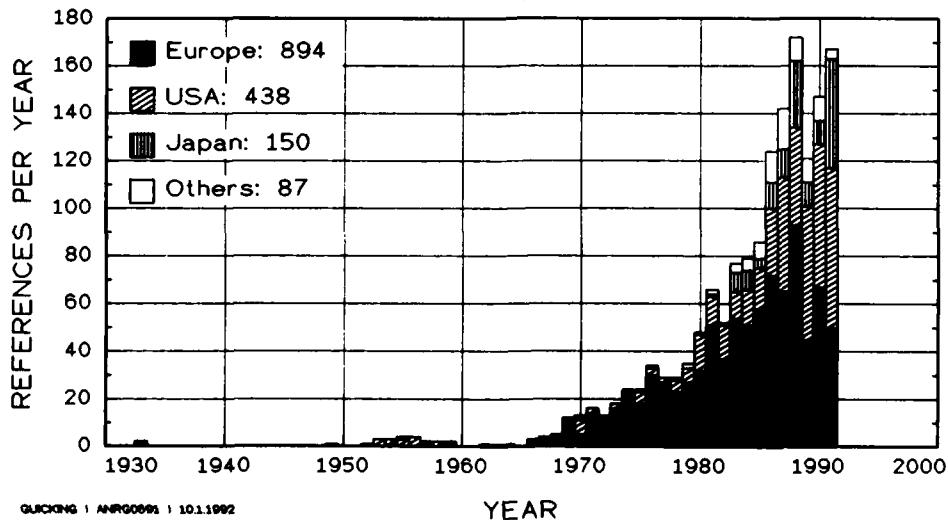
Fig. 2. Histogram of publications on active noise control.

INDUSTRIAL PRODUCTS

Broadband Duct Noise Silencers

A traditional field of active noise control research has been the cancellation of fan noise in ventilation ducts etc. where the fact of one-dimensional propagation at low frequencies facilitates the application of active controls. Since 1987, the U.S. company DIGISONIX, a division of NELSON INDUSTRIES, manufactures active systems as an alternative or supplement to their conventional passive silencers [6]. Several Japanese companies are offering lately very similar active noise control systems: EBARA CORPORATION [12] combines DIGISONIX controllers with their own transducers, while HITACHI PLANT ENGINEERING & CONSTRUCTION CO. [13] and MITSUBISHI HEAVY INDUSTRIES [14] have developed their own products. HITACHI propagates applications in HVAC installations of concert halls, auditoriums etc., while MITSUBISHI appears to favor industrial applications. Typically, stochastic noise can be reduced by 10–20 dB in the frequency range above about 30 Hz, tonal components by up to 40 dB. A new DIGISONIX product, the *DIGIDUCT* ^{TM}, combines passive absorption with active cancellation in a duct and yields 12–20 dB broadband reduction from 40 to 160 Hz in HVAC systems [15]. The lower frequency limit of the active system is determined by turbulent pressure fluctuations which must not be picked up by the input microphone (usually an antiturbulence "NEISE microphone" the maximum length of which is set by the individual installation situation), the upper limit by the cut-on frequency for higher-mode sound propagation in the duct or, in narrow ducts, by the signal processor speed (about 3 kHz).

Broadband Active Headphones

Noise cancellation at the ear by a modified headphone has first been proposed in 1949 [16]. The U.S. company BOSE [17] and the German company SENNHEISER [18] have developed noise canceling headsets for application in aircraft cockpits. They transmit speech communication signals as usual, but reduce ambient noise by 5–25 dB in the frequency range from 30 Hz to 2.5 kHz. SENNHEISER also offers noise canceling headphones without signal communication, both open-backed (with feedforward control) and closed-backed (with feedback control). The latter provides a noise level reduction of better than 25 dB above 40 Hz [19]. SENNHEISER hopes to sell active hearing protectors also for car drivers, but this will only be possible after changing the legislation (at least in Germany). All active headphones on the market employ analog electronics.

Repetitive Noise, Waveform Synthesis

The earliest digital active noise control system was developed by B. CHAPLIN in England to cancel periodic disturbances by "waveform synthesis," a conceptually simple adaptive procedure [20]. Basing on CHAPLIN's patents, the U.S. companies NCT [21] and ANVT [22] compete in developing commercial systems. Since a few years, NCT is successfully selling an accessory equipment to medical diagnostic centers by which patients in magnetic resonance imaging (RMI) scanners can be protected against the annoying impulsive noise [23]. A special feature of this system is a pneumatic headphone since no metal must be brought into the scan room.

Both NCT and ANVT have developed electronic mufflers for automobiles and hope for mass production in near future [24, 25]. NCT, in a joint venture with WALKER MANUFACTURING, have developed active mufflers for industrial applications, particularly for material handling transfer units [26]. In another project, NCT are developing active headphones that eliminate machine-related periodic components from the sound impinging on the wearer's ears [27]. NCT have also developed a local noise canceling feedback system according to an old idea of OLSON [2] and installed this in the headrest of an easy-chair. They propose aircraft cabins to be provided with their "Silentseat" [28]. With their new processor, NCT 2010, they enter the field of multichannel repetitive noise cancellation.

Repetitive Noise, LMS Controllers

Waveform synthesis is not the only way to generate the canceling signal for (quasi)periodic noise. Another method is adaptive tracking control in combination with the LMS algorithm.

The potential of this technology for canceling the interior noise in cars has been investigated in England by LOTUS ENGINEERING in cooperation with the University of Southampton [29]. The Japanese car manufacturer NISSAN has obviously started a field test of this system by series installation in a new model, which, however, is sold only in Japan so far. Many other automobile companies all over the word are known to develop their own systems.

It would be fine to have better (e. g., active) noise control in more technical equipment of everyday life. This is often a financial problem since the products should not be much more expensive with than without noise control. The first product of this type on the market is a refrigerator with active noise canceling of the periodic motor and compressor noise. It is the model GR-W 40 NVI of TOSHIBA COR-PORATION, sold in Japan for ¥ 300 000 as compared to ¥ 250 000 for the same model without active cancellation.

RECENT RESEARCH ACTIVITIES

Scanning the programs or proceedings of recent acoustics meetings and special conferences [30, 31], we observe particular emphasis on the active control of sound fields in three-dimensional spaces (rooms, vehicles), on algorithms, and on the active control of sound radiation from vibrating structures. The percentage of the formerly dominant papers on duct noise cancellation is decreasing, but it is still a subject of concern. In the following, the main directions in the different research fields of active noise control shall be outlined.

Duct Noise

The DIGISONIX and comparable Japanese systems by which low frequency stochastic noise is cancelled, employ adaptive digital feedforward controllers. Usually, the "filtered-x algorithm," a modification of the well-known LMS (least mean square) algorithm is applied which compensates for the decorrelation of the input, $x(t)$, and the error signal, $e(t)$, by (acoustic and electronic) delay in the error path. Including adaptive cancellation of acoustic feedback by another adaptive filter, both can be combined in a recursive adaptive filter (RLMS, also the "FEINTUCH" algorithm has been applied [32]). More recently this has been extended to the "filtered-u" and other recursive adaptive feedforward algorithms, also in combination with feedback control for the cancellation of repetitive signal components [33]. An independent auxiliary noise source has here been applied for the identification of the acoustic transfer functions; a newly developed circuitry with "overall modeling" utilizes the duct noise itself for this purpose [34]. The problem of optimizing the filter convergence has led to further algorithm modifications, however requiring greater computation complexity [35]. Further research activities aim at developing systems that are capable of canceling not only plane waves but also higher modes of sound propagation in the duct. This requires additional hardware (loudspeakers and microphones) and more sophisticated algorithms [36].

Structural Sound

Active noise and vibration control combine in the development of means for reducing sound radiation from vibrating structures. The interaction of structure and sound field renders special sensor and controller problems [37], but the weak coupling of sound into accelerometer signals may also reduce acoustic feedback [38]. Much work is being devoted to the investigation of possibilities for applying distributed sensors and actuators (piezoceramics and piezopolymers) [e. g., 39, 40]. Research work in this field is still in the laboratory stage; all papers deal with model experiments on plates, shells, etc. This does not only apply to airborne sound, but also to underwater noise, e. g., the reduction of sound radiation from submarines etc. [41].

Interior Spaces

Active control of noise in three-dimensional enclosures has been and is being investigated in many laboratories. At low frequencies where non-overlapping resonances occur, modal control is possible, i. e., a single loudspeaker is able to cancel the sound field in the whole room (unless it is positioned in a node of the standing wave pattern). An example is the "boom" in cars, a resonance of the air volume which is often excited by an inherent unbalance of four-cylinder engines. It can be actively controlled with a tracking controller and relatively few transducers [29]. While this problem seems to be solved, the active control of broadband noise in cars and propeller airplanes is still a matter of intense research. The difficulties encountered by poorly identified primary sources, transmission paths etc. have been outlined in [42]. Multichannel algorithms have been developed and tested in model experiments [43]. Most of the interior noise in vehicles is transmitted from vibrating parts of the hull. An alternative to cancellation by loudspeakers is therefore the compensation of wall vibrations by appropriately located and driven actuators. The concept and model experiments are presented in [44].

Much work has been devoted to the question of optimal control of 3-dim. sound fields [10 (Ch. 5–

12), 45]. Related problems in room acoustics are the equalization of sound fields [46] and the multiple channel sound reproduction [47] which is also important for natural speech reproduction in tele- and videoconference systems (including correct speaker localization) [48, 49]. A similar technique has been applied to compensate for the distortion of sonic boom signals by the test chamber [50]. Fundamental problems of power minimization and source interaction have been adressed in [51].

Algorithms

Some widely used adaptive algorithms have been mentioned above: LMS, RLMS, filtered-x, FEIN-TUCH, and also the extension to multichannel versions; for an overview, see [52]. The advantages of lattice filters are discussed in [53], stability and robustness properties of different algorithms are compared in [54–56], the applicability of intensity-related methods is discussed in [57]. As new concepts for active controls have been introduced "genetic algorithms" [58], the control of chaotic systems [59], and H^∞ control [60].

Echo Cancellation

Active noise control has benefitted from algorithm development for applications to other fields, in particular to echo cancellation on telephone lines where echoes occur at impedance steps in the "hybrid" which connects 4-wire to 2-wire lines. These echoes became audible with the long delays in satellite communication links, and it is standard technology since many years to cancel them adaptively. More difficult is the cancellation of acoustic echoes due to room reverberation. The problem occurs in teleconferencing and other hands-free telephone systems where the echoes degrade speech intelligibility and cause howling instability problems. An advanced speech controlled teleconference system is introduced in [61]. A combined acoustic and line echo canceler has recently been developed [62], and improved algorithms, e. g. reducing the time delay in digital signal processing, are presented in [63–66]. The same compensation technique can be applied in ultrasonic testing where, e. g., in composite materials echoes from internal boundaries could mask echoes from flaws [67].

Miscellaneous Applications

Some recently published subjects would not fit into the categories given above, they shall be collected in this final section. A new method of reducing propeller aircraft noise at the ground by controlled interference of propeller and exhaust noise has been developed by M. KALLERGIS [68, 69]. Active improvement of the performance of a noise barrier has been investigated by S. ISE [70]. The active cancellation technique has successfully been applied to reduce disturbing pump noise in an acoustic fault diagnosis system to monitor gear defects [71]. As an alternative to the acoustic control of exhaust noise (see above), an adaptively tuned Helmholtz resonator may be applied [72]. Vibrations excited by turbulent boundary layer flow are one noise source in aircraft cabins. They can be damped by passive and active means as has been outlined in [73]. Active compensation for loudspeaker nonlinear distortion is possible at 44 kHz sampling rate with a 20 MHz signal processor [74]. Nonlinear controllers have been applied to actively compensate for road noise in a car [75]. Coherence analysis is a necessary procedure in active noise control design if the primary sources are uncertain. Its extension to nonlinear transfer functions is possible by "transspectral coherence" [76]. Neural networks have been tested for their applicability in active noise and vibration control [77, 78].

CONCLUSION

Active noise control is no longer a laboratory curiosity; it has found numerous technical applications, and the near future will presumably bring many more. Though an occasionally observed euphoria is not justified since this technology will never solve all noise control problems, it turns out to be a reasonable supplement to traditional passive sound absorbers and insulators.

The selection and weight of topics presented in this paper—which had to be written under strong pressure of time—is naturally subjective and to my feeling not at all well balanced. I apologize to all collegues whose contributions have not been considered adequately.

REFERENCES

[1] P. LUEG: *Verfahren zur Dämpfung von Schallschwingungen.* German Patent No. 655 508. Filed: Jan. 27, 1933. Patented: Dec. 30, 1937. US equivalent: *Process of Silencing Sound Oscillations.* US Patent No. 2,043,416. Filed: March 8, 1934. Patented: June 9, 1936.

[2] H. F. OLSON and E. G. MAY (USA): *Electronic Sound Absorber.* J. Acoust. Soc. Am. 25 (1953) 1130–1136. Also: H. F. OLSON (USA): *Acoustical Engineering.* Van Nostrand, New York 1957, Chapter 9.18: *Electronic Sound and Vibration Reducers and Absorbers.*

[3] M. JESSEL: *Traduction du principe de Huygens en acoustique linéaire.* C. R. Acad. Sci. Paris 262 (1966) 1321–1324.

[4] M. A. SWINBANKS: *The active control of low frequency sound in a gas turbine compressor instal-lation.* Internoise 82, San Francisco, CA, May 17–19, 1982. Proceedings: p. 423–426.

[5] C. F. ROSS: *A demonstration of active control of broadband sound.* J. Sound Vib. 74 (1981) 411–417.

[6] L. J. ERIKSSON and M. C. ALLIE: *A Digital Sound Control System for Use in Turbulent Flows.* Noise-Con 87, State College, PA, USA, June 8–10, 1987. Proceedings: p. 365–370.

[7] G. E. WARNAKA: *Active Attenuation of Noise—The State of the Art.* Noise Control Engineering J. 18, No. 3 (1982) p. 100–110.

[8] D. C. SWANSON: *Active Attenuation of Acoustic Noise.* ASHRAE Transactions 96 (1990) 63–76.

[9] D. GUICKING: *Active Noise Control—Achievements, Problems and Perspectives.* In [30], p. 109–118. Also in: Inst. of Electronics, Information and Communication Engrs. of Japan (IEICEJ) Technical Report Vol. 91, No. 1 (April 12, 1991), p. 1–10.

[10] P. A. NELSON and S. J. ELLIOTT: *Active Control of Sound.* Academic Press, London etc. 1991, ISBN 0-12-515425-9.

[11] D. GUICKING: *Active Noise and Vibration Control.* Annotated Reference Bibliography, 3rd ed. 1988; 1st Supplement 1991 (total of 3460 References). Available: Drittes Physikalisches Institut, University of Göttingen, Bürgerstr. 42–44, D-3400 Göttingen, Germany.

[12] Anon.: *EBARA Multiple Noise Control System "EQAS".* In: [30], p. 483–486.

[13] M. TAKAHASHI, R. GOTOHDA, T. YAMADERA and K. ASAMI: *Broadband Active Noise Control of Air-Conditioning Duct Systems in Auditoriums.* In: [30], p. 273–278.

[14] H. IWATA, M. NISHIMURA, F. AOI, M. ABE and S. WATABE: *Development of Active Noise Control Duct System.* In: [30], p. 493–496.

[15] Anon.: *Broadcast Studio Quiet Assured with Active Silencing of HVAC System.* DIGISONIX Newslatter DX-SHD-4 (1991).

[16] A. V. BYKHOVSKY: *(Method of Sound Attenuation at the Ear)* (in Russian). Russian Patent No. 403 353/26. Filed: Aug. 24, 1949.

[17] R. L. MCKINLEY: *Development of Active Noise Reduction Earcups for Military Applications.* ASME Winter Annual Meeting, Anaheim, CA, Dec. 1986, Session NCA-8B. Also: Product Data Sheets of BOSE Co., USA.

[18] I. VEIT: *Gehörschutz-Kopfhörer. Elektronik kontra Lärm.* Funkschau 23/1988, p. 50–52. Also: Product Data Sheets of Sennheiser GmbH, Germany.

[19] I. VEIT: *Noise Gard—An Active Noise Compensation System for Headphones and Headsets.* Paper presented at the NATO RSG-11 Workshop, Bremen, Germany, June 5, 1991 (5 p.)

[20] G. B. B. CHAPLIN (GB): *Anti-sound — The Essex breakthrough.* Chartered Mechanical Engineer (CME) 30 (Jan. 1983) 41–47.

[21] NOISE CANCELLATION TECHNOLOGIES, INC. (NCT), Stamford, CT, and Linthicvm, MD, USA.

[22] ACTIVE NOISE AND VIBRATION TECHNOLOGIES (ANVT), Phoenix, AZ, USA.

[23] I. LEBOVICS et al.: *Siemens Approves Noise Quieting System from NCT Medical Systems for MAGNETOM MRI Systems.* NCT Pamphlet, Nov. 1, 1990.

[24] Prototype demonstration at the Conference on *Recent Advances in Active Control of Sound and Vibration,* Blacksburg, VA, USA, April 15–17, 1991.

[25] T. H. HESSE: *Commercial Considerations for the Implementation of Active Noise and Vibration Control.* In [31], p. 201–206.

[26] I. LEBOVICS et al.: *NCT and CSX Transportation Through a Co-Development Arrangement An-nounce Purchase and Installation of World's First Electronic Mufflers for Industrial Use.* NCT Pamphlet, Feb. 6, 1991.

[27] I. LEBOVICS et al.: *NCT and Foster Electric Join Forces to Produce Headset-Based Active Noise Reduction Systems.* NCT Pamphlet, March 25, 1991.

[28] G. P. EATWELL: *The Use of the Silentseat® in Aircraft Cabins.* In [31], p. 302–310.

[29] A. M. McDonald, S. J. Elliott, M. and A. Stokes: *Active Noise and Vibration Control within the Automobile.* In [30], p. 147–156.

[30] *Proceedings of the International Symposium on Active Control of Sound and Vibration ("ASJ Symposium 91"),* Tokyo, April 9–11, 1991.

[31] C. A. Rogers and C. R. Fuller (eds.): Proceedings of the Conference on *Recent Advances in Active Control of Sound and Vibration,* Blacksburg, VA, USA, April 15–17, 1991.

[32] L. J. Eriksson, M. C. Allie and R. A. Greiner: *The Selection and Application of an IIR Adaptive Filter for Use in Active Sound Attenuation.* IEEE Trans. Acoust., Speech, and Signal Processing, ASSP-35 (1987) 433–437.

[33] L. J. Eriksson: *Recursive Algorithms for Active Noise Control.* In [30], p. 137–146.

[34] L. J. Eriksson and M. C. Allie: *Active Attenuation with Overall System Modeling.* 1991 IEEE ASSP Workshop on Applications of Signal Processing to Audio and Acoustics. New Paltz, NY, Oct. 20–23, 1991 (2-page summary). And: L. J. Eriksson: *Active Acoustic Attenuation System with Overall Modeling.* US Patent No. 4,987,598. Filed: May 3, 1990. Patented: Jan. 22, 1991.

[35] E. Bjarnason: *Active Noise Cancellation using a Modified Form of the Filtered-X LMS Algorithm.* Paper to be presented at EUSIPCO '92.

[36] R. J. Silcox and S. J. Elliott: *Active Control of Multi-Dimensional Random Sound in Ducts.* NASA Technical Memorandum 102 653 (May 1990).

[37] C. R. Fuller and R. A. Burdisso: *A wave-number domain approach to the active control of structure-borne sound.* J. Acoust. Soc. Am. 89 (1991) 1:14.

[38] Y. Sato, M. Abe, T. Sone and K. Kido: *3-D Space Active Noise Control of Sounds Due to Vibration Sources.* In [30], p. 315–320.

[39] B.-T. Wang, C. R. Fuller and E. K. Dimitriadis: *Active control of noise transmission through rectangular plates using multiple piezoelectric or point force actuators.* J. Acoust. Soc. Am. 90 (1991) 2820–2830.

[40] S. E. Burke and J. E. Hubbard Jr.: *Distributed transducer vibrations control of thin plates.* J. Acoust. Soc. Am. 90 (1991) 937–944.

[41] L. D. Lafleur, F. D. Shields and J. E. Hendrix: *Acoustically active surfaces using piezorubber.* J. Acoust. Soc. Am. 90 (1991) 1230–1237.

[42] D. Guicking, M. Bronzel and W. Böhm: *Active Adaptive Noise Control in Cars.* In [31], p. 657–670.

[43] S. Laugesen and S. J. Elliott: *Multichannel Active Control of Random Noise in a Small Reverberant Room.* To be published in IEEE Trans. Acoust., Speech, and Signal Processing.

[44] S. D. Snydfr and C. H. Hansen: *Mechanisms of Active Noise Control by Vibration Sources.* J. Sound Vib. 147 (1991) 519–525. And: S. D. Snyder and C. H. Hansen: *The Effect of Modal Coupling Characteristics on One Mechanism of Active Noise Control.* In [31], p. 708–727.

[45] M. Tohyama, A. Suzuki and K. Sugiyama: *Active Power Minimization of a Sound Sorurce in a Reverberant Closed Space.* IEEE Trans. on Signal Processing 39 (1991) 246–248.

[46] S. Uto, H. Hamada, T. Miura, P. A. Nelson and S. J. Elliott: *Audio Equalizer Using Multi-Channel Adaptive Digital Filter.* In [30], p. 421–426.

[47] P. A. Nelson, H. Hamada and S. J. Elliott: *Inverse Filters for Multi-Channel Sound Reproduction.* Inst. of Electronics, Inform. and Communic. Engrs. Japan (IEICEJ) Techn. Report Vol. 91, No. 1 (April 1991), Paper No. EA91-1, p. 11–25.

[48] M. Miyoshi and N. Koizumi: *New Transaural System for Teleconferencing Service.* In [30], p. 217–222.

[49] S. Aoki and K. Matsumoto: *Stereo Reproduction Method for Teleconference.* In [30], p. 497–502.

[50] D. E. Brown and B. M. Sullivan: *Adaptive Equalization of the Acoustic Response in the NASA Langley Sonic Boom Chamber.* In [31], p. 360–371.

[51] S. J. Elliott, P. Joseph, P. A. Nelson and M. E. Johnson: *Power output minimization and power absorption in the active control of sound.* J. Acoust. Soc. Am. 90 (1991) 2501–2512.

[52] H. Hamada: *Signal Processing for Active Control – Adaptive Signal Processing.* In [30], p. 33–44.

[53] N. C. Mackenzie and C. H. Hansen: *The Implementation of a Lattice Filter Structure and Suitable Algorithm for an Adaptive Active Noise Control System.* In [31], p. 372–388

[54] D. C. Swanson: *A Stability Robustness Comparison of Adaptive Feedforward and Feedback Control Algorithms.* In [31], p. 754–767.

[55] C. C. Boucher, S. J. Elliott and P. A. Nelson: *The Effects of Modelling Errors on the Performance and Stability of Active noise Control Systems.* In [31], p. 290–301.

[56] H. Fan and R. Vermuri: *Robust Adaptive Algorithms for Active Noise and Vibration Control.* ICASSP 1990. Proceedings: Vol. 2, p. 1137–1140.

[57] J. Hald: *A Power Controlled Active Noise Cancellation Technique.* In [30], p. 285–290.

[58] A. R. D. Curtis: *An Application of Genetic Algorithms to Active Vibration Control.* In [31], p. 338–347.

[59] M. L. Spano, W. L. Ditto and S. N. Rauseo: *Exploitation of Chaos for Active Control: An Experiment.* In [31], p. 348–359.

[60] K. Nonami: *Robust Control for Mechanical Vibration Systems Using H^∞ Control Theory.* In [30], p. 165–174.

[61] J. L. Flanagan, D. A. Berkley and K. L. Shipley: *A Digital Teleconferencing System with Integrated Modalities for Human/Machine Communication; HuMaNet.* ICASSP 91. Proceedings: Vol. 5, p. 3577–3579.

[62] M. Kuo and J. Chen: *Full-duplex speakerphone with acoustic and line echo cancelers.* J. Acoust. Soc. Am. 89 (1991) 1944 (Abstract).

[63] P. J. Van Gerwen et al.: *Digital Echo Canceler.* US Patent No. 4,903,247, granted 20 February 1990. Review: J. Acoust. Soc. Am. 89 (1991) 3033.

[64] S. Makino and Y. Kaneda: *Acoustic Echo Canceler Algorithm Based on the Variation Characteristics of a Room Impulse Response.* ICASSP 1990. Proceedings: Vol. 2, p. 1133–1136.

[65] S. L. Gay and R. J. Mammone: *Fast Converging Subband Acoustic Echo Cancellation Using RAP on the WE® DSP16A.* ICASSP 1990. Proceedings: Vol. 2, p. 1141–1144.

[66] B. Hätty: *Recursive Least Squares Algorithms Using Multirate Systems for Cancellation of Acoustic Echoes.* ICASSP 1990. Proceedings: Vol. 2, p. 1145–1148.

[67] D. H. Gilbert: *Echo Cancellation System.* US Patent No. 4,875,372, granted 24 Oct. 1989. Review: J. Acoust. Soc. Am. 89 (1991) 1486.

[68] M. Kallergis: *Akustisches Modell zur Berechnung der Interferenz zwischen Propeller- und Kolbenmotor-Geräuschen.* In: Fortschritte der Akustik — DAGA'91, p. 413–416.

[69] M. Kallergis: *Method of Reducing the Overflying Noise of Airplanes Having a Propeller Driven by a Piston Engine.* US Patent No. 4,934,483, granted: 19 June 1990. Review: J. Acoust. Soc. Am. 90 (1991) 1709.

[70] S. Ise, H. Yano and H. Tachibana: *Application of Active Control to Noise Barrier.* In [30], p. 309–314. And: S. Ise: *(Study of Active Noise Control to Apply to the Field of Architectural Acoustics)*.Ph. D. Thesis (152 p.), University of Tokyo, March 1991. (In Japansese, English summary (18 p.) available from the author).

[71] W.-C. Chiu: *Application of Active Noise Cancellation for Source Identification and Monitoring in a Modal Environment.* Ph. D. Thesis, Graduate Program in Acoustics, Pennsylvania State University, University Park, PA, May 1990. Review: J. Acoust. Soc. Am. 90 (1991) 3375.

[72] T. Izumi and H. Takami: *Muffler System Controlling an Aperture Neck of a Resonator.* In [30], p. 261–266.

[73] L. Maestrello: *Passive and Active Control of Waves on Plate Structures Induced by Convective Loading.* In [31], p. 163–174.

[74] A. Goertz, D. Leckschat and W. Kippel: *Nichtlineare Entzerrung von Lautsprechern in Echtzeit mit einem Signalprozessor.* In: Fortschritte der Akustik — DAGA'91, p. 849–852.

[75] T. J. Sutton, S. J. Elliott and I. Moore: *Use of Nonlinear Controllers in the Active Attenuation of Road Noise Inside Cars.* In [31], p. 682–690.

[76] P. G. Vaidya and M. J. Anderson: *Use of the trans-spectral-coherence technique to separate signals from noise.* J. Acoust. Soc. Am. 89 (1991) 2370-2378.

[77] R. H. Cabell and C. R. Fuller: *A neural network adaptive controller for nonlinear processes.* J. Acoust. Soc. Am. 89 (1991) 1889 (Abstract).

[78] D. B. Bozich and H. B. MacKay: *Neurocontrollers Applied to Real-Time Vibration Cancellation at Multiple Locations.* In [31], p. 326–337.

SECOND INTERNATIONAL CONGRESS ON
RECENT DEVELOPMENTS IN AIR- AND
STRUCTURE-BORNE SOUND AND VIBRATION
MARCH 4-6, 1992   AUBURN UNIVERSITY, USA

Stochastic Active Noise Control

A.J. Efron   D. Graupe

Signal and Image Research Laboratory
Department of Electrical Engineering and Computer Science
University of Illinois at Chicago
Chicago, IL 60680-4348

Abstract

This paper describes an approach to adaptive active noise cancellation (ANC) that is based on adaptive control principles. The appproach aims at creating a physical noise-reduced environment at the vicinity of noisy machinery, for stochastic machine noise. The system uses a single microphone and is designed to drive the system's output to the white noise innaccessible residual which is the hypothetical generating sequence of the noise to be cancelled. Our approach is reduced to the explicit identification of noise, as actually measured at the loop's output, and to continuously forcing the cancellation network to follow the identified parameters in a manner that will whiten the output. To cancel in a complex acoustic environment an array of microphone-cancellation speaker pairs can be used.

INTRODUCTION

Several non-adaptive ANC systems have been described in the literature in recent years that use a loud-speaker to cancel a noise source. These systems are reviewed in [1]. Adaptive ANC systems as described in [2] use a steepest descent gradient-type algorithm in conjunction with a training sequence. Another important adaptive ANC design was described by Eriksson et. al. [3, 4, 5] is based on the Widrow et.al. [6] LMS algorithm. Eriksson et. al. use two LMS algorithms to drive the system's output to a minimum, employing an input-output identification scheme that requres a delayed adaptive inverse model. This requires, in similarity to [1], access to both plant input and output. The employment of delays in the channel estimation scheme of [3, 4, 5] cause estimation errors that result in the system output being a colored time series, which is the resulting cancellation minimum.

The present approach, like that of [4], aims at adaptive stochastic ANC (not being limited to one or a few deterministic peak frequencies). The presently described structure does not requried explicit removal of acoustic feedback poles since the total result of noise source and acoustic feedback is identified. Hence, a single microphone may be employed. Our time series model, which is in terms of an inaccessible residual, is what allows this savings of an input microphone and of a separate acoustic feedback model. Furthermore, our approach identifies the actual signal and forces the cancellation channel to yield an overall closed loop system whose output is forced towards the hypothetical and inaccessible generating white noise of the noise that is to be cancelled. This allows our approach to circumvent the need for both the delay elements and the delayed adaptive inverse model. The present approach thus results in a simpler ANC system structure both in algorithm and the related need for an input source microphone.

CANCELLATION ALGORITHM

Two Microphone Case

The noise to be cancelled n_k may be given in terms of ([7], chapters 4 and 8) a pure MA (moving average) model (see Figures 1 & 2):

$$n_k = \Phi(B)w_k \tag{1}$$

where w_k is inaccessible white noise, satisfying

$$
\begin{aligned}
E\{w_k\} &= 0 \\
E\{w_k w_l\} &= W\delta_{k-l}
\end{aligned}
\tag{2}
$$

δ_{k-l} being a Kronecker delta function and B^n is the shift operator i.e. $B^n w_k = w_{k-n}$. The cancellation ("anti-noise") signal y_k may be given in terms of an input-output model (see Figure 2) as:

$$y_k = C(B)G(B)e_k \tag{3}$$

The summing junctions's output (cancellation residual error), assuming no cross-coupling in the microphones, e_k satisfies, by Figure 2:

$$e_k = y_k + n_k \tag{4}$$

via Eq.(3) and (4) becomes:

$$e_k = C(B)G(B)e_k + n_k \tag{5}$$

such that:

$$[1 - C(B)G(B)]\,e_k = n_k \tag{6}$$

namely:

$$e_k = \frac{n_k}{1 - C(B)G(B)} \tag{7}$$

Substituting for n_k from Eq.(1), Eq.(7) becomes:

$$e_k = \frac{\Phi(B)w_k}{1 - C(B)G(B)} \tag{8}$$

From basic principles of filtering and prediction theory [7, 8], the linear-optimal cancellation will be achieved when e_k is driven to satisfy

$$e_k \rightarrow \pm w_k \tag{9}$$

Namely, the correction network $C(B)$ must be set to satisfy:

$$C(B) = \frac{1 \pm \Phi(B)}{G(B)} \tag{10}$$

Of the terms required to set $C(B)$ in Eq.(10) only $\Phi(B)$ is unknown and requires identification (estimation). However, the design parameter $G(B)$ should in practice always be checked (re-identified), since it is crucial for setting $C(B)$.

$\Phi(B)$ above is repeatedly identified to facilitate repeated adaptation of $C(B)$ to any changes in noise parameters. Observe that $G(B)$ represents a fixed set of parameters of the system's construction, whose repeated identification may not be necessary. The identification of $\Phi(B)$ is performed in terms of the time series model of n_k of Eq.(1), with respect to an innaccessible white noise generating sequence (w_k). Here, a pure AR (autoregressive) model $\Phi^{-1}(B)n_k = w_k$ may be first be identified, to subsequently yield $\Phi(B)$, say by polynomial division ([7] chapter 8). The identification of relatively fixed and predeterminable $G(B)$ is an input-output identificaiton based on u_k and y_k of Figure 2.
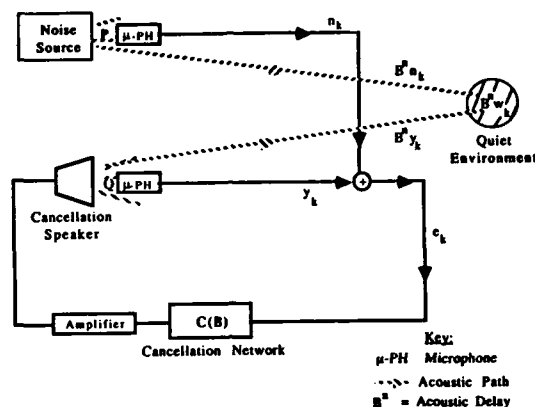
Figure 1: Schematic of Adaptive ANC System
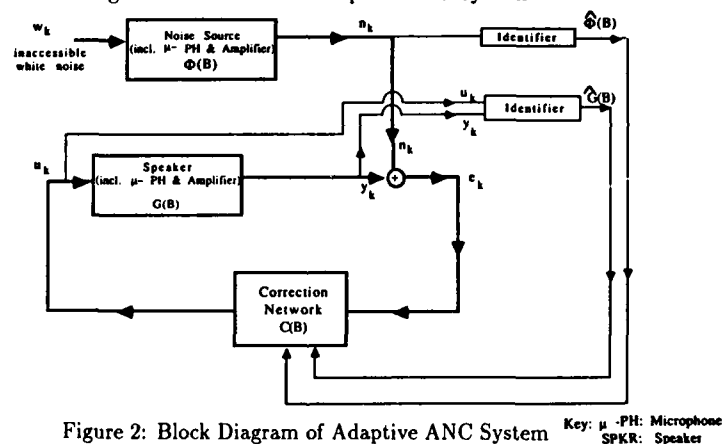
Figure 2: Block Diagram of Adaptive ANC System   Key: μ -PH: Microphone
                                                       SPKR: Speaker

Single Microphone Case

Alternatively to the system of Figure 2, a single-microphone realization of the same system can be considered as in Figure 3. In the system of Figure 3 we may substitute

$$\Phi(B) = \Psi(B)H(B) \tag{11}$$

where $\Psi(B), H(B)$ are as in that figure. We may further substitute

$$G(B) = G'(B)H'(B) \tag{12}$$

where $G'(B), H'(B)$ are as in Figure 3. $H(B)$ $(H'(B))$ above represents the acoustic link between the noise (anti-noise) source and the microphone- amplifier combination. Assuming equal distance of microphone from obth sources, we have that $H(B) = H'(B)$ in Eq.(11), (12) above. Figure 3 can thus be represented by the block diagram of Figure 4 (regardless of equality of $H(B)$ and $H'(B)$ above). In the single microphone case there is no separate identification of $\Phi(B)$ and $G(B)$ possible. Instead, $\Phi(B)$ can be identified in terms of a closed loop identification problem of the closed loop model of Figure 5 (see Reference [7], Section 8.8 pages 155-158 for details), which is a time series model for e_k in terms of an inaccessible generating white noise input sequence given by:

$$e_k = F(B)w_k \tag{13}$$

323

where, by Figure 5:

$$F(B) = \frac{\Phi(B)}{1 - C(B)G(B)} \tag{14}$$

The single microphone case suffers from the disadvantage that any delay greater than one sample length
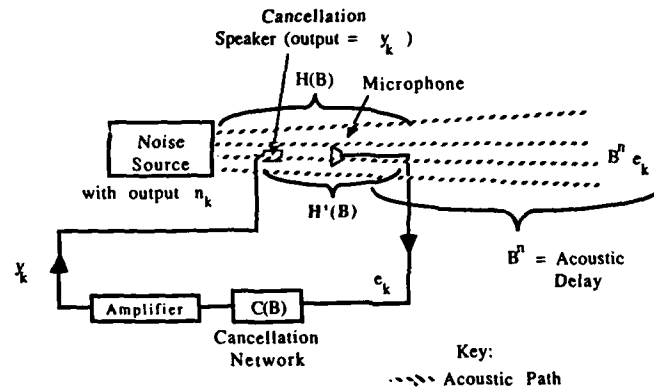
Figure 3: Single Microphone Adaptive ANC System
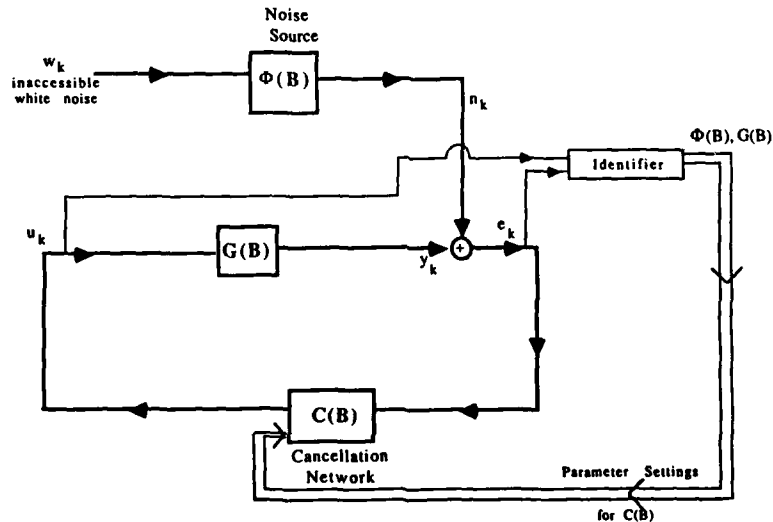
Figure 4: Block Diagram for Single Microphone ANC System

will lead to a non-minimum phase G(B). In such situations it will not be possible to totally whiten the noise. Therefore, to make the approach practical one must carefully place the cancellation speaker very close to the noise source and the microphone must be very close to the joint sound outlet of both. Cancellation will thus take place at the microphone site, however, it will hold away from it since $B^n w_k$ is also white noise as indicated in Figure 3

Considering Eq.(14), $F(B)$ may be identified from e_k, in terms of an MA (moving average) model, say via first identifying a pure AR (autoregressive) model for e_k, namely:

$$F^{-1}(B)e_k = w_k \tag{15}$$

324
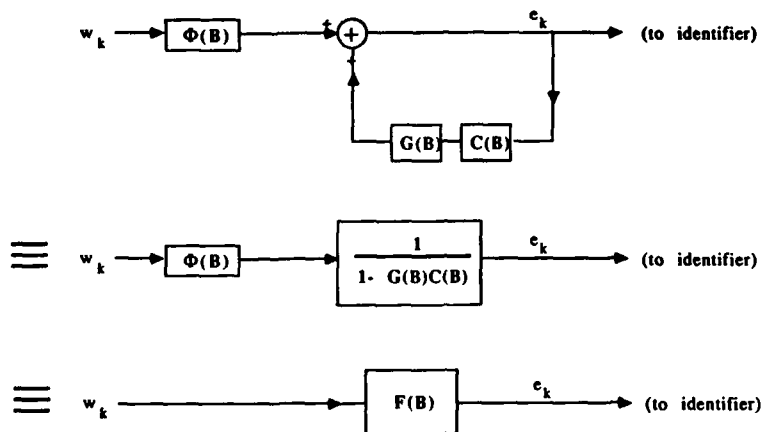
Figure 5: Time Series Model for e_k

If $G(B)$ is known (or has been identified previously) the parameters of $\Phi(B)$ are derivable from Eq.(14), since $C(B)$ is known. $C(B)$ can be updated by simply re-identifying $F(B)$ as described above and calculating $C(B)$ using Eq.(14) with the prior value of $C(B)$ and the known value of $G(B)$ (see [7], section 8.8 for details). Typically one would monitor the whiteness of e_k to determine whether any of the system parameters have changed. If $G(B)$ is not known a priori then once $F(B)$ is identified the associated ARMA model can be identified as in ([7], section 8.8). $\Phi(B)$ can be identified from the MA part and $G(B)$ from the AR part and the updating proceeds as described previously. Updating $C(B)$ is done the same manner as when $G(B)$ is known.

Array of Cancelling Speakers

More complicated environments such as a sum of random plane waves can be handled by using an array of microphone-cancellation speakers. Obviously the acoustic residual in the target array will not be white due to the differing path lengths between the different cancellation speakers. However since the noise power at each cancellation speaker is significantly reduced the overall power in the target region should be significantly reduced. This technique can be used for large diameter noise sources. The use of cancelling arrays is presently under investigation.

COMPUTATIONAL RESULTS

In this section we describe the performance of the system using recorded noise from an industrial air compressor and industrial blender. In these computations we also employ simulated speaker-microphone link with parameters as identified on-line on the actual hardware. The machine noise was recored on tape and then played through a speaker-amplifier pair. The output of the speaker-amplifier was identified as $a(B)$ which correspondes to $\Phi^{-1}(B)$ of Eq.(1). One thousand samples were used in a Sequential Least Squares algorithm to perform the identification. Also the input (recorded machine noise) along with the output of the speaker-amplifier pairs were used to identifiy its transfer function ($G(B)$). Five thousand input-output sample pairs were used in this identification to obtain an accurate $G(B)$. This realistic value of $G(B)$ was then used in the computer simulations. It was assumed that this value of $G(B)$ was known and did not need to be estimated. Figures 6 and 7 contain the results of this simulation. Reductions of

54dB and 16.7dB, respectively, were obtained.

CONCLUSIONS

We have outlined a single microphone design of an adaptive ANC system that avoids prediction of colored noise, thus achieving the optimal prediction residual. Computer simulations results using actually recorded machine noise were presented to llustrate (simulated) system performance. Real time hardware is presently being constructed at the authors Laboratory at the University of Illinois at Chicago and research into Broad-front noise sources and arrays of cancellors is being conducted.

ACKNOWLEDGEMENT

References

[1] G. Warnaka, "Active attenuation of noise - the state of the art," *Noise Control Engineering*, pp. 100-110, May-June 1983.

[2] J. Burgess, "Active adaptive sound control in a duct: A computer simulation," *Journal of the Acoustical Society of America*, vol. 70, pp. 715-726, September 1981.

[3] L. Eriksson and M. Allie, "System considerations for adaptive modelling applied to active noise control," *IEEE International Symp. of Circ. & Sys.*, June 1988.

[4] L. Eriksson, M. Allie, and R. Greiner, "The selection and application of an iir adaptive filter for use in active sound attenuation," *IEEE Transactions on Acoustics, Speech, and Signal Processing*, vol. ASSP-25, pp. 433-437, 1987.

[5] L. Eriksson and M. Allie, "A practical system for active attenuation in ducts," *J. of Sound and Vibration*, pp. 30-44, February 1988.

[6] B. Widrow, *in Aspects of Network and System Theory*. Holt, Rinehart and Winston, 1970.

[7] D. Graupe, *Time Series Analysis, Identification and Adaptive Filtering*. Kreiger, Malabar, Florida, 2 ed., 1989.

[8] G. Box and G. Jenkins, *Time Series Analysis: Forecasting and Control*. Holden Day, San Francisco, 1976.
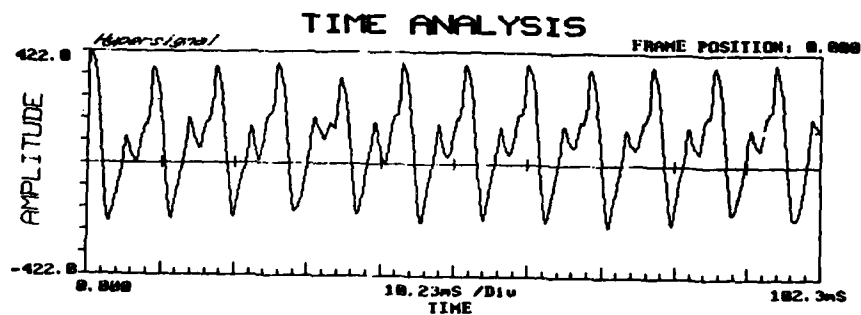
(a) prior to cancellation
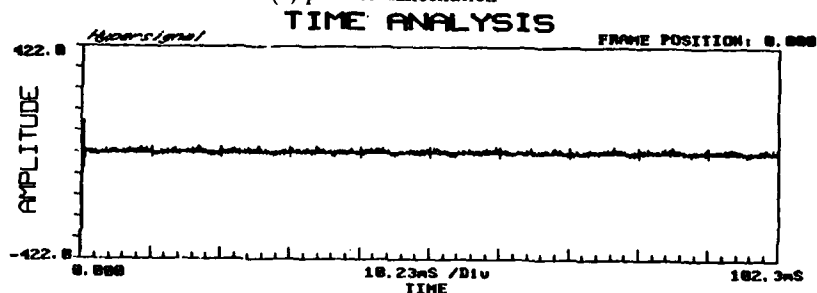
(b) after cancellation

Figure 6: Industrial Air Compressor Cancellation Results
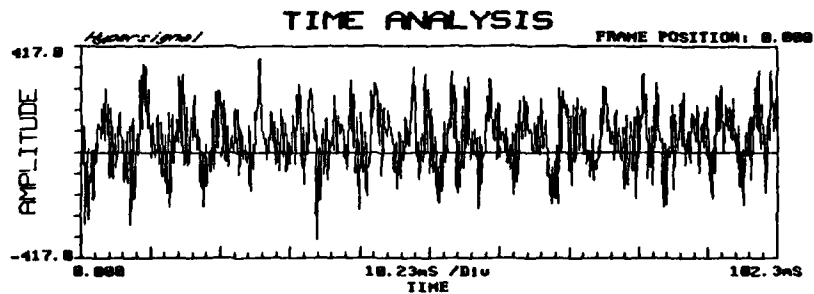
(a) prior to cancellation
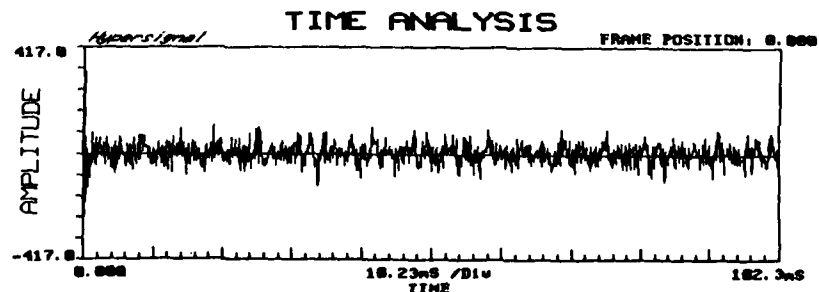
(b) after cancellation

Figure 7: Industrial Blender Cancellation Results
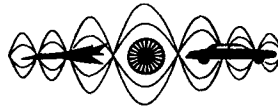
ACTIVE NOISE CONTROL
WITH INDOOR POSITIONING SYSTEM

Kenji Fukumizu, Hiroo Kitagawa, and Masahide Yoneyama
Research and Development Center, RICOH Co., Ltd.
16-1 Shin'ei-cho Kohoku-ku, Yokohama, 223, JAPAN

Active noise control (ANC) with an indoor positioning system is proposed as a method for cancelling broad-band noise in a room. When ANC is applied to broad-band noise, effective attenuation is limited to a tiny area around the control points. Many control points and loudspeakers are necessary for a large quiet zone, and calculation costs increase accordingly. To resolve this problem, a positioning system to detect the location of a person is combined with ANC. Control points and loudspeakers are arranged at appropriate intervals to cover an entire room. Only a few points and loudspeakers near the person are selectively used at any given moment. This reduces the calculation cost considerably, while providing enough attenuation to cover the entire room.

1. INTRODUCTION

In recent years amenities of living and working environments has become more essential. Quietness is an important element necessary for a comfortable environment. Undesired noise from OA processors in offices and annoying machines in factories is a serious nuisance for many workers who are sensitive to their working environment. In order to create better acoustic environments, Active noise control (ANC) technology is an attractive method for creating better acoustic environments, because (1) it can reduce the cost and space requirements for sound absorbing materials especially when attenuating low frequency noise, and (2) it can treat noise problems in a relatively general manner independent of the noise sources, if their reference signals can be measured.

The object of this research is to propose a practical system of ANC applied to broad-band noise in a room. This paper reports on the reduction of calculation costs using a practical method for maintaining a large *quiet zone*, within which noise is effectively attenuated. It is known that, when ANC is applied to noise cancellation in a room whose size is much larger than the wave length, the quiet zone is restricted physically to a very small area around the control point ([3]). A large number of control points and loudspeakers must be used in such a case. In adapting digital filters for control, it is necessary to identify and use the transfer functions for all channels between the loudspeakers and control points. This requires the control of digital filterings whose number equals the product of the number of control points times the number of loudspeakers. An attempt to obtain a large quiet zone by using many channels, thus, results in enormous calculation costs and requires super-performance processors. This is the main problem with applying ANC to a large 3-dimensional enclosure.

This paper first reports on experimental investigations into the extent of attenuation from active control of broad-band noise in a room. Suitable arrangements of control points are examined and calculation costs are discussed for the case of at least 10dB attenuation is achieved in an entire room using conventional methods.

In section 3, ANC with an *indoor positioning system* is proposed as a new method for reducing calculation costs, while maintaining sufficient noise attenuation. Detecting the location of a person's head using an indoor positioning system, the proposed system cancels only the noise around the head using a few selected control points and loudspeakers. This reduces the calculation costs considerably and makes ANC practical for even a large cavity. The effect is investigated experimentally.

2. ACTIVE CONTROL OF BROAD-BAND NOISE IN A ROOM

Theoretical results on attenuation level around a control point in a diffuse sound field ([3]) indicates that the quiet zone, within which the pressure level is at least 10 dB below that due to the primary source, is a sphere with a diameter of about one-tenth of a wavelength. The following sections report on experimental investigations into attenuation levels around multiple control points in the practical environment of a room, which is often modeled as a diffuse sound field.

2.1 Control Algorithm

The design of the controller is a feedforward model using digital FIR filters (Fig.1). To adapt the FIR filters, Multiple Error Filtered-x (MEFX) LMS ([1]) or its modification, Error Scanning (ES) technique ([2]), was adopted.

In the case of 1 noise source, L control points, and M secondary sources, MEFX LMS is summarized as follows. Let x(n) be the signal from the noise source, and $e^l(n)$ $(1 \leq l \leq L)$ be the output from the microphone Mic^l placed at the lth control point P^l (n indexes the discrete time.). W^m $(1 \leq m \leq M)$ is the FIR filter for control whose output $y^m(n)$ is emitted from the loudspeaker Sp^m as secondary sound. C^{lm} is the transfer function from Sp^m to Mic^l. Transfer functions C^{lm} must be identified as a FIR filter $\hat{C}^{lm}$ before the ordinary control process begins.

The filter output $y^m(n)$ is calculated as :

$$y^m(n) = \sum_{i=0}^{I-1} w_i^m x(n-i) . \tag{1}$$

In MEFX LMS the FIR filter W^m is adapted according as the following equation :

$$w_i^m(n+1) = w_i^m(n) - \alpha \sum_{l=1}^{L} e^l(n) r^{lm}(n-i) , \tag{2}$$

where

$$r^{lm}(n) = \sum_{j=0}^{J-1} \hat{c}_j^{lm} x(n-j) . \tag{3}$$

Note that $L \times M$ filterings are needed in each sampling time to calculate $r^{lm}(n)$. This is the main cause of the calculation cost.

2.2 Experimental Procedure

The room used in the following experiment is an ordinary office, whose dimensions are 681cm × 290cm × 270cm. A loudspeaker is placed at one side of the room as a noise source. Throughout this paper the noise is 50-250Hz band-limited white noise, whose sound pressure level is about 53-58dB(A)
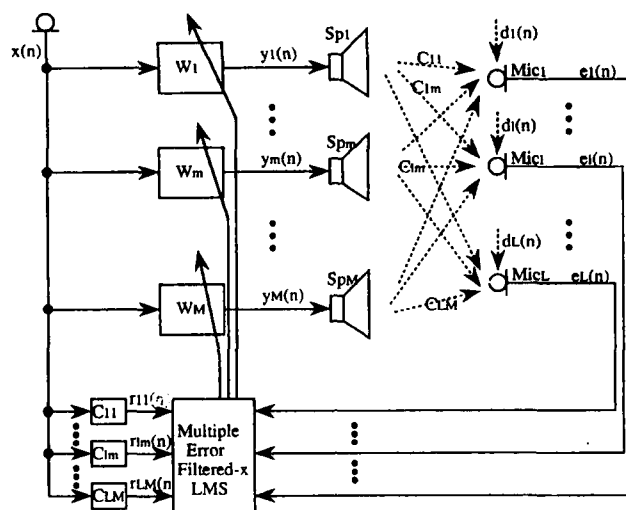
Figure 1: Multiple Error Filtered-x LMS

at control points when there is no control. The aim of the experiments is to create a 2-dimensional quiet zone.

The arrangement of the control points and loudspeakers is determined using the following principles. If the secondary source is too far from the control point, very high power output is required from the loudspeaker. The arrangement must be designed so as not to exceed the rating power and not to influence adversely on the outer area. At the same time, the loudspeakers should not obstruct the actions of the person. We investigated the suitability of various arrangements in preliminary experiments.

From the result given in [3], in the case of one-point control of 100-250Hz noise, the *quiet zone*, within which the attenuation level is at least 10dB, is 14-34cm around the control point. For multiple-control case, if each control point has a quiet zone of this size, control points must be placed rather densely, about at 30cm intervals. But we can predict on overlap of the zones in the case of using multiple control points, and therefore, the suitable interval of the control points may be greater than one-tenth of the wavelength.

Based on the reasoning above, we decided on the following speaker and control points arrangements for the experiments. Four control points, arranged at the corners of a horizontal square 170cm high from the floor, are controlled by four loudspeakers arranged to form a 150cm × 150cm square at a height of 230 cm. The size of the squares, at which the control points are arranged, is either 30, 50 or 70cm depending on the experiment. Attenuation levels of 100-200Hz octave band are measured at 10 cm intervals in an 80cm × 80cm horizontal square.

2.3 Experimental Results and Discussion

Fig.2 shows the results of experiments. The quiet zone is created around control points. According to the theoretical study in [3], the quiet zone from one control point is a sphere with a diameter of approximately one-tenth of a wavelength. This is also seen in Fig.2, where high attenuation levels are obtained around the control points. At the same time, however, *overlap* of the quiet zones can be seen where there are multiple control points, as described in the previous subsection. The center

Direction of Noise Source ↑ 10cm

1.7	3.1	5.6	8.8	8.5	8.9	4.5	4.3	3.6
3.2	5.8	6.3	8.1	10.4	9.5	7.5	6.7	4.1
3.5	4.9	7.8	9.4	14.3	11.0	10.7	5.4	3.7
3.8	6.0	7.5	11.7	12.1	12.7	9.3	6.9	3.3
5.6	7.0	8.1	11.8	15.3	16.4	12.1	7.8	4.8
5.2	6.1	8.6	11.0	14.4	14.9	12.2	7.3	4.8
3.6	5.4	6.9	9.3	11.8	14.0	10.6	7.1	2.3
2.8	4.5	4.6	6.4	9.4	9.4	8.6	6.8	3.7
1.4	3.4	3.5	6.1	5.1	6.8	5.9	6.0	2.0

(dB)

(a) 30cm

Direction of Noise Source ↑ 10cm

5.9	6.3	9.1	8.5	9.3	11.3	10.9	11.5	11.1
7.4	8.1	8.8	9.8	10.6	10.8	11.9	12.8	9.2
7.9	8.8	8.9	9.9	12.7	10.6	10.2	11.0	8.6
7.8	8.3	10.1	9.2	10.8	10.6	11.2	10.5	7.6
8.5	8.4	9.2	8.9	10.2	10.8	11.3	10.6	8.0
6.1	7.8	8.2	9.2	10.1	11.1	11.4	10.4	7.6
5.7	7.1	8.1	8.7	9.2	9.9	11.2	9.4	6.4
5.6	5.3	6.5	7.8	8.0	9.3	9.9	8.4	6.5
3.7	4.2	2.7	4.1	5.6	6.7	6.8	7.0	6.1

(dB)

(b) 50cm

O : Position of the Control Points

Direction of Noise Source ↑ 10cm

9.4	6.4	9.7	6.8	5.6	6.0	9.2	11.5	12.4
9.4	7.0	7.6	6.2	7.2	7.7	7.8	8.5	8.5
8.7	7.5	8.7	6.9	6.2	5.3	9.8	8.9	8.0
5.2	5.9	7.2	5.9	8.5	3.9	8.0	7.0	6.6
8.0	6.3	6.2	5.1	6.2	6.7	6.1	9.3	8.0
7.8	6.8	6.8	7.5	6.4	5.8	5.9	11.1	7.5
7.5	7.7	7.5	3.0	5.7	7.7	6.6	7.9	9.8
6.9	6.8	5.5	4.5	4.7	7.5	6.3	7.3	7.7
5.3	6.3	3.4	6.0	4.7	3.3	6.9	6.9	7.0

(dB)

(c) 70cm

Figure 2: Attenuation Levels

of the four control points exhibits fairly good attenuation in Fig.2 (a) and (b), when compared with the control points themselves, and generally speaking, better cancellation is achieved in the square surrounded by the four control points than in the outer area. This phenomenon is considered to be overlap of the effects from each of the control points.

These results indicates that approximately 50cm square arrangement of control points is suitable for a large quiet zone of at least 10dB attenuation. A 30cm square results in a smaller quiet zone, although the center of the control points shows very good attenuation due to the overlap phenomenon. A 70cm square, conversely, shows an ineffective zone at the center of the four control points because the overlap effect is comparatively small, and attenuation is weaker over the whole region.

We can calculate an example of the calculation cost for adapting the filters, assuming that at some height whole room should become a quiet zone. As we can see from the above discussion, control points should be arranged at intervals of 50cm over the entire room to obtain 10dB attenuation. With this assumptions, a 681cm × 290cm room requires 14 × 6 = 98 control points. If loudspeakers are arranged at 150cm intervals, they number 5 × 3 = 15. From the discussion in section 2, adapting the FIR filters requires the calculation of 98 × 15 = 1372 (!) filterings in each sampling time. This would prevent the practical implementation of ANC in a room.

3. ANC WITH AN INDOOR POSITIONING SYSTEM

In this section, ANC equipped with an indoor positioning system is proposed to resolve the calculation cost problem described in the previous section. The proposed system includes an *indoor positioning system*, to detect the location of an object in a localized area, such as a room. Various methods for indoor positioning systems are available. One uses a silicon device for a 2-dimensional position sensor, which responds to sources of light like a photo-diode and outputs the x-y coordinates of the sources. Neither digital signal processing nor image processing are necessary. By attaching an LED to a target, one can easily construct a 3-dimensional position detector using two of these devices. The detailed implementation of a positioning system is not discussed in this paper.
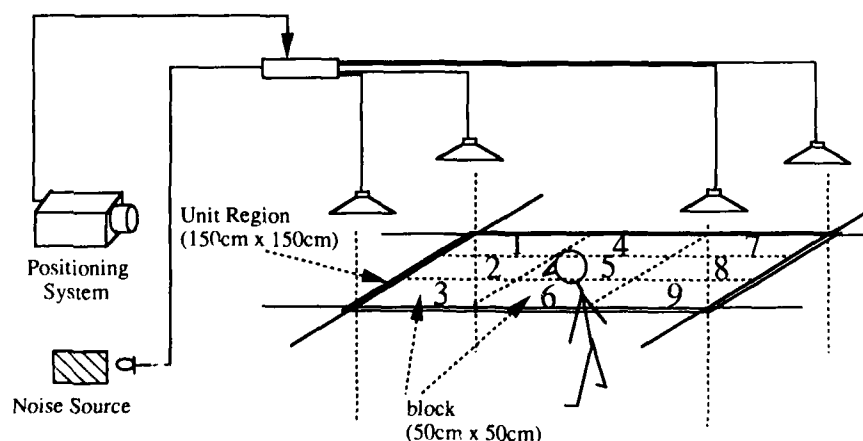
Figure 3: ANC with an Indoor Positioning System

Fig.3 is a diagram of such a system. The target space, where noise cancellation is expected, is divided into small *unit regions*. Several loudspeakers (four in Fig.3) situated above each unit

region control the noise within that region. Each unit region is further partitioned into smaller *blocks* (nine blocks in 3). Several control points (four points in Fig.3) are arranged for each block as the cancellation points for that block.

The indoor positioning system detects the location of a person's head mounted an LED, and determines which block he is in. The Active noise controller loads the filter coefficients for noise cancellation in the block, and D/A converters are switched to the loudspeakers in charge of the unit region which includes the block. Thus at any given time, only a few control points and loudspeakers (4 × 4 in Fig.3) are used.

The control strategy is a feedforward model using FIR filters. For each block, the FIR filter coefficients are prepared so that sound from the loudspeakers cancels noise at the control point for the block. Before this system is used for noise cancellation, microphones are placed at the control points and estimates of the transfer functions ($\hat{C}^{lm}$) are identified. Based on these estimates, the coefficients for the FIR filters are determined using MEFX LMS algorithm. In this case, the calculation costs are only those of the small ANC system for a block. Once determined, the filter coefficients are fixed and the microphones are removed during ordinary usage.

By determining the position of a person and switching the coefficients at each sampling time, ANC with an indoor positioning system can always create quiet zone around the person. The calculation costs for cancellation within the entire room can be reduced to that needed for a small block.

4. EXPERIMENTS

4.1 Procedure

The proposed system is being applied to practical noise attenuation within a room (the same room in section 2). The target of the control is a 2-dimensional space at a height of 170cm. One unit region is a 150cm × 150cm square. Each unit region is divided into 9 blocks, each 50cm × 50cm. Four loudspeakers are arranged 60cm above the four corners of a unit region, and four control points are placed at the corners of each block. Four FIR filters W work during cancellation, and 4 × 4 = 16 estimates of $\hat{C}^{lm}$, identified before control, are used to determine W. The filter length of W is 256 and $\hat{C}$ 128. The characteristics of the noise and the measurement method are the same as for the experiments in section 2. The attenuation level in 3 blocks in a unit region are measured assuming that each block is controlled at its control points.

4.2 Results and Discussion

Fig.4 is the result. As we can see, more than 10dB attenuation can be achieved in almost all three blocks. By arranging unit regions to cover the entire room and detecting the position of a person, the system can create a quiet zone across the whole room.

In this experiment, the calculation cost of $\hat{C}^{lm}$ filterings (Eq.3) is 128 length × 16 convolutions for each sampling time (1 msec is enough for Nyquist). 1 msec / (16 × 128) = 488 nsec can be assigned for a multiplication-and-add calculation, if these filterings only are carried out. Using current device technology, one or a few DSP can perform the calculation even if other factors increase the burden. If such a large quiet zone were created using the conventional method, the calculation cost would be about 86 times (1372 filters) of the proposed system, and the implementation would simply be a fantasy.

The proposed system uses fixed signal processing during control. The effect of changing environments is investigated in another set of experiments. After the filter coefficients are determined for an ANC system with one control point and one loudspeaker with a closed door and a closed window, changes in attenuation level are observed (1) with the door (of dimension 90cm × 200cm) open, and (2) with the window (195cm × 100cm) open.

Block #3

Block #2

Block #1

Block #6

8.9	9.9	12.7	10.8	10.2
10.1	9.2	10.8	10.6	11.2
9.2	8.9	10.2	10.8	11.3
8.2	9.2	10.1	11.1	11.4
8.1	8.7	9.2	9.9	11.2

Block #4

8.0	9.8	11.8	10.6	10.9	11.3	11.7	10.8	11.4	13.2
9.5	11.0	11.3	13.1	11.7	11.6	13.2	14.1	12.0	11.7
8.4	12.0	12.9	13.2	13.0	10.9	12.3	12.7	12.7	12.5
9.9	10.8	10.4	11.8	11.7	12.7	12.5	12.8	12.6	12.4
8.6	8.6	8.7	8.2	7.8	10.6	10.5	11.0	10.7	10.4

Block #7

(dB)   : more than 10dB
              : 8dB - 10dB

Figure 4: Attenuation Level in a Unit Region

Table 1 shows the results. With the window open, the unfavorable influence is only 3.9dB. But the open door, situated relatively close to the control point, affects rather severely the attenuation level. We can conclude experimentally that fixed signal processing works well, if the change in the acoustic environment is small. Further experimental studies and theoretical analysis are necessary to determine the limits of fixed processing as affected by change in the environment.

5. CONCLUSION

This paper has described a practical method for implementing ANC for broad band noise in a large cavity. It has been experimentally shown that, combined with an indoor positioning system, the ANC system can achieve high attenuation levels over an entire room and greatly reduce calculation costs. Even fixed signal processing works well enough for practical use if the acoustic environment changes little. The authors plan to apply the concept of ANC with an indoor positioning system to more practical problems and investigate the performance of the system.

Table 1: Effect of changing in the environment

	Att (dB)
regular	12.0
door open	5.6
window open	8.1

ACKNOWLEDGMENTS

References

[1] S.J.Elliot, I.M.Stothers and P.A.Nelson, "A Multiple Error LMS Algorithm and Its Application to the Active Control of Sound and Vibration", *IEEE Trans. ASSP* Vol. ASSP-35 No.10, 1987. pp.1423-1434

[2] H.Hamada "Signal Processing for Active Control - Adaptive Signal Processing - ", *Proc. International Symp. Active Control of Sound and Vibration (ASJ Symp. 91)*, 1991. pp.33-44

[3] S.J.Elliot, P.Joseph, A.J.Bullmore, and P.A.Nelson, "Active cancellation at a point in a pure tone diffuse sound field", *Journal of Sound and Vibration* 120 (1), 1988. pp.183-189

**SECOND INTERNATIONAL CONGRESS ON
RECENT DEVELOPMENTS IN AIR- AND
STRUCTURE-BORNE SOUND AND VIBRATION**

MARCH 4-6, 1992   AUBURN UNIVERSITY, USA

A NEW TECHNIQUE FOR THE ACTIVE CANCELLATION
OF WIDE-BAND NOISE USING MULTIPLE SENSORS

by Felix Rosenthal[*]
Annandale, Virginia 22003, U.S.A.

([*]The author is a Research Mechanical Engineer at
Naval Research Laboratory, Washington, DC 20375)

ABSTRACT

In the classical method of active noise cancellation, wide-band performance is often limited by an inability to utilize a sufficient number of sensors and actuators. A new technique is presented in which the number of such sensors and actuators is limited only by space and computational resources, and in which the utilization of all actuators is optimally controlled for every frequency of the noise to be cancelled. This technique also optimizes the cancellation process even for narrow band noise. It is applicable to methods employing Wiener, adaptive, or other types of filter mechanisms, and can be operated in either the frequency or the time domain. The new technique and its applications are the subject of pending U.S. Patent Office and Patent Cooperation Treaty applications by the author, who would be pleased to entertain possible licensing and related agreements with one or more organizations interested in utilizing this new technology.

INTRODUCTION

In many applications of classic noise cancelling procedures, it has been found that:

- It is advantageous to utilize multiple sensors and/or actuators rather than a single one. This is particularly important when the noise source consists of multiple independent components, or when a range of conditions such as a relatively wide band of frequencies is to be accommodated in the cancellation process.

- If a certain number actuators is exceeded, cancellation becomes worse instead of better.

The need for multiple sensor/actuators is readily understood in the presence of multiple noise sources which cannot all be adequately cancelled by a single cancelling microphone and loudspeaker. Multiple sensor/actuators are also needed when a relatively wide band of frequencies is to be cancelled consistently. The reason for the need in this instance is that the various frequencies generally call for various sensor/actuator locations, so that a number of these need to be available for wide-band use. This problem is graphically illustrated in the sonar example demonstrated in this paper.

The second item, the apparent limit on the number of actuators which can actually be used, is familiar to those in the industry who might have attempted to use "too many." There are of course the obvious limitations such as the availability of space and computation resources,

337

but often the process seems to degrade well before these limits are reached. The culprit in this instance is the presence of redundant information, which precludes the accurate calculation of the required filters. And unfortunately, in wide-band cancelling, the degree of redundancy generated is itself frequency-dependent. These problems and the means to solve them are also illustrated in the sonar example below.

VARIOUS KINDS OF NOISE CANCELLING

Noise cancelling may be classified[1] into sensor noise cancelling in which typically noise is to be removed from one or more primary sensor outputs, and the active variety of noise cancelling in which actual physical noise is to be removed or attenuated by adding anti-sound having opposite phase. In sensor noise cancelling, one typically wishes to separate from the primary sensor the coherent portions of noise which is simultaneously picked up by the noise or signal-free reference sensors. The differences in the case of active noise cancelling are that (1) one needs loudspeakers to produce the anti-noise, and (2) there is generally no signal to be salvaged. Noise cancelling may also be classified according to the type of filtering used: whether it is "Kalman", "Wiener" or one of several possible adaptive approximations to the Wiener algorithm. Cancellation is still further classifiable according to the width of the frequency bands to be cancelled or the geometry of the process: active cancellation can be designed for silence at a point, silence in a spatial region, or attenuation of noise around a source, and many examples exist of all of these. As far as we know, the techniques presented here are applicable to all the above instances of noise cancelling, although the experiment which is described below was done in the context of cancelling noises perceived by a sensor (signal-noise separation except that the primary or signal sensor received only noise, whose presence in the output was to be minimized).

SOME PROBLEMS WITH CLASSICAL NOISE CANCELLING

Redundancy of Noise and Loss of Signal:
In the Introduction we alluded to the fact that noises to be cancelled can under some conditions contain "redundant" information. Consider for example a case comprising two "reference" sensors both coherently receiving the same source of noise. To cancel the noise, how are the sensor outputs to be optimally combined, using some Wiener filter or approximating adaptive algorithm, when in truth either of the two sensor signals or indeed any combination of them will all work equally well? Or, in the active case, how would we properly apportion the anti-noise to the available loudspeakers? The problem amounts to nothing less than an attempt to find the intersection of two coincident lines or, in the language of linear algebra, the inversion of a singular matrix, to find the best filter constants. True, computers often produce not singular matrices but rather ill-conditioned or "rank deficient" ones, but the results are similar: large round-off errors and under extreme conditions "floating point division by zero" errors. And what happens when the number of independent sources is, say, 2 at one frequency and 6 at another? How many sensors should we then use and where should they be located? And finally, there is another question in the case of signal-noise separation: What happens if a small amount of signal enters one or more of the noise or reference sensors? Who is going to explain to the computer that this is a signal and is not to be touched? All that the computer has been instructed to do was to follow an unconstrained Wiener algorithm or some approximation to it: Find anything that you can in the reference sensors, and if it is coherent with something that also exists in the primary then cancel it, no matter how much you might first have to amplify it! A perfect prescription for cancelling the signal right along with the noise.

What is the Optimal Number of References or Loudspeakers ?
There is an interesting footnote in Widrow et al's classical 1975 paper on noise cancelling[2], reprinted as Chapter 12 of his 1985 book[3]. The footnote attempts to answer the question of why exactly four maternal chest leads were used in the reported experiments on fetal electrocardiography. "More than one input was used to make the interference filtering task

easier," according to the footnotes in References 2 and 3. "The number of reference inputs required to eliminate the maternal ECG is still under investigation."

Nonetheless, References 2 and 3 recognized very well that signal entering a reference sensor would degrade noise cancelling performance. A careful and accurate analysis is included which shows that for the most elementary case comprised of a single signal source, a single noise source, a single primary and a single reference sensor, a small amount of signal entering the reference would do no more than a correspondingly small amount of damage to the canceller performance. But whichever of the eight co-authors wrote the section on multi-reference cancelling must have assumed that what works for one will work for all, and that turns out not to be accurate.

SVD Solves Both Problems, Redundancy and Loss of Signal:
The solution to the above-described problems of noise-redundancy and possible signal cancellation, lies with implementing a procedure known in linear algebra of "singular value decomposition." Variants of this method go under the names of eigenvalue decomposition, Gram-Schmidt orthogonalization, and Karhunen-Loeve expansions. The beauty of the method is that it not only solves the two problems referred to in a robust, optimal, and entirely automatable manner, but thinking in the language of SVD, the language of n-dimensional vector spaces and of signal and noise subspaces, illuminates our understanding of the process itself by providing rational insights into what is happening. Singular value decomposition is at once an extremely powerful and robust procedure for solving linear equations, and a way of thinking rationally about the problem. But more of this later; to obtain some insight into the need for this process, we first examine a noise cancelling example based on measurements on a hydrophone.

INSIGHT INTO A FAILURE OF THE CLASSICAL METHOD AND HOW TO FIX IT: CANCELLING VIBRATION NOISE IN A HYDROPHONE

System Description:
Noise cancelling was to be performed on the output of a hydrophone belonging to a sonar system. A total of fifteen accelerometers having various locations on the sonar were available as vibration-measuring noise or reference sensors. The power spectrum (more accurately the power- or auto spectral density) for this hydrophone is shown in Fig. 1. No signal was present, but the hydrophone was driven by vibrations in three major frequency ranges labelled in Fig. 1 as Band 1, 2, and 3 respectively. A total of 15 accelerometers were also available as vibration noise cancelling sensors.

Optimal Choice of Accelerometers Depends on Frequency:
Using classical techniques only, we could never use more than four accelerometers simultaneously to cancel the vibration noise, because five or more such sensors produced an excess of redundant information and prevented the accurate calculation of the required filters. With this experience, we then wanted at least to select those four of the available accelerometers which would provide the best noise cancelling performance. The noise which is cancelled from the hydrophone is that which also appears coherently in one or more references. To facilitate a good choice, Fig. 2 shows the coherence of each accelerometer with the hydrophone in question. The accelerometers are designated as sensors 0, 1, 5, ... , 23. The coherences assume values between 0 and 1 (scales not shown in the figure) over the frequency range. From Fig. 2, we can for example try to select those four accelerometers which might best cancel the noise in vibration Band 2, by choosing those with the greatest coherence in that band. Visual inspection of Fig. 2 identifies the accelerometers labelled 0, 1, 10 and 13 as reasonable although by no means unique choices.

The result of cancelling the noise using these selected accelerometers does indeed do a creditable, even if not optimal, job of cancelling the vibration in Band 2 (see Fig. 3). But the other bands, particularly No. 1, do not fare as well.

We next look at Fig. 2 again to select accelerometers for cancelling Band 1 instead. The choice of 5, 7, 18 and 20 provides the cancellation performance shown in Fig. 4. The performance is now fairly good in Band 1 but unimpressive in Band 2.

Next -- the "obvious" choice: Why not use all 8 accelerometers and perhaps things will sort themselves out. They do not, as shown in Fig. 5. Nothing works any more! The system is suffering from a severe redundancy of information .

Frequency Dependence Makes Classical Wide Band Cancelling Difficult:
This experiment demonstrates with great clarity why wide band noise cancelling is so much harder than narrow when the classical method is used. Items such as auto muffler systems and aircraft fuselages are complicated acoustic systems, for which the optimal noise-cancelling sensor and actuator locations are frequency-dependent. Use of the classical method limits us to a relatively small number of noise sensor/actuators to assure the consistent avoidance of destructive redundancies. But clearly, the same sensor types and locations will not be optimal for all frequencies, thus making a rational choice of sensor locations very difficult.

Doing it Right:
The job is done correctly as shown in Fig. 6. The new technique permits the use of all fifteen available accelerometers, while the technique itself sorts out the signals to use their optimum non-redundant combinations. Cancellation performance is now excellent over the entire frequency range of interest, using either of two slightly different versions of the new technique. (The two corrected psd curves in Fig. 6, correspond to 20 dB and 40 dB singular value thresholds). In order to understand how it is done, it will be useful to have a working understanding of the rudiments of n-dimensional Hermitian matrices and vector spaces.

SIGNALS, NOISES, AND N-DIMENSIONAL HERMITIAN VECTOR SPACES

Analyses in the Time or Frequency Domain and their Vector Spaces:
Signals received at arrays of sensors or broadcast from arrays of loudspeakers are most readily arranged in matrix form. The matrices of interest can be general rectangular ones in which each row corresponds to a time step and each column corresponds to a signal; or they can be second order statistics of the data such as real symmetric cross correlation matrices, or their Fourier Transforms which are complex Hermitian cross spectral density matrices. The signal-cancelling and noise-redundancy considerations encountered are much the same regardless of the domain, whether time or frequency, in which the analysis is performed. In each case, matrix singular value decomposition or SVD of one type or another is a powerful method of reorganizing the data into more useful form. The present paper illustrates the concepts for the case of a frequency domain analysis using Hermitian cross spectral density matrices. In the case of the rectangular signal-vs-time data matrices, signal-noise separation is sometimes accomplished by performing generalized SVD on pairs of matrices termed "pencils."

For the purpose of calculating Wiener or adaptive filters using frequency domain analysis, the time series for each sensor is first broken up into intervals, which generally overlap to increase the sample size. For some applications, these time functions may be subjected to a windowing process. For a given interval, the series are then transformed to the frequency domain, using a Fast Fourier Transform or similar algorithm, and the required cross spectral density values are calculated. This process is then repeated for other intervals of the original time series, and the results averaged over an appropriate number of such time intervals either once-through or adaptively. This results in the expected values forming the Hermitian cross-spectral density matrices. These matrices possess dimensionality equal to the number of reference signals and/or noises being measured, and there are as many of them as there

are frequency bins in the analysis. They are used to calculate the noise cancelling filters, which are subsequently applied to the frequency-transformed time series.

Each n by n Hermitian cross spectral density matrix may be associated with an n-dimensional Hermitian vector space. A given frequency component of a, y signal or noise source, or of any quantity measured at a particular sensor, may be though: of as a vector in that vector space. In a real vector space, the vectors have magnitude and direction; in a Hermitian vector space they have magnitude, phase and a complex direction as well. Two vectors have the same direction if their corresponding signals are completely correlated or have a coherence equal to 1; they are orthogonal if they are completely independent, or have a coherence equal to 0.

A Two-dimensional Example:
To illustrate these concepts, we consider the simplest case, a single signal and a single noise source, which are received at a single primary sensor and a single "signal free" reference sensor. For the purpose of this illustration, we shall assume all phases to be zero, so that the complex Hermitian space can be depicted as a real one, with the vectors as shown in Fig. 7. The length of these vectors is the amplitude of the signal or noise represented, whereas $cos(\Theta)$ is the square-root of their coherence, where Θ is the angle between them.

In Fig. 7, we assume that there is a signal source Φ_s and a noise source Φ_n. In line with the usual assumption that the noise is statistically independent from or incoherent with the signal, Φ_s and Φ_n are shown mutually orthogonal or perpendicular. Let d denote the measurement of the primary sensor, and x that of the reference. d is shown as having both signal and noise components but is shown somewhat closer to Φ_s than to Φ_n. It is assumed that the reference sensor x picks up mostly noise Φ_n, but also a smaller component of signal Φ_s. The figure exhibits the operation of the noise cancelling process in which a Wiener Filter multiplier w is used to multiply the noise sensor output x, and subtracts it from the signal vector d to form the corrected output $q = d - wx$. It does not take a great deal of imagination to see that if the reference sensor gets mostly noise, i.e., as the angle between x and Φ_n becomes sufficiently small, then the noise cancelled output q approaches the direction of the exact signal vector Φ_s and therefore becomes perfectly coherent with it. This is what Widrow et al proved analytically for this simplest case of noise cancelling.

But now let us examine what would happen if the problem were slightly more complicated. Suppose that in our ignorance we chose to use two noise sensors, x_1 and x_2, to span our presently two-dimensional signal-noise space. The Wiener algorithm would now ask what linear combination $w_1*x_1 + w_2*x_2$ should be subtracted from d to obtain the minimum output q. If, as before, we have to contend with a signal Φ_s and a noise Φ_n, then the two references will span the entire two-dimensional space and therefore q will be minimized right down to zero: the signal will have been totally cancelled along with the noise. On the other hand, if the number of references exceeds the dimensionality of the total signal-noise space, such as would be the case if there were no signal or alternatively if there were three reference sensors, then the optimization could not be solved because the references would be redundant or linearly dependent; any one of them could as well be removed without any loss of information. The computer would respond with the equivalent of a "floating point division by zero" error and stop.

Enter SVD:
In the present context, the solution to our problems lies in applying SVD to the cross spectral density matrices of the complement of reference sensors, before attempting to use these matrices in the determination of filter constants. The classical Wiener procedure would be to form, once-through or adaptively, the filter constants f by solving the matrix equation

$$Rf = p, \tag{1}$$

where R is the matrix of cross spectral densities of the n references with each other, p is the vector of cross spectral densities of the primary sensor with the references, and f is the filter vector.

To apply SVD, the reference matrix R is first transformed into a diagonal matrix D of singular- or eigen-values using a unitary (complex orthogonal) transformation matrix U whose columns are the eigenvectors of R:

$$R = UDU^*, \qquad (2)$$

where U^* is the Hermitian, or complex-conjugate, transpose of U. D has its diagonal elements or singular values arranged in descending order. If one or more of these values are equal to zero, the matrix R is termed singular and the filter constants cannot be solved. In real problems it is more usual that R and D are merely "ill-conditioned," that is, the singular values have a relatively large dynamic range. If D is nonsingular, its inverse is simply the diagonal matrix in which the reciprocals of the singular values have been substituted for the values themselves.

The recipe for the SVD procedure, however, is to first assign a "threshold" such as 1 percent or 0.01 percent of the largest singular value, and to retain only those singular values which lie no more than 20 dB or 40 dB respectively below the largest noise singular value. We thus find the "pseudo-inverse" D^{-1} of D by taking the reciprocals of only those singular values which exceed the threshold, and putting zeros everywhere else, denoting the so-called null space of the decomposition.

Substituting (2) into (1), the filters f are determined from the condition that

$$UDU^*f = p, \qquad (3)$$

or explicitly, since for a unitary matrix $U^{-1} = U^*$,

$$f = UD^{-1}U^*p, \qquad (4)$$

where D^{-1} is the pseudo-inverse of D.

The thresholds for the retention of singular values should be set far enough below the largest noise source to include all important noises in the cancellation. At the same time, they must be set close enough to preclude redundancies, i.e., to assure that the reference matrix singular values will at all frequencies have a sufficiently low dynamic range to permit what amounts to error-free inversion. Moreover, the range of retained singular values must not include the level at which a signal could appear in the output of a reference sensor.

CONCLUSION

The classical method of active noise cancellation often limits the number of reference sensors and actuators which effectively can be utilized, because of the possibility of redundancies which would prevent accurate cancellation of the noise. The occurrence of such redundancies is in general frequency-dependent. In signal-noise separation problems, similar redundancies can occur and additionally, there is a significant chance of cancelling the desired signal itself. Both the redundancy and signal cancellation difficulties can be circumvented by cleaning up the matrix of reference signals through the use of singular value decomposition. The new technique and its applications are the subject of U.S. Patent and Patent Cooperation Treaty applications.

ACKNOWLEDGEMENTS
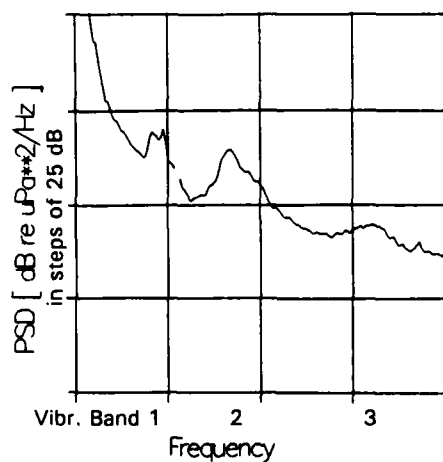
Fig. 1. Hydrophone power spectral density.
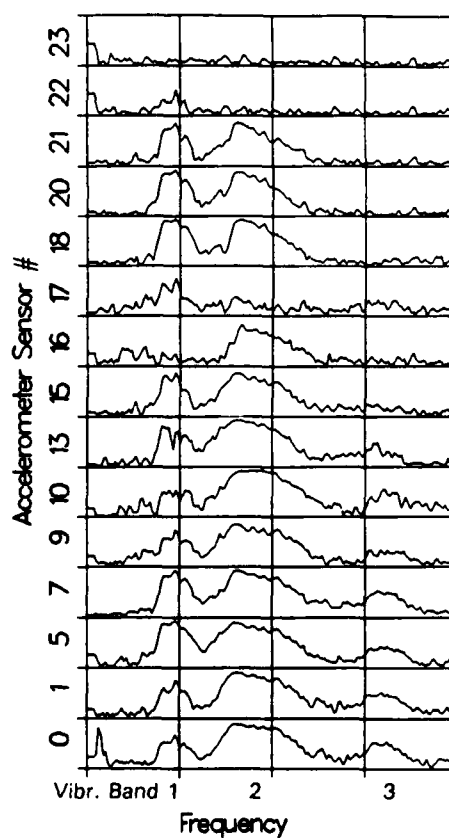
Fig. 2. Accelerometer-hydrophone coherences.

Fig. 3. Cancelling with 4 accelerometers (0, 1, 10, 13).
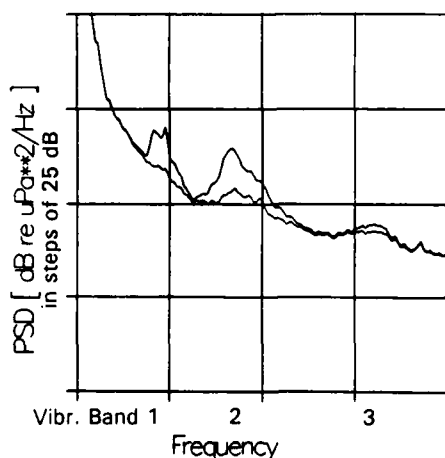
Fig. 4. Cancelling with 4 accelerometers
(5, 7, 18, 20).
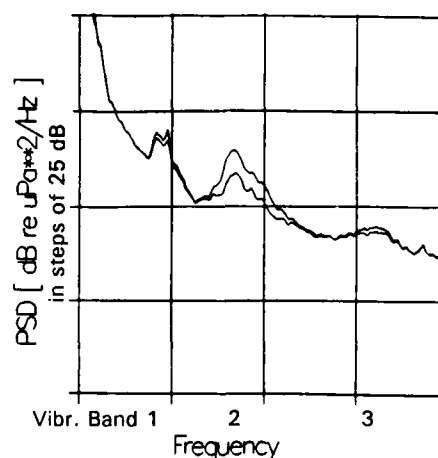
Figure 5. Cancelling with 8 accelerometers
(0, 1, 10, 13), (5, 7, 18, 20).
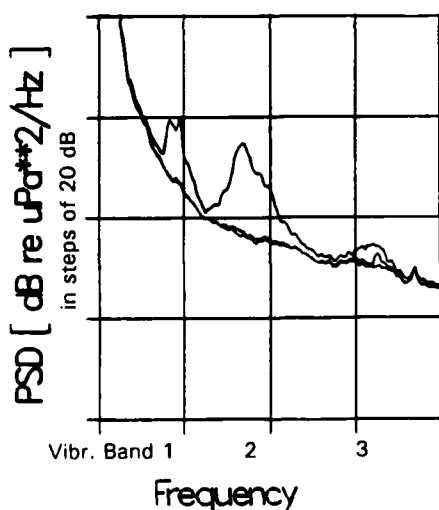
Figure 6. Cancelling at 2 levels with
all 15 accelerometers and SVD.
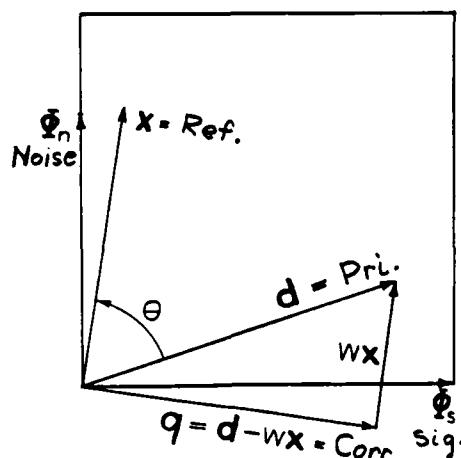
Figure 7. Sources and Sensors in a
Two-dimensional Vector Space.

REFERENCES

1. Stevens, J. C. and K. K. Ahuja, "Recent Advances in Active Noise Control", *AIAA Journal*, v. 29, no. 27, July 1991, pp. 1058-1067.

2. Widrow, Bernard, and John R. Glover, John M. McCool, John Kaunitz, Charles S. Williams, Robert H. Hearn, James R. Zeidler, Eugene Dong, Jr., and Robert C. Goodlin, "Adaptive Noise Cancelling: Principles and Applications," *Proceedings of the IEEE*, v. 63, no. 12, December 1975, pp. 1692-1719.

3. *Adaptive Signal Processing*, by Bernard Widrow and Samuel D. Stearns, Prentice-Hall, Englewood Cliffs, N.J., 1985, Ch. 12.
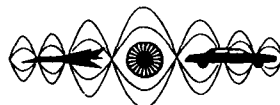
SECOND INTERNATIONAL CONGRESS ON
RECENT DEVELOPMENTS IN AIR- AND
STRUCTURE-BORNE SOUND AND VIBRATION
MARCH 4-6, 1992   AUBURN UNIVERSITY, USA

A GENERAL MULTI-CHANNEL FILTERED LMS ALGORITHM FOR 3-D ACTIVE NOISE CONTROL SYSTEMS

Sen M. Kuo and Brian M. Finn

Department of Electrical Engineering
Northern Illinois University
DeKalb, IL 60115
U.S.A

ABSTRACT

A general multi-channel filtered-x LMS algorithm with new parallel on-line error-path modeling for 3-D active noise control systems is developed and tested in this paper. An input weight vector based on the spatial placement of input microphones and cancellation speakers is proposed to mix J input signals to form a single reference signal for the adaptive filters. A modified independent cost function for each channel is used to weight the spatial significance of each error sensor output for the adaptation of the adaptive filters. The performance of the algorithm has been verified on a 3-D experimental set-up and is analyzed from both acoustical and adaptive signal processing points of view.

I. INTRODUCTION

Active Noise Control (ANC) [1] is based on the principle of superposition. Many of the successful applications to date have involved the attenuation of low-frequency noise in ducts [2,3]. The three-dimensional active noise control (ANC) system has many applications such as noise cancellation in the interior of cars, aircraft, etc. In these applications, the noise is localized, accessible and the frequency band of interest is dominated by relatively few modes. However, comparing with the conventional 1-D ANC system, the complexity of ANC in three dimensional space with many inputs and outputs is significantly higher. Many researchers have studied the problems of ANC in 3-D reverberant enclosures, from theoretical studies [4,5], computer simulation [6], to experimental testing [7,8,9].

A multiple error LMS algorithm proposed by Elliott et. al. [10] represents the first attempt to control a 3-D sound field produced by rotating machines, such as an engine, using Least Mean Square (LMS) adaptive filters. Since the undesired noise field is nearly periodic, a synthesized signal (impulse train or sinusoids) is used as a reference input. Difficulties of multiple inputs and acoustic feedback [3] are thus avoided. However, this system in not fully adaptive. A priori or separate off-line error-path modeling were required to some extent. This is only applicable in those applications where the error-paths characteristics are time invariant. In many practical applications the error-paths changes with temperature, pressure, and movement of passengers.

In this paper, a general multi-channel filtered-x LMS algorithm with fully adaptive parallel on-line error-path modeling capability is presented. An input weight vector implemented by an analog or digital mixer is proposed to combined multiple input sensor signals to form a single reference input for all channels. An individual error weight matrix for each channel is also proposed to realize the spatial significance of canceling speaker related to each error microphone. A new multi-channel on-line error-path modeling algorithm is developed based on the parallel on-line modeling algorithm proposed by Tapia and Kuo [11]. Computer simulations are conducted to demonstrate the proposed multi-channel algorithm using real transfer functions measured from the experimental setup, which consists of a 3 dimensional enclosure with approximate shape and dimension of a typical heavy equipment cabin (1.0m x 1.2m x 1.5m).

II. ACOUSTICAL CONSIDERATIONS

Acoustical phenomena, in ANC, require careful consideration for a successful transition from the signal processing domain to the overall system. As the complexity of sound fields in 3-D space is significantly

more than 1-D approximations, `he motivation for the multi-channel structure is found. ANC systems typically are focused on the elimination of noise in the lower octave bands of the audible spectrum. Because of this frequency range of interest, and the dimensions of the experimental enclosure, the normal modes are significant and well defined. Following traditional wave theory, as used to describe sound fields in rooms, specific use is made of identifying the normal modes and their associated nodal planes in the 3-D space. It is these physical phenomena which have a direct relation on the type of algorithm, number of input channels, and number of output channels used in the signal processing domain. Clearly, understanding the acoustical processes at work direct the algorithm development, but also serve to make optimal decisions on electroacoustic factors such as microphone and loudspeaker placement and selection.

The 3-D wave equation is written as

$$\frac{\partial^2 p}{\partial x^2} + \frac{\partial^2 p}{\partial y^2} + \frac{\partial^2 p}{\partial z^2} = \frac{1}{c^2}\frac{\partial^2 p}{\partial t^2}$$ (1)

where x,y,z are coordinate axes, c the speed of sound, and p the acoustic pressure. Associated with this equation for rigid wall boundary conditions are eigenfrequencies [12] given by

$$f_{lmn} = \frac{c}{2}\sqrt{\frac{l^2}{Lx^2} + \frac{m^2}{Ly^2} + \frac{n^2}{Lz^2}}$$ (2)

where l,m,n are the quantum numbers, and Lx, Ly, and Lz the dimensions of the enclosure. By predicting these lowest modes i.e. 0-0-1, 0-1-0, 1-0-0, 0-1-1 etc., for the hardwalled rectangular enclosure, empirical studies verify that characteristic frequencies very close `o these exist. Although the enclosure has damping mechanisms, and the enclosure is not a perfect rectangular box, room resonance at low frequencies follow these simplified expressions as their identity is more associated with volume than with shape [13]. With knowledge of the observed resonance frequencies, investigation of the associated mode shapes allows a view of how the ANC algorithm will interact with its acoustical environment. Three classes of modes, the axial, tangential, and oblique exist in the enclosure as solutions to the 3-D wave equation. Axial modes are typified by one non-zero quantum number, tangential by two, and oblique by the interaction of all possible states of vibration. Of these, axial exhibit the sharpest resonance features as their path length is shortest and subject to minimal decay between two sets of parallel walls. Likewise their nodal planes are easily visualized, and observed by relating the fact that cos(kx) = 0 when kx=π/2, 3π/2, ... nπ/2 where n is odd, so that spatially j nodal planes are found at distances x = λ/4, 3λ/4, ... nλ/4 where n is odd for the jth harmonic parallel to the boundary walls for the mode considered. Similarly the tangential and oblique modes have nodal planes that superimpose as the drive frequency rises to support this higher state of vibratory energy. As the normal modes are a result of standing wave patterns, and the sound pressure is assumed to be maximal at the rigid boundaries, sound pressure fields follow cosine distributions when driven at their normal modes. Some mode shapes follow to demonstrate the nodal planes.
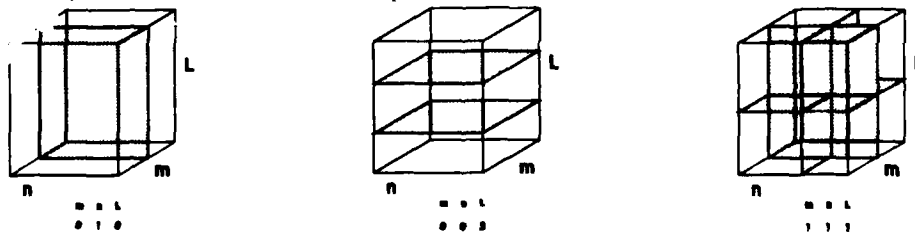
The modes and their shapes are also affected by the degree of coupling that exits between the input energy source and the 3-D space. This energy source in ANC would be the canceling speakers. It can be expected

that modes having nodal planes parallel to the canceling speakers will be excited to a higher degree than modes with nodal planes orthogonal to the canceling speakers primary wave fronts. Thus modal coupling and efficiency are considerations when determining the number of output channels and loudspeakers for the general ANC system; however, when possible to place loudspeakers close to the performance points a different strategy might be employed. This would be to place the loudspeaker in a symmetrical fashion so as not to encourage normal mode coupling, i.e. the integral of the source field is zero over the mode shape considered. As the mode shapes are important to the output, nodal planes are important to the performance input, or error microphones. For low order modes, the nodal planes are quite significant with response on a nodal plane 20-40 dB down from an anti-node. This acoustical phenomenon corrupts the error paths of the ANC system, and thus requires additional processing in the form of the filtered-X algorithm. Error microphones should be placed in positions that do not lie on the nodal planes of the several lowest modes, thus enhancing performance in this frequency bandwidth. As the bandwidth increases the modes become so numerous that statistical methods are used in their description, so likewise the response begins to smooth out and the effects of single nodal planes are greatly diminished.

Other considerations are made with respect to the input microphone not being inside the enclosure. The feedback path from the output speakers back to the reference input is now subject to the transmission loss of the enclosure after being reduced in magnitude by the noise reduction of the enclosure. By utilizing this physical barrier, it is possible to neglect acoustic feedback issues which are problematic in many ANC systems. These acoustical considerations not only serve to make the ANC system realizable, but can be used as tools for customizing the LMS algorithm for optimal performance in one or more modes of operation. Specifically, the weighting matrices can be selected for performance in the acoustic domain for a variety of situations, some with user adjustable parameters. This allows for extremely flexible and efficient use of signal processing power in the ANC system.

III. MULTI-CHANNEL FILTERED-X LMS ALGORITHM

In this paper, a general multi-channel filtered-x LMS active noise control algorithm with J input microphones, L parallel adaptive FIR filters and corresponding loudspeakers, and M error microphones to measure the performance at the desired location in 3-D space is developed. This general 3-D ANC system is illustrated in Figure 1. The global reference input signal is obtained by mixing of J input microphone signals

$$\underline{x}(n) = \underline{g}^T \underline{x}'(n) \tag{3}$$

where $\underline{x}'(n) = [x_1(n) \ x_2(n) \ ... \ x_J(n)]^T$ is the input microphone array signal vector and $\underline{g} = [g_1 \ g_2 \ ... \ g_J]^T$ is the gain vector. The value of each gain, g_j, is determined by the location of corresponding input microphone. Therefore, $\underline{g}$ provides a spatial weighting factor for each input microphone. Note that this digital mixer described in equation (3) also can be implemented by an analog circuit to release the I/O burden of 3-D ANC system.

As shown in the Figure 1, there are L canceling loudspeakers (S1, S2, .. SL) in the enclosure. $\underline{y}(n) = [y_1(n) \ y_2(n) \ ... \ y_L(n)]^T$ is an output vector from L adaptive filters to drive corresponding canceling speakers. $\underline{e}(n) = [e_1(n) \ e_2(n) \ ... \ e_M(n)]^T$ is the error vector formed by M error microphone (M1, M2, .. MM) outputs.

The simplified block diagram of the 3-D ANC system is illustrated in Figure 2. In the acoustic domain of Figure 2, $\underline{p}$ represents M main acoustic paths, $p_m(z)$, from $x(n)$ to each error microphone to be modeled by adaptive filters. H represents LxM error paths from L canceling speakers to M error microphones. Since input microphones are placed outside the enclosure, the acoustic feedback from L canceling speakers back to J input microphones can be neglected because the enclosure provides attenuation twice. Therefore, LxJ acoustic feedback paths are eliminated which greatly simplify system design.

In the electrical (processing) domain, $\underline{w}(n)$ represents L adaptive filters, that is, $\underline{w}(n) = [\underline{w}_1(n) \ \underline{w}_2(n) \ .. \ \underline{w}_L(n)]^T$ where $\underline{w}_1(n) = [w_{1,0}(n) \ w_{1,1}(n) \ .. \ w_{1,I-1}(n)]^T$ is the weight vector of l-th adaptive filter of order I. The output signal vector y(n) $\underline{y}(n) = [y_1(n) \ y_2(n) \ ... \ y_L(n)]^T$ is used to drive L speakers. Each speaker's input signal $y_l(n)$ is generated by the corresponding adaptive filter, that is,

$$y_l(n) = \underline{w}_l^T(n) \, \underline{x}(n) \quad , l = 1, 2, .. , L \tag{4}$$

where $\underline{x}(n) = [x(n) \ x(n-1) \ .. \ x(n-I+1)]^T$ is the common input signal vector for all adaptive filters. Coefficients of the adaptive filters are updated by the multi-channel filtered-x LMS algorithm [10]

$$\underline{w}(n+1) = \underline{w}(n) - 2\mu \, X^T(n) \, Q\underline{e}(n) \tag{5a}$$

where Q is the MxM diagonal matrix and

$$X(n) = \begin{vmatrix} \mathbf{h}_{11}*\mathbf{x}(n) & \mathbf{h}_{21}*\mathbf{x}(n) & . & . & \mathbf{h}_{L1}*\mathbf{x}(n) \\ . & & . & . & . \\ \mathbf{h}_{1M}*\mathbf{x}(n) & & . & . & \mathbf{h}_{LM}*\mathbf{x}(n) \end{vmatrix} = \begin{vmatrix} \underline{x}_{11}(n) & \underline{x}_{11}(n) & . & . & \underline{x}_{LM}(n) \\ . & & . & . & . \\ \underline{x}_{1M}(n) & & . & . & \underline{x}_{LM}(n) \end{vmatrix} \tag{5b}$$

where $\underline{x}_{lm}(n) = [x_{lm}(n) \ x_{lm}(n-1) \ .. \ x_{lm}(n-I+1)]^T$ for $l = 1, 2, .. , L$ and $m = 1, 2, .. , M$ is the vector of reference input signal filtered by the error path from speaker Sl to microphone M_m. The significance of M error signals $e_m(n)$ for the adaptation of L adaptive filters $w_l(z)$ is weighted by a unique weighting matrix Q. Since the speaker S_l is driven by the adaptive filter $w_l(z)$, the significance of the error microphone M_m related to the speaker S_l and its corresponding adaptive filter $w_l(z)$ should be taken into account. Therefore L independent weighting matrices

$$Q_l = \begin{vmatrix} q_{l1} & & 0 \\ & . & \\ 0 & & q_{lM} \end{vmatrix}$$

for $l = 1, 2, .. , L$ are designed. The multi-channel filtered-x algorithm in equation (5a) can be modified as

$$\underline{w}_l(n+1) = \underline{w}_l(n) - 2\times\mu\sum_{r=1}^{M}\mathbf{e}_{l_r}(n)x_{l_r}(n) \tag{6}$$

for $l = 1, 2, .. , L$, where $e'_{li}(n) = q_{li} \, e_i(n)$ are error signals weighted by Q_l for the adaptation of $\underline{w}_l(n)$.

As illustrated in Figure 2, H^ represents LxM error-path transfer functions estimated from speaker Sl to error microphone Mn, and H^ is used to filter reference signal for the adaptation of adaptive filters, $w_l(n)$. Adaptive filters are a bank of parallel FIR filters adapted by filtered-X LMS algorithm given in equation (6). The on-line estimation of H^ will be presented in the next section.

IV. MULTI-CHANNEL ON-LINE ERROR-PATH MODELING ALGORITHM
As illustrated in Figure 1, error signals of 3-D active noise control system are measured from locations where the undesired noise is acoustically combined with the anti-noise. In order for the adaptive filters to

properly converge to unknown acoustical plants, it is necessary to compensate for the transfer function of the error-path, $H_{lm}(z)$, from $y_l(n)$ to $e_m(n)$, which includes the D/A converter, smoothing filters, power amplifier, loudspeaker, acoustic path from speaker to error microphone, error microphone, preamplifier, anti-aliasing filter, and the A/D converter [15]. However, since the error-paths can be time varying, the modeling of error-path on-line is required to assure convergence of multi-channel filtered-x LMS algorithm developed in the previous section.

Real-time-on-line modeling of the error-path is a difficult problem since the error signal $e_m(n)$ pickup by the error microphone M_m is always a mixture of signals output from $P_m(z)$ and $H_{lm}(z)$ for $l = 1, 2, .. ,L$. From the system identification point of view, the adaptive filter can be used to identify $H_{lm}(z)$, however, the disturbance, $d_m(n)$, which is highly correlated with the excitation signal, $y_l(n)$, will result in a biased estimation of $H_{lm}(z)$. Most recently, the parallel on-line modeling algorithm developed by Tapia and Kuo [11] tries to eliminate the disturbance by introducing another adaptive filter $D_m(z)$ to model $P_m(z)$. In this paper, we extended this one-dimensional on-line modeling algorithm to multi-channel case for 3-D ANC systems.

We assume that response of the physical systems $P_m(z)$ and $H_{lm}(z)$ are finite and can be modeled by a digital Finite Impulse Response (FIR) filters of order N and K, respectively. The concept of this new m-th channel on-line error-path modeling scheme is illustrated in Figure 3, where the combined response of $P_m(z)$ and $H_{lm}(z)$ which is measured by the error microphone M_m can be expressed as

$$e_m(n) = \underline{p}_m^T \underline{x}(n) + \sum_{l=1}^{L} \underline{h}_{lm}^T \underline{y}(n) \qquad \text{for m} = 1, 2, .. ,M \qquad (7)$$

where $\underline{p}_m = [p_{m,0}\ p_{m,1}\ ..\ p_{m,N-1}]^T$ is the impulse response vector of $p_m(z)$, $\underline{h}_{lm} = [h_{lm,0}\ h_{lm,1}\ ..\ h_{lm,K-1}]^T$ is the impulse response vector of transfer function $H_{lm}(z)$, $\underline{x}(n) = [x(n)\ x(n-1)\ ..\ x(n-N+1)]^T$ is the input signal vector of order N, and $\underline{y}_l(n) = [y_l(n)\ y_l(n-1)\ ..\ y_l(n-K+1)]^T$ is the signal vector of order K for speaker S_l.

Defining the state vector of overall FIR system as $\underline{\Phi}_m = [\underline{p}_m\ \underline{h}_{1m}\ \underline{h}_{2m}\ ..\underline{h}_{Lm}]^T$ and the overall input vector $\underline{u}(n) = [\underline{x}(n)\ \underline{y}_1(n)\ \underline{y}_2(n)\ ..\ \underline{y}_L(n)]^T$ equation (7) can be simplified to

$$e_m(n) = \underline{\Phi}_m^T \underline{u}(n) \qquad (8)$$

This equation shows that there is an unknown overall FIR system $\underline{\Phi}(m)$ which is excited by the overall input vector $\underline{u}(n)$ and the response of system is $e_m(n)$.

Similarly, based on Figure 3, the combined output of adaptive filters $C_{lm}(z)$ and $D_m(z)$ is

$$e_m'(n) = \underline{d}_m^T(n)\underline{x}(n) + \sum_{l=1}^{L} \underline{c}_{lm}^l(n)\underline{y}_l(n) \qquad \text{for m=1, 2, ..., M} \qquad (9)$$

where $\underline{c}_{lm}(n) = [c_{lm,0}(n)\ c_{lm,1}(n)\ ..\ c_{lm,K-1}(n)]^T$ is the weight vector of adaptive filter $C_{lm}(z)$ at time n, and $\underline{d}_m(n) = [d_{m,0}(n)\ d_{m,1}(n)\ ..\ d_{m,N-1}(n)]^T$ is the weight vector of adaptive filter $D(z)$ at time n.

Likewise, by defining an overall weight vector $\underline{a}_m(n) = [\underline{d}_m(n)\ \underline{c}_{1m}(n)\ ..\underline{c}_{Lm}(n)]^T$, equation (9) can be simplified to

$$e_m'(n) = \underline{a}_m^T(n) \underline{u}(n) \qquad (10)$$

This equation shows that an overall adaptive FIR filter a_m is used to identify an unknown FIR system ϕ_m using the same input vector $u(n)$. Therefore, the parallel system identification scheme illustrated in Figure 3 can be simplified to a classical system identification problem.

The goal of this system identification scheme can be achieved by adapting coefficients of filter $A_m(z)$ to minimize the mean-square value of difference signal, $e''_m(n) = e_m(n) - e'_m(n)$ using the well-known LMS algorithm:

$$a_m(n+1) = a_m(n) + 2 \mu e''_m(n) u(n) \tag{11}$$

This combined vector equation can be partitioned into L+1 vector equations for L+1 parallel adaptive filters

$$d_m(n+1) = d_m(n) + 2 \mu e''_m(n) x(n) \tag{12a}$$

and

$$c_{lm}(n+1) = c_{lm}(n) + 2 \mu e''_m(n) y_l(n) \quad \text{for} \quad l = 1, 2, \ldots, L \tag{12b}$$

It is important to note that in equation (6), a "minus" sign is used to update weight vector of $W_l(z)$ for ANC applications instead of a "plus" sign as conventional LMS algorithm for system modeling in equation (12). This is because the residual error of the ANC system is produced by acoustical superposition (addition) instead of electrical subtraction. It is also important to point out that Figure 3 represents only a single channel of on-line modeling for error microphone Mm. For multi-channel system with M error microphones, equations (9), and (12) should be repeated for m = 1, 2, .., M.

V. EXPERIMENTS AND COMPUTER SIMULATIONS

The experimental setup consists of a 3-dimensional enclosure with approximate shape and dimension of a typical heavy equipment cabin (1.0m x 1.2m x 1.5m). The walls are considered reflective, while the floor and ceiling have some limited acoustical absorption in the frequency range of interest 50-400 Hz. Inside the enclosure is an upholstered seat, unoccupied. The setup utilizes two 6.5" cancellation speakers mounted overhead in the back corners of the enclosure. An input microphone is located behind the seat inside the enclosure, centered laterally 15cm above the floor. Two error microphones being of cardioid type further enhance the zone spatially by aiming the lobes of maximum sensitivity toward the operator's head.

For simulation purposes, nine transfer functions (1 input, 2 main, 2 feedback, and 4 error, as shown in Figure 2) were estimated with a HP 3563A control system analyzer. Using random noise with sufficient amplitude to excite the acoustical modes, a Z domain curve fit was made to the measured transfer function which includes power amplifier, loudspeaker, microphone, and preamplifier. Subsequently, IIR filters were generated through polynomial expansion of the Z domain pole/zero information, to be used in the simulations as the electro-acoustical models.

From extensive simulation results some conclusions on the performance of the algorithm follow. Shown in Figure 4 is a normalized attenuation curve and a typical error path transfer function. The power estimates used by the attenuation curve are the result of averaging the last 50 iterations in a 1000 iteration block, stepped through 5 Hz increments. As seen in the error path transfer function, resonance's following very closely to the lowest predicted acoustical modes exist. The attenuation curve shows the algorithm has no difficulty responding to the increased power demand of these resonance's, and its cancellation is correlated with the error path efficiency. This is where Q_l, the error weighting matrix, has acoustically relevance. Q_l may be designed to minimize the importance of non-efficient transfer functions that slow the convergence of the system or degrade its performance. It is also possible to have a user adjustable Q_l to optimize the system for a specific acoustical environment, such as in a car when only the driver is present or, if a more global attenuation is desired, when there are passengers.

VI. CONCLUSIONS

This paper presents a general multi-channel filtered-x LMS algorithm with new parallel multi-channel on-line error-path modeling algorithm for 3-D active noise control systems. An input weight vector based on the spatial placement of input microphones is proposed to mix J input sensor signals to form a single reference signal for all adaptive filters. A modified independent cost function for each channel is used to weight the spatial significance of each error microphone output for the adaptation of each adaptive filter. The performance of the algorithm has been verified on a 3-D experimental set-up and is analyzed from both acoustical and adaptive signal processing points of view. The robustness of the algorithm is verified by intensive simulations using real transfer functions measured from the experimental setup.

References:

[1] P. Lueg, "Process of Silencing Sound Oscillations," German Patent, DRP No. 655-508, January 1933.

[2] L. Poole, G. Warnaka, and R. Cutter, "The Implementation of Digital Filter Using a Modified Widrow-Hoff Algorithm for the Adaptive Cancellation of Acoustic Noise," IEEE Int. Conf. on ASSP, San Diego, CA, 1984. pp. 21.7.1-21.7.4.

[3] L. Eriksson, et al, "The Selection and Application of an IIR Adaptive Filter for Use in Active Sound Attenuation," IEEE Trans. on ASSP, April 1987. pp. 433-437.

[4] P. Nelson, A. Curtis, S. Elliott, and A. Bullmore, "The Active Minimization of Harmonic Enclosed Sound Fields, Part I: Theory," Journal of Sound and Vibration, (1987) 117(1), pp. 1-13.

[5] A. Bullmore, P. Nelson, and S. Elliott, "Theoretical Studies of the Active Control of Propeller-Induced Cabin Noise," Journal of Sound and Vibration, (1990) 140(2), pp. 191-217.

[6] B. Bullmore, P. Nelson, A. Curtis, and S. Elliott, "The Active Minimization of Harmonic Enclosed Sound Fields, Part II: Computer Simulation," Journal of Sound and Vibration, (1987) 117(1), pp. 15-33.

[7] S. Elliott, A. Curtis, B. Bullmore, and P. Nelson, "The Active Minimization of Harmonic Enclosed Sound Fields, Part III: Experimental Verification," Journal of Sound and Vibration, (1987) 117(1), pp. 35-58.

[8] S. Elliott, P. Nelson, I. Stothers and C. Boucher, "In-Flight Experiments on the Active Control of Propeller-Induced Cabin Noise, Journal of Sound and Vibration, (1990) 140(2), pp. 219-238.

[9] Simpson, et al, "Full Scale Demonstration Test of Cabin Noise Reduction using Active Noise Control," Proc. of Inter-Noise, 1989, pp. 459-462.

[10] S. Elliott, et al, "A Multiple Error LMS Algorithm and Its Application to the Active Control of Sound and Vibration," IEEE Trans. on ASSP, Oct. 1987.

[11] J. Tapia and S. Kuo, "New Adaptive On-Line Modeling Techniques for Active Noise Control Systems," IEEE Int. Conf. System Engineering, August 1990, pp. 280-283.

[12] V.S. Mankovsky, Acoustics of Studios and Auditoria, Hastings House, 1971, pp. 121-137.

[13] F. Alton Everest, Acoustic Techniques for Home and Studio, 1973, pp. 58-72.

[14] B. Widrow and S. Stearns, Adaptive Signal Processing, Prentice-Hall, 1985.

[15] J. Burgess, "Active Adaptive Sound Control in a Duct: A Computer Simulation," Journal of Acoustical Society of Am., Vol 70, 1981
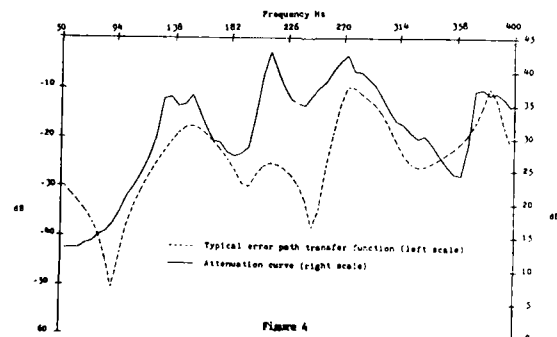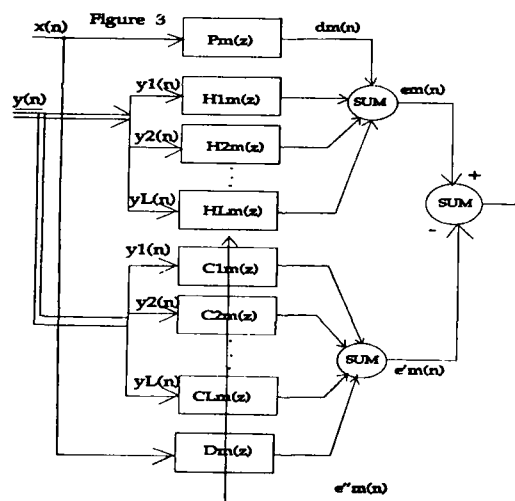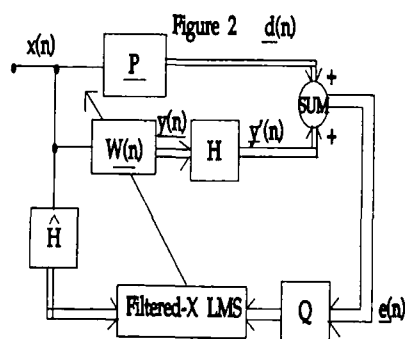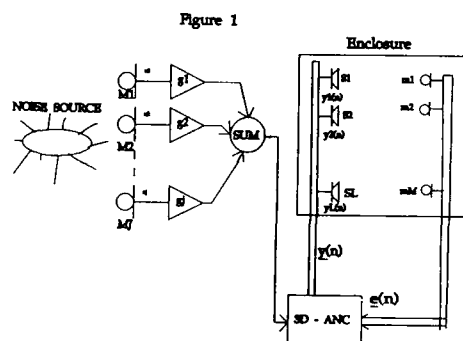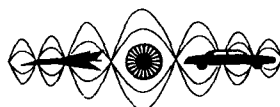
Figure 1

Figure 2

Figure 3

Figure 4

SECOND INTERNATIONAL CONGRESS ON
RECENT DEVELOPMENTS IN AIR- AND
STRUCTURE-BORNE SOUND AND VIBRATION
MARCH 4-6, 1992   AUBURN UNIVERSITY, USA

TIME AND FREQUENCY DOMAIN X-BLOCK LMS ALGORITHMS FOR SINGLE CHANNEL ACTIVE NOISE CONTROL

Qun Shen
Active Noise and Vibration Technologies
3811 E. Wier Avenue
Phoenix, AZ 85040

Andreas Spanias
Department of Electrical Engineering
Telecommunications Research Center
Arizona State University
Tempe, AZ 85287-5706

ABSTRACT

This paper is concerned with the development of block adaptive algorithms for active noise control. Time and frequency domain X-Block LMS (XBLMS) algorithms are developed for single channel active noise control applications. Analytical and experimental results are given to demonstrate the properties and the performance of the proposed algorithms. In particular, we give simulation results as well as results from the implementation of the algorithms on the Motorola DSP 56001.

I. INTRODUCTION

The sequential filtered x-LMS algorithm [1] which is often used for active noise control [2,3] is associated with two problems, namely, a) slow convergence when operating with highly correlated inputs, and b) gradient noise due to the instantaneous estimates of the errors. These problems can be tackled using block processing techniques [4]. Block LMS (BLMS) filters can be implemented in the time [4,5] or in the frequency domain [6,7]. Clark et al [4] developed the BLMS algorithm for FIR system identification and Mikhael and Wu [5] proposed a time varying convergence factor for the BLMS. A Frequency domain implementation of the BLMS was given in [6] by Ferrara and a normalized convergence factor for this algorithm was proposed by Mikhael and Spanias in [7].

In this paper, we give a block processing algorithm which is based on the structure of the filtered x-LMS algorithm. The proposed algorithm is called x-Block LMS (XBLMS) and is applied to active noise cancellation in closed structures. The XBLMS algorithm can be implemented in the time or in the frequency domain. The latter is more efficient in high order implementations and allows for the use of frequency-normalized convergence factors [8] which were shown to improve the convergence of the algorithm particularly with colored signals. Although the proposed algorithm involves block data processing, sequential (sample-by-sample) updates are also possible by block overlapping. Analytical and experimental results are given to demonstrate the performance of the algorithm. In particular, we give results from computer simulations and from the real time implementation of the algorithm on the Motorola DSP 56001. In addition, convergence analysis is given in the Appendix. The rest of the paper is organized as follows. Section II describes the filtered x-LMS algorithm, section III gives the XBLMS algorithm, and section IV presents the frequency domain XBLMS algorithm. Section V gives the computer simulations while section VI describes the real time implementation of the algorithm. Finally, section VII presents the conclusion.

II. THE FILTERED-X LMS ALGORITHM

A block diagram for an active noise control system based on the filtered-x LMS algorithm is shown in Fig. 1. The reference signal, x_k, which is associated to the external noise source, is used to drive the system. For example, the reference signal for the case of rotating machinery is periodic or quasi-periodic and is usually taken from a tachometer. The output, y_k, of the I-th order adaptive filter $W(z)$ is used as a control signal. The J-th order FIR filter $H^s(z)$ represents the acoustic path between the error signal and the secondary source and $H^P(z)$ represents the primary path between the external noise source and the error sensor.

The filtered-x LMS algorithm actually involves two operations, namely system modeling and control. In system modeling the secondary path $H^s(z)$ is modeled by a FIR or an IIR filter without the primary noise present. In the control stage, the reference signal x_k is passed through the FIR filter, $\hat{H}^s(z)$, and the filtered reference signal, r_k, is generated for the LMS algorithm.
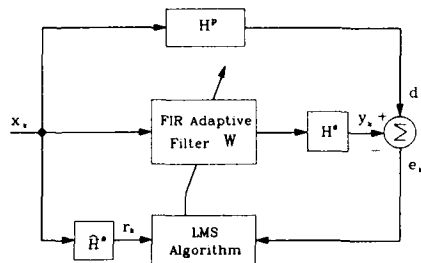
Fig. 1. The filtered-x LMS active noise control system.

The error for the system of Fig. 1 is given by

$$e_k = d_k - \underline{r}_k^T \underline{w}_k \tag{1}$$

where d_k is the desired signal. The superscript T denotes matrix or vector transpose. The vectors $\underline{r}_k$ and $\underline{w}_k$ are the filtered reference and coefficient vectors respectively, i.e.,

$$\underline{r}_k = [r_k \quad r_{k-1}, \quad \cdots \quad , r_{k-l+1}]^T \tag{2}$$

$$\underline{w}_k = [w_{0,k} \quad w_{1,k}, \quad \cdots \quad , w_{l-1,k}]^T \tag{3}$$

The filtered reference signal is given by

$$r_k = \sum_{j=0}^{J-1} h_j^s x_{k-j} \tag{4}$$

where $\{h_j^s, j = 0, 1, \ldots, J-1\}$ are the coefficients of $H^s(z)$. The mean square error (MSE), J, is defined as

$$J = E\{e_k^2\} = E\{d_k^2\} - 2\underline{w}_k^T E\{d_k \underline{r}_k\} + \underline{w}_k^T E\{\underline{r}_k^T \underline{r}_k\} \underline{w}_k \tag{5}$$

where $E\{.\}$ denotes the expectation value. In most practical applications the autocorrelation matrix, $E\{\underline{r}_k \underline{r}_k^T\}$ is positive definite and hence invertible. The gradient is given by

$$\hat{\underline{\nabla}}_k = \frac{\partial J}{\partial \underline{w}_k} = \left[\frac{\partial J}{\partial w_{0,k}} \quad \frac{\partial J}{\partial w_{1,k}} \quad , \ldots, \quad \frac{\partial J}{\partial w_{l-1,k}} \right]^T$$

$$= 2E\{\underline{r}_k \underline{r}_k^T\} \underline{w}_k - 2E\{d_k \underline{r}_k\} = -2E\{\underline{r}_k e_k\} \tag{6}$$

The coefficient vector is updated using the instantaneous estimate of the gradient, i.e.,

$$\underline{w}_{k+1} = \underline{w}_k - \mu \, \hat{\underline{\nabla}}_k$$

$$= \underline{w}_k + 2\mu \underline{r}_k e_k \tag{7}$$

where μ is the convergence factor that controls the stability and the convergence rate of the algorithm.

The filtered-x LMS is associated with a large misadjustment since the gradient is computed from only one error sample. In the following section, we introduce the XBLMS which computes the gradient from a block of errors.

III. THE X-BLOCK LMS ALGORITHM

In this section, we develop a block processing algorithm for the x-filtered structure. A block diagram for the structure of the XBLMS algorithm is shown in Fig. 2. The labels S/P and P/S stand for serial-to-parallel and parallel-to-serial conversions respectively. The secondary path is modeled first in the absence of the primary noise source. The time-varying block FIR filter is then adapted using the XBLMS algorithm.
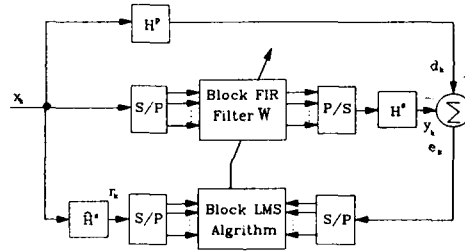
Fig. 2. An XBLMS active noise cancellation scheme.

Let us first define the following: j is the block index, L is the block length, and s is the block shift. The error, desired signal, and coefficient vectors are given by

$$\underline{e}_j = [\, e_{js} \quad e_{js+1} \quad \cdots \quad e_{js+L-1} \,]^T \tag{8}$$

$$\underline{d}_j = [\, d_{js} \quad d_{js+1} \quad \cdots \quad d_{js+L-1} \,]^T \tag{9}$$

$$\underline{w}_j = [\, w_{0,j} \quad w_{1,j} \quad \cdots \quad w_{l-1,j} \,]^T \tag{10}$$

Furthermore, the filtered reference matrix for the j-th block of data is given by

$$\underline{r}_j = \begin{bmatrix} r_{js} & r_{js-1} & \cdots & r_{js-l+1} \\ r_{js+1} & r_{js} & \cdots & r_{js-l+2} \\ \cdot & \cdot & \cdot & \cdot \\ \cdot & \cdot & \cdot & \cdot \\ \cdot & \cdot & \cdot & \cdot \\ r_{js+L-1} & r_{js+L-2} & \cdots & r_{js+L-l} \end{bmatrix} \tag{11}$$

It is noted that each component of the matrix $\underline{r}_j$ is a filtered reference signal defined in Eq.(4) and that the matrix $\underline{r}_j$ is Toeplitz. The shift s can be chosen to be between l and L. A block shift of $s < l$ implies block overlapping and therefore data reusing. Data reusing may improve convergence

speed at the expense of additional computation [5,7]. For $s = L$, the error blocks are disjoint. The error vector, $\underline{e}_j$, is given by

$$\underline{e}_j = \underline{d}_j - \underline{\Gamma}_j \underline{w}_j \tag{12}$$

The block MSE (BMSE) can then be written as

$$J_B = E\left\{\underline{e}_j^T \underline{e}_j\right\}$$

$$= E\left\{\underline{d}_j^T \underline{d}_j\right\} - \underline{w}_j^T E\left\{\underline{d}_j^T \underline{\Gamma}_j\right\} + \underline{w}_j^T E\left\{\underline{\Gamma}_j^T \underline{\Gamma}_j\right\} \underline{w}_j \tag{13}$$

The gradient estimate for the BMSE w.r.t. the coefficient vector $\underline{w}_j$ is given by

$$\underline{\hat{\nabla}}_j^B = -2\underline{\Gamma}_j^T \underline{e}_j \tag{14}$$

The update expression for the XBLMS is then given by

$$\underline{w}_{j+1} = \underline{w}_j - \mu_B \underline{\hat{\nabla}}_j^B \tag{15}$$

Note that in the XBLMS the gradient is estimated from a block of data instead of a single sample and hence the gradient noise is less than the noise associated with the sequential filtered-x LMS algorithm. In addition, the XBLMS can be implemented efficiently in the frequency domain using the Fast Fourier Transform (FFT).

IV. THE FREQUENCY DOMAIN XBLMS ALGORITHM

The frequency domain XBLMS (FXBLMS) is developed in this section. Although the FXBLMS is an exact implementation of the XBLMS, it offers computational savings in high order cases. In addition, the FXBLMS allows for direct access and control of adaptation of individual frequency components. The latter may be useful when cancelling harmonically structured noise. Firstly, the FXBLMS forms the FFT components of the 2Lx1 vector,

$$\underline{\tilde{r}}_j = [r_{js-L} \quad r_{js-L+1} \quad \cdots \quad r_{js-1} r_{js} \quad r_{js+1} \quad \cdots \quad r_{js+L-1}]^T \tag{16}$$

which consists of two L-point filtered reference vectors. Note that the block size L in this case is a radix-2 integer. The FFT components, $\{R(n), n=0,1,...,2L-1\}$ form a 2Lx2L diagonal matrix,

$$\underline{R}_j = [R(0)R(1)...R(2L-1)]^T \tag{17}$$

The frequency domain output is formed by

$$\underline{Y}_j = \underline{R}_j \underline{W}_j \tag{18}$$

where $\underline{W}_j$ is a 2Lx1 complex vector containing the frequency domain coefficients. According to the overlap-and-save method for fast convolution the last L terms of the inverse FFT of $\underline{Y}_j$ are results of a proper linear convolution, and hence

$$\underline{y}_j = [last \quad L \quad terms \quad of \quad IFFT\{\underline{Y}_j\}] \tag{19}$$

The j-th error vector is

$$\underline{e}_j = \underline{d}_j - \underline{y}_j \tag{20}$$

and the frequency domain error is formed by

$$\underline{E}_j = FFT\left\{\left[\underline{0}^T \quad \underline{e}_j^T\right]^T\right\} \tag{21}$$

where $\underline{0}$ is a Lx1 null vector. The frequency domain gradient is obtained by

$$\underline{G}_j = -2\underline{R}_j^H \underline{E} \tag{22}$$

The gradient is then constrained, i.e.,

$$\underline{\hat{\nabla}}_j^B = [first \; L \; terms \; of \; IFFT\{\underline{G}_j\}] \tag{23}$$

and

$$\underline{\hat{G}}_j = FFT\left\{\left[\left(\underline{\hat{\nabla}}_j^B\right)^T \quad \underline{0}^T\right]^T\right\} \tag{24}$$

Finally, the update equation for this algorithm is given by

$$\underline{W}_{j+1} = \underline{W}_j - \mu_B \ \underline{\hat{G}}_j \tag{25}$$

Note that the frequency domain gradient can be normalized, i.e.,

$$\underline{G}_j^n = \underline{M}^{-1} \ \underline{G}_j \tag{26}$$

where the inverse of the matrix $\underline{M} = \mathbf{R}^H \mathbf{R}$ essentially normalizes the gradient at each frequency with a sample energy of the input. The gradient must be again constrained as per Eq. (23) and Eq. (24). This type of normalization may improve the convergence of the algorithm in the case of correlated inputs.

V. SIMULATION RESULTS

A comparative simulation for the filtered x-LMS and the XBLMS is given in this section. This is based on the simulation scheme shown in Fig. 2 with a reference signal of the form:

$$x(k) = \sum_{n=1}^{4} \cos\left(\frac{2\pi nk}{N}\right) \quad \text{and} \quad N=8 \tag{27}$$

The primary path between the primary source and the error sensor is modeled by a FIR filter $H^P(z)$

$$H^P(z) = 0.6 + 0.9z^{-1} + 0.3z^{-2} + 0.5z^{-3}$$
$$+ 1.2z^{-4} - 1.5z^{-5} + 0.8z^{-6} + 0.1z^{-7} \tag{28}$$

and the secondary path between the error sensor and the actuator is modeled by FIR filter $H^s(z)$:

$$\hat{H}^s(z) = 0.7z^{-3} + 0.6z^{-5} + 0.73z^{-7} + 0.5z^{-8} + 0.45z^{-10}$$
$$+ 0.38z^{-12} + 0.9z^{-13} + 0.4z^{-16} + 0.1n(z) \tag{29}$$

where $n(z)$ is Gaussian white noise of zero mean and unit variance representing the measurement error of the plant. The convergence factor in both cases is $\mu = \mu_B = 0.01$, and the order of the adaptive FIR filter is $I = 8$. The block length is $L=8$ and the XBLMS is implemented with overlapping blocks, i.e., $s = 1$.

The convergence curves for both the filtered-x and the XBLMS algorithms are shown in Fig. 3. As it can be seen the XBLMS is associated with much less misadjustment.
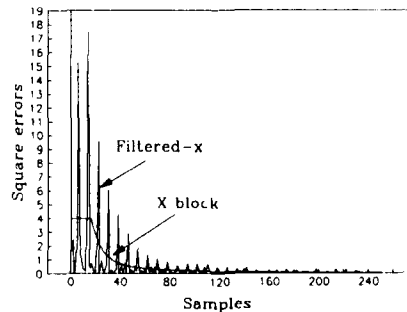
Fig. 3. Error curves for the filtered-x LMS and the XBLMS algorithms.

VI. REAL TIME IMPLEMENTATION

In order to evaluate the algorithm in an actual active noise cancellation scheme the XBLMS algorithm was implemented on the Motorola DSP 56001. The experimental setup (Fig. 4) for this

single channel active noise control consisted of two speakers, an error sensor (microphone), anti-aliasing lowpass filters, A/D and D/A converters, and a Motorola DSP 56001 controller. Speaker S1 is used to generate the primary noise and S2 is used as a secondary source.
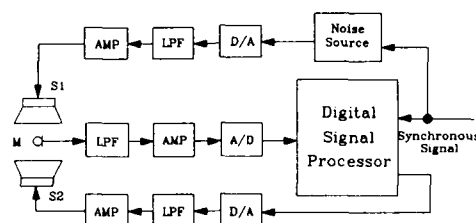
Fig. 4. Block diagram of the active noise control experiment

A sinusoidal signal of 100 Hz is used as the primary noise source. The primary noise is synchronous sampled and the sampling rate is 800 Hz. Since the reference signal is a pure tone, both block FIR filters $H^s(z)$ and $W(z)$ are of order 2 with a block length of 8. In the modeling phase, the reference signal is sent out by the secondary speaker S2 to model the secondary path between the error microphone and the secondary speaker. The BLMS algorithm is applied for the system modeling. After the algorithm converges, the FIR filter coefficients are saved in the DSP external memory to obtain the filtered reference signal in the control operation. In the control phase, the noise signal is produced by the primary speaker S1. The output of the adaptive filter $W(z)$ is sent out from the secondary speaker S2. The XBLMS algorithm is used to generate the control signal. The square of the residual error is stored in DSP memory during the adaptation. The XBLMS algorithm is adapted on a sample-by-sample basis. The convergence curve for this experiment is shown in Fig. 5 and as it is seen the misadjustment is rather small. The steady-state noise reduction in this experiment was of the order of 8 to 10 dB.
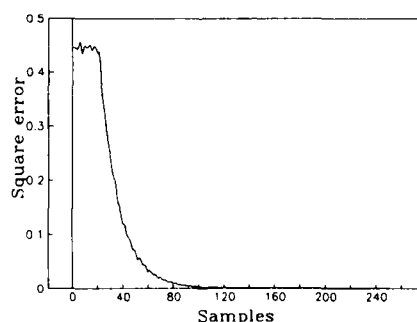
Fig. 5. Error curve of the XBLMS algorithm in the active noise control experiment.

VII. CONCLUSION

A filtered-x block LMS adaptive algorithm for active noise control was proposed. Time and frequency domain implementations of the algorithm were presented. Results from a computer simulation as well as a real time implementation were given to demonstrate the performance of the algorithm. In both cases it was shown that the algorithm is associated with a low level of misadjustment. Although the results are given for a synchronous repetitive noise source, the algorithm can also be applied to broadband random reference noise.

REFERENCE

[1] B. Widrow and S. Stearns, Adaptive Signal Processing, Prentice Hall, 1985.

[2] S.J. Elliott, I.M. Stothers, and P.A. Nelson, "A Multiple Error LMS Algorithm and its Application to the Active Control of Noise and Vibration," *IEEE Trans. Acoustics, Speech, and Signal Processing*, ASSP-35 (10), 1987, pp. 1423-1434.

[3] D.R. Morgan, "An analysis of Multiple Correlation Cancellation Loops with a Filter in the Auxiliary Path," *IEEE Trans. Acoustics, Speech, and Signal Processing*, ASSP-28(4), 1980, pp. 454-467.

[4] G. A. Clark et al, "Block Implementation of LMS adaptive filters," *IEEE Trans. Acoustics Speech and Signal Processing*, Vol. ASSP-29, June 1981, pp. 744-752.

[5] W.B. Mikhael and F.H. Wu, "Fast Algorithms for Block FIR Adaptive Digital Filtering," *IEEE Trans. Circuits and Systems*, Vol. CAS-34, October 1987, pp. 1152-1160.

[6] E.R. Ferrara, "Fast Implementation of LMS Adaptive Filters," *IEEE Trans. Acoustic Speech and Signal Processing*, Vol. ASSP-28, No. 4, August 1980, pp. 474-475.

[7] W.B. Mikhael and A.S. Spanias, "A Fast Frequency-Domain Adaptive Algorithm," *Proc. IEEE*, Vol. 76, January 1988, pp. 80-83.

[8] W.B. Mikhael and A.S. Spanias, "Comparison of Several Frequency-Domain LMS Algorithms," *IEEE Trans. CAS*, Vol. CAS-34, No. 5, May 1987, pp. 586-589.

APPENDIX: CONVERGENCE ANALYSIS OF THE XBLMS ALGORITHM

This appendix is on the convergence properties of the XBLMS algorithm. The system identification scheme for the XBLMS is different than the classical identification scheme for the LMS or the BLMS algorithm. The main difference lies in the fact that the adaptive filter function, $W(z)$, is cascaded with the transfer function $H^s(z)$. When the MSE is minimized, then we essentially have the following transfer function approximation:

$$H^P(z) \cong W(z)H^s(z) \qquad (A.1)$$

The convergence analysis assumes that $\hat{H}^s(z)$ is a good estimate of $H^s(z)$. In addition, we assume that under steady-state conditions the order of $W(z)$ and $H^s(z)$ can be reversed. The Wiener solution under these assumptions is given by

$$\underline{w}^o = \underline{r}^{-1}\underline{p} \qquad (A.2)$$

where $\underline{r}$ and $\underline{p}$ are the autocorrelation matrix and the cross-correlation vector respectively, i.e.,

$$\underline{p} = E\left\{\underline{r}_j^T \underline{d}_j\right\} \qquad (A.3)$$

and

$$\underline{r} = E\left\{\underline{r}_j^T \underline{r}_j\right\} \qquad (A.4)$$

In the following we derive the condition for the convergence of the mean of the adaptive filter vector to the Wiener solution (A.2). First we subtract the optimal vector from both sides of Eq. (15), i.e.,

$$\underline{w}_{j+1} - \underline{w}^o = \underline{w}_j - \underline{w}^o - \mu_B \hat{\underline{\nabla}}_j^B \qquad (A.5)$$

Taking the expected value of both sides of Eq. (A.5) we get

$$\underline{v}_{j+1} = \underline{v}_j - \mu_B E\left\{\hat{\underline{\nabla}}_j^B\right\} \qquad (A.6)$$

where $\underline{v}_j = E\{\underline{w}_j - \underline{w}^o\}$. Assuming that the coefficient vector and the input are independent the expected value of the gradient can be written as

$$E\left\{\hat{\underline{\nabla}}_j^B\right\} = -2\underline{p} + 2\underline{r}\underline{w}_j \qquad (A.7)$$

Substituting Eq. (A.7) into Eq. (A.6) we get

$$\underline{v}_{j+1} = (\underline{I} - 2\mu_B \underline{r})\underline{v}_j \qquad (A.8)$$

Considering the similarity transformation

$$\underline{r} = \underline{p}\underline{\lambda}\underline{p}^{-1} \qquad (A.9)$$

we rewrite the update equation as

$$\underline{\tilde{v}}_{j+1} = (\underline{I} - 2\mu_B\underline{\lambda})\underline{\tilde{v}}_j \qquad (A.10)$$

where $\underline{\tilde{v}}_j = \underline{p}^{-1}\underline{v}_j$. From (A.10) it can be shown easily that the adaptive filter vector converges in the mean to the Wiener solution if

$$0 < \mu_B < \frac{1}{\lambda_{max}} \qquad (A.11)$$

where the λ_{max} is the maximum eigenvalue of the autocorrelation matrix of the filtered reference signal. Following similar arguments one can show that the misadjustment of the algorithm is expressed by

$$M = \mu_B tr(\underline{r}) \qquad (A.12)$$

ENERGY BASED CONTROL OF THE SOUND FIELD IN ENCLOSURES

Scott D. Sommerfeldt and Peter J. Nashif
Applied Research Laboratory and
Graduate Program in Acoustics
P.O. Box 30
State College, PA 16804

ABSTRACT

A control method based on sensing and minimizing the total energy density at discrete locations is developed and compared to both the method of minimizing the squared pressure at discrete locations, as well as the optimal solution obtained by minimizing the spatially integrated potential energy density. Since total energy density is being minimized, the control system is sensitive to both pressure and velocity components, thereby preventing spillover into modes with small pressure amplitudes, but large velocity amplitudes, at the error sensor(s). The method has another distinct advantage for standing-wave fields, in that the method is much less sensitive to sensor location than the method of minimizing squared pressure. Computer simulations and experimental measurements are presented showing a comparison between the methods for the case of a one-dimensional sound field. In general, the overall attenuation obtained from minimizing the energy density is found to be superior to that obtained from minimizing the squared pressure.

INTRODUCTION

In many applications involving noise in enclosures, the desired control objective is to globally minimize the noise in the enclosure. Such applications include interior noise in aircraft, automobiles, and rooms. To obtain global minimization, it has generally been accepted that the appropriate quantity to minimize is the potential energy in the field, since the sound pressure level is a function of the potential energy density [1]. However, the total potential energy represents a quantity which is not available in practice, since it requires spatially integrating the entire acoustic field. Thus, an alternative approach which has been used in practice involves minimizing the squared pressure signal from one or more discrete "error" sensors, as an approximation to minimizing the potential energy [1-5]. To obtain optimal performance using this approach requires that one position the discrete sensors at locations corresponding to pressure maxima for all of the relevant modes of the enclosure. For regularly-shaped enclosures, where it is straightforward to determine the nature of the field in the enclosure, it is possible to locate the error sensors at optimal locations such that they are sensitive to the dominant modes in the enclosure. With such a configuration, it has been found that minimizing the squared pressure from the error sensors gives performance which is comparable to the optimal solution obtained by minimizing the total potential energy.

There are a number of applications which involve enclosures which are not regularly-shaped and where it is much more difficult to determine where to place the error sensors to achieve optimal control. In the general case, particularly for complex fields where the modes are poorly known, it has been found that the result of minimizing the squared pressure from discrete error sensor(s) is often to produce "zones of silence" in the vicinity of the error sensors while having little effect at other locations, or perhaps even increasing the sound pressure level at other locations.

Given that previous theoretical developments indicate that an optimal solution does exist to yield global minimization of the enclosed field, the question arises as to whether there is a better approach to minimizing

the noise in the field. This paper develops an alternative approach for minimizing enclosed acoustic fields based on the principle of minimizing the total energy density at discrete sensor locations. Analytical and numerical results using this approach have been reported previously [6]. Both simulation and experimental results are presented here using this energy based control method, with the results indicating that one generally obtains significant improvement in the global field using this approach as opposed to the method of minimizing the squared pressure.

MODAL REPRESENTATION OF THE CONTROLLED FIELD

The pressure in any arbitrary enclosure can be represented in terms of its normal modes. For simplicity, if one assumes a single point primary excitation source and a single point secondary control source, the acoustic field in an enclosure can be expressed as

$$p = \sum_{n=0}^{\infty} \left(A_n + B_n Q_c\right) \psi_n(\vec{x}) , \tag{1}$$

where $\psi_n(\vec{x})$ represents the nth eigenfunction (assumed to be normalized such that $\int_V \psi_n^2(\vec{x})dV = V$), Q_c represents the source strength of the control source, and the A_n and B_n represent the modal coefficients associated with the primary source and the secondary source respectively, and are given by

$$A_n = \frac{-j\omega\rho}{V(k^2 - k_n^2)} Q_p \psi_n(\vec{x}_p) ; \quad B_n = \frac{-j\omega\rho}{V(k^2 - k_n^2)} \psi_n(\vec{x}_c) . \tag{2}$$

Here, V is the volume of the enclosure, k is the disturbance wavenumber, k_n is the wavenumber for the nth mode, ω is the angular frequency, ρ is the fluid density, Q_p is the primary source strength, and $\vec{x}_p$ and $\vec{x}_c$ are the locations of the primary and control sources, respectively. The potential energy density, which is a function of position, can be expressed as

$$w_p = \frac{p^2}{4\rho c^2} , \tag{3}$$

which can be integrated over the volume of the enclosure to yield the total potential energy in the volume,

$$E_p = \frac{V}{4\rho c^2} \sum_{n=0}^{\infty} (A_n + B_n Q_c)(A_n^* + B_n^* Q_c^*) . \tag{4}$$

For global minimization, Eq. (4) represents the quantity which is to be minimized. If the A_n and B_n coefficients are represented in vector form, the potential energy can be expressed as

$$E_p = \frac{V}{4\rho c^2} \left[A^H A + A^H B Q_c + Q_c^* B^H A + Q_c^* B^H B Q_c\right] , \tag{5}$$

where the superscript ^{H} represents Hermitian transpose. From this expression, the quadratic dependence of the potential energy on the secondary source strength can be clearly seen. Following standard minimization procedures, the optimal source strength which minimizes the global potential energy is found to be

$$Q_{c,opt} = -(B^H B)^{-1} B^H A = -\frac{\displaystyle\sum_{n=0}^{\infty} B_n^* A_n}{\displaystyle\sum_{n=0}^{\infty} B_n^* B_n} . \tag{6}$$

The last expression is only valid when a single secondary source is used. For multiple secondary sources, the inverse matrix form must be used.

The modal expressions for the field can also be used to investigate the effectiveness of alternative control schemes. For simplicity, a single error sensor will be assumed in the following expressions, as the critical features to be illustrated are still apparent even with just a single sensor. If the control approach is to minimize the squared pressure, the objective function can be written as

$$J_p = p^2(\vec{x}_e) = \sum_{n=0}^{\infty} (A_n + B_n Q_c) \psi_n(\vec{x}_e) \sum_{m=0}^{\infty} (A_m^* + B_m^* Q_c^*) \psi_m^*(\vec{x}_e) , \tag{7}$$

where x_e represents the "error" location, where the squared pressure is being minimized. This expression can

also be seen to be quadratic with respect to the control source strength. If Eq. (7) is minimized with respect to the source strength, the optimal source strength for minimizing the squared pressure is found to be

$$Q_{c,p} = - \frac{\sum_{n=0}^{\infty} A_n \psi_n(\vec{x}_e)}{\sum_{n=0}^{\infty} B_n \psi_n(\vec{x}_e)} . \tag{8}$$

It can be seen from Eq. (8), that the solution obtained by minimizing the squared pressure depends on the location of the error sensors, and that the dependence on the modal coefficients is different than for the optimal solution given in Eq. (6).

An alternative method for controlling the sound field involves minimizing the total energy density at the error sensor, which can be expressed in terms of the modes as

$$w = \frac{1}{4\rho c^2} \left\{ \sum_{n=0}^{\infty} (A_n + B_n Q_c) \sum_{m=0}^{\infty} (A_m^* + B_m^* Q_c^*) \left[\psi_n(\vec{x}_e) \psi_m(\vec{x}_e) + \frac{1}{k^2} \nabla \psi_n(\vec{x}_e) \cdot \nabla \psi_m(\vec{x}_e) \right] \right\} . \tag{9}$$

Minimizing Eq. (9) yields the optimal source strength for minimizing the energy density as

$$Q_{c,e} = - \frac{\sum_{n=0}^{\infty} \sum_{m=0}^{\infty} B_n^* A_m F_{nm}}{\sum_{n=0}^{\infty} \sum_{m=0}^{\infty} B_n^* B_m F_{nm}} , \tag{10}$$

where F_{nm} is defined according to

$$F_{nm} = \psi_n(\vec{x}_e) \psi_m(\vec{x}_e) + \frac{1}{k^2} \nabla \psi_n(\vec{x}_e) \cdot \nabla \psi_m(\vec{x}_e) . \tag{11}$$

From Eq. 10, it can be seen that minimizing the energy density would yield the optimal solution if the function F_{nm} were replaced by the Kronecker delta function. Heuristically, one might anticipate the solution represented in Eq. (10) to yield a reasonable approximation to the optimal solution by observing the nature of the modal coefficients. If one considers the product $B_n^* A_m$, it can be seen from Eq. (2) that for $n \neq m$, the product will be small, since either $k^2 - k_n^2$ or $k^2 - k_m^2$ will be relatively large. On the other hand, if $n = m$, there will be large contributions from the modes where $k^2 - k_n^2 \approx 0$. Thus, one might anticipate that the method of minimizing energy density would yield better global attenuation than the method of minimizing the squared pressure.

NUMERICAL RESULTS

To gain additional insight into the various control strategies, the model of the enclosed field was reduced to a one-dimensional enclosure to simplify the numerical analysis. This paper will focus on the results obtained from the investigation of a one-dimensional enclosure. Thus, the enclosure consists of a rigid-walled closed duct of length L and cross-dimensions small enough to ensure no cross-modes in the frequency range of interest. With these assumptions, the eigenfunctions of the enclosure can be represented by

$$\psi_n(x) = \cos(k_n x) , \tag{12}$$

where k_n is given by $n\pi/L$. For the one-dimensional enclosure, it was found that retaining 50 modes achieved convergence of the infinite sums to within 0.1 dB.

The expressions for the optimal control strengths given in Eqs. (6), (8), and (10) were investigated for the case of the one-dimensional duct. The primary source strength was assumed to be located at $x/L = 0$ and to have unity magnitude, the secondary source strength was arbitrarily located at $x/L = 0.359$, and the duct length was normalized to a value of one. The relative source strengths for minimizing the potential energy, energy density, and squared pressure are shown in Fig. 1 as a function of frequency for three error sensor locations. The optimal solution for minimizing the potential energy does not depend on sensor location, whereas the other two methods do depend on sensor location. Fig. 1a) corresponds to a sensor location which should yield good attenuation for minimizing squared pressure, following the hypothesis of Nelson et al. [1] which suggests the optimal location for a pressure sensor is in a corner of the enclosure, where all modes have

363

a pressure maximum. Fig. 1b) corresponds to a location which one would expect to present problems for a control system which minimizes squared pressure, since half of the modes of the enclosure have a pressure node at the midpoint, and therefore would be unobservable. The case of Fig. 1c) was chosen to represent the situation where no particular thought was taken as to whether the sensor location was good or bad. In all cases, it can be seen that minimizing the energy density generally yields a source strength which is considerably closer to the optimal source strength than does minimizing the square pressure. Furthermore, for a given frequency, the source strength obtained by minimizing the energy density tends to be much less sensitive to the error sensor location than the source strength obtained by minimizing the squared pressure. This further suggests that better global control should be attained by controlling the energy density than by controlling the squared pressure.

Given the expressions for the source strength in Eqs.(6), (8), and (10), along with the expression in Eq. (1) for the pressure field in the enclosure, it is also possible to calculate the pressure field in the duct which one would expect with each control method for a given frequency. This result is of particular interest, as a comparable result is relatively straightforward to obtain experimentally for comparing numerical and experimental results. With the error sensor located near the middle of the closed duct, there are two cases of interest. The first case is associated with an excitation frequency corresponding to a resonance of the enclosure. The frequency chosen coincides with the seventh mode of the duct, and corresponds to 213 Hz for the experimental duct used later. Fig. 2 shows the simulation results obtained for this case. As can be seen, all three control methods yield considerably less attenuation in the region between the primary source and the secondary source than in the rest of the enclosure. Furthermore, for values of $x/L > 0.359$ (the control source location), both the squared pressure and energy density methods yield greater attenuation than the method of minimizing the total potential energy. However, if the potential energy density is integrated over the entire length of the enclosure, one finds that the method of minimizing the total potential energy yields the lowest potential energy, as it should, due to the fact that the pressure level is slightly lower for this method between $x/L = 0$ and $x/L = 0.359$. The greatest contribution to the total potential energy occurs in this region, since the pressure level is at its highest here. This result demonstrates several issues. First, for a given control configuration, the solution obtained by minimizing the potential energy may not be the best solution,
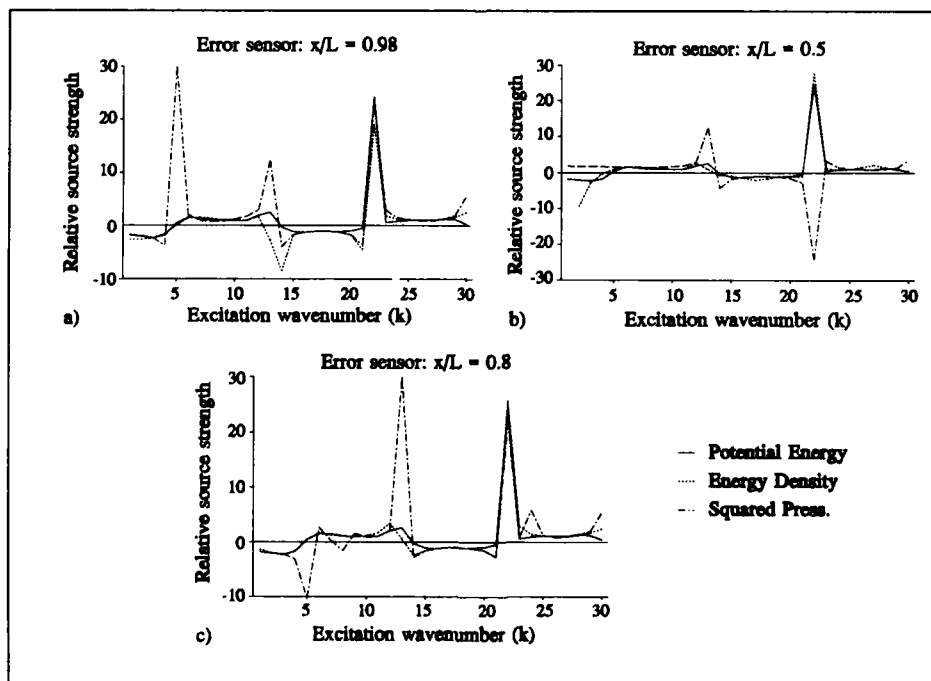

Figure 1. Optimal source strength, relative to the primary source strength, for the three control methods.

364

subjectively. Furthermore, this result illustrates the importance of looking at the issue of determining the optimal location for the secondary control source. The topic of optimal secondary source location is not addressed in this paper.

The second case of interest corresponds to an excitation frequency which is off resonance. Fig. 3 shows the case of the enclosure being excited at a frequency between the sixth and seventh modes, and corresponds to 200 Hz for the experimental duct used later. The performance of the three methods is again reasonably comparable for the region between the primary and secondary sources. However, it can be seen in the region past the secondary source, that noticeably improved performance is predicted for the method of minimizing the energy density over the method of minimizing squared pressure. This can be attributed to the fact that multiple modes contribute to the total field at this frequency, and the energy density method is sensitive to all modes since it uses both pressure and velocity. Thus, the method will not attenuate modes with large significant pressure components at the error sensor at the expense of significantly enhancing modes with a small pressure component (but large velocity component) at the error sensor location.

A final simulation result is presented in Fig. 4. This result corresponds to the error sensor again being located near the middle of the duct, but moving the secondary source to the location $x/L = 0.7$. The excitation frequency for this case is near the resonance frequency of the sixth mode, corresponding to 180 Hz for the experimental duct. Again, no attempt has been made to optimize the location, but some of the effects of source location can be seen in this example. The optimal solution now predicts that substantial attenuation can be obtained throughout almost the entire enclosure. Furthermore, it can be seen that the simulation indicates that the method of minimizing energy density gives nearly optimal results, while the method of minimizing the squared pressure actually increases the pressure level throughout almost the entire enclosure.

EXPERIMENTAL CONFIGURATION

Apparatus

The enclosure consists of a circular PVC pipe, 5.6 m in length and 0.1 m in diameter. One end of the pipe is rigidly capped, while the other end of the pipe is fitted with an enclosed speaker which serves as the primary noise excitation. The frequency of the first cross-mode associated with this closed duct is approximately 1000 Hz, so that this configuration can be considered to be a one-dimensional enclosure over the frequency range of interest. The secondary speaker is connected to the duct by means of a "T" junction, which was randomly selected to be at a location 1.93 m from the primary speaker. Since the emphasis of this research is not on the optimal location for the secondary speaker, this location was chosen with no attempt to choose a good or bad location. The emphasis of the present research is to investigate the control which can be achieved for a given arbitrary source configuration. For the error sensors, holes are drilled in the pipe, into which the error microphones can be inserted. An additional microphone is mounted on a small cart which is placed inside the duct. The purpose of this microphone is to provide a means for scanning the acoustic field in the enclosure before and after control.

The control system for the experimental apparatus is based on the Spectrum DSP96002 System Board which utilizes the Motorola DSP96002 floating point digital signal processor. An analog input/output interface is provided by means of a Spectrum Four Channel Analog I/O board, which interfaces directly with the
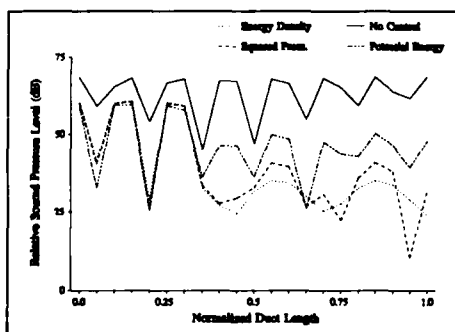
Figure 2. Predicted sound pressure level for an on-resonance excitation frequency (213 Hz).
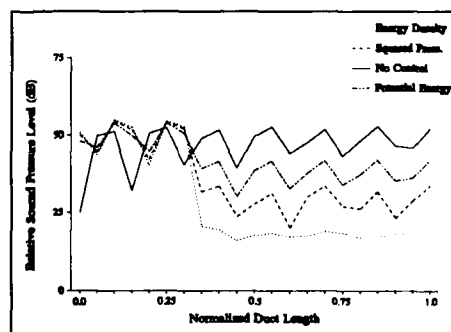
Figure 3. Predicted sound pressure level for an off-resonance excitation frequency (200 Hz).

DSP96002 System Board. A schematic of the experimental apparatus is shown in Fig. 5.

Control Algorithm

The control algorithm used in this research has been reported previously [7,8]. The adaptive algorithm is based on the filtered-x algorithm developed by Widrow and Stearns [9]. The unique feature of the control algorithm is that the control system performs simultaneous system identification and control. The system identification is necessary to provide a model of the transfer function from the controller to the error sensor, which is necessary for proper convergence of the filtered-x algorithm. A schematic of the control system is shown in Fig. 6. In this figure, W represents the transfer function of the control filter, which is updated using the filtered-x algorithm. P is the plant transfer

Figure 4. Predicted sound pressure level with the secondary source located at $x/L = 0.7$, and the error sensor at $x/L = 0.5$.

function, which represents the system to be controlled, while H represents the transfer function from the control output to the error sensor, sometimes referred to as the error path transfer function. C and D are two adaptive finite-impulse-response (FIR) filters which perform the system identification task of modelling the effects of H and P. If the squared pressure is controlled, $e(t)$ is simply the measured pressure at the error sensor, whereas if the energy density is controlled, $e(t)$ is the gradient of the energy density.

Energy Density Measurement

To actively control the energy density in an enclosure, it is important to verify that accurate measurements of the energy density can be made. This involves obtaining a measure of both the pressure and the acoustic particle velocity. Both of these quantities are required by the adaptive controller in order to adjust the control transfer function in a manner that minimizes the energy density. A method for measuring the velocity can be obtained from Euler's Equation. Integrating both sides of Euler's Equation with respect to time yields

$$v = -\frac{1}{\rho} \int \nabla p \, dt \ . \tag{13}$$

The gradient of pressure can be obtained using the two-microphone technique, such as is commonly used to measure acoustic intensity. For one dimension, the approximate pressure gradient can be expressed as

$$\nabla p = \frac{p_2 - p_1}{\Delta x} , \tag{14}$$

where p_1 and p_2 are the measured pressures from two microphones separated by an axial spacing of Δx. Substituting Eq. (14) into Eq. (13) gives the velocity in terms of the measured pressures as

$$v = -\frac{1}{\rho \Delta x} \int (p_2 - p_1) \, dt \ . \tag{15}$$

Figure 5. Experimental setup.

Figure 6. Control schematic.

To determine the integral in Eq. (15), an analog differential/integrator circuit was developed to perform the subtraction and subsequent integration. Comparison of the energy density obtained in this fashion with the energy density obtained using frequency domain processing of the two microphone signals yielded excellent agreement throughout the frequency range of interest, thereby giving confidence in the measurement method.

EXPERIMENTAL RESULTS

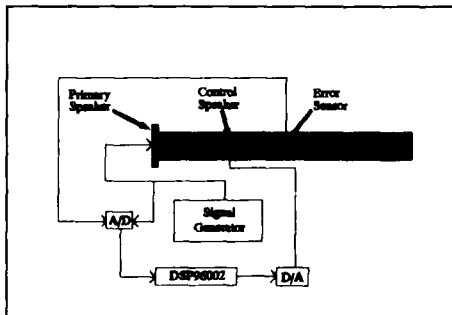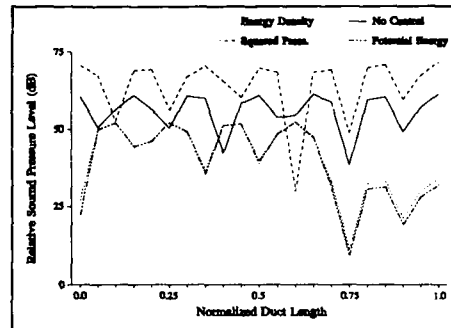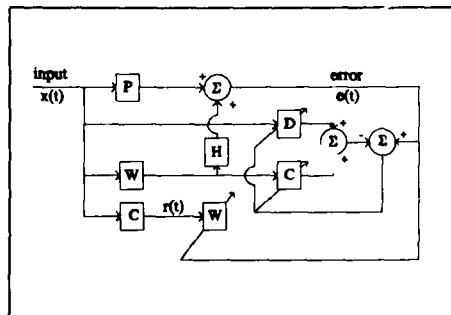Using the experimental apparatus described in the previous section, the methods of minimizing squared pressure and energy density were implemented, and results corresponding to the simulated results measured. Fig. 7 shows the results which were obtained with the error sensor located near the middle of the duct, and with an excitation frequency of 213 Hz. These results are to be compared with the simulation results in Fig. 2. The agreement is seen to be quite good, indicating that the simulation model is capturing the most important features of the problem. As with the simulation, minimal attenuation is obtained between the primary and secondary source, while approximately 35 dB attenuation is achieved with either method in the region past the secondary source.

The results of exciting the duct at an off resonance frequency of 200 Hz is shown in Fig. 8. This result is comparable to the simulation result in Fig. 3. Again, the agreement between simulation and experiment is seen to be quite good, with the method of minimizing the energy density giving markedly improved attenuation in the region beyond the secondary source. The difference between the attenuation achieved by the two methods in this region is even more pronounced experimentally than in the simulation, with the squared pressure method providing 15-20 dB attenuation, and the energy density method providing 35-40 dB attenuation.

Figs. 7 and 8 also demonstrate another property of the method of minimizing the energy density. In a standing wave field, the total energy density does not vary spatially even though the kinetic and potential energies each vary with position. The implication of this result is that the method of controlling the energy density should be relatively insensitive to the error sensor location. In Figs. 7 and 8, the modal composition of the acoustic field at the error sensor is rather different for the cases of near resonance and off resonance. This is reflected in the fact that the method of controlling the squared pressure performs considerably better for the near resonance case (Fig. 7) than for the off resonance case (Fig. 8). However, the performance achieved using the energy density method is seen to be comparable in both cases, indicating that the method is not very sensitive to the modal composition of the field. Other results obtained seem to confirm that the energy density method is much less sensitive to the error sensor location than the squared pressure method.

The effect of the secondary control source location can be seen in Fig. 9. These results correspond to those shown in Fig. 4, with the secondary source located at $x/L = 0.7$, and an excitation frequency of 180 Hz. Again, the agreement between simulation and experiment is seen to be rather good. The performance achieved by minimizing the squared pressure is seen to be poor, with the pressure field being amplified throughout most of the duct, while the method of minimizing the energy density gives global attenuation, with attenuation occurring at most locations in the duct. The attenuation achieved by the energy density method is not quite as much as predicted from the simulation, but the nature of the controlled field agrees well with the simulated result.
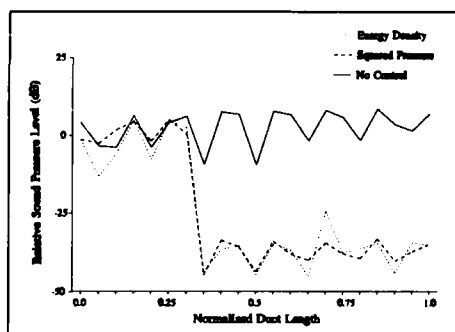

Figure 7. Measured sound pressure level for the error sensor located at a pressure maximum near the middle of the duct.
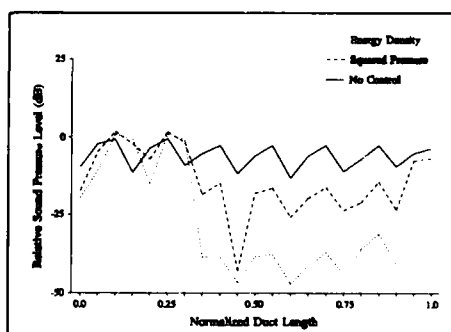

Figure 8. Measured sound pressure level for the error sensor located at a pressure minima near the middle of the duct.

367

CONCLUDING REMARKS

The method of minimizing the energy density in enclosures represents a new approach to the attenuation of noise in enclosures. If one assumes that the optimal solution consists of minimizing the total potential energy in the field, then numerical and experimental results have confirmed that the method of controlling energy density generally approximates the optimal solution considerably better than the method of controlling the squared pressure at the error sensor. It has been found that in a number of cases, minimizing the squared pressure may result in a small region of greater attenuation in the vicinity of the error sensor, i.e. a zone of silence, but the pressure level throughout the enclosure will generally be considerably higher than when minimizing the energy density. Thus, the method of minimizing the squared pressure provides

Figure 9. Measured sound pressure level for the secondary control source located at x/L = 0.7 and the error sensor located at x/L = 0.5.

a good solution when attenuation is required only over a small region, while minimizing the energy density provides the better solution when global attenuation is desired. In addition, the degree of global attenuation which is possible has also been found to depend on the primary and secondary source configuration, such that optimization of secondary source location is an issue which needs to be addressed to achieve the greatest possible control. However, the method of energy density minimization appears to yield the approximate optimal solution for a given source configuration.

A comparison has been presented between the methods of minimizing the squared pressure and the energy density for the case of a one-dimensional enclosure. The research is now being extended to the case of three-dimensional enclosures to gain further insight into the control which can be achieved for the general case of noise attenuation in arbitrary enclosures. For three dimensional enclosures, it becomes necessary to measure three velocity components to obtain the total energy density. While this involves additional microphones to obtain all of the necessary quantities, preliminary results indicate that a control system using several "energy density sensors" can control the sound field as effectively as a control system using a large number of pressure sensors. Thus, it may be possible to achieve greater control of the sound field using fewer transducers with energy density than with squared pressure.

REFERENCES

1. P. A. Nelson, A. R. D. Curtis, S. J. Elliott, and A. J. Bullmore, "The active minimisation of harmonic enclosed sound fields Parts I-III," **J. Sound Vib.**, Vol. 117, No. 1 (1987), pp. 1-58.
2. A. J. Bullmore, P. A. Nelson, and S. J. Elliott, "Theoretical studies of the active control of propeller-induced cabin noise," **J. Sound Vib.**, Vol. 140, No. 2 (1990), pp. 191-217.
3. S. J. Elliott, P. A. Nelson, I. M. Stothers, and C. C. Boucher, "In-flight experiments on the active control of propeller-induced cabin noise," **J. Sound Vib.**, Vol. 140, No. 2 (1990), pp. 219-238.
4. A. R. D. Curtis, P. A. Nelson, and S. J. Elliott, "Active reduction of a one-dimensional enclosed sound field: An experimental investigation of three control strategies," **J. Acoust. Soc. Am.**, Vol. 88, No. 5 (1990), pp. 2265-2268.
5. X. Dian and R. J. Bernhard, "Spatial extent of active noise control in an automotive vehicle," **Proc. Noise-Con 91**, Tarrytown, NY (July 1991), pp. 245-252.
6. S. D. Sommerfeldt and P. J. Nashif, "A comparison of control strategies for minimizing the sound field in enclosures," **Proc. Noise-Con 91**, Tarrytown, NY (July 1991), pp. 299-306.
7. S. D. Sommerfeldt and J. Tichy, "Adaptive control of a two-stage vibration isolation mount," **J. Acoust. Soc. Am.**, Vol. 88, No. 2 (1990), pp. 938-944.
8. S. D. Sommerfeldt, "Multi-channel adaptive control of structural vibration," **Noise Con. Eng. J.**, Vol. 37, No. 2 (1991), pp. 77-89.
9. B. Widrow and S. D. Stearns, *Adaptive Signal Processing* (Prentice-Hall, Englewood Cliffs, NJ, 1985), pp. 288-294.
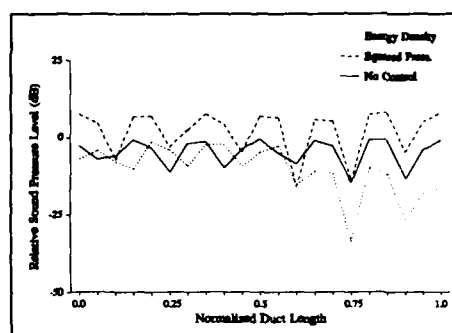
SECOND INTERNATIONAL CONGRESS ON
RECENT DEVELOPMENTS IN AIR- AND
STRUCTURE-BORNE SOUND AND VIBRATION
MARCH 4-6, 1992   AUBURN UNIVERSITY, USA

A PID CONTROLLER FOR FLEXIBLE SYSTEMS

A. Subbarao
Engineering Science Department
University of Wisconsin, Parkside
Kenosha, WI   53141

N.G. Creamer
Control Systems Branch
Swales and Associates, Inc.
Beltsville, MD   20705

M. Levenson
Control Systems Branch
Naval Research Laboratory
Washington, D.C.   20375

ABSTRACT

A systematic procedure to design a PID controller for a system with flexible modes is presented. A two-step approach is suggested to tune the controller parameters such that classical design specifications in terms of bandwidth, peak overshoot, settling time, and phase margin are approximately achieved. A numerical example illustrates the procedure.

INTRODUCTION

Feedback control of vibrations in mechanically flexib'e systems has application in spacecraft control [1] and ride quality improvement of air and surface missiles [2,3]. In theory, mechanically flexible systems require infinite dimensions to describe their behavior, but are usually modeled by a system of finite order. The on-board constraints (especially with space applications) pose a limitation on the size of the controller used. Some of the critical modes chosen are not necessarily the first few low-frequency modes.

Several authors [i.e. 4-7] have proposed methods for modeling and control of flexible systems. In the procedure followed by Moore [5], the high dimensional system is divided into strong and weak subsystems using internal dominance criterion. The weak subsystem is neglected and a state variable feedback control is derived. The high dimensional system in modal form is partitioned into two subsystems by Balas [6] and approximated by a system of lower order by dropping some modes referred to as residual modes. The effect of the residual modes is called "spillover". A prefilter is used in conjunction with the controller to minimize the effects of spillover. Gregory [7] and others have proposed modified procedures. The thrust in some of the procedures is the modeling aspect, and the control generally involves an observer design and state variable feedback. However, once a model is available it is not clear how to design a controller to meet classically required design specifications such as bandwidth, peak overshoot, settling time, and stability margins.

This paper deals with the design of a PID controller (with a lead/lag network) to achieve classical design specifications. A numerical example is added to illustrate the design.

CONTROLLER DESIGN

Consider a system with flexible modes as shown in Fig. 1. It is well known [6] that the poles and zeros representing each flexible mode will be close to each other. Figure 2 shows the pole-zero map of a system with a

rigid mode and two flexible modes. The transfer function for this system is given by

$$G(s) = \frac{K(s^2+z_1^2)(s^2+z_2^2)}{s^2(s^2+p_1^2)(s^2+p_2^2)} \tag{1}$$

In Fig. 2, the damping associated with the flexible modes is shown to be zero. In practice, the damping is known to be very small, on the order of 0.5%. Without any controller, the system shown in Fig. 2 is only marginally stable. To improve the performance a PID controller in cascade with a lead/lag network is introduced, having the transfer function

$$G_c(s) = (K_p+K_Ds+K_I/s)[(s+a)/(s+b)] \tag{2}$$

The lead/lag network provides extra flexibility for parameter tuning. The closed-loop system is shown in Fig. 3. The open-loop transfer function for the system with controller becomes

$$G(s)G_c(s) = \frac{K(K_Ds^2+K_ps+K_I)(s+a)(s^2+z_1^2)(s^2+z_2^2)}{s^3(s+b)(s^2+p_1^2)(s^2+p_2^2)} \tag{3}$$

The design of the controller in this case involves computation of K_p, K_D, K_I, a, and b to achieve required bandwidth, peak overshoot, settling time and phase margin values.

Characteristic Equation and Bandwidth

Control systems are generally low-pass filters and the performance of the closed-loop system is likened to that of a filter. By choosing the location of the filter poles, it is possible to adjust bandwidth and transient response [8]. Table 1 lists the characteristic equations for Butterworth type filters up to 8th order (similar results are available for other filters such as binomial, ITAE, etc.). For example, if a second-order Butterworth filter is chosen its characteristic equation leads to poles located at $-0.707\omega_n$ +/- $0.707\omega_n$j, therefore ensuring satisfactory transient performance. Thus the filter characteristics can be used to adjust the bandwidth and transient response. For the present design problem the characteristic equation is

$$s^3(s+b)(s^2+p_1^2)(s^2+p_2^2) + K(K_Ds^2+K_ps+K_I)(s+a)(s^2+z_1^2)(s^2+z_2^2) \tag{4}$$

If the bandwidth is specified from Table 1 the characteristic equation of the filter is known. By matching the coefficients of powers of s in Eq. (4) with the filter coefficients in Table 1, the required bandwidth and peak overshoot can be reached.

The characteristic equation of Eq. (4) is of eighth order, and matching corresponding coefficients of the Butterworth filter results in eight equations and five unknowns (K_p, K_D, K_I, a, b). In general a solution may not exist. One way of getting around this problem is to make use of results from model reduction [9].

Routh Approximate Reduced Order Models and Time Moments

Consider a high-order system whose transfer function is $G_n(s)$ and its Routh approximate reduced order model is $G_r(s)$. Let

$$G_n(s) = \frac{K_n}{s^n + a_1 s^{n-1} + \ldots + a_n} \tag{5}$$

$$G_r(s) = \frac{K_r}{s^r + a_1 s^{r-1} + \ldots + a_r} \tag{6}$$

The rth order Routh approximate model is obtained by making use of γ and δ tables [9]. The first r γ and δ coefficients depend on the parameters a_n, $a_{n-1}, \ldots, a_{n-r+1}$ and K_n. It is well known that the first r time moments of the system and the Routh approximate model are the same [10]. In other words, the low frequency behavior is dependent more on the coefficients a_n, a_{n-1}, $\ldots, a_{n-r+1}$ which are more dominant than the remaining coefficients. This result can be used to select the controller parameters K_p, K_D, K_I, a, and b. Hence, the coefficients of s^0, s^1, s^2, s^3, and s^4 in the characteristic equation given by Eq. (4) are matched with the corresponding coefficients of the Butterworth filter (eighth-order) in Table 1, and the controller parameters can be evaluated. An alternative way is to choose the parameters in a least-squares sense.

Influence of Numerator Dynamics
       When a controller with the above choice of parameters is implemented, the overall system performance may not meet the required design due to the following:

i)   In the design procedure adopted, the numerator dynamics are not taken into consideration.

ii)   For the selected values of K_p, K_D, K_I, a, and b the characteristic equation in Table 1 is not identical to the characteristic equation in Eq. (4). This may result in some deviation from the expected results.

A modification presented below can yield a satisfactory solution.

Effect of K_p, K_D, K_I, a, and b on Performance
       A change in the controller parameters causes changes in the bandwidth, peak overshoot, settling time, and stability margin. In general, for the choice of controller parameters used, all of the design requirements may not be achieved. Under these conditions, the parameter values can serve as starting estimates and can be perturbed in an attempt to meet design specifications. However, when the values of K_p, K_D, K_I, a, and b are altered, conflicting changes in bandwidth, peak overshoot, settling time, and stability margins might occur. In fact, all design criteria may not be met. Under such conflicting conditions only an "optimal" set of parameter values can be found, as described below.
       Let x_1^*, x_2^*, x_3^*, and x_4^* represent the desired values of bandwidth, peak overshoot, settling time, and phase margin, respectively. Also let x_1, x_2, x_3, and x_4 represent the corresponding actual values for a particular set of controller parameters. Consider an objective function of the form

$$J = c_1 (x_1^*-x_1)^2 + c_2 (x_2^*-x_2)^2 + c_3 (x_3^*-x_3)^2 + c_4 (x_4^*-x_4)^2 \tag{7}$$

The quantities x_1, x_2, x_3, and x_4 depend upon the controller parameters K_p, K_D, K_I, a, and b. The quantities c_1, c_2, c_3, and c_4 represent weighting coefficients. By perturbing the controller parameters a functional relationship can be developed between those parameters and the values of the bandwidth, peak overshoot, settling time, and phase margin. The optimal set of controller values are those which yield a minimal value of the objective function. The weighting factors can be chosen such that the design criteria of most importance can be most closely achieved. The following section

371

contains a numerical example illustrating the design approach.

NUMERICAL EXAMPLE

In this section the details of a controller design for a system consisting of a rigid mode and two flexible modes are discussed. For the system shown in Figures 2 and 3 the plant transfer function is chosen as

$$G(s) = \frac{1.2023(s^2+3.8^2)(s^2+4.8^2)}{s^2(s^2+4^2)(s^2+5^2)} \tag{8}$$

The flexible modes are located at +/-4j and +/-5j while the zeros are located at +/-3.8j and +/-4.8j. Let the design requirements be as follows:

i) Bandwidth around 4.5 rad/sec.
ii) Phase margin of at least 50 degrees.
iii) Peak overshoot of 20% for a step input.
iv) Reasonable settling time.

In order to meet these specifications a controller is introduced, as shown in Fig. 3, with a transfer function as given in Eq. (2). The open-loop transfer function becomes

$$G(s)G_c(s) = \frac{1.2023(s^2+14.44)(s^2+23.04)(K_p+K_Ds+K_I/s)(s+a)}{s^2(s^2+16)(s^2+25)(s+b)} \tag{9}$$

The eighth-order system characteristic equation becomes

$$\begin{aligned} s^3(s^2+16)(s^2+25)(s+b) \\ + 1.2023(s^2+14.44)(s^2+23.04)(K_Ds^2+K_ps+K_I)(s+a) = 0 \end{aligned} \tag{10}$$

To adjust the bandwidth and nature of the response as a first step, the controller parameters are estimated by comparing this polynomial with an eighth-order Butterworth filter equation as given in Table 1.

Design Step 1

As discussed in the previous section, the coefficients of s^0, s^1, s^2, s^3, and s^4 play a more significant role in the low-frequency system modes than the others. Hence, equating these coefficients of Eq. (10) with the corresponding coefficients of the eighth-order Butterworth filter and solving for the five controller parameters yields

$$a = 4.5$$
$$b = 16$$
$$K_p = 85.53$$
$$K_D = 31.1$$
$$K_I = 93.41$$

However, when this controller was implemented into the system it did not satisfy the required design specifications.

Design Step 2

Since the performance is not satisfactory, the controller parameters derived in Step 1 are chosen as starting values for an optimization design.

Using an objective function similar to the one given in Eq. (7), the optimal set was found to be

$$a = 4.5$$
$$b = 45$$
$$K_p = 85.53$$
$$K_D = 23.1$$
$$K_I = 93.41$$

When implemented, this "optimal" controller achieved the following performance values:

Bandwidth = 5.7 rad/sec
Phase margin = 105 degrees
Peak overshoot = 28%
Settling time = 8 seconds

EFFECT OF INACCURATE DYNAMICS

To find the controller parameters given above, the plant dynamics were assumed to be known exactly. Since a flexible system has infinite dimension and parameters which are known only approximately, the description by a model of finite dimension will involve some inexactness. To examine the performance under fuzzy conditions, a 2% change in the location of the poles and zeros of the flexible modes is considered and the results are provided in Figures 4 and 5. For this example the degeneration in performance is not significant (of course, larger inaccuracies in the dynamics will yield larger performance degradation). If the performance degradation is significant and unacceptable, a higher order controller such as

$$G_c(s) = (K_p + K_D s + K_I/s)[(s+a)/(s+b)][(s+c)/(s+d)] \qquad (11)$$

may be required, with the parameters chosen in a similar manner as described above.

CONCLUSIONS

A systematic procedure for the design of a controller for a system possessing flexible modes has been presented. Established results in model reduction techniques and filters are used to arrive at the controller parameters. If the design specifications are too rigid and conflicting, an optimal set of controller parameters can be found. The effect of inexactness in the model is briefly examined and a modification to take care of unacceptable performance degeneration is suggested.

REFERENCES

1. Larson, P.L. and Marsh, E., "Optimal Estimation and Attitude Control of a Solar Electric Propulsion Spacecraft," IEEE Trans. Aerospace Electr. Syst., Vol. AES-13, pp. 35-47, 1977.

2. Johnson, T., "The Aerodynamic Surface Location Problem in Optimal Control of Flexible Aircraft," Mass. Inst. Tech., Cambridge, MA, Report ESL-R-387, June 1969.

3. Klein, R., and Hughes, R., "The Distributed Parameter Control of Torsional Bending in Seagoing Ships," Proc. JACC, 1971.

4. Creedon, J.F., "Control of the Optimal Surface of a Thin Deformable Primary Mirror with Application to an Orbiting Astronomical Observatory," 3rd IFAC Symposium on Automatic Control in Space, March 2-6, 1970.

5. Moore, B.C., "Principal Component Analysis in Linear Systems: Controllability, Observability, and Model Reduction," IEEE Trans. Auto. Contr., pp. 17-31, 1981.

6. Balas, M., "Feedback Control of Flexible Systems," IEEE Trans. Auto. Contr., pp. 673-679, 1978.

7. Gregory, C.Z., "Reduction of Large Flexible Spacecraft Models Using Internal Balancing Theory," AIAA Jour. Guidance and Control, Dec 1984, pp. 725-732.

8. Graham, D. and Lathrop, R.C., "The Synthesis of Optimum Transient Response: Criteria and Standard Forms," AIEE Transactions, Vol. 72, pp. 273-287, 1953.

9. Rao, A.S., Lamba, S.S., and Rao, S.V., "Routh Approximate Time Domain Reduced Order Models for SISO Systems," Proc. IEE, London, pp. 1059-1063, Oct. 1978.

10. Hutton, M.F. and Friedland, B., "Routh Approximations for Reducing Order of Linear Time Invariant Systems," IEEE Trans. Auto. Contr., Vol AC-20, pp. 329-337, 1975.
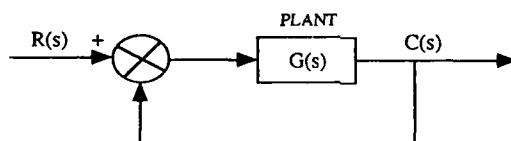
Figure 1: System with flexible modes
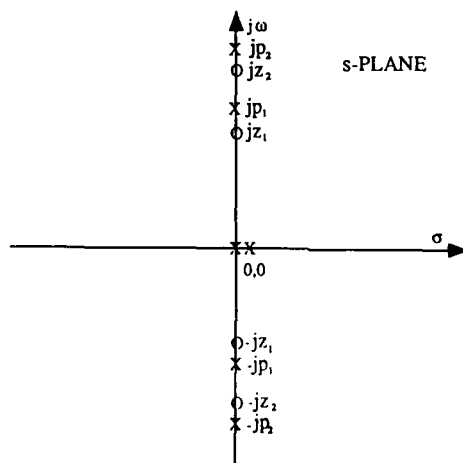
Figure 2: Pole-zero map of a system with two flexible modes
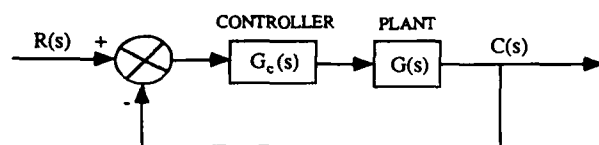
Figure 3: System with a controller

Table 1: Butterworth filter characteristic equations

$$s+w$$

$$s^2+1.4ws+w^2$$

$$s^3+2ws^2+2w^2s+w^2$$

$$s^4+2.6ws^3+3.4w^2s^2+2.6w^3s+w^4$$

$$s^5+3.24ws^4+5.24w^2s^3+5.24w^3s^2+3.24w^4s+w^5$$

$$s^6+3.86ws^5+7.46w^2s^4+9.13w^3s^3+7.46w^4s^2+3.86w^5s+w^6$$

$$s^7+4.5ws^6+10.1w^2s^5+14.6w^3s^4+14.6w^4s^3+10.1w^5s^2+4.5w^6s+w^7$$

$$s^8+5.12ws^7+13.14w^2s^6+21.84w^3s^5+25.69w^4s^4+21.84w^5s^3+13.14w^6s^2+5.12w^7s+w^8$$
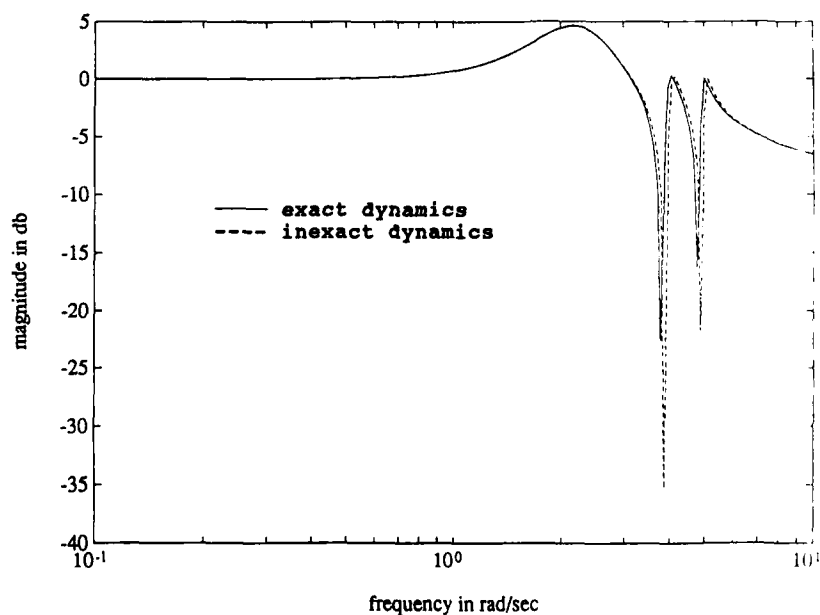
Figure 4: Magnitude plot for a system with controller; poles and zeros perturbed by 2%
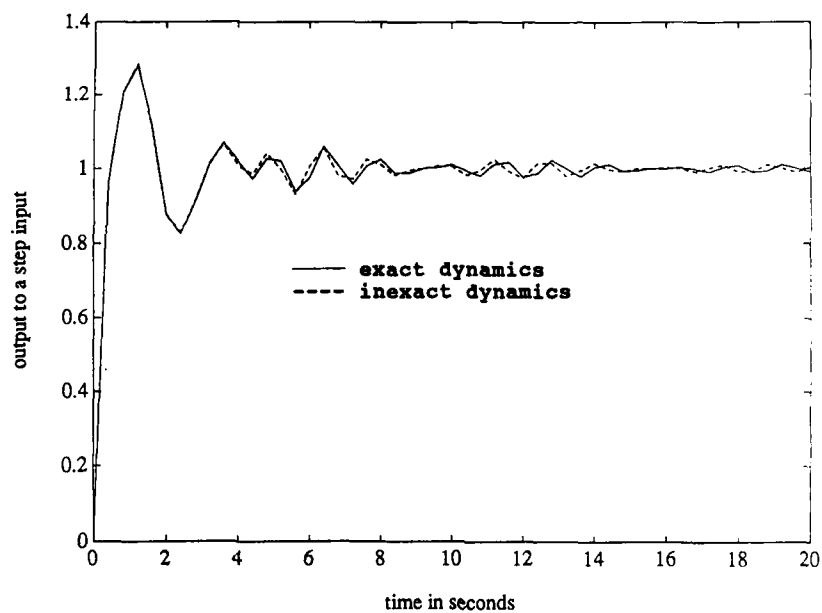
Figure 5: Step response for a system with controller; poles and zeros perturbed by 2%
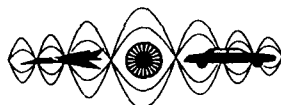
NUMERICAL SIMULATION OF ACTIVE STRUCTURAL-ACOUSTIC CONTROL FOR A FLUID-LOADED SPHERICAL SHELL

C.E. Ruckman and C.R. Fuller
Department of Mechanical Engineering
Virginia Polytechnic Institute & State University
Blacksburg, VA 24061 USA

ABSTRACT

Active structural-acoustic control (ASAC) has been demonstrated in the literature for several elementary structures using analytical models of the dynamic response. However, analytical approaches cannot be used for the practically important case of a 3-dimensional structure immersed in a dense fluid, which occurs primarily in marine applications. Such fully coupled problems, in which appreciable fluid-structure interaction takes place, require a numerical approach. This paper outlines efforts to study ASAC by computing dynamic responses of the stucture/fluid system with the computer program NASHUA. Two separate feed-forward control algorithms are developed and compared: a spatial-domain algorithm based on minimizing the radiated power, and a wavenumber-domain algorithm that does not require farfield pressure information. A spherical shell is examined to provide insight to the mechanisms by which ASAC reduces low-frequency radiation, and the results are compared with a closed-form solution.

INTRODUCTION

Active noise control is a promising technology for reducing low-frequency noise radiated from vibrating structures. Passive noise control treatments such as blankets and coatings are often adequate for mid- and high-frequency quieting, but tend to be cumbersome and massive at low frequencies. Conversely, active noise control systems usually perform best at low frequencies and become complex and ineffective as frequency increases.

Traditional active noise control methods can be thought of as active noise cancellation (ANC) because they use acoustic sources such as loudspeakers to set up an "anti-sound" field that cancels the offending noise field. If the noise field exhibits rapid spatial variations, ANC often requires many such sources to produce global changes. Furthermore, acoustic sources may be impractical if, for example, the structure is a vehicle submerged in water. For the special case of controlling radiation from flexible plates or shells, an alternate method known as active structural-acoustic control (ASAC) was first demonstrated by Fuller [1,2,3]. Rather than using acoustic sources as control actuators, ASAC uses vibrational inputs such as shakers or piezoceramic actuators applied directly on the structure. These control inputs, whose magnitudes are found by minimizing variables related to radiated pressure, alter the vibration pattern in order to reduce the vibration amplitude and/or the radiation efficiency. Hansen, Snyder, and Fuller [4] compared ASAC to ANC for a rectangular plate, and found that ASAC was a more effective approach for reducing radiated power. Other recent studies of ASAC [5,6,7] indicate that radiation from some structures can be controlled to a large extent with just one or two actuators.

Submerged shells are of significant practical interest, but they also represent a fundamental departure from existing work. All published studies of ASAC to date have used analytical approaches to obtain the

required structural-acoustic quantities. But for a general, 3-dimensional, fluid-loaded shell no such analytical expressions exist. Therefore, the present research uses a numerical approach to develop a general algorithm for investigating submerged shell structures. Predictions of the dynamic response and radiated field are obtained using the computer program NASHUA developed by Everstine [8]. NASHUA uses the finite-element program NASTRAN to compute structural quantities, and a boundary-element formulation to solve for the fully coupled structural-acoustic response. There are two significant advantages to using an approach based on NASHUA. First, no discretization of the ambient fluid is required since the fluid is modelled using boundary elements. Second, the approach can be used for any structure that can be modelled using NASHUA.

We analyze only steady-state, single-frequency forcing functions. The control algorithm used is a feedforward method in which we require *a priori* knowledge of the nature of the disturbance. After specifying the number and locations of the control actuators, we use linear quadratic optimal control theory (LQOCT) to solve for the complex optimal actuator forces that minimize a quadratic cost function.

The method is illustrated in this paper using a thin, fluid-loaded, spherical shell. The spherical shell is somewhat atypical of fluid-loaded structures because it possesses analytical solutions for certain excitation types. This simple case serves as a benchmark with which to develop methodologies and computer programs in anticipation of more complex structures. But the purpose of this paper is not to present a detailed treatise on control of the spherical shell, but rather to outline the goals of the research and give a few examples that illustrate some trends evident in preliminary results. The closed-form solution also serves to validate the numerical results.

THEORETICAL BACKGROUND

Modelling of Spherical Shell Response

Symmetry: The symmetry of a spherical shell requires more attention than might be expected. In particular, there is an important distinction between the response to a single force and the combined response to several forces. Figure 1 defines the spherical coordinate systems used. The spherical global coordinates (R,Φ,Θ) define locations in the farfield for purposes of combining the effects of multiple forces: R is the radial distance, Φ is the longitudinal angle measured from the global x-axis in the x-z plane, and Θ is the lateral angle measured from the global y-axis. The local coordinates (R,ϕ,θ) define locations relative to an individual force F. In Fig. 1, F is a normal concentrated load (point force) located in the global x-y plane at some angle α from the y-axis, and we define local axes (x',y',z) such that the force lies on the y'-axis. Then ϕ is the longitudinal angle measured from the x'-axis in the x'-z plane, and θ is the lateral angle measured from the y'-axis. For a single force, both the structural response and the radiated field are axisymmetric about the y'-axis, as in the example pressure field shown in Fig. 2a. However, if two forces are applied, then the combined response is not axisymmetric unless both forces act along the same axis. If the forces act along different axes, as in Fig. 2b, then the combined response exhibits a *plane of symmetry* that contains the two local y'-axes. If three or more forces are applied, the response is neither axisymmetric nor plane-symmetric unless one or more of the forces lie within a common plane. All loading cases examined in this paper exhibit either an axis of symmetry or a plane of symmetry.

Since the structural and acoustic responses are linear, we use superposition to obtain plane-symmetric multi-force responses. We can map the response from any individual force into the global coordinate system through a simple angular shift, and then add in the responses from other forces to find the combined response. To simplify the analysis, we only consider forces applied along the global x-y plane, that is, the $\Phi=0$ plane. This has two important ramifications: force locations can be specified with a single angular coordinate α, and the combined response to all the forces is symmetric about the $\Phi=0$ plane. Nevertheless, it is important to bear in mind that the response to each individual force remains axisymmetric.

Numerical Model: The finite-element portion of the NASHUA model uses axisymmetric plate elements that model both bending and membrane stresses. The nonuniform structural mesh contains 129 grid circles with smaller spacing near the two poles. The poles are not truly closed, but instead are approximated by grid circles of very small diameter. This implies that the point force is approximated by a normal ring force applied at the pole grid circle.

Analytical Model: For normal point force excitation, there exists an analytical solution for the dynamic response of a thin spherical shell as presented by Junger and Feit in Ref. [9]. This low-frequency solution is a

truncated summation of spherical harmonics in which the structure is assumed to experience only membrane stresses. If F is the complex magnitude of the applied force and a is the nominal shell radius, then the farfield pressure is expressed as

$$p(R,\theta) = \frac{\rho c}{4\pi a^2 kR} \sum_{n=0}^{\infty} \frac{(-1)^{n/2} F(2n+1)}{(Z_n + z_n) h_n'(ka)} P_n(\cos\theta)$$

(1)

where ρc is the specific impedance of the acoustic medium, k is the wavenumber, h_n' is the derivative of the spherical Hankel function, Z_n and z_n are the structural and acoustic impedances, and P_n is the Legendre polynomial. Reference [9] also gives expressions for the surface velocity and various other quantities.
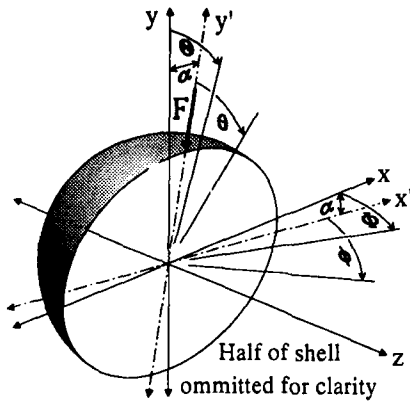
Fig. 1: Global coordinate system
(R, Φ, Θ) and local coordinate system
(R, ϕ, θ).
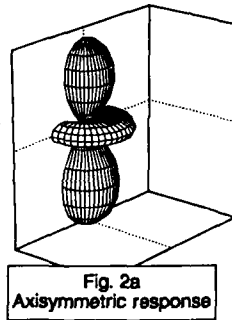
Fig. 2a
Axisymmetric response
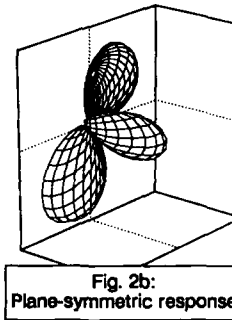
Fig. 2b:
Plane-symmetric response

Fig. 2: Examples of normalized farfield pressure magnitude.
a) Example axisymmetric response: point force at $\Theta = 0$.
b) Example plane-symmetric response: point forces at $\Theta = 0°$ and $\Theta = 75°$.

Control Approach

The control approach uses linear quadratic optimal control theory. Briefly, tne procedure is to form a positive-definite quadratic cost function, and then solve for the control forces that minimize the cost function. Interested readers should consult Ref. [3] for a more detailed derivation.

We evaluate and compare two separate cost functions. The first is a spatial-domain cost function that approximates the radiated power. This is intuitively appealing and guarantees global farfield pressure reductions, but requires error sensors in the farfield and would therefore be difficult to implement in some cases. The second cost function is a wavenumber-domain (k-domain) controller similar in concept to that discussed by Fuller and Burdisso in [10]. This cost function requires no farfield information, although computing the wavenumber spectrum requires some extra computation time. The radiated-power cost function and wavenumber cost function are denoted Π and Ψ, respectively.

Radiated Power Cost Function, Π If we had continuous expressions for farfield quantities, we could find the radiated power by integrating the acoustic intensity over an enclosing surface in the farfield. Instead for the numerical approach we know farfield responses only at discrete points, so we form our cost function as a weighted summation that approximates the radiated power when we use a large number of points. Suppose we compute the farfield pressures at a large number of farfield locations and write them in a vector $\mathbf{P}$. Furthermore, suppose we define two vectors $\mathbf{F}$ and $\mathbf{S}$ containing the magnitudes of all the control and noise forces, respectively. Since the radiated field is linear, we can sum the contributions of each of the noise and control forces (appropriately mapped into the global coordinate system) to find the total radiated field. We can write this summation in matrix form as

$$\mathbf{P}(R, \Phi, \theta) = \mathbf{A}^T \mathbf{F} + \mathbf{B}^T \mathbf{S}$$

(2)

379

The matrices A and B contain farfield pressures due to each of the forces acting individually, and they may be obtained either from NASHUA calculations or from the analytical solution. We can now define a cost function Π as

$$\Pi = \mathbf{P}^T \mathbf{G} \mathbf{P}^*, \tag{3}$$

where superscript T indicates a matrix transpose, superscript * represents the complex conjugate, and G is a diagonal matrix whose entries are constants determined by the spacing of the points in P. As the number of elements in P approaches infinity, Π approaches the total radiated power. For the low frequencies addressed in this paper, we can represent the radiated field to sufficient accuracy using 100 to 400 farfield points in P. The number of points required depends on the complexity of the radiated field; to ensure that enough farfield points are used, the radiated power can be compared to an analytical solution that uses closed-form integration to obtain the radiated power.

Wavenumber Cost Function, Ψ The wavenumber cost function is based on a one-dimensional spatial Fourier transform of the normal surface velocity. A two-dimensional transform would probably produce better results, and will be a topic for future research, but the one-dimensional transform better serves the purpose of illustrating the method. To obtain the transform, we restrict our attention to the normal velocity along along a line: the intersection between the shell surface and the global x-y plane (the Φ=0 plane.) The general spatial Fourier transform of a normal surface velocity distribution $v(x)$ is given by

$$V(k) = \frac{1}{2\pi} \int_{-\infty}^{+\infty} v(x) e^{-ikx} \, dx \tag{4}$$

where x is the linear distance along the surface and k is the wavenumber. For a general NASHUA model with uneven gridpoint spacing, the surface velocities are not evenly spaced in x; therefore we must use direct integration rather than using a Fast Fourier Transform (FFT). For the spherical shell, the domain of the integral is not infinite but rather extends only between $0 \le x \le 2\pi$. Note that because the spherical shell is a closed surface, wavenumbers exist only in integer multiples of $1/a$ where a is the shell radius.

We define a quadratic cost function Ψ that sums the squared magnitudes of the values in the wavenumber spectrum as shown below. By defining a vector V containing the spatial Fourier transform at each wavenumber k_i, we obtain a form similar to that used by the radiated power cost function Π. The size of this vector, and thus limits of the summation, are determined by the grid point spacing, which determines the largest values of k for which the transform can be reliably found. By minimizing Ψ, we reduce the magnitudes of the largest wavenumber components and, hopefully, reduce the radiated power as well. For a flat plate, Ψ would be directly proportional to the radiated power. For the present work the relation is less direct, but the formulation is straightforward and serves the purpose of illustrating the method.

$$\Psi = \sum_i V(k_i) V^*(k_i) = \mathbf{V}^T \mathbf{V}^* \tag{5}$$

It is well known that for an infinite flat plate, only subsonic wavenumber components contribute to farfield radiation. Thus for some structures, one could possibly restrict attention to the radiating portion of the wavenumber spectrum instead of including the entire wavenumber spectrum in the cost function. This could be an important topic in future research. However, such is not the case for a spherical shell. From the following expression for the acoustic radiation impedance it is clear that nearly all wavenumber components contribute to the farfield radiation:

$$z_n = i\rho c \frac{h_n(ka)}{h_n'(ka)} \tag{6}$$

Wavenumbers for which (6) is purely imaginary do not contribute to farfield radiation. But only certain discrete values of k satisfy this criterion, and there is no range of wavenumbers that can be summarily dismissed as is the case with planar radiators. Thus for the spherical shell, the wavenumber cost function should include all k for which the transform can be reliably computed.

RESPONSE OF SPHERICAL SHELL TO POINT-FORCE EXCITATION

Figure 3a shows the radiated power for a single force as a function of the frequency; the solid curve represents the results of the NASHUA model, and the broken curve represents the analytical solution. The levels agree well throughout the frequency range. At frequencies above roughly $ka=1.3$, the resonance frequencies predicted by the analytical solution are slightly higher than those predicted by NASHUA. The discrepancy is due partly to modelling approximations in the NASHUA model, which uses a small-diameter ring force to approximate a point force, and partly to simplifications used in the analytical model. Other NASHUA results agree well with analytical results, but for brevity no other direct comparisons are presented in this paper. The models are adequate for this preliminary analysis, which is aimed primarily at developing methodologies.
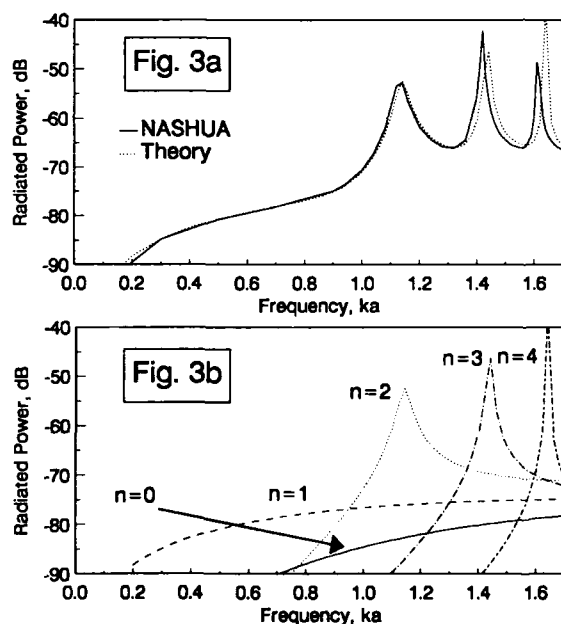
Fig. 3: Response to point-force excitation.
a) Radiated power vs. frequency. b) Modal components of radiated power vs. frequency.
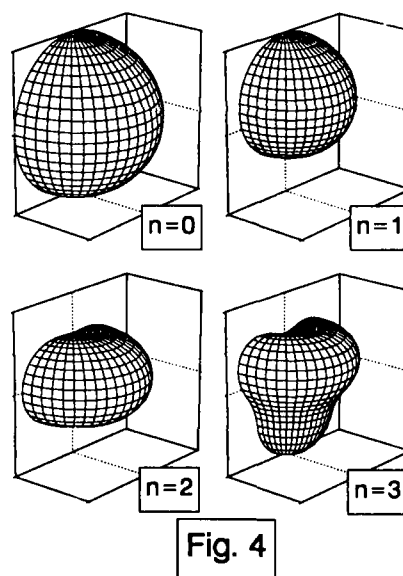
Fig. 4: Normalized mode shapes for $n=0$ (breathing mode), $n=1$ (rigid-body mode), $n=2$, and $n=3$.

In Fig. 3b the radiated power is broken into its modal components, which can be found using the analytical solution. Figure 4 shows the shapes of the first few modes; mode shapes are denoted by the number n of nodal circles present. Interestingly the $n=0$ "breathing mode" does not dominate the response anywhere in this frequency range. The $n=1$ rigid-body mode dominates the response at very low frequencies. At $ka=1.14$ the dominant mode is the axial expansion/contraction of the $n=2$ mode, and so on. These modal components provide an important tool for explaining the behavior of the controller.

ASAC USING ONE CONTROL FORCE AT OPPOSITE POLE

The simplest control setup is to place a single control force at $\Theta=180°$, directly opposite the noise force at $\Theta=0°$. By optimizing the complex control force magnitude at each frequency, we obtain the radiated power spectra shown in Fig. 5. Figure 5a shows the radiated power vs. frequency with each of the two controllers and also without control. Fig. 5b is similar except that the quantity shown is the wavenumber cost function. Note that results obtained using the radiated power cost function are referred to as "Π Controller", while results obtained using the wavenumber cost function are referred to as "Ψ Controller." In both cases, we see that a single control force reduces the cost function by 10 dB or more at resonance frequencies. (Here we consider $ka=0$ to be the resonance frequency of the $n=1$ mode.) The reductions between resonances are much smaller, generally dropping to zero at some frequency between resonances. However, the Ψ Controller does not always reduce the radiated power Π, particularly between resonances. Similarly, the Π Controller does not always reduce the wavenumber cost function Ψ. Only at resonance frequencies do the two controllers produce reductions in both cost functions. Recalling that our objective is to minimize the radiated power, and that the wavenumber cost function is merely a convenience by which we avoid the need for farfield error sensors, we must conclude that the Ψ Controller is a poor replacement for the Π Controller if we wish to control off-resonance frequencies.
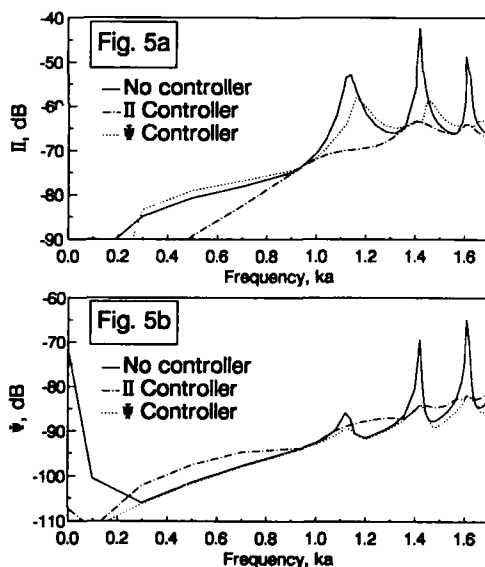
Fig. 5: Controller performance with one control force.
a) Π vs. frequency. b) Ψ vs. frequency.
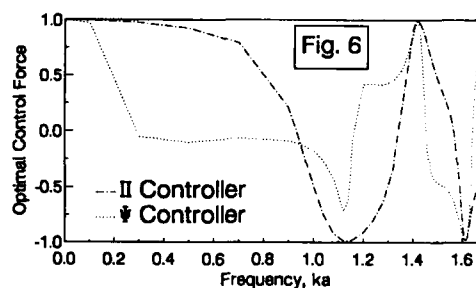
Fig. 6: Optimal Control Force vs. Frequency.

Examining the control forces specified by the two control approaches reinforces the conclusion that we need a more sophisticated design approach for the wavenumber controller. Figure 6 shows the control forces obtained with each of the two controllers. At resonance frequencies, the agreement between the two is good. But between resonances there are large discrepancies, and at some frequencies there are even sign mismatches.

The behavior of the radiated power controller becomes clear upon examining the modal components of the radiated power before and after control is applied. For example, suppose the noise force and the control force are equal in magnitude; both forces will excite the same structural modes in the same relative magnitudes because of the spherical symmetry. However, there will be phase differences between the modes excited by the noise force and those excited by the control force. Modes for which the two forces are out of phase are attenuated, and modes for which the two forces are in phase increase in amplitude. Here, with the control force

positioned 180° away from the noise force, the phase difference is always either 0° and 180°. This is a coincidental result of the spherical symmetry, since resonances always exhibit an anti-node 180° away from the force location. Furthermore, the control force magnitude at a resonance is always equal in absolute value to the noise force magnitude: *the contribution of each mode is either eliminated or doubled for a 6 dB increase.*

Figure 7a shows the modal contributions before and after applying the Π Controller at a frequency of $ka=1.14$. At this frequency the $n=2$ mode dominates the farfield response. The controller therefore applies a force that is out of phase with the $n=2$ mode, practically eliminating *its contribution to the radiated power.* As a side effect, this control force also cancels the $n=0$ mode; however, it reinforces the contributions from the $n=1$ and $n=3$ modes, both of which increase by 6 dB. This "spillover" effect explains why we cannot achieve perfect cancellation.

In Fig. 7b we see that at $ka=0.94$, an off-resonance frequency, the contributions from the $n=1$ and $n=2$ modes are nearly equal. Unfortunately, any control force which cancels the $n=1$ contribution from the noise also reinforces the $n=2$ contribution from noise, and raises the total radiated power. The optimal solution is to completely eliminate the control force, since any control force at all only increases the cost function.
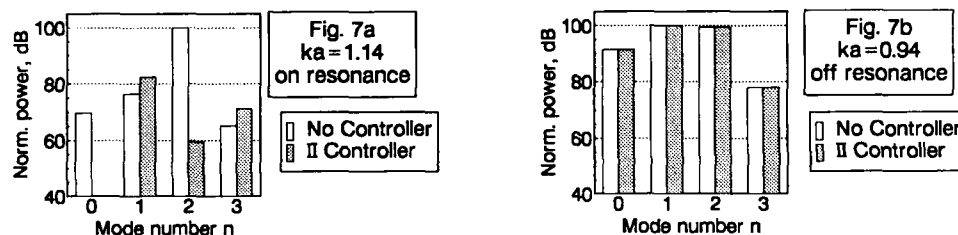
Fig. 7: Modal contributions to Π before and after applying the Π Controller. a) $ka=1.14$. b) $ka=0.94$.

ASAC USING VARIABLE-LOCATION CONTROL FORCES

Past experience has shown that controller performance can depend strongly on both the number of actuators and their locations [11]. The control algorithm as developed above can easily handle multiple control forces. In addition, to examine the effects of actuator location, we can require the control approach to optimize the actuator location as well as the complex force magnitude at each frequency. Examples from the literature [12,13] have used numerical optimization for this purpose. In this paper, since the computation times involved are relatively short, we can simply examine a large number of actuator locations and find by trial and error which location(s) produces the best results. A more general approach involving numerical optimization may be a topic for future research.

To simplify the task we apply two restrictions to the possible control actuator locations. To ensure that the combined response remains plane-symmetric, all the forces must lie in the $\Phi=0°$ plane. Furthermore, to ensure that the solution is meaningful, the control forces must not be too close to the noise force. For example, if the controller could place a control force coincident with the noise force, it would obtain perfect cancellation but would do nothing to illuminate the problem at hand. We choose to allow control forces only between $\Theta=70°$ and $\Theta=180°$ in the $\Phi=0°$ plane (see Fig. 1).

To make the results more instructive, we use a different disturbance in this section. If the disturbance is a point force, we gain little advantage by varying the control force location because the optimum control force location is almost always $\Theta=180°$. In this section the disturbance is a pair of point forces that resembles a concentrated moment: a force of +1.0 at $\Theta=0°$ combined with a force of -1.0 at $\Theta=5°$.

Figure 8 shows the radiated power vs. frequency without control and with three different control scenarios. The solid curve is the response with no controller applied. The dashed curve uses a single fixed-location control force located at $\Theta=180°$, but is barely visible because it lies on top of the solid curve. This setup achieves virtually *no reduction in the radiated power, reinforcing the importance of proper actuator* location. The dotted curve uses a variable-location point force, i.e. at each frequency we use trial and error to find the optimum location for the control force. This setup achieves large attenuations at low frequencies, but

only 3-4 dB attenuations at higher frequencies. The dash-dot curve uses two variable-location control forces, and achieves the best performance of the three.

That the controller performance improves as more control forces are added can be explained by referring again to Fig. 7b. In that case, a single control force achieves no attenuation, since any decreases in the contribution of the $n=1$ mode are accompanied by increases in the contribution of the $n=2$ mode and vice versa. But intuitively it is clear that a second control force could be arranged to counteract the increase in the $n=2$ mode, providing a net reduction in the radiated power. If the radiated power contained significant contributions from three modes instead of two, then adding a third control force would likely reduce the radiated power even further.
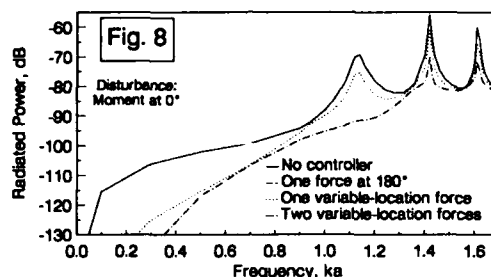
Fig. 8: Control of a concentrated moment using fixed-position and variable-position actuators.

SUMMARY

Our primary research goal is to develop a computer program for investigating active structural-acoustic control (ASAC) of 3-dimensional, fluid-loaded structures. For generality, we use NASHUA as the numerical engine for calculating structural-acoustic dynamic responses. The program thus represents a general numerical capability, and can examine almost any structure that can be modelled using finite elements. We use a feedforward control approach and investigate two different cost functions: one based on the radiated power, and one based on wavenumber concepts. We illustrate some preliminary results using the example of a thin, fluid-loaded, spherical shell. Numerical results agree well with an analytical solution.

For a point-force disturbance, a single control force can drastically reduce the radiated power at very low frequencies and at the first few resonances, although the performance between resonances is poor. The two control algorithms achieve nearly the same results at resonances. However, between resonances the wavenumber controller does not reduce the radiated power, and in many cases actually increases the radiated power. Clearly, the wavenumber controller as formulated here is too simple to allow a complete representation of the structural-acoustic field. Future research will focus on developing a more sophisticated wavenumber controller.

For a disturbance resembling a concentrated moment, a point control force located opposite the disturbance location has virtually no effect. Using a variable-location control force, i.e. finding the best actuator location at each frequency, improves performance substantially, especially at low frequencies. Adding a second variable-location control force gives further improvements, and points out the importance of choosing proper actuator locations.

ACKNOWLEDGEMENTS

REFERENCES

1. C.R. Fuller, "Apparatus and method for global noise reduction," US Patent No. 4,715,599 (1987).

2. C.R. Fuller, "Active Control of Sound Transmission/Ratiation From Elastic Plates By Vibration Inputs: I. Analysis," *Journal of Sound and Vibration*, Vol. 136, No. 1, pp.1-15 (1990).

3. H.C. Lester and C.R. Fuller, "Active Control of Propeller Induced Noise Fields Inside a Flexible Cylinder," AIAA Paper 86-1957 (1986).

4. C.H. Hansen, S.D. Snyder, and C.R. Fuller, "Reduction of Noise Radiated by a Vibrating Rectangular Panel by use of Active Sound Sources and Active Vibration Sources," Proceedings of the 1989 International Conference on Noise and Vibration, Singapore, pp.E50-E57 (August, 1989).

5. C. Guigou and C.R. Fuller, "Active Control of Edge Sound Radiation from a Semi-infinite Elastic Beam With a Clamped Edge", submitted for publication in *Journal of the Acoustical Society of America* (1991).

6. R. Clark and C.R. Fuller, "Control of Sound Radiation with Adaptive Structures," *Proceedings of the First Joint U.S./Japan Conterence on Adaptive Structures*, Maui, Hawaii, pp.227-245 (1990).

7. Y. Gu and C.R. Fuller, "Active Control of Sound Radiation Due to Subsonic Wave Scattering From Discontinuities on Fluid-Loaded Plates. I: Far-field Pressure," *Journal of the Acoustical Society of America*, Vol. 90, No. 4, Pt. 1, pp.2020-2026 (October, 1991).

8. G. Everstine and A. Quezon, "User's Guide to the Coupled NASTRAN/Helmholtz Equation Capability (NASHUA) for Acoustic Radiation and Scattering," DTRC CMLD-88/03, David Taylor Research Center, Bethesda, MD (February, 1988).

9. M. Junger and D. Feit, *Sound, Structures, and Their Interaction* (The MIT Press, Cambridge, MA, 1986), 2nd ed.

10. C.R. Fuller and R.A. Burdisso, "A Wavenumber Domain Approach to the Active Control of Structure-Borne Sound," *Journal of Sound and Vibration*, Vol. 148, No. 2, pp.355-360 (1991).

11. J.D. Jones and C.R. Fuller, "Active Control of Sound Fields in Elastic Cylinders by Multicontrol Forces," *AIAA Journal*, Vol. 27, No. 7, pp.845-852 (July, 1989).

12. G.-S. Chen, R.J. Bruno, and M. Salama, "Optimal placement of active/passive members in truss structures using simulated annealing," *AIAA Journal*, Vol. 29, No. 8, pp.1327-1335 (August, 1991).

13. B.-T. Wang, R.A. Burdisso, and C.R. Fuller, "Optimal Placement of Piezoelectric Actuators For Active Control of Sound Radiation From Elastic Plates." *Proceedings of NOISE-CON 91*, Tarrytown, NY, pp.267-274 (July, 1991).
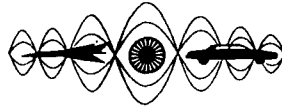
SECOND INTERNATIONAL CONGRESS ON
RECENT DEVELOPMENTS IN AIR- AND
STRUCTURE-BORNE SOUND AND VIBRATION
MARCH 4-6, 1992 AUBURN UNIVERSITY USA

OPTIMUM LOCATION AND CONFIGURATION OF AN INTRA-STRUCTURAL FORCE ACTUATOR FOR MODAL CONTROL

Captain Jeffrey S. Turcotte
USAFA/DFEM
US Air Force Academy, CO 80840
U.S.A.
Captain Steven G. Webb
USAFA/DFEM
US Air Force Academy, CO 80840
U.S.A.
Captain Daniel J. Stech
Frank J. Seiler Research Laboratory/NH
U.S. Air Force Academy, CO 80840
U.S.A.

ABSTRACT

This research investigates the damping characteristics of a force actuator using velocity feedback and compares different actuator configurations and placements on a flexible structure. Assuming a limiting value for the force available from the actuator, the best actuator configuration and placement is determined for several modes. The analytical formulation is then verified experimentally using the 20-bay planar truss located at the Air Force Academy. The results indicate that the best location for the actuator assembly is near the maximum curvature of a given mode. Further, actuator assemblies spanning several bays of the structure are better at controlling the lower modes, while assemblies spanning only two or three bays control higher modes better.

INTRODUCTION

Large flexible structures may require a multitude of control systems to eliminate unwanted vibrations. Different types of actuators can be used to control a structure's vibrations, and each has its advantages and disadvantages [1,2,3]. One type of actuator uses a coil and armature to generate forces between parts of the structure. This force generator is attached to the structure by a few truss members, and a control signal sent to the actuator causes a set of forces (but a net force of zero) to be applied to the structure; thereby reducing vibrations in certain modes.

Although this type of actuator is simple in concept, how should it be configured, and where must it be located on the structure to maximize its effectiveness? In this study, different actuator configurations, each utilizing a single force generator on the 20-bay planar truss at the U.S. Air Force Academy, are analyzed and compared in their abilities to dampen out the vibrations of a given mode. Control actuation is obtained by using a single sensor to generate velocity feedback to the actuator assembly. Though this method of control is simple, it dampens only certain modes at the possible expense of destabilizing other modes; however, if the forcing spectrum is narrow and well defined, the number of destabilized modes can be minimized. To avoid stability problems, any destabilized modes can then be stabilized by either the inherent damping in the structure or by adding passive damping.

THE CONFIGURATION

The 20 bay planar truss used for research at the Air Force Academy is composed of System M12 Meroform truss members. Steel bars at each batten

(chord wise member) were added to scale down the natural frequencies. The configuration is shown in Figure 1. The truss rests on steel balls rolling on steel plates, which provides planar motion with relatively low damping. The truss is "fixed" at one end by a steel table which is modeled as a rigid body attached by four springs to ground. Additional information concerning the hardware may be found in reference 3.
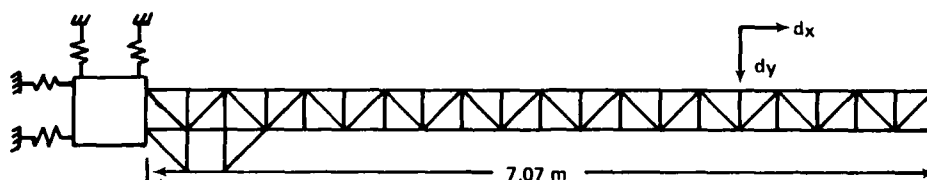

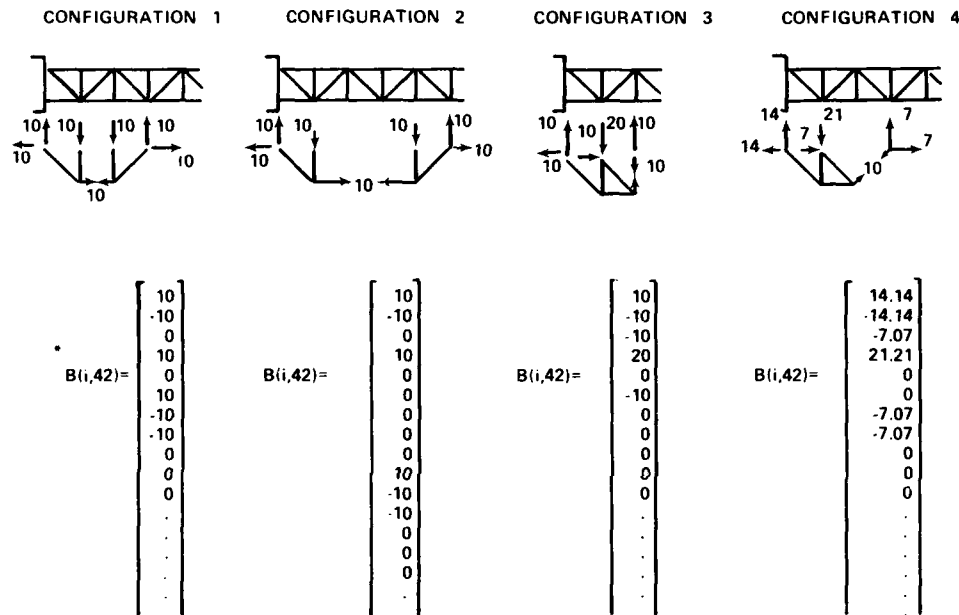FIGURE 1:   PLANAR TRUSS WITH CONTROL ASSEMBLY STRUCTURE AT BAY 1

The control system used in this study consists of a servo-accelerometer with signal conditioning circuitry, an analog computer to integrate the accelerometer output, a force generator, and some truss members to attach the force actuator to the truss. The sensor (accelerometer) is a Sundstrand Data Control Model QA-700. Since velocity feedback is used to generate the control signal, an approximate phase shift ("integration") of $\pi/2$ is effected on the accelerometer signal using a Comdyna GP-6 analog computer. The GP-6 is also used to apply an appropriate gain before sending the signal to the force generator, a BEI Kimco model LA14B-24A linear force actuator. The force generator is attached to the main structure by additional Meroform components and adaptive bracketry.

MODELING

Simplicity was a prime consideration in the modeling of the control assembly, since only comparisons and not absolutes were being sought. The truss was previously modeled by Major Steve Lamberson using MSC Nastran. For the purpose of this research, the model was reduced using Guyan reduction to the 42 degrees-of-freedom (one each x and y displacement for each bay, d_x and d_y in Figure 1) needed to allow the control planar force inputs for any location of the control assembly on the main truss. To make the control system forces determinant and thus simplify as well as speed-up the analysis, it was assumed that the control assembly members had pinned connections (no internal bending). By this assumption, each connection had forces only, and the forces were easily determined by assuming equilibrium (neglecting the mass of the control assembly). This assumption was checked for validity by actually incorporating the control assembly (configuration 1) into the finite element model at bays 1 and 18. This check revealed that the assumption caused errors ranging from 1% in mode 1 to 12% in mode 16. These errors should not affect the qualitative conclusions made.
To compare various configurations, a standard peak force per velocity input of 10 lb-s/ft (146 N-s/m) at the actuator was chosen. This corresponds to the same peak actuator force output for a given frequency and amplitude of vibration; therefore results for the same mode but different control assembly configurations and locations can be directly compared. The truss input forces resulting from the four control assembly configurations used in this study are examined in Figure 2. This figure shows the various configurations of the control assembly studied, the way they distribute the control force to the main truss, and the corresponding elements of the gain matrix (only one column of the gain or "B" matrix is non-zero -- the column corresponding to the degree-of-freedom where the

sensor is attached).

CONFIGURATION 1   CONFIGURATION 2   CONFIGURATION 3   CONFIGURATION 4

$$
B(i,42)=\begin{bmatrix} 10 \\ -10 \\ 0 \\ 10 \\ 0 \\ 10 \\ -10 \\ -10 \\ 0 \\ 0 \\ 0 \\ \cdot \\ \cdot \\ \cdot \\ \cdot \end{bmatrix}
\qquad
B(i,42)=\begin{bmatrix} 10 \\ -10 \\ 0 \\ 10 \\ 0 \\ 0 \\ 0 \\ 0 \\ 10 \\ -10 \\ -10 \\ 0 \\ 0 \\ 0 \\ \cdot \\ \cdot \end{bmatrix}
\qquad
B(i,42)=\begin{bmatrix} 10 \\ -10 \\ -10 \\ 20 \\ 0 \\ -10 \\ 0 \\ 0 \\ 0 \\ \cdot \\ \cdot \\ \cdot \end{bmatrix}
\qquad
B(i,42)=\begin{bmatrix} 14.14 \\ -14.14 \\ -7.07 \\ 21.21 \\ 0 \\ 0 \\ -7.07 \\ -7.07 \\ 0 \\ 0 \\ \cdot \\ \cdot \\ \cdot \end{bmatrix}
$$

*Elements are shifted down two rows for each bay away from the table that the assembly is shifted.

FIGURE 2:   CONTROL SYSTEM CONFIGURATIONS AND THEIR FORCE INPUTS

Neglecting any inherent damping, the system may be described by the standard second order equation:

$$[M]\{\ddot{x}\} + [K]\{x\} = \{F\} = -[B]\{\dot{x}\} \tag{1}$$

where [M] is the mass matrix, [K] is the stiffness matrix, {x} is the displacement vector, and [B] is the force per velocity (gain) matrix that reads the velocity input from the correct sensor degree-of-freedom (arbitrarily chosen as the tip y-displacement, DOF 42) and directs the actuator forces to the proper degree-of-freedom in accordance with the force distribution given in Figure 2 for each control assembly configuration. By shifting the right hand term of Eq. (1) to the left side, we get a standard damped second order homogeneous system, albeit not necessarily a stable one. This is why we used velocity feedback for control -- it gives us a simple equation of motion. The control capability of the system can then be determined by a simple complex eigenanalysis. The modal damping caused by the control system is given by:

$$\zeta_i = \cos\,\tan^{-1}\left[\frac{Im(\text{e-value}_i)}{Re(\text{e-value}_i)}\right] \tag{2}$$

where ζ_i is the fraction of critical damping c/c_{cr} in the ith mode as

389

determined by geometry of the Eq. (1) eigenvalue (e-value) in the complex plane. The damping factor, as calculated in Eq. (2), is a measure of how quickly a vibration in a given mode will dampen out. The higher the ζ, the faster the vibration will dampen out.

THE ANALYSIS

A damping factor determination was made for each mode with each control assembly configuration and each control assembly location. A short routine was set up in Matrixx to form the [B] matrix given the desired location of the control assembly. The routine assigns the peak control forces to the appropriate [B] matrix elements as indicated in Figure 2, reorganizes the equation into state space, performs the complex eigenanalysis, and executes Eq. (2) for each complex-conjugate eigenvalue pair. Executing this routine for each possible control assembly configuration and location allowed several comparisons to be performed.

The first comparison we considered was how the control damping varies as a function of control assembly location. Control assembly configuration 1 (Figure 2) was used for this comparison. If the end of the control assembly was attached at the fixed end of the truss, it was considered to be located at bay 1. Figure 3 plots the truss mode shapes for modes 1, 2, and 3; and Figure 4 plots the damping factors for each of these modes as a function of control assembly location. Comparing Figure 4 to Figure 3 shows that the best control effect for a given mode is possible when the control assembly is located at the point of maximum curvature for that mode. For example, the maximum curvature of mode 3 is at bay 16, which is precisely the location of the control assembly that yields the greatest damping factor. Note that the best location of the control assembly for damping the first mode of a cantilever structure is at the support.

Next, the damping ability of the various configurations were compared to help decide whether a long, short, or angled configuration is best. All bending modes through mode 16 (higher modes were not clearly distinguishable as bending modes) were analyzed using all four configurations, and the best damping for any location was plotted for each mode in Figure 5. This comparison cannot be used to compare damping ability for different modes because the peak forces differ with different modes (the [B] matrix holds the peak force constant only for the same modes -- the peak force is smaller for higher modes). The comparison of different configurations for the same modes, however, shows that configurations spanning more bays can better control the lower modes. On the other hand, if higher modes are to be stabilized, a shorter configuration is more effective. Note that configurations 1 and 2 are identical in design except that configuration 2 spans five truss bays, whereas configuration 1 spans only three bays. Notice from Figure 5 that configuration 2 damps mode 1 at ζ = 0.118, whereas configuration 1 damps mode 1 at ζ = 0.068 . Thus, the longer configuration (config. 2) controls the first mode much better than the shorter configuration (config. 1). The converse is true for mode 16, for which the longer configuration provides a ζ of only 0.005, and the shorter configuration yields a ζ of 0.011 . The actual damping values for mode 16 are questionable because we neglected the mass of the control assembly in the analysis, but the qualitative comparison between configurations should still be valid. This theory is further supported by the poor performance of configuration 3, which spans only two truss bays. This configuration, though the actuating force is at 90 degrees to those of configurations 1 and 2, shows that a shorter control assembly will perform poorly for the lower modes but will give at least average performance for controlling higher modes (note square data on Figure 5). Configurations that put the force actuator at a 45 degree angle to the truss (for example configuration 4, Figure 2) were found to be as effective as other configurations that span the same number of bays (compare configurations 1 and 4 in figure 5). Thus we see no analytical advantage or disadvantage to putting the actuator at an angle to the main structure.
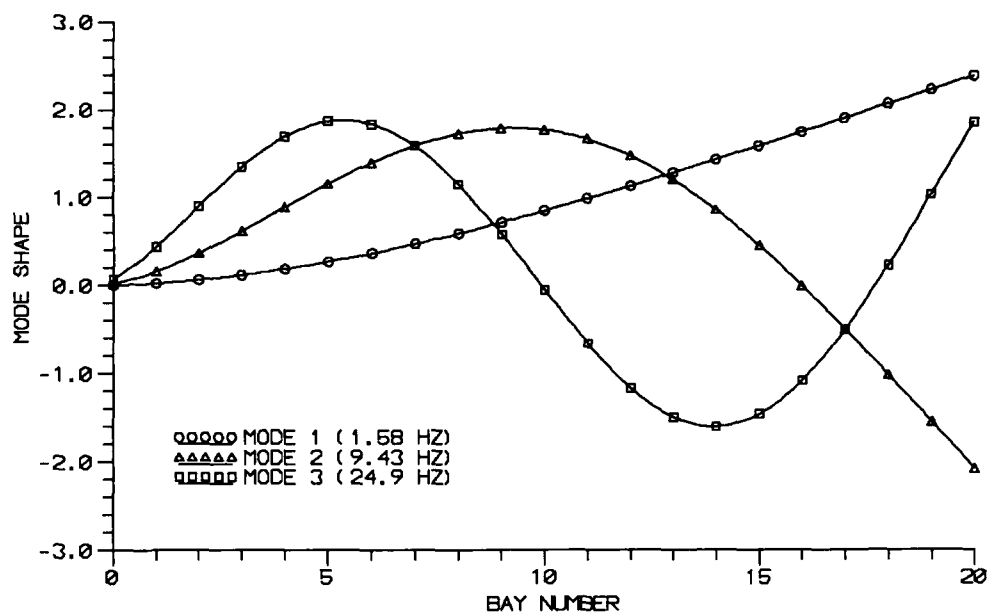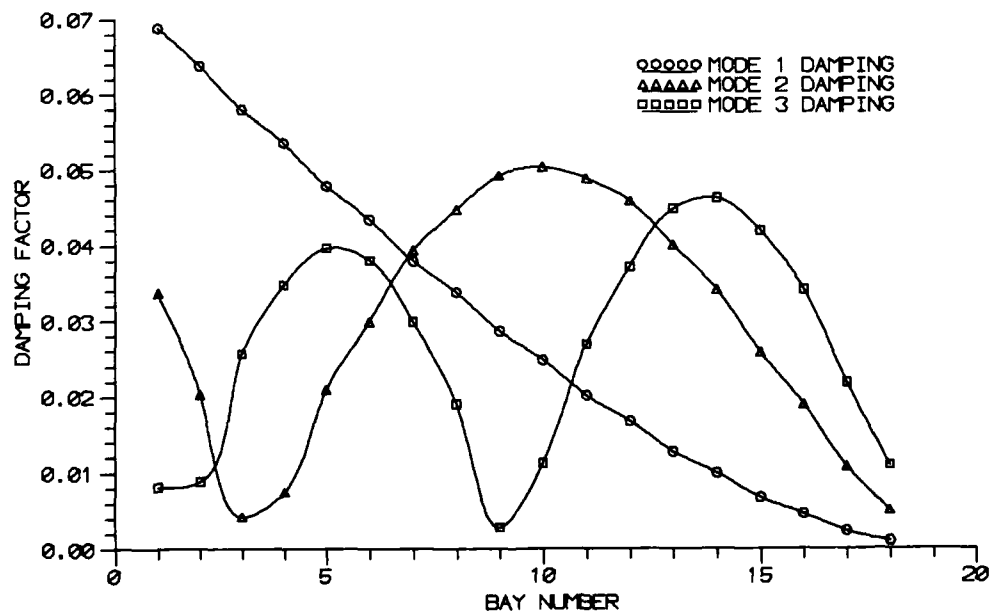
FIGURE 3: TRUSS MODE SHAPES

FIGURE 4: MODE DAMPING VERSUS ACTUATOR ASSEMBLY LOCATION
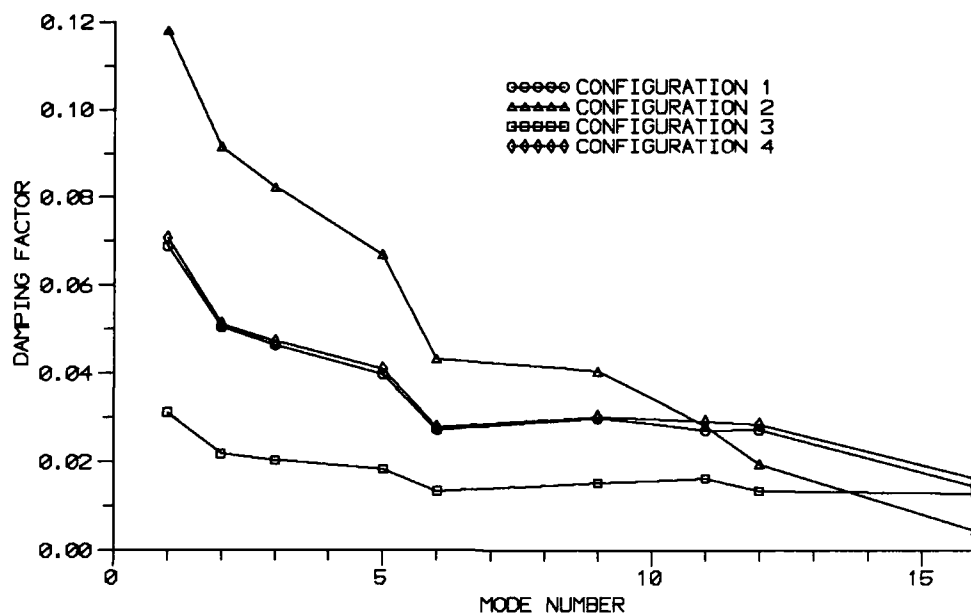CONTROL ASSEMBLY CONFIGURATION 1

FIGURE 5: COMPARISON OF CONFIGURATIONAL DAMPING CAPABILITIES

THE VERIFICATION

Although the analysis was straight-forward, we desired some experimental verification. The plan was to measure and compare the damping factors of a given mode for control power on and control power off. Recall now that the inherent damping of the structure was neglected in the analysis. The difference between the damping factors for control power on versus off should equal the damping factor calculated in the analysis; because only the inherent damping is measured with control power off, whereas both inherent and control damping are present with control power on. We could not achieve the analytical gain experimentally so we established a reasonable gain, verified it, and re-performed the analysis based on that gain. Then we performed the experiment trying to dampen out an initial vibration in mode 1 using a configuration 1 control assembly located at bay 1. Unfortunately, the inherent damping of mode 2 was not enough to avoid a mode 2 instability (the analysis indicated that mode 2 eigenvalue has a positive real root component for the sensor at the truss tip), so we were not able to measure the damping in mode 1 with control power on; therefore,this test was a failure. We could have relocated our accelerometer such that both modes 1 and 2 would be stable, but, since the inherent damping in mode 1 was large, we opted instead to reverse the control polarity and try to dampen mode 2 (again with the configuration 1 assembly located at bay 1 -- not at the optimum location for mode 2 stabilization). To do this, we used the original polarity to excite the structure (drive it unstable in mode 2) and then reversed the polarity to observe the decay. Then, we again excited the structure and allowed it to decay naturally. We used logarithmic decrement (assuming viscous inherent damping) on these decay traces to determine the damping factors for (1) inherent plus control damping and (2) inherent only damping. From these

392

two values, we calculated the experimental control damping:

$$\zeta_{control} = \zeta_{control+inherent} - \zeta_{inherent} \tag{3}$$

The experimental data for mode 2 yielded: $\zeta_{control}$ = .0089 -.0023 = .0066; whereas, the analysis (based on a configuration 1 assembly located at bay 1 with a gain of 25.5 N-s/m) yielded $\zeta_{control}$ = 0.0059 . These values compare within about 10%, which is reasonable considering the sources of error (inaccurate phase shift on integrator, truss assumption for the control force analysis, and viscous damping assumption for logarithmic decrement). Although the eigenanalysis indicated a positive (unstable) pole for mode 1 and a negative (stable) pole for mode 2, the inherent damping in mode 1 was apparently adequate to maintain stability. There were no instabilities for this test, so we deemed it successful. Because of limitations in the availability of the test article and the simplicity of the analysis, further verifications were not pursued.

PLANS FOR FUTURE WORK

The destabilization of mode 2 during our attempt to dampen mode 1 made clear the need to address the stabilization of modes with positive poles. The complex eigenanalysis, which assumes no inherent damping, indicates that some of the modes may be destabilized by the control system regardless of which sensor location is selected (whether a mode is stabilized or destabilized by the control system depends on whether the mode has the sensor motion in-phase or out-of-phase with the curvature of the truss at the control assembly location). This doesn't really happen, because some modes have enough inherent damping to overcome the control forces driving them. In space applications however, the structural damping available may not be adequate to suppress the destabilizing control forces. If a sensor location cannot be found that allows all modes to be stabilized, some passive damping must be added to the unstable modes, or else the control scheme must be improved to avoid the positive poles. This is an area for future research.

Inclusion of the actuator assembly in the finite element model would provide more accurate results and enable greater experimental verification. Even though we believe the general conclusions we make here are valid without further work, we will repeat some of the previous work with the control actuator assembly included in the model as time permits.

CONCLUSIONS

We set out to determine the best configuration and location for an intra-structural control force actuator for modal control. Trying several configurations and each possible location on the 20-bay truss at the Air Force Academy, we made two general conclusions: (1) the greatest control authority is available when the control assembly is located near the maximum curvature of the mode being controlled, and (2) control assemblies spanning more bays are better at controlling the lower bending modes and vice-versa. We verified this approach experimentally but recognized that the simple control scheme used would not be adequate in many cases, because it will likely destabilize other modes (depending on the amount of inherent damping in each mode).

ACKNOWLEDGEMENTS

393

REFERENCES

1.   Webb, Steven and Jeff Turcotte, :Analysis of a Passively Tuned
Actuator on a Low-Order Structure," Paper #90-3500, AIAA Guidance,
Navigation and Control Conference, August 1990.

2.   Hagood, N. W. and Prof. A. von Flotow, "Damping of Structural
Vibrations with Piezoelectric Materials and Passive Electrical Networks,"
Paper #ICC, Proceedings of Damping '89, February 1989.

3. Hallauer, William L. Jr. and Steven Lamberson, "Experimental Active
Vibration Damping of a Plane Truss Using Hybrid Actuation," Paper #AIAA
89-1169, 30th SDM Conference, April 1989.

SECOND INTERNATIONAL CONGRESS ON RECENT DEVELOPMENTS IN AIR- AND STRUCTURE-BORNE SOUND AND VIBRATION

MARCH 4-6, 1992   AUBURN UNIVERSITY, USA

DEVELOPMENT OF AN ACTIVE VIBRATION CONTROLLER FOR AN ELASTIC STRUCTURE

Douglas R. Browning and Raymond S. Medaugh

AT&T Bell Laboratories
Whippany, New Jersey 07981
U.S.A.

ABSTRACT

In recent years, improvements in materials and manufacturing processes and, more profoundly, advances in data-acquisition and computer technologies have made it possible to apply sophisticated active control techniques to noise and vibration problems. The challenge for the control-system engineer is to integrate these technologies into useful, reliable, and cost-effective problem solutions. The art of active noise and vibration control comprises the application of these technologies to reduce the undesirable dynamic response of the system being controlled.

This paper reviews the process of developing an adaptive structural-vibration controller and presents the details of the various analytical and experimental stages in designing the working system. An elastic test structure and rotating disturbance source is described. Experimental and analytical modal analyses results are presented. The selection of actuation and sensing technologies and spatial placement on the test structure are also described. Lastly, a discussion of the Filtered-X Least Mean Square (FXLMS) algorithm used to cancel the disturbance-generated vibrations is presented. Experimental results are described that show more than 40 dB of attenuation in measured power is achieved with the narrowband FXLMS approach.

INTRODUCTION

In recent years improvements in materials and manufacturing processes and, more profoundly, advances in data acquisition and computer technologies have made it possible to apply sophisticated active control techniques to noise and vibration problems. For example, methodologies and algorithms that in the past could not be processed fast enough to control high-frequency signals are now being demonstrated [1], and integrated into commercial products as well [2],[3]. Likewise, new material developments in rare earth magnets [4], piezoceramics [5], and magnetostrictive alloys [6] are spawning high force, high frequency actuators, availing an array of previously unsolved vibration problems to active control technology. The challenge for the control-system engineer is to integrate these technologies into useful, reliable, and cost-effective solutions for noise and vibration problems. The art of active noise and vibration control comprises the application of these technologies to reduce the undesirable dynamic response of the system being controlled.

This paper reviews the process of developing an adaptive structural-vibration controller, presenting the details of the various analytical and experimental stages in designing a working system. The paper is organized into three sections. Each section describes a major sub-process involved in completing this project. Section I introduces the test structure and rotating disturbance source. Experimental and analytical modal analyses results are presented. Section II details the selection and characterization of actuation and sensing technologies used in the control system. And Section III addresses the signal processing aspects of implementing the real-time FXLMS algorithm used to cancel the disturbance-generated vibrations. Experimental results demonstrate that more than 40 dB of attenuation in measured power is achieved for the narrowband FXLMS approach.

SECTION I

Structure and Excitation Source

An elastic structure, shown in Figure 1, was designed and built specifically for this study. The plate is a 0.584 x 0.685 x 0.0032 m (23 x 27 x 0.125 in.) Type 304 stainless steel sheet. It is passively mounted on 0.266 m (10.5 in.) high vertical supports using twenty-two 0.019 m (3/4-in.) natural rubber isolators per supported end. The vertical mounts are in turn rigidly fastened to the surface of the isolation table. A disturbance source is affixed to the surface of the plate centered along a line parallel to the supported ends. The source consists of an eccentric mass, m, mounted to a shaft coupler supported at each end by a dual bearing arrangement and driven by a speed-controlled motor. The encoder is
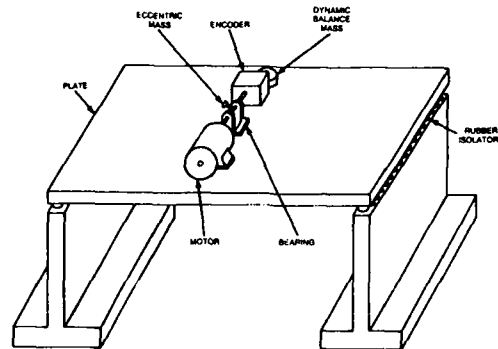
Figure 1. Experimental structure and disturbance source

attached in line with the shaft to provide a square- wave signal whose frequency is proportional to rotational speed. The balance mass located behind the encoder dynamically offsets the inertial effect of the motor.

The resultant disturbance force produced by the rotating imbalance acts through the center of the bearing base, coinciding with the geometric center of the plate. The force relationship is given by

$$\mathbf{F}(t) = F(\cos 2\pi f_o t \mathbf{u}_x + \sin 2\pi f_o t \mathbf{u}_y) = F_x(t)\mathbf{u}_x + F_y(t)\mathbf{u}_y , \tag{1}$$

where f_o is the rotating frequency of the disturbance source, F is the peak force generated and is equivalent to $mr(2\pi f_o)^2$ where r = eccentricity, and F_x and F_y are the component forces in the x and y directions, respectively. A couple, M_x, is also transmitted to the plate, equivalent to the product F_x multiplied by the height of the shaft above the surface of the plate.

Structural Characterization

A dynamic characterization study was performed on the structure after it was assembled. Identifying system dynamics is important for two reasons. First, a physical understanding of the structural dynamics must be attained prior to selection of spatial locations of error sensors and actuators for the controller. Second, transfer function information must be obtained for the structure in mathematical terms over the frequency band of interest for use in controller algorithm computations.

Experimental study. An experimental modal analysis was performed on the structure with 3 source and 48 response points. A total of 144 experimental frequency-response functions (acceleration/force) were obtained. The experimental data along with the test geometry was then ported to a post-processing package for modal parameter extraction, analytic curve-fitting, and mode shape animation. The polyreference curve fitting technique was employed to extract best-fit, real-mode, linear, dynamic parameters using all experimental data. Table 1 is a listing of parameters obtained for the first five modes. Mode frequency, damping ratio, and amplitude describe each mode's characteristics.

Table 1. Modal Parameters for Experimental Platform

Polyreference Modal Parameters (ref-1, resp-10)			
Shape Record	Frequency (Hz)	Damping (%)	Amplitude
1	13.606	5.454	-1.699+00
2	24.703	2.935	-4.624+00
3	56.769	1.466	+2.579+01
4	66.982	1.413	-4.688+00
5	75.320	1.804	+4.349+01

Using these parameters, the transfer function from point j to point k on the structure can be expressed as in Eq. (2) [7].

$$\frac{a_j(\omega)}{f_k(\omega)} = \frac{1}{M_{jk}^R} + \sum_{r=1}^{N} \frac{-(\omega^2)2A_{jk}^r\omega_r\sqrt{1-\zeta_r^2}}{-(\omega^2)+i2\omega\zeta_r\omega_r+\omega_r^2} + \frac{\omega^2}{K_{jk}^R} , \tag{2}$$

396

where
M_{jk}^R = residual mass term
K_{jk}^R = residual stiffness term
N = highest mode in frequency range of interest
a_j = acceleration response at location j due to f_k
f_k = force input at location k
ω = frequency in radians per second (rad/sec)
A_{jk}^r = residue of mode r
ω_r = natural frequency of mode r in rad/sec
ζ_r = damping ratio of mode r .

This expression assumes the form of a linear combination of second-order sections with proportional viscous damping plus residuals, which is consistent with the selected curve fit technique. The residue of mode r, A_{jk}^r, is related to the respective amplitude term listed in Table 1 by the relation

$$A_{jk}^r = \frac{amplitude_r}{\omega_r^2} . \tag{3}$$

A complete point-to-point best-fit linear description of structural dynamic behavior is therefore available using these relationships. Figure 2 is a plot of experimental data overlaid with the regenerated analytic function for response point 10 due to input source 1. Magnitude units are meters-per-second-squared per Newton.
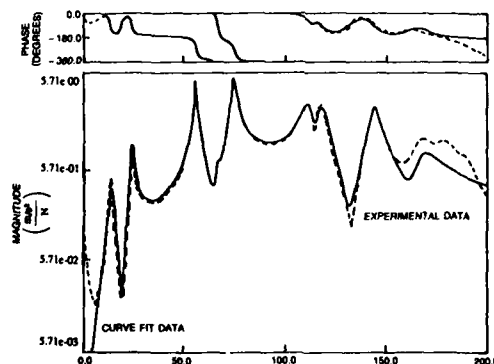

Figure 2. Experimental and curve fit frequency response function from test structure

Finite element analysis. A finite element model (FEM) was generated in tandem with the experimental study. The model consists of 650 elements and 620 nodes. The motor, bearing, and encoder are represented by effectively rigid blocks of equivalent mass and size of the real objects. All shaft and bearing intersections are modeled to allow frictionless rigid-body rotation of the shaft. Boundary conditions for the two compliantly supported sides of the plate are modeled by elastic vertical translational springs at the 44 attachment points to the rubber isolators. The spring rate for the isolators was calculated based on the linear-modeling criteria of harmonic loading and sub-150 Hz operation. With these assumptions, the spring rate is a function of the cylindrical isolator geometry and shear modulus, given by

$$k_{eff} = \frac{3G_\omega A}{L} , \tag{4}$$

where G_ω is the shear modulus of rubber, A is the cross-sectional area of isolator, and L is the height of isolator. The computed dynamic spring constant was found to be 22,210 N/m (126.8 lbf/in.). Dynamic spring rates were also experimentally obtained, varying between 21,020 and 70,050 N/m (120 and 400 lbf/in.) depending on magnitude, type (harmonic, impulse, random), and frequency of the applied load.

Modeling the plate with compliantly-supported edges and the rubber elements as vertical springs with constants of 22,210 N/m (126.8 lbf/in.) resulted in correlation of the first three mode frequencies within 7 percent of the experimental frequencies. The first three mode shapes correlated exactly. Table 2 lists the first five mode frequencies of both the FEM results and experimental results. The discrepancy in the two higher modes is associated with unmodeled rotational stiffness of the rubber supports. Further refinement of the model was deemed unnecessary since reliance on experimental information was justified for this application.

397

Table 2. FEM Modal Analysis Results

Mode Frequencies, Hz		
Mode	FEM	Experimental
1	13.83	13.61
2	26.39	24.70
3	54.37	56.77
4	90.69	66.98
5	97.01	75.32

Mode Shape Visualization

For the platform, experimental mode shapes were generated from the experimental mode shape vectors and the test geometry of the platform. The first five experimental modes are shown in Figure 3. The Finite Element Model (FEM) also provided mode shapes, displayed in Figure 4. The first three modes are identical to experimental results. Modes 4 and 5 differ due to boundary condition modeling. Notice that FEM mode shape 5 is identical to experimental mode shape 4.
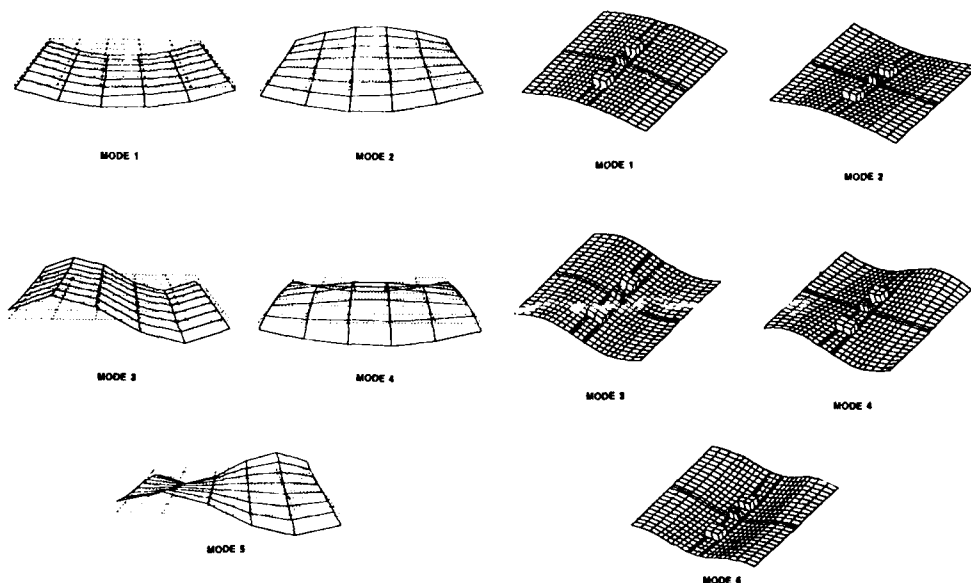
Figure 3. Mode Shapes - experimental   Figure 4. Mode Shapes - FEM

SECTION II

Actuator Selection and Characterization

Electrodynamic exciters were used in the active control system. They operate on the same moving-coil principle as loudspeakers. The magnetic field produced by coil-current flow and a surrounding permanent-magnet bias field generate attraction/repulsion forces on the coil. These forces act on the drive output part of the device.

In the active control system, control action is delivered to the structure via transduced voltage signals from D/A ports. It is desirable that the control force applied to the vibrating structure be simply proportional to this voltage over the frequency range of interest. Unfortunately, the output-force vs. input-voltage response of electrodynamic actuators is frequency-dependent. Back Electro-Motive Force (EMF) generated in the coil due to armature motion creates this dependence. Therefore, a means of generating a broadband, constant-of-proportionality relationship between force and applied voltage was developed. This equalization was accomplished by designing and constructing a transconductance amplifier. The resulting force constant is 1.45 N/volt (0.327 lbf/volt). The electromechanical theory and amplifier arrangement are described below.

Actuator electrical-to-force relationships. For the moving-coil actuator, force developed in the coil is proportional to input current through the relation $f_a(t) = \beta i_a(t)$, where β = force constant with units N/amp. When the armature is in motion, the armature coil generates a back EMF as it moves in the magnetic field of the permanent magnet assembly. The back EMF is proportional to coil velocity by a constant α. The resulting Laplace transform expression for the current in the actuator coil thus becomes

398

$$I_a(s) = \frac{1}{r_c}[V_a(s) - \alpha s X(s)] , \tag{5}$$

where
r_c = coil resistance
V_a = voltage applied to coil
α = coil velocity constant with units volts-second per meter
$sX(s)$ = Laplace-transformed coil velocity.

The developed coil force is then

$$F_a(s) = \beta \frac{1}{r_c}[V_a(s) - \alpha s X(s)] . \tag{6}$$

This expression shows the frequency-dependent relationship ($s = i\omega$) between voltage applied to the actuator coil and the coil force applied to the armature due to the presence of the coil-velocity term. In many cases the armature will be attached directly to a structure. Thus, the generated force is a function of the attached structure dynamics through the back EMF coupling term. The relationships between electrical properties of the actuator, dynamics of the actuator, and dynamics of the attached structure can be expressed in terms of the force applied to the structure by the actuator. The one-dimensional transformed equation of motion for the actuator/structure system is

$$m_a s^2 X(s) + c_a s X(s) + k_a X(s) = F_\Omega(s) - F_a(s) . \tag{7}$$

With no actuator present, the structure's force response to a displacement is given by

$$F_\Omega(s) = H_\Omega(s) X(s) , \tag{8}$$

where the Laplace transform $H_\Omega(s)$ arises from the constant-coefficient linear differential equation relating displacement, $x(t)$, and reaction force of the structure, $f_\Omega(t)$.

For the electrodynamic actuator, the coil force is proportional to input current so that $F_a(s) = \beta I_a(s)$. Substituting this expression and Eq. (8) into Eq. (7) yields

$$\frac{F_\Omega(s)}{I_a(s)} = \frac{-\beta H_\Omega(s)}{m_a s^2 + c_a s + k_a - H_\Omega(s)} . \tag{9}$$

The expression relating force applied to the structure to the applied coil voltage thus becomes:

$$\frac{F_\Omega(s)}{V_a(s)} = \frac{-\beta H_\Omega(s)}{r_c \left[m_a s^2 + \left(c_a - \frac{\alpha\beta}{r_c} \right) s + k_a - H_\Omega(s) \right]} . \tag{10}$$

For the situations where the structure's response dominates actuator armature motion, i.e., $m_a s^2 + c_a s + k_a \approx 0$, Eq. (9) and (10) reduce to

$$\frac{F_\Omega(s)}{I_a(s)} \approx \beta, \tag{11}$$

and

$$\frac{F_\Omega(s)}{V_a(s)} = \frac{\beta}{r_c + \frac{\alpha\beta s}{H_\Omega(s)}} . \tag{12}$$

399

Eq. (11) indicates current drive provides the most direct control over the force applied to the structure when compared to voltage drive, (12), which has a reactive component due to $\alpha \neq 0$.

Transconductance amplifier details. The transconductance amplifier was developed to force a constant-of-proportionality relationship between coil force and voltage. The transconductance amplifier operates to force

$$\frac{F_\Omega(s)}{V_a(s)} = \frac{\beta}{R_{ld}} ,$$

(13)

where R_{ld} = load resistance, by eliminating the actuator impedance back EMF dependence. Eq. (13) is essentially obtained by zeroing the back EMF term in Eq. (6). Figure 5 is a schematic representation of the hybrid transconductance converter.
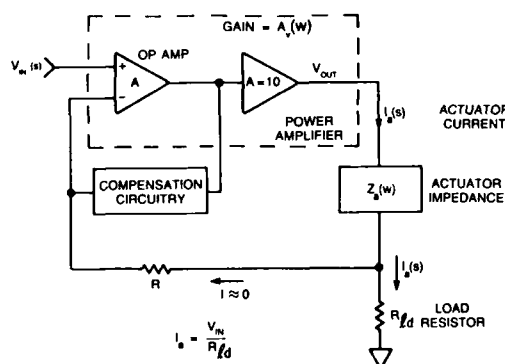

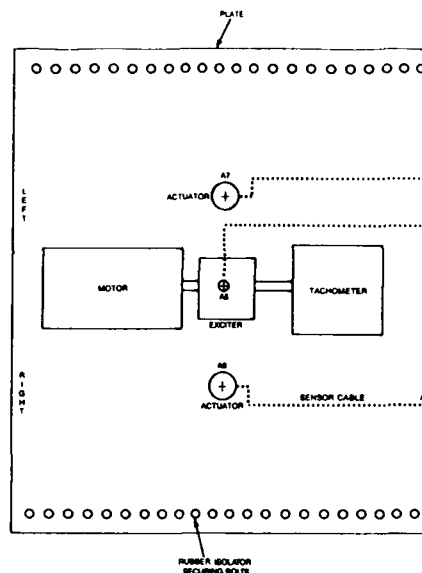Figure 5. Transconductance amplifier schematic

Figure 6. Actuator and sensor locations

Select actuator and sensor locations. Sensor and actuator locations were selected based on structural modal properties. From the derived mode shapes of the platform, it was clear that the location of the excitation source would have greatest effect on those modes that have high relative displacements at the center of the platform. Likewise, the couple introduced by the excitation source at the center of the plate would drive certain modes harder than others at various operating frequencies. Based on this information, actuator and sensor locations were selected to be capable of controlling at least the first two bending modes of the platform, modes one and three, using two actuation points. Bending modes here refer to those modes with shapes resembling half (or multiples thereof) sinusoids between constrained boundaries. Figure 6 shows the selected sensor and actuator sites. Accelerometers were chosen as the sensing technology. Factors leading to this decision were technical (high-frequency response, high sensitivity, linearity) as well as practical (availability, versatility).

Attachment of the actuators and the balancing mass to the structure slightly affected system dynamic properties. Several frequency-response measurements were performed at various locations on the structure to identify these effects. Modal frequencies were shifted at most 1 Hz within the first five modes. Modal damping, too, was altered, typically increased by a factor of 2. However, mode shapes in this frequency range were unaffected.

SECTION III

Survey and Selection of Active Control Techniques

In this application, a control method that requires minimal, approximate, a priori knowledge of the mechanical plant is preferred. Since the disturbance signals are narrow-band with unknown and slowly varying center frequency, the control method should be one that can concentrate cancellation over the narrow spectral bandwidth of the disturbances. It should be robust and self-adapting to disturbance-signal center frequency. Finally, the system has to be implementable on

400

a reasonable computation budget.

The chosen controller, based on an enhanced, narrow-band, adaptation of a FXLMS algorithm, meets these requirements well. While other approaches such as the linear quadratic Gaussian controller were considered, they did not offer the efficient narrow-band, self-adapting, characteristics of the FXLMS algorithm.

Theory

In [8] the discrete FXLMS algorithm is derived assuming an arbitrary mechanical plant transfer function. As described there, signal vector transformation matrices may be applied at actuator inputs and vibration sensor outputs to alter the residual-vibration cost function, decouple channels, and simplify stabilization. These matrices can be used to effect spatially-distributed, residual-vibration cost criterion. The controller in this study comprised a 2-input by 2-output realization of the algorithm without transformations. A 2-point, discrete, residual-vibration cost criterion was implemented to get an operating controller running quickly.

A diagonal equalization matrix, $C(z)$, was inserted in the controller output signal path to equalize and compensate the multichannel plant Frequency Response Function (FRF) in the neighborhood of the disturbance frequency. The diagonal elements of this matrix are of the form

$$\left[C(z)\right]_{ii} = 1 + az^{-1} + bz^{-2} .$$

(14)

The closed loop disturbance-to-residual-vibration relationship is now given by

$$E(z) = \left[I + \frac{\mu}{z^2 - 2z\cos(\omega_0) + 1} H(z)C(z)G(z)\right]^{-1} D(z) ,$$

(15)

where $E(z)$ is the residual-vibration vector, $D(z)$ is the disturbance signal vector, $H(z)$ is the unequalized plant transfer function matrix, $G(z)$ is the controller transfer function matrix, μ is the controller loop gain, ω_0 is the nominal disturbance frequency, and $C(z)$ is as defined. For the narrowband case, the elements of the controller transfer function matrix, $G(z)$, take the form of the discrete FXLMS notch filter described in [8] by

$$G_{\ell q}(z) = |H_{q\ell}(\omega_0)| \left[z\cos(\omega_0 - \phi_{q\ell}) - \cos(\phi_{q\ell})\right] ,$$

(16)

where q is the sensor number, ℓ is the actuator number, $H_{q\ell}$ and $\phi_{q\ell}$ are the magnitude and phase response of the actuator to sensor transfer function at ω_0. Eq. (14), (15) and (16) therefore define the frequency response of the controlled mechanical system for a given disturbance signal, $D(z)$.

Notice that Eq. (15) has the desired zeros at $e^{\pm i\omega_0}$ that cancel the disturbance on all channels. The equalizer, Eq. (14), removes or lessens the plant-FRF phase change with frequency around the first-mode resonant frequency making a faster converging closed-loop controller. From the modal theory we know that the FRF comprises a weighted sum of second-order modal filter sections parameterized by natural frequency and damping factor. To observe controller behavior, the disturbance frequency was set near the first-mode resonant frequency to produce a large, visible displacement. Because of this arrangement, without compensation the first modal-response filter would dominate the controller closed-loop response — slowing it by forcing a low loop gain to maintain stability.

The difference equation defining the FXLMS complex-weight updates in the real-time controller computations for each actuator ℓ is given by

$$w_\ell(k+1) = w_\ell(k) + \mu \sum_{q=1}^{Q} e_q(k) r_{q\ell}^*(k) ,$$

(17)

where q is the sensor number, ℓ is the actuator number, e_q is the residual-vibration signal, and r is the complex conjugate filtered-reference signal at ω_0. The filtered reference signal is computed for each time sample according to

$$r_{q\ell}(k) = |\hat{A}_{q\ell}(\omega_0)| e^{j(\omega_0 kT + \hat{\phi}_0)} ,$$

(18)

where T is the controller sample period and $\hat{A}_{q\ell}(\omega_0)$ is the estimate of the equalized actuator-to-sensor transfer function at ω_0.

Implementation

Figure 7 is a block diagram of the control system showing constituent hardware and software processes. The 200 Hz sampling of accelerometer signals and reconstruction of control signals is managed by one of three simultaneously executing processes in the control computer. Parent and child UNIX processes execute the FXLMS control algorithm. Some of the processing blocks are now further detailed.
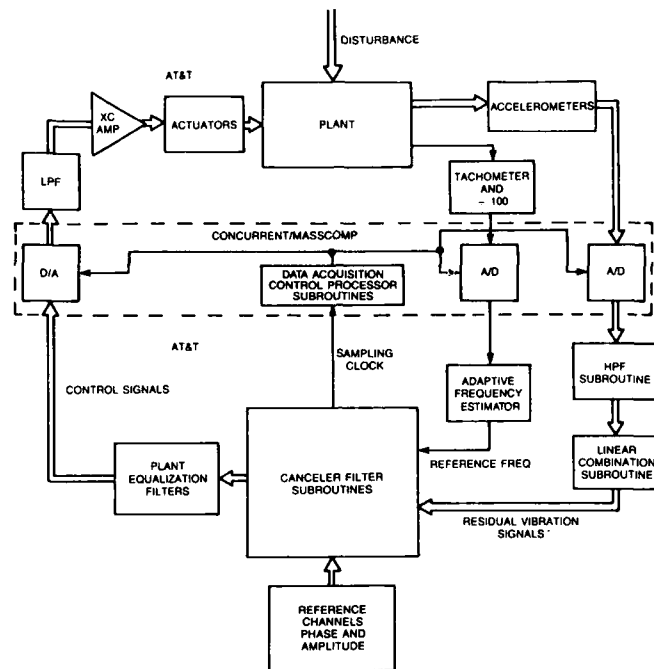
401

Figure 7. System block diagram for FXLMS adaptive vibration controller

Plant equalization filters. These are the all-zero filters, Eq. (14). The coefficients were estimated with a pole-zero mapping approach, and those that best flattened the FRF amplitude spectrum and minimized the phase change around 14.25 Hz were selected. Figure 8 displays the equalized actuator-to-sensor transfer responses from 10 to 30 Hz.

Tachometer and adaptive frequency estimator. The control algorithm requires an estimate of the disturbance-source frequency to synthesize the required quadrature, sinusoidal, filtered-reference signals. The tandemed tachometer, digital divider, and low-pass filter generate an analog sinusoidal signal at the disturbance motor rotation rate. The sampled signal is processed by a two-tap LMS adaptive filter that computes a frequency estimate for the reference signal sinusoids.

Reference channels amplitude and phase table. This table of discrete-time control-signal-to-residual-vibration amplitude and phase responses of the plant FRF matrix is used with the frequency estimate to synthesize filtered-x reference signals for the controller algorithm coefficient updates. The estimated response parameters in this table were computed with an off-line, multichannel, frequency-response estimation algorithm and are fixed during controller operation.

Results

Within 300 milliseconds of initiation of control, more than 40 dB reduction in sensor signal power was attained for the structure driven near the first mode frequency. The controller was able to track a slowly changing disturbance source frequency of up to +/- 2 Hz around the driving frequency.

System response prior to control. Figure 9 is a power spectrum measurement from an accelerometer attached between the structure and an actuator before the controller was initiated. The motor was driven at 14.25 Hz creating an acceleration magnitude of 11.76 dB root-mean-square (rms) m/s^2 (43.67 dB in/s^2). The frequency spectrum over the 50 Hz range is shown in the figure. Estimated bandwidth of the response signal at 14.25 Hz is approximately 1.7 Hz.

The higher-frequency, lower-amplitude peaks in Figure 9 may be a result of either structural nonlinear behavior or harmonic disturbances from the excitation source. For example, the 28.5 Hz peak could be caused by the structure being driven beyond its linear response range. Disturbance source effects such as shaft misalignments or looseness could also create this type of response. The other higher frequency peaks may, too, be a combination of nonlinearities and harmonic effects of the disturbance source, such as bearing noise, motor gearing, or shaft misalignments. A few of these peaks remain in the response spectrum after control.
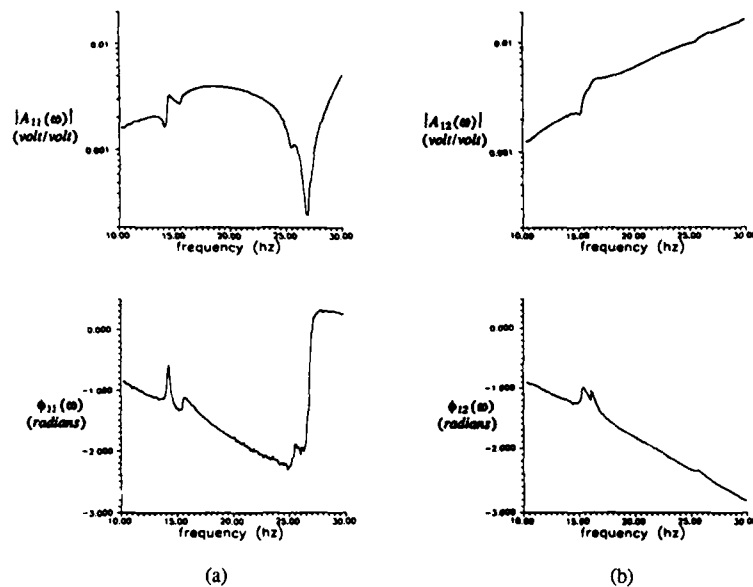
Figure 8. Equalized actuator-to-sensor transfer functions (a) point response (b) cross response

System response after control. Figure 10 is the spectral response of the same accelerometer after control. The 14.25 Hz and 28.5 Hz peaks are significantly reduced, replaced by a broader, lower amplitude spectrum. A reduction of 49.99 dB was obtained at 14.25 Hz. Notice that the amplitude and frequencies of the higher peaks are nearly identical to the pre-control situation shown in Figure 9. The low amplitude, broadband spectrum in the post-control data that does not appear in the pre-control data is caused by the dynamic range limitation of the control computer (12 bits of resolution). The data acquisition system used to monitor the performance to the controller has 15 bit D/A's; thus it is capable of *measuring the injected control computer noise-floor spectrum after controller convergence.*
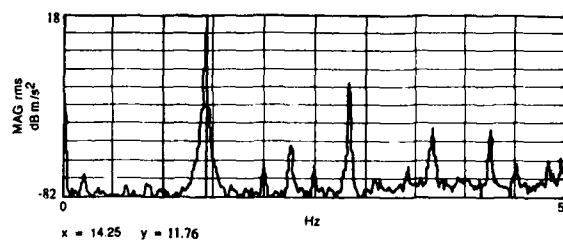

x = 14.25   y = 11.76

Figure 9. Acceleration power spectrum from accelerometer 6 before control
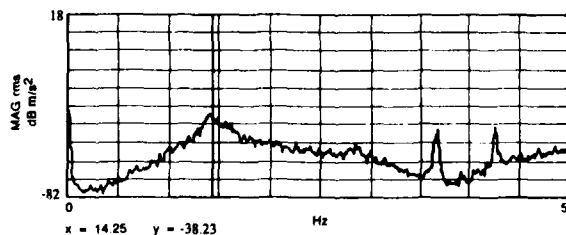

x = 14.25   y = -38.23

Figure 10. Acceleration power spectrum from accelerometer 6 after control

403

Three accelerometers were monitored before and after control. Two of them, a6 and a7, were used as the error sensors in the control algorithm and the third, a5, was located at the geometric center of the platform attached to the structure under the bearing. Table 3 compares the relative reduction levels obtained for each sensor at 14.25 Hz.

Table 3. FXLMS Active Controller Results at 14.25 Hz.

Acceleration Power Spectrum, dB rms m/s^2		
Accel	Before (dB)	After (dB)
a5	14.72	-36.43
a6	11.76	-38.23
a7	11.72	-40.36

SUMMARY

We have obtained approximately 50 dB narrowband vibration-signal level reduction on an elastic structure using a modified FXLMS control algorithm combined with plant resonance equalization. Developmental details and experimental results were presented in this paper.

Structural resonance was selected as the pre-cancellation condition. This was done to generate high signal to noise ratio in the sensor signals, visually observe the controller impact, and test the effectiveness of a simple pole-zero digital equalization technique. At the cancellation frequency, approximately 50 dB of reduction in signal power was achieved at three locations on the structure. A frequency- tracking algorithm was also developed to track changes in the tachometer reference signal. The tachometer signal could also provide an estimate of disturbance frequency content for use in a broadband version of the FXLMS algorithm.

REFERENCES

[1] C. R. Fuller, C. H. Hansen and S. D. Snyder,"Active Control of Structurally Radiated Noise Using Piezoceramic Actuators,"*Proceedings of Inter-Noise '89* , 1989, 509-512.

[2] "The Active One: Active Noise and Vibration Control System," Active Noise and Vibration Technologies , Tempe, Arizona, 1988.

[3] "BOSE Active Headphone," Excerpt from Short Course on Active Noise Cancellation, University of Maryland, April 1990.

[4] D. Ratman, "The Incredible Shrinking Speaker," *Machine Design*, June 20, 1991, 63-66.

[5] Bryant, M. D. and R. F. Keltie,"A Characterization of the Linear and Nonlinear Dynamic Performance of a Practical Piezoelectric Actuator,"*Sensors and Actuators*, 1986, 9:95-114.

[6] M. Goodfriend, "Material Breakthrough Spurs Actuator Design," *Machine Design*, March 21, 1991, 147-150.

[7] D. J. Ewins, *Modal Testing: Theory and Practice*. John Wiley & Sons, New York, NY, 1984.

[8] R. S. Medaugh, "Active Control," AT&T Bell Laboratories Internal Document, 1989.

SECOND INTERNATIONAL CONGRESS ON
RECENT DEVELOPMENTS IN AIR- AND
STRUCTURE-BORNE SOUND AND VIBRATION
MARCH 4-6, 1992   AUBURN UNIVERSITY, USA

Active Vibration Control of Flexible Structures using the Sentuator

Shin Joon, Hahn Chang-Su, Oh Jae-Eung
Dept. of Precision Mechanical Engineering
Hanyang University
Haeng dang-dong, Seong dong-ku, Seoul, 133-791
KOREA

Kim Do-Weon
Samsung Electronics
Seoul, KOREA

ABSTRACT

Undesired vibration motion of a flexible cantilever beam is controlled with piezoelectric sensor and actuator. Appropriate sensor and actuator equations are derived and implemented in a finite element analysis to simulate a feedback active vibration control algorithm. Based on it, experiments are performed. Results show that the sentuator can effectively reduce the total mode with only one sentuator regardless of location
Key Words : Piezo-electric, Laminated, Flexible, Actuator, Sensor, Cost Function, Active Vibration
         Control, Spill-over

INTRODUCTION

As automation technology advances, there have been strong requests for light weight and flexible structures. Since the measurement and vibration control of flexible structure result in very low accuracy and precision, there has been a fervant request for light, strong, accurate, and precise sensor and actuator. Under these circumstances, the development of distributed sensor/actuator became very urgent.[1],[2]

In 1969, polyvinylidene fluoride (PVDF) was first discovered by Kawai. Comparing with piezo-ceramic, it has wide frequency range, high strength, and good flexibility because of thin thickness. On the other hand, its temperature range is narrow, and DC measurement is impossible. As PVDF can do sensing along with actuating, "sentuator" is actually combined form of sensor and actuator.

In this study, the finite element method is performed on thin and flexible cantilever beam. In case of excitation with minimizes the sum of response and control force, optimal thickness ratio between sentuator and cantilever beam is determined. In addition, by comparing point control using dynamic damper with disributed control using sentuator. Spill-over is produced during control mode according to the use of actuator which is less than the modeled one. This spill-over effect is studied by varying the position of sentuator. The theoretical results are compared with experimental data. The validity of algorithm used in this study is proved, and the utilization of sentuator is presented.

THEORY

Fundamental Principle of Sentuator

Expansion/contraction is resulted from the polarity in the electric field when a voltage is supplied to sentuator (Converse effect). On the contrary, the voltage is produced as a result of expansion/contraction (Direct effect), so sentuator could be used as both actuator or sensor.

$$S_{ij} = s_{ijkl}^{E} T_{kl} + d_{kij} E_k \qquad (1)$$

Here, S_{ij} : strain s_{ijkl}^{E} : elastic compliance constant

T_{kl} : stress d_{kij} : electric constant E_{kl} : electric field

405

Finite element modelling of flexible structure

According to Eq. (2), the bending modent M_f could be calculated by taking the distance from sentuator to principle axis. And, the flexural rigidity for sentuator-beam could be obtained by Eq. (3).

$$M_f = \frac{d \cdot b \cdot E_1 \cdot V(E_2 t_1 t_2 + E_3 t_1 t_3 + E_2 t_2{}^2 + 2E_3 t_2 t_3 + E_3 t_3{}^2)}{2(E_1 t_1 + E_2 t_2 + E_3 t_3)} \tag{2}$$

$$E_i I_i = E_1 I_1 + E_2 I_2 + E_3 I_3 \tag{3}$$

Here, b : width of beam, d : piezoelectric constant, V : input voltage, t : thickness
E : Young's modulus,   I : area moment of inertial for neutral axis
subscript 1,2,3 : sentuator, bonding layer, beam

In Fig. 1, stiffness matrix at ith and (i+1)th node could be calculated from the transformation caused by load utilizing the moment-displacement relationship. The results are presented in Eq. (4).

$$\left\{ \begin{array}{c} V_{Y i} \\ M_{Z i} + M_f \\ V_{Y i+1} \\ M_{Z i+1} - M_f \end{array} \right\} = \frac{E_i I_i}{L_i{}^3} \begin{bmatrix} 12 & 6L_i & -12 & 6L_i \\ 6L_i & 4L_i{}^2 & -6L_i & 2L_i{}^2 \\ -12 & -6L_i & 12 & -6L_i \\ 6L_i & 2L_i{}^2 & -6L_i & 4L_i{}^2 \end{bmatrix} \left\{ \begin{array}{c} W_i \\ \theta_{Z i} \\ W_{i+1} \\ \theta_{Z i+1} \end{array} \right\} \tag{4}$$

Complete stiffness matrix could be calculated using superposition method and applying boundary condition. Mass matrix consists of lumped mass and rotational inertia. Using lumped mass method, it can be obtained by considering boundary condition like stiffness matrix.[3]

From the stiffness and mass matrix, Eq. (5) for flexible beam could be obtained

$$[M]\{ \ddot{q} \} + [K]\{ q \} = \{ Q(t) \} \tag{5}$$

If we transform the Eq. (5) to uncoupled coordinates and apply mode analysis, mode matrix could be found. If we set the number of sensor and actuator to N and try to control, the observed displacement and velocity are same as in Eq. (6). In mode coordinate system, force components by exciting force are divided into control dynamics and residual dynamics.[5]

$$\{y(t)\} = [C_j]\{q(L_i, t)\} + [C_j]\{\dot{q}(L_i, t)\} \tag{6}$$

Here, L_i : location of Sensor(i=1,2,...,N) $[C_j]^T$: $i \times j$ matrix composed of $[\psi_j(L_i)]$

$$\{Z(t)\} = \left\{ \begin{array}{c} Z_C \\ Z_R \end{array} \right\} = [\psi]^T \left\{ \begin{array}{c} y_C \\ y_R \end{array} \right\} = \left[\begin{array}{c|c} C_{CC} & C_{CR} \\ \hline C_{RC} & C_{RR} \end{array} \right] \left\{ \begin{array}{c} q_C \\ q_R \end{array} \right\} \qquad \{f(t)\} = \left\{ \begin{array}{c} f_C \\ f_R \end{array} \right\} = [\psi]^T \left\{ \begin{array}{c} F_C \\ F_R \end{array} \right\} = \left[\begin{array}{c|c} B_{CC} & B_{CR} \\ \hline B_{RC} & B_{RR} \end{array} \right] \left\{ \begin{array}{c} F_C \\ F_R \end{array} \right\}$$

$$f_C = B_{CC}F_C + B_{CR}F_R = B_{CC}F_C \;(\because F_R = 0) \qquad \text{Here,} \quad \{F(t)\} = \left\{ \begin{array}{c} 0 \\ Q(t) \end{array} \right\} \qquad \{y(t)\} = \left\{ \begin{array}{c} \dot{q} \\ q \end{array} \right\}$$

Control force acting physically can be expressed as Eq. (7). Also, the force component which induce control spill-over by applying to residual dynamics is calculated as Eq. (8).[8]

$$F_C = B_{CC}{}^{-1} f_C \tag{7}$$

$$f_R = B_{RC}F_C + B_{RR}F_R = B_{RC}B_{CC}{}^{-1} f_C \tag{8}$$

Optimal control law

It is possible to obtain state space representation from Eq.(5). Control force vector u is defined as Eq. (9).

$$u = - KX \tag{9}$$

To determine cost function which minimizes response and control force, feedback gain matrix K needs to be determined. This is LQR problem and feedback gain can be determinded from Riccati equation.

$$PG + G^TP + Q - PHR^{-1}H^TP = 0 \tag{10}$$

$$K = R^{-1}H^TP \tag{11}$$

COMPUTER SIMULATION RESULTS AND CONSIDERATION

Vibration analysis of a flexible structures using FEM

406

To verify the theory concerning vibraiton of flexible structure using sentuator, in Fig. 2, finite element modeling of flexible cantilever beam was done. The width and thickness were set to 1/10 and 1/1000 of total length L. The cantilever beam is divided into 3 equal length elements by attaching sentuators at the distance $X(L_1)$, $X(L_2) - X(L_1)$, and $X(L) - X(L_2)$ from the fixed end. The exciting force was applied to free end as a form of unit impulse input. As a result of eigenvalue analysis, if was possible to know that there exist six natural frequencies up to 500Hz. Since the number of divided elements is small, we can only rely on the first, second and third natural frequency. In this study, we will only pay attention to the following these three natural frequencies.

Thickness ratio decision using optimal control

Optimal thickness ratio decision under impulse exciting. Fig. 3 shows the cost function when the vibration of cantilever beam is controlled. In case of impulse excitation, the cost function has the minimum value when the thickness ratio between sentuator and cantilever beam is three.

Optimal thickness ratio decision under sinusoidal exciting. To find the possibility of controlling periodic disturbance by sentuator, simulation was performed. By setting 2nd natural frequency as exciting frequency, the optimum thickness ratio can also be found. In Fig. 4, cost function values according to the change of thickness ratio for 2nd natural frequency. Regardless of the position of control, it is found that cost function is minimum when thickness ratio is three.

Location decision of sentuator

Location decision of distributed control using sentuator. In Fig.5, the comparision of the time response according to each location of sensing for impulse and 2nd natural frequency excitation (Thickness ratio = 3) is presented. The effect is about same at any observation location. From Table 2, we could conclude that vibration effect is not affected by the position of sentuator.

Fig. 6 illustrates the transfer functions obtained by varying the sensing location controlled at fixed location. It also showns similar controlling effects throughout the intersted frequency range. In Table 3, the difference of area between original and controlled transfer function. Physically, the area of frequency domain it has the dimension of energy. Regardness of observation pcistion, energy is decresed when it is ovserved at fixed end ($X(L_1)$). In attaching sentuator, one needs to keep in mind that natural frequency mode of cantilever beam changes becaused of the bonding effect caused from sentuator thickness variation. Therefore, one needs to design the control system taking into account of the variation of system induces from sentuator attachment.[3]

Fig. 7 illustrates the comparison of the transfer functions controlled by dynamic absorber and compensated sentuator (Tr = 3). This figure tells that sentuator controlls the entire mode evenly, and the effect is greater than the one by dynamic absorber. For comparison, dynamic absorber first finds the maximum amplitude at each mode and then controls only one mode.

Fig. 8 represents the difference of peak values between the sentuator and dynamic absorber. The negative values indicate that dynamic absorber has better controlling effects. Dynamic absorber is more effective in controlling low mode, especially 2nd mode. But, calculating the difference between the controlled amount by dynamic absorber and one by sentuator, we can get the following conclusion : the higher the mode, the better the sentuator. If the control is observed at fixed end, sentuator is better in entire mode range.

Control effect according to location of sentuator. We has seen that sentuator alone is controlling entire mode very evenly. But, to see the control effect according to position, impulse and natural frequency excitation (Tr=3) were performed. Table 4 and Table 5 show the results after impulse and 2nd natural frequency excitation according to various location. From these tables, we can conclude that the observation and control effect at fixed end ((X_1)) is greatest.

EXPERIMENT

Experimental apparatus and method

This experiment was performed to prove the usuability of sentuator as a vibration sensor and actuator and the propriety of the proposed algorithm.

For this experiment, a cantilever beam was divided into three elements. Then, sentuator was attached near the fixed end to be used as a vibration sensor. After making the thickness of sentuator twice or three times of that of cantilever beam by laminating, experiment for control effect according to the change of width and adhesion position of sentuator was operated.

Cantilever beam was connected to a shaker. 20kHz white noise is produced by noise generator, amplified by amplifier, inputted to actuator. In order to reduce the effect of observation spill-over, low pass filter was used. To reduce the noise, average time was set to 30 seconds. Vibration signal, which is gained by sentuator, is inputted in DSP board (TMS320C25). After identified the property of system in DSP board, sentuator can control the vibration of cantilever beam by optimal control algorithm

proposed in this paper.

Experimental results and consideration

Vibration control effect according to the change of thickness of sentuator. The frequency response obtained by attaching sentuator (Tr = 2 or 3) at the fixed end is plotted in Fig.9 using curve fitting. From the experiment, it was found that the more effective thickness for vibration control is three.

Vibration control effect according to the change of location of sentuator. Fig. 10 and Fig. 11 shows that curve fitting obtained by varying the vibration control position while fixing the observation position at fixed end. When thickness is set to two, sentuator was possible to control at lower mode as predicted from the theory. But, the response curve is higher near resonance point. In addition, amplitude was lowered quite a lot at higher mode. Especially, when the thickness is three, overall amplitude level was reduced. The effect of vibration control was better near the fixed end.

To find the best control position, the area of response curve calculated. The results are presented in Table 6. The value gets smaller as the position is closer to the fixed end.

CONCLUSION

The optimal thickness ratio of sentuator and cantilever beam to control was determined from the simulation and experiment.

The effect of dislocation of sensor and actuator is negligable when the location of observation and control of sentator is modified. And, the best position for control is fixed end in case of impulse and sinusoidal mode excitation.

By comparing sentuator with dynamic absorber, sentuator has usefulness of controlling the total mode with only one sentuator regardless of location.

BIBLIOGRAPHIC REFERENCES

1. H. S. Tzou and M. Gadre, " Active Vibration Isolation by Polymeric Piezoelectric with Variable Feedback Gains ", AIAA, Vol. 26, No. 8, 1988, pp 1014~1017
2. H. S. Tzou and C. I. Tseng, " Distributed Piezoelectric Sensor/Actuator Design for Dynamic Measurement / Control of Distributed Parameter Systems : A Piezoelectric Finite Element Approach ", J. Sound and Vibration, 138(1), 1990, pp 17~34
3. A. Baz and S. Poh, " Optimum Vibration Control of Flexible Beams by Piezoelectric Actuators ", NASA CONTRACT # 30429-D, March, 1987
4. A. Baz and S. Poh, " Performance of an Active Control System with Piezoelectric Actuators ", J. Sound and Vibibration, 126(2), 1988, pp 327~343
5. M. J. Balas, " Feedback Control of Flexible Systems ", IEEE, Vol.AC-23, No. 4, 1978, pp 673~679
6. F. L. Lewis, " Optimal Estimation ", JOHN WILEY & SONS, 1986
7. Oh Jae-Eung, " Basic and application of structure modal analysis ", Hee-Sung Inc., 1985
8. J. Van DE Vegte, " Feedback Control Systems ", PRENTICE-HALL INC., 1990
9. D. W. Kim, J. E. Oh, " The study on the vibration control of machinary structures using dynamic absorber ", Conference proceeding : The Acoustical Society of Korea Fall Meeting, 1990, pp 245~249
10. D. K. Kim, D. W. Kim, H. S. Kim, J. E. Oh, " The study on the vibration control of flexible structures using sentuator ", Conference proceeding : KSME Spring Annual Meeting '91, 1991, pp 236~241

Table 1. The specification of cantilever beam and sentuator

	Cantilever beam	Sentuator
Length	300	100
Width	38	38
Thickness	0.5	1.0 / 1.5

(unit : mm)

Table 6 Comparison of controlled area for each sensing location

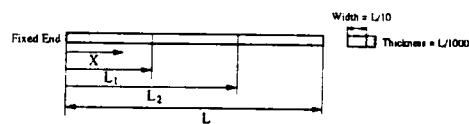| Thickness Ratio / Location	Tr = 2	Tr = 3
X(L) - X(L2)	206.4068	77.6541
X(L2) - X(L1)	1343.833	623.4733
X(L1)	246.7148	55.8655
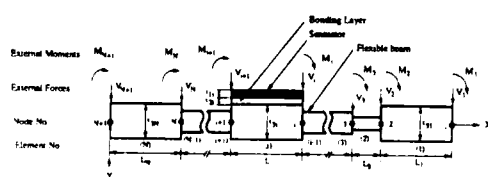
Fig.1. General layout of the sentuator - beam system

Fig.2. Finite element modeling of flexible cantilever beam
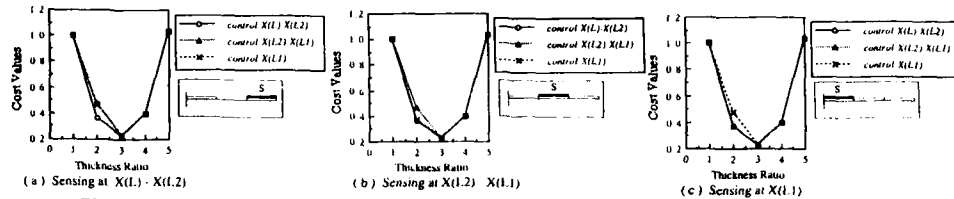
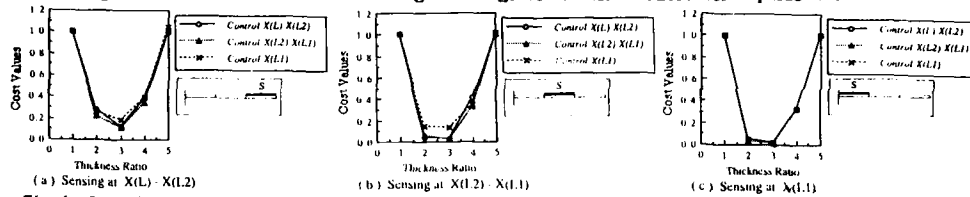Fig. 3. Cost function values according to change of thickness ratio for impulse excitation

(a) Sensing at X(L) - X(L2)　　(b) Sensing at X(L2) - X(L1)　　(c) Sensing at X(L1)

Fig. 4. Cost function values according to change of thickness ratio for 2nd natural frequency excitation

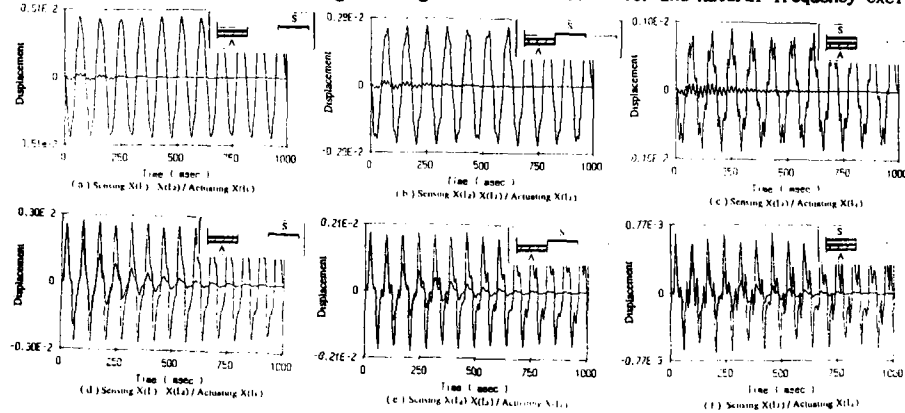(a) Sensing at X(L) - X(L2)　　(b) Sensing at X(L2) - X(L1)　　(c) Sensing at X(L1)

Fig. 5. Comparison of the time response according to each location of sensing for impulse and 2nd natural frequency excitation (Tr = 3)

(a) Sensing X(L)-X(L2) / Actuating X(L1)　　(b) Sensing X(L2)-X(L1) / Actuating X(L1)　　(c) Sensing X(L1) / Actuating X(L1)
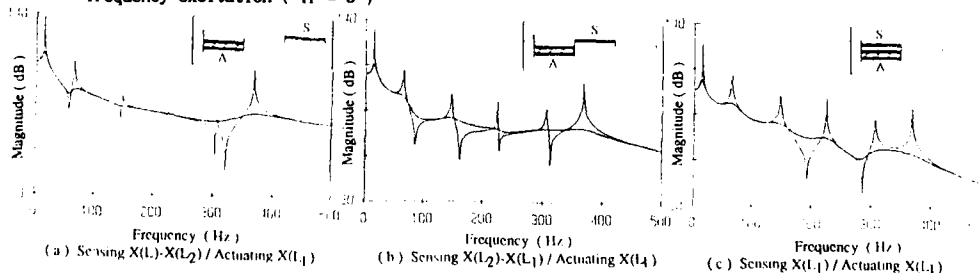
Fig. 6. Comparison of transfer functions according to each location of sensing controlled by one Sentuator (Tr = 3)

Table 2 Cost function values according to sensing and actuating location of Sentuator for 2nd natural frequency excitation (Tr = 3)

Actuating / Sensing	X(L) - X(L2)	X(L2) - X(L1)	X(L1)
X(L) - X(L2)	0.119	0.116	0.191
X(L2) - X(L1)	0.029	0.023	0.132
X(L1)	0.023	0.011	0.023

Table 3 Difference of area between original and controlled transfer function according to sensing and actuating location of Sentuator

Actuating / Sensing	X(L) - X(L2)	X(L2) - X(L1)	X(L1)
X(L) - X(L2)	4.72×10^{-4}	1.38×10^{-4}	2.99×10^{-3}
X(L2) - X(L1)	5.25×10^{-3}	6.91×10^{-4}	3.37×10^{-2}
X(L1)	1.81×10^{-2}	2.31×10^{-3}	1.17×10^{-1}

409

(a) Sensing X(L)-X(L₂) / Actuating X(L₁) (b) Sensing X(L₂)-X(L₁) / Actuating X(L₁) (c) Sensing X(L₁) / Actuating X(L₁)
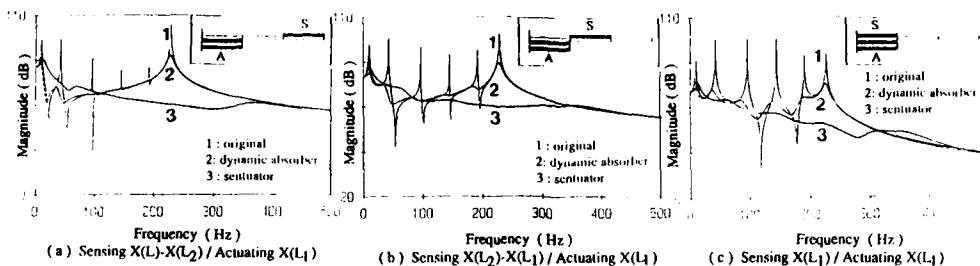
Fig.7. Comparison of transfer functions controlled by dynamic absorber and compensated Sentuator (Tr = 3)
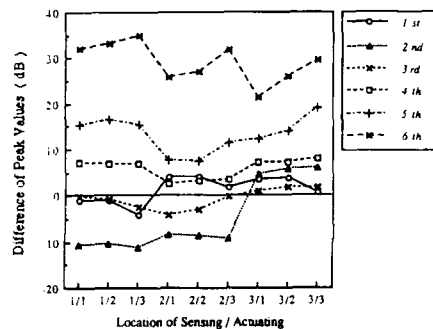

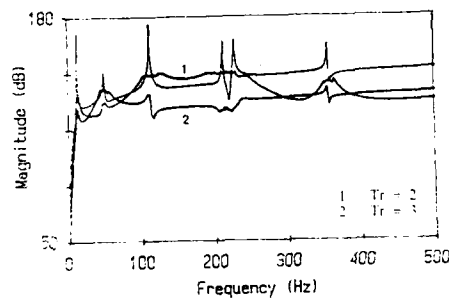Fig.8. Difference of peak values between the Sentuator and dynamic absorber

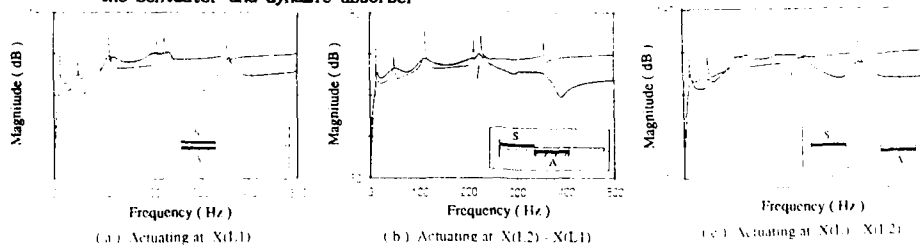Fig.9. Comparison of transfer functions according to thickness ratio

(a) Actuating at X(L1) (b) Actuating at X(L2) - X(L1) (c) Actuating at X(L) - X(L2)

Fig.10. Comparison of transfer functions according to control location of Sentuator (Tr = 2)

(a) Actuating at X(L1) (b) Actuating at X(L2) - X(L1) (c) Actuating at X(L) - X(L2)
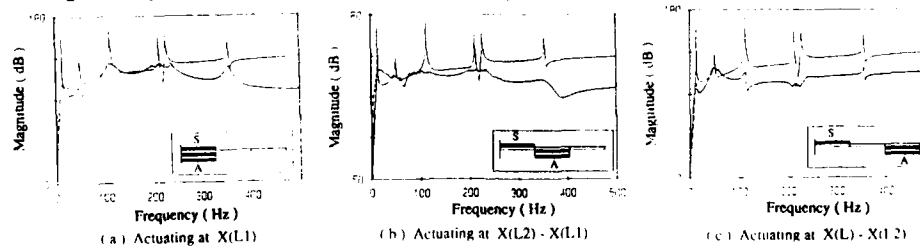
Fig.11. Comparison of transfer functions according to control location of Sentuator (Tr = 3)

Table 4 Control effect for impulse excitation

Actuating / Sensing	X(L) X(L2)	X(L2) - X(L1)	X(L1)
X(L) X(L2)	1.300 X 10⁻¹	6.610 X 10⁻⁵	6.247 X 10⁻⁶
X(L2) X(L1)	6.910 X 10⁻²	3.463 X 10⁻⁵	1.579 X 10⁻⁶
X(L1)	2.130 X 10⁻²	8.871 X 10⁻⁵	1.749 X 10⁻⁷

Table 5 Control effect for 2nd natural frequency excitation (Tr = 3)

Actuating / Sensing	X(L) X(L2)	X(L2) - X(L1)	X(L1)
X(L) X(L2)	1.877 X 10⁻¹	1.487 X 10⁻³	6.771 X 10⁻⁵
X(L2) X(L1)	7.217 X 10⁻²	4.520 X 10⁻³	2.032 X 10⁻⁵
X(L1)	7.099 X 10⁻²	2.411 X 10⁻³	1.512 X 10⁻⁵

410

STRUCTURAL VIBRATION

SECOND INTERNATIONAL CONGRESS ON
RECENT DEVELOPMENTS IN AIR- AND
STRUCTURE-BORNE SOUND AND VIBRATION
MARCH 4-6, 1992   AUBURN UNIVERSITY, USA

RADIAL IMPULSIVE EXCITATION
OF FLUID-FILLED ELASTIC CYLINDRICAL SHELLS

C. R. Fuller and B. Brévart
Mechanical Engineering Department
Virginia Polytechnic Institute and State University
Blacksburg, Virginia

ABSTRACT

The impulsive excitation of fluid-filled elastic cylinders is analytically studied using a double Fourier transform in the wavenumber and frequency domain. In particular, the contributions of various waves and their energy paths to the structural response are investigated by evaluating individual pole contributions to the total response using the method of residues. For axisymmetric excitation, the results surprisingly demonstrate that although the excitation is structural, the major path of vibrational energy to the structural observation point is through the fluid medium. For the beam mode type excitation, two paths have to be distinguished: the energy propagates either through low-frequency structural components or through the fluid medium as higher frequency components. The work adds new insight into the behavior of coupled pipe-fluid systems.

NOMENCLATURE

a	thin shell mean radius
c_f	fluid acoustic free wave speed
c_L	shell extension phase speed
E	Young's modulus
F_0	amplitude of input force
h	shell wall thickness
I_x	instantaneous intensity in the axial direction
I_x^{nd}	non-dimensional intensity in the axial direction
$J_n(\ )$	Bessel function of order n
k_{ns}	axial wavenumber
k_s^r	radial wavenumber
n	circumferential mode number
p	pressure
p_0	input force distribution
$\tilde{P}_{ns}$	spectral pressure amplitude (freq domain)
r, x, θ	cylindrical co-ordinates
R	receptance in the time domain
R_{nd}	non-dimensional receptance
s	branch number

t_0	time delay of the input force
$u,\ v,\ w$	shell displacements
$\bar{U}_{ns},\ \bar{V}_{ns},\ \bar{W}_{ns}$	shell spectral displacement amplitudes (k_{ns} and freq domains)
$\tilde{U}_{ns},\ \tilde{V}_{ns},\ \tilde{W}_{ns}$	shell spectral displacement amplitudes (freq domain only)
x_0	position of the input force
β	thickness factor
η	damping coefficient
ν	Poisson's ratio
ρ_f	density of fluid
ρ_s	density of shell
ω	circular frequency
Ω	non-dimensional frequency
χ	non-dimensional position
τ	non-dimensional time

INTRODUCTION

Practical piping systems may be subjected to several types of vibration sources, harmonic or impulsive forces applied on the shell wall. Several authors have already investigated harmonic excitation of idealized fluid-filled cylinders but little work has been done concerning any kind of impulsive point-force. Merkulov et al. [1] studied the relative transfer mobility of waves with varying branch and circumferential mode. Fuller [2] then calculated the input mobility of an infinite cylindrical elastic shell filled with fluid, including both far-field and near-field effects. He explained the pipe behaviour in terms of propagation of free waves, these waves having been previously characterized by himself and Fahy [3]. Leyrat [4] presented a solution for the mobility of a cylindrical shell system where was included the effect of an uniform internal flow. Results were given for both infinitely long shells and shells of finite length. There has been very little work on time domain methods to evaluate transient responses of cylinders. Stepanishen and Ebenezer [5] investigated the transient vibratory response of fluid-loaded cylindrical shells of finite length with axisymmetric broadband excitations acting in the radial direction. Ujihashi et al. [6] evaluated the deflection of a fluid-filled shell subjected to an impulsive axisymmetric band load, using numerical inversion of the Laplace transformation. Their results were found to be unsatisfactory when the load is varied stepwise in time.

The purpose of the present paper is to investigate the propagation paths of energy introduced in a fluid-filled elastic cylinder by an impulsive axisymmetric radial line force, with an azimuthal distribution. The displacement of the shell wall is evaluated and explained in terms of propagation of free waves. The solution is obtained by means of double inverse Fourier transform in the wavenumber and the frequency domains to express the shell displacements. The analysis is based on the fact that it is possible to separate in the solution for the displacement of the shell, the contribution of each generated wave whose characteristics are known. The instantaneous intensity in the fluid is also evaluated and used to confirm the main results and conclusions. The purpose of this work is to improve understanding of noise propagation along piping systems under more complex excitation than considered previously.

TRANSIENT DISPLACEMENT OF THE SHELL

In the present theory, the impulse response of the fluid-filled shell is considered as a resultant of individual contributions from each generated wave. Although the free wave propagation problem is taken into consideration, it is not presented here for it has been extensively studied by Fuller in a previous paper [3]. Nevertheless, for a better comprehension of the latter discussions, Figures 1(a) and (b) show the dispersion curves of a typical undamped steel shell of thickness $h/a = 0.05$ filled with water and vibrating in the n=0 and 1 circumferential modes. These graphs will be used as references for the numbering of the different branches, or waves.
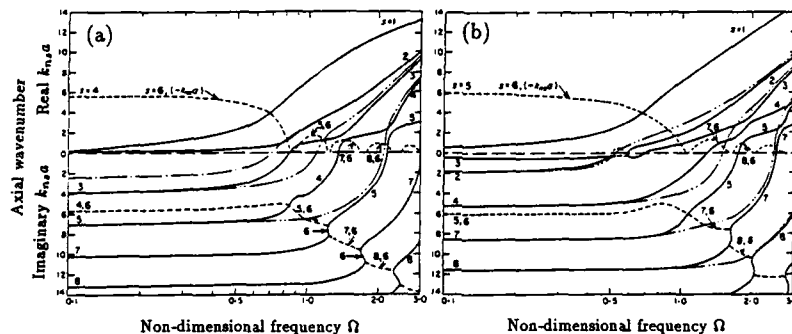
414

Figure 1. Dispersion curves for a steel shell of thickness h/a=0.05, n=0; ——, purely real and purely imaginary $k_{n_s}a$; - - - -, real and imaginary parts of complex $k_{n_s}a$; - - -, pressure release duct solution; - - - -, rigid walled duct solution. (a) n=0, (b) n=1.

The cylindrical co- .rdinate system employed in the theory is shown in Figure 2 and a list of symbols is given in the Appendix.
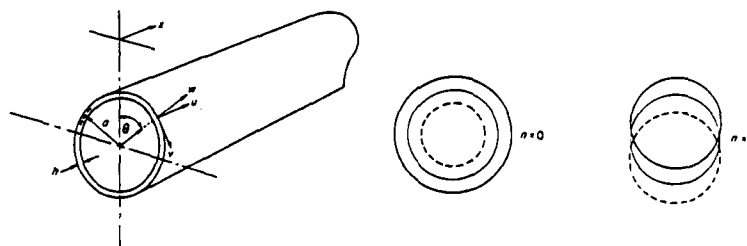

Figure 2. Co-ordinate system and mode shape.

To analyze the response of a cylindrical shell to an impulsive line force, applied around the circumference at $x = -x_0$ and at $t = t_0$, and specified by

$$p_0(\theta, x, t) = F_0 cos(n\theta)\delta(x + x_0)\delta(t - t_0),\tag{1}$$

it is convenient to express the shell displacements and applied forces as double inverse Fourier transforms in the axial wavenumber and the frequency domains,

$$u = \frac{1}{2\pi}\int_{-\infty}^{+\infty}\int_{-\infty}^{+\infty}\sum_{n=0}^{\infty}\sum_{s=0}^{\infty}\bar{U}_{n_s}cos(n\theta)e^{i(k_{n_s}x - \omega t - \pi/2)}dk_{n_s}d\omega,\tag{2}$$

$$v = \frac{1}{2\pi}\int_{-\infty}^{+\infty}\int_{-\infty}^{+\infty}\sum_{n=0}^{\infty}\sum_{s=0}^{\infty}\bar{V}_{n_s}sin(n\theta)e^{i(k_{n_s}x - \omega t)}dk_{n_s}d\omega,\tag{3}$$

$$w = \frac{1}{2\pi}\int_{-\infty}^{+\infty}\int_{-\infty}^{+\infty}\sum_{n=0}^{\infty}\sum_{s=0}^{\infty}\bar{W}_{n_s}cos(n\theta)e^{i(k_{n_s}x - \omega t)}dk_{n_s}d\omega.\tag{4}$$

$$\bar{p}_0 = \frac{1}{2\pi}F_0cos(n\theta)e^{ik_{n_s}x_0}e^{i\omega t_0}\tag{5}$$

where F_0 is a force per unit length of circumference.

415

For convenience, the vibrational motion of a cylindrical elastic shell filled with fluid is described by the Donnell-Mushtari shell equations [7],

$$\frac{\delta^2 u}{\delta z^2} + \frac{1-\nu}{2a^2}\frac{\delta^2 u}{\delta\theta^2} + \frac{1+\nu}{2a}\frac{\delta^2 v}{\delta z\delta\theta} + \frac{\nu}{a}\frac{\delta w}{\delta z} - \frac{\ddot{u}}{c_L^2} = 0, \tag{6}$$

$$\frac{1+\nu}{2a}\frac{\delta^2 u}{\delta z\delta\theta} + \frac{1-\nu}{2}\frac{\delta^2 v}{\delta z^2} + \frac{1}{a^2}\frac{\delta^2 v}{\delta\theta^2} + \frac{1}{a^2}\frac{\delta w}{\delta\theta} - \frac{\ddot{v}}{c_L^2} = 0, \tag{7}$$

$$\frac{\nu}{a}\frac{\delta u}{\delta z} + \frac{1}{a^2}\frac{\delta v}{\delta\theta} + \frac{w}{a^2} + \beta^2\left(a^2\frac{\delta^4 w}{\delta z^4} + 2\frac{\delta^4 w}{\delta z^2\delta\theta^2} + \frac{1}{a^2}\frac{\delta^4 w}{\delta\theta^4}\right) + \frac{\ddot{w}}{c_L^2} - \frac{p_a(1-\nu^2)}{Eh} = \frac{p_0(1-\nu^2)}{Eh}, \tag{8}$$

where β is the shell thickness parameter given by $\beta^2 = h^2/12a^2$, ν is the Poisson's ratio, E is the Young's modulus, c_L is the extensional phase speed of the shell material. $p_a(\theta, x)$ is the fluid loading and acts normally to the cylindrical surface of the shell.

Substitution of equations (2), (3) and (4) into (6), (7) and (8) gives the spectral equations of motion of the impulse response of the system,

$$\begin{bmatrix} L_{11} & L_{12} & L_{13} \\ L_{21} & L_{22} & L_{23} \\ L_{31} & L_{32} & L_{33} \end{bmatrix}\begin{bmatrix} \bar{U}_{ns} \\ \bar{V}_{ns} \\ \bar{W}_{ns} \end{bmatrix} = \begin{bmatrix} 0 \\ 0 \\ \frac{aF_0 e^{ik_{ns}x_0}e^{i\omega t_0}}{2\pi\rho_s c_L^2 h/a} \end{bmatrix}, \tag{9}$$

where the elements of the matrix are as given previously in several references [3, 2, 8]. Ω is the non-dimensional frequency, $\Omega = \frac{\omega a}{c_L}$, ρ_s is the density of the shell material.

Taking the inverse I of the matrix L, the spectral radial displacement amplitude for one branch and one mode is thus given by

$$\bar{W}_{ns} = \frac{aF_0 e^{ik_{ns}x_0}e^{i\omega t_0}}{2\pi\rho_s c_L^2 h/a}I_{33}, \tag{10}$$

where I_{33}, written in terms of the elements of matrix L, is

$$I_{33} = (L_{11}L_{22} - L_{12}L_{21})/(det|L|). \tag{11}$$

Application of the double inverse Fourier transform gives the radial displacement,

$$w(\chi, \tau, s) = \frac{F_0 cos(n\theta)}{(2\pi)^2\rho_s c_L h}\int_{-\infty}^{+\infty}\int_{-\infty}^{+\infty}I_{33}e^{i[k_{ns}a|\chi+\chi_0|-\Omega|\tau-\tau_0|]}dk_{ns}ad\Omega, \tag{12}$$

where χ is the non-dimensional position, $\chi = \frac{z}{a}$,
τ is the non-dimensional time, $\tau = \frac{tc_L}{a}$.

The complex integration in the wavenumber domain, giving the transfer receptance, has been previously discussed [2] and is performed by the method of residues. It has been noticed that the transfer mobility (or receptance) is convergent as the order of the waves taken into consideration increases. For this reason, the number of residues can be truncated. The second integral is also replaced by a finite sum (trapezoidal rule) over the frequency domain ($\Omega \in [-3;3]$). This is equivalent to considering that the transfer receptance at each discrete frequency is a component of a Fourier series which gives the transient response of the system. The frequency domain is limited to $\Omega < 3$ since, for frequencies greater than this, the Donnel-Mushtari shell equations become increasingly inaccurate. The receptance (w/F_0) as a function of time is therefore given by a double summation, a first summation over the poles of the determinant of the matrix L (the free waves) and a second one over the set of discrete frequencies,

$$R(\tau, \chi) = \frac{1}{(2\pi)^2\rho_s c_L h}\sum_{\Omega=-3}^{3}\Delta\Omega\left(\sum_s res\right)e^{-i\Omega(\tau-\tau_0)} \tag{13}$$

At this point, we can notice that the two summation can be easily commuted, implying that the contribution of a certain generated wave to the total transient response can be easily separated. This result is of prime importance in the determination of the energy propagation paths.

Because of the bounded frequency domain of integration, the modelled force is not perfectly impulsive and has to be rewritten as

$$p_0(\theta, x, \tau) = F_0 cos(n\theta)\delta(x + x_0) TF^{-1}\left(\sqcap_{[-3;3]}(\Omega)e^{i\omega t_0}\right)$$

$$= F_0 cos(n\theta)\delta(x + x_0)\frac{sin3(\tau - \tau_0)}{\pi(\tau - \tau_0)}. \tag{14}$$

where $TF^{-1}\left(\sqcap_{[-3;3]}\right)$ symbolizes the inverse Fourier transform of a rectangular window positioned between $\Omega = -3$ and $\Omega = 3$. The time variation of the input force is therefore as shown on Figure 3.
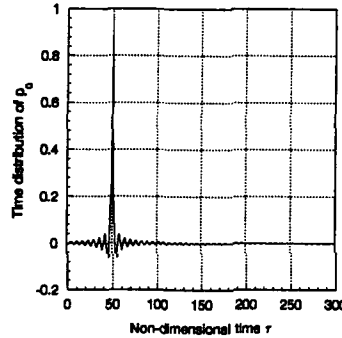
Figure 3. Time distribution of the input force; $\tau_0 = 50$.

PRESSURE AND INSTANTANEOUS INTENSITY IN THE FLUID

Using the pre-determined transfer receptance at each frequency, it is possible to evaluate both pressure and instantaneous intensity in the fluid. To perform this computation, it is convenient to express, for a paprticular circumferential mode n, the shell radial displacement and the pressure as single inverse Fourier transform in the frequency domain,

$$w = \frac{1}{\sqrt{2\pi}}\int_{-\infty}^{+\infty}\sum_{s=0}^{\infty}\tilde{W}_{ns}(\chi, \Omega, s)cos(n\theta)e^{i(k_{ns}a\chi - \Omega\tau)}d\Omega, \tag{15}$$

$$p = \frac{1}{\sqrt{2\pi}}\int_{-\infty}^{+\infty}\sum_{s=0}^{\infty}\tilde{P}_{ns}(\chi, \Omega, s)cos(n\theta)J_n(k_s^r r)e^{i(k_{ns}ax - \Omega\tau)}d\Omega, \tag{16}$$

For a particular branch s, the radial velocity of the fluid at the shell wall is related to the pressure in the fluid by the momentum equation,

$$\dot{w}|_{r=a} = \left(\frac{1}{i\rho_f\omega}\right)\frac{\delta p}{\delta r}. \tag{17}$$

Substituting expressions (15) and (16) into equation (17), we obtain the following relation

$$\tilde{P}_{ns} = \frac{\omega^2\rho_f}{k_s^r J_n'(k_s^r a)}\tilde{W}_{ns}. \tag{18}$$

Therefore, the instantaneous pressure is given by

$$p = \frac{1}{2\pi}\int_{-\infty}^{+\infty}\sum_{s=0}^{\infty}\frac{\Omega^2 c_L^2\rho_f\tilde{W}_{ns}}{a(k_s^r a)J_n'(k_s^r a)}cos(n\theta)J_n(k_s^r r)e^{i(k_{n0s}ax - \Omega\tau)}d\Omega, \tag{19}$$

417

The axial component of the particle velocity in the fluid is directly obtained from expression (19) and the momentum equation:

$$v_x = \frac{1}{2\pi} \int_{-\infty}^{+\infty} \sum_{s=0}^{\infty} \frac{\Omega^2 c_L(k_{ns}a)\tilde{W}_{ns}}{a(k_s^r a)J_n'(k_s^r a)} cos(n\theta) J_n(k_s^r r) e^{i(k_{ns}ax-\Omega\tau)} d\Omega, \tag{20}$$

In equations (19) and (20), p and v_x are made real by imposing $\tilde{W}_{ns}(-\Omega) = \tilde{W}_{ns}^*(\Omega)$ so that the instantaneous intensity is simply

$$I_x = pv_x. \tag{21}$$

RESULTS

To avoid resonance problems of the structure at the ring frequency and to insure convergence of the transient solution as we decrease the increment in the frequency domain, an artificial damping η was added to the shell material, making E, the Young modulus, complex

$$E' = E(1 - \eta i). \tag{22}$$

Typical values of 0.01 and 0.02 for η have been used for increments $\Delta\Omega = 0.02$ and $\Delta\Omega = 0.025$. The transfer receptance at each discrete frequency has been evaluated by the sum of the first seven residues, as additional residues (from the imaginary poles) did not alter the results. Convergence of the transient response was also influenced by the time step, which was set to $\Delta\tau = 1$.
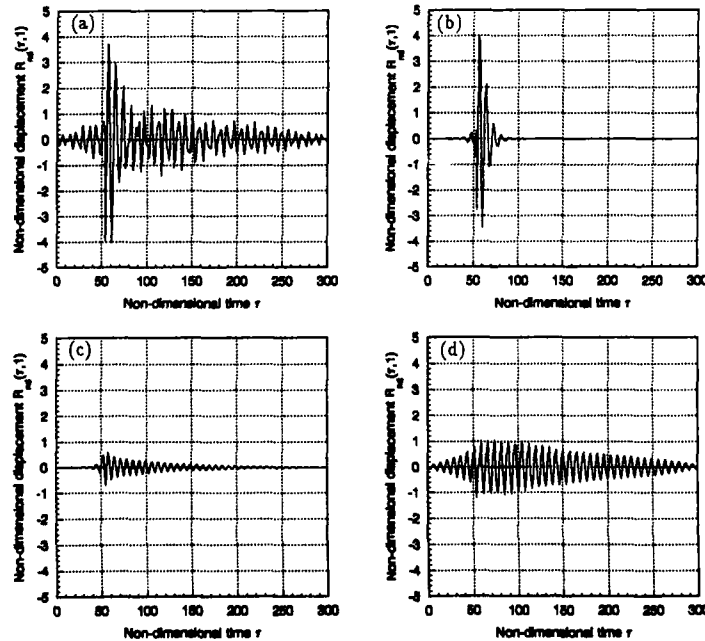
Axisymmetric, n=0, impulse distribution

Figure 4. Displacement of a steel shell, n=0, $h/a = 0.05$, $\eta = 0.02$, $x_0 = a$, $\tau_0 = 50$; (a) total response, (b) branch 1 contribution, (c) branch 2 contribution, (d) branch 3 contribution.

Figure 4(a) shows, for the n=0 circumferential mode, the total non-dimensional radial displacement $(R_{nd} = R*((2\pi)^2\rho_s c_L h))$ of a thick steel shell (h/a=0.05) filled with water one radius beyond the location of the impact. It has been noticed that this response is almost completely given ($\simeq$ 90%) by three waves numbered 1,2 and 3 on Figure 1. Their respective contribution to the transient response is given in figures 4(b), (c) and (d). It immediately appears that the branch denoted s=1 is the most important one, as it displays the most significant displacements of the shell wall.
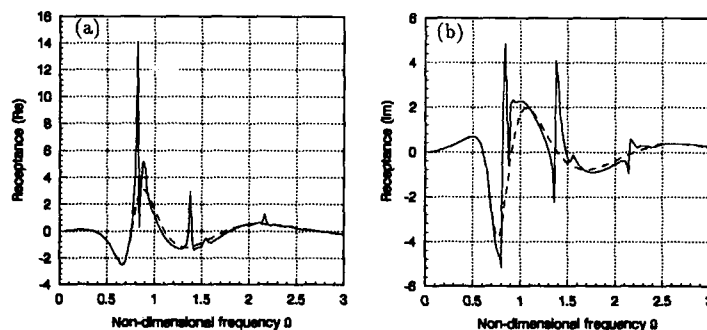

Figure 5. Transfer receptance of a steel shell, n=0, $h/a = 0.05$, $\eta = 0.02$, $x_0 = a$; ——, total transfer function; - - - -, first residue; (a) real part; (b) imaginary part

Looking now (Figure 5) at the contribution of this branch (1st residue) to the total transfer receptance (evaluated by taking the Fourier transform of the time history of Figure 4(a)), one can notice that this wave is mainly responsible for the frequency ($\Omega < 1.5$) Fourier coefficients of the series. Furthermore, Fuller showed previously [3] that this branch at low frequencies is very close to a fluid wave in a rigid walled tube. This surprising result implies that the energy introduced by the impact into the system is principally carried to the structural observation point by the fluid, as a near field pressure distribution closely hugging the wall since the radial wavenumber is imaginary at all frequencies for this particular branch. Considering now the time delay for the impulse to propagate to the observation point one radius away (the highest displacement amplitude occurs after a $\Delta\tau \simeq 4$), the corresponding phase speed of the wave is found to be very close to the fluid acoustic free wave speed,

$$c_p = c_L/\Delta\tau \simeq 1300ms^{-1}$$

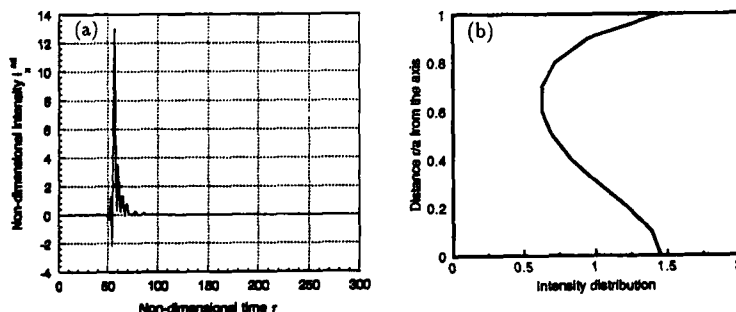This result also supports that the main propagation path of the structurally applied impulse is the fluid medium.

Figure 6. (a) Instantaneous intensity in the fluid at the shell wall. (b) Intensity distribution in the fluid; steel shell, n=0, $h/a = 0.05$, $\eta = 0.02$, $x_0 = a$, $\tau_0 = 50$.

In Figure 6(a) is plotted the non-dimensional instantaneous intensity in the fluid at the shell wall ($I_x^{nd} = I_x/(\Omega^3 c_L^3 \rho_f/a^2)$), where the intensity is the most significant. This result directly reflects the energy propagation in the fluid medium. During the time the branch s=1 contribution is important ($54 \leq \tau \leq 75$), the intensity in the fluid is steadily increased. As shown by the previous results, this is the energy responsible for the large displacement of the shell wall.

Of interest is also the radial distribution of the energy in the fluid. The time average of the instantaneous axial intensity over the period of time $T = 1/(2\pi\Delta\Omega)$ has thus been numerically evaluated for various distances r from the axis. It can be seen (Figure 6(b)) that the energy principally propagates either around the axis of the cylinder (n=0 mode) or at the shell wall (near field).

The behaviour of the other branches is also interesting. The branch known as s=2 (Figure 4(c)), which is close to the in vacuo shell wave at low frequencies, is strongly affected by the damping and of very small amplitude. These are similar results to ones previously mentioned by Fuller [9] when he investigated the free wave propagation problem. Branch s=3 is imaginary at low frequencies. Its contribution to the Fourier coefficients of the series is important as it cuts on near $\Omega = 0.75$. At this particular frequency, its phase speed is infinite and consequently information associated with this wave is immediately transmitted to the measurement point whatever its distance from the impact. Therefore, relatively small vibrations are observed to occur before most of the energy going through the fluid causes the maximum displacement of the shell (see Figure 4(d)).
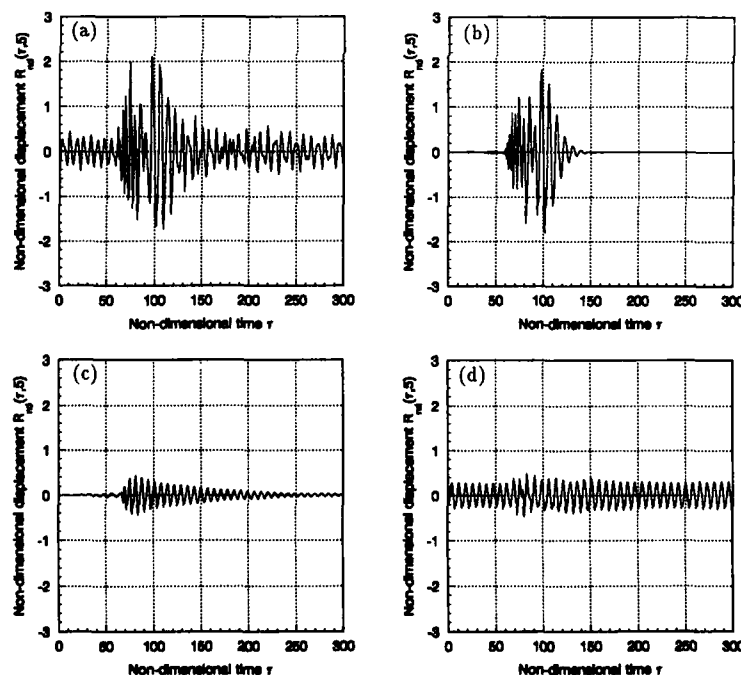

Figure 7. Displacement of a steel shell, n=0, $h/a = 0.05$, $\eta = 0.02$, $x_0 = 5a$, $\tau_0 = 50$; (a) total response, (b) branch 1 contribution, (c) branch 2 contribution, (d) branch 3 contribution.

As we evaluate the response of the shell at larger distances from the disturbance location ($x_0 = 5a$ in Figures 7 and 8), it can be seen that the overall displacement amplitudes are both smaller and spread over a wider interval, essentially because of the dispersion phenomenon created by the coupling between the fluid and the shell. The significant increase of the intensity in the fluid, shown in Figure 8, also occurs

over a longer time period and, again, this period of time exactly matches the time during which the wave s=1 contribute to the displacement of the shell. As for the radial distribution of the energy in the fluid, it tends to be more uniform but still dominant at the wall.
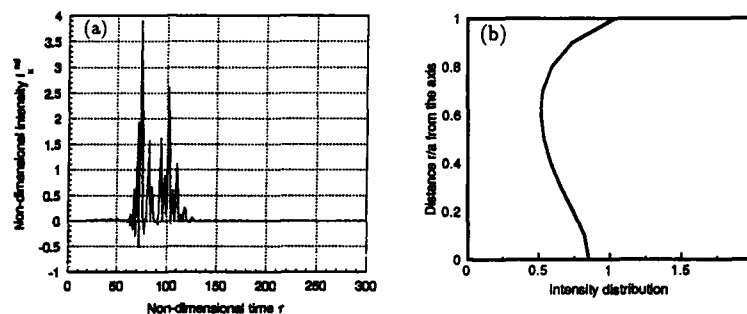

Figure 8. (a) Instantaneous intensity in the fluid at the shell wall. (b) Intensity distribution in the fluid; steel shell, n=0, $h/a = 0.05$, $\eta = 0.02$, $x_0 = 5a$, $\tau_0 = 50$.
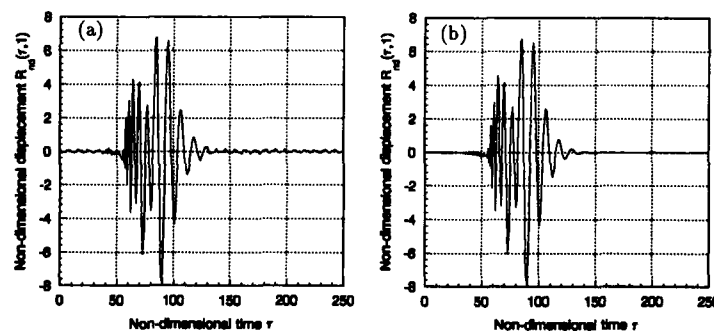

Figure 9. Displacement of a steel shell, n=0, $h/a = 0.005$, $\eta = 0.01$, $x_0 = a$, $\tau_0 = 50$; (a) total response, (b) branch 1 contribution.
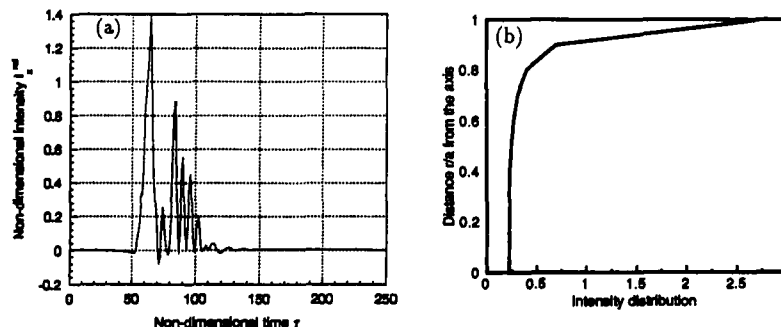

Figure 10. (a) Instantaneous intensity in the fluid at the shell wall. (b) Intensity distribution in the fluid; steel shell, n=0, $h/a = 0.005$, $\eta = 0.01$, $x_0 = a$, $\tau_0 = 50$.

With a thinner shell (h/a=0.005), the displacement of the shell wall is much shorter in time and entirely due to the wave s=1 (see Figure 9). As expected, the coupled system behaviour becomes totally

controlled by the fluid. Similar behaviour was found for free wave propagation [3]. The energy in the fluid medium (Figure 10) is now found to be almost totally concentrated at the shell wall, due to the s=1 branch being increasingly subsonic; its phase speed is now significantly lowered by the compliance of the wall.
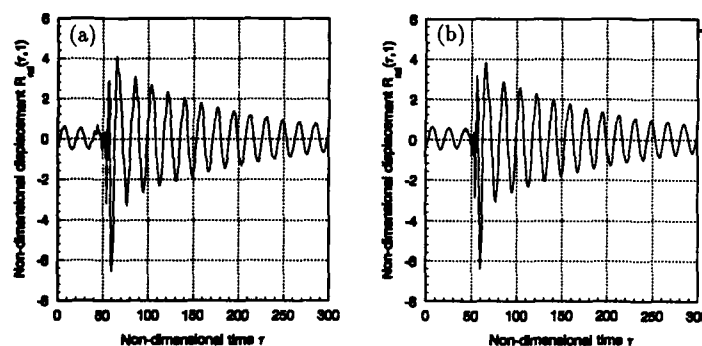
Beam, n=1, impulse distribution

Figure 11. Displacement of a steel shell, n=1, $h/a = 0.05$, $\eta = 0.02$, $x_0 = a$, $\tau_0 = 50$; (a) total response, (b) branch 1 contribution.

Figure 11(a) now shows the total non-dimensional radial displacement $(R_{nd} = R * ((2\pi)^2 \rho_s c_L h))$ of a thick steel shell (h/a=0.05) filled with water one radius beyond the location of the impact, for the beam circumferential mode (n=1). The contribution of the branch s=1 to this response is given in Figure 11(b) and is found to match the first graph almost perfectly. This implies that this wave is alone responsible for the all response of the system. This branch corresponds to the beam type shell motion [3]. That explains why the response is strongly dependent on the damping ratio added to the shell material. As explained Fuller [3], even though the s=1 branch is essentially a beam mode, the "forced" pressure amplitude in the fluid, near field at the shell wall (see Figure 12(b)), is very high. Moreover, with a thick shell (h/a=0.05), both media are strongly coupled. This can be noticed from the fact that the instantaneous intensity in the fluid (see Figure 12(a)) is found to be dependent on the damping ratio in the shell material, owing to the fluid loading appearing as a mass loading concentrated at the wall for this particular branch.
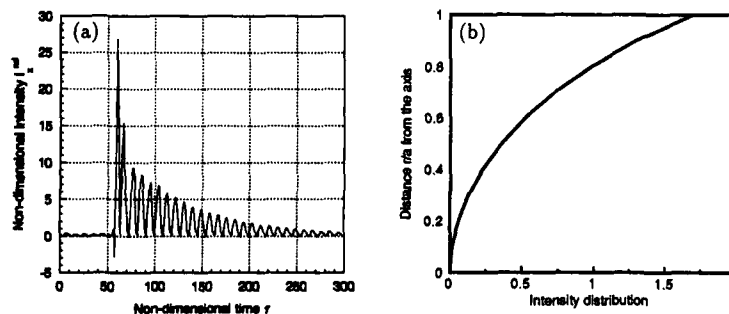

Figure 12. (a) Instantaneous intensity in the fluid at the shell wall. (b) Intensity distribution in the fluid; steel shell, n=1, $h/a = 0.05$, $\eta = 0.02$, $x_0 = a$, $\tau_0 = 50$.

Considering now a thinner shell, on Figure 13(a) and (b), the impulse response displays two distinct areas: a high frequency range (54≤ τ ≤120) and a damped low frequency one above τ=120. With this thickness of shell (h/a=0.005), it has been previously found [8] that more energy is carried by the

422

shell at frequencies below $\Omega=0.2$ and more energy is in the fluid medium between $\Omega=0.2$ and $\Omega=0.8$; higher frequencies do not induce much response of the shell wall (see Figure 14). In fact, as the wall thickness is reduced, the branch s=1, which is still very close to the *in vacuo* beam branch at very low frequencies, changes towards a fluid-type wave close to a pressure release duct solution at higher frequencies. Therefore, two propagation paths of vibrational energy appear. Most of the energy is "slowly" carried to the structural observation point by the fluid medium as high frequency components. In addition, little energy propagates through low-frequency structural components.
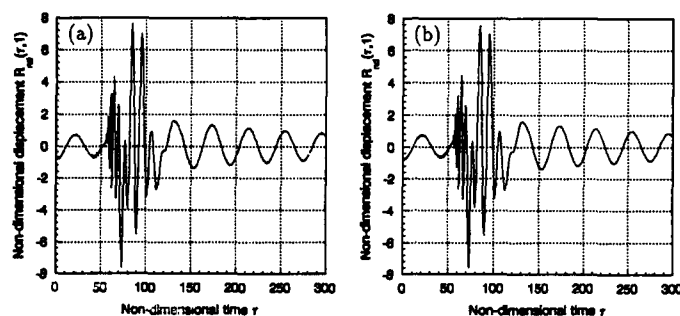

Figure 13. Displacement of a steel shell, n=1, $h/a = 0.005$, $\eta = 0.02$, $x_0 = a$, $\tau_0 = 50$; (a) total response, (b) branch 1 contribution.
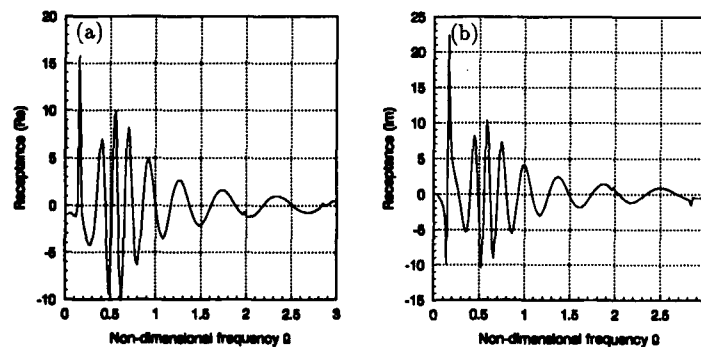

Figure 14. Transfer receptance of a steel shell, n=1, $h/a = 0.005$, $\eta = 0.02$, $x_0 = a$; ——, total transfer function; (a) real part; (b) imaginary part.

CONCLUSIONS

An expression for the radial displacement of infinite cylindrical shells subjected to an impulsive line force has been derived. Numerical results have been given for shells of different thicknesses vibrating in the n=0 and 1 circumferential modes at different distances from the impact. The results have been analyzed in terms of propagation of free waves. The contribution of each generated wave to the total response has been used to determine the propagation paths of the energy in the system.

With axisymmetric impulse distribution, most of the disturbance energy has been found to be carried to structural points by the fluid as a wave which has the characteristic of near field located near the shell wall. When the impulse distribution excites the n=1 circumferential mode, the energy is carried by a beam type wave which has also the characteristic of "forced" pressure field at the wall. This was found to

imply that the energy is carried to the observation point through both media, the structure and the fluid. More precisely, whereas low frequency components propagate through the shell wall, higher frequency components, around $\Omega = 0.5$, propagate through the fluid medium; this fluid-type frequency range can extend from $\Omega = 0.2$ to $\Omega = 0.8$ as the thickness of the shell decreases.

An expression for the instantaneous axial intensity in the fluid has been presented and the results verify those indicated by the free wave propagation interpretation.

ACKNOWLEDGMENTS

REFERENCES

1. V. N. MERKULOV, V. YU. PRIKHODKO and V. V. TYUTEKIN 1978 *Soviet Physics-Acoustics* **24**, 405-409. Excitation and propagation of normal modes in a thin cylindrical elastic shell filled with fluid.

2. C. R. FULLER 1983 *Journal of Sound and Vibration* **87**, 409-427. The input mobility of an infinite circular cylindrical elastic shell filled with fluid.

3. C. R. FULLER and F. J. FAHY 1982 *Journal of Sound and Vibration* **81**, 501-518. Characteristics of wave propagation and energy distribution in cylindrical elastic shells filled with fluid.

4. G. F. LEYRAT 1991 *Submitted to Journal of the Acoustical Society of America*. Effects of an internal flow on the vibration of infinitely long cylindrical shells.

5. P. R. STEPANISHEN and D. D. EBENEZER 1987 *Journal of the Acoustical Society of America* **82**, 1811-1817. Transient vibratory response of fluid-loaded shells with axisymmetric excitations.

6. S. UJIHASHI et al. 1987 *Jpn. Soc. Mech. Eng.* **30**, No. 262, p. 568-573. Axisymmetric impulsive responses of an infinite circular cylindrical shell filled with liquid.

7. M. C. JUNGER and D. Feit 1972 *Sound, structures and their interaction*. Cambridge, Massachusetts; M.I.T. Press.

8. B. J. BREVART and C. R. FULLER 1991 *Submitted to Journal of Sound and Vibration*. Effect of an internal flow on the distribution of vibrational energy in an infinite fluid-filled thin cylindrical elastic shell.

9. C. R. FULLER 1981 *Journal of Sound and Vibration* **75**, 207-228. The effects of wall discontinuities on the propagation of flexural waves in cylindrical shells.
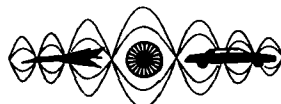
SECOND INTERNATIONAL CONGRESS ON
RECENT DEVELOPMENTS IN AIR- AND
STRUCTURE-BORNE SOUND AND VIBRATION
MARCH 4-6, 1992   AUBURN UNIVERSITY, USA

"ROTOR DYNAMIC IMPACT DAMPER TEST RESULTS FOR
SYNCHRONOUS AND SUBSYNCHRONOUS VIBRATION"
Tim A. Nale & Steven A. Klusman
Allison Gas Turbine Division
General Motors Corporation

ABSTRACT

An impact damped supercritical shaft rig is tested at operating speeds in excess of a rotor bounce, shaft first bend, and shaft second bend mode frequencies. Impactor design concepts consisting of solid steel rods, balls, and a shell housing containing a solid rod with and without a thin film are tested and demonstrated to a specific damping level. System critical speeds and mode shapes are presented with comparison of prediction and test results. Undamped as well as damped response levels are compared to predicted values for first, second, and third mode synchronous vibration. Subsynchronous vibratory levels are studied parametrically with impactor mass. Response sensitivity with unbalance is presented for two primary impactor clearance gaps and each of the design configurations. Variations in test measured damping levels with predicted levels are explained through the use of dimensionless damping curves indicating clearance gap mistuning. Preliminary test data indicates the direction in which the impactor gap must go to achieve maximum efficiency damping. Results of this testing demonstrates the ability of a single impact damper to effectively function at more than one mode frequency with acceptable levels of damping. The effects of gravity are apparent for low frequency vibration with little damping occurring but higher frequency modes show significant damping with little or no influence of gravitational acceleration. The inherent self-contained design, ability to withstand extreme operating environments, and effectiveness of damping subsynchronous vibration makes the impact damper applicable for environments too severe for conventional squeeze film dampers.

INTRODUCTION

The basic principle of impact damping is represented by the material collision property defined as the coefficient of restitution. During the instance of collision a localized elastic deformation of the damper and damped system occurs. The work in deformation and change in impactor linear momentum results in a lower energy state of the damped system. The actual magnitude of the coefficient of restitution is determined by testing and currently known to be influenced by the type of material, temperature, and relative velocity of the collision. While basic restitution data has been published in the literature, complex structure data such as shell construction, extreme environmental temperatures, and low relative velocities are not well documented.

Although numerous authors have studied the principles of impact damping over the past one-hundred and fifty years recent work initiated by NASA Lewis Research Center in 1982 has lead to the development of time history analytical models of impact damped systems. Work by Brown and North [1], Soller [2], Pyle [3], Jones [4], Nale [5], and North and Nale [6] has concentrated on the solution of the fundamental equations of motion governing an impact damped system instead of assumed solutions for steady-state motion. The combining of these published works, Allison experimental IR&D efforts, and USAF contract F33615-88-C238 work has progressed to the development of impact damper preliminary design tools. The application of these tools with rotor dynamics analysis software has given Allison the ability to design supercritical rotor shaft systems implementing impact dampers to maintain vibration limits.

Current gas turbine damper technology is focused around squeeze film oil dampers. Although the application of film dampers has been successful, several limitations currently exist. Perhaps the most critical of these limitations is the operating temperature range of damper oils. In response to this limitation the USAF Wright Aeronautical Laboratories issued contract number F33615-88-C238 in July of 1988 for the development of a high temperature damper for use in future IHPTET engines. The stated objectives of this research program were as follows:

   i) State of the art evaluations and high temperature conceptual damper
      designs.

  ii) The detail design of two high temperature dampers and one high
      temperature supercritical shaft rig.

 iii) The fabrication of the two dampers and shaft rig referenced in
      item ii.

  iv) Rig analysis, damper modeling, and correlation analysis with
      ambient and high temperature testing.

This document reports on the physical design of an elevated temperature impact damper and ambient rig test results. Details of this testing include subsynchronous and synchronous damping effectiveness. Damper unbalance sensitivity for a rotor bounce and first two shaft bend modes. Damper effectiveness changes resulting from various impactor geometries and constructions. Response sensitivity effects are indicated for changes in unbalance and impactor effective mass. Impactor orbital displacement plots are included to show impactor relative motion as it relates to gap tuning.

TEST HARDWARE

The rotor shaft rig used for this work was basic in design implementing an air turbine and squeeze film at the drive turbine end. The squeeze film damper was added for drive end stability during the test program. A second bearing was located near the opposite end with a twenty pound overhung rotor used to vary the system dynamic unbalance up to 18 g-in. The impact damper was mounted in a nonrotating containment ring located at the overhung rotor bearing, fixed to the bearing outer race and connected to ground via soft springs. The containment ring was bored at twenty angular locations to provide a nominal diameteral gap of .017 inches for the primary test impactor. End retainer plates restrict impactor axial motion to .003 inches, thereby allowing unrestricted radial motion without cylinder angular motion. Four impactor designs were tested with the first of the following the primary concept:

   i) Shell cylindrical rods with solid tungsten centers and a
      low viscosity thin film fluid, figure (1). Tested with and
      without three 10 mm flats.

  ii) Solid steel cylindrical rods with three 10 mm flats,
      figure (2).

iii) Solid steel square rods, figure (3).

iv) Steel balls, figure (4).

TEST RESULTS

The rotor rig previously described was modeled and analyzed using the Allison proprietary Finite Element Model (FEM) code, ROTORDYN, to determine the system critical frequencies and mode shapes, figures (5a) thru (5d). In addition to basic critical speed analysis, damper mass and system unbalance response sensitivity studies were performed parametrically to better understand both undamped and damped response. The basic rotor configuration is depicted in figure (5a) with the first three critical speed modes represented by the dashed lines in figures (5b), (5c), and (5d). The rotor bounce or first mode was predicted at 2571 rpm with testing showing this mode present at 97% of the predicted speed. The first bend mode was found at 89% of the predicted 7313 rpm and the second bend or third mode was determined at 91.5% of the predicted 19682 rpm. This data shows good agreement of the rig FEM and ROTORDYN solution technique with the test data, a point essential in the successful design of a damper.

Impactor Orbital Whirl
Initial testing of the rotor rig, using true cylindrical impactors, quickly indicated that the level of damping was significantly less than predicted. Preliminary review of the data gave indications that the impactors were orbiting within the containment chamber and not engaging in true collisions. The containment ring was instrumented with two Bently-Nevada proximity probes located perpendicular to each other within the same containment cell and the testing was repeated. This data, figures (6a) and (6b), confirmed the initial analysis that orbital whirl, not periodic collisions were taking place within the impact chamber at high unbalance. These two orbital diagrams, (6a) and (6b), clearly show circular motion of the impactor for the first and second bend modes. The orbital plot of the rotor bounce mode indicated rolling motion over approximately 80 degrees of the chamber. The significance of this rolling motion will be discussed later.

To address the problem of orbital whirl, three equally spaced 10 mm flats were machined on the outer diameter of the impactors, figure (1). The inclusion of these flats was undertaken in the belief that if orbital motion was to begin it would be disrupted within a maximum of one-third of an orbit and yield in a true collision. Rig testing of the impactors with flats was performed and indicated a marked improvement in damping effectiveness and non-orbital impactor motion within the containment cavity.

Impactor Design
One objective of this investigation was to determine the influence of impactor geometry and construction on the level of damping obtained for a given damper mass. For the purpose of study each of the four basic design concepts were tested and the results normalized to a common impactor mass of 5 lbs. In the case of the rotor bounce mode the inclusion of any impactors, independent of the design or mass, made no significant change in the rotor response to varying unbalances. These results prompted an acceleration analysis of the system in the impactor plane to determine if the rotor system provided accelerations greater than 110% of gravity. It was quickly determined that the rotor bounce mode did not satisfy this criteria and therefore would not experience damping by the use of impactors. This analysis and test data along with the first bounce mode orbital data confirmed that impact dampers are essentially nonfunctional unless gravity is significantly overcome by housing acceleration.

The response sensitivity for the first bend mode shows a significant decrease in rotor vibratory amplitude with the inclusion of the impactors. As seen in figure (7) the baseline dynamic amplitude was reduce from 56% to 87% with 5 lbs of added impactor mass of various design configurations.

427

Although every configuration resulted in positive results it is clear that the primary design yielded the largest reduction in amplitude with the next lowest amplitude twice that of the primary design. To better determine the importance of the thin film fluid, integral to the baseline shell design, the fluid was removed and the impactors tested again showing the response magnitude increasing approximately 11% over the baseline amplitude. The impactor oil film was then replaced with commercially pure lead and testing repeated. These results were surprising in that the shell design using lead in place of oil yielded an additional reduction in response magnitude of 7% from the baseline. These results indicate that the selection of the film material is very important and that a low shear solid material at the operating temperature achieves maximum damping.

In the case of the second bend mode the influence of the impactors is very noticeable with reductions in response magnitude from 44% to 74%. As would be expected, the reductions for the second bend mode were less than those experienced by the first bend mode that served as the damper design point. A second item quickly observed in figure (8) is that the impactor design and construction is less significant for the second bend mode. This is because the damper is operating at an off design point making it less sensitive to the coefficient of restitution. The shell impactor design was tested with oil and lead, with the lead film resulting in the lowest response amplitude even though the significance of this difference was minimal at approximately 2% of the baseline amplitude.

The results of the testing supports the primary impactor design concept of a shell containing a dense solid core and thin separating film as the most effective design. The use of a low shear solid instead of a low viscosity fluid for the separating film did improve the damping capacity of the primary design. This improvement should be further investigated to better understand the effects of film thickness.

Impactor Gap Sensitivity
Perhaps the most difficult parameter to define through analysis is the proper impactor gap for optimum damper effectiveness. The importance of this dimension is in it's ability to change the basic impactor behavior from one impact per half cycle, maximum effectiveness, to an infinite number with minimum damping efficiency. In a initial attempt to better understand the total influence of the impactor gap on system damping, two sets of solid steel cylindrical impactors were fabricated with the only difference being the effective impactor gap. The first set maintained the same gap as the shell impactors with the second set were fabricated with a gap reduced by 20%. A detailed review of the data in figure (9) shows that the gap dimension changes both the unbalance at which peak effectiveness occurs and the magnitude of this effectiveness. Both the large and small clearance impactors follow a parabolic shape when viewed as displacement verses unbalance. A third and final test was conducted where an even mix of small and large clearance impactors were run together. The resultant of this configuration was to broaden the effectiveness of the damper with unbalance. It appears that damping from the mistuned impactors is additive to that which occurs from the properly gap tuned impactors. This is a significant point that allows tuning for multiple modes using either several fixed gaps or active variable gap controls.

Synchronous Forced Response Sensitivity
Two primary goals of the synchronous response study were to determine impactor mass sensitivity correlated to Allison predictions and basic shaft response sensitivity to rotor unbalance. Parametric analysis of the damper was performed using ROTORDYN to predict the rotor response for up to five pounds of impact mass at the first three system critical speeds. These predictions were made for each mode assuming proper gap tuning resulting in one impact per half cycle, a coefficient of restitution of 0.6, and sufficient containment ring acceleration to overcome the effects of gravity. The rig used for this testing did not meet the acceleration criteria for the first, or rotor bounce mode, and therefore was not expected to behave as predicted. The second mode was used as the design

428

point for principle gap tuning since it met the acceleration criteria. The third, or second shaft bend mode also met the acceleration criteria but was knowingly gap mistuned and intuitively not expected to behave with the effectiveness shown in figure (10).

Testing was performed with no impactors, 2.5 lbs of impactors, and 5.0 lbs of impactors for comparison with calculated responses. The first mode response data in figure (11) indicates no change in response with the inclusion of any impactor mass. This was expected based on the test results presented earlier and the acceleration analysis. The second, or first bend mode data did show significant changes in response amplitude with the inclusion of impactors. Comparing the second mode test data with the predictions in figure (10) indicates good agreement at the 5.0 lb impactor point. Agreement at the 2.5 lb was not as good but is understood to be the result of gap mistuning. This decrease in damping effectiveness is better understood by examining figure (12) where it is clear that the damper designed for this rig was operating mistuned. The damped cavity amplitude is made dimensionless relative too the impactor gap and defines the x- ordinate while the y-ordinate represents damping capacity. The conclusion that can be drawn from this data is that the impactor gap was designed to large for this application. The third mode responded as would a significantly mistuned system. Although a substantial reduction in vibratory amplitude was achieved it was far less than the potential of the damper with a tuned gap.

The rig shaft response, for levels of rotor unbalance ranging from 5 to 18 gram-inches, was determine for a constant impactor mass of five pounds. The shell design was parametrically tested with oil and lead films and three flats on the shell. The first of these configurations tested was with the oil film and yielded the results in figure (13). This diagram depicts rig response normalized to the undamped response for each of the three first modes at each unbalance test condition. This data shows well ordered behavior through out the applied unbalance range with the second mode showing the lowest relative amplitude for the majority of unbalances tested. The third mode response amplitude continued to decrease with increasing unbalance, a characteristic of an impact damper both mass and gap mistuned. Testing of the shell impactor with a lead film, figure (14), depicts the same characteristics as does figure (13). The significant difference in the two sets of data is the lower response with the lead film. In this comparison it is clear that the use of a low shear solid for the thin film is better than that of a low viscosity fluid.

Subsynchronous Forced Response Sensitivity
During early rig testing, without a drive bearing damper, significant subsynchronous vibration was experienced at 9000 rpm and greater. The ability of impact dampers to control nonsynchronous vibration was characterized and found to be very good. The data presented in figure (15) shows a reduction in response amplitude from .017 inches to less than .0001 with five pounds (20 impactors) of impactor masses. Although the potential of impactors to damp nonsynchronous vibration was thought to exist the magnitude of it's effectiveness was not predicted. The flats were not present on the early dampers, showing this feature is not required for damping nonsynchronous vibration.

CONCLUSION

The use of impact dampers has now been success fully demonstrated for vibration control of a supercritical shaft. This esting confirmed the primary design concept of a cylindrical shell containing a thin separating film and solid core. The prevention of orbital whirl was found to be essential to achieve acceptable levels of damping for synchronous vibration. The inclusion of flats on the shell outer wall successfully prevents orbital whirl and causes the impact mass to engage in ordered collisions. The significance of impactor gap tuning was apparent through out the testing with the authors left with further work in understanding this area of impact damper design. Comparison of predicted and test response data shows that a single damper can be effective for multiple

429

modes even though the damper is mistuned for some. The work described herein highlights the basic critical parameters used in the optimum design of an impact damped supercritical rotor system.

REFERENCES

[1]   Brown, G.V. and C.M. North, "The Impact Damped Harmonic
       Oscillator in Free Decay", NASA Technical Memorandum
       89897, Lewis Research Center, 1987.

[2]   Soller, P.J.,"The Development of a Computer Model as an
       Aid to the Solution of the Problem of Impact Damping",
       M.S. Thesis, Rose Hulman Institute of Technology, Terre
       Haute, IN, 1985.

[3]   Pyle, S.E., "Computer Simulation of Internal Viscous
       Damping", M.S. Thesis, Rose Hulman Institute of
       Technology, Terre Haute, IN, 1983.

[4]   Jones, R.E., "Application of the Component Element Method
       to the Impact Damped Simple Harmonic Oscillator", M.S.
       Thesis, Rose Hulman Institute of Technology, Terre Haute,
       IN, 1988.

[5]   Nale, T.A., "Time History Study of a Classical Cantilever
       Beam Damped by Internal Mechanical Means", M.S. Thesis,
       Rose Hulman INstitute of Technology, Terre Haute, IN,
       1988.

[6]   North C.M. and T.A. Nale, "Time History Study of the Free
       Response of the Classical Elastic Cantilever Beam Damped
       By Internal Mechanical Means", USAF DAMPING 89, West Palm
       Beach Florida, February 1989.
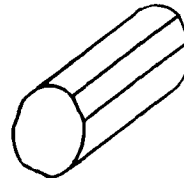
FIGURES
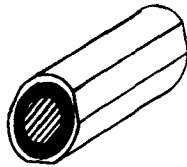
Figure 1 - Shell Impactor Design

Figure 2 - Solid Cylindrical Design
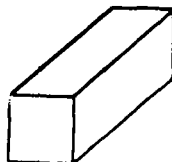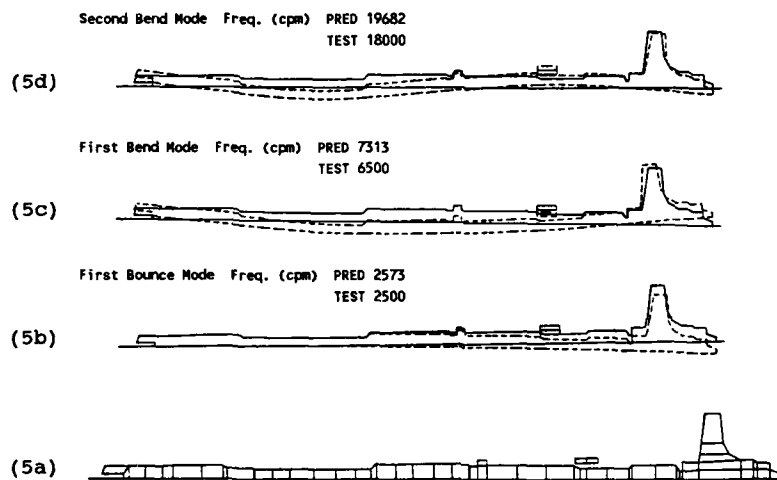

Figure 3 - Solid Square Design

Figure 4 - Solid Ball Design

Second Bend Mode Freq. (cpm) PRED 19682
                               TEST 18000

(5d)

First Bend Mode Freq. (cpm) PRED 7313
                              TEST 6500

(5c)

First Bounce Mode Freq. (cpm) PRED 2573
                                TEST 2500

(5b)

(5a)

Figures 5a thru 5d - Damper Supercritical Shaft Rig Mode Shapes
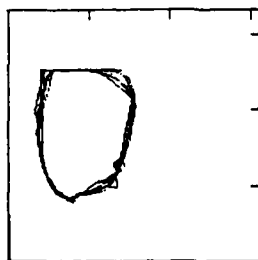
Figure 6a - Second Mode
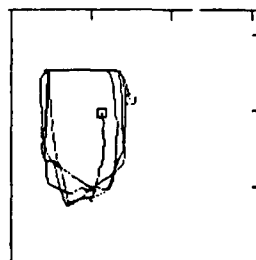Orbital Whirl at 6519 rpm
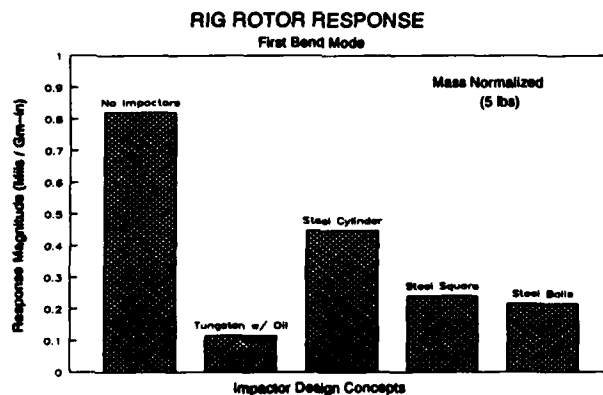
Figure 6b - Third Mode
Orbital Whirl at 18010 rpm

RIG ROTOR RESPONSE
First Bend Mode

Figure 7 - First Bend Mode Impactor Design Concept Evaluation
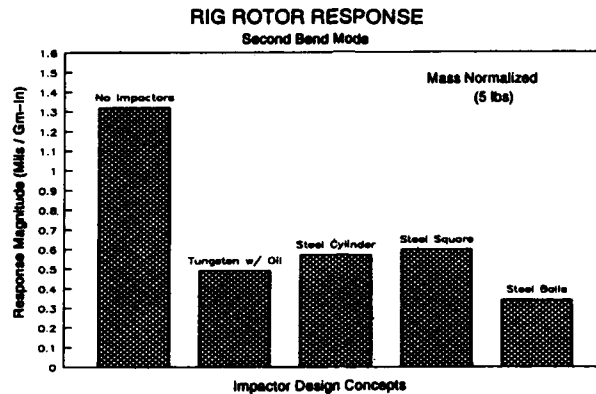
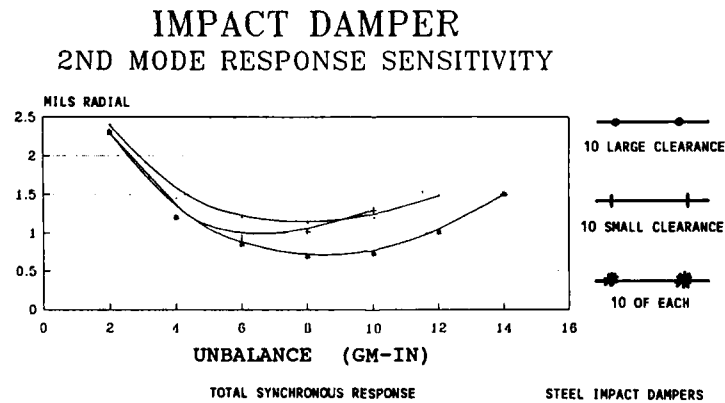Figure 8 - Second Bend Mode Impactor Design Concept Evaluation

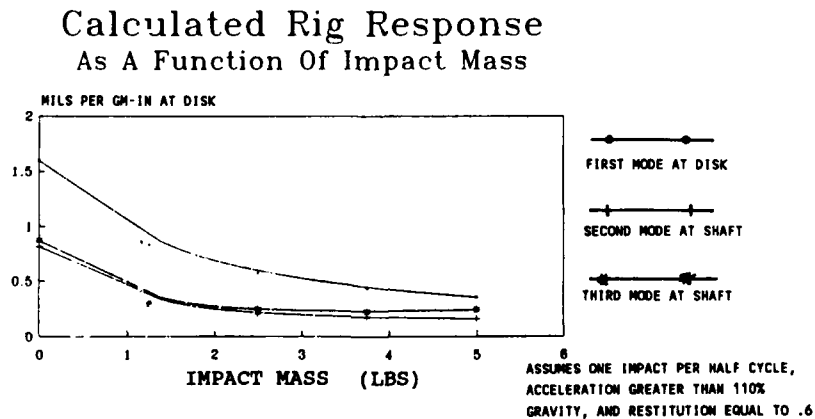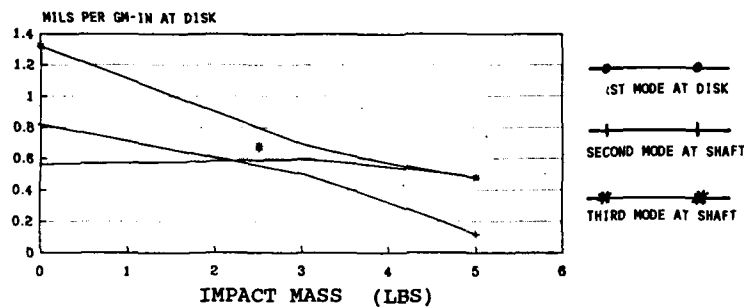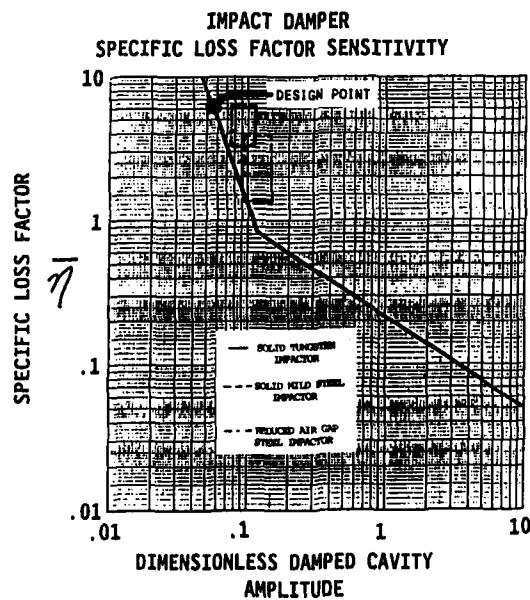Figure 9 - Impact Damper Gap Sensitivity

Figure 10 - Impact Damper Predicted Damper Mass Sensitivity

Measured Rig Response
As A Function Of Impact Mass

MILS PER GM-IN AT DISK

ıST MODE AT DISK

SECOND MODE AT SHAFT

THIRD MODE AT SHAFT

IMPACT MASS (LBS)

TUNGSTEN IMPACTORS WITH OIL FILM

Figure 11 - Impact Damper Measured Damper Mass Sensitivity

IMPACT DAMPER
SPECIFIC LOSS FACTOR SENSITIVITY

DESIGN POINT

SPECIFIC LOSS FACTOR $\overline{\eta}$

SOLID TUNGSTEN IMPACTOR

SOLID MILD STEEL IMPACTOR

REDUCED AIR GAP STEEL IMPACTOR

DIMENSIONLESS DAMPED CAVITY
AMPLITUDE

$$\overline{\eta} = f(M_{impactor}, M_{shaft}, X_i, A_e, e)$$

$M_{impactor}$ = Impactor Mass

M_{shaft} = Shaft Modal Mass
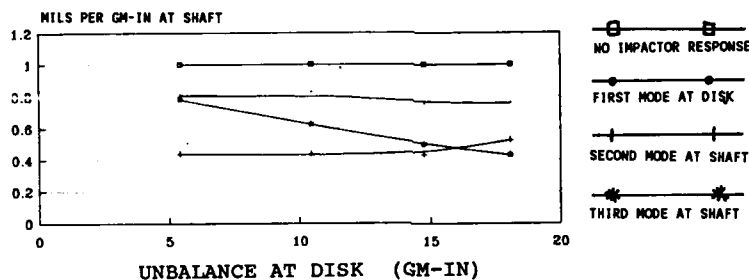
X_i = Impactor Cavity Modal Amplitude

A_e = Damped Impactor Cavity Amplitude

e = Coefficient of Restitution
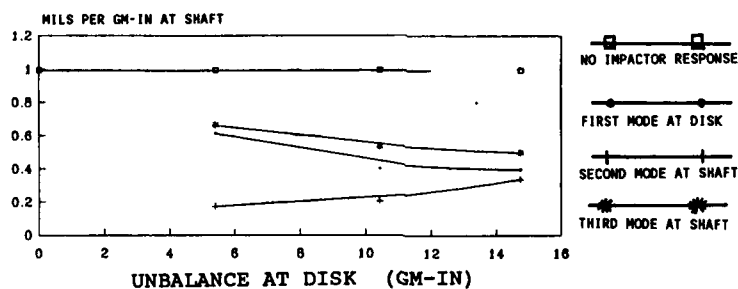
G = Impactor Gap

Figure 12 - Impact Damper Design Curve

433

Measured Rig Response
As A Function Of Unbalance

MILS PER GM-IN AT SHAFT

NO IMPACTOR RESPONSE

FIRST MODE AT DISK

SECOND MODE AT SHAFT

THIRD MODE AT SHAFT

UNBALANCE AT DISK (GM-IN)

20 TUNGSTEN IMPACTORS WITH OIL FILM AND FLATS

Figure 13 - Impact Damper Measured Response Sensitivity

Measured Rig Response Ambient
As A Function Of Unbalance

MILS PER GM-IN AT SHAFT

NO IMPACTOR RESPONSE

FIRST MODE AT DISK

SECOND MODE AT SHAFT

THIRD MODE AT SHAFT

UNBALANCE AT DISK (GM-IN)

20 TUNGSTEN IMPACTORS WITH LEAD FILM AND FLATS

Figure 14 - Impact Damper Measured Response Sensitivity
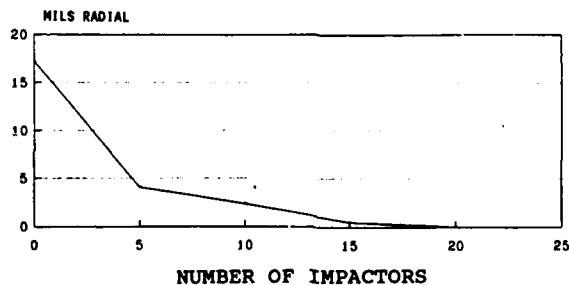
IMPACT DAMPER
SUBSYNCHRONOUS VIBRATION

MILS RADIAL

NUMBER OF IMPACTORS

Figure 15 - Impact Damper Subsynchronous Response Sensitivity

434

SECOND INTERNATIONAL CONGRESS ON
RECENT DEVELOPMENTS IN AIR- AND
STRUCTURE-BORNE SOUND AND VIBRATION
MARCH 4-6, 1992 AUBURN UNIVERSITY, USA

VIBRATION DESIGN OF SHAKERS LABORATORY OF THE NEW HONG KONG UNIVERSITY OF SCIENCE AND TECHNOLOGY

Westwood K W Hong, Nicholas J Boulter

Arup Acoustics, Ove Arup & Partners, Hong Kong

ABSTRACT

Reaction floors for powerful shakers are normally in isolated locations to minimize shaker-induced vibration from disturbing other vibration-sensitive laboratories. The compact nature of the Hong Kong University of Science and Technology (HKUST) campus requires a more exact design for the reaction floor than for a spacious campus with well separated laboratory buildings. HKUST offers a centralised laboratory service with an easy access to the major testing facilities. This resulted in the location of a Structural Laboratory housing large shakers close to vibration sensitive areas (eg micro fabrication centre). The design of the support structure for the shakers (reaction floor) to minimise vibration transmission was critical to the success of the teaching and research to be conducted in these buildings. The foundation designs of the reaction floor and the microfab centre will be presented.

1. INTRODUCTION

Vibration generating areas, such as structural laboratories, have to be carefully located if adverse effects on other sensitive spaces are to be avoided. "Green field" sites are usually chosen for these facilities which are located well away from existing and future sensitive users. The new Hong Kong University of Science and Technology is remote from any existing sensitive facilities. However, the design constraints introduced by the steeply sloping site and the users requirement for a centralised laboratory service, resulted in the Structural Laboratory (containing the shakers) being housed in the main academic building.

The upper floors of the academic building are used for teaching and research laboratories. Outside the Structural Laboratory, another wing of the academic building houses the vibration-sensitive Microfab Centre (Fig 1). This arrangement satisfied the HKUST user's requirement of providing a centralised laboratory service, but it created a potential vibration problem for the acoustic consultant. Relocation of the Structural Laboratory to an isolated location had been considered but was not feasible because of other planning constraints. An optimum solution for controlling the high level of shaker vibration had to be found. The constraints to the design of the reaction floor included cost, space, types of seismic testing and the frequency range of tests to be conducted in the Structural Laboratory. This paper presents the vibration design considerations for the shaker reaction floor.

2. VIBRATION FROM REACTION FLOOR OF STRUCTURAL LABORATORY

<u>Structural Laboratory and Reaction Floor</u>

Most of the vibration generating experiments will be carried out on the reaction floor area of the

435

Structural Laboratory. This is designed to carry high loadings and is fitted with hold-down points for fixing large structures. Experiments will include excitation of test structures by shakers with a 10 ton-force capacity between 1 to 10Hz. The proposed reaction floor is approximately 30.0m long and 13.75m wide with an overall depth of 3.5m. It weighs approximately 3000 tonnes. Within the depth of the floor will be service voids separated by 400mm thick spine walls. To maximize the bending stiffness of the reaction floor slab, the walls have been spaced at 3m centres in the longitudinal direction of the floor. Dimensions of the floor are shown in Fig 2-3.

A large amount of reinforcement steel was essential to achieve a high bending capability and pull-out strength for the reaction wall and floors. The main reinforcement bars are of 32mm diameter and are laid at 300mm centres. The spine walls significantly stiffened the 900mm thick bottom slab and the 600mm thick upper slab to assist in resisting bending moment and vertical reaction forces.

Excitation Forces from Shakers

Excitation forces will be generated by two types of shakers installed in the Structural Lab. These are the hydraulically actuated and electromagnetically actuated vibrators:-

Hydraulically actuated vibrators generate the excitation force by a hydraulic ram and a hydraulic power supply which is servo controlled in order to provide an accurate excitation forcing amplitude and frequency. The range of operating frequency is normally limited to 0 to 300Hz due to non-linearity of response at high frequency.

Electromagnetically actuated vibrators generate the excitation force by the same principle as a loudspeaker, using a drive coil located in a magnetic field of a permanent magnet or a field coil. The vibrators need a driving system comprising a signal source and a power amplifier. The range of operating frequency is from 0 to 10,000Hz, depending on the vibrator size. The excitation force generated is generally less than that of a hydraulic vibrator. The actuator capacity of the large shaker to be installed in Structural Lab is 10 ton-force.

Excitation Frequency

Vibrational forces are applied to a test structure for diagnostic purposes or for assessing the local responses throughout the structure. The diagnostic tests evaluate the ability of the test structure to perform its intended design function in a prescribed vibration environment. A survey of local resonances is usually carried out with a view to eliminating any undesirable resonances. A swept frequency sinusoidal excitation is often employed for such tests. The signal frequency is swept from low to high as well as from high to low and a sufficient time is allowed for the displacement amplitude of the test object to reach a steady state. For the design of the Structural Lab reaction floor, the excitation frequency of the shaker has been assumed to range from 0 to 500Hz.

Vibration Transmission

The vibration input forces from the shakers are to be applied to the reaction floor and the reaction wall. The reaction floor construction will modify these forces which are ultimately transmitted to the substrata and surrounding buildings by the Rayleigh surface wave and other body waves. The responses of the base slab and reaction floor due to the vibration input forces are dependent on several factors such as the mass and stiffness of the structure, damping, interface conditions of the foundation and the participating ground mass. It is essential to isolate the surface wave, which is the main vibration energy carrier, from propagating to the adjacent column footings and, in turn, setting the supported building into motion.

The surface wave also propagates to more remote areas, although decreasing in amplitude with distance. Once the foundation of a building is set into vibrational motion, individual elements of the supported building structure will respond differently according to the natural frequency of the element. The vibration will then be perceived as disturbance to sensitive equipment or subjective annoyance to people.

3. DYNAMIC DESIGN OF REACTION FLOOR

Design Concept

*Two options were investigated during the design, which were termed the 'high tuned' and 'low tuned'
foundation. The 'low tuned' design would utilise spring or rubber vibration isolators to float the
reaction floor. This would give the reaction floor a natural frequency between 3 and 12 Hz (depending
on the design of the isolators). Whilst this method could achieve a good isolation of high frequency
vibration there was a danger that the shakers would operate at the floor's natural frequency. The 'high
tuned' option did not include resilient vibration isolation material. Instead, a massive foundation
provides the inertia mass and a rigid connection to the ground.*

High-tuned Foundation Design

The 'high-tuned' structural and foundation design was eventually adopted because the users could not
guarantee that the shakers would always operate away from the resonant frequency of the 'low tuned'
option. The approach relies on the mass and stiffness of the entire structure to transmit and dissipate
the vibrational energy to the underlying rock strata. For this transmission to occur, the massive
structure and the substrata must be joined together effectively. The following parameters were
evaluated in the design:-

(a) Stiffness and mass of the reaction floor -
The test floor, reaction wall and support structures have been designed to be as stiff as it is practicable.
A stiff and massive structure is required to withstand the dynamic forces generated by the shaker during
the swept frequency test. The test floor will have a fundamental natural frequency not less than 120Hz.
This can be achieved by a suitable selection of the centre-to-centre spacing of the spine walls and a
thick reinforced concrete floor slab. The spine walls are to create a service void and to support the
test floor rigidly on the base. Therefore, these walls should also be designed to be adequately stiff and
massive. A spine wall design with 400mm thickness and 3m centre to centre spacing is adequate to
provide the required bending stiffness to the upper and lower slabs. An adequate steel reinforcement
was applied at the top and bottom junctions. The reaction wall is to provide high level anchor points
for the shakers when testing a tall structure. Besides mass, the bending stiffness of this wall is also
important. The spine walls are therefore aligned towards the reaction wall in order to counteract the
bending moment exerted on the wall and floor slab by the shaker and the test structure.

(b) Caissoned foundation -
A deep foundation is also beneficial to transmit and dissipate the vibrational energy to the substrata.
The underlying bedrock is fissured volcanic rock. In the presence of the rock joints, vibration waves
will travel predominantly as surface waves. The compression 'body' waves are scattered and reflected
to the surface following reflection at the rock interfaces, reducing the dissipation of vibrational energy
to the deeper substrata. It is therefore essential to increase the transmission energy to the substrata
by a caissoned foundation. In order to mobilise a significant soil mass, eight caissons have been
constructed, each 7m in length and 3m in diameter (Fig 4). The total mass of the eight caissons
exceeds 1000 tonnes. The optimum caisson length was determined by a finite element computer model,
as explained below in Section 4.

Bridging elements between the reaction floor and the underlying soil are eliminated by the creation
of a 600mm deep undercroft. A walkway with 1200mm high headroom in the undercroft enables the
underside of the reaction floor to be inspected. The undercroft limits the acoustical coupling of a
shallow air space, which may cause significant vibration transmission through build-up of resonances
in the air space.

The caissons have been designed with a minimum 75mm annular air gap over their entire length. The
air gap provides a high impedance mismatch to limit horizontal vibration coupling between the sides
of the caissons and the rock through which it passes. The caissons were hand-dug in order to avoid
blasting which might disturb the underlying rock strata. Concrete retaining rings were cast for every
900mm deep rock excavated. These rings and the rock surface at the bottom of the caisson were

inspected before a 3m diameter steel tube were lowered and positioned within the pit. Checks showed that a minimum 100mm sleeving air gap had been maintained around the steel tube. The steel tube forms the permanent shuttering for the concrete caisson. Every possible precaution had been taken to ensure that the 100mm air space was plugged and well protected from the fall of debris before, during and after the pouring of concrete.

(d) Perimeter vibration break -
To reduce the vibration transmission to the adjacent structure and column footings, the reaction floor has a minimum perimeter airgap of 50mm. This is sealed with a profiled neoprene rubber element and a pair of steel trims connected to the concrete structures. The steel trims can withstand the normal trolley traffic and occasional fork lift and light vehicle traffic.

A high standard of quality control was required to ensure that Contractor did not bridge the air gap with a permanent shuttering material, be it a "soft and resilient" material such as Flexcell, polystyrene foam or neoprene rubber.

(e) Services and floor cover gratings -
Electrical conduits and the drain pipes are the main items that could compromise the high standard of isolation provided by the air gap. Large electrical cable trunking was avoided so that flexible and small cables are used without the rigid armour sheath at the vibration break. Floor cover gratings across the perimeter gap are avoided and resilient vibration isolation pads are provided for the electrical conduit cover at the air gap. A drain sump to collect any spilt oil and floor cleaning water was attached to the underside of the bottom slab. The drain pipes and the small pump unit are fitted with flexible connectors.

4. DYNAMIC ANALYSIS OF REACTION FLOOR AND LABORATORY BUILDING

The high-tuned foundation and Reaction Floor have been analyzed by employing two-dimensional finite element computer models to represent the Reaction Floor and the adjacent Laboratory Building. The main objective of the analysis was to assess the effect of vibration generated by shakers on the upper floors of the building (Fig 3). Computer models using finite elements to represent the Floor and the Building have been analyzed using PAFEC, a finite element program developed by PAFEC Ltd. of Nottingham in the U.K.

Structural Representation

In the dynamic analysis, a two dimensional model was employed to represent a typical section of the reaction floor and the structural frame for the Structural Laboratory Building with unit-length geometrical properties in the longitudinal direction. Beam elements are used to represent the reaction wall, top and bottom slabs, side walls, spine walls and caissons. The underlying rock supporting the caissons are represented by spring elements. The Lab Building structure is approximately symmetrical about the centre-line of the building. Hence, only one half of the building frame is required to be represented in the model. In this model, the masses due to both dead load and live load have been lumped to the nodes. Suitable boundary conditions were also applied to the nodes along the centre-line of the model to ensure continuity. Horizontal displacement and rotation at the boundary were suppressed in this two-dimensional model.

The attenuation of vibration transmitted from the caisson footing to the building footing was calculated and also measured on site when the site formation work was being carried out on an adjoining site. Such an opportunity arose when an excavator fitted with a breaker head was working in a trench. Vibration level spectra were obtained close to the breaker and at various distances at the ground level. The loss factors over the frequency range of 0-200Hz were obtained by dividing the response at ground level by that of the trench rock bottom. These loss factors were used to calibrate the output at the caisson footing and the input at the column footing of the laboratory building.

Assumptions

The following assumptions were made in the dynamic analysis :
1. The analysis is linear elastic.
2. The footings of the caissons and laboratory building rest on soil formed from fissured volcanic rock which is represented by soil springs. A linear elastic spring system is used to simulate the soil foundation with the spring constant being the equivalent dynamic stiffness of the homogeneous and isotropic soil.
3. The structure is excited at the top slab by a shaker-induced vibration in the form of a sinusoidal force acting long enough to reach steady-state conditions.
4. The effect of reinforcing steel in the concrete is neglected.
5. The damping of the concrete structures is 5% of critical. It is anticipated that the existence of drywall partitions and false ceiling will result in a higher value of damping for the laboratory building.

The natural frequencies, mode shapes and floor response of the structures have been obtained (Fig 5-8). Results indicate that the floor response of the Laboratory Building induced by the shaker excitation on the Reaction Floor will be within the recommended vibration limit for 'Group A' laboratory equipment which requires $50\mu m/s$ (eg for optical microscopes x400 or less, or top loading weighing balances with 3 decimal place accuracy) (Fig 9-10). Vibration attenuation due to the distance will also produce a vibration environment for the more sensitive 'Group C' sensitive laboratory equipment in the Microfab Centre approximately 25m away.

Vibration Tests of Reaction Floor Caisson

Vibration testing of the finished caissons (without the reaction floor) has established the effectiveness of the design. A 200kg drop hammer, fabricated on site from steel I-sections was used as a vibration source. It was lifted and lowered by a mobile crane which provided a powered drop with a controllable fall. The test results show that the transmission loss across the top of the caisson gap was up to 40dB for the 8 caissons tested (Fig 11-12). The transmission loss for the 8 caissons do not differ significantly, indicating that the caisson gaps were not bridged.

A further vibration test was also carried out to compare the transmission loss of the caisson gap with and without trapped water. Results indicate there would be no significant difference if water is trapped in the caisson gap. The vibration testing was conducted before the construction of the reaction floor slabs. The finished construction will have a much larger mass and the transmission loss between the top of the floor and the surrounding structure is likely to be much greater than achieved with just the caissons. The structure was nearing completion at the time of writing and tests on the completed structure are expected to be undertaken in mid 1991.

5. MICROFAB CENTRE

The Microfab Centre is located at the Semi-circular Building of the Academic Complex (Fig 10). It will have four clean rooms which contain the sensitive lithography equipment, scanning electron microscopes and E-beam systems. The stringent vibration criterion of Class C ($13\mu m/s$) had been included in the clean-room design which is appropriate for wafer fabrication [1,2]. The design used a slab-on-grade process floor, taking full advantage of the exposed rock base to form a stiff ground slab foundation. A ground slab comprising of 200mm thick concrete with closely-spaced 900mm deep reinforced concrete beams was cast atop the rock foundation, giving a natural frequency well above 35Hz. The ground slab is not susceptible to footfall-induced vibration or disturbances from external road traffic and plant.

Vibration tests were conducted to measure the floor response caused by various forms of excitation. It was found that even footfall caused by a person jogging in place at a 1 metre distance from the equipment did not cause significant floor response. A hand-held breaker operating at 25m away within the Structural Lab site showed no significant effect to the floor response of the Microfab Centre. The

floor response was found to be within 5μm/s even with both footfall impacts and breaker operation.

6. ACKNOWLEDGMENTS

The authors wish to thank Mr Robin Forster of Ove Arup & Partners for his valuable advice in developing the shaker floor and undercroft design. Thanks are also to the other Ove Arup Consultants with Mr George Chan for the design of the Microfab Centre structure, Mr Michael Kwok and Mr Patrick Chan in designing and evaluating the response of the Reaction Floor and caissons

7. REFERENCES

1. D. Malam and W. Hong, "Noise and Vibration Control in Microelectronics Clean Rooms", Acoustics '85, Vol.7, : Part 2, pp 141-148, 1985.

2. D. Malam and W. Hong, "Achieving Exacting Vibration and Noise Environment for Microelectronics Clean Rooms", International Conference on Clean Rooms, IMechE, C505/88, pp 43-49, 1988.

BIOGRAPHY

Dr Westwood Hong is a senior consultant with Arup Acoustics. He received his BS degree from Imperial College and his MS and PhD degrees from King's College of University of London. He is a Fellow of the Institute of Acoustics (UK) and the Chairman of the Institute of Acoustics Hong Kong Branch. He has had many years of experience in consultancy practice in the U.K. responsible of running specialist projects in light railway, motorway and piling noise and vibration studies, acoustic design of buildings including wafer fab clean rooms, metrology buildings, and anechoic chambers. He is the author of scientific papers in active noise cancellation, vibration design of clean rooms and construction noise.

Mr Boulter is a senior consultant with Arup Acoustics in Hong Kong. He has worked in acoustical consultancy for many years and spent the last four years based in Hong Kong. He has a wide experience of vibration isolation and acoustic design in the UK and Hong Kong. His Hong Kong projects have two isolated theatres within the Hong Kong Convention and Exhibition Centre, vibration isolated studios for Metro Radio and Star TV. In the UK he has worked on FE models for large structures for the offshore oil industry.
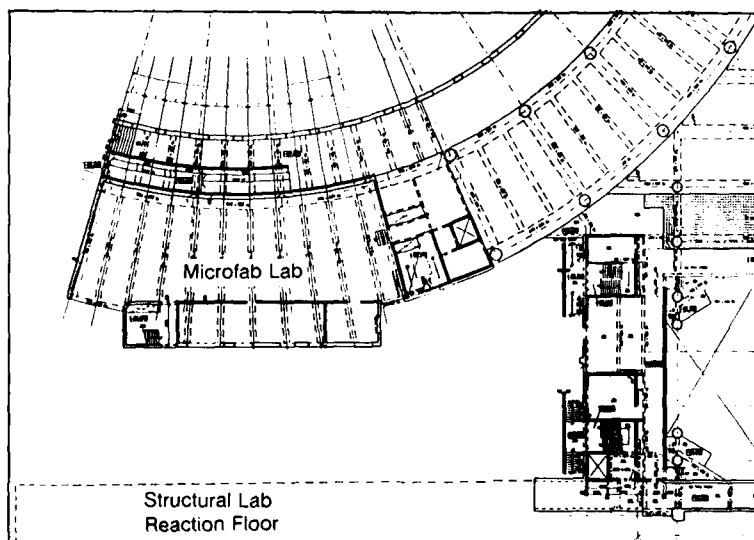
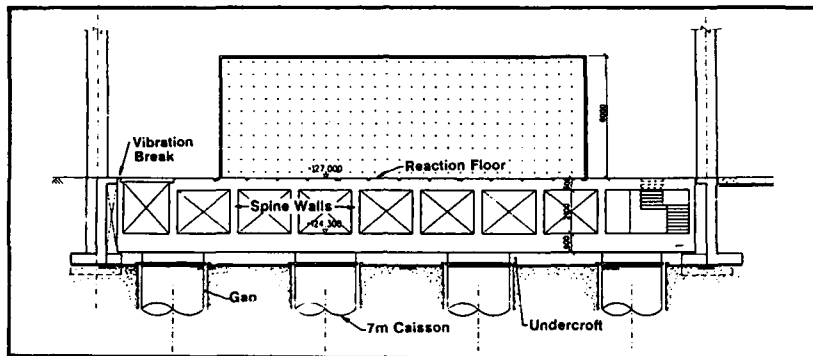**Fig. 1. Location of Reaction Floor & Microfab Centre.**

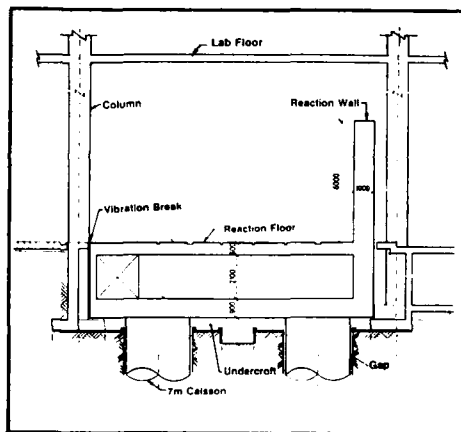Fig. 2. Reaction Floor and caisson foundation.

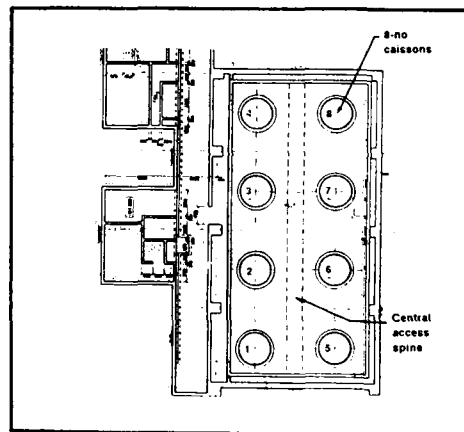Fig. 3. Typical section of Reaction Floor.

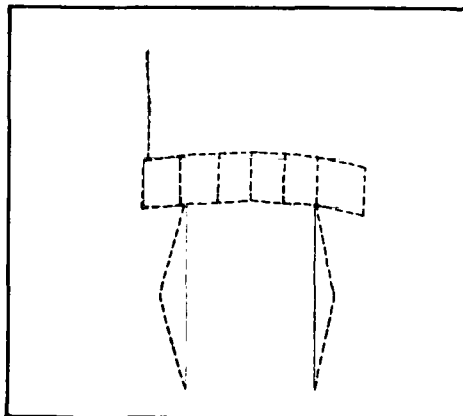Fig. 4. Plan of Reaction Floor caissons.

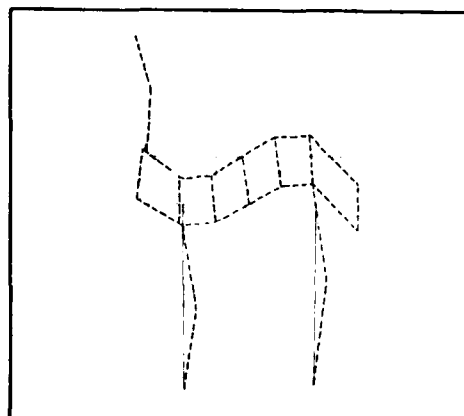Fig. 5. Reaction Floor - Mode 7 (58Hz).

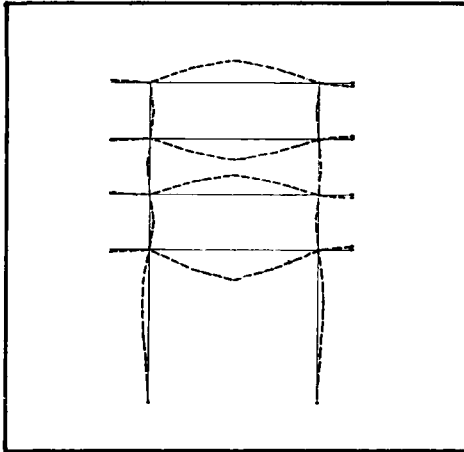Fig. 6. Reaction Floor - Mode 9 (70Hz).

441

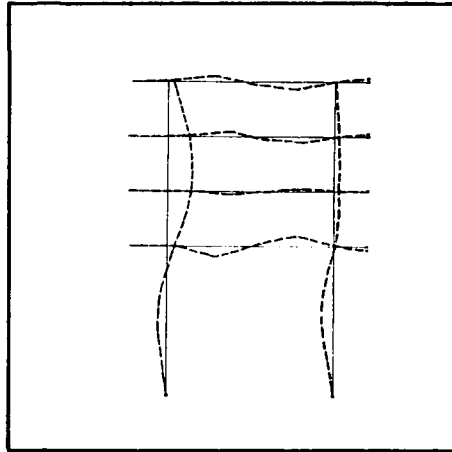Fig. 7. Structural Lab Building - Mode 6 (6.4Hz).
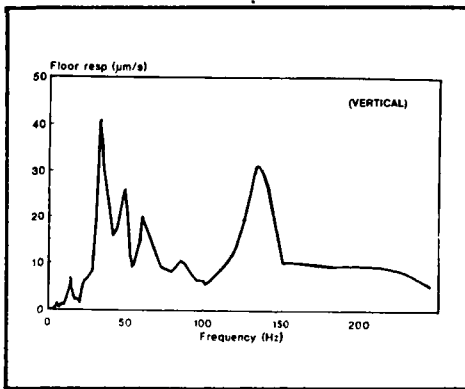

Fig. 8. Structural Lab Building - Mode 12 (15.5Hz).

Fig. 9. Predicted vertical response of
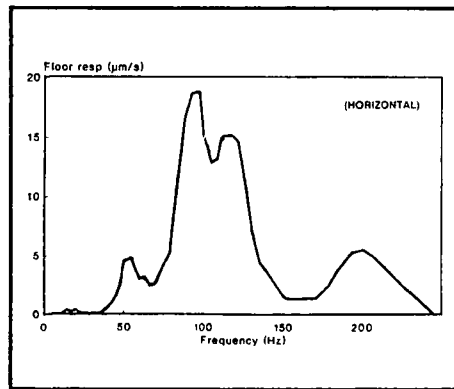Structural Lab Building.

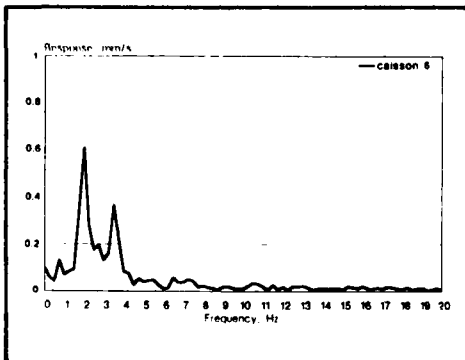Fig. 10. Predicted horizontal response of
Structural Lab Building.
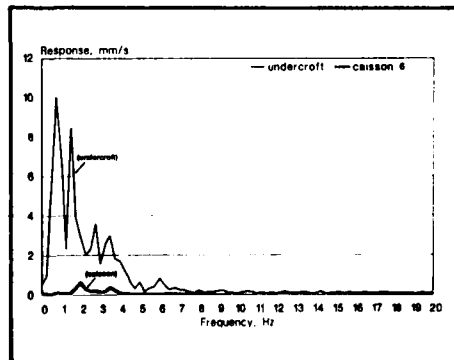

Fig. 11. Response of caisson head.

Fig. 12. Comparison of undercroft and
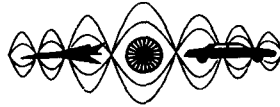caisson responses.

KEYNOTE ADDRESS

PROGRESS IN BOUNDARY ELEMENT CALCULATION
AND OPTOELECTRONIC MEASUREMENT OF STRUCTUREBORNE SOUND

Lothar Gaul, Martin Schanz and Michael Plenge

444

PROGRESS IN BOUNDARY ELEMENT CALCULATION AND OPTOELECTRONIC MEASUREMENT OF STRUCTUREBORNE SOUND

Lothar Gaul, Martin Schanz
Institute of Mechanics
University of the Federal Armed Forces Hamburg
2000 Hamburg 70
Fed. Rep. of Germany

Michael Plenge
JAFO Technology
2050 Hamburg 80
Fed. Rep. of Germany

ABSTRACT

The boundary element method (BEM) provides a powerful tool for the calculation of structureborne sound. Field equations of motion and boundary conditions are cast into integral equations, which are discretized only at the boundary. The boundary data are of primary interest because they govern the radiation into a surrounding medium. Formulations of BEM currently include conventional viscoelastic constitutive equations in the frequency domain. In the present paper viscoelastic behaviour is implemented in a time domain approach as well. The constitutive equations are generalized by taking fractional order time derivatives into account. The approach is applied for the calculation of structureborne sound in subsoil generated by soil–structure–interaction (SSI). Experimental investigation of SSI is performed by a laboratory test facility with improved measuring of structureborne sound by optoelectronics. Stationary and transient wave fields on soil surfaces have been measured successfully by holographic interferometry. The surface wave patterns allow to identify inhomogeneities and indicate the efficiency of vibration isolation by trenches.

INTRODUCTION

It is well known that the boundary element method (BEM) reduces the dimension of a boundary value problem by one. The variables in the domain of a 3-d problem are for example governed by the surface variables on the 2-d boundary via the boundary integral equation which includes the boundary conditions. The BEM provides a powerful tool for the 3-d calculation of structureborne sound because only the boundary has to be discretized, the boundary data are CAD compatible and detailed constitutive properties can be modelled [7].

In addition, the surface variables are of primary interest for structures guiding structureborne sound, because they determine the radiation into the air or another surrounding medium. Domain variables can be determined at arbitrary locations from the complete boundary data. If infinite (fullspace 3-d, fullplane 2-d) or semi infinite (halfspace 3-d, halfplane 2-d) domains are treated, no artificial boundaries with non reflecting boundary conditions need to be introduced. This is why the Sommerfeld radiation condition is fulfilled by the so called fundamental solution of the boundary integral equation. Formulations of BEM currently include conventional viscoelastic constitutive equations in the frequency domain. One aim of the present paper is to implement viscoelastic behaviour in a time domain approach as well. The elastic Stokes fundamental solution is converted to a viscoelastic one by adopting a correspondence principle. A novel viscoelastic fundamental solution is obtained analytically by inverse Laplace transformation. Viscoelastic constitutive equations are generalized by taking fractional order time derivatives into account [10].

The developed approach is adapted for the calculation of structureborne sound in a 3-d semi infinite domain. An application of practical relevance is the active or passive excitation of structures such as machine foundations interacting with subsoil. Propagation of surface waves, reflection and transmission

phenomena caused by layering, trenches and obstacles in subsoil are determined by the unknown boundary data that can be calculated from the known boundary data along with the initial conditions.

The second aim of the present paper is to improve conventional techniques of measuring structureborne sound by optoelectronics. A computerized laboratory test facility [9, 8] is presented for the experimental small scale simulation of soil–structure–interaction (SSI). The measurement of stationary and transient wave fields by holographic interferometry has been adapted to soil surfaces successfully. Detected modifications of surface wave propagation allow to identify inhomogeneities, imbedded structures or obstacles and indicate the efficiency of vibration isolation, e. g. by trenches.

GENERALIZED VISCOELASTIC EQUATIONS

Linear constitutive equations are assumed to describe the propagation of structureborne sound. Elastic-viscoelastic correspondence principles convert Hooke's law of elasticity

$$s_{ij} = 2Ge_{ij} \qquad \sigma_{ii} = 3K\varepsilon_{ii}, \tag{1}$$

with shear and bulk moduli G, K respectively to viscoelastic laws by adopting the differential operator concept or the hereditary integral concept [6]. More flexibility in fitting measured data in a large frequency range is obtained by replacing integer order time derivatives in differential operator formulations by fractional order time derivatives.

The derivative of fractional order α

$$\frac{d^{\alpha}\varepsilon(t)}{dt^{\alpha}} = \frac{1}{\Gamma(1-\alpha)} \frac{d}{dt} \int_0^t \frac{\varepsilon(t-\tau)}{\tau^{\alpha}} d\tau \qquad 0 \le \alpha < 1 \tag{2}$$

defined with the gamma function $\Gamma(1-\alpha) = \int_0^{\infty} e^{-x} x^{-\alpha} dx$ is the inverse operation of fractional integration attributed to Riemann and Liouville [17]. It can be shown that the definition by Grünwald [14]

$$\frac{d^{\alpha}\varepsilon(t)}{dt^{\alpha}} = \lim_{N \to \infty} \left\{ \left(\frac{t}{N}\right)^{-\alpha} \sum_{j=0}^{N-1} \frac{\Gamma(j-\alpha)}{\Gamma(-\alpha)\Gamma(j+1)} \quad \varepsilon\left[t\left(1-\frac{j}{N}\right)\right]\right\} \tag{3}$$

is equivalent and more convenient in constitutive equations treated by time–stepping algorithms. The generalized viscoelastic constitutive equations of differential operator type

$$\sum_{k=0}^{N} p'_k \frac{d^{\alpha_k}}{dt^{\alpha_k}} s_{ij} = \sum_{k=0}^{M} q'_k \frac{d^{\alpha_k}}{dt^{\alpha_k}} \epsilon_{ij}, \qquad \sum_{k=0}^{N} p''_k \frac{d^{\alpha_k}}{dt^{\alpha_k}} \sigma_{ii} = \sum_{k=0}^{M} q''_k \frac{d^{\alpha_k}}{dt^{\alpha_k}} \epsilon_{ii} \tag{4}$$

correspond to Hooke's law (1).

As defined by equation (2) the fractional derivative appears complicated in time domain. However both Laplace and Fourier transforms reveal the useful results

$$\mathcal{L}\{\frac{d^{\alpha}}{dt^{\alpha}}\varepsilon(t)\} = s^{\alpha}\mathcal{L}\{\varepsilon(t)\} = s^{\alpha}\bar{\varepsilon}(s), \qquad \mathcal{F}\{\frac{d^{\alpha}}{dt^{\alpha}}\varepsilon(t)\} = (i\omega)^{\alpha} \mathcal{F}\{\varepsilon(t)\}. \tag{5}$$

Laplace transformation converts equation (4) to

$$\mathcal{P}'(s)\bar{s}_{ij} = \mathcal{Q}'(s)\bar{e}_{ij}, \qquad \mathcal{P}''(s)\bar{\sigma}_{ii} = \mathcal{Q}''(s)\bar{\varepsilon}_{ii}, \tag{6}$$

with e.g. $\mathcal{P}' = \sum_{k=0}^{N} p'_k s^{\alpha_k}$.

According to the correspondence principle the elastic moduli have to be replaced by complex moduli in frequency domain ($s \to i\omega$), e.g. the deviatoric state in equation (1) leads to

$$\mathcal{F}\{s_{ij}\} = 2G^*(i\omega)\mathcal{F}\{e_{ij}\}. \tag{7}$$

The real part of the complex modulus $G^*(i\omega)$ is the storage modulus $G'(\omega)$, the imaginary part is the loss modulus $G''(\omega)$. They are related by the loss factor $\eta(\omega) = \frac{G''(\omega)}{G'(\omega)}$.

INTEGRAL EQUATION OF ELASTODYNAMICS

For consistency the boundary integral equation for elastodynamics in time domain is recalled. The field equations of a homogeneous elastic domain Ω with boundary Γ are given by

$$\left(c_1^2 - c_2^2\right) u_{i,ij} + c_2^2 \ u_{j,ii} + b_j = \ddot{u}_j \tag{8}$$

with displacement coordinates u_j and wave speeds

$$c_1^2 = \frac{K + \frac{4}{3}G}{\varrho}, \qquad c_2^2 = \frac{G}{\varrho} \tag{9}$$

with given boundary conditions

$$t_{(n)i}(\mathbf{x}, t) = \sigma_{ik} n_k = p_i(\mathbf{x}, t) \qquad \mathbf{x} \in \Gamma_t, \qquad u_i(\mathbf{x}, t) = q_i(\mathbf{x}, t) \qquad \mathbf{x} \in \Gamma_u \tag{10}$$

and initial conditions

$$u_i(\mathbf{x}, 0) = u_{0i}(\mathbf{x}), \qquad \dot{u}_i(\mathbf{x}, 0) = v_{0i}(\mathbf{x}) \qquad \mathbf{x} \in \Omega. \tag{11}$$

The 3-d Stokes fundamental solution of the Lamé equation (8) in an unbounded space, excited by $b_j(\mathbf{x}, t) = \delta(t - \tau) \delta(\mathbf{x} - \xi) e_j$ is given by (e.g. Eringen and Suhubi [4], Beskos [3])

$$\begin{aligned} \tilde{u}_{ij}(\mathbf{x}, t, \xi) = \ & \frac{1}{4\pi\varrho}\Big\{ \frac{t}{r^2} \left(\frac{3r_i r_j}{r^3} - \frac{\delta_{ij}}{r} \right) \left[H\left(t - \frac{r}{c_1}\right) - H\left(t - \frac{r}{c_2}\right) \right] \\ & + \frac{r_i r_j}{r^3} \left[\frac{1}{c_1^2} \ \delta\left(t - \frac{r}{c_1}\right) - \frac{1}{c_2^2} \ \delta\left(t - \frac{r}{c_2}\right) \right] + \frac{\delta_{ij}}{rc_2^2} \ \delta\left(t - \frac{r}{c_2}\right) \Big\} \end{aligned} \tag{12}$$

where $r = \sqrt{r_i r_i}$, $r_i = x_i - \xi_i$. The corresponding fundamental stress vector components are obtained from equation (10) after replacing the stresses by strains and displacements

$$\tilde{t}_{(n)ij} = \varrho\left(c_1^2 - 2c_2^2\right) \tilde{u}_{jm,m} \delta_{ik} n_k + \varrho c_2^2 \left(\tilde{u}_{ji,k} n_k + \tilde{u}_{jk,i} n_k\right) \tag{13}$$

with the outward normal n_k.

The dynamic extension of Betti's reciprocal work theorem combining two states of displacements and tractions $\left(\tilde{u}_{ij}, \tilde{t}_{(n)ij}\right)$ and $\left(u_{ij}, t_{(n)ij}\right)$ leads to the integral equation

$$\varepsilon_{ij}(\xi) u_j(\xi, t) = \int\limits_\Gamma \left[\tilde{u}_{ij} * t_{(n)j} - \tilde{t}_{(n)ij} * u_j \right] d\Gamma + \int\limits_\Omega \varrho \left[\tilde{u}_{ij} * b_j + \tilde{u}_{ij} v_{0j} + \dot{\tilde{u}}_{ij} u_{0j} \right] d\Omega \tag{14}$$

where $*$ denotes the convolution with respect to time and $\varepsilon_{ij}(\xi) = \frac{\delta_{ij}}{2}$ for a smooth boundary. Initial conditions being zero and vanishing volume forces reduce (14) to a boundary integral equation. The Laplace transform of the fundamental solution (12) yields

$$\begin{aligned} \tilde{u}_{ij}(\mathbf{x}, s, \xi) = \ & \frac{1}{4\pi\varrho}\Big\{ \frac{1}{r^2} \left(\frac{3r_i r_j}{r^3} - \frac{\delta_{ij}}{r} \right) \left[\frac{s\frac{r}{c_1} + 1}{s^2} \ e^{-\frac{r}{c_1}s} - \frac{s\frac{r}{c_2} + 1}{s^2} \ e^{-\frac{r}{c_2}s} \right] \\ & + \frac{r_i r_j}{r^3} \left[\frac{1}{c_1^2} \ e^{-\frac{r}{c_1}s} - \frac{1}{c_2^2} \ e^{-\frac{r}{c_2}s} \right] + \frac{\delta_{ij}}{rc_2^2} e^{-\frac{r}{c_2}s} \Big\}. \end{aligned} \tag{15}$$

The solution in frequency domain is gained by substituting $s \to i\omega$ in equation (15).

A NEW VISCOELASTIC FUNDAMENTAL SOLUTION IN TIME DOMAIN

The correspondence principle replaces the elastic moduli according to

$$3K \to \frac{\mathcal{Q}''(s)}{\mathcal{P}''(s)}, \qquad 2G \to \frac{\mathcal{Q}'(s)}{\mathcal{P}'(s)} \tag{16}$$

447

and leads to the wave speeds

$$c_{1v}^2 = \frac{1}{\varrho}\left[\frac{1}{3}\frac{\mathcal{Q}''(s)}{\mathcal{P}''(s)} + \frac{2}{3}\frac{\mathcal{Q}'(s)}{\mathcal{P}'(s)}\right], \qquad c_{2v}^2 = \frac{1}{\varrho}\frac{1}{3}\frac{\mathcal{Q}'(s)}{\mathcal{P}'(s)}, \tag{17}$$

for a viscoelastic domain. The rheological Maxwell model of a spring and dashpot in series with spring and damping coefficients $3K, F_K$ respectively corresponds to the constitutive equation (e.g. hydrostatic state)

$$\dot{\sigma}_{ii} + \gamma\sigma_{ii} = 3K\dot{\varepsilon}_{ii} \qquad \gamma = \frac{3K}{F_K}. \tag{18}$$

The correspondence (16) leads to

$$3K \to \frac{3Ks}{s+\gamma}, \qquad 2G \to \frac{2Gs}{s+\gamma} \qquad \gamma = \frac{3K}{F_K} = \frac{2G}{F_G}, \tag{19}$$

if it is assumed for simplicity, that the same damping mechanism holds for the deviatoric and the hydrostatic state. This assumption relates the viscoelastic wave speeds to the elastic ones according to

$$c_{1v}^2 = c_1^2\frac{s}{s+\gamma}, \qquad c_{2v}^2 = c_2^2\frac{s}{s+\gamma}. \tag{20}$$

The Laplace transformed viscoelastic fundamental solution is obtained by substituting the elastic wave speeds in (15) by the viscoelastic ones in (20).

A new fundamental solution has been calculated by inverse Laplace transformation. Details of the calculation, based on the theory of residues and integration along a modified Bromwich contour to assure a unique definition of complex roots, are omitted for the sake of brevity. The analytical solution is given by

$$
\tilde{u}_{ij}\left(\mathbf{x},t,\xi\right) = \frac{1}{4\pi\varrho}\left\{\frac{1}{r^2}\left(\frac{3r_ir_j}{r^3} - \frac{\delta_{ij}}{r}\right)\left[C_1\left(t\right) + \frac{r}{c_1}D_1\left(t\right) - \left(C_2\left(t\right) + \frac{r}{c_2}D_2\left(t\right)\right)\right]\right.
$$
$$
\left. + \frac{r_ir_j}{r^3}\left[\frac{1}{c_1^2}A_1\left(t\right) + \frac{\gamma}{c_1^2}B_1\left(t\right) - \left(\frac{1}{c_2^2}A_2\left(t\right) + \frac{\gamma}{c_2^2}B_2\left(t\right)\right)\right] + \frac{\delta_{ij}}{rc_2^2}\left(A_2\left(t\right) + \gamma B_2\left(t\right)\right)\right\} \tag{21}
$$

with the functions

$$
A_\beta(t) = \begin{cases} 0 & t < \frac{r}{c_\beta} \\ e^{-\frac{\gamma}{2}\frac{r}{c_\beta}}\delta\left(t - \frac{r}{c_\beta}\right) + \frac{\gamma}{2}\frac{r}{c_\beta}e^{-\frac{\gamma}{2}t}\dfrac{I_1\left(\frac{\gamma}{2}\sqrt{t^2 - \left(\frac{r}{c_\beta}\right)^2}\right)}{\sqrt{t^2 - \left(\frac{r}{c_\beta}\right)^2}} & t > \frac{r}{c_\beta} \end{cases}
$$

$$
B_\beta(t) = \begin{cases} 0 & t < \frac{r}{c_\beta} \\ e^{-\frac{\gamma}{2}\frac{r}{c_\beta}} + \frac{\gamma}{2}\frac{r}{c_\beta}\int\limits_{\frac{r}{c_\beta}}^{t} e^{-\frac{\gamma}{2}\tau}\dfrac{I_1\left(\frac{\gamma}{2}\sqrt{\tau^2 - \left(\frac{r}{c_\beta}\right)^2}\right)}{\sqrt{\tau^2 - \left(\frac{r}{c_\beta}\right)^2}}d\tau & t > \frac{r}{c_\beta} \end{cases}
$$

$$
C_\beta(t) = \begin{cases} 0 & t < \frac{r}{c_\beta} \\ e^{-\frac{\gamma}{2}\frac{r}{c_\beta}}\left(t - \frac{r}{c_\beta}\right) + \frac{\gamma}{2}\frac{r}{c_\beta}\int\limits_{\frac{r}{c_\beta}}^{t} e^{-\frac{\gamma}{2}\tau}\dfrac{I_1\left(\frac{\gamma}{2}\sqrt{\tau^2 - \left(\frac{r}{c_\beta}\right)^2}\right)}{\sqrt{\tau^2 - \left(\frac{r}{c_\beta}\right)^2}}\left(t - \tau\right)d\tau & t > \frac{r}{c_\beta} \end{cases}
$$

$$
D_\beta(t) = \begin{cases} 0 & t < \frac{r}{c_\beta} \\ I_0\left(\frac{\gamma}{2}\sqrt{t^2 - \left(\frac{r}{c_\beta}\right)^2}\right)e^{-\frac{\gamma}{2}t} + \gamma\int\limits_{\frac{r}{c_\beta}}^{t} e^{-\frac{\gamma}{2}\tau}I_0\left(\frac{\gamma}{2}\sqrt{\tau^2 - \left(\frac{r}{c_\beta}\right)^2}\right)d\tau & t > \frac{r}{c_\beta} \end{cases}
$$

where $\beta = 1, 2$ and I_n, $n = 0, 1$ denote the modified Bessel functions. Different viscoelastic constitutive equations, including those with fractional time derivatives, can be treated as well. In general this requires numerical integration of the inverse Laplace integral.

VISCOELASTIC FORMULATIONS OF BEM IN TIME DOMAIN

The integral equation (14) reduces to a boundary integral equation for vanishing volume forces b_j and initial conditions. Discretization in space and time leads to the boundary element formulation. Only the time discretization in n equal steps Δt is discussed. For simple constitutive equations the aim is to integrate the convolution terms analytically. Linear shape functions for the displacements u_i and constant shape functions for the tractions t_i in time domain

$$u_i(\mathbf{x}, \tau) = \left(U_{il}^{m-1} \frac{t_m - \tau}{\Delta t} + U_{il}^m \frac{\tau - t_{m-1}}{\Delta t} \right) \eta_l(\mathbf{x}) \tag{22}$$

$$t_i(\mathbf{x}, \tau) = 1 \cdot T_{il}^m \cdot \mu_l(\mathbf{x}) \tag{23}$$

are the simplest choice such that no terms drop out in the boundary integral equation. The actual time step is m; U_{il}^m, T_{il}^m are the modal values at time $t_m = m\Delta t$ for the corresponding boundary element Γ_l. Inserting (22,23) reduces the boundary integrals in (14) to

$$\int_0^t \int_\Gamma \left[t_{(\mathbf{n})i}(\mathbf{x}, \tau) \cdot \tilde{u}_{ij}(\mathbf{x}, \boldsymbol{\xi}, t - \tau) - \tilde{t}_{(\mathbf{n})ij}(\mathbf{x}, \boldsymbol{\xi}, t - \tau) \cdot u_i(\mathbf{x}, \tau) \right] d\Gamma d\tau =$$

$$\sum_l \sum_{m=1}^n \int_{\Gamma_l} \int_{t_{m-1}}^{t_m} \left[\tilde{u}_{ij}(\mathbf{x}, \boldsymbol{\xi}, t - \tau) \cdot 1 \cdot \mu(\mathbf{x}) \cdot T_{il}^m - \right.$$

$$\left. \tilde{t}_{(\mathbf{n})ij}(\mathbf{x}, \boldsymbol{\xi}, t - \tau) \cdot \eta_l(\mathbf{x}) \cdot \left(\frac{\tau}{\Delta t} \left(U_{il}^m - U_{il}^{m-1} \right) + U_{il}^{m-1} \frac{t_m}{\Delta t} - U_{il}^m \frac{t_{m-1}}{\Delta t} \right) \right] d\tau d\Gamma. \tag{24}$$

The associated time integrals

$$\int_{t_{m-1}}^{t_m} \tilde{u}_{ij}(\mathbf{x}, \boldsymbol{\xi}, t - \tau) \, d\tau, \qquad \int_{t_{m-1}}^{t_m} \tilde{t}_{(\mathbf{n})ij}(\mathbf{x}, \boldsymbol{\xi}, t - \tau) \tau d\tau, \qquad \int_{t_{m-1}}^{t_m} \tilde{t}_{(\mathbf{n})ij}(\mathbf{x}, \boldsymbol{\xi}, t - \tau) \, d\tau \tag{25}$$

can be integrated analytically for special constitutive equations. The traction integrals can be reduced to displacement integrals by the constitutive equation

$$\int_{t_{m-1}}^{t_m} \tilde{t}_{(\mathbf{n})ij}(\mathbf{x}, \boldsymbol{\xi}, t - \tau) \tau d\tau = \varrho \left(c_1^2 - 2c_2^2 \right) \int_{t_{m-1}}^{t_m} \tilde{u}_{mj,m}(\mathbf{x}, \boldsymbol{\xi}, t - \tau) \delta_{ik} n_k \tau d\tau +$$

$$c_2^2 \left(\int_{t_{m-1}}^{t_m} \tilde{u}_{ij,k}(\mathbf{x}, \boldsymbol{\xi}, t - \tau) n_k \tau d\tau + \int_{t_{m-1}}^{t_m} \tilde{u}_{kj,i}(\mathbf{x}, \boldsymbol{\xi}, t - \tau) n_k \tau d\tau \right). \tag{26}$$

According to the arrival times of the shear wave front $\frac{r}{c_2}$ and the compression wave front $\frac{r}{c_1}$ the time integration of the fundamental solution has to be carried out in intervals. With the abbreviations

$$f_0(r) = \frac{3r_{,i}r_{,k} - \delta_{ik}}{r^3}$$

$$f_1(r) = \frac{r_{,i}r_{,k}}{rc_1^2}$$

$$f_2(r) = \frac{\delta_{ik} - r_{,i}r_{,k}}{rc_2^2} \tag{27}$$

leads the first integral in (25) for example to

$$\int\limits_{t_{m-1}}^{t_m} \tilde{u}_{ij}(\mathbf{x},\boldsymbol{\xi},t-\tau)\,d\tau =$$

$$
\begin{cases}
0 & t-t_{m-1} < \frac{r}{c_1} < \frac{r}{c_2} \\[2mm]
\frac{1}{4\pi\varrho}\Big\{ f_0(r)\int\limits_{t_{m-1}}^{t-\frac{r}{c_1}}\Big[C_1(t-\tau)+\frac{r}{c_1}D_1(t-\tau)\Big]d\tau + \\[1mm]
\qquad f_1(r)\int\limits_{t_{m-1}}^{t-\frac{r}{c_1}}[A_1(t-\tau)+\gamma B_1(t-\tau)]d\tau\Big\} & t-t_m < \frac{r}{c_1} < t-t_{m-1} < \frac{r}{c_2} \\[2mm]
\frac{1}{4\pi\varrho}\Big\{ f_0(r)\int\limits_{t_{m-1}}^{t_m}\Big[C_1(t-\tau)+\frac{r}{c_1}D_1(t-\tau)\Big]d\tau + \\[1mm]
\qquad f_1(r)\int\limits_{t_{m-1}}^{t_m}[A_1(t-\tau)+\gamma B_1(t-\tau)]d\tau\Big\} & \frac{r}{c_1} < t-t_m,\, t-t_{m-1} < \frac{r}{c_2} \\[2mm]
\frac{1}{4\pi\varrho}\Big\{ f_0(r)\Big(\int\limits_{t_{m-1}}^{t_m}\Big[C_1(t-\tau)+\frac{r}{c_1}D_1(t-\tau)\Big]d\tau - \\[1mm]
\qquad \int\limits_{t_{m-1}}^{t-\frac{r}{c_2}}\Big[C_2(t-\tau)+\frac{r}{c_2}D_2(t-\tau)\Big]d\tau\Big) + \\[1mm]
\qquad f_1(r)\int\limits_{t_{m-1}}^{t_m}[A_1(t-\tau)+\gamma B_1(t-\tau)]d\tau \\[1mm]
\qquad + f_2(r)\int\limits_{t_{m-1}}^{t-\frac{r}{c_2}}[A_2(t-\tau)+\gamma B_2(t-\tau)]d\tau\Big\} & \frac{r}{c_1} < t-t_m < \frac{r}{c_2} < t-t_{m-1} \\[2mm]
\frac{1}{4\pi\varrho}\Big\{ f_0(r)\Big(\int\limits_{t_{m-1}}^{t_m}\Big[C_1(t-\tau)+\frac{r}{c_1}D_1(t-\tau)\Big]d\tau - \\[1mm]
\qquad \int\limits_{t_{m-1}}^{t_m}\Big[C_2(t-\tau)+\frac{r}{c_2}D_2(t-\tau)\Big]d\tau\Big) + \\[1mm]
\qquad f_1(r)\int\limits_{t_{m-1}}^{t_m}[A_1(t-\tau)+\gamma B_1(t-\tau)]d\tau + \\[1mm]
\qquad f_2(r)\int\limits_{t_{m-1}}^{t_m}[A_2(t-\tau)+\gamma B_2(t-\tau)]d\tau\Big\} & \frac{r}{c_1} < \frac{r}{c_2} < t-t_m.
\end{cases}
$$

$$(28)$$

After the time and space integration are finished, the solution of algebraic equations leads to the unknown displacement and traction boundary data for each time step [1].

## PROPAGATION OF STRUCTUREBORNE SOUND AT HALFSPACE SURFACE

Figure 1 indicates the surface discretization of a 3-d halfspace representing a subsoil. The loaded square base is of dimensions $|x| < a$, $|y| < a$. The discretization is extended in the x- and y-directions to calculate the wave propagation characteristics. The truncation of surface discretization has been studied by Klein [12]. For time harmonic excitation $F_x exp(i\omega t)$ of the base the orbits of the surface particle motion turn out to be ellipses. The path of particle motion is retrograd, which is opposite to water waves. The principle axes decrease with increasing distance from the loaded zone and change their directions. The BE results are plotted dimensionless $u_{zz} = \frac{u_z a G}{F_z}, u_{xz} = \frac{u_x a G}{F_z}$ for a frequency parameter $a_0 = \frac{\omega a}{\sqrt{G/\varrho}} = 2$. The calculated results underline the measured results by Barkan [2] shown on top of figure 1.

An impact load $F_z\delta(t)$ leads to a transient displacement response of the base plotted in figure 2 for the elastic and the viscoelastic halfspace. A conventional 3-parameter viscoelastic model was implemented and then the first derivatives with respect to time operating on the stress and the strain in the constitutive equation were generalized by fractional derivatives of order $\alpha = \beta = \frac{1}{2}$.

Figure 3 depicts the transient displacement response at three different locations. It is easily checked that the arrival time of the surface wave at $x = 3.5a$ is consistent with the arrival time of a Rayleigh surface wave.
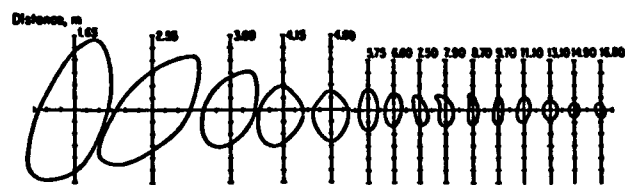
Measured (Barkan 1962)
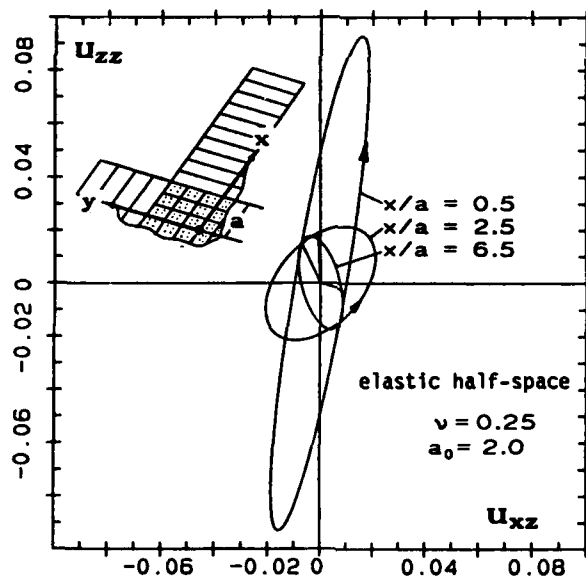
Calculated by BEM

Figure1: Orbits of motion of surface particles at varying distances from a square base with time harmonic vertical excitation
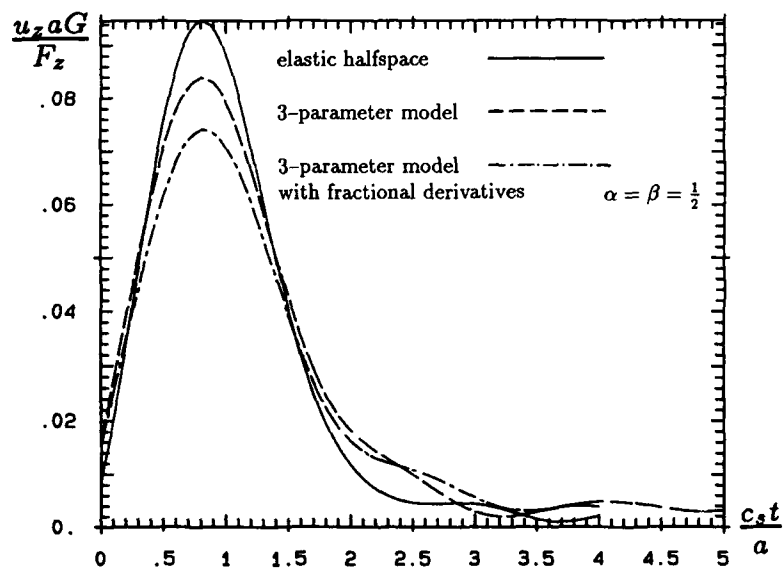
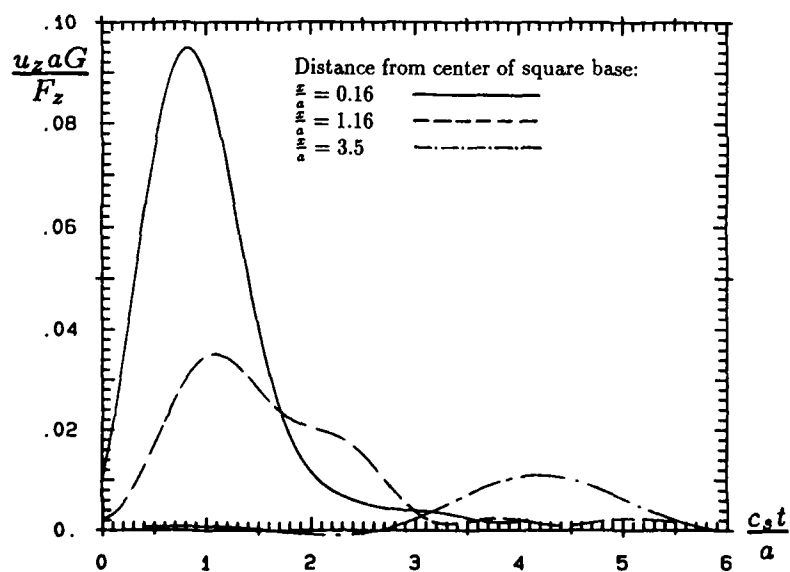Figure2: Impact response of elastic and viscoelastic halfspace

Figure3: Impact response of halfspace at 3 locations

*Figure4: Lab foundation and measuring setup for experimental static and dynamic SSI investigations*

EXPERIMENTAL INVESTIGATIONS OF SSI IN SMALL SCALE

Experimental investigations on soil–structure–interaction (SSI) are carried out at the Institute of Mechanics under the guidance of the first author. A schematic illustration and photo of the lab foundation consisting of a soil box which is equipped with conventional transducers and optoelectronic wave measurement facilities are shown in figure 4. An experimental program has been started to measure interaction phenomena as well as surface wave propagation for homogeneous and inhomogeneous soil [15, 9].

One or two rigid model footings or imbedded obstacles interact with a model halfspace consisting of homogeneous or layered sand mixed with gravel in a box. The sand is compressed in a spherical domain underneath the footings while the zone with loose sand proves to be an effective energy absorber in a suitable frequency domain. Deviations of the halfspace assumptions by trapping the energy in the finite box domain are analysed by BE calculations [12]. Static and dynamic footing tests are performed. The dynamic tests include transient vibrations excited by hammer impact or weight drop as well as forced vibrations by sine sweep and random excitation of vertical, horizontal, rocking and torsional modes of vibration. Lumped parameters of soil are evaluated from measured response impedances. Surface wave fields are detected by optoelectronic measurement.

EXPERIMENTAL STUDIES ON WAVE PROPAGATION BY OPTOELECTRONIC MEASURING

Optical methods play an important role in measurement technology since they are fast and operate without contact. The characteristic of the human eye in reading and converting optical information subjectively is balanced by adopting electrical and electronical receivers. All optoelectronic techniques share the use of light as sensitive transmitter and electronic signal processing. Because of the mentioned advantages and the progress in the development of electronic elements optoelectronic measuring techniques have a wide range of applications now. Even for the study of structureborne sound they open radically new possibilities for the contactless measurement of surface displacements and deformation of a specimen. A fibre optic vibrometer which works according to the basic principles of laser interferometry is able to measure the oscillating surface of an object pointwise [16]. Therefore it takes a long measuring time for a stationary wave field to detect the whole displacement field from multiple points. Wavefronts induced by impact excitation cannot be analysed by laser vibrometer with an acceptable amount of measurements.
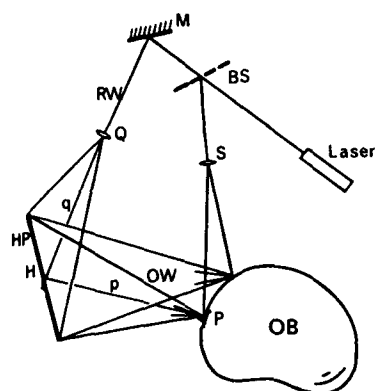
BS:	BEAMSPLITTER
M:	MIRROR
HP:	HOLOGRAM PLATE
OB:	OBJECT
Q,S:	EXPANDING OPTICS
RW:	REFERENCE WAVE
OW:	OBJECT WAVE

Figure5: Record of a hologram
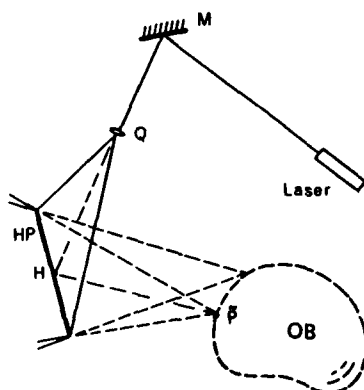
M:	MIRROR
HP:	HOLOGRAM PLATE
Q,S:	EXPANDING OPTICS
OB:	VIRTUAL OBJECT

Figure6: Reconstruction of a hologram

On the other hand holographic interferometry is able to detect the deformation state or oscillation state of 3-d objects. The basic principles of holography include the recording of an object by an interference pattern in adapted media, such as photographic plates, crystals etc. and reconstruction of an ideal virtual image of the object [20, 13]. It is, in essence, a combination of interferometry and diffraction and, as such,

requires coherent radiation for its applicability. Because of this requirement, holography became a viable imaging method only after lasers were widely available.

The basic principles of holograhic interferometry are briefly adressed first. A beam of light emitted by a laser is divided into two parts by a beamsplitter *BS* (figure 5 [19]). Each narrow ray bundle is then expanded by a lens respectively a system of lenses. The socalled 'reference wave *RW*' is directly guided onto a photographic plate of high resolution. The 'object wave *OW*' is reflected by the surface of an opaque object *Ob* and both waves interfere on the hologram plate in such a way that the variation of the relative phase from point to point is transformed into an interference pattern retaining the complete information of the object. The interference pattern is decoded by illuminating the hologram plate with reference–light and the virtual image of the object occurs. Applying holographic interferometry the photographic plate is exposed twice. During the brief intervall between exposures an object is subjected to a small change in position, e.g. two moments of a propagating wave, or a difference in shape caused by loadings. The deformation of the object measures a few μm. The reconstruction of the hologram by reference light shows both images of the object at the same time. These small deformations cannot be identified by human eye; but the object is covered with light and dark interference fringes (figure 6 [19]). These fringes are created by interference of the wave fronts of the two pictures. They represent contour lines of the deformations in the direction of the visual line of laser optics.

The deformation of the object between two light fringes is about one wave–length of the applied laser–light. Thus different deformation states are visuable by holographic interferometry and can be analysed exactly [5]. It is shown in the present paper that pulse laser holographic interferometry allows to detect imbedded obstacles and excavations in soil as follows. In an excited soil waves propagate from the source into the soil domain and at its surface. The wave field is composed of two bodywaves, the compression or P–wave and the shear or S–wave, and the socalled Rayleigh surface wave. In undisturbed soil there is a circular front of the Rayleigh wave emanating from the excitation source . If there are inhomogeneities in soil, the concentric waves are deranged, e.g. due to the boundary of obstacles. These effects can be visualized at the soil surface by holographic interferometry.

A schematic of the experimental configuration installed at the Institute of Mechanics is shown in figure 7. In a proper arrangement the double–pulsed ruby laser with 1J output energy is sufficient to
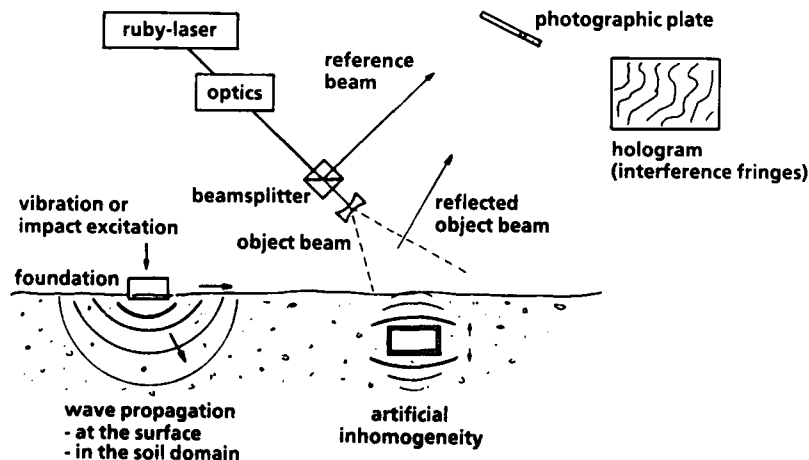
Figure 7: Application of holographic interferometry to detect wave propagation phenomena

illuminate approximately six squaremeters of the surface of the sand box. The laser beam is guided parallel by optical components before being splitted by a wedge–shaped glass into two parts according to the ratio of 96% to 4%. A dielectric mirror leads the high energy object beam to the expanding optics above the sand box. The low energy reference beam is reflected by mirrors several times in order to maintain the coherence of the laser light by optical distance compensation. After expanding it interferes with the reflected object beam on a photographic plate. All the optics and the lasers are mounted on a vibration
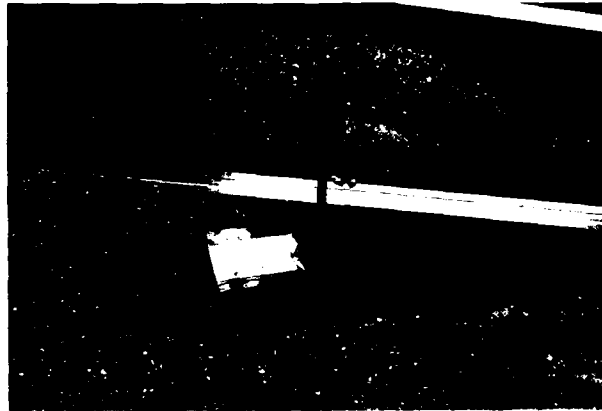
Figure8: Placing of a hollow box for simulation of soil inhomogeneity

isolated platform. A stationary wave field is generated by time harmonic excitation of a surface foundation on soil by electrodynamic shaker. An impact excitation by hammer blow generates shock-waves in the soil. Investigations were carried out with several obstacles, namely hollow boxes welded from metal sheets. They were buried in homogeneous soil and covered with a layer of up to 100 mm thickness (figure 8).

One portion of the waves propagating in soil are reflected by the obstacles and the other part is refracted. If the test parameters are chosen specifically, the buried obstacles act as wave sources themselves [11]. Thus pertubations of the wave field are generated which can be visualized by holographic interferometry.

Figure 9 depicts the interferogram of the imbedded box of rectangular shape for an exciting frequency of 500 Hz. The straight front end is clearly indicated by the straight interference fringes. Light points mark the corners of the box. The shape of the artificial inhomogeneity can be detected from the oscillation of the cover plate easily.

Figure9: Interference pattern of surface wave propagation (quadrangular box with straight front end harmonically excited at frequency of 500 Hz)

Further test series record transient wave fields on holograms. The impact excitation was generated by hammer blow or dropping of a steel ball. The wave fronts at different distances from the source can be detected by variation of the time intervalls between the laser pulses. Even in the case of impact excitation the artificial inhomogeneities can be identified by the deformation of the shock wave front clearly (figure 10). In the period of time between the two laser exposures the wave propagates a longer distance in the

Figure 10: Interference pattern of surface wave propagation (quadrangular box with circular front end, soil excitation by hammer blow)

steel skin of the box than in the surrounding soil. The circular shock wave front is disturbed by the differing wave velocities in sand and metal. This effect becomes visible in an interferogram.

SUMMARY

An improved approach has been presented for calculating the propagation of structureborne sound by BEM in time domain. In addition to the socalled geometrical damping by energy radiation the material damping is described by viscoelastic constitutive equations. Conventional viscoelastic laws and those generalized with fractional derivatives are taken into account.

One aim of the ongoing research is to validate calculated transient wave fields by optoelectronic measurement. Holographic interferometry proved to be an efficient method for interpreting wave fields. The paper at hand presents a successful application for waves on soil surfaces. Further effort has to be put in electronic analysing of holographic interferograms, e. g. by fully automatic image processing [18].

Both, numerical simulations and promising results of experimental investigation provide a good understanding of structureborne sound propagation.

REFERENCES

[1] Antes, H.; Steinfeld, B.: Das Schwingungsverhalten von Bauwerken bei Berücksichtigung von Kopplungen mit der Umgebung. Forschungsbericht, SFB 151 Ruhr–Universität Bochum, 1989/91.

[2] Barkan, D. D.: *Dynamics of Bases and Foundations, translated from the Russian by L. Draskovska, Tschebotarioff, G. P.* Mc Graw–Hill Book Company, New York, 1962.

[3] Beskos, D. E.: Boundary element methods in dynamic analysis. *Appl. Mech. Rev.*, 40:1–23, 1987.

[4] Eringen, A. C.; Suhubi, E. S.: *Elastodynamics*, Vol. II. Acadamic Press, New York, San Francisco, London, 1975.

[5] Ettemeyer, A.: *Ein neues holographisches Verfahren zur Verformungs- und Dehnungsbestimmung.* PhD thesis, Universität Stuttgart, 1988.

[6] Flügge, W.: *Viscoelasticity.* Springer–Verlag, New York, Heidelberg, Berlin, 1975.

[7] Gaul, L.: Calculation of Structurebourne Sound by Boundary Elements and Related Experiments. In *Proc. Int. Congress on Recent Developments in Air- and Structure Bourne Sound and Vibrations,* Auburn University, Vol. I, 445–454, 1990.

[8] Gaul, L.; Klein, P.; Plenge, M.: Simulations of Wave Propagation in Irregular Soil Domains by BEM and Associated Small Scale Experiments. *Int. Journal Engineering Analysis with Boundary Elements*, 8, No. 4:200–205, 1991.

[9] Gaul, L.; Plenge, M.: Randelementberechnungen und optoelectronische Messung der Oberflächenwellenfelder des inhomogenen Baugrunds. *Bauingenieur 66*, 61–68, 1991.

[10] Gaul, L.; Schanz, M.; Fiedler, C.: Viscoelastic Formulations of BEM in Time and Frequency Domain. In *Proc. Int. Conf. on Comp. Engg. Science*, Melbourne, Australia, ICES Publ., 304–310, 1991.

[11] Haupt, W.: Verhalten von Oberflächenwellen im inhomogenen Halbraum mit besonderer Berücksichtigung der Wellenabschirmung. Veröff. des Inst. f. Bodenmechanik und Felsmechanik i4, Universität Fridericiana, Karlsruhe, 1978.

[12] Klein, P.: Zur Beschreibung der dynamischen Wechselwirkung von Fundamentstrukturen mit dem viskoelastischen Baugrund durch dreidimensionale Randelementformulierungen. Bericht aus dem Institut für Mechanik, Universität der Bundeswehr Hamburg, Jan. 1990.

[13] Obermeier, E.; Schörner, J.; Rottenkolber, H.: Methoden der holographischen Interferometrie und ihre Anwendung in der Industrie. *Opto–Elektronik Magazin*, 5, Nr. 2:148–152, 1989.

[14] Oldham, K. B.; Spanier, J.: *The Fractional Calculus*. Academic Press, New York, London, 1974.

[15] Plenge, M.: *Ein Beitrag zur Untersuchung des dynamischen Verhaltens geschichteter Baugründe*. PhD thesis, Institut für Mechanik, Universität der Bundeswehr Hamburg, 1990.

[16] Plenge, M.: Erfassung der Erschütterungsausbreitung im Boden mit Hilfe optoelektronischer Meßverfahren. In Knoll, P.; Werner, D.: , Herausgeber, *Vortragsband des Kolloquiums "Erdbebeningenieurwesen und Baudynamik"*, Potsdam, DGEB-Publ. Nr. 5, 277–293, 1991.

[17] Ross, B.: Fractional Calculus. *Mathematics Magazine*, 50, 1977.

[18] Schörner, J.; Ettemeyer, A.; Neupert, U.; Rottenkolber, H.; Winter, C.; Obermeier, E.: Neue Wege in der holographischen Bildauswertung. *VDI–Berichte 731,Experimentelle Mechanik in Forschung und Praxis*, 135–144, 1989.

[19] Schumann, W.; Zürcher, J.-P.; Cuche, D.: *Holography and Deformation Analysis*. Springer–Verlag, Berlin, 1985.

[20] Wernicke, G.; Osten, W.: *Holographische Interferometrie*. Physik–Verlag, Weinheim, 1982.

SOUND-STRUCTURE INTERACTION AND TRANSMISSION OF SOUND AND VIBRATION
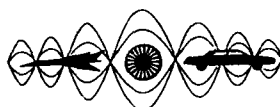
SECOND INTERNATIONAL CONGRESS ON
RECENT DEVELOPMENTS IN AIR- AND
STRUCTURE-BORNE SOUND AND VIBRATION

MARCH 4-6, 1992   AUBURN UNIVERSITY, USA

PLATE CHARACTERISTIC FUNCTIONS TO STUDY SOUND TRANSMISSION LOSS THROUGH PANELS

R.B. Bhat and G. Mundkur
Department of Mechanical Engineering
Concordia University
Montreal, Quebec H3G 1M8
Canada

ABSTRACT

Sound transmission loss through rectangular panels mounted on a rigid infinite baffle is studied using plate characteristic functions. Plate Characteristic Functions are determined by iteratively reducing the plate partial differential equation and obtaining an exact solution to the reduced equation. The plate partial differential equation is reduced by assuming an approximate solution satisfying the boundary conditions along one direction of the rectangular panel, substituting this into the differential equation and employing Galerkin's averaging technique. The Plate Characteristic Functions are used in describing the response of the panel. Normal mode analysis is employed to obtain the sound transmission loss through the panel, which is excited by a uniformly distributed harmonic pressure loading on one side. The results are compared with those obtained by analysing the problem using the frequencies and mode shapes from Rayleigh-Ritz method, in which the assumed shape functions are the beam characteristic functions and the beam characteristic orthogonal polynomials. Results obtained using the Plate Characteristic Functions are found to be quite superior and take considerably less time compared to those by the other two methods.

INTRODUCTION

There are several industrial situations where it is necessary to be able to predict the sound transmission loss properties of panels. Since the sound pressure acting on one side of the panel sets it into vibrations and the sound transmitted through depends on the vibration response of the panel, it is very essential that the response of the panel is analyzed accurately. There are several methods available to estimate the vibration response of panels such as finite element method followed by normal mode analysis [1], Rayleigh-Ritz method followed by normal mode analysis [2], or direct numerical integration methods [3].

Some form of approximation is involved in all of the above methods. To cover a certain frequency range, it is necessary to consider a large number of degrees of freedom in finite element method, or a large number of terms in Rayleigh-Ritz method such that only the lower natural frequencies computed by these methods cover the required range. This is because the higher natural frequencies and modes computed by these methods are not accurate. A small error in the natural frequency and mode shape will significantly affect the computed response [2].

461

Sound transmission loss through panels and curved plates was studied by Otsuru et al. [4] using finite element methods. In the present paper, sound transmission loss through rectangular panels mounted on rigid infinite baffle is studied employing plate characteristic functions. The plate characteristic functions are determined by exactly solving the reduced plate partial differential equation. Reduction of the partial differential equation is carried out by assuming an approximate solution satisfying the boundary conditions along one direction of the rectangular panel, substituting this into the differential equation and employing Galerkin's averaging technique. Plate characteristic functions are also the normal modes of the plate and the response of the plate to a harmonic pressure loading and the subsequent sound transmission loss are determined using normal mode analysis.

ANALYSIS

Equation of motion for plate is obtained from the minimum of the integral

$$I = \int\int_A \left\{ (\Delta w)^2 - 2(1-v)\left[\frac{\partial^2 w}{\partial\xi^2}\frac{\partial^2 w}{\partial\eta^2} - (\frac{\partial^2 w}{\partial\xi\partial\eta})^2\right] + \frac{m}{D}(\frac{dw}{dt})^2 \right\} d\xi d\eta$$

$$- 2\int_\Gamma V(s)w\,ds + 2\int_\Gamma M(s)\frac{\partial w}{\partial n}\,ds \qquad (1)$$

where $\Delta = \dfrac{\partial^2}{\partial\xi^2} + \dfrac{\partial^2}{\partial\eta^2}$, and $D = \dfrac{Eh^3}{12(1-v^2)}$

is the plate flexural rigidity, E is the modulus of elasticity, m is the mass per unit area of the plate, v is the Poisson's ratio, w is the plate deflection, and ξ and η are the Cartesian coordinates. The double integral is over the area of the plate whereas the line integral is along the boundaries of the plate, where s is along the boundary and n is a direction normal to the boundary. The necessary condition for the minimum of the integral I is obtained by considering a small variation in the deflection w as w + gϵ and then the derivative with respect to g is equated to zero. This results in [5]

$$\int\int_A \left(\Delta\Delta w + \frac{m}{D}\frac{\partial^2 w}{\partial t^2}\right)\epsilon d\xi d\eta + \int_\Gamma M(s)\frac{\partial\epsilon}{\partial n}\,ds - \int_\Gamma V(s)\epsilon ds = 0 \qquad (2)$$

where

$$\Delta\Delta w = \frac{\partial^4 w}{\partial\xi^4} + 2\frac{\partial^4 w}{\partial\xi^2\partial\eta^2} + \frac{\partial^4 w}{\partial\eta^4}.$$

When the plate is rectangular and the boundaries are parallel to the coordinate axes, the moment and shear force distribution along boundaries are given by

$$M(\xi) = \left\{ \frac{\partial^2 w}{\partial \xi^2} + v \frac{\partial^2 w}{\partial \eta^2} \right\}_{\text{at } \xi = 0,a}$$

$$V(\xi) = \left\{ \frac{\partial^3 w}{\partial \xi^3} + (2-v) \frac{\partial^3 w}{\partial \xi \partial \eta^2} \right\}_{\text{at } \xi = 0,a} \qquad (3)$$

Similar expressions describe the moments and shear forces along $\eta = 0$ and b also. For free harmonic vibration, the solution is assumed in the separable form

$$w(x,y) = X(x)Y(y)e^{i\omega t} \qquad (4)$$

where $x = \xi/a$ and $y = \eta/b$.

In order to reduce the partial equation to an ordinary differential equation, initially the deflection shape along one direction, say y direction, is assumed, satisfying all the boundary conditions along y. In the present analysis, beam characteristic functions are employed. Substituting Y(y) into Eq. (2), resulting differential equation in x direction is given by

$$\frac{ab}{a^4} \int_0^1 \int_0^1 \left[X''''Y + 2\alpha^2 X''\ddot{Y} + \alpha^4 X\ddddot{Y} - \frac{\omega^2 m XY}{D} \right] Y \delta X dx dy$$

$$+ \frac{ab}{a^4} \int_0^1 [\alpha^4 X\ddot{Y} + v\alpha^2 X''Y]\dot{Y}\delta X dx$$

$$- \frac{ab}{a^4} \int_0^1 [\alpha^4 X\ddot{Y} + (2-v)\alpha^2 X''\dot{Y}] Y\delta X dx = 0 \qquad (5)$$

where $\varepsilon = \delta w = Y\delta X + X\delta Y$. Since Y is assumed a priori, $\delta Y = 0$. Hence, $\varepsilon = \delta w = Y\delta X$ and $\frac{\partial \varepsilon}{\partial y} = \delta\dot{w} = \dot{Y}\delta X$. Further, $(\ )' = \frac{\partial}{\partial x}$ and $(\dot{\ }) = \frac{\partial}{\partial y}$. $\alpha = a/b$ is the plate aspect ratio where a and b are the side lengths of the plate along ξ and η directions respectively. After performing the integration, the ordinary differential equation in the x direction is obtained as

$$X'''' + 2\alpha^2[B - (1-v)(G_0 + G_1)]X'' + \alpha^4 \left[C - \frac{\Omega^2}{\alpha^4} + H_0 + H_1 - J_0 - J_1 \right] X = 0$$

with $A = \int_0^1 Y^2 dy$, $B = \frac{1}{A}\int_0^1 Y\ddot{Y}dy$, $C = \frac{1}{A}\int_0^1 Y\ddddot{Y}dy$, $G_0 = \frac{1}{A}(Y\dot{Y})_{y=0}$, $G_1 = \frac{1}{A}(Y\dot{Y})_{y=1}$,

$H_0 = \frac{1}{A}(Y\dddot{Y})_{y=0}$, $H_1 = \frac{1}{A}(Y\dddot{Y})_{y=1}$, $J_0 = \frac{1}{A}(\dot{Y}\ddot{Y})_{y=0}$, $J_1 = \frac{1}{A}(\dot{Y}\ddot{Y})_{y=1}$, and

$$\Omega^2 = \frac{\omega^2 m a^4}{D} \tag{6}$$

Equation 6 can be put in the form

$$X'''' + 2\beta X'' + \gamma X = 0 \tag{7}$$

where

$$\beta = \alpha^2 [B - (1 - \nu)(G_0 + G_1)]$$

$$\gamma = \alpha^4 \left[C - \frac{\Omega^2}{\alpha^4} + H_0 + H_1 - J_0 - J_1 \right].$$

Assuming $X = X_0 e^{\lambda x}$ as the solution of Eq. (7) results in

$$\lambda^4 + 2\beta\lambda^2 + \gamma = 0 \tag{8}$$

The roots are given by

$$\lambda_{1,2}^2 = -\beta \pm (\beta^2 - \gamma)^{1/2} \tag{9}$$

Further, the solution of Eq. (7) can be written as

$$X(x) = C_1 \sin p_1 x + C_2 \cos p_1 x + C_3 \sinh p_2 x + C_4 \cosh p_2 x \tag{10}$$

where p_1 and p_2 are defined as

$$p_{1,2} = \pm [\pm \beta + (\beta^2 - \gamma)^{1/2}]^{1/2} \tag{11}$$

Substituting the boundary conditions $X(x) = X'(x) = 0$, at $x = 0$ and a, into the solution in x direction given by Eq. (10), it is possible to obtain a frequency equation. Solving this equation for the appropriate root, the corresponding deflection shape along x direction can be determined. The shape function $X(x)$ determined this way is substituted now into Eq. (2) and following a similar procedure as before the partial differential equation can be reduced to an ordinary differential equation in the y direction. Solution of this equation will be of the form

$$y(y) = C_1^* \sin q_1 y + C_2^* \cos q_1 y + C_3^* \sinh q_2 y + C_4^* \cosh q_2 y \tag{12}$$

where q_1 and q_2 are given by

$$q_{1,2} = \pm [\pm \beta^* + (\beta^{*2} - \gamma^*)^{1/2}]^{1/2} \tag{13}$$

Substituting corresponding boundary conditions in Eqs. (10) and (12), two frequency equations are obtained consisting of infinite number of roots for Ω. By assuming the beam function, say $Y(y)$ corresponding to first beam mode, the first root in x direction corresponds to

464

$\Omega_{(1,1)}$. By using the resulting function X(x), the first root of the frequency equation in y direction is found which will be an improvement over the previous value of $\Omega_{(1,1)}$. The resulting functions on both x and y directions are first approximations to plate characteristic functions. Successive iterations along alternate directions is carried out until convergence for first root, to obtain the first natural frequency $\Omega_{(1,1)}$ and the corresponding plate characteristic functions. Using similar procedure for first root in y direction and second root in x direction will give natural frequency $\Omega_{(2,1)}$. Continuing in this manner for all the roots will yield frequencies $\Omega_{(1,1)}, \Omega_{(2,1)}, \dots, \Omega_{(i,1)}$. When the same process is used with second root in y direction and 1, 2, 3, ... in x direction will result in $\Omega_{(i,2)}$ (i = 1, 2, ...). Likewise, taking subsequent roots in y direction and 1, 2, 3, ... in x direction will give all the roots $\Omega_{i,j}$ (i = 1, 2, ..., and j = 1, 2, ...). In this way, it is possible to get the plate natural frequencies and the corresponding plate characteristic functions which are also the plate normal modes.

SOUND TRANSMISSION LOSS

The panel is mounted on a rigid infinite baffle and it is assumed that uniform harmonic pressure loading of the type

$$p(x,y,t) = \bar{p} \sin wt \qquad (14)$$

is exciting the panel on one side. The transformed equation of plate motion can be written as

$$D\nabla^4 \bar{w} - m\omega^2 \bar{w} = \bar{p}(w) - p_0(x,y,\omega) \qquad (15)$$

where $p_0(x,y,\omega)$ is the transmitted sound pressure acting on the panel. The plate response is assumed in terms of the normal modes as

$$\bar{w} = \sum_r \sum_s q_{rs} \phi_{rs}(x,y) \qquad (16)$$

where $\phi_{rs}(x,y) = X_r(x) \cdot Y_s(y)$ are the panel modes obtained as the product of plate characteristic functions. Expressing the pressure loading also in terms of the panel modes and following normal mode analysis we get

$$\bar{w}(x,y,\omega) = \sum_r \sum_s \frac{\bar{p}_{rs}(\omega)}{m(\omega_{rs}^2 - \omega^2 + 2i\bar{\xi}_{rs}\omega_{rs}\omega)} \qquad (17)$$

where

$$\bar{p}_{rs}(\omega) = \frac{\bar{p}(\omega) \iint \phi_{rs}(x,y)dxdy}{\iint \phi_{rs}^2(x,y)dxdy} \qquad (18)$$

and ω_{rs} are the panel natural frequencies. The equivalent viscous damping ratio is given as

$$\bar{\xi}_{rs} = \xi_{rs} + \frac{1}{2\rho c\omega_{rs}} \qquad (19)$$

465

where ξ_{rs} is the damping in the panel and the second term on the right hand side is the radiation damping, with ρ as the density of air and c as velocity of sound in air. The transmitted pressure is given by

$$p_0(x,y,\omega) = i\omega\rho c\, \overline{w}(x,y,\omega) \tag{20}$$

The sound transmission loss is expressed as

$$TL = 10 \log_{10}(R) \tag{21}$$

where

$$R = \frac{\iint |p_0|^2 dxdy}{\iint \overline{p}^2} \tag{22}$$

RESULTS AND DISCUSSION

_Sound transmission loss obtained from Eq. (21) is plotted against frequency in Figs. 1, 2 and 3 for ξ_{mn} = 0.01, 0.1 and 1. Results obtained using plate characteristic functions are compared with those obtained using frequencies and mode shapes from Rayleigh-Ritz method i) with beam characteristic functions [6] and ii) with beam characteristic orthogonal polynomials [7] as assumed shape functions. Nine modes are used in each of the three methods. Since the pressure loading is uniform, only modes with odd numbers of half waves (11, 13, 31, 33 only) in each direction respond as can be seen from the figures. The response at modes 11 and 33 are almost the same in all three methods except for the fact that the one by orthogonal polynomial gives a slightly higher value for the natural frequency of 33 mode. The response for 13 and 31 mode shows some difference, approximately 4-5 dB. The significant advantage of the present method is the enormous saving in computational time for the response.

CONCLUSIONS

Sound transmission loss through rectangular panels are obtained using the plate characteristic functions. The results are compared with those obtained by using modes and natural frequencies from Rayleigh-Ritz method. It is concluded that the present method gives results of comparable accuracy with considerable saving in computational time.

ACKNOWLEDGEMENTS

REFERENCES

1. Bathe K., "Finite Element Procedures in Engineering Analysis", Prentice Hall Inc., Englewood Cliffs, N.J., 1982.
2. Warburton G.B., "Response Using the Rayleigh-Ritz Method", Journal of Sound and Vibration, Vol. 7, 1979, pp. 327-334.
3. Goudreau G.L. and Taylor R.L., "Evaluation of Numerical Integration Methods in Elastodynamics", Journal of Computer Methods in Applied Mechanics and Engineering, Vol. 2, No. 1, 1973, pp. 69-97.
4. Otsuru T., Yamamoto H. and Yanajita H., "Sound Transmission Analysis by Computational Mechanics on Cylindrical Curved Plates", Proceedings of Inter-noise, 1988, pp. 351-354.

5. Kantorovich L.V. and Krylov V.I., "Approximate Methods of Higher Analysis", P. Nordhoff Ltd., Groningen, Netherlands.
6. Young D. and Felgar Jr., R.P., "Tables of Characteristic Functions Representing Normal Modes of Vibration of a Beam", University of Texas Publication, 1949.
7. Bhat R.B., "Natural Frequencies of Rectangular Plates Using Characteristic Orthogonal Polynomials in Rayleigh-Ritz Method", Journal of Sound and Vibration, Vol. 102, 1985, pp. 493-499.
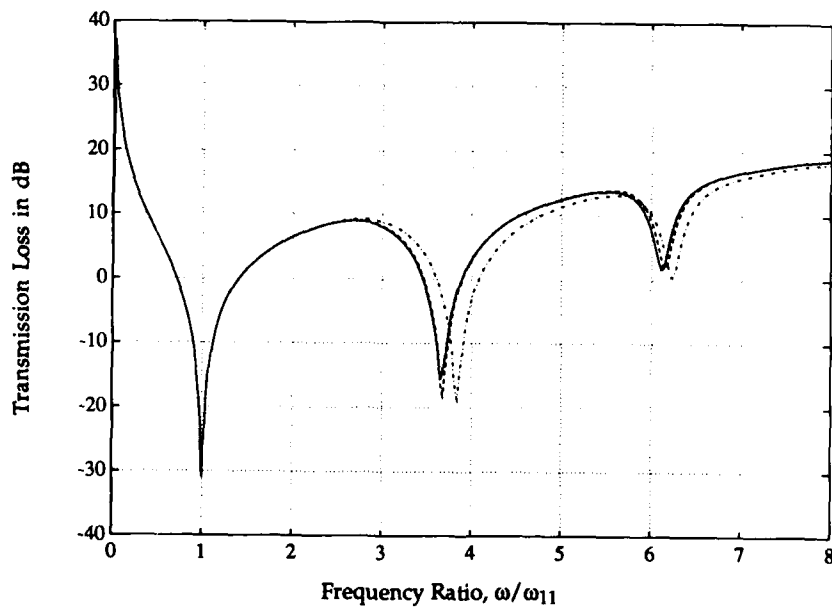
Figure 1 -- Sound transmission loss in a rectangular panel [ξ_{mn} = 0.01 in all modes, i) _____ plate characteristic functions, ii) - - - - - - - beam chartacteristic functions, iii) - - - - - - - - - - - - beam characteristic orthogonal polynomials]
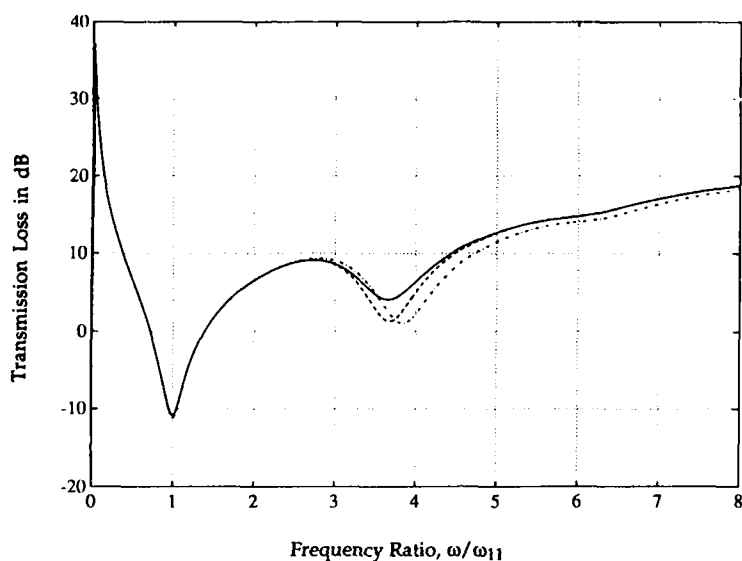
Figure 2 -- Sound transmission loss in a rectangular panel [ξ_{mn} = 0.1 in all modes, i) _____ plate characteristic functions, ii) - - - - - - beam characteristic functions, iii) -------------- beam characteristic orthogonal polynomials]
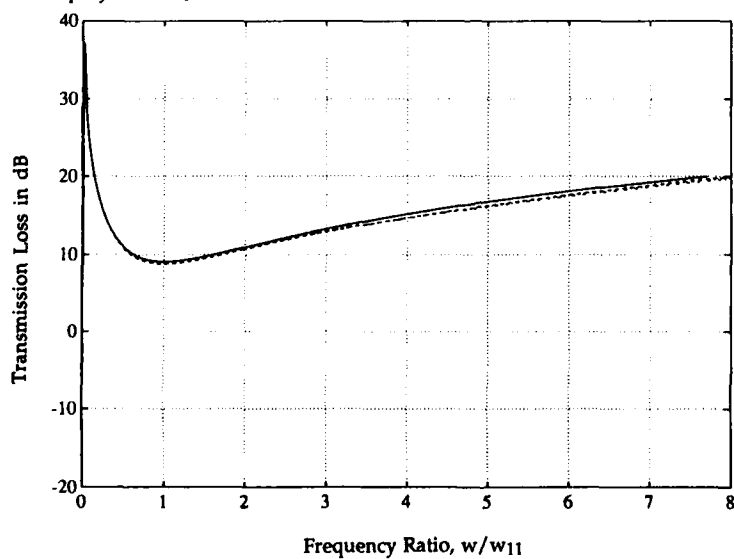
Figure 3 -- Sound transmission loss in a rectangular panel [ξ_{mn} = 0.1 in all modes, i) _____ plate characteristic functions, ii) - - - - - - beam characteristic functions, iii) --------------beam characteristic orthogonal polynomials]

SECOND INTERNATIONAL CONGRESS ON
RECENT DEVELOPMENTS IN AIR- AND
STRUCTURE-BORNE SOUND AND VIBRATION
MARCH 4-6, 1992 AUBURN UNIVERSITY, USA

SOUND TRANSMISSION LOSS OF WALLBOARD PARTITIONS

Junichi Yoshimura
Kobayasi Institute of Physical Research
3-20-41 Higashimotomachi Kokubunji
Tokyo 185 Japan

ABSTRACT

In order to study the performance of wallboard partitions in sound transmission loss (STL), the dependency of sound reduction properties on the physical parameters of wall structures was investigated. It is shown that the mass-air-mass resonance frequency (fr) has a close relation to STL of wallboard partitions and that fr shall be kept as low as possible in order to get high STL performance. It is also found that, as a result of the examination of the normalized STL according to the wallboard conditions (the type of studding and the cavity absorption), the absorptive performance of wallboard partitions becomes greater in proportion to the independency of the leaves composing the partition. The result suggests that we should select some suitable wallboard structure to meet the requirement of STL performance under the designated conditions.

INTRODUCTION

In Japan, there is an increasing demand for better sound insulation in apartment or hotel buildings. It is also required by the National Building Code that the wall structure between dwellings in an apartment building shall satisfy certain requiement on the sound transmission loss (STL) and the fire resistance. It is, however, desirable to lighten the weight of wall partitions for lessening the load of the building structure according to the increase in height of buildings. So, various kinds of wall structures using wallboards are now being developed. Wall structures between dwellings in a building are generally constructed with double-leaf partitions. Then the STL performance of double-leaf wall partitions is investigated in the following, in which STL will be, at first, discussed with relation to several physical parameters of the structures, e.g. the mass per unit area and the total thickness of the double-leaf partition, the type of studding, the number of layers composing a leaf and whether the cavity is filled with absorptive materials or not, and in the second, the procedure of wallboard attachment and the influence of coincidence dip of wallboard materials will be examined in relation to normalized frequency characteristics of STL.

The data for analyses were selected from the handbook in which STL data of wall structures had been certificated by the Japanese Government under the following conditions;

the wall structure; a double-leaf partition using thin wallboards,
the mass per unit area of the double-leaf partition; 20 - 100 kg/m²,
the total thickness of the double-leaf partition; 75 - 180 mm.

The materials of wallboards are gypsum boards (density $\rho = 0.75 - 1.0$ g/cm³), autoclaved asbestos cement silicate boards ($\rho = 0.75 - 0.8$ g/cm³), fire-resistant gypsum boards ($\rho = 0.75 - 0.8$ g/cm³), fiber reinforced gypsum sheets ($\rho = 1.4 - 1.6$ g/cm³) or asbestos cement sheets ($\rho = 1.5 - 1.7$ g/cm³).

The STL of the analyzed wall structures were independently measured by several laboratories according to the Japanese Industrial Standard (JIS A 1416); 'Method for laboratory measurement of sound transmission loss'. The handbook does not include wall structures whose STL is less than D-40 (D-value means the Japanese Standard Classification for STL). Then several tens data of simple wallboard structures were added in the analyses, and the total number of the analyzed data were 208. In the following we use the Sound Transmission Class (STC)[1] to evaluate STL performance, because the Japanese Standard classification D-value is not familiar outside Japan. Note that, as D-value is determined by the peak fitting method, it is usually lower than STC, especially for wallboard partitions in the lowest frequency region and in the coincidence frequency region.

RELATIONSHIP BETWEEN STL PERFORMANCES AND PHYSICAL PARAMETERS

The mass-air-mass resonance frequency fr of a double-leaf partition is given by the following equation[2];

$$fr=60/(m*d)^{0.5} \qquad\qquad (1)$$

where d is the width of the air space and m is the mass per unit area of each leaf of the wallboard partition. If we take the logarithm of Eq.(1), the relation among fr, m and d becomes linear. If this relation holds irrespective of the wallboard attachment procedure, it is expected to be able to analyse the STL data through a single variable, i.e. the resonance frequency fr.

Figure 1 shows a scatter diagram between fr and m in log-log scale. In the figure the data points were differently symbolized not only according to filled or not filled with absorptive materials, but also according to the type of studding, i.e.

common studding; wallboards are directly attached to common timber or metal studs,
elastic studding; wallboards are attached to the studs using resilient clips or
resilient metal channels and flexible studs,
staggered studding; wallboards are attached to the staggered studs or are
constructed as studless partitions.

As can be seen from the figure, the relationship between fr and m is relatively linear (correlation coefficient Cc=-0.802). Next, the relation of fr to d was examined, but the results scattered widely (Cc=-0.311). Using the total thickness of the double-leaf partition instead of d, the relation became better (see Fig.2). The correlation coefficient Cc was -0.826. Note that, in this case, the total thickness was plotted with linear scale.
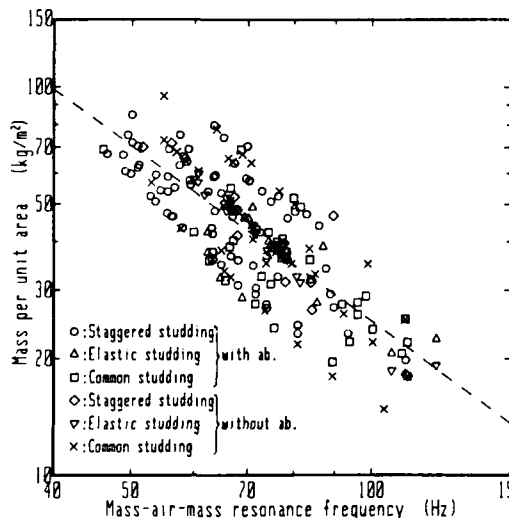
Fig.1 Scatter diagram between mass-air-mass resonance frequency and mass per unit area of partitions.
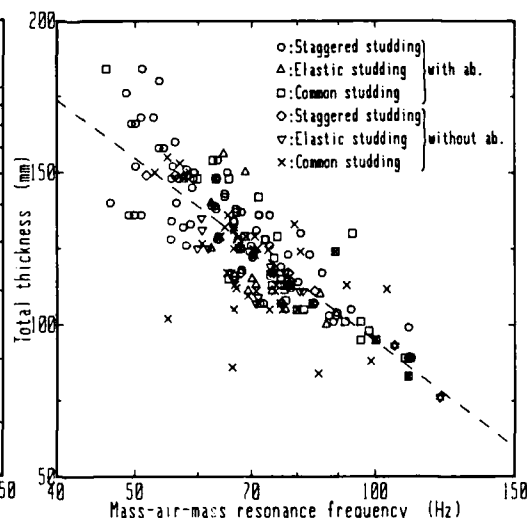
Fig.2 Scatter diagram between mass-air-mass resonance frequency and total thickness of partitions.

470

From the above results, it can be concluded that the mass per unit area and the total thickness have a good relation to fr irrespective of the wallboard attachment proced ure and that the relation does not depend upon whether the air space is filled with absorp tive material or not. Consequently, fr can be used as a single criterion for evaluating t he effective STL performance of wall structures.

Figure 3 (a) and (b) show scatter diagrams between STC and fr without and with absorptive materials respectively. From the figures, STC decreases in proportion to fr. T herefore, the resonance frequency fr shall be kept as low as possible in order to get high performance of STL. It is also found that STC changes with the wallboard attachment proce dure. Without absorptive materials, STC never exceeds 55 even if the staggered studding i s applied. On the other hand, when the common studding is applied, STC also never exceeds 55 even if the structure is constructed with absorptive materials.
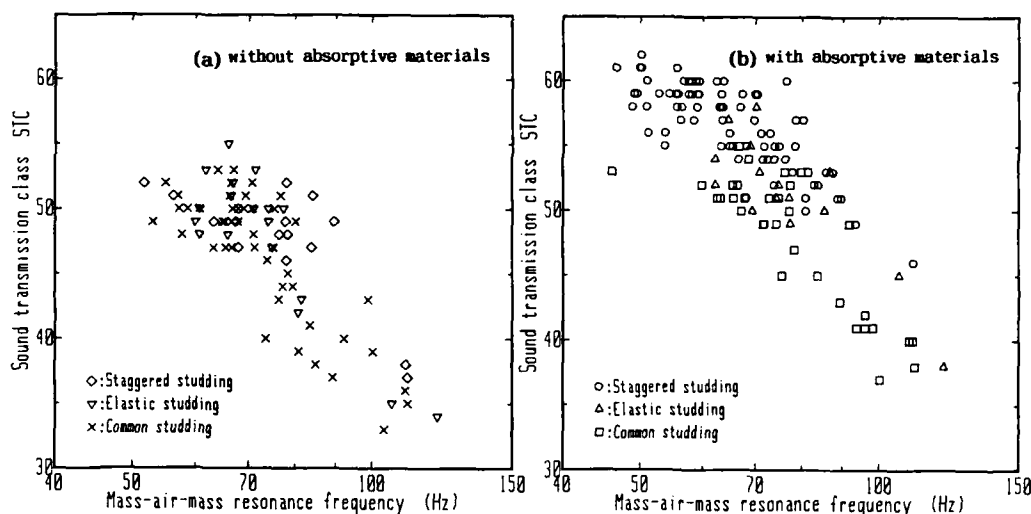
Fig.3 (a) Scatter diagram between STC and fr   Fig.3 (b) Scatter diagram between STC and fr
         without absorptive materials.   with absorptive materials.

EFFECTS OF WALLBOARD ATTACHMENT PROCEDURE AND COINCIDENCE DIP ON STL

It can be seen, from the above discussion, that STL of wallboard partitions is seriously influenced by the mass-air-mas resonance in the low frequency region. In fact, for about 30% of the analyzed data, the maximum deviation exceeds, at 125Hz, 8dB which is the tolerance provided in the STL classification procedure[1]. To make clear the influence of the resonance, the frequency characteristics of STL were normalized on the basis of the mass law and fr. That is, the STL curves were shifted so that the respective mass law values coincided each other at the resonance frequency fr. In calculating the mass law, STL was assumed to vary in proportion to the diffuse incidence mass law of an equivalent single-leaf partition having the sum of the masses of both leaves of the double-leaf partition. Note that the mass law curve was approximated by a log-linear equation, $STL=18*\log_{10}(m*f)-44$. This approximation was confirmed to hold in the range of the mass per unit area of 20 – 100 kg/m^2 and in the frequency range of 125 – 4000 Hz.

The results of the normalized STL curves for each type of studding are plotted together in Fig.4, 5 and 6. In each figure (a) and (b) are the result when the air space was unfilled and filled with absorptive materials, respectively. The frequency scale is normalized by fr. The dashed lines mean the diffuse incidence mass raw lines stated above. Although the materials of wallboards were quite different and the data were independently measured by several different laboratries, the agreement of the normalized STL curves are relatively good in each figure.

471
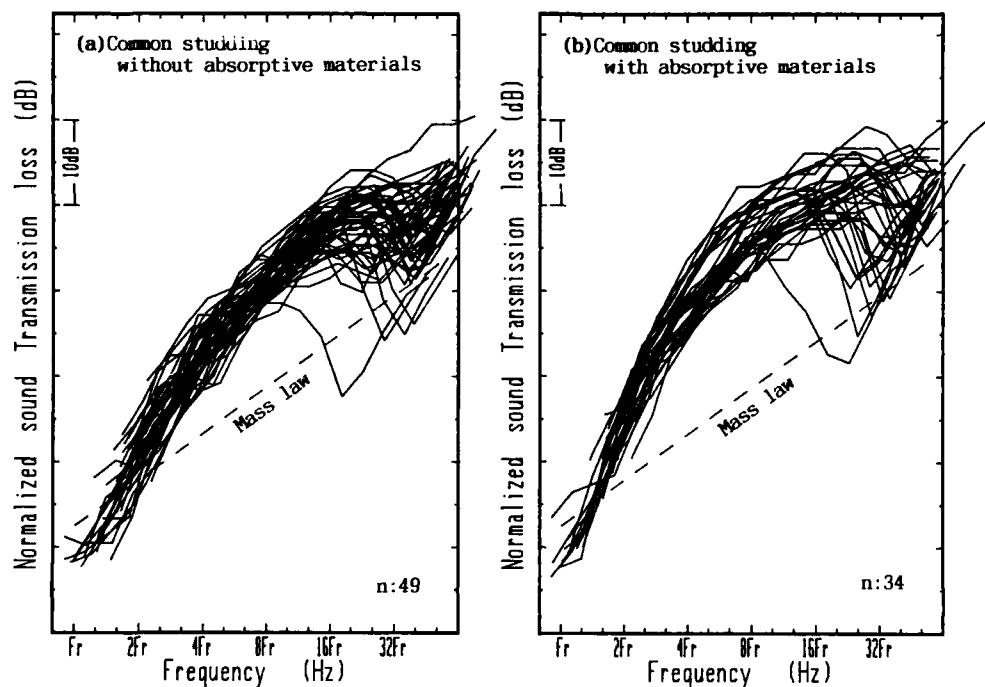
Fig.4 Normalized frequency characteristics of sound transmission loss for common studding,
(a);without absorptive material, (b);with absorptive material.
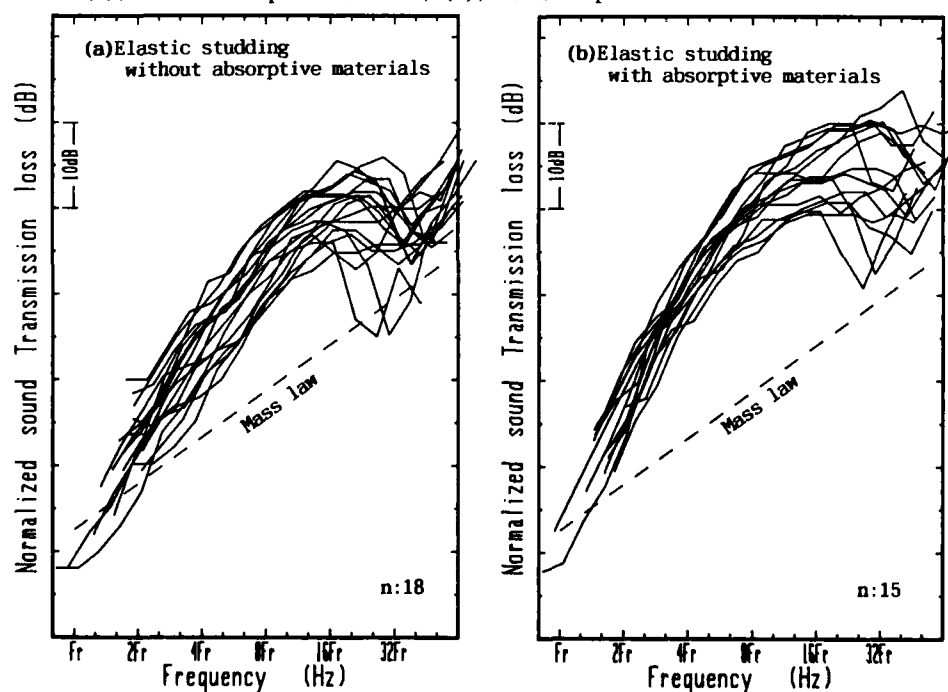
Fig.5 Normalized frequency characteristics of sound transmission loss for elastic studding,
(a);without absorptive material, (b);with absorptive material.

472
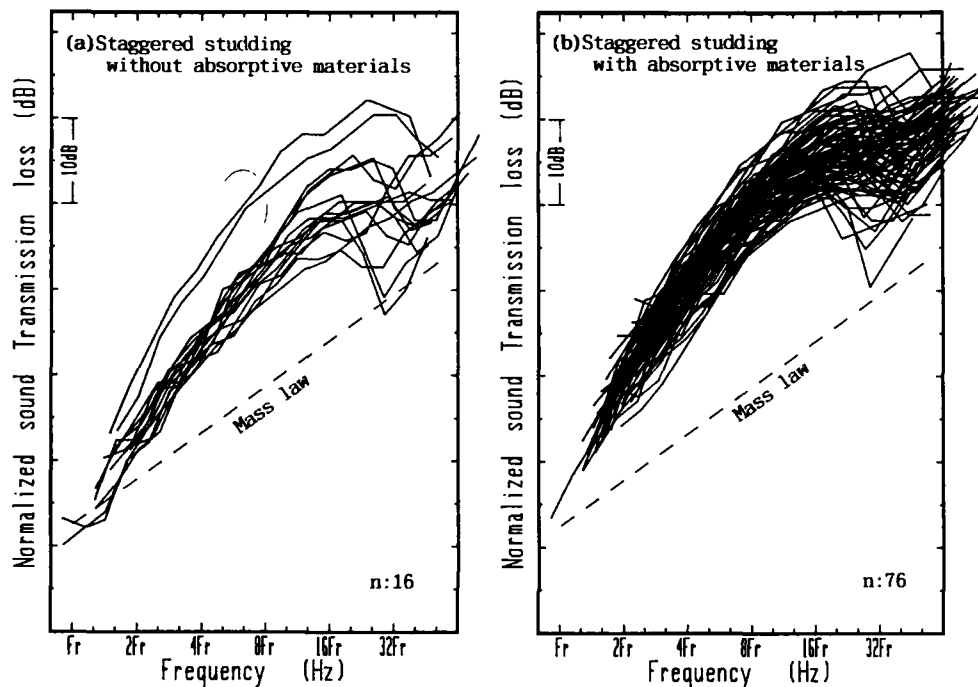
Fig.6 Normalized frequency characteristics of sound transmission loss for staggered
studding, (a);without absorptive material, (b);with absorptive material.
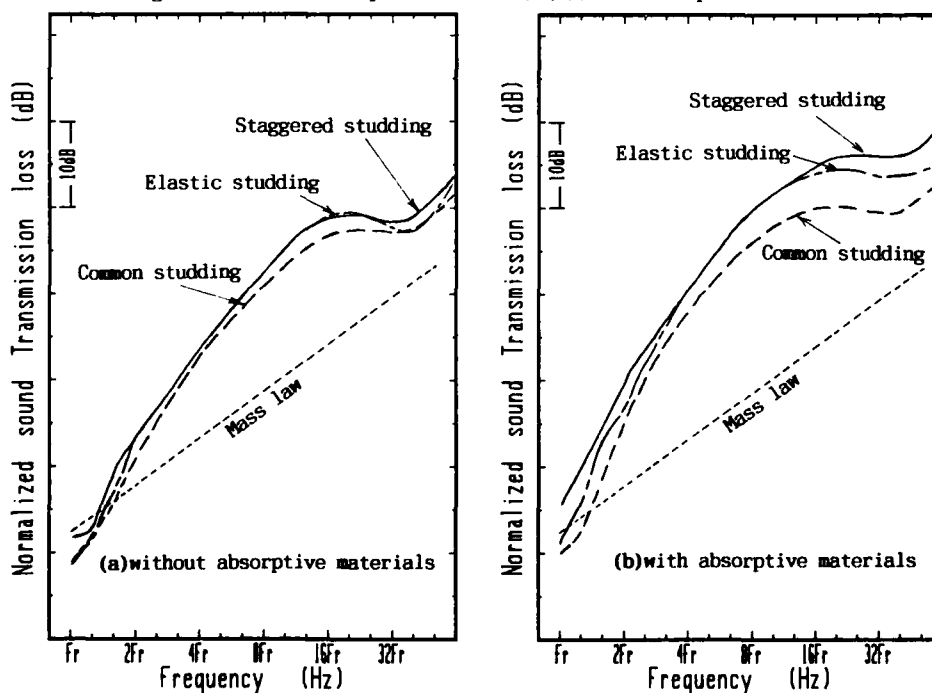
Fig.7 Comparison between the wallboard attachment procedures by averaging curves of
normarized STL; (a) without absorptive materials,(b) with absorptive materials.

473
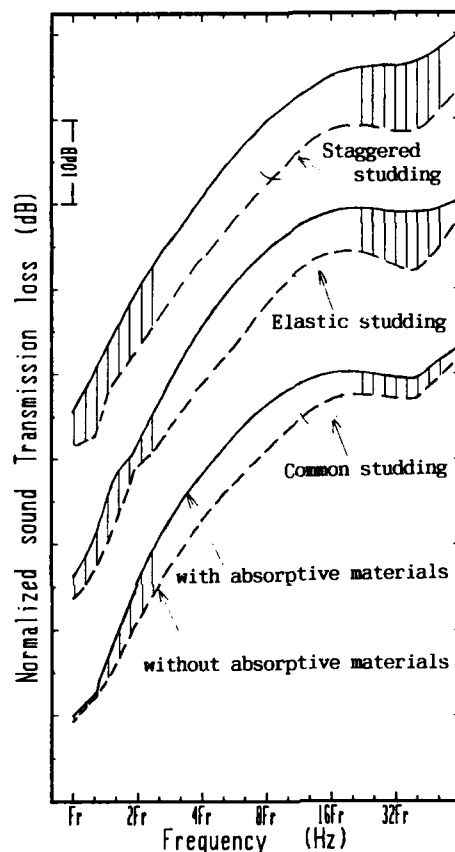
Fig.8 Effect of cavity absorption for different
wallboard attachment procedures.

To examine the effect of the difference in the wallboard attachment procedures on
STL, the normalized STL curves were averaged for each condition, resulting in Figures 7
and 8. The results of comparison are as follows;

(1)   As long as the air space was unfilled with absorptive materials, no significant
      changes were caused by the type of studding (see Fig.7(a)).

(2)   When the air space was filled with absorptive materials, the effect of the type of
      studding was better in order of staggered studding, elastic studding and common
      studding (see Fig.7(b)).

(3)   Changes of the effect of cavity absorption corresponding to the wallboard
      attachment procedure can only be seen near the resonance frequency and near the
      coincidence frequency, where the difference in the effect of cavity absorption
      becomes smaller in order of staggered studding, elastic studding and common studding
      (see Fig.8).   The reason is guessed that the effect of cavity absorption changes
      dependent on the acoustical property between two leaves of the double-leaf partition.
      In other words, it is important to reduce the stud-borne sound transmission across
      the cavity for more effective cavity absorption.

(4)   STL values of the two data marked by a circle in Fig.6 (a) are quite large,
      compared with other data. After examination of the wallboard attachment condition of
      the two data in the handbook, it was found that absorptive materials were filled in
      the top and bottom runners of the air space.

474
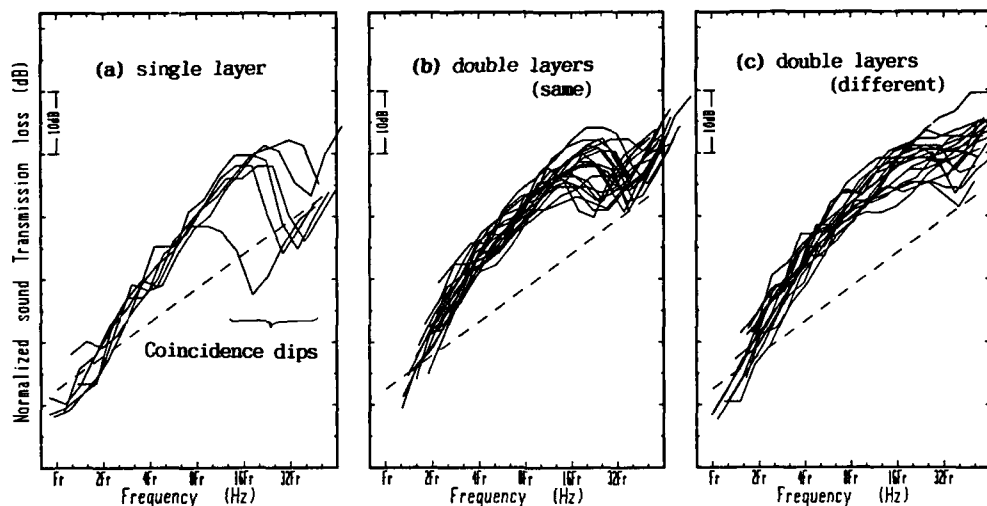
Fig.9 Comparison between the wallboards with specification;(a) single layer wallboard,
(b) double layers with same specification wallboards, (c) double layers with
different specification wallboards.

Finally, the influence of the number of layers composing each leaf of a double-leaf
partition was examined in the case of common studding without absorptive materials. The
results are shown in Fig.9 (a)-(c); (a) leaves were constructed by single layer
wallboards, (b) double layers of wallboards with the same specification of materials and
thickness, (c) double layers with different specification of materials and/or thickness.
In figure 9, the unfavourable effect of coincidence dip decreases in order of (a)-(c),
that is, by the use of double layer wallboards, especially with different materials
and/or thickness. It seems to be caused by some additional internal loss that is
produced by the friction between two layers.

SUMMARY

Wall structures between dwellings in a building are generally constructed with
double-leaf partitions for lessening the load of the building structure. In general,
mass-air-mas resonance occurs at low frequency region for double-leaf partitions. STL of
the structures is seriously influenced by the resonance. Then the STL performance of
double-leaf wall partitions and several physical parameters of the structures were
investigated. The total number of the analyzed data were 208.
    The relationship between mass-air-mass resonance frequency fr and mass per unit area
is relatively linear, and the relation of fr to the total thickness is aloso better. From
the results, it can be concluded that the mass per unit area and the total thickness are
linearly related with fr irrespective of the wallboard attachment procedure and that the
relation does not depend upon whether the air space is filled with absorptive material or
not. Consequently, fr can be used as a single criterion for evaluating the effective STL
performance of wall structures. STC decreases in proportion to fr, and changes with the
wallboard attachment procedure. Therefore, the resonance frequency fr shall be kept as
low as possible in order to get high performance of STL. Without absorptive materials,
STC never exceeds 55 even if the staggered studding is applied. On the other hand, when
the common studding is applied, STC also never exceeds 55 even if the structure is
constructed with absorptive materials.
    To make clear the influence of the resonance, the frequency characteristics of STL
were normalized on the basis of the mass law and fr for each type of studding. Although
the materials of wallboards were different and the data were independently measured by
several different laboratries, the agreement of the normalized STL curves are relatively
good.

From the results, it was found as follows;
(1) As long as the air space was unfilled with absorptive materials, no significant changes were caused by the type of studding.
(2) When the air space was filled with absorptive materials, the effect of the type of studding was better in order of staggered studding, elastic studding and common studding.
(3) Changes of the effect of cavity absorption corresponding to the wallboard attachment procedure can only be seen near the resonance frequency and near the coincidence dip frequency, where the difference in the effect of cavity absorption becomes smaller in order of staggered studding, elastic studding and common studding. The reason is guessed that the effect of cavity absorption changes dependent on the acoustical property between two leaves of the double-leaf partition.

Finally, the influence of the number of layers composing each leaf of a double-leaf partition was examined in the case of common studding without absorptive materials. The unfavourable effect of coincidence dip can be seen to decrease by the use of double layer wallboards, especially with different and/or thickness. It seems to be caused by some additional internal loss that is produced by the friction between two layers.

It is considered that there are many factors for prediction of STL performance of wallboard partition, and that greater reliance must be placed upon empirical information. Using the result of investigation, it is advisable to design an optimum wallboard structure for required STL performance with designated conditions.

REFERENCES

[1] ASTM standard,'Standard classification for determination of sound
    transmision class,' E-413-73 (1980).
[2] T.J.Schultz,in Noise and Vibration Control,McGraw-Hill,1971.

SOUND TRANSMISSION ANALYSIS BY COMPUTATIONAL MECHANICS USING CHARACTERISTIC IMPEDANCE DERIVED THROUGH A FINITE ELEMENTAL PROCEDURE

Toru Otsuru

Department of Architectural Engineering

Faculty of Engineering

Oita University

700 Dannoharu, Oita, 870-11

Japan

ABSTRACT

Here presented is a method to analyze the sound transmission loss through plates by computational mechanics based on the finite element method that uses only plate elements. The interaction between plate and air is taken into account in the form of characteristic impedance. A matrix equation to compute the characteristic impedance is set up through the finite elemental procedure with the help of a new matrix $[Se]$. The transmitted sound pressure and the transmission loss can also be obtained by solving the matrix equation presented here. Several example computations on the flat square plates with fixed edges show good agreements between the values of characteristic impedance and of transmission loss derived by this method and those by the classic analytical solutions.

1. INTRODUCTION

The purpose of this paper is to present a method to analyze vibro-acoustic phenomena from a finite elemental approach. Many studies have been done on the sound transmission characteristics through plates and walls. By using so-called classical modal analysis, almost all acoustic phenomena can basically be treated. Some complexities, however, make the classical analysis impossible. One is the complexity of the boundary conditions of the system, and another is the complexity caused by the huge amount of freedoms to be dealt with. The finite element method is a way to help solve these problems, and some studies have been successfully done on the sound transmission properties of complex structures with finite plates and closed cavities. In such studies, plate and acoustic finite elements are commonly used. [1,2]

In contrast to this, a method using only plate elements is presented below, which makes the fine modeling of plates possible and the analysis free from the effects of the cavities' boundary conditions. Such a method may be advantageous in the vibro-acoustic analysis of high frequency regions. In our previous study, to get the characteristic impedance of modal vectors through the finite elemental procedure, a new matrix, matrix $[Se]$, was proposed and, by using the matrix, some basic equations were presented. [3] With these results, several refined equations to compute the characteristic impedance and the radiated sound pressure are introduced. A practical procedure to carry out the computation is described briefly, and then, the accuracy of this method is discussed.

2. THEORETICAL DESCRIPTION

2.1 Basic Formulae

The discrete formula of a structure excited by sinusoidal force of frequency ω is,

$$[M]\{\ddot{d}\} + [C]\{\dot{d}\} + [K]\{d\} = \{F\}e^{i\omega t}$$

(1)

The nodal displacement $\{d\}$ can be got as follows.

$$\{d\} = \sum_{n=1}^{N} \alpha_n \{\phi_n\} \qquad \text{where,} \qquad \alpha_n = \frac{\{\phi_n\}^T\{F\}\ e^{i\omega t}}{\{(\omega_n^2 - \omega^2) + i\,2\,h_n\,\omega_n\,\omega\}\,M_n},$$

(2)

$$M_n = \{\phi_n\}^T[M]\{\phi_n\}, \qquad h_n = \frac{\{\phi_n\}^T[C]\{\phi_n\}}{2\,\omega_n\,M_n}.$$

The displacement to the z-direction at the co-ordinates $(x,y)_e$ is got by

$$w(x,y)_e = [N_w(x,y)_e]\{d\}_e.$$

(3)

Here, $(x,y)_e$ denotes the local co-ordinates in an element "e", and, in like manner, $\{x\}_e$ and $[X]_e$ express the vector and matrix of an element "e".

2.2 Damping Matrix [C]

Let the damping matrix, $[C]$, consist both of the damping caused by the plate's inner loss, $[C_p]$, and of the reaction of air on the plate's surfaces, $[C_a]$:

$$[C]\{\dot{d}\} = [C_p]\{\dot{d}\} + [C_a]\{\dot{d}\},$$

(4)

$$\text{here,} \qquad [C_p] = \frac{\eta}{\omega}[K].$$

The second term of Eq. (4) can be derived as follows: using characteristic impedance of the mth mode onto the nth mode, $_m\zeta_n$, the radiated sound pressure from the plate's vibrating surface can be

$$\{P_t\} = \sum_{m=1}^{N}\sum_{n=1}^{N} {}_m\zeta_n\,z_0\,\dot{\alpha}_m\{\phi_n\}.$$

(5)

Let the element's nodal displacement vector of the nth mode be written as $\{d_n\}_e$, then the work of air over an element can be

$$W_e = \{d\}_e^T \int\!\!\int_e [N_w(x,y)_e]^T[N_w(x,y)_e]\,dx\,dy \sum_m \sum_n 2\,{}_m\zeta_n\left(\frac{\dot{\alpha}_n}{\alpha_m}\right)z_0\{\dot{d}_n\}_e$$

$$= \{d\}_e^T\frac{[M]_e}{\rho\,h}\sum_m\sum_n 2\,{}_m\zeta_n\left(\frac{\dot{\alpha}_n}{\alpha_m}\right)z_0\{\dot{d}_n\}_e$$

$$= \{d\}_e^T\sum_m\sum_n [C_{a\ mn}]_e\{\dot{d}_n\}_e$$

$$\text{where,} \qquad [C_{a\ mn}]_e = 2\,{}_m\zeta_n\left(\frac{\dot{\alpha}_n}{\alpha_m}\right)z_0\frac{[M]_e}{\rho\,h}.$$

(6)

Therefore, the second term of Eq. (4) can be in the form of

$$[C_a]\{\dot{d}\} = \sum_m\sum_n [C_{a\ mn}]\{\dot{d}_n\} \propto [M].$$

(7)

Eq. (7) is a proof that modal analysis, *i.e.*, Eq. (2), can be carried out using the modal vector, $\{\phi_n\}$, which is derived from the eigen formula of Eq. (1):

$$([K] - \omega^2[M])\{\phi\} = \{0\}.$$

(8)
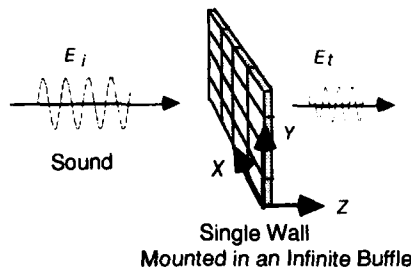
Fig.1 System to be analyzed.
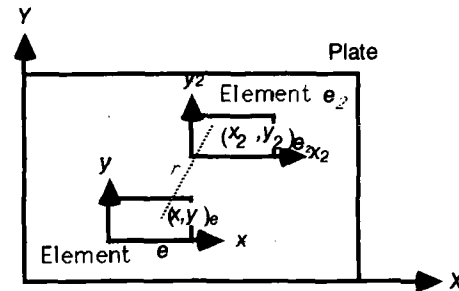
Fig.-2 Global co-ordinate system (X,Y) and local Co-ordinate system $(x,y)_e$ and $(x_2,y_2)_{e_2}$.

Accordingly, h_n in Eq. (2) is rewritten as follows:

$$h_n = \frac{\{\phi_n\}^T \left([C_p] + [C_{a\,n}] \right) \{\phi_n\}}{2\,\omega_n\,M_n}, \qquad [C_{a\,n}] = 2\,\zeta_n\,z_0\,\frac{[M]_e}{\rho\,h}. \tag{9}$$

2.3 Selecting Matrix [Se]

To make the finite elemental procedure simple and consistent, the following matrix $[Se]$ was introduced.[3] The matrix $[Se]$, which consists of "1" and "0", functions to select an elemental vector, $\{x\}_e$, from a global vector $\{x\}$, e.g.:

$$\{d\}_e = [Se]\,\{d\}, \quad \text{or} \quad [M] = \sum_e [Se]^T[M]_e[Se].$$

With the matrix [Se], the co-ordinate transformation becomes simpler from the local to the global, and vice versa.

2.4 Transmitted Acoustic Power

The transmitted sound power at an arbitrary point $(x,y)_e$ is

$$\Pi(x,y)_e = \frac{1}{2} Re\left\{ p_t(x,y)_e \cdot \dot{w}(x,y)_e^* \right\}$$

$$= \frac{1}{2} Re\left\{ [N_w(x,y)_e] \sum_{m=1}^{N} \sum_{n=1}^{N} m\zeta_n z_0 \dot{\alpha}_m \{\phi_n\}_e \cdot [N_w(x,y)_e] \sum_k \alpha_k^* \{\phi_k\}_e \right\}$$

$$= \frac{1}{2}\omega^2 z_0 Re\left\{ \left(\sum_m \sum_n m\zeta_n \alpha_m \{\phi_n\}_e^T \right) [N_w(x,y)_e]^T \cdot [N_w(x,y)_e] \left(\sum_k \alpha_k^*\{\phi_k\}_e \right) \right\} \tag{10}$$

The total sound power, E_t, radiated from plate, is got by summing up $\Pi(x,y)_e$ and integrating them over the area of all the elements,

$$E_t = \sum_e \iint_{Area\,e} \Pi(x,y)_e\, dx\, dy$$

$$= \sum_e \frac{1}{2}\omega^2 z_0 Re\left\{ \left(\sum_m \sum_n m\zeta_n \alpha_m \{\phi_n\}_e^T \right) \left(\iint_{Area\,e} [N_w(x,y)_e]^T \cdot [N_w(x,y)_e]\, dx\, dy \right) \left(\sum_k \alpha_k^*\{\phi_k\}_e \right) \right\}$$

$$= \sum_e \frac{1}{2}\omega^2 z_0 Re\left\{ \left(\sum_m \sum_n m\zeta_n \alpha_m \{\phi_n\}_e^T \right) \frac{[M]_e}{\rho\,h} \left(\sum_k \alpha_k^*\{\phi_k\}_e \right) \right\}, \tag{11}$$

with the help of matrix $[Se]$, Eq. (11) can be rewritten

$$E_t = \sum_e \frac{1}{2} \omega^2 z_0 \, Re \left\{ \left(\sum_m \sum_n m\zeta_n \alpha_m \{\phi_n\}^T \right) \frac{[Se]^T [M]_e [Se]}{\rho \, h} \left(\sum_k \alpha_k^* \{\phi_k\} \right) \right\}$$

$$\therefore E_t = \frac{1}{2} \omega^2 z_0 \, Re \left\{ \left(\sum_m \sum_n m\zeta_n \alpha_m \{\phi_n\}^T \right) \frac{[M]}{\rho \, h} \left(\sum_k \alpha_k^* \{\phi_k\} \right) \right\} . \tag{12}$$

Thus, the characteristics of transmitted sound through plates can be expressed by a simple equation. Additionally, the sound transmission loss can be obtained by

$$TL = -10 \log_{10} \frac{E_t}{E_i} .$$

2.5 Characteristic Impedance

Since the characteristic impedance plays an important role in Eq. (12), the next problem is to get it through the finite elemental procedure.

With the matrix $[Se]$, the displacement to the direction of z-axis at an arbitrary point in the plate can be

$$w(X,Y) = w(x,y)_e = [N_w(x,y)_e] \sum_{n=1}^N \alpha_n \{\phi_n\}_e = [N_w(x,y)_e] [Se] \sum_{n=1}^N \alpha_n \{\phi_n\} . \tag{13}$$

Using $[Se]$, the sound pressure at an arbitrary point (X,Y), or $(x,y)_e$, can be expressed in the following two ways.

$$p_t(X,Y) = p_t(x,y)_e = i \omega \rho_0 c \, [N_w(x,y)_e] [Se] \sum_{n=1}^N \sum_{m=1}^N m\zeta_n \alpha_m \{\phi_n\} , \tag{14}$$

$$p_t(X,Y) = p_t(x,y)_e = \sum_{e_2} \frac{i^2 \omega^2 \rho_0}{2\pi} \int\!\!\int_{Area\, 2} [N_w(x_2,y_2)_{e_2}] [Se_2] \sum_{l=1}^N \alpha_l \{\phi_l\} \frac{e^{-ikr}}{r} dx_2 dy_2 . \tag{15}$$

where, $\quad r = \sqrt{(X-X_2)^2 - (Y-Y_2)^2}$.

The following is sufficient to satisfy these two equations,

$$i \omega \rho_0 c \, [N_w(x,y)_e] [Se] \sum_{n=1}^N m\zeta_n \alpha_m \{\phi_n\} = \sum_{e_2} \frac{i^2 \omega^2 \rho_0}{2\pi} \int\!\!\int_{Area\, 2} [N_w(x_2,y_2)_{e_2}] [Se_2] \alpha_m \{\phi_m\} \frac{e^{-ikr}}{r} dx_2 dy_2 . \tag{16}$$

If we perform the following operation and rearrange them,

$$\sum_e \int\!\!\int_{Area\, e} \left\{ \left([N_w(x,y)_e] [Se] \{\phi_n\} \right)^T \times \left(\text{both members of Eq.(15)} \right) \right\} dx \, dy , \tag{17}$$

then, Eq. (16) becomes

$$\sum_e i \omega \rho_0 c \, \{\phi_n\}^T [Se]^T \left(\int\!\!\int_{Area\, e} [N_w(x,y)_e]^T [N_w(x,y)_e] dx \, dy \right) [Se] \sum_{n=1}^N m\zeta_n \alpha_m \{\phi_n\}$$

$$= \sum_e \sum_{e_2} \frac{i^2 \omega^2 \rho_0}{2\pi} \{\phi_n\}^T [Se]^T \int\!\!\int_{Area\, e} \left(\int\!\!\int_{Area\, 2} [N_w(x,y)_e]^T [N_w(x,y)_{e\, 2}] \frac{e^{-ikr}}{r} dx_2 dy_2 \right) dx \, dy \, [Se_2] \alpha_m \{\phi_m\} , \tag{18}$$

480

Using the following relation

$$\sum_e [Se]^T \left(\int\!\!\int_{Area\ e} [N_w(x,y)_e]^T [N_w(x,y)_e]\ dx\,dy \right) [Se] = \frac{[M]}{\rho_0 h}\ , \tag{19}$$

Eq. (18) is transformed as follows

$$_m\zeta_n = \frac{i\,k\,\{\phi_n\}^T [I_1]\,\{\phi_m\}}{2\,\pi\,\{\phi_n\}^T [I_2]\,\{\phi_n\}}\ , \tag{20}$$

$$[I_2] = \frac{[M]}{\rho_0 h}\ , \quad [I_1] = \sum_e \sum_{e_2} [Se]^T \int\!\!\int_{Area\ e} [N_w(x,y)_e]^T \int\!\!\int_{Area\ e_2} [N_w(x_2,y_2)_{e\,2}]\frac{e^{-ikr}}{r}\,dx_2 dy_2\,[Se_2]\,dx\,dy\ .$$

3. APPLICATIONS

To examine the accuracy of this method, the following sound transmission analysis is carried out on an aluminum plate with the dimensions of 0.78x0.39x0.012 m and with all the edges fixed. The normal sound incident condition is assumed. The element used here is A.C.M. plate element with three freedoms on each node. In the following computation, 10x6 elements (135 freedoms) and FACOM VP-200 (540 MFlopps, 128 M bytes main memory) are tentatively used.

3.1 Computation of Characteristic Impedance

The characteristic impedances can be obtained by Eq. (20) with the result of the eigen equation (8). In Eq. (20) however, the singularities make the practical integration hard to carry out. A way to eliminate the singularities is as follows:

In the finite element method, Gaussian quadrature is commonly used, which makes the practical computation simple and accurate.[4] In addition, Gaussian quadrature is suited for computations on the vector (or array) processor, since, basically, there is no recursive procedure in it. So, practical computations of Eq. (20) are performed by Gaussian quadrature: first, as no singularities exist if the element number "e" is not equal to "e_2" in Eq. (20), the integration can be performed directly. In this experimental computation, second-order Gaussian quadrature is performed: next, if "e" is equal to "e_2", the following co-ordinate transformation is performed to eliminate the singularities.

$$\begin{aligned} x - x_2 &= r\cos\Theta \\ y - y_2 &= r\sin\Theta \end{aligned} \qquad r = \sqrt{(x_2 - x)^2 - (y_2 - y)^2}\ . \tag{21}$$

Then, Eq. (20) is rewritten as

$$[I_1] = \sum_e \sum_{e_2 \neq e} [Se]^T \int\!\!\int_{Area\ e} [N_w(x,y)_e]^T \int\!\!\int_{Area\ e_2} [N_w(x_2,y_2)_{e\,2}]\frac{e^{-ikr}}{r}\,dx_2 dy_2\,[Se_2]\,dx\,dy$$

$$+ \sum_{e = e_2} [Se]^T \int\!\!\int_{Area\ e} [N_w(x,y)_e]^T \int\!\!\int_{Area\ e_2} [N_w(r\cos\Theta + x,\ r\sin\Theta + y)_{e\,2}]\,e^{-ikr}\,d\Theta dr\,[Se_2]\,dx\,dy\ . \tag{22}$$

and it is rewritten as

$$\iint_{Area\,e2} [N_w(r\cos\Theta + x, r\sin\Theta + y)_{e\,2}]\,e^{-ikr}\,d\Theta dr \quad = [J_1] + [J_2] + [J_3] + [J_4] \tag{23}$$

$$[J_v] = \sum_{\kappa=1}^{3} \int_{r^-}^{r^-} \int_{\Theta^-}^{\Theta^-} [N_w(r\cos\Theta + x, r\sin\Theta + y)_{e\,2}]\,e^{-ikr}d\Theta\,dr \tag{24}$$

The areas of Θ and r to be integrated is shown in Fig.3 and Table 1. In this case, $(e = e_2)$, third-order Gaussian quadrature is applied. That is, the integration is substituted by the summation at 108 points, _ie._ 3 (x-axis) x 3 (y-axis) x 4 (quadrant v) x 3 (area κ), in an element (see Fig. 3).

Although the number of impedances to be computed is $_{N+1}C_2$ theoretically, it is possible to reduce the number in the sound transmission analysis on the normal incidence condition by the following procedures: first, getting $_n\zeta_n$, $(m=n)$, by Eq. (20); second, computing α_n by Eq. (2) with these $_n\zeta_n$-values; then, eliminating the modes whose α_n -value is respectively small. In this trial computation, the modes whose α_n -values are 10^{-6} times as much as that of α_1 are eliminated, and the number of modes has been reduced from 135 to 37. Therefore, there are 703 $(= _{37+1}C_2)$ combinations of modes and 703 impedances per frequency point. Some of them are shown in Fig. 4 and Fig. 5, and the natural frequencies of these modes are shown in Table 2.

Since the length of an element in the computation is almost the same as the acoustic wave length of 4000 Hz, the frequency range to be discussed can be below 1000 Hz. Nevertheless, Fig. 4 shows good agreement between the impedance values obtained through the method described above and those got by the classical analytic solution in the frequency region from 31.5 to 4000 Hz. Strictly speaking, the orthogonal functions used in the latter solution are different from the modal vectors used in above mentioned method, but this agreement supports the accuracy of the method presented in this paper.

Furthermore, although it is not clear whether $_m\zeta_n$ is equal to $_n\zeta_m$ when they are derived from Eq. (20), only a slight difference can be seen in the comparison between the impedance values of modes, the natural frequency of one of which is in the high frequency region (Fig.5(c)); and there can be seen no difference between $_3\zeta_1$ and $_1\zeta_3$, and between $_8\zeta_1$ and $_1\zeta_8$ the natural frequencies of both of which are below 500 Hz. (Fig.5 (a), (b)). In addition, the required time for the computation is about 1.4 sec per one impedance value.

3.2 Computation of Sound Transmission Loss (TL)

With the impedance values thus obtained, the TL-values of the plate are computed at every 1/24 octave points in the frequency region from 31.5 to 1000 Hz. Fig. 6 shows good agreement between the TL-values got through the method presented above and those by the classical analytic solution.

4. CONCLUSIONS

A method to analyze vibro-acoustic problems by computational mechanics is presented and its accuracy is examined. The method is advantageous in the computation of the sound transmission characteristics of plates with too complicated shapes or boundary conditions to be computed by some classical analytic solutions. Besides, with the impedance obtained by this method, vibro-acoustic analysis can be carried out by the finite element method without using acoustic elements, which reduces the total amount of freedoms to be considered. Consequently, the analysis without acoustic elements makes it possible to use all the memories in a computer to model the characteristics of the plate under consideration, and also to make the analysis free from the consideration about the boundary conditions of rooms or acoustic fields on both sides of the plate.

Fig.3

y₂, y, v=2, b, v=1, Quadrant 1, y₂-y, b-y, κ=3, κ=3, κ=2, κ=2, κ=1, κ=1, r, (x₂, y₂), Θ, -x, a-x, (x,y), x₂-x, κ=2, κ=1, κ=1, κ=2, κ=3, κ=3, v=3, -y, v=4, a, x₂, x

ELEMENT e (= e₂)
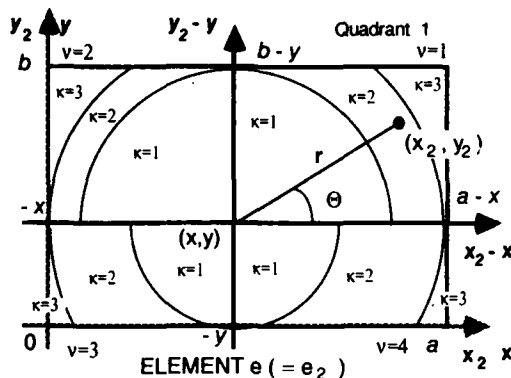
Fig.3 Co-ordinate transformation. (x,y) and (x_2,y_2) are in the same element. The Cartesian co-ordinate syatem $(x_2 - x, y_2 - y)$ is transformed to the polar co-ordinate system (r, Θ).

No.	[Hz]	No.	[Hz]	No.	[Hz]
1	48	44	720	88	1670
3	89	47	788	92	1784
8	177	51	880	103	2048
12	241	52	913	107	2295
14	266	66	1134	110	2395
17	313	67	1155	111	2428
18	328	69	1217	113	2455
27	441	73	1287	115	2507
29	492	75	1297	120	2610
34	596	77	1360	121	2653
36	599	83	1433	124	2728
37	605	85	1590		
39	632	87	1602		

Table.1 The integration area of Eq. (24). The number v corresponds to the quadrant number of Fig.3.

	v=1			v=2			v=3			v=4		
	κ=1	κ=2	κ=3	κ=1	κ=2	κ=3	κ=1	κ=2	κ=3	κ=1	κ=2	κ=3
	$(a-x \geq b-y)$			$(x \geq b-y)$			$(x \leq y)$			$(a-x \geq y)$		
r'	0	$b-y$	$a-x$	0	$b-y$	x	0	x	y	0	y	$a-x$
r''	$b-y$	$a-x$	$\sqrt{(a-x)^2+(b-y)^2}$	$b-y$	x	$\sqrt{x^2+(b-y)^2}$	x	y	$\sqrt{x^2+y^2}$	y	$a-x$	$\sqrt{(a-x)^2+y^2}$
Θ'	0	0	$\cos^{-1}\frac{a-x}{r}$	$\frac{\pi}{2}$	$\pi-\sin^{-1}\frac{b-y}{r}$	$\pi-\sin^{-1}\frac{b-y}{r}$	$\frac{\pi}{2}$	$\frac{\pi}{2}+\cos^{-1}\frac{x}{r}$	$\pi+\cos^{-1}\frac{x}{r}$	$\frac{3\pi}{2}$	$\frac{3\pi}{2}+\cos^{-1}\frac{y}{r}$	$\frac{3\pi}{2}+\cos^{-1}\frac{y}{r}$
Θ''	$\frac{\pi}{2}$	$\sin^{-1}\frac{b-y}{r}$	$\sin^{-1}\frac{b-y}{r}$	π	π	$\pi-\cos^{-1}\frac{x}{r}$	$\frac{3\pi}{2}$	$\frac{3\pi}{2}$	$\frac{3\pi}{2}-\cos^{-1}\frac{y}{r}$	2π	2π	$2\pi-\cos^{-1}\frac{a-x}{r}$
	$(a-x < b-y)$			$(x < b-y)$			$(x > y)$			$(a-x < y)$		
r'	0	$a-x$	$b-y$	0	x	$b-y$	0	y	x	0	$a-x$	y
r''	$a-x$	$b-y$	$\sqrt{(a-x)^2+(b-y)^2}$	x	$b-y$	$\sqrt{x^2+(b-y)^2}$	y	x	$\sqrt{x^2+y^2}$	$a-x$	y	$\sqrt{(a-x)^2+y^2}$
Θ'	0	$\cos^{-1}\frac{a-x}{r}$	$\sin^{-1}\frac{b-y}{r}$	$\frac{\pi}{2}$	$\frac{\pi}{2}$	$\frac{\pi}{2}+\cos^{-1}\frac{b-y}{r}$	π	π	$\pi+\cos^{-1}\frac{x}{r}$	$\frac{3\pi}{2}$	$\frac{3\pi}{2}$	$\frac{3\pi}{2}+\cos^{-1}\frac{y}{r}$
Θ''	$\frac{\pi}{2}$	$\frac{\pi}{2}$	$\cos^{-1}\frac{a-x}{r}$	π	$\pi-\cos^{-1}\frac{x}{r}$	$\pi-\cos^{-1}\frac{x}{r}$	$\frac{3\pi}{2}$	$\frac{3\pi}{2}-\cos^{-1}\frac{y}{r}$	$\frac{3\pi}{2}-\cos^{-1}\frac{y}{r}$	2π	$2\pi-\cos^{-1}\frac{a-x}{r}$	$2\pi-\cos^{-1}\frac{a-x}{r}$

(a) |ζ1|, Real Part of |ζ1|, Imag. Part of |ζ1|, — by FEM Eq.(20), by C.M.A.

(b) 3ζ3, Real Part of 3ζ3, Imag. Part of 3ζ3, — by FEM Eq.(20), by C.M.A.

frequency[Hz] frequency[Hz]

Fig.4 Comparison between the impedance-values obtained by FEM (Eq. (20)) and those by C.M.A.. (a); |ζ1|, (b); 3ζ3 .

Fig.6 Comparison between the TL-values he result of classic modal analysis
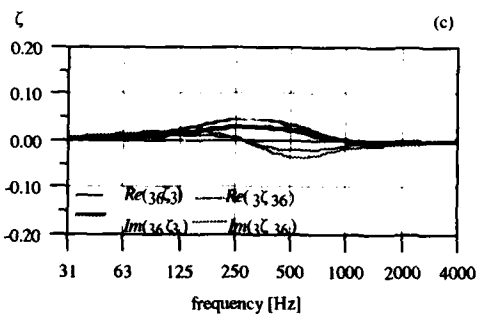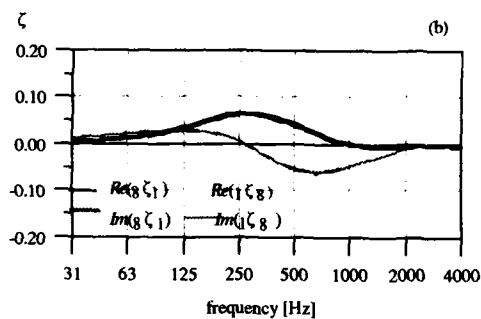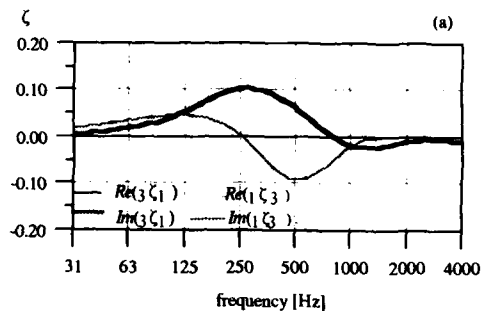
Fig.5 Comparison of the impedances obtained by FEM: (a); $_3\zeta_1$ and $_1\zeta_3$, (b); $_8\zeta_1$ and $_1\zeta_8$, (c);$_{36}\zeta_3$ and $_3\zeta_{36}$

SYMBOLS

c : Velocity of sound,
e : element number,
E_i, E_t : Incident and transmitted sound energies,
i : $\sqrt{-1}$,
k : Wave number,
N : Total number of freedoms,
w : Displacement to the direction of z-axis
z_0 : Specific acoustic impedance of air,
$[C]$, $[K]$, $[M]$: Damping, Stiffness, Mass matrices,
$\{d\}$: Nodal displacement vector,
$\{F\}$ $e^{i\omega t}$: Driving force vector,
$[N_w(x,y)]$: Shape function for the displacement w
$[Se]$: Selecting matrix of element e,
η : Inner loss factor of a plate,
ρ_0 : Air mass, ($z_0 = \rho_0 c$),
ρh : Mass density per area of a plate,
ω : Angular frequency,
ω_n, $\{\phi_n\}$: Natural frequency and modal vector of n th mode,
$_m\zeta_n$: Characteristic impedance of mth mode onto n th mode,
z^* : Complex conjugate of the complex number z,
$[X]^T$,$\{X\}^T$: Transpose of $[X]$, $\{X\}$,
$Re\{z\}$: Real part of the complex number z,
$\dot{x}$: $\partial x / \partial t$.
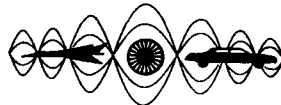
REFERENCES

1. A. Craggs, "The transient response of a coupled plate-acoustic system using plate and acoustic finite elements," J. Sound and Vib. 15, (1971), 509-528
2. J. V. Ramakrishnan and L. R. Koval, "A finite element model for sound transmission through laminated composite plates," J. Sound and Vib. 112(3), (1987), 433-446
3. T. Otsisuru and H. Yamamoto,"Sound transmission analysis by computational mechanics using characteristic impedance of mode vectors," Proc. of Inter-Noise 89, Vol1, (1989), 539-542
4. O. C. Zienkiewicz,"The finite element method." McGraw-Hill, third edition (1977)

NEW METHOD FOR CALCULATION AND DESIGN NOISE

ISOLATING ENCLOSURES

Ludmila Ph. Drozdova

Associated Prof. in the Ecology Department

at the Institute of Mechanics in St. Petersburg

Russia

ABSTRACT

This paper offers a new classification for main constructive sche-
mes of noise isolating inclosures for power plants in transportation
machines.

The author suggests a new method for the enclosure calculations
that is based on the statistical acoustic theory. This method considers:
the sound field nature inside the enclosure; the sound radiation irregu-
larity produced by various enclosure panels at the specific point; the
constructive geometry of the enclosure (general dimensions, areas of ho-
les, slots and openings); the availability of sound absorbing material in
the enclosure.

Results of the investigations have been used while developing noise
isolating enclosures for movable compressor machines with various types
of power plants.

Among the number of noise control facilities for engines the most
efficient one, the one, which allows us to meet comprehensive noise cont-
rol requirements, is the engine enclosing, i.e. the shielding of the
noise and vibrationally intensive area by an enclosed volume of some
shape - by an enclosure.

The engine being enclosed, the sound propagation character both un-
der and beyond the enclosure differs substantially from the case with an
un-enclosed being also dependent on the enclosure configuration.

Thus, the enclosing efficiency depends on a great number of factors
such as: a shape and a size of the enclosure; panels rigidity; presence
of ventilation ducts and passages; the value of the averaged sound

absorption factor; noise isolation of the enclosing structures; the loss factor for the enclosure walls; a sound field character under the enclosure etc.

It is essentially important to take into account all the factors mentioned above, because sound-isolation enclosures of simple configurations for power plants seemed to be useless.

The factor of primary importance to be solved first of all is providing air circulation under the enclosure, since all the others are substantially dependent on it. The temperature exchange between the under-enclosure space and the installation being enclosed depends on the enclosure type, the total heat conductivity of the walls, the temperature difference between the under-enclosure space and environment, being mainly provided by means of under-enclosure space ventilation.

The dependence of the enclosure sound isolation on the under-enclosure space temperature may be defined through the enclosure tightness degree, i.e. the ratio of total holes, slots and openings area to that of the external enclosure surface [1]

$$\varepsilon = \Sigma F / S_{enc.} \qquad (1)$$

where ΣF is the total area of all the holes, openings and slots of the enclosure;

$S_{enc.}$ the area of the enclosure surface.

Numerous configurations of the enclosures for different kinds of vehicles having been considered, it seemed to be possible to classify them in accordance with the following main factors: the enclosure tightness degree, the material of the enclosing structures, configuration piculiarities and the system of under-enclosure ventilation.

When designing and estimating the paticular enclosure for the actual power plant we should also take into account in addition to the mentioned above, such structural features as: area and shape of the ventilation passages (a hole, a slot, an opening); setting mufflers into the passages or acoustical shields before them; the engine size; the ventilation pasages location relaive to the specified point and some others.

Methods being available for the acoustical estimation of the enclosures in free space are based on the Wave, Geometrical and Statistical Acoustics, the latter having been widly used recently and the Statistical Energy method is of particular importance. An under-enclosure sound field is considered to be diffuse when we apply this method. The diffuse sound field is characterised by the constant time-averaged sound pressure level in all the points of the fiela and by the constant sound energy flow in all the directions. Also, amplitudes and phases of the superimposed waves are more or less random, which allows to consider them as being non-coherent and, hence, to estimate the sound energy density at each point by summing up the energy densities of all these waves.

An example of the diffuse sound field model was shown for the frequencies when the sound wave length is less than the enclosure dimensions [2]. The suggestes equation for the enclosure efficiency estimation allows only to consider the enclosure's size and availability of the sound-absorbtive coating under the enclosure.

The enclosure estimating scheme, suggested in [3], consideres more structural and other factors, including shielding area and the enclosure volume, the averaged sound absorption factor, the sound isolating ability of enclosing elements, the sound absorption factors of different enclosing structures and so on. However, the accuracy of the suggested estimating schemes is not very high, being the least in the low frequency range.

One peculiar feature of the enclosure's constructions for the transportation vehicles is the small size of the enclosed area with the configuration being uncomparable to that of the enclosed engine. Therefore, we may think of two areas in the sound field in the under-enclosure volume, the entire one being of a small size: a diffuse field beginning with the definite frequency $f \gg f_{dif}$, arising from the multiple sound wave reflections by unparalleled surfaces of the enclosure and the engine, and $f < f_{dif}$

All the variety of estimating enclosure schemes of their different configuration, influencing the acoustical efficiency of the enclosures may be reduced to the six main types:

TYPE 1 - CLOSED (in the walls there are only small configuration openings of the neglegible size; $\xi \leq 0,05$ %). It is used for enclosing engines and other power plants enclosing which do not produce too much heat.

TYPE II - OPENED (there are ventilation ducts or passages in the form of free openings on the bottom, on the side so on, through which the sound is allowed to pass free from under the enclosure; $\xi \leq 0,25$ %). It is used for the engines with the low noise level increase (up to 10 dB).

TYPE III - SEMI-CLOSED (there are ventilation passages made in the form of slots, the latter having higher impedance as comppared to the openings; $0,05 \leq \xi \leq 0,25$).

TYPE IV - SEMI-CLOSED WITH A MUFFLER (there are active noise mufflers on the ventilation system passages, reducing noise on its way through them; $\xi \leq 0,25$).

TYPE V - SEMI-CLOSED WITH A SHIELD BEFORE THE VENTILATION PASSAGE (the ventilation passage is protected from the inside by a sound reflecting shield, reducing the sound level $\xi \leq 0,25$).

TYPE VI - COMBINED (the ventilation passages are protected by both active mufflers and shields; $\xi \leq 0,25$).

For the acoustical efficiency estimation we suggest hereafter mentioned method, allowing to consider different structural peculiarities.

This method is based on the Statistical Acoustics Theory with taking into account the energetical principle of the signals summing as well as the sound diffraction resulting from different enclosure elements.

Efficiency estimations of the sound isolating enclosures are made with the following assumptions:

- the resonance phenomena in the enclosed volumes are not to be considered;

- sound sources are considered to be non-coherent sources of signals;

- the sound sources located under the enclosure are considered to be non-directed ones;

- the noise vibration contribution is not considered (the sufficient vibration isolation of the enclosure and of the whole installation is considered to be provided);

- the enclosed volume is characterised by the averaged sound absorption factor ($\bar{\alpha}$):

$$\bar{\alpha} = \alpha_c \cdot S_c + \alpha_{un} \cdot S_{un} + \alpha_{sl} \cdot S_{sl} + \alpha_h \cdot S_h + \alpha_{op} \cdot S_{op} / S_c + S_{un} + S_{sl} + S_h + S_{op} \qquad (2)$$

where: α_c; S_c; α_{un}; S_{un}; α_{sl}; S_{sl}; α_h; S_h; α_{op}; S_{op} are the sound absorption factors and the areas of the inner coated inside surfaces, of the enclosure surface itself, of the inner uncoated inside surfaces, of the slots, holes and openings respectively.

$$\alpha_{sl} = \alpha_h = \alpha_{op} = 1;$$

Let us introduce the following designations:

K is the wave mode, being $K = 2\pi f / c$;

a is an opening of the equivalent size, m;

$$B = \left[\frac{x}{2\pi r^2} + \frac{4U(1-\bar{\alpha})}{\sum_{i=1}^{6} \alpha_i S_i} \right] \cdot (1+r)^2 ;$$

$$F = \left[\frac{x}{2\pi r^2} + \frac{4U}{\sum_{i=1}^{6} \alpha_i S_i} \right] \cdot (1+r)^2 ;$$

$$G = 10^{-0.1 SI} \cdot S_p ;$$

$$T = 0.32 / (\omega^2 / 39 c^2 + 0.7 a^2 / S_{op}^2) ;$$

$$M = 2c^2 S_{op} / [c^2 + 0.7 a^2 \cdot (2\pi f)^2] ;$$

$$H = S_h \cdot \Psi ;$$

$$K_m = 10^{-0.1 \Delta L m} ;$$

$$K_{sh} = 10^{-0.1 \Delta L sh} ;$$

$$\mathcal{D} = S_{sl} \cdot K_{sl} \cdot arc tg \frac{\ell_{sl}}{2} ,$$

where $æ$ is the factor of the nearest acoustical field influence, being dependent on the ratio of the distance between the engine acoustical centre and the specified point r to the maximum dimensions ℓ_{max} of the sound source;

σ is the disturbance factor for the sound field diffuseness;

S_p is the area of the shielding enclosure panel;

SI is the sound isolation of the shielding enclosure surfaces;

Ψ is the sound radiation factor for the hole;

$K_{s\ell}$ is the sound radiation factor for the slot;

K_{sh}; ΔL_{sh}; K_m; ΔL_m are sound conductivity and acoustical efficiency factors for a shield and a muffler respectively.

Considering the designations assumed, the analitical formulae allowing to estimate the sound isolation efficiency for close-fitting enclosures of, for example, a combined type (VI) will be the following:

1) when $f < f_{dif}$; $\kappa a < 1$

$$\Delta L_{enc.} = 10\,\ell g \left\{ \left[æ/2\pi r^2 + 4\sigma(1-\bar{d})/\sum_{i=1}^{n} d_i\,S_i \right] \cdot \left[10^{-0,1SI}\,S_p + \right. \right.$$
$$+ 0{,}32/(\omega^2/39\,c^2 + 0{,}7\,a^2/S_{op}^2) + S_h\cdot\Psi\cdot 10^{-0,1\Delta L_m} +$$
$$\left. \left. + S_{s\ell}\cdot K_{s\ell}\cdot arc\,tg(\ell_{s\ell}/2)\cdot 10^{-0,1\Delta L_{sh}} \right] \cdot \left[1+r \right]^2 \right\}^{-1}, g\,\text{Б} \quad (3)$$

2) when $f < f_{dif}$; $\kappa a \geqslant 1$

$$\Delta L_{enc.} = 10\,\ell g \left\{ \left[æ/2\pi r^2 + 4\sigma(1-\bar{d})/\sum_{i=1}^{n} d_i\,S_i \right] \left[10^{-0,1SI}\,S_p + \right. \right.$$
$$+ 2c^2\,S_{op}/(0{,}7a^2\omega^2 + c^2) + S_h\cdot\Psi\,10^{-0,1\Delta L_m} +$$
$$\left. \left. + S_{s\ell}\,K_{s\ell}\,arctg(\ell_{s\ell}/2)\,10^{-0,1\Delta L_{sh}} \right]\left[1+r \right]^2 \right\}^{-1}, g\,\text{Б} \quad (4)$$

3) when $f \geqslant f_{dif}$; $\kappa a < 1$

$$\Delta L_{enc} = 10\,\ell g \left\{ \left[æ/2\pi r^2 + 4\sigma/\sum_{i=1}^{n} d_i\,S_i \right]\cdot\left[10^{-0,1SI}\,S_p + \right. \right.$$
$$+ S_h\cdot\Psi\cdot 10^{-0,1\Delta h_m} + 0{,}32/(\omega^2/39\,c^2 + 0{,}7\,a^2/S_{op}^2) +$$
$$\left. \left. + S_{s\ell}\cdot K_{s\ell}\cdot arctg(\ell_{s\ell}/2)\cdot 10^{-0,1\Delta L_{sh}} \right]\left[1+r \right]^2 \right\}^{-1}, g\,\text{Б} \quad (5)$$

4) when $f \geqslant f_{dif}$; $\kappa a \geqslant 1$

$$\Delta L_{enc.} = 10 \ell g \left\{ \left[\varkappa / 2\pi r^2 + 4\sigma / \sum_{i=1}^{n} d_i \, S_i \right] \cdot \left[10^{-0,1SI} S_\rho + \right. \right.$$
$$+ 2c^2 \, S_{op} / 0,7 \, a^2 \omega^2 + c^2) + S_h \, \psi \, 10^{-0,1\Delta Lm} +$$
$$\left. \left. + S_{s\ell} \cdot K_{s\ell} \, arc \, tg(\ell_{s\ell}/2) \, 10^{-0,1\Delta Lsh} \right] \left[1 + r \right]^2 \right\}^{-1} , \text{дБ} \qquad (6)$$

The main steps of the enclosure estimation and design are:
setting the required noise level reduction under the enclosure; selection
of the tentative scheme for the enclosure design; selection of the nomen-
clature of the enclosure shielding structures; defining the enclosure
size, shape and location for the ventilation ducts, openings, slots and
holes as well as for the acoustical shields and mufflers to be installed
on them; predictions for the acoustical efficiency of the close-fitting
enclosure of the chosen type; estimation of the thermal parameters for
the enclosed power plant [1].

The predicted estimation of the sound and thermal isolation of the
enclosure may result in specifying some possible characteristics such as:
enclosure dimensions, multiple-layer panels composition in their connec-
tion with the other enclosure elements (mufflers, acoustical shields,
peep-holes and ventilation ducts).

The obtained method for efficiency estimation of the sound isolation
enclosures gave us the possibility to carry out theoretical and experi-
mental investigations concerning the ways of their efficiency increase.
The investigations having been conducted allowed us to define that the
enclosure efficiency depends, first of all, on the following factors:
enclosure tightness degree, coating area of the inside enclosure surfa-
ces, size and shape of the ventilation ducts.

The factors only slightly influenced the enclosure efficiency are:
enclosure dimensions, presence of the protective film on the sound-absor-
btive coating, the thickness of the sound-absorbtive coating.

The main results of the theoretical and experimental investigations
were applied when designing new enclosure structures for movable compres-
sors with diesels using air and water cooling systems as well as with
electrical engines.

The enclosure for the compressor plant with the diesel engine made
of 1,5 mm-thick steel, coated inside by a 40 mm-thick sound-absorbtive
material was produce in accordance with the VI type. The coating area is
75 % of the total enclosing surfaces of the enclosure. Ventilation passa-
ges are made in the form of slots uniformly distributed along the enclo-
sure perimeter and along the hole on the roof. Before the ventilation
ducts there are acoustical shields, in the enclosure openings there are
mufflers in the form of boxes (Fig. 1).

An enclosure for the power plant with the electrical engine was ma-
de in accordance with the IV type. It is manufactured of 1-mm thick
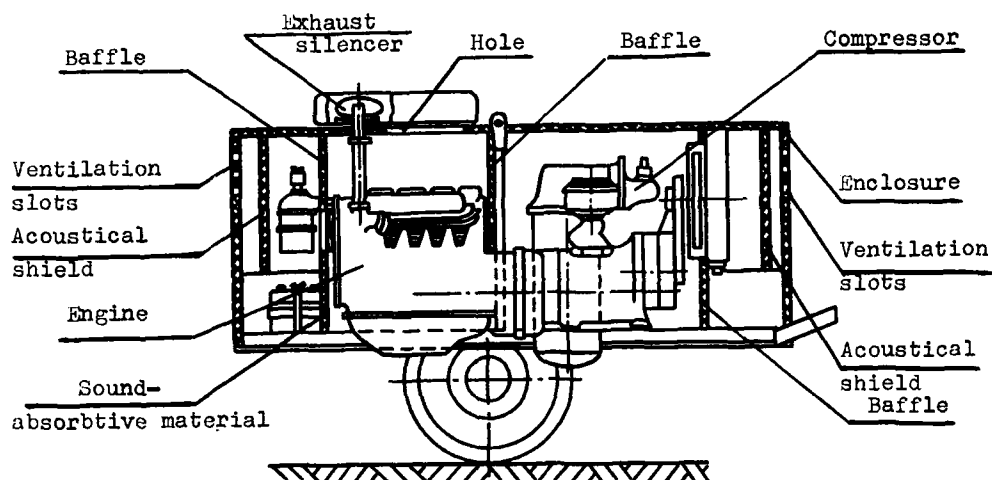
Fig.1. An enclosure for the compressor plant.
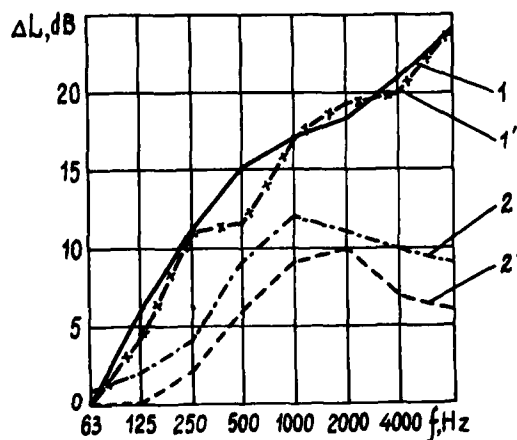
Fig.2. Efficiencies of the enclosures.
1(1') the predicted (experimental)
efficiencies of the enclosures for
compressor with the diesel engine.
2(2') the predicted (experimental)
efficiencies of the enclosures for
compressor with the electrical engine.

steel, coated by sound-absorbtive material. Ventilation ducts are made in the form of holes with the enclosure mufflers being installed on them.

Fig.2 shows the predicted and experimental efficiencies of the estimated enclosures for compressor power plants.

Thus, the obtained classification of constructive estimation for the enclosure schemes allows to select the enclosure type proceeding from the required sound-reduction value and from the thermal exchange facilities available for the given power plant to be enclosed.

The thermal regime estimation allows to define the minimum total area of the ventilation ducts. The theoretical and practical investigations being carried out also allow us to make the proper choice for the cooling surfaces structure, the shape and the location of ventilation ducts, the coating area for the inside enclosure surfaces. The suggested equations for lose-fitting enclosures efficiency may be used for the selected enclosure type in the engineering stage.

REFERENCES

1. Дроздова Л.Ф., Шаров Н.С. Особенности расчетов звукоизолирующих капотов энергетических установок.- В кн.: Проблемы акустической экологии. Сборник научных статей, разд. IУ-У - Л.: Стройиздат,1990 - с.88-93

2. Клюкин И.И. Об оценке эффективности звукоизолирующих кожухов для механизмов и о некоторых способах её увеличения.- В кн.: Труды ЛЭТИ, № 66 - Л.: ЛЭТИ, 1966.- с. 264 - 275

3. Ver I L. Reduction of Noise by Acoustic Euclousures Isolation of Mechanical Vibration Impact and Noise, (J.C) - AEME Design Engineering Technical Conference Cincinnati Ohio, September, 1973.

4. Дроздова Л.Ф. Капоты силовых установок как средство ближней звукоизоляции источников шума - В кн.: Методы и средства снижения шума мелиоративных машин, Серия 5,6, вып.3 - М.: ЦНИИТэстроймаш, 1984 - с. 22 - 33.

SECOND INTERNATIONAL CONGRESS ON RECENT DEVELOPMENTS IN AIR- AND STRUCTURE-BORNE SOUND AND VIBRATION

MARCH 4-6, 1992 AUBURN UNIVERSITY, USA

EXPERIMENTAL RESEARCHES OF AIR- AND STRUCTURE BORNE SOUND OF AGRICULTURAL MACHINES AND TRACTORS

Moissei A. Trakhtenbroit
VISKHOM Acoustic Laboratory
Moscow, 127247
USSR

ABSTRACT

Practical reduction of noise level in the cabins of agricultural machines and tractors below 80 dB(A) requires a thorough methodological approach and delicate experimental researches using special test benches and modern measuring instruments. The paper deals with practical experience and achievements in this direction.

INTRODUCTION

The standard noise level inside the cabins of agricultural machines and tractors established in the USSR at present time is 80 JB(A). However, in order to achieve competitiveness on the world market some factories are already planning to lower the noise level down to 75-76 dB(A).

Despite the fact that at the design stage of the machine necessary calculations are made and most general noise reduction means are introduced into design documentation, it is usually insufficient for obtaining such low noise levels. In most cases it is necessary to carry out an acoustic improvement of the machine test sample, which consists of a series of experimental investigations, united by common methodological approach.

Common methodological principles of the acoustic improvement of the machines, information about necessary test benches and measuring instruments are given below. As an example, the process of acoustic improvement of a grain harvester "Kedr" is shown also.

COMMON METHODOLOGICAL PRINCIPLES OF THE ACOUSTIC IMPROVEMENT

Before the beginning of an acoustic improvement the measurements of sound level and sound pressure levels within octave and/or 1/3 octave bands at particular points in cabin are carried out in the operational regimes of machines established by corresponding standards. These measurements allow to formulate the task of the acoustic improvement by comparison of actual noise parameters with those required by the customer.

The first stage of acoustic improvement includes a complex vibro-acoustic tests of the machine operating in standardized regimes with the aim to determine principal primary and secondary sources of noise as well as the ways of penetration of the same inside the cabin.

The principally basic series of measurements includes:
- measurement of the external acoustic field around the cabin;
- measurement of the internal acoustic field inside the cabin;
- measurement of vibration fields of the cabin panels;
- measurement of difference of vibration on the flexible mounts of the cabin.

The analysis of the results of the above measurements, usually, allows to detect the sources of the noise and the ways of its penetration into the cabin. In questionable cases an additional series of measurements should be carried out, the programme of which can not be specified in advance, since it depends on the results of the preceding measurements.

In the process of additional measurements the methods of successive deduction of different noise sources and of partial disassemble of the machine can be used; noise-reducing devices of different types can be applied, which are useless for practical purposes but can assist the researcher to obtain complementary data for analysis. Thus, besides the measurements of the commonly adopted parameters of noise and vibration, in some cases it appears necessary to measure the sound intensity as well as transfer functions. In any case, the process of additional measurements has an expressly creative character and its success depends, to a large extent, on the intuition and experience of the researcher.

After the principal sources of the noise and the ways of its penetration into the cabin are detected, the second stage of acoustic improvement is carried out, which includes complex stand tests of the cabin and its elements and, if necessary, of other units of the machine with the aim to discover and eliminate their design defects, causing a higher noise level. These tests can be conducted on both non-operating, assembled machine and on its separate, disassembled parts and units, mounted on special test stands.

The stand tests of the cabin and its elements include the following types of measurements:
- determination of sound insulating properties of the cabin and its separate panels by measuring the "apparent" sound insulation;
- determination of the efficiency of sound absorption in the cabin by measuring the reverberation time;
- determination of natural modes and frequencies of oscillations of the air volume in the cabin by measuring transfer functions;
- determination of natural modes and frequencies of oscillations of cabine's panels by means of modal analysis;
- determination of acoustic defects of the cabin by measuring the acoustic intensity;
- determination of the efficiency of flexible mounts of the cabin;
- determination of the efficiency of the noise protecting materials used in the cabin.

As an illustration in Fig 1-7 some stands for the above mentioned tests are shown.

During the stand tests of the cabin some technical improvements and complementary noise-reducing means are developed and introduced in its design, which allow to eliminate the discovered acoustic defects. If necessary, corresponding stand tests of other machine's elements are also carried out and improvements are brought about.

The third stage of the acoustic improvement envisages the tests of the efficiency of the improvements and complementary means of noise reducing introduced in the design, and, if necessary, the final adjustment of the machine is accomplished so, that it can meet the customer's requirements. The tests are realized while the machine is operating in standardized regimes.

First, all the improvements and complementary noise-reducing means developed at the second stage are introduced in the machine's design and the standard measurements of noise level and sound pressure levels within the octave and/or 1/3 octave bands are carried out. If these parameters correspond or are lower than the customer's requirements, the next step is taken. Otherwise, it is necessary to repeat certain steps of the first and second stages of the acoustic improvement with the purpose to eliminate hidden defects which become explicit in the process of noise lowering.

The following step of the third stage is the element-by-element check of the efficiency of each developed improvement in order to determine whether it is worthwhile to introduce it in the machine's design. In this case, the best results are obtained by so-called method of "strip-tease", in the process of which, the efficiency of each improvement is determined by way of its dismount and measurement of the increment value of noise parameters. Before the testing of the efficiency of the next improvement, the former one is mounted on the machine again.

The final result of the acoustic improvement of the machine is a list of improvements, indicating the efficiency of each of them, which enables the customer to choose the most acceptable version from the point of view of his possibilities and price.

EXAMPLE OF ACOUSTIC IMPROVEMENT

An example of the results of the acoustic improvement can be illustrated on the grain harvester "Kedr". The customer set a task to obtain in the cabin, in standard point, a sound level of 78 dB(A) and corresponding levels of sound pressure within the octave bands of frequencies of 31,5-8000 Hz. The problem was solved according to the methodology exposed in preceding section.

During the designing of the test sample the most general measures were taken to reduce the noise in the cabin. The engine, which is usually one of the main sources of noise, was installed at a maximum possible distance from the cabin and, besides, the grain hopper was mounted between the engine and cabin, which served as a sound insulating shield. The cabin was designed in the shape of a hermetically closed capsule, installed on 4 flexible mounts. The metallic parts of the cabin's walls were coated with vibration-damping material and a layer of sound-absorbing material was laid over it, except for the floor, which was covered with sound-insulating rug. The measurements of noise parameters on the test sample of the harvester showed, that the noise level in the cabin's standard point was 82 dB(A), i.e. 4 dB higher than the required one, meanwhile the

sound pressure levels, observed within the octave bands of 125, 250, 500 and 1000 Hz were higher 3, 2, 2 and 4 dB respectively (fig. 8).

The first stage of acoustic improvement consisted in that the harvester was subjected to complex vibro-acoustic tests. The measurements of the acoustic field around the cabin showed, that the main primary noise sources were the working elements, located under the cabin, and, therefore the floor proved to be the most acoustically loaded part of the cabin. The measurements of the internal acoustic field inside the cabin and vibration fields of its panels, also showed, that the floor is the most intensive secondary noise source in the cabin. The measurements of the difference of vibrations on the flexible mounts between chassis and the cabin revealed an explicit defect of the apparent vibration insulation within the frequency range of 100-300 Hz (fig. 9). Thus, it was proved, that the principal ways of penetration of noise into the cabin is the air way - through the floor and structural way - through the cabin flexible mounts.

During the second stage a set of complex stand tests of the cabin was carried out with the purpose to check and eliminate structural faults, causing a higher noise level. The cabin was dismounted from the harvester and installed on a special stand (fig. 1), which allowed to carry out the whole complex of necessary tests.

The first test was aimed at determination and increase of efficiency of sound absorption inside the cabin. In fig. 10 the characteristics of reverberation time in the cabin are given in dependence of the frequency before and after the improvement of sound-absorbing coatings. It is evident, that the efficiency of sound absorption was increased more than by two times within the octave bands of 500 and 1000 Hz, where it was a serious problem, as well as in higher frequencies. .

The next test was fulfilled in order to determine and increase the sound insulation of the floor in the cabin. In fig. 11 the characteristics of "apparent" sound insulation of the floor are given before and after the insulating properties of the rug were improved. At the same time some acoustic holes in the floor were detected and eliminated: the junction between the rear panel and floor and the entrance hole for the lever of gear box. Thus the "apparent" sound insulation of the floor was increased by 1,5-5,0 dB within the range of frequencies of 250-1000 Hz.

The next series of stand tests was aimed at the search and elimination of design defects causing an increased structure-borne noise. The global transfer functions between the principal points of penetration of sound vibration into the cabin and microphone, located near the operator's ear were measured. An example of such a function is given in fig. 12. As a result a higher sensibility of the cabin within the ranges of frequencies of 400-500 and 800-1000 Hz was detected. This proves, that the cabin has defects in its design which lead to increased structure-borne noise in these ranges of frequencies.

Then, the inertance characteristics of the cabin were measured in the points of fastening of flexible mounts. One of such characteristics is given in fig. 13. The inertance characteristic of the cabin flexible mount is also given here for comparison. The proximity of their values in the range of frequencies of 100-280 Hz accounts for vibroinsulation defect, detected during the natural tests.

Afterwards a modal analysis of the cabin was realized in 123 points, which revealed the elements of the cabin with the biggest dynamic deformations. These elements turned out to be the profiles located under the floor, cabin mount brackets and the depression under the seat. These elements are the most active in natural modes of the cabin oscillations with frequencies of 182, 220, 278 and 318 Hz. As an example in fig. 14 the deformations of the cabin's floor, rear wall and roof at the frequency of 182 Hz are given. Following the results of the modal analysis the mount brackets of the cabin were reinforced and the dynamic rigidity of proper mounts was reduced by means of slits cut in the rubber elements. The results are illustrated in fig. 15. One can see, that the difference between the inertances substantially increased, which should raise considerably the efficiency of vibration insulation. Afterwards, the profiles under the floor and the depression under the seat were also reinforced.

In fig. 16 the results of lowering of the noise inside the cabin within the octave bands of 125-1000 Hz are given due to the consecutive introduction of the developed structural improvements.

In fig. 8 the final results of the work are given. It is easily noted, that the sound level is lowered down to 77 dB(A) and the sound pressure levels in octave bands of 125, 250, 500 and 1000 Hz are reduced to 89, 79, 74 and 70 dB respectively, which are lower than the required by the customer.

CONCLUSION

The information given in this report shows the possibilities of thorough methodological approach to the problem of practical lowering of air- and structure borne noise in agricultural machines and tractors, which is used in the Acoustic Laboratory of VISKHOM. In combination with modern measuring and analytical equipment, specially developed test stands this method is a powerful tool for acoustic improvement of the machines meeting the technical specifications of the customers. The Acoustic Laboratory is ready for mutually beneficial cooperation with foreign manufacturers of machines, noise-reducing materials as well as with laboratories engaged in applied acoustic researches.

495

Fig.1 Stand for complex tests of cabins
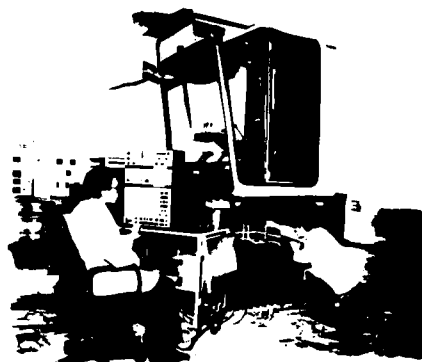
Fig.2 Stand for measurements of the sound insulation of cabin panels

Fig.3 Stand for modal analysis of the cabin
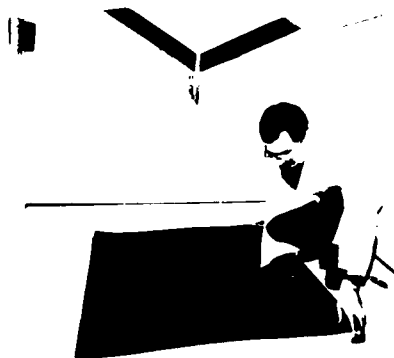
Fig.4 Stand for tests of sound-absorbing materials in reverberation mini-chamber

Fig.5 Stand for tests of vibration damping materials

Fig.6 Stand for tests of sound-insulating materials and structures

Fig.7 Stand for tests of flexible mounts
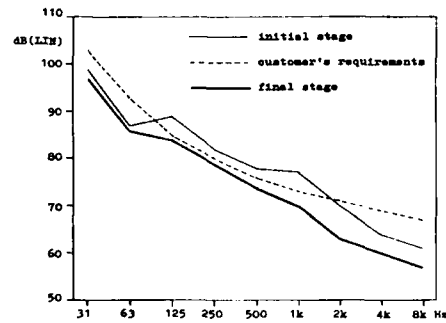
Fig.8 Noise parameters in the cabin of the combine "Kedr" before and after acoustic improvements
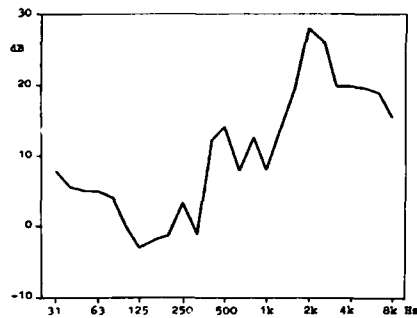
Fig.9 Difference of vertical vibration levels on the flexible mount between chassis and cabin
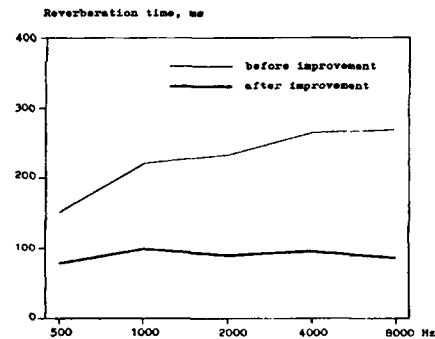
Fig.10 Reverberation time in the cabin before and after the improvement of sound absorbing coatings
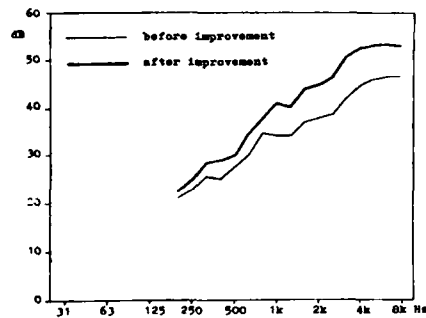
Fig.11 "Apparent" sound insulation of cabin floor before and after improvement of sound insulating rug
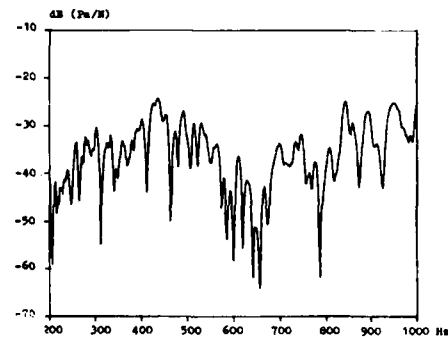
Fig.12 Global transfer function between the flexible mount fastening point and microphone near operator's ear

497
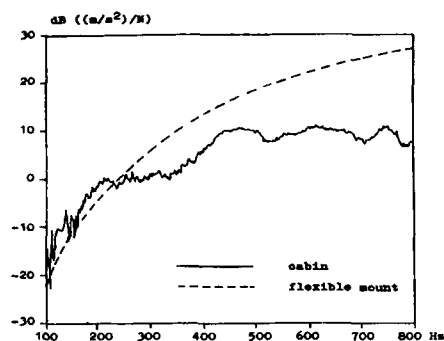
Fig.13 Inertance characteristics of the cabin in the flexible mount fastening point and of the mount itself before the introduction of structural improvements
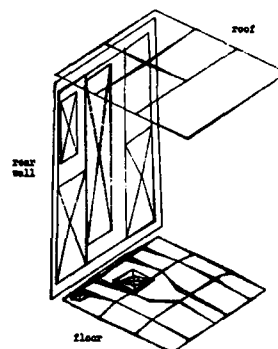
Fig.14 Example of the modal analysis of the cabin
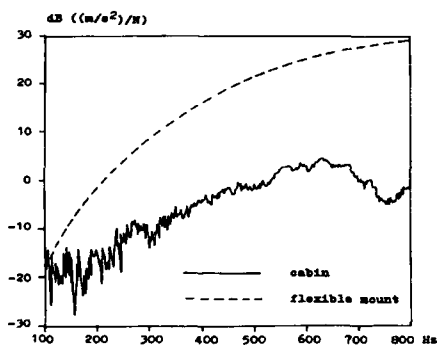
Fig.15 Inertance characteristics of the cabin in the flexible mount fastening point and of the mount itself after the introduction of structural improvements
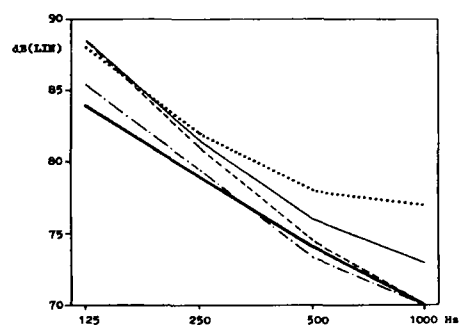
Fig.16 Lowering of noise level in the cabin of the combine "Kedr" with gradual introduction of constructive improvements

.... initial stage
——— intermediate solution (improvement of sound absorbing coatings)
— — — intermediate solution (improvement of sound insulation of the floor)
—·—·— intermediate solution (improvement of vibration insulation)
▬▬▬ final stage (reinforcement of the floor elements)

TIME DOMAIN APPROACH OF FLUID STRUCTURE INTERACTION PHENOMENAS APPLICATION TO SATELLITE STRUCTURES

D. VAUCHER de la CROIX   C.CLERC   J.M.PAROT

METRAVIB R.D.S.   METRAVIB R.D.S.   IMDYS
64, chemin des Mouilles   64, Chemin des Mouilles   Av. de Lamothe
F - 69130 ECULLY   F - 69130 ECULLY   F - 43100 BRIOUDE

ABSTRACT -

The aim of the title subject is to present an original approach combining Finite Elements and Integral Equations for solving coupled problems related to spatial structures.

Based on the fact that the interaction is moderate, the proposed method consists in a time domain calculation coupling two independant kernels , a structural and an acoustical one, in an iterative scheme. The successive resolution of their relevant equations furnishes exact interaction results with very few iterations. Preliminary requirements are the modal characteristics of the structure which can be obtained by means of any classical finite element code.

The developed code, named ASTRYD-C, has been first applied to the response analysis of a test sandwich panel in air. The recent development of a new acoustic element, suited for thin surface description, improved the accuracy of the obtained results and allowed a significant reduction of computational time.

I. INTRODUCTION -

For recent years, METRAVIB R.D.S. has been involved with industrial problems where the coupling effects between acoustics and vibrations could no more be ignored. Striking examples are encountered in the automotive and aeronautical industries (interior noise evaluation in vehicles or in aircraft cabins,...).

Another field of interest concerns spatial applications. In a context where experimental test studies are very expensive, the need for modelization techniques dedicated to fluid/structure interactions is growing. Indeed, spatial structures (ie. satellite structures and related components) become thiner and lighter than they ever were. Consequently, their sensitivity to any kind of sollicitation increases. Particularly during launching, acoustical sollicitations reach so high levels that damages could result on the satellite structure. In order to predict and possibly prevent such damages, it is necessary to estimate acceleration levels, especially at the fixation points of the various attached equipments.
In the respect fluid/structure interaction modelling can be very helpful towards a better understanding of the dynamical behavior of such structures submitted to very adverse environment conditions.

The proposed method belongs to a class of modelling techniques which couples Finite Elements with Integral Equations. However, it incorporates two essential innovations in order to allow computations in the middle frequency range without excessive CPU time increase.

499

First, the time domain approach reveals well suited to wide frequency band response problems. Indeed, it has been shown that limiting the computed results to the early times sequence did not sensitively affect the response bandspectra, except in the very low frequency region. So short time interval computations contribute reducing the total computational costs.

Moreover, the presence of a light fluid (air) produces only a moderate coupling on the structure. An iterative procedure coupling two independant kernels (describing the acoustical and structural behavior successively) is then well suited. It avoids the time consuming task of inverting strongly coupled operators as they generally appear in frequency domain methods.

The sandwich panel example discussed hereafter has been considered first for simplicity. It constitutes an excellent test case for the proposed method to be validated. After recalling some results obtained with a 3-dimensional panel geometry (finite thickness [1]), we expose new results computed in the framework of a so-called thin surface formulation.

Confrontation with measurements demonstrates the capabilities of the ASTRYD code to predict typical coupled effects that cannot be neglected.

II. FLUID/STRUCTURE COUPLING IN THE TIME DOMAIN -

II.1. Classical impenetrable acoustic elements -

As stated in the introduction, the time domain approach appears is a good compromise to evaluate fluid/structure coupling effects when these are moderate. This is typically the case for light structures in air (few hundreds g/m² to few kg/m² surface mass). Then, an iterative coupling scheme can be applied to the resolution of such problems (as was first pointed out by PARK and co-authors in refs [2-4]), advantageously replacing strong coupling algorithms. In fact, the approach implemented in the ASTRYD-C code provides an efficient way to reach the middle frequency range without exceeding computational costs.

The proposed method consists in coupling two independant kernels, a structural and an acoustical one. In fact, this relative independance has made possible to build the structural part (time domain resolution of the mechanical equations) into the original ASTRYD code developed by **METRAVIB R.D.S.** [5-7].

ASTRYD is based on a classical KIRCHHOFF's formulation (retarded potential technique). A large variety of problems in general linear acoustics can be handled with this code and a specific paper has been dedicated to its applications for solving industrial problems [8].

The generic integral equation to be solved in order to obtain the sound pressure field p on the surface of a 3-dimensional structure of arbitrary shape reads :

$$2\Pi \ p(M_0, t_0) = \int_\Sigma \ [p^* \text{grad} \ (1/d) \ - \ (1/cd) \ \dot{p}^* \text{grad} \ d] \ n_M \ d\sigma \qquad (1)$$

$$+ \ 4\Pi \sum_k S_k^*/r_k \ + \ \rho_0 \int_\Sigma w^*/d \ d\sigma)$$

where
M_0 = Calculation point on Σ
M = Arbitrary point on Σ
Q_k = Location of the kth acoustic pressure point source S_k
d = $|MM_0|$, $r_k = |Q_k M_0|$
n_M = outward normal vector to Σ in M.

The asterisc means that the corresponding variable has to be evaluated at the retarded time $\tau = t_0-d/c$ or $\tau_k = t_0 - r_k/c$, and the point denotes time derivative.

For purely acoustical radiation problems, the acceleration term w specifies the movement of the surface Σ (or part of it). This term is omitted when diffraction problems are considered.

For coupled problems however, it is always present : w expresses the vibrational behavior of the studied structure. When strongly coupled to the acoustics, the structural kernel cannot be solved separately. But, in the moderate coupling case, an independant resolution of both kernels (coupled only through the iterative algorithm exposed hereafter) leads to the correct solution. Formally the proposed approach can be expressed as follows. Quite generally, the dynamical behavior of the coupled fluid/structure system is described by operators, say L for the structural part and R for the acoustics. Using these notations, the following system of equations must be solved :

$$Lw = f \qquad (2)$$
$$p = Rw \qquad (3)$$

with w = normal surface acceleration
      p = surface pressure
      f = density of applied exterior forces.

Whenever f represents the unique sollicitations, the coupled problem is written :

$$(L-R)\, w = f \qquad (4)$$

If the moderate coupling assumption is valid, the time consuming task of inverting the operator $(L-R)$ can be avoided and the solution of (4) is obtained in form of a NEUMAN series. Explicitely, this relation corresponds to following iterative procedure :

$$w = \left\{ I + \sum_{k=1}^{\infty} (L^{-1}R)^k \right\} L^{-1} f \qquad (5)$$

At each time step, the relevant equations describing the vibrational and acoustic behavior of the structure are successively solved until convergence is achieved.
The convergence criterion applied in ASTRYD-C is expressed in terms of pressure variables. Successively iterated pressure field evaluations are compared until following global condition is fulfilled :

$$\sum_i \left| P_i^{(k)} - P_i^{(k-1)} \right|^2 / \sum_i \left| P_i^{(k-1)} \right|^2 < \varepsilon^2 \qquad (6)$$

Typical values for the parameter ε are 10^{-3}-10^{-4}, which allows the converged solution $p_i(t)$ to be obtained in few iterations at each time step (usually 4 to 5 for the studied panel).

II.1. _Thin surface element approach_ -

Although the original approach gave promising results (cf. [1]), it is poorly suited to handle coupled problems where the considered structures include acoustic cavities. A correct treatment of such problems with the classical approach (impenetrable acoustic elements) would require a double layer structure meshing : one adressing the exterior problem and the other one the interior problem. This means a substantial increase in the computational costs compared to a single layer meshing method. This is precisely the motivation for developing a so-called thin surface approach of fluid/structure coupled problems.

In this new formulation, we consider two pressure variables namely the mean surface pressure $\bar{p}$ and the pressure differential Δp, related to the external surface pressure p_e and internal surface pressure p_i through

$$\bar{p} = (p_e + p_i)/2 \qquad (7)$$
$$\Delta p = p_e - p_i$$

If the structure's surface Σ is divided into two parts, Σ_e and Σ_i so that $\Sigma = \Sigma_e \cup \Sigma_i$, it appears that both p_e and p_i are present in the KIRCHHOFF's integral equation (1). The reason why the variables defined by relations (7) are preferred to the couple (p_e, p_i) is that they satisfy a set of **uncoupled** integral equations. In the special case of plane geometry, some simplifications occur and the final form of the equations to be solved is following :

$$- 4\Pi \rho_0\, w\, (M_0, t_0) = F.P. \int_{\Sigma} \{ \Delta p^*/d^3 + \Delta \dot{p}^*/(cd^2) \}\, d\sigma \qquad (8a)$$

$$+ 4\Pi \sum_k (1/r_k)\, (\delta r_k/\delta n_{Mo})\, (\dot{S}_k^*/c + S_k^*/r) $$

$$\bar{p} = \sum_k S_k^*/r_k \qquad (8b)$$

where all the occuring symbol have the same meaning as in (1). F.P. stands for "finite part of the integral" because of the singularities that need to be integrated. When considering only the associated diffraction problem (purely acoustical application, vanishing w field), these equations have recently been discussed by KAWAI and TERAI [9].

In a first step, the results presented by these authors have been considered as a test example for the validation of the formulation implemented in ASTRYD.

Then, the coupled panel problem has been treated in this framework. It is apparent from (8a) that the form of the acoustical operator R is somewhat different from the one resultant from the integral equation (1). However, this doesn't affect the validity of the iterative procedure exposed above. The fact that the acceleration (= structural) term don't include retarded time contributions anymore simply saves some computational time. Convergence of the whole procedure is achieved with a rate comparable to the approach based on the solution of integral equation (1).

III. STUDIED CONFIGURATIONS -

The considered structure is a sandwich panel typical for spatial applications. Its material characteristics are :

Faceplates   :   Aluminium 2024
                   Thickness 0.4 mm
                   Density 2770 kg/m^3
                   Young's modulus 73 GPa
                   Poisson's ratio 0.33

Core   :   Honeycomb 5056 6/36
                   Thickness 19.2 mm
                   Density 40 kg/m^3
                   Coulomb's moduli
                        G_{xz} = 215 MPa
                        G_{yz} = 110 MPa

Dimensions   :   2.50 m x 1.60 m, total thickness 20 mm.

Two types of boundary conditions have been analyzed : all edges simply supported and free edges. For both configurations, a preliminary computation (analytical or FE model) delivers the corresponding modal basis, the knowledge of which is required to solve the structural equations in the time domain.

Typical results obtained with ASTRYD-C are discussed in the next paragraph and compared with experimental data.

IV. NUMERICAL RESULTS - COMPARISON WITH EXPERIMENTAL DATA -

The panel configurations offer two advantages : they are relatively simple to handle (and consequently well suited for validation purposes) and allow corresponding experimental tests to be performed. In this study, mechanical (point force sollicitation), modal characteristics (measurements) and acoustic (radiated pressure measurements in anechoic room) tests were conducted.

IV.1. Vibration results -

Two types of results have been analyzed :

   • transfer spectra (mean values of the normal acceleration)
   • related eigenfrequencies modal shapes.

The frequency spectrum associated with the point force time profile covers the range 0-500 Hz. Consequently, the Fourier Transforms of the time-domain results delivered by ASTRYD-C are analyzed in this frequency band.

Figure 1 illustrates typical coupling effects due to the action of the ambiant fluid (air) on the structural behavior. Frequency shifts between 4 % and 14 % vs. in vacuo eigenfrequencies have been correctly reproduced, as clearly appears from Table 1, where a comparison between observed and calculated values is summarized.

502

It is here particularly interesting to point out that the thin surface approach improved the accuracy of previously obtained results, with a significant reduction of total computational time. Indeed the CPU time required to run the iterative procedure on the finer case (192 triangular elements meshing) is about one order of magnitude smaller that the time corresponding to the associated volume meshing (thick plate with 464 elements).

Figure 2 gives a complementary comparison between model and experimentation. This typical example of a couple of modal shapes is representative of the good concordance between numerical and measured acceleration fields on the panel surface. In every case, the location of the point force sollicitation has been eccentered so that a maximum number of modes could be as clearly identified as the one presented here.

IV.2. Radiation results -

Once ASTRYD-C has evaluated the pressure response on the surface of the studied panel, a classical HELMHOLTZ integral formulation leads to radiated pressure values in every point located in the fluid.

It is particularly interesting to concentrate on the frequency evolution of the plate radiation efficiency σ_{rad}. This quantity is defined as a non-dimensional ratio of the radiated power to the quadratic velocity of the plate.

Figure 3 illustrates the incidence of the boundary conditions on σ_{rad}. In the low frequency region, the simply supported plate shows as expected, a higher radiation efficiency. The differences between the two curves reduce as the frequency is increased and above coincidence frequency (450 Hz) practically no incidence of the boundary conditions is noticed. These properties have been recently discussed on the example of rigid plates [10].

The results obtained by ASTRYD-C for thin plates where coupling effects are taken into account lead to very similar conclusions. Figure 4 confirms this fact (direct comparison between rigid and coupled results in the case of simply supported edges). Except in the very low frequency range (f < 10 Hz for mode (2,1)), the comparison of our results with [10] is excellent.

Other typical phenomenas like the increase of radiation damping near the coincidence frequency have also been recovered with ASTRYD-C , no matter the formulation ("thick" or thin plate description)..
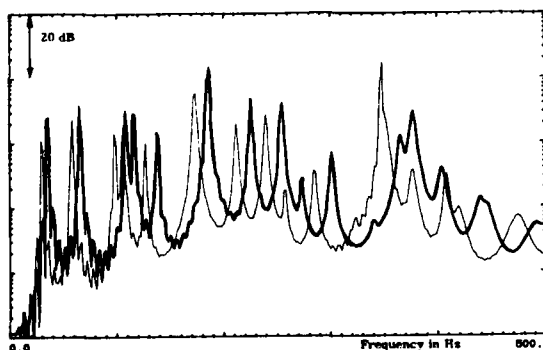
FIGURE 1 :

Typical calculated response spectra on the panel (mean values of normal surface acceleration)
— *simply supported panel in vacuo*
— *simply supported panel in air*

IN VACUO	IN AIR (1)	IN AIR (2)	MEASURES
35.4	31	30	28.5
65.9	61	59	59
108.7	104	100	108
116.4	111	106	112
138.6	133	127	134
181.1	180	175	180
226.0	215	213	223
254.7	243	240	249
274.0	261	260	261
302.2	289	285	288
341.9	326	320	312
397.7	357	349	351

TABLE 1 :

12 first modal frequencies related to the test sandwich panel

Simply supported edges - no additional equipment

(1) ASTRYD-C with 3 dim plate description

(2) ASTRYD-C with thin surface approach

503
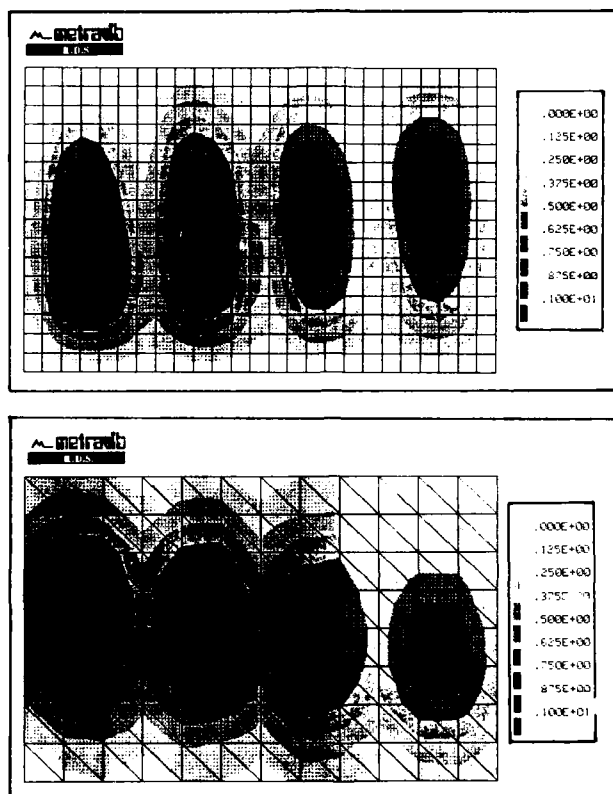
FIGURE 2 : *Couple of modal shapes comparing numerical and experimental results*
Normal surface acceleration - Simply supported panel
Measures   : f = 180 Hz
ASTRYD-C   : f = 175 Hz
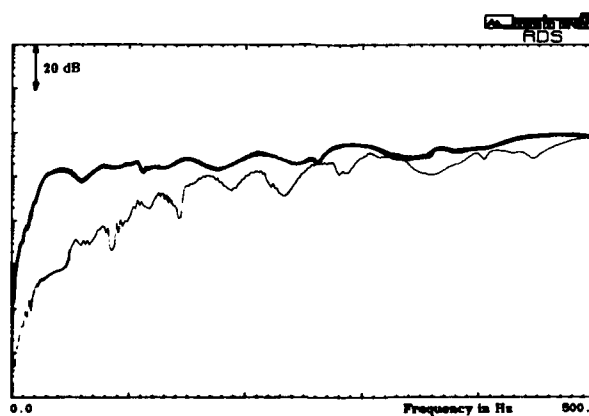
FIGURE 3 : *Global radiation efficiencies* σ_{rad}
Influence of the boundary conditions
——— simply supported edges
——— free edges
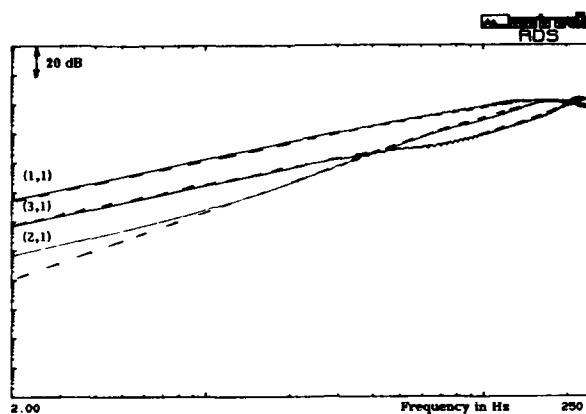
FIGURE 4 : *Single mode radiation efficiencies*
(successively modes (1,1) , (2,1) and (3,1)
Broken lines give comparison with rigid panel results [10]

V. CONCLUSION -

An original method has been presented, which is dedicated to fluid/structure interaction phenomenas. This innovative approach is particularly suited to the analysis of light structures in air, where the ambiant fluid does not strongly affect the structural behavior. Based on this assumption, an iterative coupling scheme has been developed and tested in the case of a panel structure typical for spatial applications.

The introduction of a new type of acoustical elements (so-called thin surface description) improved both accuracy and computational efficiency versus previously obtained results within the same general framework.

Comparisons between numerical and experimental results demonstrate the capabilities of ASTRYD-C to predict typical coupling effects (between 4 % and 14 % frequency shifts) on light structures in air. The proposed iterative approach seems to be promising for middle frequency calculations. And the thin surface description will enable 3-dimensional structures including acoustical cavities to be considered.

VI. ACKNOWLEDGMENTS -

505

VII. BIBLIOGRAPHIC REFERENCES -

[1].   D.VAUCHER de la CROIX, L.PERRET, J.M.PAROT
        "Fluid/Structure interaction applied to the analysis of a test sandwich panel
        typical for spatial applications".
        International Conference on Spacecraft Structures and Mechanical Testing
        ESA/CNES/DLR - NOORDWIJK - 24-26/04/91 -

[2].   K.C.PARK, C.A. FELIPPA, J.A. DE RUNTZ
        "Stabilization of staggered solution procedures for fluid-structure
        interaction analysis".
        T.BELYTSCHKO & T.L.GEERS
        Computational methods for fluid-structure interaction problems
        (A.S.M.E., A.M;D.-vol.26,1977,94-124)

[3].   C.A. FELIPPA, K.C. PARK
        "Staggered transient analysis procedures for coupled mechanical systems :
        formulation".
        Computers methods in applied mechanics and engineering 24
        (1980) - 61-111.

[4].   C.A. FELIPPA, K.C. PARK
        "Recent developments in coupled field analysis methods.
        Numerical methods in coupled systems".
        Edited by R.W. LEWIS et E.HINTON (1984)
        J.WILEY & SONS

[5].   P.AILLAUD, P.VERPEAUX, J.M.PAROT, B.BARBE
        "Calcul de diffraction d'onde par un corps de forme quelconque".
        11th International Congress on Acoustics-PARIS 1983

[6].   J.M.PAROT, D.VAUCHER de la CROIX, S.GRIOTIER
        NUMETA'87, SWANSEA 87- 3-dim
        "Acoustics of rigid or moving surfaces integral formulation
        explicit time scheme and subsequent frequency analysis".
        NUMETA'87 - SWANSEA 1987 -

[7].   J.M.PAROT, D.VAUCHER de la CROIX
        "Farfield and radiation calculations by means of a time domain
        integral equation formulation".
        INTER NOISE'88, AVIGNON 88

[8].   C.CLERC, D.VAUCHER de la CROIX
        "Space Time Analysis of Sound Radiation and Scattering"
        Air/structure borne sound and vibration Congress
        AUBURN, 4-6/03/92

[9].   Y.KAWAI, T.TERAI
        A numerical method for the calculation of transient acoustic scattering from thin rigid plates
        J.Sound Vib. 141 (1) , 1990

[10].   A.BERRY, J.L. GUYADER, J.NICOLAS
        "A general formulation for the sound radiation from rectangular
        baffled plates with arbitrary boundary conditions".
        J. Acoust. Soc. Am, 88 (6) , December 1990.
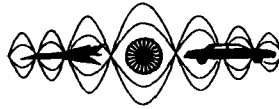
ACOUSTICS OF SHELLS WITH INTERNAL STRUCTURAL LOADING

Y. P. Guo

Department of Ocean Engineering
Massachusetts Institute of Technology
Cambridge, MA 02139, USA

ABSTRACT

An elastic shell has unique acoustic properties because of its ability to support elastic waves which may be strongly coupled to the acoustic field outside the shell. When such a shell is loaded with internal structures, its acoustic features become even richer. On the one hand, the structural loading may interact with the shell waves, changing their coupling efficiency to the acoustic field and hence altering the radiation/scattering characteristics of the shell. On the other hand, the internal structures may be resonantly excited, resulting in direct coupling between the acoustic field and the internals, which imprints the resonance signature of the internals in the acoustic field. In both cases, the acoustics of the loaded shell may be quite different from that of an empty shell. In this paper, the acoustic effects of internal structural loading is examined analytically by developing a theory that leads to explicit solutions for both the sound field and the vibrations of the loaded shell. The dependence of the acoustic field on frequency, structural loading strength, loading location and attachment style is discussed, and the dominant mechanisms that control the radiation/scattering process are identified in different parameter and spatial domains.

1. INTRODUCTION

During the past few decades, there has been quite extensive research on vibrational and acoustical properties of fluid loaded elastic shells. These studies have revealed very interesting features concerning the coupling between the shell and the surrounding fluid. Owing to these studies, the acoustic radiation/scattering characteristics of homogeneous shells have been quite thoroughly understood, especially in the low to intermediate frequency domain for shells of thickness small compared with both the overall dimension of the structure and the acoustic wavelength; these shells

can be considered as both geometrically and acoustically thin. On the other hand, for shells with some kind of discontinuity, either due to changes in the shell material or because of the attachment of internal structures, the problem is much less satisfactorily addressed, though there has been considerable interests in internally loaded shells in recent years.

An elastic shell has interesting acoustic properties because it can support elastic waves. For a homogeneous shell, these waves are strongly coupled to the acoustic field if they have supersonic phase speed; the energy in the elastic waves can then leak to the surrounding fluid as sound. For shells with internal structural loading, the coupling between the shell and the acoustic medium becomes even stronger because in this case, the subsonic components of the elastic waves are also strongly radiating, through their interactions with the structural discontinuities due to the attachment of the internals. These interactions have most profound effects on the acoustic field when they form resonances; the signatures of the empty shell are then entirely buried in the much stronger resonances. Therefore, the studies on the acoustic properties of internally loaded shells can be regarded as being mainly concerned with the conditions under which the loaded structures cause strong resonances, and hence, significantly alter the scattering/radiation characteristics of the shell.

In this paper, a theoretical study is presented, which starts with developing a formal solution for internally loaded elastic shells, including the acoustic field and the vibrational response of the shell. The solution is then used to analyze the effects of the internal structures on the acoustic field, with emphasis on the differences between empty shells and loaded shells. While the theory can easily accommodate both scattering and radiation problems, detailed results are given for the scattering of incident plane waves. In particular, analyzed is the dependence of the internal loading effects on the incidence frequency, the incidence angle, the attachment locations of the internals, the attachment style and the loading strength. The conclusions are drawn from a systematical study reported in Ref. [1-5]; details can be found in these papers.

2. FORMULATION AND SOLUTION

Consider an acoustic medium of mean density ρ_0 and sound speed c_0. By combining the conservation laws of mass and momentum, it is easy to derive the governing equation for the pressure fluctuation p,

$$\nabla^2 p + k^2 p = i\omega q + \nabla \cdot \mathbf{f}, \tag{1}$$

where $k = \omega/c_0$ is the acoustic wavenumber with ω denoting the angular frequency in the time harmonic factor $\exp(-i\omega t)$ which is here and henceforth suppressed, and q and $\mathbf{f}$ are respectively the source and the force distribution, acting as driving terms to the acoustic medium. Suppose that a cylindrical shell of mean radius a is embedded in the acoustic medium with its center coinciding with the origin of the cylindrical coordinate system (r, θ), and that the force distribution $\mathbf{f}$ is located on the shell surface $r = a$ so that

$$\mathbf{f}(r, \theta) = [f_r(\theta)\mathbf{e}_r + f_\theta(\theta)\mathbf{e}_\theta]\delta(r - a), \tag{2}$$

where f_r and f_θ are components of the force distribution respectively in the radial and the circumferential direction with e_r and e_θ being the unit coordinate vectors, and δ is the Dirac delta function. Thus, the equation (1) can be easily solved by the Green function technique. The solution is simply

$$p(r,\theta) = p_0(r,\theta) - \int_0^{2\pi} \left[f_r(\theta_0) \frac{\partial G}{\partial r_0} + f_\theta(\theta_0) \frac{1}{a} \frac{\partial G}{\partial \theta_0} \right] a d\theta_0, \qquad (3)$$

where

$$p_0(r,\theta) = i\omega \int q(r_0,\theta_0) G(r,\theta;r_0,\theta_0) a dr_0 d\theta_0, \qquad (4)$$

is the field due to the source distribution q and the integrand of the second term in (3) is evaluated at $r_0 \to a$ with (r_0, θ_0) denoting the source coordinates.

The formal solution (3) is actually the familiar Kirchoff representation of the wave equation (1) in term of the Green function G. Depending on the choice of the Green function, this representation can be reduced to integral equations of varying degree of complexity. Since the empty shell problem has been extensively studied in the past, it is convenient to choose G to be the Green function for a fluid loaded empty shell. In this case, the forces f_r and f_θ are entirely due to the structural loading inside the shell (if G is chosen to be the free space Green function, these forces also contain pressure forces due to fluid). Also, with this choice, p_0 becomes the solution for an empty shell and the integral in (3) is the field due to the internal structures. Thus, by following the procedure described in [2] with the coupling forces expended for the cases of small size attachment, the solution (3) reduces to

$$p(r,\theta) = p_0(r,\theta) - \sum_{j=1}^{N} \left[F_r^{(j)} \frac{\partial G}{\partial r_0} + F_\theta^{(j)} \frac{1}{a} \frac{\partial G}{\partial \theta_0} + M^{(j)} \frac{1}{a} \frac{\partial^2 G}{\partial r_0 \partial \theta_0} \right], \qquad (5)$$

where, $F_r^{(j)}$, $F_\theta^{(j)}$ and $M^{(j)}$ are respectively the radial force, the tangential force and the bending moment at the jth attachment point with $j = 1, 2, \cdots, N$ indicating that there are N discrete attachment points on the shell surface.

The coupling forces and bending moments are unknown quantities at this stage; they must be found by considering the dynamic balance at the attachment points, which requires the solutions of the internal structures. In linear theory, the internal structures can always be described by a set of linear equations, similar to the wave equation (1), with the coupling forces and bending moments as driving terms. Thus, the solutions for the internal structures can be symbolically written as

$$X = X[F_r^{(j)}, F_\theta^{(j)}, M^{(j)}] \quad \text{and} \quad Y = Y[F_r^{(j)}, F_\theta^{(j)}, M^{(j)}], \qquad (6)$$

where X and Y are the displacement components of the internal structures. These solutions can be related to the solution (5) by invoking the kinematic conditions at the attachment points, the equal displacement condition for example. This can be done because the pressure p is related to the shell displacements by the momentum

equations. For different attachment conditions, the dynamic balance gives different values for the coupling forces and bending moments. However, the procedure for deriving these quantities for all the cases is the same and is straightforward. When all these are done, the pressure (5) becomes an explicit solution.

The solution (5) for the pressure fluctuation can be cast into another convenient form that emphasizes different kinds of effects. By invoking kinematic conditions at the attachment points, the coupling forces and bending moments are actually found by solving a set of algebraic equations. Thus, the solution can be written in terms of matrices as

$$p(r,\theta) = p_0(r,\theta) + \mathbf{C}(\mathbf{I} - \mu\mathbf{HC})^{-1}\mathbf{U}^{(0)} \cdot \mathbf{G}. \tag{7}$$

Here, μ is a numerical constant, $\mathbf{I}$, $\mathbf{C}$ and $\mathbf{H}$ are matrices and $\mathbf{G}$ and $\mathbf{U}^{(0)}$ are vectors (see [3] for detailed definitions). Of particular concern here are the matrices $\mathbf{C}$ and $\mathbf{H}$ which respectively represent the dynamic and geometric effects of internal loading; the former is determined by the dynamics of the internals while the latter by the locations of the attachment points.

3. SOME DIRECT ANALYSES

Though the results (5) and (7) are explicit solutions which can be easily evaluated, some conclusions can be drawn from these solutions by direct analyses without any numerical calculation. Two examples are given in this section. The first concerns the relative importance of the coupling forces and the bending moments in the solution (5). This is of practical interest in determining the difference in the acoustic effects between pinned attachment and clamped attachment. At the jth attachment, the internal loading effects are given by the three terms in the summation in (5), respectively representing the contribution from the radial force, the tangential force and the bending moment. The relative magnitude of these three terms can be assessed by dimensional analysis. By noting that the empty shell Green function G varies on the lengthscale of the acoustic wavelength, namely, the inverse of the acoustic wavenumber k, it is clear that the ratio of the three terms are

$$kF_r^{(j)}\Big/ \frac{1}{a}F_\theta^{(j)}\Big/ \frac{k}{a}M^{(j)}. \tag{8}$$

On assuming that the internal structures are consist of elastic plates of the same material as the shell, and making use of the definitions for the forces and bending moments in elastic plates, the result (8) can be simplified in terms of the flexural wavenumber β as

$$k\beta\sin\theta_j\Big/ \frac{\beta}{a}\cos\theta_j\Big/ \frac{k}{a}, \tag{9}$$

where θ_j is the attachment angle at the jth connection. From this, the relative magnitude of the moment contribution, respectively in reference to that from the radial force and the tangential force, are given by

$$\frac{1}{\beta a\sin\theta_j} \quad \text{and} \quad \frac{k}{\beta\cos\theta_j}. \tag{10}$$

By using the definition for the flexural wavenumber β, it can be shown that at least one of the two ratios is much less than unity for thin shells in the low and mid-frequency domain, indicating that bending moments play a less important role in the scattering process.

The second example reveals the dependence of the internal loading effects on the loading strength, which, for the case of a single elastic plate, can be measured in terms of the thickness of the plate, in comparison with that of the shell. This can be done very conveniently by using the matrix expression (7). In this case, it can be shown that the elements of the dynamic matrix C are all proportional to the thickness of the plate. Thus, for a thin plate, the dynamic matrix is proportionally small so that the second term in the bracket in (7) can be neglected compared with the unity diagonal matrix I. The solution (7) then reduces to

$$p(r,\theta) = p_0(r,\theta) + CU^{(0)} \cdot G, \tag{11}$$

which states that the internal loading effects are directly related to the dynamic properties of the internals. Hence, the resonance properties of the internal system are directly imprinted in the acoustic field. On the other hand, for relatively thick plates, the dynamic matrix assumes large values and the unity matrix in (7) can be ignored, which leads to

$$p(r,\theta) = p_0(r,\theta) - (\mu H)^{-1}U^{(0)} \cdot G. \tag{12}$$

This shows that the loading effects are all geometrical in that the acoustic field is completely independent of the dynamics of the internals. It is the attachment locations that determine the contribution from the internal loading.

4. CALCULATION AND RESULTS

The solution (5) gives the pressure fluctuation generated by the source distribution q in the acoustic medium which contains the internally loaded shell. The effects of the internals are given by the coupling forces and bending moments, while the effects of the fluid loaded elastic shell are all contained in the Green function G. This solution can be used to study both the radiation and the scattering properties of the loaded shell by taking proper limit for the source distribution. A thorough analysis is given in [3-5] for the case of scattering of plane acoustic waves by a shell with various forms of internal structures. This corresponds to the limit of a point source located at infinity (far away from the shell). In the following, the main conclusions of that analysis are summarized here to reveal the effects of the internal structural loading on the scattered field.

The first issue we discussed is the frequency dependence of the internal loading effects. Internal loading has profound effects on the scattered field in the low and mid-frequency domain for almost all kinds of internal structures. The effects are in the form of deeply scalloped form function; for an empty shell, the scattering form function is essentially a very smooth function of the incidence frequency, while for the loaded shell, it varies very rapidly, resulting in a scallop-like curve. The amplitudes

of the scallop-like dips decrease with increasing frequency and their spacing increases with frequency, indicating that the origin of these dips is the flexural waves in the shell. These waves have significant amplitudes in the low frequency region and are dispersive, which is well correlated to the frequency dependent spacing of the dips in the scattered far field. At high frequencies, all but one class of internal loading have negligible effects on the scattering. The non-negligible class is those with structures directly mounted onto the shell, such as directly mounted concentrated masses and clamped elastic plates. For these forms of loading, the scallop-like variations in the scattered field persist to very high frequency region. For directly attached elastic plates, the resonance signatures of the plates also persist to the high frequency region. These resonances manifest themselves in the scattered field in terms of high amplitude spectral peaks with values as much as 10 dB higher than the empty shell solution.

According to whether the internal loading effects are due to waves in the shell or due to the internal structural dynamics, the loading effects can be divided into two groups. The first group can be called geometrical effects because it is the geometrical constraints provided by the attachment to the motions of the shell that significantly affect the scattering process. In this case, the attachment of the internals introduces discontinuities to the otherwise homogeneous shell, altering the coupling efficiency of shell waves to the acoustic field. This kind of loading effects has little to do with the details of the internal system; all that matters is their attachment to the shell. On a microscale, the scattering process is dominated by the individual interactions between the shell waves and the geometrical discontinuities. On a macroscale, the loading effects are in the form of shell wave resonances; the individual events of microscale interactions constructively aggregate to form overall resonances. Alternatively, this can also be considered as being due to the fact that the geometrical discontinuities divide the shell into segments which offer favourable conditions for the shell waves to resonate.

Since elastic waves in the shell play the dominant role in the case where geometrical coupling is important, it is easy to conclude that internal structural details have negligible effects on the scattered field in this case. It can be shown that changes in the values of the total internal mass, of the elasticity of the internal structures and in the distribution of the internals are not well correlated to the scattered field. This is because when geometrical effects are important, the loading impedances at the attachment points assume large values such that further changes in these values do not cause noticeable effects in the scattering. Thus, the case of geometrical coupling can be regarded as an asymptotic limit to the case of infinity loading point impedances; in this case, the attachment points are essentially hold motionless, and hence, no imformation about the internals can be leaked out.

The second group of loading effects are due to the dynamics of the internal structures, and hence, can be called dynamic coupling effects. This kind of effects are important for internal systems with strong resonance features, an elastic plate for example. At some discrete frequencies, the internal system responds to the incidence excitation with high intensity, thus causing much stronger scattering, manifested in the scattered field in terms of a series of high amplitude spectral peaks. The dynamic

effects are felt in the acoustic field only when the internal structural loading is not too strong in strength. In other words, the attachment point impedances must not be too large in order to have significant motions at the attachment points, which are necessary for the signatures of the internals to leak out to the acoustic field. This can be clearly demonstrated by the example where the internal structure is modelled by a single elastic plate pinned to the shell. The thickness of the plate, in reference to that of the shell, can then be taken as a measure of the loading strength; small and large thickness correspond respectively to light and heavy structural loading. As analysed in the previous section, for a plate thicker than the shell, the loading is heavy so that the scattered field is dominated by the geometrical coupling effects. On the other hand, for a thinner plate, the dynamic effects are dominant because the loading impedance are relatively small; the shell waves are not significantly affected while the resonances of the internal plate can easily be transmitted to the acoustic field.

The two kinds of internal structural loading effects can be clearly distinguished in the scattered field because they have different interference effects to the total scattering. The contributions due to geometrical effects are out of phase with the specular reflection from the shell because the former, due to shell waves, are in phase with the incident field (phase matching excitation), while the latter is out of phase with the incidence due to the fact that the shell essentially resembles an empty bubble; the total mass of the shell is much smaller than that of the water volume which would occupy the space of the shell. Thus, the geometrical effects cause sharp dips in the scattering form function, a manifestation of the destructive interference between the shell wave related contributions and the specular reflection from the almost pressure release shell surface. The dynamic coupling effects result in peaks in the scattering because of their constructive interference with the specular reflection. When the incident waves enter the internal structures, their phase does not change, but when these waves are reflected back to the backscattering direction, their phase changes almost by π at the other side of the shell because the internal structures have much larger density than water. Thus, the scattered field due to the waves in the internals is out of phase with the incident field, which makes them in phase with the specular reflection, and hence, results in enhanced total scattering.

Clearly, the dynamic coupling effects are independent of the locations of the attachment points. For geometrical effects, however, the dominant mechanism in the scattering process, namely, the interaction between the waves in the shell and the loading points, is strongly affected by the positions of the loading points in reference to the direction of the incident waves. It can be shown that different kinds of waves can actively participate in the interaction, depending on the relative locations of the attachment. For loading points facing the incident waves, flexural waves in the shell play the dominant role; they are converted into sound at the attachment locations, resulting in frequency dependent dips in the scattering form function because of their dispersive nature. If the attachment points are in the shadow region of the incident sound, however, flexural waves have negligible effects. Instead, the dominant interaction is between the compressional waves and the loading. As a result, the changes in the scattering form function from that of an empty shell to the loaded shell is simply

the shift of the leaky wave related dips. In between the flexural wave region and the compressional wave region, both kinds of waves interact with the loading, and their radiation interfer with each other, so that the scattered field shows very irregular and complex scattering patterns.

5. CONCLUSIONS

We have discussed the effects of internal structural loading inside an elastic shell on the acoustic field. The internals have been shown to introduce new features which result from the wave-bearing nature of both the shell itself and its internal structures. When the loaded shell is coupled to the acoustic field, weekly radiating subsonic flexural waves on the shell surface can be converted into sound by the discontinuities on the shell due to the attachment of the internals. Furthermore, the internal system can also strongly respond to the acoustic excitation which in turn causes reradiation from the shell. All these make the scattering/radiation characteristics of internally loaded shells much richer than that of empty shell.

6. REFERENCES

1. Guo, Y. P. Sound scattering from an internally loaded cylindrical shell. *J. Acoust. Soc. Am.* To appear in January 1992.
2. Guo, Y. P. On solutions of coupled problems in structural acoustics. *J. Sound Vib.* Submitted in August 1991.
3. Guo, Y. P. Sound scattering from cylindrical shells with internal structural loading: Part 1. Formulation and solution. *J. Acoust. Soc. Am.* Submitted in August 1991.
4. Guo, Y. P. Sound scattering from cylindrical shells with internal structural loading: Part 2. Mass-spring loading. *J. Acoust. Soc. Am.* Submitted in September 1991.
5. Guo, Y. P. Sound scattering from cylindrical shells with internal structural loading: Part 3. Elastic plate loading. *J. Acoust. Soc. Am.* Submitted in October 1991.
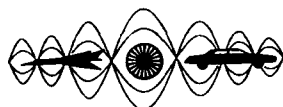
SECOND INTERNATIONAL CONGRESS ON
RECENT DEVELOPMENTS IN AIR- AND
STRUCTURE-BORNE SOUND AND VIBRATION
MARCH 4-6, 1992   AUBURN UNIVERSITY, USA

LOW-FREQUENCY SOUND RADIATION AND INSULATION
OF LIGHT PARTITIONS FILLING OPENINGS
IN MASSIVE WALLS

Roman Y. Vinokur
Engineering Laboratory
Lasko Metal Products, Inc.
West Chester, PA 19380
USA

ABSTRACT

Sound insulation of windows, doors and (in laboratory tests) vari-
ous light partitions at low frequencies is much better than it follows
from the theory of infinite models. The main reason of this phenomenon
consists in a small radiation efficiency of real partitions if their
dimensions (length and width) are little in comparison with the air-
borne sound wave length. This point of view is comfirmed by the re-
search carried out. Accelerations of single   rtitions tested are about
the same over all low-frequency region (for each plate) but the trans-
mission loss is much higher than the "mass law" prognosis. Sound radi-
ation efficiency of a vibrating rigid piston mounted on the edge wall
of a semiinfinite tunnel with a rigid inner surface has been calcula-
ted. This value is shown to vary from a small constant (at low frequen-
cies)quantity to 1. The results depend on the tunnel and piston dimen-
sions and the piston disposition on the wall.

INTRODUCTION

The theory of airborne sound insulation, based on on infinite mo-
dels of real partitions [1-4], helps to put clear physical interpreta-
tions on many important phenomena and to deduce close-form analytical
solutions. However, numerical results calculated with the aid of this
theory are often not in a good agreement with the results measured. For
instance, the theory fails to explain relatively high transmission loss
of light partitions at low frequencies. This effect was revealed more
than 40 years ago [3,5]. In part, the results [5] showed that transmis-
sion loss of single partitions made of different materials (rubber,
lead, aluminium, plywood) much exceeded the "mass law" prognosis calcu-
lated in case of normal sound incidence - at well low frequencies (for
example, not less than by 8 dB at 100 Hz). It should be noted that
transmission loss in case of normal incidence is about 6 dB higher than
in case of diffuse sound field. Regretfully, the partitions length and
width were not mentioned in that paper [5]. London [3] presumed that
a loss factor of a real (finite) plate should be much more (especially
at low frequencies) than an internal loss factor determining a vibra-
tion energy dissipation of the infinite model. This idea proved to be
valid (the exact equation expressing a total loss factor was deduced
much later [6,7]) but couldn't explain the effect discussed. As is known
a loss factor increase is able to improve essentially the sound trans-

515

mission loss only in the vicinities of the first 2-3 natural frequencies of the plate bending vibrations. The different reason is now considered to be dominating: a small sound radiation efficiency of finite plates provided that their length and width are little in comparison with a length of sound waves [8]. In such a case even severely vibrating plates deliver a weak sound radiation. If vibrations are caused by incident airborne sound one can speak about high sound insulation of the partition. A number of publications was devoted to the problem of calculation of transmission loss of finite partitions. A mathematical model used was mostly either a finite partition mounted in a rigid infinite screen ([9] and so on) or a wall between two adjacent rooms (often - two semiinfinite tunnels) [10-13 and so on]. In reality, light partitions can fill an aperture in a massive wall (this has to do with windows and doors in buildings and with samples tested at laboratories) and their sound insulation is the problem of practical interest (especially at low and middle frequencies because transmission loss at high frequencies is usually large). The case of low frequencies is investigated in this paper.

EXPERIMENT

Two different pressboard plates were tested (in one-third octave bands centered from 100 to 5000 Hz) at the Laboratory of Building Acoustics (Moscow, USSR) [14,15]. The airborne transmission loss and acceleration levels (re 9.81 m/s^2) were measured while each plate (1m*1m) was mounted (in turn) with a massive steel frame into the middle section of the test opening (1.2m*1.2m) made in the brick wall (0.62m thick) which seperated the source room (60 m^3) from the receiving room (82m^3) - see Figure 1. Thicknesses, surface dencities, critical coincidence frequencies and the first natural frequencies of the plates tested were respectively: 3 and 12 mm, 3 and 12 kg/m^2, 10000 and 2500 Hz, 6 and 24 Hz. Transmission loss was determined using the standard method of two reverberant rooms (sound pressure levels in each room were found by averaging 10 values measured). Acceleration levels were determined by averaging 10 values measured with the aide of the miniature pickup (2g weight). The pickup was (in turn) attached (using plasticine) in different points on the receiving room-side of the plates tested (Figure 1). Since the acceleration measured depended on the sound pressure in the source room (similar value in the receiving room is comparatively small and can be neglected with the point of view of partition vibrations), the modified (re sound pressure level of 100 dB) acceleration levels were calculated using the obvious relationship:

$$L_m = L_a - L_1 + 100 \text{ dB} \tag{1}$$

where L_a and L_1 are, respectively, the acceleration and the sound pressure levels measured.

ANALISIS OF EXPERIMENTAL DATA

In the frequency region $2\text{-}3 f_b < f < 0.5 f_c$ (f_c is a critical coincidence frequency, f_b is the first natural frequency of bending vibrations) a thin plate influenced by an incident sound wave may be considered to have about a pure inertial impedance. Thus, the vibration acceleration of that plate equals

$$a = \frac{2 p}{\tilde{m}} \tag{2}$$

(the "Schoch law" [2]) where p is sound pressure in the source room, $\tilde{m}$

516

Figure 1--Measurement equipment for transmission loss and acceleration levels determination: 1--the wall between reverberant rooms, 2--the partition tested, 3--steel frame, 4--doors (closed, sealed)

is the plate surface dencity, factor 2 is used to take into account both incident and reflected sound waves. In case L_1=100 dB (re .00002 Pa) one finds: p=2 Pa. Substituting this value into Eq.(2) one can obtain (in terms of acceleration levels):

$$L_a \approx -17 \text{ dB} \qquad (18 \text{ Hz} < f < 5000 \text{ Hz})$$

for the thinner plate tested ($\tilde{m} = 3$ kg/m^2) and

$$L_a \approx -29 \text{ dB} \qquad (72 \text{ Hz} < f < 1250 \text{ Hz})$$

for the thicker one (m $\approx$ 12 kg/$\tilde{m}^2$).

These results are close to experimental data (Figure 2). Hence, the plates tested have approximately a pure inertial impedance at frequencies mentioned above and their transmission loss should be controlled by the "mass law". The numerical values predicted in accordance with this rule depend on an incident sound pressure distribution on the plate surface. It's clear that the normal incidence conditions can be about accomplished if the airborne sound length is large enough in comparison with the plate dimensions (its length and width). Sound incidence angle doesn't play the essential role in such a case. One can suppose that it tooks place in frequency region

$$f < f_n = c\sqrt{b_1^2 + b_2^2} \Big/ (2b_1 b_2) \qquad (3)$$

517

Figure 2--Airborne transmission
loss (a) and acceleration levels
(b) measured:

1--for the plate with $m=3kg/m^2$
2--for the plate with $m=12kg/m^2$,

1' and 2' designate theoreti-
cal results (a--"mass law" in
case of normal sound incidence,
b--calculations using Eq.(2)),

The acceleration levels drawn
are determined in accordance
with Eq.(1).
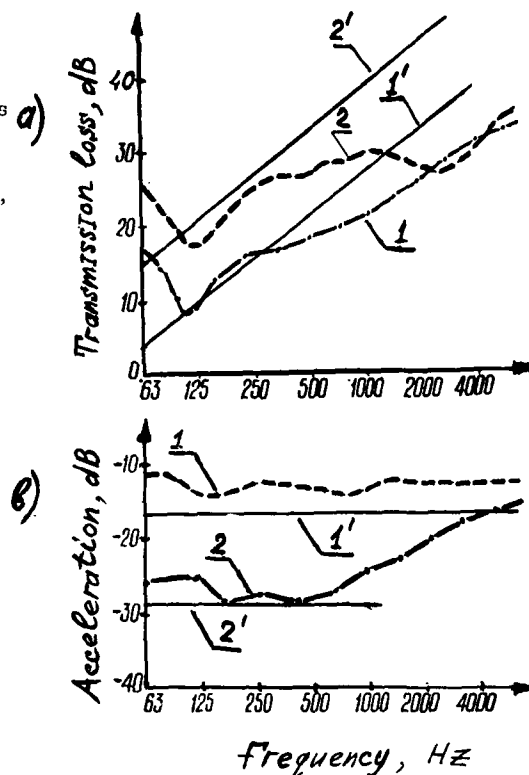
where b_1 and b_2 are the plate length and width, c is airborne sound
speed (340 m/s) [15]. Substituting $b_1=b_2=1$ m into Eq.(3), one finds $f_n=$
=240 Hz. Frequency characteristics calculated in accordance with "mass
law" for case of normal sound incidence are shown in Figure 2. One can
note that the experimental transmission loss is much bigger in both ca-
se (at frequencies below 100 Hz) than the appropriate theoretical va-
lues. It should be noted that "niche effect" (caused by interaction of
incident, reflected and radiated sound waves with the sides of the test
opening [8]) doesn't "work" at these frequencies under test conditions
used here. Its frequency region is checked to be disposed about from 125
to 400 Hz. This is the frequency range where the plate transmission loss
strongly depends on disposition of the plate in the test opening and on
the opening dimensions and shape.

   Thus, we can neglect of the "niche effect" and not to take into ac-
count the thickness of the wall in order to create mathematical model of
the phenomenon investigated.

THEORY

   As noted before, at frequencies 2-3 f_b < f < min(.5 f_c, f_n) a sin-
gle partition may be treated as a plane rigid piston with a mass equal-
led the mass of the partition. Let's find an airborne sound insulation
efficiency of a rigid piston in a semiinfinite tunnel with a rigid inner
surface (Figure 3). The piston (on the tunnel edge wall) vibrates with
 the velocity

$$V(t) = V_0 \exp(-jWt).$$
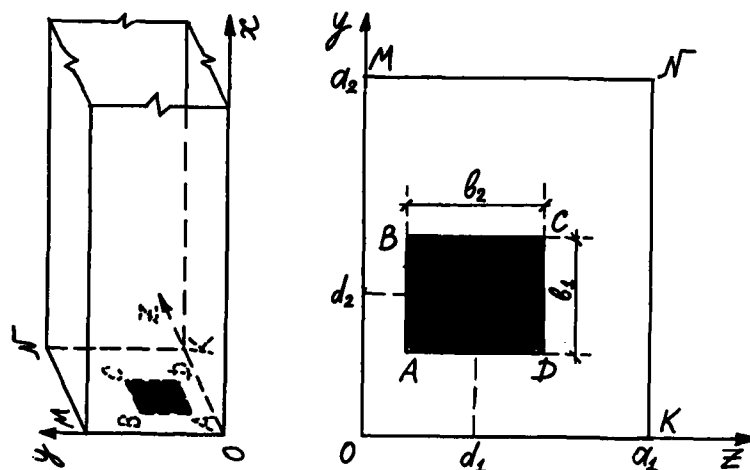
Figure 3--Semiinfinite tunnel with a rectangular piston
on the edge wall

Here V_0 is a velocity amplitude, $W = 2\pi f$ is an angular frequency, t is time, $j = \sqrt{-1}$. The piston (ABCD) and the wall (OMNK) are rectangular, the point O is the origin of the rectangular plane co-ordinate system, $|AB|=|CD|=b_2$, $|AD|=|BC|=b_1$, $|OM|=|NK|=a_2$, $|OK|=|MN|=a_1$. The geometrical center of the piston (the point E)=(d_1,d_2). Using results [16] one can write equations expressing the vibration velocity amplitude of air

$$v(z,y) = \sum_{m=0}^{\infty} \sum_{n=0}^{\infty} u_{mn} \cos(\pi mz/a_1) \cos(\pi ny/a_2)$$

and the sound pressure

$$p(z,y) = q\, c \sum_{m=0}^{\infty} \sum_{n=0}^{\infty} u_{mn} \cos(\pi mz/a_1) \cos(\pi ny/a_2) \Big/ \sqrt{Q_{mn}}$$

on the surface of the tunnel edge wall. Here:

$$u_{mn} = \frac{v_0}{a_1 a_2} \int_{h_1}^{s_1} \int_{h_2}^{s_2} \cos(\pi mz/a_1) \cos(\pi ny/a_2)\ dz\ dy,$$

$$Q_{mn}(k) = 1-[(\pi m)/(ka_1)]^2 - [(\pi n)/(ka_2)]^2 ,$$

$h_{1,2}=d_{1,2}-b_{1,2}/2$, $s_{1,2}=d_{1,2}+b_{1,2}/2$, $k=W/c$ is the wavenumber of sound waves in air, q is the air density.
Using these equations one finds the sound power radiated by the piston into the tunnel:
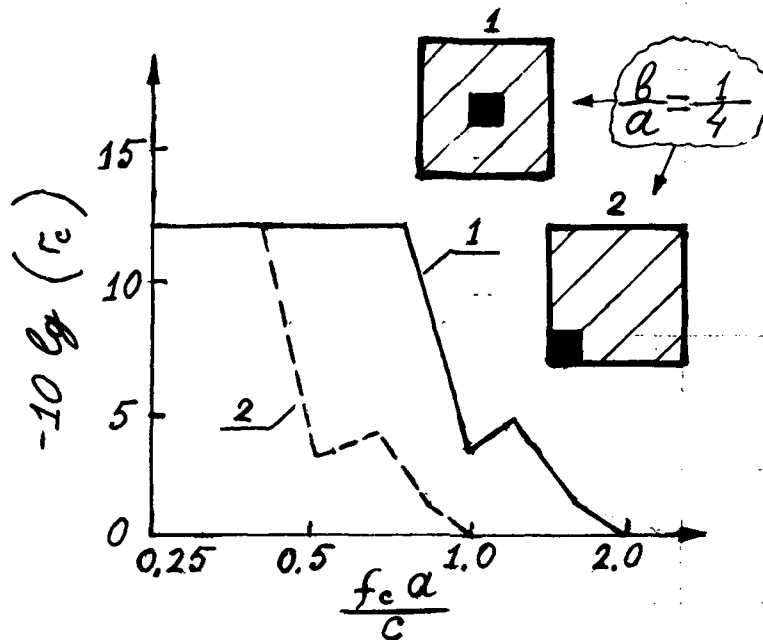
Figure 4--Frequency characteristics of the piston radiation effi-
ciency (averaged within one-octave frequency bands:

$$r_c = r(f_c) = [\int_{f_1}^{f_2} r(f) \, df] \Big/ (f_2 - f_1) \quad \text{where } f_c = \sqrt{f_1 f_2} \;, \quad f_2/f_1 = 2^{1/3} \;)$$

for different dispositions of the piston: 1 - central, 2 - corner;
$b_1 = b_2 = b$, $a_1 = a_2 = a$, $a/b = 4$

$$P(f) = .5 \; Re \; [\int_0^{a_1} \int_0^{a_2} p(z,y) \; v^*(z,y) \; dz \; dy \;] = .5qcS_0 |V_0| r(f)$$

where the piston radiation efficiency

$$r(f) = (S_0/S) \sum_m^{Q_{mn}>0} \sum_n R_1(m) \; R_2(n) \Big/ \sqrt{Q_{mn}(k)} . \tag{4}$$

Here $S_0 = b_1 b_2$, $S = a_1 a_2$, $R_i(0) = 1$,

$$R_i(N) = [\frac{sin(T_{Ni})}{T_{Ni}} cos(H_{Ni})]^2$$

($i = 1,2$; $m,n = 0, \pm1, \pm2, \pm3, \dots$; $N = \pm1, \pm2, \pm3, \dots$; $T_{Ni} = \pi N b_i/(2a_i)$;

$H_{Ni} = \pi N \; (.5 - d_i/a_i) \;)$.

Analyzing the equations obtained one could note that the piston

520

radiation efficiency is of a constant value $(r=S_0/S)$ at frequencies below the threshold $f_{20}=c/a$ ($a=\max[a_1,a_2]$) in case of central $(d_i=a_i/2, i=1,2)$ or close to the central disposition of the piston. In other[1](for instance, corner) case the threshold is half as much $(f_{10}=c/(2a))$. Using auxiliary formula

$$\sum_{n=1}^{\infty} [\sin(\pi ng)/(\pi ng)]^2 = (1-g)/(2g)$$

in the equations obtained, one finds that $\lim\limits_{f\to\infty} r = 1$.

Calculated spectrum of the radiation efficiency (averaged within one-third octave frequency bands)are represented in Figure 4 for cases of the central and corner disposition of the square piston on the square wall. Here $S_0/S=1/16$ so $10 \log_{10}(r) = 12$ dB. This should be the difference between the transmission loss measured and the "mass law" (for normal incident sound waves) prognosis.

We din't take into account a wall which is opposite to the wall with a partition tested in reality. However, it should not essentially change the evaluation: transmission loss at pretty low frequencies $(2-3\ f_b < f < f_{20}$ - for case of about the central disposition of partitions tested on the wall of reverberant rooms) is higher (in comparison with the result predicted by the theory of infinite partitions) by value $10 \log_{10}(S_0/S)$. It's important only: the length of the room should be bigger not less than twice as much than height or width of the wall with the partition tested. In reality, the ratio S_0/S is about 10. So one can speak of 10 dB - transmission loss growth at low frequencies (in case of light partitions, frequency f_b is usually not bigger than 20-30Hz; so if a=3 m then the frequency region mentioned is between approximately 60 and 100 Hz). One can also presume that this relationship is valid in case of multiple partitions consisting of two or even more plates; herein, the frequency f_b is the maximum first natural frequency of bending vibrations of the components.

The author believes that results obtained could be used in analysis of measurements of transmission loss of light partitions.

REFERENCES

1.Reissner, H.,Der senkrechte und shräge Durchtutt einer in einem flüssingen Medium erzeugten ebenen Dilatationswelle durch eine in diesem Medium befindliche planparallele, feste Platte. Helv. Phys. Acta, 11(2) (1938) 140-155.
2.Cremer,L., Theorie der Schalldämmung Wände bei schrägen Einfall. Akust.Z., 7(3) (1942) 81-104.
3. London, A., Transmission of Reverberant Sound through Double Walls. J.Acoust.Soc.Amer., 22(2) (1950) 270-279.
4. Thompson, W.T., Transmission of Elastic Waves through a Stratified Solid Material. J.Appl.Pfys., 21(2) (1950).
5. Peutz, V., Some Fundamental Measurements on Single and Double Plate Structures, Acustica, 4(1) (1954) 281-284.
6. Vinokur, R.Y., Influence of Boundary Conditions on Sound Insulation of a Thin Finite Plate at Coincidence Frequency Region. Akust.J., 26(1) (1980) 135-137 (in Russian).
7. Craik, R.Y., Damping of Building Structures. Appl. Acoust., 14 (5) (1981) 347-359.
8. Heckl, M., The Tenth Sir Richard Fairey Memorial Lecture: Sound Transmission in Buildings. J. Sound Vib., 77(2) (1981) 165-189.
9. Sewell, E.S., Transmission of Reverberant Sound through a Single -Leaf Partition Surrounded by an Infinite Rigid Baffle. J. Sound Vib., 12(1) (1970) 21-32.
10. Heckl, M., Die Schalldämmung von Homogenen Einfachwänden Endliher Fläche. Acustica, 10(2) (1960) 98-108.
11. Nilsson, A.C., Reduction Index and Boundary Conditions for a Wall between Two Rectangular Rooms. Part 1: Theoretical Results.— Acus-

tica, 26(1) (1972) 1-18.

12. Romilly, N., Exact Solution for Guided Sound Transmission through a Simply Supported Plate. Acustica, 28(4) (1973) 234-237.

13. Crocker, M.J. and Price, A.J., Sound Transmission Using Statistical Energy Analysis. J.Sound Vib., 9(3) (1969) 469-486.

14. Vinokur, R.Y. and Lalayev, E.M., Experimental Research of Transmission Loss of Ribbed Plate with High Main Resonant Frequency. In book: Komplexnoye resheniye voprosov ochrany truda, Moscow (USSR), (1982) 59-62 (in Russian).

15. Vinokur, R.Y., About Phenomenon of High Transmission Loss of Light Partitions at Low Frequncies. Akust.J., 29(3) (1983) 405-407.

16. Isakovich, M.A., Obschaya Akustika. Moscow (USSR), Nauka, 1973 (in Russian).

**SECOND INTERNATIONAL CONGRESS ON
RECENT DEVELOPMENTS IN AIR- AND
STRUCTURE-BORNE SOUND AND VIBRATION**

MARCH 4-6, 1992   AUBURN UNIVERSITY, USA

THE TRANSMISSION OF VIBRATION WAVES THROUGH STRUCTURAL JUNCTIONS

Yan TSO

Materials Research Laboratory
Defence Science and Technology Organisation
P. O. Box 50, Ascot Vale
Victoria, Australia 3032

ABSTRACT

The evaluation of transmission efficiency of structural
junctions forms an important part in the study of structure-borne
noise. In this paper, a general method for calculating the
transmission efficiency of plate-plate and plate-beam junctions is
described. This method takes into account of the effects of in-
plane *motions of plates as well as the elastic vibrations of
beams.* It is found that for typical naval ship constructions that
consist of plates coupled to light thin beams, the elastic
vibrations of the beam has a significant effect on the
transmission efficiency.

INTRODUCTION

One of the limiting factors in the analysis of vibration
transmission through complex structures, such as naval ships, is
the transmission across junctions and discontinuities in the
structure where vibration waves are partially reflected and
partially transmitted. The wave transmission properties of a
structural discontinuity may be characterised by the transmission
efficiency which is defined as the ratio between the transmitted
wave power and the incident wave power. As well as being a
parameter of intrinsic importance in the study of structure-borne
noise, the transmission efficiency may also be used to calculate
the coupling loss factor in Statistical Energy Analysis (SEA) for
prediction of vibrational response in structures.
One of the early attempts to evaluate the transmission
efficiency was carried out by Cremer and Heckl [1]. Their work
included right-angled plate junctions and plate-beam junctions
subjected to oblique incident bending waves. Other authors [2-4]
have extended the analysis to include in-plane waves. The
contribution of in-plane waves to structure-borne noise has been
investigated by Lyon [5]. In the previous studies involving
transmission efficiency of plate-beam structures, the stiffening
beam was modelled by using conventional beam theory and the effect
of bending and in-plane waves in the beam was neglected. While
this so called 'blocking mass' approach might be valid for heavy
thick beams, there are situations where elastic vibrations of the
beam have to be considered. For example, in plate-beam structures

typical of ship constructions, the beam thickness may be of the same order as the plate and hence the effect of beam vibration has to be accounted for in the evaluation of transmission efficiency.

In this paper, a general method for evaluating the transmission efficiency of structural junctions typical of those found in ship constructions is described. The effect of elastic vibrations of the beam in a plate-beam junction is investigated by modelling the beam as a finite plate coupled to a system of semi-infinite plates. Samples of calculations for some plate-beam junctions are presented.

MATHEMATICAL EXPRESSIONS FOR BENDING AND IN-PLANE WAVES

Figure 1 shows a schematic diagram of a plate-plate junction which consists of n plates coupled along a line. The plates are assumed to be infinite along the x_1 to x_n directions. It is further assumed that the plates are thin so that the boundary conditions can be applied on the plate centreline. Plate 1 is subjected to an oblique incident wave which can be either bending (B), longitudinal (L) or transverse shear (T). The incident wave is partially reflected and partially transmitted at the junction as bending and in-plane waves as shown. By using the system of co-ordinates as shown in Figure 2, mathematical expressions for the waves may be derived [1,4].

For a sinusoidal incident bending wave, the transverse bending velocity is given by:

$$V_{IBz} = \underline{V} e^{jk(\cos a)x_1} \tag{1}$$

where a is the incident angle and k is the incident wave number. For an incident bending wave, $k = k_{B1}$. The quantity $\underline{V}$ represents the y-direction dependency and time dependency of the velocity amplitude V and is given by:

$$\underline{V} = V e^{jk(\sin a)y + j\omega t}. \tag{2}$$

For incident longitudinal and transverse waves, $k = k_{L1}$ and k_{T1} respectively, the velocity components in the x_1 and y directions are given by:

$$V_{ILx} = -\underline{V}(\cos a) e^{jk(\cos a)x_1} \tag{3}$$

$$V_{ILy} = -\underline{V}(\sin a) e^{jk(\cos a)x_1} \tag{4}$$

$$V_{ITx} = -\underline{V}(\sin a) e^{jk(\cos a)x_1} \tag{5}$$

$$V_{ITy} = \underline{V}(\cos a) e^{jk(\cos a)x_1}. \tag{6}$$

The transmitted bending, longitudinal and transverse shear waves in plate i ($i = 2....n$) may be expressed in terms of a product of the incident wave amplitude and a complex transmission factor t as follows:

$$V_{TBzi} = \underline{V} t_{Bi} e^{-jk \, MBi \, xi} + \underline{V} t_{NBi} e^{-k \, MNBi \, xi} \tag{7}$$

$$V_{TLxi} = \underline{V} t_{Li} \{ML_i/(k_{Li}/k)\} e^{-jk \, MLi \, xi} \tag{8}$$

$$V_{TLyi} = -\underline{V} t_{Li} (\sin a)/(k_{Li}/k) e^{-jk \, MLi \, xi} \tag{9}$$

$$V_{TTxi} = -\underline{V} t_{Ti} (\sin a)/(k_{Ti}/k) e^{-jk \, MTi \, xi} \tag{10}$$

$$V_{TTTi} = -\underline{V}\ t_{Ti}\ \{MT_i/(k_{Ti}/k)\}\ e^{-jk\ MT_i\ x_i} \tag{11}$$

$$\text{where}\quad MD_i = \sqrt{\{(k_{Di}/k)^2 - \sin^2 a\}} \tag{12}$$

$$D = B,\ L\ \text{or}\ T$$

$$MNB_i = \sqrt{\{(k_{Bi}/k)^2 + \sin^2 a\}}, \tag{13}$$

the transmission factors t_{Bi}, t_{Li} and t_{Ti} in the wave equations represent travelling waves while t_{BNi} represents the near field evanescent bending wave.

In equation (12), if the quantity inside the square root is negative, the exponential term representing travelling wave in the wave equations becomes a real quantity and wave propagation cannot exist. One must then replace the quantity $\sqrt{\{(k_{Di}/k)^2 - \sin^2 a\}}$ by $-j\sqrt{\{\sin^2 a - (k_{Di}/k)^2\}}$ in the solution for transmission and reflection factors.

Equations (7) - (11) may also be used to express the velocity components of the reflected waves (V_{RBz}, V_{RLx}, V_{RLy}, V_{RTx} and V_{RTy}) except that in this case $i = 1$ and the transmission factors t_{Bi}, t_{NBi}, t_{Li} and t_{Ti} are replaced by their corresponding reflection factors r_{Bi}, r_{NBi}, r_{Li} and r_{Ti}. Hence, for a junction consisting of n plates coupled together, there are $4 \times n$ unknown transmission and reflection factors to describe the wave motions. These factors may be solved by the appropriate boundary conditions of the junction.

BOUNDARY CONDITIONS

Plate - plate junction

At the plate junction (i.e. x_1, x_2 ...$x_n = 0$), compatibility of plate motions requires that the velocity components of all plates along a set of reference co-ordinates (e.g. x_1, y and z_1) must be the same. In addition, the angular velocity about the y axis of all plates should be equal. Using x_1, y and z_1 as the reference co-ordinates, the compatibility requirments between plate i and plate 1 lead to the following equation:

$$\begin{bmatrix} V_{xi} \\ V_{yi} \\ V_{zi} \\ W_i \end{bmatrix}_{i=2}^{n} = \begin{bmatrix} \cos b_i, & 0 & , & -\sin b_i, & 0 \\ 0 & , & 1 & , & 0 & , & 0 \\ \sin b_i, & 0 & , & \cos b_i, & 0 \\ 0 & , & 0 & , & 0 & , & 1 \end{bmatrix} \begin{bmatrix} V_{x1} \\ V_{y1} \\ V_{z1} \\ W_1 \end{bmatrix} \tag{14}$$

where b_i is the angle between plate i and plate 1, W_i is the angular velocity of plate i at the junction and V_{xi}, V_{yi} and V_{zi} are the velocity components of plate i at the junction. The velocity components can be expressed in terms of the wave velocities given by equations (1) - (13) and the angular velocity is given by $W_i = \partial V_{zi}/\partial x_i$.

Based on the assumption of thin plates, the forces and moment per unit length of plate i ($i = 1...n$) may be expressed in terms of the velocity components, elastic modulus E, plate thickness h and Poisson's ratio μ as follows:

$$jwF_{xi} = -\{E_i h_i/(1-\mu_i^2)\}\{\partial V_{xi}/\partial x_i + \mu_i\partial V_{yi}/\partial y\} \tag{15}$$

$$jwF_{yi} = -\{E_i h_i/2(1+\mu_i)\}\{\partial V_{xi}/\partial y + \partial V_{yi}/\partial x_i\} \tag{16}$$

$$jwF_{zi} = \{E_i h_i^3/12(1-\mu_i^2)\}\{\partial^3 V_{zi}/\partial^3 x_i + (2-\mu_i) \ \partial^3 V_{zi}/\partial x_i \partial^2 y\} \qquad (17)$$

$$jw \ M_i = -\{E_i h_i^3/12(1-\mu_i^2)\}\{\partial^2 V_{zi}/\partial^2 x_i + \mu_i \partial^2 V_{zi}/\partial^2 y\}. \qquad (18)$$

Equilibrium requirements for forces and moments at the plate junction lead to four additional governing equations. The equilibrium and compatibility equations together provide the necessary boundary conditions to solve the transmission and reflection factors of interest.

Plate - beam junction (thick beam)

Figure 3 shows a schematic diagram of a system of semi-infinite plates coupled to a thick beam. The 'thick beam' assumption in the context of this paper implies that no incident wave is transmitted to the beam. It is further assumed that the beam is symmetrical about the x_b axis and the boundary conditions can be applied on the beam centreline. Hence, the compatibility requirements for plate motions in this case is exactly the same as for a plate-plate junction (equation (14)). However, the force and moment balance equations must be modified to allow for the torsional, bending and inertia effects of the beam. Detials of the derivation of force and moment equations for plates coupled to a thick beam are described in [6].

MATHEMATICAL MODEL FOR A PLATE-BEAM JUNCTION (THIN BEAM)

The structure of naval ships quite often involves the use of thin beams to reinforce plate elements. A thin beam in the context of this paper implies that the beam thickness is of the same order as the plates and is therefore subjected to bending and in-plane waves travelling in both the positive and negative directions across the beam. A schematic diagram of the structure is shown in Figure 4. By modelling the beam as a finite plate in a plate-plate junction, the expressions for bending and in-plane waves may be derived.

For bending waves:

$$V_{TBz2} = \underline{V} \{ t_{B2} \ e^{-jk \ MB2 \ x2} + t_{NB2} \ e^{-k \ MNB2 \ x2} + r_{B2} \ e^{jk \ MB2 \ x2} + r_{NB2} \ e^{k \ MNB2 \ x2} \}, \qquad (19)$$

for longitudinal waves:

$$V_{TLx2} = \underline{V} \{ML2/(k_{L2}/k)\}\{t_{L2} \ e^{-jk \ ML2 \ x2} - r_{L2} \ e^{jk \ ML2 \ x2}\} \qquad (20)$$

$$V_{TLr2} = -\underline{V} \{(\sin a)/(k_{L2}/k)\}\{t_{L2} \ e^{-jk \ ML2 \ x2} + r_{L2} \ e^{jk \ ML2 \ x2} \}, \qquad (21)$$

and for transverse shear waves:

$$V_{TTx2} = -\underline{V} \{(\sin a)/(k_{T2}/k)\}\{t_{T2} \ e^{-jk \ MT2 \ x2} + r_{T2} \ e^{jk \ MT2 \ x2}\} \qquad (22)$$

$$V_{TTY2} = -\underline{V} \{MT_2/(k_{T2}/k)\}\{t_{T2}\ e^{-j\ k\ MT2\ x2} -$$

$$r_{T2}\ e^{j\ k\ MT2\ x2}\}. \tag{23}$$

Note that in the case of a finite plate, there are four additional unknowns in the wave expressions, namely, the reflection factors r_{B2}, r_{NB2}, r_{L2} and r_{T2}. Hence, four additional boundary conditions are required to solve the transmission and reflection factors. These boundary conditions can be obtained by noting that the forces and moment must vanish at the free end, i.e.,

$$F_{x2} = F_{y2} = F_{z2} = M_2 = 0 \tag{24}$$

at $x_2 = l_w$.

TRANSMISSION AND REFLECTION EFFICIENCIES

The wave power per unit length of a junction may be expressed as the energy per unit area times the component of group velocity normal to the junction. For transmitted waves, the expression for wave power is given by:

$$P_{Di} = m_i V^2 | t_{Di}|^2\ C_{Gi}(k/k_{Di})\mathrm{Re}\sqrt{\{(k_{Di}/k)^2 - \sin^2\ a)\}} \tag{25}$$

where $D = B, L,$ or T
m_i = mass per unit area of plate i
C_{Gi} = group velocity of plate i
= $2\ C_{Bi}$ for bending waves
= C_{Li} for longitudinal waves
= C_{Ti} for transverse shear waves.

Equations (25) may also be used to express the reflected wave power by substituting $i = s$ (s is the carrier plate of the incident wave) and the transmission factors by the appropriate reflection factors.
Similarly, the incident wave power may be expressed as:

$$P_s = m_s V^2\ C_{Gs} \cos\ a. \tag{26}$$

The transmission / reflection efficiency may be calculated as the ratio of the transmitted / reflected wave power to the incident wave power:

$$\tau_{\substack{q\ u}}^{\substack{s\ i}} = P_{Di}/P_s \tag{27}$$

where i represent the carrier plate of the generated waves, q and u represent the wave type of the incident and generated waves respectively. Conservation of energy requires that the sum of all transmission and reflection efficiencies to be equal to one.
It is evident from the above analysis that the transmission and reflection efficiencies vary with the incident angle. If one assumes a diffused vibration field incident on a junction, the mean or diffuse wave transmission efficiency may be obtained by averaging the efficiencies over the entire range of incident angles (i.e. from 0 to 90 degrees). The sample calculations in the following section are based on mean transmission efficiencies.

APPLICATIONS TO PLATE-BEAM JUNCTIONS

The mathematical models for a thick beam and a thin beam coupled to semi-infinite plates were applied to the plate-beam junction shown in Figure 5. Since the beam thickness chosen in this example is the same as the plate, the beam would vibrate due to the incident wave and it is reasonable to argue that the thin beam model would give a more accurate prediction of the transmission efficiency. Figure 6 shows the bending wave transmission efficiency of the junction calculated by both models. The thick beam model predicts a low-pass characteristic of the plate-beam junction and underestimates the transmission efficiency at frequencies above 500 Hz. The effect of resonant bending frequency of the beam on wave transmission can be observed.

As a second example on plate-beam junctions, the beam thickness in Figure 5 is increased to 20 mm. Figure 7 shows the calculated transmission efficiency. Below 1 kHz, the agreement between the thick beam model and the thin beam model is reasonable. At higher frequencies, the thin beam model predicts a higher transmission efficiency, possibly due to the effect of beam resonance. It should be noted that the mathematical models used in this paper are based on thin plate theory and the assumption that the boundary conditions can be applied on the beam/plate centreline. These assumptions are not justified if the thickness of beam is large compared with the plate. The effect of plate offset from the centreline of a thick beam has been investigated by Langley and Heron [3]. Despite the assumptions used in the models, the present analysis shows that the conventional heavy beam theory may lead to a serious underestimation of the transmission efficiency when applied to plate-thin beam junctions.

CONCLUSIONS

A general method for evaluating the transmission efficiency of structural junctions has been presented. The method can be applied to junctions that consist of plates coupled to thin beams typical of naval ship constructions. A study of the transmission efficiency of plate-thin beam junctions shows that the vibrations of beam has a significant effect on wave transmission and should be considered in the analysis.

ACKNOWLEDGEMENT

REFERENCES

1. L. Cremer, M. Heckl and E. E. Ungar 1973. Structure-borne sound. Berlin: Springer-Verlag.

2. P. G. Craven and B. M. Gibbs 1981. Sound transmission and mode coupling at junctions of thin plates, part 1: representation of the problem. Journal of Sound and Vibration 77, 417-427.

3. R. S. Langley and K. H. Heron 1990. Elastic wave transmission through plate/beam junctions. Journal of Sound and Vibration 143, 241-253.

4. W. Wöhle, Th. Beckmann and H. Schreckenbach 1981. Coupling loss factors for Statistical Energy Analysis of sound transmission at rectangular structural slab joints, part 1. Journal of Sound and Vibration 77, 323-334.

5. R. H. Lyon 1986. In-plane contribution to structural noise transmission. Noise Control Engineering Journal 26, 22-27.

6. Y. K. Tso 1991. The evaluation of transmission efficiency and coupling loss factor of structural junctions. To be published as MRL technical report.
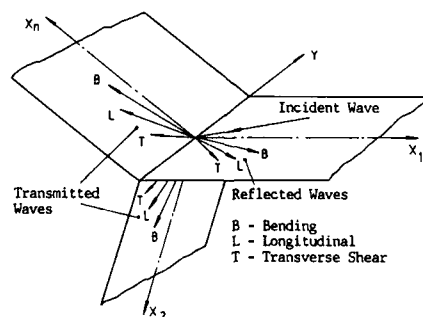
Fig. 1 Schematic Diagram of a
Plate - Plate Junction
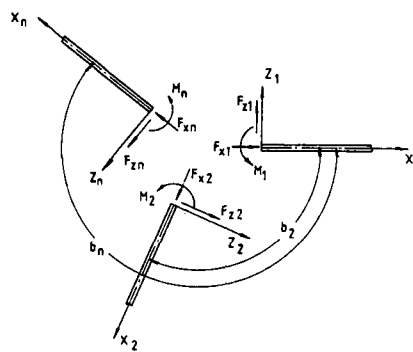
Fig. 2 System of Co-ordinates
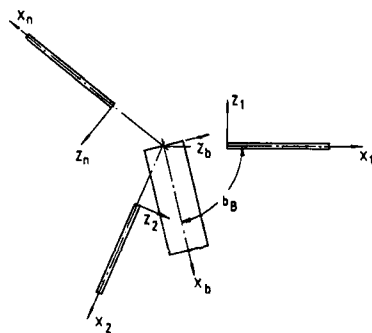
Fig. 3 Plate - Thick Beam Junction
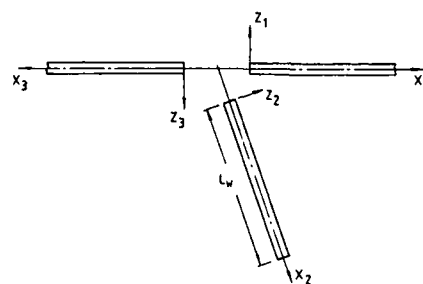
Fig. 4 Plate - Thin Beam Junction
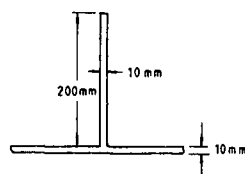
Fig. 5 A Simple Plate-Thin Beam Structure
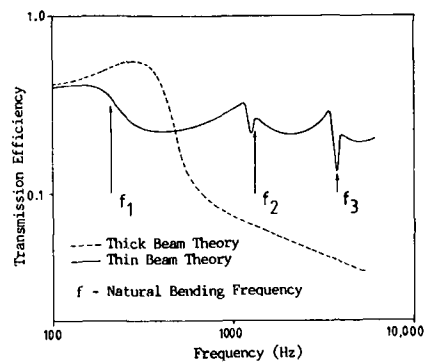
Fig. 6 Transmission Efficiencies for a
Plate- Thin Beam Junction
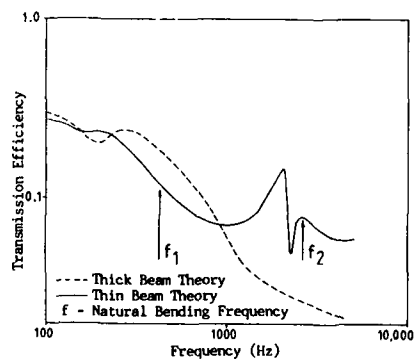
Fig. 7 Transmission Efficiencies for a
Plate- Thick Beam Junction

G. N. AVILOVA

N.N. Andreev Acoustics Institute

Moscow, USSR

ABSTRACT

The spatial characteristics of the local sound insulation are investigated for single and double wall laminated cylindrical shells. The transition-matrix method is used for the theoretical determination of the spatial frequency characteristic of sound insulation of laminated composite shells. The expression is obtained for the sound insulation value in terms of frequency and angle of observation includes the elements of a spectral matrix. The theoretical results are compared with experimental investigations in an anechoic chamber. The frequency of minimum sound insulation is identified with resonance frequency of shells.

INTRODUCTION

It is necessary to take into consideration the spatial characteristics of the sound insulation devices in the design of soundproof devices, and rational decision of other practical problems. In the last years cylindrical soundproof casings have received a wide application. Usually it is a closed angle of the diameter long. These advantages compared to rectangular casings is the higher sound insulation at low frequency region at the first resonance frequency [1].

Experimental investigations of sound insulation of cylindrical shells with source of sound inside show that the sound insulation don't depend on the viewing angle only at a low frequency. The spatial characteristic of sound insulation get short in the directional pattern with angles almost constant measured get short with the frequency rise [2].

Usually the soundproof casings are laminated covered more on metals covered with soundabsorbing and vibrodamping materials. More advanced way is employment of two-wall cylindrical casings, that is two casings inserted one in other. Each of them can be covered by soundabsorbing and vibrodamping layers. Therefore prediction of the sound insulation characteristics of such casings is of great practical significance.

The mathematical model and algorithm of computation of sound insulation of infinite laminated cylindrical shell have been developed together with processes behavior [3,4].

The theoretical analysis has been carried out on the basis of this model, and results of computation is limited plane incidence to structural regularities have been experimentally verified.

SOUND INSULATION OF AN INFINITE LAMINATED CYLINDRICAL SHELL

Let us consider an infinite laminated cylindrical shell, consisting of coaxial packets each of those in turn consist of alternating elastic and viscoelastic layers. The packets can be separated by a liquid (gas) layer. The inner radius is Rik, where i-is number of the packet, k-is number of the layer in the packet. The elastic layers are thin, that is their summary thickness is small in comparision to the radius, the liquid layer can have an arbitrary thickness.

The sound wave falls on the inner surface of the cylindrical shell and creates on it a sound pressure distributed on law:

$$p_{inc}^0 = p_0 * e^{in\varphi} e^{ik\rho z}$$

(here and further the factor e^{-iwt} is omited).

The sound pressure, created by the wave transmitted through the system of cylindrical layers, represented in the form of expansion on fundamental functions is:

$$p_{ext}^n (r,\varphi,z) = \sum_{n=0}^{\infty} C_n * H_n^{(i)} (\varkappa_{ext.}^n r) * e^{in\varphi} e^{ik\rho z}$$

where $\varkappa_{ext.}^n = k^2 - k^2$, r,φ and z - cylindrical coordinates.

Then the sound pressure on the outside surface of the external cylindrical layer ($r=R_2^n$) will be equal:

$$p_{ext.}^n (R_2^n,\varphi,z) = \sum_{n=0}^{\infty} C_n * H_n^{(i)} (\varkappa_{ext.}^n R_2^n) * e^{in\varphi} e^{ik\rho z}$$

In order to determine the factors C_n the transition matrix method is used [5]. The transition matrix method through the totality of coaxial cylindrical layers is represented in form of a product of the transmission matrix, corresponding to i-packet elastic and viscoelastic layers and intermediate liquid layer.

The transmission matrix through n_i interchangeable elastic and viscoelastic layers, limited by a liquid from both sides expressing through the components σ_{ij} and displacements u,v,w on the opposite sides cylindrical shell, have been received in rel in form:

$$\text{column} \, \{\sigma_{rr}^n , \sigma_{rz}^n , \sigma_{r\varphi}^n , u^n , v^n , w^n \} =$$

$$= [A_{n_i}]*[A_{n_i-1}]*....*[A_1]* \text{column} \{\sigma_{rr}^0 , \sigma_{rz}^0 , \sigma_{r\varphi}^0 , u^0 , v^0 , w^0 \}$$

where A_k -is the transition matrix of ik-layer. The elements of this matrix are given in the paper [6]. Taking into consideration the conditions on the boundary of the solid and liquid layers in the sound field:

$$\sigma_{rz}^0 = \sigma_{r\varphi}^0 = 0; \quad \sigma_{rz}^n = \sigma_{r\varphi}^n = 0; \quad \sigma_{rr}^0 = -p_i^0; \quad \sigma_{rr}^n = -p_i^n = -p_2^0.$$

the resulting matrix can be written as:

$$\begin{vmatrix} \sigma_{rr}^n \\ w^n \end{vmatrix} = \begin{vmatrix} a_{11} & a_{12} \\ a_{21} & a_{22} \end{vmatrix} * \begin{vmatrix} \sigma_{rr}^0 \\ w^0 \end{vmatrix}$$

where

$$a_{11} = A_{11} + \frac{A_{14} * \Delta_1 + A_{15} * \Delta_2}{\Delta_5} ; \quad a_{12} = A_{16} + \frac{A_{14} * \Delta_3 + A_{15} * \Delta_4}{\Delta_5} ;$$

$$a_{21} = A_{61} + \frac{A_{64} * \Delta_1 + A_{65} * \Delta_2}{\Delta_5} ; \quad a_{22} = A_{66} + \frac{A_{64} * \Delta_3 + A_{65} * \Delta_4}{\Delta_5} ;$$

534

$$\Delta_1 = A_{25} * A_{31} - A_{21} * A_{35}; \quad \Delta_2 = A_{21} * A_{34} - A_{24} * A_{31}; \quad (7)$$

$$\Delta_3 = A_{25} * A_{36} - A_{26} * A_{35}; \quad \Delta_4 = A_{26} * A_{34} - A_{24} * A_{36};$$

$$\Delta_5 = A_{24} * A_{35} - A_{25} * A_{34};$$

The transition for the liquid layer is obtained from the equation for the potential of the sound field and normal component of the oscillation velocity on the internal and external surfaces of the layer with $r = r_j^0 = R_1^h$ and $r = r_j^h = R_2^0$.

$$\begin{vmatrix} 6_{rr}^h \\ w^h \end{vmatrix} = \begin{vmatrix} C_{11} & C_{12} \\ C_{21} & C_{22} \end{vmatrix} * \begin{vmatrix} 6_{rr}^0 \\ w^0 \end{vmatrix} ; \quad (8)$$

where

$$C_{11} = \frac{R_1^h}{2} \times [I_n(x_j R_1^h) * N_n'(x_j R_2^0) - N_n(x_j R_1^h) * I_n'(x_j R_2^0)];$$

$$C_{12} = \frac{R_1^h}{2} w^2 [I_n(x_j R_1^h) * N_n(x_j R_2^0) - N_n(x_j R_1^h) * I_n(x_j R_2^0)];$$

$$C_{21} = \frac{R_1^0}{2 * w^2} [I_n'(x_j R_1^h) * N_n'(x_j R_2^0) - N_n'(x_j R_1^h) * I_n'(x_j R_2^0)];$$

$$C_{22} = \frac{R_1^0}{2} [I_n'(x_j R_1^h) * N_n(x_j R_2^0) - N_n'(x_j R_1^h) * I_n(x_j R_2^0)];$$

The resulting matrix D_{ij} for the two-wall shell can be written as:

$$\begin{vmatrix} 6_{rr}^h \\ w^h \end{vmatrix} = \quad \cdots \quad \begin{vmatrix} D_{11} & D_{12} \\ D_{21} & D_{22} \end{vmatrix} * \begin{vmatrix} 6_{rr}^0 \\ w^0 \end{vmatrix} ; \quad (9)$$

where ... and ... are transition matrices for the external and internal walls.

Substituting $6_{rr} = 6$ and $w = iw/w$ we will obtain the transition matrix for the shell:

$$\begin{vmatrix} 6^h \\ w^h \end{vmatrix} = \begin{vmatrix} D_{11} & D_{12} \\ D_{21} & D_{22} \end{vmatrix} \begin{vmatrix} 6^0 \\ w^0 \end{vmatrix} \quad (10)$$

After some transformations the expression for the transmission factor in the following form:

$$\cdots = \frac{D_{11} D_{22} - D_{12} * D_{21}}{\cdots} \quad (11)$$

where

$$\cdots$$

In the incident direction:

$$w \cdot \theta \quad \cdots$$

$$\quad \cdots$$

The frequency characteristic of sound insulation of double-wall shell under fixed angle of incidence is given in fig.1 (curve 1); the curve 2 in this figure corresponds to the single wall shell of the same thickness.

A numerical analysis of the expression (12) shows,that the frequency of minimum of sound insulation of the shell vibrating at the "n" mode, is displaced in the region of higher frequency; the value of the minimum of sound insulation is essentially smaller.

If the shell of finite length is exited only by one mode of vibrations,then the sound insulation can be calculated,using the expression (12). In addition it is necessary take into consideration the cavity resonances,being defined by formula:

$$\mathcal{I}_{mij} \cdot \mathcal{F}_{\text{or}} + \text{sign} + \cdots \rho_{\cdots}^{\cdots} \cdots \frac{\cdots}{\rho} \cdots \rho_{\cdots}(\omega) \cdots \cdots (13)$$

and is the complex impedance of edge.

When several modes of vibrations are exited simultaneously, it is necessary to determine the weighting factors of various modes. For this, one use the expressions, received by expansion of deformation in Fourier

$$\cdots = \cdots \cdot \frac{\displaystyle\sum_{\rho=1}^{\infty}\sum_{n=0}^{\infty} \cdots}{\displaystyle\sum_{\rho}\sum_{n} \cdots} \cdots (14)$$

In this case the frequency characteristic of sound insulation have outline caused by resonances of the shell at eigen frequencies ...

360 degree.

The experiment has confirmed the frequencies of minimum of of sound insulation are essentially depended on the incidence angle. There is an increasing of sound pressure in the surrounding space under some incidence angles, i.e. the focusing takes place. For example, for 60 degree angle it takes place in frequency band with fmid = 2500 Hz, and for 40 degree angle - in range with fmid = 1000 Hz. Negative value of sound insulation are obtained in layered shell.

The frequency bands, in which sound insulation minima take place, includes resonance frequence of inner volume shell and eigen frequency. Sound insulation minima are more strong when the shell is excited by "pure tone", that corresponds to the discrete components in the noise of machines and mechanisms.

This result is confirmed by data in Fig.4, where some angle characteristics are presented for the homogeneous cylindrical shell at its resonance frequencies. Fig.4a corresponds to the shell's cavity resonance (f = [illegible] Hz). In this case the negative sound isolation make up [illegible] dB in normal direction to the shell axis and to 15 degree solid angle and -28 dB in axis direction.

The typical characteristics of sound insulation for shell vibrating at bending modes [illegible]

[illegible]

ΔR, дБ

STATISTICAL ENERGY ANALYSIS
AND ENERGY METHODS

MODELING AND ESTIMATING THE ENERGETICS OF COMPLEX STRUCTURAL SYSTEMS

G. Maidanik and J. Dickey
David Taylor Research Center
Bethesda, Maryland 20084 USA

PREFACE

Designers of land, aero, space, and naval vehicles often demand one-to-one predictive schemes so that the performance of the vehicles can be a priori ensured. Those research scientist who humbly and truthfully "ha and dah" about their ability to comply with this demand are left out by the brokers for the designers. Under this pressure some research scientists are willing to exaggerate capabilities that lie in their models by claiming them to be bona fide predictive schemes. When one admits to a broker that his models bear only phenomenological correspondence, these models are designated academic and treated as if "academia" is a disease from which designers are to be protected at all costs. There is a need for establishing clearing houses in which competent brokers could help to transfer models that provide good phenomenological correspondence into one-to-one predictive schemes. Such honest brokers could then match-make between research scientists and designers to the bliss of both. Successful marriages of this kind could yield manufacturing of better vehicles at lower costs.

TEXT

The models to be discussed are ideal and bear a phenomenological correspondence to behavior of many complex structural systems that constitute the vehicle. In modeling for a phenomenological correspondence, one needs to ensure that the phenomenon under investigation is manifested in the model. The one-to-one correspondence is largely sacrificed so that the behavior of the model can be investigated by reasonable analytical descriptions. Reasonable analytical descriptions are those that harbor information that can be managed and deciphered. Situations exist in which despite the sacrifice of one-to-one correspondence the descriptions are still cumbersome and may be complicated. In an attempt to alleviate the cumbersomeness and the complication one may resort to introducing quadratic, and subsequently statistical, descriptions. Not withstanding that statistical descriptions may become appropriate simply because the definition of the structures cannot be specified except statistically. These quadratic and statistical descriptions basically pertain to estimating the energetics of the complex structural systems; among these kinds of descriptions is the so called statistical energy analysis (SEA).

The model approach to the derivation of SEA is briefly reviewed. Some of the advantages of using SEA are discussed and exemplified. As a counter point, some of the difficulties that may beset the use of SEA are also discussed and exemplified. An extension is introduced to SEA that accounts for the stored energy in terms of a reverberant portion as well as a non-reverberant portion. A mention is made of the wave approach to the derivation of SEA and its relationship to the modal approach is cited and compared.

SECOND INTERNATIONAL CONGRESS ON
RECENT DEVELOPMENTS IN AIR- AND
STRUCTURE-BORNE SOUND AND VIBRATION

MARCH 4-6, 1992   AUBURN UNIVERSITY, USA

AN ASSESSMENT OF THE MICROGRAVITY AND ACOUSTIC ENVIRONMENTS
IN SPACE STATION FREEDOM USING VAPEPS

Thomas F. Bergen, Dr. Terry D. Scharton, and Gloria A. Badilla*
Jet Propulsion Laboratory
California Institute of Technology
4800 Oak Grove Drive
MS 301-456
Pasadena, CA 91109
U.S.A.

ABSTRACT

The Space Station Freedom (SSF) program was established to provide a near-zero
gravity laboratory for scientific experiments which may be conducted by a human crew.
Microgravity limit requirements were established for both transient and stationary
vibration events to ensure the success of the proposed experiments. Crew acoustic noise
requirements were established to eliminate fatigue and potential hearing loss from long
term exposure, and to facilitate speech communications. The stationary noise and vibration
environments may be induced by various source classes such as fans, pumps, compressors, and
other mechanical devices. Prediction of the stationary on-orbit environments in one SSF
module was performed using the Vibroacoustic Payload Environment Prediction System
(VAPEPS).

VAPEPS is a computer program that utilizes statistical energy analysis (SEA)
techniques to predict the vibroacoustic environments in complex systems. A model of the
reconfigured U. S. Laboratory module was developed. The model included the outer
structure, equipment and payload racks, and the avionics and cabin air duct systems.
Acoustic and vibratory outputs of the various source classes were derived and input to the
model to predict their effects on the system. Analyses were performed in one-third octave
frequency bands from 10 to 10,000 Hz. Initial results showed that both the microgravity
and acoustic requirements would be exceeded in some one-third octave bands with the current
SSF design. Further analyses indicated that interior acoustic level requirements would be
exceeded even if the microgravity requirements were met.

INTRODUCTION

A major concern for SSF is the interior acoustic noise and vibration levels which
the crew and science experiments will experience. Acoustic noise requirements for SSF are
established at NC (Noise Criteria) 50 for work areas, and NC 40 for sleep compartments.[1]
Vibration requirements for SSF are established at 10^{-3} G's above 100 Hertz and decreases
linearly with frequency below 100 Hertz.[2] The SSF Office in Reston, Virginia assigned JPL
to develop a computer model to simulate the on-orbit stationary vibroacoustic environment
for SSF. This model is to be made available to all SSF contractors and sub-contractors.
The model was developed using VAPEPS, which is a computer program that predicts noise and
vibration environments and uses statistical energy analysis (SEA) methods.

The techniques used by VAPEPS to help predict the noise and vibration levels within
the SSF will be discussed. The prediction techniques prove to be very useful for this type

of analysis. They also have a rapid turn around time so that designers can get quick answers to the effects that various configurations and treatments may have on the noise and vibration levels in the SSF. The theory used within VAPEPS is presented and a description of the model is discussed. The results of the analysis and their implied effects on crew comfort and science experiments are discussed in the conclusions.

BACKGROUND ON SPACE STATION

NASA has developed various requirements for noise and vibration levels to maintain comfort and reduce stress and fatigue of its astronauts and to ensure successful microgravity experiments while on orbit in the SSF. Noise levels in both the space shuttle crew module and Skylab during orbit have caused adverse effects on astronaut communications and sleep. NASA wants to ensure that these problems are not repeated in SSF.

The principal investigators for Space Station Science experiments have determined from previous space science experiments, that a long duration, very low microgravity environment is necessary to obtain successful results. The support of microgravity experiments have been established as the primary function of SSF.

Efforts were made in the Shuttle and Skylab programs to reduce noise and vibration, however noise and vibration treatments were not designed into the vehicles. This design aspect must be considered for SSF. Including noise and vibration reduction techniques in the vehicle design will produce a quieter and lower vibration level station at reduced cost and effort. VAPEPS is a software program that can help designers in the early stages of the design to incorporate the most effective noise and vibration reduction treatments. The rapid turn around time of a prediction, as well as the simplicity of the models, allows for easy use during the concept stage.

ENVIRONMENTAL REQUIREMENTS

Acoustic levels in SSF must be low enough to ensure crew comfort and safety. The crew will be exposed to the noise levels for extended periods of time. Once permanently manned, the SSF will be able to support crews for periods of months. This varies from conventional work environments in that the crew will be unable to take rest from the noise environment. The Occupational Safety and Health Administration (OSHA) requirements for loud noise exposures assume an 8 hour exposure time with a rest period in an environment where noise levels are at least 10 dB less.

In order to account for the constant exposure to the noise, NASA developed acoustic noise requirements that are more stringent than OSHA's. Noise criteria requirements for SSF are NC-50 for the work areas, and NC-40 for the sleep areas. Figure 1 shows the NC-50 and NC-40 octave band sound pressure levels. A NC-50 curve allows for a subject (with an average male voice) to speak in a normal voice and be understood at a distance of 7 feet (a subject with an average female voice would need to be 4 feet from the other person). The following applications of the NC-40 and NC-50 design criteria help to illustrate what a person would hear if subjected to these levels: the NC-40 curve is recommended for design of open-plan offices, retail shops and stores, cafeterias, restaurants, etc.[3] The NC-50 curve is suggested design criteria for kitchens, laundries, garages, machinery spaces, power plant or mechanical equipment control rooms, etc.

Broadband vibration level requirements are established for SSF as shown in Figure 2. The broadband performance criteria was generated to assess the combined environment from multiple stationary sources, and were derived directly from the narrow band requirements. At each center frequency the narrowband criteria establishes the allowable acceleration amplitude limit. This is then reduced by 0.707 to formulate a root-mean-square (RMS) allowable. The RMS acceleration response due to the acceleration response at all frequencies within the one-third octave band must satisfy this value. Once the allowable RMS levels were determined, the equivalent power spectral density (PSD) curves were computed. The integrated values obtained from these curves within each one-third octave band corresponds to the mean square acceleration allowable over that band. Thus, the square root of the integrated sum is equal to the RMS level derived from the narrowband curve.

The broadband curve was used for comparisons with the VAPEPS predictions. This was done because all sources within the SSF lab were incorporated into the model. The combined environment from all sources is considered to be broadband even though the individual sources may have harmonics at discrete frequencies.

OVERVIEW OF VAPEPS

The primary objective of the VAPEPS activity was to develop a more consistent and
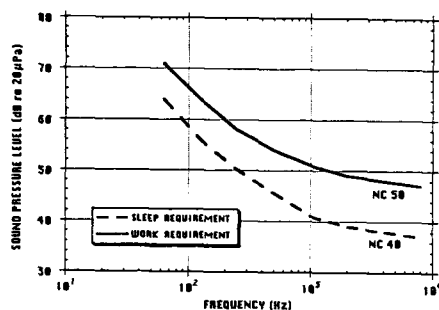
Figure 1: Noise Criteria Requirements

reliable method for establishing vibroacoustic design and test requirements for payload components. Lockheed Missiles and Space Company, (LMSC), under the sponsorship of NASA Goddard Space Flight Center and the United States Air Force Space Division was contracted to develop VAPEPS. The VAPEPS Management Center (VMC) provides the aerospace community with a cost effective tool for payload vibroacoustic environment predictions. Currently, the VMC is sponsored by NASA Lewis Research Center to perform program and modeling validations, user consultation, technology development, and program and database management.

SEA CONCEPTS

The theory incorporated into VAPEPS is Statistical Energy Analysis (SEA). This prediction scheme uses structural parameters, acoustic spaces, and excitation parameters of a space vehicle. It provides an energy balance from which the mean-

squared value of acoustic and/or vibration response can be determined in one-third octave increments from 10 to 10,000 Hertz.

The most important feature of SEA is the description of a vibrating element as a member of a statistical population (ensemble). The SEA methods identify energy as the primary variable so that the fundamental dynamic equations are simple. When steady-state condition is reached, the power input to an element must be equal to the power output of the element. This energy balance is the basis of SEA. The use of SEA leads to the statistical estimates of average modal energy. The average is taken over time and frequency bands. The average modal energy is used to calculate the spatial average mean square response.

VAPEPS ANALYSIS OF THE SSF LABORATORY MODULE

The reconfigured design of the laboratory module consists of a cylinder with bulkheads welded to the ends (see Figure 3)[4]. The aluminum module is about

Figure 2: Broadband Stationary Microgravity Requirement

Figure 3: SSF Module Outer Structure (Reconfiguration)

275 inches long, and is divided into two sections. Each section is formed of cylindrically curved waffle-stiffened skin panels that are welded together to form a 166 inch (4.2 m) diameter cylinder. Each section is welded together and reinforced at the joints with midrings. The module is additionally stiffened longitudinally with longerons and circumferentially with stability rings. Equipment racks are mounted to longerons inside the module. Equipment contained in the racks include science experiments as well as ventilation equipment, and associated duct work, which is a primary source of noise and vibration inside the module.

The following sections describe the SEA modeling of the module using the VAPEPS software. Since statistical techniques are being used, geometry and material properties are spatially averaged providing a much simpler representation of the structure (see Figure 4). A description of the SEA elements used and their energy path connections are provided. The excitation inputs are also described and the results produced by the VAPEPS analysis are presented.

SEA Element Description

Figure 4: VAPEPS Representation of Lab Module Outer Structure

Figure 5: Cross Section of SSF Module Reconfiguration
(SEA Representation)

The structural elements used to define the laboratory module include the skin panels, stiffening beams, the equipment racks, and the ventilation ducts. Material properties for aluminum were input to the model except where noted. The acoustic elements modeled include the spaces inside the racks and the ducts as well as in the living/working space.

The equivalent plate (EQPL) processor in VAPEPS was used to convert the properties of the waffle-stiffened skin panels into properties of equivalent isotropic homogeneous panels. The waffle stiffeners were treated as widthwise and lengthwise beam layers. VAPEPS does not provide for the input of curved plate parameters, so the panels were defined as flat plates with the same surface area as the curved plates in the design. The end bulkheads were similarly modeled as flat plates.

No engineering drawings of the equipment racks were available. Overall dimensions were obtained from preliminary

sketches. The racks were treated as boxes with dimensions compatible with the interior of the module. The boxes were formed of six panels of aluminum honeycomb with thin graphite epoxy face sheets. The actual materials to be used have not been determined, however lightweight composite materials are most commonly used for equipment panels. The EQPL processor was used to calculate equivalent isotropic properties of these honeycomb panels. A total of 24 racks was included in the model.

Racks and duct systems were included in the interior of the structure. The ducts were modeled as cylinders and were point connected to the primary structures at the standoffs. A duct system was defined for the avionics air and the cabin air, and crossover ducts were included. Vertical and horizontal stiffening beams representing a support structure for the racks were connected at points to the sides and corners of the racks. The racks were connected to the primary structure via the longerons. Acoustic elements were defined for each rack

Figure 6: US Lab Module Source Location

Figure 7: Small Fan Power

and duct interior space as well as for the interior acoustic space. The avionics duct spaces were acoustically coupled to the rack spaces, and the cabin air duct spaces were acoustically coupled to the interior acoustic space. Excitation of the system was provided in the form of acoustic and mechanical power, as well as turbulent boundary layer forces in the ducts. A cross-sectional view of the VAPEPS model elements is shown in figure 5.

Energy Path Connections

The basic types of energy paths used by VAPEPS are structural-to-structural element connections and structural-to-acoustic element connections. The latter provide for resonant and non-resonant (mass law) connections. Paths used in this model include the butt welding of plates and cylinders, and the point connections of beams to plates.

The outer structure was modeled as a cylinder. The forward and aft bulkheads were welded at a ninety degree angle to each end. The equivalent midring and longeron stiffening beams were point connected to the cylinder.

The rack panels were welded at ninety degree angles to form boxes. The corners of

546

Figure 8: Medium Fan Power

Figure 9: Large Fan Power

the top and bottom panels were then point connected to the longerons in the configuration shown in Figure 5.

The cabin air and avionic ducts ran the length of the module, and were point connected to the standoffs as shown in Figure 5.

Excitation Inputs

Source power levels were derived for the fans and pumps in the U.S. Laboratory system racks as identified by Boeing Aerospace. There was a total of 20 fans and 28 pumps/compressors. Power levels were estimated in one-third octave bands from 10 to 10,000 Hz for the three specified sizes of the fans and pumps/compressors: small, medium, and large. Table I summarizes the disturbance sources included in the analysis. Acoustic and mechanical (vibrational) components of the source levels were determined. Pumps and compressors were taken to be essentially the same type of equipment, and were assumed to produce the same source levels for similar horsepowers. The five small centrifugal separators included in the U. S. Laboratory rack list were not considered in this analysis. However, the Boeing Aerospace reported air flows in the laboratory ducts were used. Velocities in the 20 foot per second range generated turbulent boundary layer disturbances in the ducts beneath the rack standoffs.

TABLE I

Size of Fan	Small	Medium	Large
Quantity	7	8	5
Assumed Flow Rate (cfm)	100	400	Unknown
Assumed Static Pressure (in. water)	1	3	Unknown
Assumed Mounting Plate Thickness (in.)	1/16	1/8	1/4
Approximate Power (hp)	1/20	1/2	Unknown
Overall Sound Power (dB*)	77	93	90
Overall Mechanical Overall Power (dB*)	63	77	89

Size of Pump	Small	Medium	Large
Quantity	18	7	3
Assumed Mounting Plate Thickness (in.)	1/16	1/8	1/4
Approximate Size (hp)	0.013	0.1	0.6
Overall Sound Power (dB*)	75	84	92
Overall Mechanical Power (dB*)	83	86	98

* All power levels are in dB re 1.E-12 W

Acoustic

Acoustic levels for the large fan (THC/Avionics) were provided by Boeing Aerospace. The overall levels and frequency weighing for small and medium fans were calculated from assumed scaled down flow rate and static pressure parameters using generic results from the ASHRAE Handbook[5] for tubeaxial fans under 40 inches in diameter. Blade passage frequency increments were neglected.

The pump acoustic power levels were determined by scaling of empirical data from: "Noise Control for Building and Manufacturing Plants" taught by Laymon Miller and Bob Hoover, in November 1990[3].

Mechanical

The mechanical power inputs were based on imbalance force data provided by Boeing Aerospace for each class of equipment. The power input to a mounting structure due to the

547

mechanical imbalances were computed from an assumed impedance of the mountiag structure. The point impedance of the mounting structure was assumed to increase with equipment mechanical power since more powerful equipment will probably be mounted on heavier structure. The overall mechanical power level (total power) was computed and the mechanical power levels were assumed to have the same spectral shape as the acoustic levels for each type of equipment.

Input of Disturbances

All acoustic power inputs were injected into the acoustic spaces of the U. S. Lab system racks which supported the particular pieces of equipment. The mechanical power inputs were injected into the stiffening rails of the individual system racks that support that equipment. No inputs were assumed for payload racks. The locations of the various equipment sources were determined from configuration information provided by Boeing Aerospace. Figure 6 illustrates the proposed U.S. Laboratory layout at permanently manned capability stage (PMC). Note, that the large fans are positioned in the aft-most racks which are designated as rack number 6, ceiling, starboard, floor, and port. Figures 7-9 plot the acoustic and mechanical power input levels of small, medium, and large fans respectively, and figures 10-12 of the pumps/compressors. Plots of the source power are in one-third octave bands from 10 to 10,000 Hz. Power from assumed turbulent boundary layer excitation of ducts based on flow rates obtained from Boeing Aerospace was also input to the model. These power levels were found to be negligible compared to other sources.
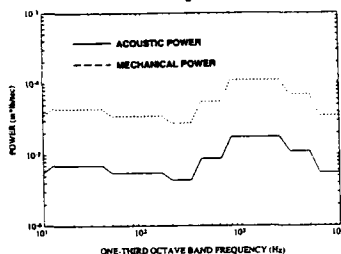
Figure 10: Small Pump Power

Figure 12: Large Pump Power

Figure 11: Medium Pump Power
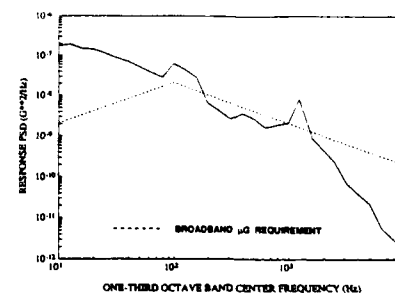
Figure 13: Average Ceiling Payload Rack Support Response

RESULTS

The responses at the 12 U.S. Lab payload racks were determined by averaging the responses of the four vertical corner beam elements of each rack. Plots of these responses are compared with the microgravity broadband requirement in figures 13-16. The response data are presented in one-third octave bands from 10 to 10,000 Hz in acceleration power spectral density (g^2/Hz) format. The ceiling racks are denoted as "lac#", the starboard racks as "las#", the floor racks as "laf#", and the port racks as "lap#". The numerical identifier can range from 1 to 6, with 1 at the forward end, and 6 at the aft end.

Preliminary analysis of the results show that predicted accelerations on the mounting posts of the payload racks exceed the microgravity requirements in the 100 Hz and 1250 Hz one-third octave bands. The 100 Hz peak is due to the peak in the large fan acoustic output. The coincidence frequency of the rack panels as they are modeled in this

548

simulation occurs in the 1250 Hz band. The coincidence is responsible for the $8*10^{-9}$ g^2/Hz peak in the 1250 Hz band, and exists at all racks, regardless of position. This results in one-third octave band root-mean-square levels in the order of 1500 micro-g which is approximately twice the 707 micro-g allowable. In the 100 Hz range, the three starboard payload racks are at or below the requirement curve. There is a continuous degradation in performance from port, to ceiling, to floor locations with no significant response differences in the forward-aft direction. The cause of these effects, or lack thereof, merits further investigation. In the worst case, the single floor payload rack acceleration response has a maximum one-third octave band root-mean-square level of 2275 micro-g which is 3.2 times the requirement. The effects from the turbulent boundary forces due to duct air flow were minimal.

Below 100 Hz, all predicted accelerations of the payload racks appear to

Figure 14: Average Starboard Payload Rack Support Response

diverge from the requirement as the frequency approaches 10 Hz. The divergence may indicate that the predictions become less accurate as the low frequencies are approached. Source assumptions and the sparse modal densities could degrade the accuracy of the SEA predictions. The results below 100 Hz require further investigation. The high frequency SEA and low frequency finite element results need to be reconciled in the 10 to 15 Hz frequency range.

Based on the simplified vibroacoustic model used, the results show that the predicted noise levels inside the untreated module do not meet the noise criteria, exceeding NC-50 by as much as 25 dBA (see figure 17). For extended periods, the overall noise level of 101 dBA inside the habitation module would indeed be agonizing if not damaging. The crew would be required to wear hearing protection while sleeping at levels above 76 dBA. It must be noted that only one noise source is included in this model, and the inclusion of additional sources will only increase the levels. In addition, this model does not include any noise control measures. Various noise control treatments are currently being investigated. These measures may be insufficient and a quieter fan may have to be used.

Figure 15: Average Floor Payload Rack Support Response

SUMMARY AND CONCLUSIONS

VAPEPS proved to be an effective tool in this analysis, allowing for the implementation of large models and the ability to change parameters easily. Parametric studies of the effects of acoustic absorption and damping are performed simply by running separate models with different absorption and damping values. VAPEPS may be employed to determine the required parameters to meet noise level requirements, however implementing the measures may be much more difficult.

Drastic damping and acoustic absorption measures will be required to bring the noise levels down. Since acoustic paths are the primary contributors to the interior noise levels, increased acoustic absorption should have a greater effect on noise attenuation

549

Figure 16: Average Port Payload Rack Support Response

than increased structural damping. Unfortunately, the use of acoustic materials such as fiberglass is not allowed since SSF is a closed system, and contamination requirements are stringent. In addition, the use of structural damping materials must be limited because they can add considerable weight to the structure. These factors present a serious problem for SSF designers. Noise sources and noise control treatments need to be considered in the design stage to ensure that noise requirements are achieved in a cost effective manner. VAPEPS is an effective tool to support this design effort.

ACKNOWLEDGEMENTS

REFERENCES

1. NASA, Man-System Integration Standards, NASA-STD-3000, Baseline, Vol. IV, 1986.

2. Space Station Engineering Integration Contractor (SSEIC), Space Station Freedom Program Office, "Space Station Microgravity Environment Definition", SSC 18270, September 1, 1991

3. Miller, Laymon N., Lecture notes for short course: "Noise Control for Buildings, Manufacturing Plants, Equipment and Products", 1990.

4. Structural Assembly Laboratory Module Space Station Freedom, Boeing Drawing, March 29, 1990.

5. American Society of Heating, Refrigerating, and Air Conditioning Engineers, Inc., "1991 ASHRAE Handbook, Heating, Ventilating, and Air-conditioning Systems and Applications," 1991

Figure 17: Predicted Cabin Acoustic Levels

550

APPLICATION OF VAPEPS TO A NON-STATIONARY PROBLEM

L. K. St-Cyr and J. T. Chon
Rocketdyne Division of Rockwell International
Canoga Park, California 91303

ABSTRACT

The VibroAcoustic Payload Environment Prediction System (VAPEPS) is an applications package for modeling interactions between vibrating structures and acoustically active spaces when the motion is statistically stationary. In particular, VAPEPS can predict sound power levels (SPLs) inside enclosures given SPLs outside. This paper presents a method of using VAPEPS to provide an upper-bound estimate of the strength of an acoustic pulse transmitted to the inside of a structural enclosure, thereby extending VAPEPS to a non-stationary problem. The method is illustrated for a particular enclosure, but the principle is general in scope.

METHOD OF ANALYSIS

VAPEPS was developed by Lockheed and JPL to assess acoustic levels in the payload bay of a rocket. It has the capability to couple structure-borne vibrations in the form of bending waves to reverberant sound in spaces. Since large structures and spaces can have thousands of relevant acoustic modes, a finite element analysis in which modes are individually characterized is not practical. Instead, VAPEPS uses statistical energy analysis (SEA). SEA solves for the density of modes within given frequency bands and assumes that the available energy is evenly distributed among all the modes in that band, a good assumption as long as there are at least a few modes per band. SEA can thus neglect the exact mode shapes since that has little effect when the modes are closely spaced in frequency.

VAPEPS accepts input in the form of an acoustic power spectrum, and assumes that this forcing is steady-state random. This is definitely not the case for an acoustic pulse. The difference between steady-state and transient cases is contained in the phase information, which VAPEPS normally discards. The approach used here was to assume a worst case: that the phase of the pulse does not change as the acoustic energy is transmitted through the walls. This assumption provides phase information inside the walls, which can then be combined with the VAPEPS-predicted magnitudes to yield a transient pressure time-history. Assuming no change in the phase portion of the pulse is a worst-case prediction because in reality, reflection and absorption will occur as functions of frequency, and this will degrade the phase alignment of the input and spread the pulse. Thus the assumption being made here should result in an upper bound for the interior acoustic environment.

Figure 1 depicts the structure; acoustic predictions are desired for the interior of the center compartment. The source of the forcing on the structure is the exterior space acting through all the outside walls. The front side of the structure faces the source of the pulse. A separate pressure time series was prescribed for the front, back, top, and bottom of the structure. The left and right ends used the same forcing function as the top. Fourier transforms of the pressure time series were created and the magnitude portions were processed to give third-octave band power spectra.
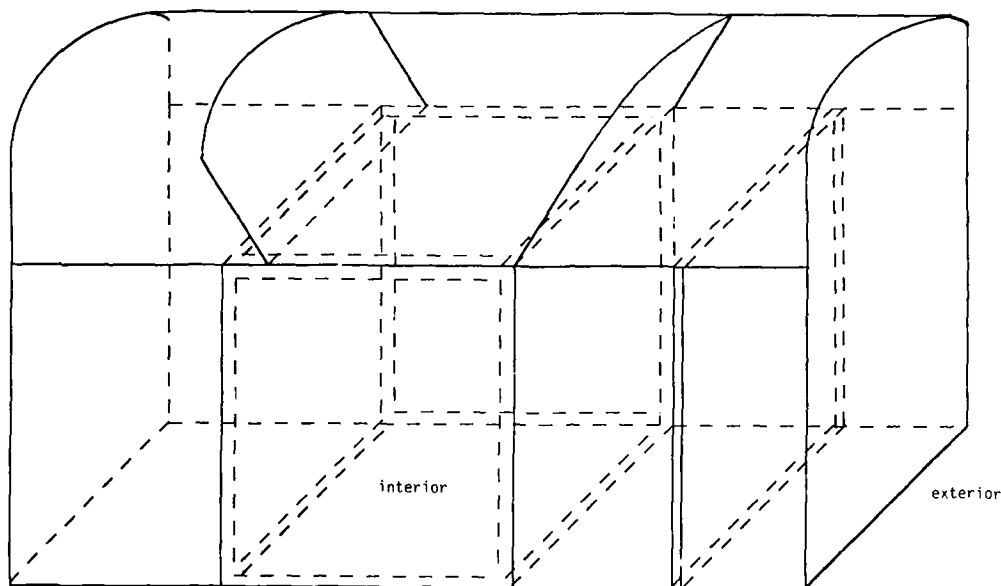
Figure 1—Geometry of structure

The next step was to apply these spectra to the VAPEPS model. Since each spectrum has its own phase information, it is only possible to recombine magnitude and phase if each spectrum is run separately through the VAPEPS model. The output from VAPEPS is an interior magnitude in the form of a spectrum. After the interior magnitude is combined with the original (unchanged) phase, one has produced a pressure history due to the pulse acting on one face of the structure. This may be repeated for all faces and summed as a function of time. The time summation implies correlated signals, which is a worst-case scenario. The entire process just described, from exterior pressures to interior predictions, is pictured schematically in the flowchart of Figure 2. The use of a finite-duration Fourier transform imposes periodicity on the prediction of the interior pressure time history, visible as the dip at the end of the pressure trace.

CONCLUSIONS

Although VAPEPS was designed for statistically stationary problems, it is possible to apply it to predictions of transmitted transients if the assumption of unchanged phase is used. Since the assumption is overly pessimistic, an upper bound for the strength of the transmitted pulse will be obtained.
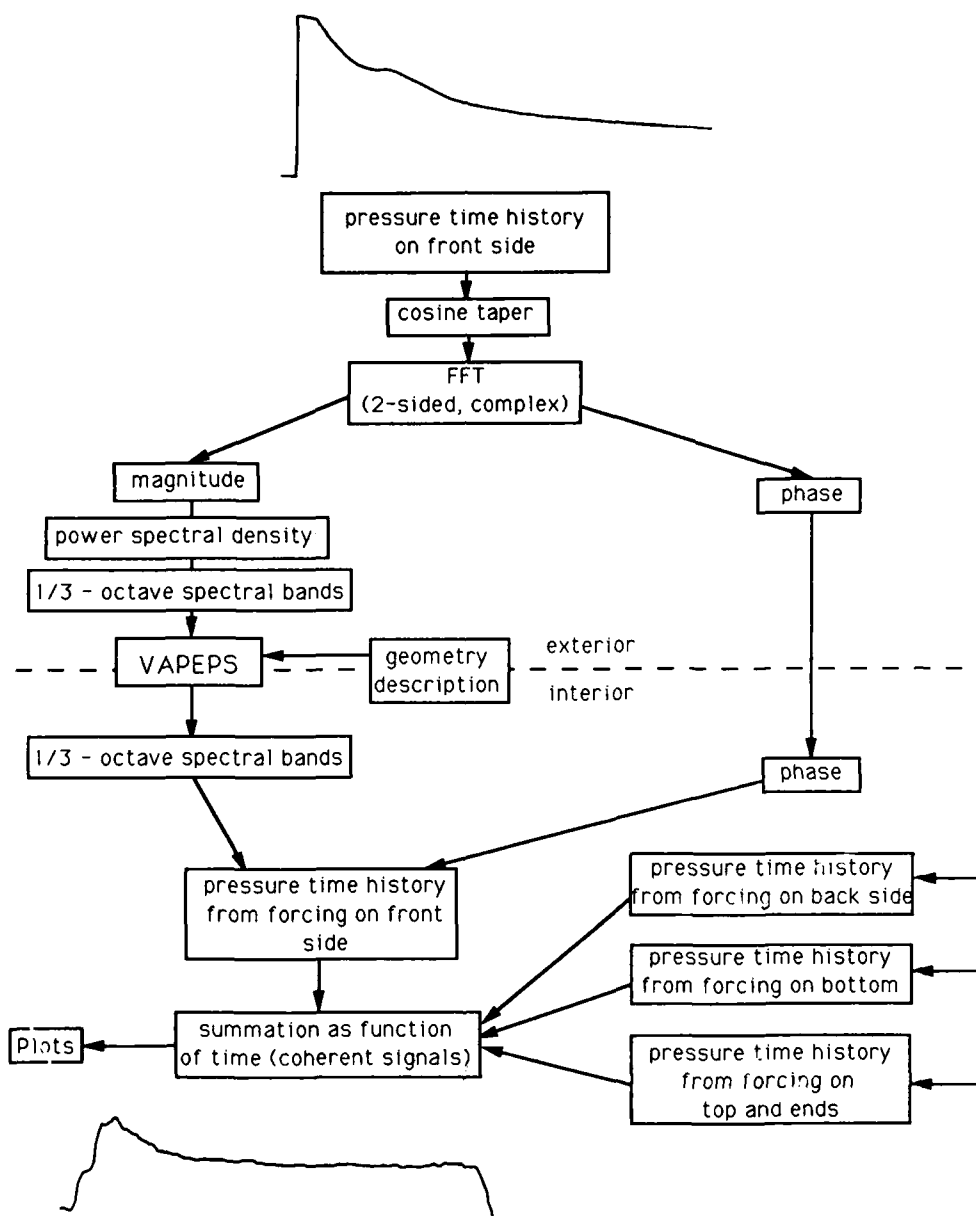
Figure 2--Process flowchart

DEVELOPMENT OF ENERGY METHODS APPLIED FOR
CALCULATIONS OF VIBRATIONS OF ENGINEERING STRUCTURES

Sergei V. Budrin and Alexei S. Nikiforov
Krylov Shipbuilding Research Institute
St.-Petersburg, 196158
USSR

ABSTRACT

Westphale's method, which is also called the SEA method and based on using of the principle of conservation of energy, is often used for calculations of vibrations of many engineering structures. Usually only appearancies of bending waves in this structures is taken into consideration. In this case the agreement between calculated and measured data will be essentially worse the further a point of observation gets from a source of vibrations.

It is shown in the report that if we consider mutual interaction of bending and longitudinal waves which take place on the structure obstacles, the above mentioned agreement is true also at the far distances from the vibration source.

The acoustic interaction between vibratory plates and air volumes limited by them is not taken into consideration in this methods. That expels the possibility of accounting energy exchange between the structure plates through the air volumes distinguishing them and in consequence reduces the accuracy of the calculations.

As it was shown in the report, if we include into scheme of the calculation the interaction between the plates and the air volumes we can calculate not only the plate vibrations but the acoustic pressure inside of the air volumes limited by plates.

1. The first article about an application of statistical energy analyse (SEA) for calculations of vibration fields in complex engineering structures was published 45 years ago. It was the article by W. Westphal [1] about a propagation of the structure-born sound in building constructions published on 1957. Usually authors cite on the more late article in this area vibroacoustic published by R. Lyon and G. Maidanik on 1964 [2]. Meanwhile this results is equal in principle. Indeed, the equation of an energy balance for the simplest structure consisting of connected between themself two plates look as:
- by Westphal

$$W_P + \alpha_{21} c_2 W_2 - \alpha_{12} c_1 W_1 - \delta_1 W_1 = 0 ;$$

$$\alpha_{12} c_1 W_1 - \alpha_{21} c_2 W_2 - \delta_2 W_2 = 0 , \tag{1}$$

where: W_1, W_2 - densities of vibration energy (VE); α_{12}, α_{21} - coefficients

describing transmissions VE from the plate 1 into the plate 2 and in the opposite direction; δ_1, δ_2 - coefficients, describing absorption VE in plates 1 and 2:

$$\alpha_{ik} = L_{ik} \tau_{ik} / \pi \; ; \quad \delta_i = \omega \eta_i S_i \; ; \tag{2}$$

L_{ik} - length of contact line between plates 1 and 2; τ_{ik} - coefficient of transmission of bending waves energy from plate i into plate k ; η_i - loss factor of plate i ; S_i - area of plate i ; ω - circular frequence; C_1 , C_2 - group speed of bending waves in plates 1 and 2; - by Lyon and Maidanik:

$$W_P - \omega \eta_{12} n_1 \left[\frac{E_1}{n_1} - \frac{E_2}{n_2} \right] - \omega \eta_1 E_1 = 0 \; ; \tag{3}$$

$$\omega \eta_{12} n_1 \left[\frac{E_1}{n_1} - \frac{E_2}{n_2} \right] - \omega \eta_2 n_2 = 0 \; ,$$

where: E_1, E_2 - total VE in plates 1 and 2; n_1, n_2 - densities of natural frequencies of plates 1 and 2; η_{12} - loss factor describing of leaving of VE from the plate 1 into the plate 2; $\eta_{12} = L_{12} \tau_{12} C_1 / (\pi \omega S_1)$. Taking account of equations $E_i = S_i W_i$ and $\eta_{ik} = \alpha_{ik} C_i / (\omega S_i)$ the identity of eq.(1) and (2) become obvious.
The demonstration of the equation

$$\frac{\eta_{ik}}{\eta_{ki}} = \frac{n_k}{n_i} \tag{4}$$

is the major result of the work [2] improving the work [1]. As showed in eq. (4) VE transmited from the plate with the greater quantity of natural frequencies exceed VE transmited in the opposite direction because each mode of one plate exite mode of other plate with an equal frequence only.

2. In above mentioned works [I] and [2] the acoustic interaction between vibratory plates and air volumes limited by them (for instance, ship accomodations) is not taken into consideration. Indeed if the exchange by VE between plates through air volumes is not taken account the accuracy of calculations is decreased. If air volumes is included in the system of energy balance's equations we can calculate besides a vibration of plates a sound pressure in air volumes also deciding the same system of equations.
M. Crocker and A. Price in their work [3] investigated a sound transmission through a partition using SEA on 1969. Probably it was the first attempt to include air volumes into a system of energy balance's equations. In this work some acoustic situations arised in one or two air volumes divided by a partition. Supplementing this situations another ones (the estimate of a vibration in the plate exited by a source of VE, the estimate of a sound pressure in the volume exited by a source of sound energy, ect.) and using more rational form of equations it was obtained the following equations for estimates of a vibration and sound pressure for cases of one and two air volumes:
- for a vibration of the plate exited by source of VE I_P :

$$W_P = \frac{I_P}{\eta_P S_P} \cdot \frac{\beta_1 + \beta_2}{1 + \beta_1 + \beta_2} \; ; \tag{5}$$

- for a vibration of the plate exited by source of sound power

$$W_P = \frac{I_c}{\eta_P S_P} \cdot \frac{\beta_1}{1 + \beta_1 + \beta_2} \; ; \tag{6}$$

- for a sound pressure in the air volume radiated bending vibrations of

the plate exited a source of VE I_P:

$$w_0 = \frac{I_P}{\gamma_0 V_0} \cdot \frac{1}{1+\beta_1+\beta_2} \; ; \tag{7}$$

- for a sound pressure in the air volume, exited a source of sound power I_0:

$$w_0 = \frac{I_0}{\gamma_0 V_0} \cdot \frac{1+\beta_2}{1+\beta_1+\beta_2} \; ; \tag{8}$$

where $w_P = m_P \langle \dot{\xi}_P^2 \rangle$; $\quad w_0 = \langle P_0^2 \rangle / (\rho_0 c_0^2)$;

m_P - mass of plate per unit of area; $\rho_0 c_0$ - acoustic resistance of air medium; $\langle \dot{\xi}_P^2 \rangle$ - meansquare vibration velocity of plate; $\langle P_0^2 \rangle$ - meansquare sound pressure in air volume.

Besides next conventional sign is assumed: $\beta_1 = \gamma_P / \gamma_0$; $\quad \beta_2 = \gamma_P / \gamma_{0P}$;

$\gamma_P = n_P \gamma_P$; $\quad \gamma_0 = n_0 \gamma_0$; $\quad \gamma_{0P} = n_P \gamma_{rad}$; $\quad \gamma_{rad} = R_{rad} / (\omega m_P S_P)$;

R_{rad} - radiation's resistance of plate; n_P - density of natural frequencies of plate; n_0 - density of natural frequencies of air volume; γ_P, γ_0 - inner loss factors of plate and air volume.

For estimates of a ratio of vibration velocity and sound pressure levels in various elements of above mentioned structures it is possible to use the following equations:

- for a ratio of vibration velocity of the plate and sound pressure in the air volume when the plate is exited by a source of VE:

$$\frac{\langle \dot{\xi}_P^2 \rangle}{\langle P_0^2 \rangle} = \frac{\gamma_0 V_0}{\gamma_P S_P m_P \rho_0 c_0^2} \cdot \frac{\beta_1}{1+\beta_2} \; ; \tag{9}$$

- for a ratio of vibration velocity of the plate and sound pressure in the air volume when the air volume is exited by a source of sound power:

$$\frac{\langle \dot{\xi}_P^2 \rangle}{\langle P_0^2 \rangle} = \frac{\gamma_0 V_0}{\gamma_P S_P m_P \rho_0 c_0^2} (\beta_1 + \beta_2) \; ; \tag{10}$$

- for a ratio of sound pressures in adjoining air volumes (sound-insulation of the partition):

$$\frac{\langle P_{01}^2 \rangle}{\langle P_{02}^2 \rangle} = SI = 1+\beta_0 \; ; \tag{11}$$

- for a ratio of vibration velocities of adjoining plates (vibro-insulation of the obstacle):

$$\frac{\langle \dot{\xi}_{P1}^2 \rangle}{\langle \dot{\xi}_{P2}^2 \rangle} = VI = 1+\beta_P \tag{12}$$

The following conventional sign is assumed in eq.(11) and (12):
$\beta_0 = \gamma_{0H}/\gamma_{00}$; $\beta_P = \gamma_{P1}/\gamma_{PP}$; $\gamma_{00} = n_{01} C_{01} S_P / (4 \omega V_0 \cdot SI_\infty)$;

SI_∞ - sound-insulation by law of mass, $\gamma_{PP} = n_{P1} \gamma_{12}$; S_P - area of partition.

Estimates of an influence of energies transmited by various paths may be fulfilled with the aid of eq.(5-12). For instance, the ratio of energies transmited into the adjoining accomodation by a partition and by external plates is equal:

$$\Delta = \frac{(1+\beta_2)(1+\beta_2/\beta_1)(1+\beta_P)}{4(1+\beta_0)} \tag{13}$$

557

3. Results of calculations by Westphal's method and measurements are not coincident in the large distance from a source of vibrations. It may be the result of the transmission of VE by ribbs for ribbed plates of the influence of the transformation types of resilient vawes wich take place on the structure obstacles and of energy's exchange between plates and air volumes. This factors may be taken into account by an idea about the propagation of an energy on several canals with the interaction between this canals. Two methods may be used in this case: the method of knot points and the method of equivalent plates.

The method of knot points is more general case of Westphal's method for limited number of canals for a propagation of an energy. This canals for ribbless plates are:
- bending, shear and longitudinal waves in structure's plates (m =1,2,3);
- sound waves in a medium contacted with a structure (m = 4).

The general equation of conversation of an energy with account of energy exchanged between ribbless plates and the medium contacting with this plates for the k-th element of structure (plates or volumes) in m-th canal have the following form:

$$ W_k^m + \sum_{j=1}^{N} \sum_{i=1}^{n} (\alpha_{ik}^{jm} q_i^j - \alpha_{ki}^{mj} q_k^m) - \delta_k^m q_k^m = 0, \qquad (14) $$

where:
W_k^m - energy entered in k-th element in m-th canal;
N^k - number of canals;
n_m - number of elements (plates and volumes);
q_k^m - flow of energy in k-th element for m-th canal;
α_{ik}^{jm} - coefficient of transmission of energy from j-th canal in i-th element into m-th canal in k-th element;
δ_k^m - coefficient of absorption of energy in m-th canal in k-th element.

Evidently $\alpha_{kk}^{mm} = 0$ for any m ; $\alpha_{kk}^{jm} \neq 0$ ($j = 1,2,3$), $\alpha_{kk}^{jm} = 0$ ($j = 4$) for $= 1,2,3; \alpha_{kk}^{mj} \neq 0$ for $m = 1,2,3;$ $\alpha_{kk}^{mj} = 0$ for $m = 4.$
Coefficients α_{ik}^{mj} & δ_k^m may be defined by [4] and [5] .
Fig.1 show flows of VE for a case of line junction of elements of a structure when N = 2.

4. The application of the method of knot points is convinient if a structure include small number of elements.

For structures included ribbed plates it is conveniently to consider their as plates with equivalent parameters. This approach allow to describe of a propagation of VE on the structure by differential equations similar to the equation of heat conductivity for a plate with radiation of heat in an environment medium.

The supposition about substitution of discrete obstacles by a parameter with unbroken distribution, is used. For one canal of propagation of VE on the orthotropic structure the differential equation described a propagation of VE have the following form:

$$ K_x \frac{\partial^2 w}{\partial x^2} + K_y \frac{\partial^2 w}{\partial y^2} - \beta w = 0, \qquad (15) $$

where: w - density of VE in equivalent plate;
K_x, K_y - coefficients characterizing of decrement of VE in direction x and y;
β - coefficient of absorption of VE in element of structure with unit surface.

The formulas for this coefficients is cited in [6] .
For a two dimensional structure with coupling canals the analogy differential equation have the following form:

$$K_{mx} \frac{\partial^2 W_m}{\partial x^2} + K_{my} \frac{\partial^2 W_m}{\partial y^2} + \sum_{j=1}^{N} \left(K_{jm} W_j - K_{mj} W_m \right) - \beta_m W_m = 0,$$

$$\left(m = 1, 2, \dots N \right), \qquad (16)$$

where: W_m - density of energy in m-th canal of propagation of VE; K_{jm}, K_{mj} - coefficients characterizing exchange of VE between j-th and m-th canals.

For a two-dimensional structure the solution of system of eq.(16) may be realized by a computer only. In some case an analys solution of this system of equations is possible. For instance, for a case of two-canal propagation of VE when one canal is excited by a poin+ source the distribution of a density of VE along axis have the following form (for O):

$$W_1 = W \left(-\frac{k_2 - \gamma_1^2}{\gamma_1} e^{-\gamma_1 x} + \frac{k_2 - \gamma_2^2}{\gamma_2} e^{-\gamma_2 x} \right) ;$$

$$W_2 = a_{12} W \left(-\frac{1}{\gamma_1} e^{-\gamma_1 x} + \frac{1}{\gamma_2} e^{-\gamma_2 x} \right) ; \qquad (17)$$

where W_0 - energy entered into structure where $x = 0$;

$$W = \frac{W_0}{2 k_{1x} \left(\gamma_1^2 - \gamma_2^2 \right)}; \qquad a_{12} = \frac{k_{12}}{k_{1x}} ;$$

$$k_1 = \frac{k_{12} + \beta_1}{k_{1x}} ; \qquad k_2 = \frac{k_{21} + \beta_2}{k_{2x}} ; \qquad a_{21} = \frac{k_{21}}{k_{1x}} ;$$

$$\gamma_{1,2} = \left[\frac{k_1 + k_2}{2} \pm \sqrt{\frac{(k_1 - k_2)^2}{4} + a_{21} a_{12}} \right]^{1/2}$$

Fig.2 shows the distribution of VE along two canals of the structure when an exchange of an energy between canals is taken into consideration. Parameters shown on the Fig.2 are connected with parameters of structure as:

$$\Delta_0 = \frac{k_2 + \gamma_1 \gamma_2}{a_{12}} ; \qquad \Delta_\infty = \frac{a_{21}}{k_1 - \gamma_1^2} ;$$

$$x_0 = \frac{\ln \Delta_y}{\gamma_1 - \gamma_2} ; \qquad \Delta_y = \frac{\left(k_2 - \gamma_1^2 \right) \gamma_2}{\left(k_2 - \gamma_2^2 \right) \gamma_1} \qquad (18)$$

Fig.2 shows also distributions of vibration's levels along a structure with periodical obstacles received by a calculation and a measurement. These results coincide.

REFERENCES

1. Westphal W. Ausbreitung von Korperchall in Gebänden, - Akustiche Beichefte, 1957, B.1, N 7, S.335-339.

2. Lyon R., Maidanik G. Statistical methods in vibration analysis AIAA Journal. 1984, V.2, N 6, p.1015.

3. Crocker M., Price A. Sound transmission using statistical energy

analysis. J. Sound Vib., 1969, V.9, N 3, p.469.

4. Nikiforov A., Budrin S. Propagation of Structure-borne Sound in Ship Structures. "Sudostrojenie", 1968 (In Russian).

5. Maidanik G. Response of Ribbed Panels to Reverberate Acoustic Fields. J.A.S.A., V.34, N 6, 1962, pp.809-826.

6. Liapunov V., Nikiforov A. Vibro-insolation in ship structures. "Sudostrojenie", 1975. (In Russian).
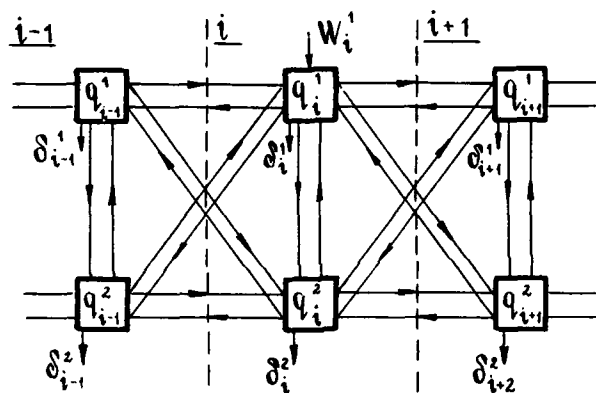
Fig. 1
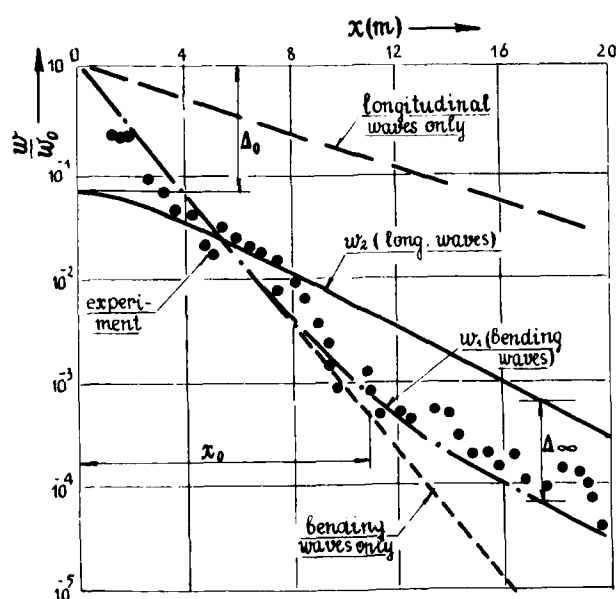
Fig. 2

SECOND INTERNATIONAL CONGRESS ON
RECENT DEVELOPMENTS IN AIR- AND
STRUCTURE-BORNE SOUND AND VIBRATION
MARCH 4-6, 1992 AUBURN UNIVERSITY, USA

THE STATISTICAL ENERGY ANALYSIS OF
A CYLINDRICAL STRUCTURE

M Blakemore
R J M Myers   J Woodhouse
Topexpress Limited   Department of Engineering
Poseidon House   University of Cambridge
Castle Park   Cambridge
Cambridge CB3 0RD UK

ABSTRACT

A test structure comprising sections of cylindrical shell connected by bolted, flanged joints has been fabricated, generically typical of aerospace structures. This is being used to explore various aspects of SEA modelling of vibration levels within the structure for given external excitation. The aim is to study coupling loss factors between the sections by a variety of approaches. These include (a) inverse estimates based on measuring mean modal energy in the subsystems under conditions of known power injection, both for a system containing many subsystems and one assembled with just two sections; (b) measurements of individual coupled modes of the system, and then calculation of appropriate averages of these; (c) calculation of modal coupling strengths or wave transmission coefficients through the joints separating the subsystems. Experimental results are compared with theoretical predictions and differences shed light on the SEA modelling of such structures.

INTRODUCTION

Laboratory and in-flight testing of aerospace structures to determine their vibrational behaviour is costly and time-consuming. Finite element and modal analysis computer packages already enable the assessment of candidate designs at low frequencies, during "drawing board" studies. A predictive tool for higher frequencies is clearly desirable. The current studies aim to validate the highly successful room acoustics theory of statistical energy analysis (SEA) applied to cylindrical structures typical of those found in the aerospace industry.

THE TEST STRUCTURE

For the purposes of this study a 'kit' of parts has been produced from which various cylindrical structures can be made, broadly representative of basic aerospace structures. It has been designed with the aim of being simple enough to be amenable to detailed theoretical analysis, whilst providing an adequate degree of non-idealism to represent a valid test of the statistical modelling techniques. It was anticipated that certain aspects of the design might expose difficulties in SEA modelling of this sort of structure: these might include the near rotational symmetry and chain connectivity of

561

the structure and the possibility of joint "coincidence" effects (see [1]).

The kit consists of five sections made from aluminium plate 1.6mm thick, bent to cylindrical form with radius 0.25m and welded with a single axial seam. The lengths of all the sections are different, ranging from 0.545m to 0.845m. There is also one section made of plate 2.5mm thick, with length matching that of one of the thinner sections. All are drilled with 12 equally spaced holes near the ends, so that bolted connections to simple L-section flanges can be made. These in turn can be used to bolt sections together, with or without an intervening plane circular baffle made of 2.5mm aluminium plate. These components can be assembled in a variety of configurations, with two or more sections, and with or without heavy wooden end-plates.

TRANSMISSION CHARACTERISTICS ACROSS MANY SECTIONS

A preliminary measurement was carried out to investigate the general characteristics of the transmission through many jointed sections of cylinder. This immediately revealed difficulties which can arise when a structure has the connectivity of a simple chain. Each section is only connected mechanically with its nearest neighbours, and if the air-borne pathway for vibration transmission is not significant then we might presume that the coupling loss factors will be zero except between neighbouring sections. Also, we expect the nature of the mechanical coupling to be rather similar across each boundary, since all the joints are nominally identical. Any SEA model obeying these two conditions predicts a very simple pattern of exponential decay along the system from excitation at one end. However, very simple observations confirm what one might expect from other such problems, that the actual decay behaviour is not of this form. Figure 1 illustrates response levels averaged over frequency bands derived from five jointed cylindrical sections with the baffles in place, to minimise acoustic coupling.

What we see is a large attenuation across the first junction, and then progressively less across the later ones. Behaviour of this kind is to be expected if there is a significant difference between different modes or travelling-wave directions in the reflection and transmission coefficients at the boundary. In the driven section we perhaps excite a broad range of modes to roughly similar energies, as assumed by standard SEA. Of these, some will be more strongly reflected than others at the first boundary, so that those which reach the adjacent section will have a much higher proportion of the ones with high transmission coefficients. Since the next boundary has similar characteristics to the first, the new mixtures of modes is better suited to being transmitted through, and a smaller attenuation is thus seen. This process repeats, the weaker-transmitting components being filtered out of the mixture more and more effectively.

Since chain-like systems are not uncommon, it is of value to investigate ways in which SEA might be used to study them. For example, straightforward application of an SEA inverse-fitting procedure to the present data produces significantly large "indirect coupling" elements in the matrix of loss factors.

DETAILED INVESTIGATION OF A TWO-SECTION STRUCTURE

Modal Analysis
Two cylindrical sections were bolted together with the baffles in place to minimise acoustic coupling between sections. A set of transfer functions was measured to a fixed accelerometer on each section from a ring of driving points equally spaced about

562

the circumference again of each section. By Fourier analysing with respect to azimuthal angle, θ, of a given drive point, the signal is decomposed into the separate contributions for each value of angular order n_c, i.e. having the form $\cos(n_c\theta)$ or $\sin(n_c\theta)$ for values of $n_c = 0, 1, 2, 3$ etc. A well-defined series of peaks is observed in the frequency spectra corresponding to the modes of the structure. It was observed that each mode "lives" predominantly in one or other of the two sections and may be associated primarily with one specific value of n_c. About 300 modes were catalogued in terms of frequency, section and n_c up to about 1800Hz, above which increasing modal overlap makes the identification process more difficult. The frequency/wavenumber characteristics of these modes correspond well with theoretical predictions of the dispersion behaviour of an infinitely-extended version of one of our cylinder sections [2]. Having identified the individual modes of each section and their associated values of n_c, a measure of the strength of coupling across the joint (as a function of frequency and n_c) was made in terms of a ratio of rms responses at the mode frequencies. A typical ratio is 10:1.

Inverse SEA Measurements
An extensive set of *in situ* SEA inverse measurements has been made on the same two cylinder sections, partly to investigate the effect of the internal and external airborne noise paths. The measurements were performed such that these paths were independently modified through combinations of baffles and fibrous filling. In each configuration a full set of 256 transfer mobilities was taken using eight points in each section, located uniformly in an axial direction and randomly circumferentially. A simple two-subsystem SEA model was assumed in the inverse procedure. The measurements allowed calculations of the mean velocity squared responses which were used to give damping loss factors (DLFs) and coupling loss factors (CLFs). A summary of the conclusions relating to coupling follows:

(1) external airborne acoustic coupling is not significant;

(2) internal airborne acoustic coupling is significant in two specific frequency ranges: i) above the equivalent flat plate coincidence frequency (~7kHz) and ii) over a range of frequencies just below the ring frequency (~3kHz) (see [3]); presumably both may be related to resonant excitation of the internal airspace(s);

(3) the presence of the aluminium baffle in the joint significantly reduces the acoustic coupling;

(4) the addition of a fibrous filling also reduces acoustic coupling;

(5) the presence of the aluminium baffle in the joint reduces the structural coupling below 2kHz. Resonant coupling through the joint is unimportant over this range of frequencies, and we believe transmission is controlled purely by joint stiffness;

(6) in contrast the aluminium baffle appears to increase the structural coupling around the ring frequency; we may be seeing the effects of resonant coupling via joint modes.

Results (2) and (6) both suggest that more subsystems need to be included in our SEA model, corresponding to the internal airspaces and the joint configuration.

563

Indirect Coupling
Work on a three-bay structure is currently in progress, to investigate the significance and physical mechanisms associated with indirect coupling.

THEORETICAL PREDICTIONS OF COUPLING LOSS FACTORS

In parallel with the detailed measurements studying the significance of various factors in determining a suitable SEA model, theoretical predictions have been made. The predictions use a variational model of the joint [4].

The first stage is to calculate transmission coefficients through the joint. To obtain these the dispersion equation for an infinite cylindrical shell (for a given frequency and angular order) is solved to obtain a total of eight modes, some evanescent and some propagating. A set of associated generalised forces and displacements is then calculated for each mode. Considering two semi-infinite cylinders connected through the joint model, it is required to match these generalised forces and displacements using an appropriate admittance matrix for the joint. This matrix is calculated from the joint model. This solves the transmission/reflection problem at the joint, for any possible incident wave field. The result is expressed in terms of a matrix of complex transmission coefficients, connecting the various propagating wave types. Coupling loss factors are obtainable from these using a wave transmission analysis (see for example Lyon [5]). These predictions are plotted on Figure 2 along with the corresponding inverse measurements for the appropriate joint geometry (no aluminium baffle included in the joint) shown with a broken line.

COMPARISON OF MEASURED AND THEORETICAL COUPLING LOSS FACTORS

The predictions are of the right order of magnitude but reveal interesting and significant differences from the inverse measurements. These differences are discussed in turn below.

Anomalies at Higher Frequencies
Above 7kHz and around 3kHz there are significant peaks in the measured CLFs, not present in the prediction. As noted earlier, 7kHz marks the position of the flat plate coincidence frequency for the current shell thickness, and so the fluid-structure coupling is particularly strong just above that frequency. Thus the associated peak in the CLFs can be attributed to internal acoustic coupling of the two cylinder sections. The peak around 3kHz is attributable to a similar mechanism, the coincident fluid-structure coupling just below the ring frequency arising as a consequence of the curvature of the shell [3]. Fluid-loading was omitted from the theoretical modelling used to obtain the CLFs. Evidently the theory will have to be extended to include such effects to obtain accurate predictions in these frequency ranges.

Anomaly at Low Frequencies
The theoretically predicted estimates for the CLFs are far too high at low frequencies. There are two possible explanations for this. The first, again, relates to fluid loading. It is well known [3] that there exist a class of cylinder modes of low angular order and over a frequency range up to the ring frequency which are strongly radiation-damped. These co-exist, over the same frequencies, with weakly damped modes of higher n_c. This invalidates the assumption of equipartition of energy between modes implicit in the standard 'wave analysis' derivation of theoretical coupling loss factors.

564

The second possible explanation arises as a consequence of low modal overlap at these frequencies, and links closely with observations made from purely theoretical calculations by Yap and Woodhouse [6]. (The modal overlap factor is less than 1 below 2kHz.) Some insight can be gained by referring to the discussion by Hodges and Woodhouse [7], Section 3.5. They discuss a simpler problem of coupled one-dimensional systems, and derive results which are qualitatively similar to the behaviour in this study by both modal and wave approaches. It is the interplay between these complementary approaches which is particularly at issue here.

From a modal standpoint it is not difficult to see that anomalous behaviour of the coupling loss factor should generally be expected when the modal overlap is low. The behaviour of the *typical* member of the ensemble (as opposed to the ensemble-average behaviour) will involve only modes which "live" in one subsystem or the other, and no coincidences of mode frequencies across the subsystem boundary should be expected. Under such circumstances the coupling loss factor will have the functional form of the underlying two-oscillator result (Hodges and Woodhouse [7] equation (3.33)). This is significantly different from the usual SEA averaged result ([7] equation (3.31)), which in turn corresponds exactly to the standard wave-method estimate which we have adopted above.

The principle difference lies in the dependence of the coupling loss factor on damping. The averaging procedure produces a factor of the order of $1/\Delta$, where Δ is the typical modal damping bandwidth. This cancels the factor of Δ appearing in the two-oscillator coupling factor, to produce a coupling loss factor independent of damping. The standard wave analysis, after all, only considers transmission behaviour near the junction, and such subsystem properties as damping simply do not enter. For low modal overlap, then, we may expect that a better estimate of the coupling loss factor will be proportional to Δ.

It remains to explain why dependence on damping should produce the anomaly we see in Figure 2, where the variable against which the CLF is plotted is frequency. We would also like to understand more clearly how this anomaly might be viewed from a "waves" standpoint. The "waves" part of the discussion by Hodges and Woodhouse [7] employs a rather special case to obtain a CLF proportional to Δ ([7] equation (3.37)). They consider systems such that the modes of the driven subsystem line up with the anti-resonances of the non-driven subsystem. The different behaviour is then traced to correlation between the wavefields on either side of the junction, with a suitable sign such that the power flow is reduced ([7] Figure 6(c)). At least for this particular case, the CLF is then found to differ from the usual one by a factor of the inverse of the modal overlap factor. Since modal spacing is not varying rapidly at low frequencies, while the modal bandwidths are approximately proportional to frequency, the result is a dependence $(1/\omega)$. This is in reasonable agreement with the low-frequency peak shown in Figure 2 for the theoretical predictions.

COUPLING LOSS FACTOR PREDICTION FROM DETAILED MODAL ANALYSIS

As previously stated, for low frequencies modal overlap tends to be low. In that range a different approach can be taken to CLFs. It yields a result which is significantly different from the wave-transmission answer discussed above, and sheds some light on the high values predicted by that method at low frequencies. The approach makes use of the detailed modal analysis on the two-bay structure. The data allow amplitude ratios of the spectra for each bay on either side of the joint, at each identified mode, to

be calculated. This information can be used to estimate the CLF, essentially by carrying through the textbook mode-averaging procedure explicitly (c.f. Lyon [5]).

We have assumed, in addition to low modal overlap, that we have weakly coupled subsystems with mode-dominated response characteristics. Furthermore, no mode frequency lies within a modal bandwidth of any other; this can be compared to the modal "anti-line-up" condition of the previous section. The resultant expressions for the CLFs η_{12} and η_{21} are:

$$\eta_{12} = \frac{\Delta}{\overline{\omega} n_1} \left\{ \sum_\alpha \frac{A_2}{A_1} \mu_\alpha + \sum_\beta \frac{A_1}{A_2} \mu_\beta \right\} \tag{1}$$

$$\eta_{21} = \frac{\Delta}{\overline{\omega} n_2} \left\{ \sum_\alpha \frac{A_2}{A_1} \mu_\alpha + \sum_\beta \frac{A_1}{A_2} \mu_\beta \right\}. \tag{2}$$

where:

   Δ is again the modal damping bandwidth or modal damping factor;
   $\overline{\omega}$ is the centre frequency of a given frequency bin;
   n_1 and n_2 are the average modal densities of each section over the frequency bin;
   A_1 and A_2 are the subsystem lengths; and
   μ_α and μ_β are the ratios of the mean squared velocities in each section for modes of section 1 and section 2 respectively.

The results from the detailed modal analysis [2] when substituted into equations (1) and (2) over bandwidths that coincide with those used for the inverse measurements mentioned earlier are shown in Figure 3. The measured results are also shown. The predictions are of the correct order of magnitude, though somewhat low in the lowest bin and perhaps high in the higher bins.

The agreement is much closer than that obtained using the purely theoretical transmission coefficients and the 'wave approach' to estimating coupling loss factors. This difference occurs despite the fact that values of the μ_α and μ_β are broadly in accordance with the typical values of corresponding theoretical transmission coefficients. The difference results from the way these numbers are combined to give CLFs, the latter including for example an explicit dependence on damping.

Two possible difficulties with the purely theoretical "wave" approach were identified earlier. One was the effect of radiation damping essentially removing the influence of a set of modes which are (potentially) particularly strongly coupled across the joint. The second was identified with the difference between the ensemble-averaged structural response and that of a typical member of the ensemble, particularly at low modal overlap. Both difficulties are circumvented by the hybrid experimental-theoretical treatment described in this section. The much-improved agreement with the inverse measurements achieved here supports the above explanations of the earlier low frequency anomaly.

REFERENCES

[1] CREMER, C, HECKL, M and UNGAR, E E. Structure-borne Sound. Berlin: Springer. 1973.

[2] BLAKEMORE, M, JEFFRYES, B, MYERS, R J M and WOODHOUSE, J. Proc. IOA, 12, 1990, pp587-593.

[3] MANNING, J E and MAIDANIK, G. J. Acoust. Soc. Am. 36, 1964, pp1691-1698.

[4] HODGES, C H, POWER, J and WOODHOUSE, J. J. Sound Vib. 101, 1985, pp219-235.

[5] LYON, R H, Statistical Energy Analysis of Dynamic Systems: Theory and Applications. MIT Press. 1975.

[6] YAP, F F and WOODHOUSE, J. Private Communication. 1991.

[7] HODGES, C H and WOODHOUSE, J. Rep. Prog. Phys. 49, 1986, pp107-170.

Section	2	3	4	5
Average total dB drop	17	29	35	36
Extra loss over 1 joint	17	12	6	1
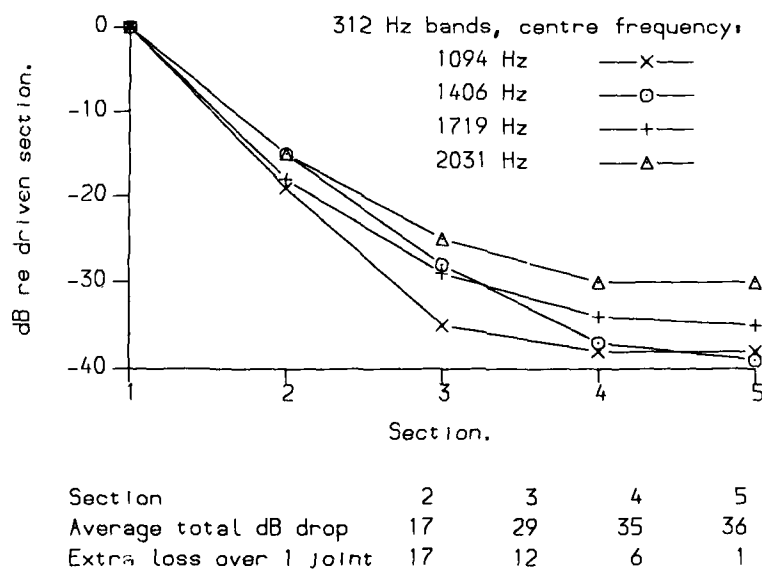
FIGURE 1 Mean square velocities averaged over frequency bands and position, derived from a structure consisting of five sections, driven in Section 1.
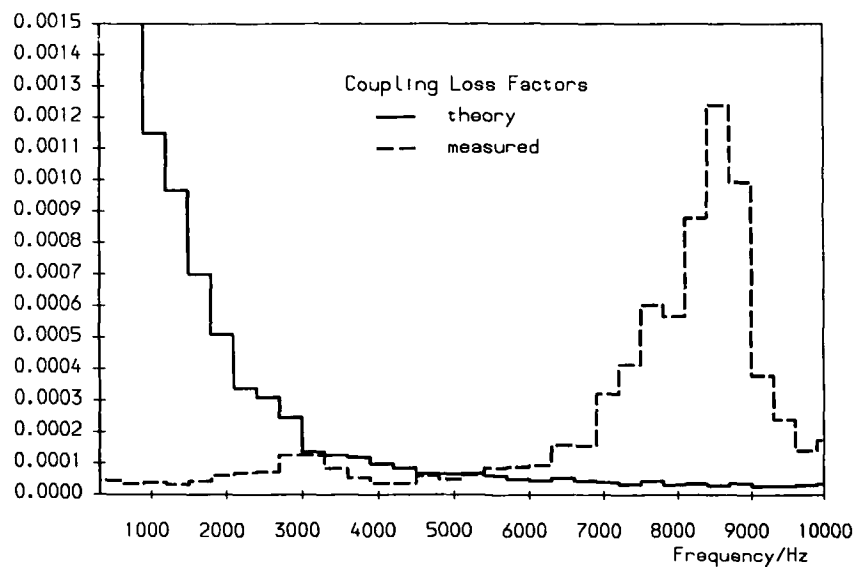
FIGURE 2 Theoretically predicted coupling loss factors compared with measured results for a two section structure.
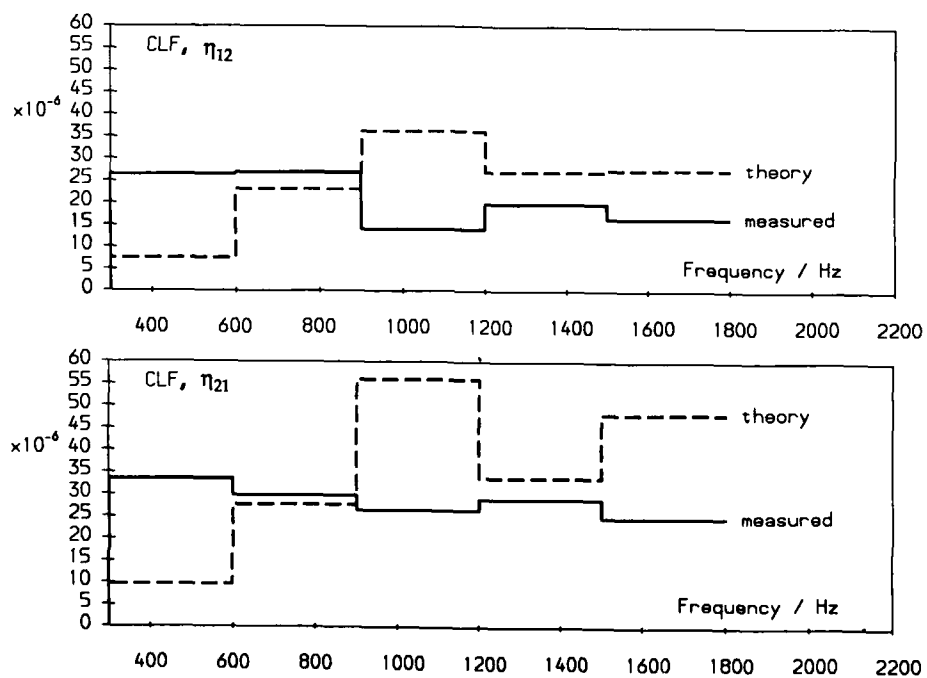
FIGURE 3 Coupling Loss Factors for a two section structure (η_{12} - top; η_{21} - lower) predicted from a detailed modal analysis compared with measured results.
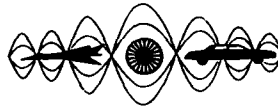
SECOND INTERNATIONAL CONGRESS ON
RECENT DEVELOPMENTS IN AIR- AND
STRUCTURE-BORNE SOUND AND VIBRATION

MARCH 4-6, 1992 AUBURN UNIVERSITY, USA

PREDICTION OF TRACKED VEHICLE NOISE
USING SEA AND FINITE ELEMENTS

David C. Rennison & Paul G. Bremner
Vibro-Acoustic Scientists Ltd
5/15 Orion Road
Lane Cove N.S.W.
AUSTRALIA, 2066.

ABSTRACT

Previous work to incorporate modal output data from finite element structural models into the more conventional framework for space- and frequency-averaged vibrational response and interior noise predictions of an armoured personnel carrier, is reviewed. The Statistical Energy Analysis (SEA) method is also applied and shown provide close estimates of the interior noise-to-force transfer functions over a wide frequency range and to complement the finite element based analysis down towards frequencies of the fundamental modes of the key structural elements.

INTRODUCTION

At low frequencies, normal mode analysis can be used effectively to model complex vibro-acoustic problems. Relationships for space- and frequency band-averaged vibrational response and acoustic power radiation are written in terms of the (modal) output parameters of numerical modal methods such as finite element analysis (FEA), to bridge between the output data of numerical methods and the conventional formalism of vibro-acoustics. At high frequencies, statistical vibro-acoustic methods such as SEA can be used but skill in modelling the coupling across joints and at power input locations is required. Both FEA and SEA are then used to predict the noise levels inside a tracked vehicle.

VIBRATIONAL RESPONSE OF A COMPLEX STRUCTURE TO MECHANICAL EXCITATION

Calculation of (i) the power flow from a source into a structure comprising beams and plates, (ii) its associated vibrational response and the (iii) ensuing radiation to the interior (and exterior) acoustic field, is quite complex for all but the simplest vibro-acoustic systems. Resort can be made to numerical modelling methods such as FEA, to provide a deterministic solution for the exact vibration response or acoustic pressure at any point in space or time for given dynamic input.

Consider a complex structure driven by an excitation force of amplitude spectrum $F(\omega)$ at frequency ω applied at $x = x_F$ and loaded by interior and exterior pressure fields. The structure is represented by its set of independent normal modes so that the total displacement response of the structure $w(x,\omega)$ at a point x on the surface is given by

$$w(x,\omega) = \sum_r \xi_r \, \psi_r(x) \tag{1}$$

where $\xi_r = \xi_r(\omega)$ is the displacement amplitude of the rth normal mode. The response to the forces and pressure fields acting is found by integrating the product of the structure's Greens function and the forces acting on the surface, all over the vibrating

569

surface. The forces developed by the pressure fields will be negligible for heavy structures vibrating in air so that the total response of the structure is given by

$$w(x,\omega) = F(\omega) \sum_r \frac{\psi_r(x)\,\psi_r(x_F)}{M_r Y_r} \tag{2}$$

where ψ_r, M_r and Y_r are the mode shape, generalized mass and admittance function for the rth structural mode. η_r is the sum of the structural and radiation loss factors.

The time average, mean square displacement at frequency ω is

$$\overline{w^2(x,\omega)} = \tfrac{1}{2}Re[w.w^*] = \frac{F^2(\omega)}{2}\left\{ \sum_r \frac{\psi_r^2(x)\psi_r^2(x_F)}{|Y_r|^2 M_r^2} + Re \sum_r \sum_{\substack{s \\ r \neq s}} \frac{\psi_r(x)\psi_s(x)\psi_r(x_F)\psi_s(x_F)}{Y_r Y_s^* M_r M_s} \right\} \tag{3}$$

As frequency increases above the fundamental structural resonance frequencies, the modes accumulate rapidly with frequency. Certain structural elements may tend to respond more strongly than connected elements, and may tend to contribute most to the structural modal mass, this situation corresponding to local panel resonances. An estimate for the space-averaged, mean-square velocity of each of the major structural elements to a band-limited force excitation of mean square force of F_Δ^2 in $\Delta\omega$ is useful in the evaluation of the effects of structural modifications on both the structural vibration response and the associated interior acoustic radiation.

The space-average, mean-square velocity, for an element A of the structure, averaged over a narrow frequency band containing several resonant modes ($r\epsilon\Delta\omega$), $\langle v_\Delta^2 \rangle_A$, is calculated by integrating $\tfrac{1}{2} Re[v.v^*]$ over the elemental area A and over the frequency band $\Delta\omega$ viz.

$$\overline{\langle v_\Delta^2 \rangle}_{,A} = F_\Delta^2 \,\omega^2 \sum_{r\epsilon\Delta\omega} \frac{\left[\frac{1}{A}\int_A \psi_r^2(x)\,dx\right]\psi_r^2(x_F)}{M_r^2} \cdot \frac{1}{\Delta\omega} \int_{\Delta\omega} |Y_r|^{-2} d\omega \;+\; \text{2nd Order Terms}$$

$$\approx \frac{\pi}{2\omega} \cdot \frac{F_\Delta^2}{\Delta\omega} \sum_{r\epsilon\Delta\omega} \frac{\left[\frac{1}{A}\int_A \psi_r^2(x)dx\right]\psi_r^2(x_F)}{M_r^2\,\eta_r} \tag{4}$$

Here the modal cross-coupling terms ($r\neq s$) do not contribute to the response and the response is assumed to be dominated by the modes resonant in $\Delta\omega$.

The contribution of structural elements to the total modal mass can be calculated for each structural element using for example FEA, as:

$$M_{r,A} = \int_A m(x)\psi_r^2(x)dx = \sum_i \sum_{j\epsilon A} m(i,j)\psi_r^2(i,j) - \sum_{j\epsilon A} m(3,j)\psi_r^2(3,j) \tag{5}$$

Here $m(i,j)$ is the nodal mass of the jth node referred to the ith coordinate direction and i=3, the surface normal displacement component, is usually most significant.

ACOUSTIC POWER RADIATED TO INTERIOR ACOUSTIC FIELD

The time-averaged acoustic power being radiated due to motion of the rth structural mode is given in terms of the modal radiation resistance as

$$W_{rad}^r(\omega) = R_{rad}^r(\omega)\,\langle v_r^2 \rangle \tag{6}$$

At those frequencies where several acoustic modes occur in the analysis band, the band averaged radiation resistance will provide a good estimate of the structural-acoustic coupling for each element. For N modes in frequency band $\Delta\omega$ and assuming equipartition of energy between these applies, the total time-average acoustic power W_Δ is

$$W_\Delta(\omega) = v_\Delta^2 \,\frac{1}{N} \sum_{r\epsilon\Delta}^N R_{rad}^r(\omega) = v_\Delta^2 \cdot \overline{R_{rad}} \tag{7}$$

where v^2_Δ is the space-averaged, mean square velocity of the radiating surface and R_{rad} is the band-averaged radiation resistance. Eq.(4) may be used to calculate v^2_Δ and R_{rad} can be calculated using the methods of SEA. For a structural element A, the band-limited radiated acoustic power is

$$W_{\Delta,A}(\omega) = v^2_{\Delta,A} \cdot \overline{R_{rad,A}} = \frac{\pi}{2\omega\,\Delta\omega} F^2_\Delta \ r\underset{\epsilon\Delta\omega}{\Sigma} \frac{\left[\frac{1}{A}\int_A \psi^2_r(x)dx\right]\ \psi^2_r(x_F)}{M^2_r\ \eta_r} \cdot \overline{R_{rad,A}} \quad (8)$$

APPLICATION TO THE HULL OF A TRACKED APC VEHICLE

The armoured personnel carrier (APC) is a box like structure comprising approximately ten thick aluminium plates. The dominant vibration source in the APC is that associated with repeated impacts of the track components on the idler wheel. These impacts produce broad-band force spectra on the idler which are then transmitted through the stub axle to the hull structure, developing a strong vibrational response on all hull structural elements. In turn these radiate acoustic power into the hull volume, producing interior noise. In terms of a vibro-acoustic systems analysis, the power radiated in the full acoustic space from the vibrating hull equals that absorbed inside the vehicle, while the power balance between the input power and that dissipated in the hull structure determines the level of the hull vibrational response.

The FEA package STARDYNE was used to compute resonance frequencies, mode shapes and modal masses for the APC hull structure. 221 nodes were used to represent half of the structure, as in Figure 1(a). Bilateral symmetry was assumed for modelling economy with the problem solved twice for symmetric and symmetric centreline boundary conditions. Figure 1 shows typical vibrational mode shapes for several modes: about 60 modes are resonant below 250 Hz while in the 200 Hz 1/3 octave frequency band, about ten modes are resonant. The latter involve flexure of top and bottom plates and the sidewalls i.e. hull plates are beginning to act as separate subsystems above 200 Hz. By comparison, the hull interior volume has about 10 and 110 acoustic modes resonant in the 200 and 500 Hz 1/3 octave bands respectively.

(a) Nodal configuration for M113A1 model.

(b) 29.5 Hz symmetric   (c) 41.3 Hz anti-symmetric

(d) 55 Hz symmetric   (e) 213.3 Hz anti-symmetric   (f) 296 Hz symmetric
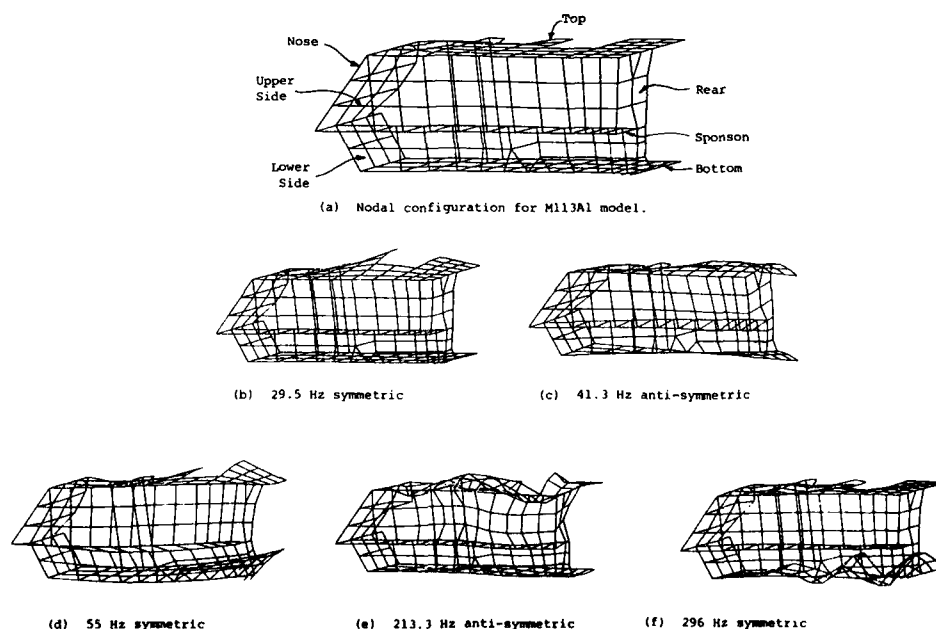
Figure 1: APC Nodal Model and Typical Vibration Mode Shapes

The total acoustic power radiated into the hull interior volume from the various structural elements in response to a driving force at the idler attachment position will be absorbed on the hull surfaces. From this power balance the interior noise-to-idler force transfer function for each structural element can be derived as

$$\frac{<p_i^2>}{F_\Delta^2} = \frac{\rho c^2}{V \eta_i} \cdot \frac{\overline{R_{rad,A}}}{\omega} \cdot \frac{v_{\Delta,A}^2}{F_\Delta^2} \quad (m^{-4}) \tag{9}$$

where $<p_i^2>$ is the space-average mean-square interior acoustic pressure, F_Δ^2 is the mean square idler force and $v_{\Delta,A}^2$ is the mean square velocity of element A. V, ρc and η_i are the volume, characteristic acoustic impedance and acoustic loss factor of the hull interior space. Then, from calculated values of $R_{rad,A}$ and measured values of V and η_i, the noise-to-force transfer functions for each major element were calculated and summed to give the overall noise-to-force transfer function. An example for vertical excitation of the idler axle is shown in Figure 2, together with measured data in 1/3 octave bands.
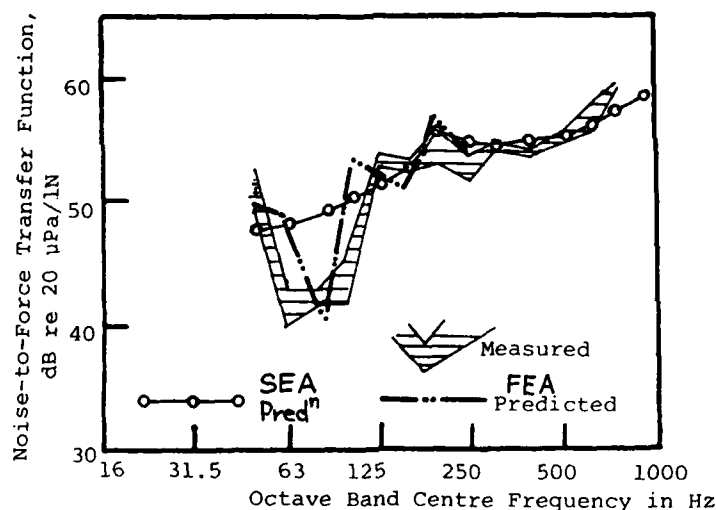
Figure 2 Comparison of Measured and Predicted Noise-to-Force Transfer Function for Vertical Excitation of M113A1 Idler Spindle.

The agreement is quite good and with refinement, improved matching between predictions and measurements and understanding of the effects of local attachment details could be made. The project duration was 5 months with 600 hours spent on FEA models and post-processing for a total cost in 1991 dollars of $50,000. There are strong costs drivers to provide more efficient analysis tools and methods for use throughout the vibro-acoustics field.

CALCULATION USING STATISTICAL ENERGY ANALYSIS

At higher frequencies and for stationary random excitations, it can be satisfactory to use other energy based methods for analysis.   Statistical Energy Analysis (SEA) is one such approach to vibro-acoustic analysis at higher frequencies and has been applied to the tracked vehicle noise transmission problem.   The analysis program used was AUTOSEA [2], developed by Vibro-Acoustic Sciences Ltd.

The SEA network for the tracked vehicle is shown in Figure 3.
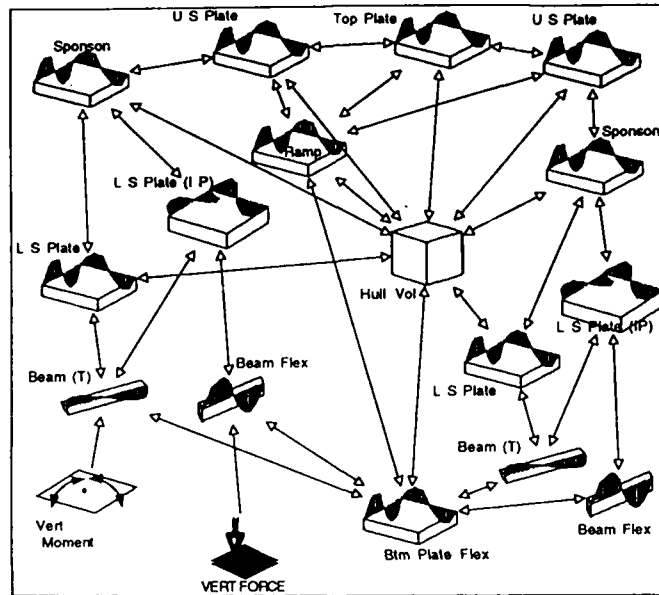
Figure 3 SEA Network for M113A Tracked Vehicle

The groups of modes in this model include the flexural modes of the various hull Plates, the acoustic modes of the Hull Volume, and the flexural and torsional modes of the Beams. Figures 4 and 5 respectively graph the number of modes resonant in 1/3 octaves bands for the various subsystems and present subsystem wavenumber plots: the intersections of acoustic and structural wavenumbers are the subsystem critical frequencies.
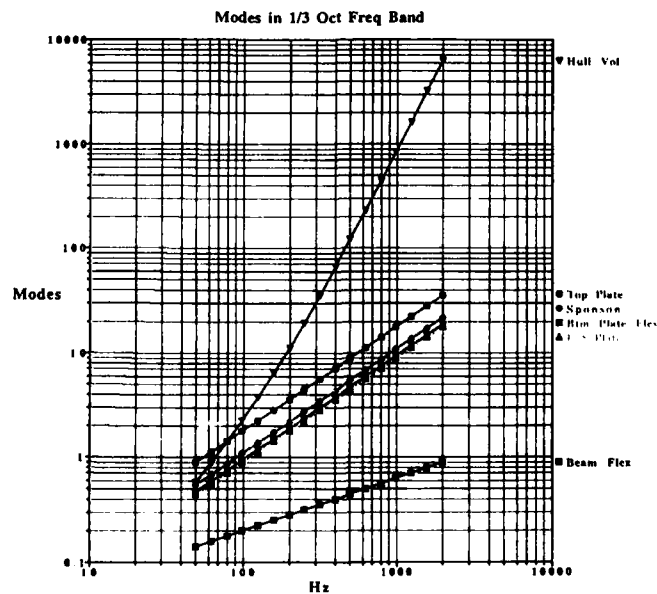
Figure 4 : Subsystem Modes in Analysis Band
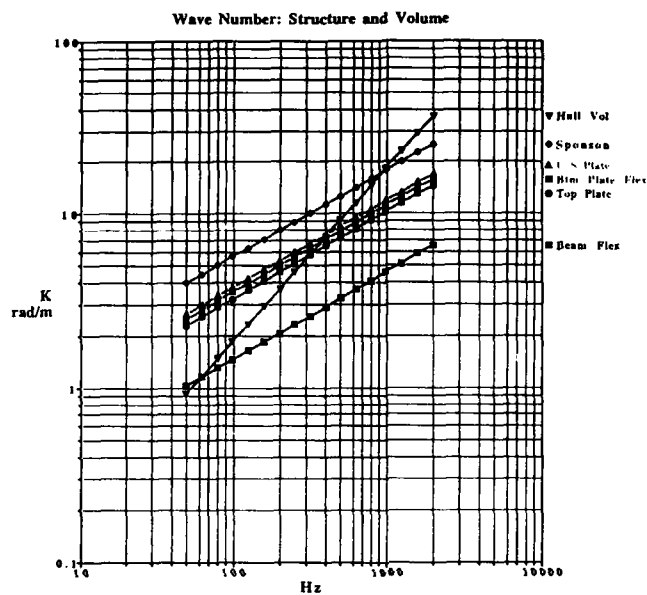
Figure 5 : Subsystem Wavenumber Spectra

Transmission paths follow subsystem physical connections so that adjacent subsystems and
their wave/mode groups are usually coupled.   Lines connecting the icons show the power
exchange between the different coupled groups of modes in each analysis frequency band.
For example, the Hull Plates are connected along their common edges to each other and and
area connected the the Hull Volume, while the Beams are line connected to the Bottom and
Lower Side Plates. Figure 6 presents Coupling Loss Factor (CLF) plots for plate-plate
and plate-acoustic space connections.
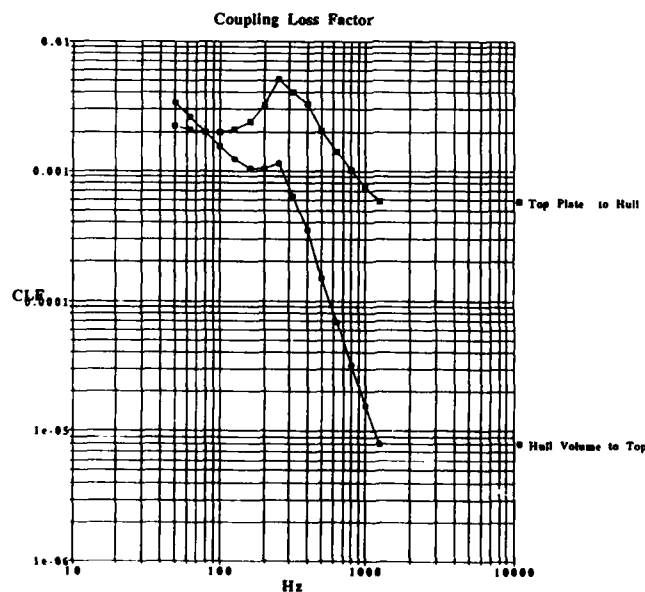
Figure 6 : Coupling Loss Factor for Top Plate/ Hull Acoustic Space

574

The input power in this case is due to a vertical Point Force which couples to the Box Beam Flexural modes and to a Point Moment which couples to Box Beam Flexural modes and Torsional modes. Power is dissipated by transmission to connected structural subsystems by the various wave groups and internally by the subsystems' mechanical and radiation damping as well as by absorption in the Hull Volume.

Figure 7 presents Power Input graphs of the spectral contribution of the various panel sources to the hull volume acoustic power levels. For this model the Bottom and Lower Side plate elements are dominant sources, with the power radiated from the Top and Upper Side plates being about 10-15 dB lower. At higher frequencies, the thinner sponsons become more important. This ranking corresponds reasonably with vibration distributions measured underway.

Power Inputs to Hull Volume
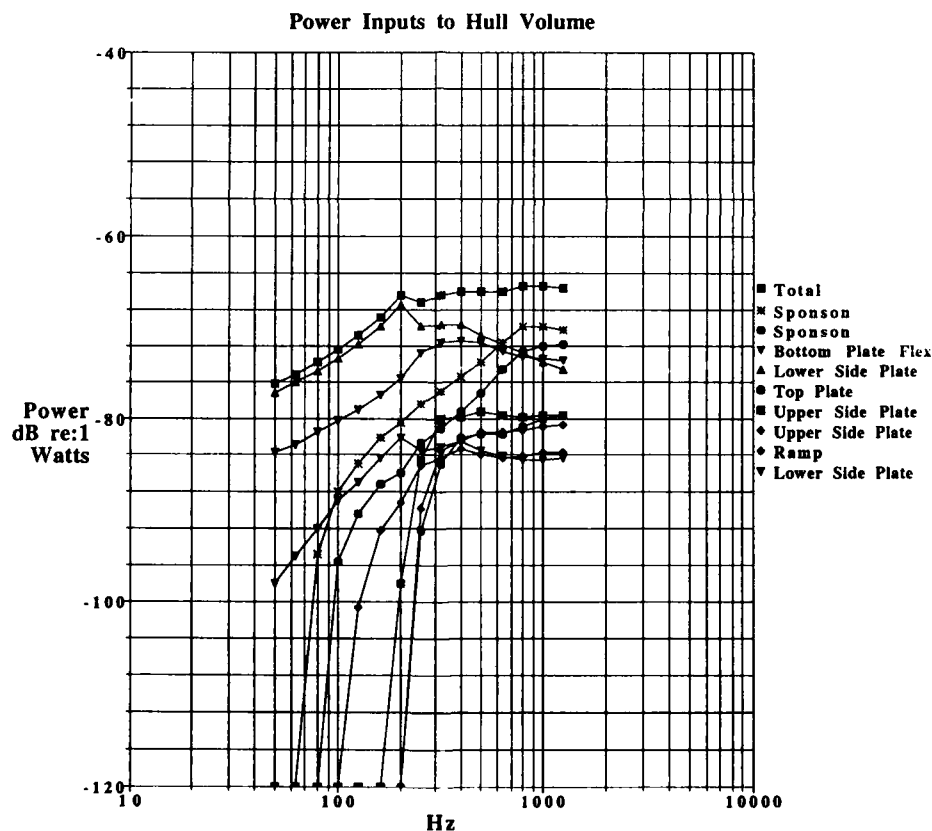
Figure 7 : Subsystem Power Inputs to Hull Acoustic Space

The power losses from the sponson are presented in Figure 8: the sponson damping controls its power dissipation but at higher frequencies, acoustic radiation from the sponson becomes as important as the power flow to coupled structural elements and to that dissipated within the sponson.

Power Losses from Sponson
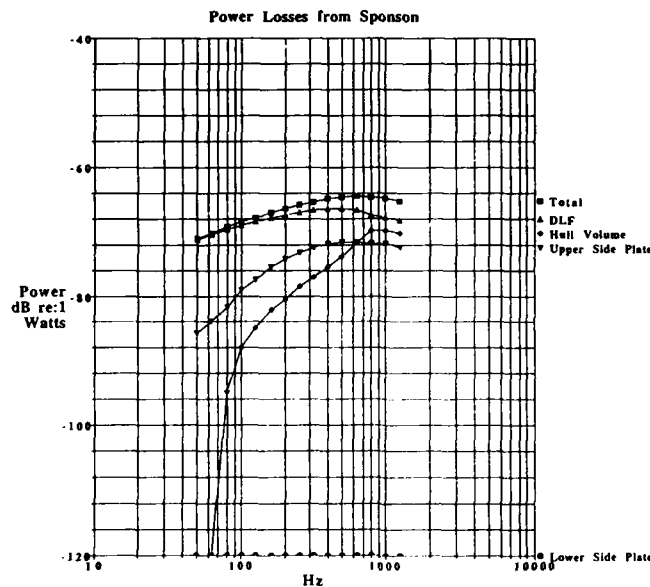
Figure 8 : Power Losses from the Sponson

Predictions of the interior noise-to-force transfer functions are superimposed on Figure 2 for comparison with the FEA predictions: the agreement is close for all frequencies above 100 Hz. It is clear that the two analysis methods are complimentary. However it would appear that SEA can provide good estimates across the broad frequency range including low frequencies. The time for development of the SEA model was about 25 hours, including collation of geometry data.

The next step in the analysis is to carry out sensitivity studies, for example, varying attachment location, plate thickness, beam properties to understand the influence of each on power transmission into the hull. SEA can enable speedy system level evaluations of such vibroacoustic problems and lead refined analysis using for example FEA.

CONCLUSIONS

A method for incorporating modal output information generated from finite element analysis models for complex structures, into the more familiar framework of frequency- and space-averaged response and transfer functions, has been developed. While the method is fully consistent with the conventional approach of using transfer function spectral densities, the averaging procedures presented are computationally efficient and provide, for vibroacoustics problems, results directly useful in understanding the effects of various structural parameters or of changes to basic structure.

SEA provides a convenient speedy method of analysing complex vibro-acoustic issues using a system level analysis. It can focus attention quickly on key design or analysis issues and lead to clearer interpretation of measured data. SEA can then be used in conjunction with other analysis methods such as Finite Element Analysis and so allow many vibro-acoustic problems to be understood in a more cost effective manner.

REFERENCES

1. Hammond S.A., Rennison D.C., Garinther G.R., etalia "Experimental Quiet Sprocket Design and Noise Reduction in Tracked Vehicles" U.S. Army Hurman Engineering Laboratory Technical Memo 8-81, April, 1981.

2. AUTOSEA User Manual, Vibro Acoustics Sciences Ltd, September 1991.

SECOND INTERNATIONAL CONGRESS ON
RECENT DEVELOPMENTS IN AIR- AND
STRUCTURE-BORNE SOUND AND VIBRATION
MARCH 4-6, 1992   AUBURN UNIVERSITY, USA

MEASUREMENT OF ENERGY FLOW ALONG PIPES

C.A.F. de Jong & J.W. Verheij
TNO Institute of Applied Physics
P.O. Box 155, 2600 AD Delft
The Netherlands

ABSTRACT

Practical methods have been developed to determine acoustic and vibrational energy flow along straight fluid-filled pipes from acceleration measurements on the pipe surface. For practical pipes only the first three circumferential modes ($n = 0$, $n = 1$ and $n = 2$) have to be considered to cover the most important frequency range. Starting from the basic shell equations, approximate expressions have been derived for the wave speed and energy flow equations. Appropriate accelerometer configurations are chosen to be able to measure the energy flow in the different wave types separately. It is shown that the existing measurement methods for structure-borne energy flow along beams can also be used for pipes, provided that some frequency-dependent correction factors are taken into account. New methods are described to measure the fluid-borne energy flow ($n = 0$) and the energy flow in $n = 2$ shell waves.

NOMENCLATURE

a	mean pipe radius	w	radial shell displacement
c_a	acoustic wavespeed in the fluid	x	axial coordinate
c_p	plate wave velocity in the shell		
D	membrane stiffness of the shell	β^2	shell thickness parameter $h^2/12a^2$
E_s	Young's modulus of the shell material	Δx	axial distance
f_{cn}	cut-on frequency for mode $n > 1$	ε_n	factor ($\varepsilon_0 = 2$, $\varepsilon_{n>0} = 1$)
f_{rng}	ring frequency $c_p/2\pi a$	ζ	wavenumber factor (eq.12)
h	shell thickness	η	fluid-shell mass ratio $a\rho_f/h\rho_s$
I_x	axial component of intensity	θ	circumferential angle
J_n	Bessel function	κ	non-dimensional wavenumber ka
k	wavenumber	ν	Poisson ratio
m	axial mode number	ρ	density
n	circumferential mode number	ψ	wave speed ratio $(c_p/c_a)^2$
N	thin shell resultant force	ω	angular frequency
p	acoustic pressure in the fluid	Ω	non-dimensional frequency f/f_{rng}
P_x	axial energy flow		
r	radial coordinate	_subscripts_	
S	auto or cross power spectrum	f,s	fluid, shell
t	time	x,r,θ	axial, radial, circumferential
u	axial shell displacement	m,n	axial, circumferential mode
v	tangential shell displacement	B,L	bending, lobar mode
v_x	axial acoustic fluid velocity	S,F,T	longitudinal, fluid, torsional mode

INTRODUCTION

Methods for measuring structure-borne energy flow along pipes have been proposed by Pavic [1] and Verheij [2]. For these methods the structure-borne energy flow along straight pipes is described using simple beam theory. This description is restricted to the low frequency range where only longitudinal, torsional and bending waves occur. However, pipes are shell-type structures and the vibrational behaviour of fluid-filled shells deviates significantly from that of beams [3,4,5]. Recently some important contributions to the subject of energy flow in pipes were presented by Fuller [3], Williams [6] and Pavic [7,8]. In this paper we will show how these ideas can be applied in practical methods to determine acoustic and vibrational energy flow along straight fluid-filled pipes.

GENERAL DEFINITIONS

We consider only axial energy flow along straight fluid-filled pipes. The total axial energy flow P_x is the sum of the axial structure-borne energy flow P_{xs} and the axial fluid-borne energy flow P_{xf}:

$$P_x = P_{xs} + P_{xf} \tag{1}$$

Structure-borne Energy Flow

The axial vibrational energy flow in the shell can be described using the axial component of the structural intensity vector [4]. In thin cylindrical shells, which have a small ratio of the shell thickness h to radius a, the energy flow is carried almost entirely by extensional and torsional stretching motion of the shell [3,4]. Radial shear stresses and bending and twisting moments of the shell are proportional to $\beta^2 = h^2/12a^2$ and therefore much smaller than the longitudinal and tangential shear stresses. The instantaneous axial structural intensity I_{xs} may be expressed in terms of the classical resultant forces $N_x, N_{x\theta}$ and of the three-dimensional displacements u,v,w of the mid-surface of the shell (figure 1), where the dot denotes a time derivative:

$$I_{xs} = - N_x \dot{u} - N_{x\theta} \dot{v} \tag{2}$$

Using the stress-strain relationships from the Donnell-Mushtary shell equations [3], the intensity can be written in terms of shell displacements only:

$$N_x = D\left(\frac{\partial u}{\partial x} + \frac{v}{a}\frac{\partial v}{\partial \theta} + v\frac{w}{a}\right), \qquad N_{x\theta} = \frac{1-v}{2}D\left(\frac{\partial v}{\partial x} + \frac{1}{a}\frac{\partial u}{\partial \theta}\right) \tag{3}$$

where D is the membrane stiffness of the shell: $D = E_s h/(1-v^2)$. The total axial structure-borne energy flow in a time-averaged sense is obtained from integration over the shell cross-section:

$$P_{xs} = \int_0^{2\pi} <I_{xs}>_t \, ad\theta \tag{4}$$

Fluid-borne Energy Flow

The axial energy flow in the fluid can be determined using the definition of acoustic intensity [4]:

$$P_{xf} = \int_0^{2\pi}\int_0^a <pv_x>_t \, rdrd\theta \tag{5}$$

Decomposition in Terms of Circumferential Modes

Due to the circular symmetry, wave propagation occurs in circumferential modes of various orders n. The shell displacements u,v,w and the acoustic pressure p can be expanded in these modes [3-8]. Each mode $n > 0$ has its own modal amplitudes $u_n(x,t), v_n(x,t), w_n(x,t)$ and $p_n(x,r,t)$ and polarization angles $\theta_n(x,t)$. The extensional stresses in the shell and the acoustical fluid velocity can be expanded similarly. The total energy flow is then obtained by summation of modes plus integration over the circumference. Intermodal cross terms do not contribute to the integral [7], so that the total energy flow can be written as:

$$P_x = \sum_{n=0}^{\infty} [(P_{xs})_n + (P_{xf})_n] \tag{6}$$

Fourier Transform

Temporal averaging in the time domain has equivalent operations in the frequency domain [2], hence the Fourier transform of the modal structure-borne energy flow can be expressed as:

$$(\tilde{P}_{xs})_n = \frac{\varepsilon_n}{2}\pi a D \omega \left\{ Im\left[\left(\frac{\partial \tilde{u}_n}{\partial x}\right)^* \cdot \tilde{u}_n\right] + \frac{1-\nu}{2} Im\left[\left(\frac{\partial \tilde{v}_n}{\partial x}\right)^* \cdot \tilde{v}_n\right] + \frac{\nu}{a} Im\left[\tilde{w}_n^* \cdot \tilde{u}_n\right] + \frac{1+\nu}{2}\frac{n}{a} Im\left[\tilde{v}_n^* \cdot \tilde{u}_n\right] \right\} \qquad (7)$$

where $\tilde{\ }$ denotes a Fourier transform, $*$ denotes a complex conjugate and Im denotes the imaginary part of a complex quantity. The factor ε_n equals 2 if $n=0$ and equals 1 if $n>0$.
Similarly the fluid-borne energy flow can be written as [4]:

$$(\tilde{P}_{xf})_n = \frac{\varepsilon_n}{4}\frac{\pi a^2}{\rho_f \omega}\left\{ \left[J_n'(k_r^n a)\right]^2 + \left(1 - \left(\frac{n}{k_r^n a}\right)^2\right)\left[J_n(k_r^n a)\right]^2 \right\} Im\left[\tilde{p}_n^* \cdot \frac{\partial \tilde{p}_n}{\partial x}\right] \qquad (8)$$

where k_r^n is the radial wavenumber, which is determined by the Helmholtz equation for the fluid with the appropriate boundary conditions, and J_n' denotes the derivative of the Bessel function J_n with respect to its argument. The acoustic pressure p in the fluid is coupled with the radial shell displacement w via the condition of continuity of velocity at the inner shell wall:

$$\tilde{p}_n = \tilde{w}_n \frac{\rho_f \omega^2}{k_r^n J_n'(k_r^n a)} \qquad (9)$$

This equation indicates that the fluid-borne energy flow can in principle be determined from measurements of adial shell displacements.

Cross Spectral Method

The equations (7-9) form the theoretical basis for the energy flow measurements. The first requirement is that the circumferential modes n can be separated experimentally (see below). The structure-borne energy flow per mode n can then in principle be determined from four cross-spectral measurements of the shell displacements, according to eq.(7). Processing is performed in the frequency domain, hence normal accelerometers can be used to determine shell displacements. The spatial derivatives that occur can be determined with a finite difference approach, as used in acoustic intensity methods [1,2]. For example:

$$\omega Im\left[\left(\frac{\partial \tilde{u}_n}{\partial x}\right)^* \cdot \tilde{u}_n\right] \approx \frac{1}{\omega^3 \Delta x} Im\left[S(\ddot{u}_n(x_1), \ddot{u}_n(x_2))\right] \qquad (10)$$

where S denotes the cross-spectrum between the modal accelerations at the axial positions x_1 and x_2, with $\Delta x = x_2 - x_1$. Practical considerations require a Δx that is large enough to be able to measure phase differences between the two acceleration signals. The finite difference approximation requires Δx to be small compared to the axial wavelength. Therefore the vibrational behaviour of fluid-filled shells has to be considered to arrive at a good choice for Δx.

Pipe and Fluid Motion

In a fluid-filled pipe an infinite number of axial modes m correspond to each circumferential mode n. In most cases only the real axial wavenumbers k are of interest for the energy flow, because complex wavenumbers are associated with exponentially decaying waves. Real wavenumber solutions of the equations of motion for $n>1$ show cut-on frequencies f_{cn}, so that no wave of mode n can propagate at frequencies below f_{cn} [3-8]. These cut-on frequencies are approximately equal to [5]:

$$f_{cn} = f_{ring}\sqrt{\frac{\beta^2 n^2(n^2-1)^2}{1+n^2+\eta n}} \qquad (11)$$

where f_{ring} is the shell ring frequency and $\eta = a\rho_f/h\rho_s$ the fluid-shell mass ratio.

LOW FREQUENCY APPROXIMATIONS

In many practical pipe systems the ring frequency lies well above the frequency range of interest. Existing methods for energy flow measurements [1,2] can only be used at frequencies below

579

the cut-on frequency of n = 2 waves. The method that is proposed here extends the frequency range of applicability up to the cut-on frequency of n = 3 waves.

Wavenumbers

Below the cut-on frequency f_{c3} of propagating n = 3 waves, only a limited number of propagating wave types can exist. At n = 0 there is a wave ('T') that is associated with torsional shell motion, a wave ('S') associated with longitudinal shell motion, coupled to fluid motion via Poisson contraction, and a plane pressure wave ('F') in the fluid that is coupled to a radial 'breathing' shell motion. At n = 1 only a bending type of wave ('B') propagates and at n = 2 the first 'lobar' wave ('L'), showing an ovalling of the pipe cross section. The axial wavenumbers k_{nm} of these waves are the real solutions of the dispersion equation for a fluid-filled shell. Using Donnell-Mushtary shell theory the following approximate expressions can be derived for non-dimensional wavenumbers $\kappa = k_{nm}a$ at low non-dimensional frequencies $\Omega = f/f_{nng}$ ($\Omega^2 \ll 1$):

$$\kappa_T^2 = \frac{2}{1-\nu}\Omega^2 \doteq \zeta_T^2\Omega^2 \, , \quad \kappa_S^2 \approx (1+\Delta)\Omega^2 + \cdots \doteq \zeta_S^2\Omega^2 \, , \quad \kappa_F^2 \approx \left(\Psi + \frac{2\eta+\nu^2}{1-\nu^2}\right)\Omega^2 + \cdots \doteq \zeta_F^2\Omega^2$$

$$\kappa_B^2 \approx \sqrt{\frac{(2+\eta)\Omega^2 - \beta^2}{1-\nu^2}} + \frac{\left[(1-\nu)(\frac{3}{4}+\eta) + \frac{3-\nu}{2} - \nu^2\right]\Omega^2 - 2(1-\nu)\beta^2}{(1-\nu)(1-\nu^2)} + \cdots \tag{12}$$

$$\kappa_L^2 = \sqrt{\frac{4(5+2\eta)\Omega^2 - 256\beta^2}{1-\nu^2}} + \frac{\left[(1-\nu)(\frac{10}{3}+2\eta) + \frac{3-\nu}{2} - \nu^2\right]\Omega^2 - 128(1-\nu)\beta^2}{(1-\nu)(1-\nu^2)} + \cdots$$

where ζ is a wavenumber factor, $\Psi = (c_p/c_s)^2$ and $\Delta = \nu^2(\Psi-1)/[(\Psi-1)(1-\nu^2)+2\eta+\nu^2]$. The first three wavenumbers were derived by Pavic [8]. The bending wavenumbers exhibit a cut-on frequency. This is not realistic, however, but is due to the simplifications of the Donnell-Mushtary shell theory [3].

Modal Amplitude Relationships

The equations of motion determine the relationships between the modal amplitudes U,V,W and P for each mode n,m [7,8]. At low frequencies ($\Omega^2 \ll 1$) these relationships are approximately equal to:

$$\left(\frac{U}{W}\right)_S \approx \frac{i\Gamma_S}{\Omega} \, , \quad \left(\frac{P}{W}\right)_S \approx -\frac{2\rho_f c_p^2}{a(\Psi-\zeta_S^2)} \, , \quad \left(\frac{U}{W}\right)_F \approx \frac{i\Gamma_F}{\Omega} \, , \quad \left(\frac{P}{W}\right)_F \approx -\frac{2\rho_f c_p^2}{a(\Psi-\zeta_F^2)} \approx \frac{E_s h}{a^2}$$

$$\left(\frac{U}{W}\right)_B \approx -i\kappa_B\left[1 - (2+\nu)\kappa_B^2 + \cdots\right] \, , \quad \left(\frac{V}{W}\right)_B \approx -\left[1 + \nu\kappa_B^2 + \cdots\right] \, , \quad \left(\frac{P}{W}\right)_B \approx \frac{2\rho_f a\omega^2}{i\kappa_b} \tag{13}$$

$$\left(\frac{U}{W}\right)_L \approx -\frac{i\kappa_L}{4}\left[1 - \frac{2+\nu}{4}\kappa_L^2 + \cdots\right] \, , \quad \left(\frac{V}{W}\right)_L \approx -\frac{1}{2}\left[1 + \frac{\nu}{4}\kappa_L^2 + \cdots\right] \, , \quad \left(\frac{P}{W}\right)_L \approx -\frac{4\rho_f a\omega^2}{\kappa_L^2}$$

where $\Gamma = \nu\zeta/(\zeta^2-1)$ and ζ is defined in eq.(12). For the torsional mode $U_T = W_T = P_T = 0$, while for the longitudinal shell and fluid modes $V_S = V_F = 0$. Thus each wave type has its most characteristic displacement amplitude, from which the other modal amplitudes can be derived.

Approximate Equations for Energy Flow per Wave Type

The amplitude relationships (13) can be applied to the energy flow equations (7,8) to determine simplified equations for the structure-borne and fluid-borne energy flow per wave type. For three wave types (T,B,L) the energy flow can be determined from single cross-spectral measurements of the appropriate modal accelerations:

$$\left(\bar{P}_{ns}\right)_T \approx \frac{1-\nu}{2} \frac{\pi a D}{\omega^3 \Delta x} Im[S(\dot{v}_0(x_1),\dot{v}_0(x_2))]$$

$$\left(\tilde{P}_{xs}\right)_{B} \approx \pi a h E_{s}\left(1 - \kappa_{B}^{2} + \cdots\right) \frac{\kappa_{B}^{2}}{\omega^{3}\Delta x} \, Im\left[S\left(\ddot{w}_{1}(x_{1}),\ddot{w}_{1}(x_{2})\right)\right]$$

$$(14)$$

$$\left(\tilde{P}_{xs}\right)_{L} \approx \frac{1}{16}\pi a h E_{s}\left(1 - \frac{1}{4}\kappa_{L}^{2} + \cdots\right) \frac{\kappa_{L}^{2}}{\omega^{3}\Delta x} \, Im\left[S\left(\ddot{w}_{2}(x_{1}),\ddot{w}_{2}(x_{2})\right)\right]$$

There is no fluid-borne energy flow associated with the torsional wave. The fluid-borne energy flow associated with bending or lobar waves is an order Ω^{2} smaller than the corresponding structure-borne energy flow and hence of minor importance. These expressions for energy flow assume that no near-fields are present. This means that measurements should be taken at positions that are at least half a wavelength away from pipe bends or other discontinuities. Note that the derivation of the approximate energy flow equation for bending waves should be performed very carefully. In [8] Pavic describes only half of the energy flow in the bending wave, the part due to bending moments. The other half, that is due to tangential shear, is described by a small term in the equations which becomes important after adding two large terms that are opposite in sign. With the dispersive wavenumber κ_{B} from eq.(12) the expression for the structure-borne energy flow in bending-type waves of eq.(14) can be used in a frequency range beyond the range where simple beam bending is valid.

The remaining two wave types (S,F) form two coupled $n=0$ waves. The energy flow equations (7,8) for these waves are complex, because cross-terms occur between the modal amplitudes of both waves. To be able to determine the energy flows, some simplifying assumptions have to be made. The energy flow for the longitudinal shell wave is mainly propagating in the shell, while the energy flow for the fluid wave is mainly propagating in the fluid [4]. It can be shown that both energy flows can be determined from shell displacement amplitudes, provided that the energy distribution over the wave types is about equal. In cases where the energy flow in one of the wave types is larger, then at least the dominant energy flow can be determined. The approximate energy flow equations, again in terms of single cross-spectral measurements, are given by:

$$\left(\tilde{P}_{xs}\right)_{S} \approx \frac{1}{\zeta_{S}^{2}} \frac{\pi a D}{\omega^{3}\Delta x} \, Im\left[S\left(\ddot{u}_{0}(x_{1}),\ddot{u}_{0}(x_{2})\right)\right]$$

$$(15)$$

$$\left(\tilde{P}_{xf}\right)_{F} \approx \frac{2}{(\zeta_{F}^{2}-\Psi)^{2}\Omega^{2}} \frac{\pi a^{2}\rho_{f}c_{p}^{2}}{\omega^{3}\Delta x} \, Im\left[S\left(\ddot{w}_{0}(x_{1}),\ddot{w}_{0}(x_{2})\right)\right]$$

EXPERIMENTAL METHODS

On the condition that a straight pipe of sufficient length is available, the energy flow in the five propagating waves at frequencies below the cut-on of $n=3$ can be determined using the approximate equations that are given above. The optimal axial distance Δx can be chosen for each wave type separately.

Circumferential mode decomposition

Below the cut-on of $n=3$ waves the circumferential modes can be separated easily, thanks to the simple θ-dependence of the shell displacements. For example:

$$\ddot{u}(x,t) = \ddot{u}_{0}(x,t) + \ddot{u}_{1}(x,t)\cos[\theta+\theta_{1}(x,t)] + \ddot{u}_{2}(x,t)\cos[2\theta+\theta_{2}(x,t)] \qquad (16)$$

Three amplitudes and two phase angles have to be determined from measurements. This means that the shell displacement should be measured at five circumferential positions at least. In practice the modal accelerations and polarization angles are determined according to figure 2:

$$\ddot{u}_{0} = \frac{1}{4}(\ddot{u}_{A} + \ddot{u}_{B} + \ddot{u}_{C} + \ddot{u}_{D}) , \quad \ddot{v}_{0} = \frac{1}{4}(\ddot{v}_{A} + \ddot{v}_{B} + \ddot{v}_{C} + \ddot{v}_{D}) , \quad \ddot{w}_{0} = \frac{1}{4}(\ddot{w}_{A} + \ddot{w}_{B} + \ddot{w}_{C} + \ddot{w}_{D})$$

$$\ddot{w}_{1}\cos(\theta_{1}) = \frac{1}{2}(\ddot{w}_{A} - \ddot{w}_{C}) , \quad \ddot{w}_{1}\sin(\theta_{1}) = \frac{1}{2}(\ddot{w}_{B} - \ddot{w}_{D}) \qquad (17)$$

$$\ddot{w}_{2}\cos(\theta_{2}) = \frac{1}{4}(\ddot{w}_{A} - \ddot{w}_{B} + \ddot{w}_{C} - \ddot{w}_{D}) , \quad \ddot{w}_{2}\sin(\theta_{2}) = \frac{1}{4}(\ddot{w}_{A'} - \ddot{w}_{B'} + \ddot{w}_{C'} - \ddot{w}_{D'})$$

Four accelerometers at $90°$ angle are used for the $n=0$ and $n=1$ modes. The amplitude and the

polarization angle of the $n = 2$ mode is determined after rotating the set of accelerometers over 45°. The advantage of using eight circumferential positions instead of five is that the decomposition can be performed with simple hardware addition and subtraction devices [11], thus reducing the number of signals which need to be recorded.

Measuring Energy Flow per Wave Type

The equations (14-15) can be applied directly to the signals that are obtained by circumferential mode decomposition, to determine the energy flow per wave type. The expressions for the structure-borne energy flow in torsional, longitudinal and bending waves are equivalent to the expressions that are used for energy flow measurements on beams [1,2]. They only contain some correction factors to account for shell behaviour. The method as presented here provides an extension of the frequency range of applicability up to the cut-on frequency of $n = 3$ waves, while it is still based on two-channel measurement techniques, using accelerometers on the surface of the pipe.

Measuring Energy Flow when Coupled Waves Occur

The equations (14-15) are bound to show errors if the separation of wave types is difficult. This can occur when measuring near discontinuities, where near-fields occur, or in cases where the energy flow is not distributed equally over the coupled axial shell and fluid waves ($n = 0$). In these cases wave-type separation may be performed by means of measuring at three or four axial positions, as has been shown for bending waves on beams by Taylor [9]. For this method longer sections of straight pipe are required, which might be a disadvantage in practical situations. An alternative approach is the direct application of eq.(7). It involves the measurement of all three components of wall displacement, for each circumferential mode, at two axial positions. Only structure-borne energy flow can be determined with this method. Nevertheless the method appears promising for application in practical situations where only short lengths of straight pipe are available. Experiments will show whether this method is practicable.

EXPERIMENT

As a first check of the theoretical results and the wave-type decomposition method the dispersion curves for bending and lobar waves were determined experimentally.

Method for measuring wavenumbers

Carniel & Pascal [10] proposed a method to measure the dispersion curve for bending waves on a beam. The method is based on a finite difference description of the second spatial derivative of the transverse displacements that are associated with the bending waves. The dispersion curve is derived from two cross power spectra (S_{21}, S_{23}) and one auto power spectrum (S_{22}) of accelerations at three equidistant axial positions (x_1, x_2, x_3) along the beam:

$$k(\omega) \approx \frac{1}{\Delta x} \sqrt{2 - \frac{S_{23}}{S_{22}} - \frac{S_{21}}{S_{22}}} \tag{18}$$

The same method can be applied to measure dispersion curves for bending ($n = 1$) and lobar ($n = 2$) waves on pipes, provided that no near-fields are present and that sets of accelerometers are used to achieve wave-type decomposition. As energy dissipation in the short length of pipe between the accelerometer positions is negligible, the imaginary parts of the two cross power spectra are expected to be equal in magnitude and opposite in sign, resulting in real wavenumbers.

Measurements and results

Measurements were performed on an empty stainless steel pipe of mean radius $a = 60.8$ mm and thickness $h = 14.0$ mm, a 1:3 scale model of a ship propeller shaft. The cut-on frequencies (eq.11) were calculated to be $f_{c2} \approx 2566$ Hz and $f_{c3} \approx 7258$ Hz. The test arrangement is shown in figure 3. The pipe was excited in the transverse direction with a periodic chirp in the range from 300 to 6000 Hz with a repetition frequency of 1.9 Hz. At the other end of the pipe some dissipation is introduced through damped plates which have many resonating modes in the frequency range. By matching accelerometers and eliminating phase mismatch between the instrumentation channels, phase errors in the cross power spectra (estimated from 400 sample records) are smaller than 0.15° [11].

Figure 4 shows the dispersion curve for bending waves on the pipe. It is compared with theoretical curves, both from beam theory and shell theory (eq.12). Below the artificial cut-on

frequency, that is due to Donnell theory [3], the beam description is satisfactory, but for frequencies above 1500 Hz ($\approx f_{c2}/2$) shell theory gives a better description. Unfortunately the wave-type decomposition method appears to be insufficient when $n=2$ waves cut on. In the frequency range above the cut-on of $n=2$ waves the wavenumber calculation becomes unreliable. This is probably caused by the sensitivity of the accelerometers to transverse acceleration. The acceleration levels for the lobar wave were 20 dB higher than the acceleration levels for bending waves, while the typical transverse to main axis sensitivity ratio of the accelerometers (B&K 4382, delta-shear type) is not much smaller than - 40 dB. Figure 5 shows the dispersion curve for the first lobar waves ($n=2$) on the pipe. This wave type is not described by simple beam theory. The cut-on frequency agrees with the value that is calculated according to eq.(11). The dispersion curve that is determined from Donnell-Mushtary shell theory shows wavenumbers that are too low, compared with the experimental result. Recently the author has shown that a more elaborate shell theory, like Flügge's [3], gives a much better description.

Figures 6 and 7 show the magnitude of the imaginary parts of the transfer functions S_{21}/S_{22} and S_{23}/S_{22} which correspond to the wavenumber curves (fig.5,6). The imaginary parts of the two different cross power spectra S_{21} and S_{23} can be used to determine the energy flow at two different cross-sections of the pipe, according to eq.(14). The close agreement between the two curves shows that reliable energy flow measurements can be performed for both wave types.

CONCLUSIONS

The theoretical foundations of energy flow measurements for quantifying sound transmission along shell-type structures are described here. Expressions have been given that form a basis for practical measurement methods, using accelerometers on the surface of the shell. They present an extension of the frequency range of applicability compared with methods that are based on beam theory. Preliminary measurements show that practical energy flow measurements on pipes are feasible, provided that a reliable wave-type decomposition and accurate phase measurements can be performed.

ACKNOWLEDGEMENT

REFERENCES

[1]   G. Pavic: "Measurement of structure-borne wave intensity, Part I: formulation of the methods", *Journal of Sound and Vibration*, 49(2), 1976, 221-230

[2]   J.W. Verheij: "Cross spectral density methods for measuring structure-borne power flow on beams and pipes", *Journal of Sound and Vibration*, 70(1), 1980, 133-138

[3]   A.W. Leissa: *Vibration of shells*, NASA SP-288, Washington DC, 1973

[4]   C.R. Fuller & F.J. Fahy: "Characteristics of wave propagation and energy distribution in cylindrical elastic shells filled with fluid", *Journal of Sound and Vibration*, 81(4), 1982, 501-518

[5]   M. Möser, M. Heckl & K.-H. Ginters: "Zur Schallausbreitung in flüssigkeitsgefüllten kreiszylindrischen Rohren", *Acustica*, 60, 1986, 34-44

[6]   E.G. Williams: "Structural intensity in thin cylindrical shells", *Journal of the Acoustical Society of America*, 89(4), 1991, 1615-1622

[7]   G. Pavic: "Vibrational energy flow in elastic circular cylindrical shells", *Journal of Sound and Vibration*, 142(2), 1990, 293-310

[8]   G. Pavic: "Energy flow through straight pipes", *CETIM 3rd International congress on intensity techniques*, Senlis (France), 1990, 91-96

[9]   P.D. Taylor: "Nearfield structureborne power flow measurements", *International congress on recent developments in air- and structure-borne sound and vibration*, Auburn (AL), 1990, 339-345

[10]   X. Carniel & J.C. Pascal: "Caracteristiques de propagation et mesure du flux d'energie vibratoire dans les barres", *CETIM 2nd International congress on acoustic intensity*, Senlis (France), 1985, 211-217

[11]   J.W. Verheij: "Measurements of structure-borne wave intensity on lightly damped pipes", *Noise Control Engineering Journal*, 35(2), 1990, 69-76
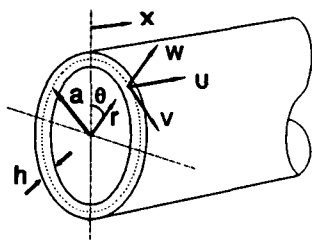
Figure 1: Geometry
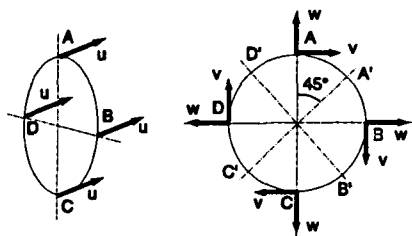
Figure 2: Accelerometer configurations for circumferential mode decomposition
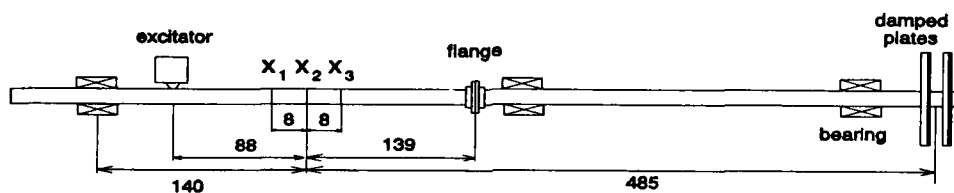
Figure 3: Test arrangement for wavenumber measurements, sizes are in cm.
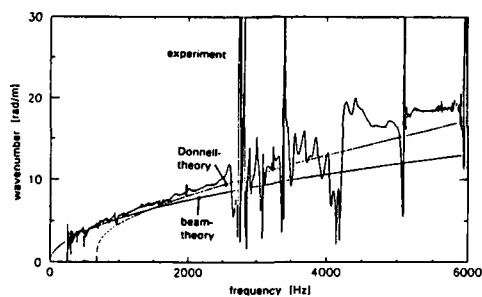
Figure 4: wavenumber for $n = 1$ waves
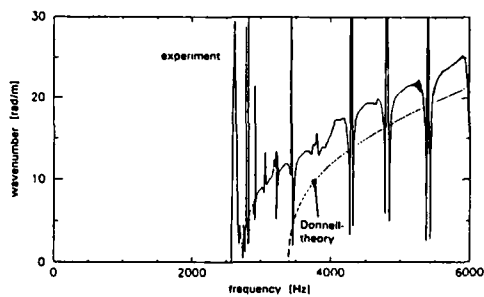
Figure 5: wavenumber for $n = 2$ waves
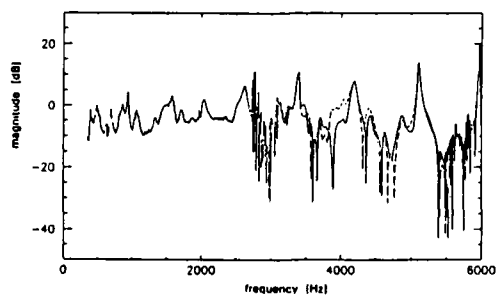
Figure 6: imaginary parts of transfer functions S_{21}/S_{22} and S_{23}/S_{22}; $n = 1$
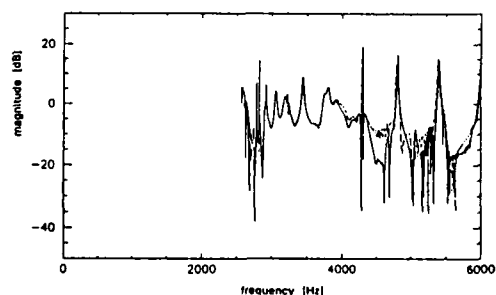
Figure 7: imaginary parts of transfer functions S_{21}/S_{22} and S_{23}/S_{22}; $n = 2$

584

COMPARISON OF MODE-TO-MODE POWER FLOW APPROXIMATION WITH GLOBAL SOLUTION FOR STEPPED BEAMS

Wu Qunli
School of Mechanical and Production Engineering
Nanyang Technological University
Nanyang Avenue
Singapore 2263

ABSTRACT

A mode-to-mode power flow approximation is derived for stepped beams based on the eigen-solutions of the uncoupled sub-beams by taking into account both the shear force and moment power flow. This approximation is compared with the global solution of the power flow for the stepped beams. It is found that the approximation agrees well with the global solutions when the weak-to-strong coupling is considered.

1. INTRODUCTION

The study of structural borne sound transmission through an engineering structure is often concerned with a wide-range frequency vibrations. The finite element method is generally used at low frequencies, while the statistical energy analysis is practicable at high frequencies. There is a lack of general analysis method for the mid-frequencies where the finite element method is too expensive and the confidence limit of the statistical energy method is relative large. The research work on a new power flow method which could bridge the mid-frequency range is intensive.   Among a number of publications, Miller and Von Flotow [1] suggested a local and global power flow analysis, through the use of travelling wave concepts. Cuschieri [2] proposed a mobility power flow method for both point and line coupled structures.

The mode-to-mode power flow was first proposed by Pope and Wibly [3] in the study of structural/acoustic coupling where the acoustic cavity was treated as a weak sub-system and the structure as a strong sub-system. This concept was adopted by Bremner and Wu [4] in the study of the weak-to-strong coupling of two plates. Due to the lack of the exact solutions for two coupled plates, the accuracy of the mode-to-mode power flow approximation is unknown.

In this paper, a mode-to-mode power flow approximation is derived for a stepped beam. This approximation is compared with the global solution.

2. GLOBAL MODE-TO-MODE POWER FLOW FORMULATION

The theoretical model considered here is for a stepped beam with total length L, as shown in Figure 1. The stepped beam consists of two sub-beams with lengths of L_1 and L_2. The beams 1 and 2 have the same Young modulus $\overline{E}$ and density ρ. The boundary conditions at the ends of the beam can be clamped, pinned or free.

Consider the transverse vibration of the Bernoulli-Euler beam, the eigenfunctions and frequencies can be solved globally from the governing equation and boundary conditions. Let $\Phi_i(x)$ be the eigenfunctions of the stepped beam. The eigenfunctions satisfied the displacement compatibility and force equilibrium conditions at the coupling boundary. The eigenfunctions are also orthogonal with the normalization factors of α_i.

Consider a harmonic force $P_0 e^{-j\omega t}$ acting on the beam 1 at location ξ, the displacement of the beam is

$$v(x) = \frac{P_0}{m_1} \sum_{i=1}^{\infty} \frac{\Phi_i(x)\Phi_i(\xi)}{\alpha_i(\overline{\omega}_i^2 - \omega^2)},$$ (1)

where P_0 is the amplitude of the external force and m_1 is the mass per unit length of the beam 1. $\overline{\omega}_i$ are the complex eigenfrequencies (angular) of the stepped beam.

The power flow from the beam 1 to beam 2 is the sum of the power flow due to the internal shear force and internal bending moment at the coupling boundary. The internal shear force at $x = L_1$ is

$$F = \overline{E}I_1 \frac{\partial^3 v(x)}{\partial x^3} = \overline{E}I_1 \frac{P_0}{m_1} \sum_{i=1}^{\infty} \frac{\Phi_i'''(L_1)\Phi_i(\xi)}{\alpha_i(\overline{\omega}_i^2 - \omega^2)},$$ (2)

where I_1 is the moment of inertia and L_1 is the length of the beam 1. The internal bending moment is

$$M = -\overline{E}I_1 \frac{\partial^2 v(x)}{\partial x^2} = -\overline{E}I_1 \frac{P_0}{m_1} \sum_{i=1}^{\infty} \frac{\Phi_i''(L_1)\Phi_i(\xi)}{\alpha_i(\overline{\omega}_i^2 - \omega^2)}.$$ (3)

The power flows associated with the shear force and moment are defined as

$$P_F = \frac{1}{2} Re\{F j\omega v^*\},$$ (4)

$$P_M = \frac{1}{2} Re\{M j\omega \left(-\frac{\partial v}{\partial x}\right)^*\},$$ (5)

where * denotes the complex conjugate. Insert equations (1) and (2) into (4) gives

$$P_F = \frac{1}{2} Re\left\{ j\omega \left(\frac{P_0}{m_1}\right)^2 \overline{E}I_1 \sum_{m=1}^{\infty} \sum_{n=1}^{\infty} \frac{\Phi_m(\xi)\Phi_n(\xi)}{\alpha_m \alpha_n (\overline{\omega}_m^2 - \omega^2)(\overline{\omega}_n^2 - \omega^2)^*} \Phi_m'''(L_1)\Phi_n(L_1) \right\}.$$ (6)

Because the eigenfunctions for the stepped beam are orthogonal, there is no power flow in cross modes. Consider the complex Young modulus $\overline{E} = E(1 + j\eta)$ where η is the loss factor of the beam, equation (6) becomes

$$P_F = \frac{1}{2} \eta\omega \left(\frac{P_0}{m_1}\right)^2 EI_1 \sum_{m=1}^{\infty} \frac{\Phi_m^2(\xi)}{\alpha_m^2 \mid (\overline{\omega}_m^2 - \omega^2) \mid^2} \Phi_m'''(L_1)\Phi_m(L_1).$$ (7)

Similarly, the power flow associated with the internal bending moment can be obtained as follows

$$P_M = \frac{1}{2} \eta\omega \left(\frac{P_0}{m_1}\right)^2 EI_1 \sum_{m=1}^{\infty} \frac{\Phi_m^2(\xi)}{\alpha_m^2 \mid (\overline{\omega}_m^2 - \omega^2) \mid^2} \Phi_m''(L_1)\Phi_m'(L_1).$$ (8)

The total power flow from the beam 1 to beam 2 is then

$$P_T = P_F + P_M = \frac{1}{2} \eta\omega \left(\frac{P_0}{m_1}\right)^2 EI_1 \sum_{m=1}^{\infty} \frac{\Phi_m^2(\xi)}{\alpha_m^2 \mid (\overline{\omega}_m^2 - \omega^2) \mid^2} P_{mn},$$ (9)

586

where

$$P_{mm} = (\Phi_m'''(L_1)\Phi_m(L_1) + \Phi_m''(L_1)\Phi_m'(L_1)).$$ (10)

It can be seen from equations (9) and (10) that the power flow can be calculated when the eigenfunctions and eigenfrequencies for the stepped beam are solved.

3. APPROXIMATION OF MODE-TO-MODE POWER FLOW FORMULATION

The global solutions of flow powers require the solutions of the global eigenfunctions and eigenfrequencies. The global eigenfunctions and eigenfrequencies of coupled systems can only obtained for limited cases. The finite element method solutions will be expensive at high frequencies. It is desirable to analyze the sub-systems individually and to calculate the power flow based on the eigen-solutions for the uncoupled sub-systems.

Consider the stepped beam with two sub-beams as shown in figure 1. Assume the beam 2 is much rigider than beam 1, i.e $EI_1 \ll EI_2$. The structural interaction can be approximated in the modal expansion of the two uncoupled beams, by considering the beam 1 "clamped" and the beam 2 "free", at the coupling boundary.

Let $\Phi_{1i}(x_1)$ and $\Phi_{2i}(x_2)$ be the eigenfunctions of the uncoupled beams 1 and 2. Consider a harmonic force $P_0 e^{-j\omega t}$ acting on the beam 1 at location ξ, the displacement of the beam 1 is

$$v_1(x_1) = \frac{P_0}{m_1} \sum_{i=1}^{\infty} \frac{\Phi_{1i}(x_1)\Phi_{1i}(\xi)}{\alpha_{1i}(\overline{\omega}_{1i}^2 - \omega^2)},$$ (11)

where $\overline{\omega}_{1i}$ is the complex eigenfrequencies (angular) of the uncoupled beam 1 and α_{1i} is the normalization factors of $\Phi_{1i}(x_1)$.

The shear force F and moment M at the end of the beam 1, $x_1 = L_1$, can be expressed as equations (2) and (3) by replacing the global eigen-variables with the uncoupled eigen-variables of the beam 1. The internal shear force F and moment M from the beam 1 will apply on the end of the beam 2. The displacement of the beam 2 due to F and M at $x_2 = 0$ is

$$v_2(x_2) = \frac{F}{m_2} \sum_{n=1}^{\infty} \frac{\Phi_{2n}(x_2)\Phi_{2n}(0)}{\alpha_{2n}(\overline{\omega}_{2n}^2 - \omega^2)} + \frac{M}{m_2} \sum_{n=1}^{\infty} \frac{\Phi_{2n}(x_2)\Phi_{2n}'(0)}{\alpha_{2n}(\overline{\omega}_{2n}^2 - \omega^2)}.$$ (12)

Insert the expressions for F and M, equation (12) becomes

$$v_2(x_2) = \left(\frac{P_0}{m_1 m_2}\right) \overline{E} I_1 \sum_{m=1}^{\infty} \sum_{n=1}^{\infty} \frac{\Phi_{1m}(\xi)\Phi_{2n}(x_2)}{\alpha_{1m}\alpha_{2n}(\overline{\omega}_{1m}^2 - \omega^2)(\overline{\omega}_{2n}^2 - \omega^2)} C_{mn}.$$ (13)

where $C_{mn} = (\Phi_{1m}'''(L_1)\Phi_{2n}(0) + \Phi_{1m}''(L_1)\Phi_{2n}'(0))$.

Following equations (4) and (5) the power flow formulation is obtained

$$P_T = P_F + P_M = \frac{1}{2}\eta\left(\frac{P_0}{M_1}\right)^2 \frac{\omega}{m_2} \sum_{m=1}^{\infty} \sum_{n=1}^{\infty} \frac{\omega_{2n}^2 \Phi_{1m}^2(\xi)}{\alpha_{1m}^2 \alpha_{2n}^2 \mid (\overline{\omega}_{1m}^2 - \omega^2) \mid^2 \mid (\overline{\omega}_{2n}^2 - \omega^2) \mid^2} C_{mn}^2.$$ (14)

Thus, the power flow can be calculated based on the solutions of two sub-systems.

4. NUMERICAL RESULTS

A numerical study was carried out to compare the results of the mode-to-mode approximation with the global solution. As an example, consider a rectangular stepped beam of clamped-clamped ends, with $L_1 = L_2 = 0.5$ meter, $E_1 = E_2 = 7.2 \times 10^{10} N/m^2$, $\rho_1 = \rho_2 = 2700\ kg/m^3$, $\eta_1 = \eta_2 = \eta = 0.01$, and $I_1 = 1.125 \times 10^{-10}\ m^4$. Let $I = I_2/I_1 = \beta^2$ and $\beta = A_2/A_1$. The power flow results for various values of I were calculated.

For the approximate solutions, the eigenfunctions and eigenfrequencies of each sub-beam were obtained from reference [5] by assuming beam 1 is clamped-clamped and beam 2 is free-clamped. The power flow was calculated from equation (14). For the global solutions, the eigenfunctions and eigenfrequencies were calculated numerically [6] and then the power flow was calculated from equation (9).

Figure 2 shows the comparison of the power flow for the stepped beam with I=5. It can be seen that the approximation matches not so well with the global solution at the first three resonances. The errors are due to the weak-to-strong assumption. At the frequencies from 120 Hz to 850 Hz the two solutions agree quite well. However, the approximate solution largely overestimates the power flow at the 880 Hz resonance. This is because two sub-beams having the same eigenfrequencies. This eigenfrequency match of the sub-beams will create a large power flow in the approximate solution. Figure 3 shows the results of the octave band average power flow. The differences of the two solutions are reduced except for the 1000 Hz band.

Figure 4 shows the comparison of the power flow for the stepped beam with I=10. The agreements of the two solutions are improved at the low frequencies. Figure 5 shows the octave band average power flow of the two solutions. It can be seen that the agreements are good over the frequency range for 31 Hz to 1000 Hz.

The power flow comparison for the case of I=40 is shown in Figure 6. The improvements can be noticed at low frequencies. However the power flow from the approximation is lower than the global solutions at the frequencies of anti-resonances. The over-estimating at 900 Hz is due to the eigenfrequency match of the two beams. The octave band results are shown in Figure 7.

5. DISCUSSION AND CONCLUSIONS

The mode-to-mode power flow approximation was derived for the stepped beam. The approximation was compared with the global solution for the weak-to-strong cases. It was found that the approximate method overestimated the power flow when the two uncoupled systems had the same eigenfrequencies. The power flow estimation for other cases showed that the approximate solutions agreed well with the global solutions.

The mode-to-mode approximation for the beams can be extended to the cases of plate-to-plate coupling. Further work is required to improve the accuracy of the mode-to-mode approximation.

ACKNOWLEDGEMENT

REFERENCES

[1] D. W. Miller and A. von Flotow 1989 Journal of Sound and Vibration 128,145-162. A travelling wave approach to power flow in structural networks.

[2] J. M. Cuschieri 1990 Journal of Acoustical Society of America 87, 1159-1165. Structural power-flow analysis using a mobility approach of an L-shaped plate.

[3] L. D. Pope and J. F. Wilby 1980 Journal of Acoustical Society of America 67, 823-826. Band-limited power flow into enclosures II.

[4] P. G. Bremner and Wu Qunli 1991 120th Meeting of Acoustical Society of America Paper No. 2SA. An approximate mode-to-mode power flow formulation for line-coupled structures.

[5] R. D. Blevins 1979 Formulas for natural frequency and mode shape. New York: Van Nortrand Reinhold.

[6] S. K. Jang and C. W. Bert 1989 Journal of Sound and Vibration 130, 342-346. Free vibration of stepped beams: exact and numerical solutions.

(a)

x

0   L

L_1

x_1

0

Beam 1   (b)

F

Beam 2

M

0   L_2 x_2
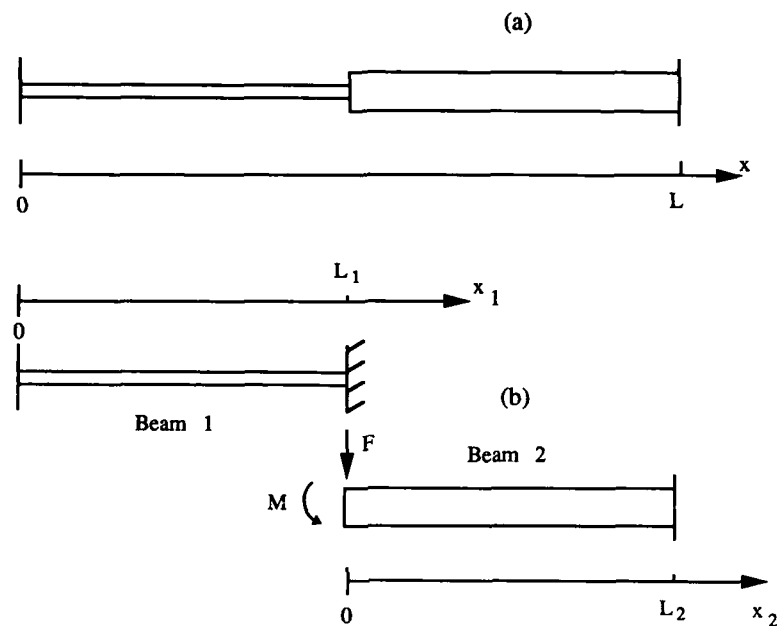
Figure 1   Stepped beams: (a) geometry for global solution,

(b) geometry for mode-to-mode approximation.

Figure 2 Power flow through stepped beam
I=5, Damping =0.01

Figure 3 Power flow through stepped beam
I=5, Damping =0.01

Global Solution + Approximation

■ Global Solution ⊠ Approximation

Figure 4 Power flow through stepped beam
I=10, Damping =0.01

Global Solution ＋ Approximation

Figure 5 Power flow through stepped beam
I=10, Damping =0.01

■ Global Solution ⊠ Approximation

Figure 6 Power flow through stepped beam
I=40, Damping =0.01

Global Solution ＋ Approximation

Figure 7 Power flow through stepped beam
I=40, Damping =0.01

■ Global Solution ⊠ Approximation

590

SECOND INTERNATIONAL CONGRESS ON
RECENT DEVELOPMENTS IN AIR- AND
STRUCTURE-BORNE SOUND AND VIBRATION
MARCH 4-6, 1992   AUBURN UNIVERSITY, USA

RECIPROCITY METHOD FOR QUANTIFICATION
OF AIRBORNE SOUND TRANSFER FROM MACHINERY

Jan W. Verheij
TNO Institute of Applied Physics
P.O. Box 155, 2600 AD Delft
The Netherlands

ABSTRACT

A substitution source method is described to enable separation of the airborne sound transfer from a particular source in situations of combined structure-borne and airborne sound transfer or in multiple source configurations.

The method describes the "source strength" of radiating surfaces by means of radiated power. This quantity is derived from sound intensity measurements close to the radiating area of interest. The transfer function for radiated power to mean square sound pressure at a receiver location is determined reciprocally. The basis for this reciprocity measurement is the assumption that the actual sound radiation can be replaced by a fictitious distribution of uncorrelated monopole sources over the radiator. The paper describes the method and a laboratory experiment in which the sound transfer from an engine-type source to an underwater receiver is modelled. A discussion is presented on limitations and on other potential applications.

METHOD

In a research project on procedures for sound path quantification from shipboard machinery, the author has explored a so-called equivalent or substitution source method to quantify the contribution of sound-radiating machine surfaces to underwater sound. The method assumes that the sound radiation of a partial surface can be replaced by a number of uncorrelated point sources evenly distributed over the surface. When the machine and all other sound sources are turned off, the substitution point sources should generate the same response at a receiver location as the original radiator if they radiate in total the same sound power as the original radiator.

To be valid, of course, it is required that the radiator has no strong directivity. It is supposed a priori that broadband sources with dimensions which are not small compared to the wavelength in air are more suited to the method than tonal or small sources.

Fig. 1 shows the type of measurements that are to be performed.

<u>Sound power</u>

The assumption is that it is easy to enclose the engine by a number m of flat measurement surfaces more or less parallel to the surfaces of the engine. For the choice of m the following considerations are applied:
- each partial surface should be small enough to allow intensity measurements to be made by hand-scanning from a stationary position
- more or less homogeneous intensity distribution over each partial surface.

For partial surface S_j the radiated power is determined according to

$$P_{rad}(j) = \int_{S_j} I_n dS \tag{1}$$

where I_n denotes the sound intensity normal to S_j.

For each surface S_j a transfer function to underwater is defined by $p_w^2(j)/P_{rad}(j)$. Then in combination with the results according to eq. (1) the contribution of the airborne path to the underwater sound pressure is obtained from

$$p_w^2 = \sum_{j=1}^m p_w^2(j) = \sum_{j=1}^m \left[p_w^2(j) / P_{rad}(j) \right] . P_{rad}(j) \tag{2}$$

Measurement of the transfer functions between brackets will now be studied.

Assume that a partial surface S_j is covered with $n(j)$ uncorrelated fictitious monopole point sources with volume acceleration $\dot{Q}_0$. Then the fictitious power radiated by these sources is

$$P_{rad}^{fic}(j) = \frac{\rho}{4\pi c} . \dot{Q}_0^2 \sum_{i=1}^{n(j)} C_{R,i} \tag{3}$$

The term $\dot{Q}_0^2 \rho/4\pi c$ equals the free field value of radiated power for a point monopole source. The correction factors $C_{R,i}$ originate from the fact that the radiation resistance of a point source against a hard wall is twice the free field value (i.e. $C_{R,i} = 2$). However, for positions close to (in terms of wavelength) edges and corners of a machine, the value will decrease, with $C_{R,i} = 1$ as a minimum (free field value).

The transfer function for each point source $\dot{Q}(i)$ is determined reciprocally using the well known relation (see fig. 1):

$$\frac{p_w^2}{\dot{Q}_0^2(i)} = \frac{p_1'^2(i)}{\dot{Q}_w'^2} \tag{4}$$

Therefore, the radiated underwater sound due to S_j follows from eqs. (2–4) as

$$p_w^2(j) = P_{rad}(j) . \left[\frac{p_w^2(j)}{P_{rad}^{fic}(j)} \right] = P_{rad}(j) . \left[\dot{Q}_0^2 \sum_{i=1}^{n(j)} \frac{p_{1,i}'^2(j)}{\dot{Q}_w'^2} \right] . \frac{1}{P_{rad}^{fic}(j)} = \frac{P_{rad}(j)}{\sum_{i=1}^{n(j)} C_{R,i}} . \frac{4\pi c}{\rho} . \sum_{i=1}^{n(j)} \frac{p_{1,i}'^2(j)}{\dot{Q}_w'^2} \tag{5}$$

In practical cases it might be justified to measure the transfer functions to just a few positions on each S_j. A selection of positions with different $C_{R,i}$ may be taken. One may distinguish between positions close to corners, close to edges and "center" positions on S_j. For each category an averaged transfer function must be multiplied with a weighting factor, taking into account the fraction of S_j which is represented by the same value of $C_{R,i}$. For the experiments in this paper this procedure has been applied.

EXPERIMENTS

Some experimental validation of the method has been performed in the laboratory. A water tank facility (360 m³) with hull-type boundaries was used as a receiver system. The sound

source was a steel box, constructed of 5 mm steel plate and profiles. The dimensions (1,6 m × 1,0 m × 0,5 m) were chosen to be approximately a 1:2 scale model of a shipboard diesel engine. Inside this box a 2 kN vibration exciter has been installed to simulate the machinery noise. This model engine has been installed in an "engine room" which has the tank hull as one of its boundaries, see figures 2 and 3.

The experiments consisted of three parts

– measurement of $C_{R,i}$

– measurement of sound intensity and underwater sound

– reciprocity measurement of transfer functions.

$\underline{C_{R,i}}$

The factor C_R is by definition the ratio of the radiation resistance of a point monopole source at the machine surface and that in the free field. Using the reciprocity principle it can be shown that this ratio can easily be estimated from measurements in a reverberation room. The reader is reminded of the well known fact that for a wall of a reverberation room: $\overline{p^2} = 2\ \overline{p_{room}^2}$, which corresponds with a radiation resistance at the walls twice as high as in the reverberation field and thus twice as high as in the free field. Based on this principle $C_{R,i}$ was estimated for three categories of positions on the engine surface using

$$C_{R,i} = \overline{p_i^2} / \overline{p_{room}^2} \quad i = 1,\ 2,\ 3 \qquad (6)$$

For category nr. 1, the "corner" positions, $\overline{p_1^2}$ was obtained from microphone positions at a distance of 0.1 m from corners. Category nr. 2 were "edge" positions at 0.1 m from edges. Category nr. 3 were "center" positions at a distance of 0.2 m or more from edges and corners.

The engine was located in a 200 m³ reverberation room which was excited by two loudspeakers driven with random noise. The microphone for measuring p_i^2, was held at 1 mm distance from the engine surface. Fig. 5 shows the measurement results of 10 lg $C_{R,i}$. Table 1 shows the approximations used for further calculations. Above 630 Hz (corresponding with 315 Hz at full scale) $C_{R,i} = 2$ is a good approximation for all positions. At lower frequencies only the "corner" positions deviate significantly from 2. Because, these "corner" positions represent only a small part of the engine surface, replacement of all $C_{R,i}$ in eq. (5) by 2 will not lead to serious deviations (see also fig. 11).

Sound intensity and underwater sound measurement

The vibration exciter inside the model engine was driven with a periodically swept sine. The spectral line distance was chosen to be 12,5 Hz to model at the reduced scale 1:2 the $\Delta f = 6.25$ Hz of a four-stroke diesel engine at 750 rpm. The sound power for eight partial surfaces A–H (see fig. 4) was determined using the averaged sound intensity vector $\tilde{I}_n(j)$ normal to S_j. The results were reduced to those of five partial surfaces by combining A and B, C and D, E and F. The bottom surface was neglected, being not accessible.

$\tilde{I}_n$ was obtained from handscanning in two perpendicular directions following grid lines 0.1 m apart. The distance of the intensity probe (B&K 4181, spacer 12 mm) to the engine surface was 0.1 m. The scanning speed was approximately 0.2 m/s. Repeatability of the 1/3 octave band results of $\tilde{I}_n$ was within 1 dB. The signal processing was performed using a multi-channel FFT-analyzer. To correct for the phase mismatch of the probe and the instrument channels, measurements with a sound intensity calibrator B&K type 3541 were used.

To get an indication of the nature of the sound field on the partial surfaces, the so-called F_3

indicator has been calculated according to

$$F_3 = L_{\bar{p}} - 10 \lg\left(|\bar{I}_n|\rho c / p_0^2\right) \quad dB \quad re\ 1 \tag{7}$$

Fig. 6 shows the results of F_3 on the partial surfaces. For measurements on the intensity calibrator the values of F_3 were at least 15 dB higher than for the measurements. This implies negligible errors due to phase mismatch for the measurements.

Fig. 7 shows the results of $P_{rad}(j)$.

The underwater sound was measured at two hydrophone positions in the tank. Due to the reverberant nature of the sound field for $f > 200$ Hz the 1/3-octave band levels at these two positions differed was less than 5 dB.

Transfer functions

Measurements according to the righthand side of eq. (4) were performed with a hydrosounder (type Dyna Empire J11) successively at the two hydrophone positions. The volume acceleration was derived from the measured piston acceleration. Omnidirectionality of the source was assumed, which becomes less correct above 2 kHz.

Sound pressures were measured against the engine surface (see fig. 1) at 1 mm distance. For ach partial surface (AB , CD, EF, G and H) three transfer functions have been determined, for "corner", "edge" and "center" positions respectively, according to

$$T_i \overset{def}{=} \left[\frac{p'^2_{1,i}}{\dot{Q}'^2_w}\right] \quad i = 1, 2, 3 \tag{8}$$

The underwater sound source was driven with the source spectrum as the model engine. Fig. 8 shows transfer functions for center positions on the partial surfaces. Surface AB is clearly predominant. This is the partial surface nearest to the hull.

For $f < 500$ Hz the transfer functions for corner and edge positions were generally lower only on AB.

Results

Fig. 9 shows calculated underwater sound pressures at one hydrophone position due to five partial surfaces. AB is predominant except at 500 Hz, where H appears predominant. The strong radiation of H at 500 Hz (see fig. 7) is caused by resonance of the ventilation grid (see figs. 3 and 4).

Fig. 10 shows the measured underwater sound pressure levels at one hydrophone position and those calculated according to eq. (5). Fig. 11 shows that replacement in eq. (5) of $C_{R,i}$ values according to Table 1 by $C_{R,i} = 2$ gives negligible differences. The agreement between measurements and calculations is within a few dB. A similar result was found for the other hydrophone position.

DISCUSSION

An attractive aspect of the proposed method is that the "source strength" measurement, i.e. of $\bar{I}_n(j)$ is relatively simple, also in cases of real engines with non-flat surfaces. At the lower end of the frequency range covered in the validation described, the length of the model engine was approximately equal to the wavelength in air, whereas the width was approximately equal to $\lambda/3$ at this frequency. Moreover the 1/3 octave filter-bandwidth contained only three spectral lines. Nevertheless, the substitution by uncorrelated point sources does not lead to unacceptable inaccuracies.

With respect to the low frequency limits of validity further tests are needed, especially for other types of spectra and other types of transfer systems. Potential applications could be to aircraft and vehicle interiors. The boundaries of such interiors may be considered as multiple radiator configurations. The sound intensity method may also be used to localize important radiators. However, as such it gives no indication on the transmission attenuation between strongly radiating components and observers. The proposed reciprocity method provides the additional information on that important aspect. This improves knowledge needed for cost-effective noise control measures.

The method would fail, however, for radiators with strong directivity due to the neglect of correlation between the substitution sources. Mason and Fahy [1] have proposed a "deterministic" method for that situation. However, this method requires detailed velocity data of the source surface. For diesel engines of the type used on board ships this would be quite difficult to obtain.

ACKNOWLEDGEMENT

REFERENCE

[1] J.S. Mason, F.J. Fahy, "Application of a reciprocity technique for the determination of the contributions of various regions of a vibrating body to the sound pressure at a receiver point". Proceedings of Institute of Acoustics, Vol. 12, Part 1 (1990), 469–476.
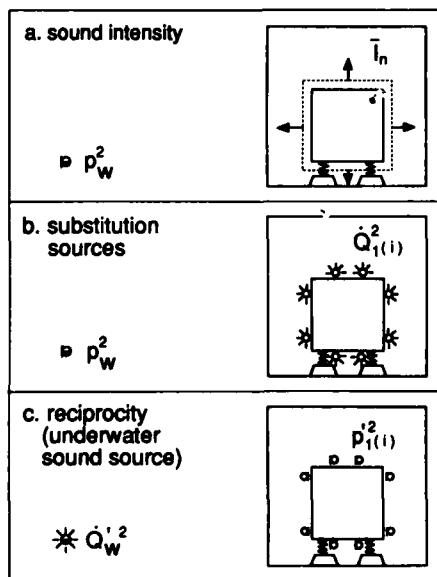
Figure 1 Substitution source principle for quantifying the airborne sound transfer from machine to underwater. An equivalent set of ficititious point sources is defined on the machine surface to generate the same sound power as the machine. The transfer function of these point sources to the water is measured reciprocally.
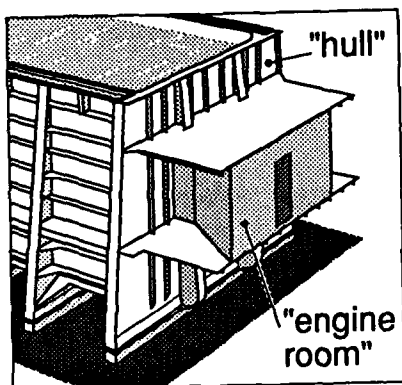
Figure 2 General overview of the "engine room" and water basin.

Figure 3 Model engine in "engine room". The wall behind the engine is the hull of the water basin.
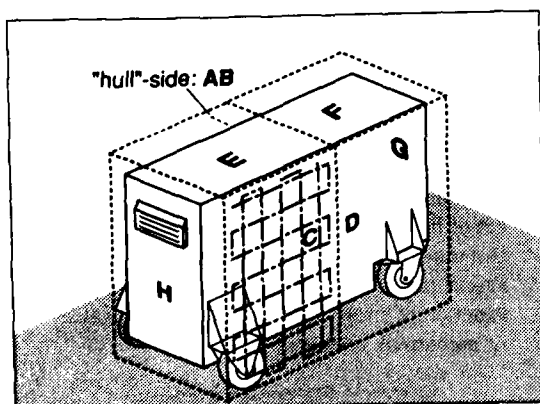
Figure 4 Enclosing surface for sound intensity measurements. Eight partial surfaces were used. Results of A and B, C and D, E and F were combined to AB, CD and EF, respectively.
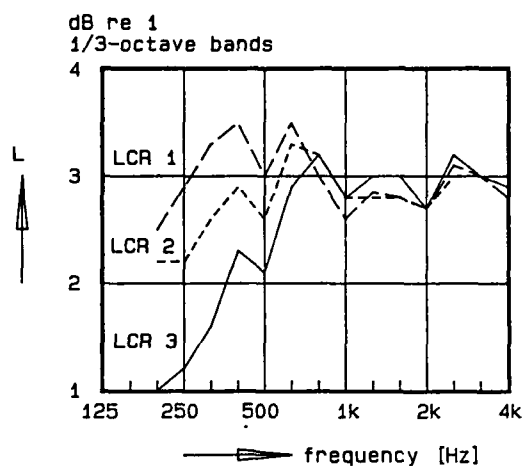
Figure 5 $10 \lg C_R$ measured according to eq. (6) for three categories of positions.
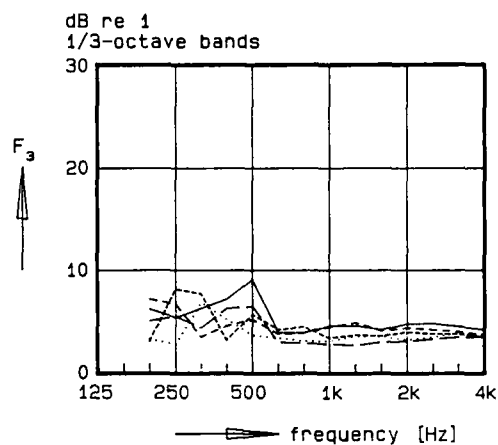
Figure 6 F_3 indicator for partial surfaces, eq. (7).
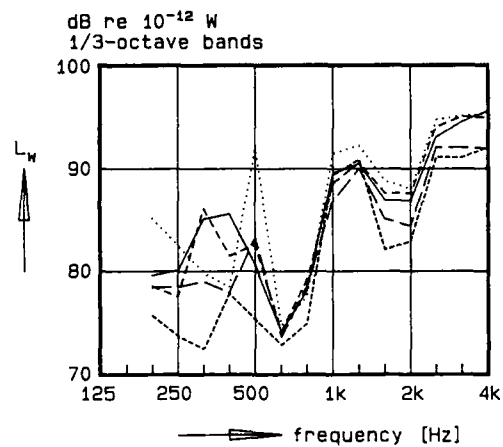
Figure 7 Radiated sound power for five partial surfaces.

———	800 partial surface AB
– – – –	801 partial surface CD
—— ——	802 partial surface EF
-------	803 partial surface G
········	804 partial surface H

Table 1 Approximate values of $C_{R,i}$ derived from fig. 5.

f (Hz)	$C_{R,1}$ corner	$C_{R,2}$ edge	$C_{R,3}$ center
200	1.25	1.5	1.6
250	1.35	1.6	2
315	1.45	1.7	2
400	1.6	1.8	2
500	1.7	1.9	2
630	1.85	2	2
800	2	2	2
1 k – 5 k	2	2	2
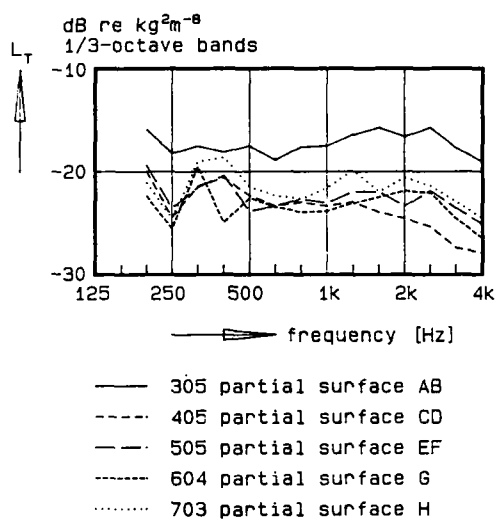
Figure 8 Transfer function 10 lg T
according to eq. (8) for center positions.
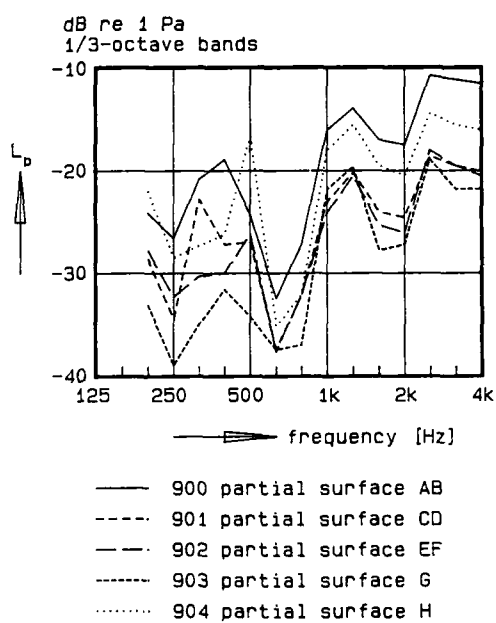
Figure 9 Underwater sound pressure levels
due to partial surfaces.
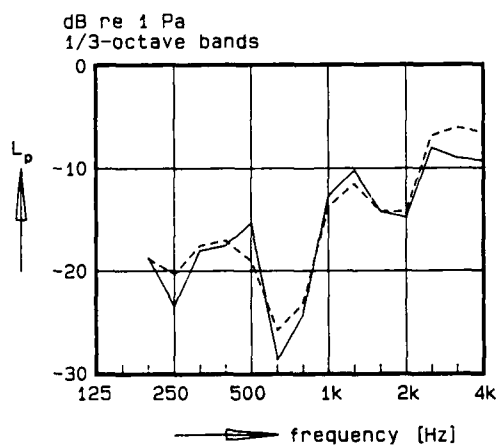
Figure 10 Measured and calculated (solid
line) underwater sound.
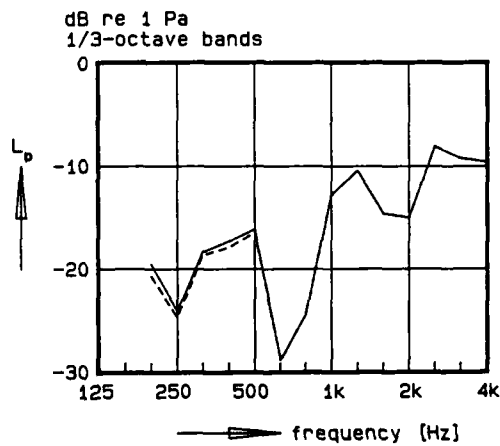
Figure 11 Calculated underwater sound
according to eq. (5) (solid line) and to eq. (5)
with $C_{R,i}$ = 2.

598

Vibrational Response of Coupled Composite Beams

C. Nataraj	and	**P. K. Raju**
Assistant Professor		Associate Professor
Department of Mechanical Engineering		Department of Mechanical Engineering
Villanova University, Villanova, PA 19085		Auburn University, Auburn, AL 36849

Abstract

The problem of two coupled unidirectional fiber composite beams is considered. For the simplifying case when pure bending occurs, the vibrational amplitudes of the two beams are obtained. Results from an experimental set-up of two graphite epoxy beams bolted together are compared to those obtained from analysis. Also presented is analytically computed power flow variation over the frequency range.

Nomenclature

A_j	area of cross-section of the jth beam
C_t	torsional rigidity of the beam
C_{mt}	mutual stiffness coefficient
$(E_{zz}I_x)_j$	flexural rigidity of the jth beam
f_j	external excitation on the jth beam
G_{xy}	shear modulus
i	$\sqrt{-1}$
J_z	polar moment of inertia about the z axis
k_j	wave number of the jth beam
l_j	length of the jth beam
m_c	coupling moment at the junction of the beams
v_j	transverse vibrational displacement of the jth beam
z_j	axial coordinate for the jth beam
α	torsional deformation about the z axis
η	$1 - [(E_{zz}I_xC_t)/C_{mt}^2]$
η_j	loss factor for the jth beam
κ	shape factor
$\phi_{n,j}$	nth eigenfunction for the jth beam
ρ_j	density of the jth beam
ψ	rotational displacement of beam cross-section
$\omega_{n,j}$	natural frequency of the jth beam
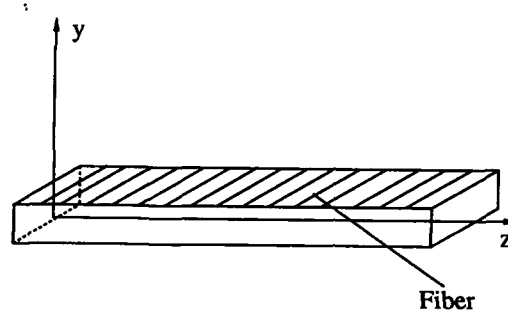
Figure 1: Fiber Composite Beam and Coordinate Systems

1 Introduction

The problem of two coupled beams in vibration has been considered by many researchers (Davies and Wahab, 1981; Lyon, 1975). However, the specific problem of fiber composite beams has not received much attention. Composite structures are used quite widely in many applications where one finds beams welded or bolted together.

In general, the vibrational problem of composite beams is quite complicated due to coupling of torsion and flexure (Teh and Huang, 1980). When two or more beams are coupled together, the problem gets further intricate since energy exchange can occur between the two beams in torsion and flexure.

This paper considers two unidirectional fiber composite beams bolted together. As a first step, the fiber angle will be chosen to be zero with respect to the symmetry axes, which essentially renders the problems of torsion and flexure independent. Results from analysis will be compared to that from a simple experimental set-up.

2 Mathematical Model

Before considering coupled beams we will first look at a fiber composite beam in free vibration. The equations of motion are quite involved and typically display coupling between torsion and flexure (Teh and Huang, 1980). Although we will be subsequently making assumptions that will obviate the need to use this coupled model, the equations are given below for completeness. Please see the nomenclature for a description of the various constants used in the equations. Fig. 1 shows the coordinate systems; the primary response variables are: v for tranverse displacement, ψ for rotation of the beam cross-section, and α for torsional deformation about the z axis.

$$\kappa A G_{xy} \frac{\partial}{\partial z}\left(\frac{\partial v}{\partial z} - \psi\right) = \rho A \frac{\partial^2 v}{\partial t^2} \tag{1}$$

$$\frac{E_{zz}I_x}{\eta}\frac{\partial^2 \psi}{\partial z^2} + \frac{E_{zz}I_x}{\eta}\frac{C_t}{C_{mt}}\frac{\partial^2 \alpha}{\partial z^2} + \kappa A G_{xy}\left(\frac{\partial v}{\partial z} - \psi\right) = \rho I_x \frac{\partial^2 \psi}{\partial t^2} \tag{2}$$

$$\frac{E_{zz}I_x}{\eta}\frac{C_t}{C_{mt}}\frac{\partial^2 \psi}{\partial z^2} + \frac{C_t}{\eta}\frac{\partial^2 \alpha}{\partial z^2} = \rho J_z \frac{\partial^2 \alpha}{\partial t^2} \tag{3}$$

When the fiber orientation with respect to the longitudinal axis differs from zero, the above set of coupled equations would have to be solved. However, in this paper, we are concerned with the special case of zero orientation (as a starting point). In that case, it can be shown the above system of equations gets decoupled. Further approximation in the form of neglecting shear effect will lead to the standard Euler beam equation as given below.

$$E_{zz}I_x \frac{\partial^4 v}{\partial z^4} + \rho A \frac{\partial^2 v}{\partial t^2} = 0 \tag{4}$$

Next, we consider two such coupled beams using the above simplifying assumptions. Since the two beams are

600
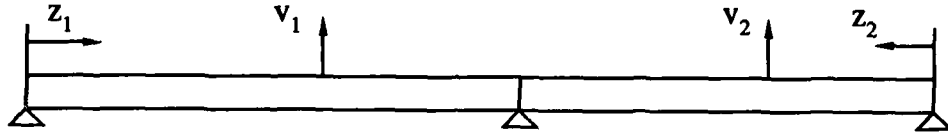
Figure 2: Coupled Composite Beams and Coordinate Systems

coupled however, the above equation gets modified with the coupling moment appearing as a forcing function. We will also include external forces and linear viscous damping. Fig. 2 shows two unidirectional fiber composite beams coupled end to end. The coupling between them could be physically achieved by bolting, welding or other means.

$$(E_{zz}I_x)_1 \frac{\partial^4 v_1}{\partial z_1^4} + c_1 \frac{\partial v_1}{\partial t} + (\rho A)_1 \frac{\partial^2 v_1}{\partial t^2} = f_1(z_1, t) + m_c \delta'(z_1 - l_1)$$

$$(E_{zz}I_x)_2 \frac{\partial^4 v_2}{\partial z_2^4} + c_2 \frac{\partial v_2}{\partial t} + (\rho A)_2 \frac{\partial^2 v_2}{\partial t^2} = f_2(z_2, t) - m_c \delta'(z_2 - l_2) \tag{5}$$

Here, f_1 and f_2 are the transverse forces acting on the two beams, and m_c is the bending moment, whose value at the coupling point is used in the equations by employing δ' which is the derivative of the dirac delta function.

The boundary conditions that need to be satisfied are:

$$v_1(0, t) = 0 \qquad v_2(0, t) = 0$$

$$\left. \frac{\partial^2 v_1}{\partial z_1^2} \right|_{z_1=0} = 0 \qquad \left. \frac{\partial^2 v_2}{\partial z_2^2} \right|_{z_2=0} = 0$$

$$v_1(l_1, t) = 0 \qquad v_2(l_2, t) = 0$$

$$\left. (E_{zz}I_x)_1 \frac{\partial^2 v_1}{\partial z_1^2} \right|_{z_1=l_1} = \left. (E_{zz}I_x)_2 \frac{\partial^2 v_2}{\partial z_2^2} \right|_{z_2=l_2} \qquad \left. \frac{\partial v_1}{\partial z_1} \right|_{z_1=l_1} = \left. \frac{\partial v_2}{\partial z_2} \right|_{z_2=l_2} \tag{6}$$

The last two statements reflect the condition that the bending moment and slope are continuous at the junction of the two beams.

Taking Fourier transforms of the equations of motion with respect to time, we get

$$(E_{zz}I_x)_1 V_1^{iv} + i\omega c_1 V_1 - \omega^2 (\rho A)_1 V_1 = F_1(z_1, \omega) + M_c \delta'(z_1 - l_1) \tag{7}$$

$$(E_{zz}I_x)_2 V_2^{iv} + i\omega c_2 V_2 - \omega^2 (\rho A)_2 V_2 = F_2(z_2, \omega) + M_c \delta'(z_2 - l_2) \tag{8}$$

$$\tag{9}$$

where, the upper case variables represent the Fourier transforms of the corresponding lower case variables.

We seek a solution to the above equations by modal analysis.

$$V_1(z_1, \omega) = \sum_m a_{m,1}(\omega) \phi_{m,1}(z_1) \tag{10}$$

$$V_2(z_2, \omega) = \sum_n a_{n,2}(\cdot) \phi_{n,2}(z_2) \tag{11}$$

where, ϕ are the eigenfunctions of free vibration of each (decoupled) beam simply supported at both ends; i.e.,

$$\omega_{m,1} = \pi^2 m^2 \sqrt{\frac{(E_{zz}I_x)_1}{(\rho A)_1 l_1^4}} \tag{12}$$

$$\phi_{m,1} = \sin \frac{m\pi z_1}{l_1} \tag{13}$$

where, $\omega_{m,1}$ are the natural frequencies of beam#1. Similar expressions can be written for the second beam.

Substituting into the above equations and using orthogonality properties of eigenfunctions, we get

$$A_{m,1}a_{m,1}l_1/2 + \phi'_m(l_1)M_c \;=\; F_{m,1} \tag{14}$$

$$A_{n,2}a_{n,2}l_2/2 - \phi'_n(l_2)M_c \;=\; F_{n,2} \tag{15}$$

where,

$$A_{m,1} \;=\; (\rho A)_1(\omega^2_{m,1} - \omega^2) - i\omega c_1 \tag{16}$$

$$\;=\; \frac{(E_{zz}I_x)_1}{l_1^4}\left(\pi^4 m^4 - k_1^4\right) \tag{17}$$

and,

$$F_{m,1} = \int_0^{l_1} F_1(z_1,\omega)\phi_{m,1}(z_1)\,dz_1 \tag{18}$$

Here, k_1 is the wave number given by

$$k_1 = \left[\frac{(\rho A)_1 l_1^4}{(E_{zz}I_x)_1}\right]^{1/4} \omega^{1/2}(1 + \eta_1^2)^{1/8} e^{\frac{i}{4}(\arctan\eta_1)} \tag{19}$$

where, η_1 is the loss factor for beam#1 which will be assumed to be the same for all the modes.

Since the slope is continuous,

$$\sum_m a_{m,1}\phi'_{m,1}(l_1) = \sum_n a_{n,2}\phi'_{n,2}(l_2) \tag{20}$$

From the above equations we can solve for the unknown moment at the junction as well as the displacement amplitudes, V_1 and V_2.

$$M_c = (N_1 - N_2)/(B_1 - B_2) \tag{21}$$

where,

$$N_1 = \frac{2}{l_1}\sum_m F_{m,1}\psi'_{m,1}(l_1)/A_{m,1} \qquad N_2 = \frac{2}{l_2}\sum_n F_{n,1}\psi'_{n,1}(l_2)/A_{n,2}$$

$$B_1 = \frac{2}{l_1}\sum_m \psi'^2_{m,1}(l_1)/A_{m,1} \qquad B_2 = \frac{2}{l_2}\sum_n \psi'^2_{n,1}(l_2)/A_{n,2} \tag{22}$$

$$V_1(z_1,\omega) \;=\; \frac{N_1 - N_2}{B_1 + B_2}\left[\frac{2l_1^2}{(E_{zz}I_x)_1}\sum_m (-1)^m \sin(\frac{m\pi z_1}{l_1})\frac{m\pi}{m^4\pi^4 - k_1^4}\right]$$

$$V_2(z_2,\omega) \;=\; \frac{N_1 - N_2}{B_1 + B_2}\left[\frac{2l_2^2}{(E_{zz}I_x)_2}\sum_n (-1)^n \sin(\frac{n\pi z_2}{l_2})\frac{n\pi}{n^4\pi^4 - k_2^4}\right] \tag{23}$$

The power flow from beam#1 to beam#2 is computed from the expected value of product of the moment and rate of change of slope at the junction of the beams; i.e.,

$$P_{12}(\omega) = \text{Re E}\left[i\omega M_c \sum_m a_{m,1}\psi_{m,1}(l_1)\right] \tag{24}$$

If we make the assumption that the forces on the two beams are statistically independent from each other, and that they are random in the sense that their modal participations, $F_{n,1}$ and $F_{n,2}$ are independent of each other, the power flow can be computed to be (Davies and Wahab, 1981)

$$P_{12}(\omega) = \frac{4}{\pi}(E_1 - E_2)\frac{\text{Im}(B_1)\text{Im}(B_2)}{|B_1 + B_2|^2} \tag{25}$$

where, E_1 and E_2 are the uncoupled modal energies given by

$$E_1 = \frac{\pi S_{n,1}}{c_1 A_1 l_1/2} \tag{26}$$

E_2 is given by a similar equation. $S_{n,1}$ is the power spectral density of the nth modal generalized force, $F_{n,1}$, which has been assumed to be white noise.

602
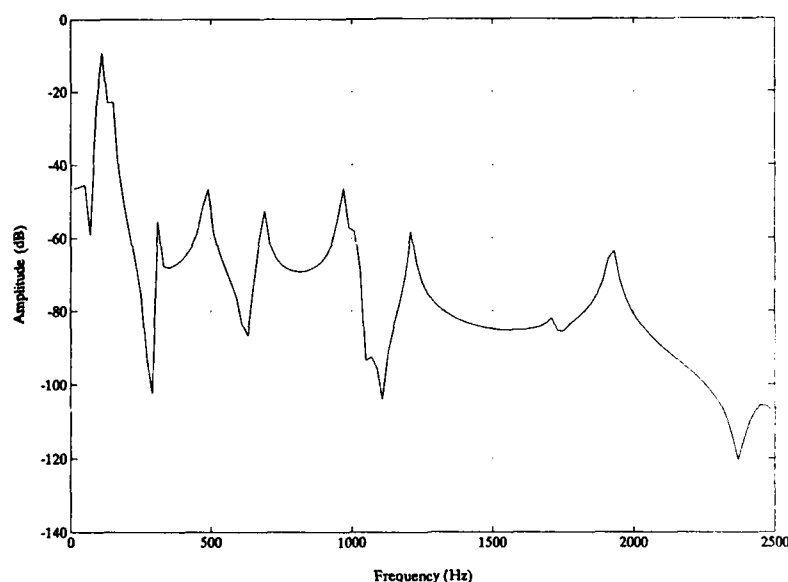
Figure 3: Computed Amplitude of Beam#1 at $z_1 = l_1/2$

3 Numerical Example

The two beams are taken to be made from unidirectional graphite epoxy composite with the fiber angle zero with respect to the longitudinal (z) axis. The material properties that are relevant to the analytical model used in this paper are as follows (Abarcar and Cuniff, 1972): $E_{zz} = 1.29E+11$ Pa, $\rho = 1550$ Kg/m^3. The geometrical dimensions are as follows: $l_1 = 10.2$ cm, $l_2 = 12.7$ cm, width (both beams) = 2.83 cm, thickness (both beams) = .027 cm. The analysis bandwidth is 0-2500 Hz. In this bandwidth, the natural frequencies of beam#1 are (in Hz): 107, 429, 966, 1717 and 2683; for beam#2, they are: 69, 277, 623, 1108, 1730, and 2492.

Beam#1 is subject to a broadband excitation, and the point of application of the force is 6.5 cm from the end remote from the junction. The vibrational amplitudes are computed from analytical expressions in the previous section and representative results are shown in Figs. 3 and 4. Experimentally measured amplitude of beam#2 at the same location is shown in Fig. 5.

It may be observed that the analytical and experimental results do not agree exactly in their peak values primarily owing to the fact that the analysis assumed the same loss factor for all the modes which is unlikely to be the case in practice. However, the peaks do occur at about the same frequencies.

Fig. 6 shows the computed power flow from beam#1 to beam#2 as a function of frequency. Future work will focus on the possible application of Statistical Energy Analysis to this problem for comparison with the ("exact") results.

4 Conclusion

Two coupled unidirectional fiber composite beams are considered. For the simplifying case when pure bending occurs, the vibrational amplitudes of the two beams are obtained. Results from an experimental set-up of two graphite epoxy beams bolted together are compared to those obtained from analysis. In addition, analytically computed power flow variation over the frequency range is presented.

Future work will involve a more general case of nonzero angle of orientation between the fiber axis and the geometric (longitudinal) axis in which case coupling between torsional and flexural vibration can not be ignored.

603
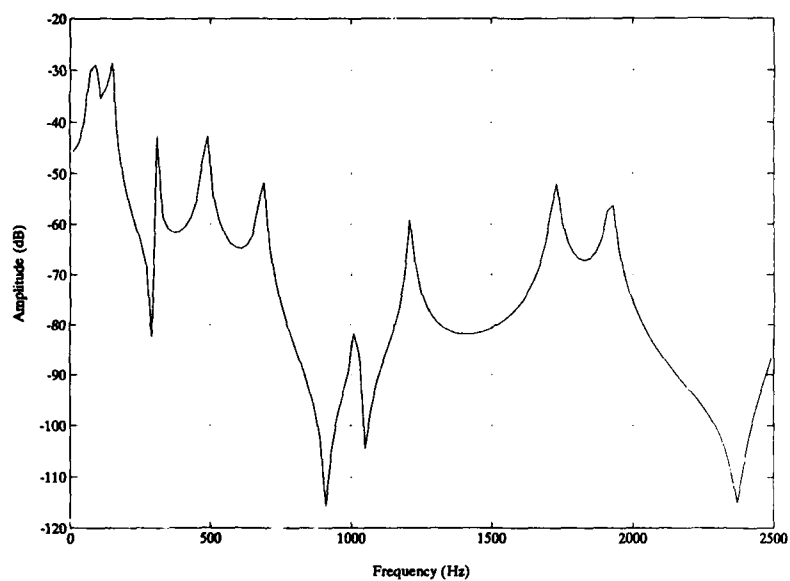
Figure 4: Computed Amplitude of Beam#2 at $z_2 = l_2/4$
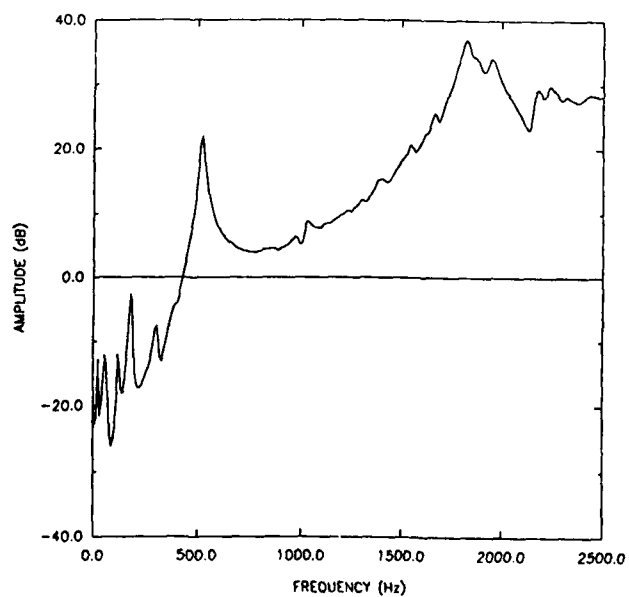
Figure 5: Measured Amplitude of Beam#2 at $z_2 = l_2/4$
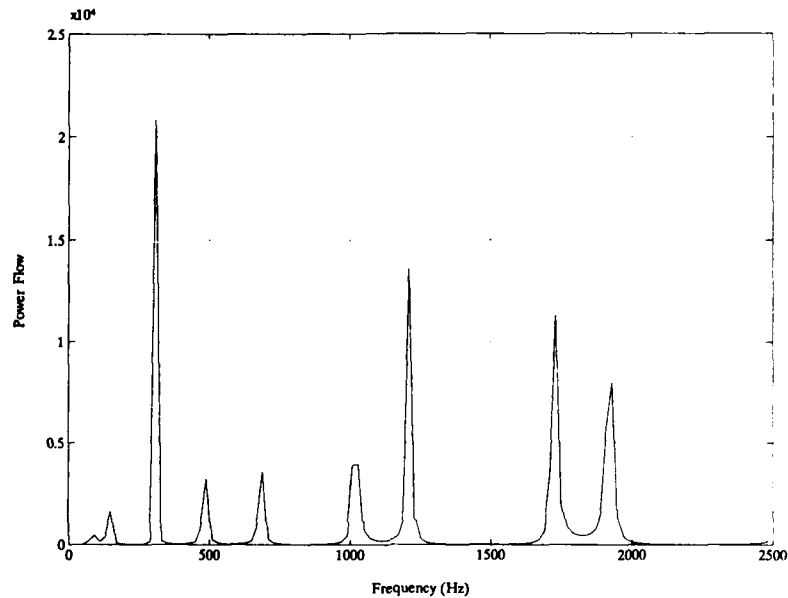
Figure 6: Power Flow from Beam#1 to Beam#2

References

Abarcar, R. B., and Cunniff, P. F., 1972, "The Vibration of Cantilever Beams of Fiber Reinforced Material," *Journal of Composite Materials*, Vol. 6, pp. 504-517.

Davies, H. G., and Wahab, M. A., 1981, "Ensemble Averages of Power Flow in Randomly Excited Coupled Beams," *Journal of Sound and Vibration*, Vol. 77, No. 3, pp. 317-321.

Lyon, R. H., 1975, *Statistical Energy Analysis of Dynamic Systems: Theory and Applications*, MIT Press, Cambridge.

Teh, K. K., and Huang, C. C., 1980, "The Effects of Fiber Orientation on Free Vibrations of Composite Beams," *Journal of Sound and Vibration*, Vol. 69, No. 2, pp. 327-337.

AUTHOR INDEX